Journal of the European Ceramic Society 16 (1996) 503–513

0955-2219(95)00163-8
0955-2219/96/$15.00

Fatigue Crack Growth Rate and Fracture Toughness of 25 wt% Silicon Carbide Whisker Reinforced Alumina Composite with Residual Porosity

A. K. Ray,[a] E. R. Fuller[b] & S. Banerjee[c]

[a]National Metallurgical Laboratory, Jamshedpur–831007, Bihar, India
[b]National Institute of Standards and Technology, Gaithersburg, MD 20899, USA
[c]Research and Development Centre for Iron and Steel, SAIL, Ranchi–834002, Bihar, India

(Received 8 December 1994; revised version received 20 July 1995; accepted 28 August 1995)

Abstract

The main purpose of this study was to determine the fracture toughness and the fatigue crack growth rate behaviour of 25 wt% silicon carbide whisker reinforced alumina ceramic composite. The fracture toughness values determined using the indentation technique depended significantly on the crack length produced at the corners of the indentation which, in turn, depended on the load used for the indentation and anisotropy in orientation of whiskers in the matrix. However, the fracture toughness values determined using the precracked four-point bend specimens were in general higher than that obtained by the indentation technique and the value was 5·96 ± 0·15 MPa $m^{1/2}$. The fatigue crack growth behaviour in this material was similar to that in the case of metals. However, the exponent for the fatigue crack growth rate was 15·5, significantly higher than that usually observed in metals. The likely micromechanism of crack growth under monotonic and cyclic loading in this composite has been identified from fractography of fatigue failed samples.

1 Introduction

Silicon carbide whiskers have been incorporated in such ceramic materials as alumina to improve the general mechanical properties[1–9] and the resistance to catastrophic failure in particular. These ceramic composite materials have potential application in the production of structural components used at elevated temperatures,[10–12] i.e. in high efficiency heat engines and heat recovery systems, and for making cutting tools to machine special materials. When used in such applications, these ceramic components often encounter monotonic and cyclic loading which produces crack extension. Accordingly, in the present investigation, the fatigue crack growth behaviour (FCGR) and the fracture toughness (K_{IC}) of a high density, 25 wt% silicon carbide whisker reinforced alumina composite have been studied.

In general, the determination of FCGR and K_{IC} of such ceramic materials is difficult since the specimens are small, Young's modulus of such materials is rather high and the material is brittle. Consequently, the load, displacement and crack length — which are all required to be measured for the determination of K_{IC} and FCGR — are very small and their precise measurement poses some problems. In addition, the permissible dimensional tolerance of the specimens and those of the grips and fixtures used to test the specimens, have to be very close. Particularly difficult is the precracking of ceramic specimens since these materials have very low toughness. Moreover, the crack initiation in such materials often requires a load which is higher than that required for crack extension. Therefore specimens fail before crack growth is achieved in a controlled manner, because the precision and dimensional tolerance of the fixture used to precrack the specimens are not adequate to avoid spurious loading, that is loading in modes other than in mode I.

2 Material and Specimen Orientation

The ceramic composite material was prepared by mixing α-alumina powder of particle size < 1 μm with 25 wt% β-silicon carbide whiskers. The average whisker diameter was 0·45–0·65 μm and the length ranged from 10 to 80 μm.[8] This mixture was hot-pressed at 1700 to 1850°C under a pressure of 25 MPa for 30 min to produce a preformed billet.

The grain size of the matrix varied between 1 and 4 μm. Details of fabrication, processing and microstructural characterization are reported elsewhere.[8]

The composite material had a porosity of 4·89%, Young's modulus of 340 GPa, fracture strength of 559 MPa and a hardness of 20 GPa, as determined by National Institute of Standards and Technology (NIST), USA, and has been reported in Ref. 8.

Four-point flexure specimens, of dimensions 3 mm × 4 mm × 50 mm, were sliced from the preformed billet and were supplied to us (National Metallurgical Laboratory, NML, India) by NIST. A sketch of the billet showing the longitudinal (L), long transverse (LT) and the short transverse (ST) planes is presented in Fig. 1(a). Opposite sides of the four-point flexure specimens were diamond-ground flat and parallel with a 30 μm diamond wheel, and the prospective tensile surface was polished with 9 μm diamond paste.[8] The specimens were soaked and rinsed in ethyl alcohol to remove the wax needed to mount them for polishing, and then dried in a hot air flow.

The location and orientation of the flexure specimens in the billet is shown in Fig. 1(a). The 3 mm × 50 mm faces of the specimen were parallel to the ST plane. The crack plane introduced later in the specimen was parallel to the LT plane and the crack propagation direction was parallel to the 4 mm dimension of the specimen. Thus the direction of crack propagation was perpendicular to the hot-pressing direction. Accordingly, the crack front was parallel to the hot-pressing direction [see Fig. 1(a)]. On the other hand, in the *R*-curve studies[8] undertaken earlier by one of the authors, while the plane of crack propagation was parallel to the LT plane like in the present investigation, the direction of crack propagation was parallel to the 3 mm dimension.

A montage of the microstructures of the 25 wt% silicon carbide whisker reinforced alumina ceramic composite, as shown in Fig. 1(b), revealed a three-dimensional 3D distribution pattern of the whiskers in the L, the LT and the ST planes of the billet. As can be seen from Fig. 1(b), the distribution of the whiskers in the L plane was non-uniform and heterogeneous. The cross-section of these whiskers measured ~0·45 μm in diameter. During hot-pressing, the whiskers which were not normal to the longitudinal plane became further inclined and therefore some of the whiskers appeared to be randomly oriented in the L plane [Fig. 1(b)]. However, a majority of the whiskers tended to be oriented normal to the hot-pressing direction. Since the material flow along this plane was high, whiskers were aligned normal to this plane. On the other hand, in the ST plane, a few

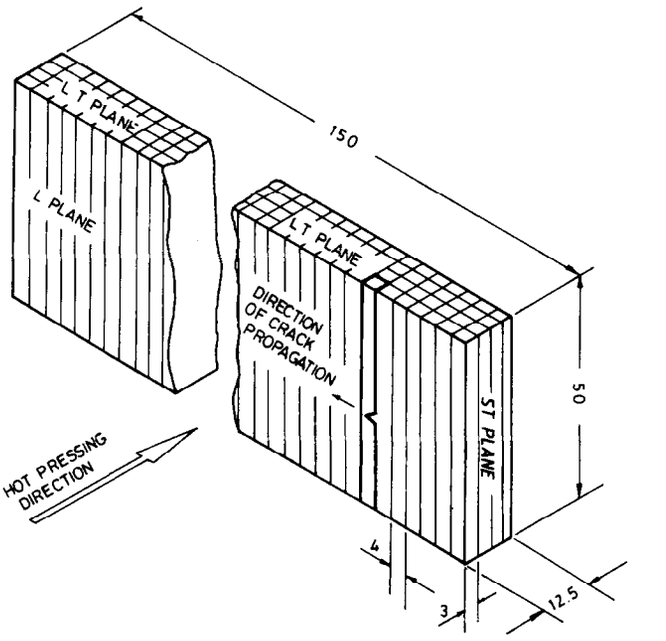

Fig. 1. (a) Billet prepared from the 25 wt% silicon carbide whisker reinforced alumina composite; (b) montage of the microstructures showing the distribution of the SiC whiskers along the three planes.

of the whiskers seemed to be embedded with random orientation; and the others were observed to be embedded normal to this plane. Probably, the friction of the walls, which in the ST planes were very close to each other, prevented easy material flow and the alignment of all the whiskers normal to the ST plane.

According to Becher and Wei,[13] whisker orientation during processing of hot-pressed SiC-whisker reinforced alumina leads to anisotropy in both fracture toughness and fracture strength of

these composites. In other words, their fracture strengths are limited by the non-uniformity of distribution of the whiskers, i.e. by the ability to disperse the SiC whiskers. They also found that dispersion of the whiskers was improved by using finer alumina powder, resulting in an increase in the fracture strength of the composite. Nevertheless, they have clearly observed[13,14] that, similar to our composite under investigation [Fig. 1(b)], the whiskers were preferentially aligned perpendicular to the hot-pressing axis. This type of distribution of whiskers suggests that a great deal of rearrangement of whiskers and powders occurred in the initial stage of densification of the composites and/or the matrix material underwent considerable deformation or creep during hot-pressing.

3 Experimental Procedure

3.1 Precracking of the specimens

The standard bridge technique is normally used for precracking four-point bend specimens. However, it did not produce satisfactory precracking and all the specimens loaded for precracking in this fixture (24 out of the 30 specimens supplied) were lost due to premature crack extension. This is probably related to fixture stiffness more than anything else. An examination of the changing crack path trajectory on the fractured surfaces of these lost specimens showed that, instead of pure mode I loading, the specimens experienced a combined mode loading with mode III loading playing a significant role in the crack extension. The bridge technique was, therefore, modified to avoid mode III loading during precracking. Accordingly, new articulated precracking bridge fixtures were designed and fabricated. These fixtures gave excellent results—achieving 100% success in precracking. The articulated bridge fixtures have been described elsewhere.[15]

A Vicker's indentation was produced at 0·8 kN load at the mid-point of the upper face (3 × 50 mm surface) of the four-point bend specimen, which acted as the crack starter. Before indention, all the specimens were coated with aluminium in a vacuum evaporator by physical vapour deposition technique to ~0·03 μm thickness, to facilitate location of the crack tip in the scanning electron microscope. Precracking was accomplished using the articulated bridge fixture at a force of 4 to 5 kN, load ratio (R) of 0·1 and frequency (f) of 20 Hz. The crack growth was measured at first on the top surface, and later on the two side surfaces, of the four-point bend specimen using the micron marker in a Jeol JSM 840A scanning electron microscope (SEM).

3.2 Crack length measurement

The crack starter indentation at the mid-point of the upper face of the specimen had cracks at all four of its corners (Fig. 2). During precracking, the crack length of the two corner cracks growing across the thickness of the specimen, which is of prime importance for the present investigation, was measured using the micron marker in the SEM at a magnification of 40×. The tip of the crack was located through observation at higher magnification, which often showed evidence of crack branching. The branch extending the furthest was considered to be the crack tip and the crack length was measured accordingly.

At first, the crack length of these two cracks growing on the tensile (3 mm × 50 mm) surface of the specimen from the two opposite corners of the indentation as crack starter, was monitored during precracking. Later, after these two cracks had spanned right across the specimen thickness, the crack lengths were measured on both the side surfaces (4 mm × 50 mm planes) from the respective upper edges. The average of the crack length measured on the side surfaces gave the crack length a.

The crack length a was measured in this manner during the precracking and also during the FCGR determination which preceded the K_{IC} testing. After the crack had advanced with regular increments of number of cycles, the specimen was unloaded from the MTS-880 servohydraulic test machine, and the current crack length was measured using the SEM. Since the determination of FCGR required precise measurement of Δa, the crack length during FCGR studies was measured with special care taken in locating the crack tip.

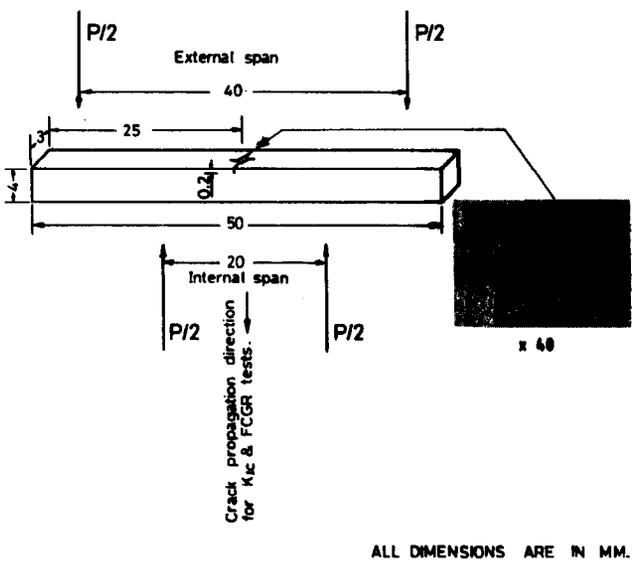

Fig. 2. Indented and precracked specimen for four-point bend loading. Cracks are located at the four corners of the indentation.

3.3 Determination of fatigue crack growth rate (FCGR)

FCGR was determined after the crack had grown significantly on the side surfaces during precracking and achieved length a equivalent to $a/W \approx 0{\cdot}05$ to $0{\cdot}1$. The four-point bend specimen is not recommended in ASTM Standard E647 and, therefore, the K_I values of the specimen were calculated using the standard formula reported elsewhere[16,17] (referred to as the ASTM STP 410 method). Except for this aspect and the use of an indentation as a crack starter, the procedure used here to determine FCGR conformed to the recommendations given in ASTM Standard E647.

The tests were conducted in an MTS-880 servohydraulic test machine using a 1 kN load cell under four-point bend loading, in laboratory atmosphere and at ambient temperature. The loading rate was $0{\cdot}25$ N s^{-1}. The frequency was 1 Hz and $R = 0{\cdot}1$. Typically, the specimens were cycled within the load range between 11 and 111 N, when $a/W \approx 0{\cdot}1$. The crack lengths were measured at regular increments of number of cycles giving ~ $0{\cdot}05$ to $0{\cdot}1$ mm of crack growth. While measuring the crack length, the specimen was first unloaded from the servohydraulic machine and the current crack length was measured with the help of the micron marker in the SEM. Thus the fatigue cracking was interrupted after a predetermined number of load cycles. This was continued until the crack length increased to a value giving $a/W \approx 0{\cdot}45$ to $0{\cdot}5$.

The test data of crack length were plotted in terms of crack length a vs. number of cycles N. The values of da/dN were generated from the a vs. N plot at any given a and plotted against ΔK (stress intensity range). With load and a known, K_I values were calculated from[16,17]

$$K_I = Y\,3P\,(L_1 - L_2)\sqrt{a / 2bW^2} \qquad (1)$$

where

$$Y = 1{\cdot}99 - 2{\cdot}47\,(a/W) + 12{\cdot}97\,(a/W)^2 - 23{\cdot}17\,(a/W)^3 + 24{\cdot}80\,(a/W)^4$$

P = load; L_1 = external span; L_2 = internal span; b = thickness of specimen; W = depth or width of specimen; a = crack length. The values of K_{max} and K_{min} were calculated using eqn (1). The ΔK value is given by $K_{max} - K_{min}$.

3.4 Fracture toughness (K_{IC}) testing

After the FCGR determination was complete and the crack had grown to a level of $a/W \approx 0{\cdot}45$ to $0{\cdot}5$, K_{IC} was determined by subjecting the precracked four-point bend specimens to monotonic loading. The test record of load vs. mid-point displacement of the specimen was obtained during monotonic loading; the ramp rate was $0{\cdot}25$ N s^{-1}. The load value corresponding to the onset of fast fracture was used in eqn (1) to obtain the K_{IC} value. Since four-point bend specimens were used, K_{IC} testing followed here conformed in all respects to the method given elsewhere.[16,17]

In addition to this procedure, the indentation fracture toughness K_C of this material was determined from the indentation technique at various loads ($0{\cdot}63$, $0{\cdot}8$, $1{\cdot}0$ and $1{\cdot}2$ kN) using the following equation proposed by Anstis *et al.*[18]

$$K_C = 0{\cdot}016\sqrt{\frac{E}{H}}\cdot\frac{P}{a^{3/2}} \qquad (2)$$

where E is the Young's modulus, H is the hardness, P is the load and a the crack length. Many emperical expressions to evaluate indentation fracture toughness have been reported in the literature.[19] However, in the case of toughened ceramics where radial cracks are emanating at the four corners of the Vickers indentation,[19] the above model [eqn (2)] has been used by Anstis *et al.*[18] to determine K_C.

3.5 SEM studies

The fracture surfaces of the test specimens were coated with a thin film of gold (thickness $0{\cdot}02$ μm) and then examined using the scanning electron microscope to identify the characteristic fractographic features of the fatigue and fast fracture regions in this material. The identification of these features gives a clue as to the likely mechanisms of fracture for this material.

At first, the SEM examination of the fatigue fracture and fast fracture zones was carried out at a low magnification of 30×. Thereafter, each of these zones was scanned at 4500× and 7500×. The fatigue crack growth at the low ΔK region and the fast fracture region (due to monotonic loading) were carefully examined in order to identify and distinguish between the characteristic fractographic features.

4 Results

4.1 Fracture toughness data

Fracture toughness values determined in this project, using both the indentation technique as well as the ASTM STP 410 method with precracked specimens, are reported in Table 1. Indentation fracture toughness test data determined with a Vickers indentation at various loads of $0{\cdot}63$, $0{\cdot}80$, $1{\cdot}0$ and $1{\cdot}2$ kN yielded K_C values of $5{\cdot}37$, $5{\cdot}45$, $5{\cdot}5$ and $5{\cdot}6$ MPa m$^{1/2}$, respectively. Figure 3 shows the variation of indentation fracture toughness values with the square root of the corresponding crack lengths. It was observed (see Fig. 3) that the

Table 1. Fracture toughness determined by indentation and by using precracked specimen for 25 wt% SiC reinforced Al_2O_3 composite

Fracture toughness (MPa $m^{1/2}$)		
Precracked specimen (ASTM STP 410 method)	*Indentation technique*	*Indentation–strength method* [8]
6·1	5·37	5·35 ± 0·17
5·8	5·45	
6·0	5·5	
	5·6	
Average: 5·96 ± 0·15	5·48 ± 0·08	

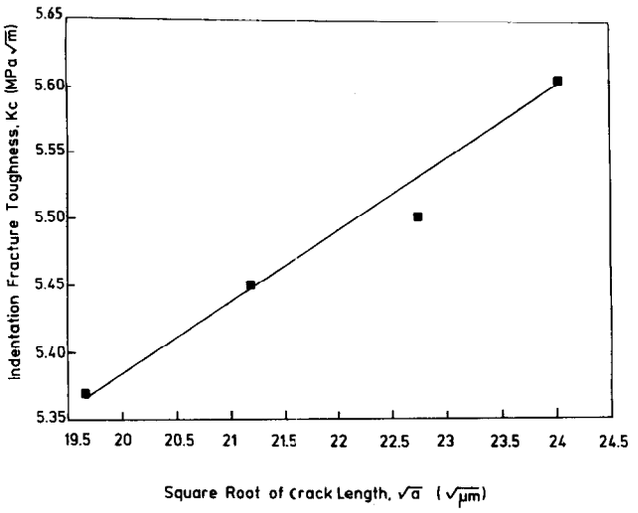

Fig. 3. Dependence of indentation fracture toughness K_C on the square root of crack length $a^{1/2}$.

indentation fracture toughness of this composite when determined using the indentation technique increased as a function of the square root of the crack length.

4.2 FCGR studies

Fatigue crack propagation behaviour of this ceramic material is reported in Fig. 4. The FCGR data of this material were fitted to the usual Paris equation $da/dN = A\ (\Delta K)^n$,[20–22] and the fatigue crack growth rate da/dN (in m/cycle) increased linearly with ΔK (in MPa $m^{1/2}$) in a log–log plot. The plot yields a value of $n = 15{\cdot}5$ and $A = 3{\cdot}4 \times 10^{-15}$ [m/cycle (MPa $m^{1/2})^{-n}$].

4.3 SEM studies

SEM fractographs of the fracture surface at the low ΔK cyclic and at monotonic loading (fast fracture region) are presented in Figs 5 to 11. It is evident that, at low ΔK (0·8 to 1·8 MPa $m^{1/2}$), a majority of the whiskers fail by producing a flat fracture surface which has a vertical level, same as the general fracture surface of the composite (see Fig. 5). On the other hand, in the fast fracture region, the whiskers fail predominantly by pull-

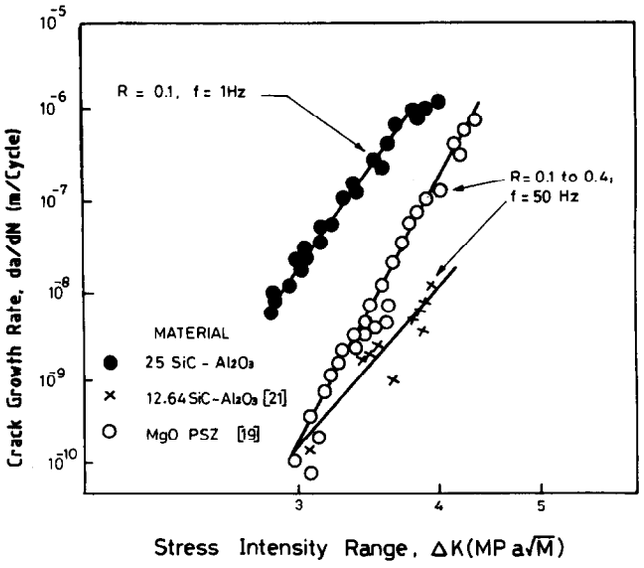

Fig. 4. Fatigue crack propagation rate data.

Fig. 5. At low ΔK (0·8 to 1·8 MPa $m^{1/2}$) region, a majority of the whiskers failed with a square fracture without evidence of large–scale pull-out.

Fig. 6. In the fast fracture region (K_{IC} = 5·9 MPa $m^{1/2}$), due to monotonic loading, whiskers failed predominantly by pull-out mechanism.

out wherein the whiskers stick out of the general fracture surface of the composite (see Fig. 6).

The matrix material failed predominantly by transgranular fracture (see Fig. 7) at low ΔK fatigue (0·8 to 1·8 MPa $m^{1/2}$). During monotonic

Fig. 7. At low ΔK (0·8 to 1·8 MPa $m^{1/2}$) region, the alumina matrix failed predominantly through transgranular fracture.

Fig. 8. In the fast fracture region (K_{IC} = 5·9 MPa $m^{1/2}$), due to monotonic loading, the alumina grains failed in a mixed mode, i.e. intergranular (~55%) and transgranular (~45%).

Fig. 9. Crack branching in the low ΔK (0·8 to 1·8 MPa $m^{1/2}$) region.

loading, the alumina grains failed in a mixed mode with about 55% by intergranular mode and the balance by transgranular mode, as shown in Fig. 8.

It is noteworthy that in the low ΔK region the crack frequently branches and deflects while it propagates (Figs 9 and 10). Correspondingly, river pattern markings with steps are also present in the cleavage facets (Fig. 11). However, in the fast

Fig. 10. Crack deflection in the low ΔK (0·8 to 1·8 MPa $m^{1/2}$) region.

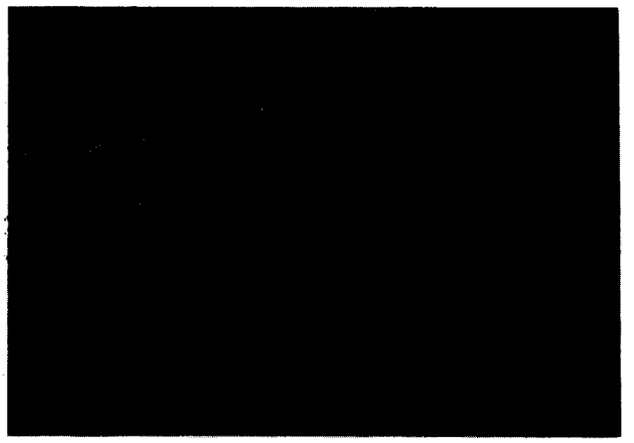

Fig. 11. River pattern marking with steps in the low ΔK (0·8 to 1·8 MPa $m^{1/2}$) region (YZ — modulation SEM image).

fracture regions, branching and deflection of the crack are virtually absent.

The distinction between the fractographic features in the low ΔK fatigue region and the fast fracture region is very evident. This is discussed further below.

5 Discussion

5.1 Indentation fracture toughness data

In the indentation fracture toughness test, the direct crack measurement technique had been adopted[18] for obtaining a rapid assessment of the indentation fracture toughness, K_C. It can be seen from Fig. 3 that the K_C values obtained by this technique increase with increase in the square root of the corresponding crack lengths. In this context, the presence of residual stresses plays an important role. A residual compressive surface stress would decrease the apparent surface crack length, while a residual tensile surface stress would do the reverse. There are various ways in which surface stresses could be introduced into a material; of

particular relevance to the production of samples for indentation testing is the process of surface grinding brittle materials, e.g. using SiC or diamond abrasive wheels on glass, ceramics and cermets.[23] It is well documented that this surface-finishing method induces residual stresses in materials such as alumina,[23] pyroceram C9606 glass-ceramic[24] and zirconia-toughened alumina.[25]

Several investigators have shown that if the slope of the K_C (indentation fracture toughness) vs. $a^{1/2}$ (square root of crack length) plot is positive, it indicates that the nature of residual surface stress present is compressive; if the slope is negative, then tensile residual surface stresses are present.[26,27] Marshall and Lawn[26] showed that such plots for tempered soda-lime glass plate produced a positive slope indicating that the nature of residual stress is compressive. In line with the Marshall and Lawn model,[26] Ikuma and Virkar[27] thus concluded that a positive linear dependence of K_C on $a^{1/2}$ for transformation-toughenable ceramics indicates the presence of residual surface compressive stresses induced by the tetragonal-to-monoclinic transformation of ZrO_2 or HfO_2 particles in the near-surface layers upon surface grinding. Based on the same theory, since the ceramic composite under investigation here shows a positive linear dependence of K_C on $a^{1/2}$, it simply indicates that the residual surface stresses present in the composite are compressive in nature.

Ponton and Rawlings[19] concluded that in indentation fracture toughness tests although the crack length a increases with increasing indenter load P as expected, plots of K_C vs. $a^{1/2}$ do not necessarily produce a zero slope for the stress-free state, a negative slope for the residual tensile stress state and a positive slope for the residual compressive stress state, as predicted by the Marshall and Lawn model.[26] According to them,[19] the sign of the slope depends both on the material and the Vickers indentation fracture toughness expression used to calculate K_C. Rather, it was suggested[19] that a strong dependence of K_C on $a^{1/2}$ is indicative of a residual surface stress. However, the sign of the slope cannot be used to distinguish between a residual compressive and a residual tensile surface stress without K_C vs. $a^{1/2}$ data for both the definite stress-free condition and the residual compressive or tensile stress condition in a given material type.[19]

Krause *et al.*[8] have reported a fracture resistance value of 5·35 ± 0·17 MPa $m^{1/2}$, measured by the indentation–strength method, in an earlier investigation on the same composite. In the indentation–strength method, strength tests were conducted in four-point bend loading with the Vickers indentation at the centre of the prospective tensile surface. The size of the radial cracks emanating from the Vickers indentation was controlled by varying the indentation load. For the same composite, these authors[8] used a parametric representation of the fracture resistance as a fractional power function in crack extension of the form:

$$K_R = K_O (\Delta C / C_O)^m \tag{3}$$

where K_R is a parameter describing the fracture resistance for an R-curve type material, m measures the relative steepness of the R-curve, K_O is the fracture resistance that corresponds to the smallest indentation crack radius, C_O is the smallest indentation crack that causes failure in flexural testing, ΔC is the crack extension (= $C - C_P$). The total crack length is C and C_P is the traction-free portion, such as exists in a pre-notched specimen. K_O and m are defined by:[8]

$$K_O = \beta^{-\beta}(1 + \beta)^{(1+\beta)} Y S_O C_O^{1/2} \tag{4}$$

$$m = (1 - 3\beta)(2 + 2\beta) \tag{5}$$

where the constant $\beta = 0{\cdot}266$, Y is the configuration coefficient and is equal to 1·174. S_O is the natural strength of the composite corresponding to the minimum indentation load P_O and is equal to 559 MPa. This is the maximum strength that could be measured for specimens with indentation cracks before failures from natural flaws dominate the strength distribution.

For their analysis,[8] indentation flaws were assumed to have traction from the outset, so $C_P = 0$. When $m = 0$, K_R is invariant with ΔC and $K_R = K_O = K_C$. The values of m, C_O and K_O for the same composite[8] were 0·08, 18·1 μm and 5·35 MPa $m^{1/2}$, respectively. Using the above expression, Fuller *et al.*[8] observed that the fracture resistance of the material K_R increases with crack extension, the so called rising R-curve phenomenon. This behaviour was explained in terms of the whiskers acting as elastic restraints to the point of rupture at small crack wall separations.

In the present study, the average value of indentation fracture toughness (Table 1) was reasonably in agreement with the fracture resistance value obtained by NIST.[8] Probably due to the non-uniform distribution of the SiC whiskers in the matrix of alumina [Fig. 1(b)], the value of K_C at a load of 1·2 kN was slightly high (Table 1 and Fig. 3). The average fracture toughness K_{IC} evaluated by using the precracked specimen was 5·96 ± 0·15 MPa $m^{1/2}$. The large difference in toughness obtained by the two methods could primarily be accounted for the difference in crack tip loading rates.

For many brittle materials, the indentation fracture toughness values were reported to be similar

to those obtained by large crack methods such as using a double cantilever beam[28] or compact tension[20,22] specimen. On the other hand, it was often contended that indentation toughness is a close approximation of the fracture from small, naturally occurring flaws.[8,28–32] However, one should make sure that the residual stress field, induced by the plastic zone[28] produced by the indentation, is small enough compared with the crack length that the indentation plastic zone has a minimum effect on the extension of cracks.

Previous investigators[8,30,33] have also reported that the considerable local branching at the corners of the indentation and small amount of deflection give rise to the appearance of local curvature in the crack path. The branching of cracks produced at the corners of the indentation was also observed in a previous study[34] and could partly account for the rising trend in the K_R (fracture resistance) values. This branching behaviour and the crack deflection observed (Figs 9 and 10) can also be explained in terms of a grain-bridging phenomenon associated with microstructural toughening. Possibly, on the scale of grain sizes, the grains of alumina were entangled with the silicon carbide whiskers in such a way that, because of the presence of a complex residual stress field, high resistance to crack propagation was created and hence the crack tended to find a new starting point at the weakest area away from this region.[29]

5.2 Fracture toughness of precracked specimens

The K_{IC} values determined using precracked four-point bend specimens could not readily be compared with those reported on this material by NIST,[8] due to the difference in the techniques used for determination of toughness. The scatter in the K_{IC} values obtained from the precracked specimens, shown in Table 1, could be due to the non-uniform distribution of the silicon carbide whiskers, apart from the system error inherent in the K_{IC} determination.

The plane of crack propagation in specimens tested was parallel to the LT plane. Since most of the whiskers were perpendicular to the crack plane, they would tend to bridge the crack plane more effectively and enhance the toughness. Therefore, the fracture toughness for the crack planes parallel to the hot-pressing direction (the L and ST planes) should be substantially higher than that for crack planes which are perpendicular to the hot-pressing direction. Hansson *et al.*[35] clearly showed that for 33 vol% SiC whisker reinforced alumina composite, the fracture toughness for crack planes parallel to the hot-pressing direction is substantially higher than that for perpendicular crack planes.

A Vickers hardness indentation introduced at a load of 0·8 kN was used as a crack starter. As a result, significant residual stresses could be induced in the specimen. If these residual stresses just ahead of the advancing crack front (i.e. within the plastic zone) were compressive in nature, they could decrease the observed fatigue crack growth rate and increase the observed K_{IC} of the material. However, if they were tensile in nature, the effect would be opposite. Some more fracture toughness tests, including those where a slot or notch is used as a crack starter, should be carried out to confirm and check the K_{IC} data reported in Table 1.

In a recent paper,[22] the K_{IC} value of 15 vol% (or 12·64% by weight) silicon carbide reinforced alumina ceramic composite using compact tension specimens was reported to be 4·5 MPa $m^{1/2}$. This toughness value is somewhat lower than the K_{IC} value determined by us. This difference could be attributed to a difference in the porosity of the materials, or in the amount or size of the silicon carbide whiskers used, or in the orientation of the crack plane or the specimen geometry. Also, as the whisker volume contents are different, the strength of the whiskers and the matrix–whisker interfacial bonding would obviously vary between the two test cases.

5.3 Fatigue crack growth rates

The results of the present study (Fig. 4) showed that 25 wt% silicon carbide whisker reinforced alumina ceramic composites were susceptible to the fatigue crack growth phenomenon, in a manner similar to metallic materials. FCGR data on 25 wt% silicon carbide reinforced alumina composite have not been reported earlier. However, recently, FCGR data of 15 vol% (which is equivalent to 12·64 wt%) silicon carbide alumina ceramic composite were given.[22] The crack growth rate in the material studied by us was about 100 times faster, at a given ΔK, than that in the other material, mainly due to larger porosity content in the former compared with the latter which is almost devoid of obvious processing flaws like porosity.[36] The difference could also be attributable to other factors, such as the strength of the whiskers and the matrix–whisker interfacial bonding.

Our material was observed to have much less resistance to fatigue than Ce-TZP–alumina composite[21] and MgO–PSZ composite.[20] As explained earlier,[20,21] the presence of the transformation zone ahead of the crack tip in these materials could result in the absorption of significant energy, and this could retard the observed fatigue crack growth rate.

Plots of da/dN vs. ΔK for the 12·64 wt% silicon carbide alumina composite and for the MgO–PSZ

composite exhibited a single linear stage with the exponent values of 15 and 28, respectively. Our material also exhibited a single linear stage (Fig. 4) without the presence of a detectable threshold. The value of the exponent was 15·5 in our material.

As already discussed, the Vickers hardness indentation when used as a crack starter could generate residual stresses which in turn could influence the FCGR. The FCGR test data on specimens where the crack starter is a slotted notch instead of an indentation, if generated, would confirm if the use of indentation as a crack starter indeed influences the FCGR or not. Such studies have been reported elsewhere.[15]

5.4 Mechanism of fracture

Since the mechanism of fracture of the whiskers and the α-alumina grains are entirely different in the low ΔK fatigue and the fast fracture regions, the scheme of crack growth in each region is discussed separately below to highlight these differences.[34]

During fatigue loading at low ΔK values, that is when $K_{max} < 2$ MPa $m^{1/2}$, the α-alumina grains of the matrix failed mainly by transgranular cleavage with frequent crack branching and crack deflection. Also, the cleavage facets revealed river patterns and steps. At the low values of ΔK, the K_{max} values are low. Consequently, the traction force ahead of the crack tip is not large enough to promote intergranular fracture.

At the same time, the whiskers could fail by three different modes: (i) pull out, (ii) tensile fracture and (iii) fatigue. Since only a few of the whiskers failed due to pull-out at low ΔK (see Fig. 5), this naturally indicates that the maximum traction forces generated ahead of the crack tip during the low ΔK fatigue was not adequate to produce pull-out. Thus it is likely that the whiskers continue to bridge the crack even after some of the surrounding alumina grains have failed by transgranular cleavage. Therefore, under these circumstances, the whiskers could fail due to tensile fracture or fatigue. Now, since the strength of the β-SiC whisker is about 6·5 to 7 times higher than that of α-alumina,[37,38] the tensile fracture of the whisker is unlikely if the traction forces ahead of the crack tip were to be distributed in proportion to the relative cross-sections of the β-SiC whiskers and α-alumina in the plane of the crack. Even if the whiskers were to carry the major part of the traction forces ahead of the crack tip, the high traction forces would produce failure by pull-out rather than by tensile fracture, as was observed in the fast fracture region (see Fig. 6) where K_{IC} values and consequently the traction forces were high. Since the possibility of large-scale pull-out or tensile fracture is thus discounted, whiskers are most likely to fail by fatigue. At low ΔK, the whiskers which had bridged the crack after the surrounding alumina grains had failed by cleavage, would continue to experience fatigue loading, then fail with a square fracture which is typical of fatigue.

During fast fracture under monotonic loading such as during the fracture toughness testing, 55% of the α-Al_2O_3 grains of the matrix failed by intergranular fracture. The value of K_I during such monotonic loading is 5·9 MPa $m^{1/2}$. At such values of K_I, the traction force ahead of the crack tip is adequate to produce intergranular failure of those grains which are favourably oriented with respect to it. The matrix failure was predominantly intergranular. Nevertheless, the whiskers were located mainly at the grain boundaries. Therefore the probability of the advancing crack front interacting with the whiskers is extremely high. The whiskers tending to bridge the advancing crack quite frequently would therefore become debonded and pull out. This hypothesis is confirmed by the fact that, during monotonic fracture, failure of the whiskers by the pull-out mechanism was frequently observed in the fractographs.

After some of the grains have failed by the intergranular mode, the other neighbouring grains—which are less favourably oriented or are bridged by the whiskers across the grain boundaries—fail by cleavage. The schematic of crack propagation during monotonic and cyclic loading is given elsewhere.[34]

To prevent fracture of this ceramic composite under monotonic loading, its microstructural features would have to be strengthened to avoid intergranular fracture of α-alumina and the pull-out of whiskers. This requires that the grain boundary strength of α-alumina and the whisker–matrix interfacial strength should be increased. Similarly, to retard crack extension during low ΔK fatigue, intergranular cleavage fracture of α-alumina grains and fatigue failure resistance of the silicon carbide whiskers should be improved, possibly by using finer α-alumina powder[13,14] and by improving the uniformity of distribution of the whiskers in the matrix during hot-pressing.[13,14]

6 Conclusions

The results of the foregoing study lead to the following conclusions.

(1) Indentation fracture toughness increased with increase in the square root of crack length. However, the K_{IC} values obtained

from the precracked four-point bend specimens were higher and had a value given by $K_{IC} = 5{\cdot}96 \pm 0{\cdot}15$ MPa $m^{1/2}$.

(2) The 25 wt% silicon carbide whisker reinforced alumina ceramic composite is susceptible to a fatigue crack growth phenomenon which is similar to that observed in the case of metallic materials. But the crack growth exponent is higher ($n = 15{\cdot}5$).

(3) At low ΔK fatigue (0·8 to 1·8 MPa $m^{1/2}$), the whiskers failed by fatigue, whereas during monotonic fracture, they failed by pull-out.

(4) The matrix at low ΔK fatigue was predominantly transgranular with frequent crack branching and deflection, in contrast to a mixed mode type (45% transgranular and 55% intergranular) failure during the monotonic fracture.

References

1. Becher, P. F., Hsueh, C. H., Angelini, P. & Tiegs, T. N., Toughening behaviour in whisker-reinforced ceramic matrix composites. *J. Am. Ceram. Soc.*, **71**(12) (1988) 1050–61.
2. Becher, P. F., Microstructural design of toughened ceramics. *J. Am. Ceram. Soc.*, **72**(2) (1991) 255–69.
3. Becher, P. F. & Tiegs, T. N., Toughening behaviour involving multiple mechanisms: whisker reinforcement and zirconia toughening. *J. Am. Ceram. Soc.*, **70**(9) (1987) 651–4.
4. Angelini, P., Mader, W. & Becher, P. F., Strain and fracture in whisker reinforced ceramics. In *MRS Proceedings Vol. 78, Advanced Structural Ceramics*, ed. P. F. Becher, M. V. Swain and S. Somuja. Materials Research Society, Pittsburgh, PA, 1987, pp. 241–57.
5. Ruhle, M., Dalgeish, B. J. & Evans, A. G., On the toughening of ceramics by whiskers. *Scr. Metall.*, **21** (1987) 681–6.
6. Warren, R. & Sarin, V. K., Fracture of whisker reinforced ceramics. In *Application of Fracture Mechanics to Composite Materials*, ed. K. Friedrich. Elsevier, Amsterdam, in press.
7. Krause Jr, R. F. & Fuller Jr, E. R., Fracture toughness behaviour of a silicon carbide whisker reinforced alumina with selected properties. In *Proc. the Fossil Energy Materials Conference, Report No. ORNL/FMP/87/G*, Martin Marietta Energy Systems, Inc., Oak Ridge National Laboratory, TN, USA, August 1987, pp. 38–55.
8. Krause Jr, R. F., Fuller Jr, E. R. & Rhodes, J. F., Fracture resistance behaviour of silicon carbide whisker-reinforced alumina composites with different porosities. *J. Am. Ceram. Soc.*, **73**(3) (1990) 559–66.
9. Campbell, G. H., Ruhle, M., Dalgleish B. J. & Evans, A. G., Whisker toughening: a comparision between Al_2O_3 and Si_3N_4 toughened with silicon carbide. *J. Am. Ceram. Soc.*, **73**(3) (1990) 521–30.
10. Solomah, A. C. & Reichert, W., Mechanical properties, thermal shock resistance and thermal stability of zirconia-toughened alumina–10 vol% silicon carbide whisker ceramic matrix composite. *J. Am. Ceram. Soc.*, **73**(3) (1990) 740–3.
11. Porter J. R. & Chokshi, A. H., Creep performance of SiC-whisker reinforced alumina. In *Ceramic Microstructure '86*, ed. J. A. Pask and A. G. Evans. Plenum Press, New York, 1986, pp. 919–28.
12. Tiegs, T. N. & Becher, P. T., Thermal shock behaviour of an alumina SiC whisker composite. *J. Am. Ceram. Soc.*, **70**(5) (1987) C-109–11.
13. Becher, P. F. & Wei, G. C., Toughening behaviour in SiC-whisker-reinforced alumina. *J. Am. Ceram. Soc.*, **67**(12) (1984) 267–9.
14. Wei, G. C. & Becher, P. F., Development of SiC whisker-reinforced ceramics. *J. Am. Ceram. Soc. Bull.*, **64**(2) (1985) 298–304.
15. Ray, A. K. & Banerjee, S., An articulated bridge fixture for precracking ceramic specimens in fatigue crack growth rate studies of 25 wt% SiC reinforced Al_2O_3 composite. *J. Am. Ceram. Soc.*, accepted.
16. Brown Jr, W. F. & Srawley, J. E., in *ASTM STP 410*. American Society for Testing and Materials, Philadelphia, PA, 1966.
17. Yamade, Y. & Kishi, T., Acoustic emission study for fracture origin of sintered mullite in 4-point bending test. *The Sumitomo Search*, **45**(3) (1991) 17–24.
18. Anstis, G. R., Chantikul, P., Lawn, B. R. & Marshall, D. B., A critical evaluation of indentation techniques for measuring fracture toughness: I, direct crack measurement. *J. Am. Ceram. Soc.*, **64** (1981) 533–8.
19. Ponton, C. B. & Rawlings, R. D., Dependence of the Vickers indentation, fracture toughness on the surface crack length. *Br. Ceram. Trans. J.*, **88** (1989) 83–90.
20. Dauskardt, R. H., Marshall, D. B. & Ritchie, R. O., Cyclic fatigue-crack propagation in magnesia–partially stabilized zirconia ceramics. *J. Am. Ceram. Soc.*, **73**(4) (1990) 893–903.
21. Tsai, J. F., Yu, C. S. & Shetty, D. K., Fatigue crack propagation in ceria-partially stabilized zirconia (Ce-TZP)–alumina composites. *J. Am. Ceram. Soc.*, **73**(10) (1990) 2992–3001.
22. Dauskardt, R. H., James, M. R., Porter, J. R. & Ritchie, R. O., Cyclic fatigue crack growth in a SiC whisker-reinforced alumina ceramic composite: long and small crack behaviour. *J. Am. Ceram. Soc.*, **75**(4) (1992) 759–71.
23. Lange, F. F., James, M. R. & Green, D. J., Determination of residual stresses caused by grinding in polycrystalline Al_2O_3. *J. Am. Ceram. Soc.*, **66** (1983) C-16–7.
24. Cook, R. F., Lawn, B. R., Dabbs, T. P. & Chantikul, P., Effect of machining damage on the strength of a glass ceramic. *J. Am. Ceram. Soc.*, **64** (1981) C-121–2.
25. Green, D. J., Lange, F. F. & James, M. R., Factors influencing residual surface stresses due to a stress-induced phase transformation. *J. Am. Ceram. Soc.*, **66** (1983) 623–9.
26. Marshall, D. B. & Lawn, B. R., An indentation technique for measuring stresses in tempered glass – surfaces. *J. Am. Ceram. Soc.*, **60** (1977) 86–7.
27. Ikuma, Y. & Virkar, A. V., Crack-size dependence of fracture toughness in transformation – toughened ceramics. *J. Mater. Sci.*, **19** (1984) 2223–8.
28. Bhattacharya, A. K. & Petrovic, J. J., Hardness and fracture toughness of SiC-particle-reinforced $MoSi_2$ composite. *J. Am. Ceram. Soc.*, **74**(10) (1991)) 2700–3.
29. Swanson, P. L., Fairbanks, C. J., Lawn, B. R. Mai, Y. W. & Hockey, B. J., Crack-interface grain bridging as a fracture resistance mechanism in ceramics: I, experimental study in alumina. *J. Am. Ceram. Soc.*, **70**(4) (1987) 279.
30. Ramchandran, N. & Shetty, D. K., Rising crack growth resistance (*R*-curve) behaviour of toughened alumina and silicon nitride. *J. Am. Ceram. Soc.*, **74**(10) (1991) 2634–41.
31. Anderson, R. M. & Braun, L. M., Technique for the *R*-curve determination of Y-TZP using indentation–produced flaws. *J. Am. Ceram. Soc.*, **73**(10) (1990) 3059–62.
32. Swain, M. V., *R*-curve behaviour and thermal shock resistance of ceramics. *J. Am. Ceram. Soc.*, **73**(3) (1990) 621–8.
33. Pezzotti, G., Tanaka, I. & Okamoto, T., Si_3N_4/SiC-whisker composites without sintering aids: 11, fracture behaviour. *J. Am. Ceram. Soc.*, **73**(10) (1990) 3039–45.
34. Ray, A. K., Das, S. K. & Banerjee, S., Fractography of the fatigued and fractured regions in a silicon carbide whisker reinforced alumina composite. *J. Eur. Ceram. Soc.*, **15** (1995) 191–9.
35. Hansson, T., Warren, R. & Wasen, J., Fracture tough-

ness mechanisms of a hot-pressed alumina reinforced with silicon carbide whiskers. *J. Am Ceram. Soc.*, **76**(4) (1993) 841–8.
36. Porter, J. R., Lange, F. F. & Chokshi, A. H., Processing and creep performance of SiC-whisker-reinforced Al_2O_3. *J. Am. Ceram. Soc. Bull.*, **66**(2) (1987) 343–7.
37. Fisher, E. S., Manghanani, M. H. & Routbort, J. L., Study of the elastic properties of Al_2O_3 and Si_3N_4 material composites with SiC whisker reinforcement. In *High Performance Composites for the 1990's*, ed. S. K. Das, C. P. Ballard and F. Marikar. The Minerals, Metals and Materials Society, 1991, p. 365.
38. Anon., Reinforcing tomorrows technology. *Ceram. Indust.*, April 1992.

Journal of the European Ceramic Society **16** (1996) 515–519

0955-2219(95)00128-X
0955-2219/96/$15.00

Cavitation Induced by High-Temperature Plastic Deformation in Aluminium Nitride Ceramics

S. Choux,[a] I. Masson,[a,b] J. P. Feiereisen,[a] A. George[a] & J. P. Michel[a]

[a]Laboratoire Métallurgie Physique & Science des Matériaux (URA CNRS 155) and [b]Laboratoire Science et Génie des Matériaux Métalliques (URA CNRS 159), Ecole des Mines, Parc de Saurupt, 54042 Nancy Cedex, France

(Received 22 July 1994; revised version received 22 June 1995; accepted 14 July 1995)

Abstract

Intergranular cavitation has been investigated in samples deformed plastically up to a few per cent in four-point bending and uniaxial compression above 1500°C. Even for strains of 0·5%, cavities with a size of several tenths of a micrometre were observed, generally nucleated at small sintering additive particles. Cavities are preferentially formed in grain boundaries perpendicular to the stress axis in areas deformed in tension but are rather isotropically distributed in samples deformed in compression. The volume fraction of cavities was found to be near the total strain.

1 Introduction

Aluminium nitride is a stoichiometric compound of formula AlN. This ionocovalent material has an ionicity factor of 0·45 and a wurzite hexagonal crystalline structure (2 H with a = 0·311 nm and c = 0·498 nm). At room temperature AlN combines a high electrical resistivity (1×10^{13} Ω cm due to a band gap of 6·3 eV), an excellent thermal conductivity as high as 200 W m^{-1} K^{-1} and a low thermal expansion coefficient, ~2·7 $\times$ 10^{-6} K^{-1}, close to that of silicon. These properties and its non-toxicity make AlN a good candidate material for substrates of electronic devices. Also AlN exhibits a good thermal stability, does not react with molten metals and shows high mechanical strength up to 1500°C. It can therefore be used for some parts in a continuous casting process. This has prompted the present work on high-temperature plastic deformation of AlN ceramics. When undergoing creep at high-temperature, polycrystalline materials often fail as a result of the growth and coalescence of voids located at grain boundaries (GBs) to form cavities. We report here on cavitation in AlN.

2 Experimental Procedures

AlN powders are sintered with additives. The materials studied were provided by ESK (Germany) in two grades: conventionally sintered (hereafter called S-AlN) or hot-pressed (HP-AlN). In both cases, the additive was La_2O_3 (5 wt%). Equiaxial grains are observed with average sizes of 7 μm (S) and 4 μm (HP). The additive is found within the GBs and especially at triple grain junctions as particles of a few tenths of a micrometre. The as-received materials have no porosity.

Samples were deformed up to a few per cent plastic strain either by uniaxial compression, in creep under constant nominal stress of 150, 200 and 250 MPa or at a fixed strain rate, $\dot{\epsilon} \cong 5 \times 10^{-6}$ s^{-1}, or by four-point bending (FPB) under constant load. In the last case, the maximum stress on the outer fibres was equal to 58, 80 and 109 MPa.

Tests were performed under Ar + He atmosphere, at temperatures ranging from 1773 to 1923 K. Samples were cooled with the final stress applied in order to freeze-in microstructures and defects. Thin foils were then cut, thinned by ion-milling and observed in a Jeol 200 CX electron microscope operating at 200 kV. Further details can be found in Ref. 1.

3 Results

3.1 Influence of thermal treatment without applied stress

To separate the possible effects of heat treatment from those due to plastic deformation, observations were made on a sample heated for 5 h at the highest investigated temperature, 1923 K, without any applied stress. Neither cavities nor any significant changes of the overall microstructure could be observed.

3.2 Cavitation after four-point bending

Observations were restricted to HP-AlN, deformed at 1873 K. FPB leads in the same sample to areas submitted to tensile stresses while others are in compression. To a good approximation, the stress (tension or compression) in a thin slice parallel to the top and bottom surfaces is practically uniaxial. Thin foils were cut parallel to these surfaces at ~100 μm beneath them. Determining the local plastic strain and stress is not straightforward. Estimates were derived from the crosshead deflection of the testing machine using the formula of Hollenberg *et al.*[2] with a stress exponent of 1·4.[1]

3.2.1 Areas deformed in tension

Plastic strains were approximately equal to 0·5% at σ = 58 MPa, 0·8% at 80 MPa and 2·2% at 109 MPa; these deformations being obtained, respectively, after 85, 110 and 285 min. Two kinds of cavities were observed (Fig. 1). Firstly, at GBs, cavities have lenticular shapes with a thickness, normal to the GB plane, roughly half the diameter in the GB plane. At a given stage of deformation, all cavities have fairly equal sizes (Table 1). And, secondly, at triple junctions, cavities are slightly larger and show concave or convex triangular cross-sections. These two classes can be labelled R and W, respectively, as proposed in Ref. 3. No cavity was ever found inside the grains.

The fraction of GBs and triple junctions where cavitation was present was estimated. Each value given in Table 1 results from counting over 100–300 GBs. The size and number of cavities increase with strain and/or stress. At ϵ = 0·8%, σ = 80 MPa, all grains have at least one cavity at their periphery and evidence of coalescence is observed. The spatial distribution of cavities is clearly anisotropic (Fig. 1) and their density is larger at GBs which are nearly perpendicular to the tensile stress axis. For each GB, the β-angle between the stress axis and the GB plane was determined in two steps:

(i) The α-angle between the stress axis and the trace of the GB in the plane of the foil was measured; α varies between a minimum value α_i and 90°.

(ii) The spectrum of α-values was then converted into β-values assuming that GBs have random orientations and that (as was easily checked) α_i is the minimum β-value. Histograms were thus obtained. For ϵ = 0·5 %, σ = 50 MPa, β varies from 45 to 90° with a maximum at 80°. For ϵ = 0·8%, σ = 80 MPa, as shown on Fig. 2, a marked anisotropy is also observed, with the same maximum and a broader spectrum. For ϵ = 2·2 %, σ = 109 MPa, the distribution is quite similar, with a maximum between 80 and 90°.

Table 1. Cavitation after four-point bending

σ (MPa)	ϵ (%)		*R cavities** Ø (μm)	*R cavities** Grain boundaries with cavities (%)	*W cavities*† Triple points with cavities (%)
58	0·5	T	0·33 (0·03)	20	21
		C	0·29 (0·08)	Very weak	Very weak
80	0·8	T	0·42 (0·09)	30	57
		C	0·37 (0·03)	5	19
109	2·2	T	0·51 (0·34)	48	66
		C	0·54 (0·22)	4	20

*R cavities: diameter (and standard deviation) and percentage of grain boundaries containing cavities are given.
†W cavities: percentage of triple points with cavities is given.
T = Area in tension; C = area in compression.

Fig. 1. Anisotropic cavity distribution in AlN after deformation by four-point bending (tension side) at T = 1873 K, σ = 80 MPa, $\epsilon = 0{\cdot}8 \times 10^{-2}$. The stress axis is parallel to the marker.

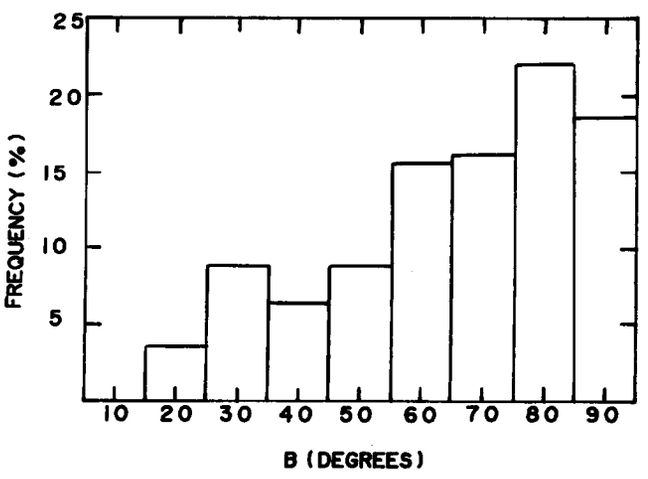

Fig. 2. Anisotropic distribution of cavities after four-point bending (tension side) for same conditions as Fig. 1. Histogram of the β-angle between the stress axis and the grain boundary plane, showing cavities (179 measurements).

3.2.2 Areas deformed in compression

Cavitation is much less developed in compressed areas, whatever the strain, as can be seen in Table 1. Cavities have the same lenticular shape and about the same size as in tension areas. Many GBs do not show cavities but the density of cavities at cavitated GBs is nearly the same as in tension. Cavitated GBs appear to be orientated at random, some being nearly parallel to the stress axis.

A significant observation is that a particle can be seen as a black dot in nearly each cavity. These particles were identified by EDS analysis and microdiffraction. They are crystallized precipitates of sintering additive (La_2O_3). Fig. 3(a) shows a GB orientated at 60° from the foil, so that cavities have elongated shapes. Particles appear at the same side of the cavities. This was not always observed. Particles may occupy diametrically opposite positions and, in a few cases, two or three particles were found in one cavity. In tension areas, in comparison, such particles were seen in a small number of cavities only. It may be mentioned that particles not attached to cavities could be found in some GBs even after 2·4% strain. Fig. 3(b) shows some particles at the GBs of a small AlN grain. The particular contrast marked by the arrow could reveal the beginning of cavitation. Such an observation, however, was extremely rare. Practically no cavities smaller than 0·1 μm were observed either in tension or compression areas in the three samples we have studied. Typically, the apparent size of particles varied from 20 to 100 nm.

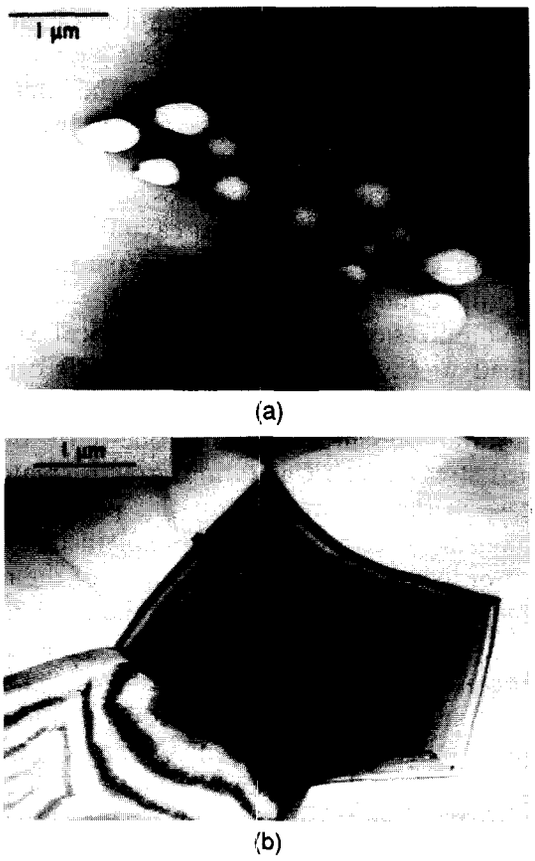

Fig. 3. Cavitation in AlN after deformation by four-point bending (compression side). (a) Cavities formed at second-phase particles in an inclined grain boundary (T = 1873 K, σ = 58 MPa, $\epsilon = 0{\cdot}5 \times 10^{-2}$) viewed using bright field TEM. (b) Second-phase particles around a small grain viewed using bright field TEM. The arrow points to the growth of a cavity (T = 1873 K, σ = 109 MPa, $\epsilon = 2{\cdot}2 \times 10^{-2}$).

3.3 Cavitation after uniaxial compression

A number of creep tests of 10^4 s to 5×10^4 s duration were performed on the two grades of AlN. Tests were interrupted after quasi-stationary creep had been established. The maximum strain attained was ~6%. Some samples were deformed in dynamic compression, under an imposed strain rate chosen in the range of steady state creep rates previously observed. The main results are as follows:

- Intragranular cavitation was never detected.
- Cavitation at GBs, on the contrary, was always observed, even after the smallest strain investigated, i.e. ~0·5%.
- R cavities initially have the lenticular shape described in Section 3.1. When growing, they change to ellipsoids with the major axis in the GB plane, as could be observed at GBs which were at a small angle from the foil plane. The rounded shape is lost for large cavities, which become facetted. The crystallographic orientation of facets could not be determined. Facets obviously depend on the orientation of the two adjacent grains (Fig. 4, marked F).
- The growth of a cavity is not necessarily symmetric inside the two adjacent grains, yet the size of cavities at a given stage of sample deformation is rather homogeneous, as observed after FPB.

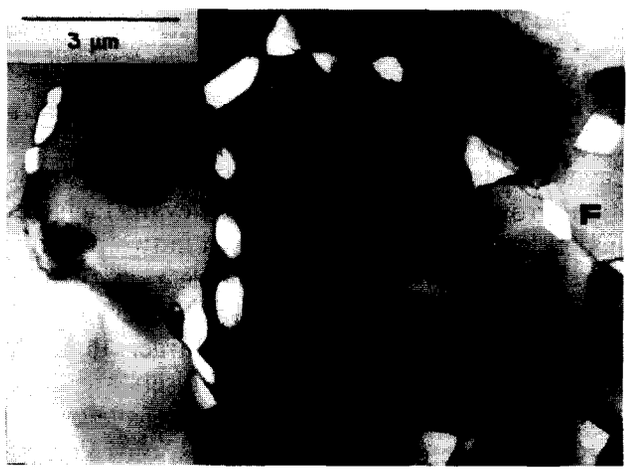

Fig. 4. Facetted cavities (F) in AlN after creep in compression (T = 1873 K, σ = 250 MPa, $\epsilon = 2{\cdot}3 \times 10^{-2}$). Dislocations (D) and one inversion domain boundary (I) can be seen in one grain.

- No clear preferential orientation of cavitated grains could be detected, in spite of observations performed in foils cut at different angles from the stress axis.
- Cavitation does not appear to be correlated with intragranular extended defects, such as dislocations or inversion domain boundaries, which can be seen in Fig. 4.
- Particles like those observed after FPB were seen in a few cavities, especially in smaller ones. It must be pointed out that cavities larger than ~1 μm are usually cut by the two faces of the thin foil, so that existing particles may have disappeared during thinning.

We are not able to state how cavity nucleation and growth are affected by each testing parameter, such as temperature, stress, strain rate and strain. We should mention, however, that the volume fraction of cavities f_v was found to be more or less equal to the total strain, for both grades of AlN, irrespective of other testing conditions. No convincing correlation between the diameter Ø of cavities (before coalescence sets in) and the strain was found. The $f_v / Ø^3$ ratio is proportional to the number of cavities per unit volume. It remains almost constant when strain is increased from 2 to 6%. This means that the number of cavities does not evolve and that the increase in the volume of cavitation is due to the growth of a constant number of cavities instead of a continuous nucleation and growth process. This is consistent with the observation that the size distribution of cavities is rather narrow in a given sample.

W-type cavities have initially the shape of concave triangles and change into convex triangles and three-branch stars as cavitation penetrates along adjacent GBs. Their size is consistently slightly larger than that of R-type cavities.

4 Discussion

Cavitation is a three-step process involving nucleation, growth and coalescence. Relevant facts and models have recently been reviewed in two papers.[4,5]

It is believed that cavity nucleation at GBs requires tensile stresses of the order of 1% of the Young modulus,[6] much larger than the applied stress in any case. Stress raisers are therefore needed, which must also create tensile stresses in samples deformed in compression. Possible stress raisers are GB ledges or second-phase particles, which both prevent GB gliding. In Al_2O_3 samples[7] containing a high density of marked GB ledges, those defects were seen to be preferred sites of cavitation. No such ledges were detected in the present work. Observations of particles acting as cavity nuclei were reported in Cu alloys[8] for large particles (~1 μm diameter), and in AlN[9] and α-SiC[10] for any particles. Here, only small particles were identified as possible nuclei. The role played by such defects was very clear especially after a slight deformation in compression (FPB) when all cavities were nucleated at particles. It is probable that in tension areas, cavitation started at defects too small to be detected by conventional TEM. It may be stressed that the very narrow size distribution of cavities within the same GB points to nearly simultaneous nucleation.

In compressed samples, tensile stresses are always developed at some GBs, especially when GB sliding is impeded by local obstacles. An example can be seen in the Fig. 19a of Ref. 4. A local concentration of tensile stresses may induce decohesion. Stress concentrations were reported by several authors. In TEM, they form patterns of concentric fringes and are called 'whorls'. Such defects are always very rare and could not be characterized. They are probably rather unstable and converted into cavities from the very beginning of deformation. The formation of cavities relaxes local stresses. Once formed, cavities take the lenticular shape which minimizes the interfacial energy, thanks to transport of matter by surface diffusion. The observation that nuclei particles remain on the same axis for all cavities in a given GB is consistent with the view that cavitation is correlated with GB gliding. This axis is parallel to the gliding direction in that particular GB.

In compression, it appears that local stresses can lead to cavitation whatever the GB orientation to the stress axis. In compression tests a hydrostatic pressure equal to one-third of the applied stress exists. Cavitation growth creates an increase in the volume against this pressure. This mechanism is only physically explained by the action of local stresses and in the rest of the material by transformations decreasing the total energy and length of the sample. Further investigation is in progress to clarify this point. As expected, however, cavitation is much more frequent in tension, where the growth of cavities can contribute directly to the total plastic strain. And lastly, it appears that coalescence merely occurs through simultaneous growth of all cavities.

References

1. Masson, I., Feiereisen, J. P., Michel, J. P., George, A., Mocellin, A. & Blumenfeld, P., *J. Eur. Ceram. Soc.*, **13** (1994) 355.

2. Hollenberg, G. W., Terwilliger, G. R. & Gordon, R. S., *J. Eur. Ceram. Soc.*, **54** (1970) 196.
3. Garofalo, F., *Fundamentals of Creep and Creep-Rupture in Metals*. MacMillan Co., New York, 1965, p. 216.
4. Chan, K. S. & Page, R. A., *J. Am. Ceram. Soc.*, **76** (1993) 83.
5. Rodriguez, P. & Bhanu Sankara Rao, K., *Prog. Mater Sci.*, **37** (1993) 403.
6. Page, R. A., Lankford, J. & Spooner, S., *J. Mater. Sci.*, **19** (1984) 3360.
7. Page, R. A., Lankford, J., Chan, K. S., Hardman-Rhyne, K. & Spooner, S., *J. Am. Ceram. Soc.*, **70** (1987) 137.
8. Fleck, R. G., Taplin, D. M. R. & Beevers, C. J., *Acta Metall.*, **23** (1975) 415.
9. Jou, Z. C. & Virkar, A. V., *J. Am. Ceram. Soc.*, **73** (1990) 1928.
10. Carter Jr, C. H., Davis, R. F. & Bentley, J., *J. Am. Ceram. Soc.*, **67** (1984) 409.

Journal of the European Ceramic Society 16 (1996) 521–527

0955-2219(95)00168-9
0955-2219/96/$15.00

Reaction Study of Aluminium Chloride with Ammonia and Mechanisms Leading to Aluminium Nitride

M. Pouget & J. P. Lecompte

Laboratoire de Matériaux Céramiques et Traitements de Surface, URA CNRS 320, Faculté des Sciences, 123 Avenue Albert Thomas, 87060 Limoges Cedex, France

(Received 20 July 1994; revised version received 11 July 1995; accepted 27 August 1995)

Abstract

The compound formed between $AlCl_3$ and NH_3 at room temperature and low temperature, characterized by different analysis methods, corresponds to the formula $AlCl_3{\cdot}6NH_3$. This intermediate was heated to 900°C under an ammonia stream to obtain aluminium nitride in low yield; as by-product NH_4Cl was formed during the thermolysis. In order to explain the decomposition mechanisms, two new pyrolysis were realized, under nitrogen and under reduced pressure. These showed formation of $Al(NH_2)NH$ in addition to NH_4Cl during the thermal decomposition. $Al(NH_2)NH$ can react with HCl, which results from the dissociation of NH_4Cl, to form AlClNH volatile combination. This is carried out by the gaseous stream during the thermolysis, thereby accounting for the low synthesis yield.

1 Introduction

The synthesis of aluminium nitride in powder or film form has been often realized from $AlCl_3$ precursor. The halide is generally heated to its sublimation temperature and then carried by a carrier gas (nitrogen, hydrogen, argon) to a reactor where ammonia is introduced. The reaction is performed at temperatures between 600 and 1400°C.[1–4] When aluminium nitride is obtained by this synthesis route, the decomposition mechanisms are difficult to describe. During the pyrolysis, a great amount of NH_4Cl is formed as a by-product. In order to explain the intermediate steps, the process used in this work is different from those proposed earlier. The reaction between $AlCl_3$ and NH_3 was first realized at room and low temperature, in order to establish its nature. This reaction results in the production of $AlCl_3{\cdot}6NH_3$.[5,6] Next $AlCl_3{\cdot}6NH_3$ was subjected to heat treatments under different atmospheres (ammonia, nitrogen or reduced pressure), and the decomposition products analysed by infra-red spectroscopy and X-ray diffraction. Comparison of the different results enabled the mechanism of aluminium nitride synthesis to be elucidated.

2 Experimental Procedures

2.1 Reactants

Aluminium chloride (bidistilled, from Atochem) was a fine, homogeneous, soft yellow and very hygroscopic powder (impurities: iron 500 ppm, Zn < 2 ppm). The ammonia used had a purity of 99·995%, its chemical composition being given by the following characteristics: H_2O < 10 ppm, O_2 < 2 ppm, N_2 < 10 ppm, CO + CO_2 < 5 ppm. The nitrogen used had a purity of 99·998%, its chemical composition being given by the following characteristics: H_2O < 2 ppm, O_2 < 3 ppm, C_nH_m < 0·2 ppm, CO < 2 ppm, CO_2 < 1 ppm.

2.2 Experimental assembly

The airtight assembly (Fig. 1) was developed for use at different temperatures (for high temperature use, a furnace is put around the quartz tube) under static conditions or under a gaseous stream.

2.3 Reaction at room temperature of $AlCl_3$ with NH_3

A definite mass (500 mg) of aluminium chloride was introduced into the quartz tube. Vacuum was realized in the assembly, then the reactor (1) was isolated. A known amount of ammonia was introduced into the rest of the assembly. The tap R_1 separating the two parts was opened, allowing ammonia gas to come into contact with the solid halide. After 24 h, when the pressure was stable, its value enabled the number of moles of ammonia still present in the assembly to be determined, and, by difference, the amount of ammonia consumed.

2.4 Reaction at low temperature of $AlCl_3$ with NH_3

The quartz tube was plunged into a dewar of

ethanol at –50°C. Ammonia was introduced, which condensed on the aluminium chloride, and the reaction was left for ~24 h. The dewar was removed from the tube, so that the excess ammonia distils. The difference between the initial volume of gaseous ammonia and the removed volume allows calculation of the number of moles of ammonia consumed.

2.4.1 Extractions with liquid ammonia

This technique was used to show the possible presence of ammonium chloride (NH_4Cl) in the reaction compound. If $AlCl_3$ undergoes an ammonolysis in liquid ammonia, the resultant product will not comprise a single compound but a melt including NH_4Cl.[7–9]

A quantity of ammonia (the order of 50 ml) was condensed on $AlCl_3$ in the reactor. The Pyrex tube (2), under vacuum and isolated from the rest of the assembly, was plunged into a dewar of liquid nitrogen in order to acquire a lower temperature than the reactor temperature; the latter was heated at the same time. Upon opening of tap R_2, the pressure difference created between the two tubes permitted the liquid to decant through the filter into the Pyrex tube. Any dissolved ammonium chloride precipitates on the Pyrex tube which is allowed to warm to room temperature while ammonia distils. This procedure was repeated about 20 times. NH_4Cl formed was quantified by titration (gravimetric technique).

2.5 Thermal decomposition

2.5.1 Under ammonia stream

After reaction, the assembly was filled with ammonia in order to maintain a gaseous stream. Heating rate, temperatures and stage times were programmed.

2.5.2 Under nitrogen stream

After reaction the assembly was filled with nitrogen, the stream obtained carrying away any gaseous products formed during the thermal decomposition. The assembly was connected via tap R_3 (Fig. 1) to a flexible tube which bubbled the nitrogen stream through hydrochloric acid solution. Thereafter, the gaseous products were determined by titration.

2.5.3 Under reduced pressure

Once the reaction between $AlCl_3$ and NH_3 was over, vacuum was realized in the assembly, and the subsequent pyrolysis followed by continuously monitoring the pressure. The volumes pressures and temperatures are known, so it is possible to determine the number of moles of gaseous products evolved. So, gaseous escape is quantified.

3 Formulation and Nature of Compound Formed Between $AlCl_3$ and NH_3

3.1 Reaction of $AlCl_3$ with NH_3

3.1.1 Room temperature

The reaction which occurs between ammonia gas and $AlCl_3$ solid is very fast and exothermic. A liquid phase transition is observed; then, very quickly, a solid layer forms and grows. Ammonia absorption, very important at the beginning of the reaction, decreases progressively and is most probably limited by the formation of the solid layer; after 24 h this absorption is over. A white fine powder is obtained which is stable under vacuum at room temperature and sensitive to the slightest moisture.

3.1.2 Low temperature

At low temperature (–50°C), the precursor saturates

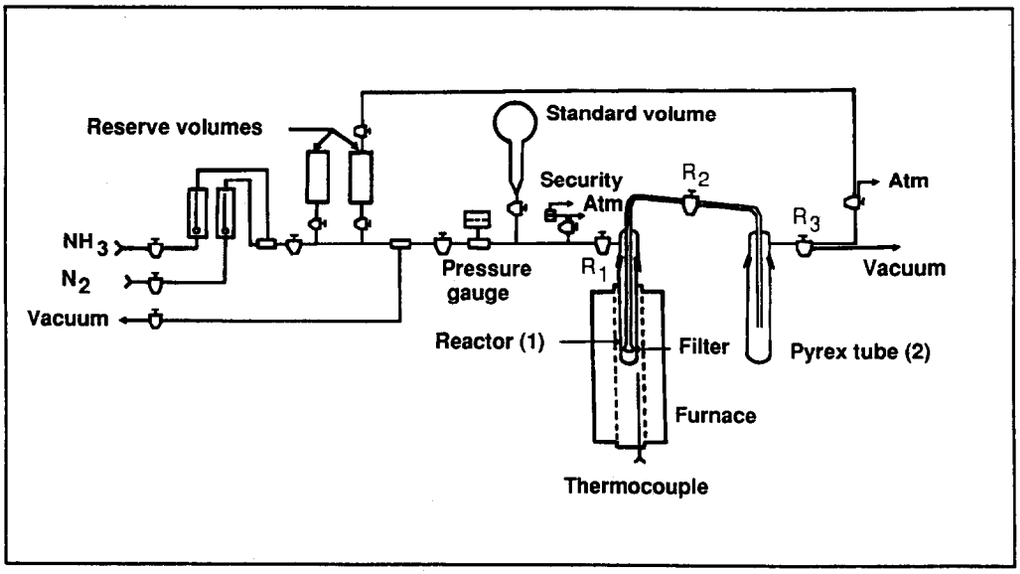

Fig. 1. Schematic illustration of the reactor assembly.

Table 1. Chemical analysis[a] of reaction compound

	Element (wt%)			
	N	*Cl*	*Al*	*H*
$AlCl_3 + NH_3$ reaction	35·4	44·0	11·8	6·8
$AlCl_3 \cdot 6NH_3$ theoretical	35·9	45·2	11·5	7·6

[a]N determined by Kjeldahl titration, Cl by gravimetric titration, Al by chelatometric titration and H by C–H–N titration.

with ammonia. A white fine powder is obtained in liquid ammonia. After 24 h, the whole is allowed to warm to room temperature and excess ammonia distils. The resultant product is the same that synthesized at room temperature during direct reaction.

3.1.3 Reaction compounds

Whatever the reaction conditions used, the compound obtained corresponds to the absorption of six ammonia molecules by one aluminium chloride molecule. The $AlCl_3 \cdot 6NH_3$ formula, which is confirmed by chemical analysis (Table 1), is established by the difference between the number of moles of ammonia introduced and remaining in the assembly.

3.2 Nature of the $AlCl_3 \cdot 6NH_3$ compound

Two assumptions have been set down: either $AlCl_3 \cdot 6NH_3$ is an adduct compound like $[Al(NH_3)_6]^{3+}$ $3Cl^-$ (Refs 5, 10 and 11) or the $AlCl_3 \cdot 6NH_3$ formulation is the result of an ammonolysis leading to a melt such as $AlCl_{3-x}(NH_2)_x$, $(6 - 2x)NH_3 + xNH_4Cl$ by analogy with other compounds.[7–9] In this last case, it is easy to show the presence of NH_4Cl by liquid ammonia extractions.

3.2.1 $AlCl_3 \cdot 6NH_3$ treated by liquid ammonia

After extraction with liquid ammonia for two weeks, the amount of chlorine removed was determined to be 4% of the theoretical chlorine content related to $AlCl_3 \cdot 6NH_3$. This low amount of chlorine indicates that the reaction between $AlCl_3$ and NH_3 is not an ammonolysis, but the resultant compound is an ammoniate adduct compound like $[Al(NH_3)_6]^{3+}$ $3Cl^-$.[12,13]

3.2.2 Physicochemical characterizations of $AlCl_3 \cdot 6NH_3$

Analysis by X-ray diffraction. As $AlCl_3 \cdot 6NH_3$ is very hygroscopic, the most airtight possible sample case has to be used. We employed a beryllium window which is transparent to X-rays and thus can form a cap isolating the powder from ambient atmosphere. The sample case has some disadvantages: it diffracts and gives two strong lines. The thickness of the beryllium window means that the sample case is not exactly in the radiation plane, leading to a low gap between the lines observed.

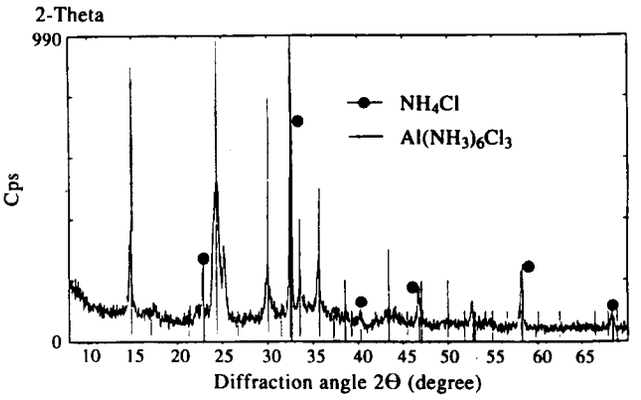

Fig. 2. X-ray diffraction pattern of the $AlCl_3 \cdot 6NH_3$ powder.

The powder is not well crystallized (Fig. 2). The X-ray diffraction pattern shows lines that can be attributed (by means of the ASTM card) to the $Al(NH_3)_6Cl_3$ compound.[10] The presence of NH_4Cl characteristic lines is observed, some of which are shared with $Al(NH_3)_6Cl_3$. The formation of a low amount of NH_4Cl during the reaction between $AlCl_3$ and NH_3 can be accepted, as 4% of chlorine was removed during the washings. The presence of NH_4Cl can also arise by partial hydrolysis of the powder during preparation or analysis.

Infrared spectroscopy. As $AlCl_3 \cdot 6NH_3$ is very hygroscopic, the preparation of pellets (a small amount of $AlCl_3 \cdot 6NH_3$ diluted in KBr) for infrared analysis was carried out in a glove box. On the other hand, during experimental measurements the samples were not protected from the air, so hydrolysis was possible.

The infra-red spectrum was recorded in the frequency range 4000–600 cm^{-1} (Fig. 3). A large but not very strong band was observed around 1600 cm^{-1} which corresponds to the antisymmetric deformation vibrations of NH_3 groups. The fine band centred around 1350 cm^{-1} is characteristic of the NH_4^+ ion. In the 800–750 cm^{-1} region the rather large band is assigned to the pendulum vibrations of NH_3 groups.

The $AlCl_3 \cdot 6NH_3$ compound can thus be described

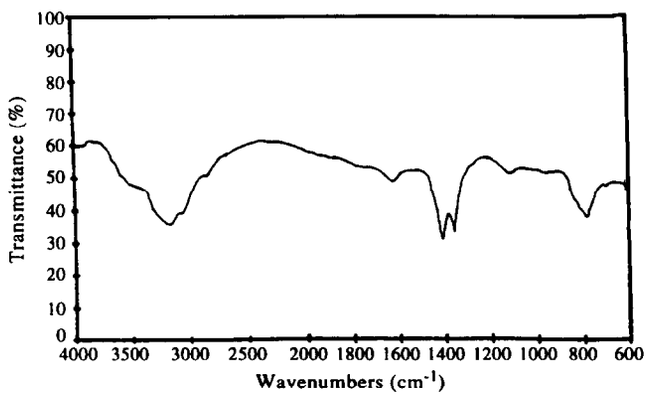

Fig. 3. Infrared spectrum of the $AlCl_3 \cdot 6NH_3$ powder.

as a complex $[Al(NH_3)_6]^{3+}$ $3Cl^-$,[10,11] with the NH_3 groups being regarded as ligands.

4 Thermal Decompositions of $AlCl_3 \cdot 6NH_3$

4.1 Under ammonia

4.1.1 Observations

A heating rate of 5°C min^{-1} was chosen, the stage temperature being 900°C (1 h). During the pyrolysis gaseous products were released from 300°C, then a fine white powder condensed on the cold areas of the assembly. At the end of the pyrolysis, a little powder remained at the bottom of the tube and a thin film which sticks strongly deposited on the reactor walls. The film and the powder were white, the powder having the appearance of transparent fine particles.

4.1.2 Characteristics of products formed

The crystalline powder that collected on the pipes was analysed by X-ray diffraction and found to have the same structure as NH_4Cl. An absorption band centred on 1400 cm^{-1}, characteristic of the NH^+_4 ion, was present in the infra-red spectrum.

The film analysed by X-ray diffraction seemed to be better crystallized than the powder collected at the bottom of the tube. The lines observed were assigned to aluminium nitride phase (Fig. 4). The maximum intensity line on the X-ray diffraction pattern and that of ASTM card No. 251133 are not the same; the nitride obtained is preferentially oriented in the (0, 0, 2) direction. The powder analysed by scanning electron microscopy (SEM) looks like big platelets: L = 150–200 μm; l = 300–350 μm; e = 15–20 μm (Fig. 5). These platelets are probably amorphous, as the crystallization occurs in part on a surface. Crystallites would be expected to form on the platelets' surface.[14] The film deposits on quartz seem to be more homogeneous (Fig. 5); the silica tube would constitute a good substrate for growth of aluminium nitride.[15]

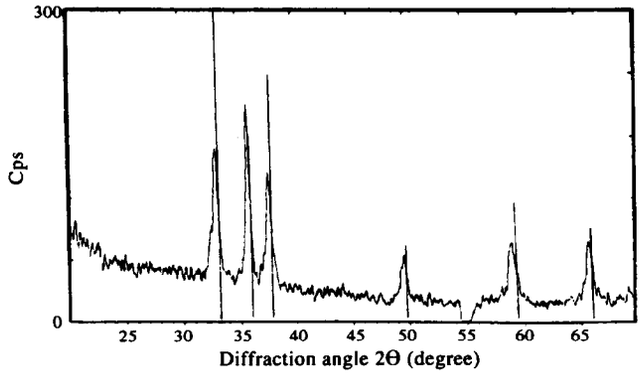

Fig. 4. X-ray diffraction pattern of the powder collected at the bottom of the tube.

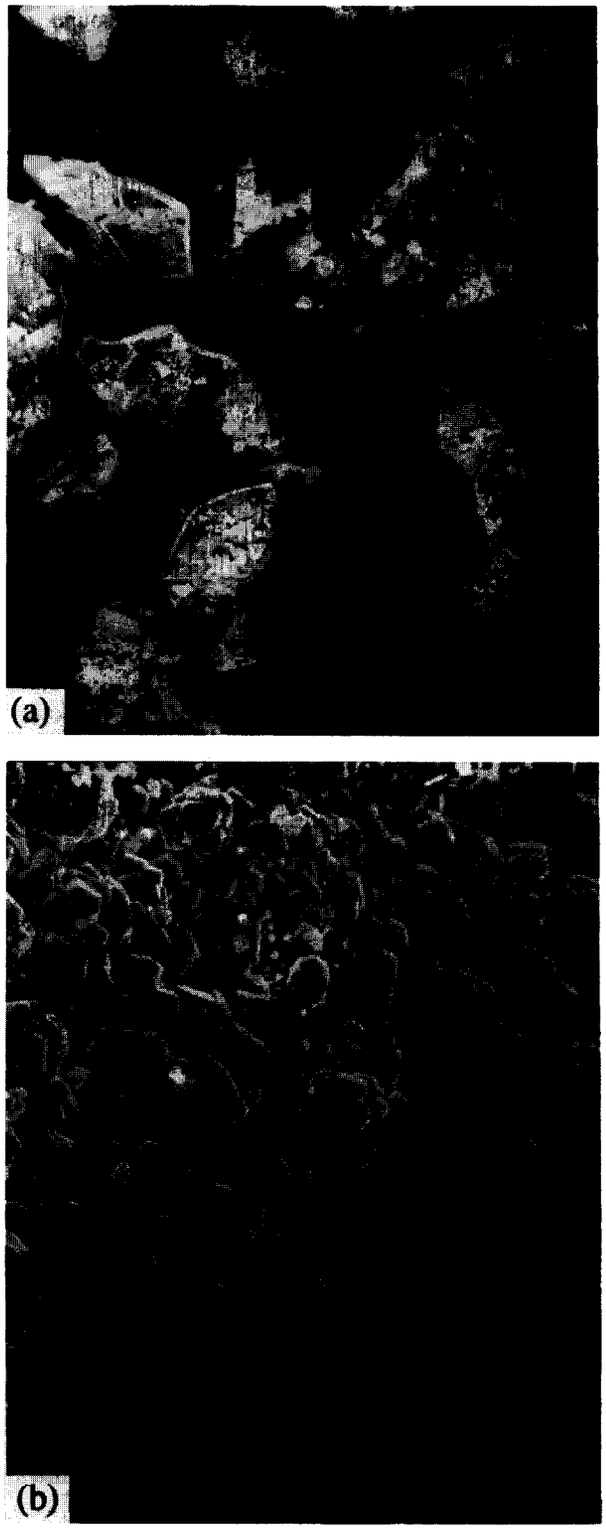

Fig. 5. Scanning electron micrographs of (a) the powder collected at the bottom of the tube (× 1000) and (b) the coated film on the silica tube (× 15000).

The specific area of the powder is of the order of 24 m^2 g^{-1}. The synthesis yield is about 10%.[12]

4.2 Under reduced pressure

4.2.1 Observations

A heating rate of 3°C min^{-1} was programmed with a stage of 900°C. A thin layer of white, rather dense deposits was observed on the tube walls. A

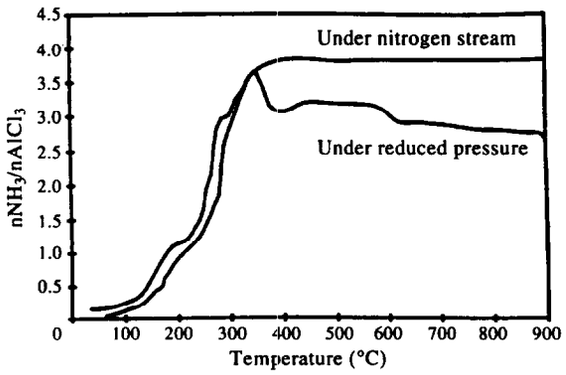

Fig. 6. Thermal decomposition curves of $AlCl_3 \cdot 6NH_3$ under reduced pressure and under a nitrogen stream.

little powder remained at the bottom of the tube. The pressure was recorded continuously and transformation to the number of moles of gaseous products permits establishment of the curve $n NH_3/n AlCl_3 = f(T)$. The gaseous product evolved was ammonia.

4.2.2 Interpretation of the curve $nNH_3/nAlCl_3 = f(T)$
The curve obtained (Fig. 6) shows several transformation areas. The first, where pressure increases rather quickly, corresponds to the escape of one mole of ammonia per mole of precursor at 175°C. Then the slope of the curve increases, expressing the escape of two additional moles of ammonia. The emanation occurs more slowly and achieves a maximum of around 4 for $n NH_3/n AlCl_3$ ratio at 350°C. Subsequently ammonia reabsorption is observed until a composition of $AlCl_3 \cdot 3NH_3$, then pressure is stabilized.

4.2.3 Contents
The sublimate which deposits on the tube walls, analysed by X-ray diffraction, has the same structure as NH_4Cl. The powder collected at the bottom of the tube is amorphous, its analysis by infrared spectroscopy not revealing the characteristic absorption band of the Al–N bond.[16] Probably, the thermal decomposition of $AlCl_3 \cdot 6NH_3$ under reduced pressure ends the formation of an ammoniate melt.[17–19]

4.3 Under nitrogen

4.3.1 Observations
A heating rate of 3°C min^{-1} was programmed with a stage of 900°C. The gaseous escape during the pyrolysis was carried out by the nitrogen stream and analysed by titration. The gaseous product comprised ammonia, acid emanation was never observed. White vapours appeared from 200°C and then condensed on the cold areas of the assembly to form a fine white powder during the whole of the thermolysis. A sublimate deposited on the walls tube at the furnace exit. There was no compound at the bottom of the tube. The results of titrations allowed the curve $n NH_3/n AlCl_3 = f(T)$ to be established.

4.3.2 Interpretation of the curve $nNH_3/nAlCl_3 = f(T)$
The thermal decomposition curves under reduced pressure and nitrogen stream are rather similar (Fig. 6), with the same transformations being present. However, ammonia refixation is avoided under the nitrogen stream. The maximum ammonia escape corresponds to a $n NH_3/n AlCl_3$ ratio of around 4. The main difference between the two types of pyrolysis is the result of the violent sublimation of NH_4Cl and particularly the absence of pyrolysis residues at the bottom of the tube.

4.3.3 Contents
The great amount of fine powder collected on the pipes was essentially NH_4Cl (infrared, X-ray diffraction analysis). The absence of pyrolysis residues is attributed to the formation of volatile compounds during the thermal decomposition. These condense on cold areas of the assembly. Thus the sublimate formed contains an important chlorine content of the order of 55 wt%, and aluminium too (≈ 5%).

4.4 Conclusions
The thermal decomposition of $AlCl_3 \cdot 6NH_3$ under an ammonia stream from 900°C leads to the formation of crystalline aluminium nitride. The by-product of the pyrolysis is NH_4Cl, which deposits on the cold areas of the assembly in great amounts and disturbs the synthesis. The presence of NH_4Cl—which can interact with aluminium compounds—results from the formation of volatile compounds that are carried out by the gaseous stream, thereby contributing to the yield decrease.

5 Decomposition Mechanisms from $AlCl_3 \cdot 6NH_3$ to AlN

From previous observations, all the reactions leading to AlN from $AlCl_3 \cdot 6NH_3$ are suggested here. These different mechanisms have been deduced from the observation of curves (Fig. 6) and the phenomena occurring during pyrolysis (ex: NH_4Cl formation perceptible).

The first escape observed corresponds to one mole of ammonia; NH_4Cl is formed at the same time which involves the formation of the compound $Al(NH_2)NH$:[20]

$$AlCl_3 \cdot 6NH_3 \rightarrow AlCl_3 \cdot 5NH_3 + NH_3 \quad T = 25\text{–}175°C$$

$$AlCl_3 \cdot 6NH_3 \rightarrow Al(NH_2)NH + 3\ NH_4Cl + NH_3$$

At higher temperatures, NH_4Cl sublimes and breaks up into NH_3 and HCl, which explains the

new ammonia escape observed. As for HCl, it fixes on $Al(NH_2)NH$ to form a volatile combination. The ammonium chloride which deposits on the cold areas is the result of the excess NH_3 and HCl recombination.

$$NH_4Cl \rightarrow NH_3\,(g) + HCl\,(g)$$

$$AlCl_3{\cdot}5NH_3 \xrightarrow{T = 225\text{–}300°C} AlCl_3{\cdot}3NH_3 +$$

$$2NH_3 \xrightarrow{T = 300\text{–}350°C} AlCl_3{\cdot}2NH_3 + 3NH_3$$

$$Al(NH_2)NH + 3\,NH_3 + 3\,HCl \rightarrow AlClNH + 3NH_3 + 2\,NH_4Cl$$

volatile chlorinated nitrogen combination — recombination on the cold areas

The volatile combination is able to fix ammonia, but the refixation is avoided in the case of the pyrolysis under nitrogen stream. The assessment corresponds well to the maximum escape observed on the curves (Fig. 6).

As AlClNH and $Al(NH_2)NH$ compounds are volatile, they can be represented by polymerized forms:[3]

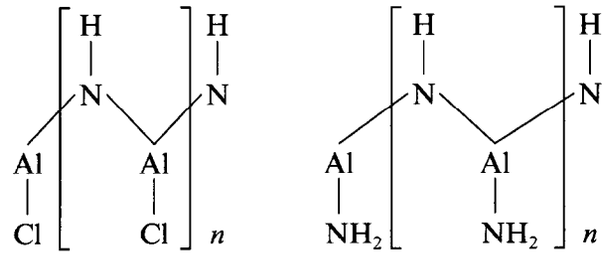

Aluminium nitride is obtained at the end of the thermolysis under ammonia whereas the thermal decomposition under nitrogen is characterized by the absence of pyrolysis residues. Under ammonia atmosphere, HCl fixation on $Al(NH_2)NH$ cannot take place in the same way:

$$Al(NH_2)NH + 3\,NH_3 + 3\,HCl \rightarrow AlN + NH_3 + 3\,NH_4Cl$$

recombination on cold areas

The equilibrium is moved towards the formation of aluminium nitride. The chlorhydrate still forms during the ammonium chloride sublimation but in a more limited way. The chlorhydrate is a volatile species and is responsible for the low yield of aluminium nitride.

6 Conclusions

The compound of formula $AlCl_3{\cdot}6NH_3$, which is the result of the reaction between $AlCl_3$ and NH_3, looks like a fine white powder and is sensitive to moisture. It is an adduct compound: $[Al(NH_3)_6]^{3+}$ $3Cl^-$. $AlCl_3{\cdot}6NH_3$ leads to aluminium nitride after a thermal treatment at 900°C under ammonia, the aluminium nitride being obtained in powder or film form by this synthesis route. The crystalline AlN is oriented in a preferential direction. Several transformations occur during the thermal decomposition of $AlCl_3{\cdot}6NH_3$; release of ammonia not only takes place at one temperature but at different temperatures between 100 and 350°C. This indicates that there are different $AlCl_3$–NH_3 bonds in the $AlCl_3{\cdot}6NH_3$ compound, the strengths of which are not the same. Intermediates such as $Al(NH_2)NH$ form during the thermal decomposition. The presence of NH_4Cl, a by-product of the synthesis, involves the formation of volatile species. These are the result of the HCl fixation on $Al(NH_2)NH$, the HCl being produced during the dissociation of NH_4Cl. The low yield of the aluminium nitride is connected with the formation of these volatiles, which are carried out by the gaseous stream.

References

1. Kimura, I., Hotta, N., Nukui, H., Saito, N. & Yasukawa, Particulate characteristics and depositions features of fine AlN powder synthetized by vapour-phase reaction. *J. Mater. Sci.*, **24** (1989) 4076–9.
2. Komiyama, H., Osawa, T., Kasi, H. & Konno, T., Rapid growth of AlN by particle precipitation aided chemical vapor deposition. *Materials Science Monographs, 38A High. Tech. Ceram.*, ed. Vincenzini. Elsevier, Amsterdam, 1987, pp. 667–76.
3. Lewis, D. W., Properties of aluminium nitride derived from $AlCl_3$–NH_3. *J. Elect. Soc.*, **117**(7) (1970) 978–82.
4. Chu, T. L. & Kelm, R. W., The preparation and properties of aluminium nitride films. *J. Elect. Soc.*, **122**(7) (1975) 995–1000.
5. Pauleau, Y., Hantzpergue, J. J. & Remy, J. C., Les composés d'addition entre l'ammoniac et les trihalogénures des éléments du groupe IIIA. *Bull. Soc. Chem. Fr.*, **5–6** (1978) 246–61.
6. Pouget, M., Les combinaisons azotées de l'aluminium formées par ammoniolyse de précurseurs halogénés lors de la synthèse du nitrure d'aluminium. Thèse, Université de Limoges, 1993.
7. Billy, M., Préparation et définition du nitrure de silicium. Thèse, Faculté des Sciences de l'Université de Paris, 1958.
8. Kottarathil, T. T., A study of the reaction between titanium tetrachlorides and liquid ammonia. Thèse, Université Catholique de Lille, 1975.
9. Fowles, G. W. A. & Pollard, F. H., Studies on the behaviour of halides of the transition metals with ammonia, Part III, The reaction of zirconium and thorium tetrachlorides with ammonia. *J. Chem. Soc.*, (1953) 4128–32.
10. Semenko, K. N., Shilkin, S. P., Kravchenko, O. V. & Polyakova, V. B., Structure of hexaammines of aluminium borohydride and chloroborohydride. *Bull. Acad. Sci. USSR, Div. Chem. Soc.*, **23** (1974) 1379–83.
11. Pino Vasquez, C., Estudio per espectrografia infraroja de los compuestos AlX_3, nNH_3. *Ana. Real. Soc. Esp. Fis. Qui*, **62**(1) (1966) 17–24.
12. Pouget, M., Lecompte, J. P. & Billy, M., Etude des composés formés lors de la réaction entre les halogénures d'aluminium et l'ammoniac dans le cadre dela synthèse du nitrure d'aluminium. I — Nature et caractérisations des composés azotés. *J. Chim. Phys.*, **91**(4) (1994) 457–71.

13. Pouget, M., Lecompte, J. P. & Billy, M., Etude des composés formés lors de la réaction entre les halogénures d'aluminium et l'ammoniac dans le cadre dela synthèse du nitrure d'aluminium. II — Thermolyse des composés azotés et préparation du nitrure d'aluminium. *J. Chim. Phys.*, **91**(5) (1994) 547–61.
14. Riedel, R., Petzow, G. & Klingebiel, V., Characterization of AlN powder produced by the reaction of $AlCl_3$ with hexamethyldisilazane. *J. Mater. Sci. Lett.*, **9** (1990) 222–4.
15. Nickel, K. G., Riedel, R. & Petzow, G., Thermodynamic and experimental study of high purity AlN formation from $AlCl_3$ by chemical vapor deposition. *J. Am. Ceram. Soc.*, **72**(10) (1989) 1804–10.
16. Makarenko, G. N., Zyatkevich, D. P., Arsenin, K. I., Karlysheva, K. F., Kosolapova, T. Ya. & Sheka, I. A., IR spectra of ultradispersed aluminium nitride powder. *Izves Akad. Nauk., Neorg. Mat.*, **15**(4) (1979) 535–7.
17. Drozin, N. N., Fridman, S. G., Gerasimenko, E. I. & Palyvchenko, G. N., Preparation of aluminium chloride monoammine. *Russian J. Inorg. Chem.*, **13**(8) (1968) 1080–2.
18. Renner, T. H., Herstellung der nitride von Bor, Aluminium, Gallium und Indium mach dem Aufwachsverfahren. *Z. Anorg. All. Chem.*, **298** (1959) 22–33.
19. Boden, G., Irmish, R., Himpel, G. & Reetz, T., Probleme bei der herstellung von nitrides chen keramischen pulvern. *Spechsall.*, **122**(3) (1989) 224.
20. Maya, L., Synthetic approaches to aluminium nitride via pyrolysis of a precursor. *Adv. Ceram. Mater.*, **1**(2)(1986) 150–3.

Journal of the European Ceramic Society **16** (1996) 529–534

0955-2219(95)00164-6
0955-2219/96/$15.00

Microstructural Features of the α to β-SiAlON Phase Transformation

Rupeng Zhao,[a] Yi-Bing Cheng,*[a] & John Drennan[b]

[a]Department of Materials Engineering, Monash University, Melbourne, Victoria 3168, Australia
[b]CSIRO, Division of Materials Sciences and Technology, Melbourne, Victoria 3168, Australia

(Received 22 July 1995; accepted 10 September 1995)

Abstract

The microstructural characteristics of Sm (α + β) -SiAlON ceramics after post-sintering heat treatment at 1450°C are investigated by analytical electron microscopy (AEM). X-ray diffraction (XRD) analyses indicate that a significant amount of the α-SiAlON (α') phase has transformed to β-SiAlON (β') during the heat treatment. It is found that the transformation is nucleated on the existing β' phase and the transformed β' grains have unique microstructural features containing a high density of dislocations and ultra-fine spherical inclusions rich in Sm and O. Similar characteristics have also been observed in the Yb (α' + β') materials. It is suggested that the transformation from α' to β' proceeds via a nucleation-growth mechanism and may require only a small amount of liquid phase to promote atomic diffusion.

1 Introduction

Post-sintering heat treatment of SiAlON ceramics is used to crystallize the glassy grain boundary phase and subsequently improve the high temperature performance of the materials.[1,2] There have been many studies exploring the grain boundary crystallization phenomenon but very little attention has been paid to the effects of post-sintering heat treatment on the stability of the SiAlON phases. Recently, Mandal *et al.*[3] revealed that some rare earth α-SiAlON (α') phases could undergo transformation to β-SiAlON (β') in the temperature range 1100 to 1600°C. α and β-SiAlONs have different mechanical properties,[4] therefore, this discovery may open new routes for tailoring the microstructures and properties of (α + β) -SiAlON ceramics.

The α' and β' phases have distinct compositions and possess different crystal structures.[5] The transformation between the α' and β' phases involves lattice reconstruction and requires a high degree of atomic diffusion. As a result of the strong covalent nature of the bonding associated with both the α' and β' lattices, the atomic diffusivity of species making up the lattice is inherently low. This poses questions of how the α' to β' transformation could take place at relatively low annealing temperatures and what is the diffusion mechanism operating. The phenomenon of α' to β' transformation has now been observed in a number of rare earth α' systems;[6–9] however, little microstructural information has been reported. This paper presents some unique microstructural features observed in heat-treated Sm- and Yb-doped SiAlON samples that have experienced a substantial α' to β' transformation and attempts to provide some explanations for the mechanism of the transformation.

2 Experimental

Samples were prepared from Si_3N_4, AlN, Al_2O_3, Sm_2O_3 and Yb_2O_3 powders with a starting composition (in wt%) of 72·50 Si_3N_4, 14·27 AlN, 2·00 Al_2O_3 and 11·23 Sm_2O_3 for the Sm α' + β' sample and 79·82 Si_3N_4, 5·24 AlN, 4·92 Al_2O_3 and 10·02 Yb_2O_3 for the Yb α' + β' sample. The samples were pressureless sintered between 1800 and 1820°C in a nitrogen atmosphere. Full details of the sample preparation can be found in Refs 10 and 11. X-ray diffraction (XRD) analyses of the as-sintered materials revealed that both samples contained mainly α' and β' phases but in the case of the Sm-containing material traces of the 21R polytypoid phase were observed and in the Yb-containing sample, yttrium disilicate ($Yb_2Si_2O_7$) was present. In each of the samples an amorphous grain boundary phase was observed by transmission electron microscopy (TEM).

*To whom correspondence should be addressed.

The Sm sample was subsequently heat-treated at 1450°C for 120 h, and the Yb sample at 1300°C for 96 h, in an alumina tube furnace in flowing high purity nitrogen. Materials characterization was performed using a Rigaku X-ray diffractometer and Philips CM20 and CM30 analytical electron microscopes (AEM) fitted with ultra-thin window energy dispersive X-ray spectroscopy (EDXS) detectors for micro-analyses. Specimens for AEM were mechanically ground, dimpled to thickness of ~20 μm, and then ion-milled to electron transparency. All specimens were carbon-coated before AEM examination to avoid surface charging.

3 Results

Figure 1 shows the XRD pattern of the Sm sample before and after the heat treatment at 1450°C. A marked difference appears in the intensities of the characteristic XRD peaks between α' and β' phases, indicating the changes in the β':(α' + β') ratio. Approximately 11% β' was found in the as-sintered Sm sample; this was increased significantly to 57% after heat treatment at 1450°C for 120 h. This is the clear evidence of the α' to β' transformation during the isothermal heat treatment. Accompanying the transformation was crystallization of the glassy grain boundary phase to form melilite (M').[11] In the case of the Yb SiAlON sample, a less dramatic transformation was noticed by XRD with the β':(α' + β') ratio increasing from 48% in the as-sintered sample to 68% after heat treatment at 1300°C for 96 h. Yb YAG was the grain boundary phase in the heat-treated sample.

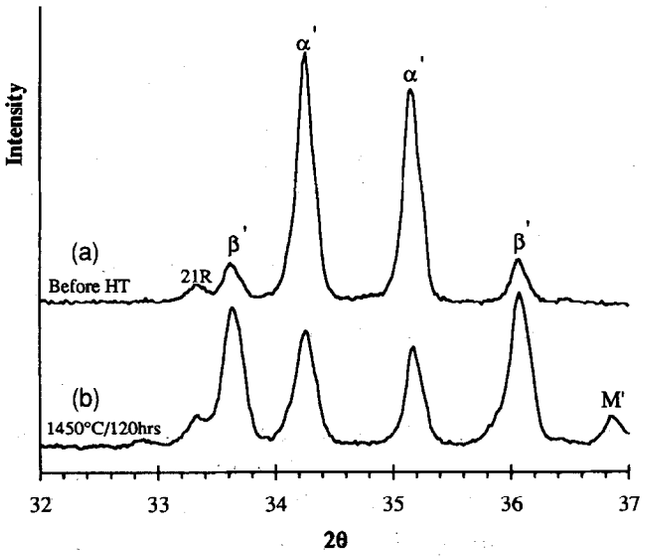

Fig. 1. XRD patterns for the Sm (α + β)-SiAlON specimens (a) before and (b) after heat treatment at 1450°C for 120 h, showing that a significant amount of α' phase has transformed to β' phase during the heat treatment. 21R and M' are 21R SiAlON polytypoid and Al-containing melilite phases, respectively.

Microstructures of the samples after the heat treatments were studied using AEM. Based on the XRD results, the microstructure should consist of two β' phases: the 'original' β' formed at sintering temperature and the transformed β' resulting from the transformation. Figures 2(a) and (b) show typical bright-field and dark-field images of the Sm sample after heat treatment, in which a β' grain with unique microstructural features is revealed. This microstructure in fact comprises two distinct grains, one is basically a defect-free β' crystal whereas the other contains a high density of dislocations and a large amount of ultra-fine (~40 nm) spherical inclusions which are often associated with the dislocations. It is emphasised that this kind of microstructure is commonly observed in the heat-treated Sm (α' + β') samples. Electron diffraction patterns in the (1 0 $\bar{1}$ 0) zone [Figs 2(c) and (d)] positively identify that both grains have the β-Si_3N_4 structure and a similar crystallographic orientation with a very small angle of misfit between them. EDXS analyses [Fig. 2(e)] from the two grains, excluding the spherical inclusions, showed the presence of Si, Al, O and N but no Sm, further confirming the grains to be β-SiAlON.

Burgers vector analysis using two-beam conditions and $\mathbf{g}\cdot\mathbf{b} = 0$ criteria verifies that the dislocations have $\mathbf{b}$ = [0 0 0 1], which is a common type of dislocations found in β-Si_3N_4/SiAlON materials.[12,13] The ultra-fine spherical inclusions, examined by nano-probe EDXS analysis, have different compositions from both the α' and β' grains and are particularly rich in Sm and O (Fig. 3). It should be noted that, although an 8 nm electron probe was used in the EDXS analysis, the surrounding β-SiAlON matrix may have made a significant contribution to the EDXS result of the inclusions, increasing their apparent Si and N concentrations. As a consequence, the actual Sm and O or even Al contents of the inclusions can be higher than that apparently observed in the spectrum shown in Fig. 3(a). It is seen from Fig. 2 that dislocations change their directions when passing through the fine spheroids. This feature discounts the possibility that the spheroidal inclusions are some artefacts of specimen preparation. Figure 4 shows a high magnification TEM image of a region that contains a number of fine spheroidal inclusions. It is clear that even within a single spheroid, the moiré pattern and lattice fringes may vary, suggesting a complex nature of these spheroids; i.e. a single spheroid may consist of several crystals as well as an amorphous region. A similar microstructure has also been observed in the Yb (α' + β') sample after heat treatment at 1300°C for 96 h (Fig. 5), which confirms the

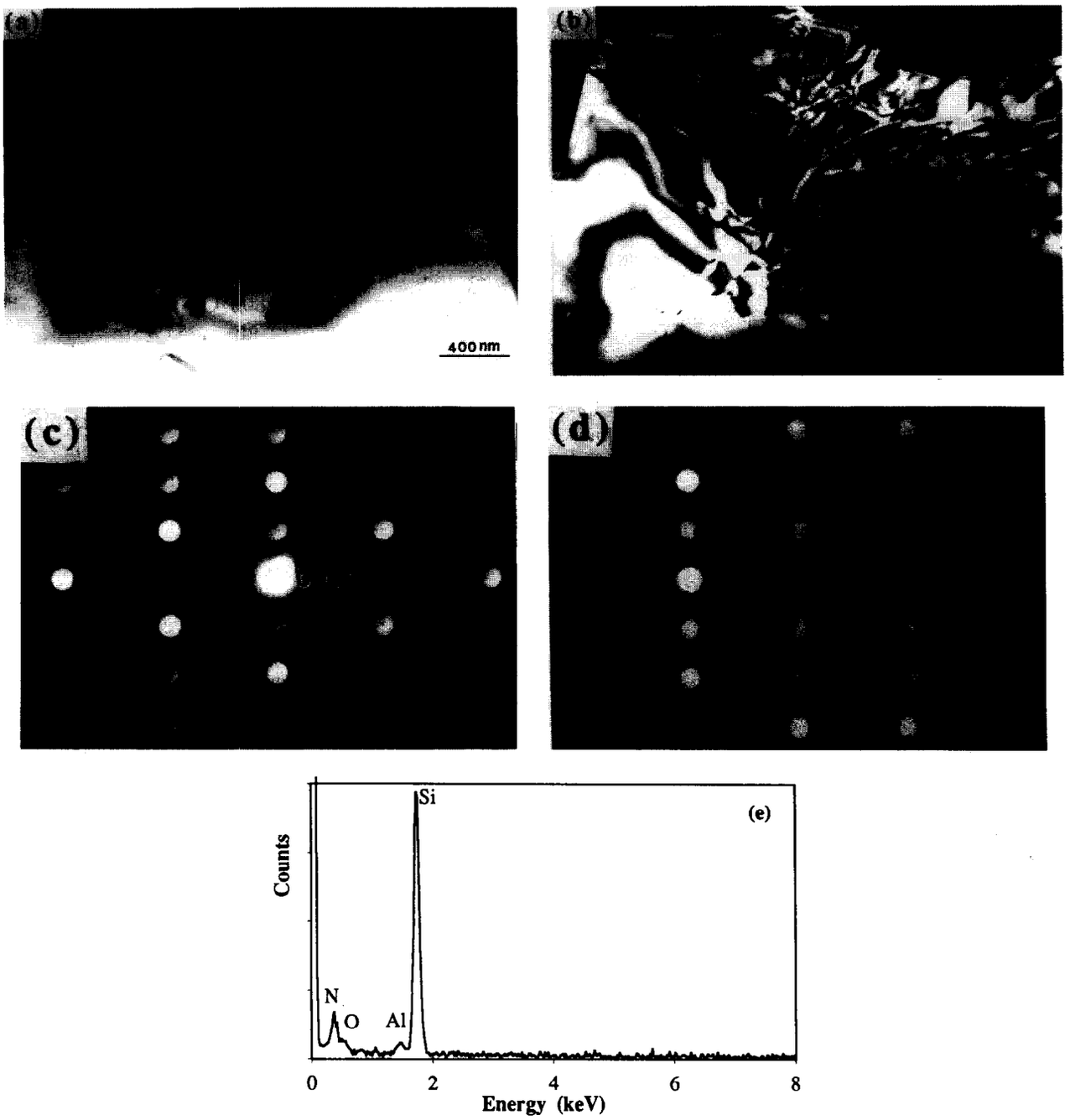

Fig. 2. (a) Bright-field and (b) dark-field TEM images of a β' grain in the heat-treated sample. Electron diffraction patterns in the (1 0 $\bar{1}$ 0) zone (c) from defect-free region and (d) from dislocated region, and (e) EDXS spectrum has confirmed both regions to be the β' phase.

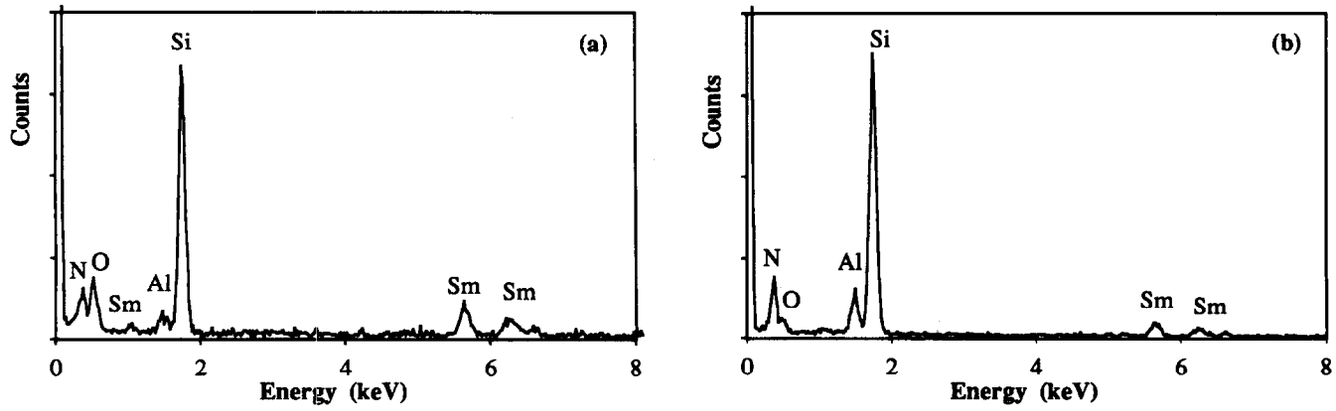

Fig. 3. EDXS spectra for (a) the ultra-fine inclusions and (b) α' grains in the heat-treated Sm sample. Note the Sm and O peaks in (a) are higher than those in (b).

Fig. 4. High magnification image of ultra-fine inclusions in a β' grain. The contrast of the inclusions shows different moiré patterns, indicating a complicated nature of the inclusions. Note the association of dislocation with the inclusions.

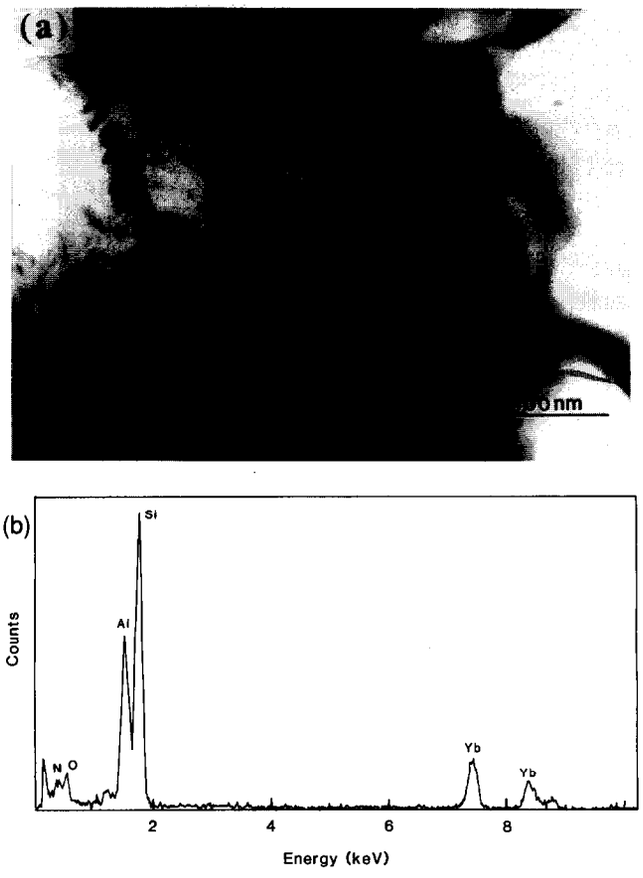

Fig. 5. (a) TEM micrograph of Yb SiAlON sample heat-treated at 1300°C for 96 h; (b) EDXS of spheroids in the microstructure.

commonality of the spheroid/dislocation features in the materials undergoing the α' to β' transformation. Extensive TEM studies failed to identify the similar feature in the Sm sample prior to the heat treatment and, to the knowledge of the authors, this type of microstructure has not been observed or reported in the as-sintered SiAlON materials. It is, therefore, suggested that this microstructure is a unique feature associated with the α' to β' transformation.

4 Discussion

4.1 Identification of the transformed β' particles

The β' form of the SiAlON structure is unable to accommodate any detectable amount of the rare earth cations; conversely the α' form requires the cations to stabilize its structure.[4] The dispersion of large amounts of Sm-rich inclusions in a β' grain represents a thermodynamically unstable state and this microstructure is unlikely to be developed during sintering at 1800°C. Post-sintering heat treatment at 1450°C produces M' ($Sm_2Al_xSi_{3-x}O_{3+x}N_{4-x}$) as a stable grain boundary phase,[11] during which the free energy of the system is reduced. Clearly redispersing of Sm from grain boundaries into β' grains would increase the free energy and hence it is unreasonable to assume these inclusions to be a result of diffusion of components from the grain-boundary phase during heat treatments. Considering the fact that the α' phase must effectively reject the stabilizing rare earth cation to proceed the transformation, we suggest that the Sm- or Yb-rich spheroids are originally a part of the α' composition which has been excluded from the structure during the transformation from α' to β' structures. Therefore the spheroidal inclusions described above are a unique feature resulting from grains which have undergone the α' to β' phase transformation.

The observed α' to β' transformation indicates that the β' phase has a lower free energy than the α' composition at 1450°C and hence the reduction in free energy ensures a thermodynamic driving force for this transformation to take place. In the α-Si_3N_4 to β-SiAlON transformation during sintering, the process can be facilitated as existing β' grains provide effective nucleation sites which would significantly reduce the interfacial energy.[13] There is no apparent reason why the two adjacent β' grains observed in Fig. 2 should develop such distinct microstructural features if they both formed in the primary sintering process. It is, therefore, very likely that the defect-free β' grain adjacent to the spheroid/dislocation-containing β' grain in Fig. 2 is a pre-existing β' phase which acts as a heterogeneous nucleus for the transformation to occur. The close crystallographic relationship between the two neighbouring β' grains provides evidence of epitaxial heterogeneous nucleation. After the phase transformation, the β' particle size is increased and its grain morphology becomes erratic (Fig. 6), further supporting that nucleation and growth is a mechanism of the transformation.

4.2 Microstructural development in the transformation

Because of the reconstructive nature of the transformation and low diffusivity of SiAlON lattices,

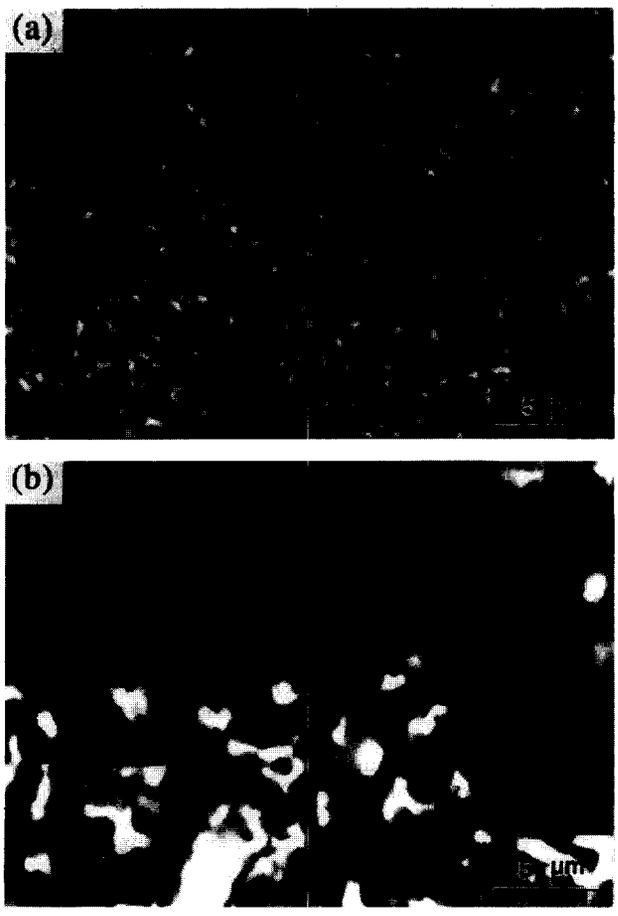

Fig. 6. SEM images of the Sm samples (a) as-sintered and (b) heat-treated at 1450°C for 120 h. The multiphase feature comprises β' (dark grey), α' (light grey), 21R (dark needle shape) and grain boundary phases (white). Note the increase in β' content and changes in its morphology after the heat treatment.

the α' to β' transformation must involve a liquid phase to promote diffusion and hence may only occur above the eutectic temperature of the system. The Sm sample shown in Fig. 2 was heat-treated at 1450°C for 120 h. It was found that after the initial 24 h heat treatment, very little glass was remained at SiAlON grain boundaries but the α' to β' transformation proceeded continuously with a constant rate in the subsequent heat treatment.[6] It seems that a large amount of liquid phase may not be a necessary premise for the α' to β' transformation although liquid is essential to this process. The spherical shape of the inclusions suggests these particles to be liquid at the heat treatment temperature but the exact origin of this liquid is equivocal at this stage. There is a possibility that, after facilitating the transformation, the residual liquid at interfaces between the nuclei and the transforming grains is left behind in the grain as the transformation frontier is advanced. It is also possible that when the transformation is initiated, the rejected Sm^{3+} cations may react with other SiAlON elements upon diffusion and create ultra-fine local liquid regions within the transforming α' grain, which could further assist the transformation. Clearly more studies are required to further understand the nature of these super-fine inclusions. The structural complication of the spheroids demonstrated in Fig. 4 indicates compositional inhomogeneity among these inclusions. This is a feature contrary to the generally homogeneous grain boundary liquid but corresponds to the local compositional fluctuation in solid solutions. In either cases, however, it seems that the amount of liquid phase involved in the phase transformation is insignificant.

The transformation from α' to β' phases depends on atomic diffusion. The formation of large amounts of dislocations in the transformed β' grains is an indication of imperfection of the diffusion, which is a combined effect of strong atomic bonding, low thermal energy and a limited amount of liquid phase. The bending of dislocations around the spheroids suggests that these super-fine aliens may also be a cause for the formation of dislocations. On the other hand, the association of these spheroids with dislocations ensures a relatively easy diffusion because the activation energy for pipe (dislocation) diffusion is less than for lattice diffusion and this is particularly evident at relatively low temperatures.[14] The feature observed in Fig. 2 may imply the characteristic of a medium stage of the transformation, in which the fine liquid regions have been solidified on cooling. During the transformation, these Sm-rich liquid spheroids would gradually diffuse out of the transformed grain along the dislocations and form a crystalline phase(s) at grain boundaries. The completion of the transformation is marked by the elimination of these inclusions from the transformed β' grains. This would further reduce the free energy of the system and induce an additional driving force to encourage the transformation. Previous studies on the Sm SiAlON samples have observed an increase in the amount of the grain boundary phase (M') and a decrease in the z value of the β' phase following the prolonged transformation process.[6,8] These results support the present assumption. In addition, it was found that the dislocation density of silicon nitride grains decreased with extending the heat treatment time.[12] This may explain why the amount of the transformed β' grains containing the spheroid/dislocation feature in the heat-treated samples is less than the proportion of the $\alpha' \rightarrow \beta'$ transformation recorded by XRD.

5 Conclusions

Unique microstructural features resulting from the α to β-SiAlON transformation have been observed in Sm and Yb ($\alpha + \beta$)-SiAlON samples.

Heterogeneous nucleation on pre-existing β' phases occurs in the transformation and the transformed grains contain large amounts of Sm/Yb-rich ultrafine spherical inclusions which are associated with dislocations. These inclusions may be a liquid phase accompanying the transformation that is solidified on cooling. The microstructure of spheroid/dislocation in a β' grain presents a unique feature of the α' to β' transformation. The diffusion of the rejected elements, namely Sm and Yb, from a transformed α' structure proceeds mainly along dislocations, which has a lower activation energy than lattice diffusion.

Acknowledgements

This work was supported by the Australian Research Council. The as-sintered Yb SiAlON sample was supplied by Dr. H. Mandal and Professor D. P. Thompson. Mr. M Staiger carried out specimen preparation of the Yb sample.

References

1. Lewis, M. H., Crystallisation of grain boundary phases in silicon nitride and SiAlON ceramics. In *Silicon Nitride 93, Engineering Materials Vol. 89–91*, ed. M. J. Hoffmann, P. F. Becher and G. Petzow, Trans Tech Publ., 1993, pp. 333–8.
2. Thompson D. P., New grain boundary phases for nitrogen ceramics. In *MRS Symposium Proceedings: Silicon Nitride Ceramics — Science and Technological Advances*, ed. I. -Wei Chen *et al.* MRS, 1993, Vol. 287, pp. 79–92.
3. Mandal, H., Thompson, D. P. & Ekström, T., Reversible $\alpha \rightarrow \beta$ SiAlON transformation in heat-treated SiAlON Ceramics. *J. Eur. Ceram. Soc.*, **12** (1993) 421–9.
4. Ekström, T., & Nygren, M., SiAlON ceramics. *J. Am. Ceram. Soc.*, **75** (1992) 259–76.
5. Hampshire, S., Nitride ceramics. In *Materials Science and Technology, Vol. 11 Structure and Properties of Ceramics*, ed. M. Swain. VCH, Weinheim, 1994, pp. 121–71.
6. Zhao, R. & Cheng, Y.-B., Phase transformation in Sm $(\alpha+\beta)$-SiAlON ceramics during post-sintering heat treatments. *J. Eur. Ceram. Soc.*, **15** (1995) 1221–8.
7. Ekström, T. & Shen, Z. J., Temperature stability of rare earth doped α-SiAlON ceramics,. In *Proc. 5th International Symposium on Ceramic Materials & Components for Engines*, Shanghai, 1994, pp. 206–10.
8. Shen, Z. J., Ekström, T. & Nygren, M., Temperature stability of samarium doped α-SiAlON ceramics. *J. Eur. Ceram. Soc.*, **16** (1996) 43–53.
9. Shen, Z. J., Ekström, T. & Nygren, M., Homogeneity region and thermal stability of neodymium doped α-SiAlON ceramics. *J. Eur. Ceram. Soc.*, in press.
10. Mandal. H., Thompson, D. P. & Ekström, T., Reversible α–β SiAlON transformation in heat-treated SiAlON ceramics. *J. Eur. Ceram. Soc.*, **12** (1993) 421–9.
11. Cheng, Y.-B. & Thompson, D. P., Preparation and grain boundary heat-treatment of samarium α-SiAlON ceramics. *J. Eur. Ceram. Soc.*, **14** (1994) 13–21.
12. Lee. W. E. & Hilmas, G. E., Microstructural changes in β-silicon nitride grains upon crystallising the grain-boundary glass. *J. Am. Ceram. Soc.*, **72** (1989) 1931–7.
13. Hwang, S. L. & Chen, I.-W., Nucleation and growth of β'-SiAlON. *J. Am. Ceram. Soc.*, **77** (1994) 1719–28.
14. Porter, D. A. & Easterling, K. E., Phase transformations in metals and alloys. *VNR*, (1982) 102.

Journal of the European Ceramic Society 16 (1996) 535–543

0955-2219(95)00126-3
0955-2219/96/$15.00

Si_2N_2O–ZrO_2 Composites Prepared by Hot Isostatic Pressing

P.-O. Olsson[a] & T. Ekström[b]

[a]National Defence Research Establishment, S-172 90 Stockholm, Sweden
[b]Department of Inorganic Chemistry, Arrhenius Laboratory, University of Stockholm, S-106 91 Stockholm, Sweden

(Received 17 February 1995; revised version received 26 June 1995; accepted 14 July 1995)

Abstract

Fully dense Si_2N_2O–ZrO_2 composites have been prepared by glass-encapsulated hot isostatic pressing at 1600 and 1700°C by two different routes. Firstly, from reacting powder mixtures of equimolar amounts of Si_3N_4 plus SiO_2 with 0, 5 and 20 wt% ZrO_2 or ZrO_2 (3 mol% Y_2O_3), and secondly by an in-situ reaction from equimolar mixtures of Si_3N_4 and $ZrSiO_4$ to form a Si_2N_2O composite with 36 wt% ZrO_2. The effects of small additions of Al_2O_3 or Y_2O_3 in the two different preparation routes were also studied. It was found that the reaction of Si_3N_4 with SiO_2 was strongly influenced by the addition of sintering aids and temperature, whereas the reaction with $ZrSiO_4$ was mainly temperature controlled and proceeded rapidly at 1700°C.

Addition of zirconia or stabilized zirconia did not appear to have any positive effect on the toughness, and the materials prepared were in general brittle with a fracture toughness of ~3 MPa $m^{1/2}$. The observed hardness was typically 12–14 GPa for the composites. The composites which consisted of more or less unreacted starting materials had a very fine-grained microstructure. In the fully reacted samples which had the highest fracture toughness the zirconia grains had increased in size compared to the more brittle samples.

1 Introduction

Improving high-temperature chemical resistance and mechanical properties, in particular of engineering ceramics, has been an important focus for some time. Oxide based ceramics are often chemically inert but are more brittle than the silicon nitride based ceramics, for instance. Non-oxide ceramics, on the other hand, are generally not very oxidation resistant when heated to high temperatures in oxidizing environments, but exceptions are found for silicon based ceramics, which develop a protective silica film on the surface, e.g. silicon carbide, silicon nitride and silicon oxynitride. From among these compounds silicon oxynitride (Si_2N_2O) has been shown to be very oxidation resistant and materials based on the oxynitride have therefore been considered as very promising candidates for high temperature engineering purposes.[1–5]

In a number of previous studies silicon oxynitride ceramics have, therefore, received attention, but it was found that formation of the Si_2N_2O phase by conventional sintering of equimolar mixtures of Si_3N_4 and SiO_2 powders at high temperatures is difficult in the absence of added sintering aids.[6–8] The Si_2N_2O phase forms and the flake-like crystals precipitate through a transient melt of silica in which the Si_3N_4 initially added dissolves. The kinetics of this process are very slow in a pure silica melt because of its extreme viscosity, even at high temperatures. Additions of small amounts of a number of metal oxides which initially react with the silica melt and thereby reduce the overall viscosity have been shown to greatly facilitate both the formation and the densification of silicon oxynitride ceramics.[9–12]

Composite ceramic materials based on Si_2N_2O with additions of pure ZrO_2 or ZrO_2 stabilized by Y_2O_3 (typically 3 mol%) have also gained attention in the past.[10,13–15] The motivation for adding zirconia to the Si_2N_2O ceramics originates from the assumption that ZrO_2 might have potential as a toughening and strengthening agent in these fairly brittle ceramics, in a similar way as has been observed for the addition of ZrO_2 to oxide matrices. Zirconia additions may also act as an effective sintering aid at preparation temperatures above 1750°C, which are normally used for nitride ceramics (see, for example, Refs 16–20). The formation of silicon oxynitride at 1700°C by hot pressing of silicon nitride and silica with ZrO_2 and ZrO_2(2·8 mol% Y_2O_3) was, for instance, studied by Ohashi and co-workers.[10] However, the dispersed

particles of zirconia were not found to contribute to toughening of the oxynitride ceramics and the indentation fracture toughness was ~3 MPa $m^{1/2}$.

The observed lack of a transformation toughening effect of zirconia in silicon oxynitride ceramics has been proposed by Cheng and co-workers[15] to be the result of dissolution of nitrogen into the zirconia structure. This N-substitution results in further stabilization of the high-temperature tetragonal ZrO_2 crystal form and thus prevents the martensitic transformation to the monoclinic form under mechanical stress. This hypothesis is in agreement with similar findings in the Si_3N_4–ZrO_2 composites where the fracture toughness at room temperature remained essentially unchanged.[20]

Two major preparation routes have been used in the past to prepare Si_2N_2O–ZrO_2 composites. The first and most well-known is from powder mixtures of equimolar amounts of Si_3N_4 and SiO_2, with ZrO_2 or $ZrO_2(Y_2O_3)$ added separately. An alternative route is via the *in-situ* reaction involving sintering of equimolar mixtures of Si_3N_4 and $ZrSiO_4$ to form a Si_2N_2O composite with 36 wt% ZrO_2.[21,22] The advantage of using the second route is the 'freedom' of preparing the materials with no or only minor additions of sintering aids, but a drawback is the substantial amount of ZrO_2 that is formed (~24 vol%). Also, there is a risk that oxidation of these materials may occur when used in air at temperatures above 1000°C. A porous oxide scale containing silica and $ZrSiO_4$ is formed and, especially at temperatures above 1250°C, a severe degradation of the materials has been observed as this oxide scale provided poor protection against further oxidation.[14] At these high zirconia contents it might also be expected that the surface stresses which result from the large volume expansion during oxidation will become significant, leading to cracking and spalling.[23]

In the present study the effects of starting materials, reaction route and overall composition on the properties of fully dense Si_2N_2O + ZrO_2 composite ceramics prepared by glass-encapsulated hot isostatic pressing (HIP) have been explored. The effects of small amounts of sintering aids (yttria or alumina) have also been studied. The results from phase analysis and microstructure characterization will be presented and discussed in relation to the observed mechanical properties.

2 Experimental Procedures

Selected Si_2N_2O + ZrO_2 compositions were prepared by two reaction routes from different starting materials. Firstly, equimolar mixtures of Si_3N_4 and SiO_2 were used (series A), with additions of 0, 5 and 20 wt% ZrO_2 or 0, 5 and 20 wt% ZrO_2(3 mol% Y_2O_3), and with 0–5 wt% Al_2O_3 added (cf. Table 1). And secondly, equimolar mixtures of Si_3N_4 and $ZrSiO_4$ (series B) were taken, which after reaction form an Si_2N_2O composite containing 36 wt% ZrO_2. With the latter materials 0–8 wt% Al_2O_3 and 0–4 wt% Y_2O_3 were added as sintering aids.

Table 1. Characteristics of the materials prepared and the densities obtained after glass-encapsulated HIP for 2 h, 200 MPa, at 1600 (HIP1600) and 1700°C (HIP1700). In series A equimolar mixtures of Si_3N_4 and SiO_2 were used as the starting materials to form Si_2N_2O and zirconia; sintering aids were added separately. In series B equimolar mixtures of Si_3N_4 and $ZrSiO_4$ were used in a sintering reaction to form an Si_2N_2O–ZrO_2 composite with 36 wt% ZrO_2

Sample series	*Additives (wt%)*				*Density (g cm^{-3})*	
	ZrO_2	*$ZrO_2(Y_2O_3)$*	*Al_2O_3*	*Y_2O_3*	*HIP1600*	*HIP1700*
A	—	—	—	—	2·827	2·829
A	5	—	—	—	2·897	2·898
A	—	5	—	—	2·896	2·893
A	5	—	2	—	2·880	2·892
A	—	5	2	—	2·875	2·891
A	20	—	—	—	3·082	3·087
A	—	20	—	—	3·075	3·078
A	20	—	2	—	3·050	3·045
A	—	20	2	—	3·042	3·042
A	—	20	5	—	3·040	3·029
B	(36)	—	—	—	3·387	3·382
B	(36)	—	1	—	3·379	3·393
B	(36)	—	2	—	3·384	3·380
B	(36)	—	4	—	3·371	3·341
B	(36)	—	8	—	3·362	3·390
B	(36)	—	—	1	3·429	3·437
B	(36)	—	—	2	3·440	3·441
B	(36)	—	—	4	3·462	3·432
B	(36)	—	2	1	3·399	3·349
B	(36)	—	2	4	3·460	3·445

The source materials used were silicon nitride (H.C. Starck-Berlin, grade LC1), silicon dioxide (analytical purity), zirconium dioxide (Chema Tex, grade SC16), zirconium silicate (Ventron), aluminium oxide (Alcoa, grade A16SG), yttrium oxide (H.C. Stark-Berlin, finest grade) and yttrium oxide stabilized with 3 mol% Y_2O_3 (TOSOH, grade TZ-3Y). The starting powders were carefully weighed, mixed in water-free propanol and milled in a vibratory mill for 17 h with sialon milling media. After drying, the powder mixes were dry-pressed (125 MPa) into compacts of size 16 × 16 × 6 mm. The samples were glass-encapsulated and hot isostatically pressed at 1600 and 1700°C for 2 h with an argon pressure of 200 MPa.

Density measurements using Archimedes principle were made on the as-sintered samples. Hardness (HV_{10}) and indentation fracture toughness (K_{IC}) at room temperature were obtained by a

Vickers diamond indenter using 98 N (10 kg) load. The fracture toughness was evaluated by the formula given by Anstis *et al.*,[24] using a value of 290 GPa for Young's modulus, and the precision of repeated measurements on the same sample was ± 0·2. The phase analysis was based on X-ray powder patterns recorded by Guinier–Hägg cameras. Scanning electron microscopy (SEM) was performed on carbon-coated materials, using a Jeol JSM 6400 microscope equipped with Tracor System EDS and WDS analysers.

3 Results

3.1 Densification

HIPed materials from both preparation routes (series A and B) sintered at two temperatures (1600 and 1700°C) were examined by optical microscopy or SEM on polished cross-sections and were found to be virtually pore-free, i.e. fully dense. Thus densification took place even if the reaction of the starting materials to yield silicon oxynitride was sometimes poor (cf. below). It can be noted in Table 1 that the density of the equimolar Si_3N_4 + SiO_2 mix was found to be 2·83 g cm^{-3}, which at first looked surprisingly close to the theoretically calculated density of the silicon oxynitride structure, 2·82 g cm^{-3},[6] despite the observation that a reaction had not taken place. The mixture of equal volumes of silicon nitride (density ~3·2 g cm^{-3}) and silica (density ~2·6 g cm^{-3}) would, however, theoretically yield ~2·9 g cm^{-3} for a fully dense body, even when the oxynitride is not formed.

It was found that the measured density of the HIPed materials of series A increased as expected with increasing ZrO_2 additions (density ~5·9 g cm^{-3}) from 2·83 to 3·08 g cm^{-3} for 20 wt% ZrO_2. In series B the amount of zirconia formed by the *in-situ* reaction was considerably higher (36 wt%) and therefore the densities were higher and varied somewhat from 3·38 to 3·46 g cm^{-3} depending on the amount of sintering aid added. Small additions of alumina generally lowered the density slightly, whereas additions of yttria gave rise to a small increase in observed density.

3.2 X-ray diffraction phase analysis

The formation of the silicon oxynitride phase from silicon nitride and silica (series A) was strongly dependent on the addition of sintering aids and sintering temperature. The X-ray diffraction results are summarized in Table 2. Without any alumina or yttria added prior to sintering, no oxynitride phase were formed even at the higher temperature, and the crystalline content of the sample mainly reflected the Si_3N_4 initially added, where the α-Si_3N_4/β-Si_3N_4 ratio determined by X-ray diffraction (XRD) was 96:4. This phase ratio is unchanged at 1600°C, whereas at 1700°C some formation of the β-phase took place during sintering.

Table 2. Results of X-ray diffraction analysis of series A, where equimolar mixtures of Si_3N_4 and SiO_2 were used as the starting materials to form the parent Si_2N_2O-matrix and zirconia and/or sintering aids were added separately

Preparation temperature (°C)	*Additives (wt%)*			*XRD results*			
	ZrO_2	*ZrO_2(Y)*	*Al_2O_3*	*Phase analysis**	*Q*	*T*	*S*
1600	—	—	—	α, β	0·96	—	—
1600	5	—	—	α, β, ZrO	0·98	0·39	—
1600	—	5	—	α, β, ZrO,	0·92	1	—
1600	5	—	2	α, β, ZrO,	0·86	—	—
1600	—	5	2	α, ZrO, SNO	1	0·14	0·27
1600	20	—	—	α, ZrO	1	1	—
1600	—	20	—	α, β, ZrO	0·95	1	—
1600	20	—	2	α, ZrO, SNO	1	—	0·76
1600	—	20	2	α, ZrO, SNO	1	—	0·90
1600	—	20	5	α, ZrO, SNO	1	—	0·90
1700	—	—	—	α, β	0·91	—	—
1700	5	—	—	α, β, ZrO	0·92	1	—
1700	—	5	—	α, β, ZrO, SNO	0·73	0·45	0·86
1700	5	—	2	α, ZrO, SNO	1	—	0·88
1700	—	5	2	α, ZrO, SNO	1	0·50	0·91
1700	20	—	—	α, ZrO	1	0·34	—
1700	—	20	—	α, ZrO, SNO	1	—	0·89
1700	20		2	α, ZrO, SNO	1	0·33	0·92
1700	—	20	2	α, ZrO, SNO	1	—	1
1700	—	20	5	ZrO, SNO	—	0·10	1

*α and β denote α- and β-Si_3N_4, respectively, and ZrO and SNO denote ZrO_2 and Si_2N_2O, respectively.
Q= α/(α + β)–Si_3N_4 phase ratio.
T= Tetragonal /(tetragonal + monoclinic + cubic)–ZrO_2 phase ratio.
S= Si_2N_2O/(α-Si_3N_4 + β-Si_3N_4 + Si_2N_2O) phase ratio.

At the lower sintering temperature only yttria-doped ZrO_2 combined with alumina addition supported formation of the silicon oxynitride phase in series A. The added zirconia was found to be present as the monoclinic and tetragonal forms in the sintered materials and the relative amount of each phase was roughly estimated by comparison of peak height ratios. Small amounts of cubic ZrO_2 present simultaneously with the tetragonal phase are difficult to detect because of extensive peak overlap. Occasionally a few very weak peaks occurred in the X-ray spectra, which were not possible to identify with any certainty. However, some of the weak peaks indicate the presence of the phases ZrN and $Zr_7O_{11}N_2$.

At the higher sintering temperature (1700°C) the composites of series A formed more silicon oxynitride, but only in the material with the highest amount of alumina added to an yttria-doped zirconia was complete reaction of the starting materials to Si_2N_2O achieved. At this temperature the yttria-doped zirconia itself also promoted a fair degree of oxynitride formation, whereas addition of pure zirconia had no observable positive effect (cf. Table 2). Again weak peaks occurred indicating the presence of small amounts of additional phases.

The phase analysis of the materials formed by reaction of silicon nitride with zirconium silicate (series B) is summarized in Table 3. At the lower temperature (1600°C) the reaction is mostly incomplete, as greater or lesser amounts of silicon nitride were identified in HIPed materials. Residual $ZrSiO_4$ is, however, only found in the materials with no addition of sintering aids or with only 1 wt% alumina added. The amount of silicon oxynitride formed seems to be relatively independent of the amounts of alumina or yttria added, and even with both sintering aids added simultaneously complete reaction was not obtained at this temperature. Weak additional X-ray peaks were also found in these samples.

The results obtained for series B at 1700°C are quite different and complete reaction to form $Si_2N_2O + ZrO_2$ has occurred for all materials. The zirconia identified in these preparations by XRD was sometimes present as either monoclinic or tetragonal ZrO_2, but often as a mixture of the two crystal modifications.

3.3 Mechanical properties

The use of the HIP technique assured that all materials were fully dense even if the formation of silicon oxynitride was not always complete. In this way the mechanical properties of the ceramics could still be evaluated. Thus, the room temperature Vickers hardness (HV_{10}) and indentation fracture toughness (K_{IC}) were measured on all materials and the results are summarized for series A and B in Tables 4 and 5, respectively.

It can be seen that in both series the hardness is ~12–14 GPa and the fracture toughness is typically between 2·2 and 3·5 MPa $m^{1/2}$. No improvement

Table 3. Results of X-ray diffraction analysis of series B, where equimolar mixtures of Si_3N_4 and $ZrSiO_4$ were used in sintering reaction to form a Si_2N_2O composite with 36 wt% ZrO_2

Preparation temperature (°C)	*Additives (wt%)*		*Phase analysis**	*XRD results*		
	Al_2O_3	Y_2O_3		*Q*	*T*	*S*
1600	—	—	α, ZrO, SNO, $ZrSiO_4$	1	—	0·55
1600	1	—	α, ZrO, SNO, $ZrSiO_4$	1	—	0·69
1600	2	—	α, ZrO, SNO	1	—	0·71
1600	4	—	ZrO, SNO	—	0·02	1
1600	8	—	α, ZrO, SNO	1	0·31	0·83
1600	—	1	α, ZrO, SNO	1	0·92	0·42
1600	—	2	α, ZrO, SNO	1	1	0·73
1600	—	4	α, ZrO, SNO	1	1	0·45
1600	2	1	α, ZrO, SNO	1	0·03	0·67
1600	2	4	α, ZrO, SNO	1	1	0·95
1700	—	—	ZrO, SNO	—	0·10	1
1700	1	—	ZrO, SNO	—	0·03	1
1700	2	—	ZrO, SNO	—	0·2	1
1700	4	—	ZrO, SNO	—	—	1
1700	8	—	ZrO, SNO	—	0·03	1
1700	—	1	ZrO, SNO	—	1	1
1700	—	2	ZrO, SNO	—	1	1
1700	—	4	ZrO, SNO	—	0·26	1
1700	2	1	ZrO, SNO	—	0·27	1
1700	2	4	ZrO, SNO	—	1	1

*α and β denote α- and β-Si_3N_4, respectively, and ZrO and SNO denote ZrO_2 and Si_2N_2O, respectively.
Q= $\alpha/(\alpha + \beta)$–Si_3N_4 phase ratio.
T= Tetragonal /(tetragonal + monoclinic + cubic)-ZrO_2 phase ratio.
S= $Si_2N_2O/(\alpha\text{-}Si_3N_4 + \beta\text{-}Si_3N_4 + Si_2N_2O)$ phase ratio.

Table 4. Room temperature hardness (HV_{10}) and indentation fracture toughness (K_{1C}) of series A. Equimolar mixtures of Si_3N_4 and SiO_2 were used as the starting materials to form the parent Si_2N_2O-matrix and zirconia and/or sintering aids were added separately

Preparation temperature (°C)	*Additives (wt%)*			HV_{10} *(GPa)*	K_{1C} *(MPa m$^{1/2}$)*
	ZrO_2	*ZrO_2(Y)*	*Al_2O_3*		
1600	—	—	—	13·0	3·5
1600	5	—	—	12·6	4·0
1600	—	5	—	12·4	2·9
1600	5	—	2	12·7	2·8
1600	—	5	2	13·9	2·3
1600	20	—	—	12·4	2·9
1600	—	20	—	12·5	2·9
1600	20	—	2	14·0	2·3
1600	—	20	2	14·4	2·2
1600	—	20	5	13·8	2·5
1700	—	—	—	12·6	2·7
1700	5	—	—	13·1	2·3
1700	—	5	—	13·8	2·1
1700	5	—	2	13·2	2·0
1700	—	5	2	12·5	2·1
1700	20	—	—	12·3	2·8
1700	—	20	—	13·1	2·3
1700	20	—	2	13·4	2·3
1700	—	20	2	14·1	2·2
1700	—	20	5	13·8	2·2

of the fracture toughness of series A seems to occur when increasing amounts of zirconia are added. In series B, which contains a considerable amount of zirconia, the ceramics are still brittle and only addition of alumina seems to have some small positive effect on the toughness. In the latter series addition of yttria alone gives a slightly higher hardness. The magnitude of the properties, however, are low compared with a typical silicon nitride based ceramic and more nearly resemble values typical for oxide ceramics. This will be discussed below as these values are correlated to either incomplete chemical reaction or the nature of the phases present.

Table 5. Room temperature hardness (HV_{10}) and indentation fracture toughness (K_{1C}) of series B, where equimolar mixtures of Si_3N_4 and $ZrSiO_4$ were used in a sintering reaction to form a Si_2N_2O composite with 36 wt% ZrO_2

Preparation temperature (°C)	*Additives (wt%)*		HV_{10} *(GPa)*	K_{1C} *(MPa m$^{1/2}$)*
	Al_2O_3	*Y_2O_3*		
1600	—	—	13·1	2·7
1600	1	—	12·5	2·6
1600	2	—	12·4	2·9
1600	4	—	12·0	3·4
1600	8	—	12·4	2·9
1600	—	1	12·4	3·0
1600	—	2	12·7	2·3
1600	—	4	12·3	2·5
1600	2	1	11·6	2·8
1600	2	4	13·4	2·6
1700	—	—	12·9	2·6
1700	1	—	13·0	2·8
1700	2	—	12·8	3·1
1700	4	—	12·5	3·5
1700	8	—	12·3	3·4
1700	—	1	13·2	2·6
1700	—	2	13·6	2·3
1700	—	4	14·1	2·2
1700	2	1	12·6	2·8
1700	2	4	12·9	2·6

3.4 Microstructure

Generally, the materials which consisted of more or less unreacted starting powders have a very small grain size, ≤ 1 μm, and only the phases rich in zirconium were easy to distinguish. This was especially true for many of the samples HIPed at 1600°C (see Fig. 1).

For series A sintered at 1700°C all samples are very brittle (see above) and thus have not been studied in detail. However, as an example of such a structure, the sample containing 20 wt% yttria-doped zirconia is shown in Fig. 2. The structure is seen to be very fine grained. Many of the zirconia grains are smaller than 0·2 μm. A few larger α-Si_3N_4 grains can also be seen.

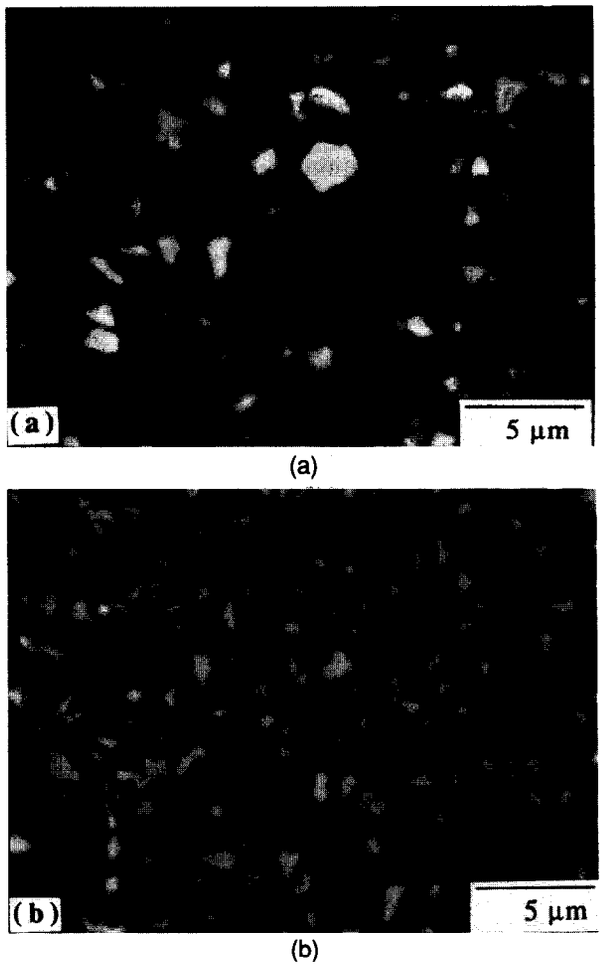

Fig. 1. SEM image of sample in series A containing 20 wt% ZrO_2 (a) and sample in series B containing 8 wt% Al_2O_3 as sintering aid (b), sintered at 1600°C. The bright areas correspond to the zirconia grains, whereas the dark area is a mixture of the other phases which formed.

Fig. 2. SEM image of sample in series A containing 20 wt% yttria-stabilized zirconia as sintering aid.

In series B sintered at 1700°C the maximum fracture toughness was achieved when only alumina was used as sintering aid (see above). When comparing the sample containing no sintering aid [Fig. 3(a)] with the one containing 8 wt% alumina [Fig. 3(c)], it can be seen that the addition of alumina increases the size of the zirconia grains. Without any sintering aid the zirconia grains are very small (< 1 μm), whereas the size of the grains has increased to ~4 μm in the alumina-containing sample. When comparing the size of the zirconia grains as the amount of alumina added increases gradually, i.e. including the sample containing 4 wt% alumina [Fig. 3(b)], it can be seen that the size of the zirconia grains is dependent on the alumina content. The composition does not, however, affect the size of the Si_2N_2O grains as much. The grains are needle-shaped with a length of ~4 μm and a short axis of ~0·5 μm. This is also true for the remaining samples in this series.

Also seen in Figs 3(a)–(c) is the effect of the zirconia grain size on the shape of the various crack paths. In the sample with the smallest grains [Fig. 3(a)] the crack path is fairly straight and transgranular and only weakly influenced by the zirconia grains. In the samples with the largest zirconia grains [Figs 3(a) and (b)] the crack path is much more winding and seems to develop in both a trans- and intragranular way.

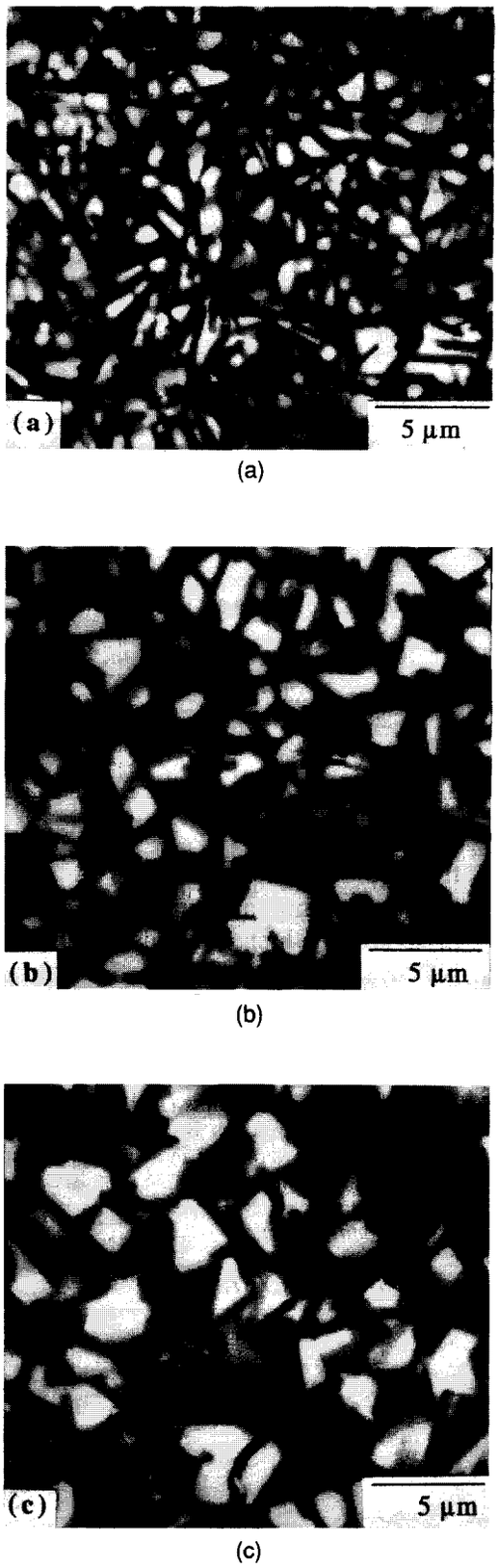

Fig. 3. SEM images showing the microstructure and representative crack deflection profiles of the undoped sample (a) and samples containing 4 wt% (b) and 8 wt% alumina (c) in series B, sintered at 1700°C.

4 Discussion

For both preparation routes, as expected, an increase in sintering temperature was found to affect the reaction to form silicon oxynitride. However, the dissolution of the starting material in the transient liquid and the transport of species by diffusion will in these cases also be important rate controlling steps. This is clearly seen for the reaction of silicon nitride with silica (series A), where additions of sintering aids to lower the viscosity is crucial. At 1600°C addition of both alumina plus yttria (released from the zirconia) was needed to lower the viscosity of the silica melt

to an extent where a sufficiently rapid diffusion occurred, whereas at the higher temperature both alumina addition or yttria from $ZrO_2(Y_2O_3)$ can achieve this effect. It should be stressed, however, that addition of pure zirconia did not help even at the higher temperature used (1700°C).

These observations are in agreement with earlier findings where silicon nitride and silica mixtures with additions of ZrO_2 or ZrO_2(2·8 mol% Y_2O_3) were hot-pressed at 1700°C.[10] It was found that the reaction rate for the Si_2N_2O formation was slow for the pure ZrO_2 additions, whereas Y_2O_3 released from ZrO_2(2·8 mol% Y_2O_3) additions increased the reaction rate considerably. The previous authors suggested that this behaviour was caused by the fairly high eutectic temperature of 1590°C found for the ZrO_2–SiO_2–Si_3N_4 system, whereas some yttrium released from the yttria-stabilized zirconia would lower both the eutectic temperature and the viscosity of the liquid significantly.

When silicon nitride reacts with zirconium silicate the decomposition of this phase will become important. As $ZrSiO_4$ is not stable at temperatures above 1675°C,[25] this will stimulate the reaction at the higher sintering temperature, and indeed all materials HIPed at 1700°C were found to be fully reacted. At the lower temperature, however, the reaction to form silicon oxynitride is surprisingly unaffected by sintering additives, which indicates that diffusion through a transient liquid is less important in determining the reaction rate. The results thus imply that the dissolution of the zirconia silicate into the liquid may be the rate controlling step in this case.

The solubilities of zirconia or zirconium silicate at 'low' temperatures in silica or silicon oxynitride liquids are not well known, but it is generally expected that the solubility is low because zirconia additions can be used as nucleation agents in glass ceramics. At higher temperatures, however, a fair amount of these zirconium compounds may dissolve as shown by Cheng and Thompson.[26] They observed that the solubility of ZrO_2 increases to ~10 wt% at 1700°C. The dissolved zirconia will, however, precipitate rapidly during cooling from this temperature. Rapid solidification of zirconia that has been partly dissolved and has acted as an sintering aid also seems to take place for Si_3N_4–ZrO_2 composites prepared at 1750°C.[20] This can schematically be illustrated in a Jänecke prism for two temperatures below and above the decomposition of $ZrSiO_4$ and is shown as the increasing solubility of Zr in the liquid in Fig. 4. The reaction of silicon nitride with zirconium silicate at the lower temperature proceeds slowly due to limited Zr solubility, whereas at the higher temperature

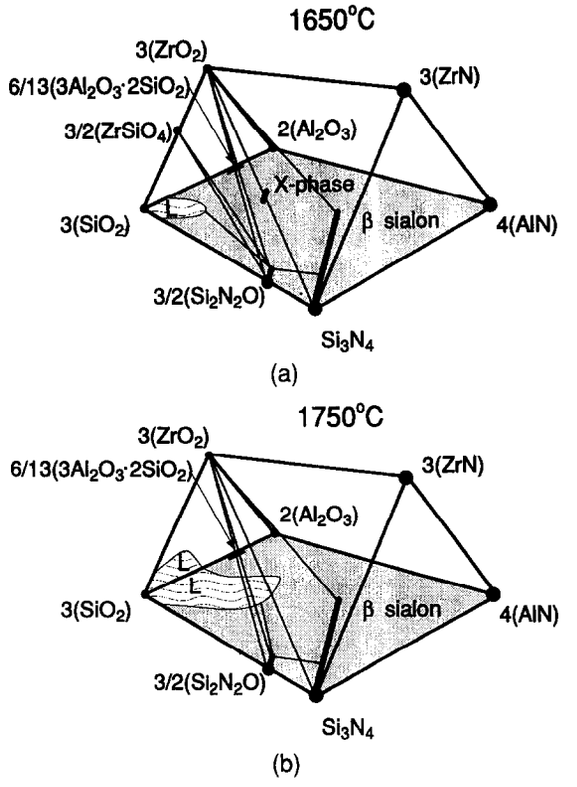

Fig. 4. Zr–Si–Al–O–N system at (a) 1650°C and (b) 1750°C, represented as Jänecke prisms.

the silicate will dissociate into zirconia + silica and the Zr solubility is drastically increased and thus opens a path for rapid reaction. Addition of up to 4 wt% yttria to the starting mix at the lower temperature does not appear to improve the degree of reaction significantly. Other sintering aids such as Sm_2O_3, however, have been reported to have a remarkably positive effect for such small additions.[21,22] Sintering temperatures of 1500–1550°C could be used, which is well below the dissociation temperature of zirconium silicate, and dense materials were obtained.

The hardness values obtained in this study were of the order of 12–14 GPa, which can be compared with 15·2 and 15·0 GPa reported for dense Si_2N_2O and O'sialon ceramics, respectively.[6,7] The reaction to the oxynitride was incomplete in many of the silicon nitride/silica preparations and the observed hardness is affected negatively by the fairly soft silica glass. In addition, zirconia does not form very hard ceramics (~10 GPa) and when present in large amounts in the composites this will lower the hardness value. In series B HIPed at 1700°C, for instance, the materials have reacted to Si_2N_2O containing ~24 vol% ZrO_2 and the expected hardness is about 13–14 GPa, in fair agreement with the observed values.

The reported fracture toughness of dense Si_2N_2O and O'sialon ceramics is of the order of 3·1–3·5 MPa $m^{1/2}$.[6,7] In this study, however, the materials are generally more brittle, with the

exception of the ceramics of series B sintered at 1700°C containing only alumina as sintering aid, which reaches this level. Since there is only a very small amount of tetragonal zirconia present ($T<0{\cdot}03$), transformation toughening is not responsible for this. However, in these samples the size of the zirconia grains has increased compared with the other samples. It thus appears that this influences the fracture toughness in a positive manner. This can be seen when comparing the different crack paths in the different samples. In the samples containing the largest zirconia grains the crack path is more irregular compared to the samples with the smallest zirconia grains. The cracks develop in both a trans- and intragranular way. Since there are a number of factors influencing the crack deflection pattern, i.e. the composition of the intergranular phase, the strength of the interfacial bonding and the different thermal expansion coefficients of the different phases (none of which has been determined), it is not easy to determine the crack growth mechanism or why the fracture toughness increases in these samples. However, it should be stressed that the addition of zirconia or stabilized zirconia does not appear to have any positive effect on the fracture toughness. This is perhaps unexpected, but similar findings have been reported previously for zirconia added to silicon nitride.[20] This phenomenon has been discussed in depth by Cheng *et al.*[15] They concluded that by dissolution of nitrogen into the zirconia, which simultaneously created oxygen vacancies in the crystal lattice, the non-transformable tetragonal zirconia (t') phase forms. No transformation toughening will therefore be possible, although a tetragonal phase might be confirmed to be present by XRD.

The preparation of Si_2N_2O–ZrO_2 composites is less straightforward and the observed mechanical properties are lower than those obtained for the O'sialon ceramics.[7] In addition, the oxygen resistance of the former materials has been reported to be inferior at high temperatures,[14] especially compared with pure Si_2N_2O.[3–5]

5 Conclusions

The reaction of Si_3N_4 with SiO_2 is strongly dependent on the addition of sintering aids, and is also affected by temperature, whereas the reaction of Si_3N_4 with $ZrSiO_4$ was mainly temperature controlled and proceeded rapidly at 1700°C. Addition of zirconia or stabilized zirconia did not appear to have any positive effect on the toughness and the prepared materials were, in general, brittle with a fracture toughness of ~3 MPa $m^{1/2}$. The observed hardness was typically 12–14 GPa for the composites. Generally, the composites which consisted of more or less unreacted starting materials had a very fine-grained microstructure. In the fully reacted samples which had the highest fracture toughness the zirconia grains had increased in size compared to the more brittle samples.

References

1. Heuer, A. H. & Lou, V. L. K., Volatility diagrams for silica, silicon nitride and silicon carbide, and their application to high-temperature decomposition and oxidation. *J. Am. Ceram. Soc.*, **73** (1990) 2785–803.
2. Billy, M. & Desmaison, J. G., High temperature oxidation of silicon-based structural ceramics. *High Temp. Technol.*, **4** (1986) 131–9.
3. Ohashi, M., Kanzaki, S. & Tabata, H., Processing, mechanical properties and oxidation behaviour of silicon oxynitride ceramics. *J. Am. Ceram. Soc.*, **74** (1991) 109–14.
4. O'Meara, C., Sjöberg, J., Dunlop, G. & Pompe, R., Oxidation of pressureless sintered Si_2N_2O materials. *J. Europ. Ceram. Soc.*, **7** (1991) 369–78.
5. Persson, J., Käll, P.-O. & Nygren, M., Interpretation of the parabolic and non-parabolic oxidation behaviour of Si_2N_2O. *J. Am. Ceram. Soc.*, **75** (1992) 3377.
6. Larker, R., Reaction sintering and properties of silicon oxynitride densified by HIP. *J. Am. Ceram. Soc.*, **75** (1992) 62–6.
7. Ekström, T., Olsson, P.-O. & Holmström, M., Formation and properties of O'-Sialon ceramics prepared by hot isostatic pressing. *J. Europ. Ceram. Soc.*, **12** (1993) 165–76.
8. Ekström, T., Holmström, M. & Olsson, P.-O., Yttria doped Si_2N_2O ceramics. In *Ceramic Materials and Components for Engines*, eds R. Carlsson., T. Johansson and L. Kahlman. Elsevier Applied Science Publishers, London, 1991, pp. 432–9.
9. Huang, Z. K., Greil, P. & Petzow, G., Formation of silicon oxynitride from Si_3N_4 and SiO_2 in the presence of Al_2O_3. *Ceram. Int.*, **1** (1984) 14–17.
10. Ohashi, M., Kanzaki, S. & Tabata, H., Effect of additives on some properties of silicon oxynitride ceramics. *J. Mater. Sci.*, **26** (1991) 2608–14.
11. Bergman, B. & Heping, H., The influence of different oxides on the formation of Si_2N_2O from SiO_2 and Si_3N_4. *J. Europ. Ceram. Soc.*, **6** (1990) 3–8.
12. Ohashi, M., Hirao, K., Nagaoka, T., Watari, K., Yasuoka, M., Kanzaki, S. & Shimamori, T., Preparation of dense silicon oxynitride ceramics by HIPing. *Br. Ceram. Trans. J.*, **91** (1992) 202–7.
13. O'Meara, C., Pompe, R. & Rundgren, K., The microstructure of Si_2N_2O/ZrO_2 composite ceramics. In *Advanced Structural Inorganic Composites*, ed. P. Vincenzini. Elsevier Science Publishers, London, 1991, pp. 179–87.
14. O'Meara, C., The microstructure and the oxidation behaviour of Si_2N_2O/ZrO_2 composites. In *Ceramic Materials & Components for Engines*, eds R. Carlsson, T. Johansson and L. Kahlman. Elsevier Applied Science Publishers, London, 1991, pp. 252–9.
15. Cheng, Y., O'Meara, C., Slasor, R. & Thompson, D. P., Some features and limitations of zirconia toughened nitrogen ceramics. In *Ceramic Materials and Components for Engines*, eds R. Carlsson, T. Johansson and L. Kahlman. Elsevier Applied Science Publishers, London, 1991, pp. 657–64.
16. Falk, L. K. L. & Rundgren, K., Microstructure and short-term oxidation of hot-pressed $Si_3N_4/ZrO_2(+Y_2O_3)$ ceramics. *J. Am. Ceram. Soc.*, **75** (1992) 28–35.
17. Lange, F. F., Falk, L. K. L. & Davies, B. I., Structural

ceramics based on Si_3N_4–ZrO_2(+Y_2O_3) compositions, *J. Mater. Res.*, **2** (1987) 66–76.
18. Claussen & Jahn, J., Mechanical properties of sintered and hot-pressed Si_3N_4–ZrO_2 composites. *J. Am. Ceram. Soc.*, **61** (1978) 94–5.
19. Dutta, S., & Buzek, B., Microstructure, strength and oxidation of a 10 wt% zyttrite–Si_3N_4 ceramic. *J. Am. Ceram Soc.*, **67** (1984) 89–92.
20. Ekström, T., Falk, L. K. L. & Knutson-Wedel, E. M., Si_3N_4–ZrO_2 composites with small Al_2O_3 and Y_2O_3 additions – prepared by HIP, *J. Mater. Sci.*, **26** (1991) 4331–40.
21. Cheng, Y.-B. & Thompson, D. P., ZrO_2/O'Sialon composites containing mixed additives. *Mater. Forum*, **16** (1992) 307–12.
22. Cheng, Y.-B. & Thompson, D. P., Densification of zirconia-containing O'Sialon composites by Sm_2O_3. *J. Mater. Sci.*, **28** (1993) 3097–102.
23. Lange, F. F., Compressive surface stresses developed in ceramics by an oxidation-induced phase change. *J. Am. Ceram. Soc.*, **63** (1980) 38–40.
24. Anstis, G. R., Chantikul, P., Lawn, B. R. & Marshall, D. B., A critical evaluation of indentation techniques for measuring fracture toughness. *J. Amer. Ceram. Soc.*, **64** (1981) 533–8.
25. Butterman, W. C. & Foster, W. R., Zirkon stability and the ZrO_2–SiO_2 phase diagram. *Am. Mineral.*, **53** (1967) 880–7.
26. Cheng, Y.-B. & Thompson, D. P., The behaviour of ZrO_2 in Y_2O_3–Al_2O_3–SiO_2 glasses. *Br. Ceram. Trans. J.*, **87** (1988) 107–10.

Journal of the European Ceramic Society 16 (1996) 545–551

0955-2219(95)00127-1
0955-2219/96/$15.00

Mechanical Property Characterization of 9 Mol% Ce-TZP Ceramic Material — II. Fracture Toughness

G. A. Gogotsi,[a] V. P. Zavada[a] & M. V. Swain[b]

[a]Institute for Problems of Strength, National Academy of Sciences, 252014 Kiev, Ukraine
[b]Department of Mechanical and Mechatronic Engineering, The University of Sydney, NSW 2006, Australia

(Received 5 August 1994; revised version received 28 June 1995; accepted 14 July 1995)

Abstract

Fracture toughness testing of four 9 mol% Ce-TZP materials with differing grain sizes has been conducted. Single edge notched beam tests revealed significant differences in the stable force–displacement response during crack extension between these materials. In all instances there was a marked difference between optical and compliance estimates of crack length. This leads to two estimates of the R*-curve response for all the materials. Acoustic emission and transformation zone size was also monitored during crack extension. The observations are discussed in terms of autocatalysis of the phase transformation in Ce-TZP materials.*

1 Introduction

Fracture toughness estimation of Ce-TZP materials has been conducted by a number of authors.[1–4] In all instances very large transformation zones and high fracture toughness values have been obtained. However, such large and non-uniform zones about the crack tip are different from other phase transforming partially stabilized ceramics (Mg-PSZ or Y-TZP). This observation has led to modelling analysis by Marshall[5] and more recently Stump[6,7] has presented a simulation of this behaviour.

In a previous study of the same Ce-TZP materials, Liu *et al.*[4] showed that the measured fracture toughness depended upon the sample testing geometry and basis of interpretation of the data. The size and shape of the transformation zone depended upon whether tests were conducted on single edge notched beam (SENB) or compact tension (CT) geometries. The fracture toughness and zone size were smaller in the SENB than the CT test pieces. Also the form of the *R*-curve was very different, depending upon whether linear elastic fracture mechanics (LEFM) or a *J*-integral approach was adopted for interpretation of the data. There is some question as to whether the *J*-integral is a valid approach because of the nature of the 'plasticity' about the crack tip and, as will be discussed here, the estimation of crack length.

This paper presents SENB observations of crack extension in relatively small samples. The crack extension is followed by monitoring changes in compliance, optical crack length and acoustic emission (AE). From such data the *R*-curves are calculated and related to AE events and transformation zone area.

2 Experimental Procedures

The materials evaluated have been described in Part I of this study.[8] Fracture toughness tests were performed in a three-point flexure rig with a 20 mm span between supports. Specimens were of dimensions 4·8 × 2·8 × 25 mm with an initial notch of 2·4 mm. To facilitate optical observations of nucleation and propagation of crack extension and transformation zone size, one of the specimen lateral sides was polished. AE signals and precision deflection were determined in the manner described in Part I.[8]

3 Observations and Discussion

3.1 Force–displacement behaviour

Force–displacement observations during crack extension of the four Ce-TZP samples are shown in Figs 1–4. In all instances the crack extension behaviour was very stable. The residual crack opening displacement increased with grain size from Ce-TZP-I to Ce-TZP-IV. Also the onset of crack growth, particularly in the case of Ce-TZP-III an Ce-TZP-IV did not occur until significant offset (marked on the figures) of the force–displacement curve. The numbers within the loops relate to the load–unloading cycles.

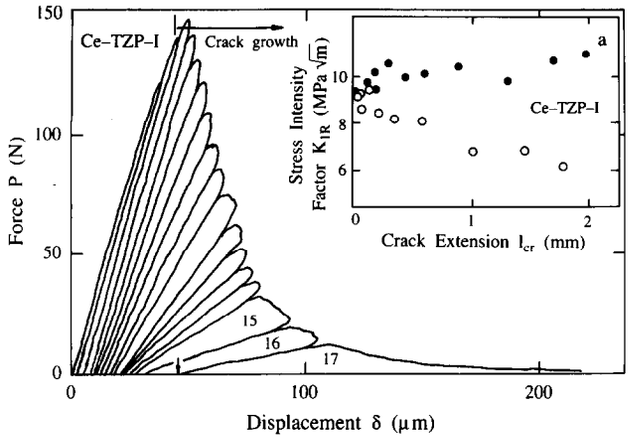

Fig. 1. Force–displacement data during crack extension of Ce-TZP-I. The arrows at the bottom of the figure are where the photographs of the crack tip were taken. The number within the loop is the fracture cycle. Inset shows the computed stress intensity factor versus crack extension l_{cr}. (●), Optically measured crack length; (○), compliance estimates of crack length.

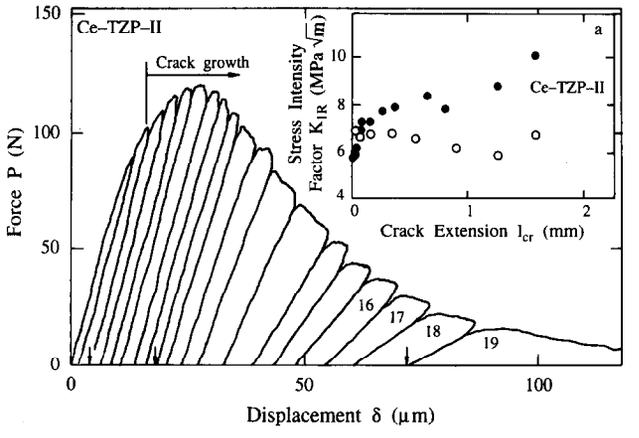

Fig. 2. Force–displacement data for crack extension in Ce-TZP-II. Inset shows computed stress intensity factor versus crack extension for optical and compliance estimates of crack length.

3.2 Fracture toughness: *R*-curves

Two approaches were used to estimate the fracture toughness, the optical measurement of the crack length and that from the compliance of the load–unloading curves in Figs 1–4. The two calculations of critical stress intensity factor versus crack length are shown in the insets to Figs 1–4. In both instances the stress intensity factor was calculated from the standard relationship:[9]

$$K = Y(a/W)\sigma \sqrt{a} \qquad (1)$$

where $Y(a/W)$ is the usual modifying factor, σ is the nominal flexure stress from peak load in the absence of a crack, a is the crack length and W the specimen width.

The *R*-curves determined from the compliance and optical observations show different trends. From the optical measurements the *R*-curve appears to increase with crack extension, whereas from the compliance measurements the toughness appears to decrease with crack extension. This

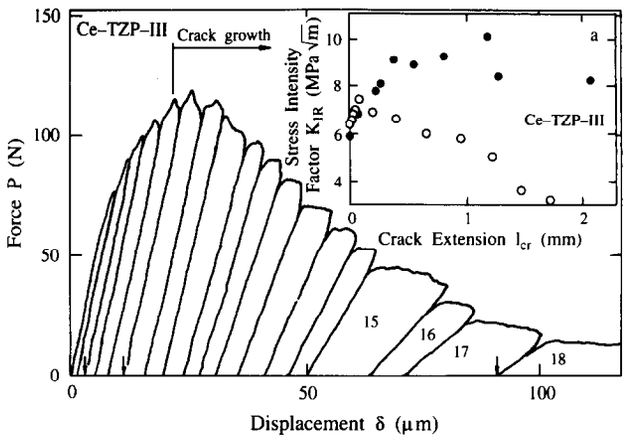

Fig. 3. Force–displacement data for crack extension in Ce-TZP-III. Inset shows computed stress intensity factor versus crack extension for optical and compliance estimates of crack length.

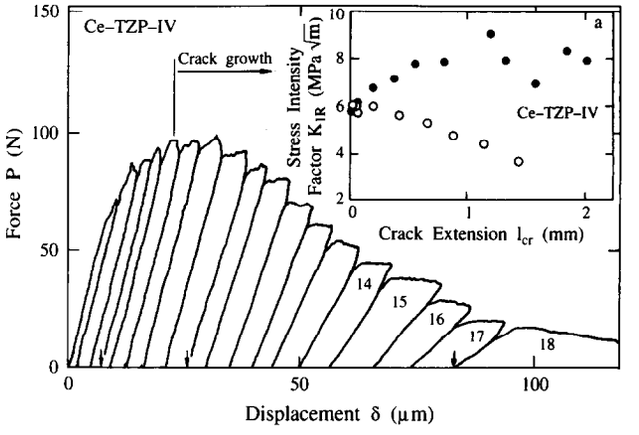

Fig. 4. Force–displacement data for crack extension in Ce-TZP-IV. Inset shows computed stress intensity factor versus crack extension for optical and compliance estimates of crack length.

Table 1. Grain size and work of fracture for Ce-TZP ceramics

Material	*Grain size (μm)*	$\gamma(J\,m^{-2})$	$K_c = \sqrt{2\gamma E}\ (MPa\ m^{1/2})$
Ce-TZP-I	1·14	308	10·4
Ce-TZP-II	1·62	454	12·6
Ce-TZP-III	2·22	494	13·1
Ce-TZP-IV	3·0	452	12·6

arises from the significant differences in the estimated crack lengths from the two approaches used. From the peak load values and calculated *R*-curves, Ce-TZP-I is tougher than the remaining samples. However, if one compares the work of fracture calculated from the area under the entire force displacement curve a different conclusion is reached; namely that Ce-TZP-III has the highest toughness, as listed in Table 1.

3.3 Compliance observations

The compliance values for all the load cycles were measured directly from the slopes of the loading-unloading cycles in Figs 1–4. The crack length was calculated from the specimen compliance using the relationship:[10]

$$\frac{C^c}{C_o} = 1 + 4{\cdot}5 \int_o^{\alpha} [Y(\alpha)]^2 \, \alpha \, d\alpha \qquad (2)$$

where C_o is the specimen compliance without a notch, C^c is the compliance measured experimentally, Y is the modifying parameter after Strawley[11] and $\alpha = a/W$.

The difference between optical and compliance estimates of the crack length are shown in Fig. 5 for all the Ce-TZP materials. In all instances the compliance estimates of crack length a^c are much less than the optically measured a^o values. More critical appreciation of the influences of the individual microstructures on this difference may be seen by comparing the ratio of the optical to the measured compliance (C^o/C^c) versus optically measured crack length, as shown in Fig. 6. A simple linear relationship was found to exist between these parameters which could be expressed by:

$$\frac{C^o}{C^c} = A + k_3 \, a^o \qquad (3)$$

The basis for these differences in compliance being caused by measurement errors is excluded, as

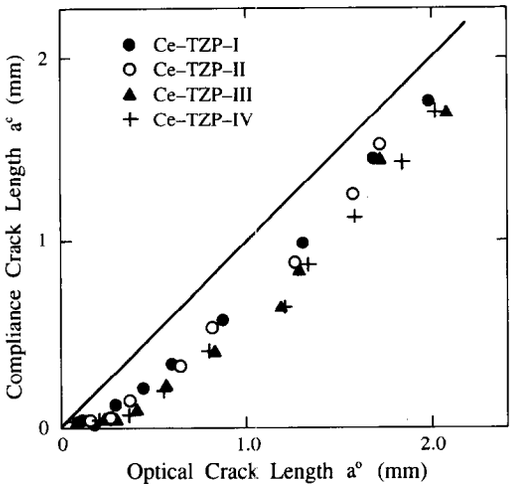

Fig. 5. Comparison between optical a^o and compliance a^c estimates of crack length for Ce-TZP materials.

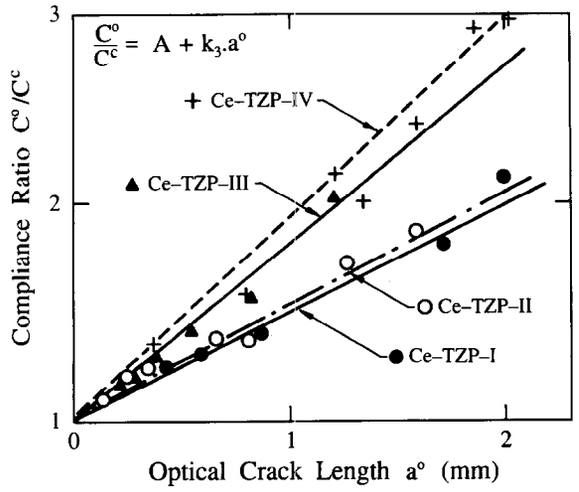

Fig. 6. Plot of ratio of optical and measured compliance (C^o/C^c) versus optically measured crack length a^o.

excellent correlation between the two approaches has been previously reported by Gogotsi *et al.*[12] for other non-transforming ceramics including glass and polycrystalline alumina. It is also argued that optical measurement errors would tend to underestimate crack length and further increase the discrepancy found in Fig. 5 because of the very narrow crack opening displacement near the crack tip. Errors in the determination of the slope of the load-displacement curves of Figs 1–4 and thereby the estimated compliance do not exceed 5%, whereas the discrepancy between the optical and determined compliance reaches more than 200%.

The slope of the ratio of C^o/C^c shows a clear increase with Ce-TZP materials I to IV, which corresponds to the increase in grain size.[8] The discrepancy between a^c and a^o, C^c and C^o leads to uncertainty in the estimation of the J-integral value for toughness. This arises because the J-integral is calculated with the aid of both load–displacement curves, as well as the actual crack length. In the current situation the contradictory features of both these measurements are likely to compound errors in its calculation.

3.4 Transformation zones

Optical observations of the transformation zone about the notch and crack tip were made at the positions marked by arrows in Figs 1–4. These micrographs are shown in Figs 7–10. No pronounced transformation zone was observed during the fracture toughness testing of the Ce-TZP-I material for different crack lengths (Fig. 7). However the force displacement observations (Fig 1) and the optical micrographs (Fig 7) show significant residual crack opening displacement. Whereas, for the remaining materials, the transformation zones were clearly visible in a manner that enabled both the complex shape of the zone and the crack length to be appreciated. For Ce-TZP-II to Ce-TZP-IV the cycle by cycle observations revealed that the zones did not grow in a continuous manner but rather in jump-like needle-shaped zones of different widths and lengths emanating from the notch region. There is a trend of increasing length and width of such zones for materials II to IV. As the load increases the number of bands increases and they coalesce forming a continuous zone at the notch tip which then re-extends as several separate needle-like zones. A crack usually nucleates within the continuous zone, and as the crack grows this continuous zone also advances ahead of the crack tip.

From the observations in Figs 7–10 the area of transformation about the crack tip as a function

Fig. 7. Optical micrograph of the notch and crack extending from the notch in Ce-TZP-I. The photograph (at × 70) was taken at the position arrowed in Fig 1.

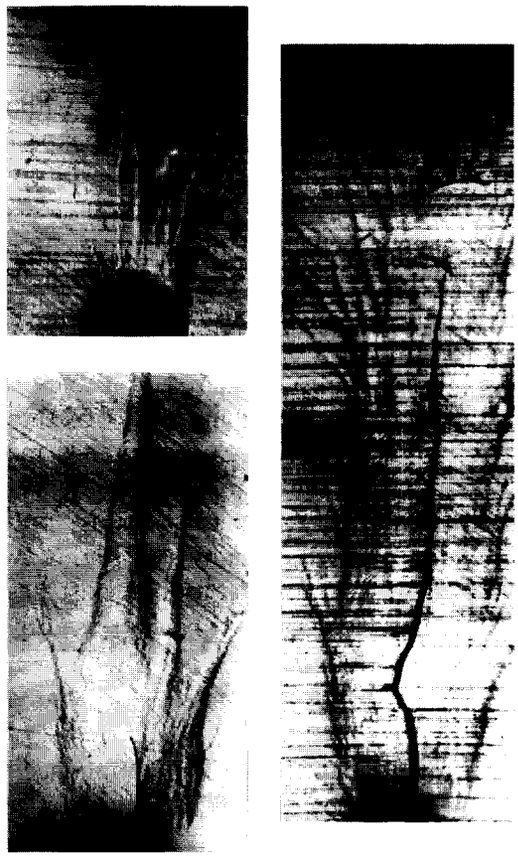

Fig. 8. Micrographs of the crack and associated transformation zone during crack extension in Ce-TZP-II. The photograph (at × 70) was taken at the positions arrowed in Fig. 2.

of crack extension may be estimated. Such measurements are shown in Fig. 11. A linear relationship may be readily fitted to the data relating the transformation zone area S to the crack length, namely:

$$S = S_o + k_4 a^o \quad (4)$$

In Fig. 11 S_o, the intercept, provides an estimate of the precrack nucleation size of the transformation zone about the initiating notch. Then, as shown schematically in Fig. 12, this zone extends ahead of the crack during propagation. Thus it is not surprising that a near one-to-one correlation exists between the slope of the data k_4 and the width of the zone W.

3.5 Acoustic emission

Considerable differences between the AE activity of the different materials were observed. The Ce-TZP-I material did not emit detectable events above the background noise.

The AE events were detected only when a pronounced t → m transformation zone is formed and there appears to be no correlation between the number of AE events (N_Σ) and the transformed area (Fig. 13). The probable reason for this behaviour is that AE activity is largely determined not by the size of the transformation zone area but the jump-like manner in which it is formed and the number of such occurrences. As shown in Part I of this study,[8] the number of AE counts was correlated with the number of bands rather than their width.

Another feature from the results in Fig. 13 is that the commencement of AE activity did not coincide with crack nucleation and growth. The absence of AE events in the Ce-TZP-I material, despite their occurrence during the beam flexure testing, suggests that crack growth is accompanied by much lower intensity activity than the burst-like t → m transformations. The results for the Ce-TZP-I would indicate that without burst activity AE events do not occur. The absence of AE activity and any discernable transformation zone about the crack tip, despite the significant residual crack opening displacement, is consistent with the observations made in Part I of this study.[8] In the previous paper the residual flexural displacement upon unloading did not correlate with the number of transformation bands and in fact the initial permanent set occurred in the absence of any bands or AE activity. It was suggested that this may be due to ferroelastic grain reorientation occurring upon the stress level exceeding a critical value and then, at a higher stress level, transformation and

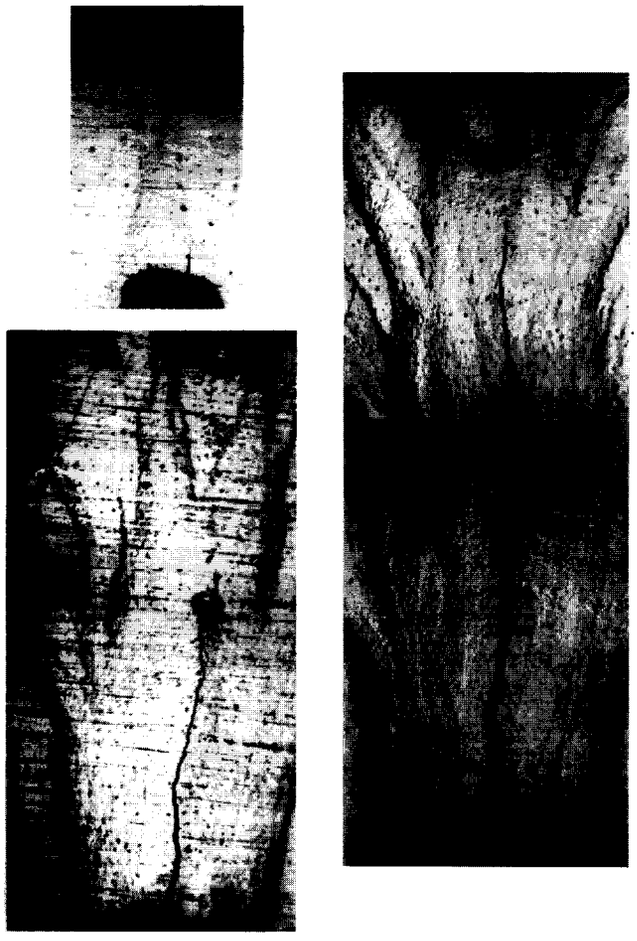

Fig. 9. Micrographs of the crack and associated transformation zone during crack extension in Ce-TZP-III. The photograph (at × 70) was taken at the positions arrowed in Fig 3.

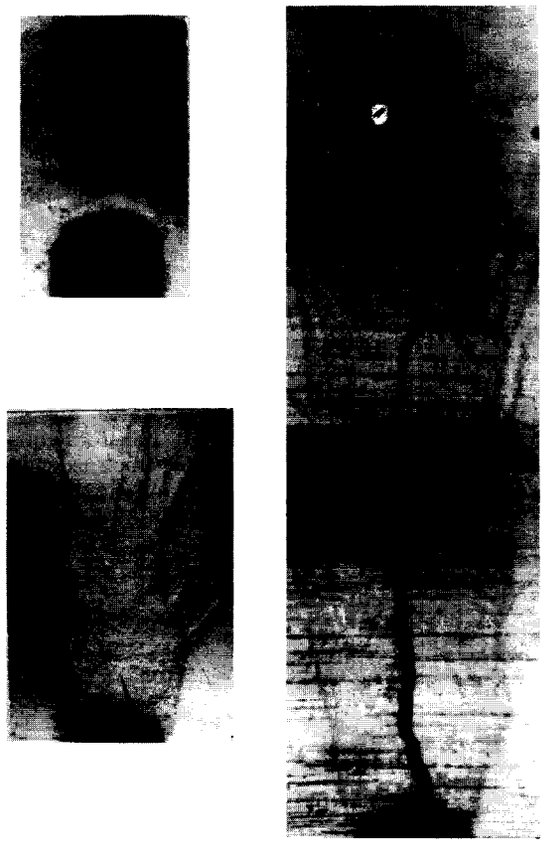

Fig. 10. Micrographs of the crack and associated transformation zone during crack extension in Ce-TZP-IV. The photograph (at × 70) was taken at the positions arrowed in Fig. 4.

the occurrence of bands on the tensile surface. Matsumoto and Virkar[13] have previously suggested such behaviour in a Ce-TZP material on the basis of X-ray analysis of ground surfaces.

Continuous AE monitoring of complete load–unload crack extension cycles revealed that events also occurred during unloading. A typical example of such behaviour is shown in Fig. 14. In this instance the unloading curve is non-linear and does not coincide with the subsequent reloading line. Such observations suggest that ligaments and bridges behind the crack tip may fracture during the unloading cycle, thereby changing the specimen compliance and also contributing AE activity. Other evidence in support of ligament formation was the regularly observed feature of the main crack arresting and a new crack either initiating from the notch or adjacent to the main crack.

3.6 Interpretation

In recent papers Stump[6,7] has addressed the issue of autocatalysis and the role of shear stresses on the transformation zone formation in this class of materials. In particular, in a simulation study where he systematically varied the shear and dilational strains associated with transforming particles, the shape of the transformation about the crack tip changed from a near cardiod form for purely dilational strain to needle-like for primarily shear strain dominated transformation.

However, in order to make use of the concepts and simulation proposed by Stump, definitions and estimates of some of the parameters he used need to be defined, where possible, for the present materials. The characteristic length dimension, comparable to the plastic zone dimension for metallic materials, is given by:[6,7]

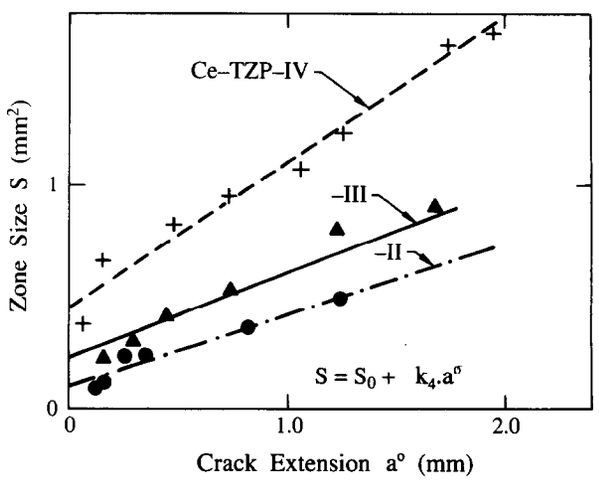

Fig. 11. Plot of the area of the transformation zone size as a function of crack length for Ce-TZP-II to Ce-TZP-IV.

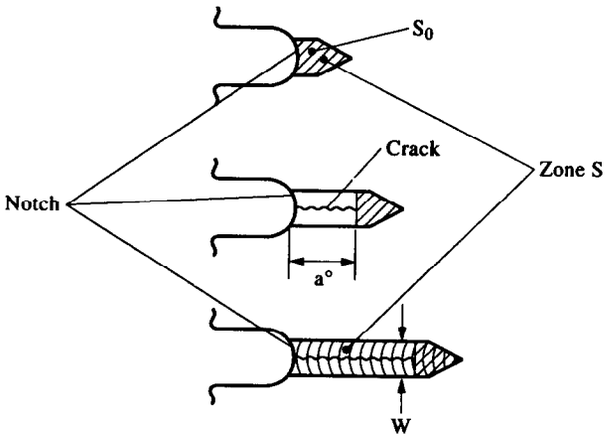

Fig. 12. Schematic illustration of the transformation zone about the notch and crack tip as the crack extends. Also marked are the dimensions of the transformation zone width W, crack length a^o and area of transformation S.

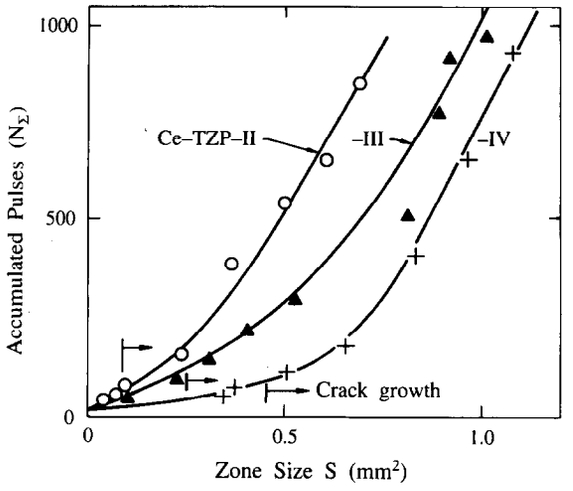

Fig. 13. Interrelation between accumulated acoustic emission events N_Σ and transformation zone area S. Arrows mark the onset where crack growth initiates.

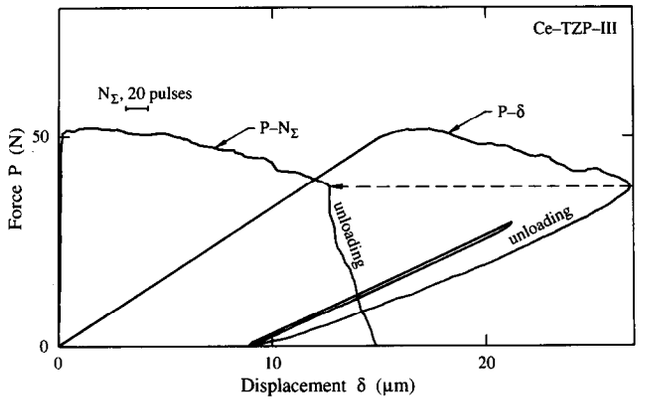

Fig. 14. Acoustic emission monitored during complete loading and unloading cycle for Ce-TZP-III. Note the acoustic emission events during unloading.

$$L_o = \frac{2}{9\pi}\left[\frac{K_m(1+\upsilon)}{\sigma^c{}_m}\right]^2 \text{ or } L = \frac{1}{8\pi}\left(\frac{K_m}{\sigma_c}\right)^2 \quad (5)$$

where K_m is the crack tip stress intensity factor for fracture (K_m ~3 MPa $m^{1/2}$), $\sigma^c{}_m$ is the critical mean stress to trigger the transformation and σ_c is the critical tensile stress for the deviation from linearity during tensile or flexure testing. The transformation-toughening parameter, or measure of the magnitude of the toughening increment is given by:[6,7]

$$\omega = \frac{Ec_t\theta^T}{\sigma^c{}_m}\left(\frac{1+\upsilon}{1-\upsilon}\right) \quad (6)$$

where c_t is the volume fraction of transformed tetragonal phase and θ^T the dilational strain associated with transformation. Stump introduces two more parameters that quantify the dilational strain β and shear strain ρ associated with the transformation of a particle; namely

$$\beta = \frac{E\theta_T}{\sigma_c(1-\upsilon)}, \quad \rho = \frac{E\gamma_T}{\sigma_c(1-\upsilon^2)} \quad (7)$$

where γ_T is the transformation shear strain. Taking typical values for the current materials, namely E from Ref. 8, $\upsilon = 0{\cdot}25$, $K_m = 3$ MPa $m^{1/2}$, $\theta_T = 0{\cdot}04$, $\gamma_T = 0{\cdot}05$ and values for σ_c again taken from the previous paper[8] (see Fig. 1), leads to the estimates for β, L and ρ given in Table 2.

Table 2. Estimates of transformation parameters for Ce-TZP materials

Material	σ_c*(MPa)*[8]	β	*L(μm)*	ρ	*E(GPa)*[8]
Ce-TZP-I	216	43·2	7·6	43·8	175
Ce-TZP-II	168	56·8	12·8	57·6	179
Ce-TZP-III	156	61·9	14·8	62·7	181
Ce-TZP-IV	138	68·0	18·9	68·9	176

The calculated values of β and ρ appear to be very large because of the low values of σ_c measured for the present Ce-TZP materials. In fact these values are all beyond the range that Stump[6] simulated. One possible explanation as to why these estimates are excessive is that no account of the extent of the phase transformation within the crack initiated transformation zone is allowed for in the expressions [eqn (7)].

Thus, possibly a better estimate for β and ρ would be to include a factor c_t in eqn (7) which is the volume fraction of phase transformation within the zone, typically ~50% or less, although not measured for the present materials. Such an approach would approximately halve the values of β and ρ estimated.

The increasing values of β and ρ for materials II to IV and the nature of the observed transformation zone shapes would appear to confirm the simulations by Stump,[6] provided that for the Ce-TZP materials the ratio of shear to mean tensile stress criteria for transformation was <1. However this approach does not account for the apparent absence of any transformation about the crack

tip for the Ce-TZP-I material. Liu *et al.*[4] also did not observe a transformation zone for the same material when tested in either SENB or CT geometries. Liu *et al.*[4] did, however, observe that the shape and size of the zone from the other materials was much greater for CT geometries, presumably because of the lower likelihood of initiating a transformation zone 'hinge' between the crack tip and the rear surface with SENB geometries.

4 Summary and Conclusions

The present studies have shown that 9 mol% Ce-TZP ceramics exhibit very extensive transformation zones about loaded notches and crack tips. The size of these zones increases with grain size and the shape of the zones are comparable to the simulations of Stump.[6,7]

The measured fracture toughness versus crack extension showed opposite trends dependent upon whether the optical or measured compliance value for crack length was used. In all instances the measured compliance was greater than that calculated from optical measurements. A linearly increasing ratio of these two estimates with crack extension was observed, the slope of which increased with grain size and transformation zone size of the Ce-TZP. No evidence of a transformation zone about the crack tip in the finer grained Ce-TZP-I was seen. It is suggested that the high toughness of this material may be due to ferroelastic grain reorientation occurring about the crack tip.

Transformation zone size area increased linearly with crack extension with an intercept at zero crack growth, indicating that transformation has occurred about the notch region prior to crack initiation. No correlation between AE events and area of phase transformation was found. More events per unit of transformation area were found for the finer grained Ce-TZP-II than for the coarser grained Ce-TZP-IV material. AE events were also detected during unloading which may have occurred because of further crack extension or phase transformation.

Acknowledgements

The authors wish to thank Drs T.-S. Liu and G. Grathwohl for provision of materials and comments on the text.

References

1. Rose, L. R. F. & Swain, M. V., Transformation zone shape in ceria-partially stabilised zirconia. *Acta Metall.*, **36** (1988) 955–62.
2. Grathwohl, G. & Liu, T., Crack resistance and fatigue of transforming ceramics: II. CeO_2 — stabilised tetragonal ZrO_2. *J. Am. Ceram. Soc.*, **74** (1991) 3028–34.
3. Yu, C.-S. & Shetty, D. K., Transformation zone shape, size, and crack growth resistance (*R*-curve) behaviour of ceria-partially-stabilised zirconia polycrystals. *J. Am. Ceram. Soc.*, **72** (1989), 921–8.
4. Liu, T., Mai, Y.-W., Swain, M. V. & Grathwohl, G., Transformation and *R*-curve behaviour of 9 Ce-TZP ceramics: Part 1, grain size and specimen geometry effects. *J. Am. Ceram. Soc.*, in press.
5. Marshall, D. B., Crack tip shielding in ceria partially stabilised zirconia. *J. Am. Ceram. Soc.*, **73** (1990) 3119–21.
6. Stump, D. M., The role of shear stresses and shear strains in transformation toughening. *Phil. Mag. A*, **64** (1991) 879–902.
7. Stump, D. M. & La Violette, R. A., Effects of shear stresses on crack growth microstructures in transformation toughened ceramics. *Phil. Mag. A*, **68** (1993) 35–47.
8. Gogotsi, G. A., Zavada, V. P. & Swain, M. V., Mechanical property characterisation of a 9 mol% Ce-TZP ceramic material: I. Flexural response. *J. Europ. Ceram Soc.*, **15** (1995) 1185–92.
9. Atkins, A. G. & Mai, Y.-W., *Elastic and Plastic Fracture.* Ellis Horwood, Chichester, 1985.
10. Kleinlein, F. W. & Hubner, H., The evaluation of crack resistance and crack velocity from controlled fracture experiments of ceramic bend specimens. *Fracture*, **4** (1977) 838–41.
11. Strawley, J. E., Wide range stress intensity factor expression for ASTM E-339 standards fracture toughness specimens. *Int. J. Fracture*, **12** (1976) 475–6.
12. Gogotsi, G. A., Zavanda, V. P. & Fesenko, A. I., Method and results R-curve determination in ceramics. Zavodsaya Laboratoriya (Ind. Lab.), **58** (1992) 40–3 (in Russian).
13. Virkar, A. V. & Matsumoto, R. L. K., Ferro-elastic domain switching as a toughening mechanism in tetragonal zirconia. *J. Am Ceram. Soc.*, **69** (1986) C224–6.

Journal of the European Ceramic Society 16 (1996) 553–560

0955-2219(95)00159-X
0955-2219/96/$15.00

Rietveld Refinement of the Crystal Structures of the Yttrium Silicon Oxynitrides $Y_2Si_3N_4O_3$ (N-Melilite) and $Y_4Si_2O_7N_2$ (J-Phase)

K. J. D. MacKenzie, G. J. Gainsford & M. J. Ryan

New Zealand Institute for Industrial Research and Development, P.O. Box 31-310, Lower Hutt, New Zealand

(Received 31 May 1995; revised 19 July 1995; accepted 28 August 1995)

Abstract

Rietveld crystal structure refinements have been carried out on the X-ray powder patterns of synthetic N-melilite, $Y_2Si_3N_4O_3$, and J-phase, $Y_4Si_2O_7N_2$. The melilite structure of $Y_2Si_3N_4O_3$ is confirmed, in which sheets containing Si_2O_7 double tetrahedra are linked by Y polyhedra in which two of the eight Y–O contacts are significantly longer (2·78Å). The present data were unable to furnish unambiguous details of O/N ordering in either N-melilite or J-phase. The structure of J-phase contains either $Si_2O_5N_2$ or Si_2O_6N ditetrahedral units containing N in the bridging position and arranged lengthwise along the a*-axis. These units are linked by Y polyhedra. Of the four distinguishable Y sites, three have seven contacts with O and N atoms within 2·8Å. One of these sites also has one longer O/N contact at 2·92Å. The fourth Y site is in 6-fold coordination.*

1 Introduction

Yttrium oxide is commonly used to promote sintering in silicon nitride and the sialons. In these systems, it reacts to form intergranular yttrium silicon oxynitrides, of which the X-ray powder patterns and compositions of several have been reported.[1] Of these, the two phases which we have most commonly encountered in our solid-state nuclear magnetic resonance studies of silicon nitride sintering[2] have been $Y_2Si_3N_4O_3$ and $Y_4Si_2O_7N_2$. The former was detected by Rae *et al.*[3] in hot pressed Si_3N_4 with yttria additions, and identified as having structural similarities with the melilite minerals, of which the end members are akermanite ($Ca_2MgSi_2O_7$) and gehlenite ($Ca_2Al_2SiO_7$). The suggested structure of the new Y-containing melilite was derived from akermanite by exchanging Y for Ca, Si for Mg and four of the seven oxygens for nitrogen.[3] A satisfactory refinement of the powder data was achieved on this basis, but it was not determined whether ordering was occurring in the O/N sites, which for the purpose of the model were assumed to be occupied randomly.

No structural refinement has been published for J-phase, although Wills *et al.*[4] have suggested it to be isostructural with cuspidine ($Ca_4Si_2O_7F_2$), and indexed the powder pattern of a hot-pressed specimen on the basis of a cuspidine-like monoclinic cell.

The present structural study was made possible by the availability of essentially monophase polycrystalline samples which have been synthesised in the course of an ^{89}Y MAS NMR study.

2 Experimental

The phases were synthesised from Si_3N_4 (H.C. Starck GmbH & Co., Grade LC 10), Y_2O_3 (Sigma Chemical Co.) and, in the case of J-phase, fine SiO_2 (Mintech NZ Ltd, Snowsil 350). Appropriately batched mixtures were ball milled for 16 h in ethanol using Si_3N_4 milling media. The solvent was removed using a rotary evaporator and the powder was pressed into pellets and fired for 2 h in a flowing atmosphere of purified oxygen-free nitrogen in a graphite furnace (Thermal Technology Inc.). N-melilite was found to be extremely sensitive to the reducing potential of the furnace atmosphere, and had to be fired at 1740°C in a powder bed of BN containing a small amount of Si_3N_4 and SiO_2, contained in a loosely covered alumina pot. J-phase was readily formed at 1650°C in a BN powder bed contained in a closed graphite pot.

The O:N ratios in both materials were determined by particle-induced γ-ray emission (PIGME), in which the sample is exposed to a deuteron beam generated in an accelerator, and the γ-rays from the resulting nuclear reactions are detected and analyzed.[5] The calibration materials were Y_2O_3, which was used as the O standard, and Si_3N_4,

which was used as the N standard after correction for its residual O content. The results indicated O:N ratios of 0·7 ± 0·1 and 3·2 ± 0·1 for N-melilite and J-phase respectively, in reasonable agreement with the ratios expected from the ideal formulae (0·75 and 3·5 respectively).

Powder diffraction data for each phase were collected using a Philips PW1700 series computer-controlled diffractometer with Philips APD1700 software, a fixed 1° divergence slit, primary beam Soller slits, 0·2 mm receiving slit and graphite secondary monochromator. The pattern was collected from 10–154° 2θ at 0·04° intervals using Co Kα radiation (40 kV, 35 mA), counting for 5 s per step. The initial cell parameters for J-phase were obtained from an indexed and refined pattern from a Huber 620 114·6 mm Guinier camera used in conjunction with a KEJ Instruments LS20 microphotometer.

The data were then converted into a form suitable for Rietveld refinement by the GSAS programme suite,[6] using λ Co Kα_1, α_2 = 1·78896, 1·79284 Å and ratio (α_1/α_2) of 2·0. The relevant refinement variables are listed in Table 1. Beam polarisation was corrected using the value for $2\theta_m$ of 31·0°.

3 Results and Discussion

3.1 N-melilite refinement

The starting point for this refinement was the preliminary structure of Rae *et al.*[3] The structure was refined in space group P-42$_1$m using fixed O/N occupancies at the N(4)O(3) sites (see discussion below). The final cell parameters are shown in Table 1 and the refined atomic co-ordinates in Table 2, corresponding to R_{wp} 0·116 and R_p 0·087, where

$$R_{wp} = (\Sigma w(I_0 - I_c)^2/\Sigma w I_0^2)^{1/2}$$

$$R_p = \Sigma|I_0 - I_c|/\Sigma I_0$$

I_0, I_c are the observed and calculated total profile intensities and w are the weights (taken as I_0^{-1}) for each point.

The final Rietveld fitted diffraction pattern for N-melilite, all the possible Bragg reflection positions for this phase (vertical bars) and the difference between the calculated and observed intensity is shown in Fig. 1.

The calculated bond lengths and angles for this structure are shown in Tables 3 and 4 respectively.

The structure consists of Si_2O_7 ditetrahedra (containing Si(2)) linked together by the Si(l)

Table 1. Final Rietveld refinement variables for N-melilite ($Y_2Si_3O_3N_4$) and J-phase ($Y_4Si_2O_7N_2$) with Y_2O_3 minor phase

	N-melilite	*J-phase*	*(+)*	*Y_2O_3*
Symmetry	Tetragonal	Monoclinic	—	Cubic
Space Group	P-42$_1$m	P2$_1$/c	—	Ia-3
a, (Å)	7·6083(1)	7·5601(2)	—	10·6020
b, (Å)	7·6083(1)	10·4411(3)	—	10·6020
c, (Å)	4·9113(1)	10·7626(3)	—	10·6020
α, (°)	90	90	—	90
β, (°)	90	110·042(2)	—	90
γ, (°)	90	90	—	90
ρ_{calc}, g/cc	4·277	4·592	—	5·034
2θ zero (°)	0·018(2)		0·009	—
Max.shift/error	0·03	0·11	—	0·01
No. contributing reflections	294	2216	—	286
No. contributing observations	3599	—	3599	—
No. profile coefficients	5	—	6	—
No. background coefficients	4	—	7	—
No. soft restraints	0	—	2†	—
No. of variables	26	—	63	—

†Si(2)–N(1), Si(1)–O/N(6) restrained to 1·61 Å ± 0·07 Å.

Table 2. Final atomic co-ordinates and isotropic temperature factors in N-melilite, $Y_2Si_3O_3N_4$. Standard deviations in parentheses

Atom	*Site multiplicity*	*x*	*y*	*z*	*100*U(iso)*	*N*†
Y	4	0·1637(1)	0·6637(1)	0·5046(3)	1·32(3)	4
Si(1)	2	0	0	0	1·17(7)	2
Si(2)	4	0·3591(3)	0·8591(3)	0·9465(7)	1·17(7)	4
O(1)	2	0	0·5	0·203(3)	0·4(1)	0·858
N(1)	2	0	0·5	0·203(3)	0·4(1)	1·142
O(2)	4	0·3553(8)	0·8553(8)	0·282(2)	0·4(1)	1·716
N(2)	4	0·3553(8)	0·8553(8)	0·282(2)	0·4(1)	2·284
O(3)	8	0·0923(7)	0·1596(7)	0·206(1)	0·4(1)	3·432
N(3)	8	0·0923(7)	0·1596(7)	0·206(1)	0·4(1)	4·568

†Total cell occupancy factor (e.g. 4 Y's per cell).

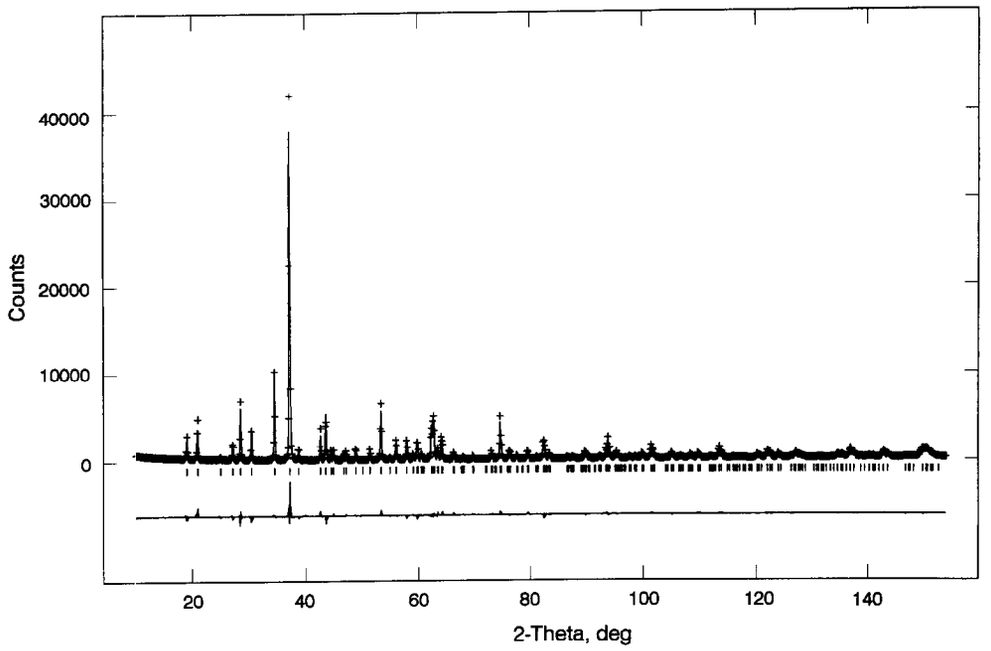

Fig. 1. Final diffractogram for N-melilite, $Y_2Si_3O_3N_4$.

Table 3. Interatomic distances in N-melilite, $Y_2Si_3O_3N_4$

Y–O/N(1)		2·303(8) Å
–O/N(2)		2·334(8)
–O/N(2')[a]	(2*x*)	2·574(6)
–O/N(3)[b]	(2*x*)	2·337(6)
Mean		2·411 Å
Y–O/N (3')[f]	(2*x*)	2·783(6) Å
Si(1)–O/N(3)[c]	(4*x*)	1·730(6) Å
Si(2)–O/N(1)[d]		1·683(6)
–O/N(2)[e]		1·648(8)
–O/N(3)[b]	(2*x*)	1·733(6)
Mean		1·699 Å

Equivalent sites are generated by symmetry operations: [a]O/N(2') *y*–1, 1–*x*, 1–*z*; 1–*y*, *x*, 1–*z*; [b]O/N(3) *y*, 1–*x*, 1–*z*; 0·5–*x*, 0·5+*y*, 1–*z*; [c]O/N(3) *x*, *y*, *z*; *y*, –*x*, –*z*; –*x*, –*y*, *z*; –*y*, *x*, *z*; [d]O/N(1) *y*, 1–*x*, 1–*z*; [e]O/N(2) *x*, *y*, 1+*z*; [f]O/N(3') –*x*, 1–*y*, *z*; 0·5–*y*, 0·5–*x*, *z*.

Table 4. Bond angles in N-melilite, $Y_2Si_3O_3N_4$

O/N(3)–Si(1)–O/N(3')	(4*x*)	110·1(3)°
–O/N(3")	(2*x*)	108·3(3)
Mean		109·5°
O/N(1)–Si(2)–O/N(2)		117·2(5)°
–O/N(3)	(2*x*)	103·5(3)
O/N(2)–Si(2)–O/N(3)	(2*x*)	114·9(3)
O/N(3)–Si(2)–O/N(3')		100·7(3)
Mean		109·1°
O/N(1)–Y–O/N(2)		111·9(3)°
–O/N(2')	(2*x*)	74·9(3)
–O/N(3)	(2*x*)	144·5(2)
O/N(2)–Y–O/N(2')	(2*x*)	142·7(2)
–O/N(3)	(2*x*)	78·3(3)
O/N(2')–Y–O/N(2")		74·4(3)
–O/N(3)	(2*x*)	77·6(2)
–O/N(3')	(2*x*)	118·4(3)
O/N(3')–Y–O/N(3)		69·7(2)

[†]See Table 3 for definitions of symmetry operators for generating primed atoms.

tetrahedra to form sheets which lie parallel to the 001 plane of the tetragonal cell (Fig. 2). The tetrahedral sheets are linked by yttrium atoms in 8-fold co-ordination with O and N. Two of the Y–O contacts are long (>2·6 Å); these are indicated with broken lines in Fig. 2. The Y site geometry of the 6 contacts <2·6 Å approximates trigonal prismatic (D_{3h}) rather than octahedral, their mean bond lengths around the Y being 2·41 Å. The question of ordering on the O/N sites was examined in further detail by refining the data on the basis of three different models.

The first model, which has been adopted by Wang and Werner (personal communication) in a Rietveld refinement of Y and N melities, places all the nitrogens in one site, corresponding to the present O/N(3). Since there appears to be no steric or stoichiometric reason for adopting this simple atom distribution, a second model was tried, in which no restrictions were placed on the occupancies of the three O/N sites. On refinement, the resulting occupancies of each site produced an inconclusive stoichiometry not consistent with the analyzed O:N ratio; furthermore, no significant improvement in the refinement was obtained. In a third model, the known O/N stoichiometry was taken into account, with 3/7 of the oxygens and 4/7 of the nitrogens being allocated to each site. Again, no significant difference was observed in the refinement, indicating that the present data are not sufficiently good to differentiate between these three possibilities.

Since this work was carried out, a ^{15}N NMR study of N-melilite (R. K. Harris, personal communication) has provided evidence of three distinct N

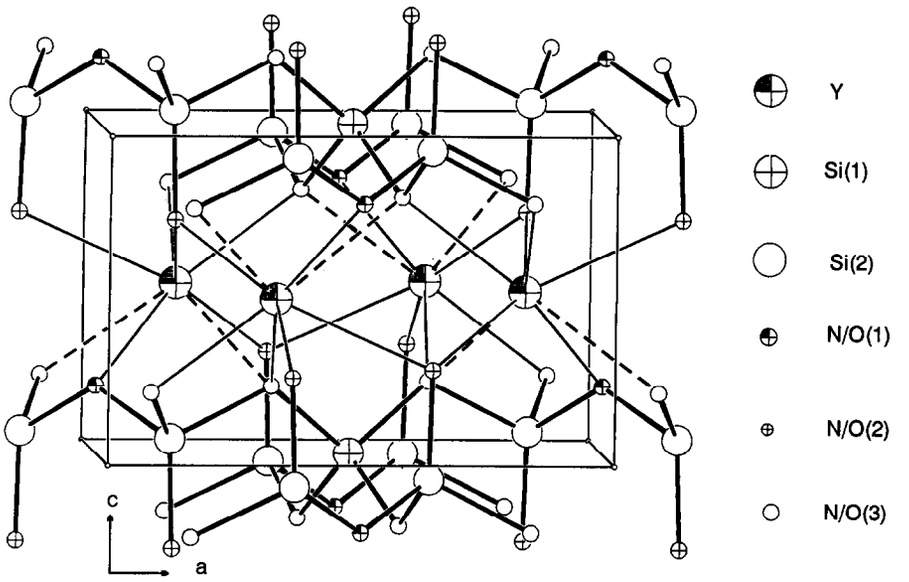

Fig. 2. View down *b*–axis of N-melilite cell, ORTEP II plot.[10] Dashed lines indicate Y contacts longer than 2·6 Å.

environments, suggesting an O/N ordering scheme in which O/N(1) contains only N, O/N(2) contains only O and O/N(3) contains an ordered arrangement of O and N. Since such a configuration would destroy the tetragonal symmetry, it was suggested that disorder must occur in O/N(3). The present Rietveld refinements can not discriminate between these levels of ordering; model 3 (above), in which the N and O are allowed to mix over all the O/N sites consistent with the compound stoichiometry, was adopted as the basis for the structural data of Tables 3 and 4.

3.2 J-phase refinement

The atom positions used as a starting point in the refinement were taken from the crystal structure of cuspidine determined by Saburi *et al.*[7] which were first transformed to conventional $P2_1/c$ co-ordinates. The original work of Wills *et al.*[4] assumed the Ca and F positions in cuspidine to be filled by Y and N respectively, but subsequent ^{29}Si and ^{15}N NMR results[8] have suggested other possible N/O ordering schemes. Hauck *et al.*[8] have observed two ^{15}N NMR signals in J-phase, which they assign to N in sites located in the bridging and terminal (non-bridging) positions of the Si ditetrahedral unit. This arrangement would lead to the presence of two Si environments (SiO_3N and SiO_2N_2); the observation of only one (albeit broad) ^{29}Si resonance was explained in terms of the overlap of these two unresolved resonances.[8] There are, however, at least two other N/O ordering possibilities which do not involve the ditetrahedral Si unit (hereafter called 'ionic' sites). These were not discussed by Hauck *et al.*[8] but could give rise to two different ^{15}N resonances and one ^{29}Si resonance. Other possibilities include the location of N in one of the sites in the ditetrahedral unit and one of the 'ionic' sites, or in the two crystallographically distinguishable 'ionic' sites. Of these possibilities, the former may be the more reasonable, since the position of one of the observed ^{15}N resonances is comparable with the position found for NSi_2 species in other oxynitride compounds; this may correspond to the bridging site, as assigned by Hauck *et al.*[8] The present Rietveld data were therefore refined on the basis of four models: (i) that of Hauck *et al* in which one N occupies the bridging site and one N is randomly distributed over the terminal sites of the ditetrahedral units; (ii) one N occupies the bridging site of the ditetrahedral unit with the other N located randomly in the 'ionic' sites; (iii) as for model (ii), but with only one of the two distinguishable 'ionic' sites occupied by N; and (iv) the N's occupy both the 'ionic' sites.

All four models gave very similar values for R_p, but with a 0·2% better value obtained for models (i) and (ii) containing a bridging N. The tabulated structural data are based on model (i), although this choice is arbitrary, since the present refinements give no reason for preferring this over model (ii).

The final refined cell parameters determined for the present J-phase are listed in Table 1. During the refinement, a small amount (ca. 5%) of unreacted Y_2O_3 was allowed for by refining it as a second phase, using the coordinates of Hanic *et al.*[9]; the same profile function was assumed for the impurity as for the major phase because the very low concentration of the former made it impossible to determine an independent profile function. As part of the refinement process, the scale factor between the two phases was also refined. The isotropic thermal parameters for the Y, Si atoms were refined as two common values and those for the remaining atoms were fixed. The Rietveld refined diffraction pattern for this sample is shown

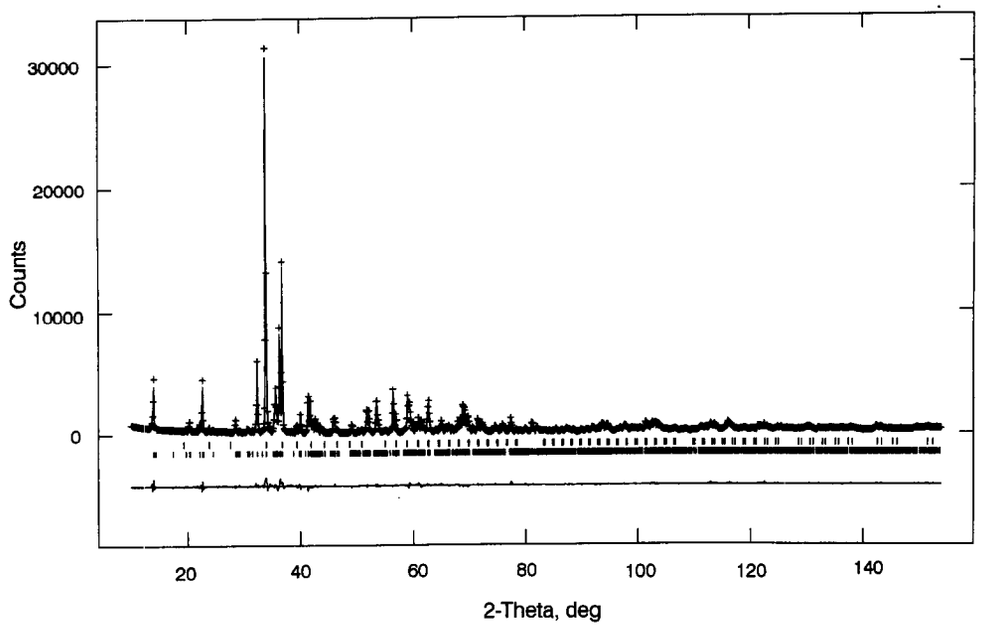

Fig. 3. Final diffractogram for J-phase, $Y_4Si_2O_7N_2$, with Y_2O_3 minor phase.

Table 5. Final atomic co-ordinates and isotropic temperature factors in J-phase, $Y_4Si_2O_7N_2$, and Y_2O_3. Standard deviations in parentheses. The multiplicities are all four in J-phase

Atom	*x*	*y*	*z*	*100*(U(iso)*
(a) J-phase				
Y(1)	0·8328(8)	0·1214(6)	0·4290(5)	1·14(3)
Y(2)	0·3358(9)	0·1227(6)	0·4173(5)	1·14(3)
Y(3)	0·5281(9)	0·4135(4)	0·3107(4)	1·14(3)
Y(4)	0·0232(8)	0·4024(5)	0·2885(4)	1·14(3)
Si(1)	0·735(2)	0·188(2)	0·132(1)	0·8(2)
Si(2)	0·155(2)	0·185(1)	0·116(1)	0·8(2)
N(1)	0·939(4)	0·240(2)	0·109(2)	0·8
O/N(2)	0·717(5)	0·035(4)	0·170(3)	0·8
O/N(3)	0·210(5)	0·031(4)	0·168(3)	0·8
O/N(4)	0·715(4)	0·275(3)	0·251(3)	0·8
O/N(5)	0·282(4)	0·265(3)	0·244(2)	0·8
O/N(6)	0·577(4)	0·233(3)	–0·013(2)	0·8
O/N(7)	0·164(4)	0·220(3)	–0·026(2)	0·8
O(1)	0·431(8)	0·494(3)	0·107(4)	0·8
O(8)	0·918(5)	0·519(2)	0·097(3)	0·8
(b) Y_2O_3				
Y(1)	0·25	0·25	0·25	1·0
Y(2)	–0·0316(8)	0	0·25	1·0
O(1)	0·376(5)	0·162(3)	0·380(7)	1·0

in Fig. 3, together with all the positions of all the calculated Bragg reflections for both phases, and the difference between the calculated and observed intensities.

The final atomic co-ordinates are shown in Table 5, corresponding to R_{wp} 0·101, R_p (both phases) 0·075. The final weight fraction of J-phase and Y_2O_3 was 0·953 and 0·047 respectively. The refinement of Y_2O_3 minor phase gave a Y(l)–O(1) bond length of 2·13(6) Å and the three Y(2)–O bond lengths of 2·27(5) Å, 2·30(6) Å and 2·41(5) Å.

The calculated bond lengths and angles for J-phase, based on model (i) are listed in Tables 6 and 7 respectively.

Table 6. Interatomic distances in J-phase, $Y_4Si_2O_7N_2$

Si(1)–N(1)	1·72(3) Å
–O/N(2)	1·69(4)
–O/N(4)	1·61(3)
–O/N(6)	1·66(2)
Mean	1·67 Å
Si(2)–N(1")	1·67(2) Å
–O/N(3)	1·67(3)
–O/N(5)	1·67(3)
–O/N(7)	1·57(2)
Mean	1·65 Å
Y(1)–N(1')	2·38(3) Å
–O/N(2)	2·78(3)
–O/N(4)	2·38(3)
–O/N(6')	2·73(3)
–O(1')	2·33(4)
–O(8")	2·27(4)
–O(8')	2·25(3)
Mean	2·44 Å
Y(2)–O/N(3)	2·72(3) Å
–O/N(5)	2·36(3)
–O/N(6')	2·28(3)
–O/N(7')	2·34(3)
–O(1")	2·32(4)
–O(1')	2·27(3)
–O(8)	2·16(4)
Mean	2·35 Å
Y(3)–O/N(2")	2·30(4) Å
–O/N(3")	2·29(4)
–O/N(4)	2·31(3)
–O/N(5)	2·28(3)
–O/N(6')	2·38(3)
–O(1)	2·20(3)
Mean	2·29 Å
Y(4)–N(1")	2·49(3) Å
–O/N(2")	2·30(4)
–O/N(3"')	2·40(3)
–O/N(4")	2·63(3)
–O/N(5)	2·58(3)
–O/N(7')	2·30(3)
–O(8"')	2·31(3)
Mean	2·43 Å

†Symmetry operations for primed atoms: N(1'), O(1'), O/N(6'), O/N(7'), O(8'): x, 0·5–y, 0·5+z; O(1"), O/N(2"), O/N(3"), O(8"): 1–x, y, 0·5+x. 0·5–z; N(1"), O/N(4"), O(8"'): x–1, y, z; O/N(3"'): –x, 0·5+y, 0·5–z.

Table 7. Bond angles in J-phase, $Y_4Si_2O_7N_2$[†]

N(1)–Si(1)–O/N(2)	118(2)°	O/N(6')–Y(2)–O/N(7')	83(1)°
–O/N(4)	106(2)	–O(1")	84(1)
–O/N(6)	102(2)	–O(1')	94(1)
O/N(2)–Si(1)–O/N(4)	106(2)	–O(8")	159(1)
–O/N(6)	114(2)		
O/N(4)–Si(1)–O/N(6)	111(2)	O/N(7')–Y(2)–O(1")	166(1)°
Mean	109·5°	–O(1')	99(1)
		–O(8")	79(1)
N(1")–Si(2)–O/N(3)	116(2)°		
–O/N(5)	98(2)	O(1")–Y(2)–O(1')	78(2)°
–O/N(7)	106(2)	–O(8")	113(1)
O/N(3)–Si(2)–O/N(5)	104(2)		
–O/N(7)	115(2)	O(1')–Y(2)–O(8")	78(1)°
O/N(5)–Si(2)–O/N(7)	117(2)		
Mean	109·3°	O/N(2")–Y(3)–O/N(3")	114(1)°
		–O/N(4)	166(1)
N(1')–Y(1)–O/N(2)	160(1)°	–O/N(5)	78(1)
–O/N(4)	101(1)	–O/N(6')	100(1)
–O/N(6)	62(1)	–O(1)	83(1)
–O(1")	123(1)		
–O(8")	109(1)	O/N(3")–Y(3)–O/N(4)	78(1)°
–O(8')	80(1)	–O/N(5)	165(1)
		–O/N(6')	112(1)
O/N(2)–Y(1)–O/N(4)	61(1)°	–O(1)	84(1)
–O/N(6')	115(1)		
–O(1")	71(1)	O/N(4)–Y(3)–O/N(5)	89(1)°
–O(8")	73(1)	–O/N(6')	82(1)
–O(8')	120(1)	–O(1)	90(1)
O/N(4)–Y(1)–O/N(6')	74(1)°	O/N(5)–Y(3)–O/N(6')	74(1)°
–O(1")	100(1)	–O(1)	88(1)
–O(8")	108(1)		
–O(8')	175(2)	O/N(6')–Y(3)–O(1)	160(1)°
O/N(6)–Y(1)–O(1')	74(1)°	N(1")–Y(4)–O/N(2")	122(1)°
–O(8")	171(1)	–O/N(3"')	123(1)
–O(8')	102(1)	–O/N(4")	63(1)
		–O/N(5)	60(1)
O(1')–Y(1)–O(8")	114(1)°	–O/N(7')	102(1)
–O(8')	76(1)	–O(8"')	76(1)
O(8")–Y(1)–O(8')	77(2)°	O/N(2")–Y(4)–O/N(3"')	105(1)°
		–O/N(4")	175(1)
O/N(3)–Y(2)–O/N(5)	62(1)°	–O/N(5)	72(1)
–O/N(6')	123(1)	–O/N(7')	93(1)
–O/N(7')	119(1)	–O(8"')	82(1)
–O(1")	73(1)		
–O(1')	128(1)	O/N(3"')–Y(4)–O/N(4")	70(1)°
–O(8")	76(1)	–O/N(5)	177(1)
		–O/N(7')	106(1)
O/N(5)–Y(2)–O/N(6')	74(1)°	–O(8"')	80(1)
–O/N(7')	78(1)		
–O(1")	103(1)	O/N(4")–Y(4)–O/N(5)	113(1)°
–O(1')	168(1)	–O/N(7')	88(1)
–O(8")	112(1)	–O(8"')	97(1)
		O/N(5)–Y(4)–O/N(7')	74(1)°
		–O(8"')	99(1)
		O/N(7')–Y(4)–O/N(8"')	173(1)°

[†]See Table 6 for definitions of symmetry operators for generating primed atoms.

The structure of J-phase according to the model whose parameters are listed in Tables 6 and 7 consists of ditetrahedral units distributed lengthwise along the *a*-axis as in Figs 4 and 5, in which the bridging atom is shown as a nitrogen N(l), with the other nitrogens distributed randomly over the terminal sites O/N(2)–O/N(7) of these $Si_2O_5N_2$ units. This represents one possible O/N ordering arrangement which is consistent with the two N sites distinguishable in the published ^{15}N NMR

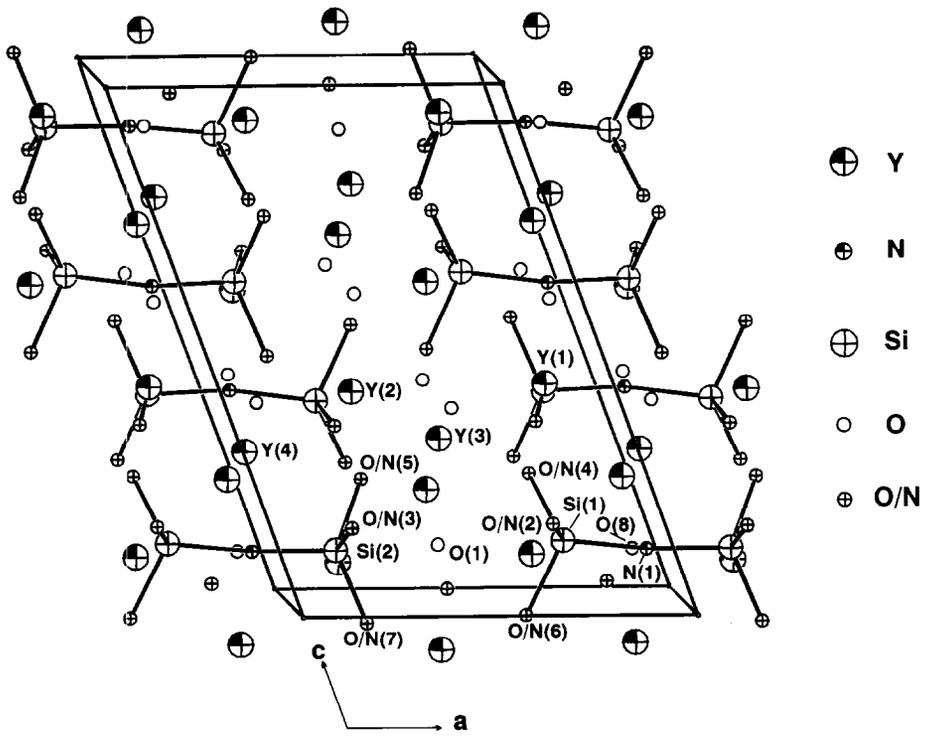

Fig. 4. Cell contents of J-phase, viewed down the *b*–axis, ORTEP II plot.[10] Only the Si ditetrahedral unit bonding is shown.

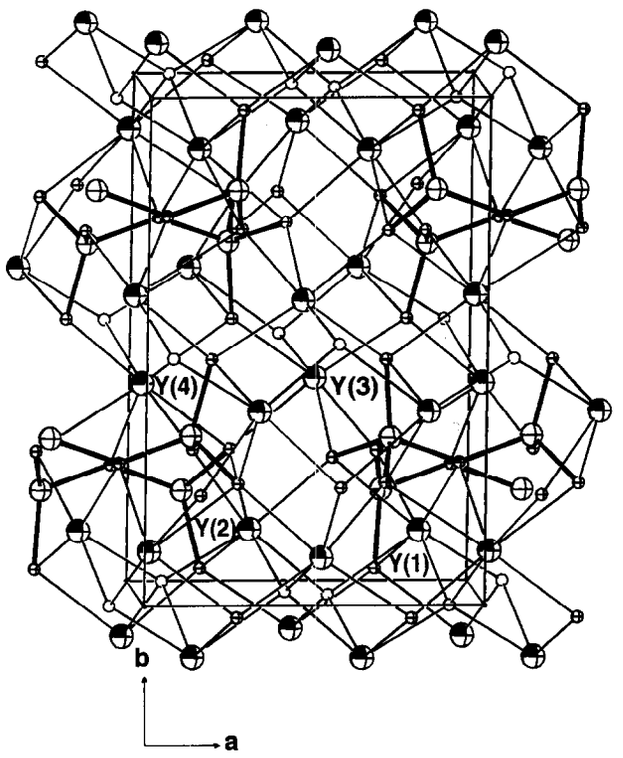

Fig. 5. Cell contents of J-phase, viewed down the *c*–axis, ORTEP II plot.[10] Thicker lines show the ditetrahedral unit, thinner lines show other bonding contacts. Atom symbols as for Fig. 4.

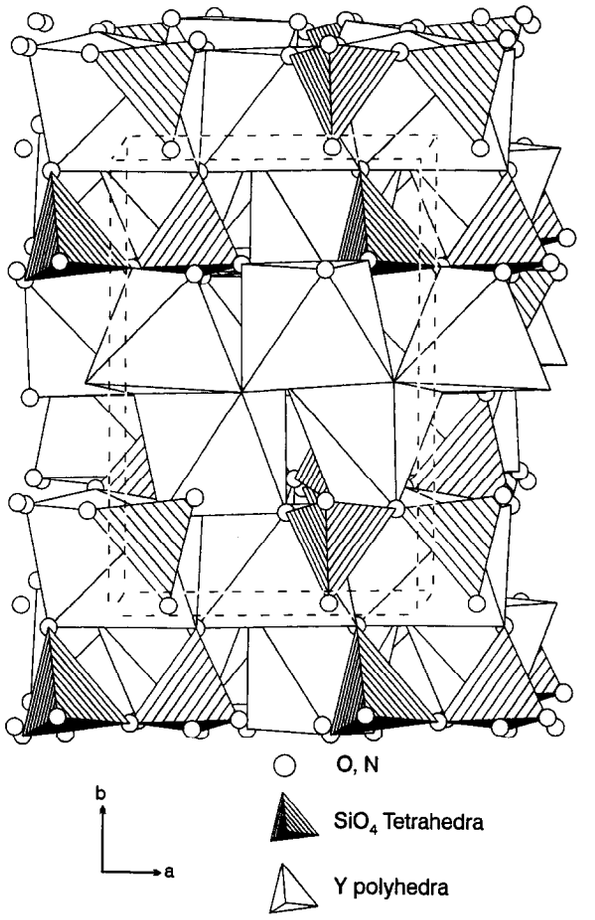

Fig. 6. Polyhedral coordination in J-phase, STRUPLO-90 plot.[11] Unit cell indicated by broken lines.

data[8]; the substitution of one N into the crystallographically distinguishable 'ionic' sites O(1) and O(8) cannot be ruled out by the present data. The ditetrahedral units are linked through O/N atoms with edge-shared Y polyhedra (Fig. 6) to form a corrugated wall in which four different Y environments can be identified (Tables 6 and 7). The Y polyhedra are linked together to form columns parallel to the *a*-axis, the columns forming three-dimensional networks by edge sharing. The Y–O, Y–O/N interatomic distances vary considerably;

on the basis of these contacts < 2·8 Å, the Y(1), Y(2) and Y(4) sites are all 7-co-ordinated. An additional contact with O/N(7) occurs at a distance of 2·92(3) Å from Y(1). Site Y(3) is 6-co-ordinated, with distorted octahedral geometry.

Acknowledgement

We are indebted to Dr I. C. Vickridge for the PIGME analyses.

References

1. Thompson, D. P., Phase relationships in Y–Si–Al–O–N ceramics. In *Tailoring Multiphase and Composite Ceramics, Materials Science Research*, Vol. 20, eds R. E. Tressler, G. L. Messing, C. G. Pantano & R. E. Newnham, Plenum, New York, 1986, pp. 79–91.
2. MacKenzie, K. J. D. & Meinhold, R. H., Role of additives in the sintering of silicon nitride: a ^{29}Si, ^{27}Al, ^{25}Mg and ^{89}Y MAS NMR and X-ray diffraction study. *J. Mater. Chem.*, **4** (1994) 1595–602.
3. Rae, A. W. J. M., Thompson, D. P., Pipkin, N. J. & Jack, K. H., The structure of yttrium silicon oxynitride and its role in the hot-pressing of silicon nitride with yttria additions. *Special Ceramics*, **6** (1975) 347–60.
4. Wills, R. R., Holmquist, S., Wimmer, J. M. & Cunningham, J. A., Phase relationships in the system Si_3N_4–Y_2O_3–SiO_2. *J. Mater. Sci.*, **11** (1976) 1305–9.
5. Vickeridge, I. C., The INS nuclear microprobe: description and applications. *NZ J. Technol.*, **1** (1985) 61–6.
6. Larson, A. C. & Von Dreele, R. B., General Structure Analysis System, Los Alamos National Laboratory, Los Alamos, NM, USA.
7. Saburi, S., Kawahara, A., Henmi, C., Kusachi, I. & Kihara, K., The refinement of the crystal structure of cuspidine. *Mineral. J.*, **8** (1977) 286–98.
8. Hauck, D. S. B., Harris, R. K., Apperley, D. C. & Thompson, D. P., Structural investigation of YAM-type yttrium silicon oxynitride by ^{15}N magic-angle spinning nuclear magnetic resonance. *J. Mater. Chem.*, **2** (1993) 1005–6.
9. Hanic, F., Hartmanova, M., Knab, G. G., Urusovskaya, A. A. & Bagdasarov, K. S., Real structure of undoped Y_2O_3 single crystals. *Acta Cryst.*, **B40** (1984) 76–82.
10. Johnson, C. K., ORTEP II. A Fortran thermal-ellipsoid plot program for crystal structure illustrations, Report ORNL 5138, (1976), Oakridge National Laboratory, Tennessee.
11. Fischer, R. X., LeLirzin, A., Kassner, D. & Rudinger, B., STRUPLO-90, version based on *J. Appl. Cryst.*, **18** (1985) 258.

Journal of the European Ceramic Society 16 (1996) 561–5.

0955-2219(95)00161-1
0955-2219/96/$15.00

Sintering of Diphasic Mullite Gel

Ladislav Pach,[a] Aicha Iratni,[a] Vladimir Kovar,[a] Peter Mankos[a] & Sridhar Komarneni[b]*

[a]Slovak Technical University, Faculty of Chemical Technology, Department of Ceramics, Glass and Cement, 812 37 Bratislava, Radlinského 9, Slovakia
[b]Intercollege Materials Research Laboratory, The Pennsylvania State University, University Park, PA 16802, USA

(Received 23 March 1995; revised version received 10 August 1995; accepted 27 August 1995)

Abstract

A monolithic colloidal gel of mullite composition, prepared from SiO_2 and boehmite sols, was sintered under isothermal conditions. The sintering process was studied by dilatometry, thermogravimetric analysis, bulk density measurements and discontinuous shrinkage measurements. The silica component of stoichiometric colloidal mullite gel prevented crystallization of α-Al_2O_3 in the system. The initial rapid part of the sintering is controlled by the alumina phase and it is not a viscous sintering process in the sense of Scherer's viscous sintering model. The final part of sintering, above approximately 80% of the theoretical density, is controlled by the silica component of the gel and agrees very well with the Scherer model.

1 Introduction

The diphasic monolithic mullite gel is a precursor, which leads to mullite ceramics with a relative density above 96% at 1250–1350°C.[1–8] It is necessary initially to calcine the gel to prevent large volume changes from occurring during sintering.[9,10] The temperature at which the required sintering processes takes place is then increased at least to 1600°C. Many quantitative studies are related to this phenomenon, such as crystallization of mullite,[11–13] phase composition,[2,14,15] sintering of crystallized mullite[9,10] and mechanical properties of mullite ceramics.[1,9,16] Sintering of the gel (amorphous phase, before crystallization of mullite) is considered to be a simple process (viscous flow or viscous deformation mechanism)[3–5,18,19] and, therefore, it has received less attention in the overall study of mullite crystallization and densification. Generally it is believed that sintering of colloidal mullite gels takes place due to the silica component of this gel. But the process has not been analysed from the view point of the role of the individual components of the gel. In this work we shall try to resolve this question.

Sintering of colloidal gels such as silica or mullite is complicated in comparison with powdered glass, because water escapes from the gel during sintering, leading to an increase in viscosity.[19] The relation between OH content in the gel and the rate of sintering, however, is not yet fully understood.[19]

This work describes the sintering kinetics of diphasic mullite gels in correlation to Scherer's viscous sintering model[19,20] as determined by the weight loss of gels at annealing, the role of silica and alumina components during sintering of a mullite gel, the pore size distribution, and the high isostatic densification (at pressure of 1·5 GPa) of gel.

The Scherer model assumes a cubic array of interconnecting glass cylinders. The microstructure of the gel is represented by a unit cell with edge length l and a cylinder with radius a. The equation relating time to density of sample is:

$$\frac{\gamma}{\eta l_0}\left(\frac{\rho_S}{\rho_0}\right)^{1/3}(t - t_0) = \int_0^x \frac{2\mathrm{d}x}{(3\pi x^2 - 8\sqrt{2}x^3)^{1/3}} \quad (1)$$

where

$$x = a/l \quad (2)$$

$$8\sqrt{2}x^3 - 3\pi x^2 + \rho/\rho_S = 0 \quad (3)$$

γ is surface energy, ρ is density at time t, ρ_S is theoretical density, ρ_0 is initial density, η is the viscosity of the gel and t_0 is the fictitious time at which $x = 0$.

2 Experimental Procedure

Monolithic colloidal gels with the stoichiometry $3Al_2O_3.2SiO_2$ were prepared from commercial boehmite (Condea, ~10 nm particle size) and silica

*To whom correspondence should be addressed.

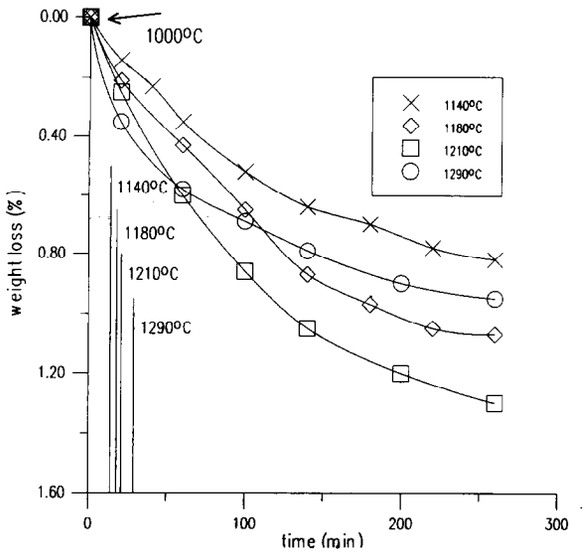

Fig. 1. Thermogravimetric analysis of diphasic mullite gels heated at the rate of 10°C min^{-1} and isothermal annealings. Weight changes of gel have been recorded from temperature 1000°C (standardized stage). Isothermal temperatures are achieved at indicated times with vertical lines on x-axis (time).

sol (Tosil, 30 wt% SiO_2, pH ≈ 9, particle size ≈ 12 nm, stabilized by NH_3). An aqueous boehmite dispersion (18 wt%) was peptized by mixing it with HNO_3 (pH ≈ 2), at 55°C. The boehmite sol was intensively mixed as the silica sol was slowly added. The mixed sol gelled within 1 h in a pan on a hot plate at about 80°C. The nearly transparent gels were extruded to rods (d ≈ 0.5 cm, l ≈ 5 cm). The monolithic gel rods were allowed to dry in air in a vertical position in order to retain their circular cross-section and shape. Dried gel rods were calcined at 550°C for 2 h. For the pressed samples, each gel rod was separately encapsulated and cold isostatically pressed at 1·5 GPa. Shrinkage of the gel rods (l = 2 cm, d = 0·5 cm) was measured during sintering using a Netsch 402 - E dilatometer at a heating rate of 10°C min^{-1} or by the discontinuous method. Rods of gels (l = 1 cm, d = 0·1 cm) were put suddenly into an oven (temperature range 1120–1220°C) and after sintering were quenched. Temperature change was about 600°C min^{-1} in the heating process. Thicker gel rods cannot be used because they disintegrated during the sudden heating. The lengths of the gel rods were measured before and after heat treatment using a micrometer. Relative density (ρ/ρ_S) curves reported in various figures were obtained from continuous dilatometric curves, thermogravimetric curves (Fig. 1) and bulk density measurements (liquid displacement method) with an error of ± 0·05 Mg m^{-3}. Relative density curves were then obtained from continuous dilatometric curves. Therefore, error bars cannot be introduced into figures.

3 Results

The specific surface area of the original gel (calcined at 550°C for 2 h) outgassed in vacuum at 350°C was 241 m^2 g^{-1}. The pore size was in a narrow range of 2–3 nm (unimodal pores). Upon isothermal heating of gels at 1140, 1180 and 1210°C [crystallization of mullite was not detected by X-ray diffraction (XRD)] and at 1290°C (mullite crystallized as detected by XRD) for 240 min, weight losses (Fig. 1) ranged from 0·8 to 1·3% compared with the standardized weight of a gel at 1000°C. If the gel is heated to the temperature at which crystallization takes place (e.g. 1290°C), the weight loss at the beginning is obviously faster than at a lower temperature, but later the weight loss is little or none as a consequence of crystallization of mullite. The standardized weight of the gels at 1000°C enables the gels to avoid the influence of physically adsorbed water (different humidity of air) on the measured weight changes.

Sintering of one-component gels (silica and alumina) and diphasic gels of mullite composition is shown in Fig. 2. Initial relative bulk densities ρ/ρ_0 of gels increase in the order boehmite < mullite < silica gel. After sintering at 1220°C for 5 h the mullite gel yielded only defect (δ,θ)-Al_2O_3 phases. Mullite, however, did not crystallize. On the other hand, both the one-component gels crystallized. The boehmite gel totally transformed to α-Al_2O_3 and the silica gel partly crystallized to cristobalite.

Mullite sintering kinetics were analysed by Scherer's viscous sintering model.[19,20] Zero time of isothermal heating reported for the kinetics studies refers to that time at which the sample reached the isothermal temperature (Figs 3, 4 and 5). Theoretical curves generated by the solution of eqn (1) are shown by the solid line in Figs 3C, 4C and

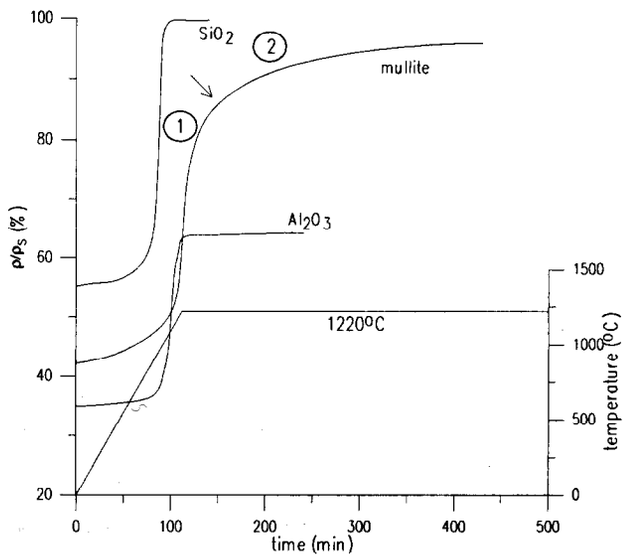

Fig. 2. Relative densities of silica, alumina and mullite colloidal gels vs. time of isothermal annealing at 1220°C: (1) the first part; (2) the second part of mullite densification.

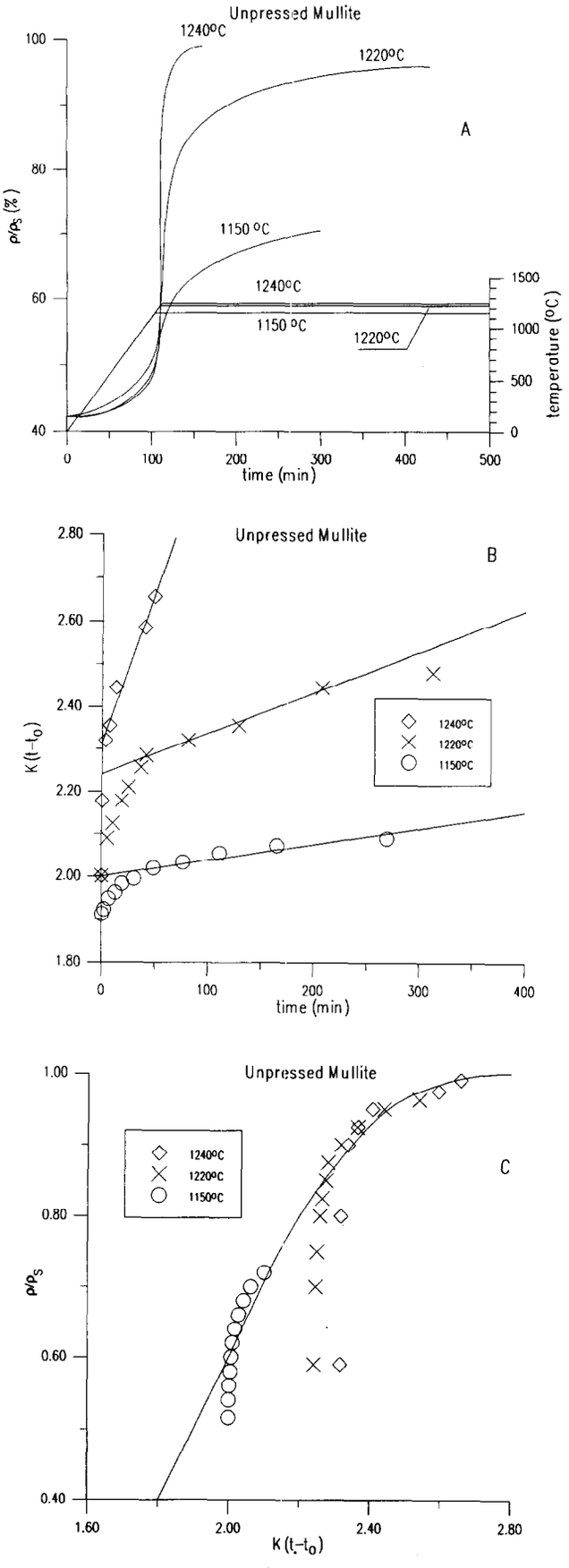

Fig. 3. Sintering of unpressed colloidal mullite gels at isothermal annealing temperatures of 1150, 1220 and 1240°C (increase of temperature 10°C min^{-1}).
A — relative bulk densities vs. time of isothermal annealing.
B, C — analysis of sintering kinetics by Scherer's model.
B — reduced time vs. experimental time.
C — relative bulk densities vs. reduced time, solid line is theoretical function of the model.

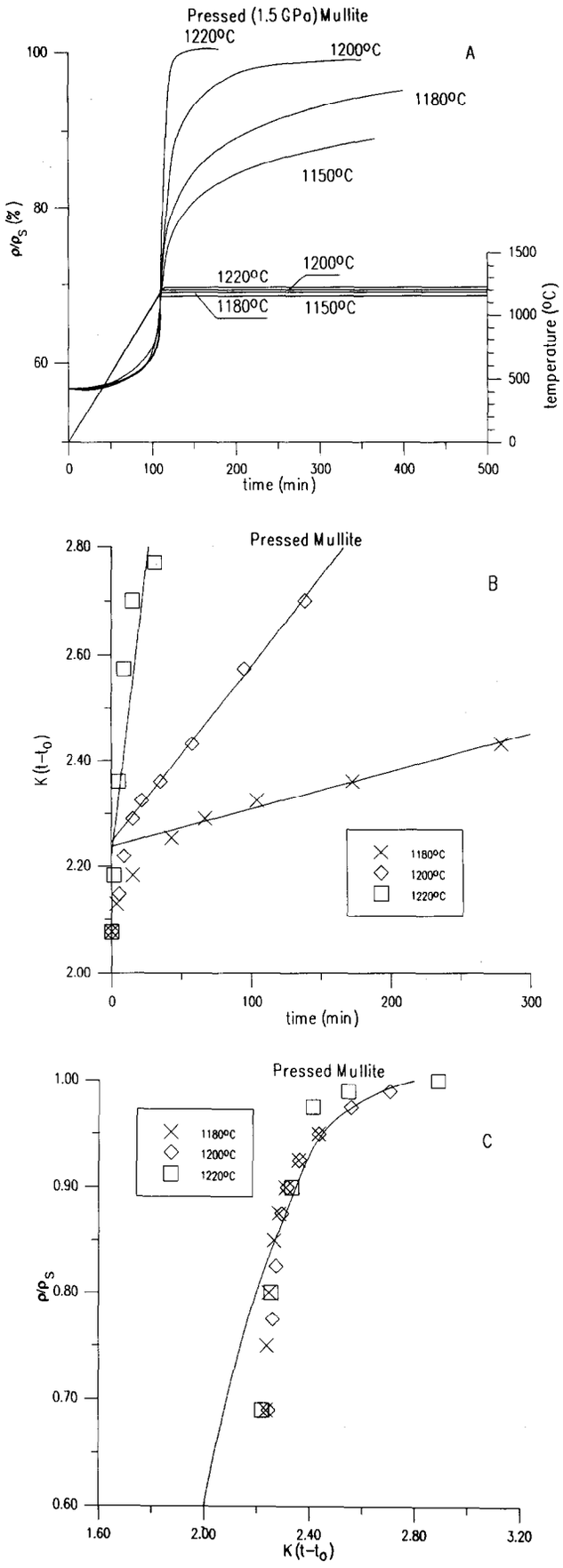

Fig. 4. Sintering of cold isostatically pressed (1·5 GPa) colloidal mullite gels at isothermal annealing temperatures of 1150, 1180, 1200 and 1220°C (increase of temperature 10°C min^{-1}).
A — relative bulk densities vs. time of isothermal annealing.
B — reduced time vs. time of experimental annealing.
C — relative bulk densities vs. reduced time, solid line is theoretical function of model.

5C. This function is used to find the reduced time $K(t - t_0)$ (where K is a constant, t is the experimental time and t_0 is a fictitious time at which $\rho = 0$) for experimental values of ρ/ρ_S. The function of these reduced times vs. the duration of isothermal heat treatment should be a straight line according to the model (Figs 3B, 4B and 5B) with slope:

$$K = \frac{\gamma(\rho_S/\rho_O)^{1/3}}{\eta l_O} \quad (4)$$

The length parameter of the model l_O can be calculated if the initial specific surface area S_O is known according to the following equation:

$$l_O = \frac{3}{S_O \rho_S x}\left(1 - \frac{\pi}{3\pi - 8\sqrt{2}x}\right) \quad (5)$$

Using eqn (5), initial relative density $\rho/\rho_S = 0{\cdot}42$ and surface area of 241 $m^2\ g^{-1}$, the length parameter of the Scherer model is 7·56 nm.

Gel viscosity was calculated from eqn (4). The required parameters K (slope of lines Figs 3B, 4B and 5B), l_O and ρ/ρ_O (Table 1) are available from the experimental measurements. For γ a value of 0·28 kJ m^{-2} was used.[19]

Initial steep parts of the sintering curves (Fig. 3A) for unpressed gels are not in agreement with theoretical functions of Scherer's model (Figs 3B and 3C). Disagreement increases with the increase in annealing temperature. In the case of the function $K(t - t_0)$ vs. time of isothermal annealing, disagreement with the model is in the deviation of experimental points from the straight line for short times (Fig. 3B). According to Scherer,[19] such deviation from the model represents an increase of viscosity caused by escape of water from the system. The above described relations for unpressed gels (Fig. 3) are nearly the same as those for cold isostatically pressed (1·5 GPa) gels (Fig. 4). However, the deviation from the model is smaller for the latter. Kinetic functions for rapidly heated samples (600°C min^{-1}) are shown in Fig. 5. Unlike the slowly heated samples (Figs 3 and 4), there is a broad agreement of experimental measurements with the model for rapidly heated samples. Kinetic parameters of gels are summarized in Table 1, and calculated functions of viscosities vs. $1/T$ are shown in Fig. 6 together with calculated activation energies. The activation energies are approximate because they were calculated based on only a few experimental points. The differences in activation energies clearly show that different processes are involved. All functions in Fig. 6 show two straight lines with different activation energies. Lines with low energies belong to viscous sintering of mullite gels without crystallization of mullite (mullite was not detected by XRD). Lines with

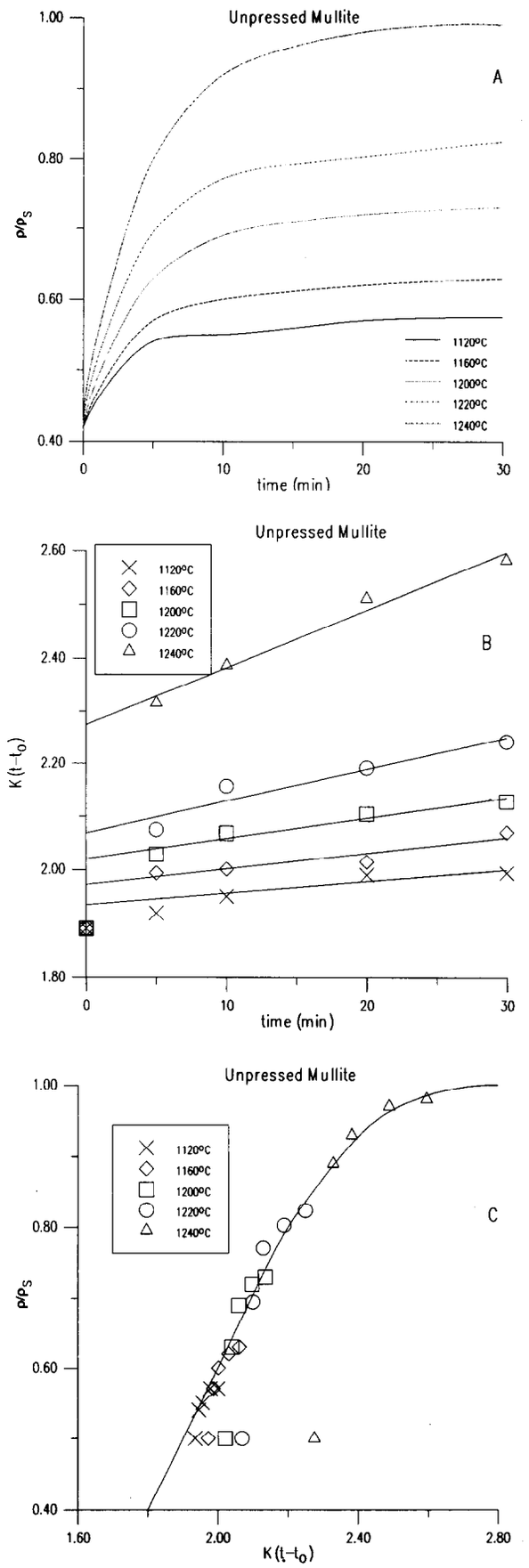

Fig. 5. Sintering of unpressed colloidal mullite gels at isothermal annealing temperatures of 1120, 1160, 1200, 1220 and 1240°C for rapidly heated samples (~600°C min^{-1}).
A — relative bulk densities vs. time of isothermal annealing.
B — reduced time vs. experimental time.
C — relative bulk densities vs. reduced time, solid lines are theoretical function of model.

Table 1. Kinetic parameters of sintering of diphasic colloidal mullite gels analysed by Scherer's model (K is constant of reduced time, viscosity is calculated for $l_0 = 7{\cdot}56$ nm, $\rho/\rho_S = 0{\cdot}42$ and $\gamma = 0{\cdot}28$ J m^{-2}; A — heating rate of ~600°C min^{-1}, B, C — heating rate of ~10°C min^{-1}; A, B — unpressed, C — pressed

Type	t (°C)	K (s)	η (Pa.s) × 10^{-12}
A	1120	$3{\cdot}6 \times 10^{-5}$	13·8
	1160	$4{\cdot}9 \times 10^{-5}$	10·1
	1200	$6{\cdot}3 \times 10^{-5}$	7·8
	1220	$10{\cdot}0 \times 10^{-5}$	4·9
	1240	$17{\cdot}8 \times 10^{-5}$	2·8
B	1150	$0{\cdot}6 \times 10^{-5}$	79·1
	1220	$1{\cdot}6 \times 10^{-5}$	30·9
	1240	$11{\cdot}6 \times 10^{-5}$	4·3
C	1150	$0{\cdot}7 \times 10^{-5}$	57·8
	1180	$1{\cdot}2 \times 10^{-5}$	41·7
	1200	$5{\cdot}6 \times 10^{-5}$	8·9
	1220	$36{\cdot}3 \times 10^{-5}$	1·4

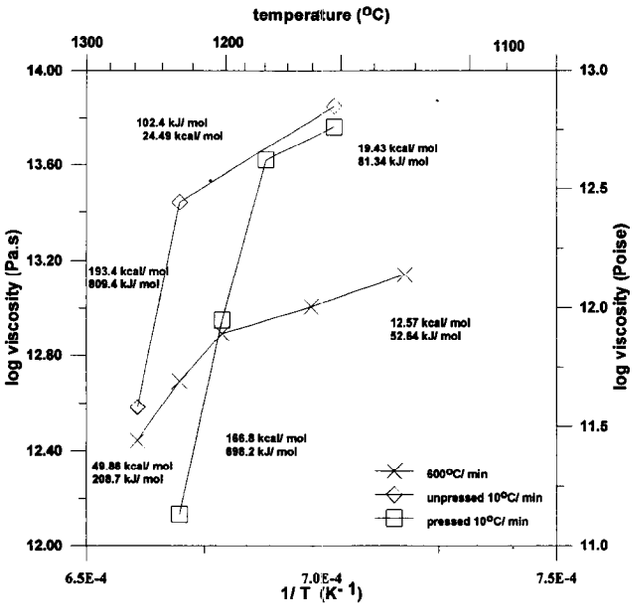

Fig. 6. Function of calculated viscosities (Scherer's model) vs. $1/T$ for diphasic mullite gels. Activation energies were calculated using an Arrhenius-type equation.

high energies belong to sintering and simultaneous crystallization of mullite. The sintering process in rapidly heated samples (600°C min^{-1}) takes place at significantly lower activation energies than in slowly heated samples (10°C min^{-1}). It is as a result of actual OH content in the samples, which can be assumed to be higher in rapidly heated samples.

4 Discussion

The diphasic mullite gel used here is composed of AlOOH or alumina particles (the latter present at temperatures >550°C), of size ~10 nm, and SiO_2 particles with size of ~11 nm. Considering stoichiometric mullite composition, a boehmite density of 3·70 Mg.m^{-3},[21] a silica density of 2·20 Mg m^{-3} and the above-mentioned particle size, the ratio of silica to boehmite (alumina) particles is 1:2·7. This means that the system is composed of 27% of silica particles and 63% of AlOOH particles (above 550°C alumina particles of the anhydrous type). Up to the temperature of intensive sintering both types of particles (i.e. silica and alumina) should form a connected network according to the percolation theory, which states that the threshold concentration to establish a connected network is about 16 vol% for a random mixture of two types of spherical particles of equal size.[22,23] This idea can be discussed by comparing the dilatometric curves of the one-component colloidal gels (SiO_2 and AlOOH) and of the diphasic gel of mullite stoichiometric composition (see Fig. 2). The silica gel used here becomes fully dense by 950°C, but the boehmite gel practically did not sinter below 1000°C. Slow sintering of the mullite gel up to about 1000°C is a result of sintering of the connected network of silica particles, leading to isolated islands of the SiO_2 phase. Above a temperature of 1000°C, sintering of boehmite derived gel is identical with sintering of the mullite gel (Fig. 2, part 1 of mullite gel). In the case of the boehmite gel, sintering was suddenly arrested by crystallization of α-Al_2O_3. If crystallization of α-Al_2O_3 did not take place, then it could be assumed that densification of the boehmite gel would not stop at a relative density of ~62% (Fig. 2) and would be continued. Such conditions are fulfilled in the mullite gels, where only direct crystallization of mullite was observed at about 1240°C. From this result, it is suggested that fast sintering of a mullite gel (Fig. 2, part 1) is controlled by the alumina phase. At this stage of sintering probably only one connected phase is present—the alumina phase. Silica enables this sintering of alumina by preventing the α-Al_2O_3 crystallization in the gel. Other influences of silica components at this stage of sintering of mullite gels are not yet clear. Further study would be needed for a better understanding of the role of the SiO_2 phase at this stage of the mullite gel sintering.

The same conclusion follows from sintering kinetic analysis by Scherer's model. The initial fast sintering of mullite (Fig. 2, part 1) as discussed above shows significant deviation from the model (Figs 3, 4 and 5). This result also indicates that the process is not a viscous sintering process in the sense of the model, where matter flows as a continuum (connected network of bonds M–O–M). It is rather flow of particles, especially flow of alumina particles. For such small particles as are

involved in the present mullite gels, viscous flow of particles and reorganization of particles are probably identical processes. These processes are influenced by the OH group content in the samples, as follows from the sintering kinetics of slow (10°C min^{-1}, Figs 3 and 4) and rapidly heated (600°C min^{-1}, Fig. 5) samples. At fast heating, the actual OH content of the samples is higher, as is observed from faster sintering at lower activation energies (Fig. 6).

Sintering of the mullite gel above ~80% of relative density (Fig. 2, part 2), is much slower than below ~80% density (Fig. 2, part 1) and agrees very well with Scherer's sintering model. The SiO_2 phase now begins to control the sintering process by the well known[19,20] viscous flow sintering mechanism. The silica phase begins to form a connected network in the sense of Si–O–Si bonds, unlike the initial gel where it is necessary to consider a network of colloidal silica particles. It is enabled by the spreading of the Al_2O_3/SiO_2 interface at the cost of Al_2O_3/vapour and SiO_2/vapour interfaces. With the increased movement of ions at this stage, crystallization of mullite also takes place. In the studied gel the crystallization of mullite had occurred at 1240°C.

Activation energies of viscous flow obtained from the (model) slopes of linear functions of K $(t-t_0)$ vs. experimental time (Figs 3B, 4B and 5C) depends on temperature, pressing and also on the heating rate (Fig. 6). The activation energies decrease as follows: unpressed gel > pressed gel > fast heated gel. These processes are significantly influenced by actual OH concentration in the sample and by crystallization of mullite.

5 Conclusion

The silica component of stoichiometric colloidal mullite gels prevents the crystallization of α-Al_2O_3. It enables the alumina component of the gel to control the sintering of the mullite gel by means of a connected network of (δ,θ)-Al_2O_3. The initial fast part of sintering is not a viscous sintering process in the sense of Scherer's sintering model. The second, slow part of sintering, above about 80% of theoretical density is controlled by the silica component of the gel and agrees very well with Scherer's model. The sintering process and also the activation energies are influenced by the rate of temperature increase, apparently as a consequence of an actual OH content in the gels.

Acknowledgement

This research was supported by NSF under grant No. 9001204.

References

1. Aksay, I. A., Dabbs, D. M. & Sarikaya, M., *J. Am. Ceram. Soc.*, **74** (1991) 2343.
2. Wang, Y., Li, D. X. & Thompson, W. J., *J. Mater. Res.*, **8** (1993) 195.
3. Komarneni, S., Suwa, Y. & Roy, R., *J. Am. Ceram. Soc.*, **69** (1986) C-155.
4. Yoldas, B. E., *Am. Ceram. Soc. Bull.*, **59** (1980) 479.
5. Jeng, D.-Y. & Rahaman, M. N., *J. Mater. Sci.*, **28** (1993) 4904.
6. Mroz Jr, T. J. & Laughner, J. W., in *Ceramic Transactions, Vol. 7, Sintering of Advanced Ceramics*, ed. C. A. Handwerker, J. E. Blendell and W. Kaysser. American Ceramic Society, Westerville, OH, 1990, pp. 664–70.
7. Rahaman, M. N. & Jeng, D.-Y., in *Ceramic Transactions, Vol. 7, Sintering of Advanced Ceramics*, ed. C. A. Handwerker, J. E. Blendell and W. Kaysser. American Ceramic Society, Westerville, OH, 1990, pp. 753–66.
8. Wu, J., Chen, M., Jones, F. R. & James, P. F., *J. Non-Cryst. Solids*, **162** (1993) 197.
9. Hirata, Y., Sakeda, K., Matsushita, Y., Shimada, K. & Ishihara, Y., *J. Am. Ceram. Soc.*, **72** (1989) 995.
10. Mroz Jr, T. J. & Laughner, J. W., *J. Am. Ceram. Soc.*, **72** (1989) 508.
11. Wei, W. & Halloran, J. W., *J. Am. Ceram. Soc.*, **71** (1988) 166.
12. Wei, W. & Halloran, J. W., *J. Am. Ceram. Soc.*, **71** (1988) 581.
13. Sundaresan, S. & Aksay, I. A., *J. Am. Ceram. Soc.*, **74** (1991) 2388.
14. Li, D. X. & Thompson, W. J., *J. Mater. Res.*, **6** (1991) 819–24.
15. Hulling, J. C. & Messing, G. L., *J. Non-Cryst. Solids*, **147–148** (1992) 213.
16. Dokko, P. C., Pask, J. A. & Mazdiyasni, K. S., *J. Am. Ceram. Soc.*, **60** (1977) 150.
17. Shinohara, N., Dabbs, D. M. & Aksay, I. A., *SPIE Vol. 683, Infrared and Optical Transmitting Materials* (1986) 19–24.
18. Sonuparlak, B., *Adv. Ceram. Mater.*, **3** (1988) 263.
19. Scherer, G. W., Brinker, C. J. & Roth, E. P., *J. Non-Cryst. Solids*, **72** (1985) 369.
20. Scherer, G. W., *J. Am. Ceram. Soc.*, **60** (1977) 236.
21. Wilson, S. J. & Stacey, M. H., *J. Colloid Interface Sci.*, **82** (1981) 507.
22. Sacks, M. D., Bozkurt, N. & Scheiffele, G. W., *J. Am. Ceram. Soc.*, **74** (1991) 2428.
23. Zallen, R., *The Physics of Amorphous Solids*. Wiley, New York, 1983, pp. 183–91.

Journal of the European Ceramic Society 16 (1996) 567–574

0955-2219(95)00165-4
0955-2219/96/$15.00

Loading of Solids in a Liquid Medium: Determination of CBVC by Torque Rheometry

J. Janardhana Reddy,[a] M. Vijayakumar,[a] T. R. R. Mohan[b] & P. Ramakrishnan[b]

[a]Defence Metallurgical Research Laboratory, Kanchanbagh, Hyderabad–500 258, India
[b]Department of Metallurgical Engineering, Indian Institute of Technology, Bombay–400 074, India

(Received 31 January 1995; revised version received 24 June 1995; accepted 27 August 1995)

Abstract

In many applications involving solid–liquid mixtures such as powder injection moulding, it is necessary to know the minimum amount of liquid necessary to provide fluidity to the powder–liquid mix. This quantity, referred to as critical binder volume concentration (CBVC), can be determined for a given powder by torque rheometry. This paper discusses the optimization of various parameters involved in the determination using torque rheometry, along with the application of the method to a variety of powders of different sizes and shapes. The CBVC value thus determined represents the minimum void volume achievable for a given powder, and thus can form the basis for deciding the amount of binder desired for injection moulding.

1 Introduction

Filling of solids in a liquid medium finds a variety of technological and commercial applications, from the formulation of common paints and pigments, to fabrication of high-tech ceramic products of complex shapes by injection moulding. In all these applications, it is useful to know the optimum quantity of the liquid medium required to disperse and mix the solids thoroughly with the liquid. Despite this, not much attention has been paid to the systematic study of this process so far. Literature records only about a dozen papers over past several decades.[1–17]

From the literature, it appears that the first sector to address this issue was the paint industry. In the early 1920s, it was noticed that the properties of a pigment–thinner mixture of a paint formulation changes drastically beyond a critical amount of solid in the liquid. Gardner and Coleman[1,2] proposed the concept of oil absorption value as an estimate of this quantity, and described a procedure for determining the same experimentally (ASTM-D1483). A slightly modified procedure, widely known as Spatula Rub-Out test,[3] was tentatively adopted in 1927 as the standard, ASTM D-281. This method was considered superior to the former one in view of the additional dispersion achieved during the rubbing operation. Klumpp[5] proposed that the oil absorption value measured is related to the pore or void volume of a closely packed pigment. However, Gardner and Coleman[1] and Baldwin[6] thought it to be simply a function of the specific surface area of the pigment.

These divergent views gave way to a somewhat coherent approach in the late 1940s with the development of the concept of critical pigment volume concentration (CPVC). According to this concept, developed largely by Asbeck and Van Loo,[7] CPVC is the pigment content, expressed as vol% pigment in the pigment–binder mix, at which the binder is just sufficient to form a strong, adsorbed layer on the pigment particles and to completely fill the inter-particulate voids (see Fig. 1). It represents the densest packing of the pigment particles commensurate with the degree of dispersion of the system. Once the pigment volume becomes more than the CPVC, the properties of the powder dominate that of the mix. Similarly, if the pigment volume is less than the CPVC, the properties of the mix are determined largely by those of the liquid.

Thus, the above definition provided a conclusive physical interpretation to the set of experimental observations of paint film properties, such as gloss, corrosion resistance, permeability, hiding power, washability, etc.[8] And, PVC/CPVC ratio became an important factor in formulating paints with desired properties. This concept can be easily extended to all situations where a powder—be it an organic or inorganic pigment, or a ceramic or a metal powder—is required to be intimately mixed with a liquid in any particular usage. The acronym CPVC can be then be suitably altered to mean critical particle volume concentration.

In many of the practical applications, the liquid

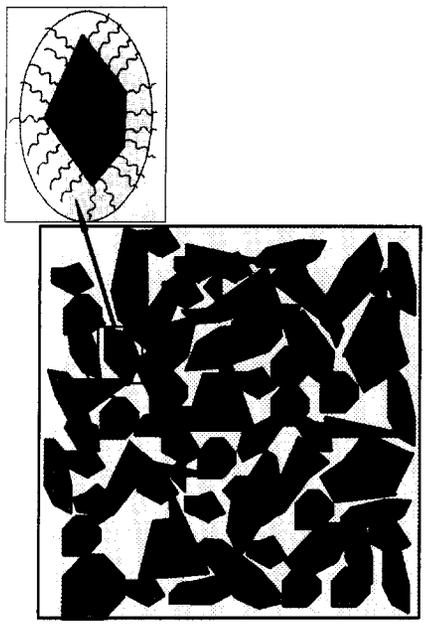

Fig. 1. Schematic particle structure at the point of CBVC showing the interparticulate voids completely filled by the binder liquid; the inset shows the adsorbed liquid forming a boundary layer around a particle.

used acts essentially as a binder for the particulate system, and the need is to know the volume of this liquid to be added. Keeping this in view, it is preferable to use the above concept in terms of its complement, the critical binder volume concentration (CBVC). In fact, the oil absorption value measured experimentally is the CBVC value itself.

In spite of the practical significance of CBVC, the Spatula Rub-Out test[3] remained the only popular method for its determination until the late 1950s. According to this method, a known weight of the pigment sample is kept on a glass plate or a marble slab. Raw linseed oil is added drop by drop to this pigment, and rubbed with a sharp edged steel spatula so as to incorporate the oil in the powder completely. The end point of the test is when a very stiff, putty-like paste, which does not break or separate on rubbing, is formed. This method is poorly reproducible and highly inaccurate because of the human subjectivity involved in the determination of the end point.

Bessey and Lammiman[9] used a density measuring technique to estimate the CBVC. In this, the powder is mixed with the binder in varying proportions, compacted and the density determined. The mix showing the peak density corresponds to CBVC. Warren and German,[10] Pujari[11] and others[12] have applied this technique to ceramic and metal powders. Hay[13] suggests that this technique is good only if complete removal of air, proper dispersion to eliminate all agglomerates and tightest possible packing of the particles is ensured. While these conditions are met easily for mixes containing binder in excess of CBVC, it is not so for sub-CBVC compositions.[14] The resulting error in densities for these samples makes the determination of the point of peak density highly subjective and inaccurate.

Wirsching and Haug[15] proposed the first instrumental method based on measuring the torque as a function of the binder content using a low shear, sigma type torque measuring mixer. Although this method is far superior to the Spatula Rub-Out test, it remained largely unknown and unexplored except for some specialized purposes.[16,17] Hay[13] re-investigated the method for the determination of oil absorption value of pigments using a Brabender Plastograph. Markhoff *et al.*[18] applied this technique for the estimation of CBVC of ceramic mixes used for fabrication of high-tech components by ceramic injection moulding. Pujari[11] proposed an alternative method based on the mechanical exotherm observed during the mixing of a molten binder with a powder in a Helicone mixer having two intermeshing blades.

Pujari's method involves a series of mixing experiments with different powder-to-binder ratios in order to estimate the CBVC, and hence is laborious and time consuming. In addition, the mechanical exotherm, which is attributed to the change of mixing from distributive to dispersive mode, was not observed in our repeated experiments in the Banbury type mixer of the Brabender Torque Rheometer. In both the work of Hay[13] and Markhoff *et al.*[18] the variation of the torque, as a function of the oil volume added to a known volume of the powder kept in the mixing bowl, is measured. A sharp change in the torque indicates the end point. In the above studies, however, the experiments were confined to only very fine powders, and limited volumes and single mixing speed. The effect of various instrumental parameters, as well as the role of particle size and shape of the powder used were not investigated in detail. This has limited the general applicability of this versatile technique for determining the CBVC of a variety of powders. This paper presents the result of our comprehensive studies on these aspects of the experimental methodology.

2 Experimental

The instrument used is a Brabender PL-2000-3 Torque Rheometer fitted with W 50 E mixing bowl and roller blades. Linseed oil of acid value 2·5 is required for mixing.

The general procedure is as follows. The torque range of the torque rheometer is calibrated for a set rotational speed (between 50 and 100 rev min^{-1}) of the blades. About 50 ml (apparent volume) of the powder is accurately weighed. Half this powder is filled into the mixing bowl and 5 ml

of linseed oil is added. After mixing for about 5 min, the balance powder is added and the mix is titrated with linseed oil. During the experiment, the oil is added to the bowl, either continuously or stepwise, using a burette. The torque is recorded continuously as a function of time using the computerized data acquisition system. The experiment is stopped after the torque value has passed through the peak value and dropped substantially. The volume of the binder corresponding to the peak value of the torque is used to estimate the CBVC.

3 Results and Discussion

3.1 Principles

The process of mixing in a Banbury type mixer, along with a typical torque vs. time curve are illustrated in Fig. 2. When an aliquot of a liquid is added to a powder mass, the torque rises sharply initially and then starts falling until it attains some stable, mean value as shown in Fig. 3 (a). The initial sharp rise is due to the immediate immobilization of the liquid by the powder particles to form a few big clusters. The immobilized liquid proceeds either to form an adsorbed liquid layer on the particles, or to bind the particles together by liquid bridging, or to fill the voids within the cluster. Both liquid bridging and void filling lead to the formation of very tight clusters which are usually tough because of the strong surface tension force involved. Considerable stresses are therefore required in order to break these clusters. Thus, during mixing at a constant shear rate, high torques are encountered initially when only a few big clusters are present. As the shearing action is continued, these big clusters break down into a large number of smaller ones, until some equilibrium distribution is reached. Corresponding to this, the torque also shows a downward trend and, ultimately, stabilizes at a certain level depending on the amount of the liquid added. If a small aliquot of the liquid is again added to this solid–liquid mix, a similar but smaller torque rise and stabilization occurs, as shown in Fig. 3(b). The mean equilibrium size of the clusters at the end of such an equilibration cycle will depend inversely on the shearing rate used (i.e. the rev min^{-1} of the mixing blades), and directly on the amount of liquid available for binding the particles.

As we continue adding the liquid, the mean equilibrium size of the clusters becomes bigger and bigger as more and more particles join together, until ultimately the whole mass becomes a coherent paste. Corresponding to this, the torque also continuously increases until it reaches a peak at the point of CBVC. From then on, addition of any further liquid serves only to dilate the solid structure and increase the interparticle distances. Therefore, the mixing torque falls as shown in Fig. 3 (c).

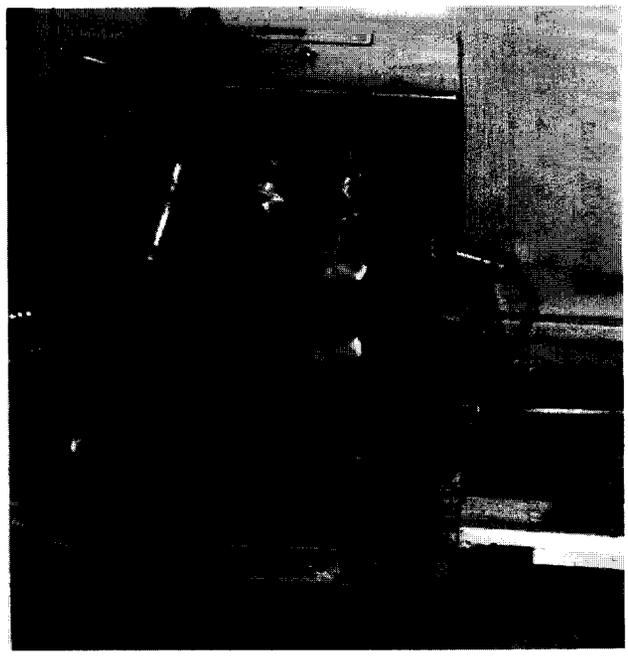

(a)

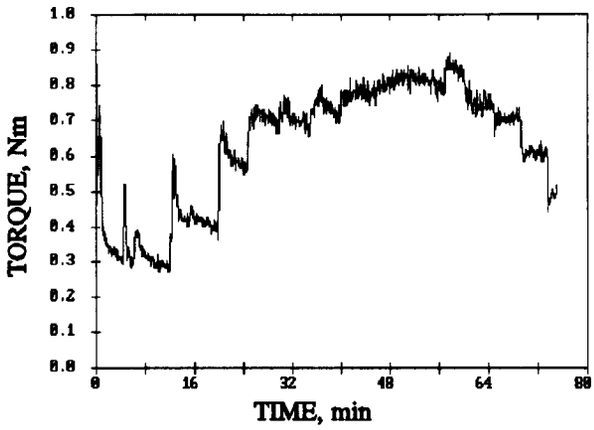

(b)

Fig. 2. (a) A Brabender mixer with roller mixing blades having a free bowl volume of 55 ml. (b) Variation of torque during a titration of 65 g of fused silica powder with linseed oil using roller blades rotating at 50 rev min^{-1}.

3.2 Optimization of experimental parameters

In standardizing the method for estimating CBVC using the above principles, various parameters such as the type of the titrant liquid to be used, the amount of powder to be filled into the mixing bowl, the rotational speed of the mixing blades and the manner in which the binder is added to the mixing bowl are to be optimized with respect to the sharpness of the endpoint and a smooth conduct of the titration. For this, two types of powders having different characteristics have been used: fused silica powder has a multimodal

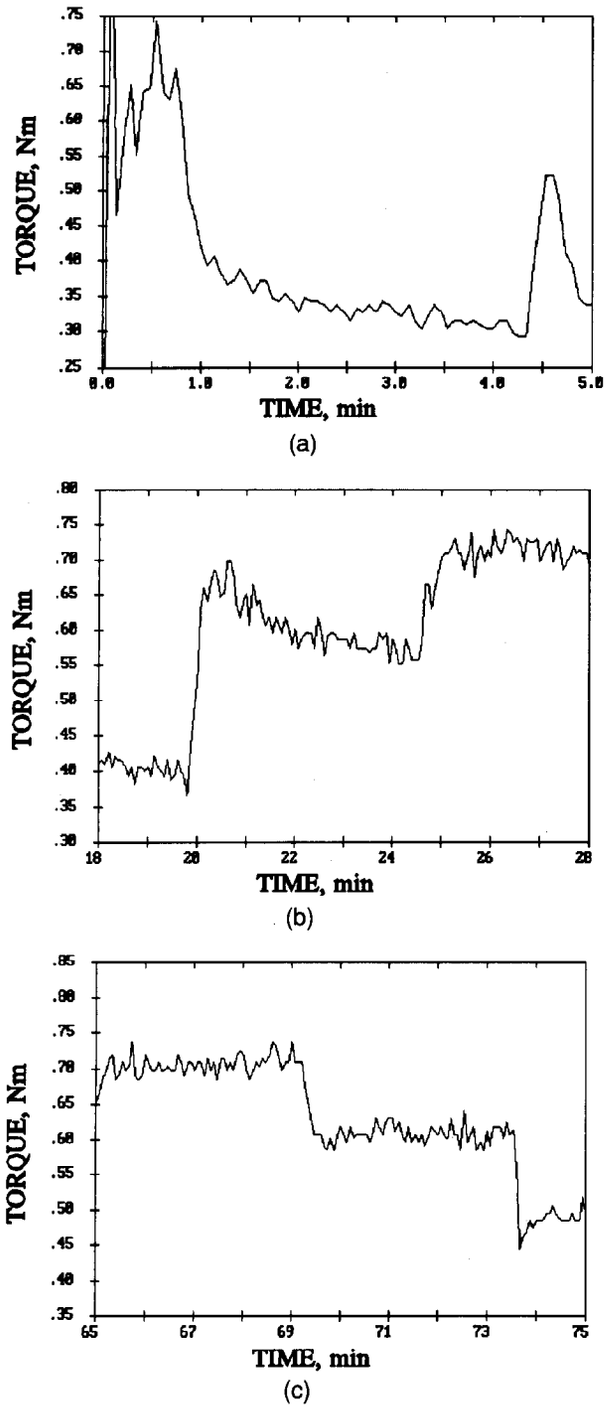

Fig. 3. Variation of torque with time: (a) On first addition of 5 ml of oil; (b) on addition of 0·5 ml of oil at some intermediate stage before the point of CBVC; (c) on addition of 0·5 ml of oil beyond the point of CBVC.

distribution of irregular shaped particles having an average particle size of about 35 μm, while alumina has a narrow monomodal distribution of irregular shaped particles centred around 2 μm.

3.2.1 Choice of the binder liquid

One of the points implicit in the application of the torque rheometer method is that the binder liquid wets the powder very well, as only a wetting liquid can flow into the interparticulate regions and give rise to interparticle bonding and hence torque. Also, as the liquid is to be added to the powder in the mixing chamber during the course of the experiment either continuously or in small aliquots using a dispenser or a burette, it must have reasonably good fluidity. Higher fluidity also facilitates faster flow into the interparticulate regions, and leads to shorter experimental times. In addition, the wear of the mixing chamber and the mixing blades will be minimized if the liquid is able to lubricate the particles. Thus the choice is essentially limited to low viscosity, wetting type liquids, having some lubricating properties. Many natural oils such as linseed oil, olive oil, sunflower oil, etc., which are multicomponent mixtures, satisfy these requirements. These oils are polar enough to wet most metal and ceramic powder surfaces which are essentially polar in nature, and they are acceptable in terms of their fluidity and lubricating behaviour. It was decided to use linseed oil as it is most commonly used in the paint industry as a vehicle, and hence is inexpensive and easily available.

3.2.2 Volume of powder

Hay[13] has suggested the total volume of the pigment and oil to be about 35 to 40 ml in 83·5 ml bowl based on his studies with diatomaceous silica and talc, while Markhoff *et al.*[18] have proposed that a theoretical powder volume of 25 ml for a 55 ml bowl be used. The former does not provide any basis for selecting the initial volume of the powder without trial and error experiments, and the latter is too arbitrary to apply for different powders.

Figures 4 (a) and (b) show the torque vs. binder volume concentration (BVC) curves for different volumes of silica as well as alumina powders. The total bowl volume is 117 ml. Out of this, the roller type mixing blades occupy a volume of 62 ml. The free bowl volume (FBV) available for holding the mix is thus 55 ml. (If cam blades are used for mixing, then the free bowl volume will be 83 ml.) In the graphs, the total volume of the mix is expressed in terms of per cent free bowl volume filled at the point of CBVC (% FBV). The y-axis in the graphs represents the torque value after mixing equilibrium is achieved and the x-axis represents the volume of the liquid added expressed as the vol% oil in the mix. Figure 4 (c) presents the CBVC values for different volumes of the mix at the point of CBVC. It is clear from the figures that, as the amount of the powder used is successively increased, the torque level increases. Except for small volumes, neither the end point definition nor the value of CBVC is significantly affected. But high volume of the powder implies higher mixing times and greater wear of the mixer, and is therefore undesirable. From this, it appears ideal that a volume of the mix sufficient enough to fill

at least 50% FBV at the point of CBVC should be used for conducting the mixing experiment.

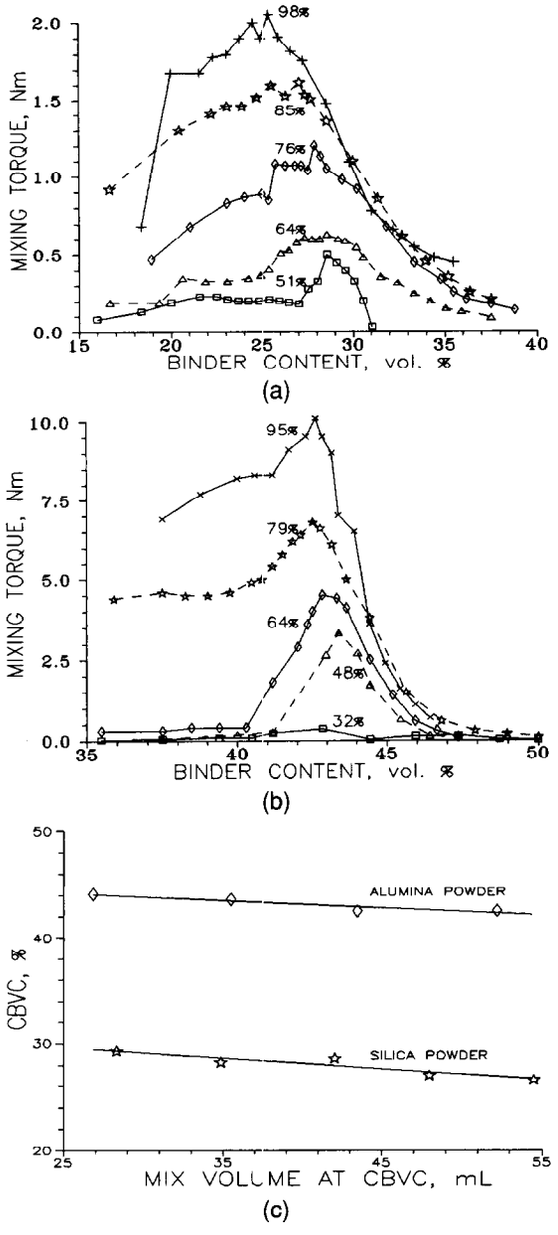

Fig. 4. Equilibrium mixing torque as a function of binder volume concentration for different volumes of the powder: (a) fused silica; (b) alumina. Roller blades at 50 rev min^{-1} were used. Values near the curves indicate the % free bowl volume filled at CBVC. (c) CBVC data from the graphs (a) and (b) vs. the total mix volume at CBVC.

However, the packing density of free powders imposes a limitation which precludes following this criterion universally. Particles of a powder mass do not flow freely and pack to their optimum level because of interparticle friction. Table 1 presents the volume of a powder pack, having an initial apparent volume of 100 ml on tapping (corresponding to the tap density) and that in the presence of a liquid (corresponding to the point of CBVC). It is clear that packing of powder particles is far more efficient in the presence of a liquid than when just tapping. This is because mixing with a lubricating liquid permits the particles to slide easily past each other and pack. The particle packing is also greatly assisted by the capillary forces due to the presence of the liquid in the interparticle regions.[19] As a consequence, the actual volume occupied by the powder when mixed with a liquid is lower than that in the absence of the liquid, and this difference becomes very pronounced especially for irregular shaped, fine powders.

In view of this, even if the powder is filled in the bowl to the topmost level of the blades in the beginning of the mixing experiment, its volume will decrease once the titration with linseed oil is commenced. For some powders, the volume may not even be sufficient to ensure good mixing by shearing action during the rotation of the blades. In fact, if the powder volume becomes very small, the powder–oil mix simply sticks to the blades and is physically carried along with them, and no mixing takes place. On the other hand, if more powder is forcibly filled with pressure into the bowl to overcome this problem, the oil flowing through the hole in the ram will form an impervious, oil–powder layer at the top of the bowl that does not allow further oil into the bowl. If the mix volume is too high to be accommodated in the bowl, either the shear pins of the blades will break or the mix is simply thrown out of the bowl. It will not be possible to continue the test under either of these situations.

Thus, there is a serious problem in specifying a

Table 1. Packing volumes of different powders

Powder	*Density ($g\ cm^{-3}$)*	*Weight (g)*	*Apparent volume (cm^3)*	*Volume after tapping (cm^3)*	*Volume at CBVC (cm^3)*
Fused silica	2·18	65·0	100	65	52
Alumina	3·97	99·2	100	83	44
Coarse SiC	3·21	160·0	100	83	75
Fine SiC	3·21	96·0	100	63	54
Zirconia	5·90	112·0	100	65	36
Fine silica	2·18	23·8	100	76	23
Fine zircon	4·70	150·4	100	53	41
Coarse zircon	4·70	126·9	100	56	43
Coarse nickel	8·90	506·4	100	97	91
Fine nickel	8·90	110·3	100	73	53
Coarse alumina	3·97	103·4	100	93	60

priori the amount of the powder that can be filled in the mixing bowl at the beginning of the titration. In order to overcome this, a different approach has been devised, following the data from Table 1 for a variety of powders with different shapes and sizes, and assuming that the maximum decrease in volume in the presence of the oil is about 80%. About 50 ml of the apparent volume of the powder is accurately weighed. Half this volume is added into the mixing bowl, and an initial 5 ml aliquot of the linseed oil is added to the bowl. After the rise and subsequent fall in the torque value, the volume occupied by the powder decreases, permitting the addition of the rest of the powder. All the powder is then added and mixing is continued until torque equilibrium is achieved. If the volume occupied by the mix appears to be very small on visual examination of the bowl, an additional volume of the powder and oil may be added at this stage. Otherwise, titration with the oil is started. Once the amount of powder to be taken to ensure that the mixing bowl is loaded to at least 50% FBV is known, a second experiment may be carried out to accurately establish the point of CBVC. Thus, the amount can be assessed by a simple, initial trial and error procedure.

3.2.3 Mixing speed

Figures 5 (a) and (b) show the variation of torque as a function of the binder content in the mix, for three different rotational speeds of the mixing blades, using coarse silica as well as fine alumina powder. It is clear from the figures that the point of CBVC is not altered significantly by the speed of the blades for both the coarse as well as the fine powders. For speeds below 50 rev min^{-1}, however, the time for attaining equilibrium torque levels after each addition of oil becomes longer and longer, thereby increasing the time required for the experiment. A rotational speed of 50 rev min^{-1} is found to be optimal, as the experiment can be completed within about 30 min. Higher speeds can lead to high wear and hence are not particularly advantageous.

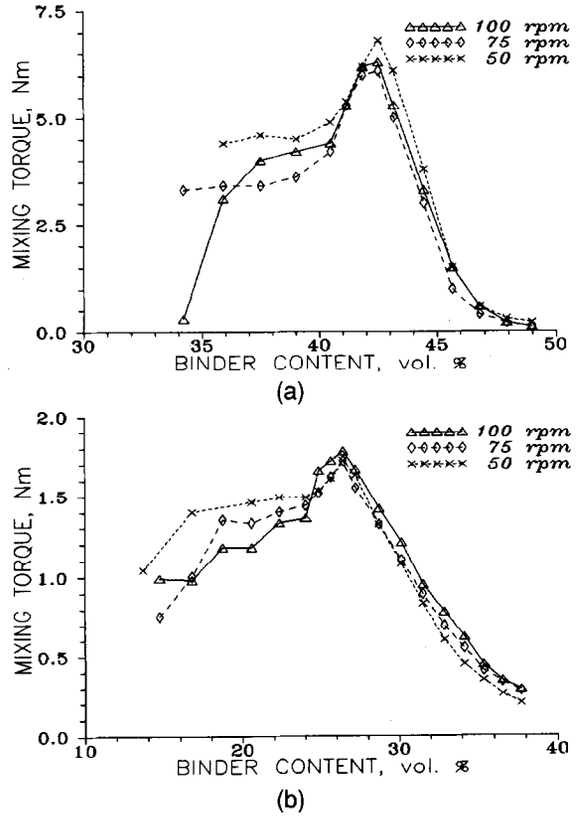

Fig. 5. Equilibrium mixing torque as a function of binder volume concentration for different speeds (rev min^{-1}) of the mixing blades: (a) 75 g fused silica and (b) 100 g alumina.

3.2.4 Mode of oil addition

Figures 6 (a)–(c) show the torque–time curves during mixing of fused silica powder, with linseed oil added in a stepwise manner as well as in a continuous fashion. Figure 7 shows the torque data from the above curves as a function of the binder content in the mix. In the case of stepwise addition of oil, the torque is allowed to stabilize before the addition of the next aliquot of oil. The shape of the torque–time curves appears distinctly different when the oil is added continuously, compare Figs 6 (b) and (c) with Fig. 6 (a). However, this apparent difference does not really manifest itself in Fig. 7, implying that the torque vs. binder content relationship remains essentially the same irrespective of the mode of addition, and that the point of CBVC can be identified quite unambiguously in all three cases. While conducting the experiment in a Brabender Rheometer, only torque–time curves are available, and therefore continuous addition of the oil at a rate of about 0·6 to 2·3 ml min^{-1} clearly offers a better alternative.

3.3 Applicability

The method has been applied to many ceramic and metal powders of different size, size distribution and shapes. Table 2 presents the particle characterization data for the different powders analysed, while the CBVC values are shown in Table 3. While the applicability of the method appears to be quite universal, special care is necessary while analysing submicrometre-sized powders. Fine and highly abrasive powders can easily penetrate the regions near the shaft of the mixing blades. Abnormal torque fluctuations signal such a possibility. The problem can be corrected normally by careful cleaning of the mixing chamber and the blades before fixing the mixing blades to the mixer.

3.4 Error analysis

The error in the method arises from the inaccurate

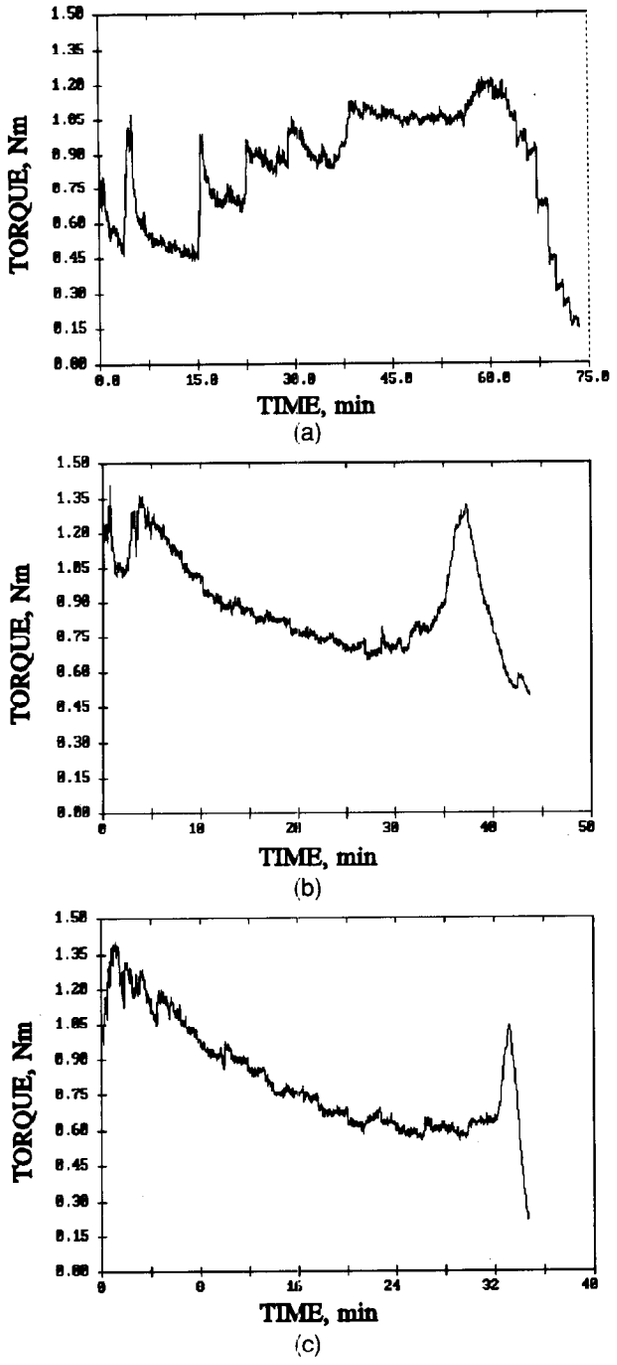

Fig. 6. Torque–time curves for 65 g fused silica at 50 rev min^{-1} using (a) stepwise addition of oil; (b) continuous oil addition at 0·6 ml min^{-1} and (c) continuous oil addition at 2·3 ml min^{-1}.

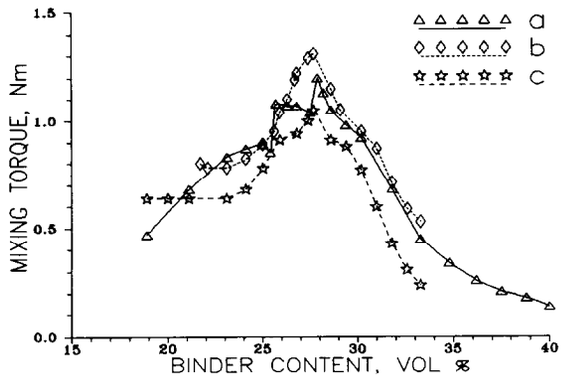

Fig. 7. Mixing torque vs. binder volume concentration graphs for the data from Fig. 6. Note the lack of any significant difference amongst the three curves in contrast to the sharpness of the end points in Fig. 6 for continuous oil addition expts.

recognition of the end point as well as from the statistical uncertainty. The torque during mixing is not a very stable value, but keeps fluctuating around a mean, even when mixing equilibrium has been achieved. Because of this, if the changes in the torque values are not significant for small additions of oil very near the point of CBVC as seen in Fig. 8, the accurate identification of the end point becomes difficult. In such a case, there will be some uncertainty in volume of oil at the end point. Table 3 presents this error data for different powders.

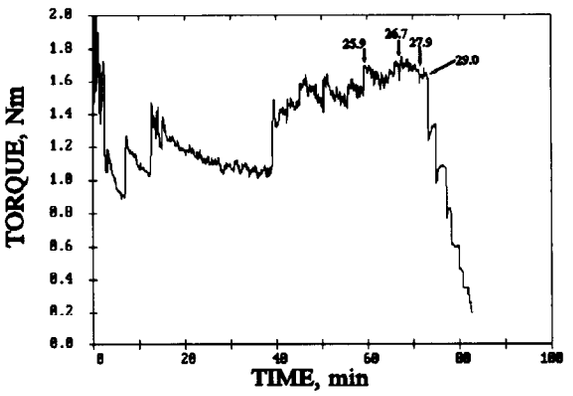

Fig. 8. Torque–time curves for a 75 g fused silica sample at 50 rev min^{-1} showing the fluctuations in the torque near the point of CBVC which leads to the uncertainty in the value of CBVC.

Table 2. Powder particle characteristics

Powder	*Particle Characteristics*			*Source*
	Average size (μm)	*Shape*	*Size distribution*	
Fused silica	35	Angular	Multimodal	Remet Corp., USA
Alumina	2	Irregular	Monomodal	Alcon, USA
Coarse SiC	58	Irregular	Bimodal	Carborundam, India
Fine SiC	16	Irregular	Bimodal	Carborundam, India
Zirconia	2	Irregular	Monomodal	IRE, India
Fine silica	< 1	–	Monomodal	Elekem, Norway
Fine zircon	6	Angular	Multimodal	Casting Supplies, USA
Coarse zircon	18	Irregular	Multimodal	IRE, India
Coarse nickel	150	Spherical	Monomodal	DMRL, India
Fine nickel	12	Irregular	Multimodal	DMRL, India
Coarse alumina	75	Irregular	Monomodal	Alcon, USA

Table 3. Error in end point recognition for different powders

Powder	*Powder Weight (g)*	*Oil volume at CBVC (cm^3)*	*CBVC (vol%)*	*Max. Relative error in CBVC (%)*
Fused silica	65	12·0	28·7	±2·7
Alumina	99	18·5	42·5	±1·6
Coarse SiC	155	26·0	35·0	±2·5
Fine SiC	110	27·0	44·0	±4·2
Zirconia	145	23·5	48·9	±3·3
Fine silica	25	15·5	57·4	±4·1
Fine zircon	150	9·8	23·4	±5·9
Coarse zircon	117	15·8	38·6	±4·9
Coarse nickel	250	20·5	42·3	±4·2
Fine nickel	160	25·2	58·4	±2·1
Coarse alumina	99	32·5	56·0	±2·3

The statistical uncertainty in the value of CBVC was obtained by repeated analysis of FSU powder. The mean value of CBVC from 11 determinations was 27·3% with a relative standard deviation of 3·5%. It is thus clear that CBVC can be determined by the proposed torque rheometric method with good reproducibility.

4 Conclusions

Critical binder volume concentration (CBVC) represents an excellent estimate of the minimum amount of a binder liquid necessary to impart fluidity to a powder mass, and its complement, the critical particle volume concentration (CPVC), denotes the maximum attainable packing density for a given powder. The method described for the estimation of CBVC is simple, fast, accurate and universally applicable to ceramic or metal powders of different sizes and shapes. Various parameters affecting the determination have been studied. The method has been applied to a variety of powder samples.

References

1. Gardner, H. A. & Coleman, R. E., *Bulletin No. 85*, American Oil and Varnish Manufacturers' Association, Farben-Zeitig, **32** (1927) 966.
2. Gardner, H. A. & Coleman, R. E., Oil absorption of pigments by Gardner–Coleman method. *Standard D1483-79*, American Society for Testing and Materials, Philadelphia, PA, 1979.
3. Gardner, H. A. & Coleman, R. E., Oil absorption of pigments by Spatula Rub-Out. *Standard D281-84*, American Society for Testing and Materials, Philadelphia, PA, 1984.
4. Sacks, M. D., Rheological science in ceramic processing. In *Science of Ceramic Chemical Processing*, ed. L. L. Hench and D. R. Ulrich. Wiley, New York, 1986 pp. 522–38.
5. Klumpp, E., *Farben-Zeitig*, **34** (1929) 2612.
6. Baldwin, J. T., *Ind. Eng. Chem.*, **21** (1929) 326.
7. Asbeck, W. K. & Van Loo, M., *Ind. Eng. Chem.*, **41** (1949) 1470.
8. Bierwagen, G. P., CPVC calculations, *J. Paint Technol.*, **44**(574) (1972) 46–55.
9. Bessey, G. E. & Lammiman, K. A., *J. Oil and Colour Chemists Assoc.*, **34** (1951) 519.
10. Warren J. & German, R. M., The effect of powder characteristics on binder incorporation for injection moulding feedstock. In *Modern Developments in Powder Metallurgy*, ed. P. U. Gummeson and D. A. Gustafson. **18** (1988) 391–402.
11. Pujari, V. K., Effect of powder characteristics on compounding and green microstructure in the injection moulding process. *J. Am. Ceram. Soc.*, **72**(10) (1989) 1981–4.
12. Anon, Injection moulding of sinterable silica based non-oxide ceramics. *Tech. Report AFML-TR-200*, Dec. 1978.
13. Hay, T. K., Reaching an objective in oil absorption measurements. *J. Paint Technol.*, **46**(591) (1974) 44–50.
14. Reddy, J. Janardhana & Vijayakumar, M., unpublished results.
15. Wirßching, F. & Haug, R., *Deut. Farben-Z.*, **11** (1957) 391 & 436.
16. Brennan J. J., Jermyn, T. E. & Boonstra, B. B., *J. Appl. Polym. Sci.*, **8** (1964) 2687.
17. Eaton, E. R. & Middleton, J. S., *Rubber World*, **52** (1965) June issue.
18. Markhoff, C. J., Mutsuddy, B. C. & Lennon, J. W., A method for determining critical ceramic volume concentration in the plastic forming of ceramic mixes. In *Advances in Ceramics, Vol. 9, Forming of Ceramics*, ed. J. A. Mengels and G. L. Messing, American Ceramic Society, Columbus, OH, 1984. pp. 246–50.
19. Cahn, J. W. and Heady, R. B., Analysis of capillary forces in liquid phase sintering of jagged particles. *J. Am. Ceram. Soc.*, **53** (1970) 406–9.

SHORT REPORTS

0955-2219(95)00162-X

Journal of the European Ceramic Society 16 (1996) 575–578

0955-2219/96/$15.00

Solute Segregations at the Space-Charge Layers of Stabilized Zirconia: an Opportunity for Ameliorating Conductivity

Xin Guo

State Key Laboratory for Synthesis and Processing of Advanced Materials, Wuhan University of Technology, Wuhan, Hubei Province 430070, People's Republic of China

(Received 23 March 1995; revised version received 16 July 1995; accepted 27 August 1995)

Abstract

According to a space-charge theory analysis, the space-charge potential of YSZ is negative, which corresponds to a $V_o^{\cdot\cdot}$ depletion in the space-charge layer. An extremely low grain-boundary conductivity of the high-purity YSZ is thus explained. Under the condition that the bulk property is ensured by the optimal dopant additions, an idea of increasing the grain-boundary conductivity by the segregations of solutes with positive effective charge is put forward. The most likely driving force for the segregations is the elastic strain energy. And the feasibility of this idea has been proved by some experimental and theoretical results.

1 Introduction

In thermodynamic equilibrium the grain boundaries of an ionic crystal may carry an electric potential resulting from the presence of excess ions of one sign, this potential is compensated by space-charge layers of the opposite sign adjacent to the boundaries. The nature of the space charge is dependent on the formation energies of point defects (vacancies and interstitials) in pure ionic crystals, it is more likely, as in almost all practical cases, that it is dictated by the effective charge of the aliovalent dopants and/or impurities.[1–3] A number of studies on the space-charge layers have appeared,[3–15] however, most of them are centered on the alkali halides.

The segregations of aliovalent solutes to the grain boundaries can be substantially affected by the presence of the space-charge layers, the space-charge segregations of Mg, Fe and Ti in Al_2O_3,[8,11] Al and Si in AgCl,[9] Sr in KCl[10] and Al in $CuCl_2$[12] have been discovered, and the segregations usually cause enhancement or diminution of some types of lattice-defect concentrations in the space-charge layers. According to Maier,[13] the grain-boundary conduction consists of the contribution from the grain-boundary interfaces and that from the space-charge layers. A space-charge layer can be treated as a normal resistor element, and its conduction mechanism is bulk-like. The variation of defect concentrations in the space-charge layers will surely change the grain-boundary conductivity, which thus suggests an opportunity for ameliorating the conductivity of ionic crystals: to increase the concentration of charge carrier in the space-charge layers by the solute segregations there. However, the bulk property can be ensured by optimal dopant additions. In the present work, an application of this idea in Y_2O_3-stabilized ZrO_2 (YSZ) is presented. Kröger–Vink notation is used throughout this paper.

2 Space-Charge Potential and Defect Distribution

In YSZ, the predominant defect is $V_o^{\cdot\cdot}$, it is produced from a defect reaction occurring as follows

$$Y_2O_3 \rightleftarrows 2Y_{Zr}' + V_o^{\cdot\cdot} + 3O_o^x \qquad (1)$$

If the effects of elastic field and solute-vacancy associates are not considered, and referencing the spatially varying electrostatic potential $\Phi(x)$ to zero at the grain boundaries ($\Phi(x)$ is a comprehensive value of space-charge potential and grain-boundary interface potential, x is the distance from the grain-boundary interfaces), it is readily shown[3,14,15] that the concentration of $V_o^{\cdot\cdot}$ as a function of distance from the interfaces is, if the dopant concentration meets the requirement of dilute solution, given by

$$[V_o^{\cdot\cdot}](x) = 2\exp\left(\frac{-G_{V_o} - 2e\Phi(x)}{KT}\right) \qquad (2)$$

where G_{V_o} is the formation free energy of $V_o^{\cdot\cdot}$. In the bulk, the electrostatic potential is $e\Phi_\infty$, then eqn (2) becomes

$$[V_o^{\cdot\cdot}]_\infty = 2\exp\left(\frac{-G_{V_o} - 2e\Phi_\infty}{KT}\right) \quad (3)$$

The potential difference between the bulk and the grain boundaries (in this convention simply the bulk potential, $e\Phi_\infty$) is determined by applying the bulk electroneutrality condition, which in this case is

$$2[V_o^{\cdot\cdot}]_\infty = [Y_{Zr}']_\infty \quad (4)$$

Equating eqns (3) and (4), the potential difference is given by

$$e\Phi_\infty = -\frac{1}{2}\left\{G_{V_o} + KT\ln\frac{[Y_{Zr}']_\infty}{4}\right\} \quad (5)$$

If the effect of Y_{Zr}' dominates over that of the intrinsic defects and there are no defect associates, we have $e\Phi_\infty < 0$, thus the space-charge potential in YSZ is negative, which corresponds to an Y_{Zr}' segregation and a $V_o^{\cdot\cdot}$ depletion in the space-charge layers at equilibrium. Whereas, the potential of the grain-boundary interfaces should be positive to compensate the negative space-charge potential, as a result, the electrostatic potential $\Phi(x)$ reaches zero at the grain boundaries, i.e. $\Phi(0) = 0$. The author has detected 17·47 mol% Y_2O_3 at the surface of a specimen with a composition of 9 mol% Y_2O_3–ZrO_2 by XPS. And the Y_2O_3 segregation at the grain boundaries has also been observed by Winnubst and co-workers.[16] These two factors together provide compelling proofs for the correctness of eqn (5). And it can be easily seen from the above analysis that the space-charge potential in Y_2O_3-stabilized CeO_2, MgO or CaO-stabilized ZrO_2 should also be negative. Usually 8–9 mol% Y_2O_3 is doped to ZrO_2, the dilute solution requirement is no longer met, but because of the negative effective charge of Y_{Zr}', the nature of the space-charge potential will not be altered. The specific conductivity of the grain boundaries for high-purity YSZ where the grain-boundary interface second phase is almost absent was found to be about 100 times smaller than that of the bulk,[17] this extremely low grain-boundary conductivity surely cannot be accounted for by the blocking effect of the second phase, it thus must be the result of the $V_o^{\cdot\cdot}$ depletion in the space-charge layers. In Y_2O_3-stabilized CeO_2,[18] the calculated thickness of the blocking layer was found to be larger than that of the second phase covering the grain boundaries. This finding further supports the idea of $V_o^{\cdot\cdot}$ depletion in the space-charge layers.

3 Experimental and Discussion

As mentioned earlier, the $V_o^{\cdot\cdot}$ depletion is related to Y_{Zr}' segregation, thus to ease or even prevent the Y_{Zr}' segregation at the grain boundaries there may be a method to increase $V_o^{\cdot\cdot}$ concentration in the space-charge layers. The feasibility of this idea is shown in Fig. 1. The grain-boundary solute segregation in a specimen with a nominal composition of 1·5 mol% Al_2O_3–9 mol% Y_2O_3–ZrO_2 was detected by an electron probe X-ray microanalyzer (JCXA-733). An obvious aluminium segregation (Fig. 1(a)) was observed, however, no yttrium segregation (Fig. 1(b)) was observed.

This observation means that the yttrium segregation can be subdued by the preferential segregations of other elements. The preferential segregation of aluminium may be due to the substantial size misfit between Al^{3+} and Zr^{4+}, thus the substantial elastic strain energy. The space-charge potential can be greatly modified by the segregations induced by the elastic strain energy. A particular case of this type is that when a minority solute

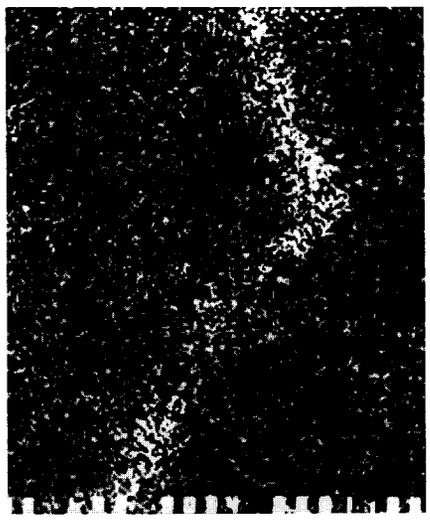

(a)

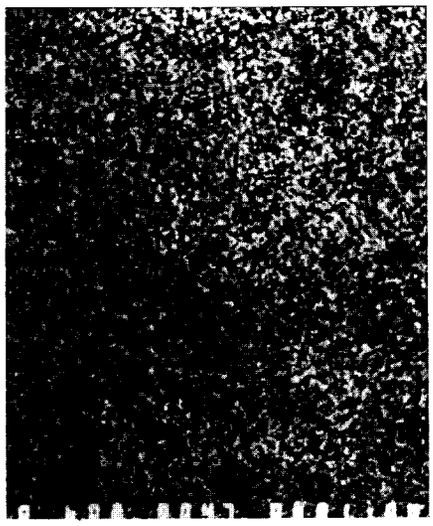

(b)

Fig. 1. Solute distributions in a specimen with a composition of 1·5 mol% Al_2O_3 –9 mol% Y_2O_3–ZrO_2 detected by an electron probe X-ray microanalyzer. (a) Aluminum distribution, (b) yttrim distribution (The bar is 1.0μm).

has a large elastic strain energy and segregates strongly to the boundaries. In this case the segregation of the majority solute will be significantly suppressed, even depleted. This phenomenon has been theoretically proved by Yan *et al.*[15] If Al_2O_3 is substitutionally dissolved in YSZ, the Al_{Zr}' segregation will not change the $V_O^{\cdot\cdot}$ depletion in the space-charge layers; if Al_2O_3 is interstitially dissolved in YSZ, $Al_i^{\cdot\cdot\cdot}$ segregation will change the sign of the space-charge potential, which corresponds to a $V_O^{\cdot\cdot}$ enrichment in the space-charge layers. The variation of the sign of the space-charge potential with doping has been observed in TiO_2.[19] It was reported that the conductivity of YSZ can be enhanced by the addition of Al_2O_3,[20,21] this enhancement was explained by the scavenging of SiO_2 located at the grain boundaries by Al_2O_3.[22] According to the above analysis, the possible influence of Al_2O_3 on the space-charge layers resulting from the Al_2O_3 segregation should also be considered. The enhanced space-charge conduction resulting from the segregations of aliovalent solutes has been found in AgCl[9] and $CuCl_2$.[12]

If pentavalent oxides M_2O_5, e.g. Nb_2O_5 and Ta_2O_5, are added to YSZ, supposing that they are substitutionally dissolved, and a defect reaction, e.g. eqn (6), occurs

$$2M_2O_5 \rightarrow 4M_{Zr}^{\cdot} + V_{Zr}'''' + 100_O^x \qquad (6)$$

The segregation of $M_{Zr}^{\cdot}$ will change the sign of the space-charge potential and cause a $V_O^{\cdot\cdot}$ enrichment in the space-charge layers. As the positively charged grain-boundary interfaces of YSZ will repulse $M_{Zr}^{\cdot}$, the only possible driving force for the segregation of $M_Z^{\cdot}$ is the elastic strain energy. Unfortunately, if the pentavalent cation solutes M^{5+} are compensated by electrons, electron conduction will be involved. However, if the amounts of the additions are very low, the electron conduction may not be a serious problem. It has been proved that pentavalent oxides, Nb_2O_5 and Ta_2O_5, do not segregate to the grain boundaries of Ce-TZP.[23] According to the study of Naik and Tien,[24] Nb^{5+} and Ta^{5+} are compensated by Ce^{3+} in CeO_2, and Ce^{3+} induces a positive charge on the grain boundaries,[22] the segregations of Nb^{5+} and Ta^{5+} are thus prevented. The addition of M_2O_5 in YSZ will not introduce Zr^{3+} in it, therefore, the M_2O_5 segregations at the grain boundaries of YSZ is possible provided that the elastic strain energy resulting from the size misfit between M^{5+} and Zr^{4+} is much larger than that resulting from the size misfit between Y^{3+} and Zr^{4+}. The solubility of Nb_2O_5 or Ta_2O_5 in ZrO_2 has been proved to be very high.[25]

4 Conclusion

According to a space-charge theory analysis, the space-charge potential of YSZ is negative, which corresponds to a $V_O^{\cdot\cdot}$ depletion in the space-charge layers and a very low grain-boundary conductivity. Under the condition that the bulk conductivity is ensured by the optimal dopant additions, e.g. 8–9 mol% Y_2O_3 or 13–14 mol% CaO, an idea of increasing the grain-boundary conductivity by the segregations of solutes with positive effective charge is thus put forward. The most likely driving force for the segregations is the elastic strain energy. However, because of the positive potential of the grain–boundary interfaces, the interfaces will repulse the positively charged solutes, then more pronounced enhancement of the grain-boundary conductivity will be obtained only if the interfaces are modified, e.g. by second phase precipitations at the same time. In the cases of dopants other than MgO, CaO and Y_2O_3, the charge compensation mechanisms are still uncertain, this makes more realistic analysis impossible.

References

1. Kingery, W. D., Plausible concepts necessary and sufficient for interpretation of ceramic grain-boundary phenomena: I. Grain-boundary characteristics, structure, and electrostatic potential. *J. Am. Ceram, Soc.*, **57** (1974) 1–8.
2. Frenkel, J., *Kinetic Theory of Liquids*. Oxford University Press, New York, 1946.
3. Kliewer, K. L. & Koehler, J. S., Space charge in ionic crystals. I. general approach with application to NaCl. *Phys. Rev.*, **140** (1965) A 1226–40.
4. Kliewer, K. L., Space charge in ionic crystals. II. The electron affinity and impurity accumulation. *Phys. Rev.*, **140** (1965) A 1241–6.
5. Kliewer, K. L., Space charge in ionic crystals. III. Silver halides containing divalent cations. *J. Phys. Chem. Solids*, **27** (1966) 705–17.
6. Kliewer, K. L., Space charge in ionic crystals. IV. Interstitial-producing impurities in the silver halides. *J. Phys. Chem. Solids*, **27** (1966) 719–25.
7. Lifshitz, I. M., Kossevich, A. M. & Geguzin, Ya, E., Surface phenomena and diffusion mechanism of the movement of defects in ionic crystals. *J. Phys. Chem. Solids*, **28** (1967) 783–98.
8. Tiku, S. K. & Kröger, F. A., Effects of space charge, grain-boundary segregation, and mobility differences between grain boundary and bulk on the conductivity of polycrystalline Al_2O_3. *J. Am. Ceram. Soc.*, **63** (1980) 183–9.
9. Maier, J., Space charge regions in solid two-phase systems and their conduction contribution: I. Conductance enhancement in the system ionic conductor—'inert' phase and application on AgCl:Al_2O_3 and AgCl:SiO_2 *J. Phys. Chem. Solids*, **46** (1985) 309–20.
10. Yan M. F., Cannon, R. M., Bowen, H. K. & Coble, R. L., Space-charge contribution to grain-boundary diffusion. *J. Am. Ceram. Soc.*, **60** (1977) 120–7.
11. Mukhopadbyay, S. M. & Blakely, J. M., Ionic double layers at the surface of magnesium-doped aluminum oxide: effect on segregation properties. *J. Am. Ceram. Soc.*, **74** (1991) 25–30.

12. Jow, T. & Wagner, J. B., Jr., The effect of dispersed alumina particles on the electrical conductivity of cuprous chloride. *J. Electrochem. Soc.*, **126** (1979) 1963–72.
13. Maier, J., On the conductivity of polycrystalline materials. *Ber. Bunsenges. Physik. Chem.*, **90** (1986) 26–33.
14. Lehovec, K., Space-charge layer and distribution of lattice defects at the surface of ionic crystals. *J. Chem. Phys.*, **21** (1953) 1123–8.
15. Yan, M. F., Cannon, R. M. & Bowen, H. K., Space-charge, elastic field, and dipole contributions to equilibrium solute segregation at interfaces. *J. Appl. Phys.*, **54** (1983) 764–78.
16. Winnubst, A. J. A., Kroot, P. J. M. & Burggraaf, A. J., AES/STEM grain boundary analysis of stabilized zirconia ceramics. *J. Phys. Chem. Solids*, **44** (1983) 955–60.
17. Verkerk, M. J., Middelhuis, B. J. & Burggraaf, A. J., Effect of grain boundaries on the conductivity of high-purity ZrO_2–Y_2O_3 ceramics. *Solid State Ionics*, **6** (1982) 159–70.
18. Tanaka, J., Baumard, J. F. & Abelard, P., Nonlinear electrical properties of grain boundaries in an oxygen-ion conductor (CeO_2·Y_2O_3). *J. Am. Ceram. Soc.*, **70** (1987) 637–43.
19. Ikeda, J. A. S. & Chiang, Y. M., Space charge segregation at grain boundaries in titanium dioxide: I. Relationship between lattice defect chemistry and space charge potential. *J. Am. Ceram. Soc.*, **76** (1993) 2437–46.
20. Guo, X., Tang, C. Q. & Yuan, R. Z., Grain boundary ionic conduction in zirconia-based solid electrolyte with alumina addition. *J. Eur. Ceram. Soc.*, **15** (1995) 25–32.
21. Miyayama, M., Yanagida, H. & Asada, A., Effects of Al_2O_3 additions on resistivity and microstructure of yttria-stabilized zirconia. *Am. Ceram. Soc. Bull.*, **64** (1985) 660–4.
22. Butler, E. P. & Drennan, J., Microstructural analysis of sintered high-conductivity zirconia with Al_2O_3 additions. *J. Am. Ceram. Soc.*, **65** (1982) 474–8.
23. Hwang, S. L. & Chen, I. W., Grain size control of tetragonal zirconia polycrystals using the space charge concept. *J. Am. Ceram. Soc.*, **73** (1990) 3269–77.
24. Naik, I. K. & Tien, T. Y., Electrical conduction in Nb_2O_5-doped cerium oxides. *J. Electrochem. Soc.*, **126** (1979) 562–6.
25. Gritzner, G., Puchner, C. & Dusza, J., Nb_2O_5 and Ta_2O_5 codoped zirconia. *J. Eur. Ceram. Soc.*, **15** (1995) 45–9.

Journal of the European Ceramic Society 16 (1996) 579–581

0955-2219(95)00167-0
0955-2219/96/$15.00

Sintering Capability of V_2O_5/Nb_2O_5 System Treated by Sol–Gel Technique

V. Kaselouri, K. Tzevelekos & G. Parisakis

Laboratory of Inorganic and Analytical Chemistry, Department of Chemical Engineering, NTU Athens, 9 Iroon Polytechniou Str., Zografou Campous, Athens 15773, Greece

(Received 21 July 1994; revised version received 18 July 1995; accepted 27 August 1995)

Abstract

Consideration of the X-ray diffraction patterns for the sintered products of V_2O_5/Nb_2O_5 mixtures, with molecular ratio 1/9, has indicated that oxide mixtures prepared by sol–gel technique show improved sintering capability compared with simply homogenized mixtures. The stable sintered product VNb_9O_{25} was produced faster, and in a better crystallized form, in the case of the sol–gel treated oxide mixtures. It was also shown that sol–gel procedures reduce the size of agglomerates in the precipitate and improve its homogeneity.

1 Introduction

Previous investigations of the V_2O_5/Nb_2O_5 system[1,2] (one of them based on the sol-gel technique[1]) have led to the conclusion that the only stable product of this system at temperatures higher than 800°C is the compound VNb_9O_{25}. The aim of the present investigation is to study the effect of the sol–gel procedure, when applied to this system, on the sintering capability, as well as to determine the grain size distribution and homogeneity of the green oxide mixtures, factors which in turn influence the sintering capability.[3]

The production of the compound VNb_9O_{25} in a well crystallized form is also desired, so that the physical and chemical characteristics of the compound can be investigated more intensively. Multicomponent oxides such as VNb_9O_{25} commonly have electronic applications.[4,5] It is also known that transition metal oxides can present superionic conduction capabilities.[6,7]

2 Experimental and Discussion

The oxide mixtures used had a molecular ratio of V_2O_5/Nb_2O_5 of 1/9, which corresponds to the compound VNb_9O_{25}. The oxide mixtures, after having been homogenized, were converted to alkoxides. Absolute ethanol was used together with benzene, which was used as the solvent. Both of the oxides were transformed to alkoxides according to the following chemical reactions:

$$V_2O_5 + 10\ EtOH \leftrightarrow 2\ V(OEt)_5 + 10\ H_2O \quad (1)$$

$$Nb_2O_5 + 10\ EtOH \leftrightarrow 2Nb(OEt)_5 + 10\ H_2O \quad (2)$$

Standard air humidity contains enough water to hydrolyse the alkoxides rapidly,[8] so the reactions were performed under high vacuum. The water produced by the reaction forms an azeotropic mixture with benzene, and is extracted from the system by fully controlled distillation at a temperature of 69·25°C.

As soon as the reactions were completed, the alkoxides were hydrolysed with an appropriate amount of water. The resulting oxide mixtures were first dried under vacuum for 2 h, and then sintered simultaneously with control samples prepared by co-grinding oxide mixtures. The reaction occurring during sintering is:[9]

$$V_2O_5 + 9\ Nb_2O_5 \leftrightarrow 2\ VNb_9O_{25} \quad (3)$$

According to our experiments, which confirm data given in the literature,[1,2] the formation of the compound VNb_9O_{25} for any mixing ratio of the oxide mixture, starts just above 600°C. The eutectic line for the quasi-binary system V_2O_5–Nb_2O_5 lies at 648°C. Especially for the 1/9 mixture, at 648°C only the non-melting product VNb_9O_{25} appears.

Using differential scanning calorimetry (DSC) analysis of the oxide mixture, it was found that at 650°C an endothermic peak appears, attributed to the melting of V_2O_5 (this was confirmed by DSC analysis of pure V_2O_5). This melting reaction promotes the formation of the non-melting product VNb_9O_{25}. The above observations led to the selection of 650°C as the sintering temperature.

An X-ray diffraction (XRD) pattern for the

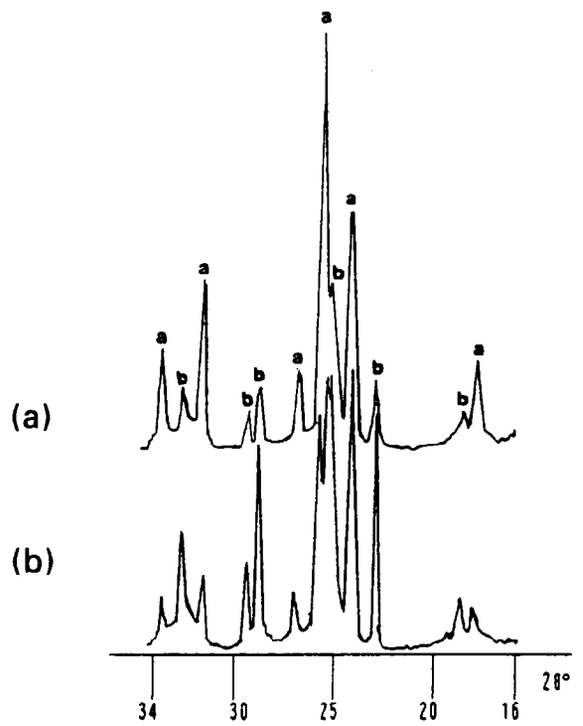

Fig. 1. XRD pattern of sintered products of V_2O_5/Nb_2O_5 1/9 sol–gel (A) and non sol–gel (B) treated mixtures, sintered for 3 h at 650°C. The peak marked (a) and (b) represent the compounds VNb_9O_{25} and Nb_2O_5, respectively.

sintered products from the sol–gel system is compared with one from the co-grinding process in Fig. 1, this showing the comparison after 3 h of firing. It is observed that the peaks corresponding to VNb_9O_{25} have a greater relative intensity for the sol–gel treated mixtures, while the peaks corresponding to Nb_2O_5 are less evident. This finding indicates that sol–gel samples can be transformed to the equilibrium product more easily, as well as in a shorter sintering time. Clear differences remain until the firing time reaches 12 h (Fig. 2), by which time the ground powders are also reacted.

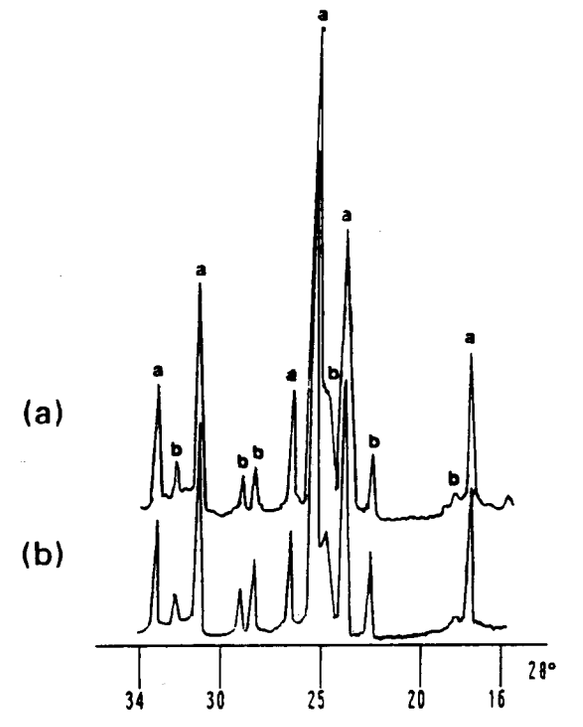

Fig. 2. XRD pattern of sintered products of V_2O_5/Nb_2O_5 1/9 sol–gel (A) and non sol–gel (B) treated mixtures, sintered for 12 h at 650°C. The peak marked (a) and (b) represent the compounds VNb_9O_{25} and Nb_2O_5, respectively.

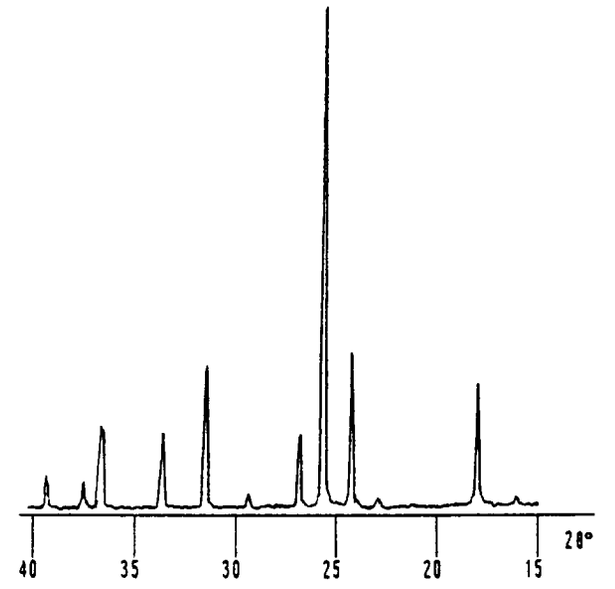

Fig. 3. XRD pattern of sintered products of V_2O_5/Nb_2O_5 1/9 sol–gel treated mixtures, sintered for 100 h at 650°C. The transformation of the initial oxide mixture to the compound VNb_9O_{25} is complete.

The XRD pattern for a sol–gel treated 1/9 oxide mixture sintered at 650°C for 100 h is presented in Fig 3. In this diagram it is observed that the starting oxide mixture has been fully transformed into the mixed compound VNb_9O_{25}, which has been produced in a well crystallized form. The crystalline form of this product is shown in Fig. 4.

The sol–gel treated oxide mixtures were also compared with co-ground mixtures, in respect to

Fig. 4. The compound VNb_9O_{25} produced from a sol–gel treated oxide mixture, sintered for 100 h at 650°C. The shape of the crystals suggests that the compound is crystallized in the orthorhombic system.

Fig. 5. The grains and agglomerates of the initial oxide mixture. The biggest agglomerate has a maximum diameter of 180 μm.

grain size distribution, by means of optical microscopy. Taking into consideration the fact that the starting oxides consisted of very small particles (< 1 μm), it was expected that the sol–gel process may not further reduce the size. Nevertheless, it was observed that the size of the agglomerates was considerably reduced: the size in the starting material (~180 μm) is shown in Fig. 5; in contrast, that in the sol–gel product has a maximum diameter of 25 μm (Fig. 6).

The homogeneity of the sol–gel treated oxide mixtures was also compared with that of the co-ground mixtures, by using electron probe microanalysis (EPMA). All the former samples showed the expected atomic ratio, as shown in Table 1.

Fig. 6. The grains and agglomerates of the sol–gel treated initial oxide mixture. The agglomerate in the centre has a diameter of 25 μm.

Table 1. Results of the EPMA analysis of sol–gel and non sol–gel treated mixtures

	Non sol–gel		*Sol–gel*	
	Weight	*Atoms*	*Weight*	*Atoms*
	5·29	9·25	5·74	10·00
% V	5·02	8·79	5·74	10·00
	3·38	11·05	5·74	10·00
	94·71	90·75	94·26	90·00
% Nb	94·98	91·21	94·26	90·00
	93·62	88·95	94·26	90·00

3 Conclusions

Sol–gel procedures have a positive effect on the sintering capability of ceramic powders. The desired sintering products are produced in a better crystallized form, after a shorter sintering period, as a result of the refined grain size and the improved homogeneity of the green powder mixtures. It was observed that these procedures reduce the size of the agglomerates and enhance the chemical homogeneity of the ceramic powder.

References

1. Schadow, H., Oppermann, H., Grossmann, O., Krzewska, K. & Wehner, B., Investigations concerning the quasi-binary system V_2O_5–Nb_2O_5. *Cryst. Res. Technol.*, **26** (1991) 401–7.
2. Waring, J. L. & Roth, R. S., Phase equilibria in the system vanadium oxide–niobium oxide. *Res. Nat. Bur. Std*, **A69** (1965) 119.
3. Bernier, J. C., Poudres et ceramiques. In *EUROGEL*, Departement Science des Materiaux, Strasbourg, 1989, p. 3.
4. Klein, L. C., *Sol–Gel Technology for Electronics and Special Shapes*. NOYES Publications, 1992, p. 305.
5. Casais, M. T., Gutierrez-Puebla, E., Monge, M. A., Rasines, I. & Ruiz-Valero, C., VM_9O_{25} (M = Nb, Ta), a combination of tetraedral VO_4 and octaedral MO_6 units. *J. Sol. State Chem.*, **102** (1993) 261–6.
6. Livage, J. & Lemerle, J., *Ann. Rev. Mater. Sci.*, **12** (1982) 105–9.
7. Barboux, P., Baffier, N., Morinau, R. & Livage, J., In *Solid State Protonic Conductors III*, ed. Odence. University Press, 1985, pp. 105–9.
8. Jones, R. W., *Fundamental Principles of Sol–Gel Technology*. The Institute of Metals, USA, 1989, p. 66.
9. Fechter, S., Kruger, S. & Oppermann, H., The phase relations in the system V/Nb/O. *Z. Anorg. Allg. Chem.*, **619** (1993) 63–9.

Journal of the European Ceramic Society 16 (1996) 583–586

0955-2219(95)00166-2
0955-2219/96/$15.00

The Corrosion Behaviour of Al_2O_3 Toughened by Ag Particles

W. H. Tuan & W. B. Chou

Institute of Materials Science and Engineering, National Taiwan University, Taipei, Taiwan 10764

(Received 7 June 1994; revised version received 16 August 1995; accepted 27 August 1995)

Abstract

The strength and toughness of alumina can be enhanced by adding silver inclusions. In the present study, the corrosion behaviour of such Al_2O_3/Ag composites in nitric acid is investigated. The strength of the composites containing 2·5 vol% silver is not affected after the corrosion test. However, the weight loss of the composites containing 10 vol% silver is increased with increasing corrosion time. The strength and the toughness of the composites after corrosion are significantly degraded. For example, the strength of the composites containing 10 vol% silver is decreased by 50% and the toughness by 30%, when the composites are soaked in nitric acid for 1000 h.

1 Introduction

Ceramics are superior for their chemical stability and therefore are frequently used in hostile environments. However, the application of ceramics as structural components has been limited by their brittleness. Recent studies suggest that the toughness of alumina can be significantly enhanced by adding silver inclusions.[1–3] A key question then arises concerning the ability of such composites to resist corrosion, since initial failure will expose the metal reinforcement to the environment. In the present study, the corrosion behaviour of silver-toughened alumina in nitric acid is investigated as a model system representing extreme conditions. The strength and toughness of the composites after the corrosion test have been determined.

2 Experimental Procedures

Alumina (AKP-50, Sumitomo Chem. Co., Ltd, Japan) and various amounts of silver oxide (Ag_2O, Johnson Matthey Co., UK) were ball milled together in ethyl alcohol for 4 h. The slurry was dried with a rotary evaporator. The powder compacts were prepared by uniaxially pressing at 56 MPa. The silver oxide was decomposed to silver and oxygen during initial heating.[1–3] Sintering was performed at 1600°C for 1 h in air.

Since the partial pressure of liquid silver at elevated temperature is high (10 mmHg at 1600°C, 23 mmHg at 1700°C),[4] a silver-free surface layer was formed.[2] After removing the silver-free layer by grinding, the volume fraction of silver after sintering was recalculated by counting the point fraction on the polished surfaces. The size of silver inclusions was determined by using the linear intercept technique. The polished specimens were thermally etched at 1500°C for 1 h to reveal the grain boundaries of alumina. The size of the matrix grains was also determined by using the linear intercept technique. More than 200 grains or inclusions were counted.

The sintered specimens were machined longitudinally with a 325-grit resin-bonded diamond wheel at a cutting depth of 5 μm/pass. The silver-free layer was removed during the grinding procedure. The final dimensions of the samples were $3 \times 4 \times 36$ mm^3. The ground specimens were soaked in an aqueous nitric acid (1 M) solution at 40°C. After a certain time, the specimens were removed, washed in deionized water and subsequently in acetone for 10 min.

The strength of the samples was determined by the four-point bend technique under ambient conditions. The upper and lower spans were 10 and 30 mm, respectively, and a loading rate of 0·5 mm min^{-1} was used. The fracture toughness was determined by the single-edge notched beam (SENB) technique, the notch being generated by cutting with a diamond saw before the corrosion test. The electrical resistivity of the composites was measured by the standard two-probe technique, using silver paint for contacts. Phase identification was performed by X-ray diffractometry (XRD), and the microstructure was observed by a scanning electron microscope (SEM) equipped with an

energy dispersive X-ray spectrometer (EDX). Chemical analysis was also conducted by applying a plasma evaporation technique (TC-136, LECO Co., USA).

3 Results and Discussion

The silver content after sintering, the relative density, the matrix grain size, the size of the silver inclusions and the electrical resistivity of the Al_2O_3/Ag composites are shown in Table 1. The fracture surfaces of the composites before sintering are shown in Fig. 1. From Table 1, both the strength and toughness of alumina are enhanced due to the addition of silver inclusions. The toughness enhancement is attributed mainly to the plastic deformation of the metallic inclusions. The strengthening effect is attributed both to the matrix refinement and the toughness enhancement.[1]

The electrical resistivity of the composite containing 2·5 vol% Ag is higher than that of the composite containing 10 vol% Ag (Table 1). This indicates that the connectivity of the silver inclusions increases with the amount of silver inclusions. The weight loss of the Al_2O_3/Ag composites is shown as a function of corrosion time in Fig. 2, while the strength and the toughness of the composites are shown in Figs 3 and 4, respectively. Each point in the figure is the average value of three testing bars; error bars show one standard deviation. The weight loss of the alumina specimens is negligible as is their strength and toughness change.

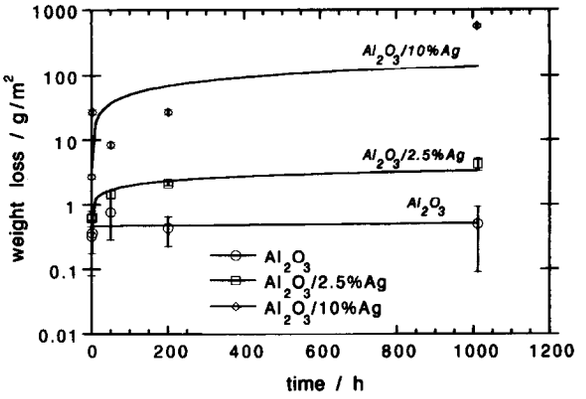

Fig. 2. Weight loss of the composites as a function of corrosion time.

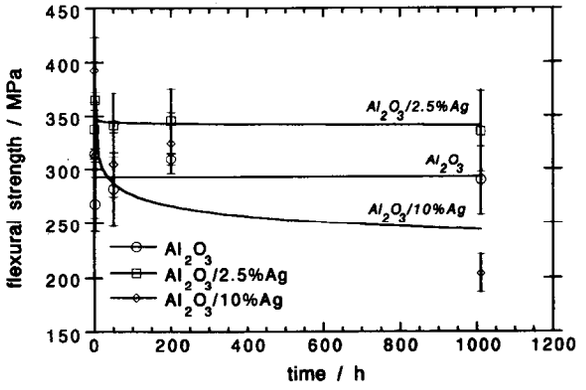

Fig. 3. Flexural strength of the composites as a function of corrosion time.

Table 1. The silver content, relative density, matrix grain size, inclusion size, flexural strength, fracture toughness and electrical resistivity of the Al_2O_3/Ag composites (composites sintered at 1600°C for 1 h)

Silver content after sintering (vol%)	*Relative density (%)*	*Matrix grain size (μm)*	*Inclusion size (μm)*	*Flexural strength (MPa)*	*Fracture toughness (MPa $m^{0.5}$)*	*Electrical resistivity (Ω cm)*
0	97·8	5·2	–	325	4·0	$1·1 \times 10^{14}$
2·5	97·9	4·5	1·2	351	4·6	$8·4 \times 10^{13}$
1·0	96·6	4·1	2·5	394	4·7	$1·8 \times 10^{13}$

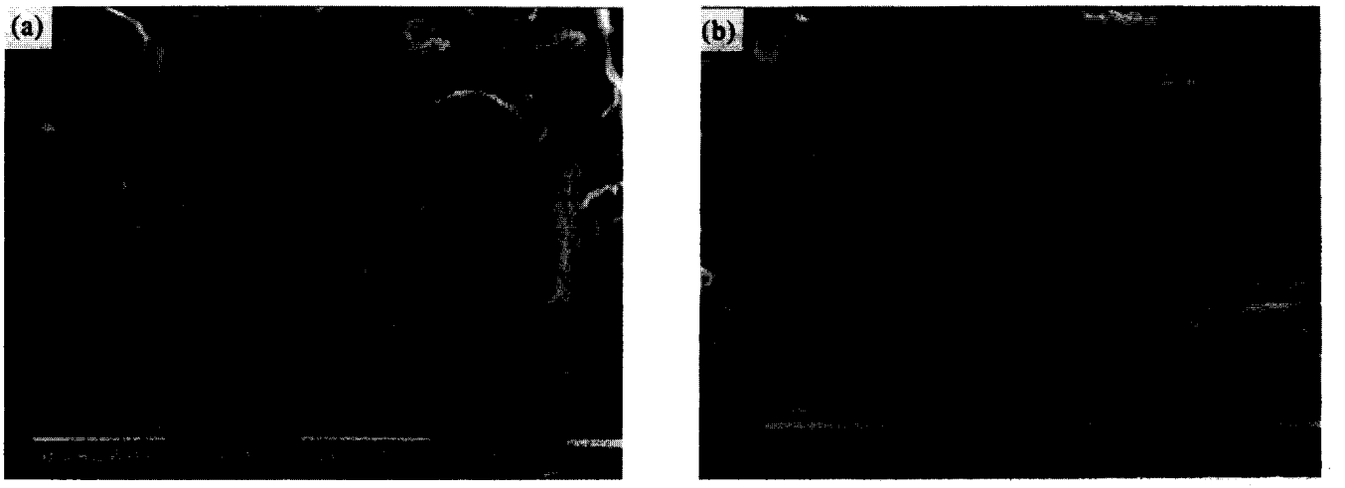

Fig. 1. Fracture surfaces of composites containing (a) 2·5 and (b) 10 vol% silver before corrosion.

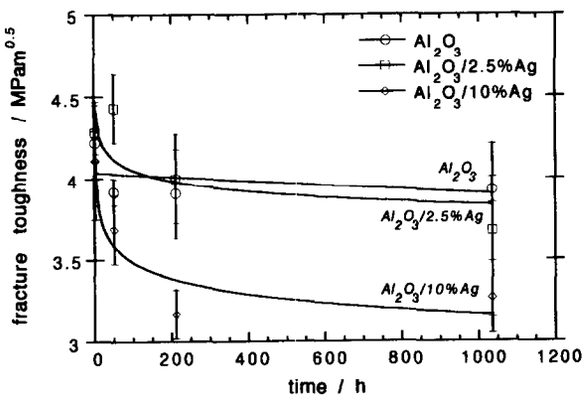

Fig. 4. Fracture toughness of the composites as a function of corrosion time.

3.1 Corrosion behaviour of Al_2O_3/2·5% Ag composite

From Table 1, it can be seen that the strength and toughness of alumina are enhanced by 8% and 15%, respectively, with 2·5 vol% silver addition. The weight loss of the composites increases rapidly during the first 2 h of exposure. This results from the dissolution of the exposed silver inclusions.[5] Subsequent weight loss is negligible. This suggests that the internal silver inclusions are well protected by the alumina matrix. Since the critical flaw size calculated from the strength and toughness (Table 1) for the as-received composite is 100 μm, the silver inclusions in the composites containing 2·5 vol% are much smaller than the critical flaw size. Therefore, the presence of the silver-depleted surface layer does not affect the strength of the composites. However, as the exposed silver inclusions are removed after corrosion, the number of silver inclusions to interact with the crack is decreased. The toughness of the composite is thus reduced as soon as the exposed silver inclusions are dissolved. Since the internal silver inclusions are well protected, the toughness of the composite after corrosion drops by only 15%.

3.2 Corrosion behaviour of Al_2O_3/10% Ag composite

The strength and toughness of alumina is enhanced by 21% and 18%, respectively, with 10 vol% silver addition. The weight loss of the composite continues to increase with increasing corrosion time. It suggests that the silver inclusions are interconnected to each other and therefore corrosion can progress through the structure by leaching out the silver phase. The strength and toughness is dramatically decreased as the composites are corroded for longer than 200 h. The fracture surface of an Al_2O_3/10% Ag composite after corrosion for 1000 h is shown in Fig. 5. Three distinct regions can be

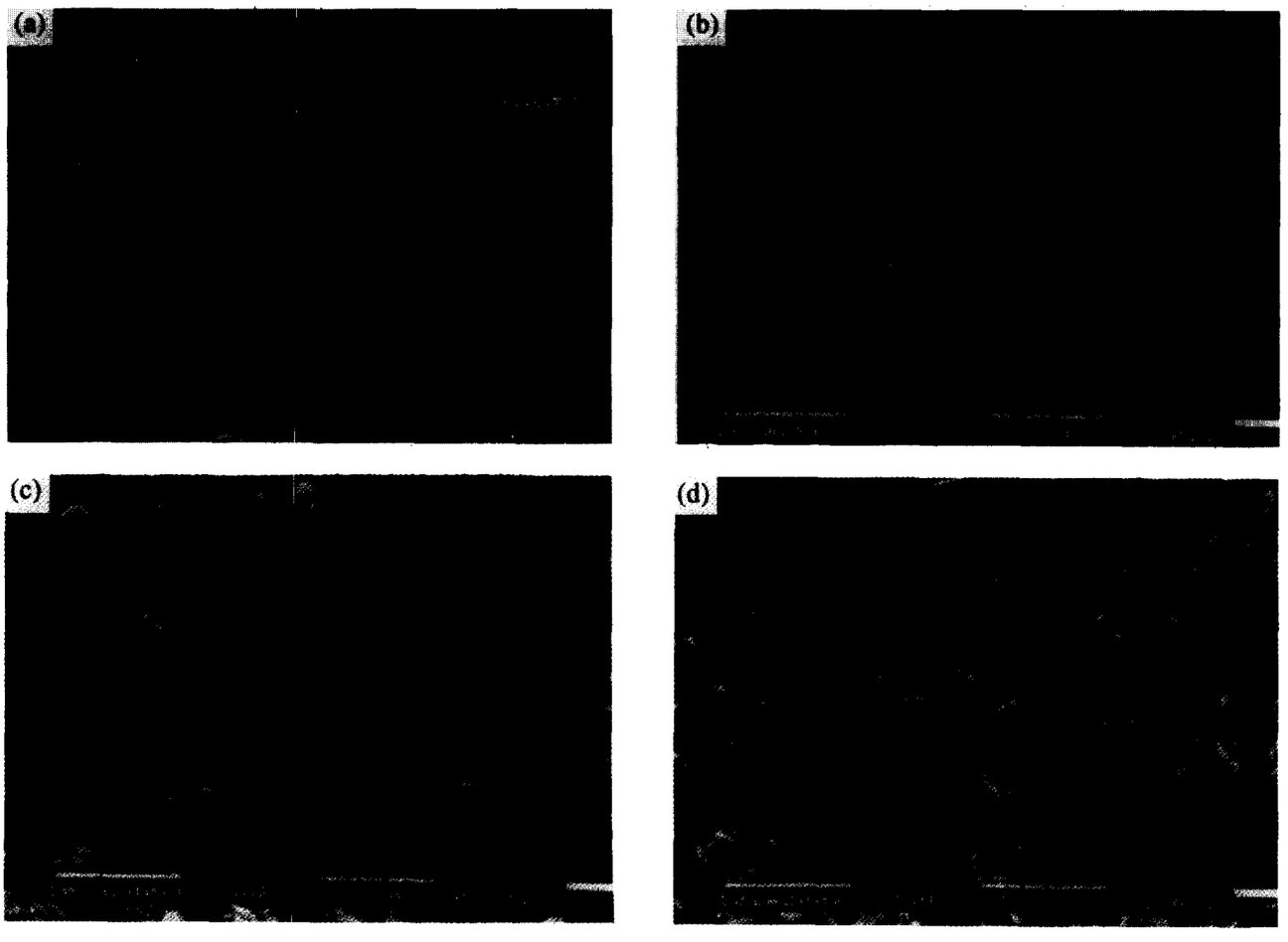

Fig. 5. (a) Fracture surface of the Al_2O_3/10% Ag composite after corrosion for 1000 h. The surface region (S), central region (C) and the intermediate region (I) are shown in (b), (d) and (c), respectively.

found on the fracture surface, Fig. 5(a). The region near the surface is shown in Fig. 5(b). The centre of the composite is shown in Fig. 5(d). The intermediate region between the surface region and central region is shown in Fig. 5(c). Only limited silver inclusions can be observed in the region near the surface. The central region of the corroded specimens is similar to the as-received composites, Fig. 1(b). In the intermediate region, the surface is covered with small particles, the amount of which is too small to be identified using XRD analysis. However, nitrogen is detected by applying the plasma evaporation technique and silver is detected by using the EDX analysis, suggesting that the small particles are silver nitrate.

After the corrosion test, the specimens were removed from the acid solution and the acid near the surface removed during the subsequent washing steps. Nevertheless, acid remained far into the structure. After drying, silver nitrate particles were deposited on the surface of the alumina grains. Since the toughening agents (silver inclusions) are almost removed completely from the crack front during corrosion, the toughness is reduced significantly. Pores are left behind after corrosion, thereby degrading the strength. For example, for the composite containing 10% Ag, the toughness is decreased by 30% and the strength by 50% after corrosion for 1000 h.

4 Conclusions

The corrosion behaviour of Al_2O_3/2·5% Ag and Al_2O_3/10% Ag composites in nitric acid has been investigated. For the Al_2O_3/2·5% Ag composites, the silver inclusions are well separated from each other. As the composites are soaked in nitric acid, only the silver inclusions exposed to the outer surface are dissolved, other silver inclusions within the composites being well protected by the alumina matrix. Therefore, the strength of the Al_2O_3/2·5% Ag composites is not affected by nitric acid. However, the toughness is reduced slightly. When 10 vol% silver is incorporated into alumina, the silver inclusions are interconnected to each other. Therefore, not only the exposed silver inclusions but also the internal silver inclusions are attacked by the acid. The weight loss of the composites containing 10 vol% silver is thus increased with increasing corrosion time. After corrosion in nitric acid, the silver inclusions within the crack front are removed and pores are formed instead, so that the strength and toughness are reduced significantly.

Acknowledgement

The valuable comments given by Prof. R. J. Brook, Oxford University, are gratefully acknowledged.

References

1. Tuan, W. H. & Chou, W. B., Toughening alumina with silver inclusions. *Proc. 2nd Conf. of European Ceram. Soc.*, ed. G. Ziegler & H. Hausner. Deutsche Keramische Gesellschaft e.V., Germany, 1991, Vol. 2, p. 1703.
2. Wang, J., Ponton, C. N. & Marquis, P. M., Silver-toughened alumina ceramics. *Br. Ceram. Trans.*, **92** (1993) 67.
3. Chou, W. B. & Tuan, W. H., Toughening and strengthening alumina with silver inclusions. *J. Eur. Ceram. Soc.*, **15** (1995) 291.
4. Wise, E. W. & Coxe, C. D., Silver and silver alloys. In *Metal Handbook*, ed. T. Lyman. Amer. Soc. Metals, OH, 1961, Vol. 1, p. 1181.
5. Leach, R. H., Silver and silver alloys. In *The Corrosion Handbook*, ed. H. H. Chlig. John Wiley & Sons, (1948), p. 314.

Journal of the European Ceramic Society 16 (1996) 587–600

0955-2219(95)00173-5
0955-2219/96/$15.00

Kinetics and Morphology of Electrochemical Vapour Deposited Thin Zirconia/Yttria Layers on Porous Substrates

H. W. Brinkman, J. Meijerink, K. J. de Vries & A. J. Burggraaf

Department of Inorganic Materials Science, Faculty of Chemical Technology, University of Twente, PO Box 217, 7500 AE Enschede, The Netherlands

(Received 2 May 1995; accepted 9 September 1995)

Abstract

By means of electrochemical vapour deposition (EVD), it is possible to grow thin (0·5–5 μm), dense zirconia/yttria layers on porous ceramic substrates. Kinetics of the EVD process, morphology and oxygen permeation properties of the grown layers are investigated. Very thin (~ 0·5 μm) layers are grown at relatively low temperatures (700 – 800°C). Water vapour as reactant enhances the surface reaction rate at the solid oxide/oxygen source reactant interface. A transition occurs from pore diffusion (above 1000°C) to bulk electrochemical diffusion (below 900°C) as rate-limiting step for layer growth. The zirconia/yttria solid solution is mainly deposited in the cubic phase; the layers grow in a typical columnar way and are polycrystalline. Oxygen permeation measurements show that the oxygen permeation flux through the zirconia/yttria layers is influenced by the layer thickness, morphology, presence of water vapour and the oxygen pressure gradient over the layer.

Introduction

The (electro)chemical vapour deposition technique (abbreviated as CVD/EVD) was originally developed by Westinghouse Electric Corporation (Pittsburg, USA) to form thin, gas-tight, solid electrolyte [e.g. yttria-stabilized zirconia, (YSZ)] layers on porous substrates for solid oxide fuel cells (SOFC).[1] Electrolyte layers with a thickness of 2–50 μm, deposited at 1000–1100°C, have been reported.[1–3] More recently proposed applications of CVD/EVD-grown layers are their use in oxygen sensors, electrocatalytic reactors and as oxygen separation membranes. In the ideal case, in dense oxygen semipermeable membranes (without pinholes or cracks) the selectivity for oxygen should be infinite, since oxygen is the only compound that can permeate through. In the case that the bulk diffusion of oxygen ions is the rate-limiting step in the separation process, membrane layers should be as thin as possible to obtain a maximum oxygen permeation rate.

The principles of the CVD/EVD technique have been outlined extensively in the literature.[1–4] A mixture of metal chlorides ($ZrCl_4$ and YCl_3, generated in the 'chloride chamber') is kept separate from an oxygen source reactant (water vapour, oxygen or a mixture, generated in the 'water chamber') by a porous ceramic substrate. Initially, under proper process conditions, the reactants diffuse into the substrate pores and react to form a metal oxide (zirconia–yttria solid solution or ZY) which deposits on the pore wall. As this process continues, pore narrowing occurs until at a certain moment the pores become totally plugged with the metal oxide. The above-mentioned stages are together known as the opposite reactant CVD (ORCVD) stage, and this stage has been discussed, for example, in Refs 5 and 6. Layer or film growth in the subsequent EVD stage is only possible in metal oxides with mixed (i.e. ionic and electronic) conducting behaviour. The oxygen source reactant is reduced at the oxygen source/film interface; oxygen ions (counter-balanced by electrons or co-balanced by electron holes) migrate through the growing film to the film/metal chloride interface, where they react at this interface with the metal chlorides to form (again) the metal oxide. These sequential steps in the EVD stage are shown in Fig. 1.

This paper deals with the kinetics and morphology of zirconia/yttria layers, grown by means of EVD on porous ceramic substrates. In the past few years, only a few groups have investigated the kinetics for the growth of YSZ by means of EVD. Only Westinghouse Electric Corporation (Isenberg[1] and Pal and Singhal[7]), Carolan and Michaels,[8] Burggraaf and co-workers,[4,9–11] Schoonman and co-workers,[12–16]

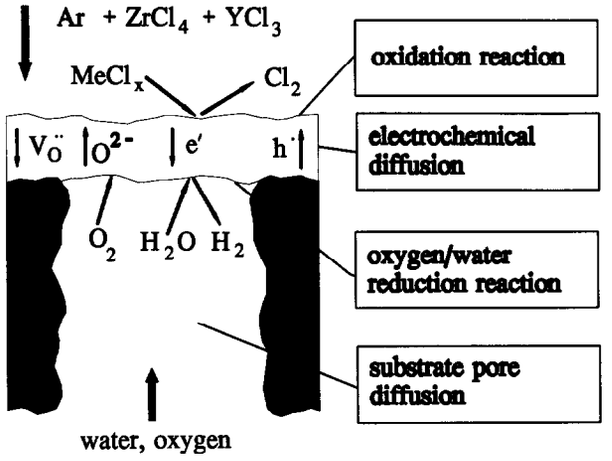

Fig. 1. Schematic view of the four steps in the EVD process.

Sasaki *et al.*[17] and Han and Lin[18] have reported these investigations. In Ref. 15 a short, systematic discussion is given on the EVD kinetics for YSZ layer growth. Some discrepancies in EVD data have been reported. Among others, Pal & Singhal[7] and Carolan & Michaels[8] have found that the EVD process obeys a parabolic law, in which the film thickness is proportional to the square root of the deposition time. On the other hand, for example Isenberg[1] showed that the deposited film thickness of YSZ doped with a small amount of CeO_2 was a linear function of time.

In this paper the optimum process conditions are investigated for growing zirconia/yttria layers that are as thin as possible on porous substrates. Therefore, the influence of the deposition temperature on the film growth rate on a 'model' substrate is investigated. The EVD process is influenced by temperature, since it relies on the electronic and ionic conductivities that are strongly temperature dependent. When the limiting step for the growth of the YSZ layer is diffusion through the bulk, and when bulk properties hold for thin layers, layer growth at 800°C is expected to be much slower than at 1000°C. Due to the large value of the activation energy for electronic conduction in YSZ as reported in Ref. 19, the diffusion resistance in the YSZ film at 800°C is three orders of magnitude larger than that at 1000°C. This would theoretically imply that when a deposition experiment is performed at 800°C, the YSZ layer will grow very slowly after reaching the stage of pore plugging. This indicates that very thin (<1 μm) dense YSZ layers can be grown on porous substrates. In the current investigation, deposition mainly occurs at 700–800°C. Besides the influence of temperature, also the influence of the addition (or removal) of water as oxygen source reactant and the influence of substrate geometries are investigated.

The experimental work performed by Lin *et al.*[10] focused on the effects of oxygen partial pressure and substrate pore dimensions on the EVD film growth rate. Experiments were mainly performed on α-alumina substrates (thickness 2 mm, average pore diameter 160 nm) at 1000°C and a total pressure of 2 mbar. H_2/H_2O, dry air and moist air were used as oxygen source reactant. Experimental results combined with theoretical predictions showed that the substrate pore diffusion was the rate-limiting step for layer growth in the first ~ 5 h, for the α-alumina substrates mentioned above (with water-containing oxygen source reactants). This linear growth rate was ~ 1·5 μm h^{-1}. For a composite substrate with a larger pore diameter/ pore length ratio (factor of 15 000 larger compared with α-alumina), the growth rate was 32 μm h^{-1}, 20 times that of α-alumina. Lin *et al.* suggested that substrate pore diffusion was still the rate-limiting step for this composite substrate. Their data indicated that the oxygen partial pressure at the oxygen source side did not have much influence on the layer growth rate. However, the presence of water had a substantial influence as can be seen in experimental data shown in Refs 9 and 10.

Morphologic aspects such as gas-tightness, phase- and microstructure of EVD-grown ZY layers are reported in the present paper. These aspects have a large influence on the performance of the devices mentioned above via material properties such as conductivity and oxygen permeability. Gas-tight layers are important for oxygen separation membranes; only then is the selectivity for oxygen infinite. The optimum in ionic conductivity in bulk YSZ is found for compositions with about 8–10 mol% Y_2O_3 with the cubic fluorite phase (at room temperature). Zirconia/yttria solid solutions with less yttria consist of tetragonal or monoclinic phases which are hardly or not ionic conducting. The microstructure of very thin layers with layer thickness comparable to the crystallite size (≤ 1 μm) is important since grain boundary effects (transport of, e.g., oxygen along the crystallite boundaries) and crystallite orientation and/or columnar structures may play an important role.

A major characterization technique used here is (*in situ*) oxygen permeation since a possible application of EVD-grown layers is as oxygen separation membranes. Besides, investigation of the oxygen permeation through EVD-grown YSZ films may help in understanding the mechanism for oxygen permeation through thin electrolyte films.

Experimental

EVD experimental conditions and procedures

Most experiments were performed in a home-built CVD/EVD reactor, known as the MM1 (mem-

Table 1. Characteristics of substrates used in CVD/EVD experiments

Coarse porous α-alumina substrate	
Diameter (mm)	12
Thickness (mm)	2
Mean pore diameter (μm)[a]	0·16
Porosity (%)[a]	50
La-doped γ-alumina membrane[b]	
Diameter (mm)	12 (12)
Thickness	5 μm (2 mm)
Mean pore diameter[c,d]	20 nm (0·16 μm)
Porosity (%)[d]	47 (50)

[a]Measured by means of mercury intrusion porosimetry.
[b]Data of top layer; support data between brackets.
[c]Measured by means of permporometry.
[d]Measured by means of nitrogen adsorption–desorption.

Table 2. Typical CVD/EVD experimental conditions for the MM1 reactor

Deposition temperature (°C)	700–1000
Reactor pressure (Pa)	200
$ZrCl_4$ sublimation bed temperature (°C)	150
YCl_3 sublimation bed temperature (°C)	625
Ar carrier gas flow rate through $ZrCl_4$ bed [ml (STP) min^{-1}]	15
Ar carrier gas flow rate through YCl_3 bed [ml (STP) min^{-1}]	7·5
Water sparger temperature (°C)	40
Air carrier gas flow rate through water sparger [ml (STP) min^{-1}]	3·5
Total pressure in water sparger (kPa)	15
Air/water ratio in vapour	1/1

brane modifier 1) reactor. An extensive description of this reactor together with the experimental procedure to deposit zirconia/yttria on porous substrates is given in Refs 4 and 5. In this section a brief outline is given of the deposition conditions and procedures.

A porous alumina substrate, either a coarse porous α-alumina substrate or a composite system consisting of a La-doped γ-alumina supported by an α-alumina substrate (the characteristics of both systems are given in Table 1), was mounted onto the end of a dense alumina tube, separating the reactor into two chambers. In the case of the composite system, the γ-alumina membrane top layer faced towards the metal chloride chamber. The preparation and characterization of these substrates is extensively described elsewhere.[20,21] The temperature inside the MM1 reactor was controlled by a six-zone furnace and an additional heating tape. Before an experiment was started, the zones were heated to their desired temperatures. When the temperature profile had been established, about 30 min before the experiment started, the sublimation beds were filled with fresh $ZrCl_4$ and YCl_3 powder, and the beds were placed at the correct position in the reactor so that metal chloride vapours were generated with a sufficiently high vapour pressure. Ar or N_2 gas flows were passed through the sublimation beds to carry the metal chloride vapours to the porous substrate. At the other side of the porous substrate, a water/air mixture (ratio 1/1) was generated by bubbling air through a water sparger.

The influence of deposition temperature on the layer growth rate was investigated with coarse porous α-alumina substrates and is reported in Ref. 22. Process conditions are shown in Table 2. First, 1 h of deposition was performed at 800°C. Then the temperature was kept at 800°C or raised to 900 or 1000°C, and deposition continued for a variable period of time (1·5, 3 or 4 h).

A small number of deposition experiments was performed in another CVD/EVD reactor, known as the MM2 (membrane modifier 2) reactor, to investigate the influence of the presence of water as oxygen source reactant. Detailed experimental procedures for these deposition experiments are extensively described elsewhere.[23] One experiment was performed for 2 h on an α-alumina substrate at 1000°C deposition temperature and 5 mbar reactor pressure with a 1/1 water/air mixture as oxygen source reactant and $ZrCl_4/YCl_3$ as metal chloride reactants. Another experiment was performed in exactly the same way, but now the water supply was disconnected so that only air was used as oxygen source reactant while the deposition time was 2·5 h.

To obtain dense zirconia/yttria layers that were as thin as possible, a number of deposition experiments was performed at 700°C on La-doped γ-alumina membrane composites. Lin *et. al.*[9] stated that the minimum thickness of a dense EVD-grown YSZ film depends on the average pore size (distribution) of the substrate surface on which the film grows. They reported films as thin as 0·2–0·5 μm, grown at 1000°C on La-doped γ-alumina membrane composites of which the top layer had a thickness of ~ 3 μm and an average pore diameter of 10 nm.[9] Typical deposition times are 30–120 min under conditions shown in Table 2. *In situ* oxygen permeation experiments were performed with these very thin layers within a few hours after the deposition had ended (see section '*In situ* oxygen permeation experiments'). Besides the depositions on membrane composites at 700°C, an additional number of depositions have been performed both on membrane composites and coarse porous substrates at higher temperatures. These samples were also used for *in situ* oxygen permeation.

A number of experiments was performed in the MM1 reactor at 800°C on α-alumina substrates under conditions mentioned in Table 2 to investi-

gate morphological aspects such as gas tightness of the layers, phase composition and crystallite size. Deposition times at 800°C were varied between 30 and 240 min, also to investigate the pore closure time for the α-alumina substrate. These results were compared with morphological results of layers grown at higher temperatures (e.g. 1000°C).

Characterization of the deposited layers

The gas tightness of CVD/EVD-grown layers was checked in two ways. The first check, which was performed *in situ* in the CVD/EVD reactor, was to get a rough indication of the gas tightness. The metal chloride room was filled with ~ 200 mbar argon while the water chamber was filled with 100 mbar argon. When the pressure in the water chamber increased with time this was considered to be an indication that the YSZ layer was not fully gas tight. The second way to check the gas tightness was performed in a home-made helium permeation apparatus as is described in Ref. 24.

By means of a scanning electron microscope [(SEM) Jeol JSM-35CF)] connected to a Kevex Delta-class EDX analyzer for energy dispersive X-ray analysis, the thickness of the EVD-grown layers was estimated. The real layer thickness was found by the back-scattered electron image (BEI) and the formed phases (elements) were checked by EDX.

The phase structure, composition, layer thickness and crystallite size of the CVD/EVD-grown zirconia/yttria layers were investigated by X-ray diffraction [(XRD) Philips PW1710 using Cu K_α radiation] and SEM. During XRD analyses, samples were measured between 2θ = 20 and 90° with scan step in the range 2θ = 0·015–0·03°; the intensity at each point was collected during 5–10 s. Additional high resolution analyses for morphological aspects were performed by means of high resolution scanning electron microscopy [(HR-SEM) Hitachi S800 field emission microscope] and atomic force microscopy [(AFM) Nanoscale II].

Of one EVD sample, grown at 1000°C for 6 h on a gel-cast porous $Sr_{0.15}La_{0.85}MnO_3$ substrate (thickness 2 mm, average pore diameter 0·9 μm, porosity 67%) in another CVD/EVD reactor (known as SOFC reactor), the zirconia/yttria layer peeled off. This layer was examined by transmission electron microscopy [(TEM) Philips CM30 operating at 300 kV] and the selected area electron diffraction facility connected to it to estimate the crystallite size and the crystallographic phases. The sample was pretreated by dimple grinding and ion milling. In this way the crystallite size found by TEM was compared with the crystallite size found by XRD to investigate the reliability of latter method.

***In situ* oxygen permeation experiments**

After the EVD film growth process several samples were used for *in situ* oxygen permeation experiments; this process has already been described.[9] The main advantage of this *in situ* process (i.e. performed in the CVD/EVD reactor) is that high temperature sealing processes and other problems related with transport of an EVD-grown sample to an oxygen permeation apparatus are avoided.

The CVD/EVD experiments were performed at 700°C for 30 min under conditions as shown in Table 2. The gas tightness of the deposited layers was checked by *in situ* argon permeation (see section 'Characterization of the deposited layers'), and when they showed some leakage another 30 min of deposition followed. This procedure was followed until the layers were gas tight. In almost all cases the layers were gas tight after 30 min deposition. Then the zone of the furnace in which the sample was placed was heated to the desired temperature (700–1000°C) to perform an *in situ* oxygen permeation measurement. When this temperature was reached, another *in situ* argon permeation measurement was performed to check whether the rise in temperature caused some leakage. The temperature of the sublimation beds was lowered (for $ZrCl_4$ < 100°C, for YCl_3 < 300°C) and in some cases the sublimation beds were removed from the furnace. The presence or absence of sublimation beds did not influence the *in situ* oxygen permeation values according to our experience. When the sample was still gas tight, a standard *in situ* oxygen permeation measurement was performed. The water chamber was flushed with oxygen and the chloride chamber with argon for about 5 min. Then the water chamber (volume 375 cm^3) was filled with pure oxygen (150 mbar, so P_{O_2} = 0·15 atm) and the chloride chamber (volume >> 375 cm^3) with argon (150 mbar; nominal P_{O_2} = 10^{-5} atm). During 30–45 min the pressure decrease in the water chamber (due to oxygen permeation through the EVD YSZ sample) was measured. With each sample a blank permeation (i.e. 150 mbar argon in both chambers) was performed to correct for possible leaks from the outside.

In a first series of *in situ* oxygen permeation experiments the relative error in the measurements was rather large (about 30–60%), mainly due to scatter, so that only an order of magnitude for the oxygen permeation value could be obtained. In further *in situ* oxygen permeation experiments the volume of the water chamber was decreased to 267 cm^3 by inserting a voluminous metal body inside this chamber. Now the error in the measurements was smaller (~ 10%).

Besides performing *in situ* oxygen permeation

with oxygen vs. argon, one experiment was performed with a water/oxygen mixture vs. argon. Also, some *in situ* permeation experiments were performed on several samples both immediately after the EVD process had ended and the day after. This was done to investigate the influence of time on the permeation results.

Results and Discussion

By means of the CVD/EVD technique it is very well possible to grow thin, dense zirconia/yttria films on porous alumina substrates. Layers are grown on the side of the substrate exposed to the metal chloride vapours. A typical SEM photograph of a cross-section of a zirconia/yttria layer deposited on a porous α-alumina substrate for 10 h at 1000°C under conditions of Table 2 is shown in Fig. 2 (sample #91041). The layer has a thickness of ~ 5 μm and has a columnar-like structure which is typical for EVD-grown zirconia/yttria layers on porous supports at high temperature. Crystallites on the surface of the layer are highly faceted; this can be seen even better in Fig. 3, where a SEM photograph of the surface of the same sample as in Fig. 2 is shown. The average size of the surface crystallites here is in the range of 2 to 3 μm. XRD analyses showed that the formed layers consisted mostly of the cubic YSZ phase, but also some amounts of monoclinic and tetragonal phases (up to about 40%) were observed.

A rough estimate of the gas tightness of the deposited zirconia/yttria layers was performed by *in situ* argon permeation immediately after the EVD process had stopped. In almost all cases the grown layers were gas tight (within the measurement accuracy, ± 0·5 mbar in 5 min) after deposition for 30 to 240 min at 700–1000°C under conditions as are shown in Table 2. Performing *in situ* argon permeations the day after, when the furnace had cooled to room temperature, showed in several cases some leakage. Further investigations showed that this was due to the fact that the ceramic seal (Autostic) between the porous substrate and the dense alumina water chamber tube became porous after cooling. The deposited samples themselves remained gas tight after cooling.

Fig. 2. SEM photograph of a cross-section of a zirconia/yttria layer deposited on porous α-alumina.

Fig. 3. SEM photograph of the highly faceted surface of an EVD-grown zirconia/yttria layer.

Detailed information about helium permeation experiments through α-alumina substrates deposited at 800°C under conditions as described in Table 2 is presented in Ref. 24. The pore closure time (i.e. the time at which the ORCVD stage ends and the EVD stage begins) is estimated to be around 40 min. This value is slightly higher than the pore closure time for α-alumina substrates, deposited at 1000°C and 2 mbar reactor pressure.[4]

Kinetics of EVD growth of zirconia/yttria layers

Zirconia/yttria layers have been grown with and without water present in the water chamber, under otherwise equal process conditions (MM2 reactor, deposition temperature 1000°C, reactor pressure 5 mbar). According to XRD analysis, both EVD-grown layers had the cubic yttria-stabilized zirconia structure. Deposition for 2 h with an air/water vapour mixture gave a YSZ layer with thickness 4–6 μm. Deposition for 2·5 h without water vapour resulted in a layer thickness of 0·5–1 μm. The influence of water vapour on the YSZ layer growth rate is obvious. Including a pore closure time of 30 min (for zirconia/yttria deposition at 1000°C and 2 mbar[4]) this means that the layer growth is around 0·4 and 3 μm per hour in the absence and presence of water vapour, respectively. So the layer growth rate is decreased by almost a factor 10 in the absence of water! The presence of water apparently influences the rate-limiting step for YSZ layer growth. Wen and Mason[25] reported the influence of water vapour on the cathodic reduction of oxygen on scandia-stabilized zirconia

coated with a porous gold electrode. The following mechanism, based on suggestions made by them, may be responsible for incorporating oxygen ions (O^{2-}) into stabilized zirconia in the presence of water (H_2O); $H_i^{\cdot}$ is an interstitial proton:

$$H_2O(g) \rightleftharpoons O^{2-} + 2H_i^{\cdot} \qquad (1)$$
$$2H_i^{\cdot} \rightleftharpoons H_2(g) + 2\,h^{\cdot}$$

When the diffusion of the oxygen source reactant (i.e. oxygen or water) through the pores is the rate-limiting step for EVD layer growth, the following equation can be used for theoretically predicting the layer growth rate dl/dt, assuming that the oxygen (or water vapour) partial pressure in the chloride chamber is negligible compared with the partial pressure of the oxygen source reactant in the water chamber (see, for example, eqns (18) and (19) in Ref. 10):

$$\frac{dl}{dt} = \frac{V_{mol} n_i D_i P_{i,OSR}}{2LRT} \qquad (2)$$

Here i is water or oxygen, and n_i is equal to 1 for water and 2 for air, including the effect that water contains one oxygen atom per molecule whereas air (i.e. molecular oxygen) contains two oxygen atoms per molecule. V_{mol} is the (average) molar volume of YSZ inside the layer, D_i is the Knudsen diffusion coefficient for compound i, $P_{i,OSR}$ is the vapour pressure of compound i at the pore entrance, L is the substrate thickness (or pore length), R is the gas constant and T is the temperature.

The experimental values found above may be compared with theoretical results from eqn (2). The Knudsen diffusion coefficients for water and oxygen at 1000°C are respectively $1{\cdot}3 \times 10^{-5}$ and $1{\cdot}0 \times 10^{-5}$ $m^2\ s^{-1}$, assuming that the α-alumina substrate has a porosity of 50% and a tortuosity value of 2·5. In the MM2 reactor, operating at 1000°C and 5 mbar total pressure, the partial water vapour pressure in the presence of water is 2·5 mbar (water/air, ratio 1/1). In the absence of water, the oxygen partial pressure is 1·05 mbar (air at 5 mbar). When pore diffusion is rate-limiting, the zirconia/yttria layer growth would be around 5·8 and 3·5 $\mu m\ h^{-1}$ in the presence and absence of water, respectively. For the situation in which water is present, the theory is in agreement with the experiment (almost a factor 2 difference), but for the situation in which only air is present, the theory does not agree with the experiment (almost one order of magnitude difference).

In conclusion it can be said that diffusion of the *water-vapour-containing* oxygen source reactant through the substrate pores is rate-limiting for EVD zirconia/yttria layer growth at *1000°C* in the Knudsen area (low pressure, small pores). Apparently, the presence of water enhances the surface reaction rate at the metal oxide/oxygen source reactant interface. When the oxygen source reactant contains no water, another step (for example, a surface exchange reaction) may be rate-limiting.

The results of the experiments in which zirconia/yttria layers are deposited as a function of total deposition time on α-alumina substrates for different deposition temperatures are discussed in Ref. 22. The observed layer growth rates, obtained from the slope of straight lines of layer thickness vs. total deposition time, are 1·6 $\mu m\ h^{-1}$ (at 1000°C), 0·4 $\mu m\ h^{-1}$ (at 900°C) and around 0 $\mu m\ h^{-1}$ (at 800°C). Due to the relatively large inaccuracy (especially at 800°C) this does not mean that the layer growth really obeys a linear growth rate behaviour. Although at 1000°C a linear relation for the layer growth is very probable, at lower temperatures other relations between the layer thickness and the total deposition time will also hold within the measurement errors. Compared with previous results, the values for the layer growth rate obtained here are almost equal. In previous papers[4,10] it was found that the layer growth rate at 1000°C and 2 mbar was about 1·5 $\mu m\ h^{-1}$; the value of 1·6 $\mu m\ h^{-1}$ reported here is within the measuring error.

The rate-limiting step for the layer growth process was evaluated in a similar way as done before in our group,[10,11] where it is suggested that one may calculate the film growth rate for each of the steps assuming it is rate-limiting. In the first place the surface exchange reactions are excluded; in the presence of water it is assumed that the surface exchange rate at the water side is fast enough, as was discussed above. Further, the facts that faceted crystallites were grown (see e.g. Fig. 3) and that the layer growth was not noticeably dependent on the metal chloride partial pressure[9] give the impression that the oxidation reaction at the metal chloride side is not a rate-limiting step. Pal and Singhal[7] have used substrates with large pores (~ 10 μm, estimated from a SEM photograph) and found an almost perfect straight line when the square of the YSZ film thickness was plotted against the deposition time, indicating that only (the electronic part of) the electrochemical diffusion process in the layer was rate-limiting.

When the bulk electrochemical transport in the EVD film is the rate-limiting step, eqn (3) displays the theoretical temperature dependence (T in K) of the layer growth rate dl/dt as derived in Ref. 22.

$$\frac{dl}{dt} = 6{\cdot}8 \times 10^4 T e^{-19379(K)/T} + 3{\cdot}8 \times 10^{14} T e^{-45024(K)/T} \quad (\mu m\ h^{-1}) \qquad (3)$$

Equation (4), also from Ref. 22, displays the theoretical temperature dependence of d*l*/d*t* when substrate pore diffusion is rate-limiting:

$$\frac{dl}{dt} = \frac{82}{\sqrt{T}} \ (\mu m\ h^{-1}) \qquad (4)$$

According to these equations it follows that the theoretical transition temperature (from pore diffusion as the rate-limiting step to electrochemical diffusion as the rate-limiting step) is around 825°C (1100K). In Ref. 22 it is stated that it is very probable that the diffusion of the water/air mixture through the substrate pores is the rate-limiting step for EVD film growth at 1000°C. At 900°C the bulk electrochemical diffusion through the zirconia/yttria layer is most probably the rate-limiting step. Extrapolating to lower temperatures, this is also the case at 800°C. At 800°C a quantitative discrepancy exists between theory and experiment: theoretically a layer growth rate (bulk diffusion limiting) of ~ 1 μm h^{-1} is expected, while experimentally the maximum layer growth rate is only a few tenths of a μm. At 900°C a discrepancy exists too; according to theory, pore diffusion is the rate-limiting step, while according to the experiments bulk diffusion is rate-limiting. There are several possible causes for these discrepancies. One possibility is that the oxygen partial pressure in the chloride chamber is higher than 10^{-17} atm, which is the assumed value in Ref. 22. But for a good agreement between theory and experiments, a high $P_{O_2,McCl}$ is necessary (only a few orders of magnitude lower than $P_{O_2,OSR}$). It is not likely, however, that the oxygen partial pressure in the chloride chamber is that high. To illustrate this, Pal and Singhal reported an oxygen partial pressure as low as $4{\cdot}3 \times 10^{-18}$ atm in the chloride chamber.[7] Another possibility to explain the discrepancy between theory and experiment is that the formed EVD layers were not totally cubic but also consisted of the monoclinic and tetragonal ZY phases. The effective values of the electron and electron-hole conductivities of cubic YSZ [present in the pre-exponential factors in eqn (3)] are then lower because the relative amount of cubic YSZ is smaller than unity (as is the fact in Ref. 19). Of course, it is also possible that data generated in Ref. 19 for YSZ bulk material may no longer hold for thin layers with a different morphology.

Very thin zirconia/yttria layers were deposited on La-doped γ-alumina membrane composites at 700°C under conditions as described in Table 2. Typical deposition times were 30 min. Layers as thin as about 0·5 μm were found to be gas tight as was checked by *in situ* argon permeation and helium permeation. Our experience is that layers could not be made thinner than several tenths of a μm (on these substrates) without showing some gas leakage. These results confirm those of Ref. 9, where thin (0·5 μm) zirconia/yttria layers were grown after 30 min on La-doped γ-alumina membrane composites at 1000°C, at similar process conditions as in Table 2. These EVD-grown layers were further used in *in situ* oxygen permeation experiments, since the very thin zirconia/yttria layers were expected to have high oxygen permeation values. A typical HR-SEM photograph of a dense zirconia/yttria layer deposited at 700°C for 120 min on a membrane composite is shown in Fig. 4.

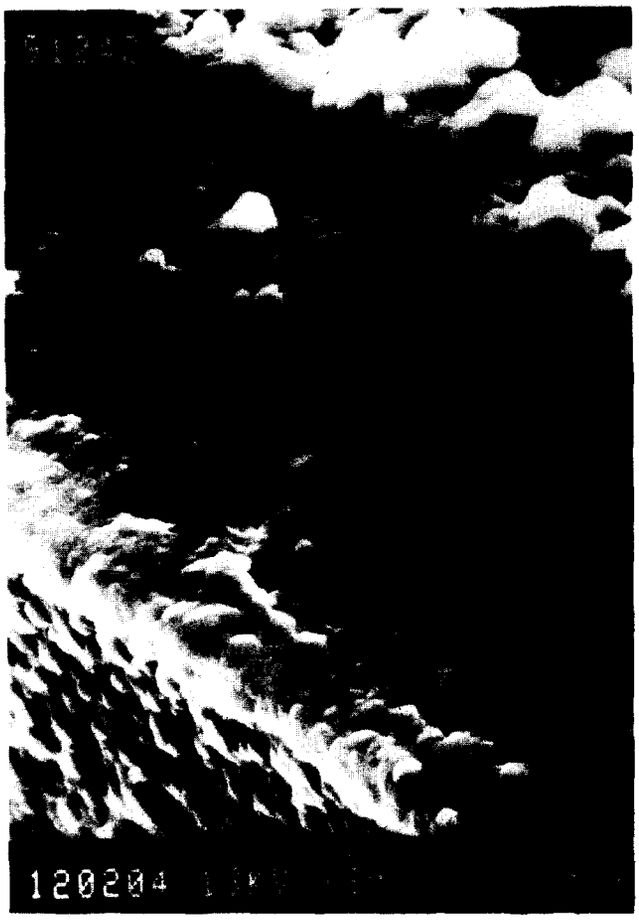

Fig. 4. HR-SEM photograph of a zirconia/yttria layer deposited for 120 min at 700°C on La-doped γ-alumina membrane. Bottom left: ZY layer (thickness ~ 0·5 μm), middle: γ-alumina membrane (thickness ~ 3 μm), upper right: α-alumina support.

Morphology of the deposited layers

The morphology of layers deposited at 800°C for 30 to 240 min under conditions as described in Table 2 is discussed here. In the XRD patterns of porous α-alumina substrates on which zirconia/yttria is deposited, several phases are observed. An example of such an XRD pattern is shown in Fig. 5 (#92032, 120 min deposition). Besides the α-alumina phase of the substrate, several zirconia/yttria phases are present: monoclinic, tetragonal and/or cubic. The α-alumina peaks are sharp, while

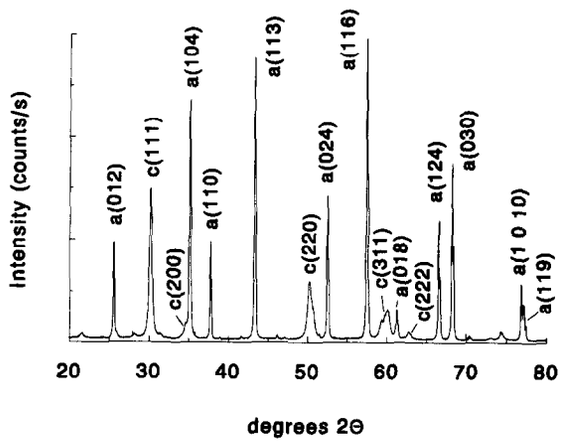

Fig. 5. XRD pattern of EVD-grown sample #92032. Cubic YSZ (c) and α-aluminia (a) peaks are indexed.

the zirconia/yttria peaks are rather broad; these peaks are indexed in Fig. 5.

It was very hard to distinguish between the tetragonal and cubic phases. In theory, the small (4 0 0) type reflections in the 2θ region between 73 and 75° are different for the tetragonal and cubic phases. In the CVD/EVD-grown samples this can hardly be seen, since the (4 0 0) peaks are small and the α-alumina (2 0 8) peak is also located in this range, which makes the analysis very difficult. However, both the tetragonal phase (see, for example, Ref. 26) and the cubic phase (see, for example, Ref. 19) exhibit oxygen ion conductivity. The bulk conductivities are similar for both phases; the grain boundary conductivity of the tetragonal phase is, however, much less.[27] Hence, with the tetragonal phase present it is preferred to have only a few grain boundaries across the layer thickness. The monoclinic zirconia/yttria phase can be easily distinguished from the tetragonal or cubic phase; the monoclinic ($\bar{1}$ 1 1) and (1 1 1) peaks at 2θ = 28·2 and 31·5° differ from the tetragonal/cubic (1 1 1) peak around 2θ = 30°. The non-linear calibration method[28,29] was used to calculate the volume fraction of monoclinic zirconia/yttria; this procedure is outlined in a previous publication from our group.[24] A computer algorithm was used for processing the XRD data of the CVD/EVD-grown layers as outlined in Ref. 30.

Table 3. Effects of deposition time and temperature on the volume fraction of monoclinic zirconia/yttria

Sample #	*Deposition temperature (°C)*	*Deposition time (min)*	V_m *(vol%)*
92030	800	30	7·8
92031	800	45	6·7
92029	800	60	13·0
92032	800	120	1·2
92047	800	240	5·1
90105[a]	1000	120	~0
91025	1000	120	~0
91027[b]	1000	120	~0

[a] $\phi_{Ar,ZrCl_4}$ = 7·5 ml(STP) min^{-1}; ϕ_{Ar,YCl_3} = 30 ml (STP) min^{-1}.
[b] T_{YCl_3} = 650°C.

In Table 3 the fraction of monoclinic zirconia/yttria is shown as a function of the deposition time. As can be seen from the table, the fraction of monoclinic phase is rather small, between 0 and 13 vol%. In a previous publication from our group[24] these values were a factor of 2–3 higher due to a wrong interpretation and calculation procedure. When the volume fraction of monoclinic phase, deposited at 800°C, is compared with that deposited at 1000°C under nearly the same conditions (samples #90105, #91025 and #91027 in Table 3), the monoclinic volume fraction is higher when the temperature is lower under current process conditions. The reason for this might be that the concentration ratio $YCl_3/ZrCl_4$ near the substrate is lower at 800°C than at 1000°C. At a deposition temperature of 1000°C, the YCl_3 bed (nominal temperature 625°C) can be heated additionally by radiation coming from the deposition zone, which is rather close to this bed. The $ZrCl_4$ bed is much less influenced by this deposition zone since the distance is larger, so the ratio $YCl_3/ZrCl_4$ can be higher than expected. When this ratio is the same in the gas phase and in the EVD-grown layers, less monoclinic zirconia/yttria will be expected in the layers at 1000°C.

From Fig. 5 it has been observed that the zirconia/yttria peaks were more broadened than the α-alumina peaks. In previous publications[24,31] this broadening has been ascribed to the existence of a very small grain size, assuming that no line broadening occurred due to local inhomogeneities and strain. The Scherrer equation[32] can be used to calculate the crystallite size D from the broadening of YSZ reflections (indexed in Fig. 5), assuming that broadening is only due to size:

$$D = \frac{K\lambda}{\beta_{CS}\cos\theta}\,\frac{360}{2\pi} \qquad (5)$$

λ is the wavelength of Cu K_{α_1} radiation (0·15405 nm), θ is the diffraction angle of the ($h\,k\,l$) reflection, K is a constant (0·94) and β_{CS} is the half width at half maximum of a step-scan profile of the ($h\,k\,l$) peak after correction for K_{α_1}–K_{α_2} separation and instrumental broadening. For the samples mentioned in Table 3 which were deposited at 800°C, the value of the (instrumental corrected) line broadening of the YSZ (1 1 1) peak around 2θ = 30° was in the range 2θ = 0·35 to 0·50°, slightly increasing with decreasing deposition time. This corresponds to a crystallite size of 17 to 25 nm, so very small. The same crystallite sizes hold for samples deposited at 1000°C in Table 3. However, this line broadening cannot be ascribed completely to the existence of small crystallites. Inhomogeneities

(i.e. the existence of more than one phase) also play a role in the occurrence of line broadening. For example, the 'assumed to be YSZ' peak around $2\theta = 30°$ consists of cubic and tetragonal parts too. Besides the existence of small crystallite sizes and inhomogeneities, another cause for line broadening is strain in the material. Thin zirconia/yttria layers which were grown at high temperatures and cooled to room temperature may contain a considerable amount of strain since the thermal expansion coefficient is different from that of α-alumina. Accordingly, it is not possible to say anything about crystallite sizes by X-ray line broadening, since other phenomena also influence the line broadening.

By means of TEM it was possible to determine the crystallite size of EVD-grown layers. The 'peeled off' YSZ layer, described in the 'Experimental' section (6 h deposition at 1000°C on a $Sr_{0.15}La_{0.85}MnO_3$ substrate), consisted of crystallites with sizes between 1 and 5 μm; most crystallites had a size of 2–3 μm. These sizes were roughly equal in all dimensions, so columns were not observed. This indicates that columns in the columnar-like structures, observed by SEM for samples grown at high temperatures (1000°C, see e.g. Fig. 2), consisted of smaller crystallites. A typical TEM photograph is shown in Fig. 6. Selected area electron diffraction revealed the cubic YSZ phase. By means of SEM, similar crystallite sizes were observed at the surface of the EVD-grown layer. This suggests that the crystallites inside the layer and at the surface of the layer are same size, about 2–3 μm. Crystallites with sizes as small as 15–25 nm were *not* observed by TEM, indicating that the crystallite size found by X-ray line broadening is not correct.

Fig. 6. TEM photograph of YSZ crystallites (text bar at the top = 1·4 μm). Deposition conditions: 6 h at 1000°C on $Sr_{0.15}La_{0.85}MnO_3$ substrate.

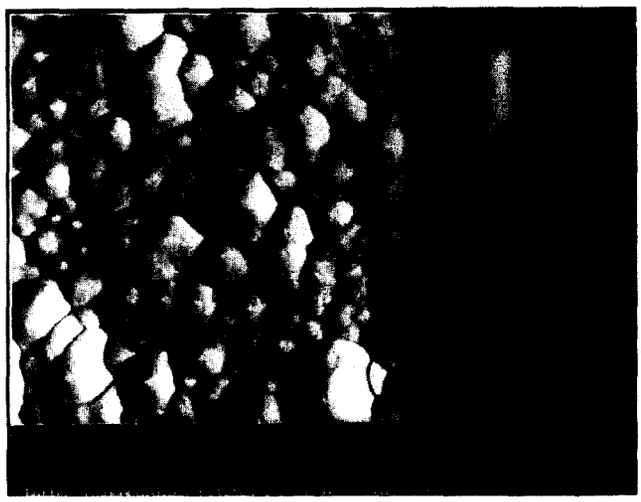

Fig. 7. AFM picture of the surface of an EVD-grown zirconia/yttria layer (#91123).

Sample #91123 (2 h deposition at 1000°C on an α-alumina substrate under standard conditions) was investigated by AFM to estimate the crystallite size. A typical AFM picture is given in Fig. 7, and by means of AFM investigation the crystallite size was found to be between 0·1 and 0·7 μm. By means of SEM similar crystallite sizes were found. Crystallites with sizes as small as 15–25 nm were not observed.

These two results suggest that there might be some influence of experimental conditions (i.e. deposition temperature, deposition time, substrate type) on the apparent crystallite size. Sample #91042 (2 h deposition at 700°C on La-doped γ-alumina membrane) resulted in a zirconia/yttria layer with a thickness of ~ 0·5 μm and an average

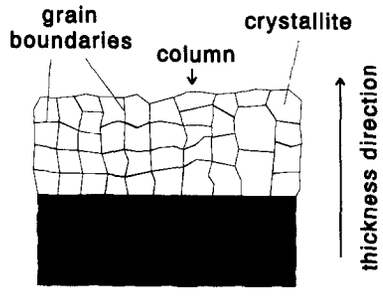

Fig. 8. Schematic view of a cross-section of a zirconia/yttria layer on a porous substrate.

(surface) crystallite size of ~ 0·1–0·2 μm. Surface crystallites of sample #91123, deposited for 2 h at 1000°C on an α-alumina substrate, were ~ 0·1–0·7 μm in size with a layer thickness of ~ 2 μm. Depositing for a longer time, e.g. 10 h at 1000°C on an α-alumina substrate (#91041, see also Fig. 2), resulted in crystallite sizes of ~ 2–3 μm with a layer thickness of ~ 5 μm. Deposition for 6 h on a $Sr_{0·15}La_{0·85}MnO_3$ substrate at 1000°C resulted in a 12 μm thick layer with crystallite sizes around 2–3 μm. According to these results, the trend is that crystallites become larger when the zirconia/yttria layer is thicker. The ratio of layer thickness and crystallite size is approximately the same for all samples mentioned here; only a few crystallites (about three to five across the membrane thickness) and grain boundaries perpendicular to the thickness direction are present. A schematic view is given in Fig. 8. Parallel to the thickness direction many grain boundaries are present. Figure 8 shows that the occurrence of many grain boundaries parallel to the thickness direction gives rise to the formation of columnar structures. This is an important microstructural feature. The influence of EVD process parameters on crystallite size is described more extensively in Ref. 23 for the system zirconia/yttria/terbia.

In situ oxygen permeation

All *in situ* oxygen permeation experiments showed a pressure decrease with time in the water chamber, after correction for leakage. The oxygen permeation values J_{O_2} were calculated from the slope of the time-dependent pressure change dp_{wc}/dt in the water chamber via:

$$J_{O_2} = \frac{V_{WC}}{RST_{av,wc}} \frac{dp_{WC}}{dt} \quad (6)$$

where V_{wc} is the volume of the water chamber (without voluminous metal body 375 cm^3; with body 267 cm^3). $T_{av,wc}$ is the average temperature in the water chamber during oxygen permeation. When the temperature of the furnace zone in which the sample is located is 700, 800, 900 or 1000°C, $T_{av,wc}$ is 51, 53, 56 or 59°C, respectively. R is the gas constant and S is the surface area of the EVD-grown YSZ sample (0·68 cm^2). The results that were obtained before decreasing the volume of the water chamber are shown in Table 4.

When the results in Table 4 are inspected, it seems that there is no large influence of the permeation temperature on the permeation value, although permeation at 1000°C seems to be somewhat larger than at lower temperatures. The permeation never has a value lower than $0·2 \times 10^{-8}$ mol cm^{-2} s^{-1} (i.e. $0·5 \times 10^{-8}$–$0·3 \times 10^{-8}$ mol cm^{-2} s^{-1}, see Table 4).

Table 4. *In situ* oxygen permeation results (without the voluminous body in the water chamber)

Sample #	*Deposition time (min)*[a]	*Permeation temperature (°C)*	dp_{wc}/dt *(mbar min⁻¹)*[b]	J_{O_2} *(mol cm⁻² s⁻¹)*
91079	120[c]	900	–0·016 ± 0·009	(0·5 ± 0·3) × 10^{-8}
91085	30	1000	–0·030 ± 0·010	(1·0 ± 0·3) × 10^{-8}
91088	30	700	–0·014 ± 0·009	(0·5 ± 0·3) × 10^{-8}
91089	30 + 30	800	–0·015 ± 0·009	(0·5 ± 0·3) × 10^{-8}
91094	30	1000	–0·022 ± 0·010	(0·7 ± 0·4) × 10^{-8}

[a]Deposition at 700°C on La-doped γ-alumina membranes under conditions as described in Table 2; all layers have a thickness of ~ 0·5 μm except for #91079 with thickness ~1 μm.
[b]Corrected for leakage, i.e. blank subtracted; average leakage –0·005 ± 0·003 mbar min^{-1}.
[c]Continuous deposition.

Table 5. *In situ* oxygen permeation results (with reduced water chamber volume)

Sample #	T_{dep} *(°C)*[a]	t_{dep} *(min)*[a]	T_{perm} *(°C)*	dp_{wc}/dt *(mbar min⁻¹)*[b]	J_{O_2} *(mol cm⁻² s⁻¹)*
91124[e]	1000	120	1000	–0·12 ± 0·01	(3·1 ± 0·3) × 10^{-8}
				–0·11 ± 0·01	(2·8 ± 0·3) × 10^{-8}
				–0·055 ± 0·009	(1·5 ± 0·3) × 10^{-8}
91125[e]	1000	120	1000	–0·11 ± 0·02	(2·8 ± 0·5) × 10^{-8}
92007[e]	1000	240	1000	–0·030 ± 0·007	(0·8 ± 0·2) × 10^{-8}
				–0·095 ± 0·009	(2·4 ± 0·3) × 10^{-8}[d]
				–0·012 ± 0·007	(0·3 ± 0·2) × 10^{-8}
92008[e]	800	120	800	–0·023 ± 0·011	(0·6 ± 0·3) × 10^{-8}
92028[e]	800	120	800	–0·146 ± 0·006	(3·7 ± 0·3) × 10^{-8}

[a]Deposition under conditions as is described in Table 2. Layer thicknesses: #91124, ~2 μm; #91125, 2–3 μm; #92007,~5 μm; #92008, ~1 μm; #92028, 1–2 μm.
[b]Corrected for leakage, i.e. blank subtracted; average leakage –0·010 ± 0·005 mbar min^{-1}.
[c]Coarse porous α-alumina substrate.
[d]Oxygen/water mixture at high oxygen partial pressure side.
[e]La-doped γ-alumina membrane composite.

However, the error in each measurement is always $0{\cdot}3 \times 10^{-8}$ mol cm^{-2} s^{-1} (absolute error) or 30–60% (relative error), which is too large to give a quantitative trend.

The accuracy was increased by decreasing the volume of the water chamber. *In situ* oxygen permeation results for this case are shown in Table 5. An EVD experiment (#91124) was performed in which an α-alumina substrate was deposited for 2 h at 1000°C under conditions as described in Table 2. After *in situ* checking for gas tightness, the deposition was followed by a number of *in situ* oxygen permeation experiments to control the reproducibility of the measurements. Two permeation experiments were performed at 1000°C, several hours after the EVD experiment was ended, in the same way as is described in section '*In situ* oxygen permeation experiments'. The volume of the water chamber was 267 cm^3 and the average temperature in the water chamber was 35°C. For these two measurements, the leakage corrected pressure decrease in the water chamber was $0{\cdot}12 \pm 0{\cdot}01$ mbar min^{-1} and $0{\cdot}11 \pm 0{\cdot}01$ mbar min^{-1}, corresponding to oxygen permeation values of $(3{\cdot}1 \pm 0{\cdot}3) \times 10^{-8}$ and $(2{\cdot}8 \pm 0{\cdot}3) \times 10^{-8}$ mol cm^{-2} s^{-1}, respectively. An *in situ* oxygen permeation experiment performed the next day gave a lower value for the oxygen permeation: $(1{\cdot}5 \pm 0{\cdot}3) \times 10^{-8}$ mol cm^{-2} s^{-1}. The experimentally observed decrease in permeation with time for sample #91124 is probably caused by the fact that the oxygen partial pressure in the metal chloride chamber increases with time. In the beginning, just after the EVD experiment has ended, considerable amounts of metal chlorides may still be present in the metal chloride chamber, for example produced by residual chloride deposits in colder parts of the reactor. This means that the oxygen partial pressure in this chamber is still very low ($<<10^{-5}$ atm), even after flushing for some time with argon or nitrogen. The large oxygen partial pressure gradient over the sample is most probably the reason that the oxygen permeation through the sample is considerably large. In the second permeation measurement, about an hour later, the oxygen partial pressure in the chloride chamber is somewhat increased due to lowered sublimation bed temperatures, flushing with fresh argon and oxygen that gets into the chloride chamber via the *in situ* oxygen permeation process. The driving force for permeation (i.e. the oxygen partial pressure difference) is now somewhat smaller, so the permeation value will decrease. This effect is even stronger in the permeation experiment performed the next day; the oxygen permeation value is half the value of the previous day.

In situ oxygen permeation experiments were also conducted with another α-alumina sample (#91125) that was deposited under the same conditions (i.e. 2 h at 1000°C) to control reproducibility. This resulted in a comparable oxygen permeation value of $(2{\cdot}8 \pm 0{\cdot}5) \times 10^{-8}$ mol cm^{-2} s^{-1} when the *in situ* oxygen permeation experiment was performed directly after the EVD experiment. So these *in situ* oxygen permeation measurements seem to be reproducible.

Of sample #92007, which had been deposited for 4 h at 1000°C (α-alumina substrate, deposited under conditions as described in Table 2), *in situ* oxygen permeation measurements were performed with both oxygen (150 mbar) and an oxygen/water mixture (150 mbar) at the high oxygen partial pressure side. These experiments were conducted the next day, after decreasing the sublimation bed temperatures and removing the sublimation beds. It can be seen in Table 5 that water has a certain effect on the permeation; the value is about three times higher than the permeation experiment performed with pure oxygen. This indicates that the surface reaction where oxygen (or water) is incorporated into the zirconia/yttria layer may be partly rate-limiting for oxygen permeation under these conditions. When another *in situ* permeation experiment was performed on this sample, again using pure oxygen at the high oxygen partial pressure side, the permeation value decreased (similar to the observation made for sample #91124).

Two *in situ* permeation experiments were performed on samples deposited at 800°C under conditions as in Table 2. Sample #92008 was an La-doped γ-alumina membrane composite and #92028 was a coarse α-alumina substrate. The oxygen permeation value through the composite was much lower than that measured through the coarse substrate. There is some contradiction in the influence of the oxygen permeation flux by the thickness of the deposited zirconia/yttria layer. Samples #91124 and #91125 with a layer thickness of 2–3 μm have a permeation of around 3×10^{-8} mol cm^{-2} s^{-1} at 1000°C while sample #92007, with a layer thickness of ~ 5 μm, has a lower permeation value. However, for all samples shown in Table 4 and sample #92008 in Table 5 the zirconia/yttria layer thickness is around 0·5–1 μm while the permeation is lower than for thicker samples. The cause for this contradiction is not clear yet. Probably the morphology of these very thin layers, i.e. the relatively large grain boundary content, is disadvantageous for oxygen permeation properties.

The rate-limiting step for *in situ* oxygen permeation may be different from the rate-limiting step during EVD layer growth, since there is a difference in experimental conditions. The largest difference is the total pressure at which the processes

were performed: for EVD layer growth the pressure is 2 mbar, for *in situ* oxygen permeation it is 150 mbar. Moreover, in *in situ* oxygen permeation experiments water is (in general) not present at the high oxygen partial pressure side. If diffusion of oxygen through the substrate pores is assumed to be rate-limiting in the temperature range 700–1000°C, the oxygen permeation value can be calculated assuming that the oxygen partial pressure in the chloride chamber is negligible compared with the oxygen pressure in the water chamber (150 mbar) and that the porosity and tortuosity values for α-alumina substrates are 50% and 2·5, respectively. In this case the oxygen permeation ranges from $1{\cdot}4 \times 10^{-6}$ to $1{\cdot}6 \times 10^{-6}$ mol cm^{-2} s^{-1} when the temperature decreases from 1000 to 700°C. These calculated values are much higher (a factor of ~ 100) than those found in current *in situ* oxygen permeation experiments (see Tables 4 and 5). So, at these relatively high pressures, the diffusion of oxygen through the substrate pores is no longer rate-limiting for oxygen permeation.

Three other steps that can be rate-limiting in the oxygen permeation process are the two surface reactions and the 'bulk' diffusion through the layer. It can be argued that for very thin (~ 1 μm) zirconia/yttria layers one of the surface reaction steps is rate-limiting. Bouwmeester *et al.*[33] reviewed the importance of surface exchange reactions as rate-limiting step in the oxygen permeation process through mixed conducting oxides. Dou *et al.*[34] have shown that for calcia-stabilized zirconia pellets under specific conditions, below a certain thickness, surface exchange reactions influence the oxygen permeation value to a large extent. In addition, since water vapour is no longer present (as is the case during the EVD process), the reduction reaction at the oxygen/metal oxide surface will no longer be catalytically activated. It is doubtful, however, whether extrapolation to ultra-thin layers is allowed. Effects of microstructure (parallel grain boundaries in columnar-like structures, defects on grain boundaries) become important here. It is stated that in very thin layers (~ 0·5 μm) the morphology of the layers becomes important. It is possible that for these thin, columnar grown layers the crystallite size is ~ 100 nm, so that surface diffusion along the boundaries of the crystallites parallel to the thickness direction is certainly possible. However, it is also possible that grain boundaries perpendicular to the thickness direction can be obstructive for oxygen transport (see Fig. 8).

An attempt has been made to observe oxygen permeation through EVD-grown zirconia/yttria under a small oxygen partial pressure gradient. Therefore, sample #92001 (deposition for 2 h at 1000°C on an α-alumina substrate; duplicate of sample #91124) was put in an oxygen permeation reactor (more extensively described in Ref. 35) with air (P_{O_2} = 0·212 atm) at the high and helium ($P_{O_2} \approx 10^{-4}$ atm) at the low oxygen partial pressure side. At 1100°C an oxygen permeation value of $\sim 6 \times 10^{-11}$ mol cm^{-2} s^{-1} was found. Comparing this value with the *in situ* oxygen permeation value of a similar sample (#91124, see Table 5) of $\sim 3 \times 10^{-8}$ mol cm^{-2} s^{-1} (at 1000°C) shows that the oxygen partial pressure gradient over the zirconia/yttria membrane has a large influence on the oxygen permeation.

Summarizing, under *in situ* oxygen permeation conditions for EVD-grown zirconia/yttria layers with thicknesses between 0·5 and 5 μm, the oxygen permeation flux is influenced by a number of parameters: the layer thickness, the layer morphology, the presence of water and the oxygen partial pressure gradient over the layer. It is very hard to establish the rate-limiting step for oxygen permeation. It is suggested that the rate-limiting step is the electrochemical diffusion through the layer, in combination with the reduction reaction at the oxygen/solid electrolyte layer. It is certain that the diffusion of oxygen through the substrate pores is not rate-limiting under *in situ* oxygen permeation conditions.

Conclusions

It is possible to deposit thin (0·5–5 μm), dense zirconia/yttria layers on porous ceramic substrates. By performing depositions at relatively low temperatures (700–800°C) and low pressures (2–5 mbar) it is possible to grow thinner layers than at 1000°C.

Water vapour enhances the surface reaction rate at the metal oxide/oxygen source reactant interface. In the absence of water in the oxygen source reactant, another step (for example a surface exchange reaction) may be rate-limiting for EVD layer growth. A layer growth rate of ~ 1·6 μm h^{-1} is observed for zirconia/yttria deposited at 1000°C and 2 mbar on an α-alumina substrate in the presence of water. Diffusion of the oxygen source reactant in the presence of water through the substrate pores is rate-limiting for EVD zirconia/yttria layer growth at 1000°C in the Knudsen regime (low pressure, small pores).

Results of kinetic experiments compared with theoretical analysis show that between 900 and 1000°C (in the presence of water as oxygen source reactant) a transition occurs from pore diffusion to bulk electrochemical diffusion as the rate-limiting step. Below 900°C, the bulk electrochemical

diffusion of oxygen through the EVD layer is the rate-limiting step. At 800°C, the layer growth rate is very slow, below several tenths of a μm per hour.

SEM and XRD analyses show that zirconia/yttria is mainly deposited in the cubic yttria-stabilized zirconia phase; relatively small fractions of monoclinic and tetragonal zirconia/yttria are obtained. The layers grow in a typical columnar-like way at high temperatures and are polycrystalline. Crystallites become larger when the zirconia/yttria layer is thicker; for a 0·5, 2–3 or 12 μm thick layer, crystallite sizes are around 0·1, 0·5 or 2–3μm, respectively. Determination of crystallite sizes by means of X-ray line broadening does not give good results due to influences of strain and inhomogeneities.

In situ oxygen permeation experiments were performed on the deposited zirconia/yttria layers in the CVD/EVD reactor. Typical conditions are: temperature 700–1000°C, pressure 150 mbar, oxygen and oxygen/water at the high oxygen partial pressure side and argon/metal chloride vapours at the low oxygen partial pressure side. Under these conditions, for EVD-grown zirconia/yttria layers with thicknesses between 0·5 and 5 μm, the oxygen permeation flux is influenced by factors such as the layer thickness, the layer morphology, the presence of water and the oxygen partial pressure gradient over the layer. Typical permeation values are around 10^{-8} mol cm^{-2} s^{-1}.

Acknowledgements

This investigation was supported by the Netherlands Foundation for Chemical Research (SON, project number 700-332-004) with financial aid from the Netherlands Organisation for Scientific Research (NWO).

Mr J. Boeijsma, Ing. C.M. Ophuis and Dr B. A. van Hassel are acknowledged for performing the XRD experiments, a number of CVD/EVD experiments and some of the oxygen permeation experiments, respectively. Dr G. W. Koebrugge is acknowledged for his assistance with AFM analysis; Prof. Dr Ir H. Verweij and Dr G. Z. Cao for many interesting discussions. Ing. M. M. A. Smithers and Dr Ir T. Kachlicki (Centre of Materials Research) are acknowledged for performing HR-SEM and TEM analyses, respectively.

References

1. Isenberg, A. O., Growth of refractory oxides layers by electrochemical vapor deposition (EVD) at elevated temperatures. In *Proc. Symp. Electrode Materials, Processes for Energy Conversion and Storage*, ed. J. D. E. McIntyre, S. Srinivasan & F. G. Will. The Electrochem. Soc. Inc., Princeton, NJ, 1977, vol. 77, No. 6, 572–83.
2. Dietrich, G. & Schäfer, W., Advances in the development of thin-film cells for high temperature electrolysis. *Int. J. Hydrogen Energy*, **9** (1984) 747–52.
3. Carolan, M. F. & Michaels, J. N., Chemical vapour deposition of yttria-stabilized zirconia on porous substrates. *Solid State Ionics*, **25** (1987) 207–16.
4. de Haart, L. G. J., Lin, Y. S., de Vries, K. J. & Burggraaf, A. J., Modified CVD of nanoscale structures in and EVD of thin layers on porous ceramic membranes. *J. Eur. Ceram. Soc.*, **8**[1] (1991) 59–70.
5. Cao, G. Z., Brinkman, H. W., Meijerink, J., de Vries, K. J. & Burggraaf, A. J., Pore narrowing and formation of ultrathin yttria-stabilized zirconia layers in ceramic membranes by chemical vapour deposition/electrochemical vapour deposition. *J. Am. Ceram. Soc.*, **76**[9] (1993) 2201–8.
6. Brinkman, H. W., Cao, G. Z., Meijerink, J., de Vries, K. J. & Burggraaf, A. J., Modelling and analysis of CVD processes for ceramic membrane preparation. *Solid State Ionics*, **63–65** (1993) 37–44.
7. Pal, U. B. & Singhal, S. C., Electrochemical vapor deposition of yttria-stabilized zirconia films. *J. Electrochem. Soc.*, **137**[9] (1990) 2937–41.
8. Carolan, M. F. & Michaels, J. N., Growth rates and mechanism of electrochemical vapor deposited yttria-stabilized zirconia films. *Solid State Ionics*, **37** (1990) 189–95.
9. Lin, Y. S., de Vries, K. J., Brinkman, H. W. & Burggraaf, A. J., Oxygen semipermeable solid oxide membrane composites prepared by electrochemical vapor deposition. *J. Membrane Sci.*, **66** (1992) 211–26.
10. Lin, Y. S., de Haart, L. G. J., de Vries, K. J. & Burggraaf, A. J. A kinetic study of the electrochemical vapor deposition of solid oxide electrolyte films on porous substrates. *J. Electrochem. Soc.*, **137**[12] (1990) 3960–6.
11. de Haart, L. G. J., Lin, Y. S., de Vries, K. J. & Burggraaf, A. J., On the kinetic study of electrochemical vapour deposition. *Solid State Ionics*, **47** (1991) 331–6.
12. Schoonman, J., Dekker, J. P., Broers, J. W. & Kiwiet, N. J., Electrochemical vapor deposition of stabilized zirconia and interconnection materials for solid oxide fuel cells. *Solid State Ionics*, **46** (1991) 299–308.
13. Kiwiet, N. J. & Schoonman, J., Electrochemical vapor deposition: theory and experiment. In *Proc. 25th Int. Soc. Energy Conv. Eng. Conf.*, ed. P. A. Nelson, W. W. Schertz & R. H. Till. AIChE, New York, 1990, Vol. 3, pp. 240–5.
14. Dekker, J. P., Kiwiet, N. J. & Schoonman, J., Electrochemical vapor deposition of SOFC components. In *Proc. 1st Int. Symp. on SOFC, High Temp. Mater. Div. Proc. Vol. 89–11*, ed. S. C. Singhal. The Electrochemical Society Inc. Pennington, NJ, 1989, pp. 57–66.
15. Dekker, J. P., van Dieten, V. E. J. & Schoonman, J., The growth of electrochemical vapor deposited YSZ films. *Solid State Ionics*, **51** (1992) 143–5.
16. Dekker, J. P., van Dieten, V. E. J. & Schoonman, J., The growth of electrochemical vapor deposited YSZ films. In *Science and Technology of Zirconia V*, ed. S. P. S. Badwal, M. J. Bannister & R. H. J. Hannink. Technomic Publishing Company Inc., Lancaster, PA, 1993, pp. 786–802.
17. Sasaki, H., Yakawa, C., Otoshi, S., Suzuki, M. & Ippommatsu, M., Reaction mechanism of electrochemical-vapor deposition of yttria-stabilized zirconia film. *J. Appl. Phys.*, **74**[7] (1993) 4608–13.
18. Han, J. & Lin, Y. S., An improved analysis on kinetics of electrochemical vapor deposition. *Solid State Ionics*, **73** (1994) 255–63.
19. Park, J.-H. & Blumenthal, R. N., Electronic transport in 8 mole percent Y_2O_3–ZrO_2. *J. Electrochem. Soc.*, **136**[10] (1989) 2867–76.

20. Lin, Y. S. & Burggraaf, A. J., Preparation and characterization of high-temperature thermally stable alumina composite membranes. *J. Am. Ceram. Soc.*, **74**[1] (1991) 219–24.
21. Cao, G. Z., Meijerink, J., Brinkman, H. W. & Burggraaf, A. J., Permporometry study on the size distribution of active pores in porous ceramic membranes. *J. Membrane Sci.*, **83** (1993) 221–35.
22. Brinkman, H. W., Cao, G. Z., Meijerink, J., de Vries, K. J. & Burggraaf, A. J., Kinetics of the EVD process for growing thin zirconia/yttria films on porous alumina substrates. *J. Phys. IV Colloque C3*, **3** (1993) 59–66.
23. Brinkman, H. W. & Burggraaf, A. J., Ceramic membranes by electrochemical vapor deposition of zirconia/yttria/terbia layers on porous substrates. *J. Electrochem. Soc.*, **42**[11] (1995) 3851–8.
24. Brinkman, H. W., Cao, G. Z., Meijerink, J., de Vries, K. J. & Burggraaf, A. J., Morphology of very thin layers made by electrochemical vapour deposition at low temperatures. In *Science and Technology of Zirconia V*, ed. S. P. S. Badwal, M. J. Bannister & R. H. J. Hannink. Technomic Publishing Company, Inc., Lancaster, PA, 1993, pp. 811–8.
25. Wen, C. J. & Mason, D. M., Electrocatalysis on solid oxide electrolytes. *J. Appl. Electrochem.*, **8** (1978) 81–5.
26. Oberländer, B., Kofstad, P. & Kvernes, I., On oxygen diffusion in tetragonal zirconia. *Mat.-wiss. u. Werkstofftech.*, **19** (1988) 190–3.
27. Chen, C. S., Boutz, M. M. R., Boukamp, B. A., Winnubst, A. J. A., de Vries, K. J. & Burggraaf, A. J., The electrical characterization of grain boundaries in ultrafine grained Y-TZP. *Mater. Sci. Eng.*, **A168** (1993) 231–4.
28. Toraya, H., Yoshimura, M. & Somiya, S., Calibration curve for quantitative analysis of the monoclinic–tetragonal ZrO_2 system by X-ray diffraction. *J. Am. Ceram. Soc.*, **67** (1984) C119–21.
29. Toraya, H., Yoshimura, M. & Somiya, S., Quantitative analysis of monoclinic-stabilized cubic ZrO_2 systems by X-ray diffraction. *J. Am. Ceram. Soc.*, **67** (1984) C183–4.
30. Brinkman, H. W., Ceramic membranes by (electro)chemical vapour deposition. Investigations on thin film and bulk mixed conducting materials. PhD thesis, University of Twente, Enschede, The Netherlands, 1994, pp. 96–101.
31. Brinkman, H. W., de Haart, L. G. J., Lin, Y. S., de Vries, K. J. & Burggraaf, A. J., Electrochemical vapour deposited zirconia/yttria layers on porous substrates. In *Proc. ECerS '91*, 11–14 Sept. 1991, Augsburg, FRG. *Euro. Ceram. II, Vol. 3*, ed. G. Ziegler & H. Hausner, 1993, pp. 2375–8.
32. Klug, K. P. & Alexander, L. E., *X-ray diffraction procedures*. Wiley & Sons, New York, 1974, pp. 687–92.
33. Bouwmeester, H. J. M., Kruidhof, H. & Burggraaf, A. J., Importance of the surface exchange kinetics as rate-limiting step in oxygen permeation through mixed-conducting oxides. *Solid State Ionics*, **72** (1994) 185–94.
34. Dou, S., Masson, C. R. & Pacey, P. D., Mechanism of oxygen permeation through lime-stabilized zirconia. *J. Electrochem. Soc.*, **132**[8] (1985) 1843–9.
35. Bouwmeester, H. J. M., Kruidhof, H., Burggraaf, A. J. & Gellings, P. J., Oxygen semipermeability of erbia-stabilized bismuth oxide. *Solid State Ionics*, **53–56** (1992) 460–8.

Notation

D	Crystallite size (nm)
D_{H_2O}	Knudsen diffusion coefficient of water vapour ($m^2\ s^{-1}$)
D_{O_2}	Knudsen diffusion coefficient of molecular oxygen ($m^2\ s^{-1}$)
J_{O_2}	Permeation flux of molecular oxygen (mol $cm^{-2}\ s^{-1}$)
K	Scherrer constant
I	EVD layer thickness (μm)
L	Substrate thickness (mm)
n_i	Number of oxygen atoms per water ($n_i = 1$) or oxygen ($n_i = 2$) molecule
$P_{i,OSR}$	Pressure of compound i in the Oxygen Source Reactant mixture (Pa)
P_{H_2O}	Water vapour (partial) pressure (Pa)
P_{O_2}	Oxygen (partial) pressure (Pa)
P_{wc}	Pressure in water chamber of CVD/EVD reactor (Pa)
R	Gas constant (8·3143 J $mol^{-1}\ K^{-1}$)
S	Surface area of EVD-grown sample
T	Absolute temperature (K)
$T_{av,wc}$	Average temperature in water chamber of CVD/EVD reactor (°C)
t	Time (min, s)
V_{mol}	Molar volume (of YSZ) ($m^3\ mol^{-1}$)
V_{wc}	Volume of water chamber in CVD/EVD reactor (cm^3)
V_m	Volume fraction of monoclinic zirconia/yttria
β	Half width line broadening ($2\theta°$)
θ	Diffraction angle (°)
λ	Wavelength of X-rays (nm)

Journal of the European Ceramic Society 16 (1996) 601–612

0955-2219(95)00181-5
0955-2219/96/$15.00

Enhanced Mechanical Properties by Grain Boundary Strengthening in Ultra-Fine-Grained TZP Ceramics

Y. J. He, A. J. A. Winnubst, C. D. Sagel-Ransijn, A. J. Burggraaf & H. Verweij

University of Twente, Faculty of Chemical Technology, Laboratory for Inorganic Materials Science, PO Box 217, 7500 AE, Enschede, The Netherlands

(Received 10 March 1995; revised version received 18 July 1995; accepted 12 October 1995)

Abstract

The mechanical properties of ceramics with the compositions of 5 mol% $YO_{1.5}$–TZP (ZY5) and 4 mol% $YO_{1.5}$–4 mol% CeO_2–TZP (ZY4Ce4) were investigated. Nanocrystalline powders of both TZPs were synthesized by a gel precipitation technique. Powder compacts were made by cold isostatic pressing, and were then pressureless sintered or sinter-forged to dense TZP ceramics (density: 96–99%) with grain sizes of 180 nm. Shear deformation during sinter-forging was found to favourably affect densification and microstructure. The mechanical properties of both types of ultra-fine-grained TZP ceramics were examined up to 760°C. The results point towards an improved grain boundary structure and the elimination of residual flaws obtained by the sinter-forging technique. The sinter-forged samples exhibited a higher Vicker hardness compared to that of pressureless sintered specimens. After sinter-forging the fracture energy value was found to be 325 J/m^2 and the fracture toughness to be 10 MPa m$^{1/2}$. A Weibull modulus of 21 was obtained for the sinter-forged samples which was significantly higher than the value of 8 for the pressureless sintered specimens. The enhancement of reliability is obviously connected to a decrease in the average size and concentration of flaws caused by inhomogeneous powder particle packing due to the presence of irregular agglomerates.

1 Introduction

Typical requirements for structural ceramics are high strength, ductility, fracture resistance, chemical inertness and a stable microstructure. For a specific ceramic material, better properties can generally be obtained by improving microstructural characteristics such as grain size, homogeneity and distribution of porosity, and process flaws.

For fine-grained ceramics, grain boundaries have a considerable effect on the properties and performance of the materials.[1,2] An example of this is the role of grain boundary morphology on fracture toughness. Watanabe *et al.*[1,3] introduced the concept of grain boundary character distribution (GBCD) in alloy polycrystals. This distribution gives the frequency of specific grain boundary configurations and is an important tool in controlling intergranular fracture by grain boundary design. They pointed out that low-energy boundaries are resistant to fracture while high-energy (incoherent) boundaries are preferential sites for crack nucleation and propagation. The toughness of polycrystals increases with the relative fraction of low energy boundaries. A similar approach to grain boundary design for polycrystalline ceramics is also indicated by Krell *et al.*[4] They suggested that the concept of grain boundary strength can be specified in three ways:

(1) As the critical stress intensity k_{IC}^{gb} required to propagate a crack along a grain boundary.
(2) As the specific fracture energy γ^{gb}.
(3) As the local, microscopic (tensile) fracture stress σ_f^{gb}.

The enhancement of the grain boundary strength for structural ceramics in the case of fracture controlled mainly by an intergranular mode will result in an improvement of mechanical properties, especially fracture toughness. High macroscopic strength is achieved, for instance, by reducing the concentration and size of flaws in the bulk[5] or by limiting the possibility of, normally occurring, subcritical growth of extrinsic flaws.[6]

Recently the possibilities of using ultra-fine-grained ceramics or even nanocrystalline materials[7,8] were explored. As suggested by Burggraaf *et al.*[7,8] the characteristic features of nano-structured materials are:

- A significant fraction of atoms is situated in the grain boundary region and/or associated with interfacial effects.

- An interaction exists between the constituent domains.

It is expected that ultra-fine-grained ceramics may possess special properties, related to the presence of a large grain boundary surface area. An example of this is surprisingly high superplastic deformation rates, obviously connected with short intergrain diffusion distances, observed by Boutz *et al.*[9] Very interesting high temperature mechanical properties are reported by Theunissen *et al.*[10] They found that Y–TZP ceramics with a smaller grain size exhibit a higher fracture toughness and bending strength at high temperature than those with a coarser grain size. Practical applications of nano-structured zirconia were limited up to now because it is difficult to produce them reproducibly with a high density (≥95%). This problem can be solved by the application of sinter-forging which is useful for the elimination of flaws and grain boundary reinforcement.[2,11,12] Hence, sinter-forging can be used to shift the full densification temperature for ceramics to a lower temperature,[13,14] so that grain growth can be limited further. This makes it possible to prepare dense ceramics with grain sizes in the nano-scale region. For sinter-forged tetragonal zirconia materials with grain sizes of 100–200 nm, densities > 97% are reported by Boutz *et al.*[15] It has also been reported that ionic conduction properties are significantly influenced by sinter-forging due to the change of grain boundary properties.[2] To our knowledge, effects of sinter-forging on mechanical strength and Weibull modulus (reliability) as well as on high temperature mechanical properties have not yet been reported before for tetragonal zirconia polycrystal (TZP) with ultra-fine structure.

The major objective of this study was to investigate the effects of sinter-forging and the influence of grain boundary properties and process flaws on fracture toughness, bending strength and Weibull modulus at temperatures up to 760°C. The sinter-forging technique was used to strengthen grain boundaries and consequently increase the mechanical properties. The effect of flaws on reliability of ceramics is discussed. Transmission electron microscopy (TEM), scanning electron microscopy (SEM), X-ray photoelectron spectroscopy (XPS) and X-ray diffraction (XRD) were used to analyze the fracture surface, flaw size and grain boundary properties.

2 Experimental Procedure

2.1 Powder preparation

Nanocrystalline tetragonal zirconia powders with high sinter reactivity were synthesized by a gel precipitation technique using metal chloride precursors. The materials studied were ZY5 (5 mol% $YO_{1.5}$–TZP) and ZY4Ce4 (4 mol% $YO_{1.5}$–4 mol% CeO_2–TZP). The precursor solution was dropped slowly into an excess of a 25 wt% ammonia solution with pH >11. The formed gel was washed subsequently with a water/ammonia mixture solution to remove Cl^-. Washing with ethanol was then used to remove the free water. A more detailed process has been given by Groot Zevert *et al.*[16] The dried gel was calcined subsequently at 500°C for 2 h followed by milling procedure using ZrO_2 balls. Compacts were made by cold isostatically pressing at 50 MPa and crushed again in an alumina mortar to obtain better powder flowability. This powder was uniaxially pressed at 80 MPa in a die to form a rectangular shape which was compacted further by cold isostatical pressing (CIP) at 400 MPa. The compacts were pressureless sintered in air at 1150°C for 10 h with heating and cooling rates of 2°C/min.

2.2 Sinter-forging

The samples for sinter-forging experiments were pre-sintered by a heating rate of 2°C/min to 1000°C for 15 min to improve compact strength. The density changed from 46% for the initial green body after CIP to 64%. These samples were subsequently machined to 26 × 8 × 6 mm^3 with plane-parallel 26 × 6 mm^2 sides. Sinter-forging experiments were performed in air at 1150°C under a constant load corresponding to an initial stress of 90 MPa. The initial stress is defined with respect to dimensions just before loading. The sinter-forging heating schedule was: heating from ambient temperature to 950°C at 600°C/h and then to 1150°C at 300°C/h. The load was imposed on the 26 × 6 mm^2 plane of the samples and raised linearly at 1150°C from zero to its final value in 5 min and then kept constant for 25 min. Details of the sinter-forging setup are given in Refs. 13, 14 and 17.

2.3 Characteristics

The densities of the green and sintered compacts were measured by the Archimedes technique in Hg. The bending strength was measured by the 4-point bending technique with an inner and outer span of 10 and 20 mm, respectively, using a crosshead speed of 0·7 mm/min. The specimens for bending strength measurement were cut into 26 × 5 × 2 mm^3 bars and polished on the 26 × 5 mm^2 side opposite to the loading piston (hence subjected to tensile stress). After machining and polishing, all specimens were annealed for 10 min at 1000°C with heating and cooling at 2·5°C/min. The fracture toughness, K_{IC}, was measured by the 3-point single-edge notched beam (SENB) method

with a span of 12 mm, a crosshead speed of 0·3 mm/min and 15 × 3 × 1 mm^3 specimens. A notch of 450 μm depth and 50 μm width was cut without pre-cracking at the notch tip. After machining, the samples were annealed at 1000°C in the same way as mentioned before.

The phase composition was measured on polished and annealed surfaces as well as on fractured surfaces by means of X-ray diffraction using CuKα radiation (Philips PW1710 X-ray diffractometer with a step scan size of 0·015° (2θ). The method proposed by Toraya[18] was used to determine the volume fraction of monoclinic zirconia. The microstructures of polished surfaces and fractured surfaces were analyzed by SEM (JSM-35CT, JEOL). The grain sizes of the sintered ceramics were measured by the linear intercept method from SEM photographs.[19] The grain boundary structure of sinter-forged materials was analyzed by transmission electron microscopy (TEM).

2.4 Weibull modulus

Weibull statistics were used in describing the strength distribution in ceramics. The statistical strength values obtained from testing of ceramics were analyzed using the cumulative probability parameter, $P(\sigma)$. This is the probability of failure at a stress $\leq\sigma$ and is given in Ref. 20:

$$\frac{1}{1 - P(\sigma)} = \exp\left(\frac{\sigma}{\sigma_0}\right)^m \tag{1}$$

where m is the Weibull modulus, which is a slope obtained from a plot of $\ln\{\ln(1/(1-P(\sigma))\}$ against $\ln(\sigma)$ curves. σ_0 is a scale parameter with the same dimension as σ.

The estimator of the cumulative probability parameter was calculated by:

$$P_j = \frac{j - 0{\cdot}5}{n} \tag{2}$$

where the jth result in the set of n samples is assigned a cumulative probability of failure, P_j. This was done by ordering the results of the stresses to rupture from the lowest to the highest values. This probability parameter $P(\sigma)$ is generally fitted to the modulus of rupture (MOR) test data, which were the four-point bending strength, σ, of a set of bars of the test materials.

2.5 Micro-hardness

The hardness of a solid is generally defined as a resistance to local deformation.[21] In this study, the classical Vickers hardness (H_V) was measured by a microhardness equipment (Shimadzu DUH-200, Japan). During the measurement, typical loading–unloading curves were recorded using a maximum load of 2 N with a loading speed of 14·4 × 10^{-2} N/s and a hold time of 5 s at the maximum load. Using this equipment, the Vickers hardness (H_V) was determined by the average values of both diagonals with a Vickers indenter apex of 136° and calculated with

$$H_V = 1{\cdot}8544\,\frac{F}{d^2} \tag{3}$$

where F is the load (N), and d is the mean value of both diagonals.

The measured Vickers hardness values (H_V) in Table 1 were nearly the same as the results (HV10) obtained by a macroindenter (Isser Stedt Garant 250RD) at a load of 100 N (10 kgf).

3 Experimental Results

3.1 Powder characteristics and densification

No significant differences in powder properties were found for the ZY5 and ZY4Ce4 systems. A crystallite size of 8 nm for both ZY5 and ZY4Ce4 powders was calculated from X-ray line broadening data (XRLB) by using the Scherrer equation[22] and measured from TEM micrographs.[23] For the same powder a large average agglomerate size of 15 μm is obtained by a laser diffraction particle size distribution analyzer (Horriba LA-500). Weak agglomerates can be fragmented gradually during isostatic compaction at a certain minimum pressure, P_y, which is defined as the agglomerate strength.[10] For both powders, P_y was found to be 70–90 MPa, but certain hard agglomerates still remained at this pressure. Relative densities of ZY4Ce4 during pressureless sintering and sinter-forging (at 90 MPa) at 1150°C are shown as a function of time in Fig. 1. The densification kinetics are significantly enhanced by creep deformation under a uniaxial pressure of 90 MPa (sinter-forging) as compared to pressureless sintering. After sinter-forging for 25 min, a creep strain of 0·5 and a density of 98–99% were reached. After pressureless sintering, however, a density of only 93–94% was obtained. To achieve a density of 96–97% by pressureless sintering at 1150°C, 600 min dwell time was required as seen in Table 2. Prolonged sintering did not result in any further density increase. Similar results were obtained for ZY5.

Table 1. The microhardness of TZP materials

Sample	*SF/PS*	H_V*(GPa)*
ZY5	SF	14·2 ± 0·5
ZY5	PS	13·3 ± 0·4
ZY4Ce4	SF	13·6 ± 0·3
ZY4Ce4	PS	12·5 ± 0·6

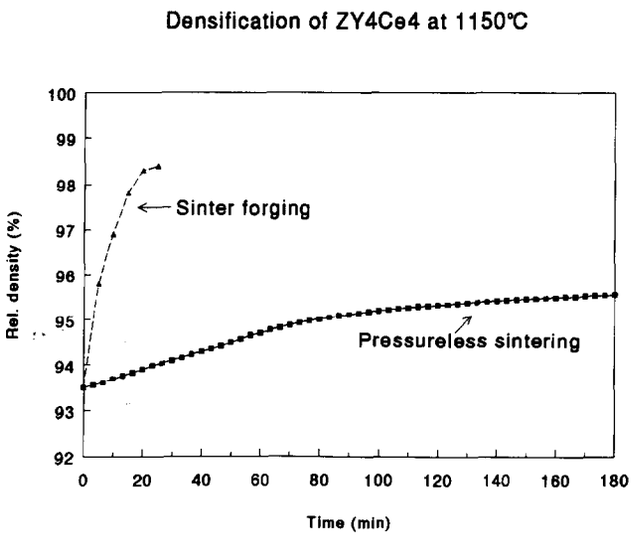

Fig. 1. Densification behaviour of ZY4Ce4 during sinter-forging and pressureless sintering. The samples were performed by sinter-forging at 90 MPa initial pressure.

Micrographs of ZY5 samples sinter-forged and pressureless sintered at 1150°C are shown in Fig. 2. Grain sizes of 0·18 and 0·19 μm were obtained for ZY5 and ZY4Ce4, respectively (Table 2). XRD analysis revealed that in all cases only a tetragonal phase was present. The residual pore sizes are less than the grain sizes in both sinter-forged and pressureless sintered samples. The microstructure obtained, however, showed large differences. At low magnification, some pore-like or crack-like

Table 2. Properties of sinter-forged (SF) TZPs (25 min) and pressureless sintered (PS) TZPs (600 min) at 1150°C

Sample	*SF/PS*	*Density (%)*	*Grain size (μm)*
ZY5	SF	98·5	0·18
ZY5	PS	96–97	0·18
ZY4Ce4	SF	98·5	0·19
ZY4Ce4	PS	97	0·19

flaws (the largest about 60 μm) were present in the pressureless sintered samples as seen in Fig. 3. Such large flaws were also found by Boutz *et al.*[13] in Y–TZP pressureless sintered at the same conditions. Such flaws, however, were not found in sinter-forged TZP, in agreement with the observations for sinter-forged ZTA (zirconia-toughened alumina) ceramics.[11]

3.2 Effects of grain boundary structure on hardness

Vickers hardness values are given in Table 1. These results show that the Vickers hardness for sinter-forged ZY5 and ZY4Ce4 samples is higher than that of the pressureless sintered samples. In all cases ZY5 has a slightly higher Vicker hardness than ZY4Ce4. The Vickers hardness can be considered as the resistance to plastic deformation. Thus a higher resistance to plastic deformation is obtained by sinter-forging compared to pressureless sintering.

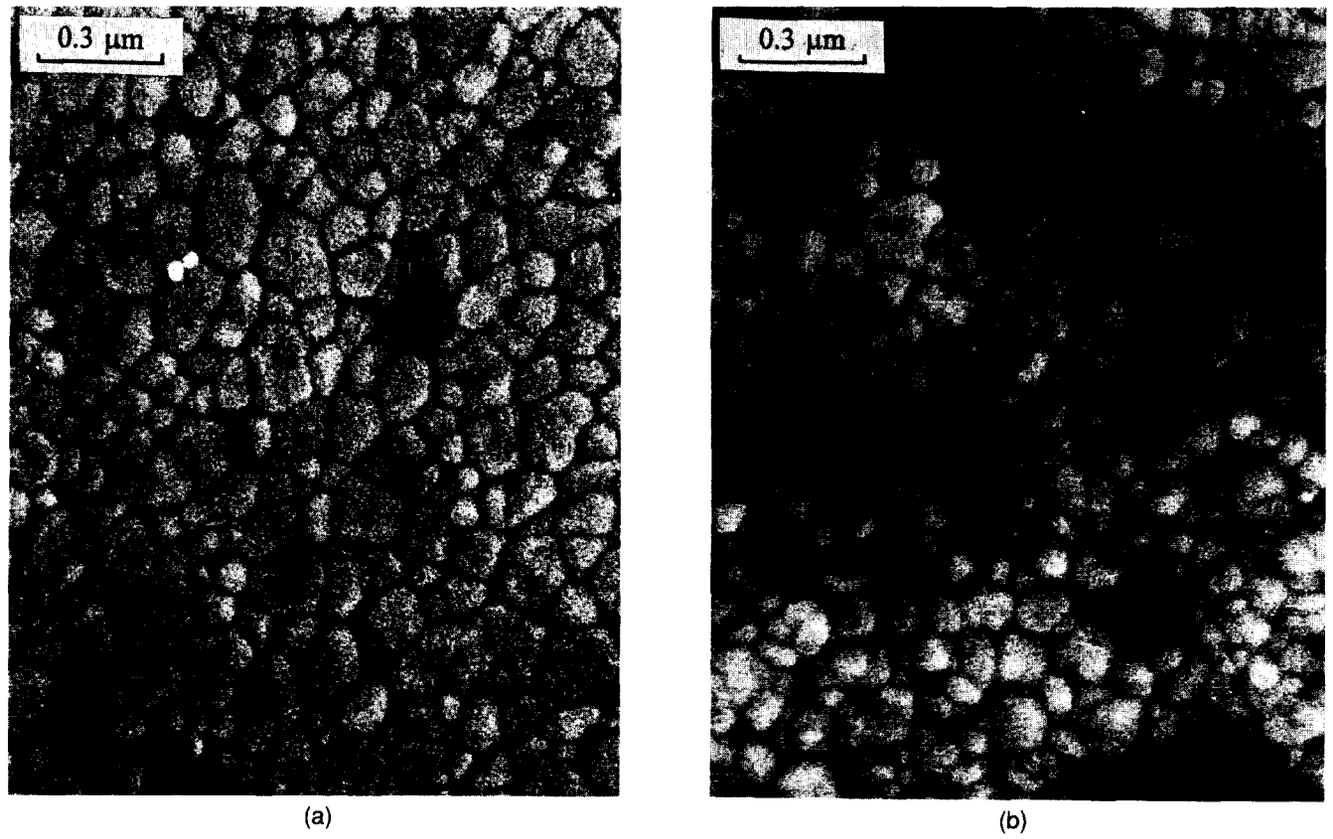

Fig. 2. Example of the microstructure of ZY5 samples after sintering at 1150°C: (a) for 25 min by sinter forging, and (b) for 600 min by pressureless sintering.

The hardness of a given material is related to microstructural parameters such as porosity, grain size, grain boundary properties and preexist dislocation structure as indicated by Krell.[24] In the present study the grain size is equal in all cases, thus grain size effects on hardnesses are eliminated. A possible difference in preexist dislocations between pressureless sintered and sinter-forged specimens is not expected as will be discussed now. Boutz *et al.*[9,13] point out that the plastic deformation of fine-grained Y–TZP takes place by interface reaction controlled grain boundary sliding. During this process the shape of the crystals does not change. That means an absence of dislocation creep. These arguments certainly hold for sinter-forging at low temperature. Bulk dislocation mobility is very low especially for the small crystals considered here. Hence, dislocations are unlikely to affect the hardness in the sinter-forged specimens. It is more likely that the differences in microhardness values between sinter-forged and pressureless sintered specimens can be ascribed to the porosity of the bulk and the property of the grain boundaries. It was attributed to the fact that the microhardness measurements were performed on parts of the microstructure without flaws. So the effect of porosity caused partly by local flaws in the pressureless sintered samples can be ignored for these microhardness measurements. Grain boundary properties such as bonding strength and micropores (or microdefects) at grain boundaries are thus the major factors that affect the hardness values. For a given ZY5 or ZY4Ce4 material, the difference in the Vickers hardness between sinter-forged and pressureless sintered samples is related to the bonding strength and micropores of the grain boundaries as will be discussed later.

Fig. 3. A typical cracklike defect is presented on the surface of pressureless sintered ZY5 samples.

3.3 Influence of strengthened grain boundaries on fracture toughness

The fracture toughness results are given as a function of temperature in Fig. 4. Sinter-forged samples show higher toughness values than pressureless sintered samples at all temperatures. X-ray diffraction results on polished surfaces and even on a ground surfaces do not show any monoclinic zirconia. This clearly indicates that no precompressive stresses at the notch tip due to machining-induced transformation can influence the mechanical properties. By XRD analyses, no monoclinic phase was detected at the fractured surface. This means that no irreversible phase transformation occurs during fracturing. As discussed by Boutz *et al.*,[13] for ultra-fine-grained TZP materials, the occurrence of reversible transformation toughening is a matter of debate, and crack deflection is commonly suggested as the toughening mechanism in this case. The toughening mechanism for all TZPs investigated in this work is expected to be the same for pressureless sintered and sinter-forged samples. So for sinter-forged samples an additional toughening mechanism should be present.

The observation of the fracture surfaces (Fig. 5) gives a clue to consider this difference between sinter-forging and pressureless sintering. All these surfaces show a considerable fraction of intergranular fracture. Hence the grain boundaries play an important role in the development of the fracture process. The fracture energy, γ_f necessary to create a unit area of new fracture surface, is directly related to K_{IC} at plane stress conditions by:

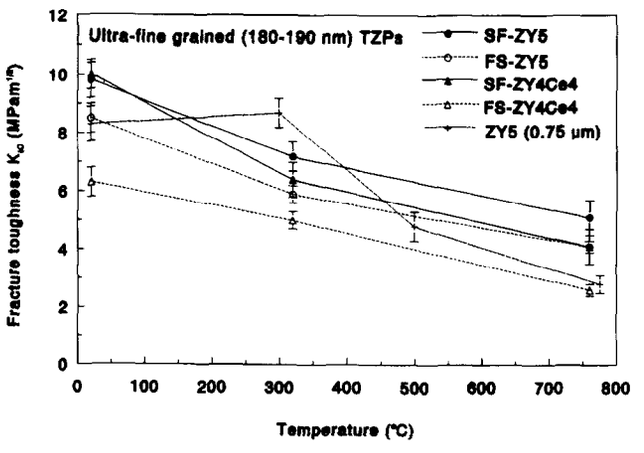

Fig. 4. Fracture toughness of ZY5 and ZY4Ce4 obtained by pressureless sintering and sinter-forging as a function of temperature.

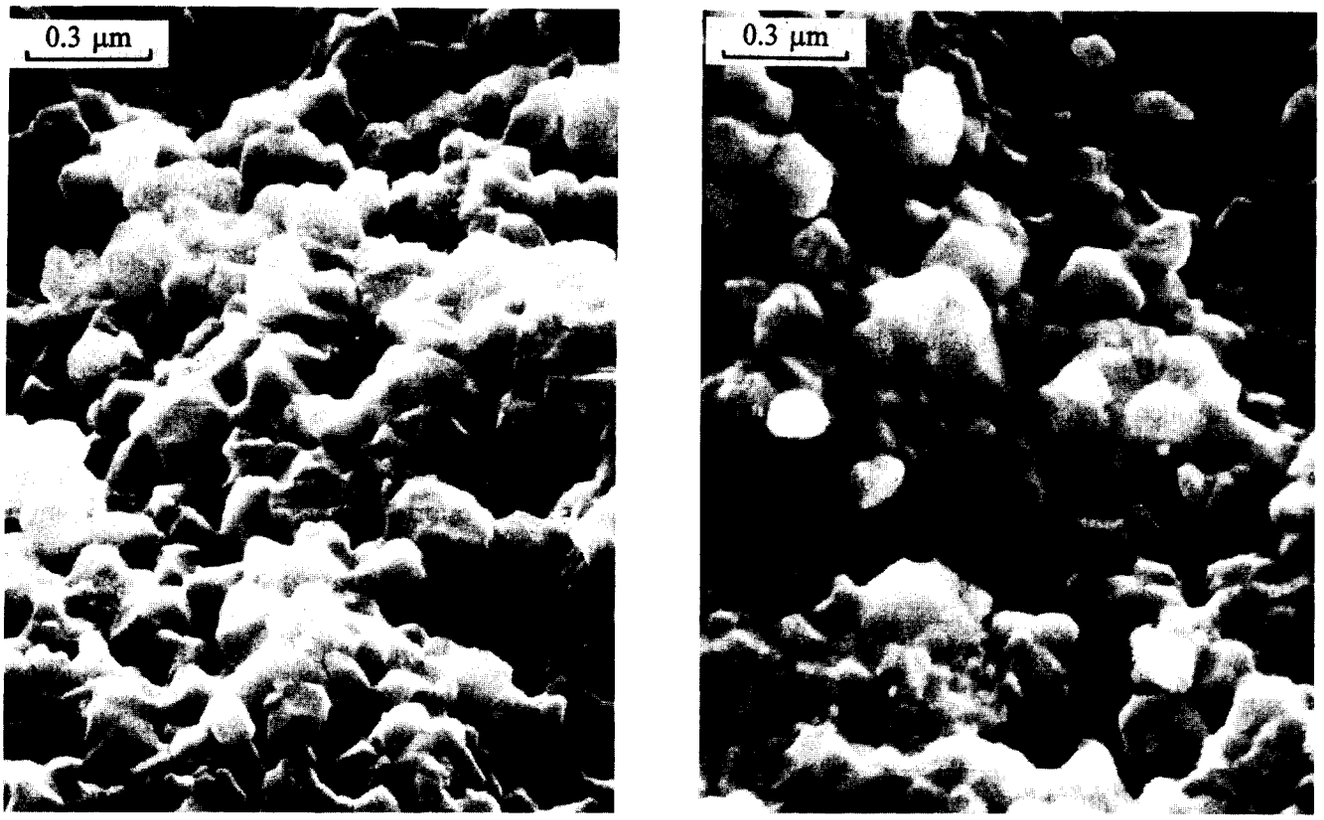

Fig. 5. Fracture surface of ZY5 sintered by (a) sinter-forging and (b) pressureless sintering, fractured at room temperature.

$$\gamma_f = \frac{K_{IC}^2}{2E} \quad (4)$$

where E is Young's modulus. An enhancement of γ_f can be caused by reduced porosity and strengthened grain boundaries. In order to compare the influence of the grain boundaries on γ_f in sinter-forged samples with that in pressureless sintered samples, it is necessary to eliminate the influence of porosity. Normally, the fracture energy, γ_f, as a function of the residual porosity (P) is given as:[25]

$$\gamma_f = \gamma_0 \exp(-bP) \quad (5)$$

where γ_0 is the fracture energy of a fully dense material and b is a numerical constant, found to be 3.4 by Boutz *et al.*[13] In Table 3, the calculated γ_0 values are given for 100% density for both sinter-forged and pressureless sintered samples, whereas the primary data are the measured K_{IC}. The γ_0 data (see Table 3) indicate that there is a significant increase in fracture energy after sinter-forging. This increase can be ascribed only to grain boundary strengthening. It is noted again that no reversible phase transformation toughening was observed in these materials.

3.4 Influence of flaws on reliability and flexural strength

In Fig. 6 the flexural strength is given for ZY5 as a function of temperature. The flexural strength gradually decreases with increasing temperature in both sinter-forged and pressureless sintered specimens because grain boundary bonding becomes weaker with increasing temperature. This variation of flexural strength as a function of temperature is the same as that obtained by Theunissen.[10]

Table 3. Fracture energies and toughness values of all investigated TZP materials

Sample	$T_{fract.}$ (°C)	*Fracture energy* $\gamma_O(J/m^2)$		K_{IC} $(MPa\ m^{1/2})$	
		SF	*FS*	*SF*	*FS*
ZY5	20	297	209	9·8 ± 0·6	8·5 ± 0·5
ZY5	320	160	101	7·2 ± 0·5	5·9 ± 0·3
ZY5	760	81	49	5·1 ± 0·6	4·1 ± 0·6
ZY4Ce4	20	325	126	10·0 ± 0·5	6·3 ± 0·5
ZY4Ce4	320	133	80	6·4 ± 0·7	5·0 ± 0·3
ZY4Ce4	760	55	21	4·1 ± 0·2	2·6 ± 0·2

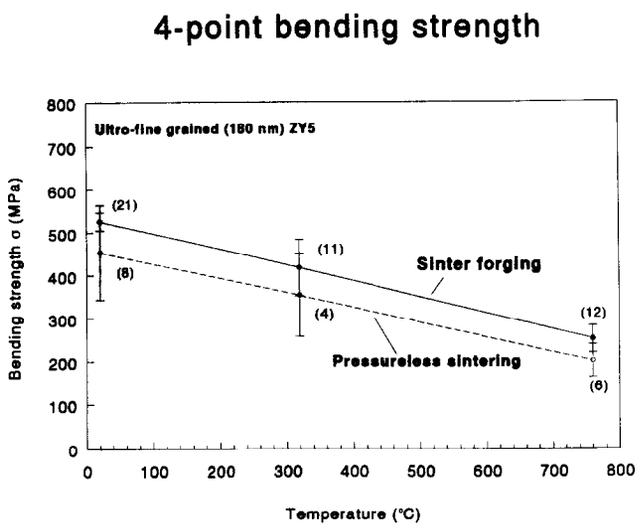

Fig. 6. Flexural strength (4-point bending strength) for sinter-forged or pressureless sintered ZY5 as function of temperature. The values in parenthesis represent the Weibull modulus.

A slightly higher flexural strength for sinter-forged samples as compared with pressureless sintered samples is observed for the full temperature region regarded (20–760°C). The Weibull modulus, m, as obtained from a Weibull plot of the flexural strength, is given in Table 4. Ten samples were used for both cases of sinter-forging and pressureless sintering. At room temperature, m-values of 21 and 8 are obtained after sinter forging and pressureless sintering, respectively. The results reveal a significant increase in the Weibull modulus for the sinter-forged samples. In all cases the Weibull modulus decreases with temperature (Table 4). It is concluded that the reliability of sinter-forged TZP ceramics is higher than pressureless sintered ones. It is well known that the bending strength of ceramics is highly sensitive to the flaws in bulks.

To investigate the effect of flaws on the reliability of materials, the fracture origins were examined by SEM. Typical morphologies of the fracture surface of pressureless sintered ZY5 samples are given in Fig. 7. As can be seen there are some Wallner lines around a certain part in the fractural surface (Fig. 7(a)). A large flaw is found at the beginning of these Wallner lines. At larger magnification it can be seen that this large flaw is a porous zone (Fig. 7(b)). Such porous zones are hardly found in sinter-forged samples (Fig. 7(c)). The same observation is made for a large area of the fracture surface of ZY4Ce4 samples as can be seen in Fig. 8. The fracture surface of the sinter-forged samples always shows a homogenous fracture surface (Fig. 8(a)), while in pressureless sintered samples it is easy to trace the stress concentration back to a specific flaw (Fig. 8(b)). As indicated in Section 3.1, crack-like or pore-like fracture origins, are present in the pressureless sintered samples and are caused by inhomogeneous sintering due to inhomogeneous packing of the green compact, while these flaws are suppressed or eliminated by a large shear deformation imposed on the material during sinter-forging. Microstructural observations indicate that the maximum dimension of the crack- or pore-like flaws is about 60 μm in pressureless sintered samples. In the sinter-forged samples, however, only residual pores are present, of which sizes are less than the grain size.

Another type of flaw is found in both sinter-forged and pressureless sintered samples (Fig. 9). Large dense, irregular-shaped particles are observed that are coherent with the local matrix. EDX analysis indicate a high Al content so that these particles are referred to as alumina inclusions. They are likely to originate from the alumina mortar used during sample preparation in the compaction-grinding-compaction processes and cannot be eliminated by the sinter-forging technique. These inclusion flaws also serve as failure initiation sites with dimensions of 25–120 μm. Nevertheless, the elimination of more severe flaws as shown in Figs 3 and 7 results in a higher Weibull modulus, enhancing the reliability of the materials after sinter-forging.

Table 4. Values of the Weibull modulus of both sinter-forged and pressureless sintered TZP ceramics

Sample	*Weibull modulus*		
	RT	*320°C*	*760°C*
FS–ZY5	8	4	6
SF-ZY5	21	11	12

RT: room temperature.
FS: free sintering.
SF: sinter-forging.

4 Discussion

A nearly theoretical density and a flaw-free microstructure are favourable in many applications of engineering ceramics. The sinterability of ceramics and the development of the final microstructure depend on the homogeneity of the pore structure in the green compacts. As suggested by Burggraaf *et al.*[7,8] a mild disorder in the green compact is preferred to obtain a homogeneous structure throughout the bulk and to minimize the size and concentration of defects. Long-range density fluctuations in the green compact may lead to the development of structural defects in materials during the sintering process. The density fluctuations are mainly caused by the presence of residual

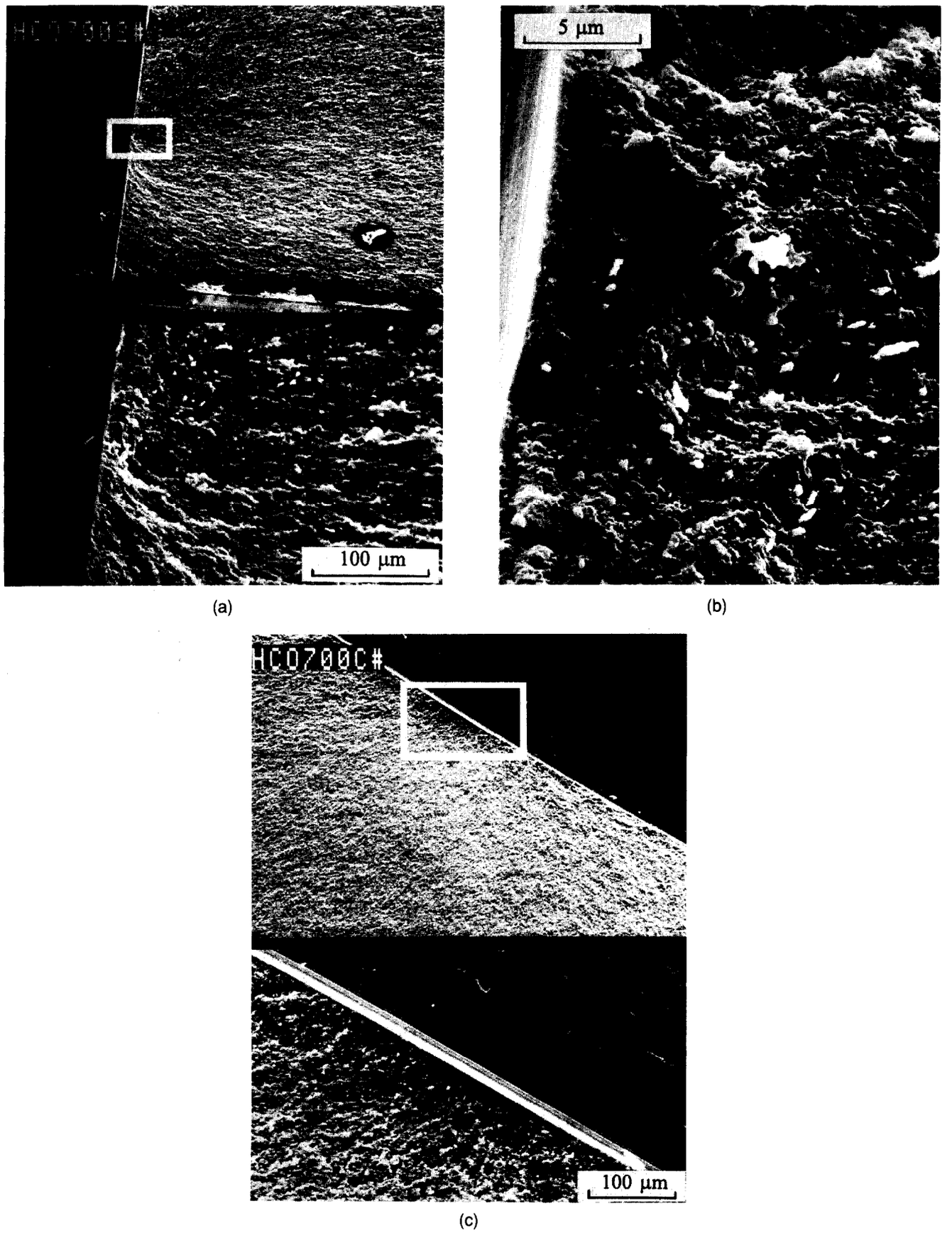

Fig. 7. Fracture surfaces of a ZY5 sample. (a) A flaw (indicated by the square) is surrounded by stress lines in pressureless sintered samples; (b) the large magnification of (a) shows a defect formed by a porous zone; (c)the sinter-forged samples.

agglomerates and/or other inhomogeneous particle packing structures.

Long-range density fluctuations result in local differences in the densification rate finally resulting in local residual tensile stresses.[26] The occurrence of such stresses during sintering may give rise to crack-like flaws or pore-like cavities.[11,27] The occurrence of porous zone flaws can be con-

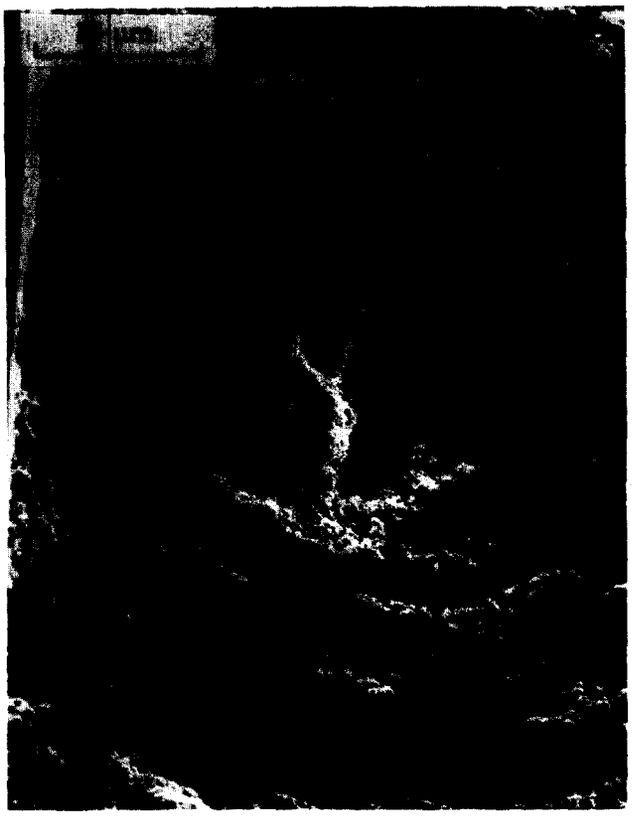

(a)

(b)

Fig. 8. Fracture surfaces of a ZY4Ce4 sample. (a) A large area of the fracture surface in pressureless sintered samples; (b) a large area of the fracture surface in sinter-forged samples.

(a)

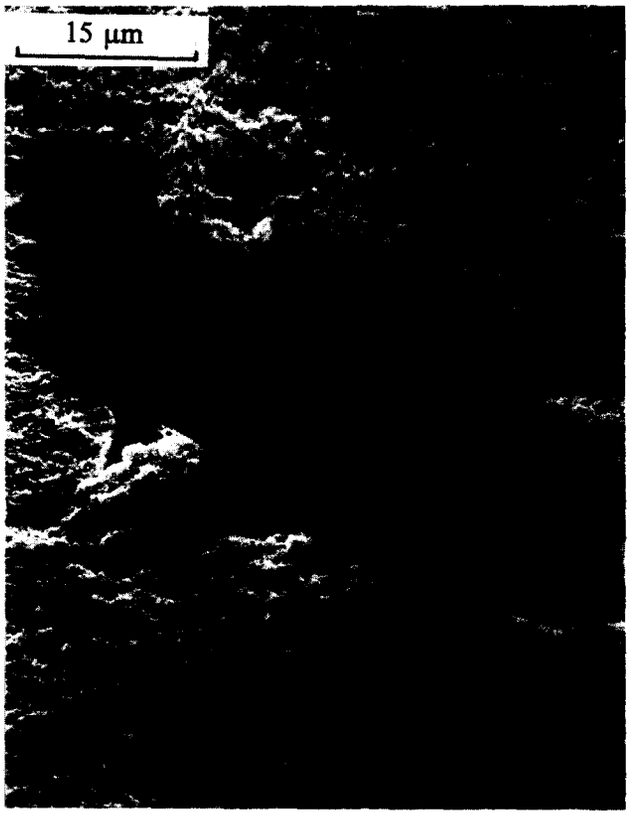

(b)

Fig. 9. An alumina inclusion acting as a fracture origin observed in the fracture surfaces of the sinter-forged or pressureless sintered samples.

sidered as being due to major inhomogeneities. The formation of processing flaws during densification makes it difficult to obtain dense materials with an ultra-fine or even nano-scale microstructure by pressureless sintering at lower temperatures such as 1150°C. During sinter-forging, a shear deformation is exerted on the compact so that large pores (or defects) can become oval-shaped

and subsequently fragmented into smaller ones as indicated in Ref. 12. The small pores can then disappear easily with increasing shear strain. The experimental results of Kellett and Lange[28] clearly show that shear deformation is responsible for the elimination of pores by a change of pore shape. The shear deformation process can even prevent the formation of crack- or pore-like flaws during the densification process. Previous experimental and theoretical results[12,28] indicate that a maximum compressive strain of 0·6 is needed to remove large pores of spherical shape. This value can be less for non-spherical pores and depends on the initial aspect ratio of the minimum and maximum diameter of the ellipsoidal pore. In our study, a final shear strain of 0·5 is obtained and leads to the elimination of process flaws. The effect of shear deformation on densification during the sinter process also leads to dense materials in shorter sintering times and even at lower sintering temperatures. The effectiveness in reducing flaws and increasing densification through sinter-forging was also observed for Al_2O_3[12] and ZTA.[11] Sung *et al.*[27] indicated that the fracture origin flaws follow an 'order of severity' in which crack-like flaws and larger pores are more severe fracture origins than inclusions. This may suggest that, even though the alumina inclusions that we found have much larger dimensions than the crack-like flaws, the latter, however, have a stronger influence on fracture strength. Hence the improvement in reliability by sinter-forging should be attributed to the elimination of more severe fracture origins such as pore-like and crack-like flaws.

The creep behaviour of ultra-fine TZP materials during sinter-forging, especially in the final sintering stage, has been interpreted as interface-reaction-controlled or grain-boundary-diffusion controlled grain boundary sliding.[13] Sinter-forging thus not only eliminates the flaws in the sintered bulk, but also changes the grain boundary morphology. In order to demonstrate the possible change of the grain boundary morphology by sinter-forging, the hard-sphere description of Gleiter *et al.*[29,30] for nanocrystalline materials is adopted. In this description the materials consist of two phases: a crystalline bulk component formed by regular lattice atoms (spheres) and an interfacial (grain boundary) component comprising all atoms which are situated in grain boundaries. A simple two-dimensional model of an ultra-fine-grained ceramic is given in Fig. 10. The interfacial atoms generally are situated in regular lattice positions, but in reality these atoms will relax from these sites (see the local area of A in Fig. 10(a)). The grain boundary phase may exhibit a different solid state structure with a more random atomic arrangement in which certain interatomic spacings are not filled completely due to incoherence between adjacent crystal lattices,[30] e.g. the local area B, C in Fig.10(a). This situation is especially probable when an irregular surface prevails frequently, as is the case for very small grains (nanocrystals). For ceramics obtained by pressureless sintering, large interatomic spacings might then be formed easily at the grain boundaries and result in a relatively thick grain boundary layer with micro-defects such as the local areas A, B and C in Fig. 10(a). If samples obtained by pressureless sintering contain an amorphous layer at grain boundaries due to impurity segregation (see Fig. 11(A)), the grain boundary component consists of the amorphous film and the interface atoms. In such cases, the presence of an amorphous layer may also make the grain boundaries weaker and lead to a further decrease in the grain boundary bonding strength. A grain boundary film with a thickness of about 1–2 nm is observed by TEM in pressureless sintered ZY5 materials[13] using the Fresnel fringe imaging technique.

During sinter-forging, shear deformation controlled by interface reaction or grain boundary diffusion[13] results in a rearrangement of the grain boundary component. Some impurities which are segregated to the grain boundaries are moved to grain boundary junctions or are partly eliminated by the crystallization during sinter-forging. The low energy traps are gradually filled and interatomic spacings are reduced. This process results in a thinner and more regular grain boundary layer (see Fig. 10(b)) as well as discontinuous amorphous films (see Figs 11(B) and (C)). The observation of the high resolution TEM image by Boutz *et al.*[13] shows the absence of amorphous phases or the existence of discontinuous amorphous films at grain boundaries of sinter-forged

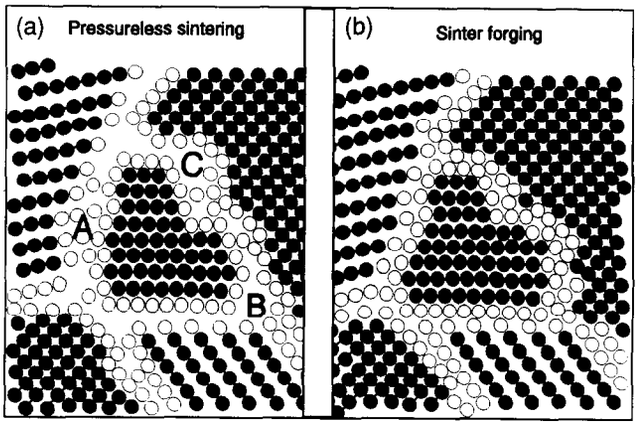

Fig. 10. Schematic representation of ultra-fine-grained ceramics distinguishing between the atoms associated with the individual crystals (solid circles) and those constituting the grain boundary network (open circles). The boundary atoms are shown in regular lattice positions, but in reality will relax to form different atomic arrangements (based on the model in Refs 29 and 30).

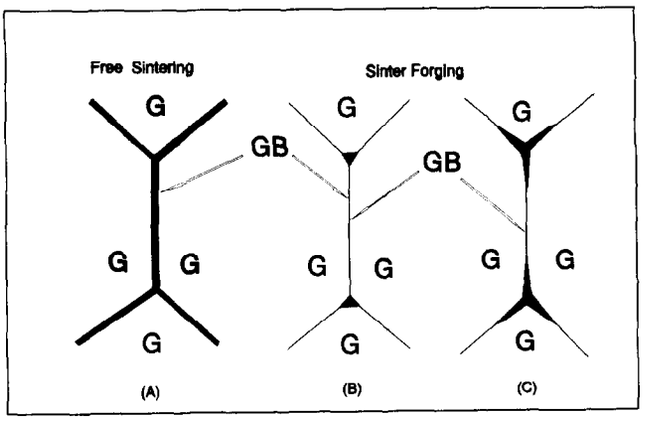

Fig. 11. Model of the physical–chemical state of the grain boundaries of TZP ceramics after pressureless sinter or sinter-forging (**G**: grain, **GB**: grain boundary).

ZY5. A more detailed discussion of this is given by Boutz *et al.*[13] XPS results obtained by Boutz *et al.*[13] show that there is a significant decrease in yttrium, aluminium and silicon concentration at the grain boundaries of sinter-forged samples. This may result in enhanced bonding strength between interface atoms from differently oriented crystallites. The improved grain boundaries might result in a higher resistance to plastic deformation in local areas, resulting in higher classical Vickers hardness for sinter-forged TZP samples than that for pressureless sintered samples.

Krell & Blank[6] pointed out that the presence of a relatively thick grain boundary layer can easily cause the formation of cracks at grain boundaries and provide an easy path for crack propagation. The improved grain boundary bonding strength by sinter-forging leads to a large fracture energy in sinter-forged samples which, in turn, increases the resistance to crack propagation. This results in an increase in grain boundary toughness (K_{IC}^{gb}). As indicated by Krell *et al.*[13] a higher grain boundary toughness (K_{IC}^{gb}) gives a higher macroscopic toughness.

5 Conclusions

(1) Dense, ultra-fine grained (180–190 nm) ZY5 and ZY4Ce4 ceramics were obtained by both sinter-forging and pressureless sintering at 1150°C. The sintering time necessary to obtain high density (> 95%) can be reduced by sinter-forging, i.e. sinter-forging can significantly improve the densification rate of TZP ceramics.

(2) Sinter-forging with a large shear strain (about 0·5) results in the absence of large pores or cracklike flaws which are present in pressureless sintered samples. It also results in an improvement of the reliability (Weibull modulus of 21) of sinter-forged samples compared to pressureless sintered ones (Weibull modulus of 8).

(3) After sinter-forging, the grain boundaries are strengthened by suppressing impurity segregation and by hindering the formation of a continuous amorphous film at grain boundaries due to shear deformation. Sinter-forging also results in a higher Vickers microhardness, an increase in fracture energies and fracture toughness compared to pressureless sintered samples. The strengthening of the grain boundaries, which is responsible for the increase of fracture toughness, is partially maintained at high temperatures. A fracture toughness K_{IC} of 10 MPa $m^{1/2}$ is obtained for ultra-fine grained TZP made by sinter-forging. A fracture energy of 300–330 J/m^2 is calculated for these materials. No irreversible phase transformation toughening was detected.

(4) The bending strength in sinter-forged samples is slightly increased by the strengthened grain boundaries. The Weibull modulus strongly increases in this case, which indicates that the strength is more sensitive to the flaw sizes and flaw size distribution. The presence of some large alumina inclusions limited the increase of bending strength in sinter-forged samples.

Acknowledgments

The authors are grateful to Miss Petra M. V. Bakker for the powder preparation, Mr Joop Snoeyenbos for machining and polishing, Mr Jaap Boeijsma for XRD measurements, Mr Marc Smithers for SEM observations. This research was partly supported by the Innovative Research Program on Technical Ceramics (IOP-TK) with the financial aid of the Dutch Ministry of Economic Affairs.

References

1. Watanabe, T., Grain Boundary Design for Desirable Mechanical Properties. *Journal de Physique*, **49** Collogue C5 (1988) 507–19
2. Boutz, M. M. R., Chen, C. S., Winnubst, A. J. A. & Burggraaf, A. J., Characterisation of Grain Boundaries in Superplastically Deformed Y-TZP Ceramics. *J. Am. Ceram. Soc.*, **77**(10) (1994) 2632–40.
3. Lim, L. C. & Watanabe, T., Fracture Toughness and Brittle-Ductile Transition Controlled by Grain Boundary Character Distribution (GBCD) in Polycrystals. *Acta Metal. Mater.*, **38**(12) (1990) 2507–16.
4. Krell, A., Woltersdorf, J., Pippel, E. & Schulze, D., On Grain Boundary Strength in Sintered Al_2O_3. *Philosophical Magazine A*, **51**(5) (1985) 765–76.

5. Griffith, A. A., *Phil. Trans. R. Soc.*, **A221** (1920) 163.
6. Krell, A. & Blank, P., Inherent Reinforcement of Ceramic Microstructure by Grain Boundary Engineering. *J. Eur. Ceram. Soc.*, **9** (1992) 309–22.
7. Burggraaf, A. J., Stuijts Memorial Lecture 1991: Some New Developments in Ceramic Science and Technology. *J. Eur. Ceram. Soc.*, **9** (1992) 245.
8. Burggraaf, A. J., Winnubst, A. J. A. & Verweij, H., Dense and Porous Nanostructured Ceramics and Composites. In *Third Euro-Ceramics*, Vol. 3, ed. P. Durén and J. F. Feméndez, 1993, pp. 561–76.
9. Boutz, M. M. R., Winnubst, A. J. A., Burggraaf, A. J., Nauer, M. & Carry, C., Low Temperature Superplastic Flow of Yttria Stabilized Tetragonal Zirconia Polycrystals. *J. Eur. Ceram. Soc.*, **13**(2) (1994) 103–11.
10. Theunissen, G. S. A. M., Bouma, J. S., Winnubst, A. J. A. & Burggraaf, A. J., Mechanical Properties of Ultra-Fine Grained Zirconia Ceramics. *J. Mater. Sci.*, **27** (1992) 4429.
11. He, Y. J., Winnubst, A. J. A., Verweij, H. & Burggraaf, A. J., Improvement of Mechanical Properties of Zirconia Toughened Alumina by Sinter-forging. *J. Mater. Sci.*, **29**(22) (1994) 5868–74.
12. Venkatachari, K. R. & Raj, R., Enhancement of Strength through Sinter Forging. *J. Am. Ceram. Soc.*, **70**(7) (1987) 514–20.
13. Boutz, M. M. R., Winnubst, A. J. A., Burggraaf, A. J., Nauer, M. & Carry, C., Low Temperature Sinter Forging of Nanostructured Y-TZP and YCe–TZP. *J. Am. Ceram. Soc.*, **78**(1) (1995) 121–8.
14. He, Y. J., Winnubst, A. J. A., Verweij, H. & Burggraaf, A. J., Sinter Forging of Zirconia Toughened Alumina. *J. Mater. Sci.*, **29**(24) (1994) 6505–12.
15. Boutz, M. M. R., Winnubst, A. J. A. & Burggraaf, A. J., The Effect of Ceria-Codoping on Chemical Stability and Fracture Toughness of Y–TZP. *J. Mater. Sci.*, **30** (1995) 1854–62.
16. Groot Zevert, W. F. M., Winnubst, A. J. A., Theunissen, G. S. A. M. & Burggraaf, A. J., Powder preparation and compaction behaviour of fine-grained Y–TZP. *J. Mater. Sci.*, **25** (1990) 3449.
17. Den Exter, P., Synthesis, Microstructure and Mechanical Properties of Zirconia-Alumina Composites. PhD Thesis, University of Twente, Enschede, The Netherlands, 1991.
18. Toraya, H., Yoshimura, M. & Sōmiya, S., Calibration Curve for Quantitative Analysis of the Monoclinic-Tetragonal ZrO_2 System by X-Ray Diffraction. *J. Am. Ceram. Soc.*,**67** (1984) C–119.
19. Mendelson, M. I., Average Grain Size in Polycrystalline Ceramics. *J. Am. Ceram. Soc.*, **52**(8) (1969) 443–6
20. Sullivan, J. D. & Lauzon, P. H., Experimental Probablity Estimators for Weibull Plots. *J. Mater. Sci. Lett.*, **5** (1986) 1245.
21. Tabor, D., The Hardness of Solids. *Rev. Phys. Techn.*, **1** (1970) 145–79.
22. Klug, K. P. & Alexander, L. E., X-ray Diffraction Procedures. John Wiley and Sons, New York, 1974.
23. Theunissen, G. S. A. M., Microstructure, Fracture Toughness and Strength of (Ultra)Fine-Grained Tetragonal Zirconia Ceramics. PhD Thesis, University of Twente, Enschede, The Netherlands, 1991.
24. Krell, A., Improved Hardness and Hierarchic Influences on Wear in Submicron Sintered Alumina. 5th Int. Conf. Science of Hard Materials, Maui (Hawaii), 20–24 Feb. 1995, *Mater. Sci. Eng. A.*, special issue.
25. Rice, R. W., Freiman, S. W., Pohanka, R. C., Mecholsky Jr, J. J. & Wu, C. C., *Fracture Mechanics of Ceramics*, ed. R. C. Bradt, D. P. H. Hasselman & F. F. Lange, Plenum Press, New York, 1978, pp. 849–76.
26. Lange, F. F. & Metcalf, M., Processing-Related Fracture Origins: II. Agglomerate Motion and Cracklike Internal Surface Caused by Differential Sintering. *J. Am. Ceram. Soc.*, **66** (6) (1983) 398–406.
27. Sung, J. & Nicholson, P. S., Strength Improvement of Yttria-Partially-Stabilized Zirconia by Flaw Elimination. *J. Am. Ceram. Soc.*, **71**(9) (1988) 788–95.
28. Kellett, B. J. & Lange, F. F., Experiments on Pore Closure During Hot Isostatic Pressing and Forging. *J. Am. Ceram. Soc.*, **71**(1) (1988) 7–12.
29. Gleiter, H., Materials with Ultrafine Grain Sizes. *1980 Deformation of Polycrystals*, ed. N. Hansen, A. Horsewell, T. Leffers & L. Libholt, 2th Risφ Int. Symp. on Metallurgy and Materials Science, Risφ Nat. Lab., Roskilde, Denmark, 1981, pp. 15–21.
30. Xhu, X., Birringer, R., Herr, U. & Gleiter, H., X-ray Diffraction Studies of the Structure of Nanometer-Sized Crystalline Materials. *Phys. Rev. B.*, **35** (1987) 9085–90.

Journal of the European Ceramic Society 16 (1996) 613–617

0955-2219(95)00171-9
0955-2219/96/$15.00

Ageing of Zirconia-Toughened Alumina Ceramics under Different Hydrothermal Conditions

D. Basu, A. Das Gupta, M. K. Basu & B. K. Sarkar

Central Glass and Ceramic Research Institute, Jadavpur, Calcutta – 700032, India

(Received 9 January 1995; revised version received 18 August 1995; accepted 9 September 1995)

Abstract

Changes in the crystalline phases of ZrO_2 in different zirconia-toughened alumina (ZTA) compositions were studied at lower temperature (150–250°C) by exposing them in a stream of humid air for a period of 24 h. Fresh samples of these compositions were also aged in an autoclave with superheated water for 2·5 h in the same temperature range, and the degree of phase transformation was compared with data from the previous samples to establish the effect of pressure on this phenomenon. It was observed for all the ZTA compositions that phase transformation increased monotonically with ageing time, temperature and pressure, although for the compositions with a lower percentage (15 vol%) of zirconia (3 mol% Y_2O_3), ageing in an autoclave was more detrimental particularly at lower temperature. As the ageing temperature increased in the composition with 15 vol% ZrO_2 (3 mol% Y_2O_3), the influence of ageing duration on phase transformation of ZrO_2 increased and the effect for 24 h of exposure time was found to be even more catastrophic than that of autoclave pressure at 250°C. On the other hand, for the ZTA compositions containing more than 15 vol% zirconia (3 mol% Y_2O_3), the damaging effect of ageing in the autoclave was greater and this difference increased with increase in temperature.

1 Introduction

Y_2O_3-doped partially stabilized zirconia (PSZ) and tetragonal zirconia polycrystals (TZP) have found application in different engineering fields as a result of their favourable room temperature mechanical properties.[1,2] High transverse rupture strength (TRS) and fracture toughness of these ceramics have been considered to be due to stress-induced martensitic transformation of the zirconia phase from its metastable tetragonal to the stable monoclinic state.[3–7] However, the use of these ceramics in the temperature range from 150 to 300°C has been reported to be severely limited as a result of degradation in mechanical properties,[8–10] due to the instantaneous phase transformation of zirconia resulting from microcracks on the surface. This degradation effect has been reported to be more severe in humid atmosphere[11–16] and even in hot non-aqueous solutions[17] of glycol, glycerol, propylamine, etc. A number of studies has been conducted to eliminate the ageing effect on Y_2O_3-doped PSZ or TZP[18,19] and it has been claimed that this degradation phenomenon can be greatly reduced by either replacing Y_2O_3 completely or partially by CeO_2, or by adding alumina in zirconia matrix.[20]

It has been reported[21,22] that the dispersion of metastable tetragonal zirconia in an alumina matrix can form a new class of ceramics with improved strength and toughness, which shows much better resistance to ageing even under humid conditions.[23] However, there has not been any systematic and extensive study on the ageing behaviour of zirconia-toughened alumina (ZTA) in hydrothermal conditions under simultaneous exposure to elevated temperature and pressure. In the present study different ZTA samples with varied amount of yttria-stabilized ZrO_2 (3Y-TZP) additions were aged in a stream of humid air in the temperature range from 150 to 250°C for 6 to 24 h. Similar samples were aged in an autoclave for 2·5 h and the effect of pressure and ageing duration on the degree of phase transformation was studied.

2 Experimental Procedure

Different ZTA compositions having 5, 10, 12, 15 and 20 vol% 3Y-TZP were prepared by milling in a planetary mill in isopropanol medium. Starting materials were A-16 grade of alumina (Alcoa, USA) having crystallite size of 7000 Å and 3Y-TZP (Tosoh Corporation, Japan) having 278 Å

Table 1. Chemical analysis of Alumina and 3Y-TZP powders, and some physical properties

Constitutent (wt%)	*Alumina*	*3Y-TZP*
Y_2O_3	–	5·07
Al_2O_3	–	0·005
ZrO_2	–	–
SiO_2	0·020	0·002
Fe_2O_3	0·006	0·002
Na_2O	0·070	0·015
Loss on ignition	—	0·710
Crystallite size (Å)	7000	278
Specific surface area ($m^2\ g^{-1}$)	—	15·4

crystallite size. Chemical analysis of these materials is given in Table 1. Test samples in the form of plates (20 × 20 × 3 mm^3) and bars (55 × 4·5 × 3·5 mm^3) were prepared in a single-acting hydraulic press at 100 MPa. The green samples were sintered at 1550°C with 1 h soaking. The bulk density of the sintered samples was measured by Archimedes' principle and thereafter the samples were thoroughly characterized for different mechanical properties (Table 2). Subsequently the samples were polished down to 0·5 μm surface finish (R_A). Photomicrographs of the polished and thermally etched samples were taken in a scanning electron microscope. The grain size was measured by the line intercept method.[24] The polished samples were aged in an air–steam mixture of controlled humidity with a steam flow rate of 10 $cm^3\ min^{-1}$ at 150, 200 and 250°C for 6 to 24 h. Fresh samples were subsequently aged in an autoclave at three different hydrothermal conditions—150°C/1MPa, 200°C/2MPa and 250°C/4MPa—to study the effect of pressure. In these cases the period of exposure was 2·5 h. The phases were identified by X-ray diffraction analysis on the plate surface before and after ageing, and the *m*-ZrO_2 content was determined by the Garvie–Nicholson method.[25]

3 Results and Discussion

Figure 1 presents the effect of 3Y-TZP content on the phase transformation of different ZTA compositions due to ageing at 150°C in a stream of humid air for up to 24 h and in an autoclave at the same temperature involving additional pressure

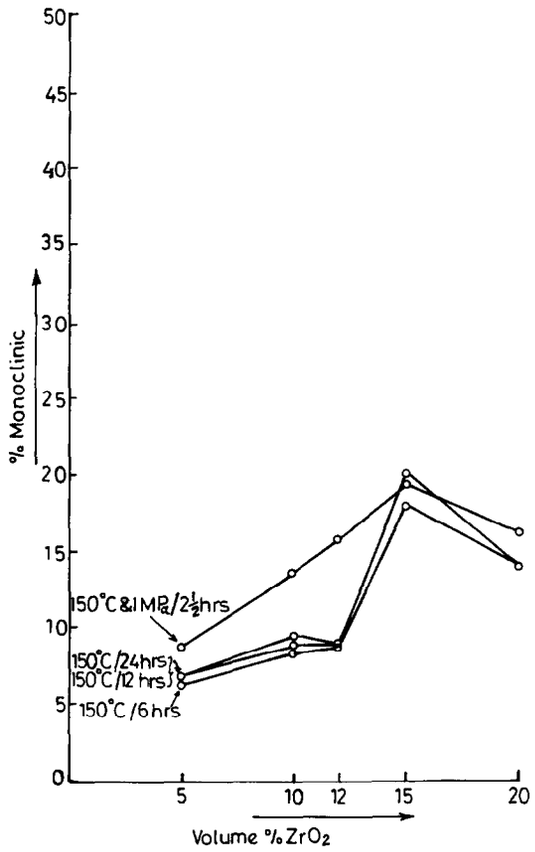

Fig. 1. Effect of ZrO_2 content on the phase transformation of different ZTA compositions when aged at 150°C in humid conditions for up to 24 h and at 1 MPa pressure for 2·5 h.

Table 2. Physical properties of different ZTA ceramics

Composition	*m-ZrO_2 content at 0 h ageing (%)*	*Density*			*Hardness (GPa)*	*TRS (MPa)*	*Fracture toughness ($MPa\ m^{1/2}$)*	*Average grain size (μm)*
		Theoretical ($g\ cm^{-3}$)	*Sintered ($g\ cm^{-3}$)*	*Relative (%)*				
A (Al_2O_3 + 5 vol% 3Y-TZP)	5·8	4·09	4·04	0·98	18·52	355·0	4·6	5·5 (Al_2O_3) + 0·5 (ZrO_2)
B (Al_2O_3 + 10 vol% 3Y-TZP)	6·6	4·18	4·13	0·99	17·40	465·0	4·6	4·5 (Al_2O_3) + 0·4 (ZrO_2)
C (Al_2O_3 + 12 vol% 3Y-TZP)	8·6	4·21	4·16	0·99	17·30	525·0	4·7	4·2 (Al_2O_3) + 0·4 (ZrO_2)
D (Al_2O_3 + 15 vol% 3Y-TZP)	10·0	4·26	4·22	0·99	17·00	775·0	5·7	3·5 (Al_2O_3) + 0·35 (ZrO_2)
E (Al_2O_3 + 20 vol% 3Y-TZP)	12·0	4·34	4·28	0·99	16·10	575·0	5·0	2·7 (Al_2O_3) + 0·3 (ZrO_2)

of superheated water. It is clear from the figure that, for 3Y-TZP additions of up to 15 vol%, the ageing effect increased with increasing ageing time and samples aged in the autoclave under pressure always showed a higher extent of phase transformation. At 15 vol% 3Y-TZP content the magnitude of transformation is maximum, and the effect of ageing for 24 h was found to be almost the same as 2·5 h hydrothermal treatment with 1 MPa pressure. Thereafter, i.e. at 20 vol% 3Y-TZP, the ageing effect decreased and the samples aged in the autoclave showed a higher degree of transformation, revealing more predominant damage. Figure 2 reveals that even at 200°C the ageing behaviour of these materials follows a similar trend, although the magnitude of transformation was found to be higher particularly in the composition with higher amount of 3Y-TZP. Furthermore, at this temperature, the difference between the effects of these two types of ageing on phase transformation was found to be much higher in ZTA compositions with 12, 15 and 20 vol% 3Y-TZP when compared with the ageing behaviour at 150°C. Figure 3 shows that during ageing at 250°C either the increase of steam pressure in the autoclave or the exposure time in hydrothermal conditions gives a lower effect up to 12 vol% 3Y-TZP. Moreover, the effect of 24 h of hydrothermal exposure was found to be more detrimental than the autoclave ageing for 15 vol% 3Y-TZP and thereafter both the effects decreased rapidly in such a fashion that the difference increased to the maximum. However, it was surprising to note that in all the cases of ageing in a stream of humid air there is very little difference between the ageing degradation of the compositions with 10 and 12% 3Y-TZP. On the other hand, when they were exposed to ageing in the autoclave, the degree of transformation was found to be much higher with the materials containing 12 vol% 3Y-TZP. Figure 4 presents the effect of 3Y-TZP content on the phase transformation of different ZTA compositions under three different hydrothermal conditions in an autoclave, involving both temperature and pressure. It shows that phase transformation of ZTA compositions was maximum at 15 vol% 3Y-TZP content in each case and for all ageing conditions.

The results indicated that the rigid alumina matrix produced a constraint which restricted the volume expansion involved in the *t–m* phase transformation of ZrO_2. This constraint decreased with increasing ZrO_2 content, resulting in an increase in ageing effect. It may be noted that the ageing effect decreased from 15 to 20 vol% 3Y-TZP addition. Table 2 shows that as the 3Y-TZP content increases in the compositions the

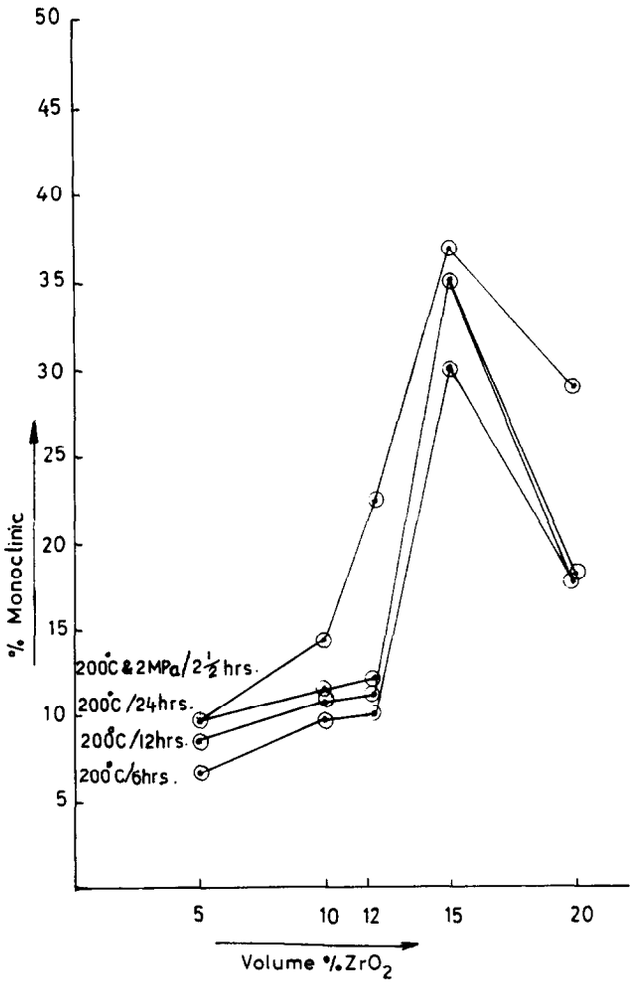

Fig. 2. Effect of ZrO_2 content on the phase transformation of different ZTA compositions when aged at 200°C in humid condition for up to 24 h and at 2 MPa pressure for 2·5 h.

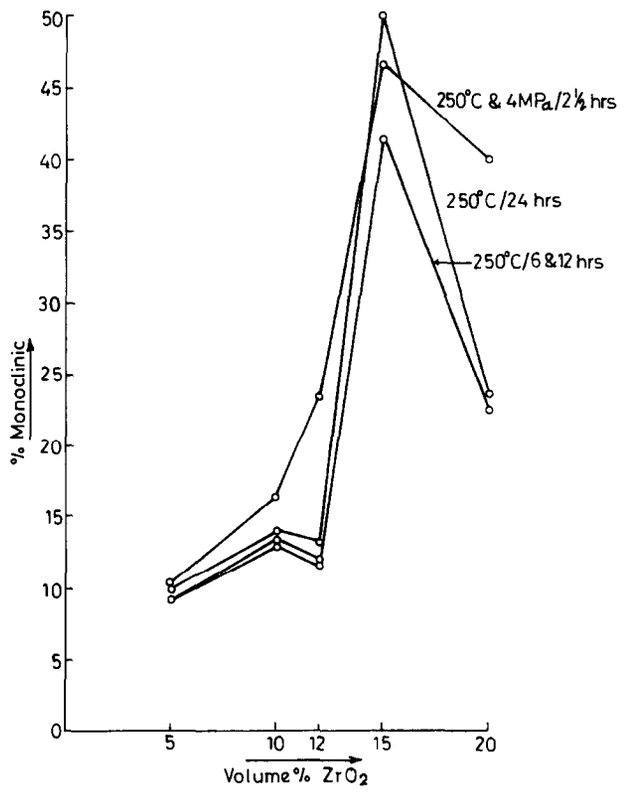

Fig. 3. Effect of ZrO_2 content on the phase transformation of different ZTA compositions when aged at 250°C in humid condition for up to 24 h and at 4 MPa pressure for 2·5 h.

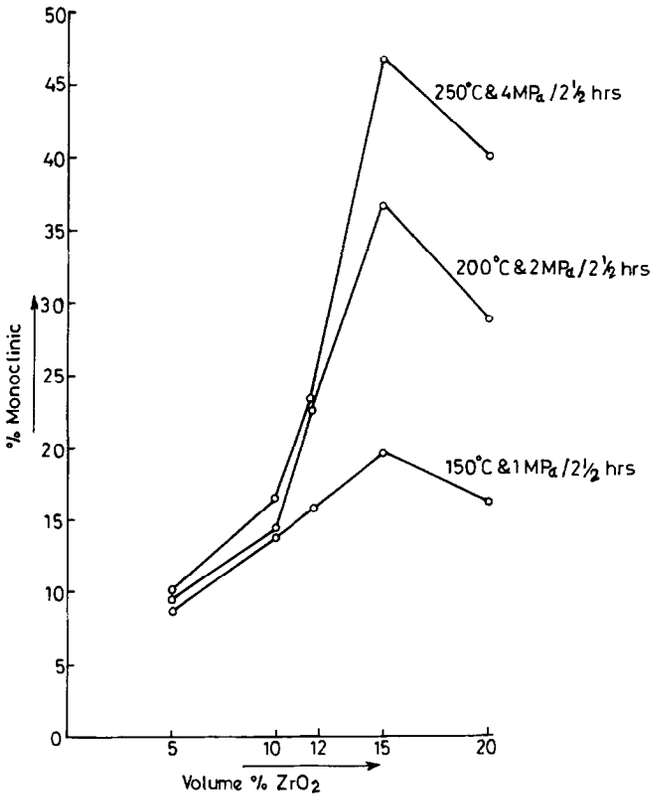

Fig. 4. Effect of ZrO_2 content on the phase transformation of different ZTA compositions under three different hydrothermal conditions: (1) 150°C/ 1 MPa, (2) 200°C/ 2 MPa, (3) 250°C/ 4 MPa.

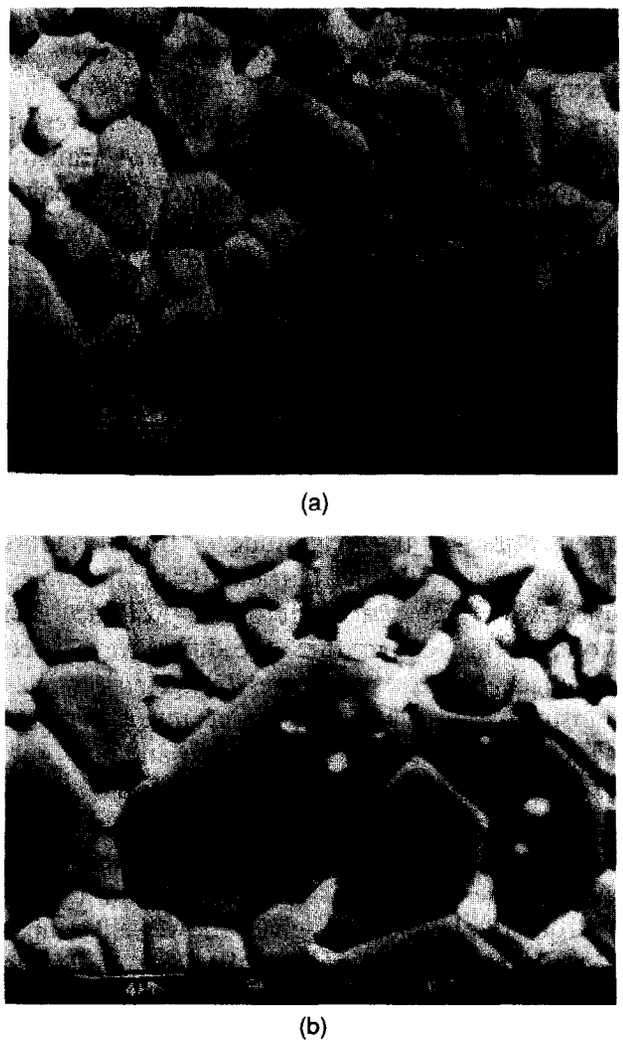

Fig. 5. Scanning electron micrographs of two sintered ZTA compositions: (a) 5 vol% ZrO_2, (b) 15 vol% ZrO_2.

average grain size of ZrO_2 decreases, and as the grain size approaches the critical value (which is between 0·2 and 0·6 μm according to Lange *et al.*[16]) the probability of the stress-induced transformation of the ZrO_2 grains is reduced. This is also reflected in the fracture toughness data of these materials: the fracture toughness decreased after attaining the maximum value at 15 vol% 3Y-TZP addition, thus indicating the reduction in transformability of the zirconia grains due to decrease in grain size. This suggests that lowering the grain size has a more dominant effect than the dilation strain. Further, the results revealed that the effect of pressure was more detrimental in most of the cases although the additional pressure should have restricted this phase change involving volume expansion. It has been hypothesized by Lange *et al.*[16] that water vapour reacts with yttrium in the zirconia to produce clustures of small α -$Y(OH)_3$ crystallites, resulting in a monoclinic nucleus on the surface of an exposed tetragonal grain. The additional pressure within the autoclave probably generated micro- and macrocracks which exposed the subsurface tetragonal grains to the ageing phenomenon, resulting in catastrophic degradation.

Figure 5 represents photomicrographs of two sintered ZTA compositions containing different amounts of 3Y-TZP. Both microstructures exhibited well-dispersed ZrO_2 grains in inter- and intragranular mode in the alumina matrix, and the average size of both the alumina and the zirconia grains was found to decrease with higher 3Y-TZP additions.

4 Conclusions

The tetragonal phase of 3Y-TZP undergoes a phase change during low temperature ageing in humid atmosphere. The degree of phase transformation in all the individual ZTA compositions increased with ageing temperature, duration and pressure. This transformability increased with 3Y-TZP content in the system up to a peak at 15 vol%. Thereafter the smaller grain size of the zirconia led to a greater stability of the tetragonal phase.

The exposure to the pressure of superheated water in the autoclave for 2·5 h greatly increased the ageing kinetics for all the compositions, and the ageing effect was found to be much greater than that of ageing in a stream of humid air even

for 24 h. However, the composition with 15 vol% zirconia addition did not show this behaviour during ageing at 250°C.

Acknowledgements

The authors would like to express their appreciation to Dr A. K. Chakrabarty and Dr S. Sen, scientists at the Institute, for X-ray analysis and scanning electron microscopy, respectively.

References

1. Garvie, R. C., Hannink, R. H. & Pascoe, R. T., Ceramic steel. *Nature (London)*, **258** (5537) (1975) 703–4.
2. Garvie, R. C., Structural applications of ZrO_2 bearing materials. In *Advances in Ceramics, Vol. 12. Science & Technology of ZrO_2 II*, ed. N. Claussen, M. R. Ruhle & A. Heuer. The American Ceramic Society, Columbus, OH, 1984, pp. 465–78.
3. Gupta, T. K., Lange, F. E. & Bechtold, J. H., Effect of stress induced phase transformation on the properties of polycrystalline ZrO_2 containing metastable tetragonal phase. *J. Mater. Sci.*, **13** (1978) 1464–70.
4. Lange, F. F., Transformation toughening. Part 3 Experimental observations in the ZrO_2–Y_2O_3 system. *J. Mater. Sci.*, **17** (1982) 240.
5. Porter, D. L. & Heuer, A. H., Mechanisms of toughening partially stabilised zirconia (PSZ). *J. Am. Ceram. Soc.*, **60** (1977) 183–4.
6. Porter, D. L., Evans, A. G. & Heuer, A. H., Transformation toughening in partially stabilised zirconia (PSZ). *Acta Metall.*, **27** (2) (1979) 1949–54.
7. Heuer, A. H., Claussen, N., Kriven, W. M. & Ruhle, M., Stability of tetragonal zirconia particles in ceramic matrices. *J. Am. Ceram. Soc.*, **65**(12) (1982) 642–50.
8. Hong Yang, Lu & San Yuan, Chen, Low temperature ageing of t-ZrO_2 polycrystals with 3 mol% Y_2O_3. *J. Am. Ceram. Soc.*, **70**(8) 1987 537–41.
9. Sato, T., Ohtaki, S. & Shimada, M., Transformation of yttria partially stabilised zirconia by low temperature annealing in air. *J. Mater. Sci.*, **20** (1985) 1466–70.
10. Watanabe, M., Jio, S. & Fukura, J., Aging behaviour of Y-TZP. In *Advances in Ceramics, Vol. 12. Science & Technology of Zirconia II*, ed. N. Claussen, M. Ruhle & A. H. Heuer. The American Ceramic Society, Columbus, OH, 1984, pp. 391–8.
11. Kobayashi, K., Kuwajima, H. & Masaki, T., Phase, change and mechanical properties of ZrO_2–Y_2O_3. *Solid State Ionics*, **3–4** (1981) 489–93.
12. Sato, T. & Shimada, M., Transformation of yttria doped tetragonal zirconia polycrystals by annealing in water. *J. Am. Ceram. Soc.*, **68**(6) (1985) 356–9.
13. Sato, T. & Shimada, M., Crystalline phase change in yttria partially stabilised zirconia by low temperature annealing. *J. Am. Ceram. Soc.*, **67**(10) (1984) C212–13.
14. Matsumoto, R. L., Strength recovery in degraded yttria doped tetragonal polycrystals. *J. Am. Ceram. Soc.*, **68**(8) (1985) C213.
15. Ruhle, M., Claussen, N. & Heuer, A. H., Microstructural studies of Y_2O_3 containing tetragonal zirconia polycrystals (Y-TZP). In *Advances in Ceramics, Vol. 12. Science & Technology of Zirconia II*, ed. N. Claussen, M. Ruhle & A. H. Heuer. The American Ceramic Society, Columbus, OH, 1984, pp. 352–70.
16. Lange, F. F., Dunlop, G. L. & Davis, B. I., Degradation during aging of transformation toughened ZrO_2–Y_2O_3 materials at 250°C. *J. Am. Ceram. Soc.*, **69**(3) (1986) 237–40.
17. Sato, T., Ohtaki, S., Endo, T. & Shimada, M., Changes in crystallographic phase and microstructure on the surface of the yttria doped tetragonal zirconia polycrystals (Y-TZP) by annealing in humid condition. In *Advances in Ceramics, Vol. 24. Science & Technology of Zirconia III*, ed. S. Somiya, N. Yamamoto & H. Yanagida. The American Ceramic Society, Columbus, OH, 1988, pp. 501–8.
18. Sato, T. & Shimada, M., Transformation of ceria-doped tetragonal zirconia polycrystals by annealing in water. *Am. Ceram. Soc. Bull.*, **64**(10) (1985) 1382–4.
19. Matsumoto, R. L., Aging behaviour of Ce-stabilised t-zirconia polycrystals. *J. Am. Ceram. Soc.*, **71**(3) (1988) C128–9.
20. Hirano, N. & Inada, H., Hydrothermal stability of Y- and Ce-doped t-zirconia + Al_2O_3 composites. *J. Mater. Sci.*, **26**(18) (1991) 5047–52.
21. Lange, F. F., Transformation toughening. Part 4 Fabrication, fracture toughness and strength of Al_2O_3–ZrO_2 composites. *J. Mater. Sci.*, **17** (1982) 247–54.
22. Claussen, N., Microstructural design of zirconia toughened ceramics (ZTC). In *Advances in Ceramics, Vol. 12. Science & Technology of Zirconia II*, ed. N. Claussen, M. Ruhle & A. H. Heuer. The American Ceramic Society, Columbus, OH, 1984, pp. 325–51.
23. Basu, D., Dasgupta, A., Sinha, M. K. & Sakar, B. K., Low temperature aging of zirconia toughened alumina under humid condition. *Ceram. Int.*, **21**(4) (1995) 277–82.
24. Fullman, R. L., Measurement of particle sizes in opaque bodies. *J. Met. Trans. AIME*, **197**(3) (1953) 447–52.
25. Garvie, R. C. & Nicholson, P. S., Phase analysis in zirconia systems. *J. Am. Ceram. Soc.*, **67**(6) (1972) 303–5.

Journal of the European Ceramic Society 16 (1996) 619–626

0955-2219(95)00183-2
0955-2219/96/$15.00

Characterisation of Sol–Gel Derived Alumina–Silica Matrices For Continuous Fibre Reinforced Composites

J. Wu, M. Chen,* F. R. Jones & P. F. James

Department of Engineering Materials, University of Sheffield, Sir Robert Hadfield Building, Mappin Street, Sheffield S1 3JD, UK

(Received 20 July 1995; revised version received 29 September 1995; accepted 12 October 1995)

Abstract

Bulk gels corresponding to an oxide composition of $3Al_2O_3{\cdot}2SiO_2$, prepared from a sol with a high solids yield using submicron alumina powder and colloidal silica sol as precursors, were sintered to over 99% of theoretical density after 2 h at 1300°C. Densification occurred by viscous flow of the amorphous silica matrix containing well dispersed alumina particles. After 2 h at 1600°C almost complete crystallisation to mullite occurred. Uniform unidirectional carbon fibre reinforced composites were produced by a single stage infiltration of fibres, using the above sol, and hot-pressing either at 1300 or at 1400°C to 98 and 97% of the theoretical density respectively. The composites, with a matrix predominantly of silica glass and dispersed alumina particles, exhibited non-brittle failure with mean flexural strengths of 720 and 766 MPa for hot-pressing at 1300 and 1400°C respectively. Extensive fibre pull-out during testing indicated a relatively weak bond between the fibres and the matrix, and transmission electron microscopy revealed no evidence of chemical interactions at the interface.

Introduction

Mullite ceramics are potential matrix materials for high temperature structural composite applications because of their excellent high temperature strength and creep resistance, good chemical and thermal stability and low thermal expansion coefficient. Fabrication of mullite ceramics by traditional methods using natural minerals as starting materials with alumina additions normally requires a high processing temperature in excess of 1700°C with lengthy sintering.[1,2] However, a mullite crystallisation temperature as low as 980°C can be achieved from alkoxide precursors using the molecular scale mixing of sol–gel methods.[3,4] Generally, the materials obtained by this technique suffer high shrinkages on drying because of the low solids content of the sols. If this disadvantage could be overcome, the sol–gel route would be extremely promising for the preparation of mullite composites especially when continuous fibre is used as the reinforcement.[5] In practice, the fabrication of composites by sol–gel methods have several inherent advantages over other methods such as slurry infiltration, melt-infiltration or CVD processing.[6] The consolidation of matrix and fibre can be realised in a single infiltration stage so that there is less damage to the fibres. It is also relatively easy to achieve a uniform fibre distribution. Organic binders are not required so porosity associated with burning-off is not a problem, and green strength remains high. However the much lower processing temperatures in sol–gel processing are a key factor. In preliminary work,[7,8] a colloidal sol with high solids yield containing up to 40% solids by volume, producing dried gels of the mullite composition, $3Al_2O_3{\cdot}2Sio_2$, was reported. This was used to prepare a highly densified monolithic mullite bulk ceramic with almost complete mullitisation at 1600°C after 2 h. It was also demonstrated subsequently[9] that highly densified continuous carbon fibre reinforced mullite matrix composites could be successfully prepared by a single stage infiltration process, followed by hot-pressing. Recently, Colomban and coworkers[10] have described the effects of a zirconia interphase on the mechanical properties of continuous oxide fibre reinforced mullite matrix composites prepared by a sol–gel route. The oxide fibres were in the form of woven fabric. Achievement of a non-brittle composite was related to the absence of a chemical reaction between the zirconia interphase and the oxide fibres.

*Present address: Department of Materials Science and Metallurgy, University of Cambridge, UK.

In this paper, densified mullite bulk gels and hot-pressed carbon fibre alumina–silica matrix composites from the high solid yield sol are characterised by X-ray diffraction (XRD), scanning electron microscopy (SEM) and transmission electron microscopy (TEM). The densification mechanism for mullite bulk gel samples is determined. The strength and elastic properties of the composites are measured under three point bending. The fracture surfaces of the composite specimens are examined by SEM, and the interface between fibre and matrix analysed by TEM.

Experimental

Monolithic samples of the mullite composition ($3Al_2O_3{\cdot}2SiO_2$) were prepared by a sol–gel process, as described in preliminary studies,[7,8] using Ludox colloidal silica sol (Dupont AS40, 40 wt% of silica, particles of 5–50 nm in diameter) and α-alumina powder (A1000 SG, Alcoa 0·5 μm) as precursors. Briefly, the pH of the Ludox sol was adjusted from 9 to 2–3 using dilute acid (HCl 1 M). Alumina powder was dispersed in the sol to achieve a uniform mixture of the required composition, using magnetic stirring. Dilute acid was again added to reduce the pH to 5–6, so that gelation occurred in 30 min. Samples of the bulk gel (discs 30 mm in diameter and 10 mm in thickness) were slowly dried at room temperature for 48 h, followed by drying at 90°C for 48 h, and calcined at 500°C for 2 h; finally they were heated at 20°C/min to the sintering temperatures (1100–1600°C) for the required holding time of 2 h.

Unidirectional carbon fibre reinforced composites were fabricated using single stage infiltration with the above sol, which had a total solids content of 40 vol%. Grafil LXA unsized high strength carbon fibre tows (density $1{\cdot}81 \times 10^3$ kg/m^3, diameter of 8 μm, theoretical strength 4 GPa, elastic modulus of 224 GPa) were employed as the reinforcement. Fibre tows were passed through the sol and wound onto a hexagonal drum to form a 10 mm thick green prepreg sheet. After drying at 90°C, the sheet was released from the drum. The dried sheet was cut into circular discs 45 mm in diameter and hot-pressed in a graphite die surrounded by a high temperature furnace. During hot-pressing, the composite prepreg was sealed by graphite powder to protect it from oxidation and a nitrogen gas flow was used to protect the die. One composite sample was heated at 20°C/min to 1300°C and held for 1 h, under a pressure of 25 MPa. Another sample was heated at 20°C/min to 1400°C and held for 0·5 h at 17 MPa. Both samples were subsequently allowed to cool naturally to room temperature overnight. By careful control of the sol viscosity, composites with a range of fibre volume fractions (0·30–0·60) could be prepared. The composites hot-pressed at 1300 and 1400°C had volume fractions of 0·40 and 0·45 respectively.

The densities of the sintered monolithic gel, and composite samples were determined by mercury immersion. The volume fraction of fibre in the composite was accurately determined from the weight change after complete oxidative removal of the carbon fibre at 900°C overnight. After this treatment, the remaining oxide matrix was white in appearance on the outside surface and on the inside after fracture, indicating that no carbon remained. The crystalline phase development in the heat treated samples was characterised by powder X-ray diffraction (Philips 1710) using a scanning speed of 2° (2θ) /min. Microstructural analysis was carried out using a Camscan 400 SEM and Philips 400 TEM. Both fracture and polished surfaces of samples were employed in the SEM study. Thin section samples for TEM study were prepared by grinding and polishing discs of 3 mm in diameter, cut from as-prepared samples to a thickness of about 100 μm and further dimpling down to about 15–20 μm in the centre, followed by final ion beam thinning to electron transparency.

The thermal expansion coefficient of the bulk gel of the alumina–silica mixture, $3Al_2O_3{\cdot}2SiO_2$, fired at 1300°C for 2 h with a density of $3{\cdot}23 \times 10^3$ kg/m^3, was measured using a dilatometer with fused silica as a reference. The measuring specimen was cut from a sintered bulk sample, and ground and polished to the diameter of 10 mm and length of 30 mm. The thermal expansion coefficient was an average result in the temperature range of 25–700°C.

The flexural strength and elastic modulus of the composite specimen were determined by three point bend test according to British Standard Methods of Testing[11] on a Mayes Universal Tester with a loading speed of 0·2 mm/min at room temperature. Rectangular test specimens cut from the hot-pressed composite were ground and polished to a span of 30 mm with a span to thickness ratio greater than 20. The reported strength is the mean of six measurements.

Results

Figure 1 shows the densification of the as-prepared bulk samples after 2 h at firing temperatures from 1100 to 1600°C. The results represent an analysis of more extensive data than given in a previous report.[8] The green density of the bulk gels was 60% of the calculated theoretical density

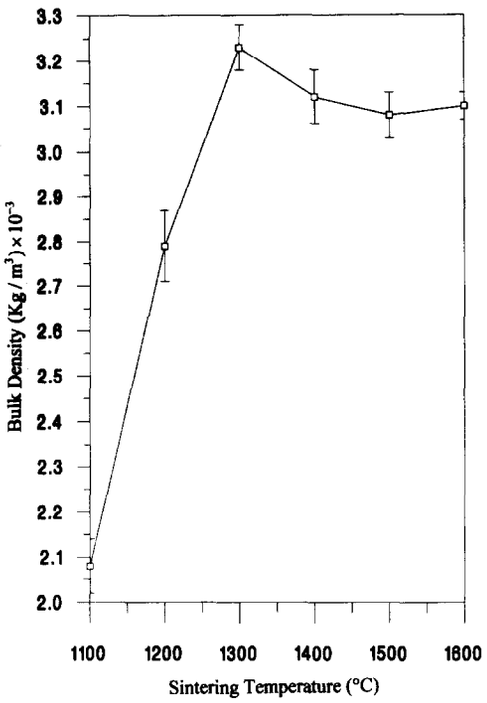

Fig. 1. Densification of the bulk gels from α-alumina powder and Ludox silica sol, corresponding to an oxide composition of $3Al_2O_3{\cdot}2SiO_2$, fired at the heating rate of 20°C/min to the sintering temperature with 2 h hold.

of $3{\cdot}25 \times 10^3$ kg/m^3 for the alumina–silica solids mixture, $3Al_2O_3{\cdot}2SiO_2$, based on the densities of $3{\cdot}98 \times 10^3$ kg/m^3)for α-alumina and $2{\cdot}22 \times 10^3$ kg/m^3 for silica glass.[12,13] Significant densification of the bulk samples began at 1100°C with substantial density increase occurring between 1200 and 1300°C. A maximum bulk density of $3{\cdot}23 \times 10^3$ kg/m^3 (over 99% of the theoretical value) was obtained at 1300°C. Sintering at higher temperatures resulted in a slightly lower bulk density of $3{\cdot}10 \times 10^3$ kg/m^3.

Figure 2 shows the XRD patterns of the as-sintered gels in the temperature range of 1200–1600°C for 2 h. The dominant crystalline phase at 1200 and 1300°C was α-alumina and no crystalline mullite was detected. The presence of a trace of cristobalite at 1200°C indicated that the amorphous colloidal silica had partially crystallised at this temperature. The extent of cristobalite formation increased after heating at 1300 and 1400°C. At around 1450°C, the crystalline mullite phase became detectable (not shown). A significant amount of mullite appeared at 1500°C at the expense of the α-Al_2O_3 and cristobalite. On firing at 1600°C, the mullite phase became dominant, with a trace of unreacted α-Al_2O_3 and cristobalite just detectable.

The high level of densification of the bulk gel is confirmed by the scanning electron micrograph shown in Fig. 3(a), where the fracture surface of a bulk sample sintered at 1300°C for 2 h, clearly demonstrates the effectiveness of the processing technique. Figure 3(b) shows the microstructure of the polished and thermal-etched (1500°C for 3 h) surface of a bulk gel which had been sintered at 1600°C for 2 h, where the fine grain structure is revealed. Based on the XRD results (Fig. 2), these grains predominantly consisted of mullite.

Figure 4 shows the transmission electron micrographs of the samples sintered at various temperatures. The submicron alumina particles were uniformly dispersed in a matrix consisting of fine colloidal silica and fine pores (diameters around 10–50 nm) at temperatures up to 900°C (Fig. 4(a)). Sintering the same gel to 1200°C resulted in a reduction in the total porosity but with significant pore coarsening to diameters around 0·1 μm (Fig. 4(b). A detailed study revealed that the pores were interconnected to form channels around dispersed alumina particles. At this temperature, as shown in Fig. 1, partial sintering had occurred, with a corresponding density of $2{\cdot}79 \times 10^3$ kg/m^3, compared with $2{\cdot}0 \times 10^3$ kg/m^3 for the unsintered gel. Almost complete densification was achieved after

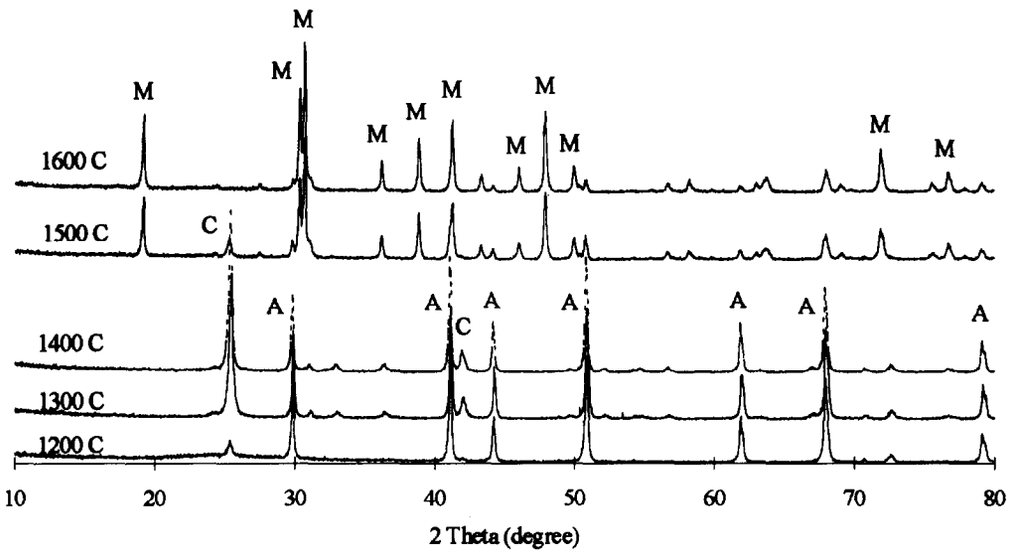

Fig. 2. XRD results of the bulk gels from α-alumina powder and Ludox silica sol, with the composition, $3Al_2O_3{\cdot}2SiO_2$, fired at the heating rate of 20°C/min to heating temperatures in the range of 1200–1600°C with 2 h hold.

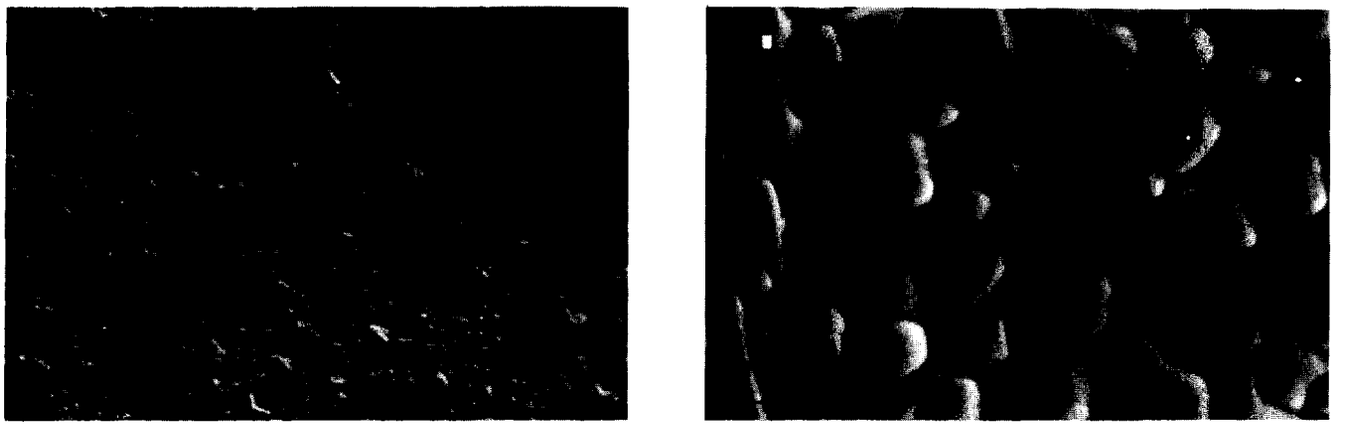

Fig. 3. SEM of a unetched fracture surface (a), and a polished and thermally etched surface (b) of the bulk gels from α-alumina powder and Ludox silica sol, with the composition, $3Al_2O_3{\cdot}2SiO_2$, fired at 1300 and 1600°C for 2 h respectively.The bars denote 3 μm for (a) and 1 μm for (b).

2 h at 1300°C, as shown by the almost pore-free microstructure (Fig. 4(c)). The fine alumina particles were individually dispersed in the already highly densified silica matrix. No agglomerates of alumina particles, which could have resulted in sintering voids were observed. From TEM and selected area electron diffraction, the silica matrix was predominantly amorphous but did occasion-

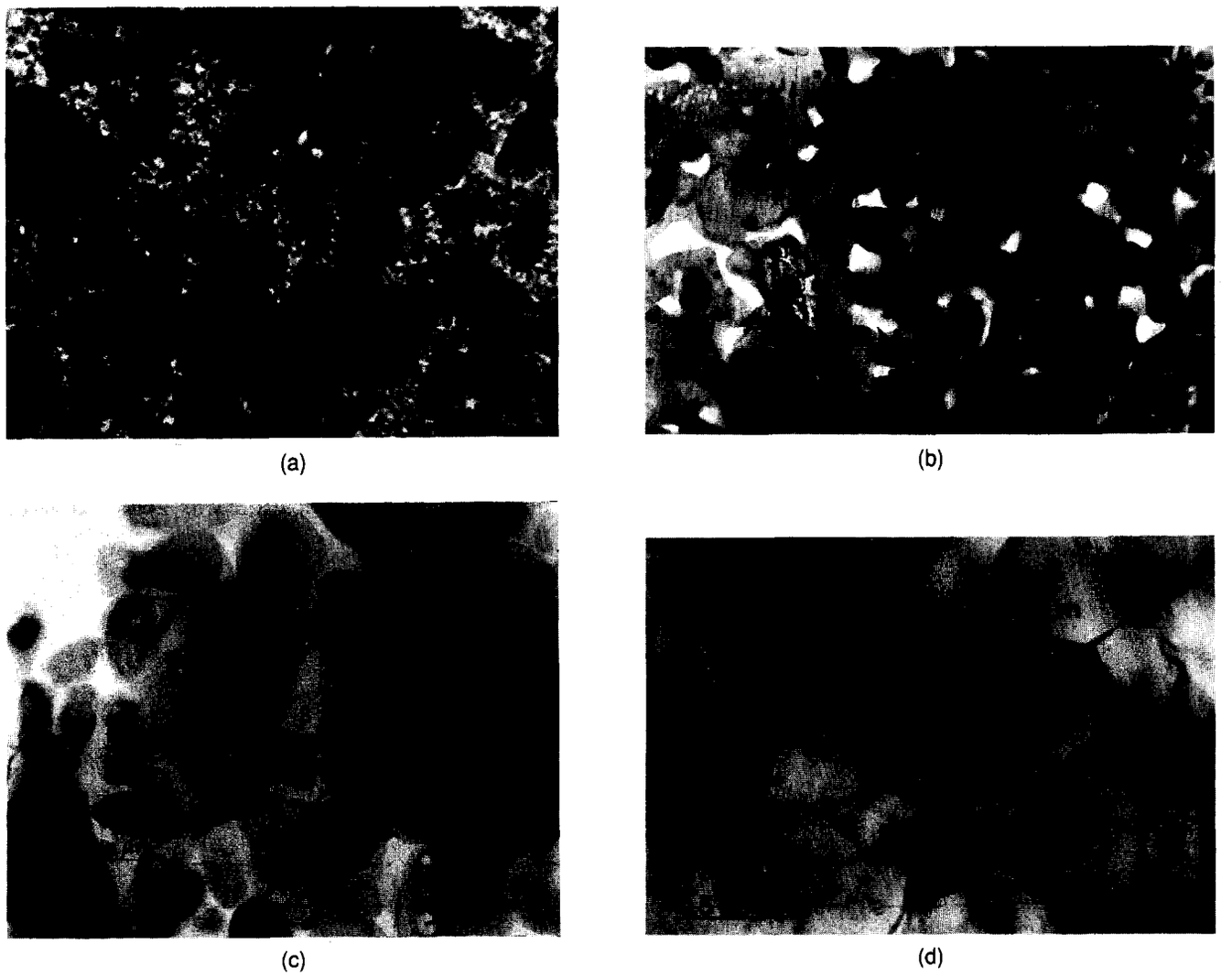

Fig. 4. TEM of the bulk samples from α-alumina powder and Ludox silica sol, with the composition, $3Al_2O_3{\cdot}2SiO_2$, fired at 900°C (a), 1200°C (b), 1300°C (c) and 1600°C (d) for 2 h respectively. The bars denote 0·5 μm for (a), 0·3 μm for (b), 0·5 μm for (c) and 0·5 μm for (d), and a, s, p and m denote α-alumina particle, silica (glass), pore and mullite grain respectively. In Fig. 4(d), a small region of unreacted alumina is arrowed.

ally contain some fine crystals, probably cristobalite since they were much finer than the alumina particles. The presence of cristobalite was also indicated by XRD. After firing at 1600°C for 2 h a uniform microstructure of crystal grains with diameters around 1 μm was observed by TEM (Fig. 4(d)), confirming SEM observations (Fig. 3(b)). XRD shows a predominance of crystalline mullite with traces of alumina and cristobalite, suggesting that most of the alumina particles had reacted with the surrounding silica matrix to form mullite, although small spherical particles within the mullite grains were occasionally visible by TEM (Fig. 4(a)), which probably represent small regions of unreacted crystalline alumina. Small regions at mullite triple grain junctions, probably of unreacted silica, were also occasionally observed.

A few small pores were also observed by TEM within the mullite microstructure, showing that the sample had not completely densified after heat treatment at 1600°C. Some of the pores may have originated not in sintering but in the precursor α-alumina particles themselves. From Fig. 1 the bulk density after 2 h at 1600°C was $3{\cdot}1 \times 10^3$ kg/m^3, approximately 98% of the theoretical density for mullite ($3{\cdot}17 \times$ kg/m^3).

Figure 5(a) shows a polished cross-section (perpendicular to the fibre direction) of the composite (V_f=0·40, hot-pressed at 1300°C for 1 h), which demonstrates the uniform distribution of carbon fibres within the matrix. The matrix was composed of unreacted alumina particles in a silica matrix (mainly silica glass). Figure 5(b) shows a polished cross-section parallel to the fibre direction. Regularly spaced transverse microcracks (average spacing 103 μm) are clearly observed running perpendicular to the fibre direction. These are probably caused by the difference in thermal expansion coefficients between the alumina–silica matrix and carbon fibre. The overall average thermal expansion coefficient of the matrix is around $4{\cdot}1 \times 10^{-6}$ K^{-1} based on measurement carried out on the bulk gel sample sintered at 1300°C for 2 h. This value compares with a value of approximately zero for the carbon fibre, producing a large thermal mismatch on cooling from the processing temperature, and resulting in transverse crack formation. Further detailed examination of the microstructure of the composite by SEM revealed no additional cracks or voids in the matrix, in good agreement with the density measurements of approximately 98% of the calculated theoretical density ($2{\cdot}67 \times 10^3$ kg/m^3) for the composite.

The microstructure of the composite hot-pressed at 1400°C were very similar to that of the composite hot-pressed at 1300°C. Properties of the composites are presented in Table 1, which shows the

(a)

(b)

Fig. 5. SEM of the fibre-reinforced composite samples hot-pressed at 1300°C for 1 h at 25 MPa. Polished cross section perpendicular to the fibre direction (a), and the polished surface parallel to the fibre direction (b). The bars denote 100 μm for (a) and 100 μm for (b).

mean values, determined by three point bending, where V_f is the fibre volume fraction σ the flexural strength, E the elastic modulus, and ρ/ρ_0 the ratio of density to the calculated theoretical density. σ_0 and E_0 are the calculated theoretical strength and elastic modulus of the composite by the rule of mixtures assuming that there is no contribution from the matrix (see Discussion). Also included is the fracture surface energy, W, for the 1300°C composite calculated from the areas under the stress–strain curves.

The hot-pressing conditions yielded composites with an average flexural strength and an average elastic modulus of 720 MPa and 107 GPa respectively at 1300°C and 766 MPa and 80 GPa respectively at 1400°C. All tested specimens showed non-brittle fracture behaviour. Figure 6 shows a typical loading stress against deflection curve for the composite under three point bending. Extensive fibre pull-out was observed in the fracture surface on the tensile side of the specimens, as shown in Fig. 7(a), suggesting a weak fibre/matrix interface. Both SEM and TEM (Fig. 7(b)) studies

Table 1. The properties of the composites

Hot-pressing condition	*1300°C, 25 MPa, 1 h*	*1400°C, 17 MPa, 0·5 h*
V_f	0·4	0·45
ρ/ρ_0	0·98	0·97
σ(MPa)	720±156	766±150
E(GPa)	107±33	80±15
W(kJ/m^3)	318±69	—
σ_0 (GPa)	1·6	1·8
E_0 (GPa)	90	100

± values are standard deviations

suggested no obvious reaction or evidence of strong bonding at the interface between the carbon fibre and the matrix.

Discussion

The bulk gel samples demonstrated high sinterability and a relatively low sintering temperature, almost full densification being achieved at 1300°C after 2 h. Similar results have been obtained previously on compacts of α-alumina particles coated with amorphous silica derived from TEOS, in which the enhanced densification was attributed to transient viscous sintering.[14] In the present case, TEM of the gel heated at 900°C shows that the alumina particles were individually dispersed in a porous silica glass matrix. Density measurement and TEM observation also indicate that during the densification process, fine pores in the silica matrix gradually collapsed and dense silica regions were formed. Moreover, the reduction in total porosity was accompanied by formation of larger interconnected pores, while the morphology of the submicron alumina particles remained unchanged. The densification mechanism consisted of viscous flow of the amorphous silica matrix, followed by rearrangement of the dispersed solid alumina particles. It is clear that at 1300°C the viscosity of the silica glass is low enough to allow collapse of remaining pores and mass transport around the alumina particles. The solid alumina particles are expected to reduce the densification rate by retarding viscous flow. However, TEM observations show that the alumina particles are well separated and do not form an interlocking network,

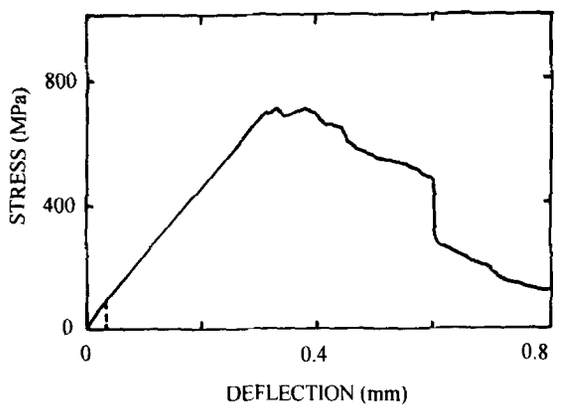

Fig. 6. A typical loading stress against deflection curve (three point bending test) for the unidirectional carbon fibre reinforced composite with the alumina–silica mixture matrix, hot-pressed at 1400°C at 17 MPa for 0·5 h, using a bar specimen with a span of 40 mm and a span to thickness ratio greater than 20. The broken line shows the curve of the bulk matrix material.

Fig. 7(a) an SEM of the fracture surface of a composite specimen after three point bend test; (b) a TEM of an interface of the composite. The bars denote 100 μm for (a) and 0·1 μm for (b). The unidirectional carbon fibre reinforced composite with the alumina–silica mixture matrix was consolidated by hot-pressing at 1300°C for 1 h at 25 MPa.

which probably explains why few residual pores were retained in the microstructure prior to crystallisation of the silica to cristobalite, and the reaction of the silica and alumina to form mullite. Mullitisation started at temperatures above 1400°C following complete densification, because of the reaction of submicron alumina particles with the silica phase. The presence of occasional unreacted alumina surrounded by the mullite and the pockets of residual silica at mullite triple grain junctions in the sample fired at 1600°C is thought to be caused by the slow diffusion rate across the mullite matrix by the end of the mullitisation.

The gradual decrease in bulk density with firing temperatures above 1300°C was noted elsewhere[7,8] and was attributed mainly to the density change caused by mullitisation, although enhanced formation of cristobalite at the higher firing temperatures, which inhibited the densification, may have been partly responsible.[8]

The matrix in the present composite samples was the alumina–silica mixture which was not converted into crystalline mullite at the processing temperatures of 1300 and 1400°C. Mullite matrix composites can be formed by hot-pressing at higher temperatures, which has been reported elsewhere[9] and the properties of these composites will be discussed in detail in a later publication. The flexural strength and elastic modulus of the composites are somewhat lower than those theoretically predicted by the rule of mixtures, according to the following equations:

$$\sigma_c = \sigma_m V_m + \sigma_f V_f \quad (1)$$

$$E_c = E_m V_m + E_f V_f \quad (2)$$

Here the subscripts c, m and f refer to the composite, matrix and fibres respectively. The observation of thermally induced transverse cracks in the matrix indicates that the matrix strength is low and that the first term in eqn (1) may be neglected. However, the experimental strengths remain much lower than the theoretical values (Table 1) which may be explained by some degradation in the strength of the carbon fibres during hot-pressing. On the other hand, the predicted and measured elastic moduli of the composite are in a reasonable agreement, also neglecting the effect of the matrix in eqn (2).

The non-brittle-mode failure of the composite was clearly shown by the loading stress against deflection curve (Fig. 6), and the extensive fibre pull-out (Fig. 7(a)) on the tensile side in the fracture surface after the three point bend test. This suggests a comparatively weak interfacial bond between the fibres and the matrix, which is supported by no apparent evidence of chemical interactions at the interface from TEM observation Fig. 7(b).

Conclusions

Bulk gels corresponding to an oxide (mullite) composition, $3Al_2O_3{\cdot}2SiO_2$, were fabricated using submicron α-alumina powder and colloidal silica sol as precursors and characterised after heat-treatment by density measurement, XRD, SEM and TEM. Bulk gels were sintered to almost full density ($3{\cdot}23 \times 10^3$ kg/m^3, over 99% of the theoretical value of $3{\cdot}25 \times 10^3$ kg/m^3) at the relatively low temperature of 1300°C. From TEM and other observations, the densification mechanism clearly consisted of viscous flow of the amorphous silica matrix and rearrangement of well dispersed solid alumina particles, which did not form an interlocking network.

X-ray diffraction revealed increasing amounts of cristobalite for heat treatments above 1200°C. Mullite was detected around 1450°C and was dominant after 2 h at 1600°C, with a trace of unreacted alumina and cristobalite just detectable. After 2 h at 1600°C an uniform microstructure of mullite grains with diameters around 1μm was obtained. The samples remained almost fully densified after mullitisation at 1600°C ($3{\cdot}10 \times 10^3$ kg/m^3 corresponding to approximately 98% of the theoretical density of $3{\cdot}17 \times 10^3$ kg/m^3 for mullite).

A sol–gel route for processing continuous unidirectional fibre composites was developed involving a simple single stage infiltration process followed by hot-pressing and avoiding the multiple impregnation often required in the use of sol–gel methods.[15]

Efficient fibre infiltration with reduced processing shrinkages was achieved by using the low viscosity sol with a high solid yield, prepared from submicron alumina powder and colloidal silica sol as precursors. The method also gave a uniform distribution of fibres and enabled the volume fraction of fibres to be adjusted. Densification of 98% to a matrix consisting mainly of alumina particles and silica glass was achieved by hot-pressing at the relatively low temperature of 1300°C.

The composites exhibited non-brittle fracture with a mean flexural strength, under three point bending, of 720 MPa for hot-pressing at 1300°C and 766 MPa for hot-pressing at 1400°C, Extensive fibre pull-out was observed after testing, indicating a relatively weak bond between the fibres and the matrix. This was supported by TEM observations which revealed a clear defined fibre/matrix interface and no evidence of chemical interactions.

Acknowledgements

Thanks are due to the Chinese Government and the British Council for financial support (J. Wu) and to the Dupont company for the supply of Ludox colloidal silica sol.

References

1. Sacks, M. D. Lee, H. W. & Pask, J. A., A review of powder preparation methods and densification procedures for fabricating high density mullite, *Ceram. Trans. Vol. 6. Mullite and Mullite Matrix Composites*, ed. S. Somiya, R. F. Davis & J. A. Pask, 1990, pp. 167–207.
2. Sing, R. N. & Gaddipati, A. R., Mechanical properties of a uniaxially reinforced mullite–silicon carbide composite. *J. Am. Ceram. Soc.*, **71** (1988) C100.
3. Yoldas, B. E., Mullite formation from aluminium and silicon alkoxides, *Ceram. Trans. Vol. 6. Mullite and Mullite Matrix Composites*, ed. S. Somiya, R. F. Davis & J. A. Pask, 1990, pp. 255–62.
4. Taylor, A. & Holland, D., The chemical synthesis and crystallisation sequence of mullite, *J. Non-Crystalline Solids*, **152** (1993) 1–17.
5. Chen, M., James, P. F., Jones, F. R. & Bailey, J. E., Alumina ceramic matrices for fibre composites prepared by modified sol–gel processing, *Inst. Phys. Conf.*, Ser No. 111, 1990, pp. 227–37.
6. Qi, D. & Pantano, C. G., Sol–gel processing of carbon-fiber-reinforced glass matrix composites. In *3rd Int. Conf. on Ultrastructure Processing of Ceramics, Glasses and Composites*, ed. J. D. Mackenzie & D. R. Ulrich. J. Wiley & Sons, NY 1987, pp. 635–49.
7. James, P. F., Wu, J., Chen, M. & Jones, F. R., Preparation of mullite using transient viscous sintering of alumina with sol–gel derived silica, presented at Conference on Advances in Amorphous State Chemistry, Dec. 1992, London (Society of Glass Technology & Royal Society of Chemistry), *Topical issues in Glass*, Vol. 1, April 1993, p. 77.
8. Wu, J., Chen, M., Jones, F. R. & James, P. F., Mullite and alumina–silica matrices for composites by modified sol–gel processing. *J. Non-Crystalline Solids*, **162** (1993) 197–200.
9. Wu, J., Jones, F. R. & James, P. F., Mullite matrix fibre reinforced composites by sol–gel processing, presented in 96th Am. Ceram. Soc. Annual Meeting, April 1994, Indianapolis, USA; *Ceram. Trans. Vol. 46: Advances in Ceramic Matrix Composites*, II, 1995, pp. 177–87.
10. Mouchon, E. & Colomban, Ph., Oxide ceramic matrix/oxide fibre woven fabric composites exhibiting dissipative fracture behaviour. *Composites*, **26** (1995), 175–82.
11. *British Standard Methods of Testing, Method 1005*, Determination of flexural properties–three point method, (British Standards Institution) BS 2782; Part 10; Method 1005; 1977, EN63.
12. Wang, J. G. Ponton, C. B. & Marquis, P. M., Effect of green density on crystallization and mullitisation in the transiently sintered mullite. *J. Am. Ceram. Soc.* **75** (1992) 3457–61.
13. Sosman, R. B., The Properties of Silica, *A. C. S. Monograph Series*, No. 37, New York: Chemical Catalog Co., 1927, p. 289.
14. Sacks, M. D., Bozkurt, N. & Scheiffele, G. W., Fabrication of mullite-matrix composites by transient viscous sintering of composite powders. *J. Am. Ceram. Soc.*, **74** (1991) 2428–37.
15. Sheppard, L. M., Enhancing performance of ceramic composites, *Am. Ceram. Soc. Bull.*, **71** (1992) 617.

Journal of the European Ceramic Society 16 (1996) 627–635

0955-2219(95)00179-4
0955-2219/96/$15.00

Sintering Behaviour of Precursor Mullite Powders and Resultant Microstructures

F. Kara* & J. A. Little

Department of Materials Science and Metallurgy, University of Cambridge, Cambridge CB2 3QZ, UK

(Received 5 April 1995; revised version received 14 September 1995; accepted 29 September 1995)

Abstract

Crystallization and sintering behaviour of two structurally different diphasic precursor mullite powders were studied. Powder derived from boehmite and colloidal silica formed mullite at around 1250°C and could be sintered to high density at this temperature by viscous flow sintering. Calcination of the powder up to 1000°C did not affect its sinterability but the weight loss decreased from 20% for the uncalcined powder to 5% for the 1000°C calcined powder. In contrast, powder derived from aluminium sulfate and colloidal silica formed mullite at around 1200°C and did not sinter much by the viscous flow, but showed enhanced solid-state sintering behaviour compared with crystalline mullite powders. Calcination of the powder at temperatures below mullite formation temperature did not affect its sinterability. Microstructural examinations revealed that dense mullite obtained by sintering of powder derived from aluminium sulfate–colloidal silica had much finer grain size (~135 nm) than that obtained from the boehmite–colloidal silica mixture (~1500 nm) and the fine grain size of the mullite was stable up to 1300°C upon long heat treatments (120 h).

1 Introduction

Although it has long been known in refractories, mullite has recently also emerged as an important ceramic material for electronic, optical and high-temperature structural applications owing to its attractive properties such as high creep resistance, retention of strength up to high temperatures, low thermal expansion, density and dielectric constant, and infra-red transparency at medium wavelengths.

Dense mullite ceramics can be produced by various methods including reaction sintering of alumina–silica mixtures and solid-state sintering of fine crystalline mullite powders. Fine crystalline mullite powder compacts require high temperatures (≥1600°C) to enable them to be sintered to high density. This is due to the low inter-diffusion rates of aluminium and silicon ions in mullite.[1] Reaction sintering temperatures of mullite precursors vary depending on the scale of mixing.

(a) Micrometre-scale alumina–silica mixtures require temperatures >1600°C for sintering and mullite formation.[2]

(b) Mixtures of fine α-Al_2O_3 and amorphous silica can be sintered to full density at ~1300°C by viscous flow of the amorphous phase. Completion of mullite formation in these mixtures in a reasonable time requires temperatures of ~1600°C.[3,4]

(c) Similarly, gels prepared from nanometre-scale (diphasic) mixtures of alumina and silica (e.g. a mixture of boehmite (AlOOH) and colloidal silica) can also be sintered to almost full density at ~1250°C by the viscous flow. However, conversion to mullite can be achieved at much lower temperatures than α-Al_2O_3–silica mixtures (1300–1350°C)[5–8] due to the finer scale of mixing of the diphasic mixtures.

Due to the intrinsic presence of crystal water, gels or powders that are prepared by using boehmite undergo large weight losses due to the decomposition of boehmite above 400°C. Such large weight losses have been observed to cause cracking of small pellets[9] and in sintering of large compacts this would be an even greater problem. In addition, the heating rate would have to be slow during sintering. Therefore, the calcination of the powders above the boehmite decomposition temperature becomes necessary to reduce weight losses. Calcination at high temperatures may also decrease the surface area of the powders which improves their processability.

In this study, two types of diphasic powders, varying in the size of the alumina component, were prepared from boehmite–colloidal silica and

*Now with Anadolu Üniversitesi, Yunusemre Kampüsü, Seramik Müh. Böl., 26470 Eskisehir, Turkey.

aluminium sulfate–colloidal silica mixtures. Their crystallization behaviour, powder characteristics, sintering behaviour after calcination at various temperatures and microstructures were studied and compared.

2 Experimental

Mullite precursor powders were produced from two different aluminium sources by the sol–gel method. A commercial pseudoboehmite powder (Cerasol, AlOOH, 99·96%, BA Chemicals, Buckinghamshire, UK) and aluminium sulfate [$Al_2(SO_3)_3 \cdot 16–18H_2O$, 99·4%, BDH Chemicals, Poole, UK] were used as the alumina source. The silica source was high purity colloidal silica (BDH Chemicals, Poole, UK).

Powder A was prepared from pseudoboehmite (surface area of 170 $m^2\ g^{-1}$) and colloidal silica (surface area of 200 $m^2\ g^{-1}$). An AlOOH sol was obtained by dispersing the boehmite powder in water for 0·5 h. The pH of the as-dispersed sol was 3·4. A silica sol was prepared by dispersing the colloidal (or fumed) silica powder in water for 0·5 h at pH 7 (adjusted by NH_4OH). The silica sol was added into the AlOOH sol under vigorous mixing by a high speed mixer and mixing was continued for 0·5–1 h. The mixture was kept in an oven at 60–80°C for gelation and drying. The dried gel fragments were crushed and ground by a motor-driven pestle and mortar, calcined at 550 and 1000°C for 2 h and then milled in methanol using ZrO_2 or alumina balls in polyethylene jars. Milling by ZrO_2 or alumina balls did not cause any detectable contamination [verified by electron probe microanalysis (EPMA) (SX50 Cameca)] or changes in the microstructure. The drying of the milled powder was carried out in an oven at 80°C.

Powder B was prepared from aluminium sulfate and colloidal silica. The alumina sol was prepared by dissolving aluminium sulfate in water. The pH in the as-dissolved condition was 2·2. The silica sol (pH 7) was then added into the alumina sol under vigorous mixing. The mixture was kept in an oven at 125°C for gelation and drying. The gel fragments were then crushed and ground by the motor-driven pestle and mortar and calcined at high temperatures (>850°C) to decompose the aluminium sulfate. Powder B was milled under the same conditions as powder A.

The sintering experiments were carried out by pressing powders into pellets (10 or 13 mm in diameter) in a die at 100 MPa which were then isopressed at 450 MPa. No pressing aid was used. All the sintering experiments were done in still air and the heating rate during sintering was 5°C min^{-1}.

The surface area and particle size of the powders were measured by the BET method using nitrogen gas absorption (Micromeritics Asap 2000) and a laser diffraction particle size analyser (Malvern, Master Sizer), respectively. The Al_2O_3/SiO_2 ratio of the sintered compacts was obtained by EPMA.

The crystallization behaviour of both powders was studied by X-ray diffraction (Philips PW 3719) after calcining them at various temperatures for a constant time.

Green and sintered densities were measured from the dimensions of the as-pressed pellets and by the water immersion technique based on Archimedes' principle, respectively. At least three samples were measured and an average was taken. Relative bulk densities were calculated by taking the theoretical density of mullite as 3·17 g cm^{-3} (JCPDS Card No: 15-776) . The difference between the relative densities of the pellets which were treated under the same conditions was always <0·5% and mostly <0·2%.

Microstructural examinations were carried out by transmission electron microscopy [(TEM) Philips 400ST].

3 Results and Discussion

Since mullite is a solid solution of alumina and silica, the production of mullite free from defects (e.g. glassy phase, cristobalite or alumina) from aluminium- and silicon-bearing compounds requires the mixing of these homogeneously. Homogeneous mixing between boehmite and silica sols can be obtained by heterocoagulation. Heterocoagulation is achieved by the preparation of stable sols of alumina and silica with opposite surface charges (ζ potential). AlOOH particles at pH 3·4 and silica particles at pH 7 bear a net positive and negative surface charge, respectively,[10] and thus mixing of these should result in maximum contact between boehmite and silica particles.

The particle size of boehmite calculated from its surface area (170 $m^2\ g^{-1}$, given by the supplier) was ~12 nm while TEM examination showed it to be ~20 nm. The particle size of colloidal silica calculated from its measured surface area (200 $m^2\ g^{-1}$) was 14 nm. Therefore, when positively charged boehmite particles are mixed with negatively charged silica particles, the silica particles are expected to surround the boehmite particles, as in Fig. 1(a).

In the case of powder B, the situation is slightly different. When aluminium sulfate is dissolved in water, it undergoes hydrolysis and condensation reactions. Under the acidic conditions (pH 2), which are used here, the condensation reactions

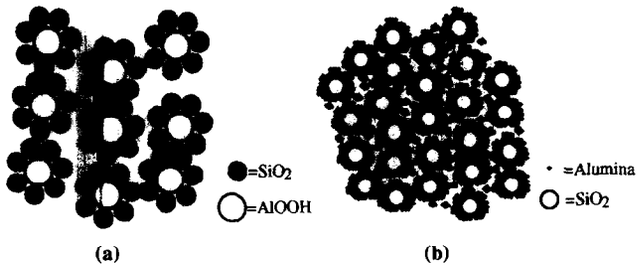

Fig. 1. Schematic representation of the expected particle arrangement of alumina and silica when (a) boehmite and (b) aluminium sulfate is used as the alumina source.

are suppressed while the hydrolysis reactions are dominant.[11] Therefore, the alumina particles derived from aluminium sulfate should be much smaller than the boehmite particles. Therefore, the mixing of the alumina sol from aluminium sulfate with the silica sol should result in the surrounding of silica particles with the aluminium oxide particles, as in Fig. 1(b).

The alumina content of mullite derived from both powders, measured by EPMA, was 72·2 wt%.

3.1 Crystallization

The development of crystalline phases from the AlOOH and colloidal silica mixture (powder A) on heating is shown in the corresponding X-ray traces in Fig. 2. At 1225°C after 2 h, the main phases present were δ-Al_2O_3 and an amorphous phase (a broad peak at around $2\theta = 20°$). After 2 h at 1250°C, the formation of mullite took place from the reaction between δ-Al_2O_3 and the amorphous phase. Although not shown in Fig. 2, the formation of mullite was not observed after 15 min at 1250°C. This indicates that mullite formation occurred after an incubation period as pointed out by others.[12–14] The incubation period was the time taken for the dissolution of transitional alumina into the amorphous phase (from which mullite nucleates[15]) to reach the critical nucleation concentration.[12,14,15] After 1300°C for 2 h, the extent of mullite formation increased with the consumption of δ-Al_2O_3 and amorphous silica but some θ-Al_2O_3 was still present. The presence of θ-Al_2O_3 together with mullite is attributed to large boehmite particles (or undispersed boehmite agglomerates) present in the starting materials which were not able to react at short times. On further heating to 1420°C for 5 h, the only crystalline phase present was mullite. The crystallization of mullite without the individual crystallization of α-Al_2O_3 and/or cristobalite indicates that the mixing method employed provided a very good degree of mixing between boehmite and silica particles.

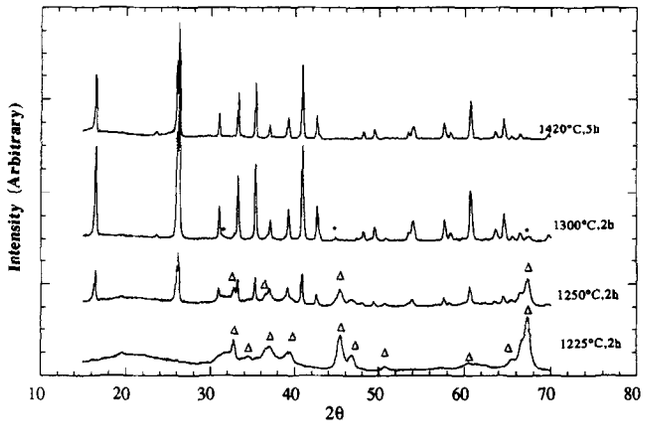

Fig. 2. Development of crystallization of powder A. (Δ) δ-Al_2O_3, (*) θ-Al_2O_3. Some of the δ-Al_2O_3 peaks at 1250°C are not labelled. Mullite peaks are not labelled.

Figure 3 shows TEM defocus images of a powder A compact sintered at 1250°C for 2 h. The amorphous phase, which shows bright contrast when imaged under-focus, was distributed homogeneously in the microstructure and surrounded the δ-Al_2O_3 particles. (An amorphous low density phase shows bright and dark contrast in under-focus and over-focus conditions, respectively.[16]) This further confirms that the processing conditions resulted in homogeneous mixing.

The development of crystallization of powder B has been reported earlier.[17] A large amount of mullite formation was observed at 1200°C in the presence of γ-Al_2O_3 type spinel and an amorphous phase. The formation of δ-Al_2O_3 and θ-Al_2O_3 was not observed.

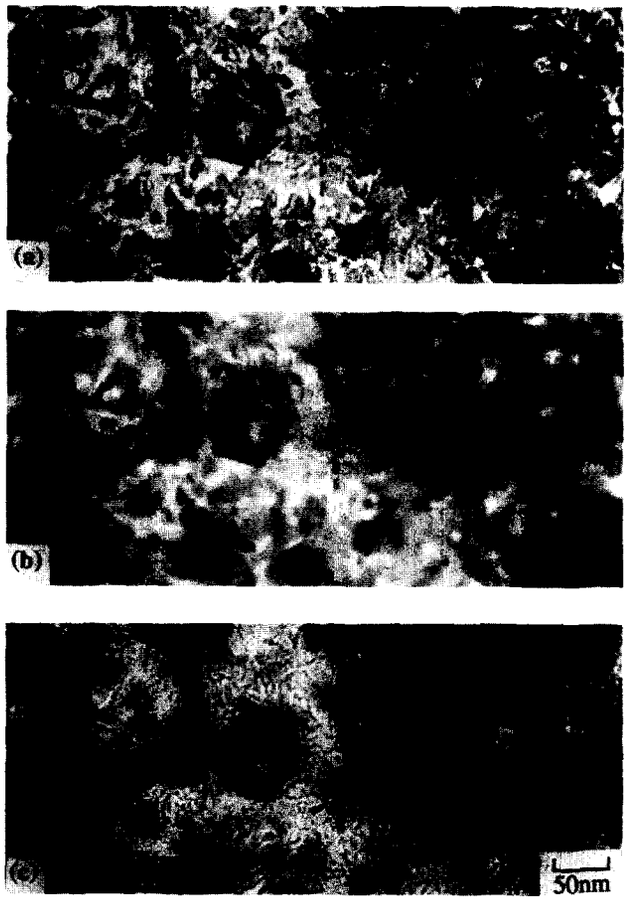

Fig. 3. TEM bright-field defocus images of a powder A compact sintered at 1250°C for 2 h: (a) under-focus (–220 nm), (b) near focus and (c) over-focus (2200 nm).

The mullite formation temperature of powder B was slightly lower than that of powder A or rather, more correctly, the rate of mullite formation at a given temperature and time was higher in powder B than in powder A. For instance, mullite formation was also observed in diphasic mixtures similar to powder A at temperatures as low as 1190°C but only after long-term isothermal heat treatment (24 h).[18] As the dissolution of alumina in the amorphous phase is rate-controlling for mullite formation and growth,[14,15] the higher rate of mullite formation in powder B can be explained by the smaller size of the alumina particles which results in higher rate of solubility at a given temperature. Therefore, more alumina becomes available for mullite formation.

3.2 Powder characteristics

The change in the surface area of each powder with calcination temperature is shown in Fig. 4. Both powders had a very high surface area which decreased with increasing calcination temperature. Assuming that powder A calcined at 550°C and powder B calcined at 940°C were mullite, the particle size of powders A and B calculated from their surface areas was 10 and 13 nm, respectively. However, both powders calcined at their respective temperature were not mullite (e.g. powder A calcined at 550°C should contain γ-Al_2O_3 and amorphous silica, both with different surface area and density). Therefore, the calculated particle size values should be considered as an approximation.

Figure 5 shows the particle size distribution of powders A and B, measured by the particle size analyser after milling for 24 h. The average particle size of both powders was ~ 2 μm. The large difference between the particle sizes calculated from the surface area and measured by the particle size analyser indicates agglomeration of nanometre-size particles.

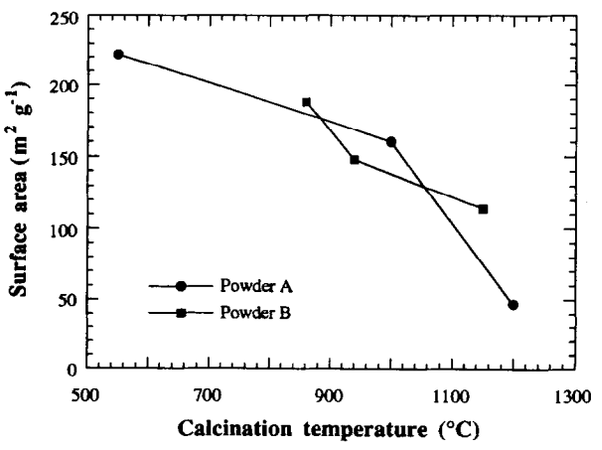

Fig. 4. Change in surface area of powders A and B with calcination temperature.

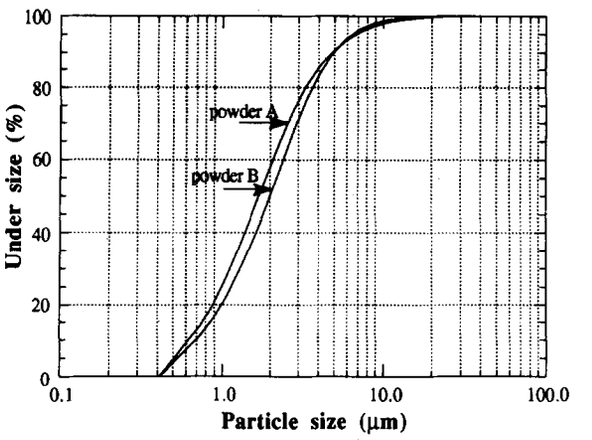

Fig. 5. Particle size distribution of powders A and B after milling in methanol for 24 h.

3.3 Sintering studies

3.3.1 Sintering of powder A

The compacts had a green density of ~45% after isopressing at 450 MPa. The effect of isothermal heat treatment on bulk density and open porosity of compacts prepared from powder A calcined at various temperatures is shown in Fig. 6. There was a sharp increase in density above 1100°C with the total elimination of open porosity at 1250°C. The location of the amorphous phase around the alumina particles and in the alumina particle grain junctions in Fig. 3 confirms that the sintering mechanism was the viscous flow of the amorphous phase. Therefore, the sharp increase in density can be attributed to the sharp decrease in the viscosity of the amorphous phase (silica-rich) with temperature. The increasing dissolution of alumina in amorphous silica also contributes to the decrease in viscosity.[19] The density of the compacts sintered at 1250°C was 3·01 g cm^{-3} (~95%). With the extensive formation of mullite above 1250°C (Fig. 2), the sintering almost stopped with only a further 3% increase in density between 1250 and 1600°C.

Optical microscope examinations of the polished surfaces of compacts sintered at 1250°C

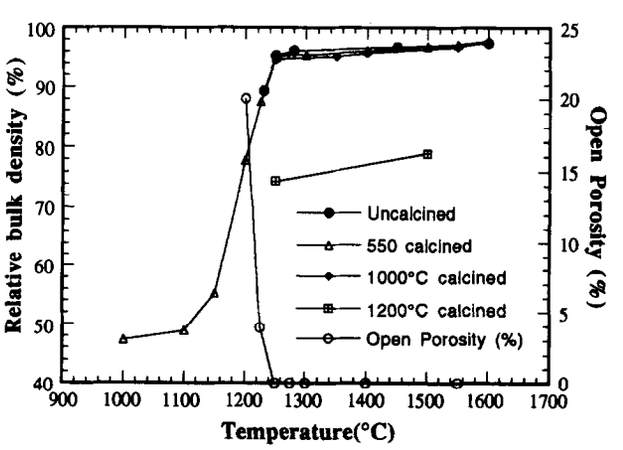

Fig. 6. Change in bulk density and open porosity of powder A compacts with sintering temperature. Sintering time is 2 h.

Fig. 7. TEM bright-field micrograph of a powder A compact sintered at 1250°C for 2 h showing the presence of micropores (some arrowed) scattered in the material.

Fig. 8. TEM bright-field micrograph of a powder A compact sintered at 1275°C for 2 h showing that pores present in the diphasic matrix are engulfed by mullite grains. White features inside the black mullite grain (M) are the pores.

showed almost no porosity although they were only 95% dense. This was due to the very small size of the pores (~30–35 nm with some as large as ~70 nm) as shown in Fig. 7, which were not resolvable in the optical microscope. The dense nature of the diphasic matrix around these pores suggests that they were the large pores inherited from the green compact. They are likely to be the result of some hard agglomerates which may be present in the powder. This is because the presence of hard agglomerates in powders causes the formation of inhomogeneous green compacts by creating two types of pores:[20] inter-agglomerate and intra-agglomerate (the pores between primary particles within the agglomerates), the latter being smaller than the former. This causes differential shrinkage and enlargement of inter-agglomerate pores since the intra-agglomerate pores are eliminated more rapidly or at a lower temperature due to their smaller size.[20] Then, the inter-agglomerate pores are eliminated, which need longer times and/or higher temperatures. It appears that these large pores could not be eliminated before mullite formation.

With the formation of mullite, the pores became engulfed by growing mullite grains as shown in Fig. 8. The mullite grain size was ~1·5 μm as shown in the figure. The elimination of the engulfed pores has to take place by diffusion of vacancies through the mullite lattice to reach the grain boundaries. Only ~3% pore elimination between 1250 and 1600°C indicates the difficulty of diffusion in the mullite lattice. Clearly, the elimination of the hard agglomerates will eliminate the large pores in the green compacts and full densification will become possible at 1250°C. For example, powders prepared by supercritical drying, which were proposed to be weakly agglomerated, sintered to ≥98% density at 1250°C.[8] If the large pores are not eliminated in the green state, high temperatures (≥1550°C) are needed for their removal.

The sintering behaviour of powder A calcined at various temperatures has already been included in Fig. 6, while Fig. 9 shows the effect of calcination temperature on sintered density at 1250°C and also on the overall weight loss of the pellets. As can be seen in these two figures, calcination temperatures up to 1000°C did not affect the sinterability of the powder but the weight loss decreased from 20% for the uncalcined powder to just over 5% for the 1000°C calcined powder. However, compacts prepared from powder calcined at 1200°C could only be sintered to 75% at 1250°C. This could be due to two reasons: (a) a decrease in the surface area of silica (as it is responsible for densification) and (b) formation of hard agglomerates during calcination which is unfavourable for packing. The occurrence of a substantial amount of sintering at 1200°C [in the

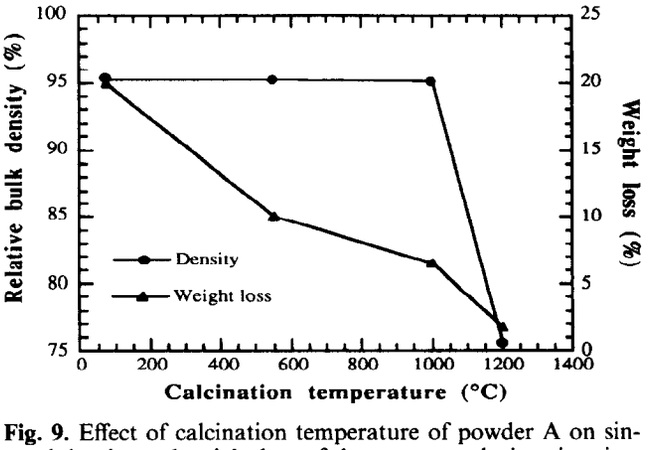

Fig. 9. Effect of calcination temperature of powder A on sintered density and weight loss of the compacts during sintering. Sintering is at 1250°C for 2 h.

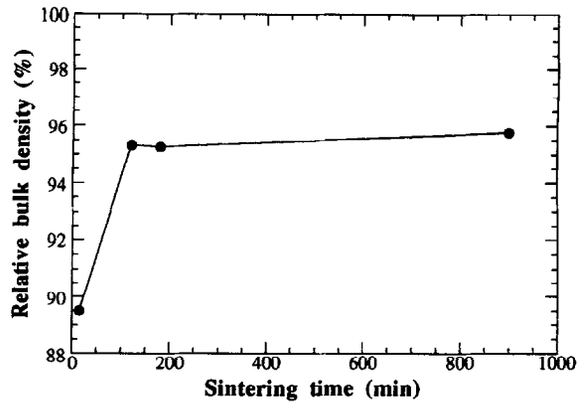

Fig. 10. Effect of sintering time on the sintered density at 1250°C.

powders calcined at ≤1000°C (Fig. 6)] is expected to cause extensive hard agglomerate formation during calcination at 1200°C. The density of 1200°C calcined compacts did not improve much on further increasing the sintering temperature to 1500°C, only 5% pore elimination taking place.

The effect of isothermal heat treatment time at 1250°C on sintered density is shown in Fig. 10. The densification at 1250°C takes place rather quickly and as high as 90% densification was achieved within 15 min. There was almost no difference in density between compacts sintered for 2 h and 15 h. This was not unexpected as mullite formation takes place after about 2 h and the densification mechanism changes into diffusion controlled. The diffusivities of related species in mullite at 1250°C are not expected to be significant.

3.3.2 Sintering of powder B

Figure 11 shows the effect of temperature on the relative bulk density of powder B compacts sintered for 5 h. There were two distinct stages of sintering. In the first stage, the densification was due to viscous flow as in powder A, where the compacts started to densify above 1100°C and showed a sharp increase in density with increasing temperature. However, since mullite formation in powder B takes place at a slightly lower temperature (~1200°C) than in powder A (1250°C), the viscous flow was disrupted at an earlier stage of sintering. Thus, powder B compacts could not be sintered to as high a density as powder A compacts by the viscous flow. The alumina–silica particle arrangement of powder B is also expected to have a detrimental effect on the densification rate in the first stage because silica surrounded by alumina is less effective for sintering due to disrupted connectivity of the viscous phase.[7] The maximum density achieved in this stage was only 70%. In the second stage (in the presence of mullite), the densification took place via solid-state diffusional processes. The temperature dependence of sintering was lower than the first stage (compare the slopes in both stages).

Figure 12 shows the effect of the magnitude of isopressure on green density and on sintered densities at various temperatures. Higher compaction pressures resulted in higher green densities and, in turn, higher sintered densities. However, the effect of green density became less pronounced with increasing temperature for a given sintering time. With the employment of isopressures as high as 1 GPa for compaction of the powder (which results in 58% green density), densities of up to 97% were achieved at temperatures as low as 1450°C.

The effect of calcination temperature on sinterability of powder B was reported earlier.[17] It was found that the sinterability of the powder was not affected when calcined up to a temperature below which there was no mullite formation (1100°C). However, if the powder was calcined at a high enough temperature to form mullite then the sinterability of the powder was reduced dramatically, demonstrating the improved sinterability of powder B when it does not contain mullite.[17] The improved sinterability of the green compacts not containing mullite compared with those made

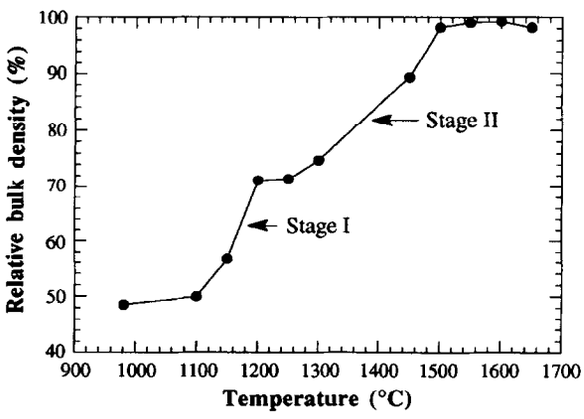

Fig. 11. Change in sintered density of powder B compacts with temperature. Sintering time is 5 h.

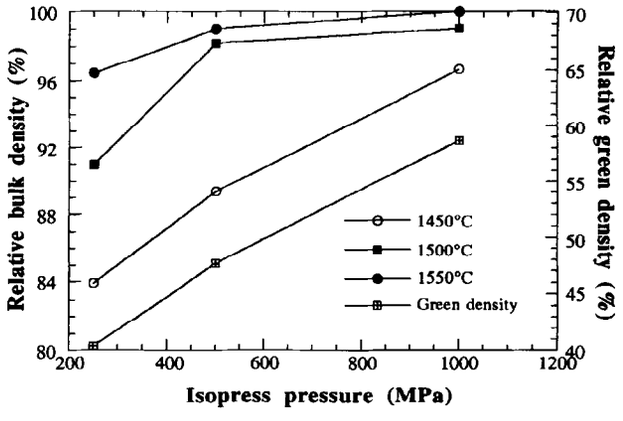

Fig. 12. Effect of isopress compaction pressure on green and sintered densities at various temperatures. Sintering time is 5 h.

from the crystalline mullite powder during solid-state sintering (stage II) (even though the mullite grain size is the same) can be attributed to the following factors :

(a) amorphous or weakly crystalline powders not containing mullite can be compacted to a smaller pore size and narrower pore size distribution due to their deformability at the contact point and due to their smaller size (i.e. better green microstructure),[21]

(b) limited viscous flow sintering causes an increase in density before solid-state sintering whereas crystalline mullite powder compacts do not show any densification up to 1400°C.[22–24]

The densification curves of powders A and B together with a fine crystalline mullite powder are compared in Fig. 13. Although powder B compacts had much more porosity to eliminate than powder A compacts by solid-state sintering (i.e. above 1250°C), powder B compacts sintered to near full density (>98%) at a lower temperature than powder A compacts. This was due to the fact that pores (engulfed inside mullite grains) in powder A compacts had to diffuse through 1·5 μm grain size mullite to reach the grain boundaries (Fig. 8), while the pores in powder B compacts were located at the multiple grain junctions as shown in Fig. 14. Even if they were located inside mullite grains, they would not have had to diffuse a long distance to reach the grain boundaries because the grain size was much finer (~0·15 μm) (Fig. 14). In addition, increased grain boundary area due to the fine grain size in powder B compacts should result in faster diffusion due to the availability of more diffusion channels. Entrapment of pores inside growing mullite grains during crystallization also appears to be the basic reason why 75% dense powder A compacts did not densify more than 5% between 1250 and 1500°C (Fig. 5).

The comparison of the sintering curves of powders A and B with that of the crystalline mullite powder in Fig. 13 shows that some 300–350°C and 150–200°C reductions in sintering temperature are possible with powder A and B, respectively, when they are reactively sintered.

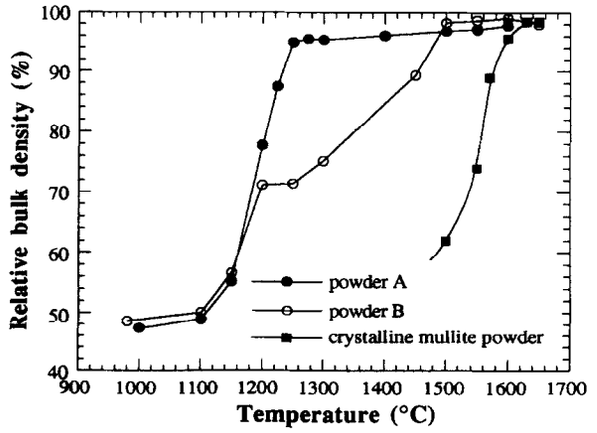

Fig. 13. Comparison of the sintering behaviour of powders A and B together with a crystalline mullite powder. Data for crystalline mullite powder are obtained from Ref. 24.

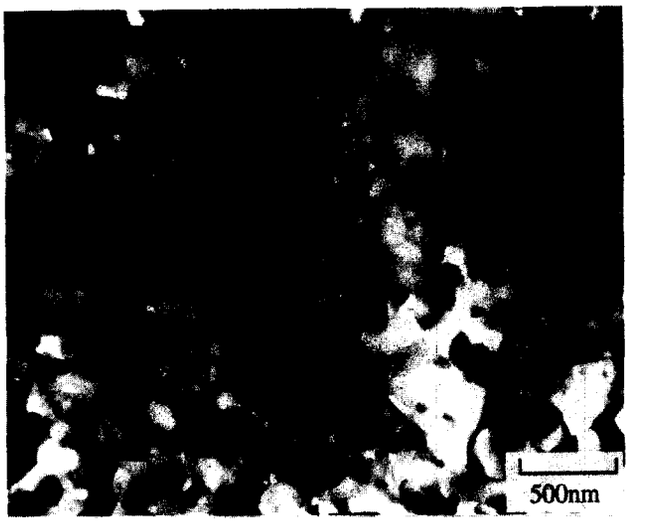

Fig. 14. TEM bright-field micrograph of a powder B compact sintered at 1450°C for 5 h (~95% dense). Arrows indicate the pores.

3.4 Stability of the fine microstructure of sintered powder B compacts

As shown previously, the grain sizes of mullite at low temperatures (where there is no appreciable grain growth) obtained from powder A and B were very different, mullite from powder B having a much smaller grain size. The only difference between the two powders was the size of the alumina particles used for preparation, these being much finer in powder B. Mullite formation from diphasic aluminosilicate mixtures occurs by self-nucleation from an intermediate amorphous aluminosilicate phase after reaching a critical alumina concentration,[25] i.e. alumina particles do not act as heterogeneous sites for mullite nucleation. After nucleation, growth of the nuclei takes place with no secondary nucleation. This means that the higher the nucleation frequency, the lower the mullite grain size. One possibility for the higher nucleation frequency in the presence of finer alumina particles could be that higher contact area between alumina and silica may cause many isolated regions reaching the critical nucleation concentration.

As powder B compacts could be sintered to high density (>95%) at low temperatures (~1450 or 1500°C for short times) when processed appropriately, grain growth of the mullite crystals was avoided (Fig. 14). Such a fine microstructure could be important in certain areas such as superplastic shaping and fibre making. Therefore, further experimental study was carried out to

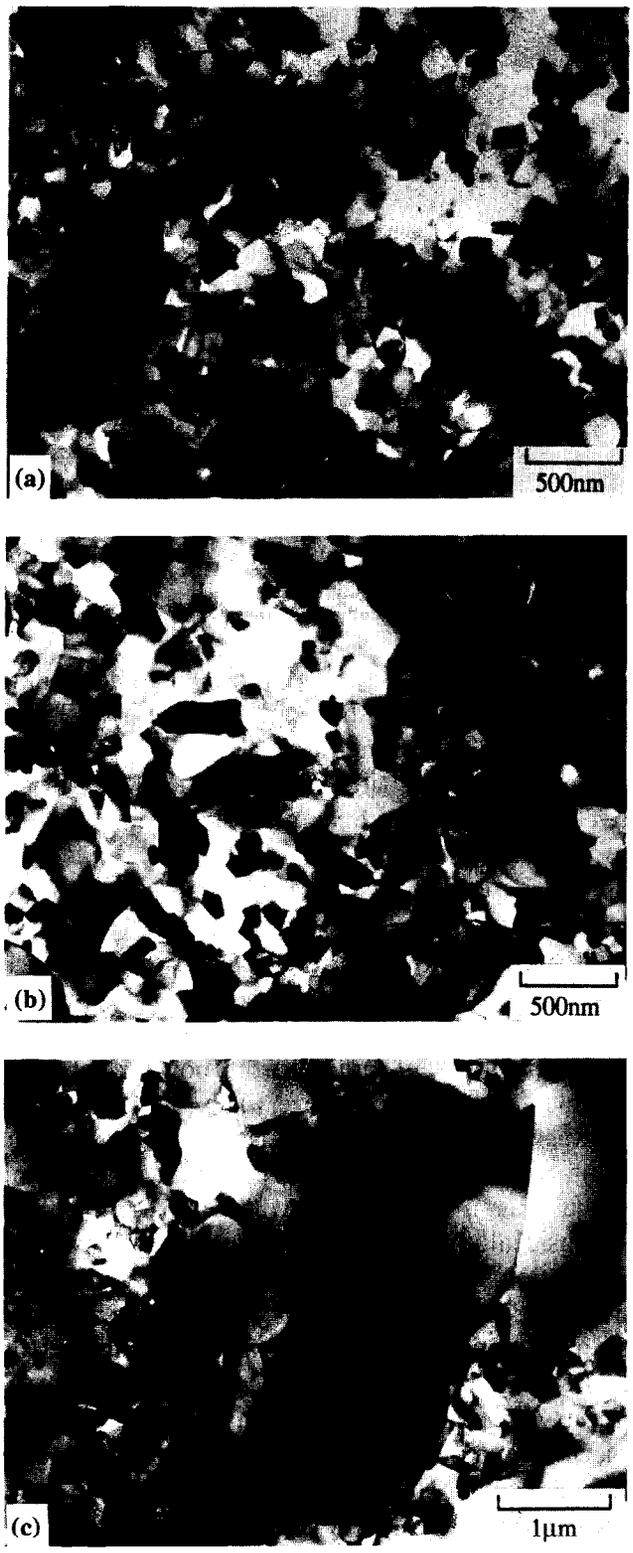

Fig. 15. TEM bright-field micrographs of powder B compacts (sintered at 1450°C for 5 h) after heat treatment at various temperatures for 120 h: (a) 1200°C, (b) 1300°C and (c) 1400°C.

measure the temperature limit of the stability of the fine grain size of the compact which was sintered at 1450°C for 5 h. This was done by conducting a constant period of 120 h heat treatment of the samples between 1200 and 1400°C.

Figure 15 shows TEM bright-field micrographs of mullite heat-treated between 1200 and 1400°C. As can be seen, the grain size did not appear to change up to 1300°C. This was confirmed by grain size measurements in TEM dark-field pictures using an image analyser. The average grain size of the as-sintered mullite (1450°C, 5 h) was ~135 nm, the smallest ever reported for dense polycrystalline mullite ceramics, and that of the 1200 and 1300°C heat-treated mullites was ~145 and 155 nm, respectively. However, at 1400°C although the grain size did not change much (~200 nm), extensive exaggerated grain growth was observed [Fig. 15(c)]. The extent of exaggerated grain growth was generally less than 1 μm, averaging about 0·5–0·7 μm, although in rare instances larger grains were also observed [Fig. 15(c)].

The occurrence of exaggerated grain growth during heat treatment at 1400°C must be due to the growth of very small amounts of larger grains which were already present in the as-sintered material (such as that indicated as A in Fig. 14). A large grain that is present in the matrix of fine grains will grow easily due to geometric (and thus free energy) considerations.[26]

Although fine and to a certain extent curved grain structure (Fig. 14) in powder B derived mullite in general aids grain growth, the stability of its fine microstructure up to ~1300°C can mainly be attributed to the low diffusivities in mullite at this temperature range as the rate of atom movement across the grain boundary is controlled by the diffusivity at grain boundaries.[26]

4 Conclusions

Homogeneously mixed precursor mullite powders were produced from boehmite–colloidal silica and aluminium sulfate–colloidal silica mixtures. The boehmite–silica mixture forms mullite at around 1250°C in the presence of δ-Al_2O_3 and an amorphous phase, and the aluminium sulfate–silica mixture forms mullite at 1200°C in the presence of γ-Al_2O_3 and an amorphous phase.

Sintering studies showed that powder derived from boehmite–silica mixture can be sintered at 1250°C to a high density (>95%) by viscous flow of the amorphous phase. Large pores, thought to be present in the green compact, could not be eliminated before mullite formation and formed the remaining ~5% porosity. With the formation of mullite the pores were engulfed by the growing mullite grains and, as a result, their elimination required high temperatures (≥1550°C). Calcination up to 1000°C did not affect the sinterability of the powder but caused a positive effect of reducing the weight loss during sintering. However, when calcined at 1200°C its sinterability was reduced dramatically.

Powder derived from aluminium sulfate–silica mixture could not be sintered to as high density as boehmite–silica mixture by viscous flow sintering as a result of the formation of mullite at an earlier stage which disrupts the viscous flow. However, sintering of the powder to almost full density was possible at around 1450–1500°C. Calcination temperatures up to 1100°C did not affect the sinterability of the powder. However, when calcined above the mullite formation temperature, its sinterability was reduced.

The nucleation frequency of mullite (and thus the grain size) appears to be governed by the size of the alumina component; the finer the alumina particle size, the higher the nucleation frequency and thus the smaller the mullite grain size. Dense and very fine grained mullite ceramics (<150 nm) can be produced from the powder derived from aluminium sulfate–colloidal silica mixture. The fine grain size was found to be stable up to temperatures of 1300°C or above on longer heat treatments.

References

1. Aksay, I. A. & Pask, J. A., Stable and metastable equilibrium in the system SiO_2–Al_2O_3. *J. Am. Ceram. Soc.*, **58** (1975) 507–12.
2. Boch, P., Chartier, T. & Rodrigo, P. D. D., High purity mullite ceramics by reaction sintering. In *Ceramic Transactions, Vol. 6, Mullite and Mullite Matrix Composites*, ed. S. Somiya, R. F. Davis & J. A. Pask. American Ceramic Society, Westerville, OH, 1990, pp. 353–74.
3. Sacks, M.D., Bozkurt, N. & Scheiffele, G.W., Fabrication of mullite and mullite matrix composite by transient viscous sintering of composite powders. *J. Am. Ceram. Soc.*, **74** (1991) 2428–37.
4. Miao, X. & Marquis, P.M., Vitreous sintering of heterocoagulated alumina silica sols. *Nanostructured Mater.*, **1** (1992) 31–6.
5. Komarneni, S., Suwa, Y. & Roy, R., Application of compositionally diphasic xerogels for enhanced densification: the system Al_2O_3–SiO_2. *J. Am. Ceram. Soc.*, **69** (1984) C155–6.
6. Sonuparlak, B., Sol–gel processing of infrared transparent mullite. *Adv. Ceram. Mater.*, **3** (1988) 263–7.
7. Fahrenholtz, W. L., Smith, D. M. & Cesarano III, J., Effect of precursor particle size on the densification and crystallization behaviour of mullite. *J. Am. Ceram. Soc.*, **76** (1993) 433–7.
8. Jeng, D.-Y. & Rahaman, M. N., Sintering and crystallization of mullite powder prepared by sol–gel processing. *J. Mater. Sci.*, **28** (1993) 4904–9.
9. Kara, F., Processing and characterisation of mullite based ceramics. PhD thesis, University of Cambridge, Cambridge, UK, 1994.
10. Hulling, J. C. & Messing, G. L., Surface chemistry effects on homogeneity and crystallization of colloidal mullite sol–gels. In *Ceramic Transactions, Vol. 6, Mullite and Mullite Matrix Composites*, ed. S. Somiya, R. F. Davis & J. A. Pask. American Ceramic Society, Westerville, OH, 1990, pp. 221-9.
11. Okada, K., Otsuka, N. & Somiya, S., Review of mullite synthesis routes in Japan. *Am. Ceram. Soc. Bull.*, **70** (1991) 1633–40.
12. Wei, W.-H. & Halloran, J. W., Transformation kinetics of diphasic aluminosilicate gels. *J. Am. Ceram. Soc.*, **71** (1988) 581–7.
13. Li, D. X. & Thomson, W. J., Kinetic mechanisms for mullite formation from sol–gel precursors. *J. Mater. Res.*, **4** (1990) 1963–9.
14. Hulling, J. C. & Messing, G. L., Epitactic nucleation of spinel in aluminosilicate gels and its effect on mullite crystallization. *J. Am. Ceram. Soc.*, **74** (1991) 2374–81.
15. Sundaresan, S. & Aksay, I. A., Mullitisation of diphasic aluminosilicate gels. *J. Am. Ceram. Soc.* **74** (1991) 2388–92.
16. Clarke, D. R., On the detection of thin intergranular films by electron microscopy. *Ultramicroscopy*, **4** (1979) 33–44.
17. Kara, F. & Little, J. A., Sintering of pre-mullite powder obtained by chemical processing. *J. Mater. Sci.*, **28** (1993) 1323–6.
18. Wei, W.-H. & Halloran, J. W., Phase transformation of diphasic aluminosilicate gels. *J. Am. Ceram. Soc.*, **71** (1988) 166–72.
19. Bansal, N. P. & Doremus, R. H., *Handbook of Glass Properties*. Academic Press, Orlando, FL, 1986.
20. Sacks, M. D. & Pask, J. A., Sintering of mullite containing materials: II, Effect of agglomeration. *J. Am. Ceram. Soc.*, **65** (1982) 70–7.
21. Kamiya, H., Suzuki, H., Takahiro, T. & Jimbo, G., Ultra-high pressure cold isostatic pressing — low temperature sintering of alkoxide derived mullite precursor powders. *Ceram. Eng. Sci. Proc.*, **13** (1992) 563–70.
22. Mizuno, M. & Saito, H., Preparation of highly pure fine mullite powder. *J. Am. Ceram. Soc.*, **72** (1989) 373–82.
23. Mitachi, S., Matsuzawa, M., Kaneko, K., Kanzaki S. & Tabata, H., Characterisation of SiO_2–Al_2O_3 powders prepared from metal alkoxides. In *Ceramic Transactions, Vol. 6, Mullite and Mullite Matrix Composites*, ed. S. Somiya, R. F. Davis & J. A. Pask. American Ceramic Society, Westerville, OH, 1990, pp. 274–85.
24. Kumazawa, T., Ohta, S., Kanzaki, S. & Tabata, H., Influence of powder characterisation on microstructure and mechanical properties of mullite ceramics. In *Ceramic Transactions, Vol. 6, Mullite and Mullite Matrix Composites.*, ed. S. Somiya, R. F. Davis & J. A. Pask. American Ceramic Society, Westerville, OH, 1990, pp. 401–11.
25. Aksay, I. A., Dabbs, D. M. & Sarikaya, M., Mullite for structural, electronic and optical applications. *J. Am. Ceram. Soc.*, **74** (1991) 2343–58.
26. Kingery, W. D., Bowen, H. K. & Uhlmann, D. R., *Introduction to Ceramics*. Wiley Interscience, New York, 1976.

Journal of the European Ceramic Society 16 (1996) 637–643

0955-2219(95)00182-4
0955-2219/96/$15.00

Phase Equilibria and Crystal Chemistry in the System Sr–Ca–Cu–O Under High Oxygen Pressure

A. D. Robertson, P. V. P. S. S. Sastry* & A. R. West

Department of Chemistry, University of Aberdeen, Meston Walk, Aberdeen AB9 2UE, UK

(Received 31 May 1995; revised version received 27 September 1995; accepted 12 October 1995)

Abstract

Phase equilibria in the system SrO–CaO–CuO have been studied under high oxygen pressures. The recently discovered non-superconducting binary phase, $Sr_{0.74(3)}CuO_2$, which is stable only under high oxygen pressure, forms a complete range of solid solutions with the structurally related phase, $Ca_{0.81(1)}CuO_2$. These materials have complicated superstructures and may form a family of Vernier phases, such as was found in $Sr_{0.74(3)}CuO_2$. Stabilities and oxygen stoichiometries of tetragonal $Sr_{2-2x}Ca_{2x}CuO_{3+\delta}$ ($0.0 \leq x \leq 0.1$) and $Sr_{14-14x}Ca_{14x}Cu_{24}O_{38+\delta}$ ($0.0 \leq x \leq 0.5$) solid solutions under high oxygen pressures are also discussed.

1 Introduction

Discovery of high temperature superconductivity in Sr–Cu–O samples prepared under pressure has renewed interest in the study of Sr–Cu–O and related phase diagrams, under both high isostatic pressure and high oxygen pressures.[1–10] In air, at one bar, there are three phases in the SrO–CuO system with compositions Sr_2CuO_3, $SrCuO_2$ and $Sr_{14}Cu_{24}O_{38+\delta}$, all of which exhibit extensive Ca $\Leftrightarrow$ Sr substitution.[6–11] Hiroi *et al.*[3] and others[4,12,13] reported superconductivity in $Sr_{n+1}Cu_nO_{2n+1+\delta}$ (n = 1, 2, 3...∞), prepared under high isostatic pressures (> 5 GPa), using $KClO_4$ as an oxidiser. Orthorhombic, non-superconducting Sr_2CuO_3, which forms in air at ambient pressure, transforms to tetragonal superconducting $Sr_2CuO_{3+\delta}$ (δ = 0·1), i.e. n = 1, when heated at 800–900°C under high pressure.[3,4,12,13] This phase has a highly oxygen-deficient K_2NiF_4 structure. A similar product prepared at 370°C in flowing oxygen using a copper hydroxometallate precursor, $Sr_2Cu(OH)_6$ had an oxygen excess of δ = 0·29 and was non-superconducting.[14] The orthorhombic to tetragonal phase transformation was also achieved by heating Sr_2CuO_3 at 400°C and 160 bar oxygen pressure.[1] TG analysis showed the oxygen content of these samples to be significantly higher, δ = 0·9, and the samples again non-superconducting.

Singh *et al.*[5] recently published results on the stability of (Ba, Sr, Ca)O–CuO binary phases as a function of oxygen pressure. The conditions used were 1, 15 and 200 bar in the temperature range 880–950°C. $Sr_2CuO_{3+\delta}$, $Sr_{14}Cu_{24}O_{38+\delta}$ and $Ca_{0.8}CuO_2$ were found to be stable under these conditions. We have recently synthesised a new high pressure phase, $Sr_{0.74(3)}CuO_2$, over the range 20–600 bar O_2 and at temperatures below 785°C;[15] this temperature range is significantly lower than that used by Singh *et. al.*[5]

A study of phase formation in the system Sr–Ca–Cu–O, at 950°C, under high isostatic pressures (10 kbar) has been reported by George *et al.*[6] and the results compared with those at 1 bar O_2. The main differences between these two sets of results are on the $SrCuO_2$–'$CaCuO_2$' join. The 'infinite-layer' phase,[16,17] $Sr_{0.15}Ca_{0.85}CuO_2$, and another ternary phase, $Sr_{0.3}Ca_{0.7}CuO_2$, are stable at 1 bar O_2 yet unstable at 10 kbar. In addition, the extent of $Sr_{1-x}Ca_xCuO_2$ solid solution is less at 10 kbar, $0 < x < 0.36$, than at 1 bar O_2, $0 < x < 0.62$.

The aim of our present studies was to better understand the phase equilibria in the Sr–Ca–Cu–O system under high oxygen pressures and to explore the possibility of tuning the oxygen content in different compositions to induce superconductivity. We report here the phase relationships in the system at 775°C and 350 bar oxygen pressure. These are lower temperatures and higher pressures than those used by Singh *et al.*[5] Results on oxygen stoichiometries and crystal chemistry of the various phases are also presented.

2 Experimental

Reagents used were $SrCO_3$ (Fisons, 99%), $CaCO_3$ (BDH, Analar) and CuO (Aldrich, A.C.S. 99+%).

*Permanent address: Chemistry Division, Bhabha Atomic Research Centre, Bombay-400 085, India.

$CaCO_3$ and $SrCO_3$ were dried overnight at 300°C and CuO at 700°C, prior to weighing. Samples were weighed out, ground together in an agate mortar and pestle with acetone to form a paste, dried and fired in gold foil boats at 800–900°C for one night in air to decarbonate. Samples were then reground, pelleted (to promote reaction) and fired at 900°C for one day then 930°C for one day and finally 950°C for a further day, with intermediate regrinding and pelleting, to attain equilibrium and complete reaction in air.

These air-reacted samples were then subjected to further heating under high oxygen pressure. For this, samples were reground, repelleted and portions, 300–600 mg, wrapped in gold foil, placed in a ceramic boat and inserted into a Morris Research Inc. High Oxygen Pressure Furnace, model number HPS 5015E7. The starting pressure was adjusted so as to give the desired pressure, at the final annealing temperature,[15] which was varied from 50 to 600 bar. The temperature was raised at 10°C min^{-1} from 25°C to a maximum of 700–850°C then held for about 16-32 h, to ensure complete reaction, before cooling back to room temperature whilst maintaining pressure. For the SrO–CaO–$CuO_{1+\delta}$ phase diagram study, a uniform annealing temperature of 775°C and a maximum pressure of 350 bar was used.

A Philips PW1710 diffractometer, Cu$K\alpha_1$ radiation, was used for routine crystalline phase identification. For accurate lattice parameter determination, a STOE STADI P diffractometer was used, in transmission mode, with a small linear position sensitive detector (PSD), Ge monochromator and Cu$K\alpha_1$ radiation. Data were collected over the range $10° \leq 2\theta \leq 80°$ with Si as internal standard. Electron diffraction (ED) patterns for selected samples were recorded using a Jeol 2000EX TEMSCAN electron microscope operating at 200 kV.

Compositional analysis was carried out by electron probe microanalysis using a CAMECA SX51 EPMA instrument. Oxygen content was determined for selected samples using a Stanton Redcroft STA 1500 combined TG/ DTA. Samples were reduced using a heating rate of 10°C min^{-1} up to 950°C under an atmosphere of flowing 5%H_2/95%N_2. The reduction reaction can be written as:

$$A_xCu_yO_{x+y+\delta}+(y+\delta)H_2 \rightarrow xAO + yCu + (y+\delta)H_2O$$

where A = Sr, Ca.

Magnetic susceptibility was measured using a Lakeshore AC 7000 Susceptometer.

3 Results and Discussion

The results on each of the binary joins are presented first, followed by results on the ternary system SrO–CaO–CuO, under high oxygen pressures.

3.1 The join SrO–$CuO_{1+\delta}$

Since there have been many studies reported on the phases that form in the system SrO–CuO at both ambient[7,8] and high pressure,[1–6] together with phase diagrams,[5–8] our studies have focused on (a) the stabilities and oxygen contents of the strontium cuprates and (b) the possible occurrence of any new phases. For each of the phases considered, results are as follows:

3.1.1 $SrCuO_2$ (1 : 1 phase)

Our results show that this phase is stable at all temperatures studied (ambient to 850°C) up to a maximum oxygen pressure of 50 bar. At higher pressures, $SrCuO_2$ decomposes to give a mixture of two other strontium cuprates, the nature of which is temperature dependent. At temperatures greater than 785°C, $SrCuO_2$ decomposes to a mixture of 2 : 1 and 14 : 24, in accordance with the results of Singh *et al.*[5] At temperatures lower than 785°C, $SrCuO_2$ decomposes to give a mixture of 2 : 1 and the new binary phase, $Sr_{0.74(3)}CuO_2$.

3.1.2 Sr_2CuO_3 and $Sr_2CuO_{3+\delta}$(2 : 1 phase)

Orthorhombic Sr_2CuO_3 is stable in air[7–9] and at high isostatic pressures[6] but transforms to tetragonal $Sr_2CuO_{3+\delta}$ on annealing under high isostatic pressures with oxidiser[3] and high oxygen pressures.[1–5] Our studies on its stability at 775°C, showed that orthorhombic Sr_2CuO_3 was stable up to an oxygen pressure of about 200 bar but transforms to tetragonal $Sr_2CuO_{3+\delta}$, in agreement with the results of Singh *et al.*,[5] at higher pressures. An indexed X-ray powder pattern for tetragonal $Sr_2CuO_{3+\delta}$ is given in Table 1; reflections marked by an asterisk are due to the supercell $4\sqrt{2}a \times 4\sqrt{2}a \times c$ which is the same as that proposed by Hiroi *et al.*[3]

The oxygen excess of the tetragonal 2 : 1 phase, determined by thermogravimetric reduction in 5%H_2/95%N_2, corresponded to δ = 0·43(2). This value is slightly greater than for the sample prepared using a hydroxometallate precursor (δ = 0·29)[14] and much smaller than reported by Lobo *et al.*,[1] δ = 0·9. These values are all significantly higher than obtained using high isostatic pressures/oxidiser[3,4] where δ = 0·1.

Magnetic susceptibility measurements showed tetragonal 2 : 1 to be non-superconducting, consistent with the oxygen content analysis which suggested an average copper valence of 2·86(4)+.

The lattice parameters of $Sr_2CuO_{3+\delta}$ are also intermediate between those obtained by Hiroi *et al.*[3] and Lobo *et al.*,[1] Table 2. There appears to be

Table 1. Indexed XRD pattern for tetragonal $Sr_2CuO_{3+\delta}$

d_{obs}(Å)	d_{calc}(Å)	I/I_o	*hkl*
6·273	6·265	4	0 0 2
3·611	3·611	4	1 0 1
2·985*	2·984*	3	5 0 3*
	2·984*	—	4 3 3*
2·969*	2·969*	1	2 6 2*
2·902?		1	?
2·799	2·798	100	1 0 3
2·666	2·666	52	1 1 0
2·647*	2·645*	8	1 8 0*
	2·645*	5	4 7 0*
2·605*	2.604*	—	4 5 3*
2·088	2·088	30	0 0 6
	2·087	—	1 1 5
2·029	2·030	23	1 1 4
2·006*	2·004*	7	3 0 6*
1·990?		1	?
1·885	1·885	19	2 0 0
1·644	1·644	35	1 1 6
1·616	1·617	8	1 0 7
1·595*	1·594*	9	1 6 7*
1·564	1·563	20	2 1 3
1·528*	1·529*	4	1 11 5*
	1·527*	—	2 7 7*
1·447*	1·446*	2	1 12 5*
1·399	1·399	13	2 0 6
	1·399	—	2 1 5
1·350	1·350	6	1 1 8

a = 3·7695(6) Å.
c = 12·529(2) Å.
Space group = I 4/mmm (No. 139).
* = Lines indexed on the tetragonal supercell $4\sqrt{2}a \times c$.
? = Unidentified lines.

a trend in that a increases and c decreases with an increase in oxygen excess, δ. Although our lattice parameters for 2:1 are very similar to those of superconducting $Sr_2CuO_{3+\delta}$[3,4] our samples are non-superconducting. The crystallographic implications for such an observation are, at present, unclear.

To date, therefore, the only synthesis route to yield superconducting tetragonal $Sr_2CuO_{3+\delta}$ (Tc = 70 K) is that using high isostatic pressures/oxidisers.

3.1.3 $Sr_{14}Cu_{24}O_{38+\delta}$ (14:24 phase)

The 14:24 phase was stable under all temperatures and pressures used during this study. Thermogravimetric measurements showed the oxygen stoichiometry to vary with pressure: in air δ = 2·01(2) whereas after annealing at 350 bar O_2, δ = 3·03(2), suggesting that the 'ideal'[10,11] composition $Sr_{14}Cu_{24}O_{41}$ can be achieved only under high oxygen pressure.

Magnetic susceptibility measurements showed that this phase is non-superconducting, even after high oxygen pressure annealing. This is perhaps surprising because the average copper valence, 2·25, is close to the value observed in most other superconducting cuprates and suggests that the '14:24' structure type is not suitable for superconductivity.

3.1.4 $Sr_{0.74(3)}CuO_2$ (3:4 phase)[15]

At temperatures lower than 785±10°C and oxygen pressures > 20 bar, the phase of approximate composition $Sr_3Cu_4O_{7+\delta}$ forms. Full details on its stability and crystal chemistry will be published elsewhere.[15] It is not stable at T>785°C even at the highest oxygen pressure used in the present investigations (600 bar) and instead, decomposes to give 14:24 and tetragonal $Sr_2CuO_{3+\delta}$. This explains why $Sr_{0.74}CuO_2$ was not observed in previous high pressure (oxygen[5] or isostatic[6]) studies, which were confined to temperatures above 880°C.

Using both XRD and ED, it was found that *two* sub-cells were required to index all the reflections in the $Sr_{0.74}CuO_2$ pattern. Both are orthorhombic, with two axes, a and c, in common.

Subcell I: a_I = 6·8182(12) Å, b_I = 3·7113(7) Å and c_I = 11·0203(17) Å;
Space group = I ba2 (No. 69) or Ibam (No. 72).
Subcell II: a_{II} = 6·8182(12) Å, b_{II} = 2·7290(3) Å and c_{II} = 11·0203(17) Å;
Space group = F mmm (No. 69).

This showed that either the sample was a phase mixture in which, remarkably, the values of two of the lattice parameters were identical, or the sample was a Vernier phase,[19] incommensurate along b. The latter interpretation was confirmed by further ED work. The coincidence (super) cell[19] is b = 92·79(1) Å (=$25b_I$ and $34b_{II}$).

$Sr_{0.74(3)}CuO_2$ is non-superconducting. This is not very surprising because the average copper valence, 2·52(6), is too large for superconductivity in layered cuprates.

3.1.5 Phase equilibria of the system SrO–CuO at 775°C with varying oxygen pressure

At 775°C, our results show that the phase equilibria

Table 2. $Sr_{2-2x}Ca_{2x}CuO_{3+\delta}$ lattice parameters, oxygen excess (δ) and average copper valence after high oxygen pressure treatment

x	a	c	δ	*Average copper valence*
0.0	3·7695(6)	12·529(2)	0·43(2)	2·86(4)+
0·05	3·7568(5)	12·528(1)	—	—
0·1	3·7531(5)	12·507(2)	0·31(2)	2·62(4)+
0·0 (Hiroi *et al.*)	3·764	12·548	0·1	2·2+
0·0 (Lobo *et al.*)	3·7907(7)	12·417(2)	0·92	3·81+

are very dependent on pressure; three areas in particular show considerable variation, Fig. 1. Between 20 and 50 bar, compositions on the Sr- and Cu-rich side of 3:4 give phase mixtures of 1:1 + 3:4 and 3:4 + 14:24, respectively. Between 50 and 200 bar, the 1:1 phase is unstable and phase mixtures of orthorhombic 2:1 + 3:4 result. Above 200 bar, orthorhombic 2:1 transforms to its tetragonal modi-fication and so phase mixtures of tetragonal 2:1 and 3:4 exist for all compositions between 2:1 and 3:4.

3.2 The join $CaO–CuO_{1+\delta}$

Our results on this system (at temperatures less than 850°C and pressures up to 600 bar) are in good agreement with those reported by Singh *et al.*[5] (for temperatures greater than 880°C and pressures up to 200 bar).

3.2.1 Ca_2CuO_3

Ca_2CuO_3 decomposes in oxygen pressures greater than 10 bar, to give a mixture of $Ca_{0.81(1)}CuO_2$ + CaO.

3.2.2 $Ca_{0.81(1)}CuO_2$

There have been several reports on the phase $Ca_{1-y}CuO_2$.[5,7,20–22] It has an upper limit of thermal stability which increases with $P(O_2)$: 775±5°C in air,[7] 835±5°C in flowing oxygen[7,20,21] and above 950°C in high oxygen pressure.[5] The exact cation stoichiometry of the phase has been variously described as between $y = 0{\cdot}15$ and 0·2. Structural studies showed it to have a cation-deficient $NaCuO_2$-related structure.[20–24] Various superstructures, commensurate and non-commensurate, have been observed and are attributed to differences in the ordering of the Ca ions.[18,19] It was proposed[18] that ordering depends on cooling rate, Ca stoichiometry and oxygen partial pressure and is, therefore, a fairly complex phenomenon.

Our results show this phase to be stable at temperatures higher than 775°C when an oxygen pressure greater than 10 bar is used, in agreement with Singh *et al.*[5] Several compositions were prepared along the join CaO–CuO, in order to determine its exact stoichiometry. Only the compositions $Ca_{0.80}CuO_2$ and $Ca_{0.82}CuO_2$ were single phase by X-ray diffraction. The phase, therefore, appears to have an average composition, $Ca_{0.81(1)}CuO_2$. Compositions on either side such as $Ca_{0.85}CuO_2$ and $Ca_{0.75}CuO_2$ were phase mixtures of CaO + $Ca_{0.81(1)}CuO_2$ and $Ca_{0.81(1)}CuO_2$ + CuO, respectively. Our formula is in general agreement with Siegrist *et al.*[20] and Singh *et al.*[5] but slightly different from that proposed by Babu and Greaves,[21] $Ca_{0.85}CuO_2$.

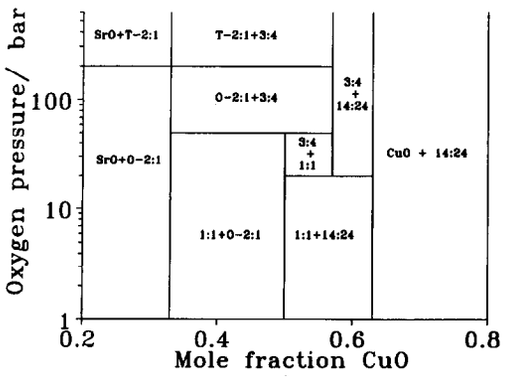

Fig. 1. Phase equilibria in the system $SrO–CuO_{1+\delta}$ at 775°C, as a function of oxygen pressure, after Ref. 15.

3.3 CaO–SrO binary join

The phase equilibria of this join at 350 bar oxygen are the same as in air at 1 bar.[25] At 775°C, there are two limited solid solutions: $Sr_{1-x}Ca_xO$ ($0 \leq x < \approx 0{\cdot}15$) and $Ca_{1-y}Sr_yO$ ($0 \leq y < \approx 0{\cdot}06$).

3.4 Phase diagram for the system $SrO–CaO–CuO_{1+\delta}$ at 775°C, 350 bar O_2

There have been several reports in the literature on phase equilibria in the system SrO–CaO–CuO in air,[7,24,25] 1 atmosphere of oxygen[6] and at 10 kbar isostatic pressure.[6] To date, however, there have been no studies under high oxygen pressures. We report here the phase relationships at 775°C and 350 bar oxygen pressure which correspond to the optimum conditions for formation of $Sr_{0.74(3)}CuO_2$. Results are summarized in Fig. 2. Compositions studied are marked, with appropriate symbols referring to whether single-, two- or three-phase mixtures resulted once equilibrium conditions were obtained.

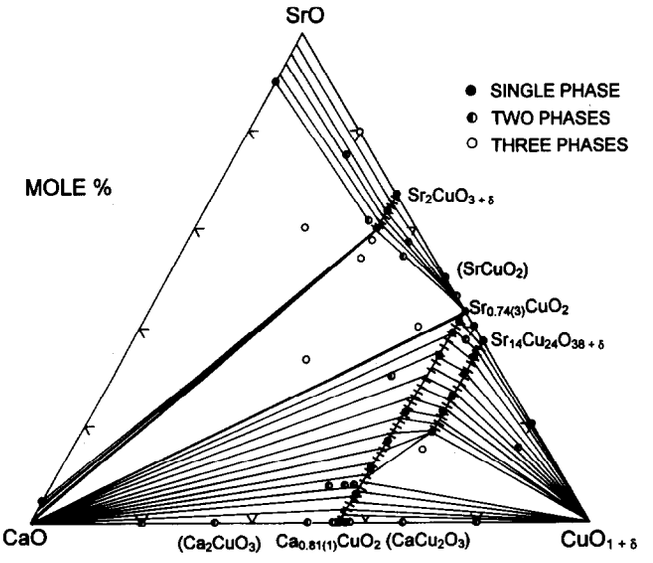

Fig. 2. Subsolidus compatibility relations in the system $SrO–CaO–CuO_{1+\delta}$ at 775°C, 350 bar O_2. It is assumed that, since XRD data were recorded at ambient temperature and pressure, no changes in the phase assemblages had occurred during cooling and release of pressure.

There are some noticeable differences in the phase equilibria between air[7,24,25] (or 1 bar O_2)[6] and 350 bar O_2 (at 775°C). The phases: $SrCuO_2$, Ca_2CuO_3, $CaCu_2O_3$, $Sr_{0.3}Ca_{0.7}CuO_2$ and $Sr_{0.15}Ca_{0.85}CuO_2$, which exist in air/1 bar O_2, do not exist at 350 bar O_2; conversely, $Sr_{0.74(3)}CuO_2$ exists at 350 bar O_2 but not at 1 bar.

The phase diagram shown in Fig. 2 is not a true ternary diagram as the oxygen content for copper oxide is not fixed. Instead, it is a ternary sub-section of the quaternary system: SrO–CaO–CuO–O. No attempt is made in Fig. 2 to show variations in oxygen excess, δ, of the phases present.

The diagram contains three single phase regions as follows:

3.4.1 $Sr_{2-2x}Ca_{2x}CuO_{3+\delta}$ ($O \leq x \leq 0{\cdot}1$) solid solutions

Tetragonal $Sr_2CuO_{3+\delta}$ can incorporate up to about 10% Ca by substitution for Sr, at 350 bar O_2. This is substantially less than in air[7] where an entire range of solid solutions forms between orthorhombic Sr_2CuO_3 and Ca_2CuO_3. The smaller range of solid solutions at high oxygen pressures appears to be associated with the instability of the K_2NiF_4/La_2CuO_4 structure when doped with smaller cations.[1] Table 2 shows the lattice parameters for x=0·0, 0·05, 0·1 at 775°C, 350 bar O_2. The unit cell contracts with x, as expected.

Thermogravimetric reduction of tetragonal $Sr_2CuO_{3+\delta}$ in $5\%H_2/95\%N_2$ showed the oxygen excess to be δ = 0·43(2). For x=0·1, the excess was less, δ = 0·31(2), perhaps because the unit cell is smaller and can accommodate less extra oxygens. Predictably, the samples are not superconducting as the average copper valences, Table 2, are too high.

3.4.2 $Ca_{0.81(1-x)}Sr_{0.74x}CuO_2$ ($0{\cdot}0 \leq x \leq 1{\cdot}0$) solid solutions

There have been various reports on $Ca_{1-y}CuO_2$[5,7,20–22] but attempts to partially substitute Sr for Ca were unsuccessful.[17] Using modest temperatures (up to 800°C) and varying the starting pressure, a complete range of solid solutions forms between $Ca_{0.81(1)}CuO_2$ and $Sr_{0.74(3)}CuO_2$.

The synthesis conditions varied with composition: $Sr_{0.74(3)}CuO_2$ formed most readily at 775°C, 350 bar O_2 whereas for $Ca_{0.81(1)}CuO_2$, higher temperatures and lower pressures were required (850°C and 50 bar). Intermediate compositions required intermediate conditions although X-ray diffraction patterns showed that a small amount (≈5%) of 'Ca-doped 14:24' and CaO were present. This was attributed to partial decomposition on cooling in the high pressure furnace. Due to operational limitations of the furnace, it was not possible to quench samples from the annealing temperature/pressure.

This range of solid solutions, $Ca_{0.81(1-x)}Sr_{0.74x}CuO_2$ ($0{\cdot}0 \leq x \leq 1{\cdot}0$) is most unusual and clearly does not form by a simple Sr⇔Ca substitution mechanism: the alkaline earth content decreases with increasing Sr content. The XRD data of all compositions, $0{\cdot}0 \leq x \leq 0{\cdot}74$, showed the same $CaCu_{0.81(1)}O_2$-type orthorhombic sub-cell (equivalent to sub-cell II for $Sr_{0.74(3)}CuO_2$) lines and a number of additional reflections attributed to either another sub-cell or supercell(s). The intensity and nature of the additional reflections varied with composition as did the intensity of one or two $CaCu_{0.81(1)}O_2$-type subcell reflections, notably the 002 reflection which decreased with x.

The lattice parameters for one sub-cell of the $Ca_{0.81(1-x)}Sr_{0.74x}CuO_2$ solid solutions, are given in Fig 3. Overall there is a gradual increase in a, c and V with x, but a decrease in b. Superimposed on these changes, however, there may be at least three regions, $0{\cdot}0 \leq x \leq 0{\cdot}2$, $0{\cdot}25 \leq x \leq 0{\cdot}55$ and $0{\cdot}65 \leq x \leq 1{\cdot}0$ where the lattice parameters,

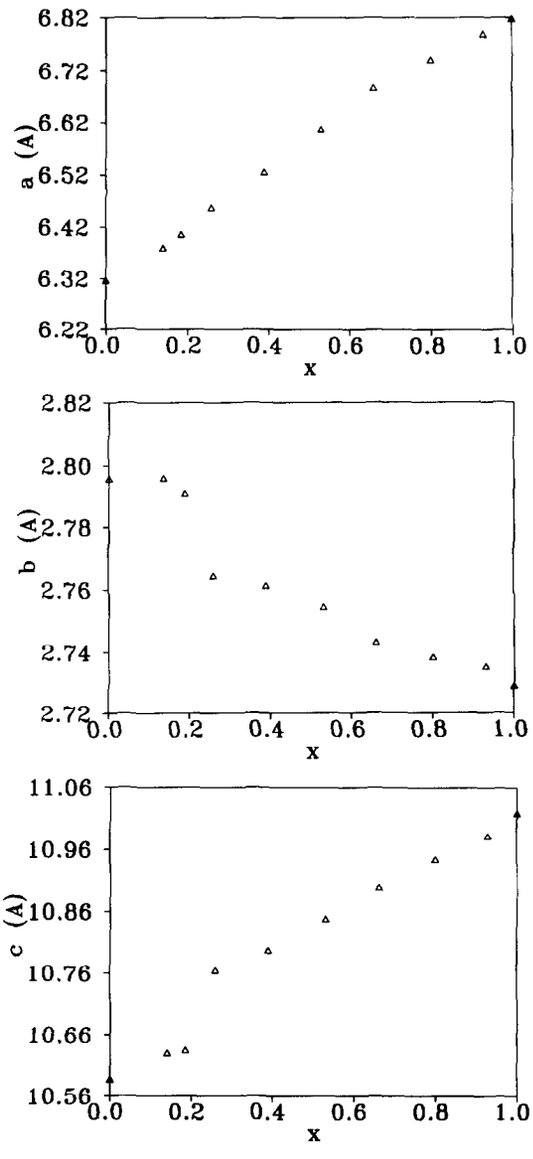

Fig. 3(a)–(c). Lattice parameters of the $Ca_{0.81(1-x)}Sr_{0.74x}CuO_2$ solid solutions, based on the $CaCu_{0.81(1)}O_2$-type orthorhombic subcell (equivalent to subcell II for $Sr_{0.74(3)}CuO_2$).

Table 3. Variation of subcell b_I and b_{II} lattice parameters with composition for $Ca_{0.81(1-x)}Sr_{0.74x}CuO_2$ solid solutions

x	b_I (Å)	b_{II} (Å)	b *coincidence cell* (Å)
1·00	3·7113(7)	2·7290(3)	92·79(1) = $25b_I$ and 34 b_{II}
0·93	3·6588(6)	2·7353(6)	10·96(2) = $3b_I$ and $4b_{II}$
0·80	3·6105(8)	2·7384(11)	79·42(1) = $22b_I$ and $29b_{II}$
0·66	3·5981(18)	2·7404(19)	57·56(2) = $16b_I$ and $21b_{II}$

especially *b*, show discrete behaviour. Instead of a homogeneous solid solution across the entire range of *x* values, a family of phases may exist; they may all have Vernier character, similar to the $x = 1·0$ end-member. For the high *x* values, $0·65 \leq x \leq 1·0$, the powder patterns may be indexed on a similar Vernier cell to $x = 1·0$, Table 3. However, the period of the Vernier 'coincidence' (super) cell in the *b* direction, changes and the structural implications are, at present, unclear. Further studies on these phases are in progress.

Magnetic susceptibility measurements suggested that none of the compositions for the range $Ca_{0.81(1-x)}Sr_{0.74x}CuO_2$, were superconducting. This is presumably because the formal copper valences for these materials are too high, ranging from: 2·38(2)+ for $Ca_{0.81(1)}CuO_2$ to 2·52(6)+ for $Sr_{0.74(3)}CuO_2$.

3.4.3 $Sr_{14-14x}Ca_{14x}Cu_{24}O_{38+\delta}$ ($0·0 \leq x \leq 0·5$) solid solutions

In air,[10,11,16,17] the 14 : 24 phase can substitute up to 50 mol% of Sr by Ca, to form $Sr_7Ca_7Cu_{24}O_{38+\delta}$. The solid solution limit, $x = 0·5$, appears to be independent of temperature and O_2; however, for a given *x*, the lattice parameters and oxygen content, δ, vary, Figs 4 and 5. The *c* parameter varies most and is about 1% greater after high PO_2 treatment (775°C, 350 bar). The oxygen content, and thus formal copper valence (FCV), is higher for samples annealed at high PO_2; in both air and high oxygen pressure, δ drops initially with *x*, then stays approximately constant beyond $x \equiv 0·2$.

Magnetic susceptibility measurements show no evidence of superconductivity. With the exception of the $x = 0·0$ sample annealed at 350 bar O_2, which had a FCV of 2·25, most of the compositions had a FCV too low for superconductivity. The non-superconductivity of $x = 0·0$ suggests that the 14 : 24 structure type is not suitable for superconductivity.

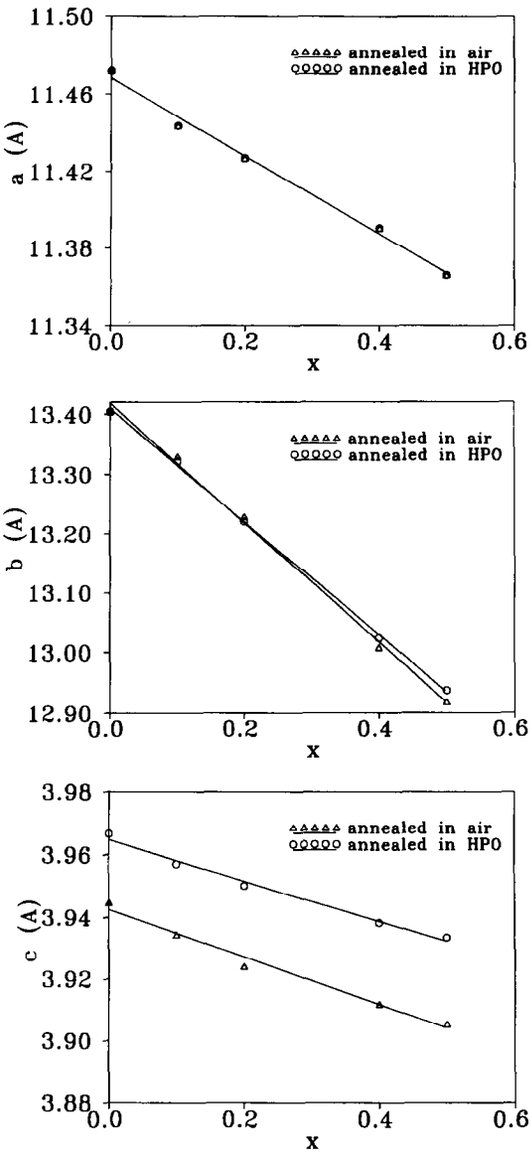

Fig. 4(a)–(c). Lattice parameters of $Sr_{14-14x}Ca_{14x}Cu_{24}O_{38+\delta}$ in air and high oxygen pressure (350 bar).

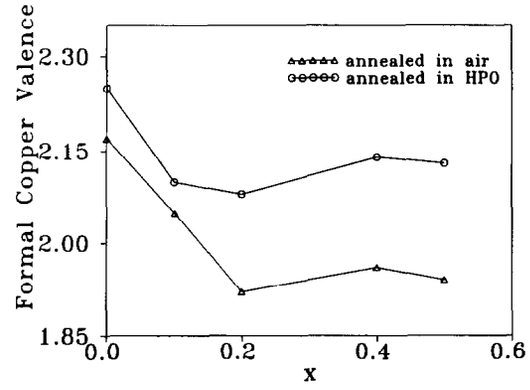

Fig. 5. Variation of Formal Copper Valence (FCV) with *x* for $Sr_{14-14x}Ca_{14x}Cu_{24}O_{38+\delta}$ in air and high oxygen pressure (350 bar).

3.4.4 Compatibility triangles in the system SrO–CaO–$CuO_{1+\delta}$ at 775°C, 350 bar O_2 (Fig. 2)

All compositions belonging to the $Sr_{2-2x}Ca_{2x}CuO_{3+\delta}$ ($0 \leq x \leq 0·1$) range of solid solutions are compatible with the $Sr_{1-x}Ca_xO$-based solid solution and the new binary phase, $Sr_{0.74(3)}CuO_2$, to form two-phase regions. The Ca-rich end-member, $x = 0·1$, is also compatible with $Ca_{1-y}Sr_yO$ to form two three-phase regions: $Sr_{1.8}Ca_{0.2}CuO_{3+\delta}$ + $Sr_{0.74(3)}CuO_2$ + CaO and $Sr_{1.8}Ca_{0.2}CuO_{3+\delta}$ + $Ca_{1-y}Sr_yO$ + $Sr_{1-x}Ca_xO$.

The complete range of solid solutions, $Ca_{0.81(1-x)}Sr_{0.74x}CuO_2$ ($0.0 \leq x \leq 1.0$), is compatible with CaO forming a very extensive two-phase region. The compatibility of $Ca_{0.81(1-x)}Sr_{0.74x}CuO_2$ with Cu-rich phases depends on composition. Ca-rich compositions, $0 \leq x \leq 0.15$, are compatible with CuO, whereas all others, $0.15 \leq x \leq 1.0$, are compatible with the 14:24 solid solutions. The 14:24 solid solutions are also compatible with CuO. There is also a small three-phase region between, $Ca_{0.64}Sr_{0.14}CuO_2$, $Sr_7Ca_7Cu_{24}O_{38+\delta}$ and CuO.

4 Conclusions

Phase equilibria in the system $SrO–CaO–CuO_{1+\delta}$ have been studied under high oxygen pressure and show significant differences from the phase equilibria in air.

The new binary phase, $Sr_{0.74(3)}CuO_2$ which only forms under high oxygen pressures and has an upper limit of thermal stability of 785±10°C, forms a nominally complete range of solid solutions with $Ca_{0.81(1)}CuO_2$. These materials have complicated superstructures and may instead form a family of Vernier phases.

Tetragonal $Sr_2CuO_{3+\delta}$ forms a limited solid solution $Sr_{2-2x}Ca_{2x}CuO_{3+\delta}$ ($0.0 \leq x \leq 0.1$) under high oxygen pressures whereas in air, orthorhombic Sr_2CuO_3 forms a complete range of solid solutions with Ca_2CuO_3.

The extent of Ca $\Leftrightarrow$ Sr solubility in the 14:24 phase remains unchanged in high oxygen pressure, although there is an increase in the oxygen content for all compositions.

All of the Sr, Ca cuprate solid solutions have formal copper valences greater than 2+ under high oxygen pressures but none exhibit superconductivity.

The lattice parameters of our tetragonal $Sr_2CuO_{3+\delta}$ are quite similar to those for the superconducting analogue.[3] It is important to determine the detailed crystal structure of both forms in order to shed some light on the crucial structural features necessary for superconductivity.

Acknowledgement

We thank EPSRC for financial support.

References

1. Lobo, R. C., Berry, F. J. & Greaves C., *J. Solid State Chem.*, **88** (1990) 513.
2. Hiroi, Z., Azuma, M., Takano, M. & Bando, Y., *J. Solid State Chem.*, **95** (1991) 230.
3. Hiroi, Z., Takano, M., Azuma, M. & Takeda, Y., *Nature*, **364** (1993) 315.
4. Laffez, P., Wu, X. J., Adachi, S., Yamauchi, H. & Môri, N., *Physica C*, **222** (1994) 303.
5. Singh, K. K., Morris, D. E. & Sinha, A. P. B., *Physica C*, **231** (1994) 377.
6. George, E., Eithon, D. & Meen, J. K., submitted to *J. Am. Cer. Soc.*, 1994.
7. Roth, R. S., Rawn, C. J., Ritter, J. J. & Burton, B. P., *J. Am. Cer. Soc.*, **72** (1989) 1545.
8. Hwang, N. M., Roth, R. S. & Rawn, C. J., *J. Am. Cer. Soc.*, **72** (1990) 2531.
9. Xu, M., Voiles, E. T., Chumbley, L. S., Goldman, A. I. & Finnemore, D. K., *J. Mat. Res.*, **7** (1992) 1283.
10. Siegrist, T., Schneemeyer, L. F., Sunshine, S. A., Waszczak, J. V. & Roth, R. S., *Mat. Res. Bull.*, **23** (1988) 1429.
11. McCarron, E. M. III, Subramanian, M. A., Calabrese, J. C. & Harlow, R. L., *Mat. Res. Bull.*, **23** (1988) 1355.
12. Han, P. D., Chang, L. & Payne, D. A., *Physica* C, **228** (1994) 129.
13. Wu, X.-J., Laffez, P., Yamauchi, H. & Môri, N., *Physica C*, **228** (1994) 292.
14. Mitchell, J. F., Hinks, D. G. & Wagner, J. L., *Physica C*, **227** (1994) 279.
15. Sastry, P. V. P. S. S., Robertson, A. D., Lachowski, E. E., Coats, A. & West, A. R. *J. Mat. Chem.*, **5** (1995) 1931.
16. Schulze, K., Majewski, P., Hettich, B. & Petzow, G., *Z. Metallkd.*, **81** (11) 1990 836.
17. Siegrist, T., Zahurak, S. M., Murphy, D. W. & Roth, R. S., *Nature*, **334** (1988) 231.
18. Morris Research Inc. High Oxygen Pressure Furnace, Model Number HPS 5015E7, User's Manual.
19. Makovicky, E. & Hyde, B. G., *Struct. Bond.*, **46** (1981) 101, and the references therein.
20. Siegrist, T., Roth R. S., Rawn, C. J. & Ritter J. J., *Chem. Mat.*, **2** (1990) 192.
21. Babu, T. G. N. & Greaves, C., *Mat. Res. Bull.*, **26** (1991) 499.
22. Mathews, T., Hajra, J. P. & Jacob, K. T., *Chem. Mater.*, **5** (1993) 1669.
23. Hestermann, K. & Hoppe, R., *Z. Anorg. Allg. Chem.*, **367** (1969) 261.
24. Brese, N. E., O'Keeffe, M., Von Dreele, R. B. & Young, V. G., *J. Solid State Chem.*, **83** (1989) 1.
25. Roth R. S., in *Proc. User Aspects of Phase Equilibria, Joint Research Centre, Petten, Netherlands*, 27–29 June 1990, Institute of Metals, London.

Journal of the European Ceramic Society 16 (1996) 645–651

0955-2219(95)00176-X
0955-2219/96/$15.00

Threshold Stress Intensity Factor in Soda–Lime Silicate Glass by Interrupted Static Fatigue Test

Vincenzo M. Sglavo & David J. Green*

Department of Materials Science and Engineering, The Pennsylvania State University, University Park, PA 16802, USA

(Received 15 August 1994; accepted 9 September 1995)

Abstract

The measurement of the threshold stress intensity factor K_{th} for sub-critical crack growth of soda–lime glass in a water environment was performed using the interrupted static fatigue test. The experimental procedures suggested in a previous paper by the current authors were followed. In the first approach, K_{th} was calculated as the stress intensity factor at which half of the specimens fail during the constant stress phase of the test. In the second approach, the fatigue limit was determined from the stress intensity factor applied to the weakest surviving sample during the stress hold. For both cases, values of the stress intensity factor were obtained for increasing hold times, which ranged from 1 hour to 20 days. The estimated K_{th} values decrease with holding time but are expected to reach a limiting value, equivalent to the true threshold at long times. For holding times of 20 days, values of 0·16 and 0·15 MPa $m^{1/2}$ were obtained by using the two different approaches. For the current test, the necessary limit in the estimated K_{th} values was not obtained, suggesting that if a threshold exists, it must be equal to or less than these values. These values are significantly lower than previous K_{th} estimates that were obtained by extrapolation from crack velocity and time-to-failure measurements (0·2 – 0·4 MPa $m^{1/2}$).

1 Introduction

Sub-critical crack growth in silicate glasses is a well-known phenomenon. As a result of such behaviour, the strength depends on loading time and environmental conditions and this fatigue effect has been extensively studied. Some works have shown that this sub-critical behaviour seems to possess a lower limit, in the sense that the crack propagation velocity tends to zero for some particular value of the applied stress intensity factor.[1–8] This value is termed the fatigue limit or the threshold stress intensity factor. From an engineering design point of view, the existence of a fatigue limit turns out to be extremely desirable, as it allows an applied stress to be defined, below which delayed failure does not occur. The determination of the fatigue limit is therefore of practical importance and this effect has aroused the interest of many researchers.

In early works on sub-critical crack growth in silicate glasses, samples were loaded at different stress levels in bending and the lifetimes were measured.[9–17] The 'endurance limit' was defined as the stress at which the fatigue curve shows asymptotic behaviour. For soda–lime glass in a water environment, values ranging from 0·15 to 0·4 times the strength measured in liquid nitrogen were extrapolated from time-to-failure measurements.[10–16] The same approach, used in more recent work by Pavelchek and Doremus[18] and Gehrke *et al.*,[19–21] furnished similar results.

Studies devoted to sub-critical crack growth velocity determination as a function of the applied stress intensity factor also showed, in some cases, the existence of a threshold below which crack motion did not occur. In these studies, double cantilever beam and double torsion fracture mechanics geometries were often used and crack advancement was measured as a function of time. Values of the threshold ranging from 0·18 to 0·40 MPa $m^{1/2}$ were put forward.[1–8,22] It must be pointed out, in these cases, that the fatigue limit corresponded to a value extrapolated from crack velocity measurements.

Although a significant number of studies have been performed, definitive proof for the existence of a fatigue limit is still an open problem and many uncertainties are present. For example, Simmons and Freiman[5] observed crack arrest in soda–lime glass in water at stress intensity factor of 0·27 MPa $m^{1/2}$ but they defined this threshold as an 'apparent' effect, because it was not associated

*To whom correspondence should be addressed.

with crack tip blunting, as predicted by the theory of Hillig and Charles.[17] Conversely, Michalske demonstrated the occurrence of crack tip blunting for stress intensity factors lower than 0·25 MPa $m^{1/2}$ using crack ageing experiments.[23]

In a previous paper,[24] a theoretical analysis of the interrupted static fatigue (ISF) test was developed. This test has been used previously for the determination of the fatigue limit in various glass and ceramic materials.[25–31] In the theoretical analysis,[24] some procedures were proposed for the correct evaluation of the threshold. In the current paper, the measurement of the fatigue limit in soda–lime silicate glass in water environment was attempted on the basis of these procedures.[24]

2 Experimental Procedure

Soda–lime silicate glass rods from a commercial source (0080 Code, Corning Glass Works) were used in this work. The composition of the glass is reported in Table 1. The rods, with a nominal diameter of 3·2 mm, were cut into 90 mm length samples and these were annealed at 520°C for 24 h in order to remove any residual stress. Heating and cooling rates of below 1°C min^{-1} were used for this purpose.

Inert strengths were determined by a four-point bend test performed in paraffin oil. Samples were initially stored in a furnace at ~120°C for 15 min and then immediately immersed in a paraffin oil bath. The bend fixture, with outer and inner spans of 80 and 20 mm, respectively, was also completely immersed in an oil bath, as shown in Fig. 1. In this way, the inert conditions were maintained during the testing of the glass rods. A crosshead speed of 15 mm min^{-1} was used for these tests. Forty rods were used for strength determination and the diameter of each sample was measured, after failure, close to the fracture surface.

The strength of 40 samples was also measured in water environment at the same crosshead speed as in the inert measurements. For these tests, the four-point fixture was immersed in a deionized water bath (Fig. 1).

The interrupted static fatigue tests were performed in a deionized water bath (pH 6·0–6·5). A constant load was applied to groups of eight samples using free-hanging weights. A schematic of the apparatus used for the ISF test is shown in Fig. 2. The glass samples were placed on two

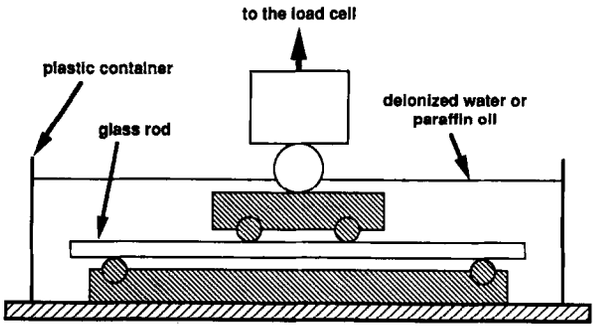

Fig. 1. Schematic of the four-point bending fixture used for strength testing in paraffin oil and in deionized water.

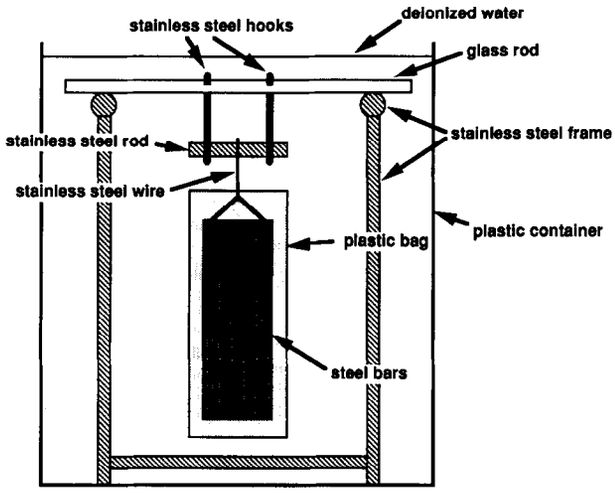

Fig. 2. Schematic of the apparatus used for the ISF test.

stainless steel rods which were suspended by a stainless steel frame. The load was applied in a four-point bend configuration by use of the two hooks. Outer and inner spans were again 80 and 20 mm, respectively. Great care was taken to avoid any contact of the hooks with the rods before the final loading. The hanging weights consisted of a set of steel bars to obtain the desired load. To avoid any contamination of the deionized water from the steel bars, each weight set was contained in a plastic bag which was carefully closed and sealed with silicone grease. The constant load was maintained on the specimens for times ranging from 1 h to 20 days. Care was taken to account for the buoyancy force acting on the steel bars, in the evaluation of the applied stress. Samples which did not fail during the constant phase of the testing were then broken in four-point bending using the same procedure as that described for the strength determination in water. Before this final testing, samples were marked on their edge in order to load them in the same orientation that was used during the static hold.

Table 1. Composition (wt%) of the soda–lime silicate glass used in the present work

SiO_2	Al_2O_3	MgO	CaO	Na_2O	K_2O	BaO	B_2O_3	Other
68·1	2·2	3·8	5·7	15·5	0·7	1·9	1·5	0·6

3 Analysis of Results and Discussion

Figure 3 shows the Weibull plot for the strength distributions determined in paraffin oil and in water. Failure probability F of each specimen was determined from the relationship:

$$F = \frac{j}{N+1} \tag{1}$$

where j is the rank in the ascending distribution and N is the total number of specimens which, in this case, is equal to 40.

The sub-critical crack growth phenomenon is responsible for a marked decrease in strength when the testing is performed in an active environment, even with the high stressing rates used in this study (~47 MPa s^{-1}). A Weibull modulus of 5·5 was determined by linear regression of the inert strength data shown in Fig. 3.

In a previous paper,[24] Sglavo and Green suggested two different approaches to measure the threshold for sub-critical crack growth K_{th} by the ISF test. In the first approach the estimate of K_{th} is calculated as the stress intensity factor at which 50% of the samples fail during the stress hold. In the second approach, the fatigue limit is estimated as the stress intensity factor corresponding to the weakest specimen in the strength distribution of samples that survive the hold stress. It was pointed out that the second approach is preferred for materials with low Weibull modulus. In this work, even if the second approach would be more opportune, the threshold measurement was attempted using both procedures. For both procedures, a critical facet of the approach is to determine the K_{th} estimates as a function of hold time.[24]

Figure 4 shows the strength S_1 measured in water, after the hold, as a function of the applied stress σ for holding times varying from 1 h to 20 days. The number of samples surviving and failing during the ISF test is also shown. The strength of the surviving specimens, S_1, is substantially equivalent to the strength measured in water on

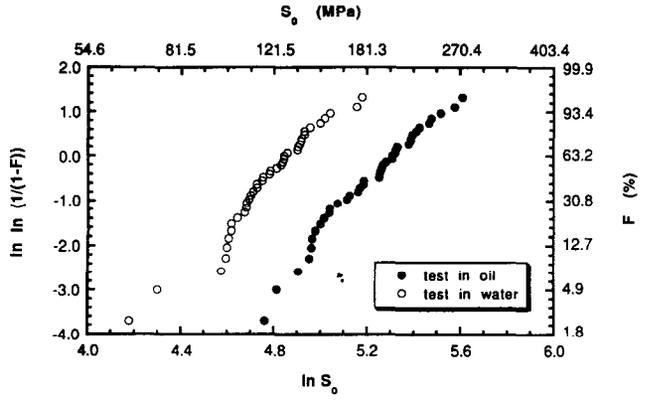

Fig. 3. Weibull plot of the strength distributions measured in paraffin oil and in deionized water.

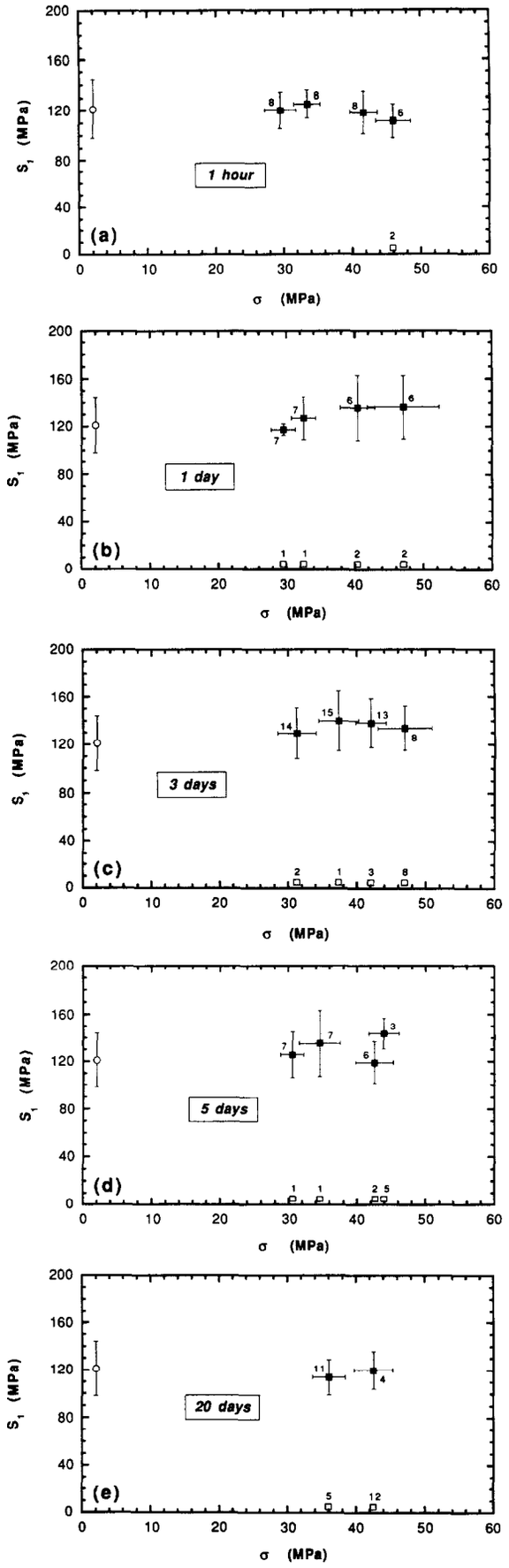

Fig. 4. Average strength S_1 measured in deionized water, after the hold, as a function of the applied stress σ for holding times of (a) 1 h, (b) 1 day, (c) 3 days, (d) 5 days and (e) 20 days. Initial strength S_0, measured in water, is shown at σ = 2 MPa for comparison. The error bars represent the standard deviation of the data. Empty square symbols correspond to specimens which failed during the stress hold. Each symbol is marked by the corresponding number of specimens.

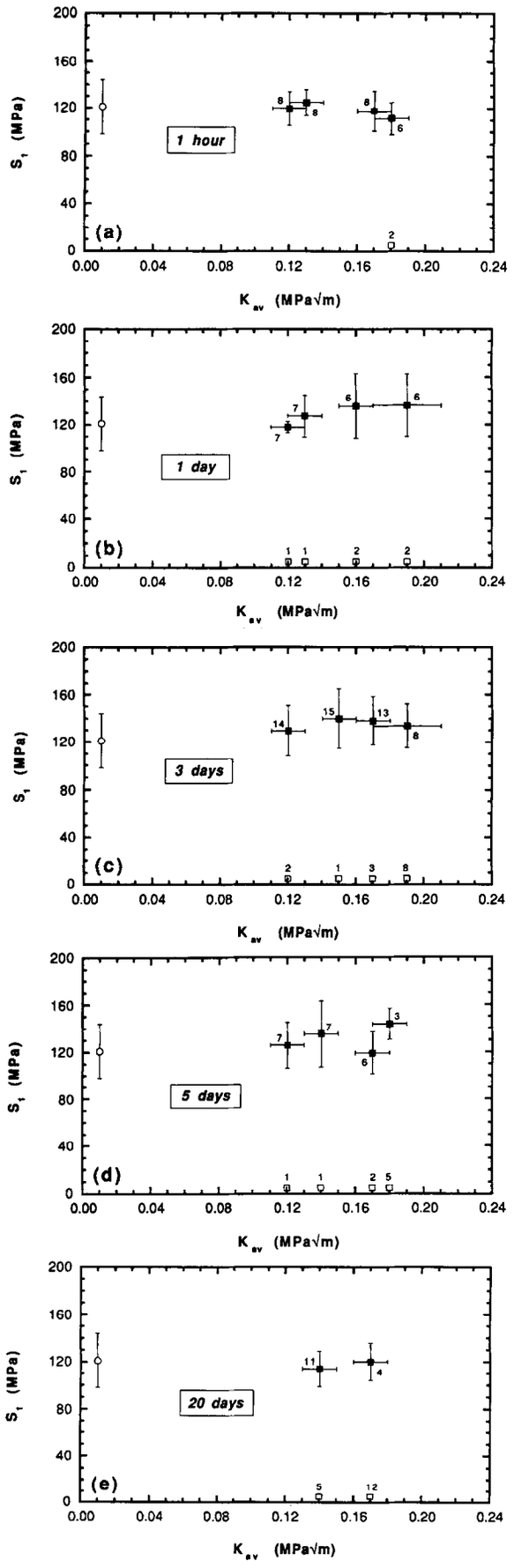

Fig. 5. Average strength S_1 measured in deionized water, after the hold, as a function of K_{av} for holding times of (a) 1 h, (b) 1 day, (c) 3 days, (d) 5 days and (e) 20 days. Initial strength S_0, measured in water, is shown at K_{av} = 0·01 MPa m$^{1/2}$ for comparison. The error bars represent the standard deviation of the data. Empty square symbols correspond to specimens which failed during the stress hold. Each symbol is marked by the corresponding number of specimens.

as-annealed samples. Some variations, probably connected to the small number of samples used in this testing, can be detected. The average stress intensity factor K_{av} applied to the samples during the hold can be calculated as:[24]

$$K_{av} = K_c\left(\frac{\sigma}{S_0}\right) \tag{2}$$

where S_0 is the average inert strength and K_c represents the fracture toughness, assumed to be equal to 0·75 MPa m$^{1/2}$ (Ref. 32). Figure 5 shows strength results of Fig. 4 as a function of K_{av}. As suggested in our previous paper,[24] the 'potential' threshold is first estimated as the value of the stress intensity factor, $(K_{av})_{50\%}$, at which 50% of samples fail during the hold. Due to the particular stresses used in this work, $(K_{av})_{50\%}$ could not be calculated for holding times of 1 h and 1 day. For these two cases, only values larger than 0·18 MPa m$^{1/2}$ could be assumed for $(K_{av})_{50\%}$. In order to take into account the scatter shown by the applied stress and, more importantly, by the inert strength, the average value of $(K_{av})_{50\%}$ was calculated, more precisely, according to the following relationship:[33]

$$(K_{av})_{50\%} = K_c\left(\frac{\sigma_{50\%}}{S_0}\right) + \frac{K_c\sigma_{50\%}}{S_0^3}V(S_0) \tag{2a}$$

where $\sigma_{50\%}$ is the applied stress corresponding to 50% of failures during the holding and $V(S_0)$ represents the variance of the inert strength, i.e. the square of the standard deviation.[33] The second term in eqn (2a), usually very small, is related to the transformation used to calculate $(K_{av})_{50\%}$ from σ and S_0, both of which are random variables.[33] Analogously, the standard deviation $[V((K_{av})_{50\%})]^{1/2}$ was calculated from:[33]

$$\left[V((K_{av})_{50\%})\right]^{1/2} = \left[\left(\frac{K_c}{S_0}\right)^2 V(\sigma_{50\%}) + \left(\frac{K_c\sigma_{50\%}}{S_0^2}\right)^2 V(S_0)\right]^{1/2} \tag{2b}$$

where $V(\sigma_{50\%})$ represents the variance of the applied stress corresponding to 50% of failures. $\sigma_{50\%}$ can be calculated by linear interpolation between two distinct applied stress values, σ_2 and σ_1, corresponding to the percentages of specimens failing during the stress hold, n_1 and n_2, with $n_1 < 0{\cdot}5 < n_2$. The variance $V(\sigma_{50\%})$ was evaluated as:[33]

$$V(\sigma_{50\%}) = \left(\frac{0{\cdot}5 - n_1}{n_2 - n_1}\right)V(\sigma_2) + \left(\frac{n_2 - 0{\cdot}5}{n_2 - n_1}\right)V(\sigma_1) \tag{2c}$$

where $V(\sigma_1)$ and $V(\sigma_2)$ represent the variance of the two applied stress values used in the interpolation. The results of these calculations are shown in Fig. 6. As was expected, a large scatter is shown by the stress intensity values, due to the low

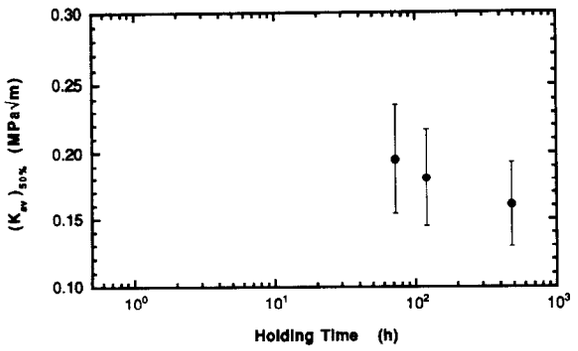

Fig. 6. $(K_{av})_{50\%}$ as a function of the holding time as calculated on the basis of the results shown in Fig. 5. The error bars represent the standard deviation of the data and are discussed in the text.

Weibull modulus associated with the inert strength. Nevertheless, a general trend is evident in Fig. 6: $(K_{av})_{50\%}$ decreases for increased holding times. A value of 0·16 ± 0·03 MPa $m^{1/2}$ is obtained at t = 20 days for the K_{th} estimate. It is important to note that $(K_{av})_{50\%}$ has not reached an invariant limit for this hold time, as required in the proper determination of K_{th}.[24]

An alternative approach to the determination of the fatigue threshold was performed by considering the strength distribution of samples that survive the hold stress.[24] Figure 7 shows the strength distributions corresponding to different holding times. A failure strength equal to zero was assigned to samples which failed during the stress hold. For each holding time, the data corresponding to the two upper applied stress shown in Fig. 4 were analysed. The weakest survivor in each distribution was considered and its inert strength S_{0w} was calculated from the data shown in Fig. 3, on the basis of its failure probability. The stress intensity factor K_w applied to this weakest surviving sample was calculated as:

$$K_w = K_c\left(\frac{\sigma}{S_{0w}}\right) \tag{3}$$

where σ is again the applied stress during the hold. Figure 8 shows the results of these calculations. The stress intensity factor applied to the specimens directly preceding and following the weakest sample in the ascending strength distribution is also shown in Fig. 8. In this way, an estimate of the possible computation error can be furnished. K_w decreases for increased holding times and for $t \geq 72$ h the trend is similar to that shown in Fig. 6. For a holding time of 480 h, K_w assumes a value of ~0·15 MPa $m^{1/2}$ but, again, no invariance is seen in K_w for the longer hold times.

The two approaches used to determine the 'potential' threshold furnished similar results. Both $(K_{av})_{50\%}$ and K_w decrease for increased holding times, according to the arguments pointed out

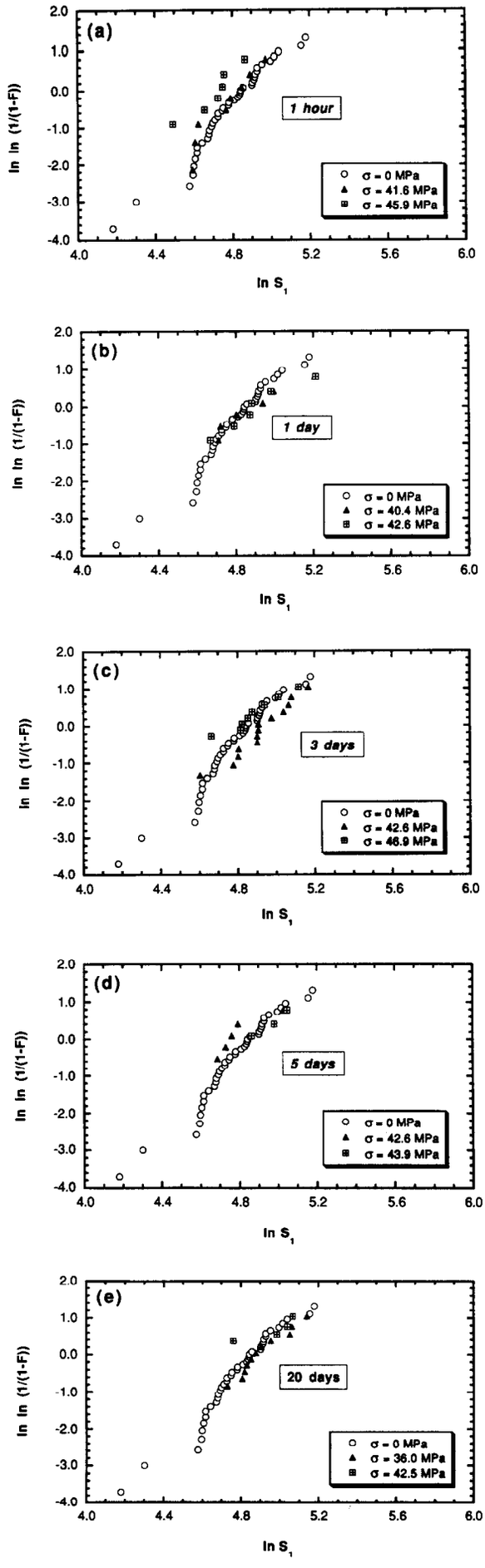

Fig. 7. Strength distribution evaluated after the stress hold, for holding times of (a) 1 h, (b) 1 day, (c) 3 days, (d) 5 days and (e) 20 days. The initial strength distribution, measured in deionized water, is shown for comparison (σ = 0 MPa).

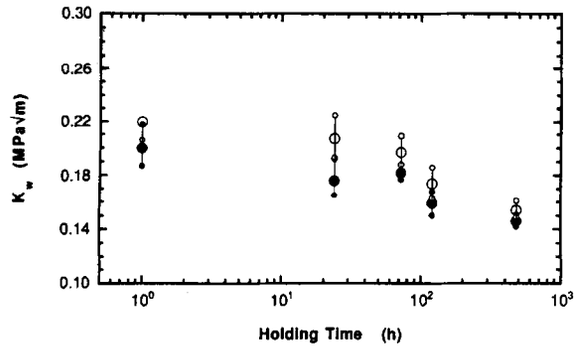

Fig. 8. Stress intensity factor K_w applied to the weakest specimen of the strength distributions shown in Fig. 7 as a function of the holding time. Empty symbols correspond to the highest applied stress defined in Fig. 7. The smaller symbols represent the stress intensity factor applied to the specimens directly preceding and following the weakest specimen in the ascending strength distribution.

previously.[24] These two parameters seem to be approaching a limiting value around 0·14–0·15 MPa $m^{1/2}$ though the holding times used in this work are not long enough to be conclusive on this point. Nevertheless, results of Figs 6 and 8 lead to some important considerations.

First of all, values of the 'potential' threshold for soda–lime glass presented in this work are lower than the fatigue limit extrapolated from crack velocity measurements and reported by other authors.[1–4,6–8] Values of K_{th} ranging from 0·18 to 0·40 MPa $m^{1/2}$ have been proposed for soda–lime glass in water environment.[1–4,6–8] Results of this work show a better agreement with data presented in early works on static fatigue of soda–lime glass where the 'endurance limit' was assumed as the stress equal to 0·2 – 0·4 times the strength measured in liquid nitrogen.[10,11,14,16] These values correspond to a stress intensity factor of 0·15 – 0·30 MPa $m^{1/2}$. On the basis of the arguments pointed out by Sglavo and Green,[24] measurement of the real value of the fatigue limit from an ISF test would require even longer hold times. The decision to use such long hold times would depend on various factors like experimental costs and the importance of the threshold information in component design.

4 Conclusions

The interrupted static fatigue test was used to determine the threshold for sub-critical crack growth in soda–lime silicate glass in water environment. The two procedures described in a previous paper were followed. First of all, the 'potential' fatigue limit was calculated as the stress intensity factor at which 50% of samples fail during the static hold for different hold times. In a second approach, K_{th} was determined as the value of the stress intensity factor applied to the weakest specimen in the strength distribution that survived the stress hold. Holding times ranging from 1 h to 20 days were used and 'potential' threshold values appeared to decrease for longer times. Theoretical calculation had shown that the estimates could be considered to be threshold values if they become invariant with hold time. Values of 0·16 and 0·15 MPa $m^{1/2}$ were obtained by the two different procedures at holding times of 20 days. Unfortunately, although an asymptotic behaviour was shown by the calculated threshold values, invariance with hold time was not shown. Nevertheless, values of K_{th} calculated at 20 days are lower than fatigue limit values presented in previous works for soda–lime glass in water environment. Only the use of longer holding times would allow a more precise evaluation of the threshold.

References

1. Wiederhorn, S. M. & Bolz, L. H., Stress corrosion and static fatigue of glass. *J. Am. Ceram. Soc.*, **53** (10) (1970) 543–8.
2. Evans, A. G., A simple method for evaluating slow crack growth in brittle materials. *Int. J. Fract.*, **9** (3) (1973) 267–75.
3. Wiederhorn, S. M., Subcritical crack growth in ceramics. In *Fracture Mechanics of Ceramics*, ed. R. C. Bradt, D. P. H. Hasselmann & F. F. Lange. Plenum, New York, 1974, Vol. 2, pp. 613–46.
4. Evans, A. G., Slow crack growth in brittle materials under dynamic loading conditions. *Int. J. Fract.*, **10** (2) (1974) 251–9.
5. Simmons, C. J. & Freiman, S. W., Effect of corrosion processes on subcritical crack growth in glass. *J. Am. Ceram. Soc.*, **64** (11) (1981) 683–6.
6. Wan, K., Lathabai, S. & Lawn, B. R., Crack velocity functions and threshold in brittle solids. *J. Eur. Ceram. Soc.*, **6** (1990) 259–68.
7. Gehrke, E., Ullner, C. & Hähnert, M., Effect of corrosive media on crack growth of model glasses and commercial silicate glasses. *Glastech. Ber.*, **63**(9) (1990) 255–65.
8. Gehrke, E., Ullner, C. & Hähnert, M., Fatigue limit and crack arrest in alkali-containing silicate glasses. *J. Mater. Sci.*, **26** (1991) 5445–55.
9. Stuart, D. A. & Anderson, O. L., Dependence of ultimate strength of glass under constant load on temperature, ambient atmosphere, and time. *J. Am. Ceram. Soc.*, **36** (12) (1953) 416–24.
10. Shand, E. B., Experimental study of fracture of glass: I, The fracture process. *J. Am. Ceram. Soc.*, **37** (2) (1954) 52–60.
11. Mould, R. E. & Southwick, R. D., Strength and static fatigue of abraded glass under controlled ambient conditions: II, Effect of various abrasions and the universal fatigue curve. *J. Am. Ceram. Soc.*, **42** (12) (1959) 582–92.
12. Mould, R. E., Strength and static fatigue of abraded glass under controlled ambient conditions: III, Aging of fresh abrasions. *J. Am. Ceram. Soc.*, **43** (3) (1960) 160–7.
13. Shand, E. B., Fracture velocity and fracture energy of glass in the fatigue range. *J. Am. Ceram. Soc.*, **44** (1) (1961) 21–6.
14. Mould, R. E., Strength and static fatigue of abraded glass under controlled ambient conditions: IV, Effect of surrounding medium. *J. Am. Ceram. Soc.*, **4** (10) (1961) 481–91.

15. Watanabe, M., Caporali, R. V. & Mould, R. E., The effect of chemical composition on the strength and static fatigue of soda-lime glass. *Phys. Chem. Glasses*, **2** (1) (1961) 12–23.
16. Shand, E. B., Strength of glass — the Griffith method revised. *J. Am. Ceram. Soc.*, **48** (1) (1965) 43–9.
17. Hillig, W. B. & Charles, R. J., Surfaces, stresses-dependent surface reactions, and strength. In *High Strength Materials*, ed. V.F. Zakay. John Wiley & Sons, New York, 1965, pp. 683–705.
18. Pavelchek, E. K. & Doremus, R. H., Static fatigue in glass — a reappraisal. *J. Non-Cryst. Solids*, **20** (1976) 305–21.
19. Gehrke, E., Ullner, C. & Hähnert, M., Strength and fatigue of some binary and ternary silicate glasses. *J. Non-Cryst. Solids*, **80** (1986) 269–76.
20. Gehrke, E., Ullner, C. & Hähnert, M., Correlation between multistage crack growth and time-dependent strength in commercial silicate glasses. Part 1. Influence of ambient media and types of initial cracks. *Glastech. Ber.*, **60** (8) (1987) 268–78.
21. Gehrke, E., Ullner, C. & Hähnert, M., Correlation between multistage crack growth and time-dependent strength in commercial silicate glasses. Part 2. Influence of surface treatment. *Glastech. Ber.*, **60** (10) (1987) 340–5.
22. Evans, A. G., A method for evaluating the time-dependent failure characteristics of brittle materials — and its application to polycrystalline alumina. *J. Mater. Sci.*, **7** (1972) 1137–46.
23. Michalske, T. A., The stress corrosion limit: its measurement and implications. In *Fracture Mechanics of Ceramics*, ed. R. C. Bradt, D. P. H. Hasselmann & F. F. Lange. Plenum Press, New York, 1983, Vol. 5, pp. 277–89.
24. Sglavo, V. M. & Green, D. J., The interrupted static fatigue test for evaluating threshold stress intensity factor in ceramic materials: a theoretical analysis. *J. Eur. Ceram. Soc.*, **15** (1995) 777–86.
25. Wilkins, B. J. S. & Dutton, R., Static fatigue limit with particular reference to glass. *J. Am. Ceram. Soc.*, **59** (3–4) (1975) 108–12.
26. Minford, E. J. & Tressler, R. E., Determination of threshold stress intensity for crack growth at high temperature in silicon carbide ceramics. *J. Am. Ceram. Soc.*, **66** (5) (1983) 338–40.
27. Minford, E. J., Kupp, D. M. & Tressler, R. E., Static fatigue limit for sintered silicon carbide at elevated temperatures. *J. Am. Ceram. Soc.*, **66** (11) (1983) 769–73.
28. Foley, M. R. & Tressler, R. E., Threshold stress intensity for crack growth at elevated temperatures in a silicon nitride ceramic. *Adv. Ceram. Mater.*, **34** (1988) 383–6.
29. Yavuz, B. O. & Tressler, R. E., Threshold stress intensity for crack growth in silicon carbide ceramics. *J. Am. Ceram. Soc.*, **76**(4) (1993) 1017–24.
30. Hayashi, K., Easler, T. E. & Bradt, R. C., A fracture statistics estimate of the fatigue limit of a borosilicate glass. *J. Eur. Ceram. Soc.*, **12** (1993) 487–91.
31. Ogasawara, T., Hori, T. & Okada, A., Threshold stress intensity for oxidative crack healing in sintered silicon nitride. *J. Mater. Sci. Lett.*, **13** (1994) 404–6.
32. Wiederhorn, S. M., Fracture surface energy of glass. *J. Am. Ceram. Soc.*, **52** (1969) 99–105.
33. Hahn, G. J. & Shapiro, S. S., *Statistical Models in Engineering*. John Wiley & Sons, New York, 1967.

Journal of the European Ceramic Society 16 (1996) 653–664

0955-2219/96/$15.00
0955-2219(95)00178-6

Microstructural Instability and the Resultant Strength of Si–C–O (Nicalon) and Si–N–C–O (HPZ) Fibres

R. Bodet,[a]* N. Jia[b] & R. E. Tressler[c]

[a]Laboratoire des Composites Thermostructuraux (UMR-47 CNRS-SEP-UB1), Domaine Universitaire, 3 allée de la Boétie, 33600 Pessac, France
[b]Analytical Sciences Laboratory, Allied Signal Inc., Morristown, NJ 07962-1021, USA
[c]Department of Materials Science and Engineering, The Pennsylvania State University, University Park, PA 16802, USA

(Received 25 March 1994; revised version received 12 September 1995; accepted 29 September 1995)

Abstract

Microstructural changes and the related strength degradation were investigated for Si–C–O Nicalon and Si–N–C–O HPZ fibres during heat treatments in air and argon at 1000–1400°C for 0·5 to 90 h. While the as-received Nicalon fibre contains β-SiC and carbon nanocrystals in an amorphous $SiO_{1\cdot12}C_{0\cdot44}$ phase, the HPZ fibre is completely amorphous. It is also inhomogeneous in surface composition compared with that of the bulk. The time-dependent strength degradation of the Nicalon fibre in argon is related to the gradual decomposition of the $SiO_{1\cdot12}C_{0\cdot44}$ phase from the surface which produces surface defects, β-SiC grain growth and intergranular porosity. The strength degradation of the HPZ fibre results from surface crystallization into α-SiO_2, Si_2N_2O and β-SiC. On the other hand, the HPZ fibre core — which has composition close to $SiN_{1\cdot02}C_{0.23}$ — shows structural stability for all heat treatment conditions.

1 Introduction

Advances in ceramic fibres are important in improving the performance of composite materials for high-temperature aerospace applications. The silicon carbide Nicalon® fibre, produced from the pyrolysis of polycarbosilane (PCS) according to Yajima's route,[1] is known to be chemically unstable at elevated temperature. Chemical reactions with the environment and thermal decomposition of the fibre lead to the formation of new populations of flaws, and result in chemical or physical modification of the fibre microstructure.[2–9] Moreover, transport processes such as viscous flow, which occurs during creep of the fibre, are highly temperature-dependent.[10] All these processes result in strength degradation in service. Recently, improvements in retained room-temperature strength and structure stability of Nicalon were observed after annealing for long periods of time in an environment containing carbon monoxide.[11] This treatment was successfully used to characterize the fibre creep behaviour with a rheological model for the viscous flow of a concentrated suspension.[12,13]

Several new ceramic fibres are currently under development. One fibre claimed to be compositionally and structurally stable to nearly 1400°C is the HPZ fibre, which is processed by pyrolysis of hydridopolysilazane.[9] Its structure can be described as a disordered $Si(N,C)_4$-based tetrahedral network containing only graphitic nanocrystals.[14] Unlike Nicalon fibre, studies on the thermal stability of HPZ fibre are still very limited. After thermal ageing in nitrogen or argon at 1200–1400°C, the fibre fracture strength was found to degrade significantly long before chemical and structural changes were evident.[3,15] Similar observations were reported after ageing in air for 2 h and in vacuum for 64 h at 1200°C, although the Young's modulus of the fibre remained unchanged after heat treatment.[16] A mechanism of property degradation involving diffusion-controlled reactions at flaw sites was postulated to explain this behaviour.[3] It was reported that the HPZ fibre aged in argon exhibits surface oxidation but much less change in the bulk compared with Nicalon.[3] Among several fibre-cordierite systems with a BN interphase, only those reinforced by the HPZ fibres experienced a strength loss (~60%) compared with the unreinforced matrix.[17] The brittle composite behaviour

*Now with Institute of Advanced Materials, Joint Research Center, Petten, The Netherlands.

was attributed to fibre degradation during the BN coating process at 600°C. Strong fibre–matrix bonding and strength degradation were also reported in the case of a chemical vapour deposition (CVD)-SiC coating (0·8 μm thick) on HPZ fibres.[16] Unlike Nicalon–glass matrix composites which develop a carbon interphase *in situ* during fabrication, those with HPZ fibres formed SiO_2-rich interfaces.[18–20] On the other hand, a deliberately formed CVD carbon coating on HPZ fibres prevented the occurrence of fibre–matrix interaction and properties approaching those of the best carbon-coated Nicalon composites were demonstrated.[18,19] The reasons for the high reactivity of the HPZ fibre with oxides, SiC and BN, and conversely its good compatibility with carbon, are not clear at this point.

Because the fibre–matrix interface is critical in many composite applications, chemical and structural characterizations of the HPZ fibre surface must be carried out. The main objective of this investigation was to compare the thermomechanical behaviours of PCS- and PCSZ-derived ceramic fibres in air and argon. The effects of long-term exposure on the microstructure and strength of these fibres were particularly studied by means of transmission electron microscope (TEM) analyses and room temperature tensile testing.

2 Experimental Procedure

Ceramic fibres investigated in this study were a commercial Nicalon fibre NLP 201 (Nippon Carbon, Yokohama, Japan) and an experimental HPZ fibre (Dow Corning, Midland, USA). The elemental compositions of the fibres obtained by EPMA are reported in Table 1. Both fibres are also known to contain some traces of hydrogen (~0·1 wt%).[14] The as-received fibres were washed in ultrasonically agitated baths of acetone, ethyl alcohol and distilled water, successively, except those exposed to heat treatments for which the organic sizing was burned off during the temperature rise.

A custom-built furnace consisting of a vertical alumina tube and six SiC heating elements was used for air and argon ageing at times from 0·5 to 90 h and temperatures between 1000 and 1400°C. Bundles of fibres were suspended by sewing them through either a carbon cloth (for argon heat treatments) or a silica cloth (for air heat treatments), which was placed inside the top part of the chamber. For argon heat treatments, a preliminary step consisting of evacuating the furnace for at least 1 h was used at the beginning of the heat treatment ($T < 550$°C) followed by a dwell time of 2 h at 550°C during which UHP argon gas (oxygen $<10^{-9}$ ppm) was introduced. An in-line oxygen sensor (zirconia cell) was used to determine the oxygen level.

Fibres were ground into powder in acetone and analysed by X-ray diffraction (XRD) (Rigaku Denki diffractometer) using Cu K_α radiation. Thermogravimetric analyses (TGA) were run on fibre bundles in dry argon with a heating rate of 100°C min^{-1}. The elemental composition of the as-received fibres was determined by electron probe microanalysis (EPMA) with a Camebax probe (model 75). X-ray photoelectron (XPS) and Auger electron (AES) spectroscopies were performed using an Al-targeted X-ray source in an ESCA/SAM/MACS system (Perkin–Elmer, model 560). The XPS data were calibrated using the Si 2p (101·1 eV) and C 1s (283·3 eV) binding energies for SiC. Samples were sputter-cleaned by 3 keV argon ion beams prior to analysis. The compositions were determined from the peak area for each element corrected for the relative sensitivity factor of XPS to the particular line. Individual filament fracture surfaces after strength tests were examined in an ISI-SX-40A scanning electron microscope (SEM). The fibre structure was analysed with a TEM microscope (Philips 420 T), using the bright field (BF), dark field (DF) and selected area electron diffraction (SAED) modes. TEM specimens were prepared either by gluing the fibres onto copper grids, followed by conventional ion-milling with argon ions (Gatan Dual Ion Mill), or by embedding the fibres in a very hard epoxy resin

Table 1. Elemental and molecular compositions of as-received Nicalon and HPZ fibres

	Elemental composition					*Molecular composition*		
Nicalon								
	Si	C	O			SiC	SiO_xC_y	C
at%	39	47	14		mol%	49	23	28
wt%	58	30	12		wt%	56	34	10
						$x = 1{\cdot}12$, $y = 0{\cdot}44$		
HPZ								
	Si	N	C	O		SiO_2	SiN_xC_y	C
at%	41	39	16	4	mol%	4	81	15
wt%	58	29	10	3	wt%	6	90	4
						$x = 1{\cdot}02$, $y = 0{\cdot}23$		

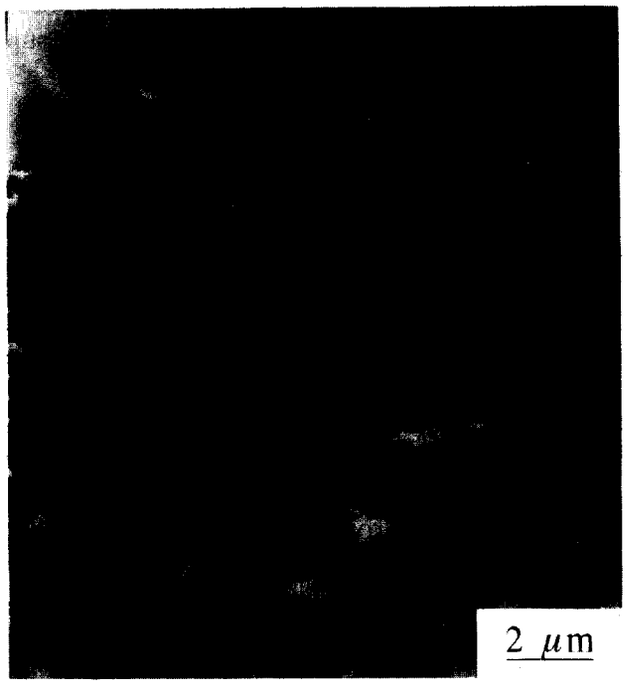

Fig. 1. Microtomed section of a Nicalon fibre after heat treatment in argon for 90 h at 1300°C, showing extensive surface degradation and grain growth.

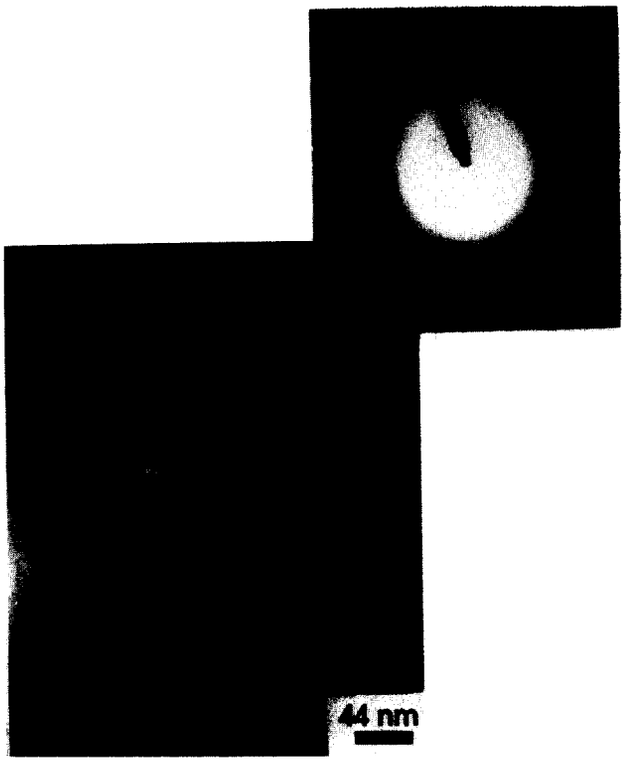

Fig. 2. TEM BF analysis of an as-received HPZ fibre. A typical globular pore found in the fibre core is shown by the arrow. The SAED pattern in the inset accounts for the amorphous character of the fibre bulk.

and subsequent microtoming of the resulting blocks with a diamond knife (Du Pont de Nemours). Although desired thicknesses could be obtained by microtomy, the fibre sections usually broke into small fragments oriented perpendicular to the knife travel. Minimum damage occurred for the most severely degraded fibres after long heat treatments, as shown in Fig. 1.

The short-term strength tests were performed on individual fibres in air at room temperature, all at the same crosshead speed of 0·5 mm min.$^{-1}$ The loading apparatus consisted of a table-top Instron tester (model 1102). The true elongation of the fibre was obtained by correcting the recorded elongation by taking into account a system compliance which is a function of both load-cell and grip deformations and fibre diameter.[21]

3 Results

3.1 Microstructure of as-received fibres

An average β-SiC grain size of 2·7 nm was obtained from an (1 1 1)-SiC dark-field image of the as-received Nicalon fibre. As pointed out in previous studies, other components found in this fibre include an amorphous SiO_xC_y phase and dispersed carbon (BSU's) nanocrystals.[7,22] The deconvolution of the Si 2p photopeak obtained by XPS after etching ~50 nm from the fibre surface accounted for an SiC to SiO_xC_y ratio of 233/110.

On the other hand, the as-received HPZ fibre is completely amorphous, as revealed by the SAED pattern in Fig. 2. The corresponding BF image indicates that the fibre contains some porosity in the 20–50 nm range. A thick (~200 nm) porous layer of different contrast was found on the surface of the HPZ fibres (Fig. 3). Such a layer has been already reported by Chang and Zangvil.[23] AES depth profiles indicated a gradual change in the layer composition from SiO_xC_y to SiN_xC_y with an intermediate $SiO_xC_yN_z$ phase showing up at a depth of 50 nm. XPS analyses were also performed at different sputtering depths from the fibre surface. All Si 2p peaks were found to be

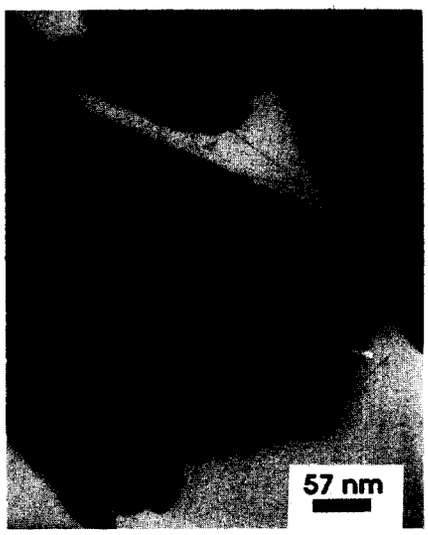

Fig. 3. TEM BF showing the porous surface of the as-received HPZ fibre, as indicated by arrows.

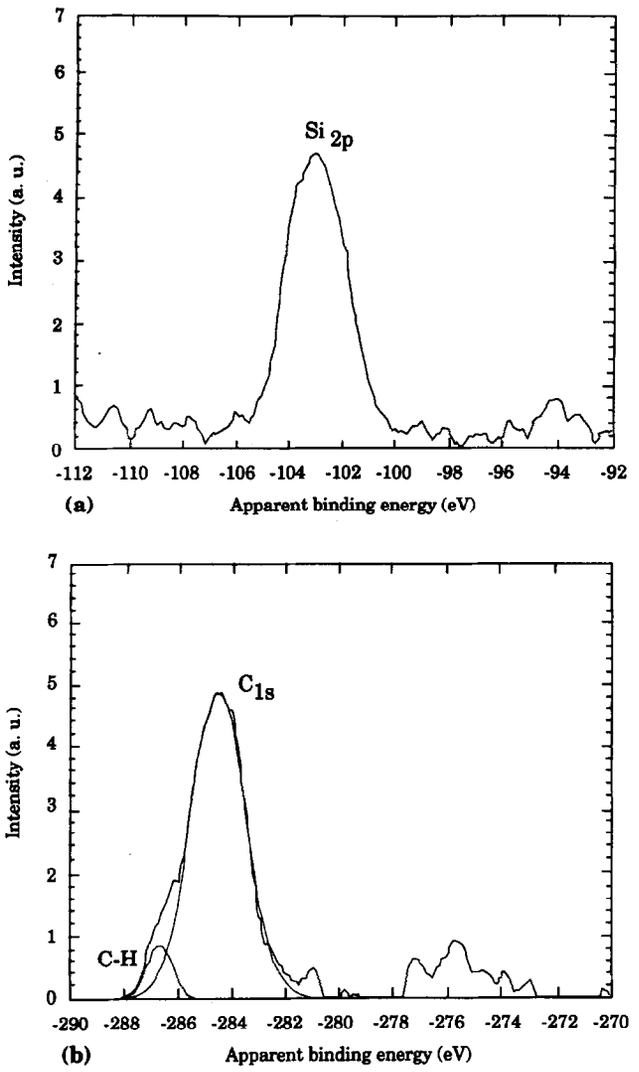

Fig. 4. XPS analysis on as-received HPZ fibres near the surface. (a) Symmetric Si 2p photopeak indicating that Si exists in a single phase. (b) Slightly shifted C 1s photopeak revealing the existence of C–H bonds originating from the polymer precursor.

symmetric, indicating a unique binding nature for Si and suggesting that Si exists in only one phase relatively to the depth. A typical Si 2p photopeak is represented in Fig. 4(a). On the other hand, the *C* 1s peak in Fig. 4(b) presents a second component bearing the feature of C–H or C–CH_3 bonds. This subpeak accounted for ~8 at% of the total carbon.

3.2 Molecular composition of as-received fibres

Attempts to quantitatively determine the fibre molecular composition required some simplifications due to the complexity of these chemical systems. First, based on the experimental observations, the 200 nm thick surface of the HPZ fibre was assumed to contain all the oxygen and its composition was taken as pure SiO_2. Second, the free carbon content in each fibre was estimated from rule-of-mixtures (ROM) calculations (normal ROM compositions can be calculated by assigning all oxygen to silicon as SiO_2; then all nitrogen to silicon as Si_3N_4; then carbon to silicon as SiC; the excess carbon is considered to be in the elemental standard state). An additional relationship, the SiC-to-SiO_xC_y molar ratio obtained by XPS, was also required for the Nicalon fibre. Then, the sets of equations given in Appendix 1 were solved. The solutions shown in Table 1 are expressed as A = mol% SiC, B = mol% SiO_xC_y for Nicalon and SiN_xC_y for HPZ, C = mol% free C, x and y. Finally, a simplification of the ternary phase formulae was performed by establishing an empirical relationship between the coefficients x and y. This led to $y = 1 - (x/2)$ for Nicalon and $y = 1 - (3x/4)$ for HPZ. The resulting formulae, $SiO_xC_{1-(x/2)}$ for Nicalon and $SiN_xC_{1-(3x/4)}$ for HPZ, can be easily verified graphically by means of mixed, $Si(C,O)_4$ or $Si(C,N)_4$, tetrahedal structures, as shown in Figs 5(a) and (b). Let α be the number of Si–O (or Si–N) bonds and $4 - \alpha$ the remaining Si–C bonds per tetrahedron, and assume that unsaturated silicon, Si–Si, O–O, C–O, N–N and multiple bonds are prohibited. The O, N and C contributions per tetrahedron normalized to one Si atom are respectively $\alpha/2$, $\alpha/3$ and $(4 - \alpha)/4$. Finally, let $x = \alpha/2$ leads to the chemical formula $SiO_xC_{1-(x/2)}$ for

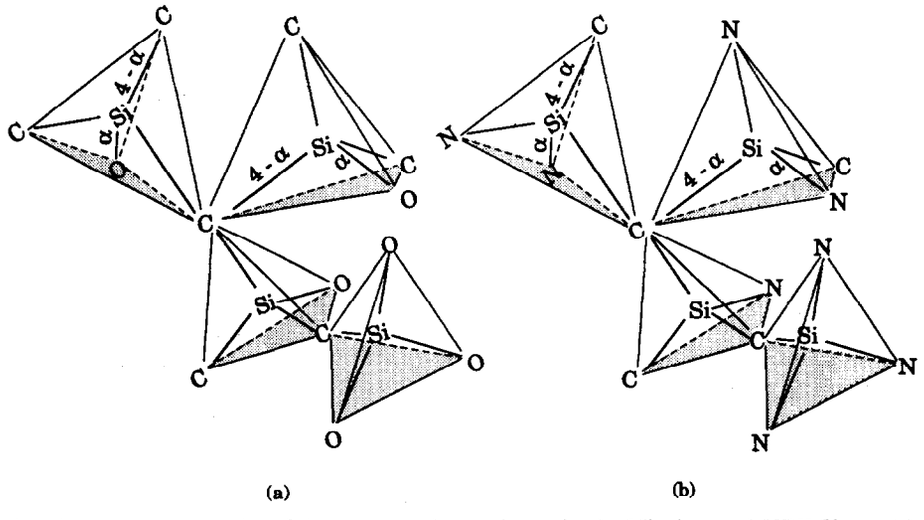

Fig. 5. Three-dimensional structure networks of the ternary glassy phases in the Nicalon and HPZ fibres: (a) SiO_xC_y, (b) SiN_xC_y.

Nicalon. Similarly, let $x = \alpha/3$ leads to $SiN_xC_{1-(3x/4)}$ for HPZ. The α value which represents the average number of oxygen or nitrogen bonded to silicon (the remaining $4 - \alpha$ being carbon bonds) signifies that 2·24 oxygen and 1·76 carbon atoms on one hand, and 3·06 nitrogen and 0·94 carbon atoms on the other hand, are bonded to every silicon atom in the respective ternary phases of the Nicalon and HPZ fibres.

Based on the above proposed formulae for the ternary phases, the fibre molecular compositions can now be varied within some limit values of x. Results are shown in Figs 6(a) and (b) along with the actual fibre compositions (dashed lines). Figure 6(a) shows that SiC vanishes in Nicalon at x = 0·36, resulting in a fibre composed of 72 mol% $SiO_xC_{1-(x/2)}$ and 28 mol% C. The fibre composition at x = 2, on the other hand, corresponds to that calculated from the ROM (mol% SiC = 59, SiO_2 = 13 and C = 28). As shown in Fig. 6(b), the HPZ fibre has the ROM composition at x = 0 and x = 4/3 (mol% SiC = 32·5, Si_3N_4 = 35·5, SiO_2 = 6·8 and free C = 25·2). Moreover, shifting x from these limits reduces both SiC and Si_3N_4 phase contents. The fibre composition at the convergent point where the stoichiometric carbide and nitride phases vanish (x = 1·02) corresponds to the actual composition of the HPZ fibre. Finally, it is shown that the free carbon content in both fibres remains constant within the entire range and thus does not depend on the composition of the other fibre phases.

3.3 Effects of heat treatments on fibre microstructure

3.3.1 Nicalon fibre

The effect of heat treatment on the Nicalon fibre crystallization was revealed by XRD and TEM. An increase of β-SiC crystallinity with ageing temperature and time was represented by a sharpening of the XRD spectrum. At the same time, the TEM analysis revealed an increased average grain size of β-SiC. As shown in Figs 7(a) and (b), the rate of grain growth in both atmospheres was found to increase with temperature and to decrease with exposure time. Figure 7(b) further indicates that a more pronounced crystallinity of β-SiC developed in Nicalon during ageing treatments in argon. An exaggerated grain growth and a well pronounced porosity resulting from exposure for 90 h at 1300°C in argon are shown in Fig. 1. The X-ray diffraction patterns also indicated that cristobalite peaks show up in air. A thick oxide scale on the fibre surface, resulting from exposure for 90 h at 1300°C, is shown in Fig. 8(a). The

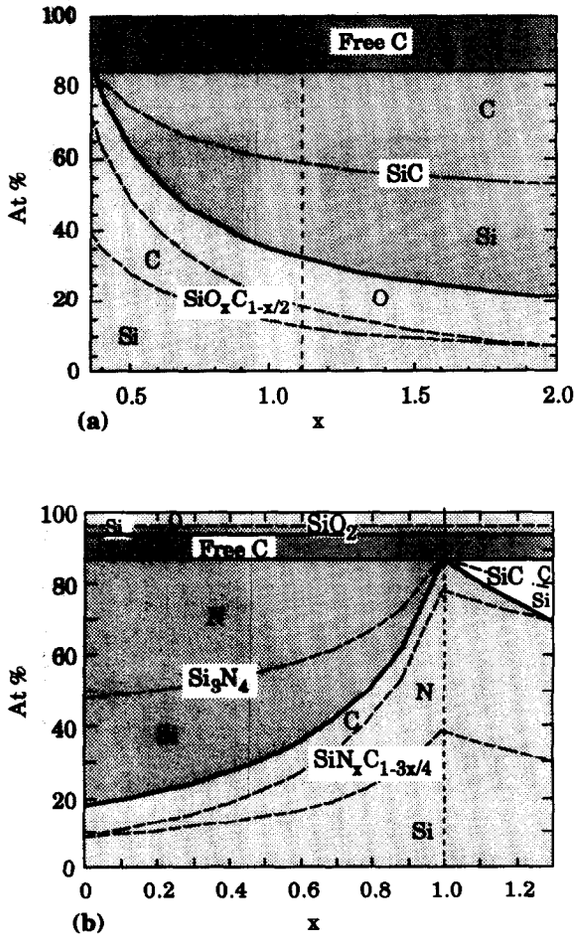

Fig. 6. Predicted variations of the fibre molecular compositions as a function of the parameter x: (a) Nicalon, (b) HPZ.

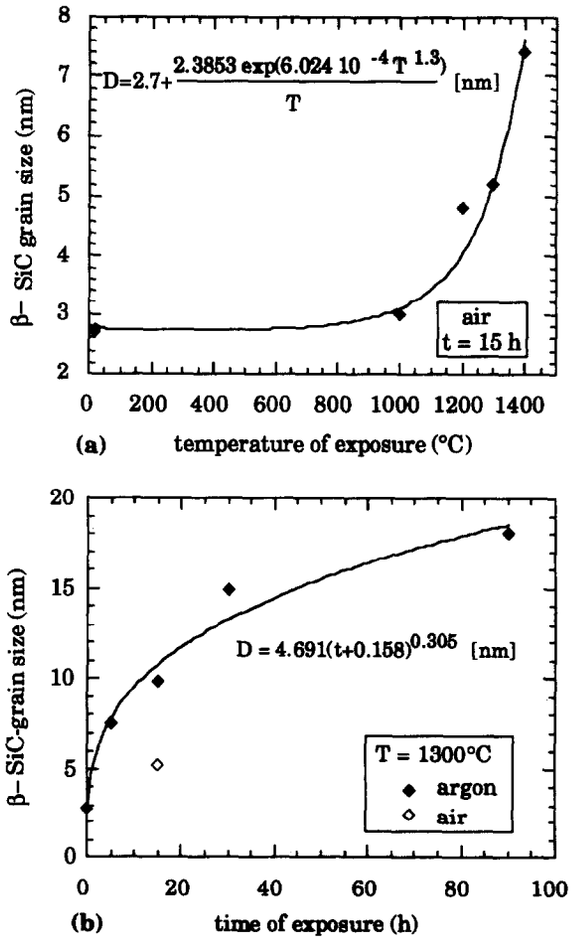

Fig. 7. β-SiC grain growth in the Nicalon fibre as a function of (a) temperature and (b) time of heat treatment in air and argon.

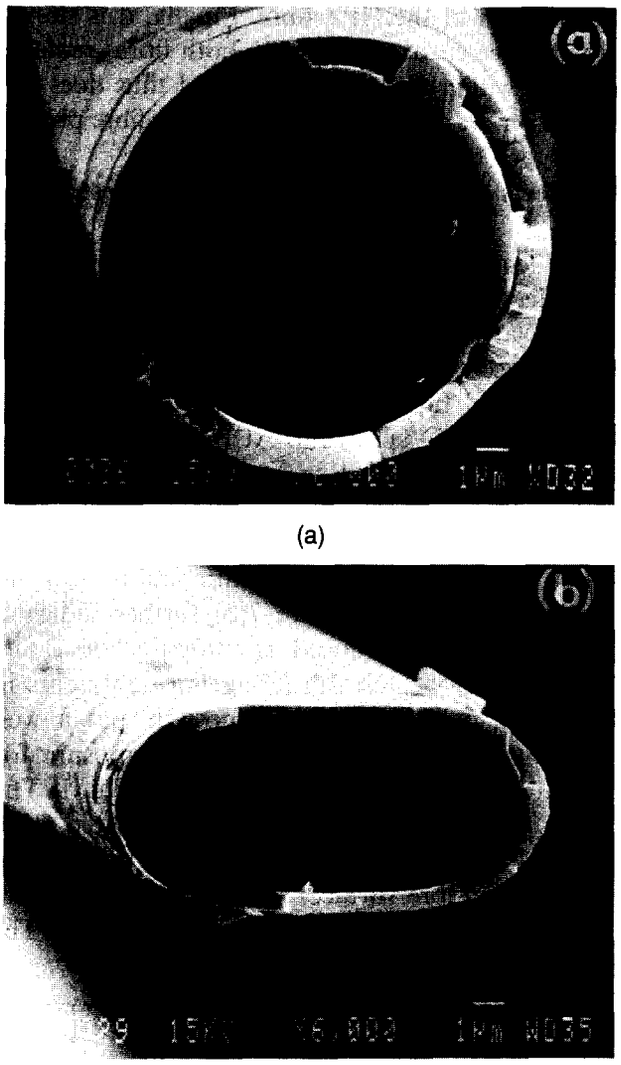

Fig. 8. SEM analysis of the fracture surfaces of fibres heat-treated for 90 h in air at 1300°C. (a) Nicalon, (b) HPZ.

composition of the heat-treated fibres in argon was analysed by means of AES depth profiling. The Nicalon fibre progressively transformed to stoichiometric SiC with increasing heat treatment time. This transformation was complete after 30 h at 1300°C and 15 h at 1400°C.

3.3.2 HPZ fibre

Crystallization of the HPZ fibre did not occur at temperatures below 1300°C in argon. After long heat treatment times at this temperature, microstructural modifications were observed near the fibre surface. A low magnification image of a surface region and the corresponding SAED pattern are shown in Fig. 9. The crystalline phase was identified as being cristobalite. Once cristobalite was transformed to amorphous silica when irradiated by the electron beam, further TEM analyses below the silica crust revealed the existence of two stable crystalline phases, Si_2N_2O and β-SiC, as well as the presence of channels of porosity within the silicon oxynitride phase [Figs 10(a) to (c)]. On

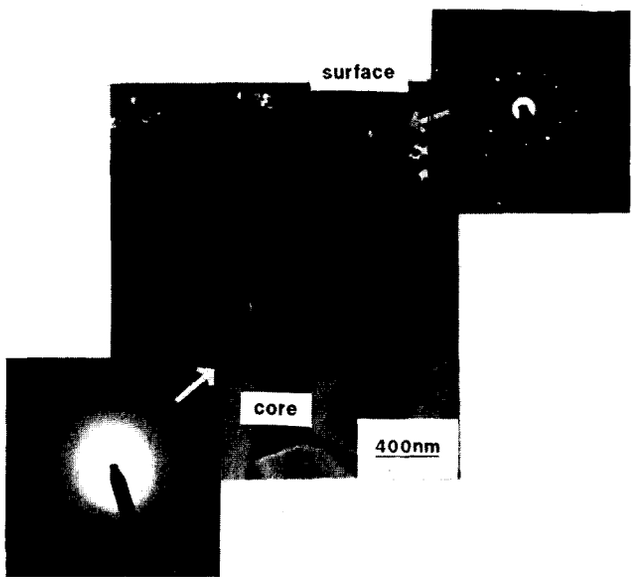

Fig. 9. SiO_2 DF micrograph of an HPZ fibre heat-treated for 90 h at 1300°C in argon, showing the crystallized fibre surface.

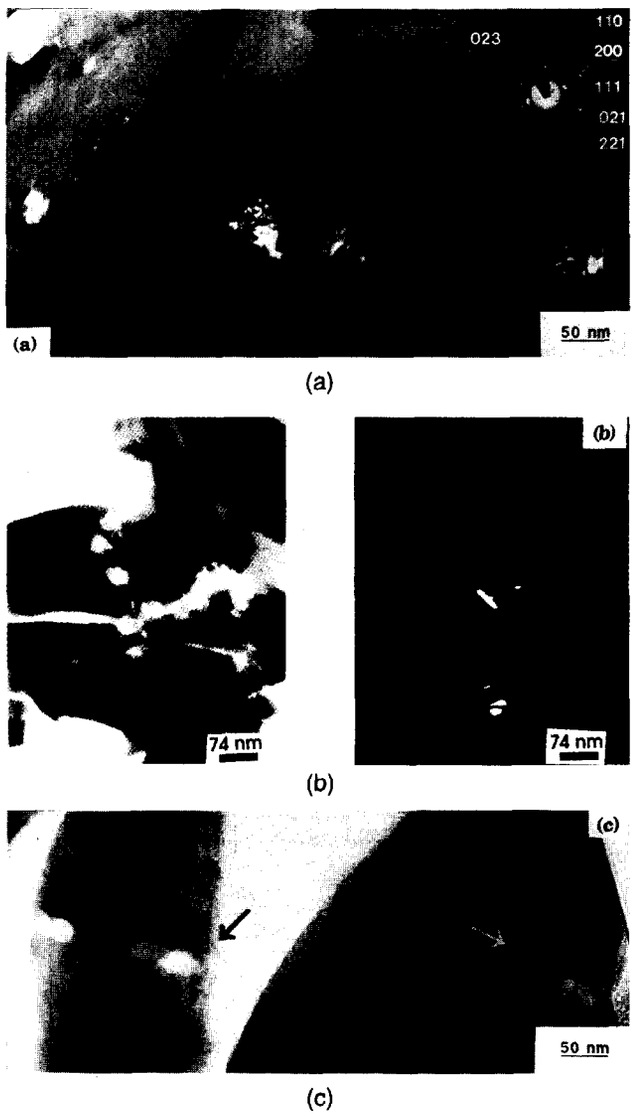

Fig. 10. TEM analysis of HPZ heat-treated for 90 h at 1300°C in argon. (a) DF image and corresponding SAED pattern of the Si_2N_2O interphase, (b) BF micrograph of the degraded near-surface region of the fibre bulk and associated SiC (1 1 1) DF, (c) BF micrograph showing the presence of channels of porosity parallel to the silica–bulk interface region.

Fig. 11. TEM image showing channels of porosity in the oxide reaction layer of an HPZ fibre heat-treated in air for 15 h at 1400°C.

the other hand, the remaining fibre after prolonged heat treatments in argon still bore the characteristics of the as-received fibre, i.e. same bulk composition and same amorphous structure (Fig. 9).

It was very difficult to establish evidence for all these microstructural changes for shorter exposure times in argon, as well as for all heat treatment conditions in air. As shown in Fig. 8(b), cristobalite again developed on the fibre surface in air. The presence of surface-connected channels in this reaction layer was also observed (Fig. 11).

3.4 Effects of heat treatments on fibre strength

Figures 12(a) and (b) show the room temperature strengths and moduli of the two fibres as a function of the exposure time in argon. It is seen from Fig. 12(a) that the heat treatment temperature greatly affected the degree of strength degradation. After heat treatments for 15 h at 1200, 1300 and 1400°C, the average strength of Nicalon was progressively lowered by 46·8, 75·9 and 91%, respectively, compared with that of the as-received fibres. By comparison, the strength of the HPZ fibre showed a decrease of 28·7, 40, and 68·1% at these temperatures. Also, the time of heat treatment was found to have an impact on the rate of strength degradation. During the first 15 h, the strength obviously reduced faster than it did during the rest of the heating period. For Nicalon this phenomenon was in apparent agreement with other changes occurring in the fibre, for example β-SiC grain growth and weight loss. Fig. 12(b) shows that the modulus of Nicalon lost 64% of its initial value after 15 h at 1400°C whereas that of

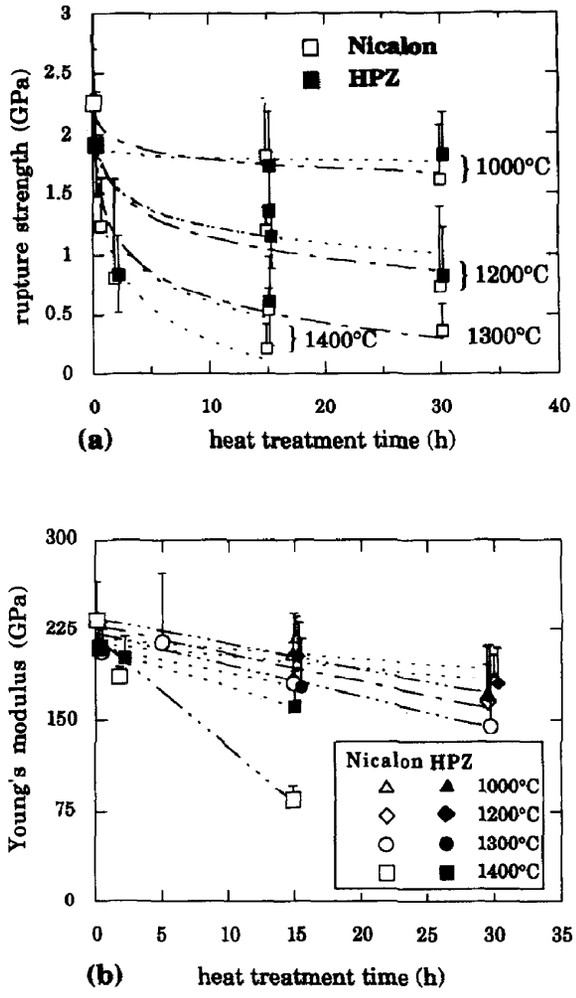

Fig. 12. Effect of time of heat treatment in argon on (a) tensile strength at room temperature and (b) Young's modulus of Nicalon and HPZ fibres. Open symbols represent Nicalon; black symbols represent HPZ. The single-sided bars represent the standard deviations.

HPZ was lowered by only 24% under the same ageing conditions.

3.5 Modelling the decomposition of the Nicalon fibre

To a large extent, heat treatments in inert atmospheres can be regarded as a continuation of the fibre pyrolysis. Many of the events taking place during heat treatments of Nicalon also occur during the last stage of pyrolysis. Among them are the crystallization of β-SiC, weight loss of the fibre, and CO and SiO evolution.[9] However, unlike pyrolysis — which is controlled to optimize the fibre properties — prolonged heat treatments often result in fibre degradation.

The overall decomposition of the Nicalon fibre can be expressed as

$$Si_{0.72}O_{0.26}C_{0.87} = (n_{SiC} + \Delta n_{SiC})\ SiC + (n_C + \Delta n_C)\ C + \Delta n_{CO}\ CO + \Delta n_{SiO}\ SiO \quad (1)$$

where $Si_{0.72}O_{0.26}C_{0.87}$ is the fibre molar formula and n_{SiC} and n_C are the initial mole ratios of SiC and C (see Table 1). Δn_{SiC}, Δn_C, Δn_{CO} and Δn_{SiO} are the variations of the mole ratios of the products.

The simplest approach used to model the decomposition is to consider the stepped progression of reaction (1) into the fibre (i.e. layer by layer), and to assume that one layer is fully decomposed when all the carbon has been consumed, i.e. $n_C + \Delta n_C = 0$. The results are shown in Figs 13(a) and (b) as a function of the molar percentage of decomposed fibre, along with the related changes in weight loss, density and porosity, which were obtained from

$$\Delta W/W_0 = \frac{\Delta W_{CO} + \Delta W_{SiO}}{M_0} = \frac{28\,\Delta n_{CO} + 44\,\Delta n_{SiO}}{M_0} \quad (2)$$

$$\rho_f = \rho_0(1-\Delta W/W_0) \quad (3)$$

$$P = 1 - \frac{\rho_f}{\Sigma\, V_i\rho_i} = 1 - \frac{\rho_f}{V_{SiC}\,\rho_{SiC} + V_C\,\rho_C + V_g\,\rho_g} \quad (4)$$

where $\Delta W_{CO} + \Delta W_{SiO}$ is the total weight of gas released, M_0 is the molar weight of the Nicalon fibre (M_0 = 34·8 g mol^{-1}), ρ_0 is the initial fibre density (ρ_0 = 2·55 g cm^{-3}), V_i is the volume fraction of the ith component ($V_i = m_i/\rho_i = n_iM_i/\rho_i$), ρ_{SiC} = 3·20 g cm^{-3}, ρ_C = 1·80 g cm^{-3}, and ρ_g is the density of the silicon oxycarbide glass which has been estimated from $\rho_0 = \Sigma V_{i\rho i}$, assuming an initial porosity of 2% in accordance with Ref. 7. The value obtained for ρ_g, i.e. 2·18 g cm^{-3}, was found to be slightly smaller than that of silica, for which ρ_{SiO_2} = 2·20 g cm^{-3}.

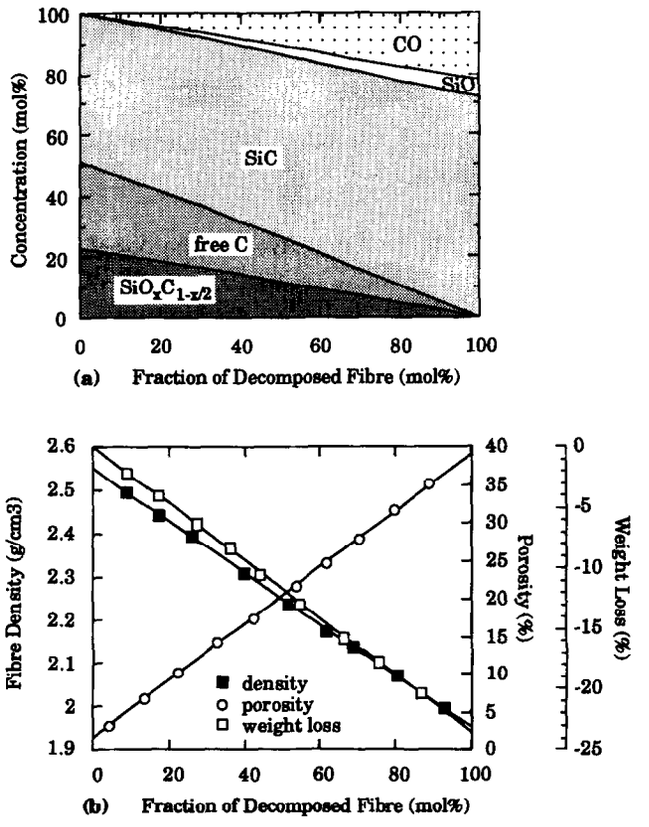

Fig. 13. Predicted variations of (a) the mole fractions of the chemical phases and (b) the porosity, density and weight loss as a function of the fraction of decomposed Nicalon fibre.

Finally, the calculated weight loss data were fitted with the experimental ones in order to plot the decomposition predictions on a time scale. The results are shown in Figs 14 and 15 for different test temperatures. In Fig. 14, the rate of decomposition is clearly expressed by the evolution of the gas phases (SiO + CO). This evolution remains limited at 1200°C even after long exposure times (~100 h). The decomposition is much faster at higher temperature and has practically ended after ~12 h at 1300°C and only ~1 h at 1400°C as it reaches a plateau which corresponds to the total consumption of carbon and silicon oxycarbide. The predicted variations of the density

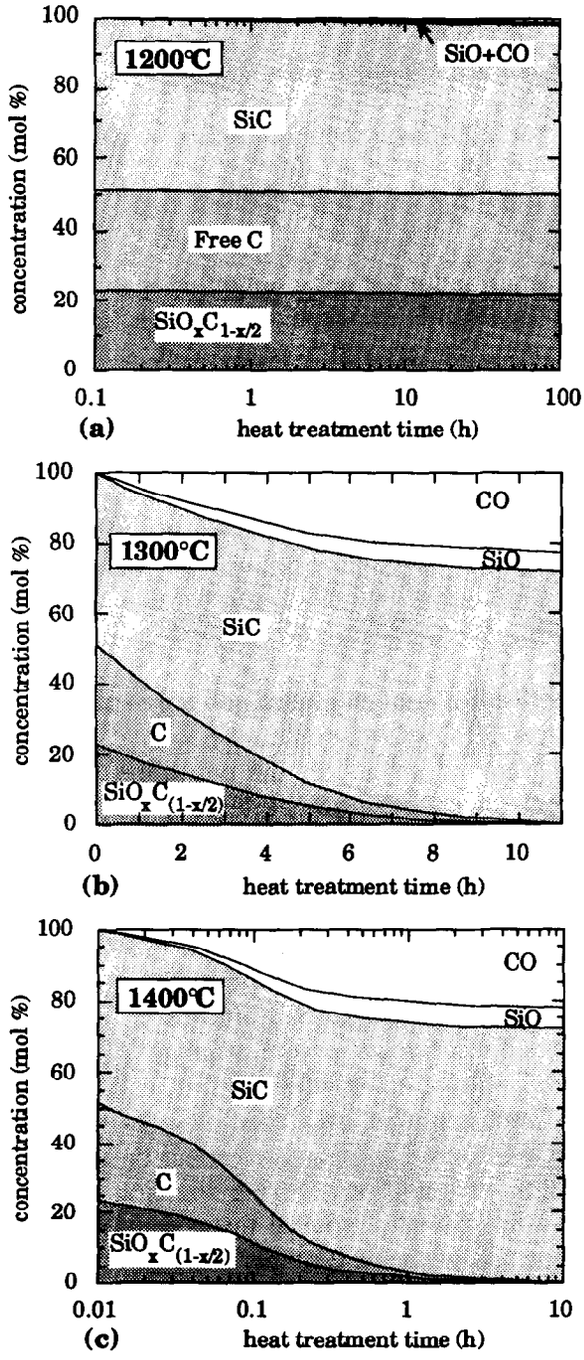

Fig. 14. Predicted variations of the molecular composition of Nicalon as a function of the exposure time in argon at (a) 1200°C, (b) 1300°C and (c) 1400°C.

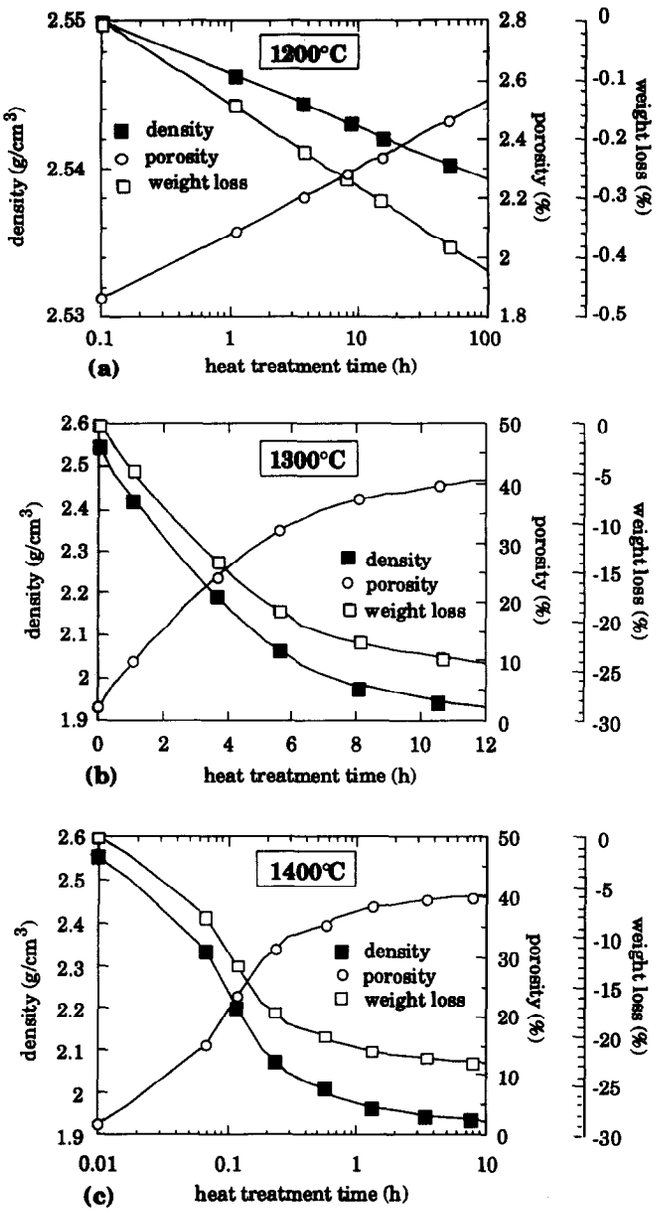

Fig. 15. Evolution of the density and porosity predicted from the experimental weight loss curve for the Nicalon fibre as a function of time of exposure in argon: (a) 1200°C, (b) 1300°C and (c) 1400°C.

and porosity along with the experimental weight loss curves are shown in Fig. 15. At the points where the experimental weight loss curves level off, the final density has dropped to ~1·9 g cm^{-3} whereas the porosity has increased to ~40%.

4 Discussion

4.1 As-received fibres

The determination of the free carbon content from rule-of-mixtures calculations is questionable. It was, however, shown in Fig. 6 that a variation of composition of the other fibre phases does not effect its initial content. Schreck *et al.*[22] attempted to determine from XPS analyses the molecular composition of the as-received Nicalon fibre. The ranges of x and y, for the silicon oxycarbide phase, were found to be $x = 1{\cdot}20 \pm 0{\cdot}11$ and $y = 0{\cdot}39 \pm 0{\cdot}06$. The empirical values obtained in the present study, $x = 1{\cdot}12$ and $y = 0{\cdot}44$, lie perfectly in these ranges. These data further correlate with the proposed relationships, $y = 1 - (x/2)$ for Nicalon and $y = 1 - (3x/4)$ for HPZ, established graphically (Fig. 5).

The porous structure and the heterogeneous oxygen-rich surface of the HPZ fibre detected by TEM and AES have already been reported.[23] Depending on processing conditions, the SiO_2-rich surface layer can be 0·1 to 0·7 μm thick. Band II in the C 1s XPS spectrum [Fig. 4(b)] suggests that carbon species carrying hydrogen or methyl groups may exist in HPZ due to incomplete decomposition of the organic precursor. It was reported that the residual hydrogen in this fibre could be as high as 0·1 wt% (~2 at%).[14] The corresponding H/C atomic ratio, i.e. 8%, has been confirmed here by XPS.

4.2 Thermal degradation of fibres

4.2.1 Nicalon fibre

Based on the microstructural observations, it is likely that the mechanical properties of Nicalon are controlled predominantly by the gradual decomposition of SiO_xC_y from the surface at elevated temperatures. If the gas diffusion is faster near the fibre surface than near the centre, the same will be true for the grain growth. This supposition was confirmed by the experimental observations which indicated a gradual grain growth in the heat-treated fibres (Fig. 1). Thus, the decomposition and related grain growth will proceed further in the fibre with time of heat treatment. The assumption used in quantification of the decomposition, that carbon is fully reacting in reaction (1), leads to a good agreement between the predicted and the experimental total weight losses (23·5 wt% vs. 24 wt%). It furthermore implies that the maximum CO is generated and results in a CO/SiO molar ratio of ~4 [Fig. 13 (a)]. This fact confirms previous statements that the major gas released from the Nicalon fibre is CO.[24]

The SiC crystallization may be reduced in air due to the formation of an oxidation layer on the fibre surface. This compact silica layer may retain the gas and consequently slow down the decomposition reaction.

4.2.2 HPZ fibre

The bulk of the HPZ fibre exhibited structural stability for all heat treatment conditions. On the

other hand, the crystallization of the surface into cristobalite, silicon oxycarbide and to a lesser extent silicon carbide was observed after prolonged exposures in argon (Figs 9 and 10). The presence of Si_2N_2O has also been noticed in HPZ/LAS matrix composites.[18,19] This phase was believed to arise from some fibre–matrix interfacial reactions. The slow formation of Si_2N_2O and SiC may be explained by the occurrence of solid-state reactions at the silica–bulk interface in the fibre, such as:

$$\frac{4}{x}\,SiN_xC_{1-(3x/4)} + SiO_2 \rightarrow 2\,Si_2N_2O + \left(\frac{4}{x} - 3\right) SiC \quad (5)$$

The stability of the silica–bulk interface is likely to persist for a long time during heat treatment because of the slow kinetics of reaction (5) which leads to the crystalline equilibrium composition.

The formation of SiC may also arise from the fibre bulk decomposition according to:

$$4\,SiN_xC_{1-(3x/4)} + 3x\,C \rightarrow 2x\,N_2(g) + 4\,SiC \quad (6)$$

In addition, reaction (6) yields nitrogen gas. Previous thermodynamic calculations indicated that the nitrogen partial pressure could be as high as 10^{-1} bar at 1300°C above Si–C–N–O fibres with an excess of carbon.[24] However, the oxide layer on the HPZ fibre may provide a good diffusion barrier for the gas. Since the β-SiC crystals were only observed after long treatments (Fig. 10), it is likely that an accumulation of N_2 prevented the formation of SiC until the gas pressure became sufficiently low for reaction (6) to proceed to the right. Where it is not related to the spinning defects, the porosity found in the near-surface region may be related to gas evolution (Figs 10 and 11).

In air, the reactions (7) and (8) are believed to occur simultaneously:

$$4\,SiN_xC_{1-(3x/4)} + \left(6 - \frac{3x}{2}\right) O_2 \rightarrow 4\,SiO_2 + (4 - 3x)CO + 2x\,N_2 \quad (7)$$

$$C + O_2 \rightarrow CO_2 \quad (8)$$

As far as the oxidation resistance is concerned, oxygen diffusion through Si_2N_2O is more difficult than through silica.[25] Thus, Si_2N_2O will provide a good protection barrier against oxidation. The thinner reaction layer on HPZ compared with Nicalon under the same heat treatment conditions supports this assumption (Fig. 8).

4.3 Strength degradation

The tensile properties of Nicalon degraded more severely than those of HPZ during heat treatments in argon. This degradation is attributed to the gradual decomposition of the SiO_xC_y phase from the surface, which causes grain growth and forms intergranular porosity. The rate of strength degradation increased with temperature and decreased with time (Fig. 12), similarly to the rate of grain growth (Fig. 7) and porosity (Fig. 15). The low modulus of Nicalon heat-treated under the most severe conditions may result from the quasi-absence of cohesion between SiC crystals due to replacement of the intergranular residual carbon and silicon oxycarbide phases by porosity.

On the other hand, the amount of compositional change was immeasurably small in the case of HPZ fibres after ageing in argon, and it is clear from the microstructural analyses that surface damage was responsible for most of the strength loss. This damage may arise during cooling from the thermal expansion mismatch between the crystallized species of the surface, i.e. cristobalite and silicon oxynitride, on one hand, and the glassy phase of the fibre bulk, on the other hand. Additionally, the porosity related to the gas evolution resulting from the bulk decomposition certainly affected the fibre mechanical properties. It is suggested that the time-dependent strength of the HPZ fibre resulted from the slow kinetics of solid–solid reactions, such as reactions (5) and (6).

5 Summary and Conclusions

The most significant results of this study can be summarized as follows.

(1) Based on the elemental and structural analyses, the molecular compositions of the Nicalon and HPZ fibres have been determined. It is proposed that the Nicalon fibre consists of three phases which are SiC, C and a $SiO_{1.12}C_{0.44}$ phase, the corresponding molar percentages of which are 49, 28 and 23. Assuming again a three-phase material for the HPZ fibre, its composition has been taken as SiO_2 = 4 mol%, $SiN_{1.02}C_{0.23}$ = 81 mol% and C = 15 mol%. It is suggested that the amorphous ternary phases can be represented by the formulae $SiO_xC_{1-(x/2)}$ and $SiN_xC_{1-(3x/4)}$ for Nicalon and HPZ, respectively. The experimental observations revealed that the HPZ fibre is amorphous, inhomogeneous in surface composition, and that it contains processing defects, such as a 200 nm thick silica-rich layer on the surface and small globular pores at the nanometre scale in the bulk.

(2) Heat treatments were performed on fibres in air and argon from 0·5 to 90 h between 1000°C and 1400°C. In Nicalon, the grain

growth was much faster in argon than in air, and it was much more sensitive to an increase in temperature than to a prolonged treatment. The gradual evolution of porosity in this fibre also decreased with time of heat treatment. Heat treatments of HPZ in argon resulted in the crystallization of the near-surface region into α-cristobalite, Si_2N_2O and β-SiC, and in the development of microporosity. It was suggested that the Si_2N_2O and SiC formations in HPZ are controlled by the slow kinetics of solid-state reactions involving the oxygen-rich scale, the silicon carbonitride and the free carbon of the bulk. On the other hand, the HPZ fibre core showed structural stability up to 1400°C.

(3) The strength degradation was for Nicalon in apparent agreement with other changes occurring in the fibre, for example β-SiC grain growth and weight loss. While the internal porosity may have contributed to the lower room temperature strength of the HPZ fibre compared with Nicalon, its strength degradation in argon was only related to surface degradation.

Acknowledgements

The authors would like to thank the Gas Research Institute for financially sponsoring this project through the Center for Advanced Materials at Penn State University, and the Société Européenne de Propulsion for a grant given to R. B. They acknowledge the assistance of Dr H. Du of the Stevens Institute of Technology for conducting the AES and XPS analyses.

References

1. Yajima, S., Hayashi, J. & Omori, M., Continuous silicon carbide fiber of high tensile strength. *Chem. Lett.*, **9** (1975) 931–4.
2. Villeneuve, J. F., Mocaer, D., Pailler, R., Naslain, R. & Olry, P., Tensile testing at high temperatures of ex-PCS Si–C–O and ex-PCSZ Si–C–N single filaments. *J. Mater. Sci.*, **28** (1993) 1227–36.
3. Sawyer, L. C., Microstructure of ceramic fibers. In *Fibre Reinforced Ceramic Composites*, ed. K. S. Mazdiyasni. Noyes Publications, Mill Road, NJ, 1990, pp. 141–81.
4. Pysher, D. J., Goretta, K. C., Hodder Jr, R. S. & Tressler, R. E., Strengths of ceramic fibers at elevated temperatures. *J. Am. Ceram Soc.*, **72** (1989) 284–8.
5. Kim, H. E. & Moorhead, A. J., Strength of Nicalon carbide fibers exposed to high-temperature gaseous environments. *J. Am. Ceram. Soc.*, **74** (1991) 666–9.
6. Shimoo, T., Chen, H. & Okamura, K., Pyrolysis of Si–C–O fibres (Nicalon) at temperature from 1473 K to 1673 K. *J. Ceram. Soc. Japan.*, **100** (1992) 48–53.
7. Le Coustumer, P., Monthioux, M. & Oberlin, A., Understanding Nicalon fibre. *J. Eur. Ceram. Soc.*, **11** (1993) 95–103.
8. Chaim, R., Heuer, A. H. & Chen, R. T., Microstructural and microchemical characterization of silicon carbide and silicon carbonitride ceramic fibers produced from polymer precursors. *J. Am. Ceram Soc.*, **71** (1988) 960–9.
9. Langley, N. R., LeGrow, G. E. & Lipowitz, J., Properties of ceramic fibers from organosilicon polymers. In *Fiber Reinforced Ceramic Composites*, ed. K. S. Mazdiyasni. Noyes Publications, Mill Road, NJ, 1990, pp. 63–92.
10. Jia, N., Bodet, R. & Tressler, R. E., Effects of microstructural instability on the creep behavior of Si–C–O (Nicalon) fibers in argon. *J. Am. Ceram. Soc.*, **76** (1993) 3051–60.
11. Bodet, R., Jia, N. & Tressler, R. E., Thermomechanical stability of Nicalon fibres in a carbon monoxide environment. *J. Eur. Ceram. Soc.*, **15** (1995) 997–1006.
12. Bodet, R., Lamon, J. & Tressler, R. E., Effects of chemical environments on the creep behavior of Si–C–O fibres. In *Proceedings of the 1st International Conference on High Temperature Ceramic Matrix Composites*, ed. R. Naslain, J. Lamon & D. Doumeingts. Woodhead Publishing, Cambridge, 1993, pp. 75–83.
13. Bodet, R., Lamon, J., Jia, N. & Tressler, R. E., Microstructural stability and creep behavior of Si–C–O (Nicalon) fibers in carbon monoxide and argon environments. *J. Am. Ceram. Soc.*, in press.
14. Lipowitz, J., Freeman, H. A., Chen, R. T. & Prack, E. R., Composition and structure of ceramic fibers prepared from polymer precursors, *Adv. Ceram. Mater.*, **2** (1987) 121–8.
15. Langley, N. R. & Li, C. T., Effects of interfacial diffusion barriers on thermal stability of ceramic fibers. In *Ceramic Microstructure '86, Role of Interfaces*, ed. J. A. Pask & A. G. Evans. Plenum Press, New York, 1987, pp. 401–7.
16. Lin, W. & Yang, J. M., Thermal stability of ceramic fibre in a CVI-processed SiC matrix composite. *J. Mater. Sci.*, **26** (1991) 4116-22.
17. Lane, J. E. & Pebler, A. R., Failure characteristics of low dielectric constant ceramic composites reinforced with BN-coated fibers. *Ceram. Eng. Sci. Proc.*, **10** (1989) 1213–22.
18. Brennan, J. J., Interfacial characteristics of glass-ceramic matrix/SiC fibre composites. *J. de Physique*, **49** (1988) 791–809.
19. Brennan, J. J., Glass and glass-ceramic matrix composites. In *Fiber Reinforced Ceramic Composites*, ed. K. S. Mazdiyasni. Noyes Publications, Mill Road, NJ, 1990, pp. 222–59.
20. Lewis, M. H. & Murthy, V. S. R., Microstructural characterization of interfaces in fiber-reinforced ceramics. *Compos. Sci. Technol.*, **42** (1991) 221–49.
21. Li, C. T. & Langley, N. R., Improvement in fiber testing of high-modulus single filament materials. *J. Am. Ceram. Soc.*, **68** (1985) C202–4.
22. Schreck, P., Vix-Guterl, C., Ehrburger, P. & Lahaye, J., Reactivity and molecular structure of silicon carbide fibres derived from polycarbosilanes. Part II: XPS analysis. *J. Mater. Sci.*, **27** (1992) 4243–6.
23. Chang, Y. W. & Zangvil, A., Characterization of Si–C–N–O fibers by analytical STEM and scanning Auger techniques. In *Ceramic Transactions, Silicon Carbide '87*, ed. J. D. Cawley & C. E. Semler. The American Ceramic Society, Westerville, OH, 1989, pp. 435–43.
24. Luthra, K. L., Thermomechanical analysis of the stability of continuous 'SiC' fibers. *J. Am. Ceram. Soc.*, **9** (1986) C231–3.
25. Tressler, R. E., Spear, K. E., Zheng, Z. & Du, H., Fundamental studies of the oxidation of silicon carbide crystals and CVD silicon nitride. In *High Temperature Corrosion of Technical Ceramics*, ed. R. J. Fordham. Elsevier Applied Science, London, 1990, pp. 69-89.

APPENDIX 1

The fibre molecular compositions given in Table 1 were obtained by solving the following sets of equations.

For the Nicalon fibre:

$$\text{Si} = \frac{39}{100} = \frac{A + B}{2A + B(y + 1 + x) + C} \quad \text{(A1)}$$

$$C_{\text{free}} = \frac{15}{100} = \frac{C}{2A + B(y + 1 + x) + C} \quad \text{(A2)}$$

$$\text{O} = \frac{14}{100} = \frac{xB}{2A + B(y + 1 + x) + C} \quad \text{(A3)}$$

$$C_{\text{bonded}} = \frac{32}{100} = \frac{A + yB}{2A + B(y + 1 + x) + C} \quad \text{(A4)}$$

$$\frac{A}{B} = \frac{233}{100} \quad \text{(from XPS analysis)} \quad \text{(A5)}$$

$$A + B + C + 1 \quad \text{(A6)}$$

with SiC = A, SiO_xC_y = B, free carbon = C.

For the HPZ fibre:

$$\text{Si} = \frac{40}{100} = \frac{A + B}{2A + B(y + 1 + x) + C} \quad \text{(A7)}$$

$$C_{\text{free}} = \frac{7}{100} = \frac{C}{2A + B(y + 1 + x) + C} \quad \text{(A8)}$$

$$\text{O} = \frac{4}{100} = \frac{2A}{2A + B(y + 1 + x) + C} \quad \text{(A9)}$$

$$\text{N} = \frac{40}{100} = \frac{xB}{2A + B(y + 1 + x) + C} \quad \text{(A10)}$$

$$C_{\text{bonded}} = \frac{9}{100} = \frac{yB}{2A + B(y + 1 + x) + C} \quad \text{(A11)}$$

$$A + B + C + 1 \quad \text{(A12)}$$

with SiO_2 = A, SiN_xC_y = B, free carbon = C.

Journal of the European Ceramic Society 16 (1996) 665–670

0955-2219(95)00185-0
0955-2219/96/$15.00

The Influence of α- and β-Si_3N_4 Precursors on Formation of α-SiAlON Ceramics

Miroslav Haviar

Institute of Inorganic Chemistry, Slovak Academy of Sciences, 842 36 Bratislava, Slovakia

(Received 21 February 1995; revised version received 5 October 1995; accepted 12 October 1995)

Abstract

During the formation of α-SiAlON from a powder mixture wet-milled in isopropyl alcohol at a temperature of 1500–1600°C there appears considerable amount of β-SiAlON. β-SiAlON is formed in high α- as well as in high β-Si_3N_4 starting powders. The β-SiAlON is dissolved at higher temperatures. The rate of dissolution of α-Si_3N_4 was observed to be higher than that of β-Si_3N_4 and the densification and rate of α-SiAlON formation is higher in high α-Si_3N_4 powder.

1 Introduction

SiAlON ceramics have attracted the attention of materials scientists during last two decades. At the very beginning of their development there was a belief that the reaction of 'transient' liquids resulting in incorporation of sintering additives into the α- or β-SiAlON structure and thus giving less or no grain boundary phase would improve the high temperature properties.[1,2] For many years this expectation was not fulfilled and the mechanical properties of Si_3N_4-based materials were superior to SiAlONs. The advantage of SiAlONs was in their different chemical properties, resulting in different corrosion resistance and ease of fabrication. The second main point focusing interest on SiAlON materials was the fact that they allowed us to have stable α-phase in the system. The α-phase is considerably harder,[5,6] which is of interest in cutting and wear applications.[3,4,7] Recent results of carefully prepared α/β-SiAlON composite materials with exceptional high temperature properties[8] are confirming early expectations.

α-SiAlON can be characterized by the formula $Me_xSi_{12-(m+n)}Al_{m+n}O_nN_{16-n}$ where Me is Li, Ca, Mg, Y and rare-earth metals except La, Ce, Pr and Eu[2,9] and $m = 3x$ when x represents the valence of the Me atom. Yttrium α-SiAlON is among the α-SiAlONs most widely investigated.[2,7,9,10] The triangle Si_3N_4–Y_2O_3·9AlN–YN·3AlN has a stability area of α-SiAlON, as shown in Fig. 1.

β-SiAlON has the formula $Si_{6-z}Al_zO_zN_{8-z}$ where $0 < z < 4{\cdot}2$.[1] α- as well as β-SiAlONs are isostructural with α- and β-Si_3N_4, respectively. The influence of different starting Si_3N_4 powders, mixing techniques, temperature and rate of temperature increase on phase composition and relative density is reported in this paper.

2 Experimental Procedure

In the present work, three starting silicon nitride powders were used. Two of them, labelled as A and B were prepared by nitridation of silicon powder in-house.[11] They were extracted from the different parts of the nitrided powder compact and due to the different thermal conditions they consisted of various α/β-Si_3N_4 proportions. The specification of the powders is shown in Table 1.

The appropriate powder mixtures, expected to produce α-SiAlON with an x-value of 0·4 were attrition milled for 4 h with Si_3N_4 balls in isopropyl alcohol. Abrasion of the milling balls (β-Si_3N_4) resulted in a 5% increase of β-Si_3N_4 in the starting powder. Alternatively, one powder mixture (C) was mixed in a rotating polyethylene bottle in isopropyl alcohol with agate balls as mixing media. This was labelled as D. The abrasion of the balls was not detected. The mixing time was 48 h. The isopropyl alcohol was dried prior to all experiments. The composition of the powder mixtures is shown in Table 2.

The powders were dried and isostatically pressed to solid bodies approximately 60% of theoretical density under a pressure of 200 MPa. The firing was performed at 1300–1900°C for 1 h under 1 MPa of static nitrogen in a graphite resistance furnace, which was evacuated before heating to 1000°C. A powder bed prepared from Si_3N_4 (86 wt%),

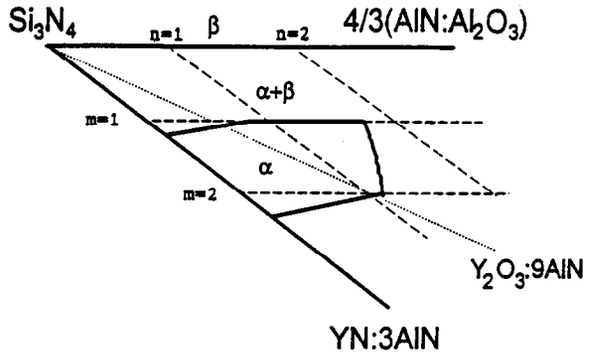

Fig. 1. Detail from the triangle Si_3N_4–$4/3Y_2O_3{\cdot}9AlN$–$YN{\cdot}3AlN$, showing composition area of α-SiAlONs, according to Ref. 9.

Table 1. Specification of the powders used

Material	*Specification*
Si_3N_4-A	Prepared in house, median grain size 0·3 μm, 85% α-phase, 15% β-phase, oxygen content 1·8 wt%
Si_3N_4-B	ditto, 10% α-phase, 90% β-phase
Si_3N_4-C	H. C. Starck Grade H1, median grain size 0·66 μm, >> 90% α-phase, oxygen content 1·6% (LECO), specific surface 9·87 $m^2\ g^{-1}$ (BET)
AlN	Fluka, No. 06280, oxygen content 1·4 wt%, median grain size 1 μm
Y_2O_3	Techsnabexport, Russia, 99·99% pure, median grain size 4 μm

Table 2. Composition of the powder mixtures (wt%)

Powder mixture	Si_3N_4	Y_2O_3	AlN
A, B and C	80·04	7·58	12·38

Al_2O_3 (7 wt%) and Y_2O_3 (7 wt%) powders were used in all experiments. Dilatometry experiments were performed in a high-temperature dilatometer heated by graphite resistance furnace. The sample was isolated from the graphite assembly by thin (0·5 mm) BN disks. Densities of the fired samples were determined by mercury immersion method. X-ray diffraction patterns were collected on the powdered samples with primary beam monochromatized CoK_α radiation ($CoK_{\alpha 1}$ = 1·788965 A) using a STOE Stadi P transmission diffractometer configured with a linear position sensitive detector. The α/β ratio in the samples was determined from the X-ray intensities of planes 102 and 210 for the α-phase and 101 and 210 for the β-phase.[12] To reveal the microstructure, polished samples were plasma etched (Fisons Instruments, model Polaron PT 7150).

3 Results and Discussion

The phase composition of powder mixtures prepared from Si_3N_4 powders A, B and C (materials A, B and C) fired at various temperatures (1300–1900°C) for 1 h is shown in Figs 2–4 (only Si_3N_4-based phases are shown). In all three powder mixtures α-SiAlON starts to form at approximately 1300°C and its formation is at the expense of α- as well as β-Si_3N_4. At approximately 1500°C there is in all powder mixtures, an increase in the β-phase. Above 1600°C the β-phase is converted to α-SiAlON. The composition of secondary β-phase (*z*-value) was, with the help of X-ray unit cell determination established in the range of $0{\cdot}2 < z < 0{\cdot}3$. These results are not in full accordance with recent work of Sheu,[8] who concluded that, while using 100% α-Si_3N_4 as the starting powder, α-SiAlON and β-Si_3N_4 phases evolved. While using 100% β-Si_3N_4 as the starting powder, only α-SiAlON evolved but the original β-Si_3N_4 decreased. The difference between these two observations can be explained by the use of various starting materials. While in the present work the difference between the pow-

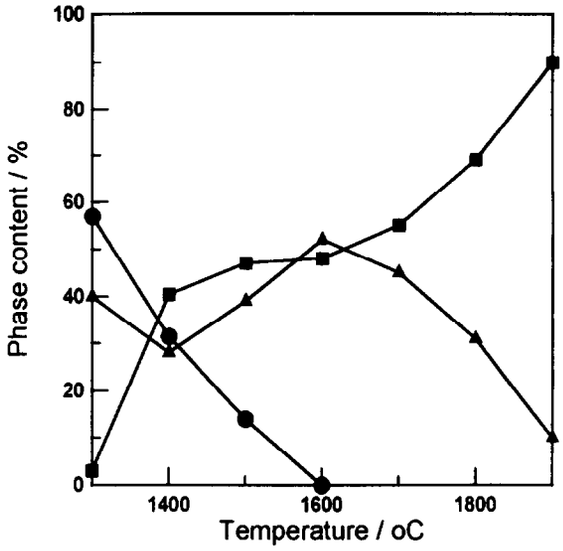

Fig. 2. Phase composition of the powder mixture A fired at various temperatures for 1 h in nitrogen. ● α-Si_3N_4, ■ α-SiAlON, ▲ β-phase.

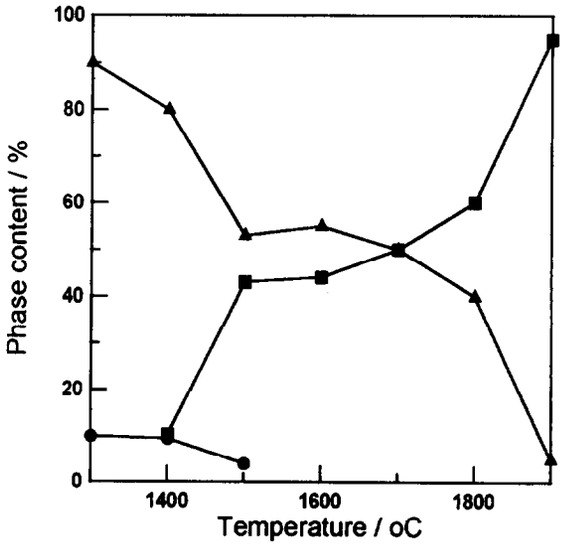

Fig. 3. Phase composition of the powder mixture B fired at various temperatures for 1 h in nitrogen. ● α-Si_3N_4, ■ α-SiAlON, ▲ β-phase.

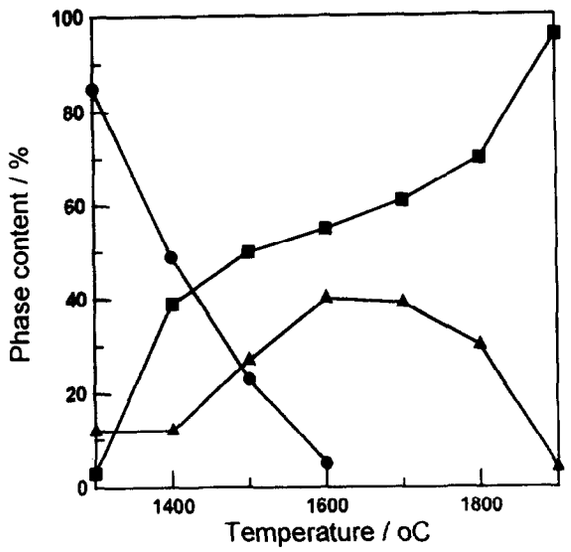

Fig. 4. Phase composition of the powder mixture C fired at various temperatures for 1 h in nitrogen. ● α-Si_3N_4, ■ α-SiAlON, ▲ β-phase.

ders A and B, as they stem from the same nitridation batch, is only in their phase composition, Sheu[8] used commercial high α-Si_3N_4 powder, which was heat treated in order to convert it to β-Si_3N_4. This treatment could result also in some change of its chemical composition. It is also possible, that the reason that Sheu[8] did not observe cooperative formation of α-SiAlON and the β-phase may have kinetic reasons, as his results represent the phase composition during heating up of the sample and not after some time lapse (1 h in present paper) at given temperature.

The phase composition of the powder mixture D, where wet milling was substituted by mixing in plastic bottle is shown in Fig. 5. Here the formation of α-SiAlON starts at lower temperatures than in attrition-milled sample, and the formation of secondary β-SiAlON is absent. The temporary formation of β-SiAlON is in agreement with the results in Ref. 13. This paper confirms this observation also in the case of the high β-Si_3N_4 starting powder. The decomposition of β-SiAlON above 1600°C suggests that the region of stability of α-SiAlON is better at higher temperatures.

The densification kinetics of powder mixtures A and B was studied in a dilatometer using various heating rates. The results are shown in Figs 6 and 7. At both heating rates, 50 and 500°C/min, the powder mixture B (consisting of 85% of β-Si_3N_4) exhibits lower densification. The densification process in the system of α-SiAlON is a very complex one. The classical sintering consisting of neck growth and pore elimination is accompanied by phase transformation, where the morphology of dissolving as well as emerging phases plays an important role. According to Hendry[14] the difference in free energies of formation of α- and β-Si_3N_4 at 1100°C is about 10%, when α modification is a more stable one. According to these data,

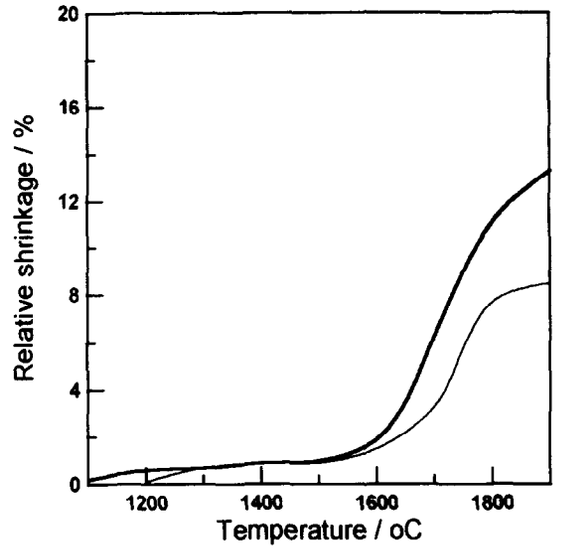

Fig. 6. Relative shrinkage versus temperature of the powder mixtures A (bold line) and B (thin line). Heating rate 50°C/min.

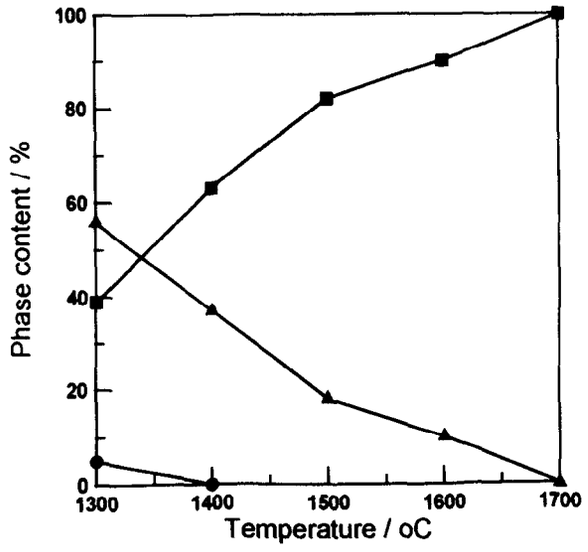

Fig. 5. Phase composition of the powder mixture D fired at various temperatures for 1 h in nitrogen. ● α-Si_3N_4, ■ α-SiAlON, ▲ β-phase.

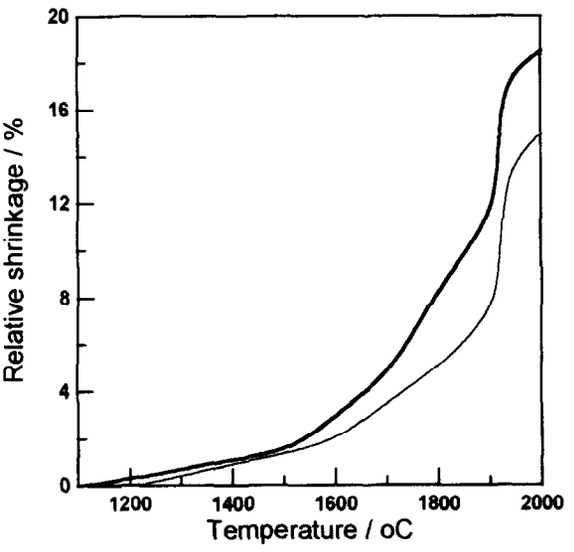

Fig. 7. Relative shrinkage versus temperature of the powder mixtures A (bold line) and B (thin line). Heating rate 500°C/min.

β-modification is supposed to become more stable above 1330°C. However, according to the recent data for β-Si_3N_4 by Pánek,[15] β-Si_3N_4 is more stable above 950°C. The earlier onset of densification of the powder mixture A is probably caused by higher dissolution rate of α-Si_3N_4. This is also in agreement with the similar observation of Šajgalík and Galusek[16] and it is the reason for higher rate of formation of α-SiAlON, specially at lower temperatures, *cf* Figs 2 and 3.

The higher heating rate (500°C/min) leads to higher relative shrinkage in the studied systems. The difference is probably caused by the amount and composition of transient liquid present in the densifying α-SiAlON system. With the ongoing phase transformation and formation of α-SiAlON (above 1300°C), this liquid is consumed. At higher heating rates the transient liquid remains, due to the kinetic reasons, in the system up to higher temperatures, influencing positively the densification. The phase composition (only major, Si_3N_4 phases are shown) of the samples after dilatometric experiments is shown in Fig. 8. At the heating rate of 50°C/min in the sample A, there is more α-SiAlON formed (61 versus 56%) compared to the sample B. This also confirms that α-Si_3N_4 from the starting powder dissolves faster than β-Si_3N_4. At the heating rate of 500°C/min the former α- and probably also β-Si_3N_4 powders did not react completely. (The resolution of X-ray diffraction analysis did not allow us, due to the close values of unit cell dimensions, to distinguish between β-Si_3N_4 and β-SiAlON quantitatively). Also in this case, the amount of α-SiAlON is higher in the sample A.

The microstructure of samples from dilatometry is shown in Fig. 9. The samples were polished and plasma etched. By plasma etching 'pure' Si_3N_4 is attacked more intensively, followed by β-SiAlON, α-SiAlON and the grain-boundary phase. Thus, the Si_3N_4 is darkest, the β-SiAlON is lighter, etc. (*cf.* Fig. 9(a)). In sample A, heated at the rate of 50°C/min (Fig. 9(a)), there is relatively low amount of original Si_3N_4 grains. The microstructure of the sample A heated with the rate of 500°C/min (Fig. 9(b)) contains a higher amount of the original Si_3N_4 grains and is considerably finer. In sample B heated at the rate of 500°C/min (Fig. 9(c)), the former Si_3N_4 grains are bigger than in sample A. This observation confirms that the rate of dissolution of β-Si_3N_4 during formation of α-SiAlON is lower in comparison with α-Si_3N_4.

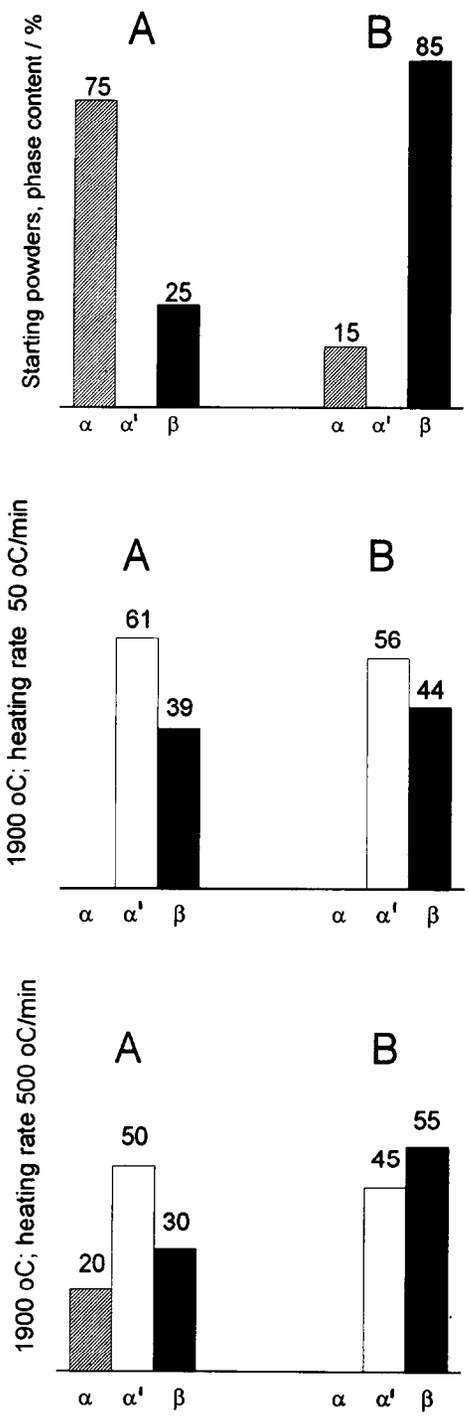

Fig. 8. Phase composition of the starting powders and samples after dilatometry.

4 Conclusions

The results of this study show that in the powder system expected to form α-SiAlON, in the temperature region 1500–1600°C β-SiAlON is formed, regardless of the α/β-Si_3N_4 starting powder composition. During the reaction producing α-SiAlON the rate of dissolution of α-Si_3N_4 is faster than that of β-Si_3N_4. The high α-Si_3N_4 starting powders thus exhibit higher densification and α-SiAlON formation.

Acknowledgement

The support of this work by the Slovak Grant Agency under the grants Nos 2/1168/94 and 2/1169/94 is kindly acknowledged.

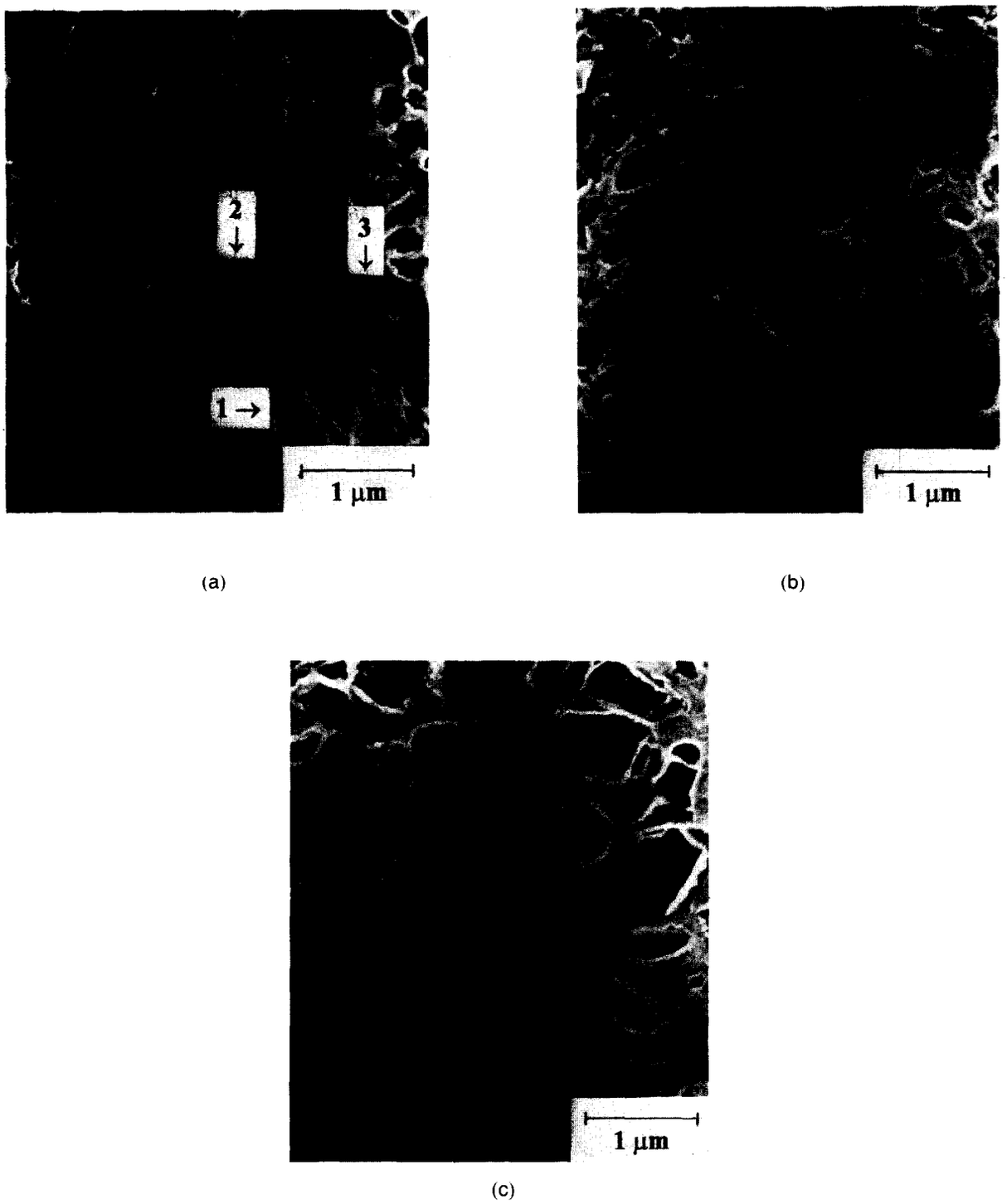

Fig. 9. Microstructure of the samples after dilatometry. (a) Powder mixture A, heating rate 50°C/min. (b) Powder mixture A, heating rate 500°C/min. (c) Powder mixture B, heating rate 500°C/min.

References

1. Jack, K. H., Review: SiAlONs and Related Nitrogen Ceramics. *J. Mater. Sci.*, **11** (1976) 1135–58.
2. Hampshire, S., Park, H. K., Thompson, D. P., & Jack, K. H., α'-SiAlON Ceramics. *Nature*, **274** (1978) 880–92.
3. Lumby, R. J., Butler, E. & Lewis, M. H., Lucas Syalons: Composition, Structure, Properties and Uses. In *Progress in Nitrogen Ceramics*, ed. F. L. Riley. Martinus Nijhoff Publ., The Hague, 1983, pp. 683–94.
4. Bessenyei, E. & Porat, R., Performance of Silicon Nitride Cutting Tool Inserts Prepared by Gas Pressure Sintering. *Refr. Metals & Hard Mater.*, **11** (1992) 121–6.
5. Greskovich, C. & Gazza, G. E., Hardness of Dense α- and β-Si_3N_4 Ceramics. *J. Mater. Sci. Lett.*, **4** (1985) 195–6.
6. Ekström, T. & Nygren, M., SiAlON Ceramics. *J. Am. Ceram. Soc.*, **75** (1992) 259–76.
7. Bartek, A., Ekström, T., Herbertsson, H. & Johansson, T., Yttrium α-SiAlON Ceramics by Hot Isostatic Pressing and Post-Hot Isostatic Pressing. *J. Am. Ceram. Soc.*, **75** (1992) 432–9.
8. Sheu, T. S., Microstructure and Mechanical Properties of the *in situ* β-Si_3N_4/α'-SiAlON Composite. *J. Amer. Ceram. Soc.*, **77** (1994) 2345–53.
9. Huang, Z. K., Tien, T. Y. & Yen, T. S., Subsolidus Phase Relationships in Si_3N_4–AlN–Rare-Earth Oxide Systems. *J. Am. Ceram. Soc.*, **69** (1986) C241–2.
10. Ukyo, Y. & Wada, S., Formation and Stability of Y–α'-SiAlON Co-existing with β'-SiAlON. In *Euro-Ceramics*,

ed. G. de With, R. A. Terpstra & R. Metselaar. Elsevier, London, 1991, pp. 1566–71.
11. Lenčéš, Z., Influence of Cr, Fe, Ni and Ti Additions on the Nitridation Kinetics of Silicon Powder Compacts. *Ceramics - Silikáty*, **38** (1994) 61–7.
12. Käll, P. O., Quantitative Phase Analysis of Si_3N_4-Based Materials. *Chem. Scr.*, **28** (1988) 439–43.
13. Haviar, M., Influence of Oxygen Content on Formation of Yttrium α-SiAlON Ceramics. *J. Am. Ceram. Soc.*, **77** (1994) 2425–8.
14. Hendry, A., Silicon Nitride Ceramics. In *Structural Ceramics: Processing, Microstructure and Properties.*, ed. J. J. Bentzen & I. B. Bild-Sovensen, Proc. of the 11th RISØ, Int. Symp. on Metall. and Mat. Sci., Denmark, 1990, pp. 27–38.
15. Pánek, Z., Standard Gibbs Energy of Formation of β-Silicon Nitride. *J. Am. Ceram. Soc.*, **78** (1995) 1087–8.
16. Šajgalík, P. & Galusek, D., α/β Phase Transformation of Silicon Nitride: Homogeneous and Heterogeneous Nucleation. *J. Mater. Sci. Lett.*, **12** (1993) 1937–9.

Journal of the European Ceramic Society 16 (1996) 671–678

0955-2219/96/$15.00
0955-2219(95)00172-7

Surface Charge and Viscosity of Mixed Si_3N_4–Y_2O_3 Suspensions Containing Lignosulphonate

Heidi Fagerholm,[a] Leena-Sisko Johansson,[b] Mats Graeffe[a] & Jarl B. Rosenholm[a]

[a]Åbo Akademi University, Department of Physical Chemistry, Porthansgatan 3–5, FIN–20500 Åbo, Finland
[b]Materials Research Centre, University of Turku, ElectroCity 4D, FIN–20520 Turku, Finland

(Received 20 June 1994; revised version received 31 August 1995; accepted 9 September 1995)

Abstract

We have studied the surface charge and the dispersion behavior of silicon nitride–yttrium oxide–lignosulfonate powder dispersions, prior to sintering. In our previous study we reported on the effect of pH on the adsorption of yttria (Y_2O_3) and lignosulfonate (LS) on the surface of silicon nitride (Si_3N_4) powder. The adsorption was studied by particle size measurements, scanning electron microscopy, X-ray photoelectron spectroscopy (ESCA) and carbon analyses. In this study, we report the results from the electrophoretic mobility and surface charge determinations and viscosity measurements of the slip. The viscosity measurements were performed as a function of the LS concentration added in the dispersion. This was done in order to determine the optimum concentration of lignosulfonate added in the dispersion, i.e. the concentration which would result in the lowest viscosity for the highest possible dry content of the slip. The surface charge was determined via potentiometric titrations and by measuring the electrophoretic mobility.

Introduction

Silicon nitride based ceramics have great potential for high-temperature, high-stress applications. In order to obtain defect-free ceramic bodies it is of importance to avoid aggregation of the dispersed powder and to be able to sinter the green body at sufficiently low temperatures.[1]

In our previous publication[2] we reported on the effect of pH on the adsorption of yttria (Y_2O_3) and lignosulfonate (LS) on the surface of silicon nitride (Si_3N_4) powder. In this paper we report on the suspension properties of Si_3N_4 matrix with an addition of sintering agent, yttria.

Electrophoretic mobility measurements were used to determine the change in the surface charge on the interface of the silicon nitride and yttria particles after conditioning in aqueous solutions of pH 7 and pH 10. Potentiometric titrations of the Si_3N_4–Y_2O_3–LS system were performed to quantify the surface charge and determine the isoelectric point (IEP) and to investigate if any specifically adsorbed positive or negative surface groups were present.

The viscosity of the slip was studied as a function of the concentration of lignosulfonate added to the dispersion. This is to obtain the lowest viscosity/highest dry content of the powder in the slip. In general the homogeneity and viscosity of the slip relate to the sintering properties of the green body.

Experimental

Raw materials

The silicon nitride powder (SN E-10) used in this study was supplied by Ube Industries, Yamaguchi, Japan. According to the manufacturer, the specific surface area was 10 $m^2\ g^{-1}$ and the particle size ~0·4 μm. The yttrium oxide powder (grade fine) was supplied by H. C. Starck, Berlin, Germany. The BET specific surface area according to the manufacturer was 13·7 $m^2\ g^{-1}$. The particle size distribution was given to be $X_{90} < 2{\cdot}5$ μm, $X_{50} <$ 0·8 μm and $X_{10} < 0{\cdot}35$ μm. The lignosulfonate used was Wargonin extra (calcium–sodium lignosulfonate) supplied by Lignotech Sweden.

The powders were used without further purification. The water used was distilled and purified with a Milli Q system to obtain a minimum resistivity of 18 $M\Omega\ cm^{-1}$.

Sample preparation

The list of samples is given in Table 1. The samples contained silicon nitride, yttrium oxide and/or lignosulfonate. The amount of the sintering agent, Y_2O_3, was kept at a constant level of 5 wt% and the concentration of the dispersing agent added to the solution was 0·05, 0·5 or 2·0 wt% for the electrophoretic mobility measurements. Viscosity was

Table 1. List of the samples. All samples except pure lignosulfonate specimen were treated in solutions of pH 7 and pH 10

Si_3N_4
Y_2O_3
Lignosulfonate (LS)
Si_3N_4 + 5 wt% Y_2O_3
Si_3N_4 + 5 wt% Y_2O_3 + 0·05 wt% LS
Si_3N_4 + 5 wt% Y_2O_3 + 0·5 wt% LS
Si_3N_4 + 5 wt% Y_2O_3 + 2·0 wt% LS

determined against the concentration of LS added to the dispersion, the amount of LS added being in the range 0·05–1 wt%. Percentage additives were calculated for the dry content of the slip. All samples were prepared by first adding the lignosulfonate powder (when used) in Milli Q purified water, then adding Y_2O_3 and finally Si_3N_4.

The pH 7 was chosen in order to obtain countercharged particle surfaces, thus ensuring an electrostatic adsorption of Y_2O_3 on the surface of Si_3N_4.[3] This pH is close to the natural pH of the slurry, and, according to Lidén *et al.*,[3] the colloidal yttria particles are stable and positively charged only in the pH range close to pH 7. However, the solubility of yttria at pH 7 might cause problems in the interpretation of the surface charge measurements.[4] According to the literature,[5] yttria is insoluble in bases and soluble in acids, and the solubility of yttria into cold water is 0·0018 g dm^{-3} (ie. 18 ppm). In our experiments the solubility of yttria into water was still insignificant at pH 7 (100 ppm). We did not measure the solubility of yttrium in aqueous silicon nitride dispersions but Rosenholm *et al.*[6] have reported that in aqueous ZrO_2 dispersions stabilized with 3 mol% Y_2O_3, the solubility of yttrium was at its minimum at a pH range of 6–7·5.

The pH 10 was chosen for our experiments, since pH 9–10 is typically used in processing of silicon nitride powders.[7] The pH of the respective slurries was adjusted using 0·1 M HCl or NaOH (Merck titrisols).

Sample preparation for electrophoretic mobility measurements

The dispersion was prepared by first adjusting the pH of the water. The dispersions were processed in an ultrasonic stirrer, after which the pH of the dispersion was readjusted. The dispersion was allowed to equilibrate for 24 h under stirring to ensure a sufficient conditioning time. The concentration of each slurry was about 20 wt%.

Prior to the measurements the pH of the dispersions was readjusted once more, after which the dispersion was centrifuged (3000 rev min^{-1}, 30 min) and separated from the supernatant. The dispersion was then diluted according to the requirements of the instrument manufacturer.

Sample preparation for surface charge measurements

Samples were prepared by adding 40 ml of the electrolyte (NaCl) to a preweighted amount of powder. This addition resulted in a suspension containing 15–21 m^2 powder. The suspensions were dispersed by an ultrasonic device and then allowed to equilibrate for about 20 h in a sealed container in normal atmosphere under stirring.

The supernatants used as blanks were obtained by centrifuging identically prepared suspensions at 3500 rev min^{-1} for 3 h. The supernatant was filtrated through a 0·22 μm Millipore filter paper before the titration.

Sample preparation for viscosity measurements

The viscosity was measured on dispersions containing 20–34 vol% powder. The measurements at the native pH of the slurry (close to pH 7) were made on freshly made slips, after 15 min treatment with an ultrasonic rod (model 450 Sonifer® Branson). The conditioned slips were prepared by allowing the powder dispersion to condition for 24 h. The alkaline slips were prepared by adding 5 ml 0·1 M NaOH in water; measurement of the pH of the slip after conditioning revealed a value of ~10–11. For the slips at conditioned native pH, the pH measured after conditioning was ~7–8.

Electrophoretic mobility

The electrophoretic mobility measurements were carried out using a Zetasizer IIc instrument from Malvern Instruments. The results of the measurements are reported as electrophoretic mobility since the size/diffuse layer thickness ratio is outside both the Huckel and the Smoluchovski limits and the transformation to zeta potential is not at all straightforward.

Surface charge

The surface charge density was determined using the method first developed by Parks and de Bruyn.[8] A Titrino 702 titroprocessor (from Metrohm) was used for potentiometric titrations. We measured the surface charge density as a function of pH, using HCl, NaOH and three different electrolyte concentrations.

Both the electrolytes used in the suspensions and the supernatants of the suspensions were used as blanks. Differences between titrations can be expected depending on whether the electrolyte or supernatant is used as a blank, since a larger amount of titrant is required for neutralizing the ions leached into the supernatant.

Titrations were conducted between pH 3 and 11. The dispersion rate for the titrate was 0·02 ml min^{-1} which gave a titration rate of 4 to 8 pH units per hour.

The surface charge as a function of pH was determined from the net adsorption densities (Γ/mol cm^{-2}) by

$$\sigma_0 = F(\Gamma_{H^+} - \Gamma_{OH^-}) = \frac{F}{s}[(n_{H^+} - n_{OH^-}) - (n^b_{H^+} - n^b_{OH^-})]$$

where n_{H^+} and n_{OH^-} are the total number of moles H^+ and OH^- added to the suspension, $n^b_{H^+}$ and $n^b_{OH^-}$ are the number of moles added to the blank to give the same pH, s is the available surface area and F is the Faraday constant.

According to Gibb and Koopal,[9] the surface charge of the oxides and their mixtures as a function of pH in various electrolyte concentrations and the isoelectric points (IEPs) can be determined via potentiometric titrations. According to Lyklema,[10] the presence of specifically adsorbed cations or anions may be observed from shifts of the common intersection point (cip) of the potentiometric titration curves measured in various electrolyte concentrations. For an inert electrolyte, in absence of specific adsorption cip may be identified as the point of zero charge (PZC). The electrolyte used in our experiments was, according to Bergström and Pugh,[11] found to be inert for silicon nitride.

Viscosity

The shear stress and viscosity measurements were made using a Bohlin VOR Rheometer System

Results and Discussion

Electrophoretic mobility

Results from the electrophoretic determinations are given in Fig. 1.

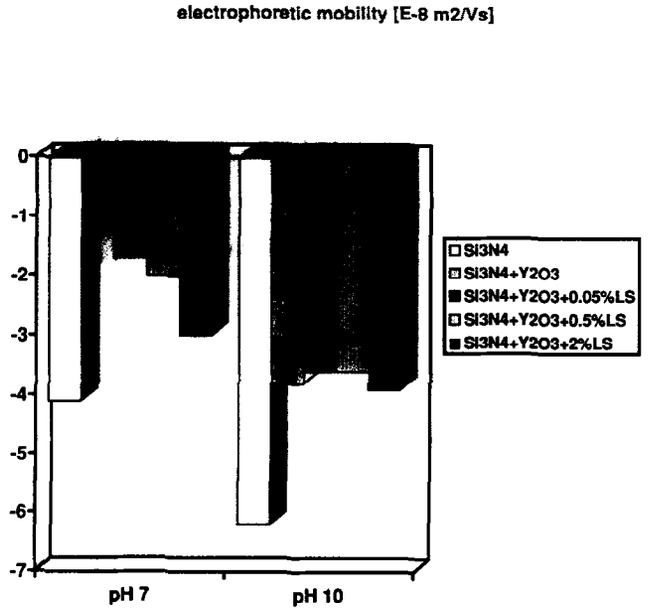

Fig. 1. Si_3N_4 + Y_2O_3 + lignosulfonate.

Si_3N_4–lignosulfonate

The Si_3N_4 slip conditioned at pH 7 showed a clearly negative electrophoretic mobility which was not significantly changed in samples with an increasing addition of LS in the dispersion. The slip conditioned at pH 10 showed an enhanced negative electrophoretic mobility. As in the case of pH 7, treatment with an increasing amount of LS at pH 10 also resulted in no significant change in the electrophoretic mobility.

Si_3N_4–Y_2O_3–lignosulfonate

The results from the electrophoretic mobility measurements are given in Fig. 1. An addition of yttria in the Si_3N_4 matrix at pH 7 resulted in a less negative electrophoretic mobility of the powder particles in the suspension, compared with that of pure Si_3N_4. This was expected as yttria is known to have a positive surface charge at pH 7 and also is expected to adsorb on the silicon nitride surface covering the Si_3N_4 particles. An increasing addition of lignosulfonate in the Si_3N_4–Y_2O_3 matrix was detected as an increasing negative electrophoretic mobility of the particles. However, this was detected only at pH 7, as increasing the amount of LS added to the slip at pH 10 did not change the electrophoretic mobility of Si_3N_4–Y_2O_3–LS particles. Thus these results support the previous assumption that lignosulfonate does not cover the Si_3N_4–Y_2O_3 particles.[2]

Surface charge

Native pH of the slips

Results from surface charge measurements of Si_3N_4 and Si_3N_4–Y_2O_3 are shown in Fig. 2. Our titration curves for Si_3N_4 showed decreased relative surface charge densities when supernatant was used as blank at pH values > 8. This is in agreement with the results reported by Bergström and Pugh, although in our experiments the decrease was smaller. The difference in Si_3N_4 titration curves (electrolyte vs. supernatant) was explained to be due to a large amount of titratable species leached from the powder surface.

The isoelectric point (IEP) for the Si_3N_4 suspensions was determined to be at pH 7·2 when using either electrolyte or supernatant as blank, indicating no leaching of titratable ions. Since the common intersection point of titration curves (cip) was also at pH 7·2, no specific adsorption was observed and cip coincides with PZC.

An addition of 5 wt% Y_2O_3 in the Si_3N_4 matrix resulted in more positive surface charge densities than those of Si_3N_4. This could be explained by the electrostatic adsorption of positive yttria particles on negative silicon nitride particles, as shown

by electrophoretic mobility measurements. Moreover, the titration curves of Si_3N_4–Y_2O_3 were less dependent on the blank used than the titration curves of Si_3N_4. This would indicate that less titratable ions were leached out from Si_3N_4–Y_2O_3.

A shift in the IEP value of Si_3N_4–Y_2O_3 from 8·4 to 9·2 was detected when the ions leached from the powder were taken into account, i.e. by using the supernatant as a blank. In addition, the cip value differed slightly from the IEP value suggesting

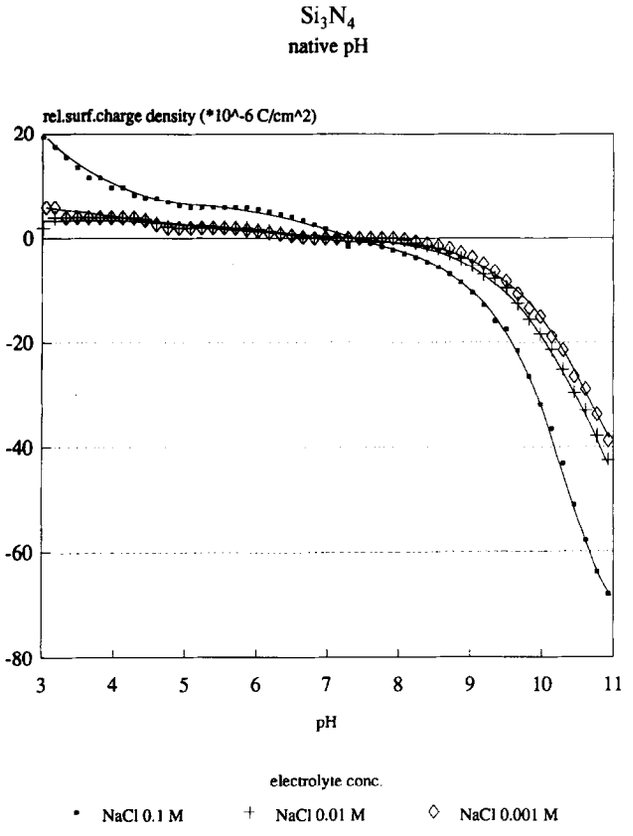

(a)

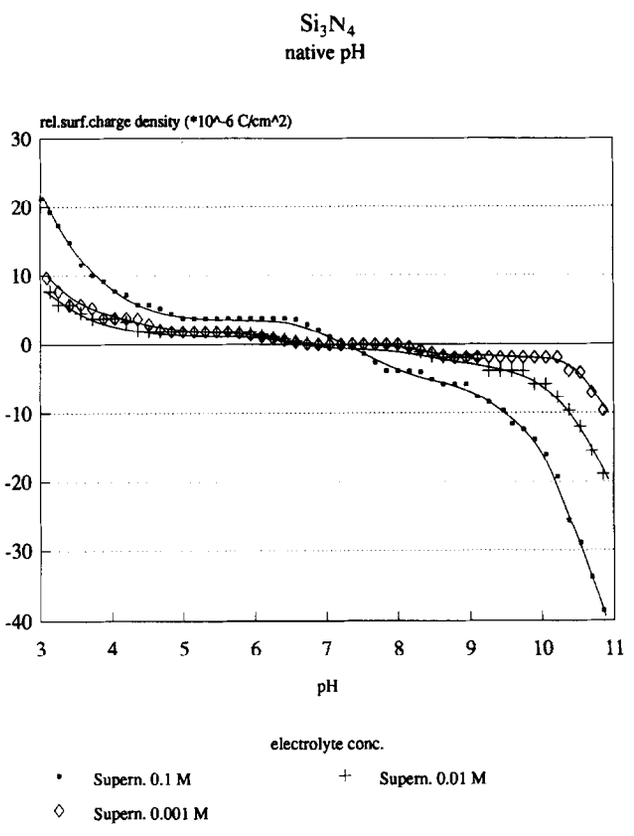

(b)

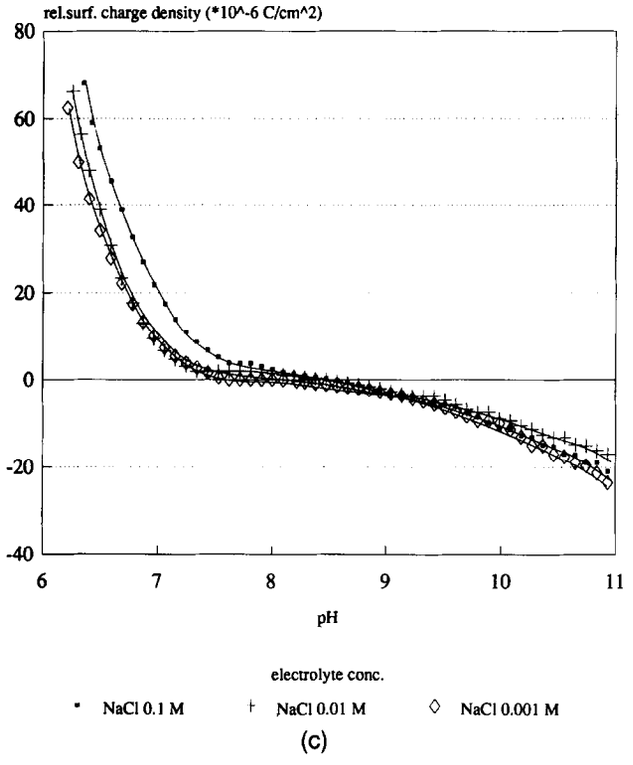

(c)

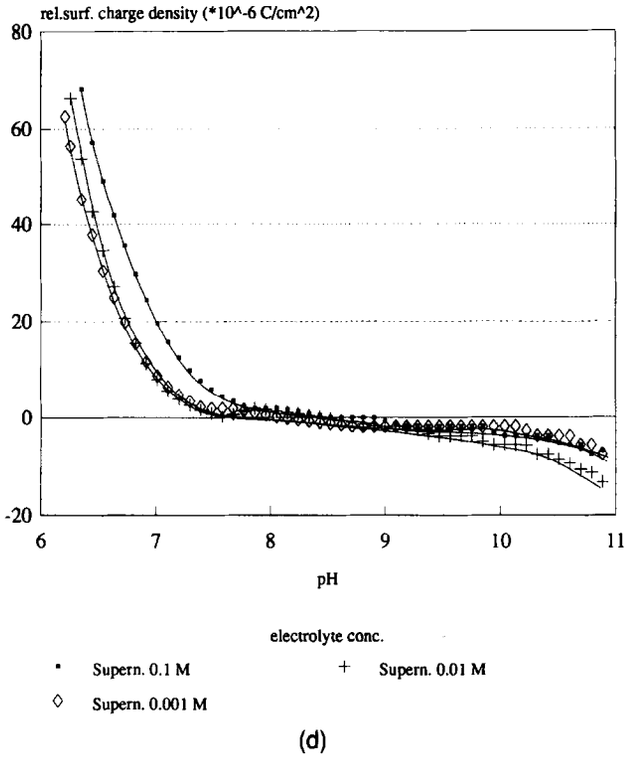

(d)

Fig. 2. Surface charge of (a) Si_3N_4 using pure electrolyte as blank; (b) Si_3N_4 using supernatant as blank; (c) Si_3N_4–Y_2O_3 using pure electrolyte as blank; (d) Si_3N_4–Y_2O_3 using supernatant as blank.

a specific adsorption of cations, presumably ammonia. According to Pollinger,[12] the IEP value for Y_2O_3 appears at pH 9·25. Thus, our results support the assumption of yttria particles covering the silicon nitride particles, preventing the leaching of ions from Si_3N_4 matrix. This explains why the Si_3N_4–Y_2O_3 system behaves rather like pure yttria when the supernatant is used as blank. On the other hand, when the electrolyte was used as blank the IEP value of Si_3N_4–Y_2O_3 was closer to that of pure Si_3N_4 (8·4).

Slip conditioned at pH 7

Results from surface charge measurements of Si_3N_4 and Si_3N_4–Y_2O_3 conditioned at pH ≈ 7 are shown in Fig. 3. Titrations for pH conditioned slips were performed only using the supernatant as blank, thus taking the titratable leached species into account. The ionic strengths referred here are given as the original ionic strengths for the pure electrolyte, although they will be changed during the conditioning due to the leaching of ions from the matrix into the supernatant.

For pure Si_3N_4 the cip and IEP appeared at about pH 7, suggesting no specific adsorption of ions. Thus the cip can be identified as PZC. This is in agreement with the surface charge measurements of the non-conditioned slip, since the native pH of the slip is at about pH 7.

Once again, an addition of 5 wt% Y_2O_3 in the Si_3N_4 matrix resulted in more positive surface charge densities than those of pure Si_3N_4. This was explained by the electrostatic adsorption of the positive yttria particles covering the negative silicon nitride particles. However, the surface charge densities of the Si_3N_4–Y_2O_3 suspension conditioned at pH 7 were slightly less positive than the ones for the non-conditioned slip. A shift in the IEP value from 9·2 to 8 was detected as a result of the conditioning. The cip was also shifted from 8·5 to 7·3. This supports again our assumption of specific adsorption of cations.

Slip conditioned at pH 10

Results from surface charge measurements of Si_3N_4 and Si_3N_4–Y_2O_3 conditioned at pH ≈ 10 are shown in Fig. 4. For pure Si_3N_4 conditioned at pH 10, the IEP appears at about pH 10 and the cip at pH close to 11. This could be due to the dissociation of silicon nitride in strong alkaline solutions which drastically increases the solubility of Si from Si_3N_4 matrix in the suspension.

An addition of 5 wt% Y_2O_3 in the Si_3N_4 matrix and conditioning of the suspension at pH 10 resulted in an IEP at pH 7·2, which is similar to the IEP of pure Si_3N_4. According to these results yttria does not adsorb colloidally on Si_3N_4 particles. Neither does it cover the silicon nitride particles in slips conditioned at pH 10 as suggested in Part 1 of this study. The common intersection of electrolyte

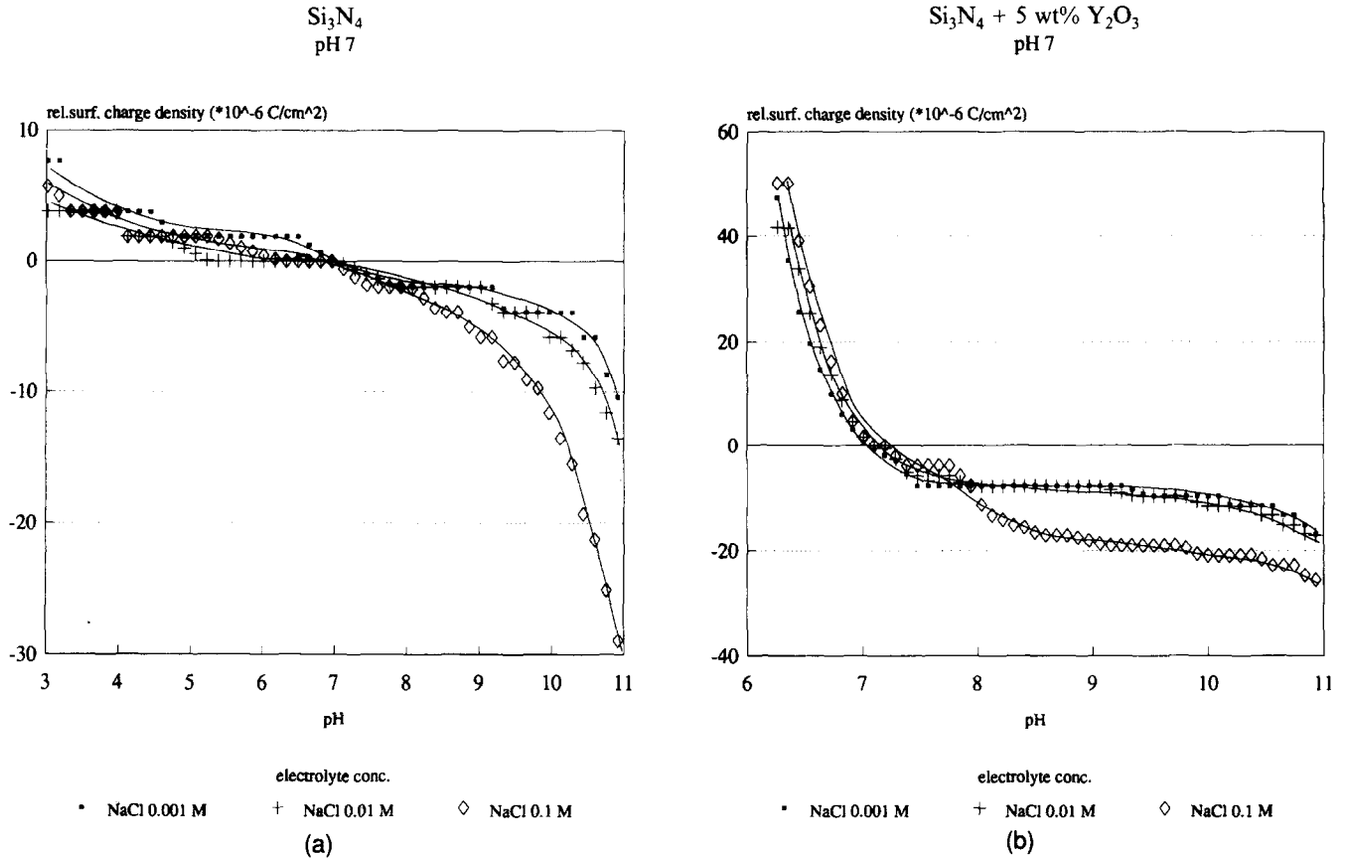

Fig. 3. Surface charge of (a) Si_3N_4 using supernatant as blank; (b) Si_3N_4–Y_2O_3 using supernatant as blank.

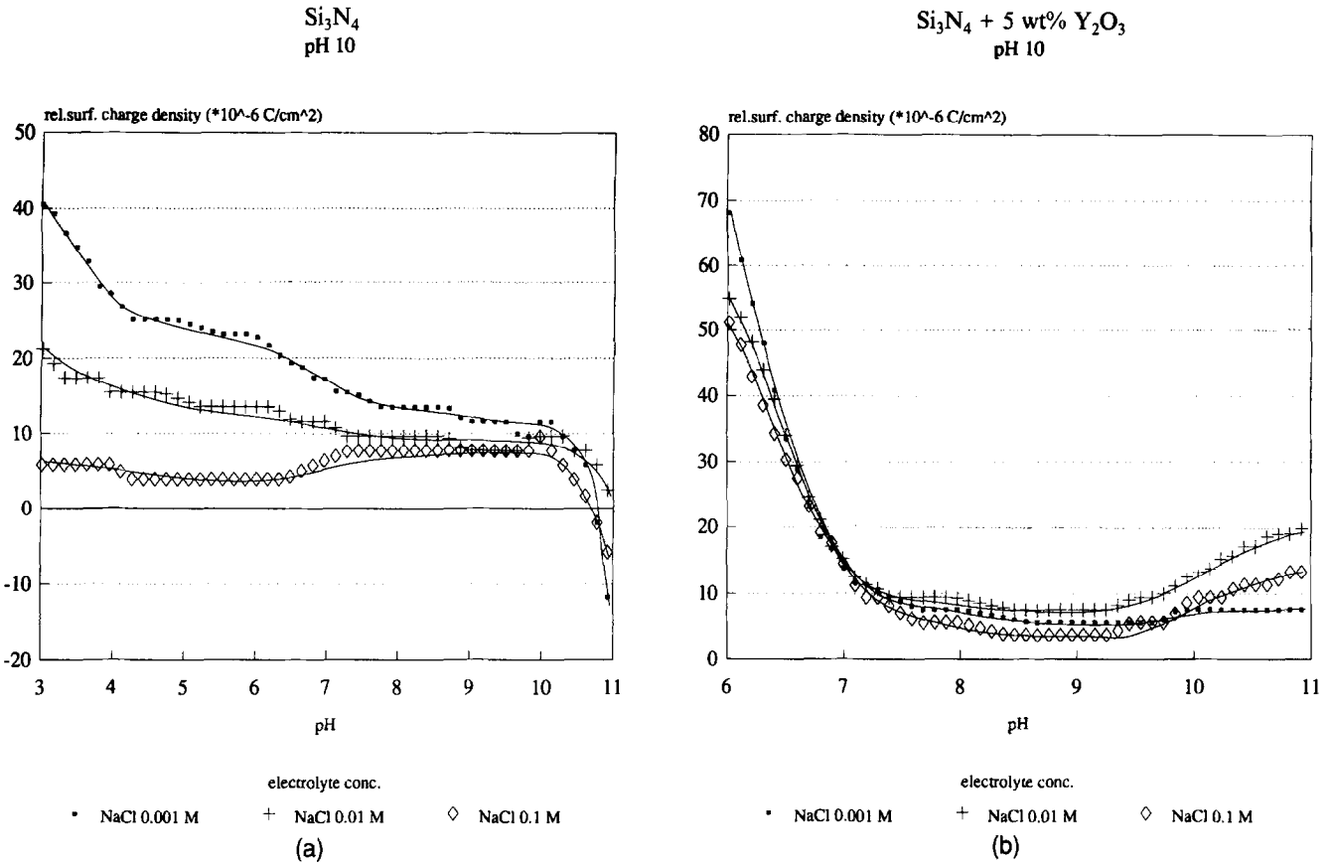

Fig. 4. Surface charge of (a) Si_3N_4 using supernatant as blank; (b) Si_3N_4-Y_2O_3 using supernatant as blank.

curves for the Si_3N_4–Y_2O_3 slip conditioned at pH 10 was never reached. However, the addition of yttria in the Si_3N_4 matrix caused a clear change in the surface charge density towards more positive values.

Viscosity

The results from viscosity measurements are shown in Figs 5 (for Si_3N_4 + LS slip) and 6 (for Si_3N_4 + Y_2O_3 + LS slip). The viscosity of the slips was measured for freshly made slips (native pH) and for slips that had been conditioned in solutions of about pH 7 and in alkaline solution of pH 10–11 for 24 h.

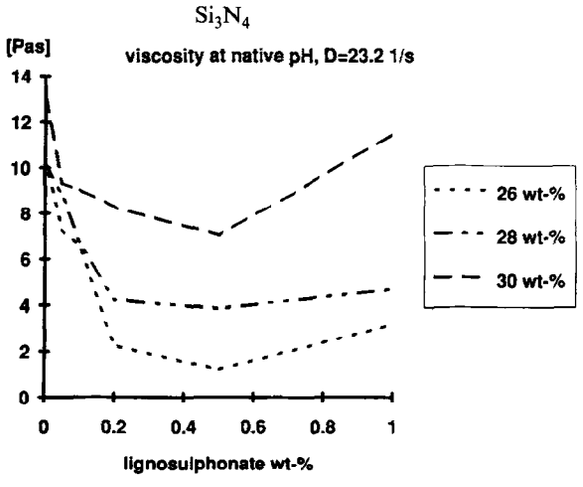

Fig. 5. Viscosity of Si_3N_4–LS slip at native pH.

The results from the viscosity measurements at a shear rate of about 23 s^{-1} for the Si_3N_4 slips at the native pH are presented in Fig. 5. The lowest viscosity for the slips appeared to be at ~ 0·4 wt% addition of LS.

The results from similar viscosity measurements for the Si_3N_4–Y_2O_3 slips at three different pH treatments (native, conditioned at pH 8 and pH 10–11) are presented in Fig. 6. The viscosities of the non-conditioned slip and the slip conditioned at pH 8 were found to be similar, and the lowest viscosity was achieved with an addition of 0·5 wt% LS. The viscosity of the Si_3N_4–Y_2O_3 slip conditioned at pH 10–11 was markedly lower. Also, the viscosity behaviour of this slip was different: the lowest viscosity was achieved with an addition of 0·05–0·2 wt% LS. This is in good accordance with the results for silicon nitride powders with a specific surface area of 11 m^2 g^{-1} reported by Rabinovich *et. al.*[13]

Since the optimal slip casting properties are achieved by using proper conditioning with minimum amount of dispersing agent, to ensure the best slip casting properties an LS addition of ~ 0·2 wt% is required for the Si_3N_4–Y_2O_3 slip.

Unfortunately we were unable to record the viscosity for the slips without LS addition due to problems with dispersability of the powders.

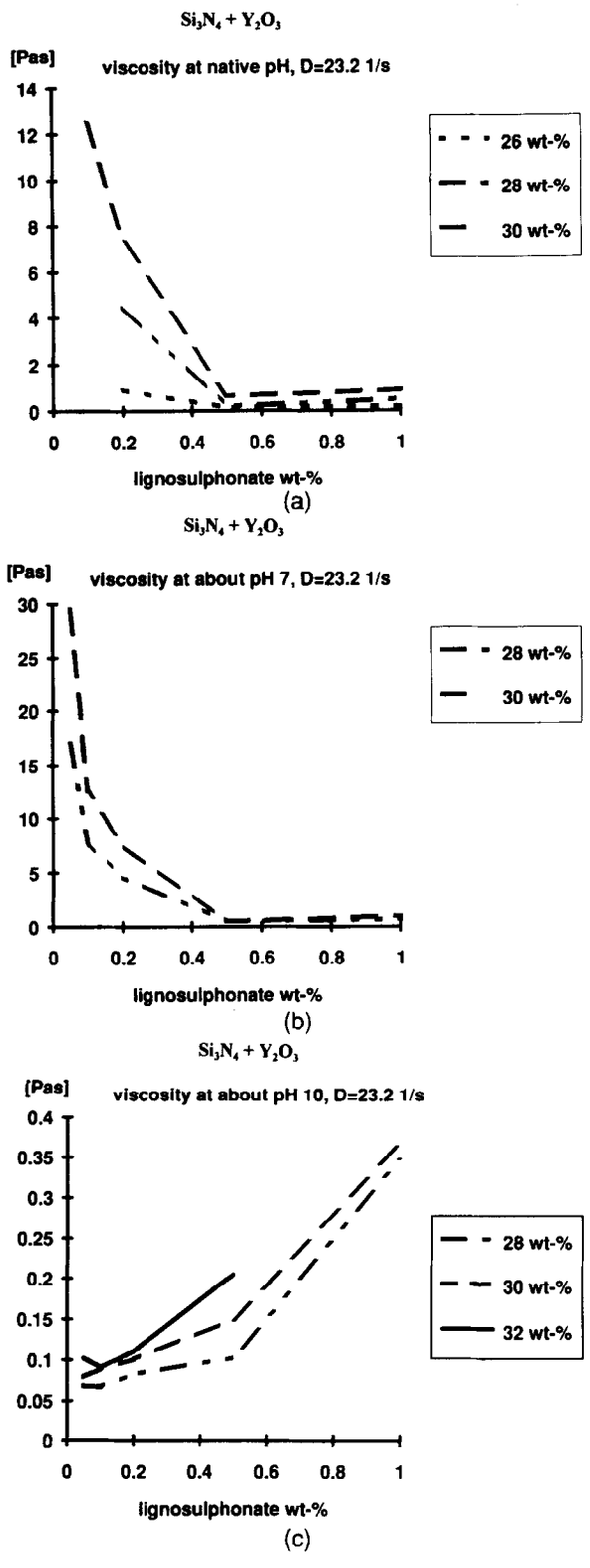

Fig. 6. Viscosity of (a) Si_3N_4–Y_2O_3–LS slip at native pH; (b) Si_3N_4–LS slip conditioned at pH 7–8; (c) Si_3N_4–LS slip conditioned at pH 10–11.

Concluding Remarks

The results presented in Parts 1[2] and 2 of this study enable the following conclusions to be made.

Dispersion mechanism

According to the results from X-ray photoelectron spectroscopy (ESCA), particle size and carbon analyses, the dispersion mechanism of LS is dependent on the pH of the slip.

At pH 7 the dispersability of the Si_3N_4–Y_2O_3 powders increased with increasing amount of LS added to the solution, as indicated by the viscosity measurements and particle size analyses. In this case the carbon content of the dried Si_3N_4–Y_2O_3 – LS powder dispersion was also increased and LS was found to adsorb on the Si_3N_4 and Y_2O_3 particle surfaces (ESCA). These results indicate that at pH 7 LS acts as an adsorbing dispersant, suggesting steric stabilization of the suspension.

At pH 10, the viscosity of the Si_3N_4–Y_2O_3–LS powder dispersion was drastically lower than that at pH 7, indicating an enhanced dispersability of the powders. However, now the viscosity of the suspension increased with increasing amount of LS added to the solution, indicating a decrease in dispersability of the powders. ESCA, particle size and carbon analyses indicated that LS was not adsorbed on the Si_3N_4 and Y_2O_3 powder particles, although the carbon content of the matrix still increased slightly with increasing amount of LS added to the solution. According to these results, at pH 10 LS acts as a non-adsorbing, free polymer dispersant in the solution. Thus we propose that the dispersion mechanism of LS at pH 10 is of depletion stabilization.

Colloidal/specific adsorption

The addition order of the powders in water, ie. LS, Y_2O_3 and Si_3N_4, supports the colloidal adsorption of LS on the powder particles especially at pH 7 due to the formation of counter-charged LS and yttria particles. This was confirmed by ESCA results.

Leaching of ions from the matrix in the dispersion was confirmed by the surface charge measurements and specific adsorption of cations at pH 7 is suggested.

Processability

In the colloidal processing of silicon nitride based ceramics, an addition of sintering agents typically in the range of 0·05–2 wt% is required. The typical pH used in processing is pH 9–10. Treatment in the alkaline environment at pH 10 ensures the lowest viscosity values and the smallest particle sizes for the powder dispersion, indicating a good dispersability in water. The dispersion stability found for Si_3N_4–Y_2O_3 powder dispersion treated at pH 10 indicates that the stability is enhanced by small additions of LS although no adsorption of LS was confirmed.

Applicability of methods

Great care must be taken when the results from

'dry' characterization techniques are related to the surface conditions present in a real slurry. Traditional 'wet' methods, such as viscosity, surface charge, electrophoretic mobility and particle size analyses, are considered to represent the prevailing process conditions of (for example) high-performance ceramics in a realistic way. Dry methods, such as ESCA, scanning electron microscopy and carbon analysis, yield information on chemical or structural composition of the dried samples.

In this study we have applied both wet and dry methods in order to understand the observed processing behaviour of silicon nitride based ceramics. Results gained from different methods were found to be in accordance with each other, verifying that dry analyses can be related to the characteristics of the slurry. Due to the complexity of the system studied, the use of several independent characterization techniques proved to be a proper way to extract reliable and complementary information.

Acknowledgements

We wish to thank Ms Kirsi Haapoja and Mr Jukka Kujanpää for assistance with the measurements. Financial support from the Research Councils for Technology and the Natural Sciences of the Academy of Finland is gratefully acknowledged.

References

1. Richerson, D.W. (ed.), *Modern Ceramic Engineering: Properties, processing, and use in design, 2nd edition.* Marcel Dekker Inc., New York, 1992.
2. Fagerholm, H. M., Johansson, L.-S. & Rosenholm, J. B., *J. Eur. Ceram. Soc.*, **14** (1994) 403–9.
3. Lidén, E., Persson, M., Carlström, E. & Carlsson, R., *J. Am. Ceram. Soc.*, **74**(6) (1991) 1335–9.
4. Pugh, R. J. & Bergström, L. (ed.), *Surface and Colloid Chemistry in Advanced Ceramic Processing, Surfactant Series, Vol. 51*, Marcel Dekker, NY, 1994, pp. 99–101.
5. *Handbook of Chemistry and Physics, 60th edition.* CRC Press Inc., Boca Raton, FL, 1981, p. B141.
6. Rosenholm, J., Manelius, F., Fagerholm, H. Grönroos, L. & Byman-Fagerholm, H., *Progr. Colloid Polym. Sci.*, **97** (1994) 51–8.
7. Persson, M., Hermansson, L. & Carlsson, R., *Ceramic Powders,* ed. P.Vincenzini. Elsevier Scientific Publ, Holland, 1983, pp. 735–42.
8. Parks, G. A., & de Bruyn, P. L., *J. Phys. Chem.*, **66** (1962) 967–73.
9. Gibb, A. W. M. & Koopal, L. K., *J. Colloid Interf. Sci.*, **34**(1) (1990) 122–38.
10. Lyklema, J., *J. Colloid Interf. Sci.*, **99**(1) (1984) 109–17.
11. Bergström, L. & Pugh, R. J., *J. Am. Ceram. Soc.*, **72**(1) (1989) 103–9.
12. Pollinger, J. P., *III Int. Symp. on Ceramic Materials & Components for Engines, 1988.* Am. Ceram. Soc., 1989, pp. 369–79.
13. Rabinovich, E. M., Leitner, Sh. & Goldenberg, A., *J. Mater. Sci.*, **17** (1982) 323–8.

SHORT REPORTS

0955-2219(95)00177-8

Journal of the European Ceramic Society 16 (1996) 679–683

0955-2219/96/$15.00

Structural Nano-Defects in α-Silicon Nitride

Chong-Min Wang & F. L. Riley*

School of Materials, University of Leeds, Leeds LS2 9JT, UK

(Received 5 December 1994; revised version received 18 September 1995; accepted 29 September 1995)

Abstract

Two types of α-silicon nitride powder have been examined by transmission electron microscopy. Clustered, nano-dimension, coffee-bean shaped features can be seen: these are believed to be dislocation loops. The features are concentrated towards particle centres and appear to be formed by the condensation of lattice point defects during cooling from powder production temperatures probably in the region of 1300 to 1500°C. Similar concentrations of features confirmed to be vacancy dislocation loops have been seen in the unconverted α-silicon nitride grains in hot-pressed silicon nitride. Calculations based on estimates of precursor defect concentrations suggest a very speculative value for the activation energy of formation of the Schottky type of lattice defect in α-Si_3N_4 of 670 kJ mol^{-1}.

1 Introduction

There has recently been considerable interest in the production of nano-dimension intragranular precipitates of silicon carbide within the silicon nitride grains of composite materials.[1] This work revives interest in the more general question of the possible defect nature of the silicon nitride crystal lattice, its capacity to accommodate localized structural defects, and in the nucleation and growth of second phases within the lattice. Ten years ago, Jack reported the observation of 25 nm intragranular, amorphous, disc-like, features in a black chemical vapour deposition (CVD) silicon nitride, which on annealing at 1850°C coalesced and then disappeared. It was postulated at the time that the discs were precipitates of amorphous silica.[2] More recently, internal microstructural features which were assumed to be nano-dimension copper- and tin-rich precipitates have been observed in grains of otherwise very high purity polycrystalline CVD α-silicon nitride; these features similarly disappeared after annealing at 1800°C.[3] Three recent publications[4-6] describe the observation of ~15 to 25 nm dimension dislocation loops in high purity CVD α-phase silicon nitride and in residual (untransformed) α-silicon nitride grains in hot-pressed or hipped silicon nitride. In the CVD materials the loops were characterized in some detail with respect to type, Burger's vector, and habit plane[4,5] The development of vacancy loops in the hot-pressed silicon nitride was attributed to the condensation of thermally activated vacancies during rapid cooling from densification temperature in the region of 1700°C.[6] It was assumed that any loops present in the starting (a high α-phase) powder would have been redissolved or annealed out during hot-pressing, and that those seen in the α-grains of the dense material had developed subsequently. However, since silicon nitride powder is itself produced at high temperature, followed by more or less rapid cooling to room temperature, it might be expected that the powder particles would contain their own populations of loops. Dislocation loops might therefore be a general feature of all rapidly cooled silicon nitride (and similar) materials.

The object of the work reported here was to extend the earlier high resolution transmission electron microscope (TEM) examinations,[6] in a search for similar structural features in silicon nitride powders. In this continuation study on two commercial powders we have observed moderately high densities of 'coffee-bean' nano-dimension features, which are postulated to be dislocation loops. The first powder from H.C. Starck (FRG) was produced by the nitridation of silicon powder at 1300 to 1400°C followed by mechanical milling to break down agglomerates;[7] the second was a high purity powder from Ube (Japan) produced by the lower temperature imide route followed by annealing at 1300 to 1500°C to crystallize the amorphous material.[8] Estimates of the point defect concentrations necessary to generate loops of concentration corresponding to the defects seen have been attempted.

*To whom correspondence should be addressed.

2 Experimental

Silicon nitride powders, H.C. Starck LC12N (specific surface area 17 $m^2 g^{-1}$, 96% α-phase, oxygen content 1.6%) and Ube E-03 B15X02 (specific surface area 3.2 $m^2 g^{-1}$, 95% α-phase, oxygen content 0.9%), were dispersed without preliminary treatment in isopropanol at 0.1 g dm^{-3} with 10 min ultrasonic agitation. A drop of suspension was dried on a 3 mm diameter copper grid, covered with Formvar polyvinyl, and ~3 nm carbon, films and examined in a Jeol 200 kV TEM/STEM microscope with a rotation angle of ±30°.

The dense hot-pressed silicon nitride reported on here had been formed by pressing Starck LC12N powder in a boron nitride lined graphite die at 1700°C under 20 MPa for 500 s. The densification aid consisted of 3% Al_2O_3 and 7% TiO_2 added to the powder as the metal alkoxides dissolved in isopropanol, followed by hydrolysis and drying at 120°C. On completion of the hot-pressing period the temperature fell by 200°C in the first 500 s of cooling and room temperature was reached in 2 h. X-ray diffraction analysis showed the material to contain ~70% of unconverted α-phase.

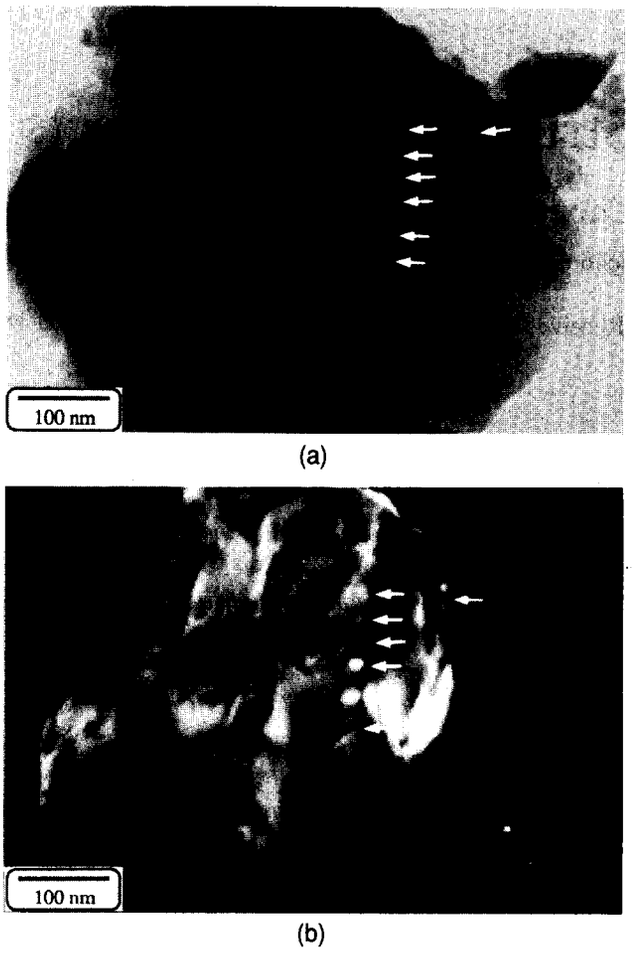

Fig. 2. Intragranular spherical features (arrowed) in a selected particle of H.C. Starck powder: (a) bright field; (b) dark field.

3 Results and Discussion

3.1 Powders

The two silicon nitride powders used were chosen because of their quite different production routes. The H.C. Starck powder had been subjected to milling, carrying with it the possibility of mechanically induced lattice strain and associated dislocation networks. This powder, while of small (~100 nm) mean particle size, had a relatively wide size range (Fig. 1), and the tendency for smaller particles to adhere to the larger made the observation of internal features in the smaller electron transparent particles difficult. Moreover, the larger particles, within which it would have been expected that most defects would be found, tended to be electron opaque. Therefore only a narrow range of particle sizes was in practice amenable to examination. Most particles picked out were additionally partially opacified by the presence of tangled dislocation networks, presumed to be the consequence of the post-nitridation milling. Randomly selected suitable particles were rotated to optimize the contrast of the characteristic coffee-bean strain fields of the defect features; dark field was used to aid confirmation of observations. Figures 2(a) and (b) show features, seen in bright field and dark field, in particles of Starck powder. Unambiguous identification of the nature of the internal features seen (vacancy or interstitial loop, or precipitate) was impossible because of the size of the larger particles (500 nm) which did not lend themselves to high resolution microscopy, and the disturbance of contrast caused by the attached smaller particles. It is believed, however, because of their transparency to the electron beam and on the basis of previous observations made using high resolution TEM with the positive identification of missing lattice planes,[6] that they may be vacancy loops.

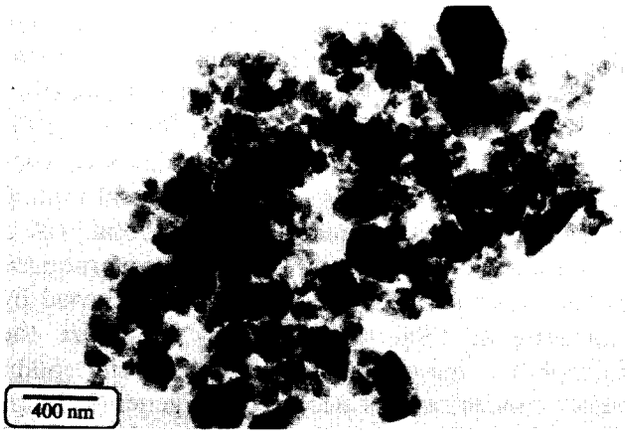

Fig. 1. H.C. Starck powder: general overview showing the wide particle size range.

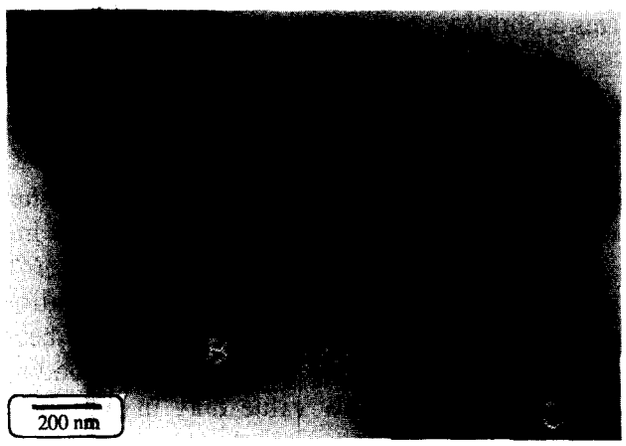

Fig. 3. Three UBE powder particles at low magnification, showing typical features under bright field.

The Ube powder particles were more easy to examine because of their narrow size range and uniformity of particle shape, although the range of picture contrast obtainable was narrow because of the particle thickness. Because their production route did not involve milling it was considered that there was a much greater chance that they would be strain-free. Internal 10 to 30 nm dimension strain centres similar in every respect to those seen previously exist also in these particles, three of which are shown in Fig. 3. Figures 4(a) and (b) show in higher magnification the features of particle A in bright and dark field; Figs 5(a) and (b) similarly show those in particle C. As with the Starck powder, the degree of resolution possible with samples of such thickness makes positive identification of their nature impossible; however, it is suggested that they are vacancy dislocation loops, for the reasons given above, and because of the likelihood that the formation of vacancy (rather than interstitial) point defects will be intrinsically energetically more favourable in the largely covalent silicon nitride.

We therefore suggest that nano-dimension precipitates or dislocation loops are a normal feature of α-silicon nitride grains and particles, and a consequence of the standard quite rapid cooling from fabrication temperature, resulting in the sudden development of supersaturated concentrations of point defects. A common feature in the two types of powder particles, as with the dislocation loops in the hot-pressed silicon nitride grains, is the existence of a defect-free zone at the particle perimeter, here of about 75 nm width and seen most clearly in Fig 5(b). This suggests that in all cases the features have formed by the condensation of high concentrations of a lattice defect which is partially able to escape by diffusion to grain

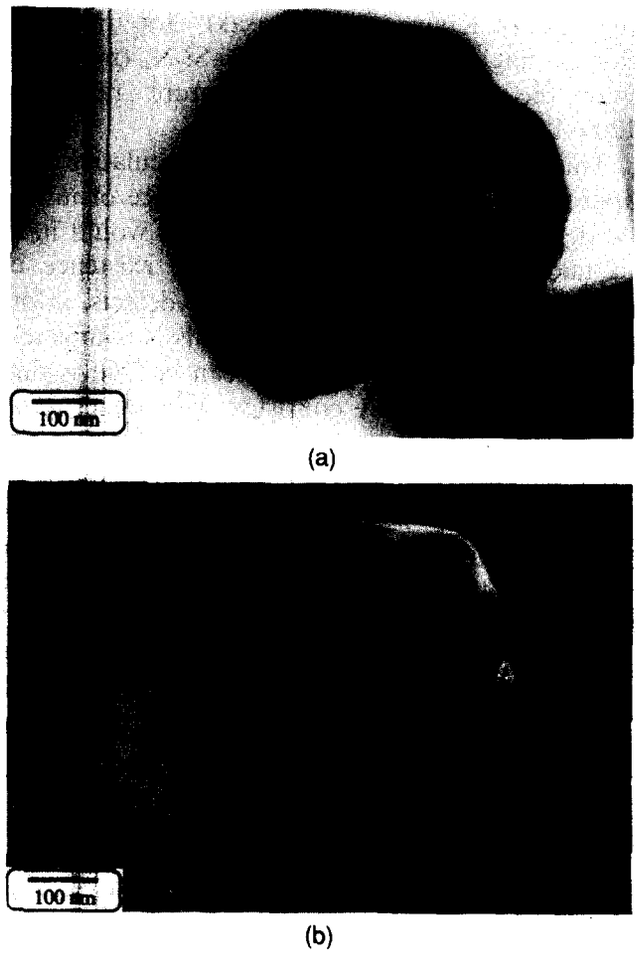

Fig. 4. UBE particle A at higher magnification: (a) bright field; (b) dark field.

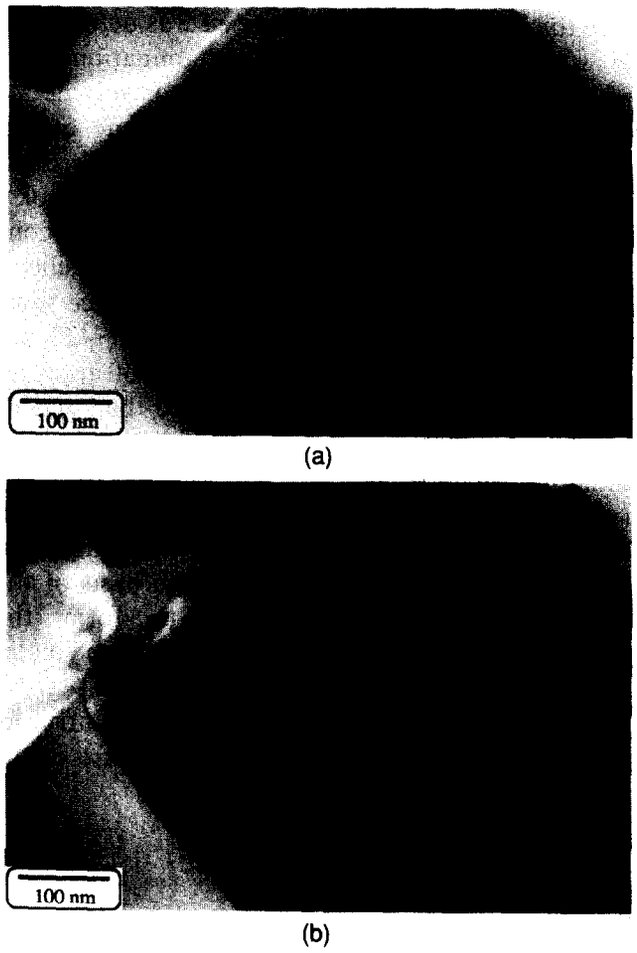

Fig. 5. UBE particle C at higher magnification: (a) bright field; (b) dark field.

boundaries or particle surfaces. If the powder features are dislocation loops they would be likely to redissolve or be annealed out during heating (for an hour or more) at sintering temperature, although to secure absolute proof of this would require more precise information about vacancy mobility in silicon nitride at these temperatures. On the basis of the width of the defect-free zones measured earlier,[6] and using the Einstein–Smoluchowski relationship, the very approximate value of 2×10^{-18} m^2 s^{-1} at ~1700°C was estimated for the silicon nitride 'vacancy' diffusion coefficient in α-Si_3N_4.

3.2 Hot-pressed material

It is possible to try to quantify the point defect concentration required for the precipitation of the dislocation loops in the α-Si_3N_4 grains of the hot-pressed material. For simplicity it is assumed that the condensation of thermally activated point defects is solely responsible for the formation of the dislocation loops, and that all the vacancies present further than ~50 nm from the grain surface form loops. Examination of an α-Si_3N_4 grain section of area 700 x 130 nm^2 in a thinned foil of hot-pressed silicon nitride showed 62 loops of diameter ~25 nm (the grain was rotated to ensure that all the loops within this area were counted). The thickness of the foil examined was determined *in situ* using the standard contamination spot technique[9] to be 175 nm, giving a volume of examination of 0.0159 μm^3. The volume of the unit cell of α-Si_3N_4, which contains four formula units, is 0.293 nm^3 (Ref. 3) and, following Brook[10] and assuming that an Si_3N_4 'vacancy' ($V_{Si_3N_4}$) consists of a Schottky type of defect with three silicon ($V_{Si}^{''''}$) and four nitrogen ($V_{N\cdots}$) vacant lattice sites, the mean linear dimension for $V_{Si_3N_4}$ is ~420 pm (indicating that the average loop disc of approximate volume 206 nm^3 should require the condensation of ~2800 $V_{Si_3N_4}$). An estimate for the minimum Schottky defect concentration [$V_{Schottky}$] (where the square brackets are used to indicate a fractional concentration) at the hot-pressing temperature of 1700°C, calculated on the basis of the volume of vacancies required to form the number of loops divided by the volume of material in which they were counted, is thus 8×10^{-4}. Assuming that the vacancies are entirely intrinsic, thermally activated defects and making use of the relationships

$$0 = 3[V_{Si}^{''''}]+4[V_{N\cdots}] \quad (1)$$

where

$$[V_{Si}^{''''}] = 3\,[V_{Schottky}] \quad (2)$$

and

$$[V_{N\cdots}] = 4\,[V_{Schottky}] \quad (3)$$

gives a Shottky equilibrium constant (K_s) of:

$$K_s = 3^3 \times 4^4 \times [V_{Schottky}]^7 \quad (4)$$

or

$$K_s = 6912\,[V_{Schottky}]^7 \quad (5)$$

and ~ 1×10^{-18}. On the assumption as before that precipitation of the loops occurs rapidly after initiation of cooling from 1700°C, $\Delta G_{Shottky}$ is ~670 kJ mol^{-1}. This value for the Schottky formation energy is perhaps not as high as might have been expected, given the strong and directional bonding of silicon nitride: a low value may in part be a result of the strain energy of the α-silicon nitride lattice, although the disorder entropy term arising from the seven vacant atomic lattice sites must also be a favouring factor.

On the basis that the rate-controlling step in the diffusion of the Si_3N_4 'vacancy' is that of the slowest species, believed to be N,[11] a very approximate estimate can also be made for the self-diffusion diffusion coefficient for N (D_N) in the α-Si_3N_4 grains at the hot-pressing temperature (1700°C). This is calculated using the relationship $D_N = 4D_V[V_{Si_3N_4}]$, setting $D_V \approx 2 \times 10^{-18}$ m^2 s^{-1} on the basis of the width (~20 nm) of the defect-free zone and $[V_{Si_3N_4}] = 8 \times 10^{-4}$, to give $D_N \approx 6 \times 10^{-21}$ m^2 s^{-1}. This value compares reasonably well with that of 10^{-19} m^2 s^{-1} estimated by extrapolation of the data of Kijima and Shirasaki[11] for ^{15}N diffusion in single crystal grains of α-Si_3N_4 (measured over the much lower temperature range of 1200–1410°C).

This analysis, which is both speculative and approximate, assumes only the presence of intrinsic defects; a more realistic treatment would need to take into account the probable existence of extrinsic, impurity generated, point defects, information on which for these materials is completely lacking. Perhaps the least that can be said is that the values derived are consistent with other data, but it is clear that a more complete study of the defect chemistry of silicon nitride is needed, focusing on the influence on atomic mobility of low concentrations of metallic impurity elements. The failure so far to detect dislocation loops in grains with the β-Si_3N_4 structure may be a result of higher atomic diffusivities in a lattice containing high concentrations of extrinsic defects associated with impurity atoms.

4 Conclusions

Distinctive nano-dimension 'coffee-bean' strain centres associated with structural defects appear to be a normal feature of α-Si_3N_4 grains and powder particles. While some may be associated with

impurity precipitates, those seen in the hot-pressed Si_3N_4 grains examined here are believed to be vacancy dislocation loops, condensing (most probably during rapid cooling from production temperature) in a lattice which is supersaturated with respect to Schottky defects. Very approximate estimates of the Schottky defect concentration at 1700°C and of the defect formation energy, made on the basis of dislocation loop densities in the α-Si_3N_4 grains of a hot-pressed material, are 8×10^{-4} and 670 kJ mol^{-1} respectively.

It is recognised that these are very tentative values, based on a speculative approach; it is hoped that this brief study will serve to stimulate more work on the subject.

Acknowledgements

Dr Y.Q. Sun of the Department of Materials of the University of Oxford is thanked for helpful discussions and advice on the interpretation of data.

References

1. Sawaguchi, A., Toda, K. & Niihara, K., Mechanical and electrical properties of silicon nitride–silicon carbide nanocomposite materials. *J. Am. Ceram. Soc.*, **74** [5] (1991) 1142–4
2. Jack, K. H., The characterization of α-sialons and the α-β relationship in sialons and silicon nitride. In *Progress in Nitrogen Ceramics*, ed. F. L. Riley. Martinus Nijhoff, The Hague, 1983, pp. 45–60.
3. Kunz, K. P., Sarin, V. K., Davis, R. F. & Bryan, S. R., Self-diffusion in silicon-30 and nitrogen-15, in α-phase silicon nitride. *Mater. Sci. Eng.*, **A105/106** (1988) 47–54C.
4. Moore, K. L., Defect characterization in a CVD α-Si_3N_4. *Proc. Electron Microsc. Soc. America*, **49** (1991) 936–7.
5. Suematsu, H., Petrovic, J. J. & Mitchell, T. E., Dislocation loops in α-silicon nitride single crystals. *Proc. Electron Microsc. Soc. America*, **50** (1992) 342–4.
6. Wang, C. M., Riley, F. L., Castro, F. & Iturriza, I., Dislocation loops in α-silicon nitride. *J. Am. Ceram. Soc.*, **76** [8] (1993) 2136–40.
7. Haag, H., Glaeser, W. D. & Krismer, B., Preparation and characterization of silicon nitride powders for hot-pressing. In *Nitrogen Ceramics*, ed. F. L. Riley. Noordhoff-Leyden, 1977, pp. 315–6
8. Arakawa, T., State of the art silicon nitride powders obtained by thermal decomposition of $Si(NH)_2$ and the injection moulding thereof. In *Silicon Nitride—1*, ed. S. Somiya, M. Mitomo & M. Yoshimura. Elsevier Applied Science, London, 1989, pp. 81–91.
9. Scott, V. D. & Vove, G., Foil thickness measurements in the transmission electron microscope. *Mater. Sci. Technol.*, **31** (1987) 600–8.
10. Brook, R. J., Defect equilibria in the solid state. In *Nitrogen Ceramics*, ed. F.L. Riley. Noordhoff-Leyden, 1977, pp. 187–200.
11. Kijima, K. & Shirasaki, S., Nitrogen self-diffusion in silicon nitride. *J. Chem. Phys.*, **65** [7] (1976) 2668–71.

Journal of the European Ceramic Society 16 (1996) 685–686

0955-2219/96/$15.00
0955-2219(95)00184-0

Synthesis of Crystalline Ferrites Below 60°C

Midori Ueda,* Shiro Shimada & Michio Inagaki

Faculty of Engineering, Hokkaido University, Kita-ku, Sapporo 060, Japan

(Received 29 June 1995; revised version received 29 September 1995; accepted 12 October 1995)

Abstract

The ranges of aging temperature and time were determined for the preparation of zinc, cobalt, nickel and iron ferrites in crystalline form by their direct precipitation from aqueous solutions of the corresponding metal chlorides with ammonia below 60°C.

Introduction

In our previous papers,[1,2] it was shown that fine powders of zinc ferrite can be successfully synthesized at a temperature near room temperature. The relatively simple procedure involved addition of either ammonia or hydrazine monohydrate in an aqueous solution of $FeCl_2$ and $ZnCl_2$, followed by aging at a constant temperature within the range 30–60°C. The particles of zinc ferrite obtained were very fine, less than 0·1 μm in size, but had relatively high crystallinity, comparable to that found in powders heated up to 600°C.[1] Using hydrazine monohydrate, the concentration of metal solution had to be low in order to get crystalline powders of zinc ferrite, avoiding the formation of hydrazine complexes of metals.[2]

We have now extended the work to other ferrites, $CoFe_2O_4$, $NiFe_2O_4$ and Fe_3O_4, and determined the conditions for the synthesis of these materials in crystalline form near room temperature.

Experimental Procedure

Experimental procedure was very simple: into the mixed-metal solutions of MCl_2 (M = Ni, Co and Fe) and $FeCl_2$ having the metal ratio M/Fe of 1/2, ammonia was mixed at a constant temperature between 0 and 60°C by shaking. The concentration of each metal in aqueous solution was kept at 0·05 mol/dm^3 and that of ammonia at 15 mol/dm^3. After aging at a constant temperature for 0·5–8 h, the precipitates were collected by filtering and washing using water at room temperature. They were examined by X-ray powder diffractometry and scanning electron microscopy. The detailed experimental procedure was the same as was reported in our previous paper.[1] The temperature of aging was limited to between 0 and 60°C. Below 0°C, the handling of the aqueous solution was not easy and at 80°C it was difficult to keep the conditions of metal concentration because of the evaporation of water.

The formation conditions of the ferrites crystallized in a spinel structure are summarized in Fig. 1 in terms of aging temperature and time. In this figure, the results on zinc ferrite reported before are included for comparison.[1]

$ZnFe_2O_4$

Aging at a temperature between 30 and 60°C for more than 2 h resulted in the formation of a single phase of zinc ferrite in the crystalline state. Below 30°C, an amorphous phase was obtained even after a considerable aging time. This amorphous phase could be changed to spinel structure only by heat treatment above 400°C. Short time aging gave a so-called green-rust phase[3] which was expected to contain Fe^{2+}, Fe^{3+}, Zn^{2+}, OH^- and Cl^-. The representative X-ray powder patterns are shown in Figs 2(a) and (b) for zinc ferrite spinel synthesized by aging at 40°C for 8 h and for the green-rust phase prepared at 0°C for 4 h, respectively. The powder pattern for the green-rust phase is characteristic, with two broad peaks which can be indexed as 003 and 006. The crystallinity of the spinel which was measured by the half width of the 311 diffraction line was found to depend strongly on both aging temperature and time, the half width of the spinel obtained by aging at 60°C for more than 4 h corresponding to that heated up to 600°C. The atomic ratio of Fe/Zn was determined by atomic absorption spectrometry to be 2·2, corresponding to $Zn_{0.94}Fe_{2.06}O_4$.

*Present address: Kitami Institute of Technology, Kouen-cho, Kitami-shi, Hokkaido 090, Japan.

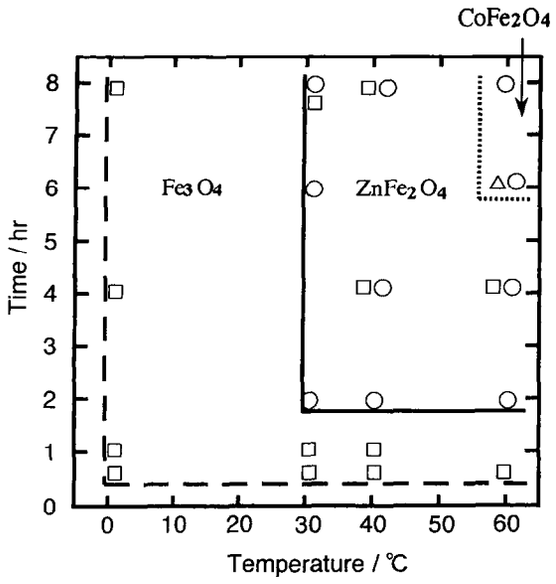

Fig. 1. Formation range of aging temperature and time for the crystalline ferrites. △ $CoFe_2O_4$; ○ $ZnFe_2O_4$; and □ Fe_3O_4.

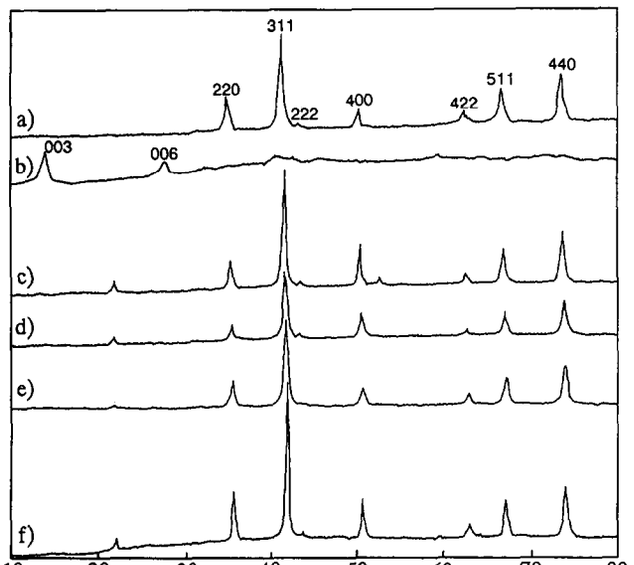

Fig. 2. X-ray powder patterns of the products: (a) $ZnFe_2O_4$; at 40°C for 8 h; (b) green-rust containing Zn^{2+}; at 0°C for 4 h; (c) $CoFe_2O_4$; at 50°C for 6 h; (d) $NiFe_2O_4$; at 40°C for 8 h; (e) (Ni, Zn)Fe_2O_4; at 40°C for 8 h; (f) Fe_3O_4; at 60°C for 0·5 h.

$CoFe_2O_4$

After aging at 60°C for 6 h, a single phase of spinel was obtained. As its X-ray powder pattern in Fig 2(c) shows, it has rather high crystallinity. The atomic ratio of Fe/Co determined was 2·2.

The aging at 60°C for 2 h and also at a temperature below 50°C for 6 h, gave a mixture of the green-rust phase and spinel, the former being the main phase at the low aging temperature.

$NiFe_2O_4$

No single phase of nickel ferrite was synthesized by the present procedure, by aging at temperatures from 0 to 80°C for up to 5 days. In most cases, the green-rust phase coexisted with a spinel having a low crystallinity. By heat treatment of this mixture to 600°C, a well-crystallized nickel ferrite associated with a small amount of Fe_2O_3 was obtained, where the overall ratio of Fe/Ni was 2·2.

Because the green-rust phase was soluble in dilute HCl, the spinel phase could be isolated. One of the powder patterns is shown in Fig 2(d). However, its atomic ratio of Fe/Ni was determined to be 5·0, indicating an Fe-rich composition.

An attempt was made to synthesize the mixed ferrites of zinc and nickel by the present procedure. Only in the mixed-metal solution of Zn/Ni = 4/1 was a single phase of spinel obtained (Fig. 2(e)). The metal composition determined by atomic absorption spectrometry, however, was $(Zn_{0.87}Ni_{0.13})_{0.91}Fe_{2.09}O_4$, namely, a much smaller ratio of Zn/Ni in the precipitates than in the starting metal solution. From the metal solutions containing more nickel ions, the mixture of the spinel and the green-rust phase was always obtained. These results show the difficulty in incorporating nickel ions into the spinel structure by the present procedure.

By solid-state reaction between Fe_2O_3 and NiO, it was reported that spinel formation was so suppressed that a single phase of $NiFe_2O_4$ was not obtained even at 900°C, the single phase being prepared only from a mixture of precursor raw materials ($FeCl_3$ and $NiCl_2$) using ethylene glycol.[4]

Fe_3O_4

At all temperatures examined, Fe_3O_4 with spinel structure (magnetite) is obtained, as shown in Fig. 1. In this case also, the green-rust was formed at short aging times (less than 0·5 h). The structural conversion from the green-rust to spinel was easily followed by observing the color change of the colloidal particles from deep green to black. In the sample synthesized at 0°C, a small amount of FeOOH was detected by X-ray diffraction; this was seen under scanning electron microscopy to have needle-like morphology The powder pattern of the sample after aging at 60°C for 0·5 h is shown in Fig. 2(f). SEM shows that Fe_3O_4 obtained at 60°C was composed of aggregates of minute particles of less than 0·1 μm in size.

References

1. Ueda, M., Shimada, S. & Inagaki, M., *J. Mater. Chem.*, **3** (1993) 1199.
2. Ueda, M., Shimada, S. & Inagaki, M., *J. Europ. Ceram. Soc.*, **15** (1995) 265.
3. Bernal, J. D., Dasgupta, D. R. & Mackay, A. L., *Clay Miner. Bull.*, **4** (1959) 15.
4. Ueda, M., Shimada, S. & Inagaki, M., *J. Soc. Mater. Eng. Reso. Japan*, **7** (1994) 46.

Journal of the European Ceramic Society **16** (1996) 687–694

0955-2219(95)00190-5
0955-2219/96/$15.00

Influence of Grain Size on the Toughness and Thermal Shock Resistance of Polycrystalline $YBa_2Cu_3O_{7-\delta}$

F. Osterstock,[a,*] I. Monot,[b] G. Desgardin[b,†] & B. L. Mordike[a]

[a]Institut für Werkstoffkunde und Werkstofftechnick, TU Clausthal, 38678 Clausthal — Zellerfeld, Germany
[b]Laboratoire CRISMAT — CNRS URA 1318 — ISMRA — Université de Caen, Boulevard du Maréchal Juin 14050 Caen Cedex, France

(Received 3 November 1994; revised version received 16 October 1995; accepted 24 October 1995)

Abstract

The toughness and thermal shock resistance (quenching from RT in air into liquid nitrogen) have been investigated on four grades of polycrystalline 'YBaCuO' of almost equal porosity using the Vickers indentation technique. The mean grain sizes varied from 1·5 to 10 μm. The change in toughness with increasing grain size is described by a bell-shaped curve as already published by Rice et al. *for the case of other non-cubic ceramics. For the determination of the thermal shock resistance, an original method, based on the relative increase of the length of Vickers indentation radial cracks, as the sample is quenched, has been used. The ranking of the four grades can only be explained if the increase of the thermal residual mismatch stresses, as the samples are put into liquid nitrogen, is taken into account such as to predict a shift of the bell-shaped change of toughness with increasing grain size as the temperature reaches that of liquid nitrogen. The proposed methodology delivers a powerful tool for investigating non-cubic polycrystalline structural or functional ceramics in the R&D stage.*

Nous avons utilisé la technique de l'indentation Vickers pour étudier la tenacité et la résistance au choc thermique (trempe de la température ambiante à l'air dans l'azote liquide) de quatre nuances de 'YBaCuO' polycristallin et de porosités semblables. Les tailles moyennes des grains varient de 1·5 à 10 μm. La variation de la tenacité lorsque la taille des grains augmente suit une forme en cloche, telle que celle proposée par Rice et al., *pour d'autres céramiques non-cubiques. Une méthode originale, basée sur l'augmentation relative de la longueur des fissures radiales de l'indentation Vickers lorsque l'échantillon est trempé, a été utilisée pour déterminer la résistance au choc thermique. Le classement des quatre nuances nécessite la prise en compte d'un accroissement des contraintes thermiques résiduelles entre les grains lorsque les échantillons sont refroidis dans l'azote liquide. Ceci permet de proposer un décalage de la courbe en cloche qui décrit la variation de la tenacité avec la taille des grains lorsque le matériau atteint la température de l'azote liquide. La méthodologie proposée se révèle comme un bon outil pour l'étude de céramiques fonctionnelles ou structurales à structure non-cubique dans le stade de recherche et développement.*

Die Bruchzähigheit und der Thermoschockwiderstand (Abschrecken von Luft bei Raumtemperatur in flüssigen Stickstoff) wurden an vier vielkristallinen 'YBaCuO' Sorten von beinahe gleicher Porosität, mittels der Vickershärteeindrucksmethode untersucht. Die mittlere Korngrösse varierte zwischen 1·5 und 10 μm. Die Anderung der Bruchzähigheit mit steigender Korngrösse wird durch eine glockenartige Kurve beschrieben, wie schon von Rice et al., *für andere nicht-kubische Keramiken vorgeschlagen. Der Thermoschock-widerstand wurde mittels einer Methode, die auf der relativen Verlängerung der Vickerseindruck-risse während des Abschreckens beruht, untersucht. Zur Einordnug der vier Sorten muss die Zunahme der thermischen Eigenspannungen zwischen den Körnern während des Abhühlens in flüssigem Stickstoff in Betracht gezogen werden. Dies hat eine Verschiebung der glockenartigen Anderung der Bruchzähigkeit mit steigender Korngrösse bei der Temperatur des flüssigen Stickstoffs zur Folge. Die vorgeschlagene Methodik erweist sich als sehr angebracht für die Untersuchung von vielkristallinen nicht-kubischen Funktions-oder-Baukeramiken in der Entwicklungsphase.*

*This work was done during the time F. Osterstock was on leave from LERMAT — CNRS URA 1317 — ISMRA.
† To whom correspondence should be addressed.

1 Introduction

Although much attention is currently paid to the fabrication of high-temperature superconducting materials, either in the shape of thin films or being textured, a potential still exists for the use of polycrystalline ones. It has been recognised very early that, for the latter, the grain size plays an important role in the density of the critical current.[1,2] Microcracking along the grain boundaries under the action of thermal mismatch stresses is a common feature of non-cubic functional and structural polycrystalline ceramics. However the grain sizes for which a dramatic decrease in critical current density has been detected by Refs 1 and 2 differ. This reveals a general problem of grain boundary engineering about which it has been speculated for this family of materials[3,4] or in a more general way.[5]

It appears from these works that the quality of a grain boundary is often best approached by the grain boundary energy, γ_{gb}, which describes its mechanical resistance, but also depends on the geometrical orientation of the two neighbouring grains on the one hand and on the nature and amount of impurities located in it on the other hand. The latter also influence the quality and the coherency of the superconducting domains.

Furthermore the mechanical resistance of 'YBaCuO' and other high-T_c superconducting cuprates is only poorly documented. In addition to the determination of usual mechanical properties,[6,7] the indentation method has been used for the measurement of more specific properties[8,9] of single crystals or of polycrystals.[10] The latter encompasses the toughness which provides more reliable information on the quality of a sintered microstructure than the single rupture stress which depends on the size of the largest defect and is thus inadequate for judging materials in the state of research and development. Also the toughness appears in treatments of thermal shock resistance, which is of importance when the functional part is cooled from room temperature to that of liquid nitrogen.

In the present paper, the indentation method has been used to determine toughness at room temperature and thermal shock resistance of polycrystalline YBaCuO when quenched into liquid nitrogen, as a function of grain size. Existing models are used in order to discuss the experimental results.

2 Materials and Experimental Procedures

Mixtures of Y_2O_3, CuO and $BaCO_3$ have been calcinated at 880°C, then milled and calcinated again and remilled. The resulting powders were then uniaxially pressed at room temperature and subsequently pressureless sintered at 920°C in air such as to yield various grain sizes.

Afterwards the resulting discs (5 mm in thickness and 25 mm in diameter) were refired and then ground and polished to remove the outer skin, which may have been fitted with thermal stresses of the first kind, and for metallographical purposes. The density of these discs was measured using Archimedes' principle in toluol. Four different microstructures were obtained; their characteristics are given in Table 1 in addition to the toughness as it will be deduced below. Electron scanning micrographs are shown in Fig. 1 in order to see the microstructures under investigation.

Thoughout this study, the indentation method was used for determining the toughness and evaluating the thermal shock resistance with the help of Wolpert and Zeiss durometers. Details will be given below concerning the working-out scheme

Table 1. Designation of the samples and main characteristics

Sample	*920 B*	*920 C*	*920 D*	*920 A*
μ structure	Very fine	Fine	Medium	Coarse
Porosity vol.%	19	19	22	16
K_c, MPa $\sqrt{m}$	0·70	0·84	1·64	0·24
Grain size, μm	1·5	3·5	5·5	10

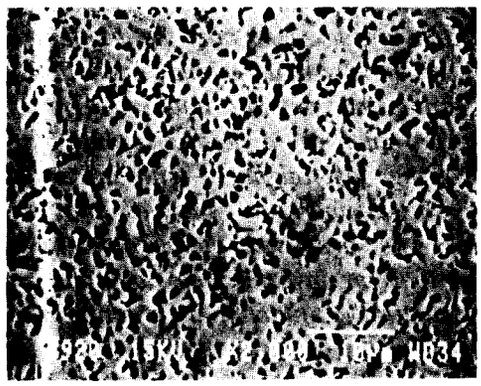

(a)

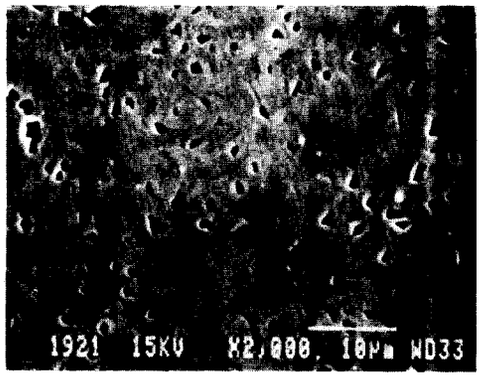

(b)

Fig. 1. Electron micrographs of samples 920B (a) and 920A (b)

and procedures, A well defined procedure was used for determining the toughness, via the direct crack length measurement method.[11] Thermal shock was realized in putting as-indented samples into liquid nitrogen, within a Dewar. Care was taken during reheating to avoid condensation of ambient humidity, which may cause sub-critical crack extension due to stress enhanced corrosion, in isolating the sample into water absorbing paper after it had been swept a first time. This also reduced the reheating rate.

3 Results

3.1 Toughness using the Vickers indentation method

The procedure used here is that initially outlined by Anstis *et al.*[11,12] Due to the elasto-plastic mismatch between the deformed zone under the indentor and the remaining elastic matrix a symmetric crack pattern appears during unloading the Vickers diamond. These cracks are in equilibrium between the residual central opening and the toughness, K_c of the material. Such a pattern is shown in Fig 2; Fig. 3 gives details concerning the parameters used. A dimensional analysis yields a relation between indentation load, P, crack length, c_0, and the toughness:

$$K_c = \xi(E/H)^{1/2} \cdot P \cdot c_0^{3/2} = \chi r \cdot P \cdot c_0^{-3/2} \qquad (1)$$

where: E is Young's modulus and H the hardness; ξ and χr are dimensionless proportionality factors, with:

$$\chi r = \xi(E/H)^{1/2} \qquad (2)$$

Values of the microhardness H_v = 8·7 GPa[8] and Young's modulus E = 180 GPa[6] were used to verify whether the ratio (EH) fits with the values used by Anstis *et al.*[11,12] They obtained $(E/H) \approx 30$ for a range of glassy and crystalline materials, whereas $(E/H) \approx 20$ holds in the present case. Thus toughness was deduced from:

$$K_c = 0{\cdot}77\ P \cdot c_0^{-3/2} \qquad (3)$$

despite the fact that porosity may yield densification before plastic deformation occurs beneath the indentor. Furthermore, as can be deduced from the scatter of the Young's moduli published by Alford *et al.*[6] the value of the Young's modulus of the bulk may depend on grain size due to thermal mismatch stress induced microcracking of the grain boundaries. The values of the proportionnality factors may thus vary with grain size too. The purpose of this paper is however to underline the resulting behaviour.

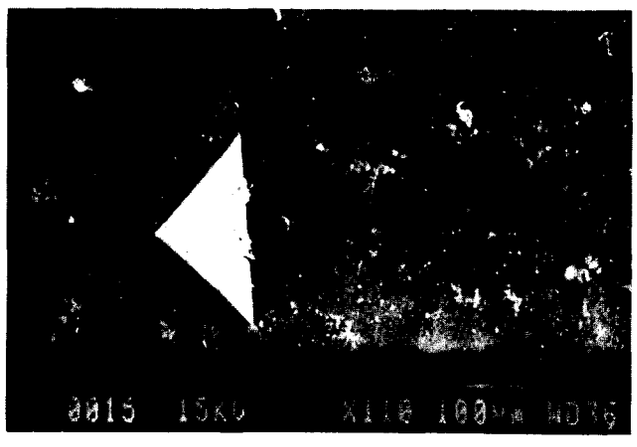

Fig. 2. Electron micrograph of a Vickers indentation and associated radial cracks in grade 920D.

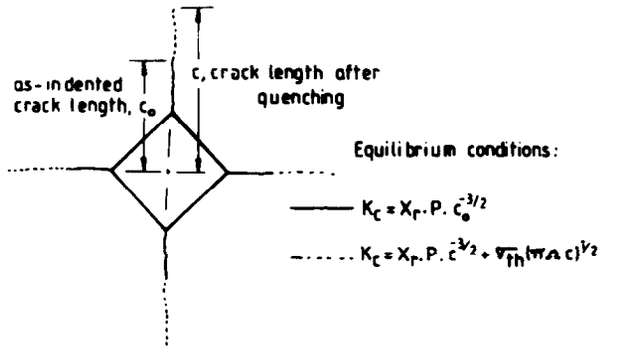

Fig. 3. Schematic of the Vickers indentation induced median-radial crack system, its extension during quenching and the associated parameters. In the quenching it has been assumed that the indentation crack system is located within a skin of homogeneous and constant peak stresses.

A comparison has been made between the medium grain-sized grade 920 D and three materials for which the indentation crack system is already well established: Palmquist cracks for WC–Co and the median-radial crack system for Al_2O_3 and SiC. The former is characterized by the fact that a level of indentation load is needed for the occurrence of the first crack, whereas for the latter the identation load versus radial crack length plot passes the zero point in accordance with eqn (1). It can be seen in Fig. 4 that the YBaCuO 920 D follows the behaviour of a median-radial crack system.

In Fig. 5, the results of the four grades are plotted and compared with Al_2O_3 (K_c = 3·5 MPa Vm) and SiC (K_c = 3·2 MPa Vm) in a $P^{2/3}$ versus c_0 plot. This coordinate system, $P^{2/3}$ versus c_0, has been chosen, because, as can be deduced from eqn (1), the slope is directly proportional to $K_c^{2/3}$, and, in addition to the verification made just above, it is less subject to errors than measurements made with only one indentation load. The values of K_c deduced in this way are given in Table 1 and plotted as a function of grain size in Fig. 6. As can be seen, as grain size increases, the toughness first increases and then decreases. This is a feature which has already been observed for non-cubic

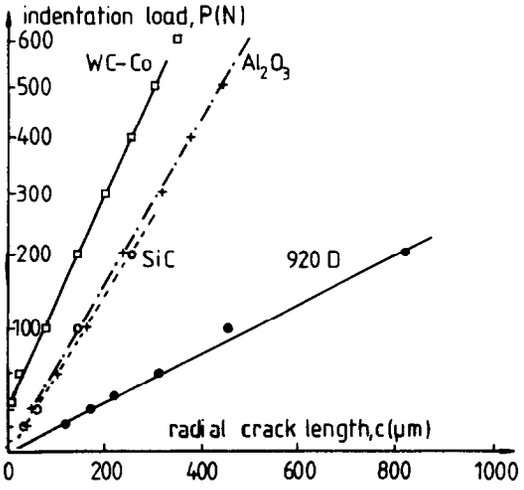

Fig. 4. Indentation load versus radial crack length plots for a material exhibiting Palmquist cracks (WC–Co) and others exhibiting a median-radial crack system (SiC, Al_2O_3 and YBaCuO).

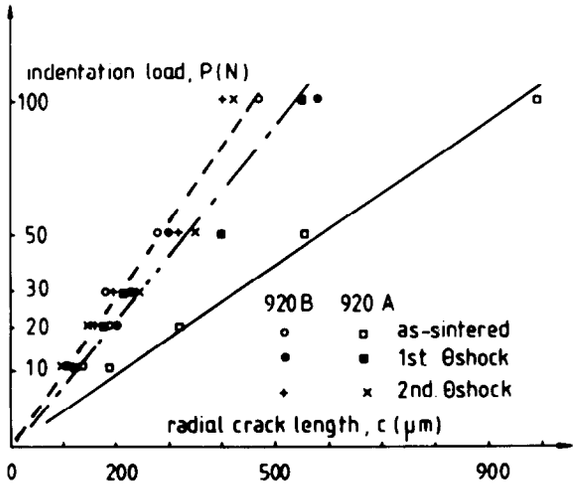

Fig. 5. Indentation load versus radial crack length for the four grades of YBaCuO and comparison with SiC and Al_2O_3.

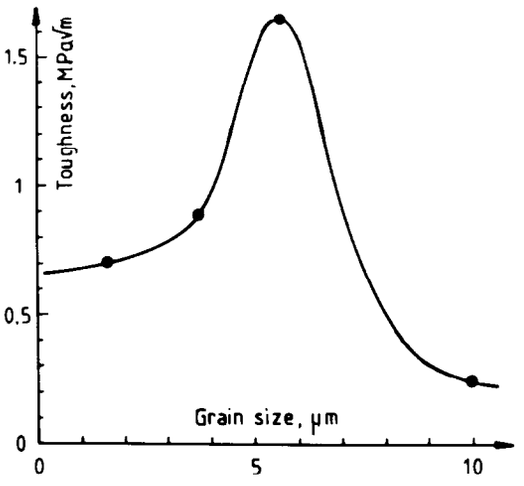

Fig. 6. Variation of Vickers indentation toughness with grain size for the four YBaCuO grades.

ceramics[13–15] and will be discussed later in conjunction with the results of thermal shock testing. The maximum value of K_{1c} is detected at a grain size of about 6 μm which is much larger than the value of 1 μm computed by D. R. Clarke *et al.*[3] for spontaneous microcracking of polycrystalline YBaCuO. This discrepancy may be due to the values of the toughness of the grain boundaries which are higher than that used in ref. 3. Additionally, the polycrystalline YBaCuO investigated here is porous, thus lower values of the residual thermal mismatch stresses are expected.

3.2 Thermal shock resistance

High-temperature ceramic superconductors are aimed to be put to work at the temperature of liquid nitrogen and because an in-between stage at room temperature is technically necessary, the investigation and the knowledge of the resistance against sudden temperature changes are necessary. Since the works of Buessen[16] and Kingery[17] many efforts have been devoted to the thermal shock resistance of structural ceramics.[18] These approaches, however, propose to rank the materials in determining a critical quenching temperature difference, ΔT_c, following a method which needs a large number of specimens having the same microstructure. This is hardly achievable for materials in the R&D stage and, in the case investigated here, the relative resistance of materials against given quenching conditions is looked for. For this purpose a test based on the conditions of the stable extension of Vickers indentation cracks has been developed[19,20] and will be briefly outlined below.

The principle is based on the existence of residual contact stresses which act as a central opening force, or wedge, such as to extend the radial cracks until its driving force is counterbalanced by the crack resistance of the indented material (eqn (1)). Now if an external stress of mechanical or thermal origin σ_{th} is added to this wedge effect, the indentation cracks increase their size, c. The critical stress intensity factor is then:[11,12]

$$K_c = \chi r \cdot P \cdot c^{3/2} + \sigma_{th}(\pi \Omega c)^{1/2} \qquad (4)$$

It corresponds to the superposition of the residual indentation stress intensity factor and that due to the external stress, $K_e = \sigma_{th}(\pi\ \Omega\ c)^{1/2}$ where Ω is a geometrical factor taking into account the shape and size of the semi-elliptical surface cracks (Ω = 0·405) The occurence of a negative and a positive exponent for the actual radial crack length, c, indicates the possible existence of stable crack extension during the superimposition of stresses given above. The differentiation of σ_{th} with respect to the actual crack length, c, shows that stable crack growth occurs between the initial, or as-indented (see Fig. 7), crack length, c, and a given crack length, c_m Both depend on the indentation load, P, and on the material toughness, K_c The value of c_m is obtained as:

$$c_m = (4\chi r \cdot P/K_c)^{2/3} \quad (5)$$

in conjunction with a stress level, σ_m; both defining the end of stable and the onset of uncontrolled crack extension:

$$\sigma_m = 3K_c/4((\pi\Omega c_m)^{1/2} \quad (6)$$

These bell-shaped curves are schematically shown in Fig. 2 of ref. 2 and reproduced for several indentation loads in Fig. 7. The aim is to show how indentation cracks due to different indentation loads increase in length for a given external applied stress, which is the peak of the thermal transient stress, σ_{th} in the present case. For a value of the applied stress, $\sigma_{th} = 0$, the radial cracks have their initial length, c_o (eqn (3)). In Fig. 7, a level of $\sigma_{th} = 58$ MPa has been arbitrarily chosen such as to correspond to a maximum of one of the curves (P=100 N). It shows that the radial cracks extend in a stable, and then possible unstable way, depending on the indentation load, as shown by the thick parts of the bell-shaped lines. It is a special case, since it defines the conditions for the onset of unstable extension as the curve describing the behaviour of a crack system obtained with an indentation load of P = 100 N where the crack length attains $c = c_m$. The ratio c_m/c_0 is 2·52, independently of the indentation load.

Values of c/c_o, the relative increase in radial crack length, can thus be calculated as a function of indentation load, P, and for various levels of applied stress and toughness of the materials, K_c. Some features are shown in Fig. 8. It appears that the relative increase in radial crack length c/c_o, tends as a function of the indentation load, the more rapidly towards $c_m/c_o = 2{\cdot}52$, the higher the level of the applied stress or the lower the toughness of the material.

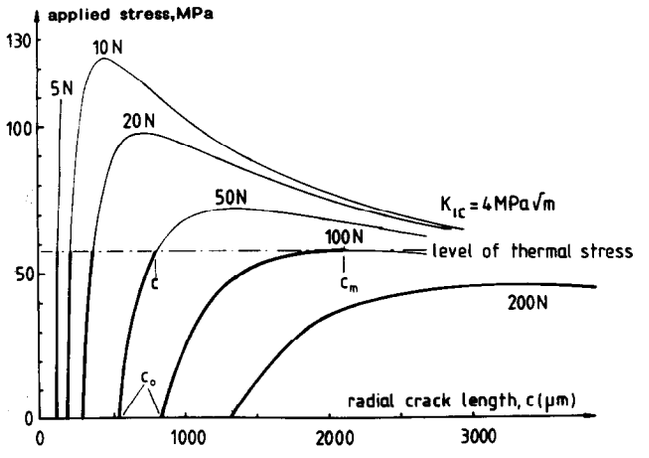

Fig. 7. Stable (increasing) and unstable (decreasing) branches of the extension of Vickers indentation radial cracks under the action of an applied stress. The value of the indentation load is given on the top of each curve. The extensions for a given level of applied stress are the thick part of the lines (χr = 1).

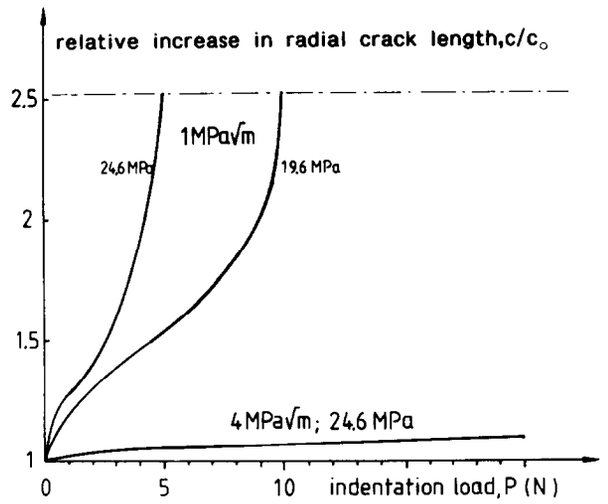

Fig. 8. Comparative effects of toughness and given applied, mechanical or thermal stresses on the relative increase in length of the radial cracks from Vickers indentation, as a function of indentation load. The limit of stable and thus measurable crack extension (c/c_o = 2·52) is indicated.

In the present case, since the YBaCuO samples differ only by the grain size and since they have all the same shape and dimensions, it is assumed that the value of the peak of the thermal transient stress, σ_{th}, appearing when the samples are put into liquid nitrogen, is the same for the four grades. The response of the sample to quenching is thus solely dictated by the toughness and the relative increase in radial crack length, c/c_o, is some indicator of the thermal shock resistance.

The experimental results are shown in Fig. 9. It can be seen that the shape of the experimental curves follows that predicted in Fig. 8. From the way these curves have been derived, it means that, the higher or the steeper the curve, the less thermal shock resistant is the material. In the present

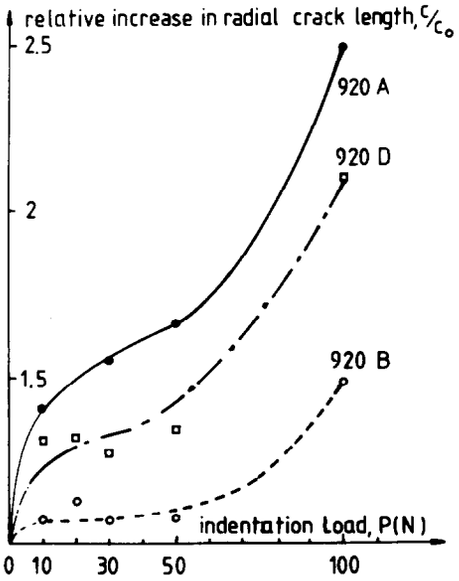

Fig. 9. Relative resistances against thermal shock of three YBaCuO grades when quenched from room temperature in air into liquid nitrogen.

case, it shows that the thermal shock resistance decreases with increasing grain size. It can be noted that this ranking is not the same as that for the toughness which exhibited first an increase and then a decrease with increasing grain size. This apparent discrepancy will be discussed on the basis of existing models and results obtained on both functional and structural ceramics.

Further toughness measurements made on quenched samples give some information for speculating on the role of residual thermal mismatch stresses. The state of the residual stresses depends solely on the testing temperature (room temperature in the present case), if they have not been, at least partly, released by spontaneous microcracking, which is an irreversible process. Microcracking during the stage in liquid nitrogen can thus be detected at room temperature through toughness measurements using the indentation method. The results are shown in Fig. 10 for grades 920B (finest grain size) and 920A (coarsest grain size). The toughness of grade 920B did not change after the first, nor after the second quenching, indicating that no microcracking had occurred. Grade 920A behaves differently. After the first quenching a sharp and apparent increase in toughness is observed. A second quenching does not yield further changes. The change observed after these quenchings indicates a change in the internal stress state which may be due to microcracking as detected by other means by D. S. Smith *et al.*[2] and M. Aslan *et al.*[1] The reasons why the release of residual stresses through microcracking yields an apparent increase in toughness are not clear. Previously obtained results on thermally shocked fine-grained alumina[21] and coarse-grained chromium-magnesia refractories[22] indicate opposite changes of toughness after thermal shock. Grade 920A would be in accordance with the refractory. They have also the common features of being porous and coarse-grained. This problem however should be discussed within further papers. An explanation may be that nuclei of microcracks are created which would not have been activated otherwise.

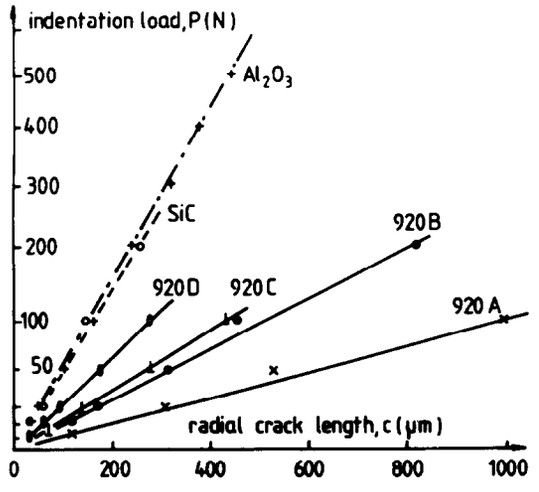

Fig. 10. Detection of microstructural damage in the coarse-grained 920A grade after quenching into liquid nitrogen.

4 Discussion

The shape of the curve describing the change in toughness with grain size is similar to that already shown by Rice, Freiman, Becher and Pohanka.[13–15] Their model is based on the existence of thermal residual mismatch stresses at the grain boundaries due to the anisotropy of the thermal expansion coefficients. These residual stresses are also investigated for their role in dielectric failures[23,24] and the influence of grain size (the tendency to grain boundary microcracking increases with increasing grain size) has been established[25].

Residual thermal mismatch stresses may enhance toughness. The case must be considered when an external stress is applied and superimposed to these already existing stresses in order to reach the conditions for grain boundary microcracking. Rice and Freiman[14] considered an arithmetic contribution of the grain boundary energy per unit area of primary crack growth. Other models consider the superimposition of applied and residual stresses (stress-induced microcracking) for deriving models of toughness based on the shielding effect of a frontal microcracked, or process zone.[26–28] It appears from these models that as grain size increases, the density of microcracks ahead of the primary crack increases in a first time, enhancing the shielding effect and thus toughness. However above a critical grain size, the strain energy of the grains is high enough that the decrease in applied stress necessary for inducing microcracking counterbalances more and more the shielding effect. Toughness decreases then towards zero for a grain size at which spontaneous microcracking occurs.[23–31]

When the YBaCuO samples are cooled to the temperature of liquid nitrogen (77 K), the residual thermal mismatch stresses and the associated strain energy of the grains, increase with respect to their level at room temperature. This results in a shift, towards smaller grain sizes, of the bell-shaped curve describing the variation of toughness with grain size at room temperature (see Fig. 6). This shift is illustrated in Fig. 11 as well as the expected changes in toughness for a temperature of 77 K.

This shift may explain the apparent discrepancy between the ranking of the toughness measured at room temperature and the ranking of the thermal shock resistance as a function of grain size. Extension of the radial crack during thermal shock

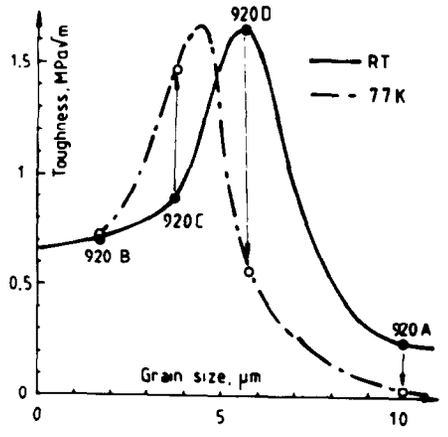

Fig. 11. Speculated shift of the toughness versus grain size as testing temperature varies from room temperature to that of liquid nitrogen.

takes place at the temperature of liquid nitrogen and the toughness at that temperature must be considered. The speculated shift may yield the same ranking for the toughness at 77 K and the thermal shock resistance. Unfortunately the lack of testing materials and facilities did not allow of an experimental confirmation.

5 Conclusion

In the present work the influence of grain size on the toughness and thermal shock resistance of polycrystalline YBaCuO has been investigated in using the Vickers indentation method. It has been shown that this experimental methodology yields valuable quantitative and qualitative informations on these materials in the R&D stage. The changes of toughness and thermal resistance with grain size can be correlated within the frame of models taking residual thermal mismatch stresses into account.

In view of the discrepancies of published results on the decrease of critical current density with increasing grain size, inquiries on the nature and structure of the grain boundaries should be undertaken in order to become able to tailor microstructures exhibiting both high toughness, thermal and microcracking resistance, as well as satisfactory current densities and reliability.

References

1. Smith, D. S., Suasmoro, S. & Gault, C., Demonstration of grain growth induced microcracking and its role in the electrical response of $YBa_2Cu_3O_{7-\delta}$. *J. Eur. Ceramic Soc.*, **5** (1989) 81–5.
2. Aslan, M., Jaeger, H., Kaiser, G., Gröner, R., Schulze, K. & Pezow, G., Influence of microstructure on the superconducting properties of polycrystalline $YBa_2Cu_3O_{7-\delta}$. *J. Eur. Ceramic Soc.*, **6** (1990), 129–35.
3. Clarke, D. R., Shaw, Th. M. & Dimos, D., Issues in the processing of cuprate ceramic superconductors. *J. Am. Ceramic Soc.*, **72**(7) (1989) 1103–13.
4. Zhu, Y., Tafto, J. & Suenage, M., Defects in high T_c cuprate superconductors. *MRS Bulletin*, Nov. 1991, 54–9.
5. Clarke, D. R., Grain boundaries in polycrystalline ceramics. *Ann. Rev. Mater Sci.*, **17** (1987) 57–74.
6. Alford, N. McN., Birchall, J. R., Clegg, W. J., Hormer, M. A., Kendall, K. & Jones, D. H., Physical and mechanical properties of $YBa_2Cu_3O_{7-\delta}$ superconductors. *J. Mat. Science*, **13** (1988) 761–8.
7. Ochiai, S., Hayashi, K., Hosoda, A. & Osamura, K., Tensile strength and its scatter of superconducting $YBa_2Cu_3O_{7-\delta}$ in silver sheathed wires and tapes estimated from multiple cracking. *J. Mat. Sci. Letters*, **10** (1990), 117–19.
8. Cook, R. F., Dinger, T. R. & Clarke, D. R., Fracture toughness measurements of $YBa_2Cu_3O_{7-\delta}$ single crystals. *Appl. Phys. Letters*, **51**(6) (1987), 454–6.
9. Fujimoto, H., Murakami, M. & Koshizuka, N., Effect of Y_2BaCuO_5 on fracture toughness of YBCO prepared by a MPMG process. *Physica C*, **203** (1992), 103–10.
10. Osterstock, F., Strauss, S., Mordike, B. L., Monot, I. & Desgardin, G., Toughness and thermoshock resistance of polycrystalline $YBa_2Cu_3O_{7-\delta}$. *J. Alloys and Compounds*, **195** (1993), 679–82.
11. Anstis, G. R., Chantikul, P., Lawn, B. R. & Marshall, D. B. A critical evaluation of indentation techniques for measuring fracture toughness; I, Direct crack measurements. *J. Am. Ceramic Soc.*, **64**(9) (1981) 533–8.
12. Chantikul, P., Anstis, G. R., Lawn, B. R. & Marshall, D. B., A critical evaluation of indentation techniques for measuring fracture toughness: II, Strength method. *J. Am. Ceramic Soc.*, **64**(9) (1991), 539–43.
13. Rice, R. W., Freiman, St. W. & Becher, P. F., Grain size dependence of fracture energy in ceramics; I, Experiment. *J. Am. Ceramic Soc.*, **64**(6) (1981) 345–55.
14. Rice, R. W. & Freiman, St. W., Grain size dependence of fracture energy in ceramics; II, A model for non-cubic materials. *J. Am. Ceramic Soc.*, **64**(6) (1981), 350–54.
15. Freiman, St. W. & Pohanka, R. C., Review of mechanically related failures of ceramics capacitors and capacitor materials. *J. Am. Ceramic Soc.*, **72**(12) (1989) 2258–63.
16. Buessem, W. R., Thermal shock testing. *J. Am. Ceramic Soc.*, **38**(1) (1955) 15–17.
17. Kingery, W. D., Factors affecting the thermal shock resistance of ceramic materials. *J. Am. Ceramic Soc.*, **38**(4) (1955) 3–15.
18. Hasselman, D. P. H., Unified theory of thermal shock fracture initiation and crack propagation in brittle ceramics. *J. Am. Ceram. Soc.*, **52**(11) (1969) 600–4.
19. Osterstock, F., Contact damage submitted to thermal shock: a method to evaluate and simulate thermal shock resistance of brittle materials. *Mat. Sci. Eng.*, **A168** (1993), 41–4.
20. Osterstock, F., Caplan, D. & Prouteau, C., Effect of thermal shock and related transient stresses on the stable and unstable extension of Vickers indentation cracks in brittle solids. *3. ECRS*, Vol. 3, eds P. Duran & J. F. Fernandez, 1993, pp. 997–1002.
21. Osterstock, F. & Moussa, R., Thermal shock resistance of ceramics: influence on fracture mechanical parameters. *Ceram. Forum Int.*, **3** (1988) 71–84.
22. Themines, D. & Osterstock, F., Linear non-elastic fracture mechanics: application on refractories. *2nd Int. Conf. on Residual Stresses, ICRS-2*, eds G. Beck, S. Denis & A. Simon, Elsevier Applied Science, 1989, pp. 985–90.
23. Kishimoto, A., Kounioto, K. & Yanagida, H., Mechanical and dielectric failure of $BaTiO_3$ ceramics. *J. Mat. Science*, **24** (1989) 698–702.
24. Chano, H. T., Shin, B. C. & Kim, H. G. Grain size dependence of electrically induced microcracking in ferroelectric ceramics. *J. Am. Ceram Soc.*, **72**(2) (1989) 327–9.
25. Davidge, R. W. & Tappin, G., Internal strain energy and the strength of brittle materials. *J. Mat. Science*, **3** (1968), 287–301.

26. Buresh, F. E., Fracture toughness testing of alumina. In *Fracture mechanics applied to brittle materials*, ed. St. W. Freiman. ASTM STP 678, 1979 pp. 151–65.
27. Kreher, W. & Pompe, W., Increased fracture toughness of ceramics by energy-dissipative mechanisms. *J. Mat. Science*, **16** (1981) 694–706.
28. Hutchinson, J. W., Crack tip shielding by microcracking in brittle solids. *Act. Metall.*, **35**(7) (1987) 1605–19.
29. Evans, A. G., Microfracture from thermal expansion anisotropy; I, Single phase system. *Acta Metall.*, **26** (1978), 1845–53.
30. Case, E. D., Smyth, J. R. & Hunter, O., Grain size dependence of microcrack initiation in brittle materials. *J. Mat. Science*, **15** (1980) 149–53.
31. Tvergaard, V. & Hutchinson, J. W., Microcracking in ceramics induced by thermal expansion or elastic anisotropy. *J. Am. Ceramic Soc.*, **71**(3) (1988) 157–66.

Journal of the European Ceramic Society 16 (1996) 695–702

0955-2219(95)00197-2
0955-2219/96/$15.00

Critical Notch-Root Radius Effect in SENB-S Fracture Toughness Testing

R. Damani, R. Gstrein & R. Danzer*

Christian Doppler Laboratorium für Hochleistungskeramik am Institut für Struktur- und Funktionskeramik, Montanuniversität Leoben, A-8700 Leoben, Austria

(Received 20 September 1995; revised version received 20 October 1995; accepted 30 October 1995)

Abstract

The brittle behaviour of ceramic materials makes imperative the development of accurate and reproducible methods of measuring their resistance to fracture. To this end, a European round robin was set up to investigate the relative merits of five different methods of fracture toughness testing. Of these the single edge notch bend – saw cut (SENB-S) method seemed to deliver the most reproducible results, both within and between laboratories. However, it has been observed empirically that if notches are cut too thick, the values of fracture toughness determined are systematically too high. An explanation and a theoretically based relationship to describe this behaviour are presented. It is suggested that this effect results from the interaction of the stress field around the notch tip and defects related to the microstructure or machining damage. Measured data from a number of materials seem to correlate well with the theory. It is shown that if correct values of fracture toughness are to be determined with the SENB-S method, the notch width must be of the order of the size of the relevant microstructural or machining-induced defects (e.g. large pores and weak grain boundaries).

Introduction

The greatest limitation in the use of ceramic materials for load-bearing applications is their brittleness. To overcome this problem tougher materials must be engineered. More accurate and reproducible methods of fracture toughness testing are required to enable an objective evaluation of the progress made in improving the resistance to crack propagation of ceramic materials.

With this in mind, The European Structural Integrity Society-Technical Committee 6 (ESIS TC6) set up a round robin to evaluate five commonly used methods of fracture toughness testing: the chevron-notched beam (CVN); the indentation fracture (IF); the indentation strength in four-point bending (IS); the single-edge precracked beam in four-point bending (SEPB–B) using popped in bridging cracks, and the single edge notch bend – saw cut (SENB-S) methods. The results of this round robin showed that the SENB-S method, although not always the most accurate, seems to be the most reproducible both within and between laboratories.[1] Furthermore, the SENB-S method requires very little specialized apparatus and specialist skill. It is therefore cheap and applicable in most standard mechanical laboratories. The major limiting feature of this method, however, is the appearance of a limiting *critical notch root radius*, above which the values of K_{Ic} determined are systematically too high. In this work an explanation is presented that relates the occurrence and magnitude of this critical notch root radius, ρ_c, to microstructural features of the ceramic material. A relationship that allows a first approximation of the magnitude of ρ_c is suggested.

Fracture Toughness Testing in Ceramics

A major problem of fracture toughness testing of ceramics is the difficulty in reliably introducing reproducible and easily measurable sharp cracks into the samples. In metals fatigue cracks are initiated and grown in a controlled manner, but this is too difficult, if not impossible, in ceramic samples. Various other methods have been devised to initiate such cracks in ceramic samples, e.g. by using the bridging method or a chevron-notched sample (where the initial cracks run into a field of decreasing stress intensity),[2] but they tend to produce long cracks that are difficult to measure and difficult to reproduce. In the SENB-S method most of these problems are avoided since it is relatively

*To whom correspondence should be addressed.

easy to machine an accurate notch, the exact depth of which is easily discernible in an optical microscope. The machined notch is then assumed to act as a long, sharp crack.

It should be noted that there are ceramic materials with more or less constant crack resistance, and other ceramic materials where the crack resistance increases as the crack grows. In the following analysis emphasis is placed on the first type of material.

The SENB-S Method and the Critical Notch Root Radius

The SENB-S method involves taking small-beam samples (typically of breadth b = 3 mm, height w = 4 mm and length L = 45 mm), sawing a suitable notch to a depth a_0 and then testing to fracture in four-point bending [see Figs 1(a) and 1(b)]. The depth of the notch is determined by optical analysis of the fractured surfaces. It is assumed that fracture initiates from some statistically distributed small flaw in front of the notch. The size of this flaw, δa, correlates with some microstructural feature. The total crack length at failure is then: $a_f = a_0 + \delta a$. However, since $\delta a << a_0$, and δa is difficult to find and measure, the approximation $a_f \approx a_0$ is usually applied. The stress at failure, σ_f, is used to calculate the critical stress intensity factor (i.e. the fracture toughness), K_{Ic}, from a relationship based on the standard linear elastic fracture mechanics relationship:

$$K_I = Y \sigma \sqrt{\pi a} \tag{1}$$

where Y is a correction factor allowing for the influence of sample geometry and crack configuration. The following relationship,[3] applicable to long, sharp crack configurations with values of α between 0·4 and 0·6, was used in the round robin investigation for calculating K_I:

$$K_I = \frac{F}{b\sqrt{w}} \frac{S_1 - S_2}{w} \frac{3\sqrt{\alpha}\, \Gamma_M}{2(1-\alpha)^{3/2}} \tag{2}$$

where

$$\Gamma_M = 1{\cdot}9887 - 1{\cdot}326\,\alpha - \frac{(3{\cdot}49 - 0{\cdot}68\,\alpha + 1{\cdot}35\,\alpha^2)\,\alpha\,(1-\alpha)}{(1+\alpha)^2}$$

$\alpha = a_f/w$, F is the load, and S_1 and S_2 are the outer and inner roller spans of the four-point bending fixture, respectively. The critical stress intensity factor K_{Ic} is obtained if the maximum load before failure, F_{max}, is used in eqn (2). (Note: If, for instance, w = 4 mm, a_0 = 2 mm, and δa = 50 μm the error made by applying the approximation $a_f \approx a_0$ in calculating K_{Ic} from eqn (2) is about 3·8%.)

The notches are typically cut to half the depth of the beam ($\alpha \approx 0{\cdot}5$). The half-width of the saw cut is taken to be the notch root radius, ρ.

It is commonly presented in literature[3–5] that, if the notches are too wide, i.e. the notch-root radius ρ is too large, the values of K_{Ic} will be systematically determined too high. Only below some critical value of notch-root radius ρ_c will the values of K_{Ic} remain constant and correct (Fig. 2). Indeed, some such behaviour is to be expected if the differences in stress distribution in front of a notch and in front of an infinitely sharp crack are considered and, in fact, is often observed empirically.

Thus, by treating the notch as a blunt crack and by considering the true role of small cracks at the notch tip, an explanation for this critical notch-root radius effect becomes evident. These small cracks can be assumed to be in-plane material

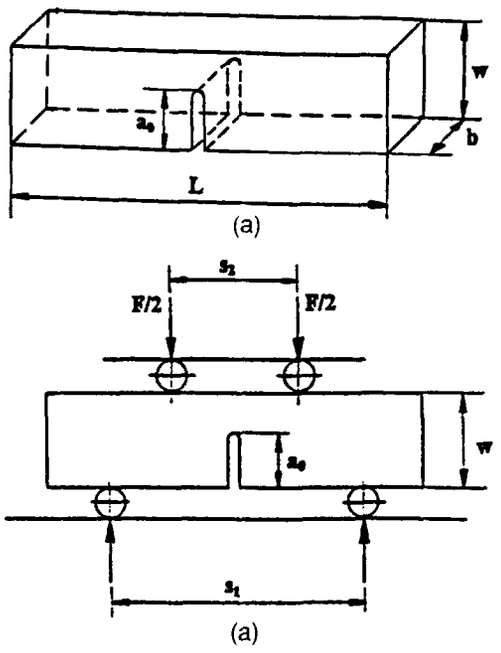

Fig. 1. (a) Geometry of edge-notched small beam sample; (b) schematic arrangement of sample in a four-point bend test.

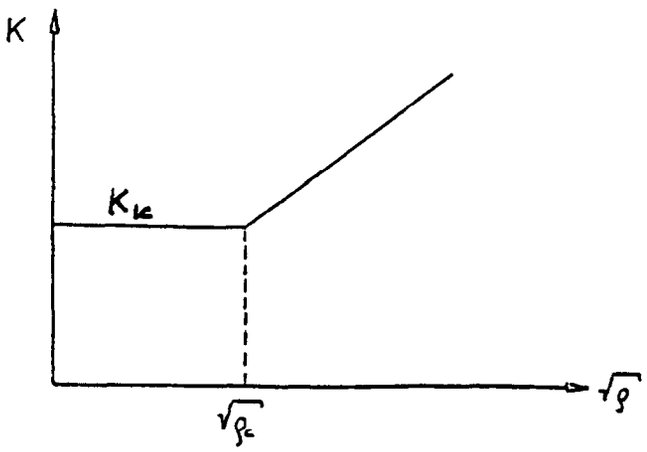

Fig. 2. Schematic representation of dependence of measured fracture toughness K_{Ic} on notch-root radius ρ (from Munz & Fett[3]).

flaws, or machining damage, statistically distributed along the notch front [Fig. 3(a)]. For analytical simplicity it is convenient to replace the true notch-crack configuration with an assumed idealized configuration, e.g. a through-thickness edge crack [Fig. 3(b)] or a half-penny crack [Fig. 3(c)]. The true configuration will be somewhere in between. The conventional concept of a long crack, i.e. $a_f \approx a_0$, in which the influence of the notch is neglected, may then be replaced by the configuration of a small crack in front of a notch, which lies in a stress field under the influence of the notch. In the following the ratios of the corresponding stress intensity factors are calculated.

By using a standard fracture mechanics approach to blunt cracks to calculate the notch tip stress,[6] and by re-applying (1) with the appropriate geometric correction factor (e.g. for a through-thickness edge crack $Y = 1{\cdot}12$ and for a half-penny shaped crack $Y \approx 2/\pi$), the ratio of the true stress intensity factor seen by a small notch-tip crack K_{ntc} to the stress intensity factor for long sharp cracks K_{lsc} calculated by (2) is given as

$$K_{ntc} / K_{lsc} \approx 2\ Y \sqrt{\delta a / \rho} \tag{3}$$

This relationship is valid for very small cracks where $\delta a << \rho_c$ and may be applied as an approximation for small cracks. The stress intensity factor calculated from eqn (2), however, is valid for long cracks where $\delta a >> \rho_c$. The change in stress intensity as the fracture-initiating crack varies from short to long crack may be given by suitably weighting the two functions (2) and (3). To this end, Fett[7] suggested the following simple function

$$X \approx \tanh (2\ Y \sqrt{\delta a / \rho}) \tag{4}$$

where

$$X = \frac{K_{ntc}}{K_{lsc}} \tag{5}$$

(note that $\tanh x \approx x$ for $x << 1$, and $\tanh x \to 1$ as $x \to \infty$).

The validity of the above weighting function has been corroborated by applying the boundary collocation method. In Fig. 4(a) stress intensity is plotted against the relative notch depth α and small crack size δa. It shows schematically the curves of K for long cracks as obtained from eqn (2) and for small cracks according to eqn (3) in the area around the notch tip as functions of α and δa, respectively, when all other conditions are kept constant. The solid line shows the weighted function for K_{ntc} using eqn (4). Figure 4(b) shows the strong dependence of the weighted function on ρ.

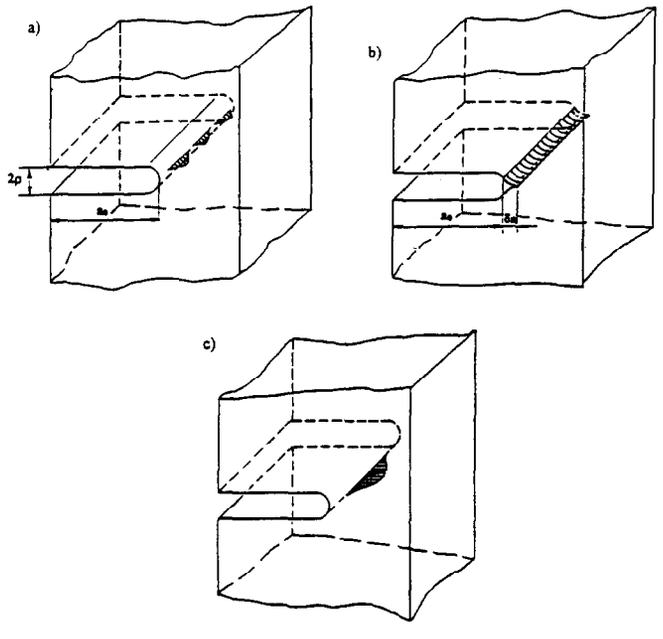

Fig. 3. (a) Schematic representation of notch and natural, in-plane notch-tip defects (true notch-crack configuration); (b) idealized edge-crack configuration; (c) idealized half-penny configuration.

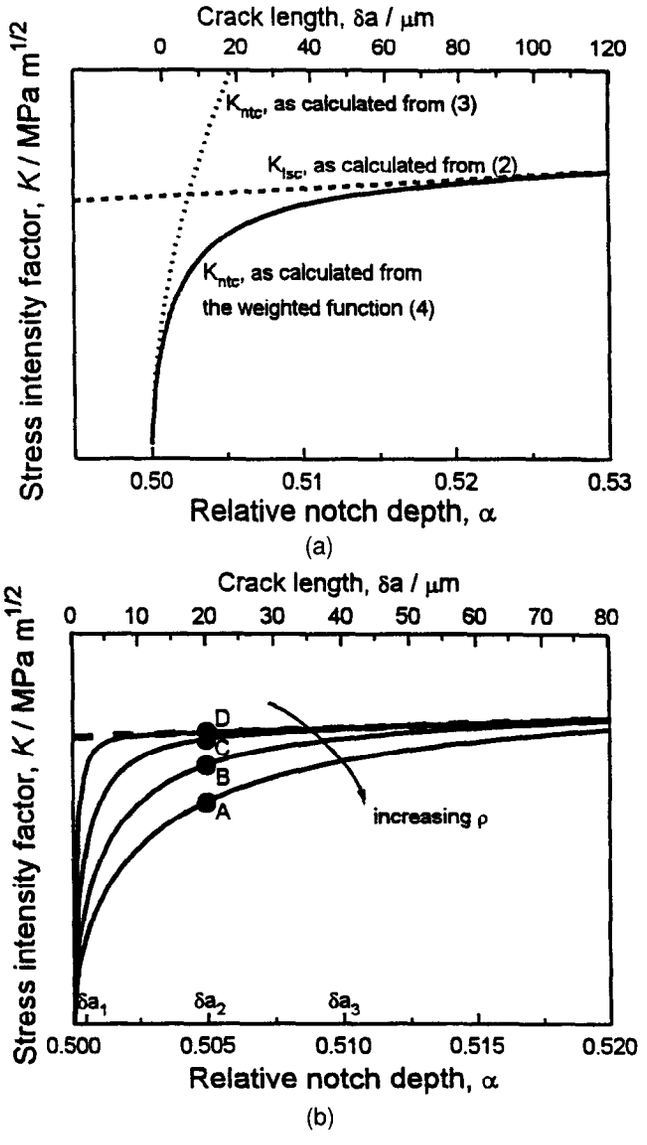

Fig. 4. (a) Stress intensity factors for long sharp cracks and small notch-tip cracks as calculated from eqns (2) and (3) respectively, and the weighted function, eqn (4). (b) Dependence of the weighted function (4) on notch-root radius ρ.

Points A, B, C and D mark the stress intensity factors that would be seen by a small crack of length δa_2 in front of the notch. The dashed line represents the K_{Ic} that would be calculated for long sharp cracks under the same conditions.

Figure 5(a) shows schematically the variation in K_{Ic} values determined from the notch-crack configurations suggested above, i.e. varying notch width and δa kept constant. The scatter bars give an idea of the magnitude of empirical scatter typically observed. Figure 5(b) shows schematically the types of curves that would be attained for three different small crack sizes, where $\delta a_1 < \delta a_2 < \delta a_3$, as shown in Fig. 4(b).

It can clearly be seen that small cracks in front of notches can actually experience significantly lower stress intensities than the corresponding long cracks, i.e. $K_{ntc} < K_{lsc}$ [see points A and B in Fig. 4(b)]. Bearing in mind that the ceramic materials considered behave in a predominantly brittle fashion and do not show increasing crack resistance as cracks grow, the small cracks will not grow before fracture occurs. Therefore, to initiate fast fracture from such a small crack, it is necessary to apply significantly higher forces, compared with a system with the corresponding long crack, before $K = K_{Ic}$ at the crack tip. Thus, assuming eqn (4) is correct, fracture toughness values calculated using eqn (2) would be higher than the true fracture toughness. How much higher depends on the magnitude of the effect of the notch and the size of the starting defect. Generally, the wider the notch the more force is required and the higher the value of K_{Ic} determined [see corresponding points A' and B' in Fig. 5(a)]. If, however, the notch is thin enough, the stress intensity at the tip of the small crack does not greatly differ from that seen by an equivalent long crack [see points C and D and dashed line in Fig. 4(b)]. Thus a correct value (within the scatter) of fracture toughness is measured [see corresponding points C' and D' in Fig. 5(a)].

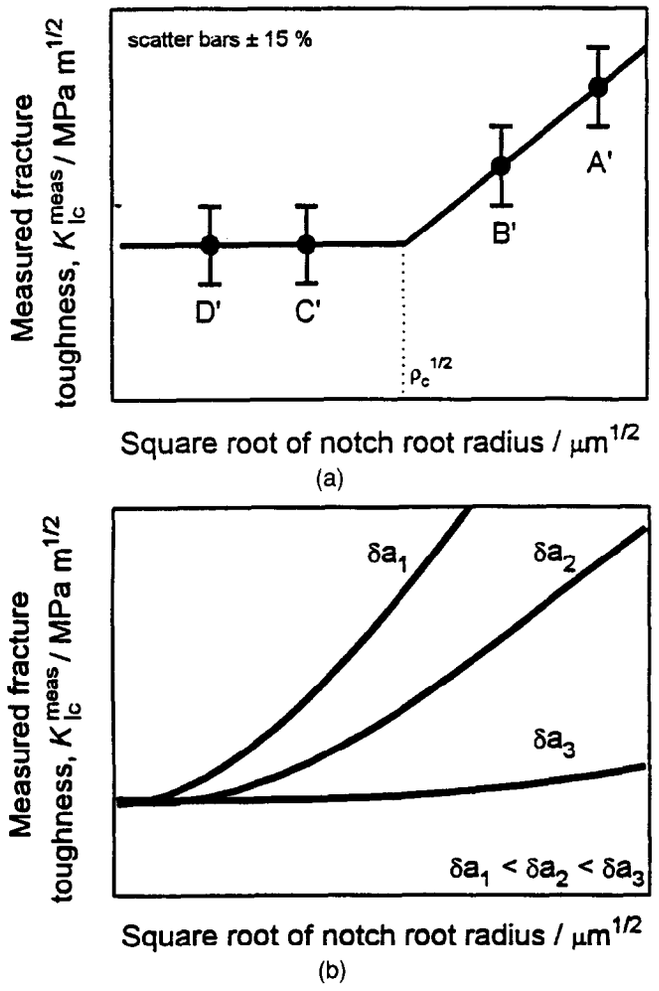

Fig. 5. (a) Schematic representation of the experimentally observed variation in fracture toughness, K_{Ic}^{meas} for constant starting crack size δa and varying notch-root radius ρ. (b) Schematic representation of the theoretical dependence of measured fracture toughness K_{Ic}^{meas} [as calculated from eqn (2)], on varying notch-root radius ρ for different sizes of a starting crack δa.

From eqn (4) X may be calculated as a function of ρ for any given Y and δa. It is clear that, unless δa is sufficiently large, a small crack will not experience a critical stress intensity factor at the same applied stress as would a long crack. It can be assumed that for any such small crack to see a critical stress intensity factor, the stress intensity experienced at the small crack tip must be K_{lsc} raised by $1/X$. Hence the variation in measured fracture toughness, K_{Ic}^{meas}, with increasing ρ may be calculated:

$$K_{Ic}^{meas} = \frac{K_T}{X} \tag{6}$$

where K_T is the true fracture toughness, K_{Ic}.

Relationship (4) may be rearranged so

$$\rho \approx \frac{4\ Y^2}{[\tanh^{-1} X]^2}\ \delta a \tag{7}$$

Then, in order to estimate the critical value of the notch root radius ρ_c, the assumption can be made that the X-ratio must reach a certain value before the method delivers constant results. However, since large scatter is usually observed in practice, there is little reason to demand that this ratio be unity. It should suffice to set X at a value between 0·9 and 0·95, in which case from eqn (6) it follows

$$\rho_c \approx A\ \delta a \tag{8}$$

where both A and δa are constants.

It is suggested here that in many cases δa is a feature of the microstructure, e.g. weakly bonded grain boundaries or large pores, etc. The determination of δa by microstructural analysis before mechanical testing thus enables the a priori

estimation of ρ_c, and gives an idea of the validity of the fracture toughness value determined.

Comparison with Experimental Data

To investigate the validity of eqns (4) and (6), SENB-S tests were made on small beam samples (b = 3 mm, w = 4 mm, L = 45 mm) of five ceramic materials: alumina (Al_2O_3); zirconia (ZrO_2); magnesia partially stabilized zirconia (MgPSZ); hot-pressed silicon nitride (HPSN); and sintered silicon carbide (SSiC). Notches were cut using high-speed rotary saws and diamond-tipped (diamond grit size between 15 and 25 μm) blades. The samples were tested in four-point bending at a load rate of 0·2 to 0·25 mm s^{-1}. The testing fixture was made of hardened steel and had freely movable rolls. The results of the tests are plotted in Figs 6 to 10.

The curves in Figs 6(b) to 10(b) were obtained by applying eqn (6). For any given values of δa and

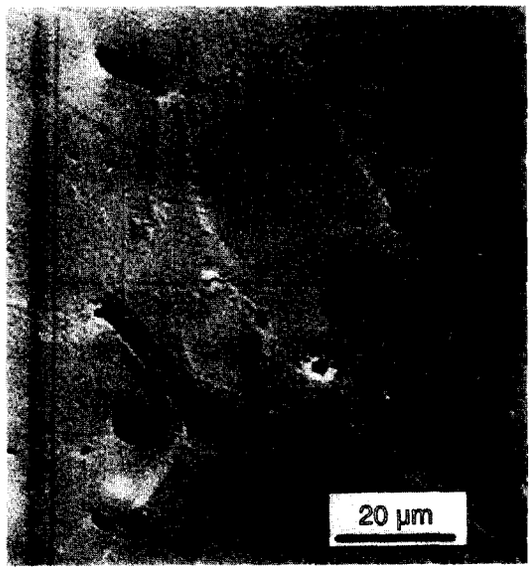

(a)

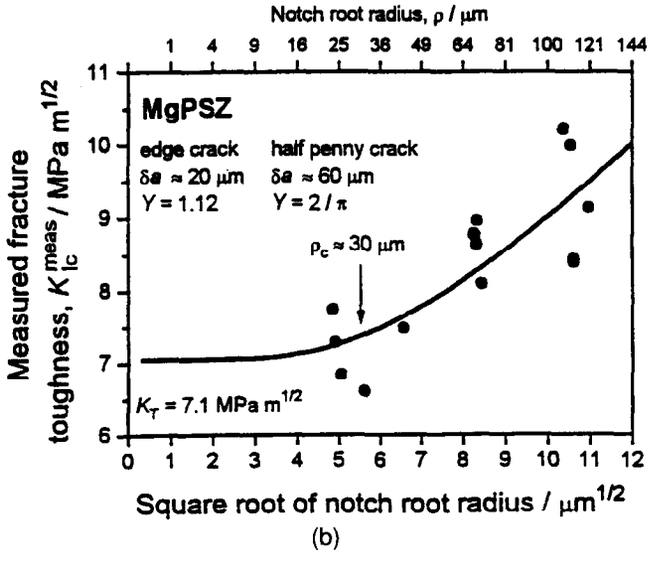

(b)

Fig. 6. (a) Microstructure of MgPSZ; (b) the best fit through the measured data points according to eqn (6).

(a)

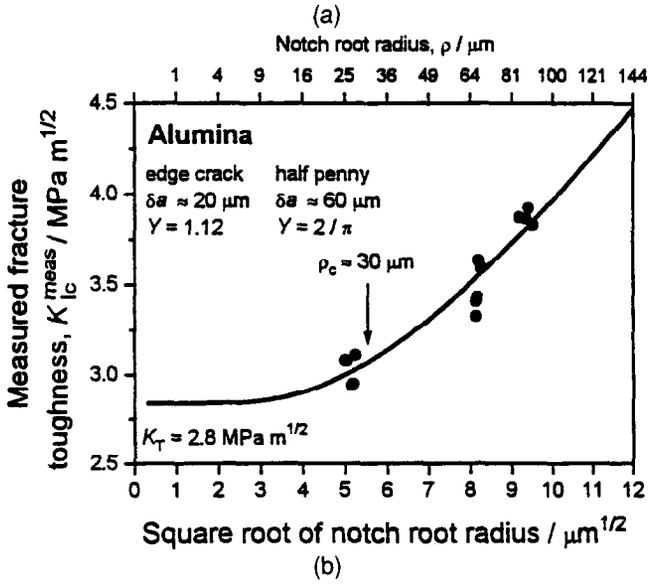

(b)

Fig. 7. (a) Microstructure of Al_2O_3; (b) the best fit through the measured data points according to eqn (6).

Y, the value of X follows from eqn (4) as a function of ρ. There are two possibilities to fix the parameters δa and Y, either by mathematical fitting or by microstructural analysis. The course of the curves may be determined by the product of Y^2 and δa, hence this has been used as one fitting parameter. By changing K_T the whole curve is shifted up or down. Both features have been used to get a reasonable fit to the experimental data points.

The parameters may also be fixed by microstructural analysis. The notch-tip small cracks were assumed to be related to some characteristic feature of the microstructure so δa was roughly approximated for each material on the basis of microstructural studies. Where no obvious suitable microstructural feature was found δa was assumed to be related to machining damage, e.g. the size of scratches from the diamond-tipped saw (approximately 10 μm). If isolated open grain boundaries or other obvious isolated defects in the microstructure

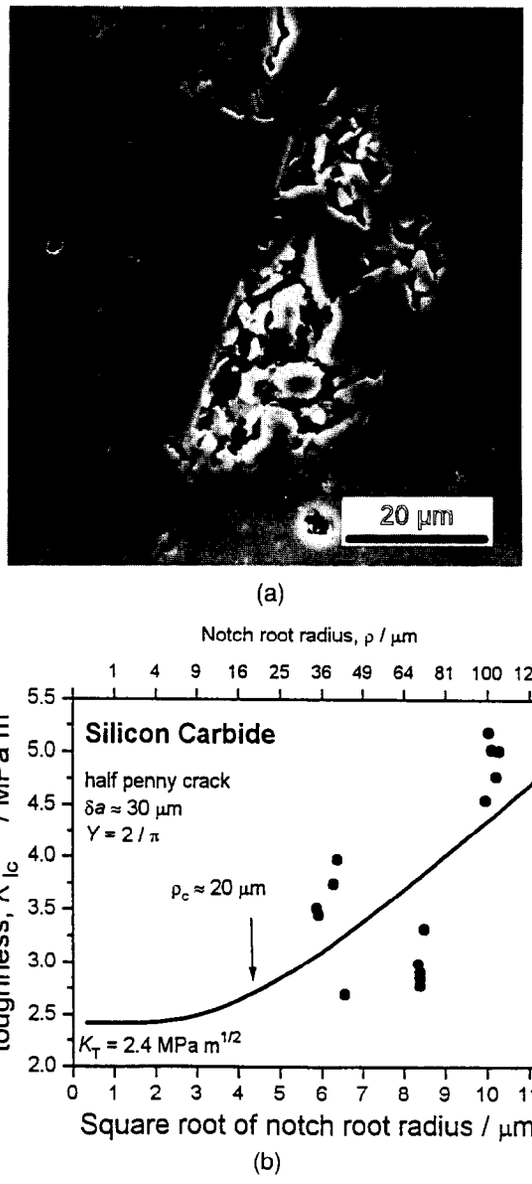

Fig. 8. (a) Microstructure of SSiC; (b) the best fit through the measured data points according to eqn (6).

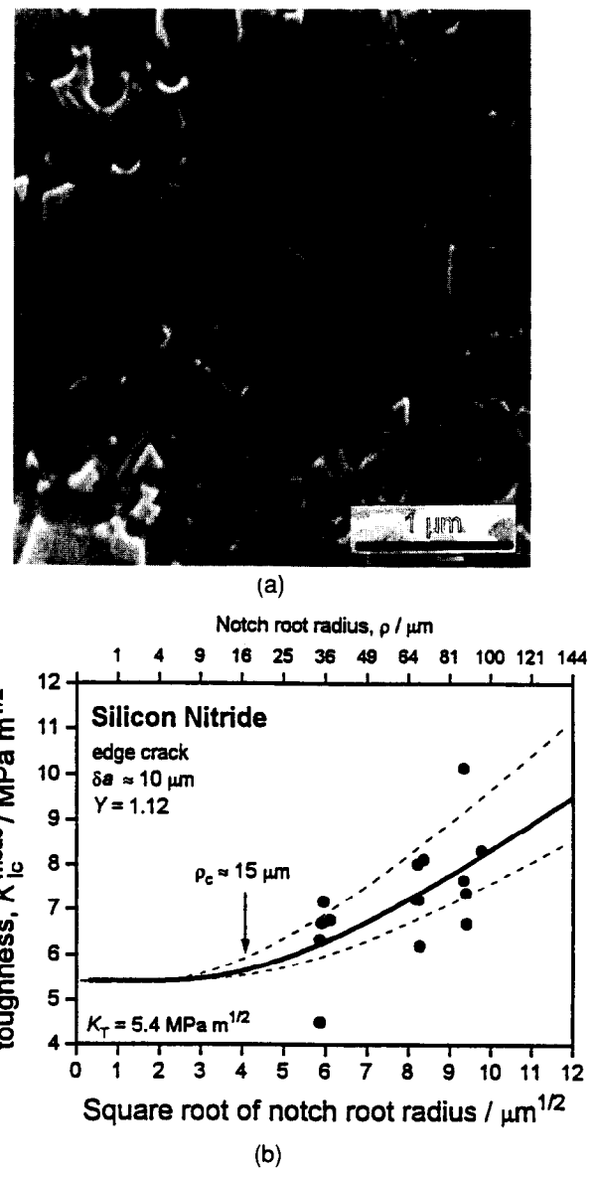

Fig. 9. (a) Microstructure of HPSN; (b) the best fit through the measured data points according to eqn (6) for scratches from diamond grit.

were observed, a half-penny crack configuration may be assumed for which $Y \approx 2/\pi$. If the spacing between defects is small or there is excessive porosity, an edge-crack configuration seems to be more plausible where $Y \approx 1{\cdot}12$. In reality any intermediate configuration is possible. The fitting procedure and the microstructural analysis yield similar results for the parameter $Y^2\,\delta a$ (within a factor of two).

The critical values of the notch root radii ρ_c shown in Figs 6(b) to 10(b) were estimated from eqn (8), by setting the value of X at 0·95, whereby A takes values of about 0·5 and 1·5 for half-penny or edge cracks, respectively.

Discussion of Results

Magnesia partially stabilized zirconia (MgPSZ)

The measurements on and the microstructures of MgPSZ are shown in Fig. 6. The mean grain diameter is about 40 μm. Some grain boundaries are badly sintered as is shown in Fig. 6(a). There are also regions where several open grain boundaries join giving a possible defect radius of 40 to 80 μm. The fitted curve in Fig. 6(b) gives a half-penny crack radius of 60 μm. However, the possibility of straight-through edge cracks cannot be completely excluded. To get the same curve for this notch-crack configuration a crack depth of 20 μm would be required, which correlates with a typical grain facet length. If it is assumed that one line of grain facets breaks open under the action of the sawing wheel, this would be the depth of the corresponding type edge crack. For this material the critical notch root radius is estimated to be about 30 μm and the measurements performed with the narrowest notch width (50 μm blade) are believed to be valid.

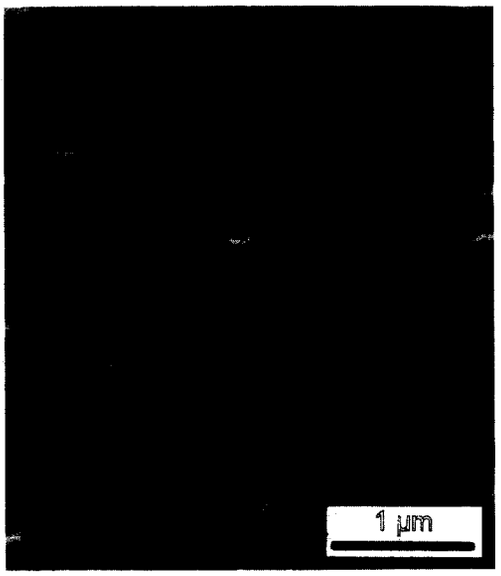

(a)

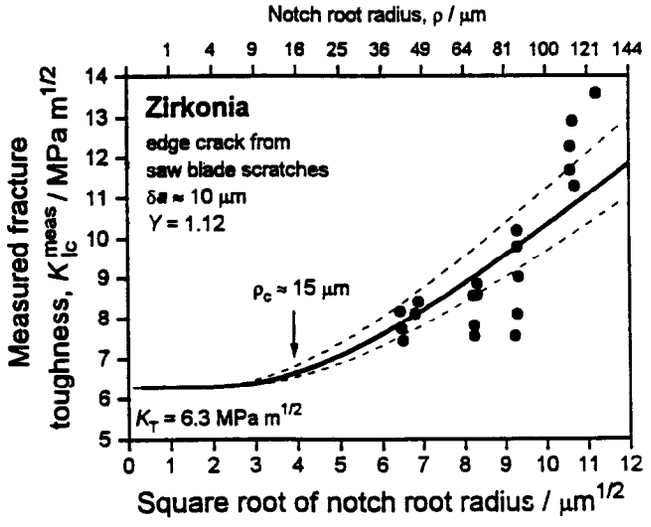

(b)

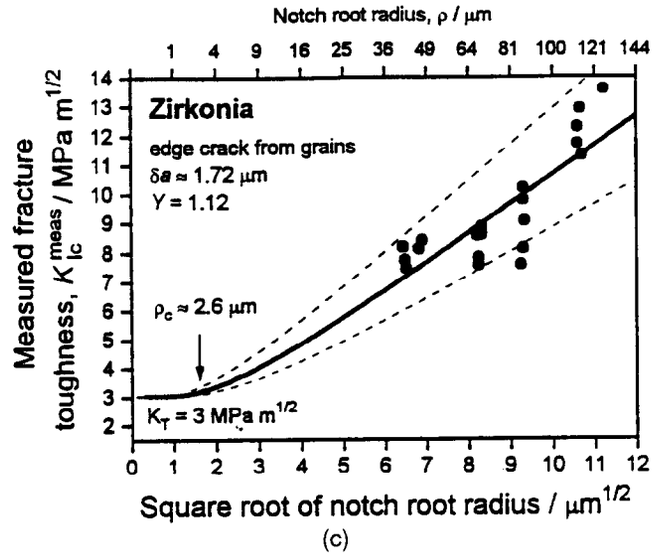

(c)

Fig. 10. (a) Microstructure of ZrO_2; (b) the best fit through the measured data points according to eqn (6) for the scratches from diamond grit; (c) the best fit through the measured data points according to eqn (6) for scratches as predicted by regressional fit. (The micrograph was provided courtesy of Dr F. Hoffer of the ZFE at the Forschungs Institut für Elektronenmikroscopie at the Technischeuniversität Graz, Austria.)

Alumina (Al_2O_3)

The results for alumina are shown in Fig. 7. The mean grain diameter is about 10 μm, and a lot of porosity was observed. The polishing also resulted in large amounts of grain breakout, even at the lowest loads used [see Fig. 7(a)]. It is assumed that such breakouts will also occur under the action of a saw. Both porosity and breakout would act together resulting in a more or less straight-through edge-type crack with a depth of about a few grain diameters .The best-fit curve in Fig. 7(b) is obtained for the through-thickness edge-crack configuration with a crack depth of 20 μm. An analogous fit for a half-penny shaped crack would require a crack depth of 60 μm, which does not seem to be justifiable from the microstructure. Again, the critical notch root radius is estimated to be about 30 μm and the measurements performed with the narrowest notch width (50 μm blade) are believed to be close to the true value.

Sintered silicon carbide (SSiC)

Sintered silicon carbide has a bi-modal microstructure consisting of isolated large grains (diameter of about 30 μm) embedded in a matrix of very fine grains (about 7 μm in diameter). Many fine pores are observed all over the material. Around the large platelet-like grains there is an exceptionally high level of porosity [see Fig. 8(a)], which is believed to be responsible for the fracture-initiating crack. The fitted curve in Fig. 8(b) gives a depth of 30 μm for a half-penny crack, which corresponds exactly to the observed feature. Due to the relatively small defect size the critical notch-root radius is determined to be only 20 μm and all the measured values should be too high.

However, one set of values [as shown in Fig. 8(b)] seems to agree with the theoretically predicted true fracture toughness. This set of tests was carried out using different apparatus from the other two sets. If this apparatus was slightly misaligned a slight hammering action could result. This would cause an increased crack size or a different crack geometry, both of which would result in lower apparent K_{Ic}.

Hot-pressed silicon nitride (HPSN)

The HPSN used has a very fine grain structure, the grain morphology of which is shown in Fig. 9(a). Needle-like grains, up to 3 μm in the long axis, were observed. Microstructural analysis revealed no obvious features that could be thought of as fracture-initiating defects. It may be assumed that scratches from the saw blade act as starting cracks. The size of the diamond saw grit was between 15 and 30 μm, so the depth of the resulting scratches would therefore be about half this size

(between about 7 and 15 μm). The value of δa predicted by the mathematical fit of eqn (7) shown in Fig. 9(b) seems to support this assumption. However, the prediction cannot be seen as definitive due to the large experimental data scatter.

The critical notch-root radius is small, about 15 μm. The measured values were therefore all too high. The large scatter in measured values may possibly be explained if the initial starting crack size is varied between the smallest assumed crack and the largest assumed crack, from about 7 to about 15 μm respectively. The dashed lines in Fig. 9(b) show the scatter band that could be expected from such a variation in starting crack size.

Zirconia (ZrO_2)

The microstructure of zirconia shown in Fig. 10(a) is very fine. The grains are equiaxed and generally less than 1 μm in size; a reasonable amount of porosity was observed, but nothing much larger than the grains. No obvious microstructural feature that acts as a fracture-initiating crack could be observed. The same assumption could be made as in case of HPSN, i.e. that the starting cracks are the scratches from the saw blade of about 10 μm [see Fig. 10(b)]. As before, the scatter band describes the variation in scratch depth resulting from the varying diamond grit size.

Although the data are described properly by the fit above, a slightly better fit may be achieved by mathematical regression [Fig. 10(c)]. The regression suggests a starting crack of about 1·7 μm. The dashed lines here represent the scatter resulting from varying the starting crack size by about one grain diameter. It should, however, be noted that this regression also yields a K_T that is very low. In indentation experiments no cracks at all were seen, even at indentation loads of 30 kg. This would indicate a much higher fracture toughness.

In both cases the fit quality is not very high and a clear distinction between the two cannot be made from the mathematical point of view.

Conclusions

In general, the SENB-S method of fracture toughness testing is reliable, easily applicable and shows low scatter both within and between laboratories. However, the appearance of the critical notch-root radius effect is unavoidable. Therefore, to obtain valid and consistent results it is imperative to cut suitably thin notches.

The notch-root radius effect may be explained if the fracture-initiating crack is assumed to be some small crack in front of the notch tip, under the influence of the stress interaction field of the notch. The theory presented shows that the values of K_{Ic} are valid only if the notch thickness is below some critical value, ρ_c. The magnitude of ρ_c is shown to be proportional to the size of the critical, fracture-initiating defect. The proportionality factor depends on the defect geometry but is of the order of unity. Equation (8) presented in this paper enables the a priori estimation of ρ_c if microstructural studies can reveal an appropriate defect-like microstructural feature. If no such feature can be found, the lower limit of defect size, i.e. machining scratches of about 10 μm, may be adopted.

For coarse-grained materials (of diameter about 50 μm) there will always be some defects (e.g. open grain boundaries or broken grains) of the order of magnitude of the grain size. Therefore it is possible with simple contemporary technology to make notches thin enough to obtain valid measurements from these materials. The same is true for materials containing a reasonable number of large defects (diameter of about 50 μm or more).

However, for materials with very fine and clean microstructures, the starting defects are most probably machining scratches and more advanced technology or methodology will be required to make notches thin enough to deliver valid results.

Acknowledgement

This work was supported by the Ministerium für Wissenschaft und Forschung der Republik Österreich under the contract no. Gz 49·929/3-II/4/94, Mechanische Eigenschaften keramische Hochleistungswerkstoffen.

References

1. Primas, R. J. & Gstrein, R., ESIS TC6 round robin on fracture toughness (Draft Nov. 1994). EMPA Report No. 155'088, Eidgenössische Materialprüfungs- und Forschungsanstalt, Dübendorf, Switzerland, 1994.
2. Amin, K. E., *Toughness, Hardness and Wear*, Engineered Materials Handbook: Vol. 4 Ceramics and Glasses. ASM International, Metals Park, OH, 1991, pp. 599–609.
3. Munz, D. & Fett, T., *Mechanisches Verhalten keramischer Werkstoffe: Versagensablauf, Werkstoffauswahl, Dimensionierung*. Springer-Verlag, Berlin, 1989.
4. Bertolotti, R. L., Fracture toughness of polycrystalline Al_2O_3. *J. Am. Ceram. Soc.*, **56**[2] (1973) 107.
5. Nishida, T., Hanaki, Y. & Pezzotti, G., Effect of notch-root radius on the fracture toughness of a fine-grained alumina. *J. Am. Ceram. Soc.*, **77**[2] (1994).
6. Schwalbe,K.-H., *Bruchmechanik metallischer Werkstoffe*. Carl Hanser Verlag, München–Wien, 1980.
7. Fett, T., Stress intensity factors and weight functions for cracks in front of notches. KfK 5254, Kernforschungszentrum Karlsruhe, Karlsruhe, Germany, 1993.

Journal of the European Ceramic Society 16 (1996) 703–713

0955-2219(95)00199-9
0955-2219/96/$15.00

Mechanical Behaviour of Silicon–Silicon Carbide Composites

E. Scafè,[a] G. Giunta,[a] L. Fabbri,[a]* L. Di Rese,[a] G. De Portu[b] & S. Guicciardi[b]

[a]Eniricerche SpA, via E. Ramarini 32, 00016 Monterotondo (Roma), Italy
[b]Istituto di Ricerche Tecnologiche per la Ceramica, CNR, via Granarolo 64, 48018 Faenza (Ravenna), Italy

(Received 5 September 1994; revised version received 24 October 1995; accepted 1 November 1995)

Abstract

The dependence on the composition of Young's modulus, fracture toughness and flexural strength of a reaction-sintered (RS) silicon–silicon carbide (Si–SiC) composite was determined at room temperature over a wide range of SiC content (0–90 vol%). The results were compared with those of two commercial reaction-bonded (RB) Si–SiC materials. Young's modulus follows two-phase models over the whole compositional range when a value of 432 GPa is assumed for the Young's modulus of β-SiC. At low SiC contents (<60 vol%), the RS composites show fracture behaviour consistent with a crack-deflection toughening model, while at SiC content higher than about 70 vol%, they exhibit much higher surface energies than the equivalent RB commercial Si–SiC. Between 60 and 70 vol% SiC an abrupt change of fracture behaviour is observed. Such differences in surface energies are attributed to quite different microstructures and crack propagation mechanisms.

1 Introduction

In the late 1970s, researchers at General Electric proposed a new way to prepare silicon carbide-based ceramics;[1] they succeeded in obtaining a reaction-sintered (RS) Si–SiC material (Silcomp®) from the reaction between liquid silicon and aligned carbon fibres without the addition of silicon carbide powder. At Eniricerche an alternative method for preparing a fully dense, reaction-sintered Si–SiC composite (ER RS) was developed,[2] by direct reaction between silicon and carbon powders.

Both these preparation procedures allowed the almost continuous variation of SiC volume fraction, and each phase was continuous and interpenetrating through the microstructure.[3] The main differences between the materials obtained by the two methods were in the microstructure: the Silcomp® had an aligned SiC fibre in a silicon matrix structure, whereas the ER RS composite was formed by a sponge-like structure of the silicon carbide reinforcement filled with silicon. In the first material some residual unreacted carbon and porosity were present (about 5 vol%), while the second resulted in an almost dense and carbon-free material (≤ 0·5 vol%). Due to its very low porosity, the latter material represents a model suitable for studying the influence of microstructure on mechanical properties. At low SiC content it will be shown that the composite behaves like a brittle matrix with rigid inclusions. At high SiC content it approaches a fully dense polycrystalline β-SiC with some silicon regions acting as defects. In the intermediate region an abrupt change in the fracture behaviour is observed.

In order to better understand the microstructure–properties relationships of these composites at high SiC contents, two well-known materials, Refel[4] and Sigri,[5] were also evaluated and compared with the ER materials. These commercial materials can also be defined as 'interpenetrating phase composites',[3] due to their microstructure and preparation procedure (i.e. silicon infiltration), even though the high SiC content could have broken down the interconnectivity of the silicon phase. As, in general, very different features are reported for Si–SiC materials which have quite similar chemical composition, it will be shown that, as expected, the microstructure has a strong influence on the fracture properties; at the same time however, it does not affect the elastic properties, which follow the two-phase models. In particular, the high SiC content ER RS composites are characterized by the highest value of fracture toughness reported to date for this class of materials. In a previous study,[6] it was proposed that such a feature could be attributed to the different crystalline phases (α- and β-SiC). Now, further microstructural

*Present address: JRC, Ispra (VA), Italy.

investigations, with particular SEM operating conditions, allow us to consider the observed fracture toughness values as primarily being due to other microstructural features.

2 Experimental

A group of RS Si–SiC composites (ER RS-1...8) was prepared in the Eniricerche laboratories. Their properties were analysed and compared with those of three Si–SiC composites: two commercial reaction-bonded materials (rectangular plates, Sigri* 5 × 50 × 50 mm and Refel† type 5 × 50 × 150 mm), and one RS Si–SiC (Silcomp®, literature data only).

The ER RS Si–SiC composites were made by using silicon and carbon powders. The powders were prepared by ball-milling (agate jar) high purity feed-stock materials. Silicon was obtained from a single crystal electronic-grade ingot (B-doped, 1–10 ppma). The impurity content of carbon was of the order of 0·3 wt% (mainly Ca, Al, Fe oxides). After milling, the size distributions of silicon and carbon powders were both below 25 μm with average particle sizes of ~5 μm, as measured by laser scattering method. The SiC content in the final composite material was controlled by varying the relative amount of silicon and carbon powders. These powders were dry-ball mixed and die-pressed (200 MPa) to their final shape (i.e. plates 4 × 10 × 50 mm). The reaction sintering was carried out under vacuum ($\leq 10^{-2}$ Pa), at temperatures higher than the silicon melting point (1450–1700°C). The resulting sponge-like SiC structure was filled with a suitable amount of liquid silicon. The cooling cycle was performed in order to control the volume expansion of silicon (~9%) during solidification. The sintered components did not show any shrinkage for high SiC content (>50 vol%), according to published data on similar materials.[1,4] SIMS–AES analyses[7] on the sintered ER RS Si–SiC materials show ~0·2 at% of Al, due to a contamination from the furnace.

To evaluate phase composition and texture, X-ray powder diffraction was carried out using Cu K_α radiation and a graphite monochromator (Philips, APD 1700).

Microstructural analysis was performed using a Cambridge Stereoscan 360 scanning electron microscope, employing both the backscattering and the secondary mode. The instrument was equipped with a high brightness gun (LaB_6 cathode) and a solid-state backscattered electron detector having high collection efficiency and operating with beam energy ranging between 6 and 30 keV.

To obtain the crystallographic features of grains (down to ~0·5 μm), the electron channelling pattern (ECP) technique was used at low beam energy (6–8 keV).[8,9] ECP conditions were verified by observing the contrasting changes of the polished surface at different orientation angles, relative to the beam, according to the literature.[10]

The volume fractions of each phase (Si, SiC, C and porosity) were determined using image analysis (IA) by sampling at least 50 random regions on samples polished down to 1 μm diamond paste, at 1000× magnification corresponding to an area of 100 × 150 μm. Measurements were taken with a metallographic optical microscope connected to a Quantimet 970. IA was used in order to determine the size distribution of the minority phase regions. Density was obtained by the Archimedes' method according to ASTM C693-84.[11]

Young's modulus was measured by an improved flexural resonance method, described elsewhere,[12,13] based on electrostatic excitation and a laser modulation technique for detecting vibration amplitude. Three different compositions of ER RS Si–SiC (30, 50, 70 vol% SiC) were prepared to select the most appropriate two-phase model, which was used to calculate all Young's modulus values necessary to evaluate the fracture energy γ. Due to the sample thickness (4 × 10 × 50 mm), its effect on the shear modulus was corrected following the ASTM suggestions;[14] three polycrystalline silicon samples, with different thicknesses, were measured in order to check the effectiveness of Pickett's correction term.[15] The reproducibility of the method of Young's modulus determination was of the order of 0·01%; the absolute accuracy was limited by the accuracy of the dimensional measurements. By using adequate machining and measuring procedures, an absolute accuracy better than 1% was obtained.[12,13] In addition, sound velocities (longitudinal and transversal) of some selected samples (50 and 70 vol% SiC) were measured by using an automated cross-correlation method.[16] Ultrasonic measurements were carried out with a buffer rod, while the centre frequencies of the transducers were 10 and 5 MHz for longitudinal and transversal velocity, respectively. The time-domain cross-correlation function of the selected echoes allows the time-of-flight measurements with an uncertainty of ±2 ns. Young's modulus and Poisson's ratio were calculated by the equations reported elsewhere.[16] The ultrasonic data agreed quite well with those measured by flexural resonance on the same samples (Table 2), whereas our values, measured with both methods on commercial RB Si–SiC,

*Silit-SK 308, trade mark for Sigri Elektrographit GmbH, was purchased by 'Elettrocarbonium', Milano, Italy.
†Refel RB Si–SiC, trade mark for UKAEA material, was purchased by TenMat Ltd, Manchester, UK.

were slightly lower in the case of Refel and higher in the case of Sigri (Table 2), than those reported in the literature.[4,5,17–19]

For mechanical testing, samples were machined in order to obtain test-bars (4 × 4 × 40 mm). The surface in tension was polished down to 9 μm grit and the edges were rounded to avoid stress concentration. Three-point flexural strength was measured over a 35 mm span using an Instron 1195 universal testing machine with a crosshead speed of 0·5 mm min^{-1}.

Fracture toughness values were obtained by the single edge notched beam (SENB) technique. The samples (4 × 4 × 20 mm) were carefully notched with a 0·10 mm diamond saw down to one-third of their thickness. They were then broken in three-point bending over a 16 mm span with a crosshead speed of 0·5 mm min^{-1}. The agreement between our experimental values for Sigri and Refel and those previously reported in the literature[5,17–19] on commercial Si–SiC composites was quite good.

The density and Young's modulus values represent the average of at least three samples. Toughness data were averaged on four specimens while, for strength determinations, more than six test-bars were used for each point. Matrix properties were measured on commercial polycrystalline silicon (purchased from Dynamit Nobel Silicon).

3 Results and Discussion

3.1 Microstructure

X-ray diffraction analyses of RB Si–SiC show, as reported in the literature,[20] the presence of the different α (hexagonal) and β (cubic) SiC polytypes, with some texturing effect. The exothermicity of the reaction between silicon and carbon results in a large increase in temperature. A local temperature rise in excess of 400°C, in addition to the operating temperature (1600–1700°C), has been reported for Refel RB Si–SiC.[4] Since, in the RS process, silicon and carbon powders are not diluted by the presence of α-SiC particles, the reaction front temperature is expected to be higher than in the corresponding RB case, approaching the self-propagating reaction regime.[21] In this case, a temperature higher than 2000°C should be attained. As a result, a fraction of an α polytype was expected in the RS composites, as reported in the literature for similar experimental conditions.[22] By contrast, we have observed only the β-SiC polytype in our RS material.

For the two commercial RB composites, quite different microstructures were observed. Refel material shows an enhanced bimodal SiC grain size distribution and exhibits silicon regions with an average diameter of ~11 μm [Figs 1(a) and (b)]. In agreement with the literature data,[20] metallic inclusions (Al, Fe, Ni) and some residual carbon were also observed.[7] Sigri material [Figs 2(a) and (b)] shows much coarser SiC grain size and less enhanced bimodal distribution. Larger silicon regions, with an average diameter of ~17 μm, and metallic inclusions (mainly Al) were also found.

Typical microstructures of ER RS composites show polycrystalline continuous SiC and Si phases belonging to the interpenetrating-type class, that, according to Schulz,[23] can be described as being formed by infinitely long cylinders. ER RS materials exhibit two different morphologies at low (<60 vol%) and high (>70 vol%) SiC content. At low concentrations, large textured silicon regions are found and the SiC polycrystalline regions (Fig. 3) have an average diameter that ranges from 10 to 18 μm as the SiC content varies from 50 to 35 vol% (Figs 4 and 5) respectively. At high SiC concentration, large silicon carbide regions are found, with average silicon domains of ~11 μm [Figs 6(a) and (b)], and some residual carbon. The SiC microstructure maintains the sponge-like polycrystalline morphology, with reduced crystalline domains size

(a)

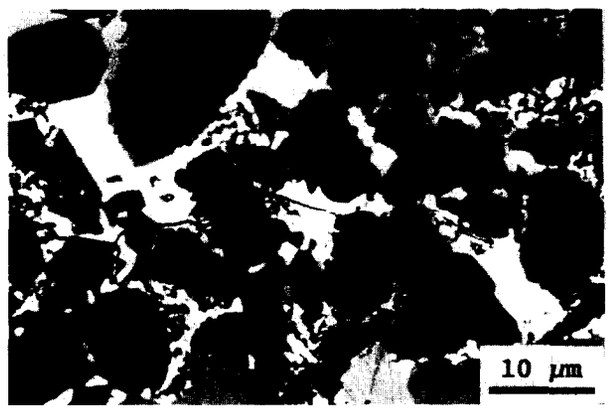

(b)

Fig. 1. (a) Backscattered SEM micrographs of commercial RB Si–SiC composites (Refel material); nearly transgranular fracture is observed. Silicon (grey regions), silicon carbide (89 vol%) (dark regions), carbon (black regions), metallic inclusions (white regions); phase morphology is similar to those reported in the literature.[20] (b) As (a) but using ECP technique.

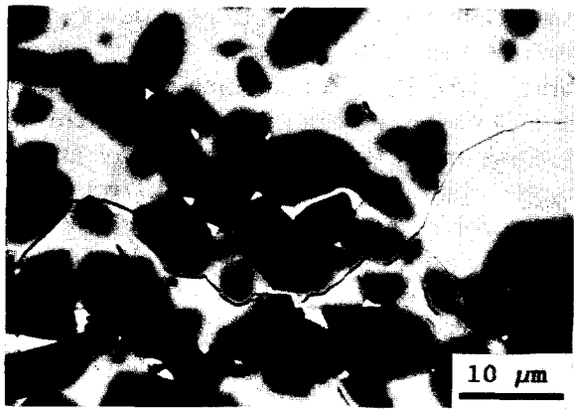

(a)

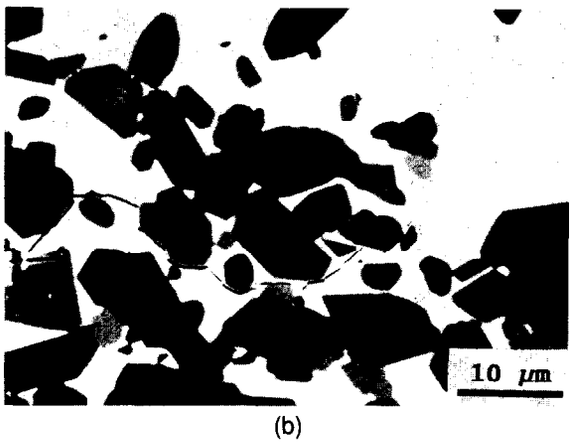

(b)

Fig. 2. (a) Backscattered SEM micrographs of commercial RB Si–SiC composites (Sigri): silicon carbide (82 vol%). Crack deflection is evidently operating. (b) As (a) but using ECP conditions.

Fig. 3. Backscattered SEM ECP micrograph of ER RS Si–SiC composites: silicon and polycrystalline silicon carbide (35 vol%). SiC grain exhibits different orientations.

(Fig. 7) containing a high density of twins. SiC grains did not show crystallographic texture effects.

The total amount of residual unreacted carbon and porosity (V_{ext}), measured by using IA, was generally less than 0·5 vol% (Table 1); these values were lower than those reported in the literature for the Silcomp® material.[24] The SiC volume fraction values used for the analysis of material properties were calculated using the 'rule of mixtures' and the experimental density data as measured by Archimedes' method, considering 2·33 and 3·21 g cm^{-3}

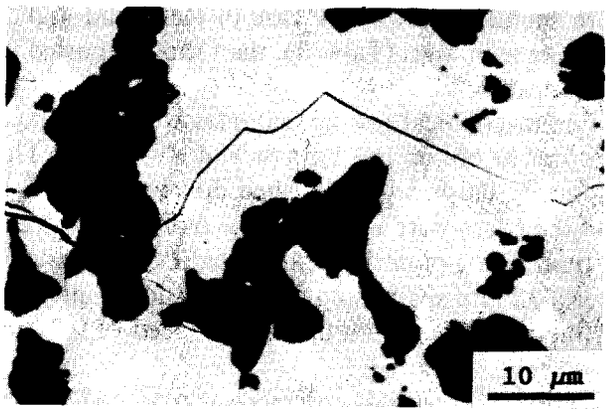

Fig. 4. Backscattered SEM micrograph of ER RS Si–SiC composites; polycrystalline silicon carbide (35 vol%). Crack moves mainly in silicon region and is deflected by SiC grains.

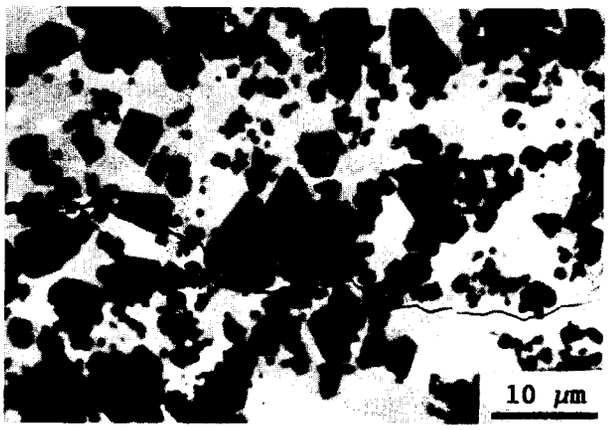

Fig. 5. Backscattered SEM micrographs of ER RS Si–SiC composites; polycrystalline silicon carbide (50 vol%). Also, at this SiC content, the crack moves mainly in the silicon region and is deflected by SiC grains.

as the density of Si and SiC respectively. The comparison between density data and density values, calculated using the same procedure, and the volume fractions obtained by IA, leads to reasonable agreement due to the low values of unreacted carbon and porosity (Table 1 and Fig. 8).

3.2 Elastic properties

The experimental data obtained on Si–SiC materials were compared with the values obtained from the composite theory. Among the different two-phase models available in the literature, the near fully dense Si–SiC composites follow quite well the absolute bounds models as already reported.[12,25] In particular, because more stringent hypotheses about the microstructure of the composite could be formulated, such as an isotropic and quasi-homogeneous distribution of phases, a more accurate model having narrower limits may be applicable: the Hashin–Shtrikman (HS) model.[26] Homogeneous phase distributions were observed for all Si–SiC composites. In this case the HS model could be applied once the elastic properties of the phases were known. The theoretical upper limits

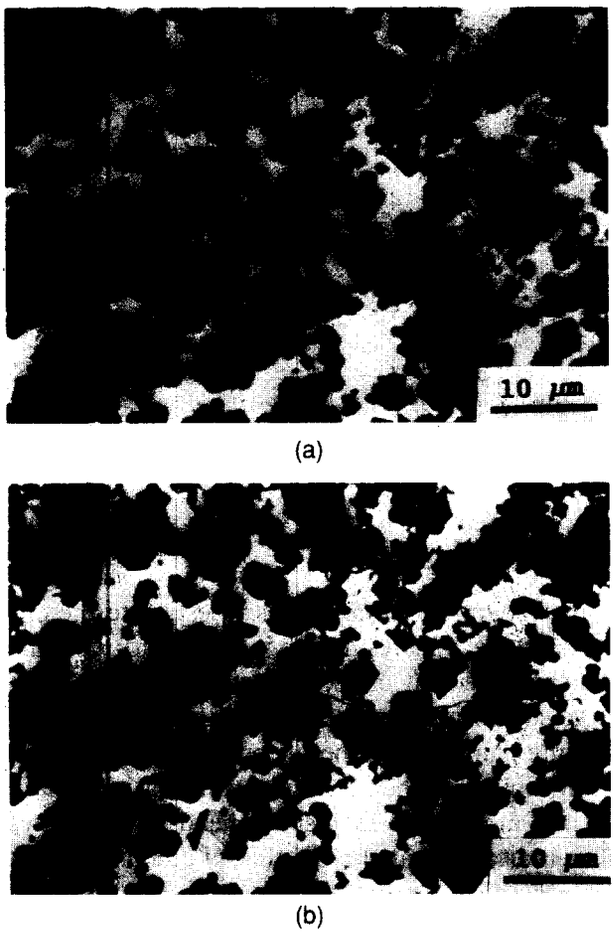

Fig. 6. (a) Backscattered SEM micrographs of ER RS Si–SiC composites: sponge-like polycrystalline SiC morphology (70 vol%) (dark regions); residual carbon (black regions). The crack passes mainly in the polycrystalline SiC regions. (b) As (a) but using ECP technique.

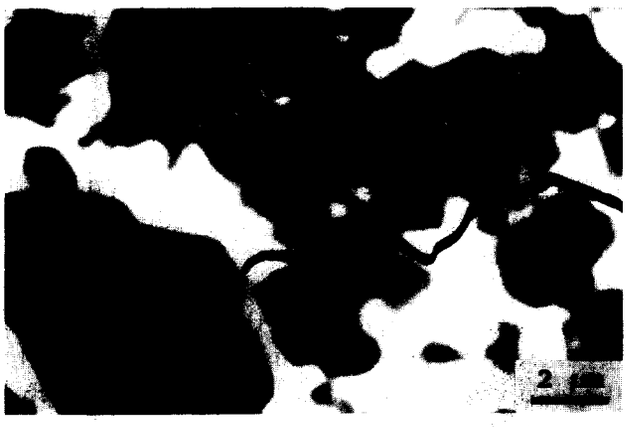

Fig. 7. SEM backscattered ECP micrograph at high magnification of ER RS Si-SiC composite: the crack is also deflected inside the SiC grain (dark region) according to its polycrystalline structure.

for bulk (K_u) and shear moduli (G_u) can be calculated by the following relationships:[26]

$$K_u = K_2 + \frac{V_1}{1/(K_1 - K_2) + 3V_2/(3K_2 + 4G_2)} \quad (1)$$

$$G_u = G_2 + \frac{V_1}{1/(G_1 - G_2) + 6V_2\,(K_2 + G_2)/5G_2(3K_2 + 4G_2)} \quad (2)$$

where V, K and G are volume fraction, bulk modulus and shear modulus, respectively, and the subscripts 1 and 2 refer to Si and SiC phases, respectively. The lower limits (K_1, G_1) are obtained from the previous equations by interchanging the indices 1 and 2.

In order to compare our experimental data with the predicted elastic properties, the upper bounds to Young's modulus (E_u) and Poisson's ratio (ν_u) were calculated by the following relationships:

$$E_u = 9K_uG_u/(3K_u + G_u) \quad \nu_u = (3K_u - 2G_u)/(6K_u + 2G_u) \quad (3)$$

The lower limits (E_1, ν_1) were calculated by interchanging the indices u with 1.

Due to the availability of high-quality large silicon single crystals, very accurate values of the elastic constants, measured by acoustical methods, are reported in the literature.[27] By using these data, in addition to the averaging procedure due to Voigt, Reuss and Hill,[25] the calculated Young's modulus of silicon (E_{ref} in Table 2) was 164 GPa. The calculated average Poisson's ratio, obtained by using the same procedure, was 0·22. Our experimental results on reference samples of polycrystalline silicon are in quite reasonable agreement (168 ± 2 GPa).

Reliable data for elastic constants of SiC single crystals are lacking due to the difficulties in obtaining single crystals large enough to perform accurate acoustic measurements.[28,29] Therefore the elastic properties of polycrystalline β-SiC were derived by using a non-linear least-squares analysis of the whole set of our experimental values. The result was E_{ref} = 432 GPa (Fig. 9). This value is one of the few data reported to date on polycrystalline β-SiC, and can be compared only with the results of theoretical calculations, e.g. 496 GPa[29] or 402 GPa.[30] The experimental values reported in the literature are measured either on whiskers or on α-SiC polytypic, polycrystalline ceramic samples, resulting in 436 GPa[31] and 448 GPa,[23] respectively.

By using these values (168 and 432 GPa for Si and SiC phases, respectively) the commercial RB Si–SiC composites can also be fitted to the same theoretical model, even though there is a mixture of α–SiC and β–SiC polytypes.

3.3 Mechanical properties

As mentioned above, Figs 11 and 12 illustrate the complex behaviour of fracture toughness and strength as a function of SiC content. Two different regions are clearly identifiable, below and above the value of about 65 ± 5 vol% SiC, which is inferred from our experimental points that are at 59 and 69 vol% SiC. The value 65 ± 5 vol% SiC could be regarded as a sort of percolation threshold for silicon in the SiC matrix.

Table 1. Microstructural characteristics of Si–SiC composites. ρ_{calcul} represents the bulk density as measured by using image analysis data

Sample	*Grain size* (μm)	ρ_{exp} ($g\ cm^{-3}$)	V_{SiC} (*vol%*)	V_{Si} (*vol%*)	V_{ext} (*vol%*)	ρ_{calcul} ($g\ cm^{-3}$)
Poly-Si	100	2·33	0	100	0	2·33
Sigri	17[a]	3·051	82·4	17·4	0·2	3·050
Refel	11[a]	3·110	84·6	15·3	0·1	3·072
ER RS-1	n.m.	2·612	32·8	67	0·2	2·614
ER RS-2	18[b]	2·642	35·4	64·4	0·2	2·637
ER RS-3	n.m.	2·674	37·2	62·5	0·3	2·650
ER RS-4	n.m.	2·735	46·5	53	0·5	2·728
ER RS-5	10[b]	2·779	51·4	48·4	0·2	2·778
ER RS-6	n.m.	2·845	59·1	40·7	0·2	2·845
ER RS-7	11[a]	2·923	68·9	30·6	0·5	2·925
ER RS-8	n.m.	3·101	87	12	1·0	3·072

[a]Silicon region.
[b]Silicon carbide regions.
n.m.: not measured.

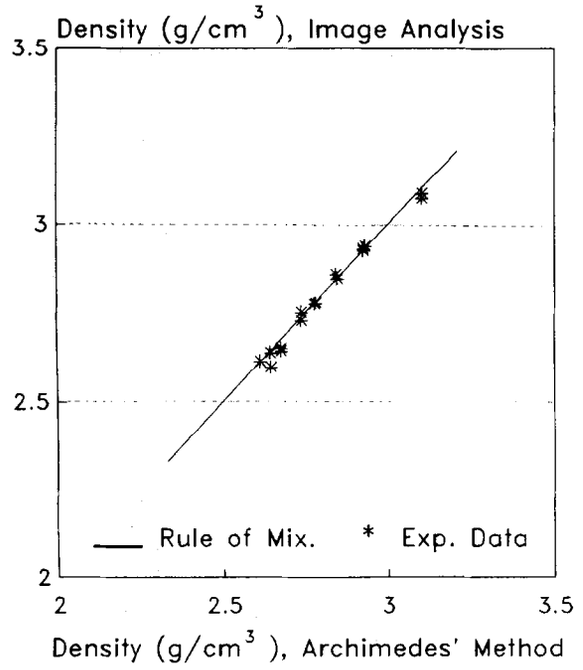

Fig. 8. Experimental values of density measured by the Archimedes' method (*x*-axis) vs. values obtained by image analysis (*y*-axis).

For SiC content between 0 and 60 vol%, the ER RS Si–SiC composites behave like the particulate composites described in the literature by Faber and Evans (FE):[33] the toughness increases rapidly at the first introduction of the reinforcement, and slowly thereafter (Fig. 11). At low SiC content, the fracture toughness values of ER RS material agree quite well with those reported for Silcomp® (longitudinal direction[24]) even though the two RS composites, which contain β-SiC crystals in both cases, have quite different morphologies: Silcomp® exhibits longitudinally aligned grains up to 50 μm in size[24] and the ER composite has a sponge-like microstructure with 2 μm grains.

To identify toughness mechanisms, stable cracks were produced by indentation (Knoop indenter, with a load of 20 N) of the polished surfaces of both RB and RS composites to estimate the crack front profile. Figures 4 and 5, relative to RS materials, show evident crack deflection examples inside large silicon regions. Apart from hypothetical weak fracture planes inside the silicon region, this phenomenon happens when a crack, running in a matrix, finds a more rigid inclusion ahead and deviates.[34] This indicates that the FE theory could be applied. To utilize FE results, the shape of the reinforcing phase has to be determined. Due to the interpenetrating-type microstructure, the second phase can be described as being formed by infinitely long cylinders; therefore the aspect ratio value is taken as equal to 12.[33] For these concentrations the experimental values of fracture toughness, K_{exp}, were compared with those calculated according to FE theory:

$$K_{th} = A\,(2\gamma_{Si}E_c)^{1/2} \qquad (4)$$

where A, which depends on the aspect ratio of the second phase, was assumed to be equal to 2;[33] γ_{Si} is the silicon matrix fracture energy (2.7 J m^{-2}, Ref. 35); and E_c is the Young's modulus of the composite calculated using the HS model, which fits our experimental results. Table 3 shows that the agreement can be considered very satisfactory and could justify a posteriori the assumed crack-deflection toughening mechanism for these composites at low SiC content.

In the neighbourhood of 65 vol% SiC, an abrupt change in fracture toughness of the ER RS composites is observed. A possible explanation could be attributed to the fact that at this SiC content the interconnectivity of the silicon region may have broken down to give discrete silicon particles[3] which act mainly as defects. This fact is consistent with the different behaviour of the other RS composite (Silcomp®), which is reinforced with fibres. Concerning RB commercial materials, we did not find any data about composites with low SiC

Table 2. Elastic properties of Si–SiC composites obtained by using different techniques (ultrasonic and resonance methods). Numbers within brackets represent the experimental errors

Specimen	*Thickness (mm)*	V_{SiC} *(vol%)*	E_{reson} *(GPa)*	E_{ultras} *(GPa)*	ν	E_{ref} *(GPa)*
Poly-Si-1	2·06	0	168 (2)			164[e]
Poly-Si-2	3·01	0	168 (2)			164[e]
Poly-Si-3	3·48	0	167 (2)			164[e]
Sigri	3·98	82[a]	375 (4)	371 (3)	0·17	375[e]
Sigri		82[b]				310[b]
Refel	3·97	89[a]	382 (4)	387 (3)	0·17	386[e]
Refel		90[c]				409[c]
ER RS-2		35[a]	234 (4)			230[e]
ER RS-5		51[a]	258 (2)	260 (3)	0·20	260[e]
ER RS-7		68[a]	322 (4)	323 (3)	0·19	320[e]
Silcomp-1		20–25[d]				200[d]
Silcomp-2		40–45[d]				303[d]
Silcomp-3		80–85[d]				350[d]

[a]Averaged on four samples.
[b]Literature data.[5]
[c]Literature data.[18,19]
[d]Literature data.[24]
[e]Calculated from theory.

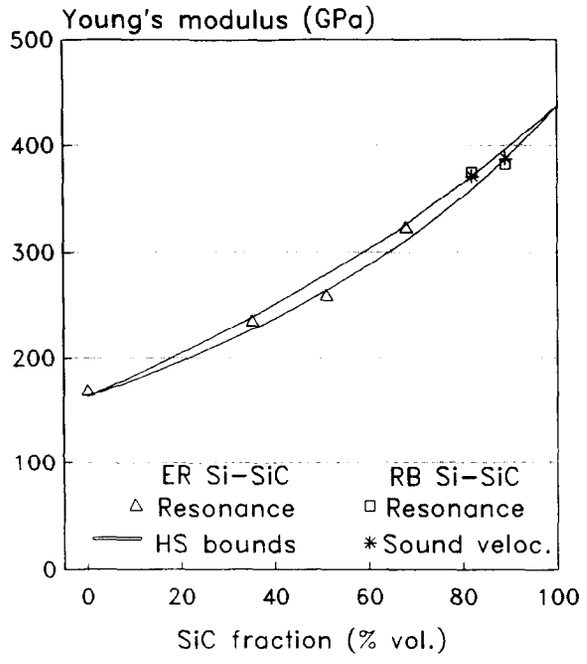

Fig. 9. Experimental values of Young's modulus vs. SiC volume fraction. Solid lines represent the Hashin–Shtrikman bounds.

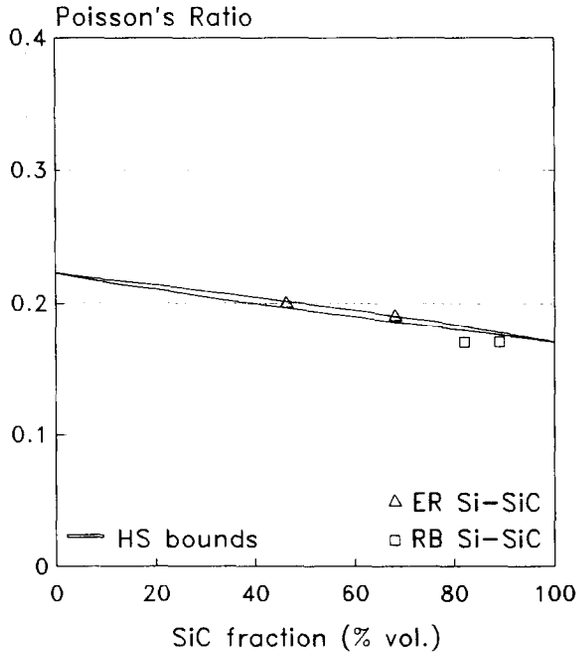

Fig. 10. Experimental values of Poisson's ratio vs. SiC volume fraction. Solid lines represent the Hashin–Shtrikman bounds.

content; some Refel materials were studied as a function of composition[19] but the SiC content was in the range 75–95 vol%, well above the supposed percolation threshold of silicon. From this point of view, the properties of RB commercial materials should be compared with those of the RS composites in the range >65 vol% SiC.

At SiC content >65 vol%, the two composites (ER RS-7 and ER RS-8) show a slight increase in fracture toughness which probably is associated with the similar increase in Young's modulus. The comparison between the RB and RS composites, at similar SiC volume fraction, shows a much tougher behaviour of RS Si–SiC materials. In particular, the γ values of ER RS-7 and ER RS-8 composites, calculated from $\gamma = K_{IC}^2/(2E)$, are higher than the value of 30 J m^{-2} reported in the literature for SiC ceramics,[36] and are also considerably higher than the corresponding values calculated for the RB Si–SiC commercial materials which, for the Refel composite (Table 3), agree reasonably with those already published.[18,19]

It is reported in the literature that interpenetrating-phase composites could benefit from further toughening mechanisms such as crack-bridging,[3,37,38] therefore the load–displacement curves and the corresponding micrographs were carefully examined. In all the tests the load–displacement curves did not show any curvature before fracture, indicating no evidence of *R*-curve in these materials.[37,38] The

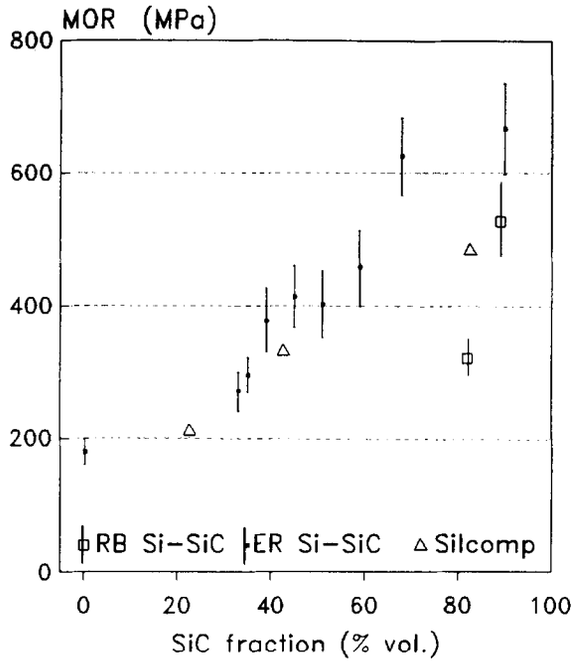

Fig. 11. Experimental values of flexural strength vs. SiC volume fraction.

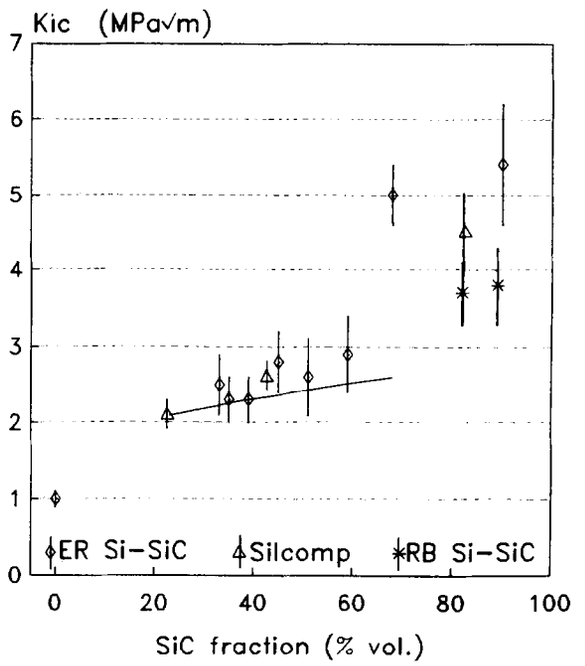

Fig. 12. Experimental values of fracture toughness by SENB method of different Si–SiC composites. Solid line shows the behaviour according to the Faber–Evans crack-deflection theory.

Table 3. Mechanical properties of Si–SiC composites. Numbers within brackets represent the experimental errors

Specimen	V_{SiC}[c] *(vol%)*	E_{calc}[d] *(GPa)*	ν_{calc}[d]	K_{IC} *(MPa m$^{1/2}$)*	K_{th}[e] *(MPa m$^{1/2}$)*	σ *(MPa)*	c *(μm)*	γ *(J m^{-2})*
Poly-Si	0	164	0·22	1·0 (0·1)	–	180 (20)	20	2·7
ER RS-1	33	226	0·20	2·5 (0·4)	2·2	270 (30)	56	13·0
ER RS-2	35	230	0·20	2·3 (0·3)	2·2	295 (27)	40	11·0
ER RS-3	39	239	0·20	2·3 (0·3)	2·3	378 (30)	24	10·0
ER RS-4	45	253	0·20	2·8 (0·4)	2·3	413 (46)	30	12·0
ER RS-5	51	268	0·19	2·6 (0·5)	2·4	402 (50)	27	12·0
ER RS-6	59	289	0·19	2·9 (0·5)	2·5	456 (56)	26	14·0
ER RS-7	68	316	0·18	5·0 (0·4)	–	625 (59)	42	38·0
ER RS-8	90	390	0·17	5·4 (0·8)	–	667 (69)	43	38·0
Sigri	82	–	–	3·7 (0·4)	–	320 (30)	87	18·0
Refel	89	–	–	3·8 (0·5)	–	525 (60)	34	19·0
Refel[a]	90	–	–	3·4	–	539	26	14·0
Silcomp-1[b]	20–25	–	–	2·1 (0·2)	–	210 (20)	65	11·0
Silcomp-2[b]	40–45	–	–	2·6 (0·2)	–	331 (20)	41	11·0
Silcomp-3[b]	80–85	–	–	4·5 (0·5)	–	483 (50)	57	29·0

[a]Literature data.[18]
[b]Literature data.[23]
[c]Averaged on eight samples.
[d]Calculated with the HS two-phase model.
[e]Calculated with the Faber–Evans model.

sudden load drop at fracture could also have been caused by too large a notch width but, as can be seen on the crack micrographs, behind the crack tip we did not find any indication of the main mechanism of *R*-curve in ceramics, i.e. crack bridging.[37] Moreover, the fracture toughness, as measured by SENB, is representative of the material as a whole and not of any specific individual phase: such fracture toughness values have to be considered relative to a crack that sees the microstructure around it as a homogeneous medium.

The overall fracture energy of these classes of composites can be described as the combination of two main mechanisms. The first one is related to the low/high fracture energy regions (i.e. Si and SiC and Si–SiC interface) intersected by the crack. The second one is the energy absorbed by any other toughening mechanism, such as crack deflection. Stable cracks, such as those introduced by indentation, have been reported to preferentially follow low energy paths in monolithic ceramics.[39–40] By the same principle, therefore, they should allow the features indicative of the crack propagation path between the different phases in our materials to be revealed. Moreover, by this technique, one should be able to ascertain

if the Si–SiC interface is the basic strength-controlling factor of these materials, as already reported.[20]

In the Sigri composite, the crack appears to move preferentially at Si–SiC interface or, at least, quite close to it (Fig. 2). In the Refel composite, the crack crosses both phases with a straighter path (Fig. 1); the crack follows the Si–SiC interface much less than in Sigri material, if at all. The single-crystal SiC grains appear to be cleaved. The similar experimental values of fracture toughness in both RB composites seem to indicate that the fracture of Si and SiC regions and crack deflection lead to the same balance for the overall fracture toughness of this type of composite.

In the ER RS composites, the crack profile crosses both phases and apparently in a way similar to that of Refel material [Figs 6(a) and (b)], with some occasional crack branching. Again, no evidence of a weak Si–SiC interface is found. But SEM micrographs of ER RS composites, at higher magnification (Fig.7) and in ECP conditions, show that the crack was also deflected inside the SiC grains, because of their polycrystalline structure. In a previous work[6] we proposed that such differences in surface energy were attributable mainly to the different amounts of the cubic and hexagonal crystalline SiC phases present in the RB and RS classes of composites. Now, more accurate SEM analyses enable us to attribute such differences to the quite different microstructures of the materials. In fact, the SiC regions intersected by the crack in the Refel composite [Fig. 1(a)] were mainly rounded single crystals, as detected by ECP [Fig. 1(b)], while in the ER composite complex-shaped polycrystalline SiC regions were observed [Fig. 6(b)]. The more complicated fracture process of polycrystals could account for the higher fracture energies calculated for RS composites than for RB commercial materials.[41] Unbroken SiC or Si grains were never observed behind the crack tip.

From all the facts presented above, we argue that the Si–SiC interface is not the determining factor for the fracture properties of this class of composite. If this were the case, it would not be possible to explain the decisive difference in fracture toughness between Sigri, Refel, Silcomp® and ER RS composites with nearly the same SiC content (see Table 3). Moreover, in the case of ER RS composites, if the Si–SiC interface were the controlling parameter then the γ values would have to remain almost constant for the entire compositional range investigated. The very large values of γ for SiC contents higher than 65 vol% and the fractographic evidence indicate that other microstructural features are responsible for the fracture properties.

The flexural strength of the ER composites shows the same trend as their fracture toughness, with an initial increase followed by a sort of plateau between 40 and 60 vol% SiC (Fig. 12). At lower SiC content (33–35 vol%) the strength values were slightly lower than those expected from toughness data. For SiC content higher than 65 vol%, the flexural strength jumps to higher values. In this region, as reported also for Refel material,[19] the flexural strength increases as silicon content decreases. On this subject, it is noteworthy that our experimental values on Refel material agree well with those reported in the literature over many years and from different sources, thus demonstrating the high reproducibility of the preparation procedure. At the maximum SiC content, the ER composite exhibits the highest values of flexural strength, followed by Refel, Silcomp® and Sigri, respectively.

The critical flaw size (c) of the composites was roughly estimated by $c = (YK_{IC}/\sigma)^2/\pi$, where Y is the shape factor, taken as 1·43 for a surface penny-shaped crack,[42] and K_{IC} is the experimental value measured by the SENB technique. It is very likely that in these materials, at the very first loading, the crack tends to grow inside the silicon regions, which have lower toughness, and then spreads catastrophically into the rest of the material. By using the macroscopic K_{IC}, we intended to estimate the critical flaw size just before the sudden failure. From Table 3, one can see that the critical flaw size is almost the same for ER, Refel and Silcomp®, while Sigri shows larger calculated values. The critical flaw size of ER composites ranges between 24 and 56 μm for all the composition ratios. For the composites with high SiC content, these dimensions match reasonably with the silicon regions present in the microstructure. Some fractographic investigations on broken test-bars indicated silicon-rich regions as effective fracture origins. Nevertheless, by considering the wide range of SiC contents investigated, there seems to be only a minor influence on the second phase on this parameter (see Table 3).

4 Conclusions

Si–SiC composites are statistically homogeneous and isotropic materials that do not show interface effects, so that they can be adequately described by the Hashin–Shtrikman two-phase model when 432 GPa is assumed as the Young's modulus of the cubic SiC phase. In the ER RS composites, crack deflection appears to be the dominant fracture toughening mechanism for SiC content up to 65 ± 5 vol%, if rod-shaped particles with high aspect

ratio are assumed as the reinforcing phase. In Sigri material this mechanism still seems to be evident, even though a larger SiC content is present. At high SiC concentration (>65 ± 5 vol%) the fracture toughness of RS composites is higher (especially for the ER composites) than that of corresponding RB materials. It is proposed that such behaviour depends upon SiC phase morphology (polycrystalline grains) in RS Si–SiC. Silicon–silicon carbide interface does not seem to be the determining factor for the mechanical properties.

Acknowledgements

This work was partially supported by the 'Progetto finalizzato Materiali Speciali per Tecnologie Avanzate' of the Consiglio Nazionale delle Ricerche. The authors are grateful to F. Petrucci, V. Adoncecchi and G. Di Passa for their valuable technical assistance, S. Loreti for X-ray diffraction analyses and P. Alessandrini for scanning electron micrographs. We also thank H. Willems and W. Arnold (Fraunhofer Institut for Nondestructive Testing, Saarbrucken, Germany), for fruitful scientific discussion on ultrasonic characterization techniques.

References

1. Hillig, W. B., Mehan, R. L., Morelock, C. R., De Carlo, V. J. & Laskow, W., Silicon/silicon carbide composites. *Am. Ceram. Soc. Bull.*, **54**[12] (1975) 1054–6.
2. Scafè, E., De Rese, L., Petrucci, F., De Portu, G. & Guicciardi, S., Mechanical properties of reaction sintered Si–SiC composites. In *Advanced Structural Inorganic Composites*. ed. P. Vincenzini. Elsevier Science Publishers B.V., Amsterdam, 1991, pp. 269–75.
3. Clarke, D. R., Interpenetrating phase composites. *J. Am. Ceram. Soc.*, **75**[4] (1992) 739–59.
4. Forrest, C. W., Kennedy, P. & Shennan, J. V., The fabrication and properties of self-bonded silicon carbide bodies. In *Special Ceramics*, Vol. 5, ed P. Popper. British Ceramic Research Association, Stoke-on-Trent, 1972, pp. 99–123.
5. Richter, H., Kleer, G., Herder, W. & Röttebacher, R., Comparative study of the strength properties of slip-cast and of extruded silicon-infiltrated SiC. *Mater. Sci. Eng.*, **71** (1985) 203–8.
6. Scafè, E., Giunta, G., Di Rese, L., Petrucci, F., De Portu, G. & Guicciardi, S., Toughening mechanisms in Si–SiC composites. In *Euro-Ceramics II*, Vol. 2, Structural Ceramics and Composites, ed. G. Ziegler and H. Hausner. Deutsche Keramische Gesellschaft e.V., 1991, pp. 1715–20.
7. Scafè, E., Grillo, G., Fabbri, L. & Vittori, V., SIMS–AUGER and thermal conductivity characterization of Si–SiC materials. *Ceram. Eng. Sci. Proc.*, **13**[9–10] (1992) 918–28.
8. Parretta, A., Camanzi, A., Giunta, G. & Mazzarano, A., Morphological aspects of silicon carbide chemically vapour-deposited on graphite. *J. Mater. Sci.*, **26**, (1991) 6057–62.
9. Joy, D. C., Electron channelling patterns. In *Advanced Techniques for Microstructural Characterization*, ed. R. Krishnan, T. R. Anantharaman, C. S. Pande & O. P. Arora. Trans Tech Publications, Switzerland, (1988), Vol. 16, pp. 81–94.
10. Camanzi, A., Giunta, G., Parretta, A. & Vittori, M., Characterization of ceramic coating by channelling effects in scanning electron microscopy. In *Inst. Phys. Conf. Ser. 93*, Vol. 2, ed. P. J. Goodhew & H. G. Dickinson. Institute of Physics, Bristol, 1988, pp. 525–6.
11. Standard test method for density of glass by buoyancy. *ASTM C693-84*, American Society for Testing and Materials, Philadelphia, PA, 1984.
12. Scafè, E., Di Rese, L., Grillo, G. & Petrucci, F., Young's modulus of Si–SiC two-phase particulate composites. In *Advanced Structural Inorganic Composites*, ed. P. Vincenzini. Elsevier Science Publishers B.V., Amsterdam, 1991, pp. 309–15.
13. Scafè, E., Fabbri, L., Grillo, G. & Di Rese, L., Improved technique for Young's modulus determination by flexural resonance. *Ceram. Eng. Sci. Proc.*, **13**[9–10] (1992) 1094–102.
14. Standard test method for Young's modulus, shear modulus, and Poisson's ratio for ceramic whitewares by resonance. *ASTM C848-78, reapproved 1983*, American Society for Testing and Materials, Philadelphia, PA.
15. Pickett, G., Equations for computing elastic constants from flexural and torsional resonant frequencies of vibration of prisms and cylinders. *Proc. Am. Soc. Testing Mater. ASTEA*, **45** (1945), 846–65.
16. Panakkal, J. P., Willems, H. & Arnold, W., Nondestructive evaluation of elastic parameters of sintered iron powder compacts. *J. Mater. Sci.*, **25** (1990) 1397–402.
17. Sigri Elecktrographit GmbH, Technical notes 834 01 20. Germany.
18. McLaren, J. R., Tappin, G. & Davidge, R. W., The relationship between temperature and environment, texture and strength of self-bonded silicon carbide. *Proc. Br. Ceram. Soc.*, **20** (1972) 259–74.
19. Kennedy, P., Effect of microstructural features on the mechanical properties of REFEL self bonded silicon carbide. In *Non-oxide Technical and Engineering Ceramics*, ed. S. Hampshire. Elsevier, Amsterdam, 1986, pp. 301–17.
20. Ness, J. N. & Page, T. F., Microstructural evolution in reaction-bonded silicon carbide. *J. Mater. Sci.*, **21** (1986) 1377–97.
21. Pampuch, R. & Stobierski, L., Solid combustion synthesis of refractory carbides: (a review). *Ceram. Int.*, **17** (1991) 69–77.
22. Yamado, O., Miyamoto, Y. & Koizumi, M., Self-propagating high-temperature synthesis of the SiC. *J. Mater. Res.*, **1**[2] (1986) 275–9.
23. Schulz, B., Thermal conductivity of porous and highly porous materials. *High Temperature–High Pressure*, **13** (1981) 649–60.
24. Mehan, R. L., Effect of SiC content and orientation on the properties of Si–SiC ceramic composites. *J. Mater. Sci.*, **13** (1978) 358–66.
25. Grimvall, G., Thermophysical properties of materials. In *Selected Topics in Solid State Physics*, Vol. XVIII. North-Holland, Amsterdam, 1986, p. 257.
26. Hashin, Z. & Shtrikman, S., A variational approach to the theory of the elastic behaviour of multiphase materials. *J. Mech. Phys. Solids*, **11** (1963) 127–40.
27. McSkimin, H. J. & Andreatch, P. Jr, Elastic moduli of silicon vs. hydrostatic pressure at 25·0 °C and −195·8°C. *J. Appl. Phys.*, **35** (1964) 2161–5.
28. Lambrecht, W. R. L., Segall, B., Methfessel, M. & van Schilfgaarde, M., Calculated elastic constants and deformation potential of cubic SiC. *Phys. Rev. B*, **44** (1991) 3685–94.
29. Fischer, E. S., Manghnani, M. H., Wang, J. F. & Routbort, J. L., Elastic properties of Al_2O_3 and Si_3N_4 matrix composites with SiC whisker reinforcement. *J. Am. Ceram. Soc.*, **75** (1992) 908–14.

Journal of the European Ceramic Society 16 (1996) 715–719

0955-2219(95)00205-7
0955-2219/96/$15.00

Thermal Shock Behaviour of Si_3N_4/SiC Composites

A. Kaiser, R. Vaßen & D. Stöver

Institut für Werkstoffe der Energietechnik Forschungszentrum Jülich GmbH KFA, 52425 Jülich, Germany

(Received 15 July 1995; revised version received 6 November 1995; accepted 13 November 1995)

Abstract

In the present study the thermal shock behaviour of Si_3N_4/SiC composites with and without Y_2O_3 as additive was investigated using the KFA electron beam test facility JUDITH at energy densities of up to 9 MJ m^{-2}, which is designed for disruption simulations of materials for the first wall of a fusion reactor. The influence of SiC content, microstructure, additive and density on thermal shock behaviour and mass loss is discussed. Composites with additive have a slightly higher mass loss rate, but show no catastrophical thermal shock behaviour as do the composites without additives. Samples with lower density in the system with additive revealed no visible difference in mass loss and fracture behaviour.

1 Introduction

Most investigations on the properties of Si_3N_4 concern optimization of the fracture toughness K_{IC} and bending strength, but Si_3N_4 also exhibits good corrosion resistance and thermal shock resistance. Si_3N_4 powder without additive can only be densified by hot-isostatic pressing (HIP) and the resulting dense specimens have good oxidation resistance because of the low amount of the silica grain-boundary phase.[1] But the microstructure consists of equiaxed grains and these samples therefore have relatively low values of K_{IC}. It is well known that using sintering agents leads to the self-reinforcement of Si_3N_4 during sintering via the formation of a needle-like structure, and fracture toughness is increased.[2] The oxidation resistance is more or less significantly reduced, depending on the additive system used, because of the higher amount of glassy phase.[1] It is therefore of interest to study the influence of additives as a secondary phase and microstructure (i.e. grain morphology) on the thermal shock behaviour. When SiC was added to the system Si_3N_4/additive the needle-like structure was changed and almost equiaxed grains appeared,[3] as is known for Si_3N_4/SiC without additives,[4] and thus the influence of additive on the thermal shock behaviour can be elucidated.

2 Experimental

2.1 Processing and sample characterization

Mixtures of α-Si_3N_4 (450 nm) with 10 and 20 wt% β-SiC (500 nm), both supplied by H. C. Starck Germany, or nanosized β-SiC (20 nm)[5] and 8 wt% Y_2O_3, also supplied by H. C. Starck, were used as starting materials. HIPing of these powders using quartz capsules at temperatures of 1750–1800°C for composites with Y_2O_3 and 1900°C for the Si_3N_4/SiC system and pressures of 200 MPa, respectively, resulted in compacts with densities >98% of theoretical density.[3,4]

The microstructure of Si_3N_4/SiC/Y_2O_3 revealed a bimodal grain size distribution of Si_3N_4 grains, with equiaxed micrometre-sized α- and β-Si_3N_4 grains (2–4 μm) surrounding larger needle-like β-Si_3N_4 grains. Aspect ratios up to 10 were found. The amount of equiaxed grains increased with higher SiC contents, because SiC particles suppressed the phase transformation of α- to β-Si_3N_4. Transmission electron micrographs of Si_3N_4/10% SiC/8% Y_2O_3 indicated that nanometre-sized SiC particles were uniformly dispersed in the Si_3N_4 matrix as well as along the grain boundaries. The majority of grain boundaries seemed to be free of any second phase. The additive was predominantly located as amorphous phase in triple points at the grain-boundary junctions. The grain boundary phase consisted of $Y_2O_3{\cdot}SiO_2$, $Y_2Si_2O_7$ and $Y_5N(SiO_4)_3$. These were formed by a reaction of Y_2O_3 and SiO_2 or Si_3N_4, with silica coming from the surfaces of Si_3N_4 and SiC.

Equiaxed Si_3N_4 grains with average grain sizes of 1·5 μm were found in the case of Si_3N_4/SiC composites. In the case of addition of nano-SiC, nanometre-sized SiC particles are believed also to be found inside Si_3N_4 grains as in the case of composites with Y_2O_3.

Vickers hardness H_v10 of Si_3N_4/SiC composites[4] increased from 15·5 to 18 GPa, and in the case of

composites with Y_2O_3[3] from 14 to 16 GPa, with increasing SiC content. Hardness was decreased by the addition of Y_2O_3 because of the glassy structure of the grain-boundary phase. Fracture toughness K_{Ic} of the composites, measured by the indentation technique, was nearly independent of SiC content. If Y_2O_3 was used as an additive fracture toughness increased from 3·5 to 6·5 MPa $m^{1/2}$. The grain boundaries are weakened by the additive and the appearance of crack deflection is intensified.

2.2 Thermal shock tests

Thermal shock tests were performed with electron beam loadings in the JUDITH facility with energy densities of 2·3, 4·5 and 9·1 MJ m^{-2} and pulse duration of 3 ms. The acceleration voltage was 120 kV and the size of the scanned beam was 3 × 3 mm^2. Mass loss decreases strongly after the first pulse and after 5 pulses is nearly constant. Therefore 10 pulses were applied and the averaged mass loss per pulse was determined. Specimens had a diameter of about 8 mm and a height of 4 mm. During thermal shock at the JUDITH facility the surface is heated to temperatures close to 3000°C[6] and thermal stresses arise.

A model to calculate the erosion rates of weight loss is presented in Refs 6 and 7, and is very briefly described here. This model is based on the equivalence of the different energy density currents, i.e. the incoming energy density j_Q is compensated by several outgoing energy density currents:

$$j_Q = j_{sub} + j_{rad} + j_\lambda + j_{cp} + j_m \qquad (1)$$

with j_{sub} and j_{rad} as the energy density currents due to sublimation and radiation from the surface. j_λ describes the heat current into the sample by thermal conductivity. The electrons penetrate into the solid and heat up a surface layer with a given heat capacity c_p. This energy current is described by j_{cp}. During the heating phase the erosion rate dm/dt is determined by the sublimation term j_{sub}. After reaching a critical temperature, which corresponds to the maximum compression stress the sample is able to sustain,[7] the heating rate is set equal to zero and the energy balance is now achieved by an additional term, j_m. This term, $j_m = c_p \rho T\, dm/dt$ with ρ the density of the sample and T the temperature, decribes the energy required to heat up the cooler parts of the sample after erosion of hot surface elements. Creep can be introduced into the model by simply reducing the thermal expansion by the integrated creep rate. Reduction of surface stress by creep reduces particle erosion (j_m) and increases surface temperature. This leads to an increase of the sublimation rate and a reduced erosion rate, because sublimation consumes more energy than the mechanism described by j_m.

This model will serve as an aid to explain the effects of decomposition temperature, thermal conductivity and compression strength on the erosion rates, but can give no information about the thermal shock behaviour.

In the theory developed by Hasselmann *et al.*,[8] catastrophic crack propagation caused by thermal shock is reduced by maximizing the parameter

$$R'''' = NGE/\sigma_f^2 \qquad (2)$$

with N as the number of cracks nucleated during fracture, G as the fracture energy expended in creating unit area of new fracture surface, E as the Young's modulus and σ_f as the fracture stress. Using the equation of Griffith ($\sigma_f \approx K/\sqrt{a}$) and with the fracture energy $G \approx K^2/E$ gives

$$R'''' \approx a \qquad (3)$$

with a as the defect size. This parameter R'''' will serve to explain recent thermal shock behaviour.

3 Results and Discussion

3.1 Results

3.1.1 System without additive

In Table 1 results of JUDITH tests of the system Si_3N_4/SiC are summarized. No sample could bear the energy density of 9·1 MJ m^{-2}, even for one pulse. This high energy led to breakage of the samples into many small and larger pieces. Mass loss of these samples could not be determined because not all small parts of one broken sample, which were widely spread in the large vacuum chamber of the JUDITH facility, could be found after the experiment.

3.1.2 System with additive

Figure 1 shows the mass losses of Si_3N_4/SiC/Y_2O_3 systems for various energy densities, while Fig. 2 reveals the influence of density on mass losses of the same systems for various energy densities. At 2·3 MJ m^{-2} sometimes high values of mass losses

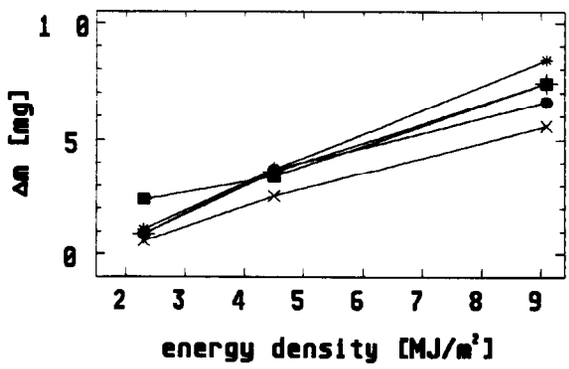

Fig. 1. Averaged mass losses after test in JUDITH facility of composites with 8 wt% Y_2O_3: X; Si_3N_4 (98·1%); ■, Si_3N_4/10% HCS-SiC (97·9%); ●, Si_3N_4/20% HCS-SiC (98·3%); +, Si_3N_4/10% nano-SiC (97·9%); *, Si_3N_4/20% nano-SiC (98·1%).

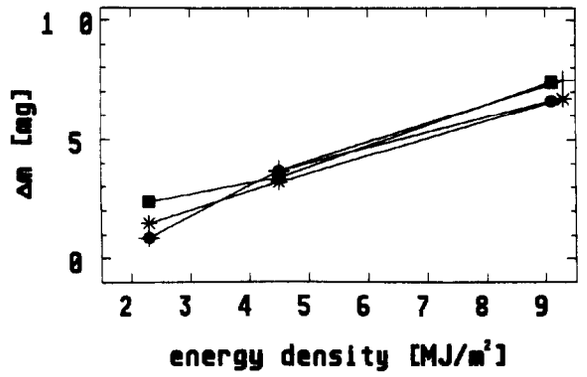

Fig. 2. Averaged mass losses after test in JUDITH facility of composites with 8 wt% Y_2O_3 and different densities: ■, Si_3N_4/10% HCS-SiC (97·9%); ●, Si_3N_4/20% HCS–SiC (98·3%); +, Si_3N_4/10% HCS-SiC (85·9%); *, Si_3N_4/20% HCS-SiC (93·8%).

were found (Figs 1 and 2: ■). This effect was attributed to breaking off of larger particles, which increased mass loss significantly especially at low averaged mass losses found at low energies.

3.2 Discussion

3.2.1 System without additive

Mass loss increased with increasing energy density in the system Si_3N_4/SiC (Table 1). At the energy density of 2·3 MJ m^{-2} all samples showed no difference in mass loss, whereas mass loss at an energy density of 4·5 MJ m^{-2} was decreased if SiC was added. The explanation of this effect is the higher decomposition temperature (j_{sub}) and higher thermal conductivity (j_λ) of SiC. This is also indicated by the lower mass loss rate of pure SiC[6] compared with pure Si_3N_4 of these results. Because of the energy balance higher terms of j_{sub} and j_λ lead to a lower term j_m, thus giving a lower erosion rate. Additionally, the higher compression strength of SiC compared with Si_3N_4 leads to a higher critical temperature (see section 2.2) and a longer time, when sublimation (j_{sub}) determines mass loss. Lower values of dm given by j_{sub} than by the term j_m (see section 2.2) result in a decrease of mass loss with higher compression strength.

Residual stress because of thermal mismatch between SiC and Si_3N_4 after sintering will lead to

Table 1. Averaged mass losses (mg) after 10 pulses in the JUDITH facility for the Si_3N_4/SiC-system (* indicates mass loss for one pulse)

	Energy (mJ m^{-2})	
System	*2·3*	*4·5*
Si_3N_4	1·1	5·1
Si_3N_4+10% HCS-SiC	0·9	3·1
Si_3N_4+20% HCS-SiC	1·1	2·0
Si_3N_4+10% nano-SiC	1·0	3·1
Si_3N_4+20% nano-SiC	—	<3·0*

Fig. 3. SEM micrograph of Si_3N_4/10 wt% nano-SiC after 2·3 MJ m^{-2}: the bar indicates 100 μm; ← beam direction.

an increased number of nucleation centres of thermal fracture and therefore to a higher crack density and additional energy absorption. Figure 3 shows a micrograph of the transition zone of the loaded region to the bulk Si_3N_4/10 wt% nano-SiC after a JUDITH test. In the system Si_3N_4/SiC cracks parallel to beam direction were found. These cracks were responsible for the catastrophic behaviour of this system. At higher energy densities the tensile thermal stress at the disc edge was too high and led to the growth of cracks through the samples and consequent breakage.

No visible influence of SiC content or SiC powder on the fracture behaviour was found, probably because of the small resolution of energy density. More experiments with energy densities between 4·5 and 9·1 MJ m^{-2} should give more information.

3.2.2 System with additive

In the system Si_3N_4/SiC/Y_2O_3 the addition of SiC led to an increase of mass loss (Fig. 1). No dependence of SiC content or type of SiC powder on mass loss could be found. Si_3N_4/Y_2O_3 has the most pronounced needle-like structure and no preferred direction of the elongated grains exists. The elongated grains improve the thermal conductivity[9] compared with an equiaxed structure, which has a higher amount of grain boundaries. This leads to a higher j_λ term and therefore a lower erosion rate, given by the term j_m, is reached. This overcompensates the positive effect of SiC on j_{sub} and j_λ and of higher compression strength on mass loss (see section 3.2.1). Figure 4 shows a micrograph of the transition of the loaded region to the bulk Si_3N_4/10 wt% nano-SiC/8 wt% Y_2O_3 after a JUDITH test. No cracks as they exist in the system Si_3N_4/SiC were found. In this system a small layer at the surface within the loaded region broke off the bulk. The high temperature during the JUDITH test leads to weakening of the grain-boundary

phase, especially in the case of samples with additives. Therefore small layers exist at the surface with weakened grain boundaries, while in the inner regions the temperature is lower than the melting point of the grain-boundary phase and interface strength is higher. Cracks are favoured to propagate in the direction of the weak grain boundaries parallel to the surface.

Assuming a similar distribution of defect size [eqn. (3)] in samples with and without additive, no improvement in thermal shock behaviour is reached. The positive effect of the grain-boundary phase Y_2O_3 to the thermal shock behaviour of Si_3N_4/SiC/additive is explained by the higher creep rate of samples with additive,[10] which decreases the thermal stress, and the lower Young's modulus of the grain-boundary phase as the second phase, leading to a high *E*/low *E* composite with improved thermal shock behaviour.[8,11] Also, the higher number *N* of nucleated cracks in Si_3N_4/SiC/Y_2O_3 samples has to be regarded. In the system with additive grain boundaries are weaker than without additive, especially at high temperatures. Therefore crack initiation is favoured and *N* is increased.

Samples with and without SiC were also tested at the highest possible energy density of 22·3 MJ m^{-2}. All samples survived. Therefore no statement about the influence of SiC on the fracture behaviour can be made.

Figure 2 shows the mass losses of Si_3N_4 with 10 and 20% HCS-SiC with Y_2O_3 for different densities (94 and 86%) and various energy densities. Mass loss increased with increasing energy density, but there were no significant differences found between dense and porous samples. In Ref. 12 even smaller mass losses were found for samples made of SiC/B_4C/C, if they had lower density (ρ = 75%). This effect is currently not understood, because it is difficult to describe the dependence of mass loss on microstructure, but it will be taken into consideration in the model. Pores in samples with lower density can be regarded as second phase with lower Young's modulus, leading to better thermal shock behaviour.[8] A higher density of pores increases the number *N* of nucleated cracks [eqn (2)]. Also, larger pores in porous samples increase R'''' [eqn (3)]. However, due to limitations of the test facility, energy density could not be further increased to reveal a different behaviour of dense and porous samples.

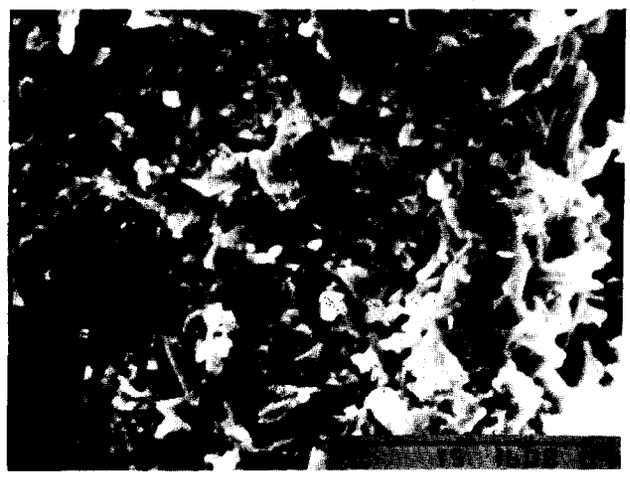

Fig. 4. SEM micrograph of Si_3N_4/10 wt% nano-SiC/8 wt% Y_2O_3 after 4·5 MJ m^{-2}: the bar indicates 10 μm; ← beam direction.

4 Summary

Si_3N_4/SiC composites with 10 and 20 wt% HCS- or nano-SiC with and without Y_2O_3 as additive were tested by the KFA electron beam test facility at energy densities of up to 9·1 MJ m^{-2}. The system Si_3N_4/SiC breaks catastrophically at energy densities of 9·1 MJ m^{-2}, while in the system with Y_2O_3 addition no such cracks were formed. The positive effect of Y_2O_3 on the thermal shock behaviour is explained by the effect of microstructure and high(Si_3N_4/SiC)/low(Y_2O_3) modulus composites. SiC decreases the mass loss in the system Si_3N_4/SiC and increases mass loss in the system Si_3N_4/SiC/Y_2O_3.

Acknowledgements

The authors thank Dr Förster, Institut für Laser und Plasmaphysik, Universität Düsseldorf, for producing the ultrafine SiC powder; Mr Coenen and Mr Gelissen, our Institute, for assisting this work and the other members of the Forschungszentrum Jülich who contributed to the present work; Dr Duwe and Mr Münstermann, Heiße Zellen (HZ), for performing the JUDITH tests; Mr. D'Orsaneo and his colleagues, Zentralabteilung Technologie (ZAT), for the preparation of quartz capsules.

References

1. Jacobson, N. S., Corrosion of silicon-based ceramics in combustion environments. *J Am. Ceram. Soc.*, **76** (1993) 3–28.
2. Wötting, G., Gugel, E., Schwier, G. & Lange, H., Processing for improved fracture toughness of dense silicon nitride. In *Ceramic Powder Science IV, Ceram. Trans. vol. 22*, ed. S. Hirano, G. L. Messing & H. Hausner. The American Ceramic Society, Inc., Westerville, OH, 1989, pp. 647–54.
3. Kaiser, A., Vaßen, R., Stöver, D., Buchkremer, H. P. & Kesternich, W., Composites of Si_3N_4 and nanosized SiC. To be published in *Silicates Industriels, Proceedings of Ceramic Ceramic Composites III*, Mons, October 1994.

4. Kaiser, A., Vaßen, R., Stöver, D., Buchkremer, H. P., Förster, J. & Uhlenbusch, J., Si_3N_4 SiC composites using conventional and nanosized powders. *Nanostructured Mater.*, **6** (1995) 917–20.
5. Förster, J., Hoesslin, M. v., Schäfer, J. H., Uhlenbusch, J. & Viöl, W., Optimization of CO_2 laser assisted synthesis of ultrafine silicon and silicon carbide powders. In *Proceedings of the 10th International Symposium on Plasma Chemistry*, Bochum, Germany, 1991, pp. 1–6.
6 Vaßen, R., Förster, J., Yehia, A., Hammelmann, K., Buchkremer, H.-P., Bolt, H. & Stöver, D., Development of low-Z materials for plasma facing, structural applications in fusion reactors. In *Proceedings of the 18th Symposium on Fusion Technology*, Karlsruhe, 1994, Elsevier Science BV, The Netherlands, pp. 259–62.
7. Vaßen, R., Kaiser, A. & Stöver, D., Potential of nanocrystalline low-Z materials for plasma facing, structural application in fusion reactors. To be published in *J. Nuclear Mater.*, 1995.
8. Hasselmann, D. P. H., Becher, P. F. & Mazdiyasni, K. S., Analysis of the resistance of high-E, low-E brittle composites to failure by thermal shock. *Z. für Werkstofftechnik*, **11** (1980) 82–92.
9. Ziegler, G., Thermal properties and thermal shock resistance of silicon nitride. In *Progress in Nitrogen Ceramics*, ed. F. L. Riley. Martinius Nijihoff Publisher, The Netherlands, 1983, pp. 565–88.
10. Hvidos, P. & Dusza, J., Deformation and fracture behaviour of two Si_3N_4 ceramics with different sintering additives. *Scripta Metall. Mater.*, **32** (1995) 1459–64.
11. Mazdiyasni, K. S. & Ruh, R., High/low modulus Si_3N_4–BN composite for improved electrical and thermal shock behaviour. *J. Am. Ceram. Soc.*, **64** (1981) 415–19.
12. Yehia, A., Vaßen, R., Duwe, R. & Stöver, D., Ceramic SiC/B_4C/TiC/C composites as plasma facing components for fusion reactors. To be published in *J. Nuclear Mater.*, 1995.

Journal of the European Ceramic Society 16 (1996) 721–737

0955-2219(95)00186-7
0955-2219/96/$15.00

Thermal Behavior of (Organosilicon) Polymer-Derived Ceramics. V: Main Facts and Trends

M. Monthioux & O. Delverdier

Centre d'Elaboration des Matériaux et d'Etudes Structurales, UPR A8011 CNRS, BP 4347, F31055 Toulouse Cedex, France

(Received 24 April 1995; revised version received 5 October 1995; accepted 12 October 1995)

Abstract

Extensive investigations of polymer-based ceramic materials taken within the Si–C–N–O–(H) system have been performed and previously published as Parts I – IV. This paper reports the main results, facts, trends and conclusions which can be drawn from them, regarding the physical and chemical behavior of these materials submitted to an increasing thermal treatment. Both similarities and discrepancies are described and explained, whatever the chemical composition of the ceramic, (i.e. containing Si–C or Si–C–N, Si–C–O, Si–C–N–O). Emphasis is made on the mechanisms, and the role of various parameters, either intrinsic (e.g. the role of compositional C, O, or N) or extrinsic (e.g. influence of the atmosphere), is examined. The overall results indicate, among others, that excess carbon (relative to the SiC stoichiometry) is always beneficial both to the structural stability of the ceramic and the mechanical properties (when measurable), while heteroatoms (O, N) are always finally detrimental. They thus sustain the current efforts to develop ceramic fibers from chemical systems as simple as possible, using oxygen-free curing processes. More generally, they provide guidelines for understanding, and somewhat predicting, the thermochemical behavior of any related materials.

A partir d'études approfondies de matériaux céramiques issus de polymères et appartenant au système Si–C–N–O–(H), dont les résultats ont été publiés au préalable (Parties I – IV), les principaux évènements chimiques et physiques intervenant durant un traitement thermique croissant sont rappelés. Les similitudes comme les différences sont décrites et expliquées, quelle que soit la composition des céramiques (c'est-à-dire contenant uniquement Si–C, ou Si–C–O, Si–C–N, Si–C–O–N–O). L'accent est mis sur les mécanismes, et le rôle des paramètres intrinsèques (par exemple présence des éléments O, N, ou C) ou extrinsèques (par exemple influence de l'atmosphère) est examiné. D' une manière générale, les résultats indiquent, entre autres, que du carbone en excès (par rapport à la stoechiométrie de SiC) est toujours bénéfique à la fois à la stabilité structurale du matériau et à sa tenue mécanique (quand celle-ci est mesurable), alors que la présence d'hétéroatomes (O, N) est toujours préjudiciable en finale. Ces résultats vont dans le sens des efforts actuellement consentis pour développer des fibres céramiques appartenant à des systèmes chimiques aussi simples que possible, en utilisant des procédés de réticulation exempts d'oxygène. Plus généralement, ils fournissent des données de base pour comprendre, et éventuellement prédire, le comportement thermochimique de tout matériau céramique apparenté aux matériaux étudiés.

1 Introduction

Extensive studies have been performed in the past — and still are — by several French laboratories on the polymer-derived ceramics within the Si–C–N–O–(H) system. The number of papers published from these studies is huge and covers the whole field of science involved in materials preparation, so that all of them cannot be cited herein. However, a sample of related literature is proposed.[1–20] The overall goal of this governmental funded program (see Acknowledgements section) was to investigate various Si-based polymer routes and their ability to provide ceramics with high thermal stability, either for fiber or matrix purposes. Indeed, although still the best ceramic fiber commercially available nowadays, the polycarbosilane (PCS)-based NL-200 Nicalon^{R} fiber (Si–C–O system) is not able to respond to the needs of the 21st century (engines for aerospace or aeronautics for instance). On the other hand, polymer-based ceramic matrices (Si–C system for instance) always contain a free carbon phase, the role and behavior of which are still controversial. Thus, ceramics prepared from PCS and oxygen-cured PCS were considered as a reference series,

as far as the NL-200 Nicalon^R fiber is known around the world to people involved in ceramic reinforcements for composites.

The part of the work our laboratory devoted itself to was to investigate the way the mineralized polymers (i.e. become amorphous ceramics) transform into crystallized ceramics then withstand, evolve, and degrade when submitted to an increasing thermal treatment. Because revealing the nucleation and the relative agencement of the phases was of an utmost importance, transmission electron microscopy (TEM) was used as the main investigation technique. The TEM observations, together with data from additionnal techniques such as elemental analysis, thermogravimetry, X-ray diffraction and electrical properties, all of them performed by our co-authors, were mainly reported in previous papers about ceramics from the Si–C and Si–C–O systems (Part I),[19] from the Si–C–N system (Parts II and III),[12,13] and from the Si–C–N–O system (Part IV).[20] Considering the results — in addition to some unpublished data — with some hindsight allows general trends to be revealed which are likely to help in the understanding of the thermochemical behavior of any related materials.

2 Materials

Preparation of the polymeric precursors were performed either by the Laboratoire de Chimie Organique et Organométallique (Bordeaux, France) or the Institut de Chimie Fine (Montpellier, France). The chemical aspects of the preparation have been thoroughly studied and already published or patented,[1-4,9] as has the organic/mineral transition.[7,8,10,15] Precursors for Si–C and Si–C–O ceramics were polycarbosilane (PCS) polymers, either modified from a commercial Mark 1 (ideally $[-CH_3HSi—CH_2-]$)[2] or a new polymer ($[-CH_3PhSi-]_{0.5}[-CH_3HSi-CH_2-SiHCH_3-]_{0.5}$ copolymer).[1] Precursors for Si–C–N and Si–C–N–O ceramics were new polyvinylsilazane[9] ([–HSi(CH=CH_2)NH–]) polymer (PVSZ) or polycarbosilazane ($[-CH_3CH_3Si-]_{1-x}[-CH_3HSi-N-SiHCH_3-]_x$) copolymers (PCSZ),[3,4] where a changing x value allowed various chemical compositions to be obtained. Si–C–O and Si–C–N–O ceramics were fibers, prepared from the related oxygen-free precursors (PCS or PCSZ) by melt-spinning then curing in a nitrogen/oxygen mixture atmosphere at the Laboratoire des Composites Thermostructuraux (Bordeaux, France).[11,14,16,17] Thermal mineralisation of the polymers and further heat-treatment of the ceramic products were mainly performed by the Laboratoire des Composites Thermostructuraux for the PCS- and PCSZ-derived materials[10,11,14-18] and by the Laboratoire des Céramiques Nouvelles (Limoges, France) for the PVSZ-derived materials.[7] The mineralisation was considered to be achieved when the weight loss had become negligible, which occurred in the 800–1000°C range. At this stage, the bulk chemical compositions (obtained from Electron Probe MicroAnalysis) of the starting materials for the TEM study are (Table 1):

- $SiC_{1.4}O_{0.05}$ for the so-called Si–C ceramic (from commercial PCS);
- $SiC_{2.1}O_{0.2}$ for the so-called C-enriched Si–C ceramic (from PCS copolymer). Oxygen content originates from contamination. It mainly appears as local concentration of superficial silica and therefore does not interfere with the intrinsic evolution of the bulk ceramic. This is ascertained by the comparison between another oxygen-contaminated Si–C ceramic[9,10] and the

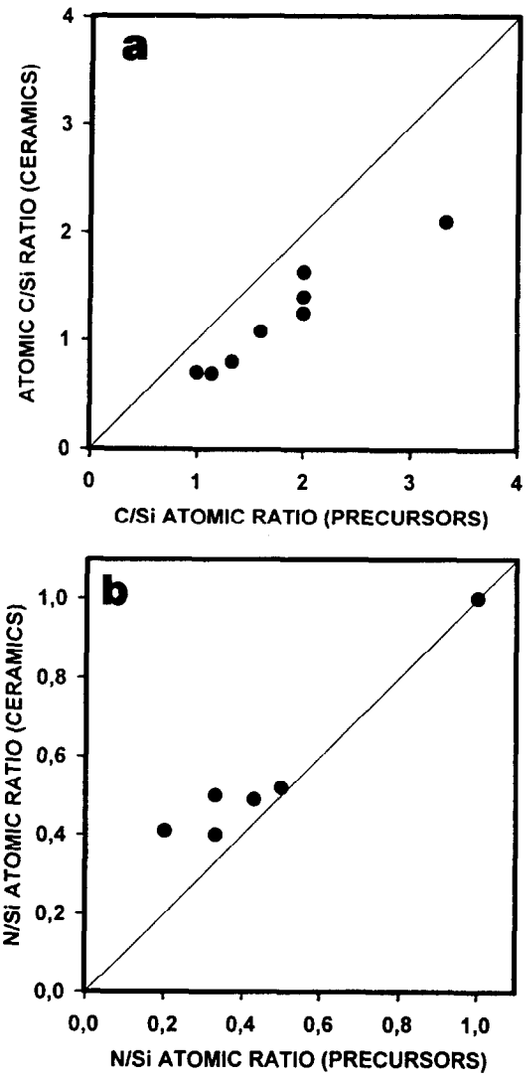

Fig. 1. Correlation between the theoretical chemical composition of the precursors and the chemical composition of the ceramic materials derived from them. (a) C/Si atomic ratio; dots below the solid line (slope = 1) indicate a depletion in C relative to the precursor. (b) N/Si atomic ratio, dots above the solid line (slope = I) indicate a depletion in Si relative to the precursor.

Table 1. Correspondence between the empirical formulae of the precursors and the elemental composition of the ceramic materials derived from them

Precursor		*Related ceramic*	
Name in the text	*Formula*	*Formula*	*Name in the text*
PCS	SiC_2H_6	$SiC_{1.4}O_{0.05}$	Si–C ceramic
PCS	id. (oxygen-cured)	$SiC_{1.25}O_{0.54}$	Si–C–O ceramic
PCS Copolymer	$SiC_{3.33}H_{6.33}$	$SiC_2O_{0.2}$	C-rich Si–C ceramic
PVSZ	$SiC_2N\ H_5$	$SiC_{1.63}N\ O_{0.07}$	PVSZ-based Si–C–N ceramic
PCSZ x=0·25	$SiC_{1.6}N_{0.2}\ H_{5.2}$	$SiC_{1.08}\ N_{0.41}\ O_{0.05}$	
x=0·75	$SiC_{1.14}\ N_{0.43}\ H_{4.28}$	$SiC_{0.69}\ N_{0.49}\ O_{0.05}$	PCSZ-based Si–C–N ceramic
x=1	$SiC\ N_{0.05}\ H_4$	$SiC_{0.7}\ N_{0.41}\ O_{0.06}$	
x=0·5	$SiC_{1.33}\ N_{0.33}\ H_{4.66}$	$SiC_{0.8}\ N_{0.5}\ O_{0.05}$	
PCSZ x=0·5	id. (oxygen-cured)	$Si\ C_{0.8}\ N_{0.41}\ O_{0.6}$	Si–C–N–O ceramic

same but contamination-free ceramic,[19] the thermal behaviour of which are similar;

- $SiC_{0.8}N_{0.5}O_{0.05}$ for the so-called Si–C–N ceramic (from PCSZ copolymer, for x = 0·5);
- $SiC_{1.25}O_{0.54}$ for the so-called Si–C–O ceramic (from commercial PCS)
- $SiC_{0.8}N_{0.4}O_{0.6}$ for the so-called Si–C–N–O ceramic (from PCSZ copolymer, for x = 0·5).

Whatever the chemical system the ceramic samples belong to (Si–C, Si–C–N, Si–C–O, Si–C–N–O), differences in their chemical composition at the end of the mineralisation stage are somewhat well-related to the basic differences in the chemical composition of the precursors, specifically regarding the carbon content (see Table 1 and Fig. 1). The fact that the C/Si atomic ratios are always lower in the ceramics than in the precursors (Fig. 1(a)) has to be related to the weight loss occurring during the organic/inorganic transition episode which is mainly due to the removal of gaseous hydrocarbon species. However, the fact that the N/Si atomic ratios are higher or equal in the ceramics compared to the precursors (Fig. 1(b)) may indicate that Si-containing species are also removed during the mineralisation stage.

Thermal stability of the above ceramics was then investigated through further heat treatments under a high purity argon flow (N56 grade) up to 1600°C or more using a 3600°C/h heating rate and a 0·25 or 1 h isothermal stage (graphite crucible in a radio frequency coil). Weight losses with increasing temperature were most often measured in a graphite crucible and furnace in N56 grade argon flow (SETARAM TAG 24). Some other treatments may have been using specific conditions and will be mentioned in the text. Attention has to be paid that, as far as possible, treatment conditions were standardized for all the samples above. Conditions were different for the Si–C–N ceramic prepared from the PVSZ polymer (lower heating rate, nitrogen atmosphere,...). Comparison with the ceramics above is then not allowed, except in some cases. Therefore, the chemical composition (from chemical analysis) of the related starting material is now given for information ($SiC_{1.63}NO_{0.07}$) but cannot be compared to the compositions above without caution. Results on PVSZ-based ceramics will be only used in Sections 3.3.4, 3.4.4, 3.5.2, and 3.5.3.

TEM investigations were performed using high resolution microscopes from PHILIPS (EM400 and CM12). Conventional bright field (BF), lattice fringes (LF) and selected area diffraction (SAD) modes were used, in addition to a peculiar dark field mode (DF) the principle of which is detailed in refs 5 and 19. Aperture sizes used provided a resolution limit of 0·65 nm in DF mode, and allowed lattice periods higher than 0·23 nm to be imaged in LF mode. Observations and previous conclusions were mainly published in references 12, 13, 19, and 20.

Further experimental details were provided in the previous papers already cited.

3 Results and Discussion

3.1 Thermal behavior of the polymer-based ceramics: common trends

All the starting materials of the study are amorphous ceramics, as evidenced from SAD patterns

and DF images, exhibiting a fine (<1 nm) porosity. Regarding the chemical system they belong to, crystallyzed phases such as SiC, Si_3N_4, SiO_2, and C were expected to occur at a given time of the thermal treatment. Specifically, regarding the C/Si at. ratio values, one could expect the occurrence of a 'free' carbon phase for materials with a C/Si at. ratio higher than 1 (i.e. above the value for the SiC stoichiometry). In fact, any of the materials develops a free carbon phase, whatever the C/Si at. ratio, even for values as low as 0·70 (Si–C–N ceramic for $x = 1$). Of course, this indicates that part of the Si atoms are mobilized by the N atoms (and/or O atoms) and are therefore no longer available to make SiC. Actually, free carbon is always the first phase to nucleate, generally as so-called Basic Structural Units (BSUs) which are small stacks of 2–3 polyaromatic layers (graphenes) of 1 nm in lateral extension and piled up as plates in turbostratic order (Fig. 2). Because BSUs have also been observed in other 'immature' carbon-containing ceramic materials (such as Nicalon^R NL200 or Tyranno^R Fibers)[21,22] on the one hand, and have been demonstrated to be the primary state of solid carbon in most of the polyaromatic carbon materials[23] on the other hand, it is believed that nucleation of BSUs must be a common event for any polymer-based ceramic, as soon as excess carbon is available. According to previous studies on the Nicalon^R NL200 fiber[21] and as sustained by other investigation methods such as NMR,[24] BSUs are found to act as independent entities, and the peripheral carbon atoms of graphenes tend to be saturated with hydrogen atoms rather than to be linked to the surrounding medium. Modelling the BSUs as shown in Fig. 2 then taking into account the H content may thus be a way to estimate the free carbon content of the ceramics through simple calculations, and good concordances have been found when possible.[12,21,24] Aromatic CH groups are not stable at high temperature and, as in any carbon material,[25] hydrogen is removed mainly as gaseous H_2 in the 1000 – 1250°C range, as revealed by elemental analysis,[12] mass spectrometry,[21] or NMR.[24] This induces unsaturations which are fixed by the edge-to-edge linkage of neighboring BSUs into larger distorted graphene stacks (Fig. 3). As the thermal treatment continues to increase, the distorted graphene stacks continue to associate each other edge-to-edge and, in a lesser extent, face-to-face. They thus increasingly build a polyaromatic carbon network, which may finally be possibly interconnected at long distance depending on the amount of free carbon phase relative to the bulk. According to the scenario above, a hydrogen-depleted immature ceramic, (i.e. having not enough remaining H atoms to saturate the peripheral C atoms of the coronene-like graphenes of the BSUs, the H/C atomic ratio of which is ~ 0·5)

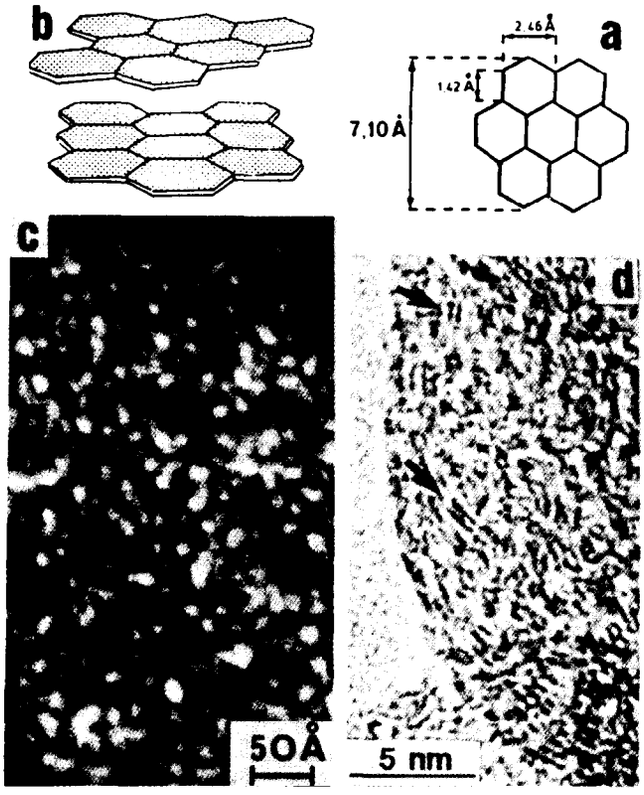

Fig. 2. (a) Sketch of a coronene molecule. (b) Sketch of a BSU. (c) Because of their tiny size, BSUs appear only as bright dots in DF mode the size of which is close to the resolution limit. (d) Imaging them in LF mode is possible (arrows) but requires drastic conditions of sample thickness and focussing values.[21]

Fig. 3. LF image of distorted graphene stacks obtained from the removal of peripheral hydrogen atoms of BSUs and subsequent BSU edge-to-edge association (example taken from a PCSZ-based Si–C–N ceramic with $x = 0·1$).

needs to make the amount of peripheral aromatic C atoms match with the amount of available H atoms, and then may have a very narrow temperature window between the occurrence of BSUs and their subsequent edge-to-edge association. The step of BSU occurrence may thus be missed.[19]

SiC is always the second phase to nucleate, as nanometric crystals, even for the N-containing ceramics, which probably has to be related to the fact that the N/Si atomic ratios of the starting ceramic materials are always lower than the value N/Si = 1·33 required for the stoichiometry of Si_3N_4. As soon as the grain sizes are large enough to provide reliable LF images, the SiC crystals appear associated to the carbon phase, in the manner that the graphenes tend to lie flat upon the crystal faces (Fig. 4). This suggests that, as far as BSUs nucleate first, they could act as nuclei for

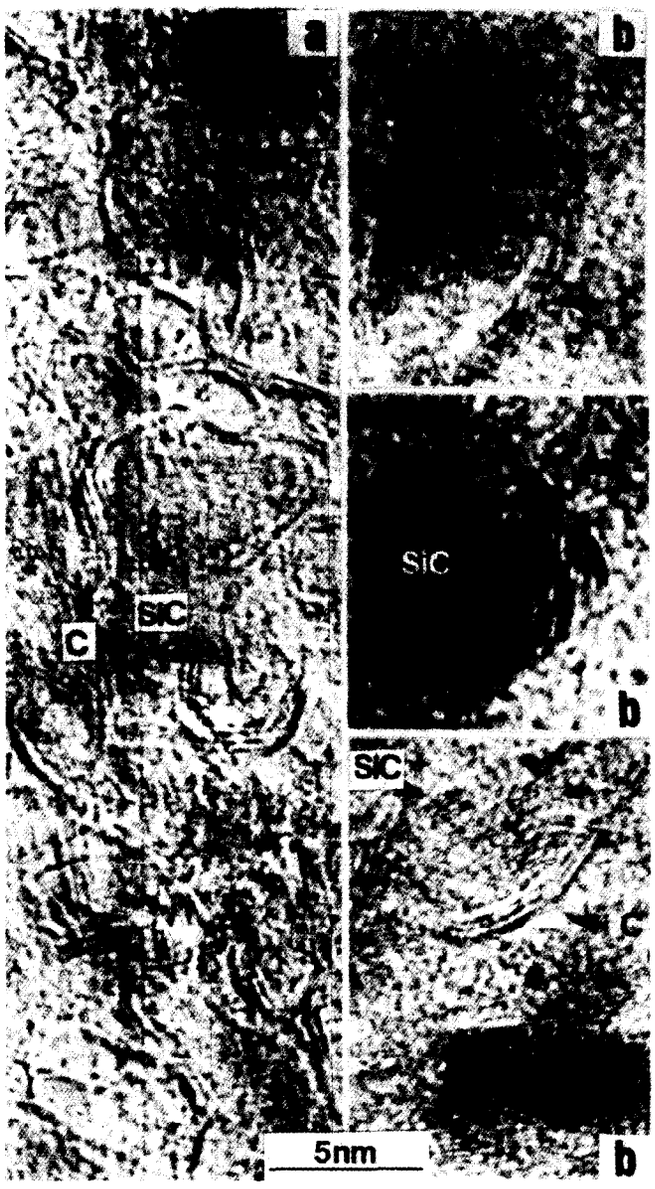

Fig. 4. LF images of distorted graphene stacks lying flat upon SiC crystal faces. (a) example taken from a Si–C ceramic (with C/Si at. = 1·4).[19] (b) Examples taken from a PCSZ-based Si–C–N ceramic with $x = 0{\cdot}5$.[13]

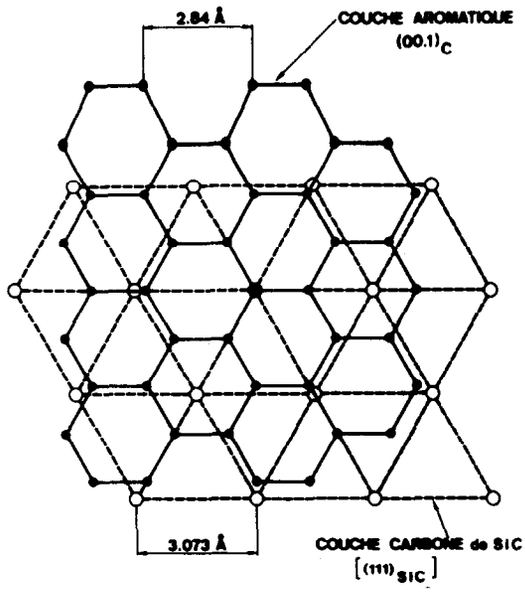

Fig. 5. Sketch of the superimposed lattices of a graphene and of a C layer in a β-SiC crystal seen following the [111] direction.[26]

SiC, by promoting the stacking of alternate Si then C atom layers from the graphene faces. Indeed, on the one hand the BSU and SiC primary grain sizes are similar (about 1 nm), and on the other hand the lattice parameters of a graphene and of SiC are somewhat compatible (Fig. 5).[26] However, this remains a mere assumption and would require further investigations, such as looking at C-depleted ceramics, which were not available materials. Whatever, the graphene stacks / SiC grains association is an undoubted fact, which at least may originate from the structural rearrangements from BSUs to distorted layers, which naturally will tend to dispose according to the minimal free energy state, i.e. flat upon any free surface (specifically when the surface somewhat presents a lattice compatibility).

At this stage of their thermal evolution, all the polymer-based ceramics investigated are made up

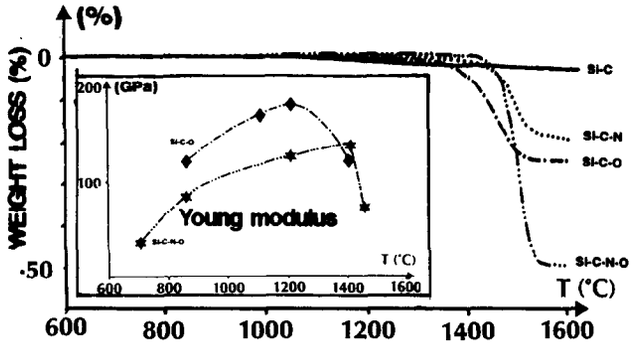

Fig. 6. Weight loss versus heat-treatment temperature for various ceramics submitted to standard conditions of heat-treatment (the Si–C–N ceramic is PCSZ-based with $x = 0{\cdot}5$). The temperature of weight loss corresponds to the temperature of degradation of the heteroatom-containing intergranular phase. Consequently, Si–C appears as the only stable system. In inset: example of mechanical property degradation for fibered ceramics, to be related to the time of the intergranular phase degradation.[11,17,19,20]

of more or less large SiC crystals (but generally less than ~ 10 nm), a more or less interconnected polyaromatic carbon network in which SiC crystals are inserted as within uncomplete carbon cages, and a more or less abundant intergranular amorphous $SiC_xO_yN_z$ phase (thus containing the heteroatoms — O, N – when any). SiC crystals are not like dry hazelnuts in their shells relative to the intergranular phase but must be linked to it, in order to account for the level of mechanical properties observed (E ~ 200 GPa, see inset in Fig. 6 for instance). Whether Si–C ceramics (i.e. not containing any heteroatoms) also have a real amorphous SiC_x intergranular phase or merely SiC_4 grain boundaries is a question, which cannot be ruled out by TEM. It cannot be easily answered either by spectroscopic methods such as NMR or XPS for instance, because of the coexistence of both ordered but nanometric (SiC crystals) and disordered (amorphous SiC) structures, both containing SiC_4 tetrahedra. Considering the fact that SiC grains do not appear much larger nor more frequent in Si–C ceramics than in heteroatom-containing ceramics, it is doubtful that the whole bulk of the Si–C ceramic is able to completely transform into crystalline SiC nuclei in a same time. Kinetic effects are expected, depending on how favorable to arrange into a β-SiC structure neighboring SiC_4 tetrahedra are. We thus assume that a remaining amorphous SiC_x intergranular phase is still present between SiC grains in Si–C ceramics, from which the SiC crystals will be built then will grow up, at least during the first growth step.

Actually, SiC crystals always grow up slowly in a first step then drastically in a second step, following various and multiple growth mechanisms which depend both on the temperature range and the chemical system the materials belong to (see Section 3.3). As expected from thermodynamic calculations,[27] the Si–C system is very stable and does not exhibit any weight loss, contrary to the heteroatom-containing ceramics (Fig. 6). Thus, in any system but the Si–C system, the second growth step originates in the diffusion-controlled thermochemical degradation of the heteroatom-containing intergranular phase, which in turn is able to degrade the free carbon phase through solid–solid reactions (Si–C–N ceramic)[13] or gas–solid reactions (Si–C–O and Si–C–N–O ceramics),[19,20] as illustrated in Fig. 7. Since depending on the diffusion of gaseous species through the material towards the outer surface, the degradation rate is slow enough to induce skin/core effects. The degradation starts in areas close to the outer surfaces then proceeds towards the inner parts. The coexistence of two grain growth mechanisms in a

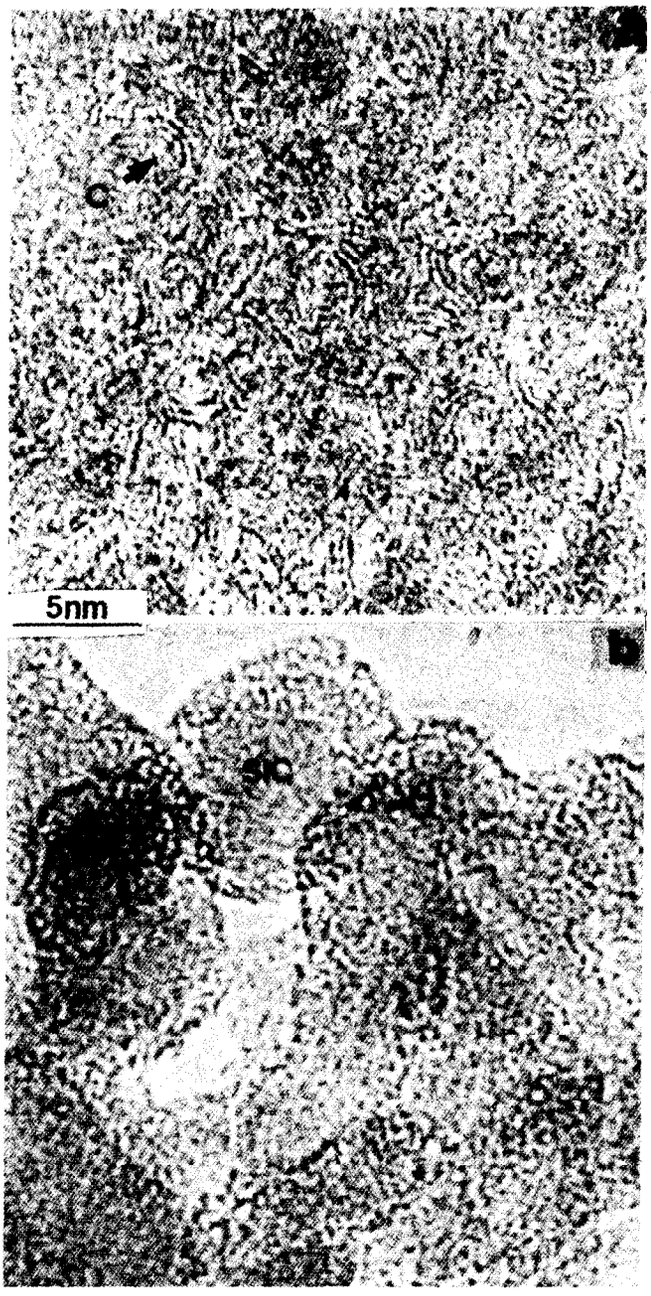

Fig. 7. LF images of Si–C–O ceramic materials in the vicinity of the degradation temperature. (a) In inner parts, where the material is not degraded yet, polyaromatic carbon stacks still are well visible (arrows). (b) In outer parts, where the thermochemical degradation has started, carbon stacks are destroyed and are no longer visible.[19]

ceramic is thus possible for a while, the low rate growth in the core, and the high rate growth in the skin.[19,21] When ceramics are under a filamentous shape (oxygen-containing systems), the thickening of the skin with the increasing temperature is measurable,[14] somewhat revealing the diffusion ability of the gaseous species involved. Also, testing the mechanical behavior is possible in that case, and performances fall down drastically (inset in Fig. 6) as soon as both the intergranular phases (i.e. the amorphous and the carbon ones) degrade. As far as the second SiC crystal growth step always occurs both at high temperature and corresponds to a high rate growth, stacking faults become

frequent, and the mere β structure is progressively replaced by polytypes.

3.2 Chronology of events

All the chemical, structural and textural events described above are common to any of the ceramics here studied, and even to other related materials.[21,22] However, for similar heating rate, they occur at temperatures which may vary depending on the chemical system. Table 2 gathers all the data[12,13,19,20] about the temperature of occurrence for the main events which are likely to characterize the thermal evolution of polymer-based ceramics. Following the general trends above, these events are: the nucleation of BSUs ('BSU'), the edge-to-edge association of BSUs into distorted graphene layers ('d'), the nucleation of SiC crystals ('Cr'), then the thermochemical degradation of the heteroatom-containing intergranular phase ('★'). Attention has to be paid that the edge-to-edge association of the BSUs ('d' event) is related to the building of the carbon network, but does not mean whether the network is interconnected at long distance or not. The interconnection event is not reported in Table 2, since it is related to the amount of free carbon content, which cannot directly be quantified by TEM images. Table 2 only involves ceramic materials heat-treated in similar conditions (i.e. Si–C–N ceramics from PVSZ are excluded). The comparison between the various systems is believed to be as more accurate as the architectures of the starting polymers are close. Also, Si–C–N ceramics from PCSZ with x values other than 0·5 are not considered in Table 2, since they have not been investigated following enough accurate temperature steps. When between parenthesis '(BSU)' indicates that the stage of BSU nucleation was missed because of the inadequate temperature step for the final temperatures of the heat-treatments, which were sometimes not narrow enough. However, knowing that the BSU nucleation must occur after the amorphous state but before the edge-to-edge BSU association helped us to estimate the temperature of BSU nucleation in these cases. Generally speaking, the temperatures of event indicated are rigorously the temperatures at which the related events have been observed for the first time rather than the temperatures at which they have really occurred, i.e. the event may have occurred sooner, within a temperature range which has not been investigated.

As already mentioned in Section 3.1, nucleation of BSUs is then the first event to occur. Despite the tiny size of the BSUs (< 1 nm), a specific use of the TEM technique allows them to be identified and distinguished from the background.[19] Attention has to be paid that nucleation and concentration of polyaromatic carbon may pre-exist as single graphenes without being revealed by TEM, as far as our imaging procedure needs the stacking period between graphenes to occur (corresponding to the 002 reflection). However, developments of such single graphenes are very limited, since thermodynamic indicates[28] that face-to-face association of graphenes are favored as soon as the graphene size reaches that of the coronene molecule (about 0·7 nm). We thus assume that the BSU occurrence may really be considered as the starting point of the development of a 'free' carbon phase. From Table 2, it is clear that heteroatoms (O, N) unfavor the BSU nucleation. Coarsly, the temperature of BSU nucleation is as higher as the atomic C% is lower (Fig. 8), unsurprisingly due to an effect of increasing dilution which acts against the necessity for carbon atoms to be close to each other to be able to associate into graphenes then into graphene stacks. More in detail, the correlation in Fig. 8 is not very

Table 2. Chronology of the main physicochemical events characterizing the thermal evolution of some of the polymer-based ceramic materials investigated. Heat-treatment conditions were similar. BSU = BSU nucleation. d = edge-to-edge association of BSUs into distorted graphene stacks. Cr= SiC crystal nucleation ★ = thermochemical degradation of the heteroatom-containing intergranular phase. The Si–C–N ceramic reported is PCSZ-derived with x = 0·5.

chemical system		heat-treatment temperature									
	C/Si	900	950	1000	1100	1200	1250	1350	1400	1450	1600
Si-C	1.4	domain of the amorphous	(BSU)	d/Cr	ceramic	d/Cr	domain of the crystallized				
	2.1			BSU	(d/Cr)	d/Cr					
Si-C-N					(BSU)	d/Cr			ceramic	★ degradation domain	
Si-C-O							BSU	d/Cr	★		
Si-C-N-O									BSU	Cr ★	

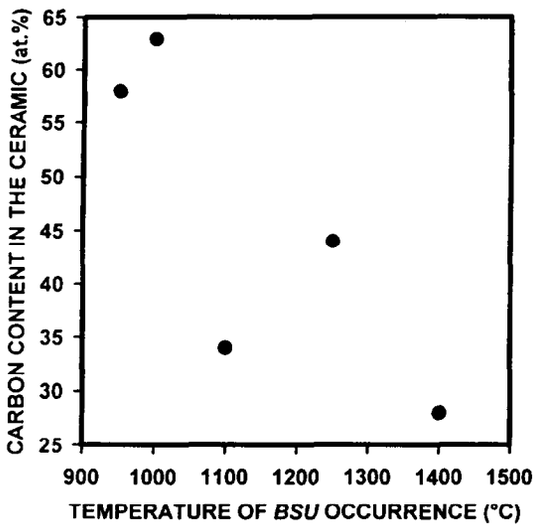

Fig. 8. Correlation between the temperature of BSU occurrence and the carbon content for the various ceramics listed in Table 2.

good, because of various and multiple reasons which would be too much speculative to discuss (differences in the polymer architecture, relative affinity of O and/or N for Si and/or C, role of the remaining H atoms,...). At least, as discussed in Section 3.1, the lack of sufficient amount of remaining H atoms in the Si–C ceramic relative to the C-enriched Si-C ceramic may have caused an early building of the carbon network, while the highest atomic C content — as in the C-enriched Si-C ceramic — would have been expected to induce the earliest BSU nucleation, statistically speaking.

As soon as BSU nucleation has occurred, the edge-to-edge association of the BSUs into distorted graphene stacks ('d' event in Table 2) follows quickly, generally related to a release of gaseous H_2. Building the carbon network is thus the second event to occur (together with the SiC nucleation), except in the Si–C–N–O ceramics. Indeed, BSUs nucleate as late as 1400°C in the latter, while the bulk material degrades within the following 50°C only. Obviously, BSUs do not have the time to associate in that case. In addition, it may be questionable whether BSUs which are that late could behave exactly the same way than earlier BSUs, specifically regarding the saturation by peripheral hydrogen atoms, as far as aromatic CH groups may not exist at this temperature.

Except for the Si–C–N–O ceramics, the nucleation of SiC crystals ('Cr' event in Table 2) then appears to be concomitant to the edge-to-edge association of BSUs. It is thought to be a coincidence, since studying the Si–C–N ceramics from PVSZ (which are not reported in Table 2 because of the discrepancies in the heat-treatment conditions) has shown that both events could be successive, the BSU association occurring first.[12] Indeed, as assumed above, the BSU association is believed to be a consequence of the removal of the hydrogen atoms peripheral to the graphenes, while the nucleation of SiC crystals has to be related to structural rearrangements at the solid state within the remaining amorphous $SiC_xN_yO_z$ matrix (where y and/or z may be equal to 0 depending on the chemical system, of course). Actually, Table 2 indicates that the nucleation of SiC is logically the earliest in the Si–C ceramics, as far as structural rearrangements towards SiC_4 tetrahedra are expected to be much easier in a SiC_x matrix than in a heteroatom-containing matrix. On the opposite, the SiC nucleation is the latest in the Si–C–N–O ceramics, i.e. containing two types of heteroatoms having no affinity one to each other but with Si atoms, which is also assumed to be the best situation to unfavor structural rearrangements towards SiC_4. Again, using TEM to evidence the nucleation of the SiC crystals is probably the most convenient technique, but induces some limitations. Primary SiC crystals are revealed both through the SAD and DF modes, based on the cristallographic reflections of pure β-SiC. Therefore, local concentrations of SiC_4 tetrahedra which would be non-ordered or ordered otherwise (as clusters for instance) would be missed, while possibly acting as the nuclei. However, the first β-SiC imaged may be as low as 1 nm large, which only corresponds to few elemental cells (about 8, containing about 30 SiC_4 tetrahedra).

Finally, the last event is, of course, the thermochemical degradation of the ceramics ('★' event in Table 2), which occurs through the thermochemical degradation of the remaining amorphous $SiC_xN_yO_z$ matrix. From Table 2 (no '★' event in Si–C ceramics) and Fig. 6, it is obvious that the threshold of thermal stability of the ceramics is governed by the presence and the type of heteroatoms, while the amount of them must be more related to the intensity of the degradation. Nitrogen (Si–C–N ceramic in Table 2) appears more likely to induce a thermally stable intergranular phase than oxygen (Si–C–O ceramic in Table 2). This has to be related to the stability of Si–N bond relative to the Si–O bond in the specific environment of the carbon-containing ceramic materials investigated, which would need thermodynamic calculations. It at least has probably to be related to the value of the N/Si atomic ratios which are always by far under the stoichiometry of Si_3N_4 (1·33), and obviously remain so even after the mobilisation of some of the Si atoms due to the crystallisation of SiC. As a matter of fact, ceramics containing both O and N (Si–C–N–O

ceramic in Table 2) exhibit a degradation temperature intermediate between that of Si–C–O and Si–C–N ceramics.

3.3 Mechanisms of crystal growth

Depending on the chemical system the ceramics belong to the temperature range of the heat-treatment, and the composition of the atmosphere, various mechanisms of SiC crystal growth may occur, which are described below.

3.3.1 Annealing type

Figure 9 summarizes the evolution of the SiC grain sizes for the ceramic materials also reported in Table 2 (again, Si–C–N ceramic from PVSZ are excluded because of the discrepancies in the treatment conditions). The SiC grain size is represented by the modal size, i.e. the class of the most frequent size. Actually, SiC grain sizes never have a single value at a given temperature but a range of values with various frequencies. A complete description of the grain size evolution thus should require to draw histograms from a statistical investigation. This has been performed sometimes, in this study[19] or — mainly — in a previous one.[21,29] However, such work is very time-consuming and using the modal size, which is rather easily estimated by a mere but carreful eye-examination of the DF images, has been most often preferred. Figure 9 shows that at least two growth rates may be identified for all the ceramics, whatever the system. The first one is low and corresponds to the growth of SiC grains within the domain of thermal stability of the bulk material. It is encountered in every ceramics — but the Si–C–N–O ceramic, (see Section 3.3.2 below) — as soon as the SiC crystals have nucleated. Indeed, the SiC nucleation necessarily goes with the formation of grain boundaries (either between SiC grains or between SiC grains and the remaining amorphous phase). They concentrate internal stresses, the energy of which is higher as the mismatch between the two adjacent lattices is higher. With the

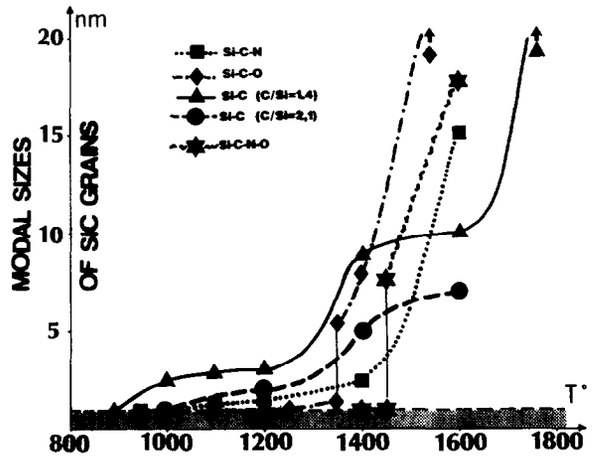

Fig. 9. Modal size of SiC crystals versus heat-treatment temperature for various ceramics submitted to standard conditions of heat-treatment.[13,19,20] Strictly speaking, the modal size is the class of the most frequent size, and therefore may be different from the mean size. Two values are given for the Si–C–O and Si–C–N–O fibered ceramics at 1350 and 1450°C respectively, since a skin/core effect occurs at these temperatures (see text). For the latter (Si–C–N–O), the grain sizes value are indicative only, since a size gradient occurs in addition to the skin/core effect.[20]

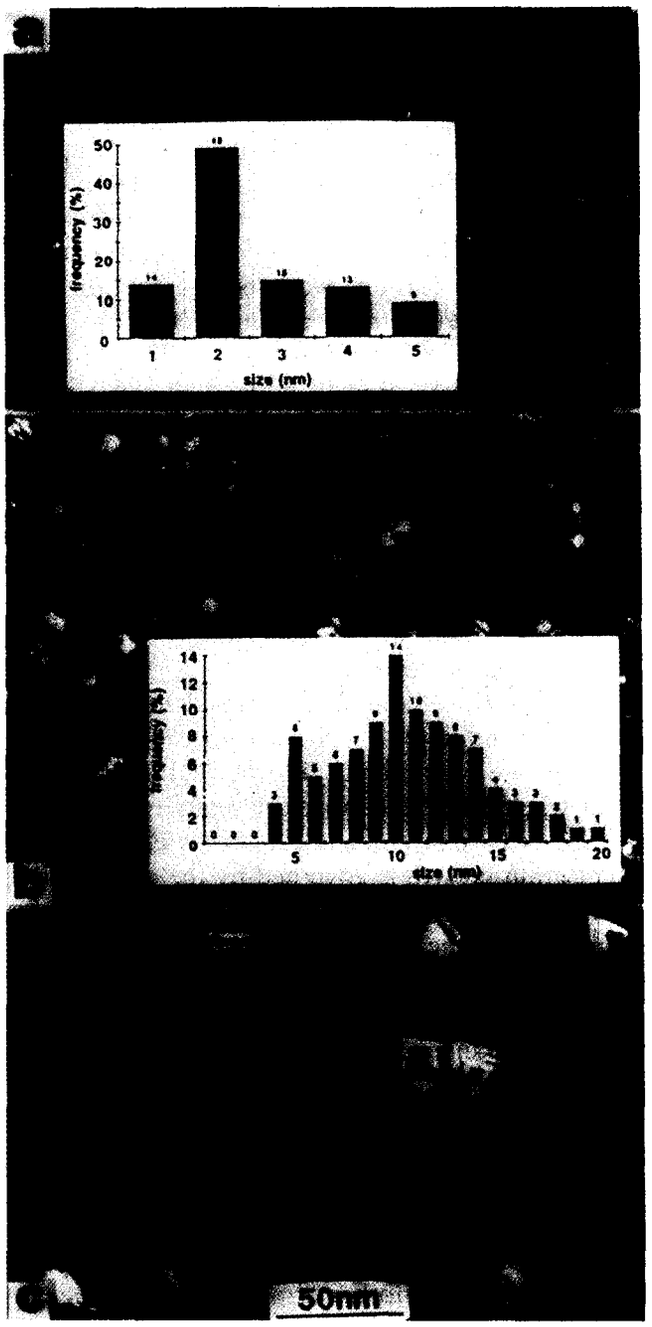

Fig. 10. Typical DF images and some related grain size distributions for various grain growth mechanisms. (a) Within the stability domain. The image is typical from a nucleation then low rate growth step following the annealing mechanism. Example taken from a Si–C ceramic (with C/Si at. = 1·4). In inset, the related grain size histogram.[28] (b) Within the degradation domain. The image is typical from a rapid grain growth through the coalescence mechanism. Example taken from a Si–C–O ceramic. In inset, the related grain size histogram.[29] (c) Peculiar case of the Si–C–N–O ceramic, in which the SiC nucleation and the $SiC_xN_yO_z$ phase degradation are concomitant.[20] Note the difference in grain shapes between (b) — round grains — and (c) — triangular grains. The image suggests a low rate growth step following an atom-by-atom feeding mechanism.

increasing temperature, stresses tend to relax and structural rearrangements occur at the grain boundaries, through the diffusion and migration of the structural defects. The crystal growth cannot occur otherwise than following random directions, since depending on only the interfacial energy which governs the defect migration, instead of following specific crystallographic directions. Crystal shapes are therefore isometric (Fig. 10(a)), and crystal sizes increase as the temperature increases. The growth rate remains low since occurring at the solid state, and at a relatively low temperature. Crystal size distributions are generally narrow and asymetric, i.e. the most frequent size classes are the lowest (Fig. 10(a)), since the memory of the nucleation event is not far and the chances of structural rearrangements are low. However, they of course increase as the temperature increases. As already pointed out in Section 3.2, at a given temperature within the low growth rate domain, crystal sizes tend to be higher in the Si–C ceramics than in the Si–C–N or Si–C–O ceramics (Fig. 9), due to the better chemical compatibility of the surrounding matrix regarding the SiC crystals, making easier the structural rearrangements.

3.3.2 Atom-by-atom feeding

In Si–C–N–O ceramics, SiC crystal nucleation is completely inhibited by the presence of O and N atoms in the bulk matrix. The nucleation can only occur when the heteroatoms are removed, i.e. when the $SiC_xN_yO_z$ phase degrades. Likewise, the subsequent grain growth is governed by the degradation rate. Since N and O do not leave the system at the same speed,[20] the material is structurally and texturally deeply transformed but the transformations may be slow enough to induce a crystal size gradient within the skin in addition to the skin/core effect mentioned in Section 3.1. Because the nucleation step and the subsequent grain growth step occur almost in the meantime and at high temperature, the stable intergranular phase cannot form, but the coalescence growth mechanism (see Section 3.3.3 below) cannot occur at this stage either. Finally, features suggest another growth type. Actually, crystals formed no longer exhibit isometric shapes but elementary crystallographic shapes such as tetrahedral, which are evidenced by triangular projections when the crystals are lying on a (111) face relative to the electron beam (Fig. 10(c)).[20] This reveals a low rate growth mechanism able to respect the respective expansion rate of the various crystal faces of the face centered cubic, thus promoting the 'slow' faces (111) to the detriment of the 'fast' faces (100) and (110). This is consistent with an atom-by-atom feeding mechanism, similar to that occurring in oversaturated solutions (when the required atoms are easily available, every crystal faces may take the number of atoms they need to grow up). The mechanism is likely to proceed as long as the 'feeding' matrix remains in an amount high enough to prevent crystal impingements. As soon as this condition is no longer fulfilled, the coalescence type growth mechanism may occur (see Section 3.3.3 below).

3.3.3 Coalescence type

The mechanism of growth by coalescence corresponds to the high growth rate domain in Fig. 9 and finally occurs in any ceramic, as supported by the slopes of the curves which are the same for all of them. It appears as soon as SiC crystals become free of any linkage to the surrounding medium. Because of the high temperatures on the one hand and of the relatively small size of crystals on the other hand, SiC crystals may be led to move and to impinge, due to thermal energy supply. Impingements lead to coalescence and subsequent high rate crystal growth. Again the growth cannot be oriented following specific crystallographic directions and the grain shape tends to be isometric (Fig. 10(b)). Since larger crystals are relatively less likely to move than smaller ones, chances of coalescence are lower for them. The subsequent grain size distributions therefore tend to provide wide and symetric histograms (inset in Fig. 10(b)). Crystals are less and less numerous, but larger and larger.

It is amazing to state that all the ceramics develop this peculiar growth mechanism, whatever the chemical system they belong to, while they do not all behave identically under thermal stress. Why SiC crystals become free to move in Si–C–N and Si–C–O ceramics is clear. As long as the remaining matrix which partly surrounds the SiC crystals as an intergranular phase and which they are linked to is stable, the grain growth is limited to the structural solid-state rearrangements mentioned in Section 3.3.1. As soon as the temperature becomes high enough to make the bonds the heteroatoms (O, N) are involved in break, the SiC crystals are liberated and may start to move, impinge, then coalesce with the neighboring crystals. For most of the materials, the intergranular carbon network cannot prevent this mechanism to occur, since generally also being degraded in the meantime. The high temperature growth mechanism is the same for the Si–C–N–O ceramics, and it is noteworthy that the grain shapes change from tetrahedric (Fig. 10(c)) to isometric as soon as the coalescence mechanism occurs.[20]

It has been assumed that an SiC_x intergranular phase may also exist in Si–C ceramics (see Section 3.1). Specifically in these materials, as long as the

intergranular phase exists, SiC crystals are built from it, and the building rate may increase quickly as the temperature increases, much more quickly than in the heteroatom-containing ceramics because of the chemical compatibility between the crystals and the surrounding matrix. This explains the intermediate rapid growth episode in Fig. 9 for SiC ceramics. Afterwards, because both the possibilities of structural rearrangements are exhausted and because the intergranular carbon network partially hinders the coalescence growth mechanism, the grain growth is limited for a while. This explains the intermediate slow growth episode in Fig. 9. Finally, the grain growth may start again following the expected coalescence mechanism as soon as the energy supply and the subsequent thermal 'shaking' is high enough to make the crystals go out from the uncomplete carbon cages and finally impinge on to each other. Another reason for the SiC crystals leaving the carbon cages is that, as the temperature increases, the carbon structure improves, rigidifies, and become less and less able to accommodate the SiC grain growth. This may induce internal stresses able to finally expel the SiC grains. Anyway, from this point, the carbon phase is no longer systematically intricated with the SiC phase but tends to evolve apart.[19]

Consistently, it is doubtful that, for the very large crystals which are obtained in any ceramic at very high temperatures, the coalescence mechanism remains the main one. Sizes may have become high enough to oppose to wide movements, which would be needed. Thus, other mechanism — such as that occurring in thermally sintered materials — are expected to occur and progressively replace the previous one, but they have not been able to be revealed in the study.

3.3.4 Vapor growth type

Because the intergranular phase degradation involves gaseous species such as N_2 (in Si–C–N ceramics), SiO and CO (in Si–C–O and probably Si–C–N–O ceramics), and possibly radicals, vapor growth mechanisms in heterogeneous (gas–solid) or homogeneous (gas–gas) phases are expected at high temperature within the high rate growth domain, according to reactions such as:

$$Si(g) + CO(g) \rightarrow SiC(s) + 1/2\ O_2(g) \quad (1)$$

$$SiO(g) + CO(g) \rightarrow SiC(s) + O_2(g) \quad (2)$$

$$SiO(g) + 2\ C(s) \rightarrow SiC(s) + CO(g) \quad (3)$$

$$Si(g) + C(s) \rightarrow SiC(s) \quad (4)$$

which are amongst the most probable.

Homogeneous reactions such as (1) and (2), specifically, are believed to be responsible for the occurrence of polytypes, always revealed in high temperature SAD patterns (Fig. 11(a)) or DF images (Fig. 11(b)). Actually, a growth mechanism such as coalescence is more likely to provide twin crystals, for instance, than the peculiar alternance of polytypes stacked and aligned following the [001] (regarding the regular α-SiC structure) or [111] (regarding the regular β-SiC structure) directions as observed in Fig. 11(b). Such structural features are rather found in rapidly grown SiC crystals such as that obtained from chemical vapor deposition process[30] or whisker preparation process,[31] which both occur following the quick propagation of a screw dislocation in conditions of undersaturation (when few atoms are available, it is more easy to promote the grain growth by only adding them at the step of a dislocation). The mechanism must be thus concomitant to the coalescence mechanism, since it requires the intergranular phase degradation to occur. However, the latter is certainly generally prevalent, at least for a while, since it is more likely to explain why grain size histograms are symmetrical (see Section 3.3.3), while a vapor growth mechanism may affect any crystal regardless its size and should much more quickly induce asymetrical histograms with a predominance of the largest size classes.

Heterogeneous reactions such as (3) and (4) are also likely to participate in SiC grain growth, to an extent which may be very variable from one

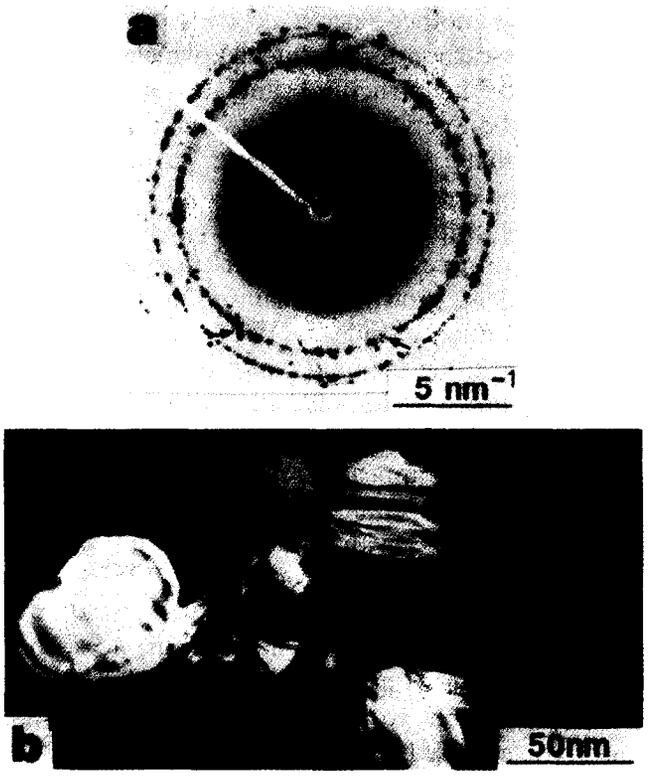

Fig. 11. Examples of evidence for polytypism in ceramic materials. (a) SAD pattern: peculiar features of polytypism are arrowed. (b) DF image: the spiral aspect (arrow) suggests a helicoidal growth mechanism, as for whiskers.

ceramic to another since it depends on the ability of the free-carbon to be attacked, which is directly related to the structural and textural features of the carbon network, if any. Actually, the chemical reactivity of polyaromatic carbon mainly occurs by the edges as it is nearly nil by the faces. Therefore, graphene edges or, at least, structural defects, are necessary. Such a mechanism may be the prevalent growth mechanism in PVSZ-based Si–C–N ceramics. Indeed, PVSZ-based ceramics were found to be the only ones the SiC nucleation step was not a widespread occurrence at a given temperature everywhere in the material.[12] SiC crystals, when they appear, are randomly distributed but seldom, with grain size distributions which are not consistent with that of a regular nucleation then growth process (Fig. 12). Because of the early development of a widespread, well formed and complete carbon network (the free-carbon content is about 32 at%),[12,24] very few carbon atoms remain available to make SiC, and the SiC_xN_y matrix is enclosed in carbon cages. The formation of SiC crystals thus appear to be related to the random occurrence of available graphene edges, due to the breaking of graphene–graphene grain boundaries induced by thermally promoted internal stresses (Fig. 13).

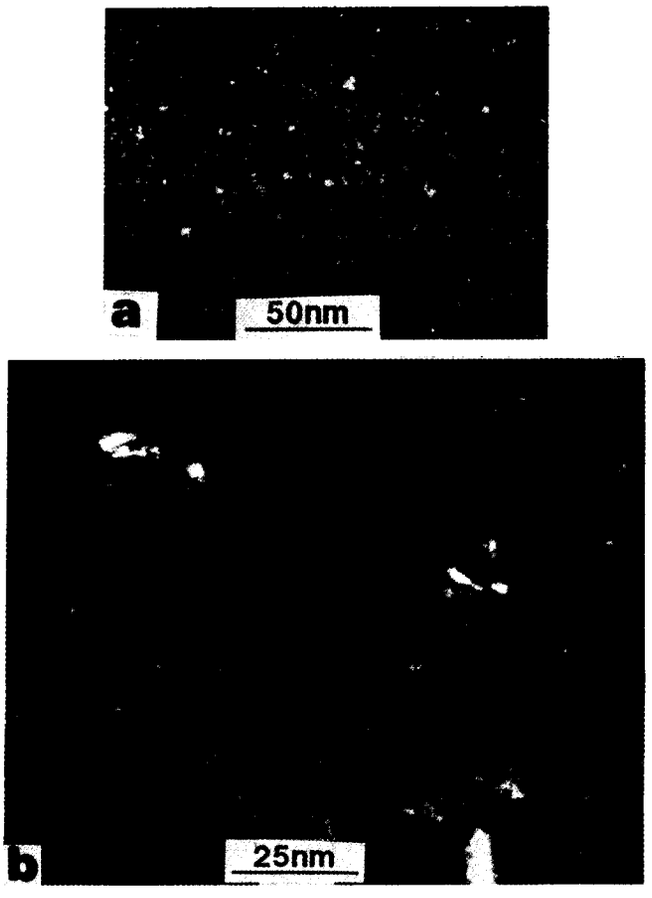

Fig. 12. DF images of the SiC crystal distribution at temperatures close to the step of SiC nucleation in (a) a PCS-based ceramic material, taken as a reference for a regular nucleation mechanism: there are many small crystals and (b) a PVSZ-based Si–C–N ceramic: the crystals are rare and large.

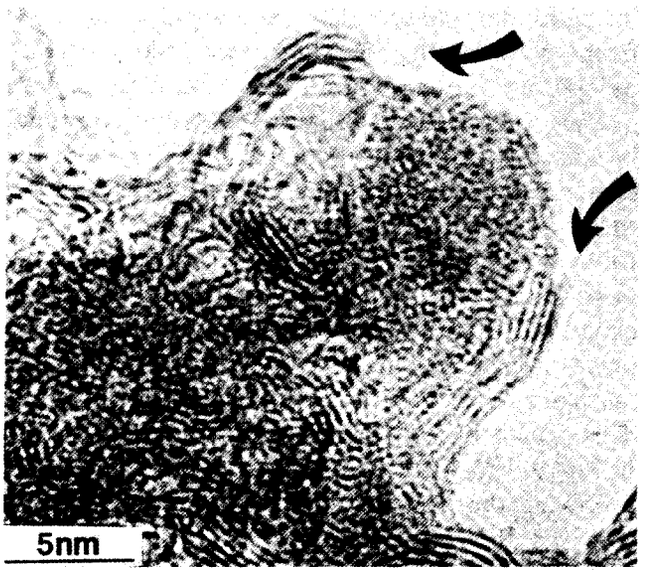

Fig. 13. LF image as an example of graphene edges become accessible due to the breaking of a carbon cage in a PVSZ-based Si–C–N ceramic.[12]

Contrarily, Si_3N_4 crystals are never formed in Si–C–N ceramics (under argon atmosphere), while the gaseous species cited in the following reactions have been directly detected[17] or are very probable:

$$3\ Si(g)+2N_2(g) \rightarrow Si_3N_4(s) \quad (5)$$

$$3\ SiO(g) + 2N_2(g) + 3\ CO(g) \rightarrow Si_3N_4(s) + 3\ CO_2(g) \quad (6)$$

This indicates that the required amounts of some of the related species are not available, either because they may have been preferentially used for SiC-promoting reactions (see above), or merely because quantities released were not sufficient.

3.4 Influence of intrinsic parameters (i.e. related to the polymer composition)

3.4.1 Role of the carbon content

Increasing the carbon content within the polymer always goes with increasing the free carbon content in the subsequent ceramic. A well developed carbon network is always favorable to the thermal stability of the ceramics, as far as it is detrimental to the SiC grain growth, either because opposing to the structural rearrangements as an intergranular phase, or because preventing the coalescence mechanism as uncomplete carbon cages. For instance, the comparison between the Si–C ceramic and C-enriched Si–C ceramic in Fig. 9 is clear regarding that point. Within the same simple chemical system (Si–C), SiC modal sizes are always lower for the latter than for the former at given temperatures, though the bulk behavior of growth remains identical. The carbon phase may even improve some mechanical features such as the Young modulus as soon as the carbon network

interconnects at long distance.[21] As long as it is not chemically destroyed by the thermochemical degradation of heteroatom-containing intergranular phase, it is also assumed to help in maintaining the mechanical cohesion of the ceramic material within the coalescence growth domain or, at least, in providing some flexibility to the bulk material. As a matter of fact, the latter feature may be required for the weaveability of heteroatom-free (or poor) SiC fibers, such as the new Hi-Nicalon^R or Tyranno^R Lox-E which are now being studied.[32–34]

It also appears clearly that the electrical behavior of the ceramic is deeply and mainly influenced by the behavior of the carbon phase, at least for temperatures up to 1400°C (Fig. 14), beyond which the contribution of the SiC phase becomes prevalent (because of the carbon phase degradation) or no longer subordinate (when the carbon phase does not degrade). In Fig. 14, the materials are as more conductive (less and less semi-insulator) as E_a decreases.[10,11,13,17,19,20] and the slope of the curve $E_a = f(T)$ must at least partly be related to the speed the carbon network becomes long-range interconnected at. Indeed, considering the temperature of events the SiC phase is involved in (nucleation, crystal growth) does not correlate well with the electrical behavior of the various ceramics. For instance, the nucleation of SiC occurs later in the C-enriched ceramic (with C/Si at. = 2.1) relative to the Si–C ceramic (with C/Si at. = 1.4), while the resistivity decreases more rapidly for the former. On the contrary, taking (arbitrarily) the Si–C ceramic as the reference sample, it appears that the respective pathes of the various ceramics may be directly related to the carbon phase behavior. Actually, the beginning of the loss of the semi-conductor feature occurs the earliest in the C-enriched ceramic because of the quick carbon network interconnection expected from the higher free carbon content, it occurs later in the Si–C–N ceramic due to the later carbon network building, and it occurs the latest in the Si–C–N–O ceramic because no carbon network is able to build. Likewise, the fact that the behavior for the Si–C–O ceramic seems not to follow the same general path as for the other ceramics could be explained by the fact that the carbon network is probably destroyed before being long-range interconnected, making the electrical behavior mainly controlled by the non-carbon phases. Also, an insufficient amount of free-carbon may be a reason. Finally, tentatively characterizing the carbon network interconnection event by the inflexion point of the curves in Fig. 14, we could say that the interconnection occurs around 1050°C for the C-enriched Si–C ceramic, around 1100°C for the reference Si–C ceramic, and around 1200°C for the Si–C–N ceramic.

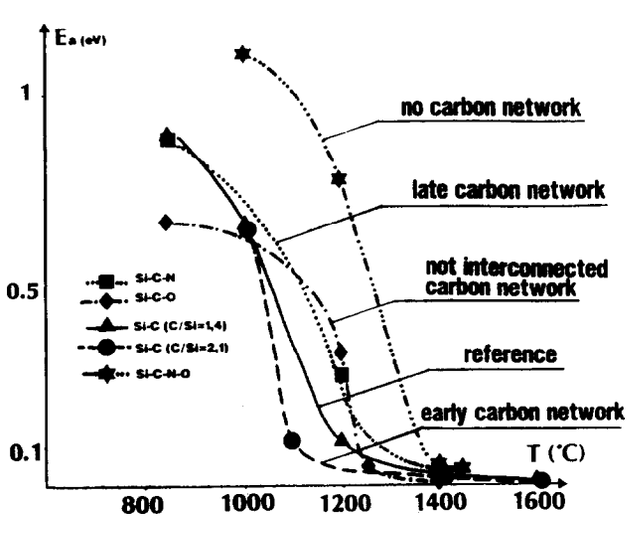

Fig. 14. Electrical behavior of some ceramic materials versus the increasing final temperature of heat-treatments (as measured T_f θ = 230°C, in order to avoid any possible machine effect for insulating materials). The plot is based on the variation of the apparent activation energy E_a calculated from the slope of log10 $\sigma = f(1/\theta)$ instead of the absolute conductivity values, in order not to have to take into account shape factors, which could be unknown or unprecise for bulk materials (four-point method, measurements from room temperature to ~ 600°C, helium atmosphere).[10,11,13,17,19,20] The Si–C ceramic (with C/Si at. = 1·4) is arbitrarily taken as the reference material which the others are compared to.

3.4.2 Role of the oxygen content

Oxygen is not involved in the primary chemical composition of the polymer precursor, strictly speaking, since added during the organic/inorganic transition process as a curing step. However, it is incorporated very early and is therefore considered here as an intrinsic parameter. Using such oxygen-containing polymers allows both the nucleation of SiC (and of BSUs) and the subsequent grain growth to be delayed, through the development of an intergranular phase the oxygen atoms are concentrated in. Oxygen atoms thus hinder the structural rearrangements towards SiC. From a structural standpoint, oxygen-containing ceramics (Si–C–O, Si–C–N–O) evolve less quickly than the related oxygen-free ceramics (Si–C, Si–C–N), and therefore may be considered more structurally stable within the thermochemical stability domain. However, the oxygen-containing intergranular phase is always thermally unstable, which finally results in a deep chemical alteration of the bulk material. From this standpoint, oxygen is detrimental to ceramic materials devoted to high temperature applications.

3.4.3 Role of the nitrogen content

Of coarse, using nitrogen-containing polymers allows the same nucleation then growth inhibition effects to be obtained than with oxygen, i.e. nitrogen-free ceramics (Si–C, Si–C–O) evolve more quickly than the related nitrogen-containing ceramics

(Si–C–N, Si–C–N–O), structurally speaking. Nevertheless, as mentioned in Section 3.4.2 above, nitrogen is less efficient than oxygen regarding these inhibition effects. On the contrary, the intergranular phase the nitrogen atoms are concentrated in is thermochemically more stable than the oxygen-containing intergranular phases. From this standpoint, nitrogen is less detrimental than oxygen to ceramic materials devoted to high temperature applications. However, the role of nitrogen cannot be that simple. Because the N content appears to act both on the nucleation, the free carbon content, and the degradation of the material, increasing the N content does not lead to monotonous changes in the ceramic behavior.[13] For instance, a high N content unfavors the nucleation then growth of the SiC phase, and also unfavors the development of the C phase by delaying the BSU nucleation and enhancing the carbon network degradation. Both events are antagonist, since the former prevents the SiC growth while the latter is likely to enhance it. Such a compromise effect is also expected for varying the oxygen content, though the related materials were not available to be investigated.

3.4.4 Role of the polymer architecture

In addition to differences in the mere chemical composition of the system, differences in the architecture of the polymeric precursor within the same chemical system may be important. Both polycarbovinylsilazane (PVSZ)[7,9,12] and polycarbosilazane (PCSZ)[3,15] polymers were used as precursors for Si–C–N ceramics. They were not often compared until now in this paper because of the discrepancies in their heat-treatment conditions. However, comparisons remain reliable on some aspects. For instance, a main difference is the presence of vinyl groups in PVSZ instead of methyl groups in PCSZ. The existence of such primary C–C bonds may have a dramatic effect on the subsequent ceramic, regarding the carbon content. Actually, the carbon yield in the PVSZ-ceramic — calculated from the C/Si at. ratios in the polymer and the ceramic, respectively 2 and 1·6 — is higher (~ 82%) than in the PCSZ-based ceramics (60–70%, depending on the x value) — where C/Si at. ratios for the polymer and the ceramic are 1·6 and 1·08 respectively for the highest (for $x = 0{\cdot}25$). As a matter of fact, TEM investigations account for a much higher free-carbon content in the former material.[12,13] Though NMR investigations have shown[24] that the primary π C=C bonds transform into σ C–C bonds during the organic/inorganic transition (which occurs at low temperature, i.e. mainly below 500°C), a PVSZ precursor is thus more likely to finally promote a well and early developed polyaromatic carbon network, inducing dramatic consequences on the SiC nucleation then growth, as described in Section 3.3.4. Obviously, the fact that carbon atoms are neighboring in the starting polymer thus helps to promote the formation of aromatic rings as soon as the temperature of carbonisation is reached (>500°C) during the ceramisation step.

3.5 Influence of extrinsic parameters (i.e. related to the treatment conditions)

Using a gaseous N_2 atmosphere instead of an argon atmosphere during the heat-treatment of nitrogen-containing ceramics delays the SiC growth by maintaining the N content longer is the intergranular phase.[12,17,20] This indicates that gaseous N_2 is a by-product of the thermal evolution in the related chemical systems, and that nitrogen-containing intergranular phases such as SiC_xN_y may somewhat behave as Si_3N_4 relative to the free-carbon phase:

$$Si_3N_4(s) + 3\ C(s) \rightarrow 3\ SiC(s) + 2\ N_2(g) \quad (7)$$

which provides a vague idea of how the SiC_xN_y phase degrades. Maintaining the N atoms within the system long enough, regarding the temperature,

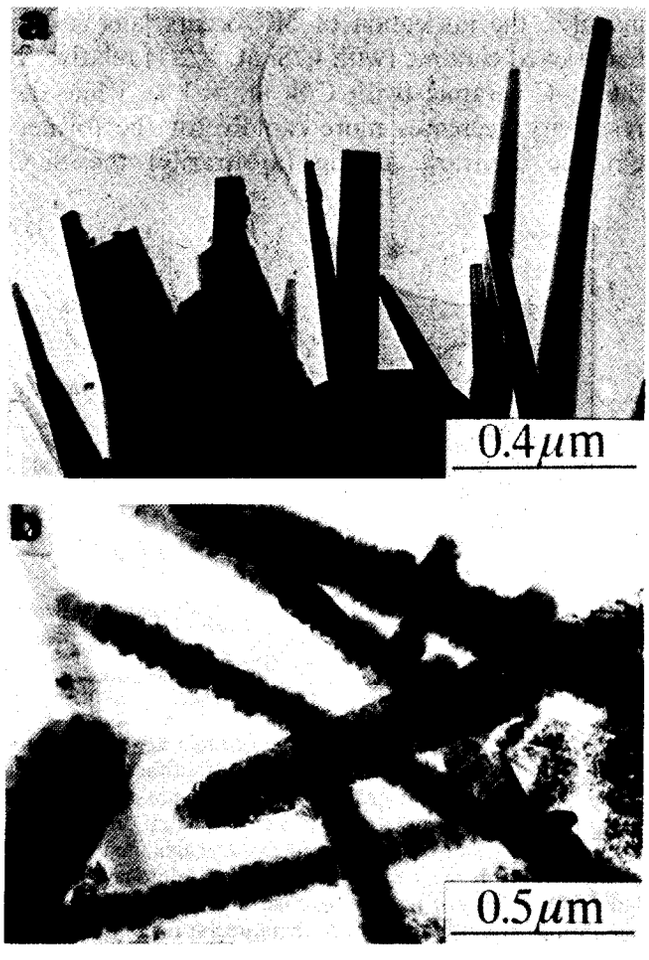

Fig. 15. BF images of (a) Si_3N_4 whiskers upon a Si–C–N–O ceramic surface[20] and (b) SiC whiskers grown upon the surface a PCSZ-based Si–C–N ceramic ($x = 0{\cdot}5$).[13]

might also of course lead to the formation of β-Si_3N_4 crystals in the bulk.[12] However, specific conditions may be required, such as a limited previous SiC crystallisation in order to maintain sufficient amounts of available Si atoms. The conditions were fullfilled in the PVSZ-based Si–C–N ceramics only,[12] though it is not ascertain whether they are due to the use of non-standard pyrolysis conditions (50°C/h instead of 3600°C/h) or to the specificity of the polymeric precursor (see Sections 3.4.4 and 3.3.4). Whatever, further studies should be made in order to investigate the extent of the reaction

$$3\ SiC(s) + 2\ N_2(g) \rightarrow Si_3N_4(s) + 3\ C(s) \quad (8)$$

in these chemical systems.

In contrast, a N_2 atmosphere and high temperatures ($\sim$ 1600°C) may promote α-Si_3N_4 whisker growth at the ceramic surface following reactions (5) and (6) for instance,[17,20] supporting the statement made in Section 3.3.4 that the partial pressure of self-induced released gaseous N_2 was not sufficient to allow these reactions to occur in argon atmosphere (Fig. 15(a)).

SiC-whiskers were also observed at high temperature (under argon atmosphere) at the surface of the PCSZ-based Si–C–N ceramic[13,15] (Fig. 15(b)). Likewise, this indicates that at least one of the gaseous species required was absent — or not in sufficient amount — in the inner atmosphere (i.e. filling the material porosity) but present in the surrounding atmosphere. O_2 traces are suspected (leaks, impurities in argon), able to promote the SiC whisker growth through reactions (1) and (2) from the gaseous Si species exiting the material. Previous reactions such as

$$C(s) + O_2(g) \rightarrow CO_2(g) \quad (9)$$

$$C(s) + CO_2(g) \rightarrow 2\ CO(g) \quad (10)$$

$$C(s) + 1/2\ O_2(g) \rightarrow CO(g) \quad (11)$$

$$Si(g) + 1/2\ O_2(g) \rightarrow SiO(g) \quad (12)$$

may have to occur depending upon the partial pressure of the species and the temperature in order to provide the oxygenated gaseous species required. In reactions (9) – (11), the C(s) species is provided by the graphite-body of the furnace. Indeed, previous studies on related materials have shown that environmental carbon added to oxygen traces may lead to unexpected events.[35] The fact that no SiC whiskers are formed for Si–C ceramics is explained by the lack of Si species exiting the material, since quite thermally stable (see Fig. 6).

Attention has to be paid that, as far as bond-breaking at high temperatures is involved, specifically when nitrogen-containing intergranular phases thermally degrade, radicals and radical reactions may also intervene in the whisker formation instead of or in addition to the regular gaseous species and chemical reactions listed above.

Finally, changing the heating rate also appears not to be subordinate. Because of the low porosity size, diffusion rates of gaseous species are low. Then, partial pressures of the gaseous species released by the materials are as higher as the heating rate is higher, i.e. the system acts as a more and more confined one. Therefore, as soon as any inner event is diffusion-controlled because involving a gaseous species (e.g. intergranular phase degradation and subsequent SiC growth in heteroatom-containing ceramics, or intrinsic Si_3N_4 crystallisation in PVSZ-based Si–C–N ceramic in N_2 atmosphere), its occurrence will be delayed and possibly inhibited by the use of high heating rate.[12]

4 Conclusion

The long-term investigation of polymer-based ceramics from the Si–C–N–O system which is reported and summarized in this paper has allowed the respective role and behavior of excess C, O, or N atoms to be revealed. An overall conclusion of the study could be that heteroatoms (regarding the SiC phase) should be avoided since finally always detrimental to the ceramic material at high temperatures. On the contrary, excess carbon may be considered beneficial to the stability of the ceramic material since limiting the SiC nucleation and SiC growth extent, and also beneficial to the mechanical properties since adding its own qualities to the properties of the bulk provided that the carbon amount is high enough to make the formation of an interconnected carbon network possible. As a matter of fact, recent development and investigations of heteroatom-free (or poor) fibers[32–34,36–46] exhibiting high thermal stability seems to sustain the idea that the binary Si–C chemical system is the more suitable for high temperature reinforcement applications. In some extent, it is true. However, although quite chemically stable, Si–C ceramics are found not to be as stable from a structural standpoint. Structural rearrangements occur continuously within the material, which could lead to fatal internal stresses when incorporated as a reinforcement within a brittle matrix such as SiC from chemical vapor deposition. In contrast, Si–C–N ceramics, although condemned to degrade at high temperatures, has been found to be thermochemically more stable than oxygen-containing systems, and more structurally stable than the Si–C system, at

least within the stability domain. Therefore, Si–C–N fibers (prepared through an oxygen-free curing process)[18,47] may exhibit a stability domain wide enough to have a suitable potential as reinforcement for high temperature composites for uses below ~1400 – 1500°C, definitely better than oxygen-cured fibers, and possibly better than Si–C fibers. Furthermore, using nitrogen-containing polymers may help in limiting the extent of the carbon network in addition to inhibiting the structural rearrangements into SiC_4 tetrahedra. Actually, although demonstrated to be beneficial to the ceramic materials on the one hand, a well-developed long-range interconnected carbon network may be fatal for a use in oxygen-containing atmospheres on the other hand. Whatever, carbon is found to be the leading element in the SiC-based ceramics, since acting directly on the thermochemical and structural stabilities, the mechanical properties, the electrical behavior, and possibly the weavability of fibers. Further investigations of ceramics with various carbon content should therefore be necessary, and are actually currently performed in our laboratory.

Acknowledgements

The authors thank the National Program 'Précurseurs de Céramiques à Base Si, C, N, O' for its financial support and specifically the Centre National de la Recherche Scientifique (CNRS), the French Ministry of Defence (DRET), Rhône-Poulenc, and Société Européenne de Propulsion.

References

1. Pillot, J. P., Bacqué, E., Dunoguès, J. & Olry, P., Copolymérisation de dichlorosilanes avec des bischlorosilylmethanes, les produits obtenus et les utilisations desdits produits, *French Patent*, 2 599371, 1986.
2. Birot, M., Bacqué, E., Pillot, J.-P. & Dunoguès J., Etude de la transformation polydimethylsilane-polycarbosilane. I. Analyse des gaz dégagés. *J. Organomet. Chem.*, **310** (1986) C41–4.
3. Bacqué, E., Dunoguès, J., Biran, C., Olry, P. & Pillot, J.-P., *French Patent*, 2 599037, 1986.
4. Bacqué, E., Pillot, J.-P., Dunogués, J. & Olry, P., *European Patent*, 296028, 1988.
5. Monthioux, M., Oberlin, A. & Bouillon, E., Relations between microtexture and electrical properties during heat-treatment of SiC fiber precursor. *Compos. Sci. Technol.*, **37** (1990) 21–35.
6. Delverdier, O., Monthioux, M. & Oberlin, A., Rôle de l'oxygène dans l'evolution thermique de céramiques issues de polycarbosilane. In *Proceedings 7èmes Journées Nationales sur les Composites*, eds G. Fantozzi & P. Fleischmann. Lyon, France, 1990, pp. 391–400.
7. Lavedrine, A., Bahloul, D., Goursat, P., Choong, K. Y. N., Corriu, R., Leclercq, D., Mutin, H. & Vioux, A., Pyrolysis of polyvinylsilazane precursors to silicon carbonitride. *J. Europ. Ceram. Soc.*, **8** (1991) 221–7.
8. Richard, C., Bacqué, E., Pillot, J.-P., Birot, M., Dunoguès J., Mocaer, D. & Pailler R., In *Actes Journées Spéciales Fibres Minérales*. Paris, France, 1991, pp. 7–16.
9. Choong, K. Y. N., Corriu, R., Leclercq, D., Mutin, P. H. & Vioux, A., Polyvinylsilazane: a new precursor to silicon carbonitride. *New. J. Chem.*, **15** (1991) 85.
10. Bouillon, E., Langlais, F., Pailler, R., Naslain, R., Cruège, F., Huong, P. V., Sartrou, J. C., Delpuech, A., Laffon, C., Lagarde, P., Monthioux, M. & Oberlin, A., Conversion mechanisms of a polycarbosilane precursor into a SiC-based ceramic material. *J. Mater. Sci.*, **26** (1991) 1333–45.
11. Bouillon, E., Mocaer, D., Villeneuve, J.-F., Pailler, R., Naslain, R., Monthioux, M., Oberlin, A., Guimon, C. & Pfister, G., Composition-microstructure-property relationships in ceramic monofilaments resulting from the pyrolysis of a polycarbosilane precursor at 800 to 1400°C. *J. Mater. Sci.*, **26** (1991)1517–30.
12. Delverdier, O., Monthioux, M., Oberlin, A., Lavedrine A., Bahloul, D. & Goursat, P., Thermal behaviour of polymer-derived ceramics. II. Si–C–N system from a new PVSZ precursor. *J. High Temp. Chem. Process.*, **1** (1992) 139–49.
13. Delverdier, O., Monthioux, M., Mocaer, D. & Pailler, R., Thermal behaviour of polymer-derived ceramics. III. Si–C–N system from a new PCSZ precursor. In *5th European Conference on Composite Materials Proceedings*, eds A. R. Bunsell, J. F. Jamet & A. Massiah. Bordeaux, France, 1992, pp. 691–6.
14. Pailler, R., Jaymes, I., Naslain, R., Richard, C., Pillot, J. P., Dunoguès, J., Olry, P., Mocaer, D. & Chassagneux, E., Effects of oxygen content on mechanical properties and oxidation resistance in ex-PCSZ Si–C–N–O model filaments. In *5th European Conference on Composite Materials Proceedings*, eds A. R. Bunsell, J. F. Jamet & A. Massiah. Bordeaux, France, 1992, pp. 631–6.
15. Mocaer, D., Pailler, R., Naslain, R., Richard, C., Pillot, J.-P., Dunoguès, J., Gérardin, C. & Taulelle, F., Si–C–N ceramics with a high microstructural stability elaborated from the pyrolysis of new polycarbosilazane precursors. Part I. The organic-inorganic transition. *J. Mater. Sci.*, **28** (1993) 2615–31.
16. Mocaer, D., Pailler, R., Naslain, R., Richard, C., Pillot, J.-P. & Dunoguès, J., Si–C–N ceramics with a high microstructural stability elaborated from the pyrolysis of new polycarbosilazane precursors. Part II. Effect of oxygen curing on properties of ex-PCS monofilaments. *J. Mater. Sci.*, **28** (1993) 2632–8.
17. Mocaer, D., Pailler, R., Naslain, R., Richard, C., Pillot, J.-P., Dunoguès, J., Delverdier, O. & Monthioux, M., Si–C–N ceramics with a high microstructural stability elaborated from the pyrolysis of new polycarbosilazane precursors. Part III. Effect of pyrolysis conditions on the nature and properties of oxygen-cured derived monofilaments. *J. Mater. Sci.*, **28** (1993) 2639–53.
18. Mocaer, D., Pailler, R., Naslain, R., Richard, C., Pillot, J.-P., Dunoguès, J., Darnez, C., Chambon, M. & Lahayc, M., Si–C–N ceramics with a high microstructural stability elaborated from the pyrolysis of new polycarbosilazane precursors. Part IV. Oxygen-free model monofilaments *J. Mater. Sci.*, **28** (1993) 3049–58.
19. Delverdier, O., Monthioux, M., Mocaer, D. & Pailler, R., Thermal behavior of polymer-derived ceramics. I. Si–C and Si–C–O systems from both commercial and new polycarbosilane (PCS) precursors. *J. Europ. Ceram. Soc.*, **12** (1993) 27–41.
20. Delverdier, O., Monthioux, M., Mocaer, D. & Pailler, R., Thermal behavior of polymer-derived ceramics. IV. Si–C–N–O fibers from an oxygen-cured polycarbosilazane. *J. Europ. Ceram. Soc.*, **14** (1994) 313–25.
21. Le Coustumer, P., Monthioux, M. & Oberlin, A., Understanding Nicalon^R fiber. *J. Europ. Ceram. Soc.*, **11** (1993) 95–103.
22. Bourgerette, C., Le Coustumer, P., Monthioux, M. & Vahlas, C., TEM characterization of a heat treated

Tyranno^R fiber. In *6th European Conference on Composite Materials. Proceedings, vol: High temperature ceramic matrix composites,* eds. R. Naslain, J. Lamon & D. Doumeingts, Woodhead Publishing Limited, UK. Bordeaux, France, 1993, pp.67–74.
23. Oberlin, A., Carbonization and graphitization. *Carbon*, **22** (1984) 521–41.
24. Gérardin, C., Caractérisation par résonance magnétique nucléaire de matériaux céramiques à base de carbure ou carbonitrure de silicium obtenus par voie polymérique. PhD Thesis, University of Paris VI, France, 1991.
25. Oberlin, A., Boulmier, J.-L. & Villey, M., Electron microscopy study of kerogen microtexture Selected criteria for determining the evolution stage of kerogen. In *Kerogen*, ed. B. Durand, Technip, Paris, France, 1980, pp.191–241.
26. Goma, J., Oberlin, A., Kerrand, E. & Bélouet, C., Résistance du substrat de carbone au silicium fondu dans le procédé RAD. *Rev. Phys. Appl.*, **19** (1984) 297–306.
27. Greil, P., Thermodynamic calculations of Si–C–O fiber stability in ceramic matrix composites. *J. Europ. Ceram. Soc.*, **6** (1990) 53–64.
28. Vorpagel, R. E. & Lavin, J. G., Most stable configurations of polynuclear aromatic hydrocarbon molecules in pitches via molecular modelling. *Carbon*, **30** (1992) 1033–40.
29. Le Coustumer, P., Monthioux, M. & Oberlin, A., Mécanismes de dégradation d'une fibre Nicalon série 200. In *AMAC-CODEMAC Colloquium: Matériaux Réfractaires pour Applications Hautes Températures*, eds. R. Naslain, J. Lamalle & J. L. Zulian. Bordeaux, France, 1990, pp. 43–53.
30. Schamm, S., Mazel, A., Dorignac, D. & Sevely, J., HREM identification of 'one dimensionally disordered' polytypes in the SiC (CVI) matrix of SiC/SiC composites. *Microsc. Microanal. Microstruct.*, **2** (1991) 59–73.
31. Madigou, V., Monthioux, M. & Oberlin, A., Microstructure et microtexture d'un composite Si_3N_4 renforcé whiskers et de ses constituants. In *AMAC-CODEMAC Colloquium: Matériaux Réfractaires pour Applications Hautes Températures*, eds R. Naslain, J. Lamalle & J. L. Zulian. Bordeaux, France, 1990, pp. 221–35.
32. Chollon, G., Laporte, C., Pailler, R. Naslain, R. Laanani, F., Monthioux, M. & Olry P., Thermal stability of a PCS-derived fiber with a low oxygen content (Hi-Nicalon). *J Mater. Sci.* (submitted).
33. Chollon, G., Fibres céramiques à base de carbure de silicium et à faible taux d'oxygène. PhD Thesis, University of Bordeaux I, France, 1995.
34. Laanani, F., Monthioux, M., Guimon, C., Chollon, G. & Pailler, R., A comparative study of some heat-treated oxygen-cured or radiation-cured ceramic fibers: chemical, structural, and nanotextural aspects. *J. Europ. Ceram. Soc.* (to be submitted).
35. Le Coustumer, P., Monthioux, M. & Oberlin, A., Further studies of the stability of PCS-based ceramic fibres at high temperatures. 2. Effect of all-carbon environments. *Br. Ceram. Trans. J.*, **94** (1996) 185–90.
36. Matsuzawa, T., Okamura, K. & Sato, M., Microstructure and mechanical properties of SiC fiber. In *International Meeting on Advanced Materials*, Vol. 4, Materials Research Society, 1989, pp.191–6.
37. Okamura, K., Sato, M., Seguchi, T. & Kawanishi, S., Preparation of high temperature strength SiC fiber. In *Controlled Interphases in Composites Materials*, ed. H. Ishida, Elsevier, 1990, pp. 209–18.
38. Takeda, M., Imai, Y., Ichikawa, H., Ishikawa, T., Seguchi, T. & Okamura, K., Properties of the low oxygen content SiC fiber on high temperature heat-treatment. *Ceram. Eng. Sci. Proc.*, **12** (1991) 1007–18.
39. Yamamura, T., Tyranno fibers. In *Euro-Japanese Colloquim on Ceramic Fibers, 6th European Conference on Composites Materials,* eds A. R. Bunsell & I. Kimpara, Bordeaux France, Japan Society for Composites Materials, 1993, pp. 187–201.
40. Xu, Y., Zangvil, A., Lipowitz, J., Rabe, J. A. & Zank, G. A., Microstructure and microchemistry of polymer-derived crys-talline SiC fibers, *J. Am. Ceram. Soc.*, **76** (1993) 3034–40.
41. Ishikawa, T., Recent developments of the SiC fiber Nicalon and its composites, including properties of the SiC fiber Hi-Nicalon for ultra-high temperature. *Compos. Sci. Technol.*, **51** (1994) 135–44.
42. Toreki, W., Batich, C. D., Sacks, M. D., Saleem, M., Guang, J. C. & Morrone, A. A., Polymer-derived silicon carbide fibers with low oxygen content and improved thermomechanical stability. *Compos. Sci. Technol.*, **51** (1994) 145–59.
43. Hasegawa, Y., New curing method for polycarbosilane with unsaturated hydrocarbons and application to thermally stable SiC fibre. *Compos. Sci. Technol.*, **51** (1994) 161–6.
44. Lipowitz, J., Barnard, T., Bujalski, D., Rabe, J & Zank, G., Fine-diameter polycristalline SiC fibers. *Compos. Sci. Technol.*, **51** (1994) 167–71.
45. Takeda, M., Sakamoto, J., Imai, Y., Ichikawa, H. & Ishikawa, T., Properties of stoichiometric silicon carbide fiber derived from polycarbosilane. *Ceram. Eng. Sci. Proc.*, **15** (1994) 133–41.
46. Zhang, Z.-F., Scott, C. S. & Laine, R. M., Pure silicon carbide fibers from polymethylsilane. *Ceram. Eng. Sci. Proc.*, **15** (1994) 152–61.
47. Sato, M. Okamura, K., Kawanishi, S. & Seguchi, T., Preparation and mechanical properties of silicon oxynitride fiber and silicon nitride fiber. In *International Meeting on Advanced Materials*, Vol. 4, Materials Research Society, 1989, pp. 197–202.

Journal of the European Ceramic Society 16 (1996) 739–744

0955-2219(95)00203-2
0955-2219/96/$15.00

Aluminium Nitride–Molybdenum Ceramic Matrix Composites: Characterization of Ceramic–Metal Interface

A. A. Khan & J. C. Labbe*

Laboratoire de Matériaux Céramiques et Traitements de Surface (LMCTS), URA CNRS 320, Groupe 'Céramiques Nouvelles', 123 Av. Albert Thomas, Faculté des Sciences, Université de Limoges, 87060 Limoges Cedex, France

(Received 10 July 1995; revised version received 1 November 1995; accepted 7 November 1995)

Abstract

Pure aluminium nitride can be hot pressed with an addition of molybdenum powder. With this technique we obtain a ceramic matrix composite having a dispersed metallic phase. Composites produced in this manner present a homogeneous structure with very little open porosity. Electrical resistivity measurements done over a series of composites show a sharp decrease in electrical resistivity when the molybdenum volume fraction in the material increases from 0·2 to 0·22. This value corresponds to the percolation threshold of metallic phase in the ceramic matrix. The interface between molybdenum particles and aluminium nitride grains is established through a fine oxide or oxynitride layer present at the surface of AlN grains.

Le frittage d'un mélange des poudres de nitrure d'aluminium et de molybdène est effectué sous charge. Par cette technique on obtient des composites à matrice céramique avec une phase métallique (Mo) dispersée dans la matrice de AlN. Les échantillons frittés de cette façon présentent une structure dense et homogéne. Les mesures de la résistivité électrique effectuées sur une série de mélanges montrent une chute brutale de celle-ci lorsque la fraction volumique du molybdène dans le matériau passe de 0·2 à 0·22. Cette composition correspond au seuil de percolation des grains métalliques. L'interface entre les particules de molybdène et les grains de AlN s'établit à travers une fine couche d'oxyde ou d'oxynitrure qui se trouve à la surface des grains de AlN.

1 Introduction

Aluminium nitride has many attractive properties for applications which need high thermal conductivity, good mechanical strength, low density value and a low thermal expansion coefficient. Aluminium nitride single crystals exhibit thermal conductivity[1] values of up to 320 W m^{-1} K^{-1}, whereas the thermal conductivity of polycrystalline AlN varies between 80 and 200 W m^{-1} K^{-1} according to the microstructure and composition of the sintered ceramic.[2–5] Hot pressed pure AlN[6,7] shows bend strength values of about 250 to 300 MPa and an elastic modulus ranging between 300 and 310 GPa. It presents a good thermal stability at temperatures higher than 2400°C, under normal conditions. Thus aluminium nitride presents itself as a potential material for thermomechanical applications.

On the other hand, aluminium nitride possess a brittle nature, as is the case for other ceramic materials. Attempts have been made to improve the fracture toughness of AlN by adding a dispersed second phase in the ceramic matrix, usually in the form of whiskers having a similar thermal expansion to AlN. In an effort to improve the mechanical characteristics of AlN, and thereby to expand its application field, silicon carbide whiskers (SiC_w) were employed[8] as a dispersed second phase. Solid solution formation in the AlN–SiC_w system results not only in a chemical phase change, but also in a morphology change. Whiskers are consumed as SiC diffuses into equiaxed AlN grains, resulting in the formation of a solid solution. Bend strength of hot pressed whisker-reinforced AlN composites increases up to 370 MPa but no important change takes place in the fracture toughness.[8] On the other hand, the thermal conductivity of AlN is dramatically reduced due to Si contamination.

Another way of improving the mechanical and thermomechanical properties of AlN could be the addition of a metallic phase with higher mechanical and thermal properties. Added metallic particles should present a high melting point (in order to

*To whom correspondence should be addressed.

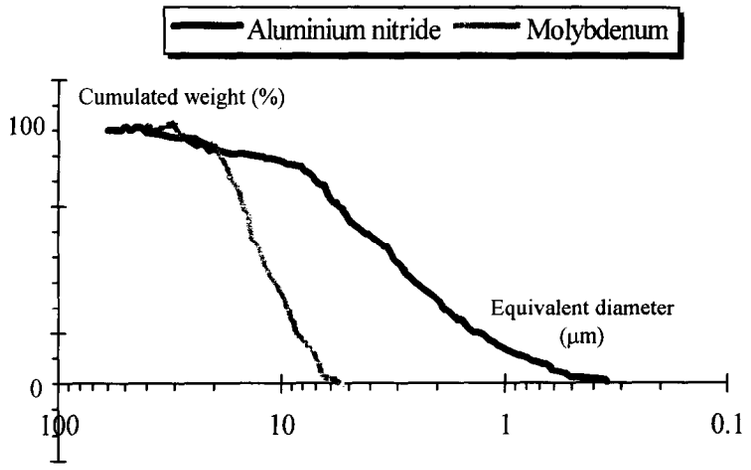

Fig. 1. Size distribution of AlN and Mo powders measured by X-ray sedigraphy technique.

preserve the refractoriness of AlN) and low solubility in the AlN lattice (to preserve high thermal conductivity), in view of high temperatures employed during the sintering of AlN. To keep the density of the composite at its optimum value, a refractory metal with relatively light weight is preferable for this purpose.

Since AlN is a covalent compound, limited atomic mobility prevents complete densification of pure AlN at temperatures lower than 1700°C. At higher temperatures (1700 to 1800°C), pressures or sintering aids are required to achieve respectable densification rates. The hot pressing technique helps to obtain more than 97% densification of AlN, where pressure plays a very important role during sintering. Samples obtained by hot pressing show better mechanical properties than those obtained by pressureless sintering because of the absence of low melting point secondary phases at the grain boundaries and a fine microstructure. Sintering cycles during hot pressing are relatively shorter and hot pressed sample dimensions are closer to the finished product dimensions due to better shrinkage control during hot pressing. But at the same time, this technique remains difficult to apply in the case of large-sized samples and for those having complex shapes because of the high pressures necessary to obtain the required densification.

In this work, aluminium nitride is co-sintered with molybdenum using a hot pressing cycle commonly employed for pure aluminium nitride. AlN–Mo composites are produced with the aims of understanding and verifying the influence of the molybdenum phase on the aluminium nitride ceramic matrix. Molybdenum is a relatively light refractory metal (theoretical density = 10·2 g.cm^{-3}) with a melting point of 2610°C. Earlier studies[9] have shown the presence of adequate bonding between plates of sintered pure AlN and Mo, heat-treated under pressures of 20 MPa at 1850°C for 4 h. Molybdenum equally shows high thermal conductivity (138 W m^{-1} K^{-1}). Because of its ductile nature, the addition of molybdenum is supposed to improve the mechanical as well as the thermomechanical properties of aluminium nitride, whereas better thermal conductivity can be expected in the case where the AlN–Mo interface is clean and devoid of any secondary phases. In this work we study the influence of molybdenum addition on the electrical properties of AlN–Mo composites in order to investigate the percolation threshold, the composition for which the material becomes an electrical conductor, and to verify the state of the metal–ceramic interface in the as-sintered samples.

2 Experimental Procedure

2.1 AlN and Mo powders

Aluminium nitride powder from H. C. Starck (Berlin), with a specific surface area of 4 m^2 g^{-1}, was used. Principal elements of this powder are presented in Table 1 where we note that oxygen is the main impurity. The size distribution of this powder, as studied by the sedigraphy technique (Sedigraph 5000 D, Micromeritics), is presented in Fig. 1. We observe in this figure that the majority of particles have sizes varying between 0·3 and 5 μm. This result is confirmed by the scanning electron micrograph shown in Fig. 2(a).

Molybdenum powder was supplied by Prolabo. This powder is 99·9% pure showing a size distribution of 5 to 30 μm (Fig. 1). Figure 2(b) presents

Table 1. Composition of AlN powder as given by H. C. Starck (Berlin)

Element	*Al*	*N*	*O*	*C*	*Fe*
% weight	>64·5	33·2	1·8	0·05	0·01

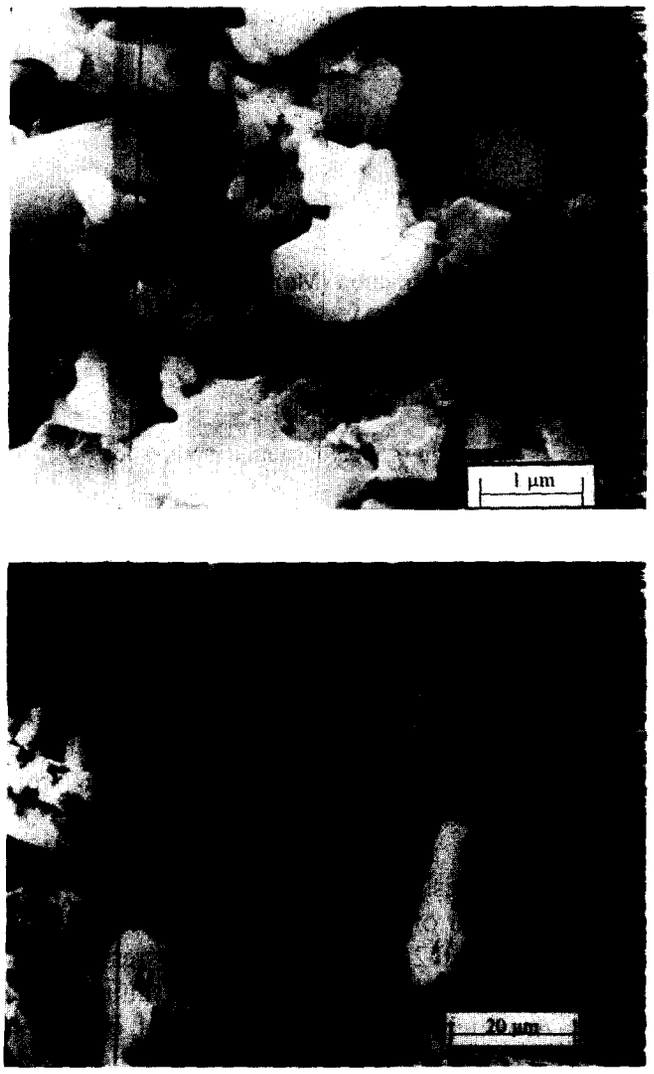

Fig. 2. SEM photomicrographs of AlN (a) and Mo (b) powders, showing size distribution and particle form.

the structure of powder particles which is relatively uniform compared with that of AlN.

2.2 Sintering conditions

Powders were mixed in different proportions, varying the molybdenum concentration by volume in AlN from 5 to 35%. The mixtures were prepared by dry milling for a period of 24 h. Since AlN forms the continuous majority phase (molybdenum concentration never exceeds 35% by volume) and the molybdenum particles are supposed to be embedded inside the AlN matrix, the

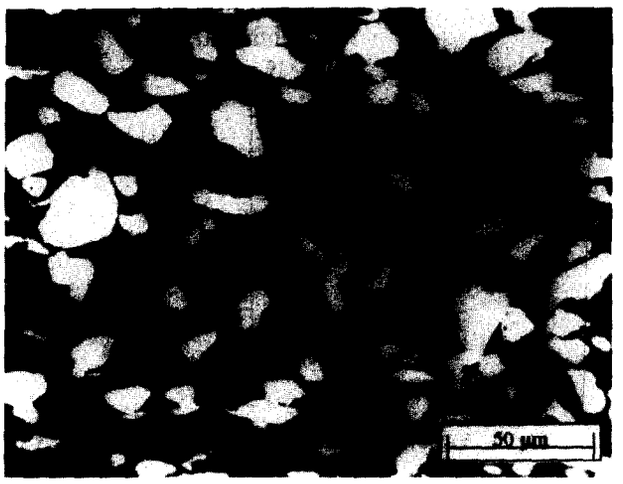

Fig. 3. Microstructure of hot-pressed AM25 (25% Mo and 75% AlN by volume).

sintering conditions are kept similar to those commonly employed for the hot pressing of pure aluminium nitride,[10,11] in order to obtain a dense composite.

Sintering powder was placed inside a graphite mould with its inner walls coated with a BN slurry to avoid any interaction between the powder and graphite and also to facilitate the demoulding process. An LPA 2000 (La Physique Appliquée) hot pressing furnace was used, which allowed 20 MPa pressure on the mould during the sintering cycle to be obtained. Sintering was performed under a dynamic nitrogen atmosphere, at a temperature of 1800°C and for a dwell time of 1·5 h. Pressure was applied once the temperature reached 1400°C. Sintered samples were in the form of discs with 30 mm diameter and were rectified to a 4 mm thickness.

The mercury penetration technique was employed to measure the density and open porosity content. Results concerning five compositions are presented in Table 2, where it is found that all the samples presented show a densification rate of more than 94% and an open porosity content of less than 1·5%. Figure 3 illustrates the structure of a hot pressed AlN–Mo sample containing 25% molybdenum by volume. The structure is relatively homogeneous, showing metal particles almost the same size as the powder particles and only traces of porosity in the AlN matrix.

Table 2. Values of theoretical density, measured density, total porosity and open porosity obtained by the mercury penetration technique, for five different mixtures after hot pressing

Ref.	*Volume fraction of AlN*	*Volume fraction of Mo*	*Theoretical density,* $d_{th}(g.cm^{-3})$	*Apparent density,* $d_a(g.cm^{-3})$	*Total porosity (%)*	*Open porosity (%)*
AM5	0·95	0·05	3·605	3·4	5·93	0·75
AM10	0·9	0·1	3·954	3·77	4·66	1·31
AM15	0·85	0·15	4·301	4·2	2·88	0·47
AM20	0·8	0·2	4·648	4·42	4·91	0·98
AM25	0·75	0·25	4·995	4·85	2·93	0·32

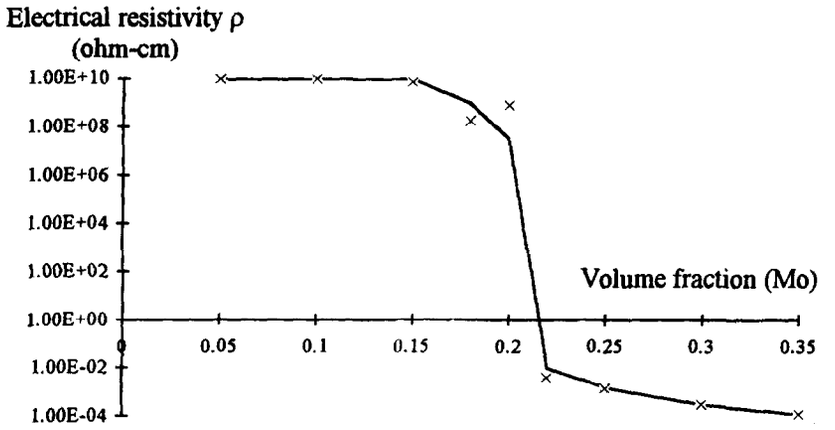

Fig. 4. Variation of the electrical resistivity ρ of Aln–Mo composites, as a function of molybdenum concentration.

Molybdenum particle growth is prohibited due to the high pressures employed during sintering and the absence of sufficient contact between the molybdenum particles at sintering temperatures, whereas the angular structure of initial molybdenum powder particles is not preserved in the sintered structure. The particles have a tendency to acquire rounded forms which are thermodynamically more stable and the particle size is increased wherever a contact is established.

3 Electrical Resistivity Measurement

Electrical resistivity measurements were performed with the help of four-point Valdes method. In this method we employed four fine needle-shaped points in line, 1 mm apart, which were brought in contact with the sample surface. Two outer contacts were used to inject current I into the sample and inner contacts gave the potential difference v between the given points. The electrical resistivity ρ is calculated using a simple Valdes relation which can be written in the case of four points in line, separated through a distance d, as:

$$\rho = 2\ \pi d(v/I) \qquad (1)$$

Samples were prepared under conditions similar to those mentioned in Section 2.2. Molybdenum concentration in the samples was varied from 5 to 35% by volume. Samples, in the form of discs having 30 mm diameter and 4 mm thickness, were rectified and polished to obtain a clean parallel surface.

Table 3 gives the values of current intensity I, potential difference v and electrical resistivity ρ, measured by the above-mentioned technique, for samples having different volume fractions of metallic phase. The results show that the value of electrical resistivity falls rapidly when the volume fraction of molybdenum in the composite increases from 0·2 to 0·22. The same results are illustrated in the form of a semilogarithmic curve in Fig. 4, which shows the variation of electrical resistivity of AlN–No composites as a function of molybdenum volume fraction. This insulator to conductor transformation can be attributed to a percolation phenomenon due to the presence of metal particles in the ceramic matrix. Earlier studies[12,13] showed the same type of results in the case of composites containing Ni, Pd, Cu and Ag particles dispersed in NiO matrix. As can be seen in Fig. 3, the metal particles for a 25% volume concentration are not in contact with each other. Electron conduction in this case can only take place through a modification in AlN matrix properties, produced by the presence of a ceramic–metal interface.

Table 3. Values of electrical resistivity for different AlN–Mo composites, measured by the four-point Valdes method

Ref.	*Volume fraction of AlN*	*Volume fraction of Mo*	*Current intensity, I (A)*	*Potential difference, v (V)*	*Electrical resistivity, ρ (Ω cm)*
AM5	0·95	0·05	$0{\cdot}1 \times 10^{-9}$	0·8	$8{\cdot}6 \times 10^{9}$
AM10	0·9	0·1	$0{\cdot}1 \times 10^{-9}$	0·824	$8{\cdot}85 \times 10^{9}$
AM15	0·85	0·15	$0{\cdot}1 \times 10^{-9}$	0·65	$6{\cdot}98 \times 10^{9}$
AM18	0·82	0·18	$0{\cdot}1 \times 10^{-9}$	0·026	$0{\cdot}16 \times 10^{9}$
AM20	0·8	0·2	$0{\cdot}1 \times 10^{-9}$	0·12	$0{\cdot}75 \times 10^{9}$
AM22	0·78	0·22	0·1	$6{\cdot}3 \times 10^{-4}$	$3{\cdot}95 \times 10^{-3}$
AM25	0·75	0·25	0·1	$2{\cdot}2 \times 10^{-4}$	$1{\cdot}41 \times 10^{-3}$
AM30	0·7	0·3	0·1	5×10^{-5}	$3{\cdot}14 \times 10^{-4}$
AM35	0·65	0·35	0·1	2×10^{-5}	$1{\cdot}25 \times 10^{-4}$

3.1 Percolation through a space charge layer

When two surfaces having different work functions are in contact, a charge transfer takes place in such a manner that the surface having higher value of work function is enriched in electrons. This transfer of charge at the interface between a metallic particle and the ceramic matrix is responsible for the formation of a space charge layer[12] at the particle surface. The electrical resistivity in such a system depends upon the electronic concentration in the space charge layer, the thickness of the space charge layer and the distance between the two particles.

When the distance between metal phase particles in the solid material is decreased due to an increase in the metal phase concentration, the free electron population in the region between the two particles is increased. Critical concentrations corresponding to electronic conduction in ceramic–metal composites depend essentially on the nature of the interface. Any type of interaction at the interface or the presence of a secondary phase between the two surfaces, formed during sintering, will modify to a large extent the nature of the interface and consequently the electrical and thermal properties of such a material will be modified. Results of electrical resistivity measurements for the AlN–Mo composites show, knowing that the percolation threshold is situated around 22% of metallic phase, that no reaction takes place between molybdenum grains and the AlN matrix during sintering that is capable of modifying the interface properties, and thus the electrical properties, in a significant manner.

4 AlN–Mo Interface

The physical and chemical conditions of adhesion between AlN and molybdenum metal have been studied by Quériaud and Lefort.[9] Their samples were obtained by placing two discs, one of molybdenum and the other of aluminium nitride, one on top of the other and treating under pressures of 20 MPa for 4 h under flowing argon atmosphere at 1850°C. Adhesion studies at the interface showed that only AlN samples sintered without additives and those with 3% Y_2O_3 remained attached with molybdenum. Samples of aluminium nitride sintered in the presence of CaO showed very little adhesion to molybdenum. In all cases, AlN samples with higher additive content (10 to 15% by weight) do not show any adhesion to molybdenum. According to these results,[9,14] we can say that the presence of oxide secondary phases is undesirable for a good quality AlN–Mo interface.

EDAX (energy dispersion analysis by X-rays) at the AlN–Mo interface, performed by Quériaud[14] on the samples mentioned previously, after treatment at 1850°C, showed the diffusion of a small quantity of aluminium (less than 4 at%) over a thickness of a few μm inside the molybdenum layer. In cases where a secondary phase was present, molybdenum diffused into the liquid oxide phase with concentrations up to 9 at%. However, no molybdenum traces were found inside the AlN grains. These results can be explained by the fact that the diffusion either takes place after slight decomposition of AlN, which is possible under conditions described by Quériaud,[9,14] or in the presence of an oxide phase present at the grain boundaries.

Microanalysis EDAX studies undertaken in the case of AlN–Mo composites obtained after hot pressing under conditions specified in the earlier part of this work, do not show the presence of free aluminium. Aluminium signalled by Quériaud[14] is provided by a slight decomposition of AlN under argon at 1850°C signalled by different authors.[15] This difference in results can be explained by the difference in sintering conditions of AlN–Mo composites and those employed by Quériaud during his experimentation (sintering under nitrogen and at 1800°): the latter prevents AlN decomposition and, as a result, the diffusion of free aluminium inside molybdenum grains is prohibited.

X-ray diffraction analysis of the sintered AlN–Mo surface does not show any extra peaks except those attributed to AlN and Mo. The presence of a stable oxide layer at the AlN grain surface, belonging to the Al–O–N system and being favourable for good densification of AlN in the absence of sintering additives, has been shown by many authors.[10,16] This phase cannot be identified on the X-ray diffraction pattern because it exists superficially in very small quantity and perhaps in the amorphous state, which makes it impossible to be identified by this technique. Its formation can be explained by the presence of oxygen (1·8% by weight), the majority of which is found at the surface of AlN powder particles in the form of aluminium oxide. Under these conditions we can admit that the adhesion between the molybdenum grains and the AlN matrix is produced through a fine oxide or oxynitride layer. We thus find a complex three-phase system which is composed of:

(1) a nitride phase (AlN), which is the majority phase and which forms the matrix;
(2) a metallic phase (Mo), which is dispersed in the matrix, having particle sizes between 5 and 45 μm; and
(3) a secondary phase of the Al–O–N system, in the form of a fine superficial layer, whose quantity and composition depend on the quantity of oxygen in the starting powder and the sintering conditions.

The presence of a small quantity of oxygen is helpful in the sintering process[16] but, on the other hand, a high oxygen content can produce negative effects which could result in modification of the AlN–Mo interface due to the presence of an interphase and in eventual degradation of electrical and thermal properties. Studies[15] on the properties of sintered aluminium nitride have shown that good densification during sintering is obtained for oxygen concentrations in AlN powder of around 0·6 to 1·4% by weight.

5 Conclusions

In an attempt to improve the mechanical, thermal and electrical properties of pure aluminium nitride, it is found useful to add a refractory metal dispersed phase in the AlN matrix. Molybdenum seems to be the best choice as a refractory metal, due to its good thermal and electrical properties, its melting point of 2610°C and its thermal expansion coefficient close to that of aluminium nitride. Powder mixtures of AlN–Mo were sintered with AlN as the majority phase, varying the molybdenum concentration between 5 and 35% by volume. Hot pressing was performed under conditions similar to those employed for pure AlN powders. Samples sintered under these conditions present a homogeneous structure, very little open porosity and more than 94% densification rate.

Electrical resistivity measurements were performed using the four-point Valdes technique. Results have shown that the electrical resistivity varies as a function of molybdenum concentration and that the material becomes an electrical conductor in the case of molybdenum volume fractions of more than 0·22. This insulator to conductor transformation is attributed to a percolation phenomenon in the metal phase. The presence of a space charge layer at the AlN–Mo interface modifies the electronic structure in the region closer to the interface and thus participates in the conduction of electrons between the metal phase. Consequently, the material becomes a conductor with concentrations of metallic phase for which the metallic particles are not really in contact.

X-ray studies of the sintered AM25 surface have shown the absence of any secondary phase at the interface between AlN matrix and molybdenum particles. Phase studies undertaken for the ternary system Mo–Al–N are in conformity with these results.[17] The presence of a very fine oxynitride layer at the AlN grain boundaries, which has been verified by earlier studies, aids in the densification of AlN grains during sintering and is probably helpful in obtaining an adherent interface between AlN grains and Mo particles. The presence of this layer does not affect, in a notable manner, the interface properties, the electrical conductivity or the critical metal phase concentration corresponding to the percolation threshold. In any case, a secondary oxide phase present in higher quantities would be expected to modify the AlN–Mo interface to a large extent, and degrade the electrical and thermal properties.

References

1. Slack, G. A., Non metallic crystals with high thermal conductivity. *J. Phys. Chem. Solids*, **34** (1973) 132–5.
2. Partridge, G., Ceramic materials possessing high thermal conductivity. *Adv. Mater.*, **4**(1) (1992) 51–4.
3. Slack, G. A., Tanzilli, R. A., Pohl, R. O. & Vandersande, J. W., The intrinsic thermal conductivity of AlN. *J. Phys. Chem. Solids*, **48**(7) (1987) 641–7.
4. Böcker, W. D. G., Hamminger, R., Heinrich, J., Huber, J. & Roosen, A., Covalent high performance ceramics. *Adv. Mater.*, **4**(3) (1992) 169–78.
5. Sheppard, L. M., Aluminium nitride: a versatile but challenging material. *Ceram. Bull.*, **69**(11) (1990) 1801–12.
6. Hirano, M., Kato, K., Isobe, T. & Hirano, T., Sintering and characterisation of fully dense aluminium nitride ceramics. *J. Mater. Sci.*, **28** (1993) 4725–30.
7. Witek, S. R., Muller, G. A. & Harmer, M. P., Effects of CaO on the strength and toughness of AlN. *J. Am. Ceram. Soc.*, **72**(3) (1989) 469–73.
8. Mroz, T. J. & Groat, E. A., Fabrication and properties of AlN–SiC whisker composites. In *Advances in Ceramic Matrix Composites, Ceram. Trans.*, **38** (1993) 375–82.
9. Lefort, P. & Queriaud, R., Compatibility between molybdenum and aluminium nitride. *J. Eur. Ceram. Soc.*, **13** (1994) 329–33.
10. Ado, G., Bernache, D., Billy, M., Han, K. S. & Lefort P., Mécanisme de frittage sous charge du nitrure d'aluminium et de l'oxynitrure (AlON). *Rév. Chim. Minér.*, **22** (1985) 473–83.
11. Kurokawa, Y., Utsumi, K. & Takamizawa, H., Development and microstructural characterisation of high thermal conductivity aluminium nitride ceramics. *J. Am. Ceram. Soc.*, **71**(7) (1988) 588–94.
12. Kieffer, J. & Wagner Jr, J. B., Electrical conductivity of metal–metal oxide composites. *J. Electrochem. Soc.*, **135**(1) (1988) 198–205.
13. Dudney, N. J., Effect of interfacial space charge polarisation on the ionic conductivity of composite electrolytes. *J. Am. Ceram. Soc.*, **68**(10) (1985) 538–45.
14. Queriaud, R., PhD thesis, University of Limoges, France, 1991.
15. Yefsah, S., PhD thesis, University of Limoges, France, 1984.
16. Sakai, T & Iwata, M., Effect of oxygen on sintering of AlN. *J. Mater. Sci.*, **12** (1977) 1659–65.
17. Schuster, J. C. & Nowotny, H., Phase relationships in the ternary systems (V, Cr, Mo, Mn, Re)–Al–N. *J. Mater. Sci.*, **20** (1985) 2787–93.

Journal of the European Ceramic Society 16 (1996) 745–752

0955-2219(95)00187-5
0955-2219/96/$15.00

Nickel–Alumina Bonds: Mechanical Properties Related to Interfacial Chemistry

P. Lourdin, D. Juvé & D. Tréheux

Ecole Centrale de Lyon, Laboratoire Matériaux, Mécanique Physique, URA CNRS 447 69131 Ecully Cédex, France

(Received 13 March 1995; revised version received 5 October 1995; accepted 12 October 1995)

Abstract

Mechanical properties of solid state bonded $Ni–Al_2O_3$ interfaces have been investigated as a function of several bonding parameters (temperature, pressure, time) and purity of the starting alumina.

It has been shown that they depend upon the plastic deformation of the metal, on the damages induced at the ceramic surface and on both the nature and amount of interfacial phase that appears during the bonding process.

According to the processing conditions used, the nickel aluminate spinel has not been found at the interface, but it has been shown that bonding arises from the magnesium aluminate spinel or sodium magnesium silicate and that nickel silicide is formed on the nickel side of the bond near by the interface.

Les propriétés mécaniques d'interfaces $Ni–Al_2O_3$ obtenues à l'état solide ont été étudiées en fonction des différents paramètres d'élaboration (température, pression, temps) et de la pureté de l'alumine de départ.

Il a été montré qu'elles sont fonction de la déformation plastique du métal, des défauts créés à la surface de la céramique ainsi que de la nature et de la quantité de phase interfaciale qui apparait au cours du processus de liaison.

Compte tenu des conditions expérimentales utilisées, la spinelle $NiAl_2O_4$ ne se forme pas à l'interface mais il a été montré que la liaison s'établit par l'intermédiaire soit de la spinelle $MgAl_2O_4$ soit d'un silicate mixte de sodium et de magnésium et qu'un siliciure de nickel se forme dans le nickel près de l'interface.

1 Introduction

Modern engineering components that often contain a metal bonded to a ceramic have been subject to extensive studies according to the variety and the complexity of the phenomena controlling the mechanical behavior of the interface.

When solid state bonding is used to obtain a metal–ceramic interface, the fracture resistance measured by conventional tests (shear, tensile tests) strongly depends upon the defects present along the interface such as pores and unjoined areas,[1] damage and cracks induced either by thermal stresses[2] or by friction between the two materials[3] especially in the ceramic close to the interface. Chemical interactions at the interface also play an important role. It has been shown that contaminants at the materials surfaces such as carbon, sulphur and chlorine atoms generally reduce the adhesion.[4] On the other hand, during bonding, chemical reactions often occur at the metal–ceramic interface influenced by the materials themselves, the welding temperature and the atmosphere.[5–7] The bond quality depends upon the reactions and on the properties of the reaction products. In addition, the diffusion of the metallic species in the ceramic body can reduce the toughness of the ceramic close to the interface which then affects the mechanical resistance of the bond.[8] Since bonds are often exposed in service to both temperatures and environments different from the one used for their formation, chemistry at the interface is likely to change, as well as the mechanical properties.[9] The nickel–alumina interface made by solid state bonding has been the subject of many studies.[3,5,10–16] From a physical point of view, it has been shown that strong bonds can be obtained when intimate contact between the two materials is effective depending upon the plastic deformation of the nickel, that varies with the applied pressure. Consequently the yield strength of the metal (function of the temperature and fabricating conditions) has to be taken into account as well as the friction coefficient at the interface and the thickness of the metal bonded.[3]

From a chemical point of view, the conditions leading to a reaction between solid nickel and alumina are now very well known: the aluminate formation ($NiAl_2O_4$) requires a threshold concentration of oxygen dissolved in the metal which is of the order of 1/5 the solubility limit.[5] From a mechanical point of view, contradictory results are published in the literature. Ni–Al_2O_3 bonds are reported to be either strong[11,14] or weak.[12,13] In both cases, the mechanical properties obtained were explained by the presence of nickel aluminate spinel at the interface. This paper reports results of the mechanical properties of solid state bonded Ni–Al_2O_3 interfaces investigated at room temperature with flexure and tensile tests. It focuses on the interfacial chemical dependence of interfacial fracture resistance.

2 Experimental Procedure

Two kinds of polycrystalline alumina have been investigated in this study: A99 'standard' (S) and 'high purity' (HP) from SCT (Société des Céramiques Techniques, Tarbes, France) and used as sintered, the average roughness value being about 0·3 μm R_a. The compositions of the starting alumina powders are given in Table 1. In both cases MgO has been introduced to inhibit the growth of alumina grains on sintering.

The nickel used has the following composition: Cu<0·01, Si=0·14, C=0·051, Mn=0·08, Fe=0·98, Co<0·01, Ni balance. Push-out tensile test samples (Fig. 1) were fabricated in order to measure the fracture strength of bonds and the four-point bending test (delamination specimen) (Fig. 2) was also performed to measure the interfacial fracture energy G_c.

The Al_2O_3–Ni–Al_2O_3 assembly was solid state bonded in a dynamic vacuum (5 10^{-3} torr) in the range 1050–1410°C for 1–48 h, with an applied pressure varying from 2 to 21 MPa. The dimetral ratio r/t (radius/thickness) of the metallic foil was varied in the range of 5–25. The heating rate to the bonding temperature was 150°C/h, the cooling rate to room temperature was 200°C/h. The applied pressure was maintained during all the thermal cycle. Following mechanical testing, SEM observations coupled with EDS analyses and grazing incidence X-ray scattering (GIXS) were carried out on both alumina and nickel sides of the bond after the nickel has been removed by peeling to detect the presence of interfacial phases.

3 Results

3.1 Pressure and temperature effects

From push-out specimens made with S alumina, the trends in bond strength with applied pressure and temperature are shown in Fig. 3.

The bond strength firstly increases with increasing values of applied pressure and temperature, then decreases at constant time and r/t ratio. Thermally actived microdeformation and diffusion act simultaneously to achieve the contact between metal and ceramic.[17] Plastic deformation of the metal is needed depending on the applied pressure, the yield strength of the metal (function of the temperature, work hardening), the friction

Table 1. Analysis of Al_2O_3 powders

	A99 standard (ppm) (S)		*High purity (ppm) (HP)*	
	Specification	*Typical value*	*Specification*	*Typical value*
Na_2O	<800	700	<60	40
K_2O	<5	<15	<30	<20
CaO	<220	<180	<30	20
SiO_2	<560	400	<100	50
Fe_2O_3	<360	300	<30	<10
Cr_2O_3	<50	10	<30	10
MgO	2000		2000	

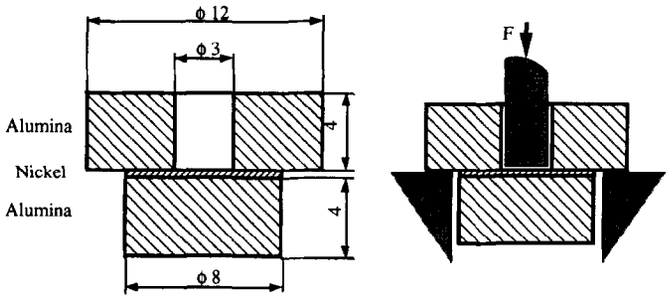

Fig. 1. Push-out specimen. Loading rate: 0·1 mm/min.

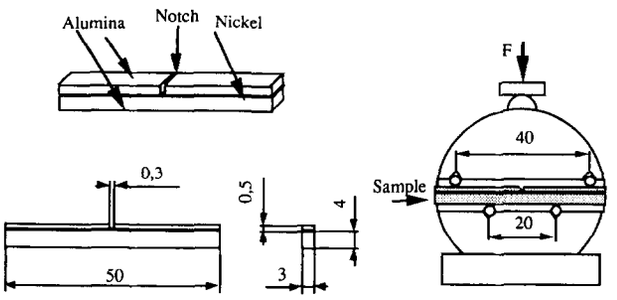

Fig. 2. Delamination specimen. Loading rate: 0·1 mm/min.

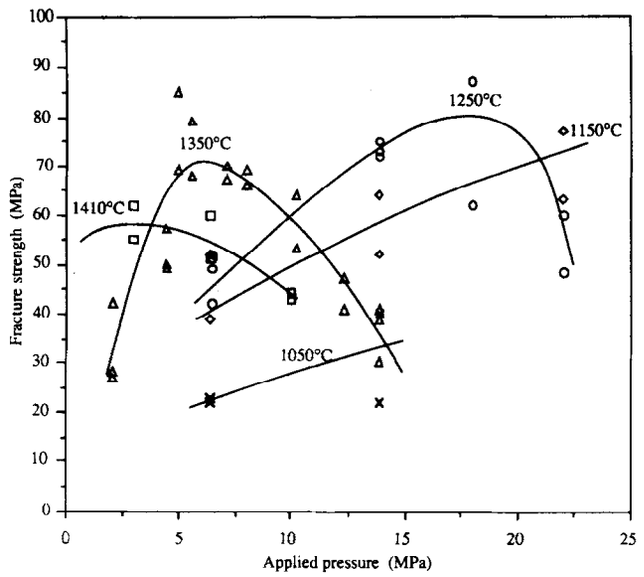

Fig. 3. Bonding strength versus applied pressure at different bonding temperatures, (S alumina).

coefficient at the interface and the dimetral ratio of the foil.[18] It can lead to full contact between the two materials without any overflowing of the metallic foil out of the interface. In these conditions, the maximum bond strength is obtained.

3.2 Influence of *r/t* ratio

It is shown in Fig. 4 that the parameter *r/t* acts on the bond strength in the manner described for both applied pressure and temperature. When the applied pressure is higher than that required to achieve the full contact, the metal is squeezed outside the interface. Sliding damages the outer junction ceramic surface by friction weakening the bond. Examples of such edge defects are shown in Fig. 5.

Whatever applied pressure, time and *r/t* ratio, up to 1150°C, bonds always fail within the interface. GIXS and EDS analyses performed on both

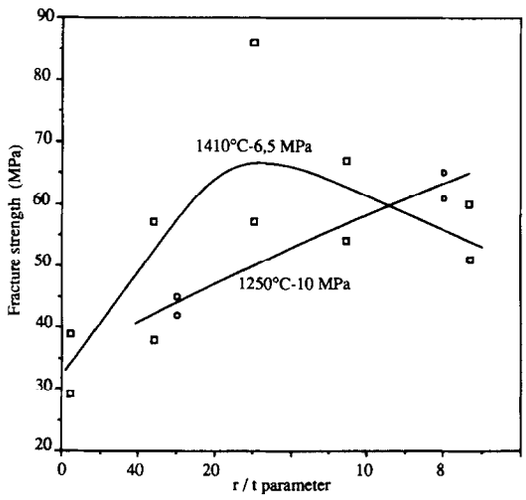

Fig. 4. Bonding strength versus *r/t* ratio (radius/thickness), (S alumina).

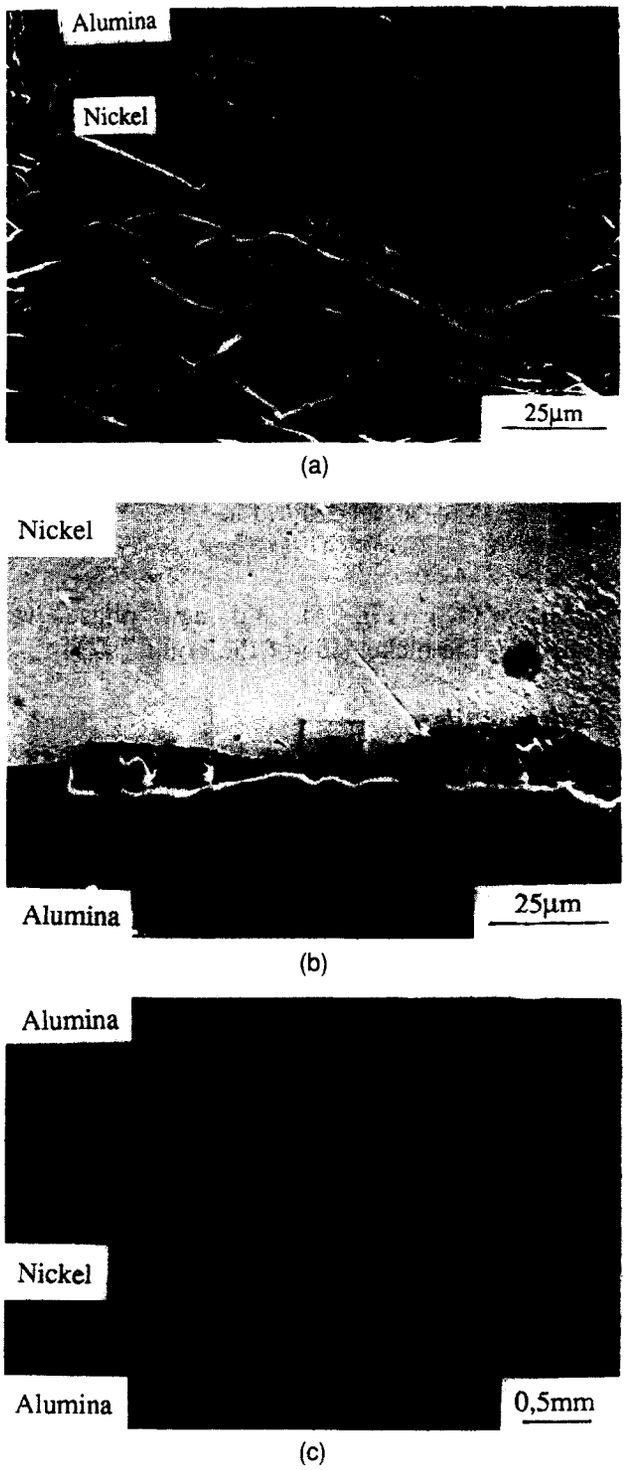

Fig. 5. Examples of flaws observed at the edge of Ni/S Al_2O_3 interfaces: (a) scratches on the nickel surface at high temperatures; (b) alumina grains detached by nickel on sliding at medium temperatures; (c) external 'chipping' of alumina at low temperatures.

alumina and nickel contact surfaces after a bonding time of 1 h indicate that only Al_2O_3 and Ni are present. Above 1150°C, the bonds fail within alumina at very different strength levels. At 1250°C and above, a crystalline film has been detected at the interface for a bonding time one hour long. Although the diffraction patterns were complex, the best fit between ASTM data and patterns was obtained for a sodium magnesium silicate

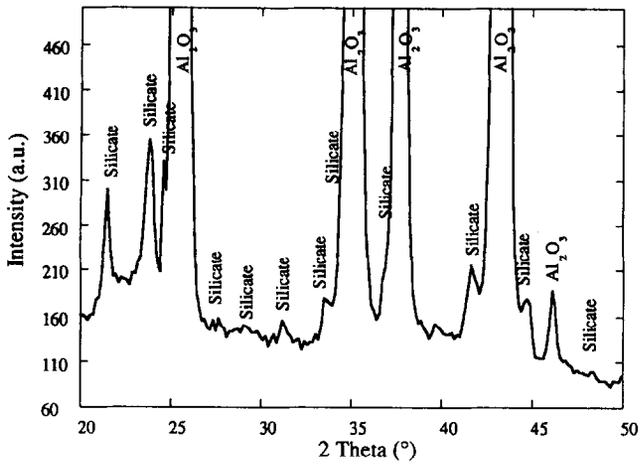

Fig. 6. GIXS diffraction pattern of standard alumina bonding area, (1350°C, 1 h).

($Na_2Mg_5Si_{12}O_{30}$) (Fig. 6). No new phase was detected on the nickel side of the bond.

3.3 Effect of time

Varying the bonding time at 1250°C, mechanical trends similar to those previously described were found (Fig. 7). In this case, the pressure chosen (6·5 MPa) was not suitable to produce a plastic macro-deformation of the metal. So the decrease observed in the bond strength associated to an interfacial fracture cannot be attributed to edge defects: other factors govern the mechanical resistance of the bond. SEM observations performed on the standard alumina side of bonds made after 10 and 48 h indicate that the contact area includes two zones having different morphologies, an inner zone (1), where alumina grains are badly defined and an outer one (2) where alumina grains are very well defined (Fig. 8). The extent of each zone varies with the duration of bonding, the inner zone being strongly reduced by the time. Some triple grain boundary points were found to be free of second phase, as previously observed by Drillet.[15]

GIXS analyses reveal after 10 and 48 h that the interfacial film corresponds to a spinel phase, $NiAl_2O_4$ or $MgAl_2O_4$, since both have the same lattice parameter. Nevertheless, as the characteristic blue colouration of $NiAl_2O_4$ was not observed, $MgAl_2O_4$ was assumed to be the compound present. It is confirmed by EDS analysis, since Mg has been detected in the bonding area but not Ni. Also, Mg concentration in the inner contact area was important while no Mg was detected in the outer area. Furthermore, no Ni, nor Ca, Si or Na were detected at the interface within the resolution limits of EDS (Fig. 9). On the nickel side of the bond a nickel silicide (Ni_3Si) was detected by GIXS.

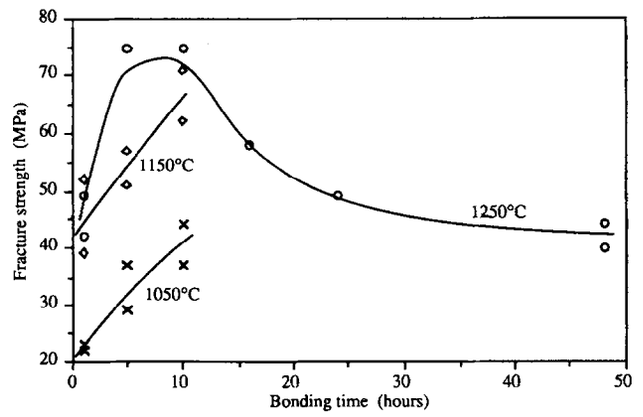

Fig. 7. Bonding strength versus bonding time. Applied pressure: 6·5 MPa, (S alumina).

In conclusion, for standard alumina, with a varying bonding time at 1250°C, it has been shown that the nature of the interfacial film changes from silicate, (1 h) to spinel, (5–48 h) and so the bonding strength which is first increased from 45 to about 75 MPa and then decreased to about 40 MPa, though the chemistry at the interface seems to be the same. According to the previous observations it is suggested that the interfacial area covered with $MgAl_2O_4$ (zone 1 Fig. 8) is responsible for the mechanical resistance of the bond. In support of this, the extent of zone 1 has been measured on bonds performed at 1250°C at 5, 10 and 48 h. Then the 'true' fracture strength was calculated with respect to the area measured but not to the macroscopic initial area (43·2 mm^2) of contact as for Fig. 3 (that leads to an apparent fracture strength). The results are given in Table 2. In all the cases the maximum strength value was obtained showing that the bond resistance is proportional to the area covered with $MgAl_2O_4$.

Using the four-point flexure delamination test[2] which has a mode mixity angle $\Psi \approx 45°$ (Fig. 2), the interfacial fracture energy of bonds made in the range 1050–1350°C was measured. It is shown in Fig. 10 that the maximum fracture energy (30 J m^{-2}) is reached at about 1150°C.[3] This temperature is the threshold temperature for the interfacial microstructure leading to the maximum bond strength to occur.

3.4 Role of alumina

Bonds made with high purity alumina with processing conditions identical to those precedently described, always fail within the interface at strength levels 30–60% smaller than those measured for standard alumina as shown in Fig. 11. As for S alumina, it is shown in Fig. 12 that the morphology of the HP alumina contact surface of a sample bonded at 1400°C during 1 h does not correspond to that of the starting polished surface and seems also covered with a phase. GIXS and EDS analyses indicate the presence of $MgAl_2O_4$ on the alumina side and of Ni_3Si on the nickel side of the bond (Fig. 13).

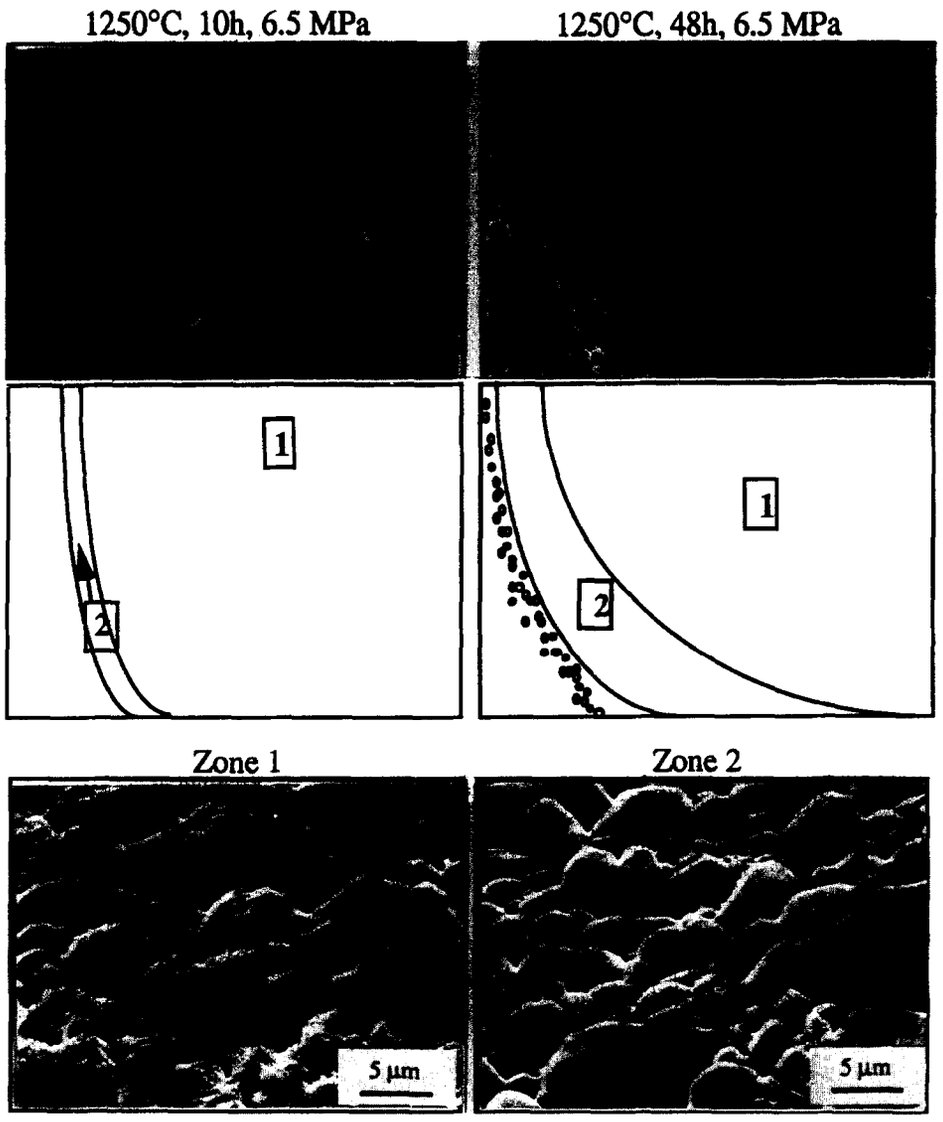

Fig. 8. SEM micrograph and repartition of zones 1 and 2 at the standard alumina interface.

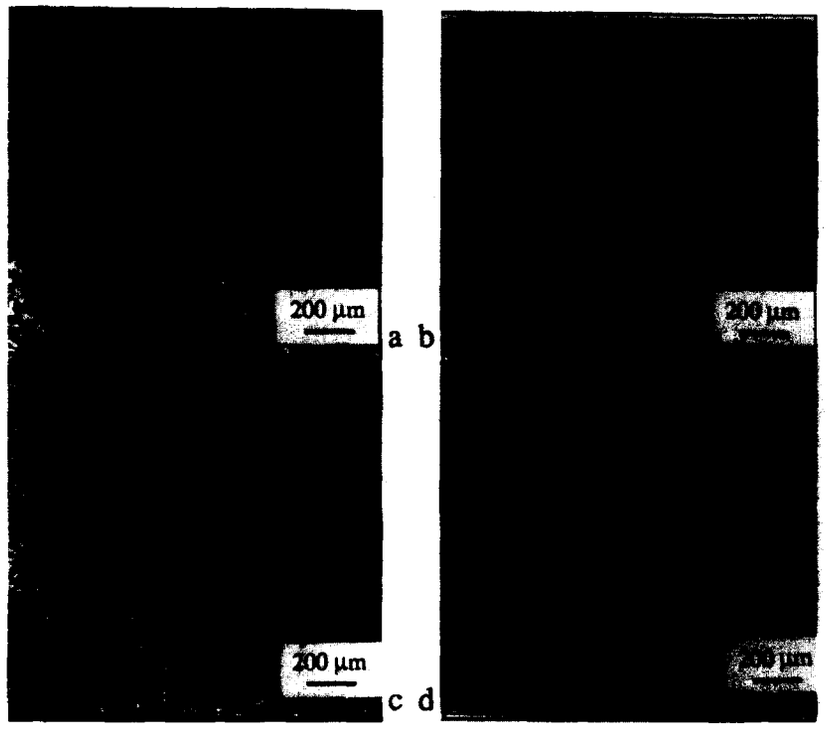

Fig. 9. Standard alumina area of contact after bonding at 1250°C under 6·5 MPa during 48 h: (a) SEM micrograph; (b) Mg map; (c) Al map; (d) Ni map.

Table 2. Fracture strength associated to the area covered with magnesium aluminate spinel

Time at temperature	*Surface of zone 1 (mm^2)*	*Fracture strength (MPa)*
	Maximum contact area:	
5 h 1250°C	43·2	75
10 h 1250°C	41·6	76
48 h 1250°C	35·5	60

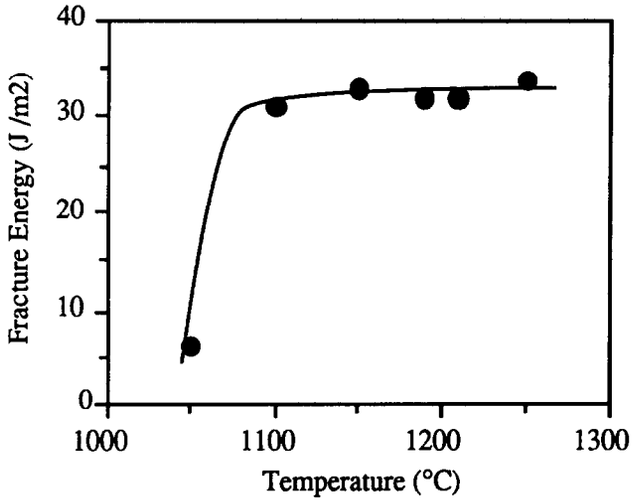

Fig. 10. Interfacial fracture energy versus bonding temperature. S alumina/Ni, 4 MPa, 0 h.

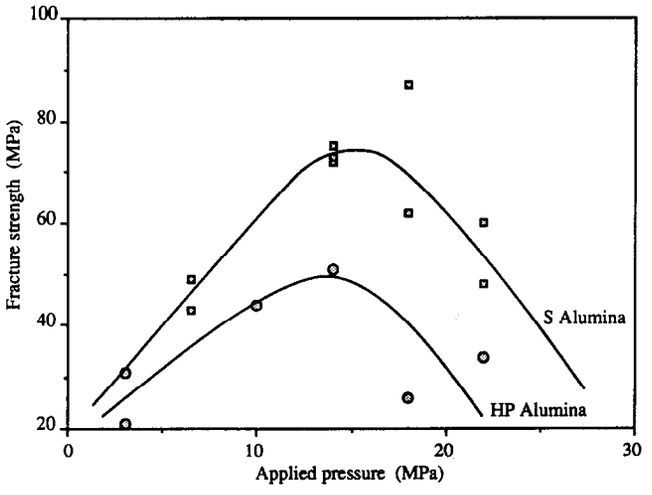

Fig. 11. Bonding strength versus applied pressure. 1250°C, 1 h, Ni = 0·5 mm (r/t = 5).

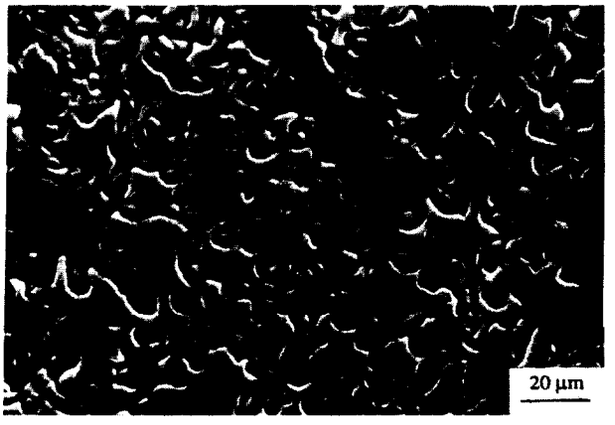

Fig. 12. SEM micrograph of high purity alumina bonding area.

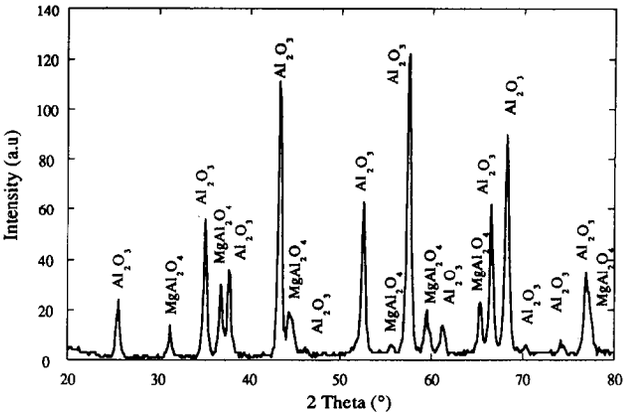

Fig. 13. GIXS diffraction pattern of high purity alumina bonding area (1400°C, 1 h).

4 Discussion

The experimental conditions used in this study to obtain Ni–Al_2O_3 bonds have not led to the formation of $NiAl_2O_4$ at the interface whatever the starting alumina (HP or S) but other, different phases have been identified.

Up to 1150°C, no new phases have grown at the interface on bonding, only nickel and alumina were observed.

Above 1150°C, it is suggested that a capillary mechanism acts firstly on bonding, favouring the migration of secondary phase material from the alumina triple grain boundaries points, allowing high concentrations of impurity at the interface. Then, reactions between the different components lead to the growth of new phases which vary with bonding time, temperature and alumina.

After 1 h, since 1250°C has been identified on the sides of the interface:

— in the case of HP bonds, magnesium spinel and nickel silicide
— in the case of S bonds, magnesium silicate and nickel

When bonding time is increased, magnesium spinel and nickel silicide have been observed for S bonds too.

The two aluminas studied contain the same amount of MgO, in return the quantity of SiO_2 is lower for the HP alumina than for the S alumina.

It is then propounded that the bonding arises firstly from magnesium silicate whatever the

purity of the starting alumina, the amount of which depends only on the initial SiO_2 level, the quantity of silicate formed being smaller with the HP alumina than with the S alumina. All the silicate has quickly transformed into spinel in the former, while it was always observed in the latter after a bonding time of 1 h.

Increasing bonding time diffusion mechanisms at the multiphase interfacial region and reactions between the alumina and the silicate lead to $MgAl_2O_4$, the silicon so released diffuses into nickel where it forms a silicide.

Towards the mode of fracture and the fracture strength measured, Ni–Al_2O_3 bonds also exhibit drastic changes with the solid state bonding variables and alumina purity. Such mechanical features can be connected with the nature and amount of the interfacial products formed, for bonds without edge defects.

SEM observations of S alumina contact area after a bonding time 1 h long, have shown that the alumina surface in the contact was progressively covered with magnesium silicate up to 1250°C. At this temperature the overall contact surface contains silicate and the maximum fracture energy G_c is reached (30J m^{-2}). Up to this temperature failures are adhesive (within the interface), above they are cohesive (within bulk alumina).

A major question is then asked: why does the $MgAl_2O_4$ become unstable in the time leading to debonding? The mechanism by which $MgAl_2O_4$ decomposes is not yet understood. It is suggested that oxygen is the determining factor since $MgAl_2O_4$ progressively disappears from the periphery to the middle of the junction: the outer region of the bond is in contact with an atmosphere having an oxygen level smaller than that required to stabilize the magnesium spinel. Such an hypothesis is consistent with other results and analyses that clearly show the critical role of oxygen in stabilizing spinels such as $CuAlO_2$, $NiAl_2O_4$ and $FeAl_2O_4$.[5–7]

5 Conclusion

The results presented raise the importance of both physical and chemical effects on the mechanical properties of metal–ceramic bonds examplified by Ni–Al_2O_3 interfaces.

From a physical point of view, to obtain strong Ni–Al_2O_3 interfaces using the solid state bonding process, a pressure leading to the greatest contact area between the two materials is needed. However it cannot give any flaws nor decohesion at the edge of the bond where high residual and applied stress are located. These defects acting as notches will be the fracture origin.[19,22]

From a chemical point of view, no direct reaction between Ni and Al_2O_3 has been observed. In our case (vacuum 5 10^{-3} torr), bonding depends only on the sintering alumina additives, especially MgO and SiO_2, capable of reaching the interface. Magnesium silicate and magnesium spinel have been observed at the alumina side and nickel silicide on the nickel side. It has been also shown that magnesium-based phases were metastable.

Mechanical properties of bonds are connected with the nature and amount of interfacial phases when physical defects are avoided. Providing that all the contact area between alumina and nickel is covered with an interfacial film magnesium silicate is associated with cohesive failures whereas magnesium spinel and nickel silicide lead to adhesive failures.

Acknowledgements

The authors wish to thank SCT for financial support and G. Thollet for EDS analyses.

References

1. Reimanis, I. E., Pore removal during diffusion bonding of Nb–Al_2O_3 interfaces. *Acta Metall. Mater.*, **40** (1992) S67.
2. Evans, A. G., Dalgleish, B. J., Charalambides, P. G. & Rühle, M., The fracture energy of bimaterials interfaces. *Mater. Sci. Engng*, **53** (1990) A126.
3. Lourdin, P., Les liaisons Ni/Al_2O_3 à l'état solide. Elaboration, état des contraintes thermiques, comportement mecanique. Thesis ECL No 92–31, 1992.
4. Korn, D., Elssner, G., Fischmeister, H. F. & Rühle, M., Influence of interface impurities on the fracture energy of UHV bonded niobium–sapphire bicrystals. *Acta Metall. Mater.*, **40** (1992) S355.
5. Trumble, K. P. & Rühle, M., The thermodynamics of spinel interphase formation at diffusion bonded Ni/Al_2O_3 interfaces. *Acta Metall. Mater.*, **39** (1992) 1915.
6. Trumble, K. P., Thermodynamic analysis of aluminate formation at Fe/Al_2O_3 and Cu/Al_2O_3 interfaces. *Acta Metall. Mater.*, **40** (1992) 105.
7. Béraud, C., Courbière, M., Esnouf, C., Juvé, D. & Tréheux, D., Study of copper-alumina bonding. J. Mater. Sci., **24** (1989) 4545.
8. Berroug, A., Juvé, D., Tréheux, D. & Moya, E. G., Silver–alumina solid state bonding: study of diffusion and toughness close to the interface. *J. European Ceram. Soc.*, **12** (1993) 385.
9. Allen, R. V. & Borbidge, W. E., Solid state metal ceramic bonding of platinium to alumina. *J. Mater. Sci.*, **18** (1983) 2835.
10. Klomp, J. T., Solid state bonding of metals to ceramics. *Science of Ceramics*, **5** (1970) 501.
11. Calow, C. A. Bayer, P. B. & Porter, I. T., The solid state bonding of nickel, chromium and nichrome sheets to α-Al_2O_3. *J. Mater. Sci.*, **6** (1971) 150.
12. Calow, C. A. & Porter, I. T., The solid state bonding of nickel to alumina. *J. Mater. Sci.*, **6** (1971) 156.
13. Vardiman, R. G., Preferred orientation of $NiAl_2O_4$ spinel grown on sapphire. *Mater. Res. Bull.*, **7** (1972) 699.
14. Bailey, F. P. & Bordidge, W. E., Solid state metal–ceramic bonding. *Mater. Sci. Res.*, **14** (1981) 525.

15. Drillet, P., Contribution à l'étude des liaisons céramique-métal: élaboration et étude structurale d'interfaces alumine/nickel. Thesis, University of Rennes, 1992.
16. Wan, C., Etude de la liaison métal-alumine élaborée par voies liquide et solide: mouillage, thermocompression. Thesis, University of Grenoble, 1992.
17. Derby, B., The formation of metal/ceramique interfaces by diffusion bonding. *Acta Scripta Metall. Proceedings series*, **4** (1991) 161.
18. Avitzur, B., Limit analysis of disc and strip forging. *Int. J. Mach. Tool. Des. Res.*, **9** (1969) 165.
19. Dalgliesh, B. J., Lu, M. C. & Evans, A. G., The strength of ceramic bonded with metals. *Acta Metall.*, **36** (1988) 2029.
20. Evans, A. G., Lu, M. C., Rühle, M. & Schmauder, S., Some aspects of the mechanical strength of ceramic/metal bonded systems. *Acta Metall.*, **34** (1986) 1643.
21. Mader, W. & Rühle, M., Electron microscopy studies of defects at diffusion bonded Nb/Al_2O_3 interfaces. *Acta Metall.*, **37** (1989) 853.
22. Dalgleish, B. J., Trumble, K. P. & Evans, A. G., The strength and fracture of alumina bonded with aluminium alloys. *Acta Metall.*, **37** (1989) 1923.

Journal of the European Ceramic Society 16 (1996) 753–758

0955-2219(95)00188-3
0955-2219/96/$15.00

Growth, Preparation and Surface Modification of Microcrystalline Diamond Powder for the Synthesis of Diamond Ceramics

O. Semchinova,[a] D. Uffmann,[a] H. Neff[b] & E. P. Smirnov[c]

[a]Laboratorium für Informationstechnologie, Universität Hannover, Schneiderberg 32, 30167 Hannover, Germany
[b]TZN Forschungs- und Entwicklungszentrum Unterlüß GmbH, Neuensothrier Str. 18-20, 29345 Unterlüß, Germany
[c]Technological University, Moskovsky pr.26, 198013 St. Petersburg, Russia

(Received 30 June 1995; revised version received 6 October 1995; accepted 12 October 1995)

Abstract

Chemically modified microcrystalline diamond surfaces have been prepared and investigated on the basis of thermodesorption measurements, X-ray diffraction and X-ray photoemission spectroscopy. X-ray investigations and SEM-images show that the synthesized diamond powder consists of pure carbon crystals of cubic modification with unbroken facets. Investigation of acidic functional groups, having different oxygen content and bound on the diamond surface by an oxidizing process, was carried out by the method of neutralization with different alkaline reagents. It has been shown that the concentration of the groups neutralized by each reagent decreases as the temperature of the heat treatment during preparation is raised. Under thermal treatment, the oxy- functional groups decompose at T>600°C, leaving a hydrogen terminated diamond surface. Hydrogen desorbs at T>1000°C, thus generating an atomically clean surface, such as is required for direct bonding of the nano- and microcrystals during sintering.

Gegenstand der vorliegenden Veröffentlichung ist die Synthese von Diamantpuder, sowie dessen chemische Reinigung und Modifikation der Oberfläche. Chemisch modifizierte mikrokristalline Diamantoberflächen wurden präpariert und auf der Basis von Thermodesorptionsmessungen, Röntgenbeugung und Röntgen-Photoemissionsspektroskopie untersucht. Die Röntgenuntersuchungen und rasterelektronenmikroskopische Aufnahmen zeigen, daß die synthetisierten Puder aus reinen Kohlenstoffkristallen kubischer Modifikation mit ungebrochenen Facetten bestehen. Mit Hilfe der Neutralisationsmethode wurde das Verhalten saurer funktionaler Gruppen mit unterschiedlichem Sauerstoffgehalt, die durch einen Oxidationsprozeß an der Diamantoberfläche gebunden wurden, unter Verwendung unterschiedlicher alkalischer Reagenzien untersucht. Es wurde gezeigt, daß die Konzentration der Gruppen für jede der verwendeten alkalischen Reagenzien mit zunehmender Temperatur bei der Wärmebehandlung abnimmt. Durch die Wärmebehandlung zersetzen sich die funktionalen Gruppen bei T>600°C und hinterlassen eine mit Wasserstoff terminierte Oberfläche. Der Wasserstoff desorbiert bei T>1000°C and erzeugt so eine atomar reine Oberfläche, die für die direkte chemische Bindung der Nano- und Mikrokristalle beim Sintern erforderlich ist.

Introduction

Due to its extreme physical properties, diamond is an attractive material for a broad range of applications that include high power, high temperature electronics and optical and superhard mechanical components.

Use of natural or synthetic diamond has already resulted in considerable progress towards the fabrication of discrete electronic devices.[1] High materials cost and device integration problems, however, limit single crystalline bulk diamond to very selected applications. A possible alternative, for some applications, is presented by polycrystalline diamond films[2] already employed as heat spreaders for the effective operation of high power semiconducter lasers. These films, made by chemical vapor deposition (CVD) posess a unique structure that is polycrystalline in nature but with some degree of orientation. However, these films are more expensive than such optical materials as zinc selenide and sapphire and have a very limited application. Because the production of diamond powder is already a relatively cheap high volume technology, the fabrication of bulk diamond ceramics may became an attractive solution to the problem. However, there are a number of technological

difficulties to overcome. Surface graphitization of the microcrystals during sintering is one example. In this work, the surface properties of chemically modified microcrystalline diamonds have been investigated. The surface phenomena, which are determined by the composition, structure and reactivity of the functional groups on the diamond surface are of great interest for the synthesis of diamond ceramics. Various functional groups have been added to the crystallite surface to minimize, and possibly avoid graphitization at the surface during the ceramic sintering process. The surface condition critically affects interfacial bonding between adjacent grains and, hence, the mechanical properties of the ceramic material itself.

There are several reasons for the uncommon occurrence of diamond:[3,4]

- —the entropy of diamond is less than the entropy of graphite by 0·78 cal/Kmol;
- —a large activation energy barrier exists between graphite and diamond, which prevents even small particles from forming at room temperature under equilibrium conditions. The density of diamond (3·51 g/cm^3) is significantly higher than that of graphite. Therefore the former becomes the equilibrium form of carbon only at high pressure.

These facts certainly also apply to the formation of the nano- and microcrystalline diamonds used in this study.

Figure 1 displays the phase diagram of carbon, summarizing the different experimental routes for diamond synthesis, and the phase separating lines, a, b, c.

Although diamond would be the stable phase at room temperature at a pressure of 2 GPa, it does not form under these conditions, primarily due to the extremely low kinetics of the process. Bulk diamond grows from graphite only when the temperature increases to at least several hundred degrees, or in the presence of a catalyst like molten nickel or manganese, with P>6 GPa and T>1200°C. The difficulties of diamond formation are largely due to the high thermodynamic stability of the graphitic planes, melting above 4000 K.[5] Thus the transformation from the planar sp^2-structure to the three-dimensional sp^3-network accounts for the required high temperature and pressure.

Experimental

In this work, microcrystalline diamond has been synthesized from doped graphite, employing the spontaneous crystallization method under high static pressure corresponding to zone 1 of Fig. 1. Crystal growth was carried out in an apparatus of

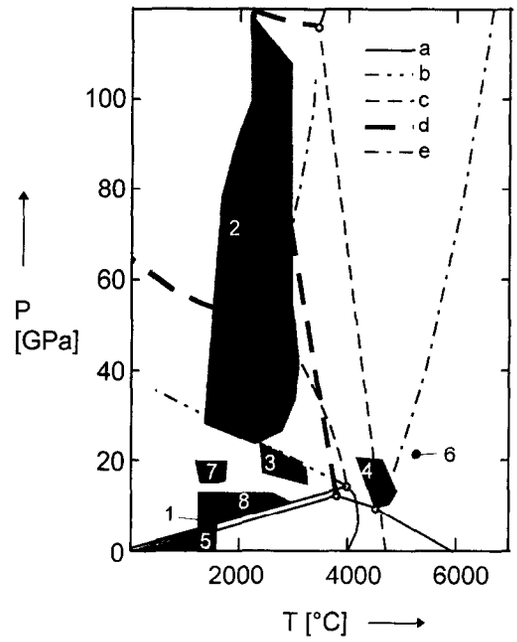

Fig. 1. P-T phase diagram of carbon. Experimental methods of diamond synthesis: (1) Statical method. (2) Dynamical method. (3) The method of the graphite–diamond direct junction at the statical conditions. (4) High-temperature synthesis using the detonation wave. (5) Epitaxial method. (6) The melt-solution method (from graphite). (7) Graphite Longsdailit direct junction at the statical conditions. (8) Direct synthesis from the elementary carbon and organical combinations. Phase separating lines: (a) Graphite–diamond, graphite–liquid. (b) Metastable graphite. (c) Diamond–liquid. (d) Diamond - metallic carbon. (e) Metallic carbon–liquid.

the anvil type. Growth conditions were as follows: pressure 4·5 GPa, temperature 1200°C. The Mn–Ni system has been used as the catalytic agent. The catalyst dissolves carbon from the graphitic phase, which then precipitates the 'allotropic' stable phase under equilibrium conditions, where diamond is formed. A defined size of the diamond particles can be achieved by controlling the duration of the process, usually around 2 min. Subsequently, the samples have been purified and classified by their grain size. Impurities from the metallic catalyst and graphitic fragments have been removed in a boiling acidic solution of H_2SO_4+ CrO_3.The surface of the microcrystals finally has been purified by boiling in a concentrated $HClO_4$ solution, which also forms the highly reactive oxygen groups on the surface of the microcrystals.

Diamond has a very high surface energy resulting in modified bonding properties upon exposure to chemically reactive species. To minimize the surface free energy, so-called functional groups are formed on the surface, which are strongly bonded to the outer carbon surface atoms. The removal (disposal) of the oxy-functional groups obtained is feasible at relatively high temperatures only. The products of their decay should be in this case CO and CO_2 that means the graphitization

of the diamond surface. Boehm and Suppok show[6,7] that the concentration of the oxy-functional groups is strongly dependent on the oxidizing temperature (by using gas-phase oxidation) and oxidizing reagent (by chemical treatment). Oxygen gives rise to different oxy-functional groups (see Fig. 2(b)) which affect the chemical activity of the diamond surface differently. Because of this, there is opportunity to control the colloid-chemical properties of the diamond by the modification of the oxy-functional groups. The formation of the different oxy-functional groups and their modification by temperature treatment was investigated in the present work. As outlined above, oxidation of the crystals in concentrated $HClO_4$ solution is the final preparation step of the diamond powder, resulting in the formation of oxy-functional groups on the surface. According to the standard modern chemical structural model diamond consists of the skeleton and surface functional groups (see Fig. 2(a) and 2(b) respectively). The application of alkali neutralization to the oxy-functional groups on the diamond surface after boiling in $HClO_4$ solution shows an acidic reaction. Consequently the bonding of definite functional groups by oxidizing reactions has been investigated in order to find a method to adjust the surface conditions of the crystallites. As object under study, natural and synthesized diamond powder with crystallite sizes up to 14 μm were considered. The oxidizing process of the diamond samples was established in the boiling $HClO_4$ solutions or from the gas phase using oxygen. Duration of the boiling in acid was 2 h. The concentration of the oxy-functional groups on the diamond surfaces has been determined via the titration method by neutralization with $NaHCO_3$, Na_2CO_3, NaOH and $NaOC_2H_5$ in a 0.05 mol solution. The specific surface area of the material ranges from 30 m^2/g to 1 m^2/g.

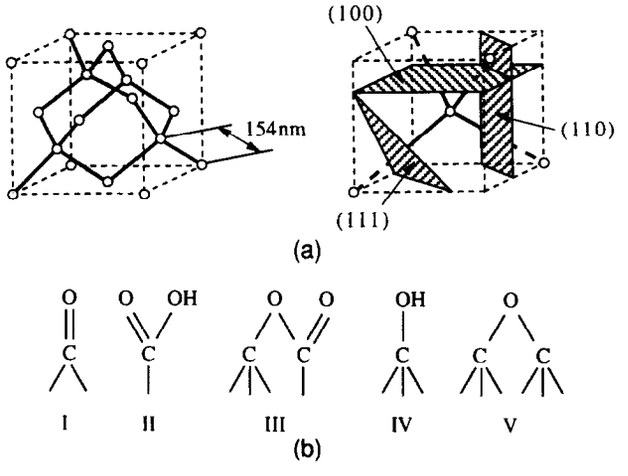

Fig. 2. (a) Structure of diamond skeleton. (b) Surface of diamond, functional groups: I carbonyl; II carboxyl; III lactonic; IV tertiary alcohol; V ether groups.

Results and Discussion

Figure 3 displays a scanning electron microscopic (SEM) image of the microcystalline material under study. The size of the crystals ranges from below 1 to 14 μm and crystal surfaces are undistorted.

The crystallographic properties of the synthesized diamond samples were investigated by X-ray diffraction (XRD). Figure 4 shows the X-ray diffraction pattern of the powder. CoKα-radiation has been used for excitation. The pattern shows the typical diamond structure. No other, i.e. graphitic modification has been observed. The concentration of the different functional groups bound on the diamond surface due to the oxidizing process was investigated and is shown in Table 1. The selective neutralization of these groups, having different oxygen contents, was carried out by the use of $NaHCO_3$, Na_2CO_3, NaOH and $NaOC_2H_5$ 0.05 mol solutions. Neutralization through the $NaHCO_3$ solution occurs due to the presence of the strong acidic carboxyl group, as indicated in Fig. 2(b), case II. For $NaOC_2H_5$, neutralization at the surface occurs due to both the strong acidic groups and the weak hydroxyl groups, as indicated in Fig. 2(b), case IV. Na_2CO_3 and NaOH account for another type of neutralization than the strong or weak acidic groups. With increasing temperature during sample treatment (boiling in the acids or oxidizing in dry oxygen atmosphere at T=100–570°C) the amount of neutralized functional groups decreases, as indicated in Table 1. To estimate the concentration and structure of the functional groups, thermodesorption and X-ray photoelectron spectroscopy of the crystals have been used.

Thermodesorption experiments have been performed under He-flow at a pressure of 0·1–0·15 MPa at a flow rate of 0·4–0·6 cm^3/s by slow ramping up of the temperature. Thermodesorption spectra are displayed in Fig. 5. Typically, CO and CO_2 from the thermally decomposing oxy-functional groups desorb at a temperature of 500–600°C. This leaves a hydrogen terminated diamond surface in this range of temperature. Desorption of hydrogen from the surface is observed at a temperature of 1000°C, generating finally an atomically clean diamond surface. The thermal decomposition of the oxy-functional groups is described by the following reactions:

$$C(OH)\rightarrow C(H) + CO \text{ and } C(OOH)\rightarrow C(H) + CO_2;$$

and results in the emission of CO and CO_2, respectively and hydrogenation of the surface.

The data in Fig. 5 also indicate that oxidation in hot $HClO_4$ solution is more effective than

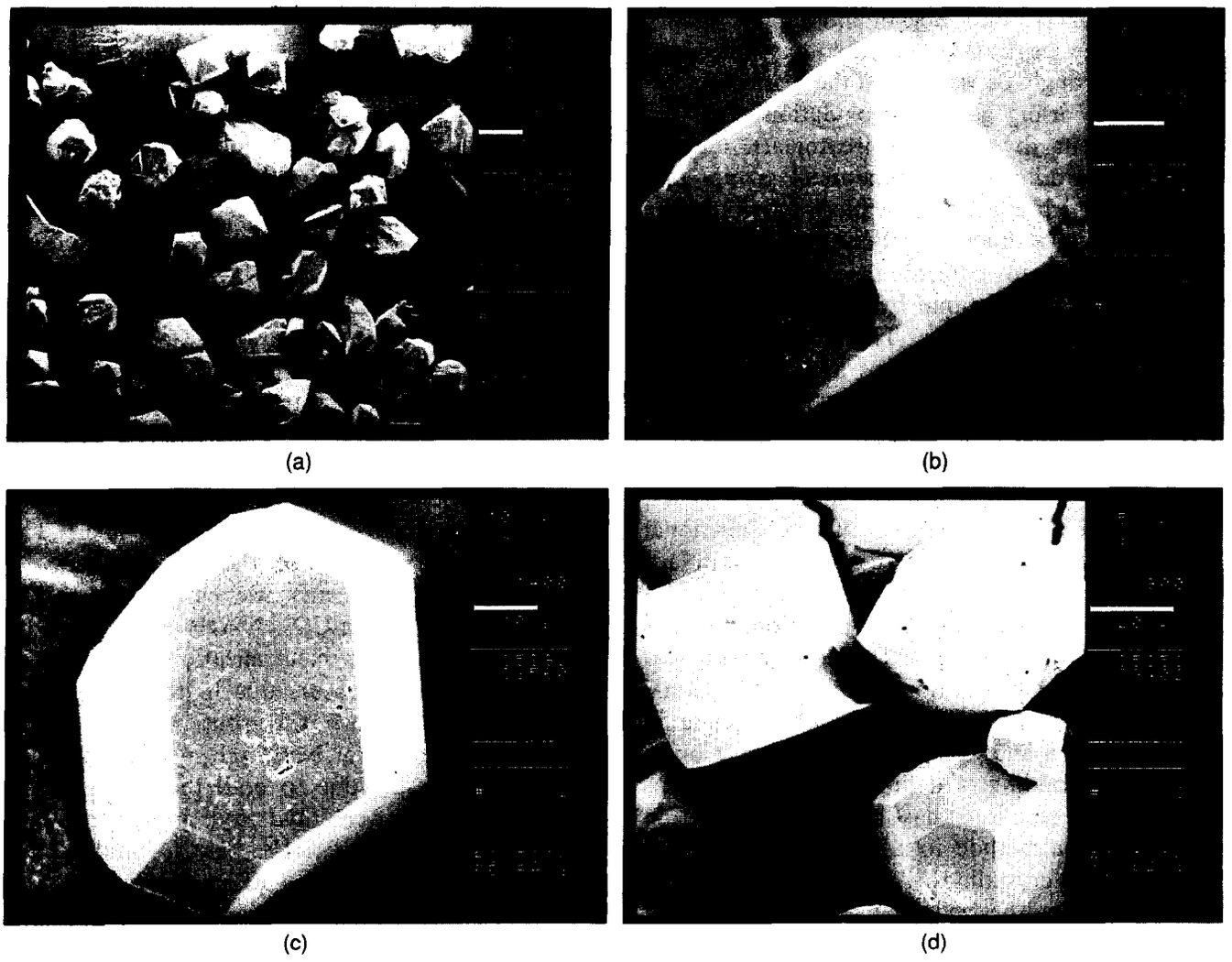

Fig. 3. SEM image of the diamond powder.

oxidation in a dry oxygen atmosphere at T=400°C. For the estimation of the desorption energy E of CO and CO_2 the approximation of the maximum in the linear program-simulated thermodesorption spectrum was used. Taking into account the approximation restrictions[8] the energy of the activation reactions of thermodesorption from the diamond surface is found as following:

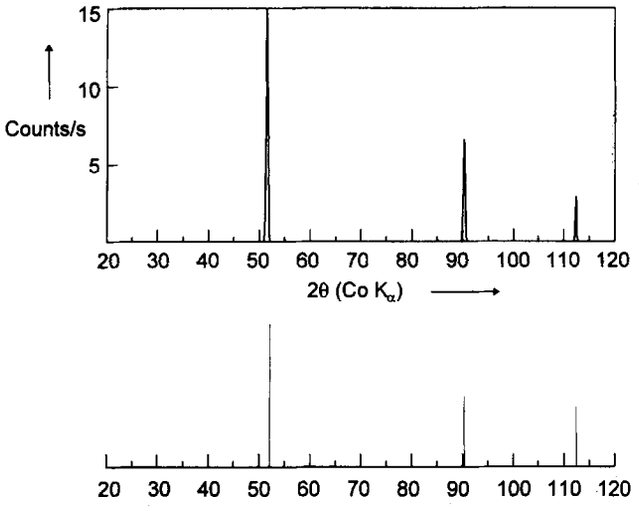

Fig. 4. XRD spectrum of the diamond powder (CoKα).

E_{CO_2}=230–260 kJ/mol and E_{CO}=230–290 kJ/mol.

The findings from the thermodesorption experiments are corroborated by X-ray photoemission spectroscopy (XPS) with the resulting spectra shown in Fig. 6. This surface sensitive method provides information on the chemical bonding state, degree of coverage and chemical composition.

Data have been recorded with the ESCALAB-5 installation, using AlKα- radiation for photoelectron excitation and the constant energy mode of the energy analyzer.

The complete spectra (not shown) reveal an impurity level at the diamond surface of approximately 1 at% or less. Figure 6, finally, shows the oxygen 1s XPS-peak, centered at a binding energy of 531·6 eV, upon exposure of the diamond crystal to treatment in $HClO_4$ solution. For comparison, also the spectrum upon treatment in He-atmosphere at 800°C is shown. The acidic treatment of the diamond surfaces results in a very broad O1s-peak, extending up to a binding energy of 537 eV. The unusual broadening is attributed to the presence of various species of the oxy-functional

Table 1. Concentration of oxy-functional groups on the diamond surfaces after oxidation, determined using different alkaline reagents for neutralization

Temperature of sample treatment (°C)	*Concentration of oxy-functional groups (mg-equiv/m²)*			
	$NaHCO_3$	Na_2CO_3	$NaOH$	$NaOC_2H_5$
100	2·27	2·94	4·42	4·75
220	1·56	2·08	3·59	3·81
350	0·91	1·25	2·34	2·62
570	0·1	0·21	0·45	0·55

groups on the surface, as illustrated in Fig. 2. Not shown is the carbon 1*s*-peak, since only a very small chemical shift has been observed. Taking into account the total peak area of the carbon and oxygen 1*s*-levels and normalization to the respective photo-ionization cross-sections, the concentration ratio between oxygen and carbon is estimated to be 0·1.

For estimation following equation was used:

$C_O/C_C = [T(O1s)\ \sigma(C1s)]/[T(C1s)\ \sigma(O1s)]$;

where:

C_O — oxygen atoms concentration;

C_C — carbon atoms concentration;

T — total area peak;

σ — photo-ionization cross-section of electronic level.

$\sigma(C1s)/\sigma(O1s) = 0{\cdot}36$ then yields $[C_O]/[C_C] = 0{\cdot}10$.

The ratio $[C_O]/[C_C] = 0{\cdot}1$ corresponds to one monolayer coverage of the surface (approximately one atom of oxygen per one atom of carbon).

These data are in a good agreement with the thermodesorption data.

Concluding Remarks

The formation of nanosized diamond powders by the statical method under the conditions mentioned above is satisfactorily stable. The result of the interaction between the atomically-clean diamond surface and the low-molecular compounds is the formation of functional groups. The removal of the oxy-functional groups obtained is possible only at high temperatures. Because the products of their decay should be CO and CO_2 the decay could be accompanied by the destruction of the diamond skeleton too. The reactivity of the surface functional groups is especially important for the synthesis of diamond ceramics. Consequently the bonding of definite functional groups by oxidizing reactions has been investigated in order to find a method to adjust the surface conditions of the crystallites. It was shown that the formation process of the oxy-functional groups was strongly dependent on the oxidizing reagent and was a function of temperature. As the temperature during treatment rises the concentration of the diamond oxy-functional groups neutralized by each investigated reagent decreased. The highest density of free bonds of the diamond surface was demonstrated for the $HClO_4$ treatment. The XPS investigations show the ratio $[C_O]/[(C_C]=0.10$, which corresponds to one monolayer coverage of the diamond surface. The energy of the activation reactions of thermodesorption from the diamond was found as following: E_{CO_2}= 230–260 kJ/mol and E_{CO}= 230–290 kJ/mol.

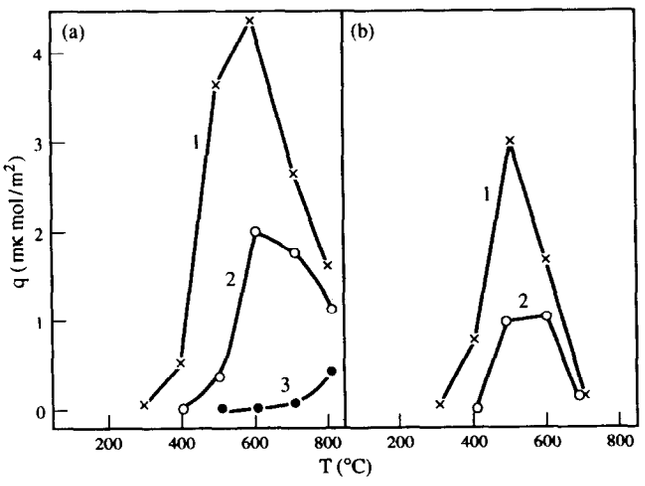

Fig. 5. Thermodesorption spectra of diamond powder CO (a) and CO_2 (b). (1) Sample after oxidizing in $HClO_4$. (2) Sample after oxidizing in O_2 atmosphere at T=400°C, duration 30 min. (3) Treatment in He, at T=800°C, then in environmental atmosphere at T=20°C.

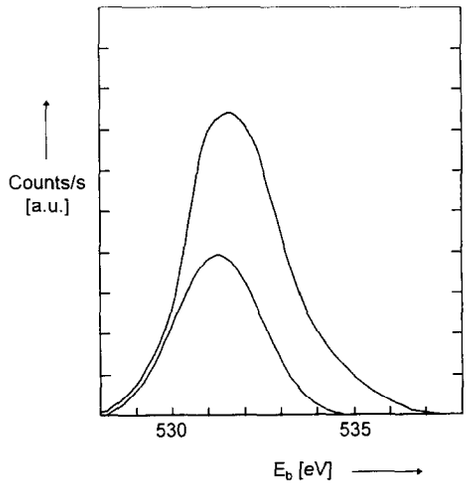

Fig. 6. XPS spectra of diamond surface: (a) C1*s*, (b) O1*s*. (1) after treatment in $HClO_4$. (2) after treatment in He atmosphere at T=800°C.

References

1. *Diamond Films and Coatings (Development, Properties and Applications)*, Ed. Robert F. Devis, N.C. State University, USA, 1993.
2. Weiss, Stefanie A., Diamond-Film Optics Ready to take the Heat. *Photonics*, **29**(3) 37–80.
3. Davis, Robert F., The Films and Devices of Diamond, Silicon Carbide and Gallium Nitride. *Physica B*, **185** (1993) 1–15.
4. Bent, H. A., Second Law of Thermodynamics. Oxford University Press, N.Y., 1965, p. 325.
5. Regueiro, Manuel Nunez, Monceau, Pierre & Hodeau, Jean-Lois, Crushing C_{60} to Diamond at Room Temperature. *Nature*, **355** (1992) 237–9.
6. Suppok, R. & Boehm, H., Chemie der Oberfläche des Diamanten. I. *Carbon*, **6** (1968) 283–93.
7. Suppok, R. & Boehm, H., Chemie der Oberfläche des Diamanten. II. *Carbon*, **6** (1968) 573–83.
8. Luk'janov, I. M. & Smirnov, E. P., ESCA investigations of the Graphite and Diamond Surface. *J. of the Theor. and Experimental Chemistry*, **N4** (1989) 490.

Journal of the European Ceramic Society 16 (1996) 759–766

0955-2219(95)00201-4
0955-2219/96/$15.00

The Influence of Crystallization and Washing Medium on the Characteristics of Nanocrystalline Y-TZP

C. D. Sagel-Ransijn, A. J. A. Winnubst, A. J. Burggraaf & H. Verweij

University of Twente, Faculty of Chemical Technology, Laboratory for Inorganic Materials Science, Enschede, The Netherlands

(Received 30 July 1995; revised version received 26 October 1995; accepted 7 November 1995)

Abstract

A zirconia–yttria gel, made by coprecipitation, was treated in six different ways to obtain a nanocrystalline Y-TZP powder: one large gel batch was split into six parts of which one was crystallized in air and the others crystallized either in water with a high pH or in methanol. The batches were subjected to several post treatments. Powder properties and densification characteristics of the six powder batches obtained in this way are described. The air-calcined powder can be sintered to a relative density of about 93% at 1070°C/10 h, but reproducibility of the sintering characteristics is poor. Optimal hydrothermal treatment of the powder yields a reproducible sintering process, resulting in a relative density of 96% at 1070°C/10 h and an average grain size between 120 and 130 nm.

1 Introduction

Nanostructured materials currently receive considerable attention. The percentage of atoms present in the grain boundary region becomes significant once the grain size enters the nanometre regime (i.e. grain size less than 100 nm).[1,2] It is expected that the properties of these nanocrystalline ceramics will be different from those of more conventional materials with phase or grain structures on a coarser scale.[2] He *et al.*[3] have shown that fine-grained zirconia exhibits better wear resistance than the coarse-grained material. For the same material, Theunissen[4] found that both bending strength and fracture toughness at high temperatures are improved with smaller grain sizes. The evaluation of mechanical properties (at low to moderate temperatures) requires the production of bodies with near-theoretical densities. However, preparing bulk materials with near-theoretical densities, while simultaneously keeping the grain size below 100 nm, is not yet possible. The sinterability of the material should permit densification to proceed at such a low temperature that only limited grain growth occurs.

To obtain good sinterability at low temperatures, ultra-fine powders with a low degree of agglomeration are required. The compaction and sintering behaviour of such fine powders is determined, to a large extent, by the strength of their agglomerates. At a given crystallite size, the agglomerate strength can be lowered by increasing the intra-agglomerate porosity and/or decreasing the strength of the interparticle bonds.[5]

Fine powders of ZrO_2 solid solutions can be prepared by a gel precipitation technique using metal chlorides as precursor chemicals.[6,7] This so-called chloride method involves coprecipitation of metal chlorides, followed by water/ammonia and ethanol washing steps. Subjecting the gel to ethanol washing is a crucial step in lowering the strength of the agglomerates. The reduction in strength has been ascribed to the formation of ethoxide groups on the surface[8] and to lower packing density within the agglomerates due to the lower surface tension of ethanol compared with water during the drying process of the powder[9,10] The ethanol washing step doubles the intra-agglomerate porosity after calcination (at 500–550°C) compared with a gel that has been treated with water/ammonia only.[11] The intra-agglomerate porosity of these alcohol-washed powders is sufficiently high to make the agglomerates collapse to a large extent under moderate pressures (50–150 MPa).[7,12] In this way, compacts of uniform pore size distribution are obtained.

Under hydrothermal conditions, crystallization of ZrO_2 solid-solution gels proceeds at temperatures well below 500°C. For example, temperatures of 190–250°C have been reported for the hydrothermal

crystallization of ZrO_2–CaO,[13] ZrO_2–Y_2O_3[14–16] and ZrO_2–CeO_2.[17] Several investigations suggest that the formation of strong interparticle bonds under hydrothermal conditions is greatly diminished or even avoided.[13] Crystallization in organic solvents might be a way to reduce the agglomerate strength even further. Sato *et al.*[17] conclude that crystallization in organic solvents gives better results than hydrothermal crystallization to improve the sinterability, indicating the formation of softer agglomerates in organic solvents. Supercritical drying, which can be performed at a reasonable temperature and pressure for organic solvents, eliminates the effects of capillary forces and might result in even softer agglomerates.

Limited work has been done to address the differences in sinterability of ZrO_2 solid solutions prepared via crystallization in air, hydrothermal crystallization and crystallization in methanol. In the case of ZrO_2–CaO,[13] ZrO_2–CeO_2[17] and ZrO_2–Y_2O_3,[15,16] it has been observed that the sinterability is strongly improved by the hydrothermal treatment. None of these investigations focused on the effect of the washing medium after hydrothermal crystallization. It is expected that this step is important because it affects the surface condition and impurity level of the particles forming the agglomerates.

In this paper, Y-TZP (yttria-stabilized tetragonal zirconia polycrystals) powders are prepared from a dried ethanol-washed gel obtained by coprecipitation and crystallization in air, crystallization under hydrothermal conditions or methanol crystallization. After hydrothermal crystallization, a part of the powder is washed with ethanol. The influence of crystallization medium and post-hydrothermal crystallization treatments on powder properties, green compact structure and sinterability is examined and the synthesis route leading to dense, nanostructured Y-TZP is reported.

2 Experimental Procedure

2.1 Powder synthesis

Appropriate amounts of $ZrCl_4$ (>98% pure) and YCl_3 (99·9% pure) for the preparation of TZP with 5 at% Y on the Zr-site were dissolved in a 0·2 M aqueous HCl solution. The solution was filtered and added drop-wise to an excess of a 25 wt% ammonia solution, with the pH maintained at a value >11. A precipitated gel was obtained and allowed to settle overnight, after which the clear supernatant was removed. The gel obtained was washed with water/ammonia mixtures until the washing liquid no longer became turbid on addition of 0·1 M $AgNO_3$. This indicated that the washing liquid was chloride-free. The gel was subsequently filtered, redispersed and washed twice in ethanol. After drying at 120°C, the gel was divided into four parts as follows.

Table 1. Explanation of codes used

Code	*Explanation*
AC	Air-crystallized
HC	Hydrothermally crystallized
MC	Methanol-crystallized
W	Water-washed
E	Ethanol-washed
SD	Supercritical drying
400	Finally heat-treated at 400°C

(1) The first part was dry milled, calcined in static air at 500°C for 2 h and dry milled again (AC500) (explanation of codes is given in Table 1).

(2) The second part was used for hydrothermal crystallization in a stainless steel autoclave equipped with poly(tetrafluoroethylene) liner. Crystallization of the gel took place at 200°C for 2 h in a basic medium (ammonia solution) at a pressure of 20–30 bar. After hydrothermal treatment, the pH of the slurry was 9–11. The slurry was divided into three parts:
   (a) one part was filtered, dried at 120°C and dry milled (HC-W);
   (b) the second part was treated as above (HC-W) and additionally heat-treated at 400°C for 1 h (HC-W400);
   (c) the third part was redispersed and washed three times in ethanol, filtered and dried at 120°C. The dried powder was subsequently dry milled and heat-treated at 400°C for 1 h to remove residual organics (HC-E400).

(3) The third part was used for crystallization in methanol. Crystallization took place at 250°C for 2 h at a pressure of 130 bar. The powder was supercritically dried at the same temperature and pressure, dry milled and heat-treated at 400°C for 1 h (MC-SD400).

(4) The fourth part was also used for crystallization in methanol. Crystallization also took place at 250°C for 2 h at a pressure of 130 bar. After crystallization, the powder was washed three times in ethanol, dry milled and heat treated for 1 h at 400°C (MC-E400).

In all cases, dry milling was performed with zirconia balls.

For the above-mentioned syntheses, the effects of crystallization medium and post-hydrothermal crystallization treatments (washing, drying and/or temperature treatment) on powder and sintering characteristics were researched.

2.2 Green compact formation and sintering

Green compacts were prepared by cold-isostatic pressing in two steps: initially at 80 MPa and finally at 400 MPa with a 3 min holding time. Sintering was studied by means of dilatometry using a Netzsch 402 E dilatometer. The dilatometer's thermocouple was carefully calibrated by the melting method proposed by Henderson *et al.*[18] Densities were calculated from the green density and the observed linear shrinkage of the specimens, and corrected for thermal expansion and weight loss (due to removal of absorbed water). Final densities calculated in this way were in good agreement with those measured by Archimedes' technique (in Hg). All experiments were performed using cylindrical specimens with initial dimensions 7–15 mm (height) by 6–7 mm (diameter).

Non-isothermal sintering experiments were done at a heating rate of 120°C h^{-1} to 1200°C, immediately followed by cooling with a rate of 240°C h^{-1}. Isothermal experiments were done at 1050°C for 5 h and at 1070 and 1150°C for 10 h (heating rate 120° h^{-1}, cooling rate 240°C h^{-1}).

2.3 Characterization techniques

A PL Thermal Sciences system (STA 625) was used for thermogravimetric and differential thermal analysis (TGA/DTA) (in air, heating rate 600°C h^{-1}). Nitrogen sorption isotherms were obtained at 77 K using a Micromeretics ASAP 2400 system. Specific surface areas were calculated by the BET method; no corrections for microporosity were necessary. Mesopore size distributions were calculated from the adsorption branch assuming cylindrical pore shape. The phase composition was analysed by X-ray diffraction (XRD) using a Philips PW 1370 diffractometer with Cu K_α radiation. Peaks were corrected for the $K_{\alpha1}/K_{\alpha2}$ doublet and instrumental broadening. Crystallite sizes of the powders were determined by X-ray line broadening assuming Cauchy line profiles. Grain sizes in sintered specimens were determined by the lineal intercept technique from scanning electron micrographs (Hitachi S800) of polished, thermally etched cuts using $D = 1{\cdot}56\ L$, where L is the average lineal intercept.[19] Corrections for residual porosity were made by the method proposed by Wurts and Nelson.[20] The surfaces of specimens for examination by scanning electron microscopy (SEM) were coated with Au/Pd to prevent charging.

3 Results

3.1 Powder characteristics

Phase analysis by XRD revealed that all powders are tetragonal with only traces of monoclinic zirconia. The primary crystallite size as calculated from X-ray line broadening data (XRLB) of the AC500, HC-W, HC-W400 and HC-E400 powders is ~8 nm, while that of the MC-SD400 and MC-E400 powders is ~5 nm.

DTA/TGA analyses were performed in air up to 800°C for all powders before heat treatment or calcination. The DTA pattern of the AC powder showed three peaks at 300, 430 and 475°C. The first two peaks are related to the oxidative decomposition of ethoxy groups; the peak at 475°C coincides with the crystallization temperature of zirconia.[11,12,15] The total weight loss of this material upon heating is 25%. The DTA pattern for HC-W material did not show any peaks. The weight loss of this material upon heating was only 4%. The DTA pattern of the HC-E powder showed two peaks at 310 and 380°C. The TGA pattern of the HC-E powder shows a distinct decrease in weight of ~1·5% between 300 and 400°C. Both peaks observed in the DTA pattern are therefore likely to be related to the oxidative decomposition of chemisorbed ethoxy groups. The total weight loss of the HC-E material upon heating is 5%. The MC-SD material shows two peaks in the DTA pattern at 310 and 420°C. These peaks correspond to a strong weight loss and are probably related to adsorbed methanol groups. The total weight loss of the material upon heating is 14%. The DTA pattern of the MC-E powder showed only a single peak at 420°C; weight loss upon heating for this material is 16%.

As a consequence of the DTA results, the AC powder was calcined at 500°C (AC500) to make sure that all powder crystallized. The HC-E powder was treated at 400°C (HC-E400) in order to eliminate the chemisorbed ethoxy groups. The MC-SD and MC-E powders were both treated at 400°C. DTA measurements performed after these heat treatments indicated that the powders were free of chemisorbed species and were fully crystalline.

The specific surface area of the powders is dependent on the crystallization medium. Crystallization in methanol (samples MC-E400 and MC-SD400) results in the largest surface area and the smallest average crystallite size, as shown in Table 2. After heat treatment at 400°C, the specific surface areas of both HC-E400 and HC-W400 are equal (91 $m^2\ g^{-1}$).

Assuming that the volume V_p of the pores measured by N_2 adsorption/desorption can be ascribed to (intra)-agglomerate porosity, the porosity P was calculated using.[7]

$$P = \frac{V_p \rho_{th}}{(V_p \rho_{th} + 1)} \quad (1)$$

Table 2. Powder and agglomerate properties of the powders investigated [S_{BET} is specific surface area; P is agglomerate porosity; P_y is yield point; m is constant from eqn (2)]

Material code	*Crystallite size (nm)*	S_{BET} *($m^2 g^{-1}$)*	P*(%)*	P_y *(MPa)*	m	*Modus pore size (nm)*
AC500	8	103	73	80	14	9·5
HC-W	8	117	56	62	8	6·5
HC-W400	8	91	56	130	7	9·5
HC-E400	8	91	67	64	11	9·5
MC-SD400	5	144	77	41	11	6·5
MC-E400	5	144	77	55	12	6·5

where ρ_{th} is the theoretical density (6.06 g cm^{-3}). In Table 2, it can be seen that the agglomerate porosities are in the range 56 to 77% for all powders. These results indicate that the agglomerate porosity is dependent on both crystallization medium (air, water or methanol) and washing liquid used before final heat treatment. The largest porosities (77%) are obtained for methanol crystallized materials (MC); the supercritical drying after treatment (MC-SD400) did not affect the final porosity.

3.2 Compaction behaviour

The relative density of the powders as a function of the logarithm of isostatic compaction pressure is given in Fig. 1. The curves show two linear parts (parts 1 and 2) with a point of intersection at pressure P_y. Below P_y, the increase in density is rather low.

According to Van de Graaf *et al.*,[21] the intersection P_y is a measure of the strength of the agglomerates. After compaction at a pressure around P_y, the agglomerates are gradually fragmented, while they are only rearranged at pressures below P_y. Above P_y, rearrangement of the internal agglomerate structure takes place. This part of the compaction curve (part 2) can be described by the empirical equation.[7,12,22,23]

$$\rho - \rho_y = m \times \ln [P/P_y] \quad (2)$$

where m is a constant, ρ the density and P the pressure. The subscript y stands for yield point. The values of P_y and m are given in Table 2. The P_y values of the HC-W and the AC500 powder are 62 and 80 MPa, respectively. Because the HC-W powder shows a lower agglomerate porosity and the same crystallite size, the lower P_y value for the HC-W powder can be related to weaker intercrystalline bonds in the HC-W powder than in the AC500 powder. This is in accordance with results reported by Haberko and Pyda,[13] who studied hydrothermal crystallization of ZrO_2–CaO.

If HC-W and HC-W400 are compared it is clear that the heat treatment at 400°C results in a strengthening of the intercrystalline bonds, because agglomerate porosity and crystallite size remain the same while P_y increases. The influence of washing medium used after hydrothermal crystallization on agglomerate strength is demonstrated by the powders HC-W400 and HC-E400, which have an agglomerate strength of 130 and 64 MPa, respectively. The smaller agglomerate strength of HC-E400 is, in this case, probably related to the larger agglomerate porosity and/or a difference in strength of the intercrystalline bonds. The slightly higher agglomerate strength of the HC-E400 material compared with the MC-E400 material is probably related to the smaller agglomerate porosity of the former. The agglomerate strength of the MC-SD400 material (P_y = 41 MPa) is smaller than of the MC-E400 material (P_y = 55 MPa). This shows the influence of supercritical drying in this case.

A large value of m (the slope of the high pressure curve) corresponds to a relatively rapid increase in relative density with compaction pressure. A large value of m might be an indication of a large

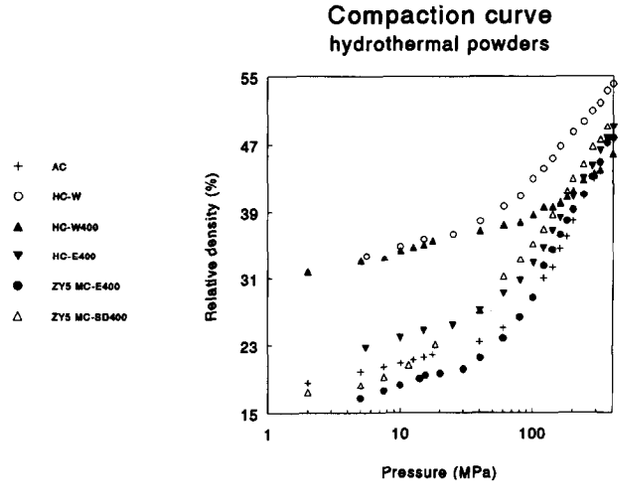

Fig. 1. Densification behaviour of the ZY5 powders during isostatic compaction.

density distribution in the green compact. Some sources of density variations are the friction between the powder and the die wall and between the powder particles. The specimen may fracture during unloading or ejecting of the pressed part, especially when large specimens are made. The m values of the various powders range between 7 and 14, as can be seen in Table 2. It is expected that the stresses created during compaction of the HC-W and HC-W400 material are small, therefore it should be easy to prepare large samples of this material.

3.3 Green compact properties

Figure 2 shows adsorption/desorption isotherms of green compacts (pressed at 400 MPa). The shape of the hysteresis loop is an indication of the pore morphology. The hysteresis of the HC-W and MC-SD400 materials is predominantly of type E, following the classification of De Boer.[24] The AC500 material is of a mixed type A/E, while the MC-E400 and HC-E400 (≈HC-W400) materials are in between (curves of the HC-W400 and MC-E400 materials are not shown here). Type E is indicative of tubular capillaries with strongly varying widths (as expected in powder compacts), while type A corresponds to a cylindrical pore shape. During sintering of a AC500 powder compact, the hysteresis shape becomes more and more similar to type A due to progressive neck formation.[25] The differences in green porous texture between the powders are most probably caused by partial sintering already taking place during crystallization in air (500°C) or heat treatment (400°C) after crystallization in water or methanol of the normal dried powder, while partial sintering does not take place when the hydrothermally crystallized powder is only filtered and dried at 120°C (HC-W). Neck formation during heat treatment is reduced in the case of supercritical drying

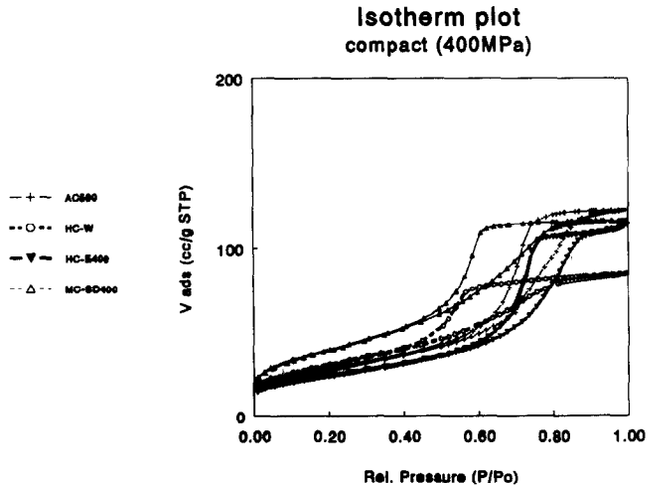

Fig. 2. N_2 sorption isotherms of green compacts.

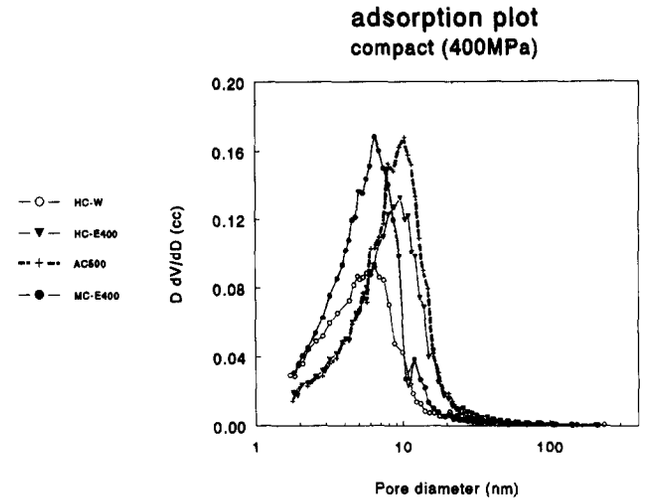

Fig. 3. Pore size distributions in the powder compacts after isostatic pressing at 400 MPa.

(MC-SD400), resulting in an E type hysteresis and low P_y values.

The pore size distributions of green compacts are given in Fig. 3. The width of the pore size distribution is similar for all powders, with the exception of the HC-W powder, which has a slightly broader distribution. The most frequently found pore diameter of the HC-E400, HC-W400 and AC500 compacts is the same and equals 9.5 nm, whereas the HC-W, MC-SD400 and MC-E400 materials have a maximum at 6.5 nm. Since the crystallite sizes of the AC500, HC-W, HC-W400 and HC-E400 materials are the same, the smaller average pore diameter of the HC-W green compact results from improved compactability resulting in a better particle stacking.

3.4 Sinterability and microstructure

The increase in relative density with temperature was measured using a heating rate of 120°C h^{-1} to 1200°C. The results for the AC500, HC-W, HC-W400 and MC-SD400 materials can be seen in Fig. 4.

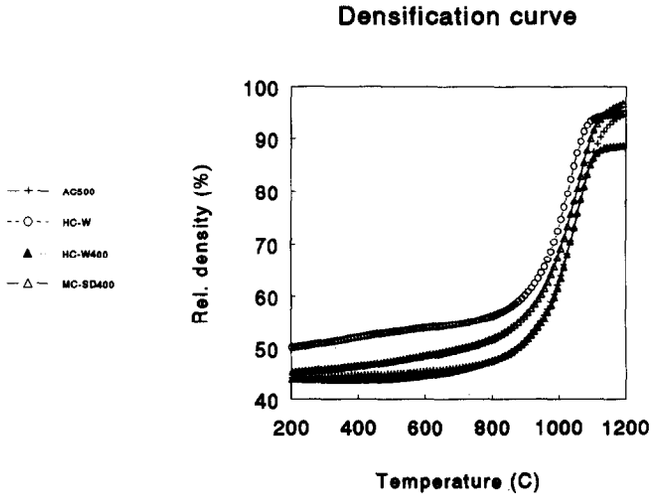

Fig. 4. Increase of relative density with temperature during heating at 120°C h^{-1}.

The HC-E400 and MC-E400 materials show approximately the same densification behaviour as the AC500 material. The maximum in densification rate is found at a temperature of around 1040°C for all cases. The HC-W400 material has the lowest final density (90%), probably due to the harder agglomerates present in the powder. The other materials show only small differences in sinterability, these samples being 95% dense at 1150°C. From the non-isothermal sintering behaviour, it is evident that it should be possible to sinter the five systems to full density at a temperature below 1100°C. For the AC500, HC-W, HC-E400, MC-E400 and MC-SD400 materials, isothermal sintering experiments were performed at 1050°C. The increase in relative density with time during sintering at 1050°C is illustrated in Fig. 5. The AC500 material is 90% dense and the HC-E400, MC-E400 and MC-SD400 materials are 93, 93 and 94% dense, respectively, after 5 h of sintering. The HC-W material is 94% dense after 2 h of sintering at this low temperature. The average grain size of the materials after sintering at 1050°C/5 h is between 95 and 100 nm in all cases. The microstructure is homogeneous, as is shown for the HC-E400 material in Fig. 6. HC-E400 and MC-SD400 were also sintered at 1150°C for 10 h, resulting in a density of 98% and a grain size of 180 nm. Sintering the AC500 and HC-E400 materials at 1070°C for 10 h resulted in a grain size between 120 and 130 nm and a relative density of 93 and 96% for AC500 and HC-E400, respectively. In the HC-W material, small cracks were observed by SEM, as is shown in Fig. 7. No cracking was observed for the other materials. A drawback of the AC500 material is that it results in irreproducible final densities. After sintering for 10 h at 1150°C, densities varied between 92 and 97%. The densification

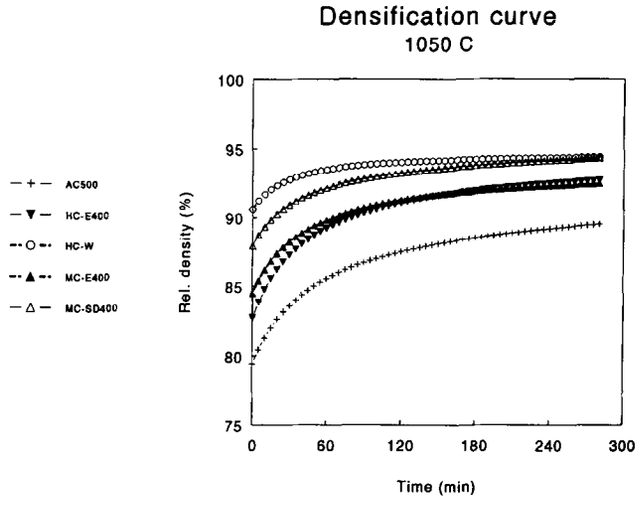

Fig. 5. Increase of relative density with time during sintering at 1050°C.

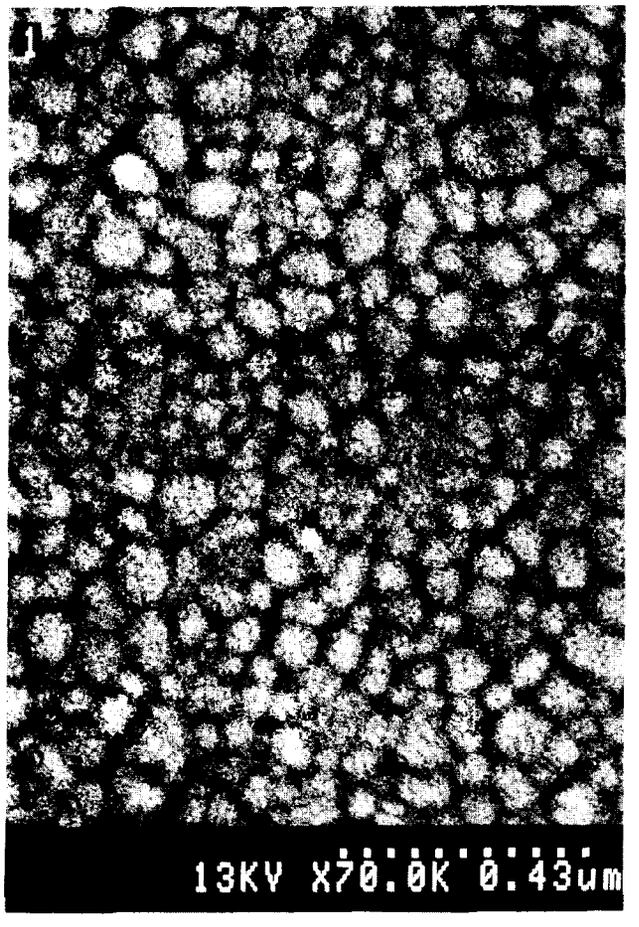

Fig. 6. Microstructure of the HC-E400 material sintered for 5 h at 1050°C.

Fig. 7. Microstructure of the HC-W material sintered at 1050°C for 5 h showing a crack.

characteristics of the hydrothermal powders are very reproducible.

4 Discussion

4.1 The effect of liquid medium before final heat treatment on powder properties

Final heat treatment of hydrothermal powder results in a larger pore size and smaller pore size distribution. The neck area is also increased by this heat treatment. Boutz *et al.*[25] observed that an increase in heat treatment temperature of an air-crystallized powder compact (starting at 500°C) leads to an increase in pore size, narrowing of the pore size distribution and increase in neck area. The results observed for the HC-W and HC-W400 materials indicate that the same holds for hydrothermally crystallized powders for temperatures down to 200°C (hydrothermal crystallization temperature). After hydrothermal crystallization, the liquid medium does not influence the pore size, pore size distribution or the pore shape. Materials HC-W400 and HC-E400 show identical results.

The agglomerate strength of air-crystallized powder can be reduced if water is replaced by ethanol before crystallization. This reduction is extremely large. It was found that the agglomerate strength of a water-washed air-crystallized powder is >400 MPa, whereas the agglomerate strength of ethanol-washed air-crystallized powder varies between 60 and 90 MPa. This reduction in strength has been ascribed to the formation of ethoxide groups on the surface[8] and to the lower compaction pressure during drying due to the lower surface tension of ethanol compared with water.[9,10] In the case of hydrothermally crystallized powder, the agglomerate strength is reduced to a lesser extent if water is replaced by ethanol after crystallization: 130 MPa for HC-W400 compared with 64 MPa for HC-E400 powder. This means that the effect of the washing medium can be reduced by crystallization before final heat treatment. However, this influence cannot be neglected yet. The reduction in agglomerate strength is likely to result from the increase in agglomerate porosity. The increase of agglomerate strength with heat treatment temperature (HC-W and HC-W400) is caused by an increase in neck area.

The hydrothermally crystallized powders show good sintering characteristics. The observed cracking of the HC-W material might be related to stresses forming in the temperature range 200–700°C during densification of agglomerates containing a large number of pores with a diameter <6 nm. Cracking of the HC-W material can be avoided if a lower heating rate is used until 700°C.

4.2 The effect of crystallization medium on powder properties

A comparison will be made between crystallization in air, water and methanol. Crystallization in methanol results in a smaller crystallite size than is obtained by hydrothermal crystallization or crystallization in air. The difference in pore size between AC500 and HC-E400 on one hand, and MC-E400 on the other hand might be caused by this difference in crystallite size.

More neck area is obtained by crystallization in air than by crystallization in liquid media. This might be caused by the higher crystallization temperature. To a large extent, the strength of the intercrystalline bonds and agglomerate porosity determine the agglomerate strength of the material.[5] It is reasonable to assume that the strength of the intercrystalline bonds is increased if the neck area is increased. Therefore, the agglomerate strength of the methanol-crystallized material is expected to be the smallest; this is in agreement with experimental results (as indicated by P_y values).

The sinterability of the material is not influenced by the crystallization medium. The low reproducibility of achieving high final densities of the air-calcined material can have several causes. Some of these are: a large agglomerate-strength distribution; the irregular agglomerate shape; and the large differences in agglomerate sizes in the powder. The synthesis of Y-TZP with reproducible high final densities from air-crystallized material is still under investigation.

4.3 The effect of supercritical drying of methanol-crystallized material on powder properties

The effect of supercritical drying on powder properties has been analysed for methanol-crystallized material. The results obtained for the methanol-crystallized materials show that supercritical drying has no influence on pore size, pore size distribution, agglomerate porosity or sinterability of the material. Supercritical drying does, however, result in less neck area compared with normal drying which, with the same agglomerate porosity, leads to a smaller agglomerate strength. This will lead to a more homogeneous microstructure in the green and sintered compact.

5 Conclusions

(1) Pressureless sintering of the hydrothermally or methanol-crystallized material that was ethanol-washed and subsequently heat-treated, results in relatively dense (93–94%), nanostructured (<100 nm) Y-TZP at a sintering temperature as low as 1050°C.

(2) Densities can be increased to 96% at 1070°C and 98% at 1150°C, with resulting grain sizes of 130 and 180 nm, respectively.
(3) The as-dried hydrothermally crystallized material (HC-W) exhibited small cracks after sintering, probably caused by stresses associated with the densification of agglomerates. Cracking can be avoided by low heating rates up to 700°C.
(4) The effects of supercritical drying after crystallization in methanol are minor.
(5) The powder characteristics, compactability, green compact properties and sinterability of the air-calcined and hydrothermally crystallized materials that were ethanol-washed and heat-treated, are almost the same.
(6) Crystallization in methanol instead of water or air results in smaller crystallites and softer agglomerates.
(7) Replacing water by ethanol directly after hydrothermal crystallization results in an increase in agglomerate porosity.

Acknowledgements

These investigations were partly supported by the Innovative Research Program on Technical Ceramics (IOP-TK) with financial aid from the Dutch Ministry of Economic Affairs.

References

1. Burggraaf, A. J., Stuijts Memorial Lecture 1991: Some new developments in ceramic science and technology. *J. Eur. Ceram. Soc.*, **9** (1992) 245–50.
2. Burggraaf, A. J., Winnubst, A. J. A. & Verweij, H., Dense and porous nanostructured ceramics and composites. In *Proceedings of the Third Meeting of the European Ceramic Society*, ed. P. Duran & J. F. Fernandez. Faenza Editrice Iberica, 12–17 1993, pp. 561–76.
3. He, Y. J., Winnubst, A. J. A., Burggraaf, A. J., Verweij, H., van der Varst, P. G. Th. & De With, B. G., Grain size dependence of sliding wear in tetragonal zirconia polycrystallines. Submitted to *J. Am. Ceram. Soc.*
4. Theunissen, G. S. A. M., Microstructure, fracture toughness and strength of (ultra)fine-grained tetragonal zirconia ceramics. PhD thesis, University of Twente, Enschede, The Netherlands, 1991, Ch. 7.
5. Rumf, H., Grundlagen und Methoden des Granulierens. *Chemie Ing. Techn.*, **30** (1958) 144–58.
6. Haberko, K., Characteristics and sintering behavior of zirconia ultrafine powders. *Ceramurgia Int.*, **5** (1979) 145–58.
7. Groot Zevert, W. F. M., Winnubst, A. J. A., Theunissen, G. S. A. M., & Burggraaf, A. J., Powder preparation and compaction behaviour of fine-grained Y-TZP. *J. Mater. Sci.*, **25** (1990) 3449–55.
8. Kaliszewski, M. S. & Heuer, A. H., Alcohol interaction with zirconia powder. *J. Am. Ceram. Soc.*, **73** (1990) 1504–9.
9. Roosen, A. & Hausner, H., The influence of processing conditions on the sintering behaviour of coprecipitated calcia-stabilized zirconia powders. In *Ceramic Powders* (Materials Science Monographs 16), ed. P. Vincenzini. Elsevier, Amsterdam, 1983, pp. 773–82.
10. Dogan, F. & Hausner, H., The role of freeze-drying in ceramic powder processing. In *Ceramic Trans., Ceramic Powder Science (II)*, Vol. 1, ed. G. L. Messing, E. R. Fuller Jr & H. Hausner. American Ceramics Society, Westerville, OH, 1988, pp. 127–34.
11. Mercera, P. D. L., Van Ommen, J. G., Doesburg, E. B. M., Burggraaf, A. J. & Ross, J. R. H., *J. Mater. Sci.*, **27** (1992) 4890.
12. Theunissen, G. S. A. M., Microstructure, fracture toughness and strength of (ultra)fine-grained tetragonal zirconia ceramics. PhD thesis, University of Twente, Enschede, The Netherlands, 1991, Ch. 2.
13. Haberko, K. & Pyda, W., Preparation of Ca-stabilized ZrO_2 micropowders by a hydrothermal method. In *Advances in Ceramics*, vol. 12, American Ceramics Society, Westerville, OH, 1984, p. 774–83.
14. Pyda, W., Haberko, K. & Bucko, M. M., Hydrothermal crystallization of zirconia and zirconia solid solutions. *J. Am. Ceram. Soc.*, **74** (1991) 2622–9.
15. Boutz, M. M. R., Olde Scholtenhuis, R. J. M., Winnubst, A. J. A. & Burggraaf, A. J., A hydrothermal route for production of dense, nanostructured Y-TZP. *Mater. Res. Bull.*, **29** (1994) 31–40.
16. Rossi, G. A. & Pelletier, P. J., Y_2O_3 doped ZRO_2 powder prepared in nonaqueous medium. Influence of the crystallization method on powder sinterability and properties of Y-TZP ceramics. In *Advances in Ceramics, Vol. 24: Science and Technology of Zirconia III*, ed. S. Somiya, N. Yamamoto & H. Yanagida. American Ceramics Society, Westerville, OH, 1988, pp. 173–81.
17. Sato, T., Dosaka, K., Yoshioka, T., Okuwaki, A., Torii, K. & Onodera, Y., Sintering of ceria doped tetragonal zirconia crystallized in organic solvents, water, and air. *J. Am. Ceram. Soc.*, **75** (1992) 552–6.
18. Henderson, J. B., Emmerich, W.-D. & Wassmer, E., A method for the temperature calibration of pushrod dilatometers. *J. Thermal Anal.*, **32** (1987) 1905–13.
19. Mendelson, M. I., Average grain size in polycrystalline ceramics. *J. Am. Ceram. Soc.*, **52** (1969) 443–6.
20. Wurts, J. C. & Nelson, J. A., Lineal intercept technique for measuring grain size in two-phase polycrystalline ceramics. *J. Am. Ceram. Soc.*, **55** (1972) 109.
21. Van de Graaf, M. A. C. G., Ter Maat, J. H. H. & Burggraaf, A. J., Microstructure and sintering kinetics of highly reactive ZrO_2–Y_2O_3 ceramics. *J. Mater. Sci.*, **20** (1985) 1407–18.
22. Halloran, J. W., Role of powder agglomerates in ceramic processing. In *Advances in Ceramics*, Vol. 9, ed. J. A. Mangels & G. L. Messing. American Ceramics Society, Inc., Columbus, OH, 1984, pp. 67–75.
23. Halloran, J. W., Agglomerates and agglomeration in ceramic processing. In *Ultrastructure Processing of Ceramics, Glasses and Composites*, ed. L. L. Hench & D. R. Ulrich. John Wiley and Sons, New York, 1984, pp. 404–17.
24. De Boer, J. H., *The Structure and Properties of Porous Materials*. Butterworth Scientific Publications, 1958, pp. 68–93.
25. Boutz, M. M. R., Winnubst, A. J. A. & Burggraaf, A. J., Yttria-ceria stabilized tetragonal zirconia polycrystals sintering, grain growth and grain boundary segregation. *J. Eur. Ceram. Soc.*, **13** (1994) 89–102.

Journal of the European Ceramic Society 16 (1996) 767–771

0955-2219(95)00202-2
0955-2219/96/$15.00

Synthesis and Structural Characterization of a New System: ZrO_2–Y_2O_3–RuO_2

E. Djurado, C. Roux & A. Hammou

Laboratoire d'Ionique et d'Electrochimie du Solide de Grenoble, associé au CNRS (URA 1213), ENSEEG, BP 75, 38402 Saint Martin d'Héres Cedex, France

(Received 20 September 1995; revised version received 25 October 1995; accepted 7 November 1995)

Abstract

New compounds belonging to the pseudo-ternary system ZrO_2–Y_2O_3–RuO_2 have been synthesized from nitrates as precursors. The general formula was $[(ZrO_2)_{0.91}(Y_2O_3)_{0.09}]_{1-x}(RuO_2)_x$ with $0 \leq x \leq 20$ mol% RuO_2. In order to avoid thermal decomposition and to obtain the best sample crystallinity, the last firing was performed at 900°C. X-ray diffraction measurements provide evidence of a solid solution limit at $10 \leq x < 12.5$ mol% RuO_2 with the cubic fluorite-type structure. Microstructural analyses show samples with high porosity and heterogeneity in grain size and ruthenium composition.

De nouveaux composés appartenant au système pseudo-ternaire ZrO_2–Y_2O_3–RuO_2 ont été synthétisés à partir des nitrates comme précurseurs. La formule générale était $[(ZrO_2)_{0.91}(Y_2O_3)_{0.09}]_{1-x}(RuO_2)_x$ avec $0 \leq x \leq 20$ mol% RuO_2. Dans le but d'éviter la décomposition thermique et d'obtenir la meilleure cristallinité de l'échantillon, le dernier recuit a été effectué à 900°C. Des mesures de diffraction des rayons X ont permis de mettre en évidence une solution solide dont la limite a été déterminée à $10 \leq x < 12.5$ mol% RuO_2 dont la structure est cubique de type fluorine. Des analyses microstructurales montrent des échantillons avec une grande porosité et une hétérogénéité en granulométrie et en composition du ruthénium.

1 Introduction

Ruthenium oxide RuO_2 is a transition metal dioxide with a rutile-type structure. Its thermal dissociation is described by the reaction

$$RuO_2\ (s) \rightarrow Ru\ (s) + O_2\ (g)$$

at 1461°C under 0·21 atm pO_2.[1] Furthermore, RuO_2 is considered one of the main active components in so-called dimensionally stable anodes due to its remarkable electrocatalytic properties.[2] It is well known that its anodic overpotential for oxygen evolution is very low.[3–5] For these reasons, we thought that it would be worthwhile to use it as an electrode in oxygen sensors and solid oxide fuel cells in the form of a ZrO_2–Y_2O_3–RuO_2 solid solution. Taking into account that very few data are available in the literature related to this aspect,[6] many problems were posed:preparation technique, RuO_2 solubility and phase stability in stabilized zirconia, thermal stability, electrical conductivity, electrode polarization, etc.

The present paper mainly describes the different attempts to prepare a stable solid-state solution, and the structural characteristics of the powdered and sintered material.

2 Experimental

Ternary oxide samples of ZrO_2, Y_2O_3 and RuO_2 were prepared to give compositions with $[(ZrO_2)_{0.91}(Y_2O_3)_{0.09}]_{1-x}(RuO_2)_x$, $0 \leq x \leq 20$ mol% RuO_2. In the following, yttria-stabilized zirconia–ruthenia will be labelled $YSZRu_x$. Samples were prepared from a stoichiometric mixture of ruthenium nitrosyl nitrate $Ru(NO)(NO_3)_3$, zirconyl nitrate $ZrO(NO_3)_2$ and yttrium nitrate $Y(NO_3)_3$ dissolved in water. The solution was then dried under continuous stirring at 100°C until total evaporation of water. The products were calcinated at 500°C for 6 h to decompose the nitrates. The complete thermal decomposition of the nitrates used as precursors was observed at 500°C by thermogravimetry using a Netzsch Thermal Analyser (Fig. 1). This result is in agreement with those reported by Ardizzone *et al.*[7] concerning the decomposition of $Ru(NO)(NO_3)_3$.

After pyrolysis at 500°C, subsequent grinding and annealing of the sample was undertaken at different temperatures—800, 900, 1100 and 1400°C—to investigate its thermal stability. Firings were carried out in air at a heating rate of 5°C min^{-1} for 12 h

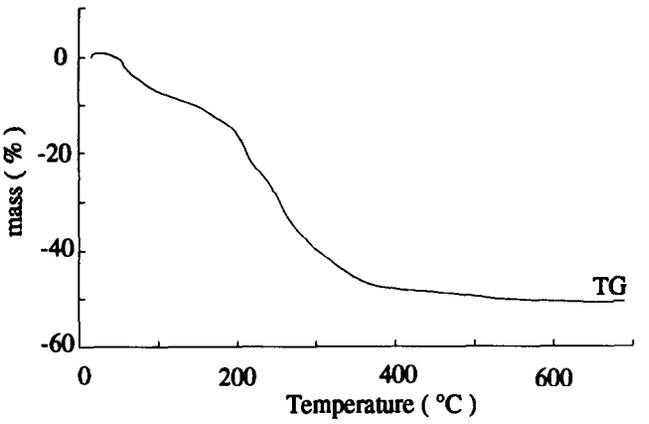

Fig. 1. Thermogravimetric analysis of $ZrO(NO_3)_2$ + $Y(NO_3)_3$ + $Ru(NO)(NO_3)_3$.

duration at each temperature. Samples were furnace-cooled to room temperature.

Note that two further preparation methods were used in unsuccessful attempts to synthesize a new single phase with YSZ/RuO_2. RuO_2 was mixed with different yttria-stabilized zirconia (YSZ) materials:

(1) commercially available YSZ powder (9 mol% Y_2O_3, from Tosoh) and
(2) YSZ powder prepared from calcination of Zr and Y hydroxides at 500°C. The mixture of Zr and Y hydroxides was obtained using the butylate method.[8]

These methods, based on the solid-state route, led to a two-phase mixture of RuO_2 and YSZ.

$YSZRu_x$ powder was pressed in a uniaxial die at 1500 kg cm^{-2} to form a pellet (12·8 mm in diameter and 3·1 mm thick). X-ray characterization at room temperature was carried out using a Siemens D500 diffractometer equipped with a linear detector (Cu $K_{\alpha 1}$ radiation, λ = 1·5406 Å). Silicon was used as the internal reference for all scans (0·04°, 2θ steps, 5 s counting time).

Scanning electron microscopy (SEM) and electron probe micro analysis (EPMA) (Cameca SX50) were performed to characterize the crystal microstructure. Two $YSZRu_{10}$ samples synthesized at 900 and 1400°C were studied by EPMA. Four elements were analysed: standard no. 1 is pure Ru calibrated on line L_α at 15 kV using a polyethylene terephthalate (PET) ($C_5H_{12}O_4$) crystal; standard no. 2 is Zr in YSZ (wt% = 62·67) calibrated on line L_β at 15 kV using a PET crystal and not on the L_α in order to avoid overlap of the Y L_β; standard no. 3 is Y in YSZ (wt% = 12·08) calibrated on line L_α at 15 kV with a thallium acid phthalate (TAP) ($C_8H_5O_4Tl$) crystal; standard no. 4 is O in YSZ (wt% = 25·25) calibrated on line K_α at 15 kV with a PCl multilayer (W–Si) crystal. Note that Zr, Y and O standards come from the nominal $((ZrO_2)_{0.91}(Y_2O_3)_{0.09})$ composition which was prepared via nitrates up to 1400°C and gave satisfactory quantitative results compared with calculated values.

3 Results and Discussion

The first section deals with the new material prepared as a powder and the second part with the new material prepared as sintered ceramics.

3.1 $YSZRu_x$ powder

The firing procedure (successive grinding and annealing) proved to be essential to keep the RuO_2 in the yttria-stabilized zirconia matrix giving rise to a black compound. The main advantage of the nitrate method compared with the classical solid-state reaction route is that it stabilizes RuO_2 in solid solution at low temperatures, which otherwise decomposes into Ru and RuO_4 at temperatures higher than 1000°C.[9] The minimum temperature at which RuO_2 could be incorporated into YSZ was 500°C.

X-ray diffraction patterns of $YSZRu_x$ compounds with $0 \leq x \leq 10$, fired at 500°C, showed one single cubic phase, similar to that of YSZ, with very broad peaks indicating poor crystallinity. To improve the crystallinity of the compounds, treatments were carried out at 800 and 900°C. These firings yielded well-crystallized monophase samples. A typical XRD pattern of the $YSZRu_{10}$ powder after a 900°C treatment for 12 h is shown in Fig. 2. Based on this profile, a cubic fluorite-related structure could be assigned to $YSZRu_{10}$ solid solution. The unit-cell parameter changed from 0·5129(3) nm for pure YSZ to 0·5098(2) nm for $YSZRu_{10}$ solid solution.

The influence of temperature on the variation of full width at half maximum (FWHM) of the (2 2 0) peak for $YSZRu_{2.5}$ was investigated. FWHM values of 0·81°, 0·73° and 0·49° (±0·04°) were found at

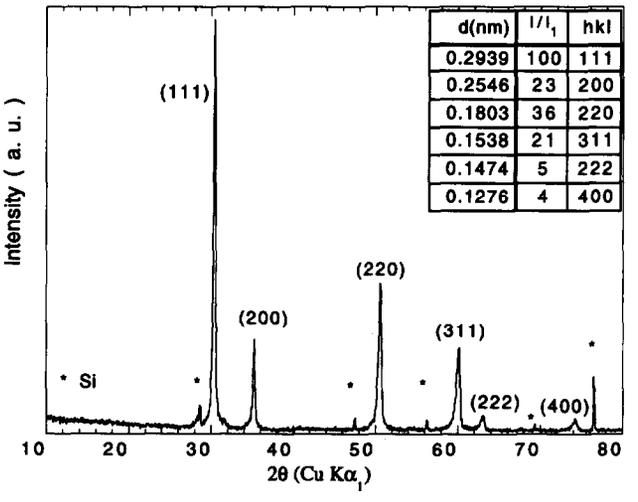

Fig. 2. Typical X-ray powder diffraction pattern of $[(ZrO_2)_{0.91}(Y_2O_3)_{0.09}]_{0.9}(RuO_2)_{0.1}$ fired at 900°C.

500, 800 and 900°C, respectively. The decrease in FWHM with increasing temperature is consistent with a better crystallinity and larger grain size.

To study the chemical stability of the new oxides with temperature, special attention was paid to the temperature dependence of the (1 1 1) and (2 0 0) reflections of $YSZRu_{10}$ sintered at 800, 900, 1100 and 1400°C (Fig. 3). The (1 1 1) peak of pure RuO_2 appears at 1100°C, indicating the thermal decomposition of the solid solution. At 1400°C, the X-ray profile is quite similar to that of pure YSZ.

In Fig. 4, simultaneous examination of the (1 1 1) and (2 0 0) positions indicates a 2θ shift towards lower angles from 1000°C due to the loss of ruthenium and recovering of the YSZ configuration. In an oxidizing atmosphere, during the volatilization of RuO_2, Bell and Tagami[10] reported that the main vapour species are RuO_3 and RuO_4 in the range 1465 to 2090°C. We may conclude that the best com- promise between thermal stability and crystallinity appears to be achieved with calcination at 900°C.

To determine the solubility limit of RuO_2 in YSZ, samples containing 2·5, 5, 10, 12·5, 15 and 20 mol% RuO_2 were prepared. Up to 10 mol% RuO_2, all the samples were single phase with the cubic fluorite-type structure. For higher RuO_2 content, peaks characteristic of the excess of RuO_2 appeared, indicating that the limit of the solid solution was reached between 10 and 12·5 mol% RuO_2 (Fig. 5).

In the solid solution domain, the lattice parameter variation (Fig. 6) follows the linear relationship:

$$a\ (\text{nm}) = 0{\cdot}5128(6) - 0{\cdot}2(8) \times 10^{-3}\ x$$

These data suggest that the contraction of the unit cell is correlated to RuO_2 dissolution in YSZ. Ru^{4+} is six-fold coordinated in its rutile structure and has an ionic radius of 0·62 Å. In the YSZ, Zr^{4+} is eight-fold coordinated and its ionic radius is 0·84 Å.[11] Thus, it is not ruled out that Ru^{4+} could be

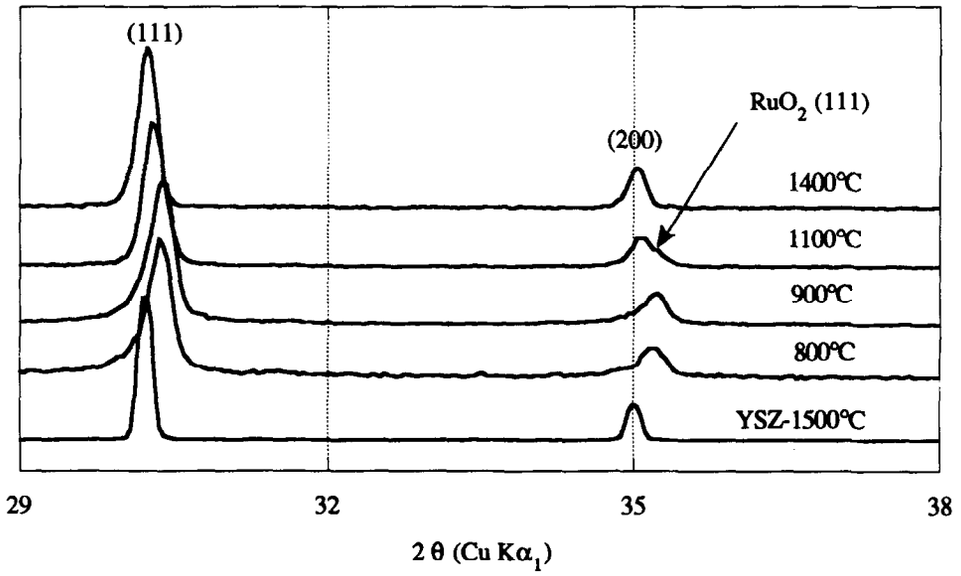

Fig. 3. Temperature dependence of the (1 1 1) and (2 0 0) X-ray positions of YSZ/10 mol% RuO_2.

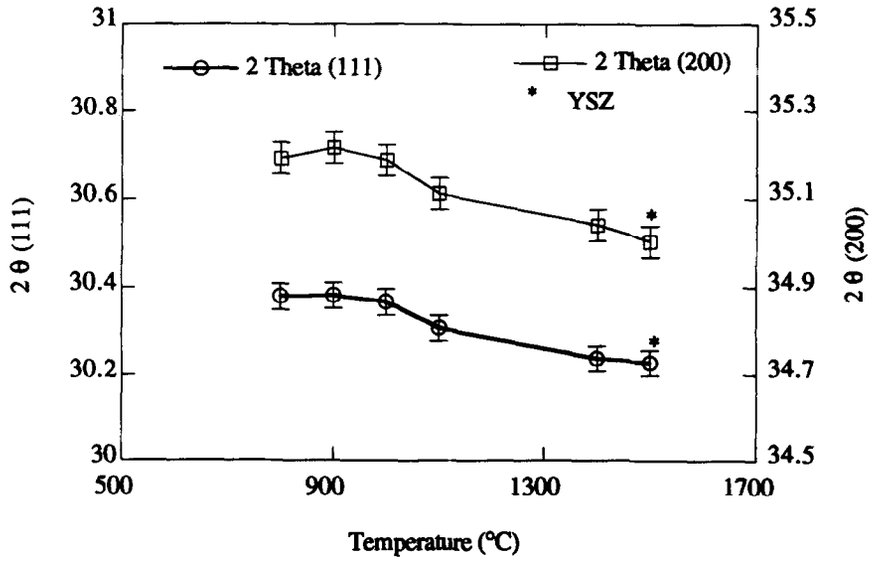

Fig. 4. The 2θ shifting with temperature of the (1 1 1) and (2 0 0) X-ray positions of YSZ/10 mol% RuO_2.

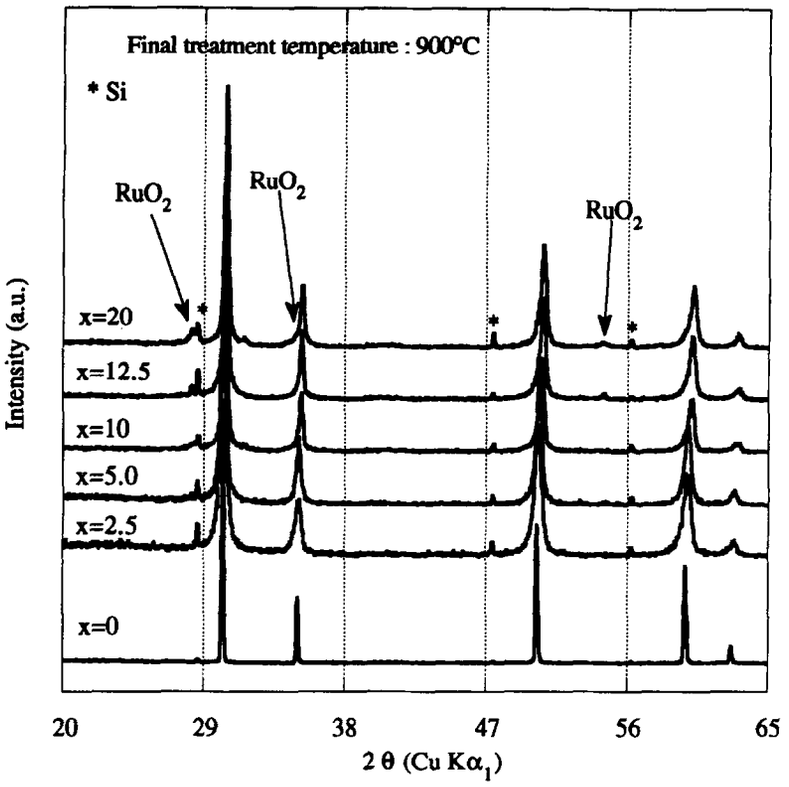

Fig. 5. X-ray diffraction spectra as a function of x mol% RuO_2 in $[(ZrO_2)_{0.91}(Y_2O_3)_{0.09}]_{1-x}(RuO_2)_x$.

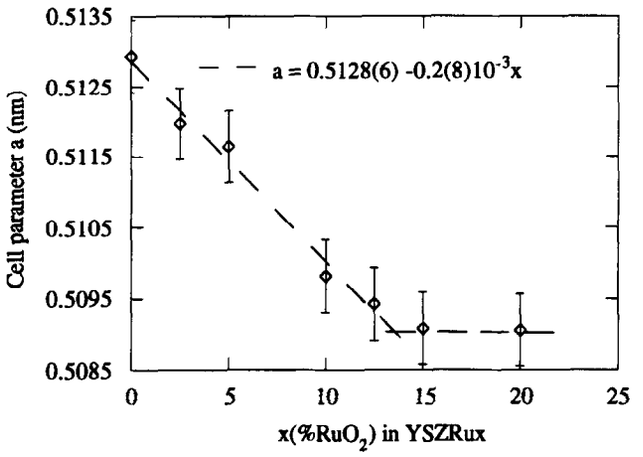

Fig. 6. Variation of the cell parameter with RuO_2 content in the system $[(ZrO_2)_{0.91}(Y_2O_3)_{0.09}]_{1-x}(RuO_2)_x$.

incorporated in the YSZ matrix as a substitutional dopant on Zr^{4+} sites. Ru^{4+} may also occupy interstitial sites. X-ray diffraction did not allow us to conclude the nature of the local environment of Ru because the dopant (Ru^{4+}) has an atomic number very close to the doped value (Zr^{4+}). Raman measurements at the K threshold of ruthenium (22118 eV) are planned to determine the local environment of Ru^{4+} in YSZ.

3.2 $YSZRu_x$ ceramics

The final sintering temperature of 900°C and the 12 h sintering duration were selected to avoid thermal decomposition of the solid solution. This was confirmed by X-ray analysis (Fig. 3).

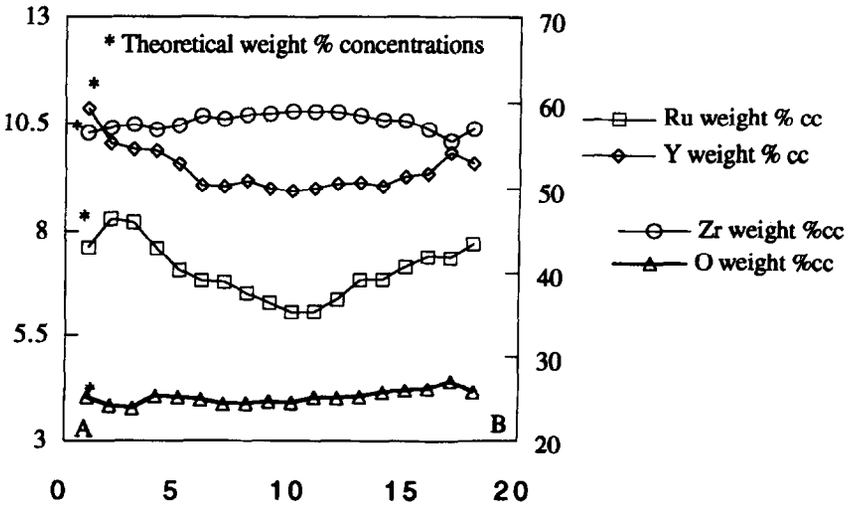

Fig. 7. Change of Ru, Y, Zr and O wt% through the 25 μm grain. A and B are the extremities of this path.

Table 1. Quantitative analysis on $YSZRu_{10}$ prepared at 1400°C

Element	*Theoretical wt%*	*Measured wt%*
Ru	7·62	0·42
Zr	56·38	65·30
Y	10·86	8·08
O	25·13	25·73

No shrinkage was found in a dilatometry experiment in air on $YSZRu_{10}$ up to 1000°C. The density of $YSZRu_{10}$ pellets sintered at 900°C for 12 h was ~3·6 g cm^{-3}.

Porosity was detected using SEM. In addition, heterogeneity in the grain size (from 1 to 25 μm) as well as in the composition of particles was observed. A composition profile was determined through the particles of around 25 μm in size. It shows a small gradient of ruthenium composition in the grain (Fig. 7), ruthenium being located on the periphery of the particle.

A sintering study needs to be carried out to increase the density of samples, which is too low at present because of the synthesis technique.

Finally, a microprobe analysis on the $YSZRu_{10}$ prepared at 1400°C in air confirms that a significant amount of ruthenium is lost under these conditions (Table 1).

4 Conclusion

In the present work, new oxides, $[(ZrO_2)_{0.91}(Y_2O_3)_{0.09}]_{1-x}(RuO_2)_x$, belonging to the cubic solid solution with $0 \leq x < 12{\cdot}5$ mol% RuO_2, have been synthesized by solid-state chemistry from nitrates as precursors. The last 900°C firing step was carried out to obtain the best possible crystallinity and good thermal stability of the monophase fluorite-related compound. The contraction of the unit cell parameter has been correlated to RuO_2 incorporation into the YSZ matrix. Further work is planned to investigate the local environment of Ru^{4+} in the new compounds by Raman spectroscopy and Extended X-ray Absorption Fine Structure (EXAFS).

On the other hand, SEM and EPMA results mainly show heterogeneity in the grain size and ruthenium composition. Moreover, high porosity is observed inside and between grains. Our future experiments will aim at reducing the porosity and enhancing the microstructural homogeneity.

Acknowledgement

The authors would like to thank the Commission of the European Communities for their financial support (Project JOUE-004C).

References

1. Tagirov, V. K., Chizhikov, D. M., Kazenas, E. K. & Shubochkin, L. K., *J. Inorg. Chem.*, **20** (1977) 1133.
2. Beer, H. B., *J. Electrochem. Soc.*, **127** (1980) 303C.
3. Trasatti, S. & Buzzance G., *J. Electroanal. Chem. Interfacial Electrochem.*, **29** (1971) 635.
4. O'Grady, W., Twakura, C., Huang, J. & Yeager, E., in *Electrocatalysis*, ed. M. W. Breiter. The Electrochemical Society Softbound Symposium Series, Princeton, NJ, 1974, p. 286.
5. Burke, L. D., Murphy, O. J., O'Neill, J. E. & Venkatesan, S., *J. Chem. Soc., Faraday Trans. 1*, **73** (1977) 1659.
6. Long, Y. C., Zhang, Z. D., Dwight, K. & Wold A., *Mater. Res. Bull.*, **23** (1988) 631.
7. Ardizzone, S., Falciola, M. & Trasatti, S., *J. Electrochem. Soc.*, **136** (1989) 1545.
8. Koch, M. & Nair K. M., *Cermugia Int.*, **2**[2] (1976) 88.
9. Pascal P., *Nouveau Traité de Chimie Minérale*. Masson et Cie editors, Paris, Vol. XIX, 1958, p. 85.
10. Bell, W. E. & Tagami, M., *J. Phys. Chem.*, **67**[11] (1963) 2432–6.
11. Shannon, R. D. & Prewitt, C. T., *Acta Cryst.*, **B25** (1969) 925.

Journal of the European Ceramic Society 16 (1996) 773–779

0955-2219(95)00191-1
0955-2219/96/$15.00

Growth of Cubic Paraelectric Perovskite La-Modified $PbTiO_3$ Thin Films by RF Magnetron Sputtering

B. Jaber, D. Remiens & B. Thierry

Laboratoire des Matériaux Avancés Céramiques — CRITT Céramiques Fines, Université de Valenciennes et du Hainaut-Cambrésis, Z. I. Champ de l'Abbesse, 59600 Maubeuge, France

(Received 21 February 1995; revised version received 13 October 1995; accepted 24 October 1995)

Abstract

Thin films of lead titanate doped with 28% lanthanum (PLT28) have been deposited on sapphire and silicon substrates using RF magnetron sputtering. Film deposition was performed without substrate heating and the sputtering gas was pure argon. The process conditions required to prepare dense, crack-free and stoichiometric perovskite films, from different kinds of targets, have been determined. Cracking of PLT28 films on silicon substrates has been prevented by heating the substrate to 300°C during deposition. After post-annealing the films were very dense.

Les films minces de titanate de plomb dopé avec 28% en lanthane (PLT28) ont été préparés sur des substrats de saphir et de silicium par pulvérisation cathodique RF magnetron. Les dépôts sont effectués sans chauffage du substrat et le gaz de pulvérisation est de l'argon pur. Les conditions de process nécessaires pour préparer des films PLT28 stoechiométriques, de structure pérovskite, denses et sans fissures ont été determinées. Les fissures apparaissant sur les films déposés sur silicium ont été supprimées par chauffage du substrat à 300°C durant la croissance du film. Après le traitement thermique les films sont très denses.

1 Introduction

Ferroelectric ceramics belonging to the solid solution system PLZT (lead–lanthanum zirconate–titanate) have undergone substantial technology development due to their many interesting properties. These materials can be piezoelectric, ferroelectric, electrooptic, pyroelectric, ... but in the bulk form, the use of these ceramics has been limited by the relatively high switching voltages required.

Many techniques[1–4] have been developed to grow these materials in thin films form. Such films allow the inherent limitations of monolithic ceramics to be overcome and to attain compatibility with semiconductor technologies.

Among these methods, cathodic sputtering, DC or RF, is the most developed[5,6] to prepare ferroelectric thin films such as lead titanate (PT), lead zirconate–titanate (PZT) and PLZT. There have been numerous proposals for the application of the PLZT thin films in optoelectronic devices, in particular the (28/0/100) composition which exhibits interesting electrooptic effects superior to those of $LiNbO_3$ as shown in Table 1.

The purpose of this paper is to report the preparation of PLT28 thin films on sapphire and silicon substrates. Deposition conditions and post-annealing parameters have been optimised in order to produce stoichiometric thin films with perovskite structure.

2 Experimental Procedure

The radio-frequency magnetron sputtering system used was described previously.[9] For easy target fixation, the deposition has been performed in the 'sputter-down' mode. The substrate temperature was measured by a chromel-alumel-type thermocouple placed just behind the substrate. The measured temperature, as reported in this paper, represents the substrate block temperature. Films are deposited on substrates of (0001) sapphire and (100) oxidised silicon. The properties of the substrates

Table 1. Comparison of the linear electrooptic coefficient r for some materials

Material	r 10^{-10} *(m/V)*	*Ref.*
PLZT (9/65/35)	0·22	7
PLZT (28/0/100)	0·35-0·41	7
$LiNbO_3$	0·17	8

Table 2. Characterisation of the substrates used and of PLT28 ceramics

Material	*Structure*	*(hkl)*	*Lattice parameter (Å)*	*Thermal expansion coefficient* $10^{-6}K^{-1}$	*Ref.*
Al_2O_3	Rhombohedral (α-Al_2O_3)	(0001)	a = 4·759 c = 12·991	7·5	10
Si	Diamond cubic	(100)	a = 5·4301	3	10
PLT28	Perovskite cubic	—	a = 3·9277[11]	6·6 $623 \leq T \leq 773$ K	12

used and of PLT28 ceramics are summarised in Table 2.

Before deposition, all substrates were cleaned in a series of organic solvents and deionised water.

Different types of targets were studied:

— A mixture of PbO, TiO_2 and La_2O_3 powders (purity >99·95%) with the composition of $Pb_{1-x}La_xTi_{1-x/4}O_3$ where x = 0·28. The target diameter and thickness were 3" and 3 mm, respectively. This chemical formula has been used assuming the B-site vacancies to neutralise the extra-positive charge from the La addition–creation (La^{3+} occupies the A-sites (Pb^{2+}) in the tetragonal perovskite structure of $PbTiO_3$). Films made using this formula had better optical and electrical properties.[13]

— Reacted powder prepared by calcination of a mixture of oxides for 6 h at 1100°C. The stoichiometry of this powder was confirmed by Inductively Coupled Plasma (ICP) analysis. X-ray diffraction showed the powder to have the cubic perovskite structure with lattice parameter of a = 3 9303 Å.

— Sintered target prepared by pressureless sintering of the reacted powder at 1250°C for 4 h, using a powder bed of $PbZrO_3$ (to prevent the lead evaporation). The latter two targets had a 1" diameter and 2 mm thickness.

In order to stabilise the target surface composition (formation of the 'altered layer') and to remove the adsorbed gas, a pre-sputtering run was necessary:

— 3 h for the new target.

— 30 min before each deposition for a previously used target.

The pre-sputtering conditions were identical to those of deposition.

After carrying out many depositions, cracks appeared in the erosion track of all targets probably due to local heating provoked by the presence of the magnetron system.

3 Film Characterisation

The thickness and its uniformity of the PLT28 films were measured by profilometry with 200 Å precision. The film was then chemically etched (hydrochloric acid) to make a step between the film and the substrate (obtained by photolithography). The film composition was analysed by ICP. The structure was determined by X-ray diffraction (XRD) with a counter diffractometer using θ–2θ geometry and Cu Kα radiation. The film morphology was examined by scanning electron microscopy (SEM).

4 Results and Discussion

It is well known that the deposition conditions such as RF power density, gas pressure, target–substrate distance, ..., affect the properties of films, primarily the deposition rate, the film composition as well as the microstructure.

4.1 Deposition rate

The effect of argon pressure on different types of target (1" diameter) have been studied. Figure 1 shows the deposition rate variations versus the

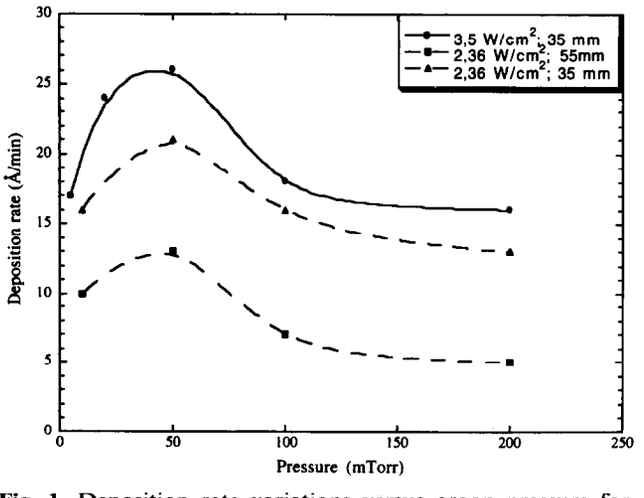

Fig. 1. Deposition rate variations versus argon pressure for two values of power density: 2·36 and 3·5 W/cm^2 and two inter-electrode distances: 35 and 55 mm. A mixed oxide powder target (1" diameter) and a silicon substrate were used.

argon pressure for two values of power density: 2·36 and 3·5 W/cm^2 and two inter-electrode distances: 35 and 55 mm, in the case of the mixed oxide powders target. The deposition rate was deduced by the film thickness measurement divided by the duration of sputtering.

Below 50 mTorr, the deposition rate increased with the argon pressure, since the ion density increased. The deposition rate decreased when the pressure become larger than 50 mTorr; the number of collisions in the reactor increased therefore the ion efficiency decreased. Above 100 mTorr, the deposition rate was constant; in the order of 15 Å/min for an RF power density of 2·36 W/cm^2 and an inter-electrode distance of 35 mm. It was likely that the backscattering effect contributed to these effects at high pressure.

The increase of RF power density involved an increase of the deposition rate since the Ar^+ energies increased which causes an increase in the density of sputtered neutrals and their average energy. However, the deposition rate decreased when the distance between the target and substrate increased, in effect, the energy of the Ar^+ decreased as the number of collisions increased and in addition the sputtered neutrals were thermalised near the target which increased the diffusion path.

As can be seen in Fig. 2, the deposition rate also depended on the type of target. For fixed deposition conditions the highest film deposition rate was obtained using the sintered target. These variations were presumably due to the large differences in the kinds of sputtered neutrals and in the bonding energies of species at the surface of each target types.

Sintered targets which often broke after each deposition were rejected. This behavior was probably due to the large stress generated in the material because of the large quantity of dopant (28% lanthanum) incorporated.

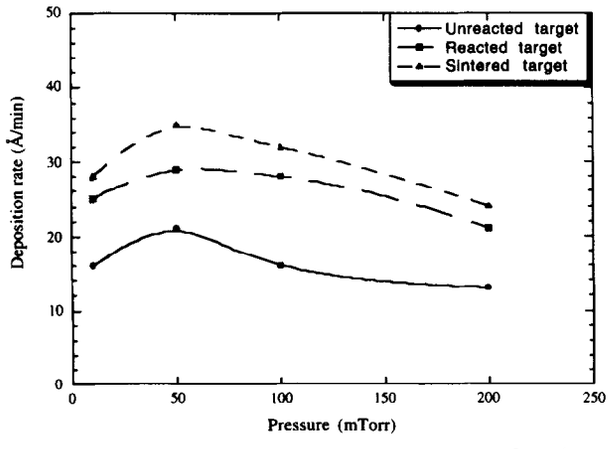

Fig. 2. Deposition rate versus gas pressure as a function of target type, RF power density density P_{rf} = 2·36 W/cm^2, sputtering pressure P = 100 mTorr, target–substrate distance d = 35 mm.

4.2 Film composition

In this study two types of targets were used.

4.2.1 Target of reacted powder (1" diameter)

As previously mentioned, film deposition was carried out at room temperature. The substrate temperature reaches about 50°C during the deposition phase due to electron/ion bombardment. Figure 3 shows the film composition variations versus the RF power density; the sputtering pressure and the inter-electrode distance were fixed at 50 mTorr and 35 mm respectively. Whatever the RF power density the concentrations of Pb and Ti were far from the desired composition. However the desired concentration of La is obtained for RF power density of 1·2 W/cm^2. Therefore this RF power density was selected to study the pressure effect on the film composition. As can be seen in Fig. 4, a working point for this type of target was found for an Ar pressure about 110 mTorr. Contrary to that found previously for $PbTiO_3$ films,[9] PLT28 films investigated in this study did not contain an excess of Pb. These is presumably due to the large quantity of La^{3+} (28%) occupying the Pb^{2+}-site in the $PbTiO_3$ perovskite and to the

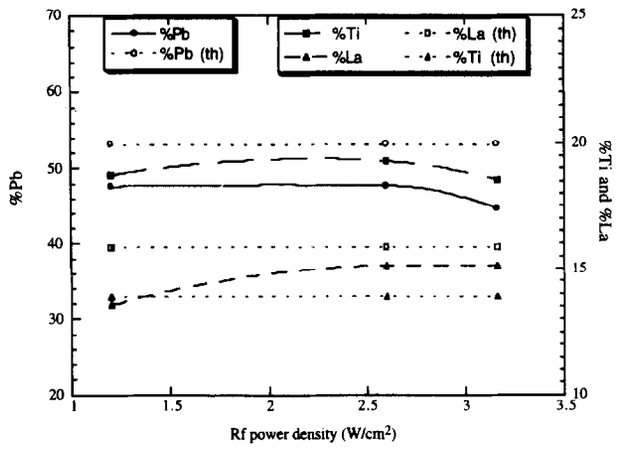

Fig. 3. Film composition versus RF power density for Al_2O_3 substrate with the reacted powder target (1" diameter); P = 100 mTorr and d = 35 mm.

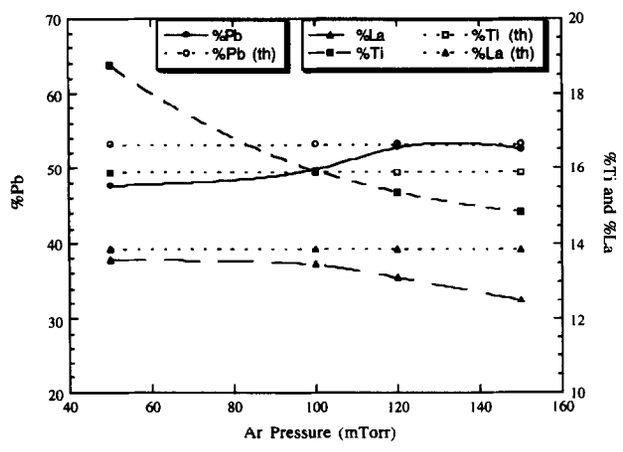

Fig. 4. Film composition versus argon pressure for Al_2O_3 substrate with the reacted powder target (1" diameter); P_{rf} = 1·2 W/cm^2 and d = 35 mm.

difference in the transfer process of the sputtered species.

4.2.2 Target of mixed oxide powders (3" diameter)
The object with this type of target was to attain an excellent uniformity of film thickness and composition.

In this context, the distance between target and substrate was fixed at 70 mm for 50 mTorr pressure (the thermalisation regime was certainly attained). Figure 5 illustrates the composition variation versus the RF power density for a fixed argon pressure of 50 mTorr. Elemental concentration varied very little with the RF power density.

The composition variations versus the sputtering pressure (RF power density fixed at 2·6 W/cm^2) are shown in Fig. 6. The observed behavior was different to that obtained in the case of the reacted powder target particularly for Ti and La elements.

From these studies, optimised deposition conditions were defined and are summarised in Table 3.

For these sputtering conditions and with these target diameters the substrate temperature reaches about 170°C during deposition due to the ion bombardment. Using this target and the optimal

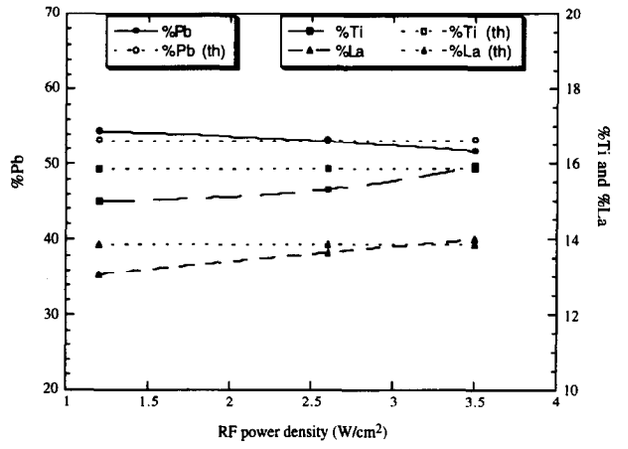

Fig. 5. Variation of the film composition as a function of the RF power density for Al_2O_3 substrate with the unreacted powder target (3" diameter); P = 50 mTorr and d = 70 mm.

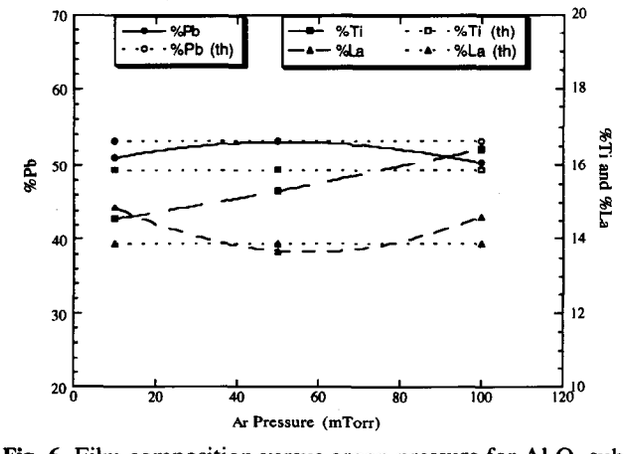

Fig. 6. Film composition versus argon pressure for Al_2O_3 substrate with the unreacted powder target (3" diameter); P_{rf} = 2·6 W/cm^2 and d = 70 mm.

Table 3. Optimal deposition parameters of unreacted powder target

Inter-electrode distance	70 mm
RF power density	2·6 W/cm^2
Sputtering gas	100% Ar
Gas pressure	50 mTorr
Substrate temperature	~170°C

conditions, the effect on the film composition of the oxygen concentration in the sputtering gas (argon) has been investigated. As can be observed in Fig. 7, the incorporation of 5% O_2 in Ar resulted in a decrease of different element concentrations. Above this quantity of O_2 the composition remained constant. These observed variations are likely to arise from the high reactivity of O_2 with these elements at the target surface as well as in the plasma.[14]

4.2.3 Composition reproductibility
In Fig. 8 the results obtained for films made under the optimised conditions (Table 3) from 3" targets (mixed oxide powders) are presented. Composition reproducibility of 4% was found for films produced from the same target (data points 1 and 2) as well as for films obtained from different targets

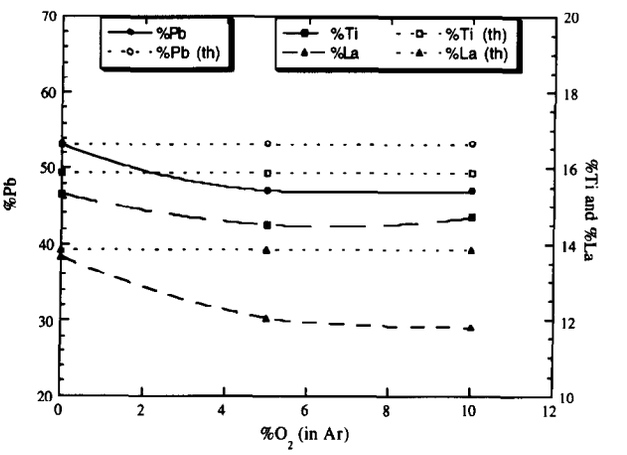

Fig. 7. Effect of oxygen concentration in the sputtering gas (Ar) on the film composition.

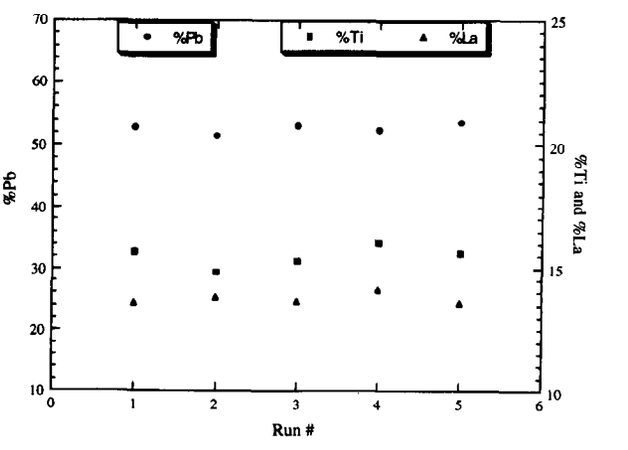

Fig. 8. Film composition reproducibility for the unreacted powder target (3" diameter).

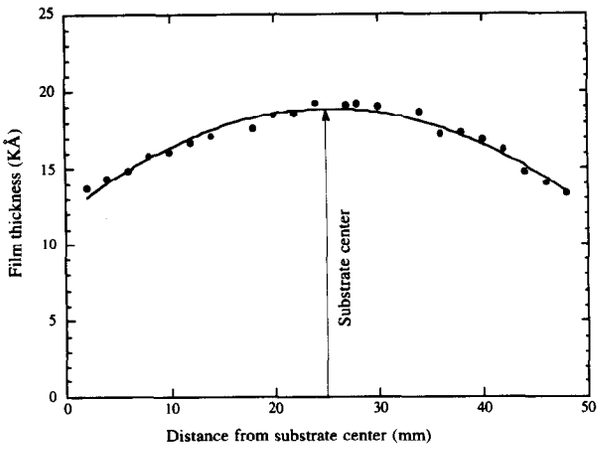

Fig. 9. Variation of the film thickness as a function of the radial distance from the substrate centre.

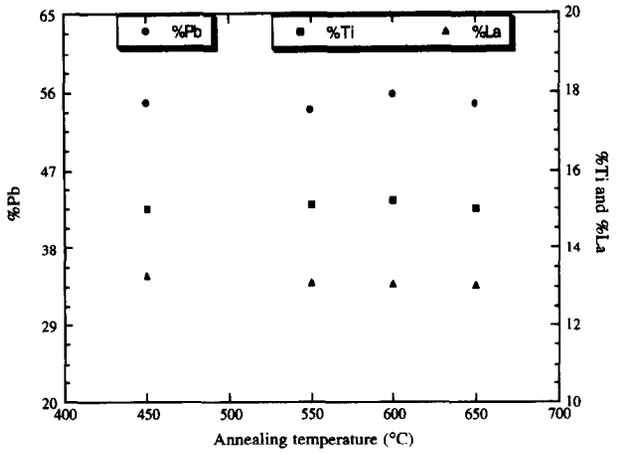

Fig. 11 Film composition as a function of the annealing temperature. Annealing time = 2 h.

(data points 3, 4 and 5). These composition deviations were attributed to the analysis error of the ICP.

4.2.4 Thickness uniformity

Films were deposited on silicon substrates 2" in diameter from 3" diameter targets of unreacted powder. The desired film thickness was about 1·9 μm (for our future applications). Figure 9 shows film thickness as a function of the radial distance from the substrate centre.

The observed variation was due to the inner and outer diameters of the plasma ring (magnetron effects) and to the variations in the ejection angles for the sputtered species.[15] For the present deposition conditions the inner and the outer diameters of the plasma ring (Fig. 10) are estimated to be 1·7 and 2·7 mm respectively. A 5% film thickness uniformity was measured on a diameter of about 20 mm.

4.2.5 Composition after post-deposition annealing

A post-deposition annealing step was necessary in order to crystallise amorphous films obtained on unheated substrates.

This study was carried out on films deposited on (0001) Al_2O_3 and (100) oxidised Si substrates using a 3" target of unreacted powder and optimal deposition conditions (Table 2).

The annealing temperature was limited to 700°C for pratical reasons (to reduce the loss of Pb, to avoid film–substrate interactions).

Figure 11 shows film composition as a function of the annealing temperature. It can be seen that the film composition was not sensitive to annealing temperature variations up to 650°C regardless of whether sapphire or silicon substrates were used.

4.3 Film structure and microstructure

The development of the film structure was examined by XRD. Figure 12 illustrates the structural development as a function of the annealing temperature (annealing time fixed to 2 h) for films deposited on (0001) Al_2O_3. The film thicknesses were about 0·75 μm. In order to suppress microcracking (due to the large difference in the coefficients of thermal expansion between film and substrate), the heating and cooling rates were optimised at 3 and 1°C/min respectively. Annealing was carried out in air.

As-deposited films produced X-ray diffraction patterns consistent with an amorphous structure.

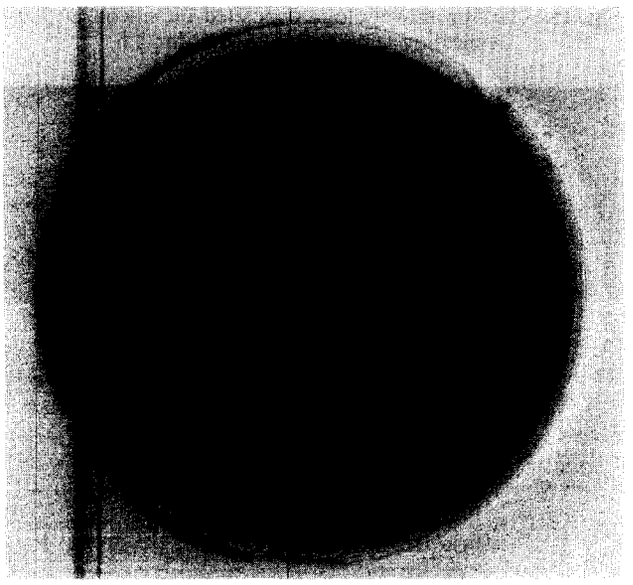

Fig. 10. Target photography after sputtering process in deposition conditions summarised in Table 3.

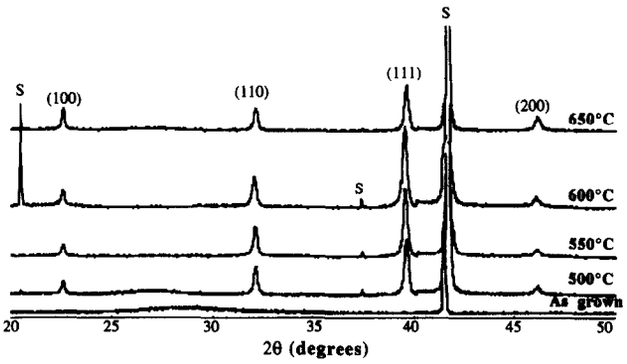

Fig. 12. XRD pattern as a function of annealing temperature for films deposited on sapphire.

The cubic perovskite structure was initiated at a temperature as low as 500°C without evidence of pyrochlore second phase. The perovskite phase formation was completed between 550 and 600°C. The same result had been reported by A. R. Kan *et al.*[13]

The PLT28 films had (111) preferred orientation on this type of substrate. At an annealing temperature of 600°C, the lattice parameter was 3·9286 Å, a value very close to that of the bulk ceramic.

It is well known that the substrate also affects crystallisation. For silicon substrates, optimal crystallisation was obtained at 650°C as can be seen in Fig. 13. These films have (110) preferred orientation. However, using the annealing parameters optimised for sapphire substrates, microcraking occurred in films deposited on silicon (Fig. 14). This was presumably due to the high stress generated at the SiO_2/PLT28 interface (large difference in the coefficients of thermal expansion). After several trials, microcracking was prevented by depositing the film with a substrate temperature of about 300°C (Fig. 15). This reduced stress in the film and perhaps initiated film crystallisation.

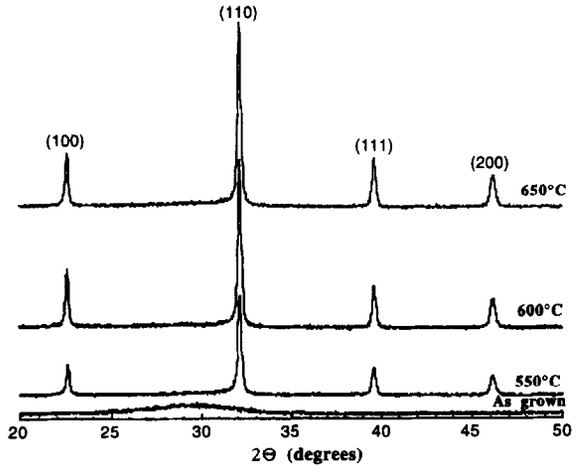

Fig. 13. XRD pattern as a function of annealing temperature for films deposited on silicon.

Fig. 14. Microcracking observed in the film deposited (at room temperature) on silicon after thermal treatment (600°C, 2 h).

After thermal treatment, the films were very dense as can be observed in the SEM micrograph (Fig. 16) showing the cross-section of the film annealed at 600°C for 2 h in air.

5 Conclusions

PLT28 thin films have been prepared successfully on sapphire and silicon substrates by RF magnetron sputter deposition from targets of unreacted as well as reacted powder.

The sputtering parameters have been optimised in order to assure the composition transfer between the stoichiometric target (1" and 3") and the thin film

Post-deposition annealing conditions have also been optimised to obtain crack-free PLT28 thin films with a perovskite structure on sapphire as well as on silicon substrates.

The PLT28 thin films have a (111) and (110) preferred orientation on (0001) sapphire and (100) oxidised silicon respectively.

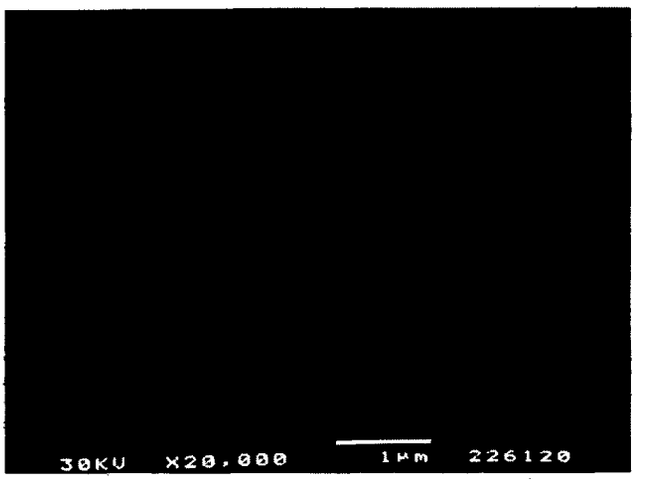

Fig. 15. The film morphology deposited on silicon at 300°C. Annealing temperature: 600°C for 2 h.

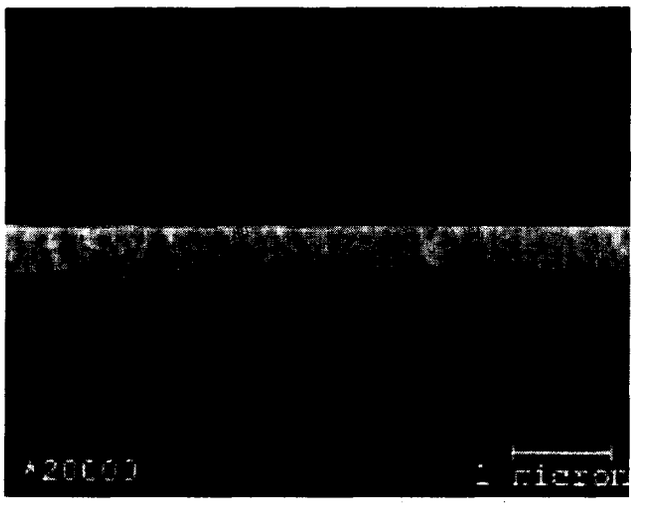

Fig. 16. Cross-section of the films deposited on silicon annealed at 650°C for 2 h in air.

References

1. Budd, K. D., Dey, S. K. & Payne, D. A., *Bl. Ceram. Proc.*, **36** (1985) 107.
2. Xu, J. J., Shaikh, A. S. & Vest, R. W. In *IEEE Transactions on Ultrasonics, Ferroelectrics and Frequency Control*, 1989 p. 307.
3. Okada, H., Takai, S., Amemiya, M. & Tominaga, K., *Jpn. J. Appl. Phys.*, **28** (1989) 1030.
4. Lijima, K., Terashima, T., Yamamoto, R., Hirata, K. & Bando, K., *Appl. Phys. Lett.*, **56** (1990) 527.
5. Ishida, M., Matsunami, M. & Tanaka, T., *J. Appl. Phys.*, **48** (1977) 951.
6. Okamura, T., Adachi, H., Shiosaki, T. & Kawabata, A., *Jpn. J. Appl. Phys.*, **30**(5) (1991) 1034.
7. Wu, A. Y., Wang, F., Bustamante, C., Yeh, C. Y. & Diels, J. C., *IEEE 7th Int. Symp. Appl. Ferro.*, Urbana-Champaign, 1990, p. 135.
8. Haertling, G. H., *Ferroelectrics*, **75** (1987) 25–55.
9. Remiens, D., Tirlet, J. F., Jaber, B., Joire, H., Thierry, B. & Moriamez, C., *J. Eur. Ceram. Soc.*,**13** (1994) 493.
10. Ishida, H., Isuji, S., Kimura, K., Matsunami, H. & Tanaka, T., *J. Crystal Growth*, **45** (1978) 393.
11. Huang, Y., Luo, W., Din, A., Ge, M. & Chen, X., *SPIE Electro-Optic and Magneto-Optic Materials and Applications*, **1126** (1989) 36.
12. Tossell, D. A., Obhi, J. S., Shorrocks, N. M., Patel, A. & Whatmore, R. W. *IEEE, Int. Symp. Appl. Ferro.*, 1992 p.11.
13. Khan, A. R., Yoo, I. K. & Desu, S. D., *Int. Symp. Appl. Ferro.*, 1992 p. 412.
14. Vassant Kumar, C. V. R. & Nansingh, A., *J. Appl. Phys.*, **65**(3) (1989) 1270.
15. Castellano, R. N., Notis, M. R. & Simmons, G. W., *Vaccum*, **27** (1977) 103.

Journal of the European Ceramic Society 16 (1996) 781–789

0955-2219(95)00200-6
0955-2219/96/$15.00

Synthesis and Phase Transformations of Mullites Obtained from SiO_2–Al_2O_3 Gels

Manuela Sales & Javier Alarcón*

Departamento de Química Inorgánica, Facultad de Ciencias Químicas, Universidad de Valencia, 46100 Burjasot (Valencia), Spain

(Received 7 September 1994; revised version received 25 October 1995; accepted 1 November 1995)

Abstract

Synthesis and structural characterization of mullite phases obtained from three nominal compositions in the SiO_2–Al_2O_3 system is reported and comparisons between them are established. Monosized gels with Al/Si atomic ratios of 2:3, 3:1 and 9:1 were obtained and thermally treated at temperatures between 700 and 1500°C. The thermal evolution of amorphous gels was followed by thermal analysis, X-ray diffraction and infra-red spectroscopy. The microstructural changes were studied by scanning electron microscopy and transmission electron microscopy. The formation of Al_2O_3-rich mullite started around 1000°C for all samples and was fully developed at 1400°C. The chemical composition of mullites changed as a function of calcining temperature. An anomalous low value of the lattice parameter a *was obtained for the sample with Al/Si atomic ratio of 9:1 compared with the 3:1 sample at 1400°C, which may be due to the slow reaction rate of Al_2O_3 with SiO_2-rich glassy phase during mullite formation.*

1 Introduction

Mullite is the only stable phase in the SiO_2–Al_2O_3 binary system. The properties of this phase are of great technological importance because of its high mechanical strength at high temperatures and its optical characteristics,[1] so that mullite has long been the subject of intense research. However, research at a fundamental level on thermodynamics, kinetics and crystal structure is needed to clarify some aspects that are not completely understood yet.

An early way for synthesizing mullite, reported some years ago, was the thermal decomposition of kaolinite: in this process, by maintaining an almost topotactic relationship between phases and with the release of SiO_2, mullite is obtained as end product. The so-called 'sol–gel' process, widely used for the preparation of materials during the past few years, has recently been applied to the preparation of aluminosilicates. Two methods have been used to achieve the synthesis of pure mullite powders, these ways differing in the degree of homogeneity of the precursor. Thus, when the scale of chemical homogeneity is at the atomic level, mullite formation is observed at ~980°C through an exothermic reaction. In contrast, when the scale of chemical homogeneity is in the nanometer range (the so-called diphasic precursors), the formation of mullite is delayed to temperatures higher than 1200°C. Both crystallization processes are evidenced by exothermic effects in differential analysis curves. The mullite formation kinetics in both cases has been observed to follow a nucleation and growth process but whereas in the single-phase precursor the process of mullitization is consistent with a nucleation rate-controlled mechanism, in the case of diphasic precursors it has been found that the growth rate of the mullite grains is controlled by dissolution of the alumina particles into the amorphous silica-rich phase.[2,3] Another way of synthesizing mullite is from the so-called hybrid gels, defined as gels from mixtures of polymeric and colloidal derived sols. By low temperature treatment, *in situ* crystallization of the polymeric gel is effected, thus obtaining mullite seed crystals in an untransformed matrix; then mullite nucleates homoepitactically from the viscous densified colloidal gel. Further research may be interesting to achieve new processing methods at lower temperatures mainly to obtain precursors in which aluminium and silicon are at a real atomic level of mixing.

The structure of mullite may be thought of as being derived from the disordered sillimanite $SiO_2 \cdot Al_2O_3$, by the exchange of Al^{3+} for Si^{4+} and the removal of oxygen anions.[4] The stoichiometric phase may be written as $[Al_2]^{VI}(Si_{2-2x}Al_{2+2x})^{IV}O_{10-x}$

*To whom correspondence should be addressed.

and corresponds to a crystalline phase with variable composition, i.e. a solid solution. In order to accommodate this compositional variation, mullite develops an incommensurate structure whose periodicity varies continuously with composition.

The metastability of the pseudo-tetragonal crystalline modification and the tetragonal ↔ orthorhombic transition have been dealt with previously. Cameron[5] showed the possibility of obtaining a tetragonal phase for x about 0·65, corresponding to 79 mol% Al_2O_3. However, mullites containing more than 77·3 mol% Al_2O_3 have not been reported, this being the main reason why Cameron's suggestion on the occurrence of mullite with tetragonal symmetry has not been confirmed or denied. Schneider *et al.*[6] have recently reported a metastable orthorhombic mullite phase with $a > b$ obtained from a starting mixture of aluminium sec-butylate and silicon chloride with an Al/Si ratio of 8 : 1 (i.e. $x = 0{\cdot}67$, corresponding to 80·2 mol% Al_2O_3). That metastable mullite has a composition richer than $x = 0{\cdot}65$ in Cameron's diagram, at which point the curves of a and b cell parameters cross.

Many studies on mullite formation from gel precursors with different Al/Si ratios have been reported. The reactions leading to the formation of mullite can vary considerably depending on the method of preparation of gels, i.e. single phase or diphasic gels. Several reports have examined the effect of Al/Si ratio on the formation temperature and the microstructure of mullite from diphasic gels.[7] However, when alumina and silica are mixed on a molecular level as in the case of single-phase gels, little information exists concerning the effect of Al/Si ratio on mullitization temperature and microstructure[8] for compositions placed far away from the stable or metastable mullite solid-solution boundaries in the SiO_2–Al_2O_3 binary system. Some experimental factors can affect directly the precursor gel structure which determines the further thermal evolution. One of the key points is to avoid the occurrence of alumina segregation while hydrolysis and condensation reactions take place. One of the possible ways to overcome this difficulty is, as previously reported for other systems,[9] to use prehydrolysed tetraethylorthosilicate (TEOS) solution as silicon source.

The aim of this work was the preparation and characterization of mullite powders in the binary system starting from mixtures of prehydrolysed TEOS and aluminium alkoxides. Three different compositions, corresponding to $Al_2O_3 : SiO_2$ molar ratios of 1 : 3, 3 : 2 ($x = 0{\cdot}25$) and 9 : 2 ($x = 0{\cdot}70$) — the former and latter placed in both sides of the solid solution limit composition for mullite, have been prepared as single-phase gels. The structural evolution with thermal treatment for specimens of different Al/Si ratios and the microstructural features of starting gels and final products were also examined.

2 Experimental Procedure

2.1 Preparation of gel samples

Gels with compositions (in mol%) 25 Al_2O_3 : 75 SiO_2 (hereafter denoted as sample A, with composition in wt% 36·1 Al_2O_3 and 63·9 SiO_2) and 60 Al_2O_3 : 40 SiO_2 (hereafter denoted as sample B, with composition in wt% 71·8 Al_2O_3 and 28·2 SiO_2) were prepared using as starting chemicals tetraethylorthosilicate (TEOS, $Si(OC_2H_5)_4$) and aluminium ethoxide ($Al(OC_2H_5)_3$), both from Merck & Co. (Darmstadt, Germany) by the following procedure.

The $Al(OC_2H_5)_3$ was dissolved in ethanol (EtOH) by refluxing and added to a prehydrolysed TEOS solution. The TEOS : H_2O molar ratio used was 1 : 2 and prehydrolysis performed at 40°C for 20 h. The resultant mixture was refluxed at 70°C for 5 days. After several days sample B, with the larger amount of aluminium alkoxide and consequently requiring a higher molar ratio of TEOS/EtOH (1/30) than sample A (1/20), gave rise to a transparent gel. On the other hand, sample A gelled after mixing both starting solutions and gave a gel that was opaque.

A gel with composition (in mol%) 81·8 Al_2O_3 : 18·2 SiO_2 (hereafter denoted as sample C, with composition in wt% 88·4 Al_2O_3 and 11·6 SiO_2) was prepared using aluminium tri-sec-butylate ($C_{12}H_{27}AlO_3$) from Merck as raw material and isopropanol as solvent. These changes in reagents facilitate the dissolution of a great amount of aluminium raw material. The procedure followed for preparing gel C was the same as for gels A and B, using a molar ratio TEOS/Si-PrOH = 1/30. After several days a transparent gel was obtained.

To check possible differences in structure and phase transformation of dried and heated gels when aluminium tri-sec-butylate and isopropanol were used instead of aluminium ethoxide and ethanol in the preparation of gels, composition B was prepared with both aluminium alkoxides and solvents.

All gels were first slowly dried by covering the beaker containing the gel with a holed plastic film and allowing the solvent to evaporate for several weeks; they were then dried in oven at 120°C. Dried gels A and B showed a yellow colouration while dried gel C was colourless.

Precursor glass gel was obtained by preheating the dried samples at 750°C for 3 h, products derived from this process were either grey (sample B) or white (samples A and C). Glass powder was

calcined at temperatures in the range 900 to 1400°C for 3 to 15 h, or at 1500°C for 30 min.

2.2 Characterization of samples

The chemical and structural evolution of dried gels and crystalline specimens was examined using several techniques.

Infra-red (IR) absorption spectra were obtained in the range 2000–400 cm^{-1} using the KBr pellet method on a Perkin–Elmer model 882 spectrometer (Beaconsfield, UK).

Differential thermal analysis (DTA) [Perkin–Elmer model 1700 instrument (Norwalk, CT)] and thermogravimetric analysis [Perkin–Elmer model 7 instrument (Norwalk, CT)] were carried out in air with α-Al_2O_3 liners, using a heating rate of 10°C min^{-1}. Finely powdered alumina was used as reference substance.

X-ray diffraction (XRD) analysis (model D-500 diffractometer, Siemens, Karlsruhe, Germany) was performed using graphite-monochromated Cu $K\alpha$ radiation. The diffractometer had two 1° divergence slits, a 1° scatter slit, and a 0·05° receiving slit. Eleven overlap-free reflections between 20° and 70° (2θ) were measured with a scanning speed of 0·12° 2θ min^{-1} using CaF_2 as internal standard. Determination of the lattice constants of mullite was made using LSQC and POWCAL programs.

The microstructure of the as-prepared and thermally treated samples was determined by scanning electron microscopy (SEM) and field-emission SEM working at 20–30 kV and 5–10 kV, respectively (models S-2500 and S-4100, Hitachi Ltd, Tokyo, Japan). To check the quality of the observation, some of the samples were etched with dilute HF solution for 10 s, and subsequently washed with H_2O. All specimens were coated with gold in an ion-beam coater. The morphology of dried gels and mullite particles was also examined using transmission electron microscopy (TEM) (model H-800, Hitachi Ltd, Tokyo, Japan) at an accelerating voltage of 200 kV. Samples were prepared by dispersing as-produced and calcined powders in absolute ethanol and setting dropwise on copper grids that had previously been coated with a holey thin carbon film.

3 Results and Discussion

3.1 Structural development of gel samples

Since two kinds of aluminium precursor were used for gel preparation, we think it is worthwhile to comment that the gel structure and experimental results for thermal-treated specimens B prepared from both types of aluminium source and solvent are very similar. Therefore, it can be assumed that experimental results of all three compositions prepared in this work are comparable with each other.

IR spectra of dried gels and crystalline samples are depicted in Figs 1, 2 and 3. In comparison

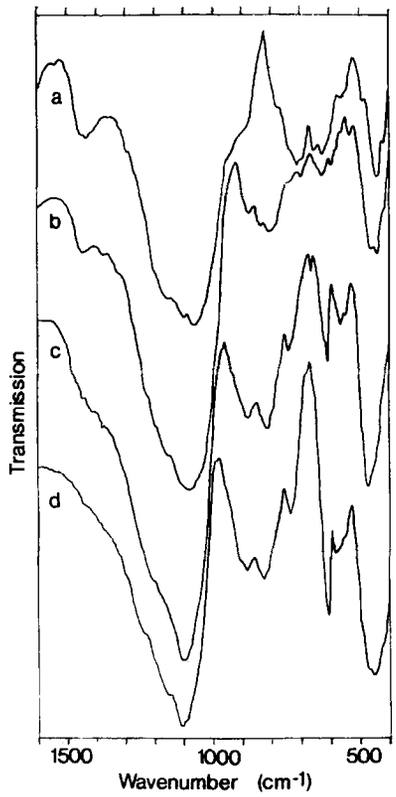

Fig. 1. IR absorption spectra of sample A gels after several heat treatments: (a) dried gel; (b) 750°C/3 h; (c) 1000°C/3 h; (d) 1300°C/3 h.

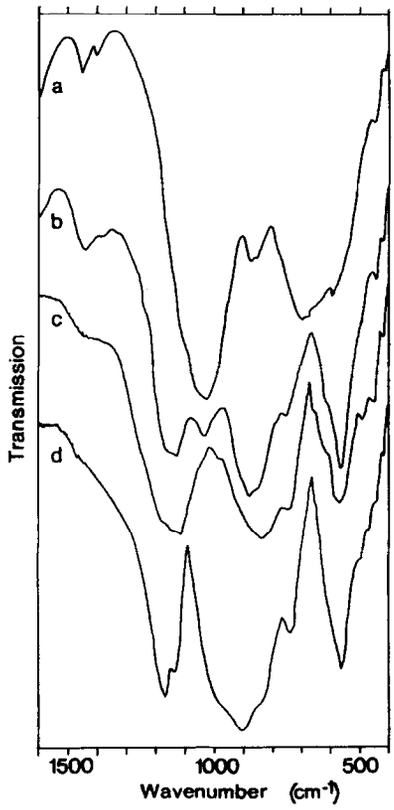

Fig. 2. IR absorption spectra of sample B gels after several heat treatments: (a) dried gel; (b) 750°C/3 h; (c) 1000°C/3 h; (d) 1300°C/3 h.

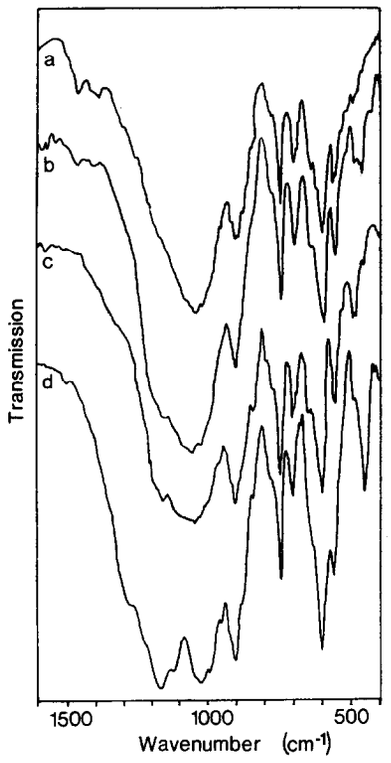

Fig. 3. IR absorption spectra of sample C gels after several heat treatments: (a) dried gel; (b) 750°C/3 h; (c) 1000°C/3 h; (d) 1300°C/3 h.

with IR spectra observed in previously reported binary systems,[10,12] the characteristic vibration modes associated with Si–O bonds were not so clearly distinguished in samples B and C. On the other hand, peaks in the 500 to 800 cm^{-1} region were clearly observed in both samples (although more intense in sample C), and can be attributed to Al–O bonds both in tetrahedral and octahedral coordination. For both samples B and C a band centred at 875 cm^{-1} was observed over the full range of temperature, increasing its intensity with higher temperatures. This band could be associated with Si–OH and/or Al–OH at low temperature; however it also may be attributed to Si–O–Al bond vibrations.[13,14] The peak at 1020 cm^{-1} was attributed to Si–O bond stretching vibration modes. Other authors associate this band with Si–O–Al bond vibrations because the absorption band of Si–O bonds at 1100 cm^{-1} for amorphous silica is shifted to lower energies by introducing Si–O–Al bonds.[10,12] This band shifted to higher energies with increasing temperature: thus, at 1300°C the band from 1020 cm^{-1} was centred at 1165 cm^{-1} with a shoulder at 1130 cm^{-1} associated with SiO_4 and AlO_4 tetrahedra vibration modes, respectively. It should be noted that in samples treated at temperatures higher than 1300°C all characteristic bands of mullite were observed (1175, 1120, 905, 845, 750 and 460 cm^{-1}).[11]

In general, there was an apparent difference between the IR spectra of sample A and those of samples B and C. As can be seen, bands around 1200, 1100, 750 and 460 cm^{-1} attributed to Si–O bonds were detected in the former dried gels. In samples of gel A shifting to higher wavenumber with the formation of mullite at 1000°C was very small compared with the deviations detected in sample B, richer in Al_2O_3. An increase of band intensity associated with Si–O–Si bonds was observed, mainly for the peaks around 440 and 1030 cm^{-1}, compared with both bands in sample B. This fact could be due to an increasing amount of SiO_2 which does not form mullite.

Some authors[12,15] have reported the chemical composition of mullite as a function of the absorbance bands at 1130 and 1165 cm^{-1}. When the chemical composition of mullite is rich in Al_2O_3, the 1130 cm^{-1} peak is stronger than the 1170 cm^{-1} peak in intensity. In samples B and C at 1300°C, the 1165 cm^{-1} peak was stronger than that at 1130 cm^{-1}. It was not possible to draw comparisons between peaks in sample A because bands associated with the excess silica overlapped with the corresponding bands of mullite. It is noteworthy, however, that the band at 1130 cm^{-1} in mullite B is also stronger at 1000°C, i.e. at the first stage in mullite formation. This fact suggests the initial formation of an Al_2O_3-rich mullite and reflects the change in chemical composition of mullite.

3.2 Thermal analysis

Figure 4 shows DTA curves of samples A, B and C that had been thermal treated at 750°C for 3 h. Sharp exothermic peaks were observed at 989 and 975°C in samples A and B, respectively; whereas two well-defined exothermic peaks were detected in sample C at ~945 and 983°C. XRD analysis of the former samples after the exothermic peaks indicated the presence of mullite as crystalline phase in both samples, whereas for sample C the crystalline phases associated with the first and second exothermic effects were γ-Al_2O_3 and mullite, respectively. In general, the first exothermic peak

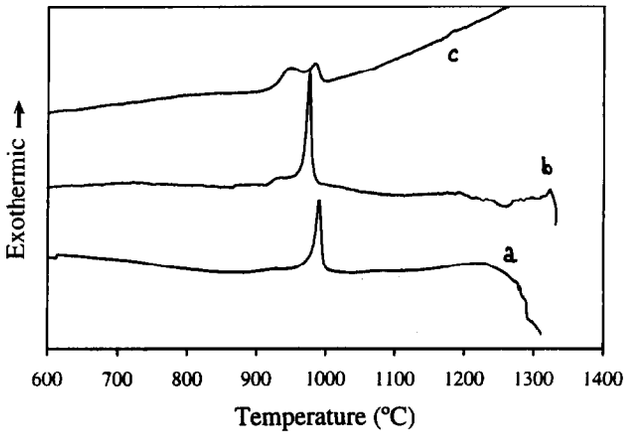

Fig. 4. DTA curves of gel-derived glass powders: (a) sample A; (b) sample B; (c) sample C.

was shifted to lower temperatures for samples with higher alumina content. This tendency was in agreement with previously reported results for systems richer in alumina than composition A.[12,16]

3.3 Thermal evolution of crystalline samples

X-ray diffractograms of samples A, B and C fired at different temperatures are shown in Figs 5, 6 and 7, respectively. At 1000°C the sample of gel A showed mullite as the only crystalline phase. In samples B and C, however, γ-Al_2O_3 was also detected at this low temperature. The amount of γ-Al_2O_3 was very small for the stoichiometric sample B; however, it was the major crystalline phase for sample C. This fact is in agreement with results obtained when the preparation of mullite takes place from a single-phase precursor in which a high degree of chemical homogeneity is reached.[2,17]

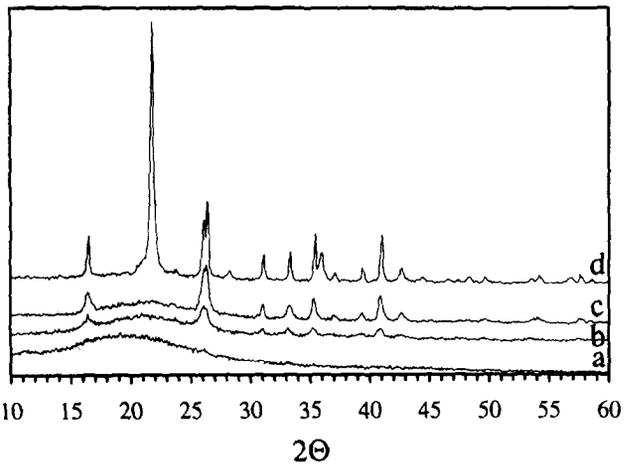

Fig. 5. XRD patterns of sample A gels fired at: (a) 750°C/3 h; (b) 1000°C/15 h; (c) 1200°C/15 h; (d) 1500°C/0.5 h.

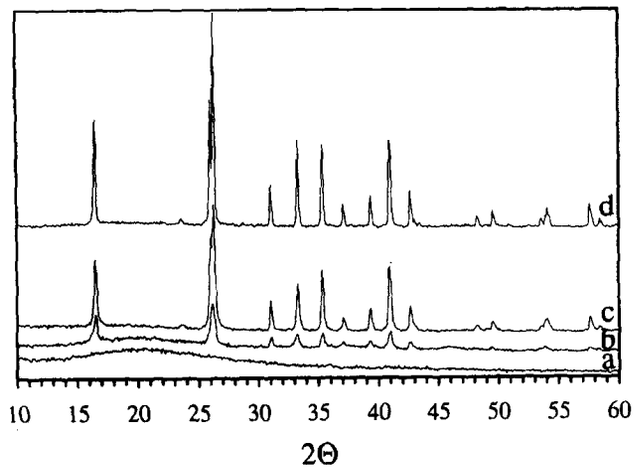

Fig. 6. XRD patterns of sample B gels fired at: (a) 750°C/3 h; (b) 1000°C/15 h; (c) 1200°C/15; (d) 1400°C/15 h.

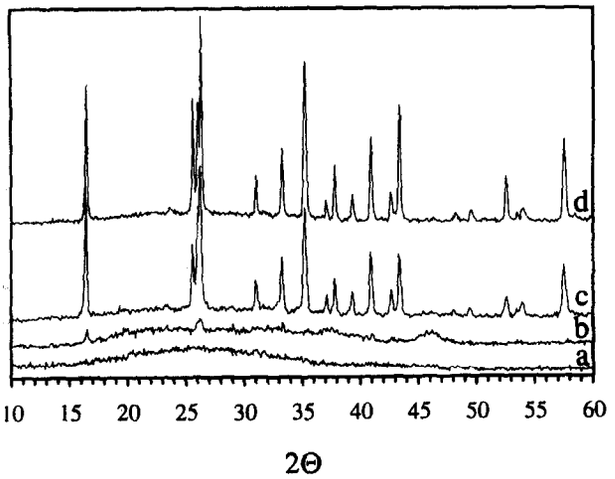

Fig. 7. XRD patterns of sample C gels fired at: (a) 750°C/3 h; (b) 1000°C/15 h; (c) 1200°C/15 h; (d) 1400°C/15 h.

In fact, some doubts about whether gels B and C were single-phase or not could arise. However, the DTA curves for gels B and C indicated that the exothermic peaks could be ascribed to mullite and to γ-Al_2O_3 and mullite, respectively. Reports on mullite formation from diphasic gels have indicated the formation of Al–Si spinel without detecting an exothermic peak around 1000°C and only showed a small rounded peak at ~1250°C associated with the formation of mullite.[18–20] Thus our specimens, which showed mullite and spinel as the crystalline phases at ~1000°C after thermal treatment, could be considered as single-phase gel precursors. The formation of spinel together with mullite has been interpreted in terms of favourable experimental conditions leading to the segregation of alumina and silica in alkoxide-derived gels. The prevention of that alumina–silica segregation, as has been previously reported in the literature,[20] is especially problematic in dual alkoxide systems even for the method of preparation used in this work, in which water was not really added as a separate reagent but was homogeneously distributed in the prehydrolysed TEOS solution before adding the aluminium alkoxide solution.

By increasing the temperature mullite was completely developed in sample B at temperatures as high as 1400°C but cristobalite and corundum were also detected as secondary crystalline phases in samples A and C, respectively. This result was in accordance with the phase diagram for compositions placed on either side of the solid solution limit for mullite.[21] Variation of the lattice parameters of mullite with increasing temperature for samples A, B and C is given in Tables 1, 2 and 3. The change of the parameter a as a function of temperaure, i.e. lowering a with increasing temperatures, can be related to changes in the mullite composition in accordance with Cameron's results.[5] Thus, mullites formed at the first stage of crystallization were richer in Al_2O_3 than those formed as the calcining temperature was raised. It should be noted that end mullites produced in composition B (3 : 2 as Al_2O_3/SiO_2 molar ratio) between 1400 and 1500°C were as rich in Al_2O_3 as composition C (with 9 : 2 as molar ratio). This fact can be related to the initial formation of a mullite very rich in SiO_2

Table 1. Lattice parameters for sample A fired at different temperatures

Temperature (°C)	a(Å)	b(Å)	c(Å)
1000	7·577 ± 0·016	7·702 ± 0·017	2·8867 ± 0·0023
1200	7·565 ± 0·006	7·692 ± 0·004	2·8829 ± 0·0009
1300	7·551 ± 0·004	7·688 ± 0·002	2·8851 ± 0·0006
1400	7·542 ± 0·003	7·691 ± 0·002	2·8797 ± 0·0005
1500	7·543 ± 0·003	7·690 ± 0·002	2·8806 ± 0·0005
JCPDS 15-776	7·5456	7·6898	2·8842

Table 2. Lattice parameters for sample B fired at different temperatures

Temperature (°C)	a(Å)	b(Å)	c(Å)
1000	7·584 ± 0·006	7·682 ± 0·005	2·8802 ± 0·0010
1200	7·554 ± 0·007	7·686 ± 0·003	2·8828 ± 0·0006
1300	7·553 ± 0·003	7·687 ± 0·002	2·8851 ± 0·0005
1400	7·552 ± 0·003	7·688 ± 0·002	2·8852 ± 0·0005
1500	7·552 ± 0·003	7·690 ± 0·002	2·8852 ± 0·0004

Table 3. Lattice parameters for sample C fired at different temperatures

Temperature (°C)	a(Å)	b(Å)	c(Å)
1000	7·565 ± 0·008	7·690 ± 0·005	2·8845 ± 0·0024
1200	7·554 ± 0·006	7·679 ± 0·005	2·8849 ± 0·0010
1300	7·557 ± 0·003	7·688 ± 0·003	2·8875 ± 0·0008
1400	7·553 ± 0·003	7·685 ± 0·002	2·8840 ± 0·0004
1500	7·552 ± 0·002	7·687 ± 0·002	2·8843 ± 0·0004

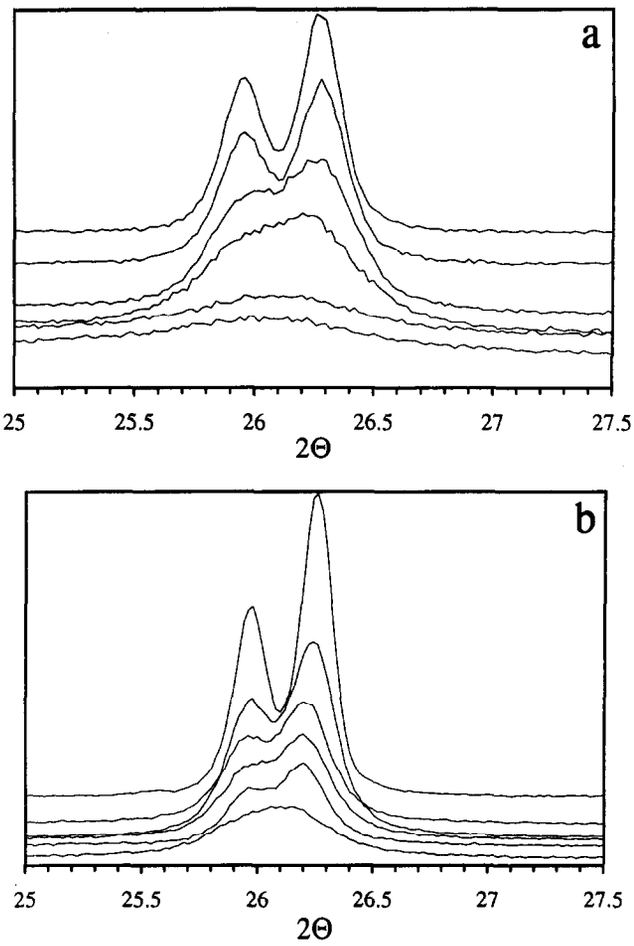

Fig. 8. 1 2 0/2 1 0 reflection pair for powders fired at different temperatures (from 1000 to 1500°C in 100°C intervals) recorded at low goniometer speed: (a) sample A; (b) sample B.

together with the large crystallization of γ-Al_2O_3 in sample C. Further, mullite evolution by solution of α-Al_2O_3 in the SiO_2-rich glassy phase is unfavoured kinetically.

Primarily crystallized mullite at 1000°C could be associated with pseudo-tetragonal mullite because no splitting of peaks with Miller indices of 1 2 0, 2 4 0, 0 4 1 and 2 5 0 was observed. However, the latter could be the result of poor crystallization of mullite and consequently low resolution. Increasing the soaking time led to an initial splitting in the peaks. Likewise, a further increase of calcining temperatures gave rise to a clear angular separation of diffraction lines that was more evident at high temperatures, as displayed in Fig. 8. So it can be considered that the first crystalline phase at 1000°C was pseudo-tetragonal or near orthorhombic and that the phase transformed into a truly orthorhombic one upon increasing either holding time or heating temperature.

The attempt to obtain results related to the controversial occurrence of tetragonal or orthorhombic mullite from sample C, which has an initial composition with $x = 0{\cdot}70$, i.e. (in mol%) 81·8 Al_2O_3, has not been successful. Thus, XRD analysis is of crystalline Al_2O_3-richer mullite obtained by calcining a gel-like glass sample at 1000°C/3 h indicated the formation of orthorhombic mullite with $a < b$, like mullites from samples A and B. However, it was remarkable that sample C was very poorly crystallized at 1000°C even though peaks of mullite were clearly identified. Except at 1000°C, in the overall range of temperature the composition of mullite C was similar to that of mullite B, and is considered to be due to the crystallization of γ-Al_2O_3 at the first step along with poor chemical homogeneity of the precursor gel so that, as consequence, reactivity in the system is very slow. This finding for sample C did not allow us to check the recent results of Schneider *et al.*,[6] which appeared to suggest that mullites very rich in Al_2O_3 were actually orthorhombic instead of tetragonal, as first suggested by Cameron.[5] The former authors have identified mullites with $a > b$, which supposedly must correspond to compositions higher in Al_2O_3 than that corresponding to 79 mol% Al_2O_3. However, this Al_2O_3-rich mullite phase was thermally unstable and above ~1050°C, the lattice parameters gradually shifted back to those of conventional mullite.[6]

3.4 SEM and TEM observations

Figures 9 and 10 display scanning electron micrographs of dried and fired gels of samples A, B and C. As can be distinguished from Fig. 9, large agglomerates with a flat outer surface were present; their fracture surfaces revealed that the agglomerates were made up of small particles. The size of the mullite particles obtained upon heating the amorphous gel particles seemed to be independent of temperature for specimen B, see Fig. 10(b). Also, note that directional growth displayed in particles of specimen C, Fig. 10(c), could be due to the presence of liquid phase. For samples A and C a second phase was observed, characterized by XRD as cristobalite and corundum, respectively.

TEM images of samples A and B are also presented in Figs 11 and 12. Some evidence for the presence of very small particles with size <10 nm is found for the dried gel in Fig. 11. This picture was obtained by deviation from the exact focus condition, and allowed the observation of a fine microstructure that differed somewhat from the irregularly mottled appearance generally associated with fully dense amorphous materials.[22] Examination of sample B at 1500°C showed small, relatively equiaxed particles as displayed in Fig. 12. The particle size of mullite in sample A at 1500°C was the same as that in sample B.

4 Conclusions

Monophasic gels with Al/Si atomic ratios of 2 : 3, 3 : 1 and 9 : 1 were prepared to examine the effect of nominal composition on either mullite formation pathway or microstructural evolution of mullite. Formation of an Si–O–Al network was detected by IR spectroscopy for compositions B and C, while the network present in sample A was built up of Si–O bonds. Al_2O_3-rich mullite was first observed at 1000°C for the three compositions. Full development of mullite took place at 1400°C. On heating the samples, changes in the composition of initial mullites to SiO_2-richer mullite were detected in agreement with the phase diagram. Differences in the compositions of the mullites developed (obtained from lattice parameters) were as expected, except for the case of mullite C which

Fig. 9. SEM micrograph of sample B dried gels (120°C/24 h); bar = 5 μm.

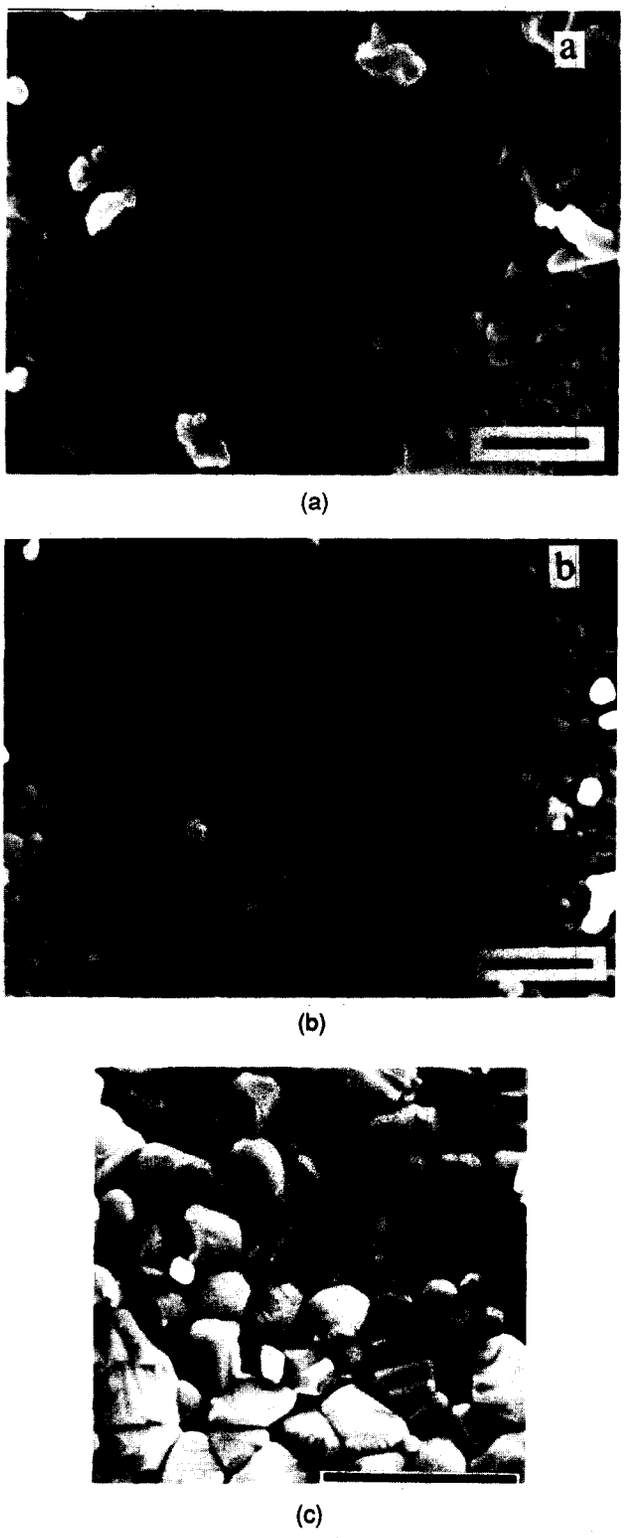

Fig. 10. SEM micrographs of powders fired at 1500°C: (a) sample A; (b) sample B; (c) sample C; bar = 1 μm.

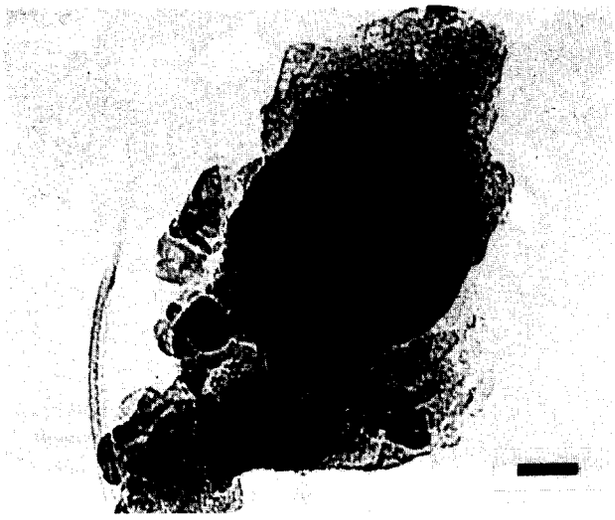

Fig. 11. TEM micrograph of sample B dried gels; bar = 50 nm.

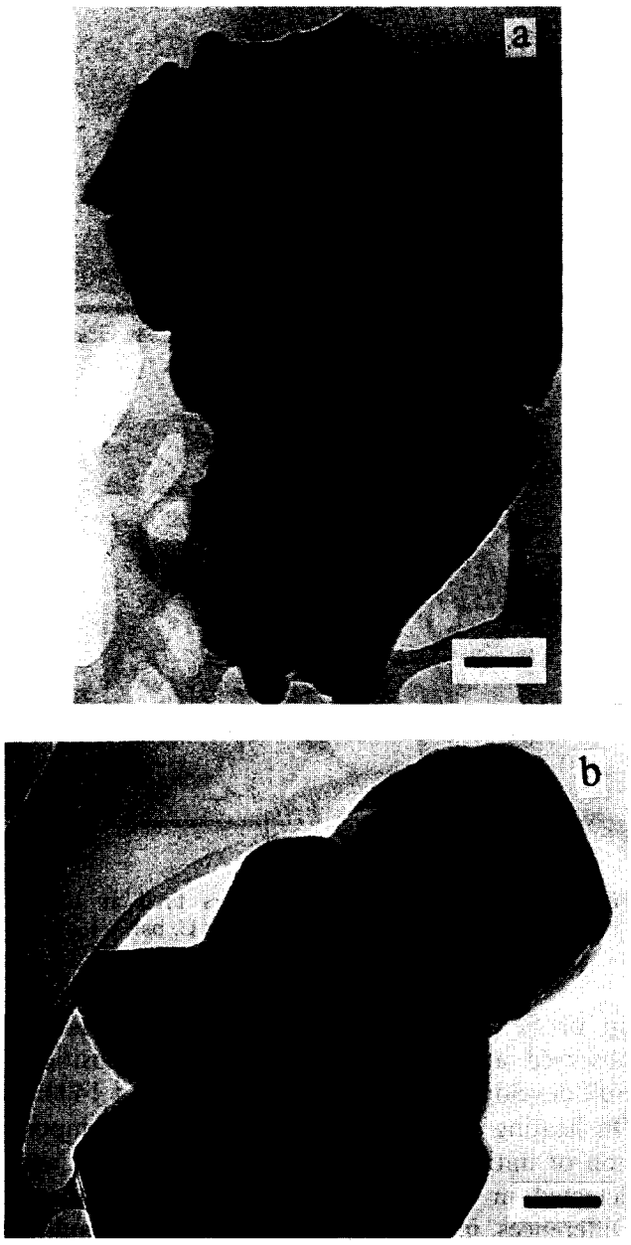

Fig. 12. TEM micrographs of powders fired at 1500°C: (a) sample A; (b) sample B; bar = 50 nm.

seemed to be poorer in Al_2O_3 than mullite B. Microstructural study by SEM indicated that in samples B and C the particle size at higher temperatures is almost constant. However, specimen C displayed a directional growth which was due to presence of liquid phase.

Acknowledgement

Financial support for the present work was provided by CICYT (Project MAT92-0423).

References

1. Aksay, I. A., Dabbs, D. M. & Sarikaya, M., Mullite for structural, electronic and optical applications. *J. Am. Ceram. Soc.*, **74**[10] (1991) 2343–58.
2. Li, D. X. & Thomson, W. J., Mullite formation kinetics of a single-phase gel. *J. Am. Ceram. Soc.*, **73**[4] (1990) 964–9.
3. Sundaresan, S. & Aksay, I. A., Mullitization of diphasic aluminosilicate gels. *J. Am. Ceram. Soc.*, **74**[10] (1992) 2388–92.
4. Angel, R. A. & Prewitt, C. T., Crystal structure of mullite: a re-examination of the average structure. *Am. Mineral.*, **71**[11/12] (1986) 1476–82.
5. Cameron, W. E., Mullite: a substituted alumina. *Am. Mineral.*, **62**[7/8] (1977) 747–55.
6. Schneider, H., Fischer, R. X. & Voll, D., Mullite with lattice constants a > b. *J. Am. Ceram. Soc.*, **76**[7] (1993) 1879–81.
7. Li, D. X. & Thomson, W. J., Mullite formation from nonstoichiometric diphasic precursors. *J. Am. Ceram. Soc.*, **74**,[10] (1991) 2382–7.
8. Hoffman, D. W., Roy, R. & Komarneni, S., Diphasic xerogels, a new class of materials: phases in the system Al_2O_3–SiO_2, *J. Am. Ceram. Soc.*, **67**[7] (1984) 468–71.
9. Monrós, G., Carda, J., Tena, M. A., Escribano, P., Sales, M. & Alarcón, J., Synthesis and characterization of V_2O_5–SiO_2–ZrO_2 pigments by sol–gel method, *J. Non-Cryst. Solids*, **147 & 148** (1992) 588–93.
10. Hirata, Y., Sakeda, K., Matsushita, Y., Shimada, K. & Ishihara, Y., Characterization and sintering behavior of alkoxide-derived aluminosilicate powders. *J. Am. Ceram. Soc.*, **72**[6] (1989) 995–1002.
11. Percival, H. J., Duncan, J. F. & Foster, P. K., Interpretation of the kaolinite–mullite reaction sequence from infrared absorption spectra. *J. Am. Ceram. Soc.*, **57**[2] (1974) 57–61.
12. Okada, K. & Otsuka, N., Characterization of the spinel phase from SiO_2–Al_2O_3 xerogels and the formation process of mullite. *J. Am. Ceram. Soc.*, **69**[9] (1986) 652–6.
13. Nogami, M., Ogawa, S. & Nagasaka, K., Preparation of cordierite glass by the sol-gel process. *J. Mater. Sci.*, **24**[12] (1989) 4339–42.
14. Pancrazi, F., Phalippou, J., Sorrentino, F. & Zarzycki, J., Preparation of gels in the CaO–Al_2O_3–SiO_2 system from metal alkoxides. *J. Non-Cryst. Solids*, **63** (1984) 81–93.
15. Cameron, W. E., Composition and cell dimensions of mullite. *Am. Ceram. Soc. Bull.*, **56**[11] (1977) 1003–11.
16. Hori, S. & Kurita, R., Characterization and sintering of Al_2O_3–SiO_2 powders formed by the chemical vapor deposition method. In *Proceedings of the 1st International Workshop on Mullite*, Tokyo, Japan, 1987, ed. R. F. Davis, J. A. Pask & S. Somiya. American Ceramic Society, Westerville, OH, 1990, pp. 311–22.

17. Okada, K., Hoshi, Y. & Otsuka, N., Formation reaction of mullite from SiO_2–Al_2O_3 xerogels. *J. Mater. Sci. Lett.*, **5**[12] (1986) 1316–18.
18. Pask, J. A. & Tomsia, A. P., Formation of mullite from sol–gel mixtures and kaolinite. *J. Am. Ceram. Soc.*, **74**[10] (1991) 2367–73.
19. Pask, J. A., Zhang, A. W., Tomsia, A. P. & Yoldas, B. E., Effect of sol–gel mixing on mullite microstructure and phase equilibria in the α-Al_2O_3–SiO_2 system. *J. Am. Ceram. Soc.*, **70**[10] (1987) 704–7.
20. Huling, J. C. & Messing, G. L., Epitactic nucleation of spinel in aluminosilicate gels and its effect on mullite crystallization. *J. Am. Ceram. Soc.*, **74**[10] (1991) 2374–81.
21. Aksay, I. A. & Pask, J. A., Stable and metastable equilibria in the system SiO_2–Al_2O_3. *J. Am. Ceram. Soc.*, **58**[11–12] (1975) 507–12.
22. Hietala, S. L., Smith, D. M., Brinker, C. J., Hurd, A. H., Carim, A. H. & Dando, N., Structural studies of anomalous behavior in the silica–alumina gel system. *J. Am. Ceram. Soc.*, **73**[10] (1990) 2815–25.

SHORT REPORTS

0955-2219(95)00204-9

Journal of the European Ceramic Society 16 (1996) 791–794

0955-2219/96/$15.00

Sintering and Electrical Conductivity of Doped WO_3

V. O. Makarov[a] & M. Trontelj[b]

[a]University of Dnepropetrovsk, Gagarina 72, 320625 Dnepropetrovsk, Ukraine
[b]J. Stefan Institute, University of Ljubljana, Jamova 39, 61000 Ljubljana, Slovenia

(Received 30 March 1995; accepted 22 June 1995)

Abstract

The influence of a series of oxide additives, namely Al_2O_3, Co_3O_4, MnO_2 and Na_2O, on the sintering capacity and electrical conductivity of WO_3-based binary ceramic systems was studied. The densification behaviour and the microstructures obtained after firing were dependent on the additive oxide type. A small addition of Na_2O shifts the onset of sintering to lower temperatures, whereas the addition of Al_2O_3 shifts the onset of sintering to higher temperatures compared with undoped WO_3. The inhibition of grain growth was observed in Al_2O_3-doped WO_3. The electrical conductivity of these WO_3 ceramics depends on the additive oxide type and varies in the range from 2×10^{-2} to 9×10^{-7} Ω^{-1} cm^{-1}.

The WO_3–Na_2O system was found to exhibit non-linear current–voltage characteristics and a low breakdown voltage. The non-linearity coefficient of the current–voltage characteristics of the Na_2O-doped WO_3 ceramics increases with sintering temperature and attains a maximum value of around 5.

1 Introduction

Tungsten oxide (WO_3) is a nonstoichiometric n–type semiconductor and even a very small decrease in its oxygen content gives rise to an increase in the electrical conductivity.[1] The electrical conductivity of WO_3 single crystals ranges from 10 to 10^{-4} Ω^{-1} cm^{-1}, depending on the stoichiometry.[1–3] Studies on the electrical conductivity of WO_3-based ceramic materials have been reported.[4,5] The conductivity of doped WO_3 ceramics is claimed to be increased by the addition of La_2O_3, Co_2O_3 and Li_2O.[5] Although several authors have reported sintering studies of WO_3,[6–8] the influence of various additives on the sintering properties and the electrical conductivity has not been systematically investigated.

The present work describes new data on the influence of Al_2O_3, MnO_2, Co_3O_4 and Na_2O on the sintering capacity and electrical conductivity of WO_3-based binary systems.

2 Experimental

Tungsten trioxide powder and 0.5 mol% of additive oxide, either Al_2O_3, MnO_2, Co_3O_4 or Na_2O, were mixed using alcohol as a medium. Sodium oxide was added as Na_2CO_3. After drying, the mixture was then pressed into pellets of 6 mm diameter at a pressure of 200 MPa. Samples were sintered at 1200°C in air for 2 h. The samples doped with Na_2O were sintered at temperatures of 1050 to 1250°C. For investigation of the sintering behaviour of the WO_3-based composites, the pellets were heated to 1300°C at a rate of 10°C min^{-1}. Apparent densities of sintered pellets were determined using Archimedes' method.

For electrical measurements, liquid In–Ga alloy was used as the electrode material. Current–voltage (I–V) measurements were made in the d.c. mode in the current range up to 1 mA at room temperature. The non-ohmic I–V characteristics were expressed empirically by $I = kV^{\alpha}$, where α is a non-linear coefficient and k is a constant. The non-linear coefficient was calculated in the current density range from 0.1 to 1 mA cm^{-2}. The specific conductivity (σ_0) was measured at an electric field of 1 V mm^{-1} in the ohmic region.

Sintered samples were examined by scanning electron microscopy (SEM) and energy dispersive X-ray microanalysis (EDX).

3 Results and Discussion

The shrinkage curves of pure and doped WO_3 are shown in Fig. 1. The addition of Na_2O shifts the onset of sintering to lower temperatures, compared with the undoped WO_3. On the other hand, for the WO_3–Al_2O_3 system shrinkage begins at a higher temperature. For the WO_3–MnO_2 and WO_3–CO_3O_4 systems two different types of shrinkage can be noticed: a slow stage and then a rapid stage when a liquid phase appears. The second stage starts at around 1050°C for both compositions. The appearance of a liquid phase at ~1100°C for

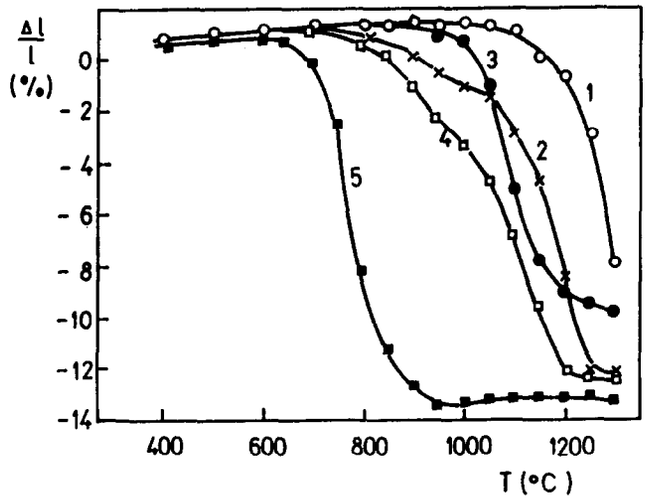

Fig. 1. Dimensional changes as a function of sintering temperature for pure WO_3 (3) and WO_3 doped by 0.5 mol% of Al_2O_3 (1), Co_3O_4 (2), MnO_2 (4) and Na_2O (5).

MnO_2-doped and at ~1050°C for Co_3O_4-doped WO_3 was confirmed by differential thermal analysis (DTA), and is responsible for the sudden rise of the shrinkage rate. The DTA curves for all compositions also showed two endothermic peaks at 760 and 910°C associated with phase transitions in the WO_3.[4]

Fig. 2 shows the microstructure of pure and doped WO_3 ceramics sintered at 1200°C for 2 h. A microstructural comparison showed that all the additives studied except Al_2O_3 enhance grain growth in WO_3. The grain sizes in the WO_3–Al_2O_3 system are smaller than those in the other binary systems, and therefore the addition of Al_2O_3 inhibits grain growth in WO_3. According to phase diagrams of the WO_3–Na_2O system, the liquid phase appears at 665°C whereas for the WO_3–Al_2O_3 system it appears at 1190°C.[9] Microstructural analysis of the polished ceramic surface showed a second intergranular phase for all the binary systems studied. Obviously, the sintering of these systems takes place in the presence of a liquid phase. All compositions have a porous microstructure.

Data on the apparent density, final shrinkage and average grain size of the WO_3-based systems studied, after sintering at 1200°C for 2 h, are listed in Table 1. The bulk density of the samples varied from 80% (pure WO_3) to 93% of the theoretical density, depending upon the composition. The data show an increase in the final shrinkage of doped samples for all compositions compared with undoped WO_3.

The specific electrical conductivity of tungsten oxide ceramics depends on the dopant oxide type and varies in the wide range from 2×10^{-2} to

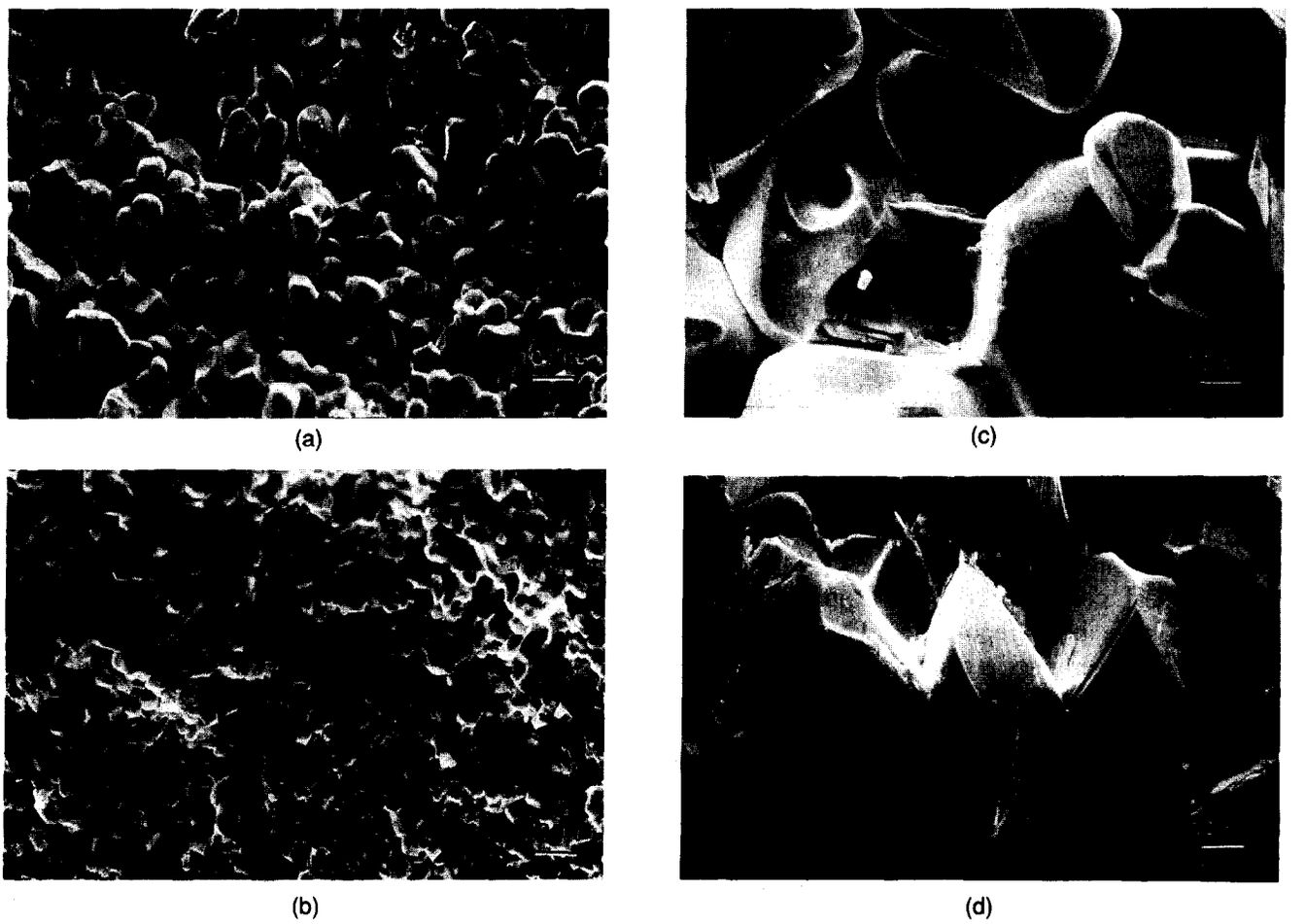

Fig 2. Microstructures of pure (a) and 0.5 mol% doped WO_3 samples after firing at 1200°C for 2 h: (b) WO_3 + Co_3O_4, (c) WO_3 + Al_2O_3 and (d) WO_3 + Na_2O.

Table 1. Apparent density, final shrinkage, average grain size and electrical parameters of various WO_3-based binary ceramic systems, sintered at 1200°C for 2 h

System	*Apparent density* ($g\ cm^{-3}$)	$\Delta l/l$ (%)	*Average grain size* (μm)	*Electrical conductivity* ($\Omega^{-1}\ cm^{-1}$)	*Non-linearity coefficient,* α
WO_3	5.8	11	10	8×10^{-6}	1
WO_3–Al_2O_3	6.7	14	6	2×10^{-2}	1
WO_3–Co_3O_4	6.7	14	65	5×10^{-5}	1
WO_3–MnO_2	6.5	13	150	1×10^{-6}	3
WO_3–Na_2O	6.8	14	30	9×10^{-7}	4

$9 \times 10^{-7}\ \Omega^{-1}\ cm^{-1}$ (Table 1). It is well known that for polycrystalline materials the conductivity depends on the specific conductivity of the grain, the grain size and the grain boundary resistance. From Table 1 it can be seen that high conductivity WO_3–Al_2O_3 samples have linear *I–V* characteristics. It is believed that there are no barriers at the grain boundaries and the measured conductivity is close to the specific conductivity of WO_3 crystallites.[1–3] The *I–V* characteristics of WO_3 ceramics doped with MnO_2 and Na_2O are non-linear. It is assumed that the conductivity of the WO_3–MnO_2 and WO_3–Na_2O systems is controlled by the grain boundaries. The electrical conduction within the WO_3 grain is believed to be ohmic and non-linearity arises due to the boundaries between the WO_3 grains.

The Na_2O-doped WO_3 ceramic is interesting because of its high non-linear coefficient. The *I–V* characteristics of WO_3–Na_2O samples as a function of sintering temperature are shown in Fig. 3. The effect of the sintering temperature on the non-linearity coefficient α and the electrical conductivity σ_0 are summarized in Fig. 4. It can be seen that α increases and σ_0 decreases with increase in the sintering temperature. It seems that a high temperature increases the grain boundary resistance of Na_2O-doped WO_3 ceramics. Further increase of the sintering temperature does not improve the non-linear characteristics due to partial sublimation of WO_3.

It was also observed that the average grain size for the WO_3–Na_2O system increases from 15 to 40 μm on increasing the sintering temperature from 1050 to 1250°C.

The presence of a second phase between the matrix grains is clearly visible in Fig. 5. This phase is located at multiple grain junctions and probably originates from solidification during cooling of the liquid phase. EDX analysis revealed that this phase is rich in Na and W. Semiquantitative EDX analysis allowed

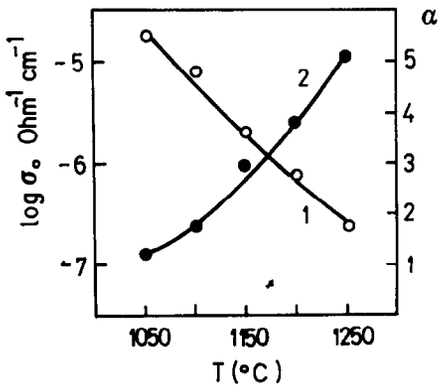

Fig. 4 Variation of conductivity (1) and non-linearity coefficient (2) with sintering temperature for the WO_3–Na_2O ceramics.

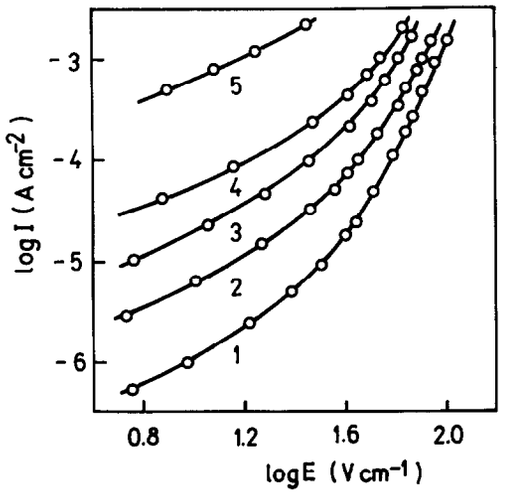

Fig. 3. *I–V* characteristics of WO_3–Na_2O ceramics sintered at different temperatures, 1250°C (1), 1200°C (2), 1150°C (3), 1100°C (4) and 1050°C (5), for 2 h.

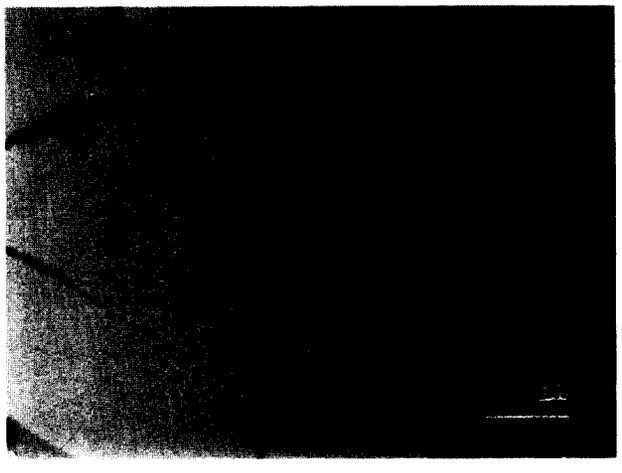

Fig. 5 SEM micrograph of a polished cross-section of a WO_3–Na_2O ceramic showing the presence of the intergranular phase at the corners of the matrix WO_3 grains.

its identification as sodium tungstate Na_xWO_3, where $x = 0.4$–0.5. According to the EDX analysis no dopant was found within the WO_3 grains.

It is important to note that the Na_2O-doped WO_3 ceramic is characterized by a low breakdown voltage. Since the non-linearity coefficient of about 3 to 4 obtained for the WO_3–Na_2O binary systems is inadequate from the practical point of view, it might be possible to improve it by adding other oxides.

4 Conclusions

Based on experimental data, the following conclusions can be drawn on the influence of oxide additives on the sintering capacity and electrical conductivity of WO_3-based ceramics.

(1) Doping of WO_3 by Al_2O_3, Co_3O_4, MnO_2 and Na_2O promotes better densification. The addition of Na_2O shifts the onset of sintering to lower temperatures, whereas the addition of Al_2O_3 shifts the onset of sintering to higher temperatures, compared with pure WO_3. The addition of Al_2O_3 inhibits the grain growth in WO_3. All the other additives studied enhance grain growth. Sintering of the doped WO_3 takes place in the presence of a liquid phase.

(2) The electrical conductivity of tungsten oxide ceramics strongly depends on the oxide additives. It reaches a maximum value of 2×10^{-2} Ω^{-1} cm^{-1} for the WO_3–Al_2O_3 system and a minimum value of 9×10^{-7} Ω^{-1} cm^{-1} for the WO_3–Na_2O system. It was found that the Na_2O-doped WO_3 ceramics exhibit non-linear current–voltage characteristics.

References

1. Sahle, W. & Nygren, M., Electrical conductivity and high resolution electron microscopy studies of WO_{3-x} crystals with $0 \leq x \leq 0{,}28$. *J. Solid State Chem.*, **48** (1983) 154–60.
2. Berak, J. M. & Sienko, M. J., Effect of oxygen-deficiency on electrical transport properties of tungsten trioxide crystals. *J. Solid State Chem.*, **2** (1970) 109–33.
3. Grunin, V. S., Makarov, V. L., Patrina, I. B. & Razumienko, M. V., Defects of nonstoichiometry and electrical conductivity of WO_3 crystals. *Sov. Phys. Solid State*, **30** (1988) 3091–5.
4. Sawada, S. & Danielson, G. C., Electrical conduction in crystals and ceramics of WO_3. *Phys. Rev.*, **113** (1959) 803–5.
5. Kaneki, N., Hara, H., Shimada, K. & Shimuzu, T., Effect of atmosphere on resistivity of WO_3 ceramics. *J. Am. Ceram. Soc.*, **59** (1976) 368–9.
6. Hanafi, Z. & Khilla, M. A., The colour problem of tungsten trioxide electrical conductivity. *Z Physik C. Chem. Neue Folge*, **82** (1972) 209–16.
7. Lefkowitz, I., Dowell, M. B. & Shields, M. A., Phase transitions in tungsten trioxide at low temperatures. *J. Solid State Chem.*, **15** (1975) 24–39.
8. Gehlig, R. & Salje, E., Dielectric properties and polaronic conductivity of WO_3 and $W_xMo_{1-x}O_3$. *Phil. Mag. B*, **47** (1983) 229–45.
9. *Phase Diagrams for Ceramists, Vol. 2, 1969 Supplement*, ed. M. K. Reser. The American Ceramic Society, Westerville, OH, 1969, p. 82 & 97 (after Mokhosoev, M. V. & Fedorov, P. I.) *Russ. J. Inorg. Chem.* (Engl. Transl.), **124** (1961); and Waring J. L., *J. Am. Ceram. Soc.*, **48**(9) (1965) 494.

Journal of the European Ceramic Society 16 (1996) 795–798

0955-2219(95)00192-1
0955-2219/96/$15.00

Correlation between Microstructure, Phase Transformation during Fracture and the Mechanical Properties of Y–TZP Ceramics

J. L. Shi, B. S. Li, Z. L. Lu & X. X. Huang

Shanghai Institute of Ceramics, Chinese Academy of Sciences, 1295 Ding-Xi Road, Shanghai 200050, People's Republic of China

(Received 20 June 1994; revised version received 11 October 1995; accepted 24 October 1995)

Abstract

The mechanical properties of Y–TZP(yttria-stabilized tetragonal zirconia polycrystalline) materials with different microstructures have been studied and related to the phase transformation capability during fracture. It has been found that the microstructure of the materials affects the phase composition and also the phase transformation volume (tetragonal to monoclinic) on the fracture surface during fracture. Higher densities lead to higher phase transformation volume; and both of them contribute to higher fracture toughness and strength.

Introduction

The relation between mechanical properties and microstructure is fundamental for structural ceramics, and also one of the most interesting and extensively studied themes.[1–4] The presence of large defects (pores, flaws, etc.) in the microstructure degrades the mechanical properties of the materials, for example, the strength. Although many relations have been suggested between the fracture strength (σ_f) and the relative density (ρ) of a ceramic, commonly this relation is written as:[5]

$$\sigma_f = \sigma_o \exp[-b(1-\rho)] \quad (1)$$

where b is a constant, σ_f, σ_o are the material strength at $\rho = \rho$ and $\rho = 100\%$, respectively.

For phase transformation toughened Y–TZP ceramics, the phase transformation in the front (or vicinity) area of a crack tip is also a critical factor for the enhancement of the fracture toughness. A higher phase transformation volume from tetragonal to monoclinic will lead to higher fracture toughness.[6–8] Factors affecting the phase transformation volume are the grain size of the tetragonal phase,[8–11] the amount of stabilizer,[12–14] and the restraining conditions.[15–16] However, in investigating the effect of these parameters on the phase transformation, dense materials (often manufactured by hot-pressing or hot isostatic pressing) have commonly been used, and the effect of density has been surprisingly ignored. This paper investigates the relation between density and phase transformation behavior and the effects of both of them on the mechanical properties of pressurelessly sintered Y–TZP ceramics.

Experimental Procedure

Materials preparation

The Y–TZP powders were first prepared via coprecipitation. For the preparation of the mixed solutions of zirconium oxychloride ($ZrOCl_2.8H_2O$) and yttrium chloride ($YCl_3.8H_2O$), the Zr^{4+}/Y^{3+} ratio was controlled to give an yttria content of 3 mol% in the final powders. The mixed solutions of different concentrations were added to ammonia solution of concentration of 12 vol%, and the coprecipitates were obtained. The pH value was maintained above 9·5 during the coprecipitate. The coprecipitates were washed with distilled water to remove Cl^- until Cl^- contents in the filtrates was lower than 2–40 ppm. The coprecipitates were then dried in an oven overnight at 110°C, and finally calcined at 750°C for 120 min. The resulting powders were composed mainly of tetragonal zirconia with no monoclinic phase.

PVA(polyvinyl alcohol) was used as a binder. Powders were compacted by uniaxial pressing at 50 MPa and then by a cold isostatic pressing at 250 MPa. The compacts were presintered at 750°C for 120 min to burn out the binders and then sintered at 1450 or 1550°C for 120 min with a heating rate of 3°C/min. To maintain the homogeneity of the temperature distribution and to prevent evaporation of components from the sample surface, the green bodies were embedded for sintering in powders of the same composition.

Property measurement

The densities of the sintered samples were measured by the Archimedes method in distilled water. The fracture strength was determined by the three point bend method with a load speed of 0·5 mm/min with samples of 2·5 × 5 × 26 mm, and a testing span of 20 mm. Fracture toughness was measured by the single edge notched beam (SENB) method with a loading speed of 0·05 mm/min. The notch width was 0·2 mm and notch depth was 2·5 mm on 2·5 × 5 × 26 mm. The strength and toughness measurement was made on an Instron 1195 materials tester. The Vickers hardness of the sintered bodies was measured on an Akashi-AVK-A micro-hardness tester with a constant punch load of 98 N.

Determination of the phase compositions

The phase compositions of the sintered bodies were determined by X-ray diffraction (Rigaku Denki, RAX-10) with the tetragonal content being given by:

$$t(\%)=I_{t(111)}/[I_{t(111)}+I_{m(111)}+I_{m(11\bar{1})}] \quad (2)$$

where $I_{t(111)}$, $I_{m(111)}$ and $I_{m(11\bar{1})}$ are the diffraction line intensities of the tetragonal (111), monoclinic (111) and monoclinic ($11\bar{1}$) lattice places. The samples were ground to remove a surface layer of 0·5–1 mm in depth, and then polished with 0·5 μm diamond particles. The phase compositions of the sintered samples were determined on the polished surface. X-ray diffraction was also conducted on newly fractured surfaces. The difference between the tetragonal contents of the polished surfaces and the fractured surfaces is taken as a measure of the phase transformation volume during fracture.

Results

Relation between the mechanical properties and the sintered densities

Figures 1, 2 and 3 show the dependence of fracture strength (σ_f), fracture toughness (K_{1c}) and Vickers hardness (H_v) on sintered density. The relation between Vickers hardness and relative density is approximately linear:

$$H_v\,(\text{GPa}) = 11{\cdot}43\text{–}0{\cdot}439(1-\rho) \quad (3)$$

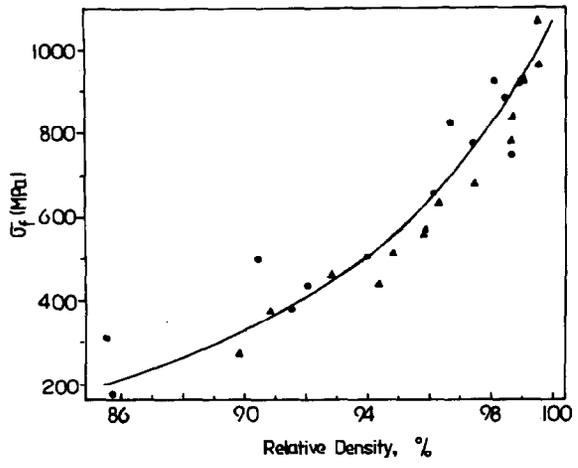

Fig. 1. Density dependence of the fracture strength (σ_f) of sintered 3Y–TZP bodies at (●) 1450°C, and (△) 1550°C.

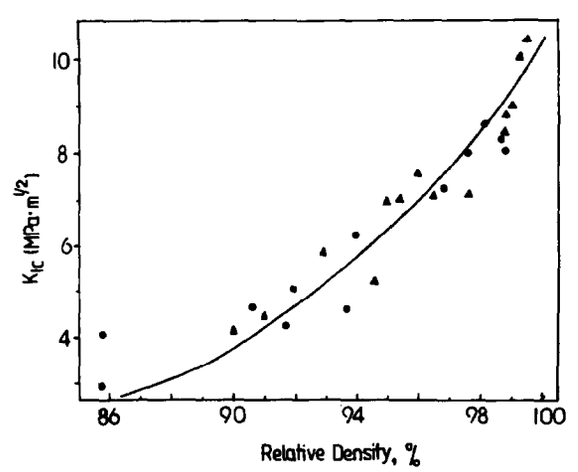

Fig. 2. Density dependence of the fracture toughness (K_{1c}) of sintered 3Y–TZP bodies at (●) 1450°C, and (△) 1550°C.

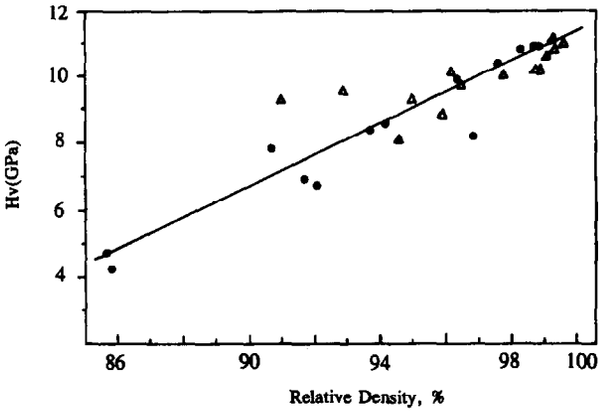

Fig. 3. Density dependence of the Vickers hardness (H_v) of sintered 3Y–TZP bodies at (●) 1450°C, and (△) 1550°C.

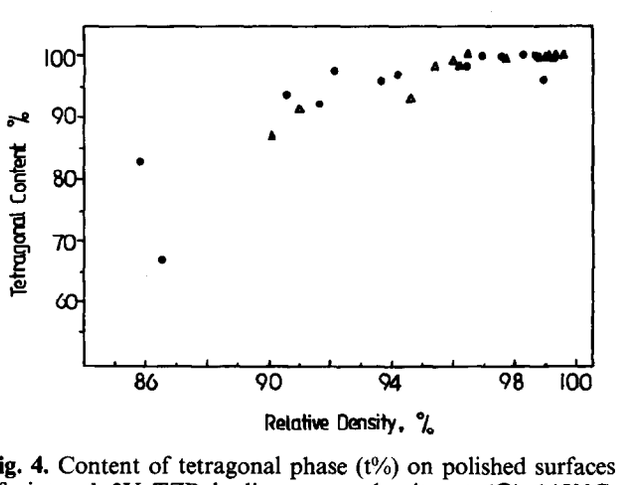

Fig. 4. Content of tetragonal phase (t%) on polished surfaces of sintered 3Y–TZP bodies versus density at (●) 1450°C, and (△) 1550°C.

The fracture strength obeys eqn (1) with:

$$\sigma_f(\text{MPa}) = 1045\exp[-0{\cdot}116(1-\rho)] \quad (4)$$

The results for fracture toughness follow eqn (1) also satisfactorily with:

$$K_{1c}(\text{MPa m}^{1/2}) = 10{\cdot}4\exp[-0{\cdot}10(1-\rho)] \quad (5)$$

The relation fits least well in the lower density region.

The effect of density on phase composition and phase transformation volume

Generally there is no monoclinic phase in high density 3Y–TZP ceramics pressurelessly sintered at or below 1550°C; however, if the sintered density is low, the sintered bodies may contain some monoclinic phase, as illustrated in Fig. 4. The sintered density also affects the phase transformation volume during fracture, as shown in Fig. 5. In addition, sintering temperature also affects the phase composition and the phase transformation volume: at densities of ≥96%, higher sintering temperature leads to lower tetragonal content and higher phase transformation volume. This is due to the larger grain size at the higher sintering temperature, which results in greater instability of the tetragonal phase.[12]

Once chemical compositions and grain size are fixed, the main factor affecting the tetragonal stability is the restraint imposed on the grains by the surrounding material. Lower sintered densities result in lower restraining force and the tetragonal phase content is consequently lower.

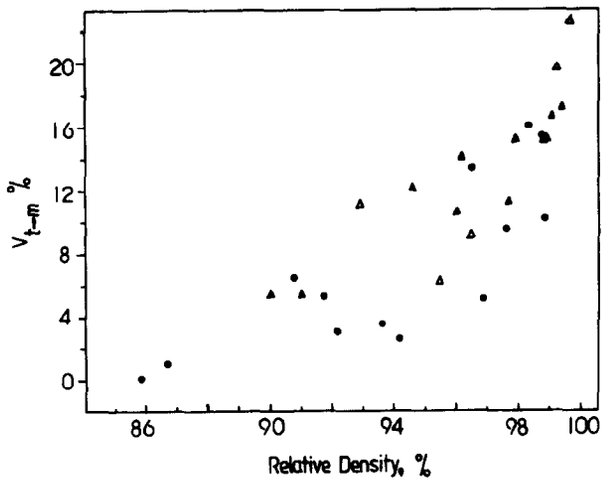

Fig. 5. Volume ($V_{t\to m}$) of phase transformation from tetragonal to monoclinic during fracture of sintered 3Y–TZP bodies versus density at (●) 1450°C, and (△) 1550°C.

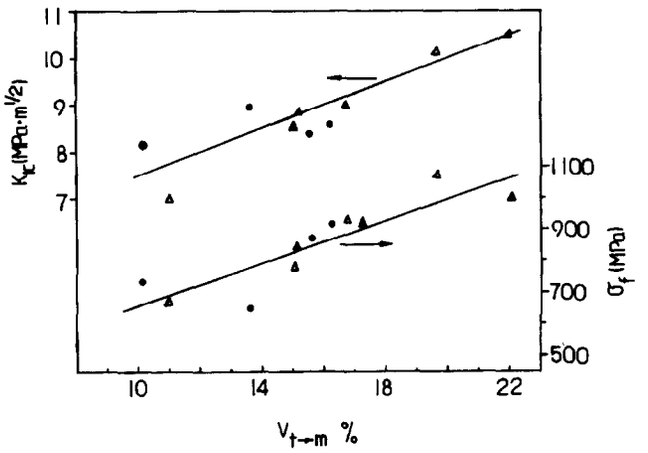

Fig. 6. Dependence of fracture toughness and strength on fracture phase transformation volume, (●) 1450°C, and (△) 1550°C.

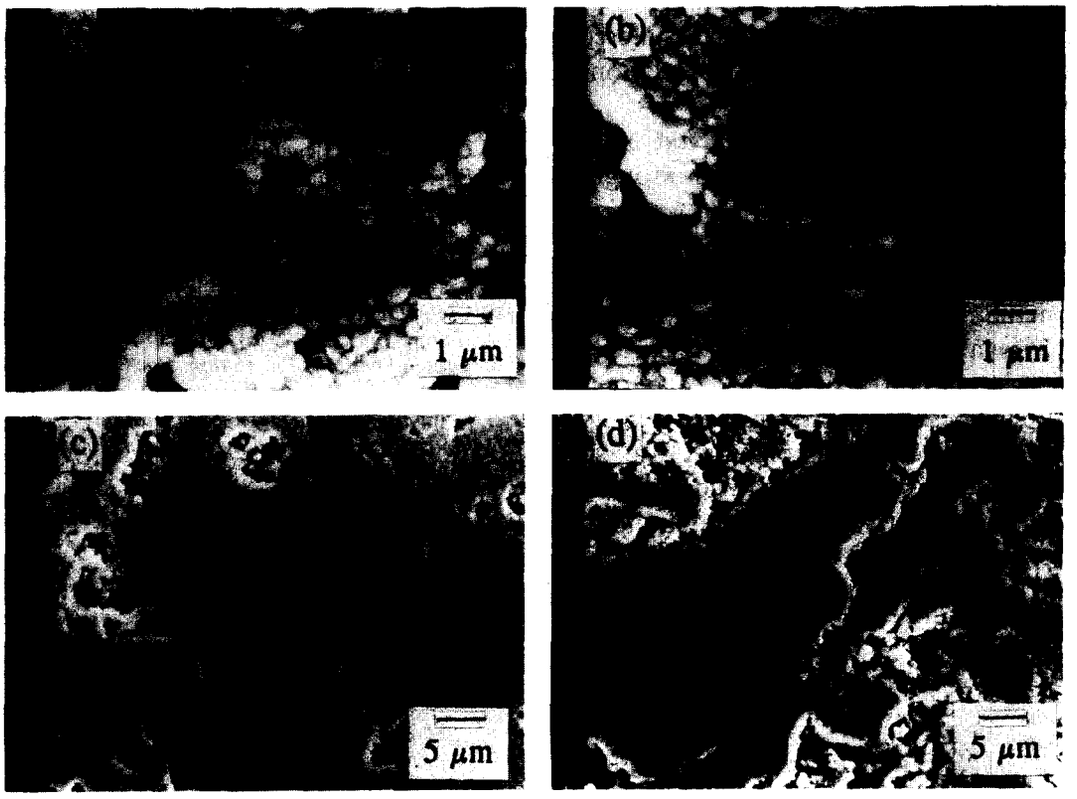

Fig. 7. SEM Micrographs of sintered 3Y–TZP bodies at 1550°C for: (a) 99·0%; (b) 97·4%; (c)90·6%, and at 1450°C for (d)85·8%.

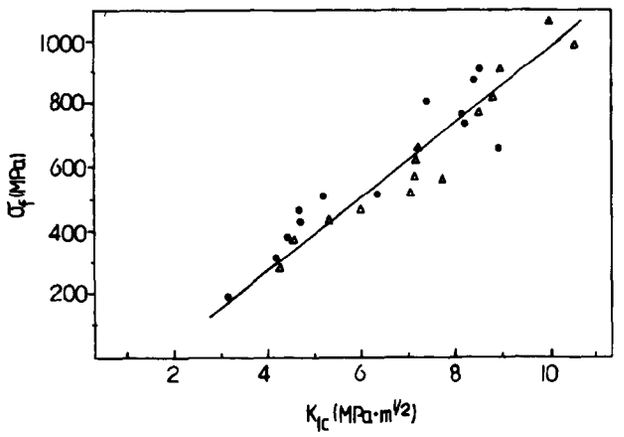

Fig. 8. Relations between fracture strength and fracture toughness of the sintered Y–TZP bodies at (●) 1450°C, and (△) 1550°C.

Discussion

For phase transformation toughened materials, the toughening contribution of stress-induced phase transformation volume $V_{t\to m}$ can be formulated as:[6,8]

$$K_{Ic} = K^{o}_{Ic} + AV_{t\to m} \quad (6)$$

or[7]

$$K_{Ic} = (K^{o}_{Ic}{}^{2} + BV_{t\to m})^{1/2} \quad (7)$$

where K_{Ic} and K^{o}_{Ic} are the fracture toughness with and without the phase transformation toughening effect, $V_{t\to m}$ is the phase transformation volume and A and B are constants related to materials properties and the phase transformation process.

Figure 6 shows the relations between the fracture strength, fracture toughness and the phase transformation volume when the relative sintered densities are higher than 97%. The two relations are approximately linear.

According to the Griffith equation,[17] the relation between fracture strength and fracture toughness can be written as:[18,19]

$$K_{Ic} = Y(\pi C)^{1/2}\sigma_f \quad (8)$$

where C is one half of a critical defect (e.g. crack) length and Y is a geometrical factor. Figure 7 shows the microstructures of the Y–TZP materials with different densities. Materials of lower density contain larger pores, i.e. defects of larger size, so the change of fracture toughness with decreasing density will be less than that of fracture strength, as found in eqns (4), (5), and Figs 1 and 2. Figure 8 demonstrates the relation between the fracture strength and the fracture toughness for 3Y–TZP ceramics with various densities. At higher densities, where the strength and toughness are also higher, the calculated critical defect length, if the geometric factor Y is assumed to be one, is around 60 μm; at lower density where the strength and toughness were also lower, the defect length is up to 160 μm; both of them are much greater than the grain sizes of the pressureless sintered materials.

References

1. Spriggs, R. M., *J. Am. Ceram. Soc.*, **44** (1961) 628.
2. Evans, A. G. & Tappin, G., Effects of Microstructure on the Stress to Propagate Inherent Flaws. *Proc. Brit. Ceram. Soc.*, **20** (1972) 275–7.
3. Kirchner, H. P. (ed.), *Strengthening of Ceramics, Treatments, Tests, and Design Applications* , Marcel Dekker, Inc., New York & Basel, 1979, Chapter 1, pp. 1–12.
4. Lawn, B. R. & Wilshaw, T. R., *Fracture of Brittle Solids*, Cambridge University Press, London, 1975.
5. Duckworth, W., *J. Am. Ceram. Soc.*, **36** (1953) 68.
6. Evans, A. G., Marshall, D. B. & Hurlingame, N. H., *Advances in Ceramics, Vol. 3, Science and Technology of Zirconia I*, eds A. H. Heuer & L. W. Hobbs, The Am. Ceram. Soc. Inc., Columbus, Ohio, 1981, p.202.
7. Lange, F. F., *J. Mater. Sci.*, **17** (1982) 235.
8. Evans, A. G., *Advances in Ceramics, Vol. 12, Science and Technology of Zirconia II*, eds N. Claussen, M. Ruehle & A. H. Heuer, The Am. Ceram. Soc. Inc., Columbus, Ohio, 1988, p. 193.
9. Garvie, R. C., Hannink, R. H. & Pascoe, R. T. *Nature (London)*, **258** (1975) 703.
10. Lange, F. F., *J. Mater. Sci.*, **17**, (1982) 225, 240.
11. Gupta, T. K., Hechtold, J. H. & Kuznicki, R. C., *J. Mater. Sci.*, **12** (1977) 1421.
12. Haberko, K. & Pampuch, R., *Ceram. Int.*, **9** (1983) 8.
13. Matsu, M., Somda, T. & Oda, I., *Advances in Ceramics, Vol. 12, Science and Technology of Zirconia II*, eds N. Claussen, M. Ruehle & A. H. Heuer, The Am. Ceram. Soc. Inc., Columbus, Ohio, 1984, p. 371.
14. Tsukuma, K., Kubota, Y. & Tsukidate, T., *Advances in Ceramics, Vol. 12, Science and Technology of Zirconia II*, eds N. Claussen, M. Ruehle & A. H. Heuer, The Am. Ceram. Soc. Inc., Columbus, Ohio, 1984, p. 382.
15. Claussen, N., *J. Am. Ceram. Soc.*, **61** (1978) 85; *J. Am. Ceram. Soc.*, **59** (1976) 49.
16. Green, D. J., *J. Am. Ceram. Soc.*, **65** (1982) 610.
17. Griffith, A. A., The Phenomena of Rupture and Flow in Solids, *Phil. Tran. Roy. Soc.*, **221A**(4) (1920) 163.
18. Cottrel, A. H., *The Mechanical Properties of Matter*, John Wiley and Sons, New York, 1964.
19. Davidge, R. W. & Evans, A. G., *Mater. Sci. Eng.*, **6** (1970) 281.

Journal of the European Ceramic Society 16 (1996) 799–802

0955-2219(95)00198-0
0955-2219/96/$15.00

Effects of Silicon Carbide Nano-phase on the Wet Erosive Wear of Polycrystalline Alumina

R. W. Davidge, P. C. Twigg & F. L. Riley*

School of Materials, University of Leeds, Leeds LS2 9JT, UK

(Received 12 October 1995; revised version received 30 October 1995; accepted 30 October 1995)

Abstract

Wet erosive wear rates for alumina–silicon carbide nanocomposites have been measured and compared with those for pure polycrystalline aluminas of similar grain size. In pure materials for mean grain sizes >2 μm the dominant wear mechanism appears to be grain-boundary microfracture, leading to grain pull-out; for finer grain sizes the worn surfaces are smooth. Within both grain size ranges significant reductions in wear rate are found for the nanocomposite materials, thus extending the span of established benefits obtained through the incorporation of silicon carbide nanoparticles into ceramic materials.

Introduction

The wear behaviour of hard ceramic materials such as alumina is a subject of considerable industrial importance, even more so when 'wear' is taken to include the material removal processes of cutting and grinding. The wear of alumina is known to be strongly dependent on the microstructure, and on the mean grain size (G) in particular. For a wide range of wear and abrasion processes the wear rate decreases as G decreases.[1–10] For pure alumina with G in the range 2 to 50 μm, the predominant wear mechanism is grain-boundary fracture. For very fine-grained materials (<1 μm) plastic deformation or polishing seems to be the preferred wear mechanism and it is likely that in these cases an underlying slow tribochemical wear mechanism may become the dominant process.

A tentative model for the wear of polycrystalline ceramics of grain sizes in the range 1 to 12 μm has been proposed,[11] based on microcrack propagation. This model assumes the preferred passage of cracks along two-grain boundaries, with delays in crack propagation occurring at multiple boundary junctions for readjustment of the direction of crack propagation. This 'stop–go' crack propagation process is a product of the fluctuating stress field experienced under bombardment by multiple erodent particles.

The time (t) for the crack to progress a specified distance (d) is given by:

$$t = 2(t_f + t_j)\, d / G \tag{1}$$

where t_f (proportional to the mean grain dimension, G) is the time to traverse a two-grain boundary face of dimension ~$G/2$ at a mean rate characteristic of the material, and t_j (a constant) is the time taken to realign at a three-grain junction. The experimentally observed wear rate (W) given by:

$$W = Ad / t \tag{2}$$

thus becomes

$$W = AG / 2\,(t_f + t_j) \tag{3}$$

where A is a constant related to the microstructural crack linking process and the experimental conditions of the test. t_f can be eliminated by defining a characteristic grain size (G_o) for which $t_f = t_j$. Thus:

$$t_f = (G/G_o)\, t_j \tag{4}$$

and substitution into eqn (3) gives:

$$W = A\, G\, G_o / [2\, t_j\, (G + G_o)] \tag{5}$$

There should therefore be a proportionality between W and $G / (G + G_o)$ with the plot passing through the origin, a prediction supported by a wide range of wear data for which the value of G_o ranges from 1 to 100 μm, depending on the nature of the process.[11] The G_o term is expected to vary with the nature of the wear process and conditions, which affect in particular the scale of the damage and the way that individual cracks propagate and link. This wear model specifically focuses on grain size effects and ignores possible contributions from other material removal processes less likely to be grain-size dependent, such as plastic-deformation-dependent and tribochemical wear. The model is therefore considered to be applicable to ceramics with grain sizes above a lower limit of ~1 μm;

*To whom correspondence should be addressed.

microfracture is not observed in ceramics of grain size <1 μm. Porosity has a detrimental effect on wear properties, but for levels ≤2% the effects would be expected to be small.[12]

The incorporation of nanoparticles (<1 μm) of silicon carbide (SiC) into polycrystalline alumina materials is known to confer marked improvements in their mechanical properties (for example, increased strength, toughness and creep resistance).[13–15] This paper reports the results of a preliminary investigation into whether these advantages extend to the wear properties of hot-pressed aluminas containing varying proportions of three grades of nanoparticle SiC powder. The study was based on a simple system of wet erosion, using a slurry of alumina grit in water. Direct comparisons of the wear rates for these materials with those for alumina, silicon nitride and zircon materials are possible because the experimental technique for wearing the materials was identical to that used in previous investigations.[10,16,17]

Experimental

Alumina (Sumitomo AKP53) and silicon carbide (Lonza α-SiC, UF45, UF32 and UF15 at levels of 5 and 10 wt%) powders were used. The mean particle size (d) for the alumina was 90 nm and the maximum (d_{max}) 320 nm; d for SiC ranged from 90 nm (UF45) to 110 (UF15) and d_{max} from 320 nm (UF45) to 500 nm (UF15). The powders were blended by attrition milling in water with Dispex A40 dispersant (Allied Colloids, Bradford, UK), and then freeze-dried. One sample of freeze-dried alumina without SiC additions (Al_2O_3-I) was used as a control material; a second sample of alumina was also prepared using a spray-drying alumina powder (Al_2O_3-II). Discs of material 50 mm in diameter and ~6 mm thick were hot-pressed in a graphite die at temperatures in the range 1400 to 1700°C and under pressures of 25 MPa. Selected hot-pressed discs were given subsequent annealing treatments under a non-oxidizing atmosphere at <1900°C to cause grain growth. This process was carried out under an argon gas flow (100 cm^{-3} min^{-1}) and the discs were further embedded in fine SiC powder as an oxygen getter to prevent oxidation of the nanoparticle SiC. Densities were measured by the water immersion method using BS7134. Discs of 25 mm diameter were core drilled from the larger discs for the wear rate measurements, and surfaces were ground using a steel-bonded 75 μm diamond wheel. Worn disc surfaces were gold-coated and examined by scanning electron microscopy (SEM); other surfaces were ground and polished to 1 μm diamond, embedded in SiC powder and thermally etched at 1400°C for 40 min under flowing argon, gold-coated and photographed by SEM for grain size measurements.

Wet erosion was carried out in a modified high-torque attritor mill using 0·5 to 1 mm dimension crushed fused alumina aggregate in water.[10,16] The alumina discs (25 mm diameter and ~5 mm thick) were clamped between shaped discs of hard polyurethane attached to the shaft of the mill, with ~50% of the disc exposed. The sample holder was immersed in an externally water-cooled slurry consisting of 700 g of alumina grit (of stated purity 92·2% Al_2O_3, with SiO_2 and TiO_2 as the major impurities) in 250 cm^3 of deionized water and rotated at a speed of 8 Hz with a disc track radius of 36 mm (giving a disc perimeter linear velocity of ~1.9 m s^{-1}). After wearing for 2 h (t_1) and 6 h (t_2) discs were ultrasonically cleaned in deionized water, dried for 20 min at 110°C, and weighed to ±0·1 mg (w_1 and w_2). A wear rate (R) measured in m s^{-1} was calculated on the basis of the expression:

$$R = [(w_1 - w_2) / (t_2 - t_1) / (Ap)$$

where A, arbitrarily, is the area of the exposed leading quadrant of the 6 mm thick disc rim (approximately 1/4 of the total rim area): experience showed that with this wear configuration very little wear took place on the disc faces and the face area (although much larger) was therefore ignored. This time period was chosen in order to minimize any effects of initial surface finish at short times and the significant smoothing of the grit particles at longer times. The slurry was replaced by a fresh batch after use for two tests (total time 12 h). Worn and fracture surfaces of the discs were gold-coated and examined by SEM.

Mean alumina grain size (G) was measured using a standard line intercept technique from SEM photographs. At least 100 grains were measured for each material, and G obtained by multiplication of the mean intercept length by the factor 1·56.[18]

Results

The alumina and alumina–silicon carbide nanocomposite materials were produced by hot-pressing and, for one composition, subsequent annealing, alumina and SiC powders using the conditions set out in Table 1, which also summarizes material characteristics and wear rates (the means of two determinations).

The microstructure of a typical nanocomposite is illustrated by Fig. 1; the uniform distribution of the nanoparticles of SiC (darker phase) at the grain boundaries and within the alumina grains is clear.

Wear rate data for the coarser-grained nanocomposite materials, compared with those for a series of pure aluminas,[10] are shown in Fig. 2. For

Table 1. Materials' fabrication conditions and properties

Material	*Hot-pressing temperature (°C)*	*Density*		G *(μm)*	R *(nm s^{-1})*
		(g cm^{-3})	*%Theoretical*		
1 Al_2O_3-I	1450	3·95	99·3	1·3	11·8
2 Al_2O_3-II	1400	3·93	98·7	0·7	2·2
3 +5% UF45	1550	3·87	98·2	0·5	1·2
4 +5% UF45	1700	3·92	99·5	2·0	14·2
5 +5% UF45	as 3 + 1900 anneal	3·80	95·4	5·0	16·1
6 +5% UF32	1550	3·88	98·5	1·0	1·8
7 +5% UF15	1550	3·89	98·8	1·1	4·6
8 +10% UF45	1550	3·78	97·0	0·8	1·4
9 +20% UF45	1550	3·48	91·2	0·4	5·9

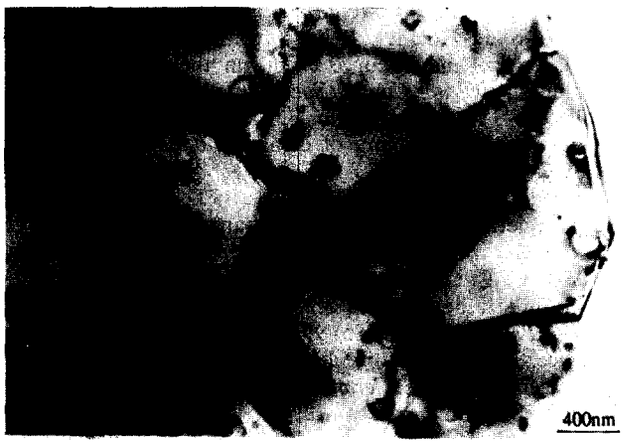

Fig. 1. Microstructure of a typical nanocomposite.

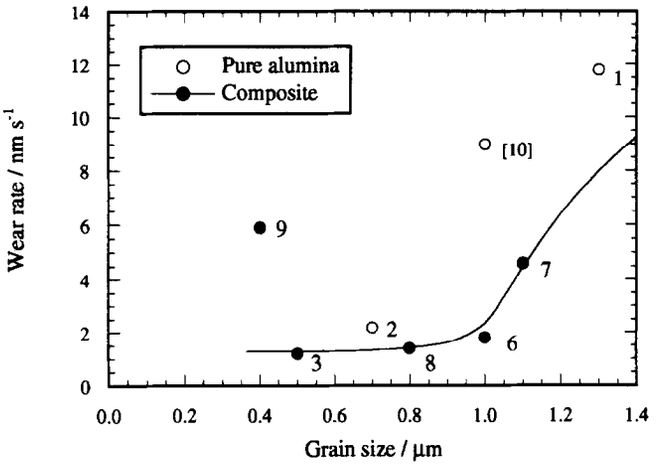

Fig. 3. Wear rate data for the finer grain nanocomposite materials, and fine grain size pure alumina.

greater clarity, data for finer-grained ($G \leq 2$ μm) materials, for which wear is by mechanisms other than microfracture, are shown separately in Fig. 3. Examination of the worn surfaces of the pure aluminas of grain size ≥2 μm predominantly showed grain-boundary fracture; all the nanocomposites, including the 5 μm grain size material, although showing some indication of grain detachment, showed a predominantly smooth wear surface similar to that of a very fine-grained pure alumina and indicative of plastic deformation or tribochemical wear. Figure 4 is that of a worn surface of a 2·5 μm pure alumina;[10] Fig. 5 shows a typical surface of a worn 5 μm nanocomposite material.

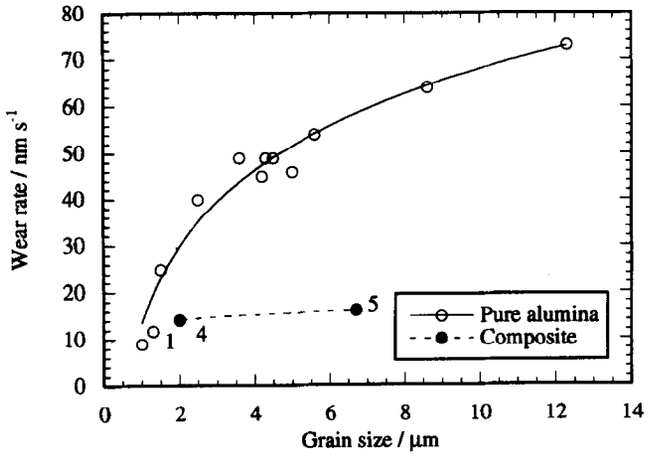

Fig. 2. Wear rate data for the coarser grain nanocomposite materials, compared with those for pure alumina.[10]

Fig. 4. Typical surface of a worn 2·5 μm grain size pure alumina.

Fig. 5. Typical surface of a worn 5 μm grain size nanocomposite material.

Discussion

There is a clear improvement in the wear behaviour of the nanocomposites in comparison with that of the pure aluminas of equivalent grain size. For nanocomposites of $G \geq 2$ μm the wear rates were reduced by a factor of 2 to 3. The data for the finer-grained materials are less conclusive, but the wear rate appears to be reduced by a factor of 1·5 to 2. The deleterious effect of a high porosity level (9%) is indicated by the poor wear resistance of sample 9 prepared with the addition of 20% of SiC powder, and therefore less easy to densify fully.

One of the best established effects concerning Al_2O_3/SiC composite materials is the 'strengthening' of the alumina grain boundaries by the nanophase. This is manifested, for example, by relatively smooth transgranular fracture paths in the nanocomposites, compared with those of pure alumina, and the smoother surfaces during polishing (indicative of a reduced degree of grain pull-out).[15] These effects of the SiC nanoparticles on wear rate are also associated with a change in the nature of the wear process, from that typical of a large grain material (where there is relatively easy material removal by grain-boundary fracture) to that typical of a smaller-scale material removal process with mechanisms involving much slower localized plastic deformation or atomic removal of material. The nanocomposites thus have much better wear resistance than that predicted by the microfracture model, because of inhibition of the grain-boundary fracture process by the SiC particles. However, even when the worn surfaces of the small-grained pure alumina and the nanocomposites are similar, the wear rate of the nanocomposite is much slower. It is known that dislocation substructures form in nanocomposites[13] and these may reduce the efficiency of processes involving plastic deformation.

Conclusions

The incorporation of nanoparticle SiC into dense polycrystalline alumina leads to a significant reduction in wear rate and parallels the action of this type of SiC in improving other mechanical properties of ceramic materials. Although grain size is the single most important parameter in determining the wear rate of pure polycrystalline aluminas, the presence of nano-phase SiC has (at equivalent grain sizes) a significant additional beneficial effect. The presence of the fine SiC particles in the sintering alumina powder also inhibits grain growth so that, for given densification conditions, the nanocomposites tend to possess desirable fine grain sizes.

Acknowledgements

The support of the EPSRC through research grant GR/J86513 is acknowledged. The nanocomposites were prepared as part of BRITE-EURAM Project BRE CT920358, and the Partners are thanked for provision of materials.

References

1. Evans, A. G. & Wilshire, T. R., Quasi static solid particle damage in brittle solids—I: Observations, analysis and implications. *Acta. Metall.*, **24** (1976) 939–56.
2. Cho, S. J., Hockley, B. J., Lawn, B. R. & Bennison, J., Grain-size and R-curve effects in the abrasive wear of alumina. *J. Am. Ceram. Soc.*, **72**(7) (1989) 1249–52.
3. Rice, R. W. & Speronello, B. K., Effect of microstructure on rate of machining of ceramics. *J. Am. Ceram. Soc.*, **59**(7–8) (1976) 330–3.
4. Wiederhorn, S. M. & Hockley, B. J., Effect of material parameters on the erosion resistance of brittle materials. *J. Mater. Sci.*, **18** (1983) 766–89.
5. Wu, C. Cm., Rice, R. W., Johnson, D. & Platt, B. A., Grain size dependence of wear in ceramics. *Ceram. Eng. Sci. Proc.*, **6**(7–8) (1985) 995–1011.
6. Rice, R. W., Micromechanics of microstructural aspects of ceramic wear. *Ceram. Eng. Sci. Proc.*, **6**(7–8) (1985) 940–58.
7. Marshall, D. B., Lawn, B. R. & Cook, R. F., Microstructural effects on grinding of alumina and glass ceramics. *J. Am. Ceram. Soc.*, **70**(6) (1987) C139–40.
8. Gee, M. G. & Almond, E. A., The effects of surface finish on the sliding wear of alumina. *J. Mater. Sci.*, **25**(1A) (1990) 296–310.
9. Cho, S. J., Moon, H., Hockley, B. J. & Hsu, S. M., Wear transformation phenomenon in alumina during sliding. In *C-MRS Int. Symp. Meeting 1990*, Vol. 5, ed. B. Wu. North-Holland, Amsterdam, 1991, pp. 387–9.
10. Miranda-Martinez, M., Davidge, R. W. & Riley, F. L., Grain size effects on the wet erosive wear of high purity polycrystalline alumina. *Wear*, **172** (1994) 41–8.
11. Davidge, R. W. & Riley, F. L., Grain size dependence of the wear of alumina. *Wear*, **186–187** (1995) 45–9.
12. Miranda-Martinez, M., Davidge, R. W. & Riley, F. L., The reduction of erosive wear rates of advanced technical ceramics. In *Ceramics in Energy Applications*, Proc. Institute of Energy's 2nd Int. Conf., London, 20–21 April 1994. The Institute of Energy, London, 1994, pp. 239–52.
13. Niihara, K., New design concept of structural ceramics—ceramic nanocomposites. *Ceram. Soc. Jap.*, **99**(10) (1991) 974–82 (Centennial Memorial Issue).
14. Zhao, J., Stearns, L. C., Harmer, M. P., Chan, H. M., Muller, G.A. & Cook, R. E., Mechanical behaviour of alumina–silicon carbide 'nanocomposites'. *J. Am. Ceram. Soc.*, **76** (1993) 503–10.
15. Walker, C. N., Borsa, C. E., Todd, R. I., Davidge, R. W. & Brook, R. J., Fabrication, characterization and properties of alumina matrix nanocomposites. *Br. Ceram. Proc.*, **53** (1995) 249–64.
16. Miranda-Martinez, M. & Riley, F. L., Wet abrasive wear of technical ceramics. *Br. Ceram. Trans. J.*, **90** (1991) 118–21.
17. Wootton, A., Miranda-Martinez, M., Davidge, R. W. & Riley, F. L., The wet erosive wear behaviour of fine-grain zircon ceramic. *J. Eur. Ceram. Soc.*, in press.
18. Mendelson, M. I., Average grain size in polycrystalline ceramics. *J. Am. Ceram. Soc.*, **52**(8) (1969) 332–46.

Journal of the European Ceramic Society 16 (1996) 803–811

S0955-2219(96)00003-9
0955-2219/96/$15.00+.00

Grain Size Dependent Residual Microstresses in Submicron Al_2O_3 and ZrO_2

Andreas Krell,[a] Angelika Teresiak[b] & Dietrich Schläfer[b]

[a]Fraunhofer-Institut für Keramische Technologien und Sinterwerkstoffe (IKTS), D-01277 Dresden, Germany
[b]Institut für Festkörper- und Werkstofforschung Dresden, Postfach 270016, D-011071 Dresden, Germany

(Received 12 October 1995; revised version received 27 November 1995; accepted 5 December 1995)

Abstract

X-ray measurements of lattice spacings are used to determine residual microstresses present in sintered alumina and in tetragonal zirconia polycrystals due to thermal expansion anisotropy (TEA). In Al_2O_3 with grain sizes larger than 1 μm the microstresses are 30–100 MPa, in submicrometer samples the grain size influence becomes small and residual stresses range between 20 and 30 MPa. For the grain sizes between 0·3 and 9 μm there is no indication of a change in the high-temperature relaxation mechanism. In ZrO_2 with grain sizes of 0·5–1 μm the residual stresses are similar as observed in Al_2O_3 (20–60 MPa), they decrease further at grain sizes 0·2–0·4 μm. The results are independent of technological approaches like powder processing or sol/gel used to produce the sintered bodies.

1 Introduction

The need for residual stress measurements results from their complex influences on the mechanisms of the microstructural development during sintering, on crack propagation and energy dissipation, and on the macroscopic technical performance (e.g. strength, toughness, wear). Whereas the present work was focused on *micro*stresses, other components have to be considered as well because X-ray measurements on ground surfaces comprise contributions from different (microscopic and macroscopic) stress components. A threefold classification of residual stresses in polycrystals adopted here was given e.g. by Kloos.[1]

First kind residual stresses are macroscopic along at least one dimension (e.g. within a surface, possibly with a steep gradient along the perpendicular z-direction). A frequent origin is microplastic deformation (dislocations, twins)—important for all measurements on ground or polished ceramic surfaces.[2,3] The size of subsurface grinding damage decreases with smaller grain sizes.[4] Extended subsurface damage is present in the upper layer of grains only, and even in 40 μm coarse grained alumina it occurs only within a 20 or 2 μm thin surface region after grinding or polishing, respectively.[2] In sintered alumina with 2 μm grain size the resulting macroscopic residual compressive stresses are about −35 MPa in a depth of 25 μm, higher stresses of −150 MPa are present within a 10 μm thin surface layer,[5] and only the upper 1–3 layers of grains exhibit a stress level of −450 MPa.[6]

Second kind residual stresses develop on cooling of sintered polycrystals due to thermal contraction differences between the crystallites. In polyphase ceramics there is a thermal misfit between grains of different phases, in single-phase non-cubic polycrystals thermal expansion anisotropy (TEA) produces residual stresses due to the different thermal contraction of randomly oriented neighbouring grains. Sintered alumina was studied first by Evans.[7] In a first approximation these stresses do not depend on grain sizes, but their relaxation introduces an important grain size effect discussed below. Second kind residual stresses are of outstanding importance for the ratio of trans- and intergranular fracture, for crack branching or bridging,[8] microcracking,[7,9] stress-induced phase transformation,[10,11] and subcritical crack growth.[12] In this way, microstresses govern crack-propagation-induced energy dissipation[13,14] and affect the macroscopic toughness and strength. Their investigations contribute to an improved understanding of the technologically important correlation of grain size and macroscopic mechanical behaviour. These microstresses were the central subject of our study.

Third kind residual stresses on the scale of lattice defects within the grains influence the hardness and the tribological behaviour, but their effect on the macroscopic toughness and strength is usually small. These stresses are not a subject of the present investigation.

In sintered alumina with a random orientation of grains and at a temperature difference on cooling of $\Delta T = -1500$ K, a first approach gives an average tensile component $\sigma_c \approx 250$ MPa in the direction of the c-axis.[7] A more realistic evaluation has to consider the statistical character of the orientation relationship of neighbouring grains and needs statistical calculations as proposed by Kreher.[15] In his paper, simple analytical expressions for the average TEA microstresses in the grains were derived under the assumption that the elastic anisotropy of the single crystals can be neglected, i.e. one has to approximate the elastic stiffness tensor by isotropic constants. Kreher and Molinari demonstrated different approaches which can be used for this purpose,[16] but for a first qualitative estimation it is sufficient to use known macroscopic effective elastic constants of the polycrystalline materials (actually, no unambiguous anisotropic data are available for tetragonal zirconia doped with different amounts of Y_2O_3). Hence, with the exact statistical solutions derived by Kreher[15] an average tensile microstress along the c-axis is calculated for Al_2O_3 as $\sigma_c = 148$ MPa with a corresponding compressive stress $\sigma_a = -\sigma_c/2 = -74$ MPa in the plane perpendicular to the c-axis (Al_2O_3: $E \approx 400$ GPa, Poisson's ratio $\nu \approx 0{\cdot}23$, $\Delta\alpha = \alpha_c - \alpha_a = 0{\cdot}9 \times 10^{-6}$ K^{-1}, $\Delta T = -1500$ K). This result is considerably lower than Evans' approach. For zirconia the use of $E = 217$ GPa, $\nu = 0{\cdot}32$, $\Delta\alpha = 1{\cdot}55 \times 10^{-6}$ K^{-1}, $\Delta T = -1400$ K yields $\sigma_c = 126$ MPa. Figure 1 shows these stresses after an appropriate tensor transformation in the sample-fixed coordinate system as a function of the orientation of the considered grain. Note the very *similar* results in spite of the high thermal anisotropy in ZrO_2 (caused by its low Young's modulus).

Second kind TEA stresses are subject to high-temperature visco-elastic relaxation during a cooling interval when the grain boundary viscosity is yet low, and all measurements are expected to give results lower than indicated by Fig. 1. Two similar approaches describe visco-elastic relaxation in a form[17,18] that is equivalent with

$$<\sigma> = \sigma_0 + \int \frac{<\sigma> E}{\dot{T}\eta_{\text{eff}}} \, dT \qquad (1)$$

$$\eta_{\text{eff}} \sim G^2 / D_{\text{eff}} \qquad (2)$$

where $<\sigma>$ is the statistical average of the residual stress, σ_0 is the stress before relaxation, $\dot{T}$ is the cooling rate (<0!), η_{eff} is the effective grain boundary viscosity which is proportional with the square of the grain size G and with the inverse effective diffusion coefficient D_{eff}; E and ΔT have the meaning as introduced above. Due to the strong grain size effect in eqn (2), the relaxation term in eqn (1) reduces the residual stress $<\sigma>$ the smaller the grain size. With only grain boundary diffusion considered, an approximation gives $D_{\text{eff}} \sim 1/G$, and the grain size effect can be described by $<\sigma> = \sigma_0 - (1/G^3) \int A \, dT$ where a term with an inverse grain size appears which is not affected by the integration.[18] However, the limitations of the validity of such approximations are not obvious, and none of the models claims a simple stress–grain size relationship. On the contrary, Blendell and Coble emphasize the requirement of a numerical integration (in their work this procedure gives a rather weak grain size effect: 6 MPa difference for grain sizes between 50 and 150 MPa).

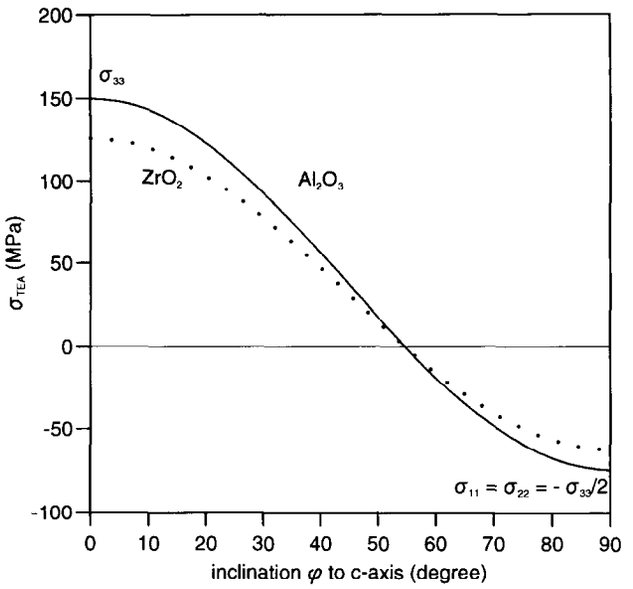

Fig. 1. Theoretical evaluation of residual stresses σ_{TEA} in Al_2O_3 and ZrO_2. The shape of the curve with the given relationship of σ_{33} and σ_{11} and with zero stresses at 55° is a consequence of the tensor transformation and the required balance of forces.

With relaxation stimulated by progressively smaller grain sizes, the driving force $<\sigma>$ of the relaxation term in eqn (1) decreases. Therefore, whereas $<\sigma>$ decreases continuously with reduced grain sizes, the *degree* of the grain size influence will decrease significantly at very small grain sizes.

Elaborated X-ray diffraction methods measure macroscopic first and second kind surface stresses when the average of the stress over the examined phase is not zero ($\sin^2 \psi$ approach; ψ is the angle between the normals of the specimen surface and of diffracting {hkl}-planes);[19,20] it is also possible to incorporate the effect of elastic anisotropy into the analysis.[21] In single phase materials, however, the $\sin^2\psi$ approach cannot be used to investigate *thermal anisotropy micro*stresses in the bulk (without influences of macroscopic surface stresses) because the associated strains are fixed at each of the randomly oriented crystallites (in their isotropic surroundings). Without any relationship of these

*micro*strains to the macroscopic surface, a variation of the macroscopic direction ψ for one reflex (hkl) would find the same lattice spacing d for all ψ—an incorrect pretence of a zero strain due to the circumstance that the reflecting crystallites exhibit a constant strain independent of different ψ. Hence, second kind microstresses in single phase materials have to be derived by other techniques. Three methods were described:

(i) Precision X-ray measurements of lattice parameters comparing the sintered body with a powder standard resulted in $\sigma_c \approx 40$–70 MPa for an alumina with 3 μm grain size; there were indications of increasing relaxation with increasing impurity and doping concentrations (MgO, SiO_2, PbO).[22] This result is in fair qualitative agreement with Fig. 1 if one assumes a high degree of relaxation.

(ii) The same agreement holds for a measurement which analysed the broadening of spectroscopic R lines (due to Cr^{3+} impurities).[17] For 50–130 μm coarse alumina with probably low relaxation activity σ_c was 100–130 MPa.

(iii) Inconsistent results were derived from a new method which analyses the frequency shift of the optical fluorescence from Cr^{3+} impurities. Measurements in Al_2O_3/ZrO_2 composites with alumina grain sizes of 2–8 μm resulted in $\sigma_c = 56$ MPa for the alumina phase which agrees well with other published data.[23] In single phase alumina, however, surprisingly high values ranging from 100–160 MPa (grain size 2 μm) to 200–300 MPa (16 μm) were reported.[24]

At present, attention has focused on microstructures with grain sizes smaller than 1 μm, but measurements of TEA microstresses were published for coarser grained ceramics only (in alumina for the 50–150 μm[17] and for the 2–20 μm range[24]). The present study was, therefore, concentrated on the grain size influence in σ_{TEA} microstresses down to about 0·2 μm. The comparison of residual stresses in alumina and in zirconia was intended to give an insight into the role of different grain boundary structures in both materials.

2 Materials and Methods

2.1 Materials and measurements

Table 1 gives a survey of the investigated materials. All but one sample were fabricated by usual powder processing, sintering in air and diamond grinding (40–50 μm grit size). An additional alumina batch was prepared from boehmite with a sol/gel technology (+ α-Al_2O_3 seeds <0·2 μm) to test whether TEA stresses depend on special technological approaches or on surface conditions. Therefore, this sample was broken down to a grit size of about 0·2 mm before X-ray investigations and measured in this fractured state (with a crystallite size of about 0·5 μm the broken grit size of 200 μm is large enough to represent real polycrystals with a level of residual microstresses as typical in this microstructure).

The monoclinic phase content was zero in most of the ground ZrO_2 surfaces. Only the coarsest of the zirconia microstructures (0·77 μm) exhibited a slight increase of the monoclinic content from zero to 3% on grinding.

The orientation dependent lattice strain was derived from very precise X-ray measurements of lattice parameters in the sintered bodies and in powder standards. For this procedure it is essential to have specimens and standards with the same state of possible solid solutions of impurities and dopants. Therefore, the powder standards were taken off from

Table 1. Investigated sintered ceramics. The raw materials are given as footnotes

Material	*Impurities, additives (wt%)*	*Grain sizes (sintered microstructure) (μm)*	*Grain boundary microstructure (Results of high resolution TEM studies)*
Al_2O_3*	0·001 Si, 0·001 Fe	0·4–2·5	Grain boundary facets free of amorphous phases, very few amorphous triple junctions
Al_2O_3 from boehmite†	0·16 Ti, 0·018 Si	0·5	Not investigated
Al_2O_3††	0·095 Si, 0·085 Mg, 0·065 Pb	2·5–9	Coexistence of interfaces with an amorphous phase and of facets free of any glass
ZrO_2(3 mol% Y_2O_3)‡	0·015 Na, 0·015 Fe, 0·010 Al	0·25–1	Continuous very thin amorphous interface in all grain facets (<1 nm)

*Taimicron DAR, Taimei Chemicals, Japan; 99.99% purity, specific surface (BET) 14 m^2/g, median particle size 0·2 μm.
†Disperal, Condea Chemie, Hamburg, Germany, specific surface (BET) 170 m^2/g, median particle size 5–10 nm.
††Alcoa A16SG, Aluminum Corp. of America, Bauxite, AR, 99.9% purity, specific surface (BET) 9 m^2/g, median particle size 0·6 μm.
‡TZ-3Y, Tosoh, Japan; 99.95% purity, specific surface (BET) 17 m^2/g, median particle size 60 nm.

the batches used to fabricate the sintered specimens *after* processing with all additives just before compaction and sintering, and they were annealed with the same temperature regime as applied to sinter the polycrystalline samples.

The X-ray measurements for alumina microstructures with grain sizes <3 μm and for all zirconia specimens were performed with Co–K$_\alpha$ radiation at 40 kV/40 mA; for coarser alumina microstructures (≥3 μm) Cu–K$_\alpha$ was used. The goniometers had a symmetric Bragg–Brentano arrangement (pw1820 with an analysing software APD1700* for alumina specimens with grain sizes <1 μm, HZG4† for all other samples). A secondary monochromator was used to improve the peak–background ratio. The software calculates the exact peak positions by a Marquardt non-linear least-squares fit. The algorithm continues the iterations until either a maximum number of 25 iterations has been performed or convergence has been reached. The default convergence criterion is ≤0·0001 or less fractional change per iteration in each of the twelve intrinsic parameters. After each iteration, the weighted sum of the squares indicates profile fitting's progress. The accuracy of the determined peak positions was ±0.005–0.010° due to a long measuring time of 20 s per step and a narrow step width $\Delta(2\Theta) = 0.02°$ which is less than 1/30 of the typical half-width of investigated reflexes.

The measuring range was $110° < 2\Theta < 145°$ with cobalt radiation. It contains sufficiently strong reflexes with different orientations of lattice planes with respect to the c-axis (Table 2). Due to the special preparation of the standards, only the residual stresses give rise to the measured difference in the X-ray peak positions

$$\Delta\Theta_{hkl} = \Theta_{hkl}^{specimen} - \Theta_{hkl}^{standard} \qquad (3(a))$$

and the related orientation dependent strain[26]

$$\varepsilon_{hkl} = -\Delta\Theta_{hkl}\cot\Theta_{hkl}\,, \qquad (3(b))$$

where Θ_{hkl} is the Bragg angle. The accuracy of the determined peak positions as stated above means errors of $0{\cdot}3 \times 10^{-4}$–$0{\cdot}5 \times 10^{-4}$ in the strain and of 10–20 MPa in the tension component of the residual microstress.

The use of eqn (3(b)) to derive an information about second kind residual microstresses requires that (i) the sample is free of macroscopic residual stresses or can be corrected for such effects, (ii) the microstresses are hydrostatic, (iii) surface effects resulting from small penetration depths and large grain sizes can be neglected. The first condition we shall discuss in Section 2.2. As to the other conditions, Fig. 2 demonstrates that the penetration depth

*Philips Ind. Electr. BV, Almelo, Netherlands.
†Richard Seifert & Co. Freiberger Präzisionsmechanik GmbH, Freiberg, Germany.

Table 2. Characterization of investigated reflexes (Al_2O_3: hexagonal indices for structural cell with c/a = 2·73). φ is the inclination of the lattice-plane normal to c-axis, Φ is the angular direction around the c-axis in Al_2O_3 as defined by Wachtman *et al.*[25] The Bragg angle Θ refers to Co–K$_\alpha$ radiation. The asterisk marks reflexes measured for coarser alumina microstructures (>3 μm) only

Material	*Reflexes*	*Orientation* φ	Φ	*Bragg reflection* 2Θ
Al_2O_3	(000·12)	0·0°	—	111·3
	(11$\bar{2}$·15)*	20·0°	0·0°	142·3
	(21$\bar{3}$·10)	40·0°	−10·5°	127·3
	(04$\bar{4}$·10)*	51·6°	−30·0°	145·2
	(22$\bar{4}$6)	61·2°	0·0°	118·1
	(41$\bar{5}$6)*	67·4°	−19·0°	136·1
	(13$\bar{4}$4)	71·0°	+16·0°	112·1
	(40$\bar{4}$4)	72·4°	−30·0°	131·2
	(04$\bar{4}$2)	81·0°	+30·0°	123·0
ZrO_2	(105)	16·0°	—	127·8
	(204)	36·0°	—	116·6
	(303)	55·0°	—	130·1
	(312)	66·0°	—	118·0
	(321)	79·0°	—	131·3

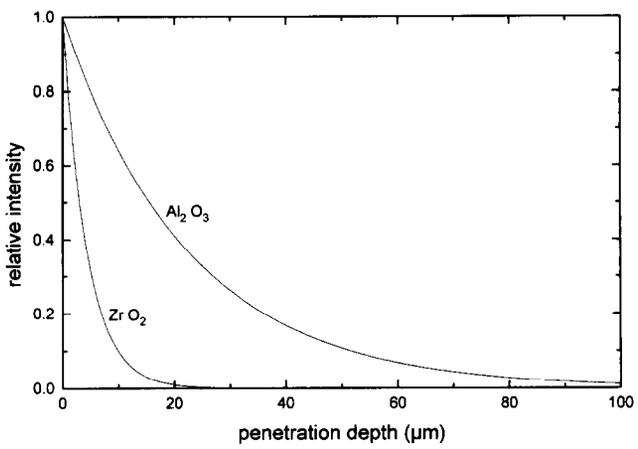

Fig. 2. X-ray intensity of Co–K$_\alpha$ radiation at $2\Theta = 120°$ as a function of the penetration depth in alumina and in zirconia.

of the X-rays is much larger than the grain sizes of the examined ceramics. Calculations show that the penetration depth (perpendicular to the surface) is almost independent of (hkl): the width of the range for the reflexes in Table 2 is 10·5% for Al_2O_3 and 6·5% for ZrO_2. Hence, most of the reflecting grains are in a depth below the surface that avoids surface effects.

2.2 Analysis of measured data

In Figs 3(a) and (b) the full curves exemplify the orientation dependence of the thermal anisotropy strains ε_{hkl} in Al_2O_3 and ZrO_2 calculated with an isotropic approximation by the same procedure as used for Fig. 1 (orientation averages of the elastic parameters E and ν as given in the introduction. As an example, strain states are selected which finally would give a corresponding maximum tension in c-axis direction of $\sigma_{33} = +100$ MPa in both materials.

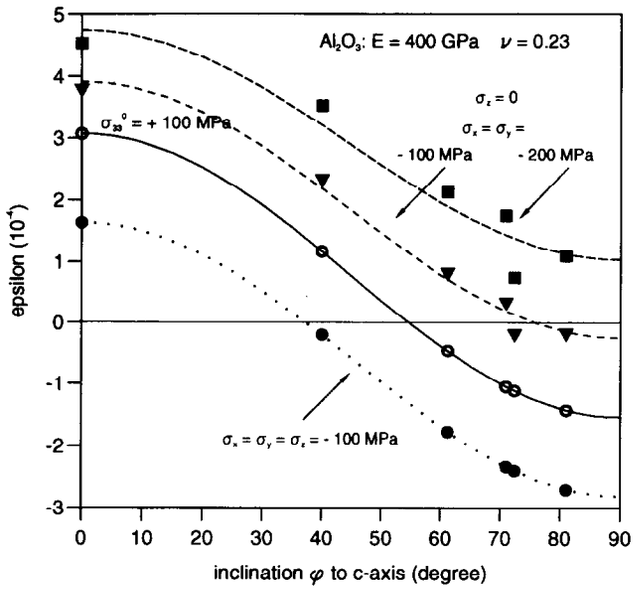

(a)

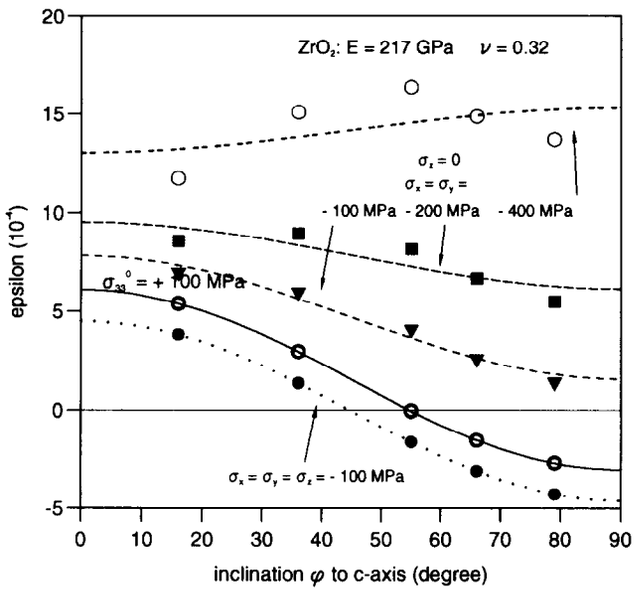

(b)

Fig. 3. Influence of elastic anisotropy and of superpositioned first kind residual surface stresses in Al_2O_3 (Fig. 3(a)) and in ZrO_2 (Fig. 3(b)) on deviations of TEA strain ε_{hkl} from an isotropic (cosine-like) approximation. Full symbols give results for selected reflexes calculated by eqns (5) and (6). Full lines—pure TEA stresses; broken lines—effect of superpositioned plain surface compression; dotted lines—superposition with hydrostatic compression.

With the exception of the broken sol/gel derived reference sample, all X-ray investigations were performed on ground surfaces where first kind residual stresses should be present. In comparison with the macrostress-free material (full curves in Fig. 3), the probable compressive character of these plane macrostresses (component normal to the surface $\sigma_z = 0$) produces an additional *positive* strain perpendicular to the surface because all reflecting lattice planes are oriented here with their normals parallel to the surface normal (Fig. 3 also demonstrates that *hydrostatic* compression would be required to reduce the TEA strain). Of course, these macrostresses would violate the condition (i) given above for the application of eqn (3(b)), and an appropriate correction is required.

It has been shown that under the assumption of elastic isotropy macrostresses simply shift the orientation dependent strain curves which characterize the pure type II microstresses in Fig. 3; the amount of this shift equals the level of the superpositioned macrostress.[27] This behaviour provides a way to calculate both the TEA microstress and the macrostress by re-shifting the measured strain curves to a zero position at an inclination angle = 54·7° or, in other words, to a position where $\varepsilon_{33} = -2\ \varepsilon_{11}$ (the characteristics of the macrostress-free state in Fig. 3). Unfortunately, the situation becomes more complicated if elastic anisotropy causes systematic deviations from the cosine-like curve derived under the assumption of elastic isotropy and alters the character of the curve-shift produced by macrostresses. In Al_2O_3, these effects are probably small: no systematic and significant deviation was observed for 6 investigated reflexes in 7 specimens. Investigations of 5 reflexes in 7 ZrO_2 samples sometimes showed (105) data below and (321) strains above the cosine-like fit, but generally the deviations were of random character either in ZrO_2. It was, nevertheless, decided to separate the actually interesting TEA stresses and possible macrostresses with consideration of elastic anisotropy. The reason was to be sure that deviations of the measured ε_{hkl} (φ) curve from the form expected for pure type II TEA-stresses are really associated with the superposition of macrostresses and not generated by elastic anisotropy alone.

Grigoryev described a way to take into consideration the elastic anisotropy for the analysis of these first kind surface stresses.[28] Generally, the strain component perpendicular to the specimen surface in the laboratory-coordinate system of the measurement (where the z-axis is perpendicular to the surface) is calculated with the compliances s_{33ij} according to

$$\varepsilon_{33} = \sum_{j=1}^{3} (s_{331j}\,\sigma_{1j} + s_{332j}\,\sigma_{2j} + s_{333j}\,\sigma_{3j})\,. \qquad (4)$$

The tensor components s_{33ij} and the stresses σ_{ij} have to be derived from the data in the crystallographic-coordinate system by corresponding transformations. Grigoryev gives solutions for the cubic system[21,28] which are used here as a sufficient approximation for ZrO_2 (3 mol% Y_2O_3) with its very small tetragonality. Tensorial calculations for the trigonal system were performed for Al_2O_3. Since hydrostatic stress fields

cannot exist in single phase polycrystals by physical reasons, only results for plane surface compression $\sigma_{SF} = \sigma_x = \sigma_y$ ($\sigma_z = 0$) are given here. With the orientation angles φ (inclination of the lattice-plane normal to c-axis) and Φ (the angular direction around the c-axis) as defined by Wachtman *et al.*[25] the resulting equations are:

Al_2O_3

$$\varepsilon_{33}/\sigma_{SF} = (s_{11} + s_{33} - s_{44})\sin^2\varphi\cos^2\varphi + s_{12}\sin^2\varphi + s_{13}(\sin^2\varphi + 2\cos^4\varphi) + 2s_{14}\sin^3\varphi\cos\varphi\sin\Phi(1 - 4\cos^2\Phi) \quad (5)$$

For the quantitative evaluation, the s_{mn} matrix components published by Wachtman *et al.*[25] were used here.

ZrO_2

$$\varepsilon_{33}/\sigma_{SF} = 2s_{12} + 2(s_{11} - s_{12} - 0{\cdot}5s_{44})\Gamma \quad (6)$$

orientation factor $\Gamma = (h^2k^2 + k^2l^2 + h^2l^2)/(h^2 + k^2 + l^2)$

The elastic compliances were derived for ZrO_2 (3 mol% Y_2O_3) from data published by Ingel *et al.*[29]: $s_{11} = 2{\cdot}735 \times 10^{-3}$ GPa^{-1}, $s_{12} = -5{\cdot}763 \times 10^{-4}$ GPa^{-1}, $s_{44} = 1{\cdot}842 \times 10^{-2}$ GPa^{-1}.

The individual points in Fig. 3 represent these calculations for some of the reflexes (Table 2); the broken and dotted lines are results of a least squares fit. Contrary to hydrostatic first kind residual stresses, with a plane surface stress ($\sigma_z = 0$) elastic anisotropy causes considerable deviations from the (isotropic approximation) TEA fit, and in zirconia the whole character of the ε_{hkl} (φ) dependence can change.

The analysis of the measured ε_{hkl} data was performed as illustrated in Fig. 4 for the example of an alumina microstructure with a grain size of 1·9 μm:

(1) The measured Θ_{hkl} of sintered specimen and powder standard give ε_{hkl} by eqn (3).

(2) The measured ε_{hkl} (φ) are influenced by superpositioned first kind surface stress as demonstrated by Fig. 3: compared with the macrostress-free curve, a result of higher measured ε_{hkl} (φ) requires a correction for plane compression σ_{SF} (lower ε_{hkl} (φ) would indicate hydrostatic compression σ_{HY}). A cosine-like least squares fit of measured (1) and corrected (2) ε_{hkl} was achieved with a stepwise variation of the macrostresses σ_{SF} by a computer program that finally stopped at $\varepsilon_{33} = \varepsilon_{fit}$ ($\varphi = 0°$) $= -2\,\varepsilon_{11} = -2\varepsilon_{fit}$ ($\varphi = 90°$). The use of a cosine-like function minimizes the fitting error in the final result ε_{33}. Note that the significance of this ε_{33} is high because it represents the full information of *all* measured ε_{hkl}. The relevant equations for Al_2O_3 and ZrO_2 are (5) or (6) for plane surface compression $\sigma_{SF} = \sigma_x = \sigma_y$ ($\sigma_z = 0$), the macrostress levels are given by the end point of the variation procedure.

Most of the specimens exhibited measured ε_{hkl} as in the example of Fig. 4 and enabled a ready analysis assuming plane surface compression (σ_{SF} is –50... –100 MPa for the coarsest and –100...–200 MPa for the fine grained alumina microstructures; similar values are observed for most ZrO_2 samples with one exception of –370 MPa in the 0·3 μm microstructure).

However, a measurement of two submicron alumina specimens with extremely low resulting microstresses of 20–30 MPa (i.e. close to the limit given by the measuring accuracy of 10–20 MPa) showed all negative ε_{hkl} the interpretation of which would require the assumption of a small *hydrostatic* compression or of a plane *tension* stress in the surface. Both explanations must be discarded, the first by physical reasons and the second due to the known compressive character of macrostresses in ground ceramics. More probably, such (small) apparently negative ε_{hkl} are associated with occasional slight stresses in the annealed powder standards: sintering of submicron samples requires raw materials with grain sizes of 150 nm and less, and due to this fine grain size the annealing procedure of the powder standards may well happen to cause some slight degree of sintering even in the loose powder. The consequence is an additional error in $\Theta_{hkl}^{standard}$ in eqn (3(a)) which is insignificant when $\Delta\Theta_{hkl}$ is large but may become important if this difference is close to zero. The contribution to the possible error in σ_{33} is about 5 MPa.

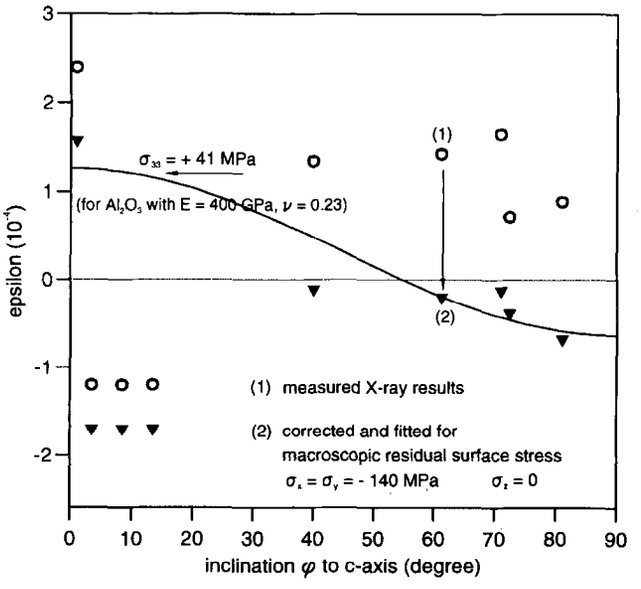

Fig. 4. Illustration of the subsequent steps of the analysis (example: measured strain data ε_{hkl} in a 1·9 μm alumina microstructure). Step (2) also considers elastic anisotropy (eqns (5) and (6)).

The final ε_{33} resulting from the variation procedure gives the average TEA tensile stress component for c-axis orientation with the elastic isotropic approach discussed in the introduction by

$$\sigma_{33} = \frac{E_{\text{eff}}}{(1 + \nu_{\text{eff}})} \varepsilon_{33} \qquad (7)$$

with the given orientation averages for E_{eff} and ν_{eff}. The total amount of all contributions to a possible maximum error is about ±25 MPa in σ_{33}.

3 Results

Figure 5 displays the grain size influence on the TEA residual stress measured for alumina microstructures with grain sizes between 0·3 and 9 μm. Here as in the following figure the tensile component in the c-axis direction resulting from the cosine-like fit of all measured ε_{hkl} is used as a representative parameter that contains all information about the whole orientation dependence of TEA stresses in a microstructure. Note that this double-logarithmic plot must not be used for extrapolations into the range of coarser grain sizes because it neglects the existence of an upper (relaxation-free) stress limit (calculated in Fig. 1).

In Fig. 5, the data point at a grain size of 0·5 μm represents the sol/gel derived broken reference sample. This microstress is in no way distinguished from the results obtained on ground surfaces and gives convincing evidence for the sound basis of the procedure adopted here to separate type I and type II residual stresses in the analysis.

Figure 6 compares TEA residual stresses for ZrO_2 and Al_2O_3 in analogy with Fig 5. The measured TEA stresses are similar in Al_2O_3 and in ZrO_2 for

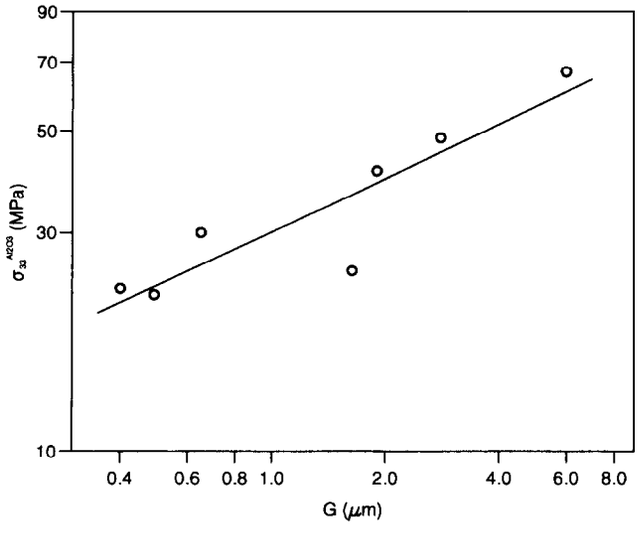

Fig. 5 Double-logarithmic presentation of the grain size influence on TEA residual stress in alumina.

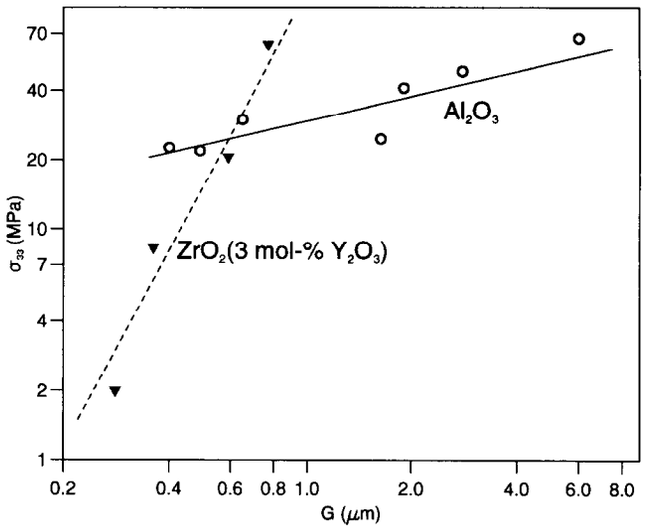

Fig. 6. Comparison of TEA residual stresses in submicron zirconia and alumina.

grain sizes in the range 0·5 – 1 μm, but considering the results of the finer grained microstructures, Fig. 6 suggests different grain size effects. However, the error of ±25 MPa as discussed above indicates a limited reliability of all stress results <30 MPa. Since most of the zirconia data are within or close to this range, no final conclusion about the grain size effect in tetragonal zirconia should be derived here. As a consequence, it is also impossible to advance reliable suggestions about the residual stresses in coarser zirconia ceramics, and the experimental comparison with alumina in analogy with the calculated data in Fig. 1 remains an open issue.

4 Discussion

Due to relaxation, the thermal expansion anisotropy stresses σ_{33} in alumina given in Fig. 5 are lower than the relaxation-free solution in Fig. 1. Figure 5 corresponds well with the result of +56 MPa obtained by optical fluorescence[23] for 2–8 μm grain size alumina in Al_2O_3/ZrO_2 composites, but there is poorer agreement with the published 100–160 MPa reported for single phase alumina of the same grain size.[24] Two comments are possible. On the one hand, the consistency of our results for the whole grain size range 0·3 μm < G < 9 μm in Fig. 5 indicates a fairly high degree of significance of the present results on a qualitative level. On the other hand, the limits of accuracy indicate that also the present results do not exclude a TEA tensional component σ_{33} close to + 100 MPa with grain sizes of about 10 μm, and present and previous results will come close to each other. This idea becomes further substantiated if we remember that just the coarser

alumina specimens in the present investigations contain dopants and impurities which favour relaxation.[22] Hence, slightly higher TEA stresses than the upper limit observed in the present investigations are probable with an improved purity at grain sizes of about 10 μm.

Contrary to the comparison with previously published experimental data, it is difficult to compare the present results for alumina with a *theoretically* predicted grain size effect. As outlined in the introduction, the existing models do not provide a ready functional dependence of residual stresses on the grain size, and approximations that give an inverse grain size effect $1/G^3$ are ruled out by our results. Replotting the data of Fig. 5 as a function of $1/G^3$ gives a linear relationship but with σ_0 = 60–70 MPa which is an unlikely result compared with the calculated relaxation-free stress level of 150 MPa suggested by Fig. 1.

The double-logarithmic plot of all alumina σ_{33} data between 0·3 and 9 μm in Fig. 5 indicates *one* grain size dependent relaxation mechanism of the TEA microstresses σ_{TEA} in fine and in medium grained alumina according to $\sigma_{TEA} \sim G^m$ with m $\approx$ 0·39. This value is close to m $\approx$ 0·37 which may be derived by a logarithmic plot of the data obtained by Ma and Clarke[24] for alumina microstructures with grain sizes ranging from 2 to 16 μm. If we compare with the much smaller grain size effect calculated by Blendell and Coble[17] (6 MPa difference for grain sizes between 50 and 150 MPa) we have to consider that the influence of the grain size must decrease when approaching the relaxation-free conditions at very large grain sizes.

A similar decrease of the grain size influence occurs at extremely fine grain sizes. A closer inspection of Fig. 5 considering the logarithmic character reveals a behaviour which actually is similar to a lower limit of the relaxation. To reduce the grain sizes from about 5–10 μm to approximately 1–2 μm causes a drop of the residual stress component σ_{33} by about 50% (about –35 MPa). In the investigated submicrometer range, however, the absolute changes in σ_{33} become very small. This behaviour compares well with general expectations and is, of course, consistent with the theoretical models as discussed in the introduction.

The TEA residual stresses of the 0·5 μm sol/gel-derived alumina microstructure are consistent with all other data in Fig. 5. Obviously, the TEA microstresses as obtained here are independent of special technological approaches and surface conditions.

The evaluation of the results at very small grain sizes and low microstresses is considerably influenced by the accuracy of the measurements. The extremely thin amorphous grain boundary interface in ZrO_2 (0·5 nm) that is know to promote superplastic deformation (at very *slow* rates) and may cause a stronger grain size effect with extremely small residual microstresses in tetragonal zirconia at grain sizes <0·5 μm. However, at present no sufficiently precise measuring approach is available to draw valid conclusions about microstress components <15 MPa in single phase ceramics. Most of the investigated zirconia microstructures exhibit results close to or lower than the accuracy of the measurement. With the present data it is, therefore, impossible to draw final conclusions about the relaxation behaviour of microstresses in zirconia. Experiments with coarser microstructures would be required to compare the relaxation-free state of zirconia with the calculated result in Fig. 1, but the known phase instability of tetragonal zirconia at larger grain sizes will make such investigations very difficult if not impossible.

5 Conclusions

In sintered alumina, the average tensional component in x-axis direction is about 30–100 MPa with grain sizes of 1–9 μm. With smaller grain sizes 0·3–1 μm, this stress component is reduced further due to known relaxation processes, but the absolute changes are small in the submicrometer range: the investigations suggest a level of about 20–30 MPa. However, at present no sufficiently precise measuring approach is available to draw valid conclusions about microstress components <30 MPa in single phase ceramics.

A double-logarithmic plot gives a consistent grain size dependence close to $\sigma_{TEA} \sim G^{1/3}$ for the whole range of investigated grain sizes 0·3 μm < G < 9 μm. It is, therefore, suggested that there is no change in the fundamental relaxation processes within the investigated range of grain sizes. At present, there is no basis for a ready comparison of the observed grain size influence with existing theoretical models.

With grain sizes between about 0·5 and 1 μm, the residual stresses measured in tetragonal zirconia polycrystals are similar as observed in alumina (20–60 MPa). However, the stresses in microstructures with grain sizes 0·2–0·4 μm are actually smaller than the limit of accuracy (probably <10 MPa). Therefore, no final conclusions can be derived here for the grain size effects in this material.

The comparison of residual TEA stresses in compact, ground alumina samples produced by a powder technological approach and in equally dense grit samples of sol/gel origin reveals that the present results are independent of special processing routes and surfaces states.

Acknowledgments

The investigations at the Dresden Fraunhofer Institute have been supported in part by the Deutsche Forschungsgemeinschaft under contract Kr 1398/1-1. We gratefully acknowledge the cooperation with Dr W. Kreher at the Max-Planck-Group of the Mechanics of Heterogeneous Solids in Dresden (Germany) and with Dr E. Pippel and Dr J. Woltersdorf at the Max-Planck-Institute of Microstructural Physics in Halle (Germany).

References

1. Kloos, K. H., Eigenspannungen, Definition und Entstehungsursachen (Residual stresses, definition and origin). *Z. Werkstofftechnik*, **10**(9) (1979) 293–302.
2. Hockey, B. J., Observations by transmission electron microscopy on the subsurface damage produced in aluminium oxide by mechanical polishing and grinding. *Proc. Brit. Ceram. Soc.*, **20** (1972) 95–115.
3. Hockey, B. J., Plastic deformation of aluminum oxide by indentation and abrasion. *J. Am. Ceram. Soc.*, **54**(5) (1971) 223–31.
4. Xu, H. & Jahanmir, S., Effect of microstructure on subsurface damage and material removal in grinding of alumina ceramics. Paper SXI-35-94 in *96th Annual Meeting Abstracts*, The America Ceramic Society, Westerville, Ohio, 1994.
5. Samuel, R., Chandrasekar, S., Farris, T. N. & Licht, R. H., Effect of residual stresses on the fracture of ground ceramics. *J. Am. Ceram. Soc.*, **72**(10) (1989) 1960–6.
6. Scholtes, B., Recent investigations on the origin and distributions of residual stresses in ceramics and metal-ceramic compounds. In *Constraints Résiduelles et Nouvelles Téchnologies*, CETIM, Paris, 1990, pp. 61–71.
7. Evans, A.G., Microfracture from thermal expansion anisotropy—I. Single phase systems. *Acta Metall.*, **26**(12) (1978) 1845–53.
8. Wu, C. Cm., Freiman, S. W., Rice, R. W. & Mecholsky, J. J., Microstructural aspects of crack propagation in ceramics. *J. Mater. Sci.*, **13**(12) (1978) 2659–70.
9. Green, D. J., Microcracking mechanisms in ceramics. In *Fracture Mechanics of Ceramics*, Vol. 5, ed. R. C. Bradt, A. G. Evans, D. P. H. Hasselman & F. F. Lange. Plenum Press, New York, 1983, pp. 457–78.
10. Heuer, A. H. & Rühle, M., On the nucleation of the martensitic transformation in zirconia (ZrO_2). *Acta Metall.*, **33**(12) (1985) 2101–12.
11. Schmauder, S. & Schubert, H., Significance of internal stresses for the martensitic transformation in yttria-stabilized tetragonal zirconia polycrystals during degradation. *J. Am. Ceram. Soc.*, **69**(7) (1986) 534–40.
12. Becher, P. F. & Ferber, M. K., Grain-size dependence of the slow-crack growth behaviour in noncubic ceramics. *Acta Metall.*, **33**(7) (1985) 1217–21.
13. Fu, Y. & Evans, A. G., Microcrack zone formation in single-phase polycrystals. *Acta Metall.*, **30**(8) (1982) 1619–25.
14. Pompe, W. & Kreher, W., Theoretical approach to energy-dissipative mechanisms in zirconia and other ceramics. In *Advances in Ceramics, Vol. 12 (Zirconia 11)*, ed. N. Claussen, M. Rühle & A. H. Heuer. The American Ceramic Society, Columbus, Ohio, 1983, pp. 283–92.
15. Kreher, W., Residual stresses and stored elastic energy of composites and polycrystals. *J. Mech. Phys. Solids*, **38**(1) (1990) 115–28.
16. Kreher, W. & Molinari, A., Residual stresses in polycrystals as influenced by grain shape and texture. *J. Mech. Phys. Solids*, **41**(12) (1993) 1955–77.
17. Blendell, J. E. & Coble, R. L., Measurement of stress due to thermal expansion anisotropy in Al_2O_3. *J. Am. Ceram. Soc.*, **65**(3) (1982) 174–8.
18. Evans, A. G. & Clarke, D. R., Residual stresses and microcracking induced by thermal contraction inhomogeneity. In *Thermal Stresses in Materials and Structures*, ed. D. P. H. Hasselman & R. A. Heller. Plenum Press, New York, 1980, pp. 629–48.
19. Green, D. J., Lange, F. F. & James, M. R., Factors influencing residual surface stresses due to a stress-induced phase transformation. *J. Am. Ceram. Soc.*, **66**(9) (1983) 623–9.
20. Eigenmann, B., Scholtes, B. & Macherauch, E., Determination of residual stresses in ceramics and ceramic–metal composites by X-ray diffraction methods. *Mater. Sci. Eng. A*, **118**(5) (1989) 1–17.
21. Grigoryev, O. N. & Krivoshei, G. S., Determination of thermal stresses in heterogeneous materials (in Russian). *Zavodskaya Laboratoria*, 7/8 (1992) 30–2.
22. Krell, A. & Grigoryev, O. N., Residual stresses and microporosity in oxide ceramics. *Sprechsaal*, **123**(10) (1990) 1012–15.
23. Ma, Q., Pompe, W., French, J. D. & Clarke, D. R., Residual stresses in Al_2O_3–ZrO_2 composites: A test of stochastic stress models. *Acta Metall. et Mater.*, **42**(5) (1994) 1673–81.
24. Ma, Q. & Clarke, D. R., Piezospectroscopic determination of residual stresses in polycrystalline alumina. *J. Am. Ceram. Soc.*, **77**(2) (1994) 298–302.
25. Wachtman Jr., J. B., Tefft, W. E., Lam Jr., D. G. & Stinchfield, R. P., Elastic constants of synthetic single crystal corundum at room temperature. *J. Res. Nat. Bureau of Standards - A.*, **64**(3) (1960) 213–28.
26. Grigoryev, O. N., Krell, A., & Trefilov, V. I., Determination of thermal residual stresses in single-phase ceramic materials (in Russian). *Zavodskaya Laboratoria*, 7 (1990) 36–9.
27. Kreher, W., Pompe, W., *Internal Stresses in Heterogeneous Solids*. Akademie-Verlag, Berlin, 1989.
28. Grigoryev, O.N., Thesis submitted for the degree of a Doctor of Sciences (habilitation). Ukrainian Academy of Sciences, Kiev, 1992.
29. Ingel, R. P., Lewis III, D., Elastic anisotropy in zirconia single crystals. *J. Am. Ceram. Soc.*, **71**(4) (1988) 265–71.

Journal of the European Ceramic Society 16 (1996) 813–818

S0955-2219(96)00005-2
0955-2219/96/$15.00 +.00

Influence of Residual Stresses on the Mechanical Properties of a Layered Ceramic Composite

O. Sbaizero & E. Lucchini

Dipartimento di Ingegneria dei Materiali e Chimica Applicata, Università di Trieste, Via Valerio — 34127 Trieste, Italy

(Received 7 June 1995; revised version received 6 December 1995; accepted 12 December 1995)

Abstract

A layered Al_2O_3–ZrO_2 ceramic composite has been fabricated using a colloidal processing method. The technique uses sequential centrifuging of slurries containing suspended ceramic powders to form a three-layered structure. The outer layers have a high alumina content while the central layer contains mainly stabilized zirconia. These laminae are subjected to residual stresses due to their different thermal expansion coefficients. These stresses depend on the configuration of the system as well as on the amount of the zirconia in the two layers.

If the residual stresses exceed the strength of the inner layer, periodic parallel cracks are produced. Such cracks of course adversely influence the structural performance of the composite and should be avoided. A model for this problem is presented.

Vickers indentations were also placed into the tensile layer with the intent to explore the crack propagation in such system. Cracks were split after they reached the compressive layer. The effects of the layer thickness on the depth of the cracks beneath the interface were systematically explored.

1 Introduction

The majority of attention in the production of reliable ceramics for structural applications has been paid to either the development of stronger materials through processing and microstructural refinements, in order to minimize the flaw size or in the activation of an *R*-curve behaviour introducing toughening mechanisms using platelets, whiskers or fibres to reinforce ceramic matrices.[1-7]

Concerns about both methods include the correct choice of the components, their availability and price as well as the processing cost. It is in fact difficult to imagine the market competitiveness of ceramics with a very high price. Besides, there are applications in which structural ceramics must exhibit above all high strength and hardness combined with some degree of resistance to damage introduced in service.

A well recognised and inexpensive method of achieving the aforementioned results is the introduction of surface compressive stress, an approach normally used in glasses.[8,9] In the ceramics this goal can be obtained through the production of laminate ceramic composites[10-14] using the build-up of residual stresses due to the thermal expansion mismatch between the different layers to enhance the mechanical properties.

The variable 'layer composition' as well as the system's geometry allows the designer to control the magnitude of the residual stresses in such a way that compressive stresses, in the outer layers near the surface, increase strength, hardness, flaw tolerance and probably also fatigue strength and stress corrosion cracking.

During this investigation a three-layered structure has been fabricated using colloidal techniques[1-5] combined with sequential centrifuging of the slurries to consolidate the layers.

The outer layers are made of alumina containing different amounts of zirconia while the inner layer contains mainly zirconia with a small amount of alumina. This system was selected because both oxides are mutually insoluble, there are no intermediate phases and pressureless sintering produces materials with near theoretical density. At high temperature, all stresses relax due to thermally activated processes. During cooling, the alumina rich layers contract less than the zirconia rich inner layer, since the outer layers' thermal dilatation is lower. As a consequence there will be a distribution of tensile and compressive residual stresses. A symmetrical layered material, with zirconia as the inner layer, is therefore expected to exhibit the desired compressive stress near the surface. If the system geometry is maintained constant, the residual

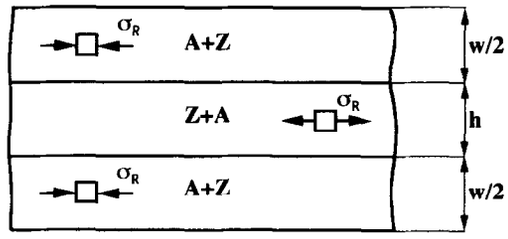

Fig. 1. Schematic of an ideal layered material.

stress depends on the composition, in any case the inner layer is under tensile residual stress while the outer layers are subjected to compressive stresses. Figure 1 shows a schematic of an ideal specimen. The magnitude of these stresses can also be tailored by varying the Al_2O_3/ZrO_2 ratio in the layers.

The aim of the present study is to characterize the mechanical properties of a trilayer laminate composite as well as to compare crack path predictions with experimental observations.

2 Experimental Procedure

The layers were produced starting from aqueous slurries containing 25 vol% powders: α-alumina (Sumitomo Chemical Co. AKP-20) and zirconia+3 mol% yttria (Dynamit Nobel); these powders were chosen because their particles have comparable sizes. The slurries were prepared by dispersing the powders with a blender (6000 rpm) in deionized water. The pH values of the dense slurries were adjusted to ≈ 4 using HNO_3 (1 M) to provide large electrostatic repulsive forces between the particles, the slurry was also ultrasonically homogenized for 3 min at 300 W in order to break down the aggregates. After ultrasonication, slurries were equilibrated for 4 h in a planetary mixer and then NH_4NO_3 was added to induce strong short range repulsive forces between the particles. The slurry in this situation is called 'coagulated'[15] and the short range repulsive potential is able to induce a weakly attractive particle network that allows particles to pack to a high relative density by centrifugation preventing also mass segregation.

Quantities of slurries enough to yield the desired thickness of layer were placed in a Teflon cylindrical container (diameter = 50 mm) and were centrifuged for 60 min at 2000*g*. After that the supernatant liquid was poured off, another volume of suspension, containing a solid phase with different composition, was placed in the container in order to deposit the next layer. This procedure was repeated until multilaminar composites with layer thickness ranging from 0·1 to 0·3 mm were obtained. Consolidated bodies were air dried for 24 h at 65°C and then cold isostatically pressed at 100 MPa. The disk-shaped samples were heated from room temperature to 200°C over a 3 h period, after which the temperature was raised to 1550°C at 10°C/min and ultimately held at this temperature for 3 h after which it was lowered to room temperature over the next 4 h.

The bending strength at room temperature was measured with a universal testing machine, using a 4-point bending with outer and inner span of 40 and 20 mm respectively and a crosshead speed of 0·01 mm/min on $4 \times 3 \times 45$ mm bars cut from the disk-shaped samples produced by centrifuging. These tests were also carried out on samples with different outer/inner layer thickness with the total thickness remaining constant in order to assess the influence of the stress magnitude on the total strength.

The assesment of the residual stresses requires knowledge of Young's modulus, Poisson's ratio and the thermal expansion coefficient for the single layers; the former two data were derived from the longitudinal and shear ultrasonic wave velocities, the latter with a dilatometer up to 1450°C.

Vickers indentations were used to assess the hardness and also when placed into the central layer to explore the crack propagation in such systems. Residual stresses were also emphasized placing Vickers indentations in the different layers. Polished sections of the samples were examined before and after thermal etching. Secondary electron and back scattered images were obtained in a scanning electron microscope.

3 Results

As far as the microstructure is concerned, in bodies produced with coagulated slurries, Al_2O_3 and ZrO_2 were observed to be uniformly mixed, see Fig. 2. Another observation is that thermal expansion mismatch sometimes produced periodic parallel cracks in the inner layer, see Fig. 3. Such cracks of course adversely influence the structural performance of the composite and should be avoided.

As far as the indentations are concerned, the compressive stress in the outer layers reduces the crack propagation toward the interface with the tensile layer, see Fig. 4, whereas if enough load (> 60 kg) was applied in the inner layer, a crack propagated through it, but after reaching the interface with the layer in compression it bifurcates, see Fig. 5.

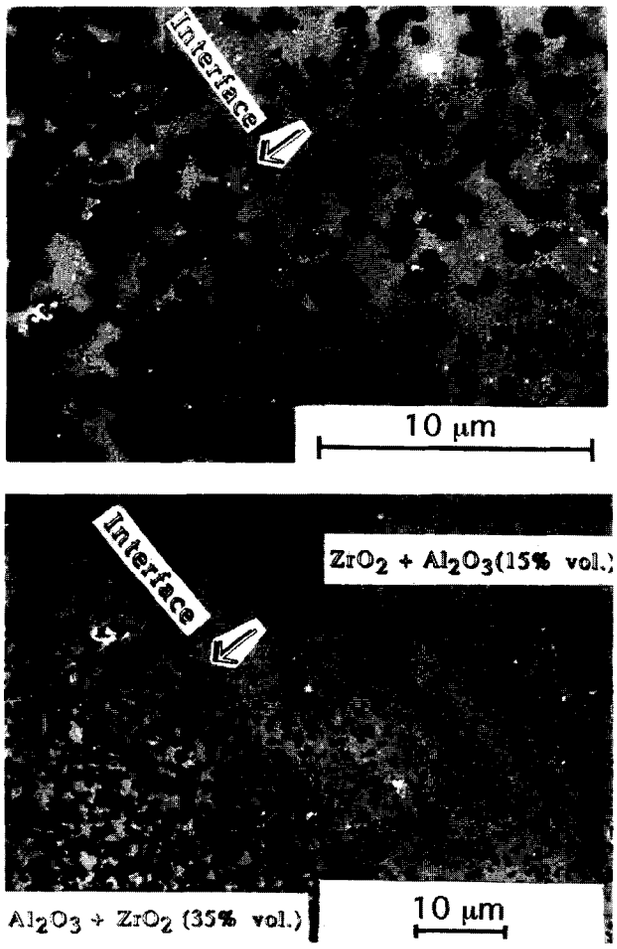

Fig. 2. Backscattered images of an interface between two layers of different composition.

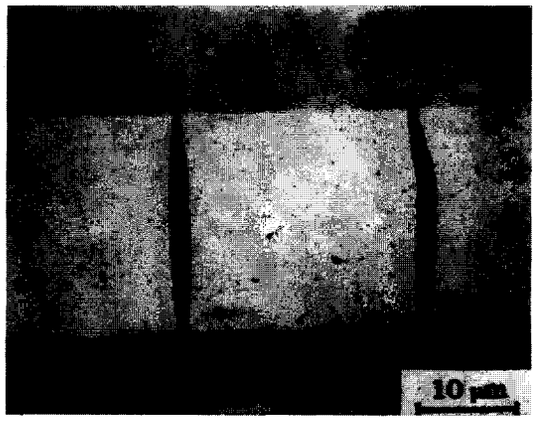

Fig. 3. Periodic cracks developed in an inner layer due to residual stress.

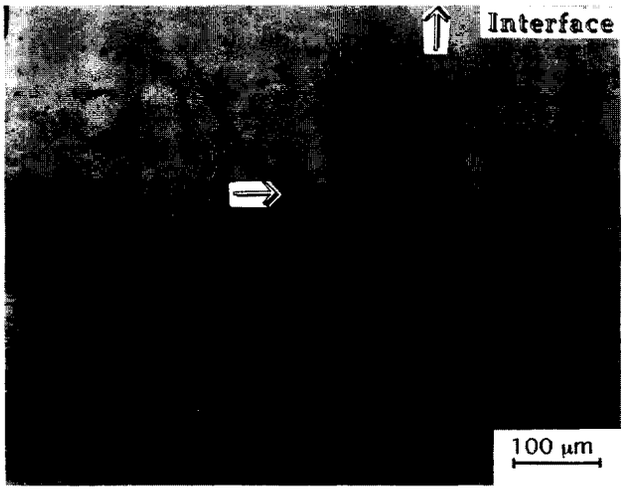

Fig. 4. Vickers indentation in an inner layer.

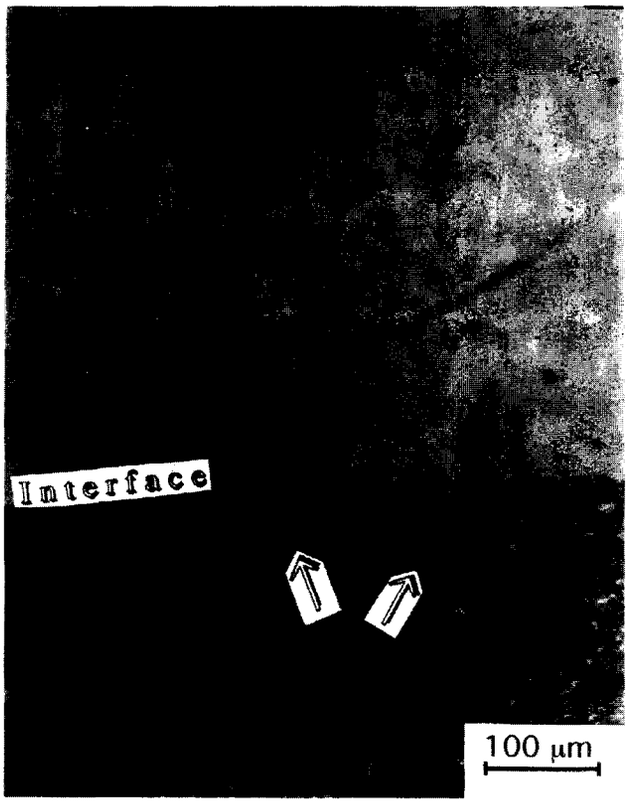

Fig. 5. Crack bifurcation during the propagation in outer layer.

4 Discussion

4.1 Matrix cracking

The residual thermal stress in a layer bonded between two identical substrates (Fig. 1) is biaxial, with the magnitude:[16]

$$\sigma_R = \frac{\epsilon_R E_i}{1 - \nu_i}\left[1 + \frac{h\,E_i/(1-\nu_i)}{w\,E_o/(1-\nu_o)}\right]^{-1} \quad (1)$$

where ν is Poisson's ratio, E is Young's modulus, h the thickness of the inner layer and $w/2$ the thickness of each outer layer, the subscripts o and i distinguish the outer and inner layer respectively.

ϵ_R is the thermal mismatch strain and is given by:

$$\epsilon_R = \int_T^{T_0} (\alpha_i - \alpha_o)\,dT \quad (2)$$

where T_0 and T are the processing and the current temperature and α is the thermal expansion coefficient. The two outer layer thickness being the

same, the stressed sandwich remains flat, so that the residual stresses are difficult to detect. When these residual stresses, in the layer under tension, exceed the strength of the material, transverse cracks start to develop.

Previous investigations[17–20] have recognized that a critical non-dimensional group of parameters $\mathcal{R}$ exists, below which cracking does not occur. $\mathcal{R}$ is defined as:

$$\mathcal{R} = R\,(E_m\,\Delta\alpha\,\Delta T / K_m)^2 \qquad (3)$$

Where R is the reinforcement size, E_m the Young's modulus matrix, $\Delta\alpha$ the thermal expansion mismatch, ΔT the processing temperature range and K_m the matrix toughness. The significance of this coefficient is that cracking, in the matrix under tension, is found to be suppressed when $\mathcal{R}$ is less than a critical value, $\mathcal{R}_c$. The magnitude of the cracking coefficient, $\mathcal{R}_c$, depends on the volume fraction of the reinforcement as well as the elastic modulus and Poisson's ratio between reinforcement and matrix.

The model has been developed for cracking around elastic inclusions[21] but it has been used also for ceramic matrix composites containing elastic reinforcements[22] with periodic parallel cracks normal to the fibre axis; the present study might extend the aforementioned results for ceramic composites, to include also sandwich structures. In this case the 'matrix' will be the inner layer whereas the 'reinforcements' will be the outer layers, therefore $\mathcal{R}$ is given by:

$$\mathcal{R} = (w/2)\,(E_i\,\Delta\alpha\,\Delta T / K_i)^2 \qquad (4)$$

where $(w/2)$ is the outer layer thickness, E_i the inner layer Young's modulus, K_i the outer layer toughness, $\Delta\alpha$ and ΔT being, as before, the processing temperature range and the difference in thermal expansion coefficient.

For a well-bonded interface $\mathcal{R}_c$ has the form:[21]

$$\mathcal{R}_c = \sqrt{6}\,B^2(1-\nu)^3(1+\nu)^{1/2} / f(1-f) \qquad (5)$$

where B is a coefficient between 0·8 and 1, f is the volume fraction of the reinforcement. The trend for $\mathcal{R}_c$ in the case of a well bonded interface and with B=0·8 is plotted in Fig. 6. The two dashed lines highlight the sample geometry used in this study. Transverse cracks are found to be suppressed provided that $\mathcal{R}$ <3–4, whereas profuse cracking should be expected when $\mathcal{R}$>5.

In order to compare the results of our observations with the calculations we focused our attention on several compositions. For every one we assessed the thermal expansion coefficient as well as Young's modulus and toughness. Results are reported in Table 1. Keeping constant the inner layer composition (either ZrO_2 + 15% Al_2O_3 or ZrO_2 + 35% Al_2O_3, the first set of observations establishes the lack of matrix cracking in those systems containing at least 50% of zirconia, the residual stress is in fact depleted as the amount of zirconia in outer layers is increased. Matrix cracks could not be detected even at the ends of the beams where edge effects are present; and in fact $\mathcal{R} < \mathcal{R}_c$ is therefore consistent with the absence of matrix cracks.

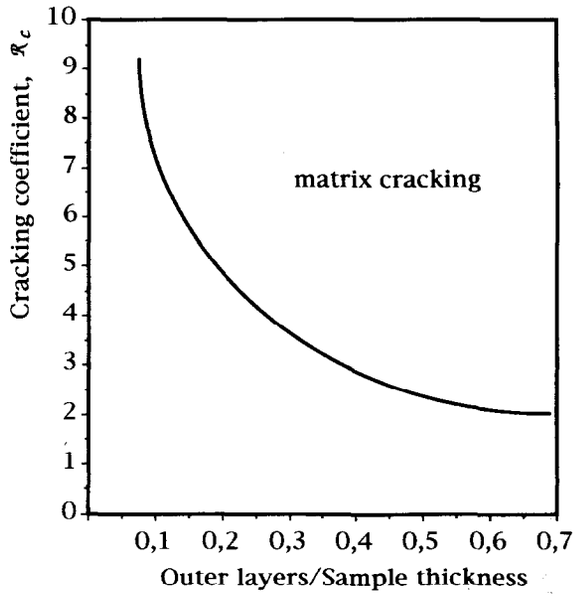

Fig. 6. Trend in the cracking coefficient, $\mathcal{R}_c$ with inner layer/sample thickness ratio for materials with well-bonded interfaces.

Table 1. Experimental results for the formation of the periodic parallel cracks in the tensile layer

Outer layer composition	*α ($10^{-6}K^{-1}$)*	*$\mathcal{R}$*	*Observation*
Alumina	8·4	31	Cracks
A+20%Z	9·58	8·6	Cracks
A+35%Z	9·8	6	Cracks
A+50%Z	10·25	2	No cracks
A+70%Z	10·5	0·8	No cracks

Inner layer composition: ZrO_2+15% Al_2O_3.
(E = 222 MPa, α = 10·9 × 10^{-6} K^{-1}, K_{Ic} = 4·9 MPa $\sqrt{m}$, ΔT = 1550°C).
Outer layer thickness = 2000 μm. Outer layer/sample thickness = 0·3.

Outer layer composition	*α (10^{-6} K^{-1})*	*$\mathcal{R}$*	*Observation*
Alumina	8·4	32	Cracks
A+20%Z	9·58	5·4	Cracks
A+30%Z	9·75	3·4	Cracks
A+40%Z	10	1·3	No cracks
A+50%Z	10·25	0·18	No cracks
A+70%Z	10·5	0·08	No cracks

Inner layer composition: ZrO_2+35% Al_2O_3.
(E = 260 MPa, α = 10·4 × 10^{-6} K^{-1}, K_{Ic} = 4·5 MPa $\sqrt{m}$, ΔT = 1550°C).
Outer layer thickness = 2000 μm. Outer layer/sample thickness = 0·5.

Further confirmation of the analysis is provided by results of the outer layer without zirconia (pure alumina), in this case $\mathcal{R} = 31$ and profuse cracking is present, in fact $\mathcal{R} >> \mathcal{R}_c$.

4.2 Crack bifurcation

Vickers indentations were placed into the tensile layer with the intent to explore the crack propagation in our system. Cracks were split after they reach the compressive layer. A simplified model has been developed, see Fig. 7. Assuming that the layers have different thermal expansion coefficients but identical elastic constants as well as thickness, after the propagation the material between the bifurcated crack and the interface is stress free and therefore the residual stress, is given by:

$$\sigma_R^* [1 + h / y] = 2 \sigma_R \tag{6}$$

Where σ_R is the residual stress obtained using eqn (1) while $y/2$ is the crack length propagation in the outer layer (see Fig. 7). Upon loading, the energy release rate is the same at every point of the crack front and if the crack perpendicular to the interface propagates straight into the outer layer, the magnitude is given by:[23]

$$\frac{E \mathcal{G}}{\sigma_R^2 h} = (1 + y / h) \frac{\pi}{2} \left[\frac{4}{\pi} \sin^{-1} \left(\frac{1}{1 + y / h} \right) - 1 \right]^2 \tag{7}$$

Whereas if the crack after penetrating into the outer layer bifurcates, the energy release rate magnitude is:[23]

$$\frac{E \mathcal{G}_\perp}{\sigma_R^2 h} = \frac{1}{2} [1 - 3y / h] \tag{8}$$

Therefore the strain energy release rate varies linearly with (y/h) in the case of bifurcated cracks whereas there is a different behaviour for the crack that propagates straight into the layer; see Fig. 8. From this figure and from eqns (7) and (8) it is possible to find out that $\mathcal{G} \geq \mathcal{G}_\perp$ at $y/h \approx 0{\cdot}09$.

Practically the cracks propagate into the outer layers for about 1/20 of ZrO_2 rich layer thickness before bifurcating. To account for this bifurcation phenomenon, the concept of the T-stress[24] can also be used. For a mode I crack the T-stress is defined as:

$$\sigma_{ij}(r, \theta) = \frac{K}{\sqrt{2\pi r}} f_{ij}(\theta) + T\delta_{ij} \tag{9}$$

where T is the stress acting parallel to the crack. A crack in an isotropic, homogeneous, brittle solid, selects a trajectory with mode I loading and according with Cotterell and Rice[25] a mode I crack is stable if $T<0$, but unstable if $T>0$. The T-stress after a crack penetrates into another layer was computed by Suo and Evans, using finite elements.[26] From their calculation it appears that conditions exist near the interface with $T>0$ for value of y/h close to that of our model. The observed bifurcation may be plausibly explained by this effect. To confirm our model we measured the crack penetration in several samples (five for each system) with different inner/outer layer thickness ratio and different compositions. The experimental results are reported in Fig. 9. It is evident that a reasonable agreement exists between the model and experimental results.

4.3. Mechanical properties

Strength was assessed on layered samples with varying outer/inner thickness ratio, with the total

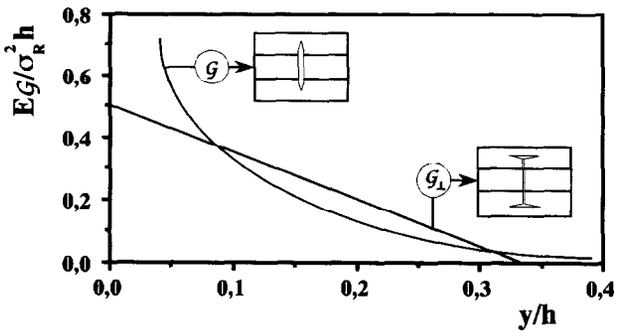

Fig. 8. Trend in the strain energy release rate versus (y/h) for the crack that propagates straight into the layer and for the crack that bifurcates.

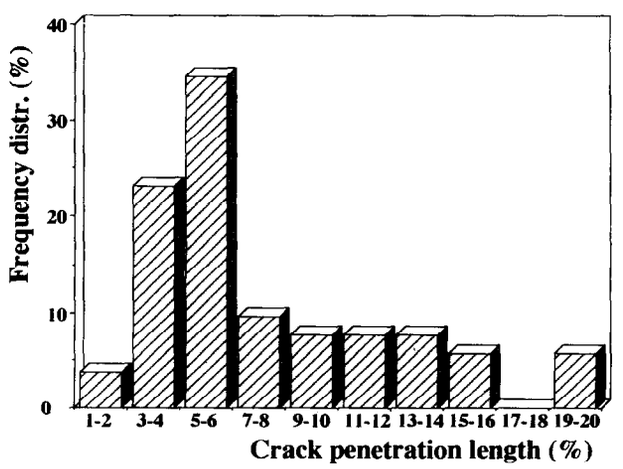

Fig. 9. Experimental results for the crack penetration length before bifurcation.

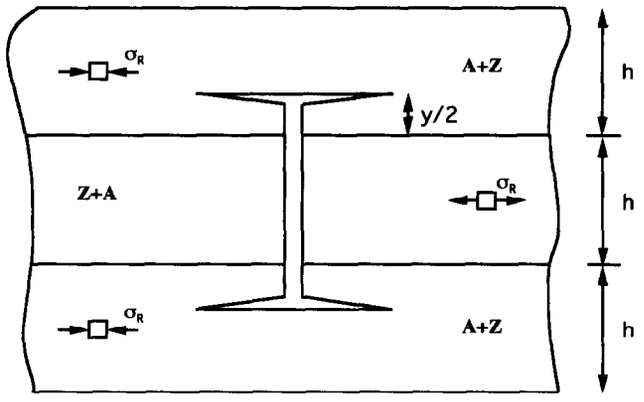

Fig. 7. Schematic example for the crack propagation from the inner layer and subsequent bifurcation.

sample's thickness remaining constant. Strength data are reported in Fig. 10. Over the range of thickness tested, the strength was found to increase with increasing thickness of the inner layer, in fact, for a given total thickness, the magnitude of the predicted surface compressive stress increases with increasing inner layer thickness. The presence of such surface compressive stress makes it more difficult to initiate a failure from flaws in the near surface regions and therefore the material will be less sensitive to degradation caused by surface damage due to contact or abrasion. Fractured samples were examined using scanning electron microscopy, in every case examined the failure was observed to have originated from pre-existing processing flaws. It is evident therefore that much higher strengths should be attainable by improving processing.

5 Conclusions

This work has shown that it is possible to produce, by centrifuging, layered ceramic composites with surface compressive stresses using materials with different thermal expansion coefficients. Although substantial increases in strength have been found, it is clear that better results will occur when processing flaws are reduced. The microstructure obtained when coagulated slurries were sequentially centrifuged was homogeneous. The residual thermal stresses sometimes generate periodic parallel cracks in the tensile layer; a critical non-dimensional parameter $\mathcal{R}$ was used and experimental results confirm that cracks will be suppressed when $\mathcal{R}$ is less than a critical value $\mathcal{R}_c$.

When a crack propagates from the inner towards the outer layer it deviates just after it penetrates the layer under compression. A model was presented taking into account the strain energy release rate of the crack that penetrates straight into the layer compared with that of the crack that bifurcates. The model predicts that bifurcation should occur after the crack propagates for about 1/20 of the outer layer thickness. Experimental results are in good agreement with the model.

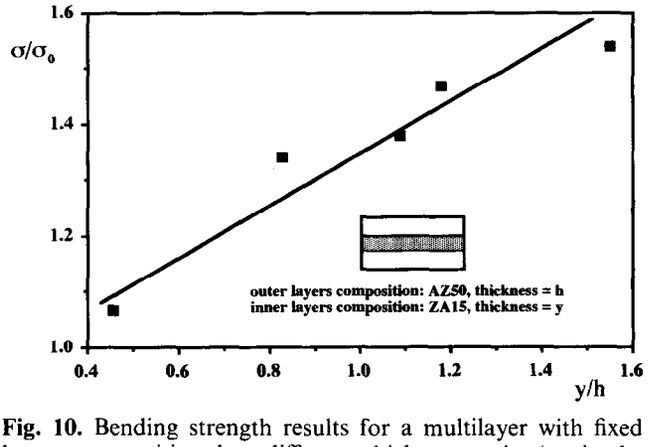

Fig. 10. Bending strength results for a multilayer with fixed layers composition but different thickness ratio (σ_0 is the strength of the outer layer).

References

1. Evans, A. G., *J. Amer. Ceram. Soc.*, **73**(2) (1990) 187–206.
2. Becher, P. F. & Wei, G. C., *J. Amer. Ceram. Soc.*, **67**(12) (1984) C267–9).
3. French, J. D., Chan, H. M., Harmer, M. P. & Miller, G. A., *J. Amer. Ceram. Soc.*, **75**(2) (1992) 418–23.
4. Padture, N. P., *J. Amer. Ceram. Soc.*, **75**(7) (1992) 1870–5.
5. Cook, R. F. & Clarke, D. R., *Acta Metall.*, **36**(3) (1988) 555–62.
6. Masaki, T. & Sinjo, K., *Ceram. Int.*, **13** (1987) 109–12.
7. McMurtry, C. H., Boecker, W. D. G., Seshadri, S. G., Zanghi, J. S. & Garnier, J. E., *Am. Ceram. Soc. Bull.*, **66**(2) (1987) 325–9.
8. Kirschner, H. P., *Strengthening of Ceramics*, Marcel Dekker, New York, 1979.
9. Lange, F. F., *J. Amer. Ceram. Soc.*, **63**(1–2) (1980) 38–40.
10. Virkar, A. V., Huang, J. L. & Cutler, R. A., *J. Amer. Ceram. Soc.*, **70**(3) (1987) 164–70.
11. Chartier, T. & Besson, J. L., *Science of Ceramics*, Vol. 14, ed. D. Taylor, The Institute of Ceramics, UK, 1988, pp. 639–44.
12. Chartier, T., Besson, J. L. & Boch, P., *Advances in Ceramics, Science and Technology of Zirconia III*, Vol. 24, eds S. Somiya, N. Yamamoto, H. Yanagida, Amer. Ceram. Soc., Westerville, Ohio, 1988, pp. 1131–8.
13. Sathyamoorthy, R., Virkar, A. & Cutler, R., *J. Amer. Ceram. Soc.*, **75**(5) (1992) 1136–41.
14. Russo, C. J., Harmer, M. P., Chan, H. M. & Miller, G. A., *J. Amer. Ceram. Soc.*, **75**(12) (1992) 3396–400.
15. Velamakanni, B. V., Chang, J. C., Lange, F. F. & Pearson, D. S., *Langmuir*, **6** (1990) 1323–5.
16. Ho, S. & Suo, Z., *J. Appl. Mech.*, **60** (1993) 890–4.
17. Davidge, R. W. & Green, T. J. *J. Mater. Sci.*, **3** (1968) 629.
18. Ito, Y. M., Rosenblatt, M., Cheng, L. Y., Lange, F. F. & Evans, A. G., *Int. J. Fract.*, **17** (1981) 483.
19. Evans, A. G., *J. Mater. Sci.*, **9** (1974) 1145.
20. Lange, F. F., *Fracture Mechanics of Ceramics*, Vol. 2, Plenum Press, New York, 1976. p. 599.
21. Budiansky, B., Hutchinson, J. W. & Evans, A. G., *J. Mech. Phys. Solids*, **34** (1986) 167.
22. Lu, T. C., Yang, J., Suo, Z., Evans, A. G., Hecht, R. & Mehrabian, R., *Acta Metall. Mater.*, **39**(8) (1991) 1883–90.
23. Tada, H., Paris, P. C. & Irwin, G. R., *The Stress Analysis of Cracks Handbook*, Del Research, St. Louis, MO, 1985.
24. Zak, A. R. & Williams, M. L., *Jnl Appl. Mech.*, **30** (1963) 142–3.
25. Cotterell, B. & Rice, J. R., *Int. J. Fracture*, **16** (1980) 155–69.
26. Ye, T., Suo, Z. & Evans, A. G., *Int. J. Solids and Structures*, in press.

Journal of the European Ceramic Society 16 (1996) 819–824

S0955-2219(96)00002-7
0955-2219/96/$15.00 +.00

Cathodic Electrosynthesis of Ceramic Deposits

I. Zhitomirsky & L. Gal-Or

Israel Institute of Metals, Technion-Israel Institute of Technology, Haifa, 32000, Israel

(Received 10 October 1995; revised version received 28 November 1995; accepted 5 December 1995)

Abstract

Cathodic electrosynthesis of TiO_2, ZrO_2 and $ZrTiO_4$ deposits on platinum substrates was performed via hydrolysis of $TiCl_4$ and $ZrOCl_2$ salts dissolved in a mixed methanol–water solvent in presence of hydrogen peroxide by an electrogenerated base. The deposits were characterized by XRD, TG/DTA, SEM and EDS. Deposits as obtained were amorphous. The crystallization behaviour of the deposits has been studied. Crystallite sizes were derived at different temperatures from X-ray broadening data. A possible mechanism of electrosynthesis and the role of hydrogen peroxide are discussed.

1 Introduction

A cathodic electrodeposition process has recently enabled the formation of films of different ceramic materials. These materials encompass individual oxides (Al_2O_3, ZrO_2, CeO_2, PbO *et al.*[1–7]) as well as complex compounds, including ferroelectric materials ($BaTiO_3$ and PZT[8,9]), high temperature superconductors ($YBa_2Cu_3O_{7-x}$[10,11]), and biomaterials.[12,13] Cathodic electrodeposition is achieved via hydrolysis of metal ions by an electrogenerated base to form metal oxide/hydroxide films on the cathodic substrate. Different chemical reactions available for the generation of base were discussed in literature.[1,3] It should be noted that reduction of water and nitrate are important cathodic reactions used for the electrodeposition process. However, the electrodeposition of titania in this way presents difficulties. The titanium nitrate salt is an unstable compound and is not available commercially. Difficulties are also associated with the use of other inorganic salts of Ti^{4+} in aqueous solutions since they are easily hydrolyzed in water to form a titanium hydroxide precipitate. Matsumoto and coworkers used $TiCl_3$ salt for electrodeposition.[8,9] They suggested that Ti^{3+} ions do not exist in the solution since they transform to Ti^{4+} or TiO^{2+}.[8,9] In their experiments on electrodeposition of important ferroelectric materials such as $BaTiO_3$ and PZT difficulties were encountered with the control of deposit stoichiometry due to different deposition rates of individual components. No deposition was achieved by the authors on platinum substrates. It should be noted that electrodeposition holds important perspectives for the development of various ferroelectric thin film devices. Since titanates constitute one of the important groups of ferroelectric materials currently used in industry, it is important to develop an electrodeposition process for formation of titania and stoichiometric complex titanates on platinum substrates.

In previous works,[14,15] a novel approach has been advanced for the electrodeposition of oxide films. The problem of titania electrodeposition was solved by use of a peroxocomplex[16] of titanium instead of titanium ions. The peroxocomplex of titanium is stable under certain conditions in aqueous solutions,[16] therefore water can be used as a solvent and a source of OH^- groups which are necessary for the deposition process. Deposition was performed from mixed *N,N*-Dimethylformamide(DMF)–water solutions.[14] It was pointed out that non-aqueous solvents are preferable for morphology optimization, however the deposition process needs certain amounts of water for base generation and for prevention of formation of non-stoichiometric titania. Deposition of titania was achieved via hydrolysis of the peroxocomplex by electrogenerated base and thermal decomposition of the obtained deposit (hydrated peroxocompound). This approach has been further expanded to formation of complex compounds. $ZrTiO_4$ has been deposited on graphite from a mixed water–methanol solvent.[15] It was established that the use of a peroxoprecursor provides equal deposition rates of the individual components and allows to obtain a deposit of desired stoichiometry. However, the exact mechanism of $ZrTiO_4$ electrodeposition is not fully understood. The purpose of this work is to study the deposition of titania, zirconia and $ZrTiO_4$ on platinum substrates and to get a better understanding of the mechanism of deposition via peroxoprecursors.

2 Experimental Procedures

As starting materials commercially guaranteed salts of $TiCl_4$, $ZrOCl_2 \cdot 8H_2O$ and hydrogen peroxide H_2O_2 (30 wt% in water) were used. Three different solutions in a mixed methanol–water (3:1 volume ratio) solvent were prepared. Stock solution 1 contained 0·005 M $TiCl_4$ and hydrogen peroxide additive in a ratio of $TiCl_4$:H_2O_2 = 1:1·2. Stock solution 2 contained 0·005 M $ZrOCl_2$ and hydrogen peroxide, $ZrOCl_2$:H_2O_2 = 1:1·2. For preparation of stock solution 3 reagents were mixed in a ratio $ZrOCl_2$:$TiCl_4$:H_2O_2 = 1:1:2·4, total concentration of $ZrOCl_2$ and $TiCl_4$ was 0·005 M. Rectangular Pt specimens (40 × 15 × 0·1 mm) were used as cathodic substrates. The electrochemical cell for deposition in a galvanostatic regime included the cathodic substrate centered between two parallel platinum counterelectrodes. Electrodeposition experiments were performed at 1°C. Cathodic deposits were obtained at a constant current density of 20 mA/cm^2. Deposition times were in the range of up to 20 min. After drying at room temperature deposits were removed from the substrates and subjected to X-ray and TG/DTA study. The phase content was determined by X-ray diffraction with a diffractometer (Phillips, PW-1820) using monochromatized CuK_α radiation. The Scherrer relationship

$$D = \frac{0{\cdot}9\ \lambda}{\beta \cos\theta}$$

was used for calculation of the crystallite size from X-ray line broadening measurements, where D is the average crystallite size, λ is the X-ray wave length, β is the full width at half maximum of the peak and θ is the Bragg angle. A commercially available computer program has been utilized for the profile fitting procedure. Correction for instrumental broadening has been performed. Thermal analysis was carried out in air between room temperature and 800°C at a heating rate of 10°C/min using a thermoanalyzer (Setaram, TGA92). The microstructure of the obtained deposits was studied using a scanning electron microscope (Jeol, JSM-840) equipped with EDS. EDS studies were performed on powder specimens which were obtained by removing green deposits from the substrates and annealing them in air at 800°C for 1 h.

3 Results

Performed experiments revealed the formation of deposits from all the stock solutions used. X-ray analysis was made on fresh deposits and those thermally treated in air at different temperatures for 1 h. The X-ray diffractograms of fresh deposits exhibit their amorphous nature (Figs 1, 2 and 3). Results of X-ray studies of deposits obtained from stock solution 1 (deposits 1) show that faint peaks of the anatase phase appear at 300°C. In Fig. 1 it can be seen that deposit 1 thermally treated at 400°C displayed anatase peaks, which are broadened due to the fine size of the crystallites. Deposits 1 heated at higher temperatures possess an anatase structure up to 700°C. Further increase of the annealing temperature results in an anatase–rutile

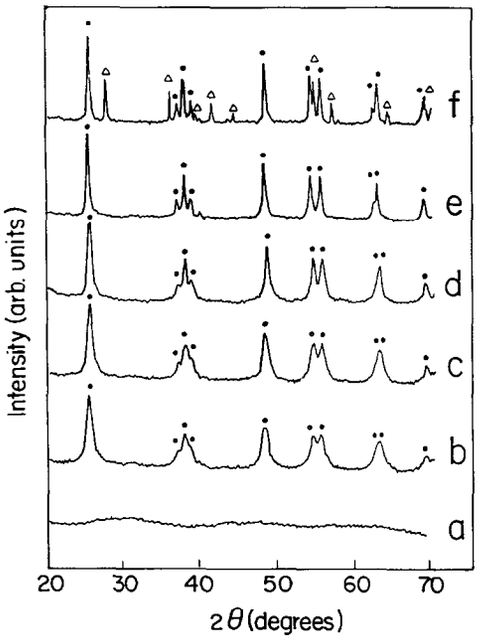

Fig. 1. X-ray diffraction patterns of deposits 1 obtained at a c.d. of 20 mA/cm^2: as-prepared (a) and after thermal treatment at different temperatures for 1 h: 400 (b); 500 (c); 600 (d); 700 (e) and 800 (f) °C. (• anatase, Δ rutile).

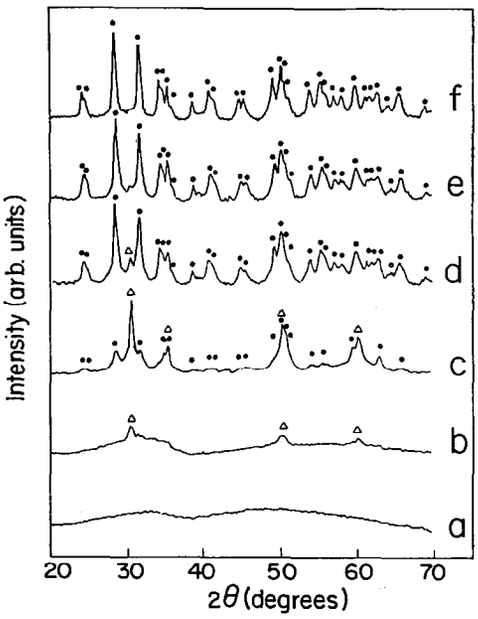

Fig. 2. X-ray diffraction patterns of deposits 2 obtained at a c.d. of 20 mA/cm^2: as-prepared (a) and after thermal treatment at different temperatures for 1 h: 400 (b); 500 (c); 600 (d); 700 (e) and 800 (f) °C. (• monoclinic zirconia, Δ tetragonal zirconia).

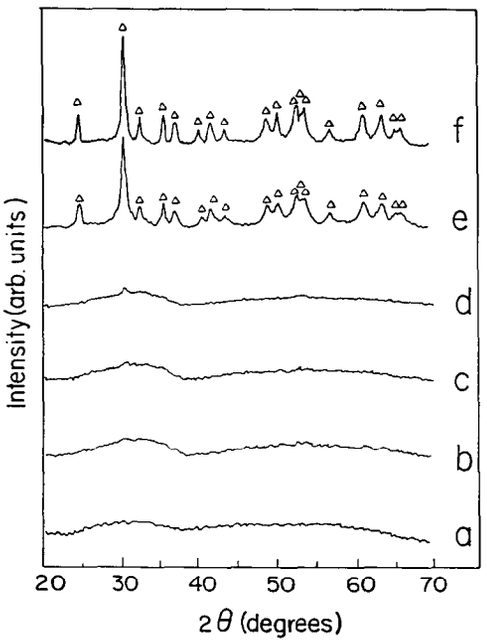

Fig. 3. X-ray diffraction patterns of deposits 3 obtained at a c.d. of 20 mA/cm^2: as-prepared (a) and after thermal treatment at different temperatures for 1 h: 400 (b); 500 (c); 600 (d); 700 (e) and 800 (f) °C (Δ $ZrTiO_4$).

transformation. Figure 1 indicates that XRD spectra taken from deposit 1 annealed at 800°C displayed reflexes of rutile in addition to those of anatase. On exposure of deposits 1 to the temperature of 1000°C, X-ray diffraction patterns exhibit only peaks of rutile. In Table 1, experimental data are given on crystallite size of deposits 1 thermally treated at different temperatures. From this table it can be seen that nanometer-sized anatase forms at 400°C and crystallite size increases with temperature. It is interesting to notice, that rutile crystallites at 800°C are significantly larger than the anatase ones from which they were derived.

Figure 2 shows XRD data for deposits obtained from stock solution 2 (deposits 2). Small reflexes appear at 400°C, which become more clear and sharp at higher temperatures. It is reasonable to attribute these peaks to tetragonal zirconia. However it should be noted that it is difficult to distinguish between the cubic and tetragonal zirconia phases owing to peak broadening. After annealing at 500 and 600°C the samples consisted of mixtures of tetragonal and monoclinic zirconia. At 600°C monoclinic zirconia is dominant, at 800°C the tetragonal phase was not detected in the XRD pattern. As is seen from Table 1, sizes of tetragonal and monoclinic crystallites are on the nanometric scale, while crystallites of the monoclinic phase at 500°C were smaller than those of the tetragonal phase.

XRD data for deposits obtained from stock solution 3 (deposits 3) are summarized in Fig. 3. Deposit crystallization was observed at temperatures exceeding 600°C. The only crystalline phase in deposits 3 thermally treated at 700 and 800°C is $ZrTiO_4$, no peaks due to individual oxides were detected. The observed *d*-values match well with the Joint Committee on Powder Diffraction Standards (JCPDS) data for this material. It is remarkable, that in the temperature region of 400–600°C deposit 3 remains amorphous, whereas crystallization of deposits 1 and 2 was detected. Data presented in Table 1 indicate formation of nanosize $ZrTiO_4$. However it should be noted again that the calculations performed in this work were based on the suggestion that small particle size is the only reason of XRD line broadening.

Figure 4 shows an assemblage of TG/DTA curves for deposits 1, 2 and 3. For deposit 1 the total weight loss in temperature region up to 800°C was about 29% of the initial sample weight, however essentially most of the weight loss occurred below 300°C. The DTA curve exhibits a broad endotherm around 130°C and an exotherm at 440°C. For deposit 2, two distinct steps in the TG curve are distinguished. A sharp reduction of sample weight was observed up to ~200°C and in the region 330–415°C, then the weight fell gradually. Weight losses at 330 and 415°C were 29 and 34% respectively, the total weight loss in the temperature region up to 800°C was 36%. Two endothermic peaks around 130 and 350°C and an exothermic

Table 1. Crystallite sizes of different phases obtained from X-ray line broadening measurements. Reflexes used for calculations are designated

Temperature (°C)	*Particle size (nm)*				
	Titania		*Zirconia*		*Zirconium titanate*
	Anatase (101)	*Rutile (110)*	*Tetragonal (111)*	*Monoclinic (11-1)*	*$ZrTiO_4$ (111)*
400	13				
450			12		
500	15		31	11	
600	20			17	
700	34			20	17
800	59	147		27	18

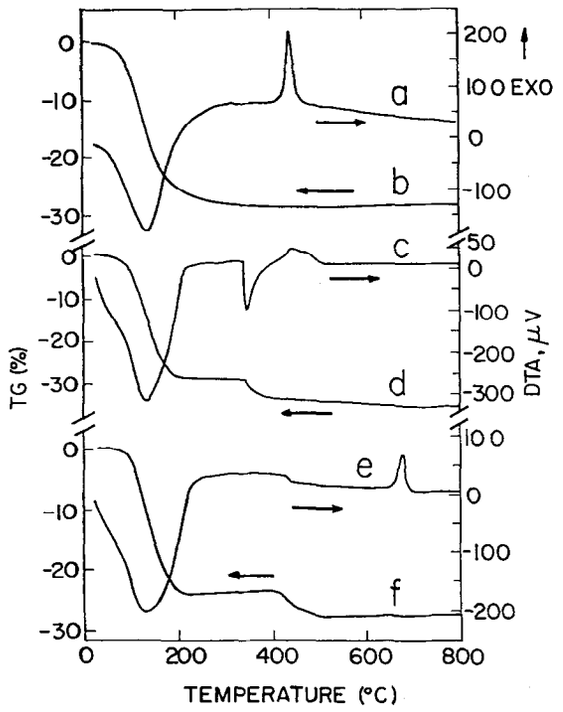

Fig. 4. DTA ((a),(c),(e)) and TG ((b),(d),(f)) data for deposits 1((a),(b)) deposits 2 ((c),(d)) and deposits 3 ((e),(f)) obtained at a 10°C/min heating rate.

effect around 460°C were observed in the DTA curve. The endothermic peak around 130°C and the exothermic peak were very broad. It is thought that the two endothermic peaks correspond to two steps in weight losses.

TG records for deposits 3 show two distinct steps in weight loss up to 200°C and in the region 410–500°C. Weight losses at 235, 540 and 800°C were 23, 27 and 28%, respectively. A very broad endotherm around ~130°C is seen in the DTA curve, a small endothermic effect could be also distinguished at ~430°C. When the specimen was heated to higher temperatures an exothermic peak at ~680°C was observed. For deposits 3, as for deposits 2, a possible link emerges between the observed endothermic effects and the steps in weight loss in corresponding temperature regions.

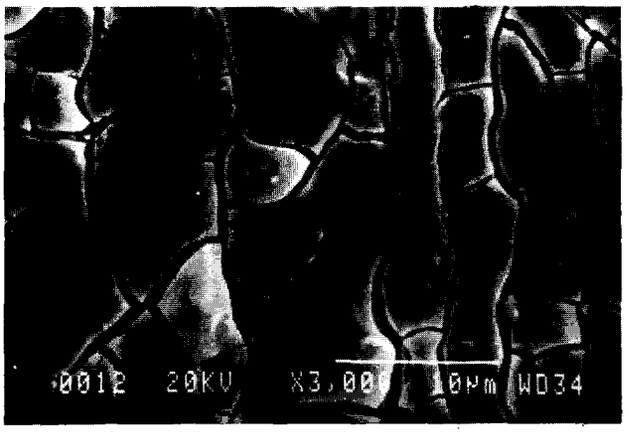

Fig. 5. SEM picture of green deposit 3 on a Pt substrate.

SEM observations indicate a fine particle structure of the deposits. A SEM picture of the green deposit 3 on a Pt substrate is shown in Fig. 5. The sample also shows cracks which arise owing to drying shrinkage. EDS data taken from 15 powder samples show the Ti/Zr ratio to be in the region 0·98–1·05.

4 Discussion

The reported results indicate that the proposed approach has no restriction with regard to platinum being used as a substrate in the deposition process. The mechanism of film formation via a peroxocomplex was discussed in previous works[14,15] and can be used to provide an explanation of the experimental data described above. It is implied that the peroxocomplex of titanium $[Ti(O_2)(OH)_{n-2}]^{(4-n)+}$ is hydrolized by the electrogenerated base to form the cathodic deposit. According to Ref. 16, below pH 1 the peroxocomplex is mononuclear, increase of the pH value causes transformation to a dinuclear and then to a polynuclear complex. Further pH increase results in precipitation of the peroxotitanium hydrate $TiO_3(H_2O)_x$. In the electrosynthesis method the high pH of the cathodic region brings about formation of a peroxotitanium hydrate, which precipitates on the electrode. The cathodic reaction that generates OH^- is:

$$2H_2O + 2e^- \Leftrightarrow H_2 + 2OH^- \quad (1)$$

The following anodic reaction occurs simultaneously:

$$2H_2O \Leftrightarrow O_2 + 4H^+ - 4e^- \quad (2)$$

Phase evolution of deposits obtained from stock solution 1 with temperature are in good agreement with Ref. 14. According to the X-ray data, crystallization of anatase was observed after thermal treatment at 400°C. It is important to note that particle size of titania is on a nanometric scale, (Table 1). This is remarkable, because nanostructured titania exhibits important properties and is now a subject of intensive investigation.[17–19] Recently it has been established that electrodeposition can be used for formation of nanostructured oxides.[2,20] Obviously, the extension of this method to titania electrodeposition is of significant interest. Crystallite sizes of electrodeposited titania at different temperatures are close to those for chemically precipitated titania.[19] A higher crystallite size of rutile than that of anatase observed at 800°C is also in agreement with Ref. 19. Observed weight losses (Fig. 4) are attributed to decomposition of the peroxocomplex and liberation of water and oxygen:

$$2TiO_3(H_2O)_x \Rightarrow 2TiO_2 + O_2 + 2xH_2O \quad (3)$$

The exothermic peak on the DTA curve at 440°C is associated with crystallization of titania.

It is reasonable to expect that in analogy to titania the formation of zirconia can be achieved via a peroxoprecursor. Indeed, according to literature,[21] the hydrated zirconium peroxide $ZrO_3(H_2O)_x$ can be precipitated from zirconium salt solutions in presence of hydrogen peroxide. However, the mechanism of zirconia deposition remains questionable taking into account $ZrO_3(H_2O)_x$ non-stability.[21] Moreover, in contrast to titania, electrodeposition of zirconia can be achieved without hydrogen peroxide.[3,20] Turning again to the wet chemical method of powder processing it should be pointed out that zirconium forms different ionic species depending on the experimental conditions,[22,23] moreover hydrolysis conditions have a significant influence on crystallization behaviour of precipitated hydrous zirconia subjected to thermal treatment.[23] A detailed study of the influence of hydrogen peroxide on zirconia deposition is in progress and will be reported in due time.

As seen from Fig. 2 the main crystalline phase in region 400–500°C is tetragonal zirconia. However, the size of tetragonal crystallites exceeds the critical value of about 10 nm,[24] as a result transformation to monoclinic phase was observed. The crystallite size of the tetragonal phase at 500°C is higher than that of the monoclinic phase. This result is consistent with Refs 23 and 25. Results of thermal analysis exhibit two steps in weight losses and corresponding endotherms which probably can be attributed to a gradual decomposition of the green deposit to form zirconia. It is in this regard that different stages in weight losses were reported[26] in thermal analysis experiments performed with chemically precipitated zirconia. The exothermic effect at around 460°C is associated with crystallization of zirconia phases and is in agreement with the X-ray data. The crystallization temperature of electrosynthesised zirconia is close to that for the chemically precipitated material.[23,25,26] The results of $ZrTiO_4$ electrodeposition experiments described in previous work[15] showed that the deposit remains amorphous up to 600°C, whereas according to Refs 4 and 14 crystallization of titania and zirconia was observed at ~400°C. However it is reasonable to assume that the crystallization behaviour depends upon electrolyte composition, nature of solvent and substrate. In the light of the above, experimental data should be compared for experiments performed in similar conditions. The results of this work provide such a possibility. Results of X-ray studies show that $ZrTiO_4$ crystallizes directly from the amorphous phase. No peaks of individual components were observed in diffraction patterns obtained at different annealing temperatures. Comparison of X-ray data for deposits 1–3 indicates that crystallization of individual oxides is observed at temperatures at least by 200° lower than the crystallization temperature for zirconium titanate. With this fact in mind, it can be expected that in the case of composition fluctuations in deposit 3, peaks of individual components can be observed. This is especially evident taking into account the nanometric size of zirconia and titania crystallites obtained from stock solutions 1 and 2 respectively.

At this point it is important to note that no exotherms corresponding to crystallization of individual components were detected in the DTA curve for deposit 3. From the results of X-ray studies it can be concluded that the exotherm at ~ 680°C can be attributed to $ZrTiO_4$ crystallization. In this respect, results of Okamoto *et al.*[27] of thermal analysis of titania and zirconia mixtures of different degrees of homogeneity should be mentioned. Remarkably, in the case of composition fluctuations in the mixture of two gels, DTA curves have a quite different behaviour from that for coprecipitated gel, exhibiting additional peaks at temperatures lower than temperature of $ZrTiO_4$ crystallization.[27]

Observed weight losses are associated with the decomposition of the peroxoprecursor. According to the experiments and calculations performed in Ref. 28 the composition of the peroxocompound obtained via the chemical precipitation method was established as $ZrTiO_{3.43}(OH)_{1.13}xH_2O$. According to Ref. 29, the amorphous peroxoprecursor undergoes three structural transformations as the temperature increases. It can be supposed that the steps in weight losses observed in this work correspond to different stages of structural transformations.[29] Going on to Ref. 28 the width of the endothermic peak for deposit 3 around ~130°C can also be attributed to a gradual decomposition of the hydrated peroxide.

On the basis of the above experiments it can be concluded that the temperature of $ZrTiO_4$ formation via electrosynthesis is in agreement with the temperature of formation of this material via the chemical precipitation method.[28,29] It is important to see that the electrodeposynthesis is similar to the wet chemical method of powder processing making use of electrogenerated base instead of alkali. Obviously, electrosynthesis not only produces ceramic materials but also provides their deposition. Going on to Murata *et al.*[30] we can conclude that hydroden peroxide allows us to prevent different hydrolysis rates of individual components and enables us to obtain material of a desired stoichiometry. Hydroxide ions generated in cathodic reactions allows us to perform hydrolysis and obtain colloidal particles near

the cathode. It was supposed[12,15] that the deposition can be achieved via electrophoretic motion of these particles towards the cathode.

Results of this work provide a basis for electrosynthesis of different ferroelectric titanates and solid solutions on Pt substrates, which are important for electronic applications. As an extension of this work recently we have shown the possibility of electrosynthesis of lead zirconate-titanate (PZT) on Pt and on platinized silicon wafers. Results of these studies will be published soon.

5 Conclusions

The feasibility of electrosynthesis of titania, zirconia and zirconium titanate ceramic deposits on platinum substrates has been demonstrated. Obtained materials were found to be amorphous, while their crystallization temperatures are in agreement with those of corresponding powders produced by chemical precipitation methods. The reported data show that the sizes of the obtained crystallites are on a nanometric scale, and their variation with temperature as well as phase evolution has been studied. Results of X-ray studies, thermal analysis and EDS showed that the electrosynthesis of zirconium-titanate via a peroxoprecusor route enables control of its stoichiometry. The obtained results pave the way for the electrodeposition of ferroelectric titanates and their solid solutions.

References

1. Switzer, J. A., Electrochemical Synthesis of Ceramic Films and Powders. *Am. Ceram. Soc. Bull.*, **66** (1987) 1521–4.
2. Zhou, Y., Phillips, R. J. & Switzer, J. A., Electrochemical Synthesis and Sintering of Nanocrystalline Cerium (IV) Oxide Powders. *J. Am. Ceram. Soc.*, **78** (1995) 981–5.
3. Gal-Or, L., Silberman. I. & Chaim, R., Electrolytic ZrO_2 Coatings. I. Electrochemical Aspects. *J. Electrochem. Soc.*, **138** (1991) 1939–42.
4. Chaim., R., Silberman, I. & Gal-Or, L., Electrolytic ZrO_2 Coatings. Microstructural Aspects. *J. Electrochem. Soc.*, **138** (1991) 1942–6.
5. Zhitomirsky, I., Gal-Or, L., Kohn, A. & Hennicke, H. W., Electrochemical Preparation of PbO Films. *J. Mat. Sci. Lett.*, **14** (1995) 807–10.
6. Chaim, R., Stark, G., Gal-Or, L. & Bestgen, H., Electrochemical ZrO_2 and Al_2O_3 Coatings on SiC Substrates. *J. Mat. Sci.*, **29** (1994) 6241–8.
7. Chatterjee, A. P., Mukhopadhyay, A. K., Chakraborty, A. K., Sasmal, R. N. & Lahiri, S. K., Electrodeposition and Characterization of Cuprous Oxide Films. *Mater. Lett.*, **11** (1991) 358–62.
8. Matsumoto, Y., Morikawa, T., Adachi, H. & Hombo, J., A New Preparation Method of Barium Titanate Perovskite Film using Electrochemical Reduction. *Mat. Res. Bull.*, **27** (1992) 1319–27.
9. Matsumoto, Y., Adachi, H. & Hombo, J., New Preparation Method for PZT Films Using Electrochemical Reduction. *J. Am. Ceram. Soc.*, **76** (1993) 769–72.
10. Abolmaali, S. B. & Talbot, J. B., Synthesis of Superconductive Thin Films of $YBa_2Cu_3O_{7-x}$ by a Nonaqueous Electrodeposition Process. *J. Electrochem. Soc.*, **140** (1993) 443–5.
11. Slezak P. & Wieckowski, A., Aqueous Electrochemical Synthesis of $YBa_2Cu_3O_{7-x}$ Superconductors. *J. Electrochem. Soc.*, **138** (1991) 1038–40.
12. Royer P. & Rey, C., Calcium Phosphate Coatings for Orthopaedic Prosthesis. *Surface and Coatings Technology*, **45** (1991) 171–7.
13. Shirkhanzadeh, M., Bioactive Calcium Phosphate Coatings Prepared by Electrodeposition. *J. Mat. Sci. Lett.*, **10** (1991) 1415–17.
14. Zhitomirsky, I., Gal-Or, L., Kohn, A. & Hennicke, H. W., Electrodeposition of Ceramic Films from Non-aqueous and Mixed Solutions. *J. Mat. Sci.*, **30** (1995) 5307–12.
15. Zhitomirsky, I., Gal-Or, L. & Klein, S., Electrolytic Deposition of $ZrTiO_4$ Films. *J. Mat. Sci. Lett.*, **14** (1995) 60–2.
16. Mühlebach, J., Müller, K. & Schwarzenbach, G., The Peroxo Complexes of Titanium. *Inorg. Chem.*, **9** (1970) 2381–90.
17. Hahn, H. & Averback, R. S., Low-Temperature Creep of Nanocrystalline Titanium (IV) Oxide. *J. Am. Ceram. Soc.*, **74** (1991) 2918–21.
18. Siegel, R. W., Ramasamy, S., Hahn, H., Zongquan, L., Ting, L. & Gronsky, R., Synthesis, characterization, and properties of nanophase TiO_2. *J. Mater. Res.*, **3** (1988) 1367–72.
19. Hague, D. C. & Mayo, M. J., The Effect of Crystallization and a Phase Transformation on the Grain Growth of Nanocrystalline Titania. *NanoStruct. Mater.*, **3** (1993) 61–7.
20. Chaim. R., Fabrication and Characterization of Nanocrystalline Oxides by Crystallization of Amorphous Precursors. *NanoStruct. Mater.*, **1** (1992) 479–89.
21. Clark, R. J. H., Bradley, D. C. & Thornton, P., *The Chemistry of Titanium, Zirconium and Hafnium*. Pergamon Press, Oxford, New York, Toronto, 1975, p. 453.
22. Zhang, W. & Glasser F. P., Condensation and Gelation of Inorganic ZrO_2–Al_2O_3 Sols. *J. Mater. Sci.*, **28** (1993) 1129–35.
23. Srinivasan, R., Harris, M. B., Simpson, S. F., De Angelis, R. J. & Davis, B. H., Zirconium Oxide Crystal Phase: The Role of the pH and Time to Attain the Final pH for Precipitation of the Hydrous Oxide. *J. Mater. Res.*, **3** (1988) 787–97.
24. Garvie, R. C. & Goss, M. F., Intrinsic Size Dependence of the Phase Transformation Temperature in Zirconia Microcrystals. *J. Mater. Sci.*, **21** (1986) 1253–7.
25. Mercera, P. D. L., Van Ommen, J. D., Doesburg, E. B. M., Burggraaf, A. J. & Ross J. R. H., Zirconia as a Support for Catalysts. Evolution of the Texture and Structure on Calcination in Air. *Appl. Catal.*, **57** (1990) 127–48.
26. Mercera, P. D. L., Van Ommen, J. G., Doesburg, E. B. M., Burggraaf A. J. & Ross J. R. H., Influence of Ethanol Washing of the Hydrous Precursor on the Textural and Structural Properties of Zirconia. *J. Mater. Sci.*, **27** (1992) 4890–8.
27. Okamoto, Y., Isobe, T. & Senna, M., Mechanochemical Synthesis of Non-crystalline $ZrTiO_4$ Precursor from Inhomogeneous Mixed Gels. *J. Non-Cryst. Solids.*, **180** (1995) 171–9.
28. Navio, J. A., Marchena, F. J., Macias, M., Sanches-Soto, P. J. & Pichat, P., Formation of Zirconium Titanate Powder from a Sol–gel Prepared Reactive Precursor. *J. Mater. Sci.*, **27** (1992) 2463–7.
29. Navio, J. A., Macias, M. & Sanches-Soto, P. J., On the influence of chemical processing in the crystallization behaviour of zirconium titanate materials. *J. Mat. Sci. Lett.*, **11** (1992) 1570–2.
30. Murata, M., Wakino, K., Tanaka, K. & Hamakawa, Y., Chemical preparation of PLZT powder from aqueous solution. *Mat. Res. Bull.*, **11** (1976) 323–8.

Journal of the European Ceramic Society 16 (1996) 825–831

0955-2219(95)00214-6
0955-2219/96/$15.00 + .00

Enhanced Toughness of a Partially Stabilised Zirconia at Elevated Temperatures

D. G. Jensen*

Department of Materials Engineering, Monash University, Clayton, Victoria, 3168 Australia

(Received 31 May 1995; revised version received 15 November 1995; accepted 29 November 1995)

Abstract

A ternary partially stabilised zirconia alloy has been developed by doping 10·8 mol% Mg–PSZ with 1·25 mol% CeO_2. This material has a microstructure that has oblate spheroidal precipitates that have twice the diameter and aspect ratio of those in Mg–PSZ. These precipitates, by enhancing toughening mechanisms other than the usual transformation toughening mechanism allow a considerable increment to toughening at elevated temperatures, despite transformation toughening not being operative at these temperatures. There is a measurable toughening at high temperature that cannot be attributed to transformation toughening. However, more work is required in the processing to reduce the porosity of the material.

1 Introduction

Optimally aged partially stabilised zirconia alloys at room temperature consist of a dispersion of metastable tetragonal precipitates in a cubic matrix. These precipitates transform to the monoclinic phase when some of the constraint imposed by the matrix is relieved by, for example, the nearby propagation of a crack. This transformation is accompanied by a 4% volume increase; the expansion of the precipitate absorbs some of the energy normally used in driving the crack and thus shields the crack tip from the crack driving force. Toughening of the material by this mechanism is known as transformation toughening.[1]

A significant limiting factor with this toughening mechanism is that an increase in the temperature of the material serves to stabilise the tetragonal phase, thus reducing the propensity for the precipitates to undergo a stress-induced transformation to the monoclinic phase.[2,3] This limits the service temperature of partially stabilised zirconias. In order to circumvent this problem, an attempt has been made to utilise other potential toughening mechanisms that are temperature insensitive to improve the high temperature toughness of PSZ-type materials, while retaining the transformation mechanism at low temperatures.

2 Background

With a view to retaining the transformation mechanism at room temperature, but tailoring the precipitate morphology in such a way as to enable other toughening mechanisms to become operative at high temperatures, we embarked on the development of an alloy that would incorporate precipitates having a morphology that would allow both of these aspects.

Toughening mechanisms other than transformation toughening that may benefit the toughness of PSZ-type materials at high temperature are crack deflection, particle pullout and crack bridging. Although particle pullout is a bridging mechanism, we will use the term to differentiate it from bridging where the bridge itself finally ruptures.

Crack deflection[4] serves to increase toughness by deflecting the crack out of its propagating plane, thereby increasing fracture surface area and, as the crack driving force and the crack direction no longer coincide, results in the decrease of the crack driving force. Faber & Evans[4] have proposed that increasing the aspect ratio of rod-shaped inclusions from 1 to 12 would serve to increment the toughness by 50%; their model is independent of particle size.

Crack bridging as used in our case[5,6] is a result of thermal expansion mismatch resulting in regions of residual compressive stress that result in these areas remaining intact following the passage of a crack, bridging the crack and serving to reduce the crack driving force until the bridge fails.

Particle pullout[7] utilises the frictional sliding energy loss that results from a particle being pulled out of the surrounding material in order to reduce the crack driving force; this continues until one side of

*Present Address: CSIRO Division of Wool Technology Geelong Laboratory, Belmont, Victoria, 3216, Australia.

the particle slides out of the surrounding material. It would obviously be desirable to have longer particles in order to maximise this contribution; however, it should be noted that very long particles would fail as opposed to frictionally sliding as the frictional force would be greater than the strength of the particle.

By carrying out calculations of potential toughening increments by the various mechanisms that would be operative at high temperature (crack bridging, particle pullout and crack deflection), it was determined that the ideal microstructure would be one in which the precipitates were large and had a high aspect ratio. To this end the calculation of precipitate morphologies by the minimisation of the elastic strain energy was carried out.

It is known that the metastable tetragonal precipitate's size is determined by solute content; in an attempt to maximise the solute in the precipitate, it was decided to use CeO_2 which has a high solubility in tetragonal zirconia. The precipitate, by having a higher solute content than Mg–PSZ, should remain tetragonal to a larger size than were there little solute present in the precipitate, as is the case for Mg–PSZ.

The aspect ratio of the precipitates is controlled by a combination of elastic anisotropy and the lattice parameter mismatch,[8] or 'tetragonality parameter':

$$t_1 = \frac{(a_t - a_c)}{(c_t - a_c)} \quad (1)$$

where a_c is the cubic lattice parameter, and a_t is the smaller and c_t is the larger of the tetragonal lattice parameters.

As zirconia has low elastic anisotropy,[9] it is the tetragonality parameter that dominates, and calculations show that a very low tetragonality parameter results in a high aspect ratio. For the system under investigation, the calculations based on the elastic constants at 1400°C given by Kandil *et al.*, and from lattice parameters derived from using Guinier XRD, an equilibrium aspect ratio of 7·7 is obtained; this is almost twice that obtained for Mg–PSZ.

3 Experimental

Powders in the ratio 1·25 mol% CeO_2, 10·8 mol% MgO and ZrO_2, to which was added 0·25 mol% SrO were attritter milled in a binder-isopropanol mixture for 6 h, thence spray-dried. This material is hereinafter referred to as 1·25 CM–PSZ. The resulting powder was then pressed into bars uniaxially at 30 MPa and the bars were then isostatically pressed at 200 MPa. These bars were then fired in an electric furnace at 1700°C for 2 h and cooled at 500°C/h to room temperature. Subsequent to this, the bars were aged for varying periods at 1400°C in order to allow precipitate growth and coarsening.

Mechanical testing was undertaken using an Instron 1122 with a crosshead speed of 0·1 μm/min for strength testing and 0·05 μm/min for toughness testing. A three-point rig with a span of 3 cm was employed for all testing, this rig was placed inside a furnace designed for high temperature testing when the high temperature (600°C) testing was carried out. Toughness testing was carried out in accordance with ASTM E399/83[10] for plane strain toughness testing; indentation toughness was carried out in accordance with the method of Anstis.[11]

For strength testing, bars were machined to about 40 × 4 × 2 mm; the tensile surface was polished to a mirror finish in order to remove the compressive zone as a result of grinding-induced surface transformation of the precipitates to monoclinic. The edges were chamfered to prevent cracks from propagating from the corners, which would give a false indication of the strength. Toughness testing was carried out using bars of the approximate dimension 40 × 8 × 4 mm, into which were cut notches 170 μm wide of various depths, in order to do single-edge, notched bend (SENB) testing. In order to remove the compressive zone at the notch tip, the bars were annealed at 1000°C for 20 min.

Scanning electron microscopy (SEM) was carried out in a Hitachi SF450 by observing the carbon coated fracture surfaces. Cracks propagating from the corners of Vickers indents on the polished surfaces of the sample aged 16 h were etched in HF for 4 min; the sample was then carbon coated for observation in the SEM. Transmission electron microscopy (TEM) was carried out using a Philips EM420 microscope, thin foils prepared by cutting a 5 mm diameter sample, thence thinning to 80 μm and then dimple grinding to 25 μm. Samples were then ion beam milled to perforation and given a light carbon coat. Precipitates were observed near the $<001>_c$ direction, the precipitate habit plane. Energy dispersive spectra (EDS) analysis was carried out in order to determine approximate solute content within the precipitates; no correction for absorption was carried out. The transformable tetragonal phase fraction was determined by the ratio of the areas under the {111} cubic/tetragonal and monoclinic X-ray peaks.[12]

4 Results and Discussion

4.1 Microstructural investigation

Observation of precipitates, and the measurement of precipitate diameter and aspect ratio has been documented elsewhere,[13] but the results are given in Table 1; additionally, we have added the solute content of the precipitates and the transformable tetragonal phase percentage.

Table 1. Comparison of various microstructural details of materials with regard to ageing time

Ageing time (h)	*MgO in precipitate. (MgO in 10·8 mol% Mg–PSZ)*	*Precipitate diameter (μm)*	*Precipitate aspect ratio*	*Transformable tetragonal (%)*
1	11·3 ± 0·7 (10·1) ± 1·0	0·167	4·39	2·3
4	11·8 ± 1.1 (5·9) ± 0·7	0·274	6.10	4·3
8	7·4 ± 0·5 (3·0) ± 0·6	0·371	6·30	5·2
16	3·8 ± 0·9 (0·8) ± 0·4	0·482	8·18	8·9

It should be noted that the CeO_2 concentration is remarkably stable at 1·3% in both the matrix and the precipitates for all ageing times. Additionally, the CeO_2 serves to reduce the diffusion of the MgO from the precipitates, which allows the precipitates to grow to a larger size before they have insufficient solute to remain tetragonal.

Comparing data for 9·4 mol% Mg–PSZ with those presented in Table 1, the diameter of precipitates in Mg–PSZ is about 0·2 μm and the aspect ratio is approximately 5 : 1; this illustrates the improvement in these morphological factors, which should result in improved high temperature toughness.[14,15]

4.2 Mechanical properties

The strength, although low in comparison to that for Mg–PSZ, shows an incremental increase with increasing ageing time to 4 h at room temperature, whereafter the strength reduces (see Fig. 1). Although the strength would be expected to reach a maximum after 16 h ageing (with Mg–PSZ, peak strength and toughness both coincide with peak ageing), the strengths of the samples aged for 4 h and 16 h do fall within experimental error. The samples tested at 600°C show a small rise with increasing ageing time to 16 h, whereafter the strength degrades. This degradation in strength of the materials aged for 32 h is due to the large (approximately 30%) monoclinic phase content in this overaged material. A feature worthy of comment is that the strength of material aged for 16 h tested at 600°C is very close to that of as-fired material tested at room temperature.

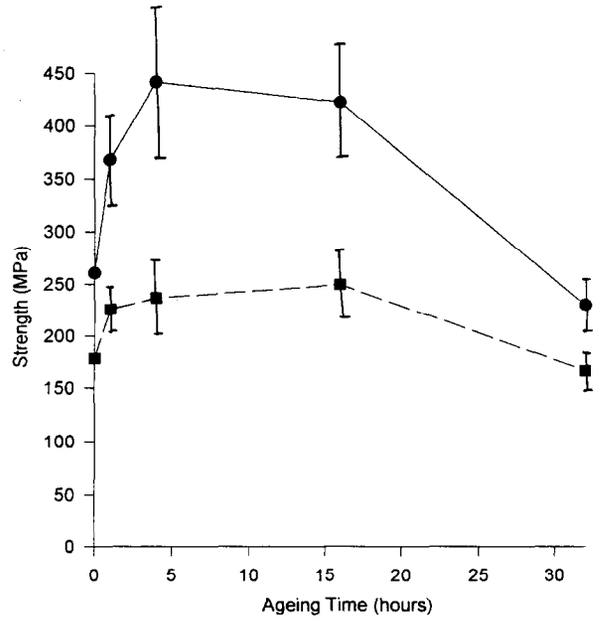

Fig. 1. Graph of strength versus ageing time. For all graphs, circles represent room temperature values, whereas squares represent measurements conducted at 600°C.

Toughness testing of these materials proved very interesting (see Fig. 2), firstly in that the toughness calculated by the indent method proved to be an underestimate of the true toughness measured. The materials show a considerable increment to toughness with increasing ageing time, both at room temperature and at 600°C. It should be noted that tests conducted at 800°C of samples aged for 4 h and 16 h gave the same toughness values as for 600°C (in other words, about 4·4 MPa$\sqrt{m}$). Swain *et al.*[2] have shown that for conventional Mg–PSZ, there is only about a 5% increment to toughening at 600°C, whereas our peak-aged material shows an increment of about 60%. Furthermore, the data given by Swain *et al.* show that the toughness for peak-aged Mg–PSZ at 600°C is less than that for as-fired material at room temperature. With regard to the decrease in toughness with increasing temperature, it is interesting that the toughness of eutectoid-aged Mg–PSZ decreases by about 50% when the testing temperature is increased to 600°C, whereas the decrease for 1·25 CM–PSZ is only about 33%. It should also be noted in Fig. 2(a) that the toughness of peak-aged 1·25 CM-PSZ at 600°C is measurably greater than that for as-fired material tested at room temperature. This would suggest that the proposed, non-transformation-based toughening mechanisms are at work. In order to validate this, it was decided to carry out an SEM evaluation.

4.3 SEM study

As fractography alone does not give an accurate indication of mechanisms, such as crack bridging

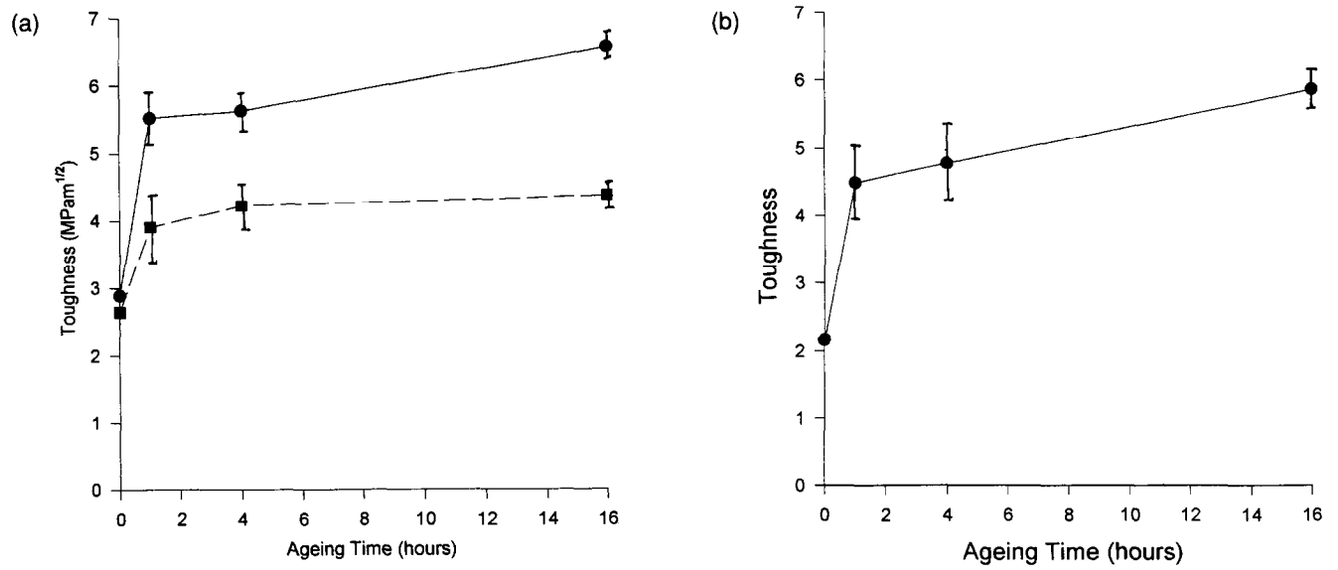

Fig. 2. (a) Graph of toughness versus ageing time, measured by SENB. The toughness of peak-aged CM–PSZ tested at 600°C is measurably greater than that of as-fired CM–PSZ tested at room temperature. (b) Graph of toughness versus ageing time for samples tested at room temperature by measuring the diagonal cracks emanating from a Vickers indent. Note that the toughness values obtained are an underestimate of the values obtained by using SENB.

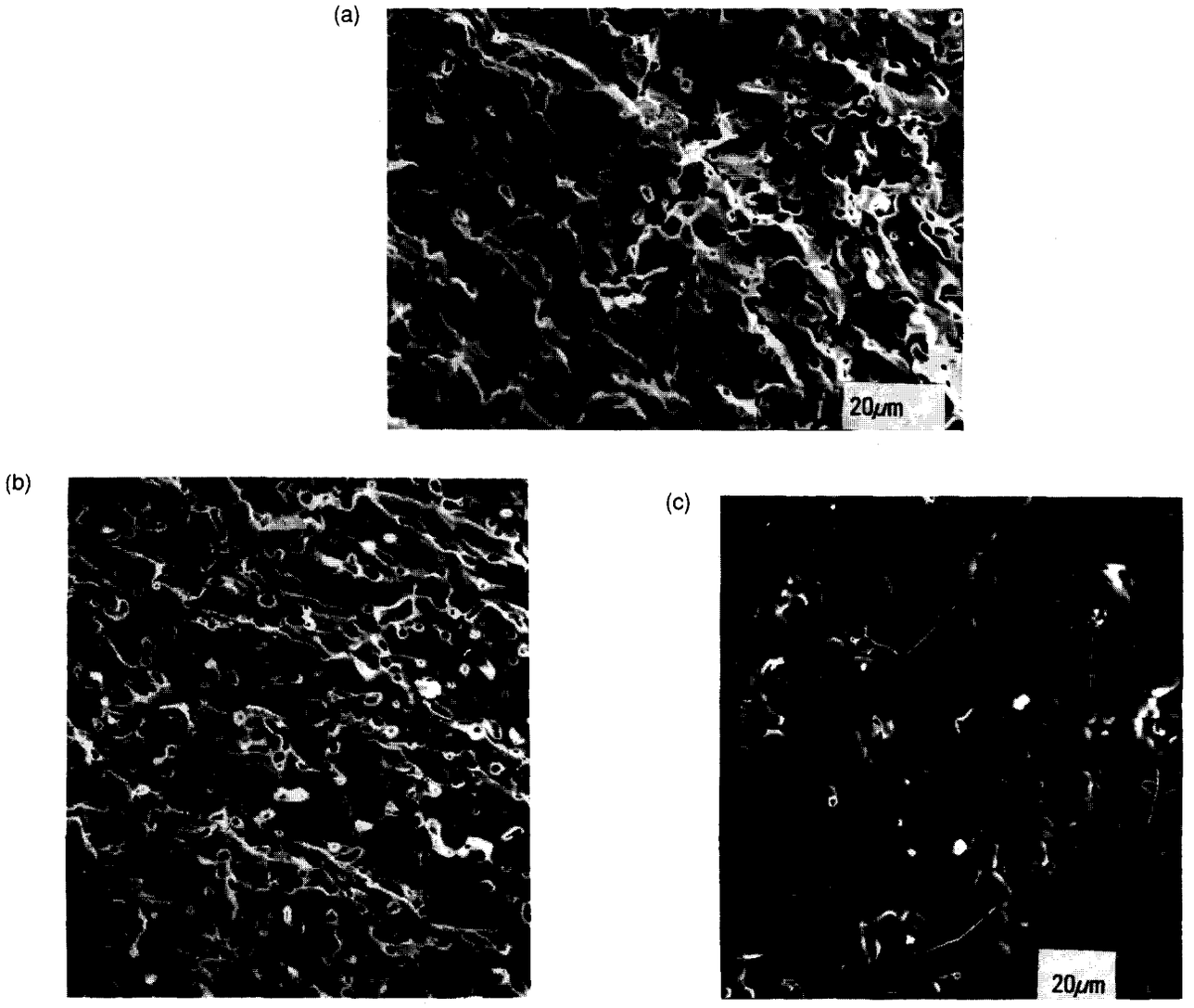

Fig. 3. (a) Fracture surface of as-fired material fractured at room temperature. Note the high apparent pore density exhibited by the preferred cleavage direction of the material. Both inter- and intra-granular fracture are evident. (b) Fracture surface of as-fired material fractured at 600°C. Notice the similarity of the fracture surface as compared with the material tested at room temperature. (c) Surface of diamond-sawn region of sample shown in (b). Note that the porosity is not as high as that for a fracture surface.

due to any bridges already having failed, it was decided also to study the cracks emanating from a Vickers indent in the aged 16 h sample in order to ascertain whether such processes were occurring.

Samples were found to have a grain size of 15–40 μm; the porosity was approximately 5% as measured by the comparison of measured and theoretical densities. The porosity was evenly distributed throughout the material.

It is interesting to note that the as-fired material exhibits cleavage-type fracture, with the preferred cleavage direction coinciding with that of the highest pore density. This is evident at both room and high temperatures (see Fig. 3), the true porosity of the bulk is not as high as is evident with the fracture surfaces (see Fig. 3(c)) resulting from the nature of the fracture.

Samples aged for 1, 4, and 16 h exhibit predominantly intra-granular fracture, and considerable crack–precipitate interaction is in evidence (see Figs 4, 5 & 6). This interaction clearly contributes to the enhanced toughness at high temperatures. Material aged for 32 h, having very large regions of grain boundary, monoclinic phase present, has predominantly intergranular fracture, which contributes to the reduced strength and toughness evident in this material (see Fig. 7).

The observation of cracks emanating from the corners of Vickers indents (see Fig. 8) provides evidence of crack deflection, precipitate pullout and crack

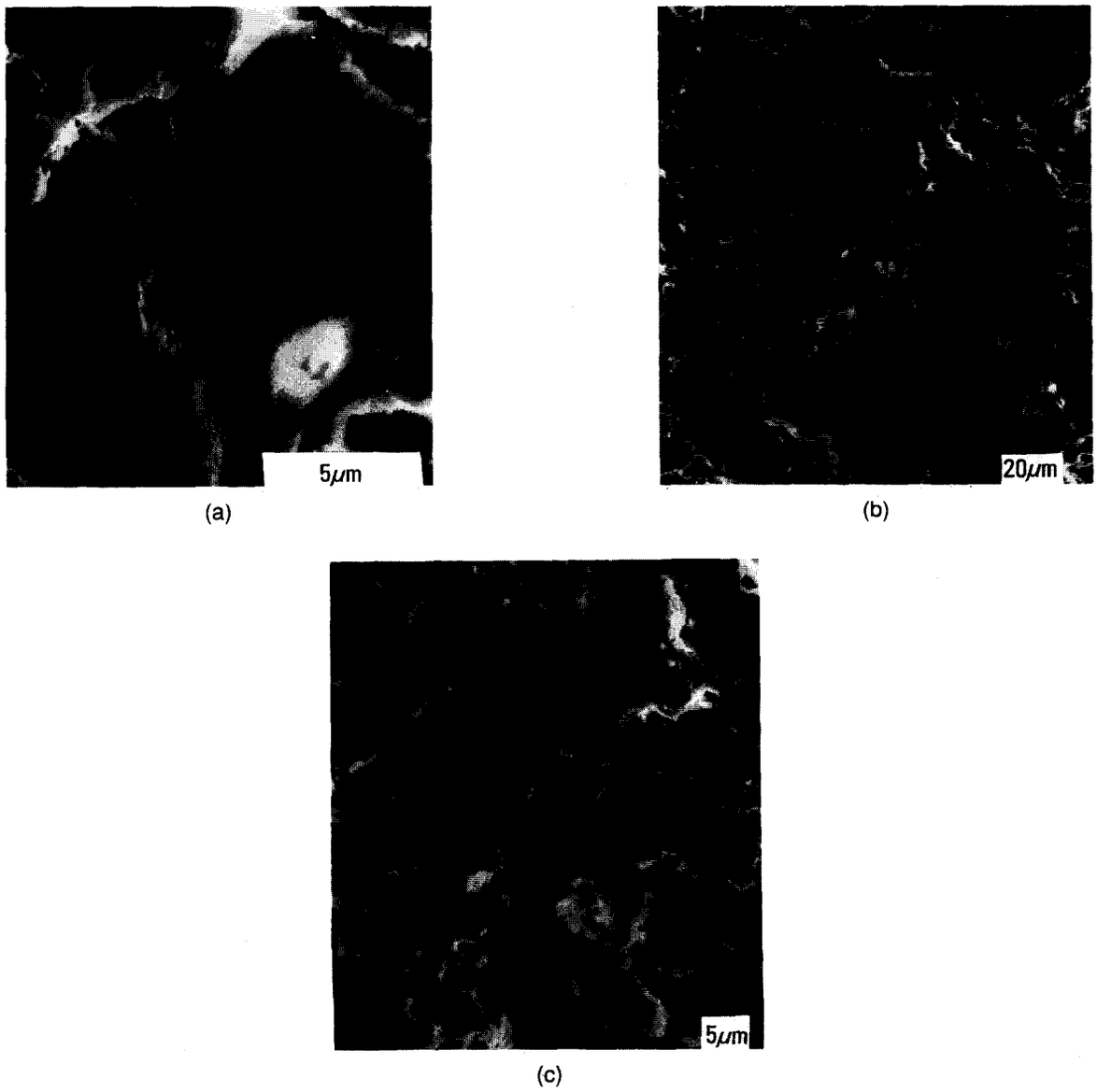

Fig. 4. (a) Fracture surface of material aged for 1 h fractured at room temperature. Note that there is considerable crack–precipitate interaction; the textured effect on the fracture surface is due to deflection of the crack about the precipitate. Some of the exposed precipitates could also be a result of crack bridging and pullout. Precipitates in the material aged for 1 h have approximately the same morphology as those in peak-aged Mg–PSZ. (b) Fracture surface of aged for 1 h material fractured at 600°C. Note that some of the fracture appears to have occurred inter-granularly, but that for intra-granular fracture, there is considerable crack–precipitate interaction. (c) Higher magnification micrograph of part of the region in (b), showing evidence of crack–precipitate interaction.

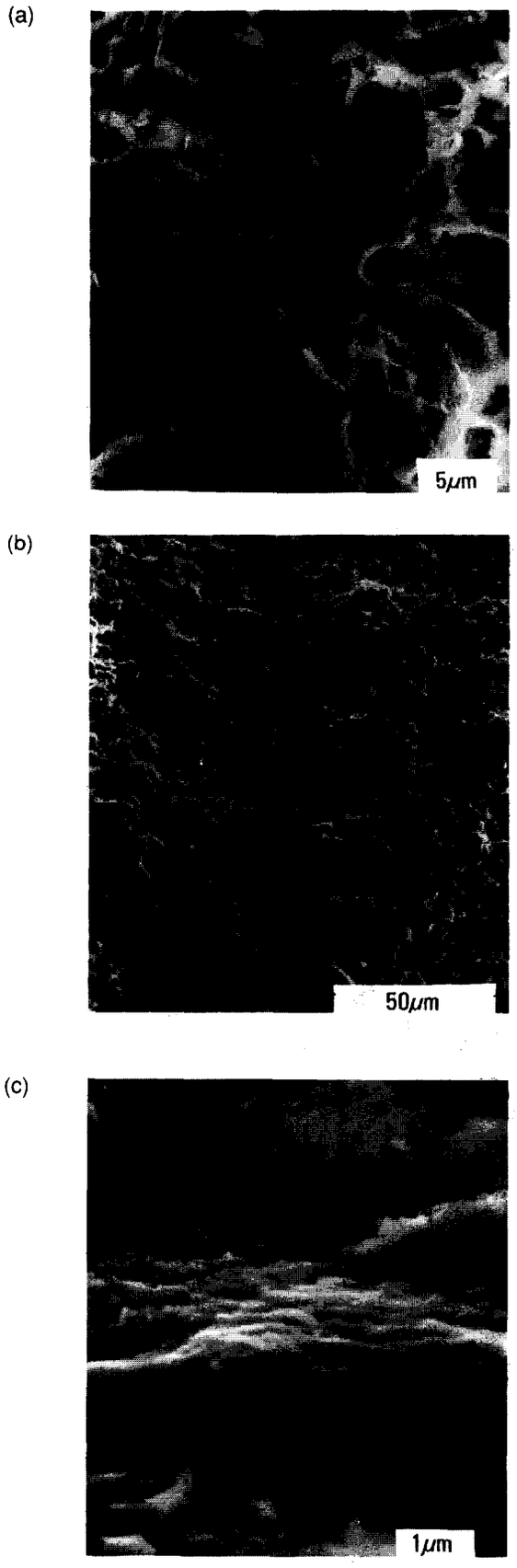

Fig. 5. (a) Fracture surface of material aged for 4 h fractured at room temperature. Most of the fracture is intra-granular, with some inter-granular fracture occurring. (b) Fracture surface of material aged 4 h fractured at 600°C. The fracture is primarily intra-granular. (c) Higher magnification micrograph of part of the region in (b). Note considerable crack–precipitate interaction; it is this type of interaction that accounts for the improved high temperature fracture toughness of this material.

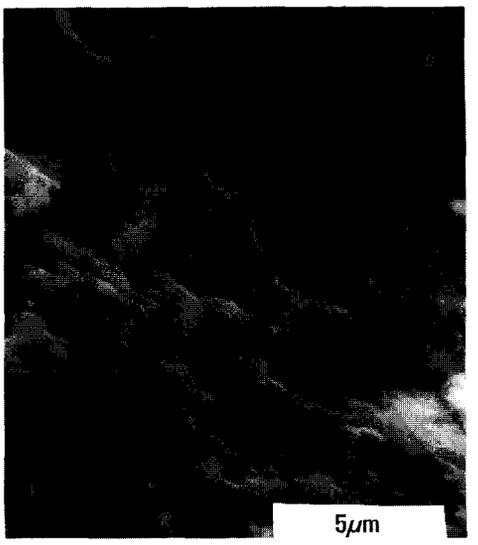

Fig. 6. Fracture surface of material aged for 16 h fractured at 600°C. Note the considerable extent of crack–precipitate interaction. Clearly, crack deflection has occurred, but it is difficult to say whether precipitate pullout has occurred, and impossible to tell whether crack bridging has occurred.

Fig. 7. Fracture surface of material aged for 32 h fractured at room temperature. Note that although there is some crack–precipitate interaction present, the fracture is predominantly inter-granular, and that there are regions of grain boundary monoclinic phase (A) through which the crack has preferentially propagated.

bridging. With regard to crack bridging, both elastic and plastic bridging elements are in evidence. These mechanisms, as previously discussed, are all temperature insensitive toughening mechanisms, and as such could be expected to contribute to the enhanced high temperature toughness evident in this material.

Another feature that is worthy of comment is that of the apparent morphology of many of the precipitates in Fig. 8. Although it appears that many of the precipitates have a kinked morphology, TEM observations point to these precipitates being the

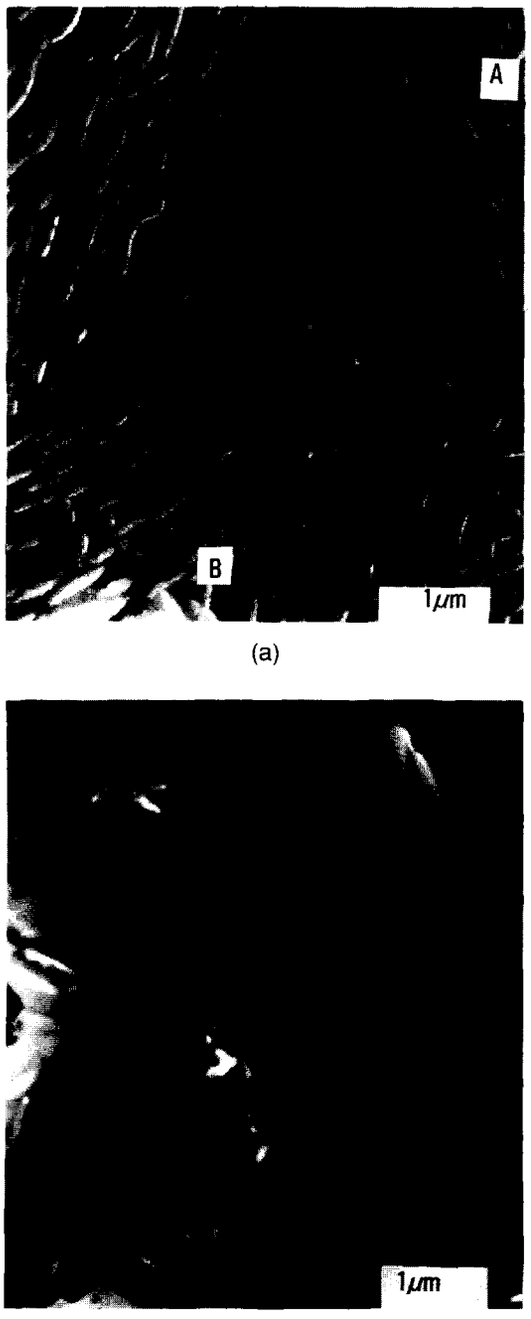

Fig. 8. Crack emanating from the corner of a Vickers indent in material aged for 16 h. (a) Particle pullout (A) and crack deflection (B) are clearly in evidence. (b) Crack bridging.

result of precipitates that have nucleated and grown in a rafted manner, having grown together.[13,14] In detail, however, the precipitates have been shown to deviate from an assumed oblate spheroid shape, but not to the extent as it appears in the SEM images.

5 Conclusions

(1) The high-temperature toughness shows a considerable increase with increasing ageing time giving promise to PSZ-type ceramics that may be used for high-temperature applications. The toughening increment at room temperature is similar to that for eutectoid-aged Mg–PSZ.

(2) Improved processing is required to reduce the porosity in order to improve the strength of the material.

(3) Sub-eutectoid ageing should improve the increment to transformation toughening in the same way as for Mg–PSZ.

Acknowledgements

The author wishes to acknowledge Alan White, who cut the notches in the toughness testing samples. The helpful advice of Professor Paul Rossiter and Associate Professor Trevor Finlayson is gratefully acknowledged, as is the critical reading of the document by Trevor. Much of this work was carried out at the CSIRO Division of Materials Science and Technology. This work was supported by an APA Award.

References

1. Green, D. J., Hannink, R. H. J. & Swain, M. V., *Transformation Toughening of Ceramics*, CRC Press, Boca Raton, FL, 1989.
2. Swain, M. V., Hughan, R. R., Hannink, R. H. J. & Garvie, R. C., *Magnesia-Partially-Stabilised Zirconia (Mg–PSZ) Microstructure and Properties*. Zirconia Conference, Japanese Ceramic Soc., Tokyo Inst. Tech., 1983.
3. Becher, P. F., Swain, M. V. & Ferber, M. K., Relation of Transformation Temperature to the Fracture Toughness of Transformation-Toughened Ceramics. *J. Mat. Sci.*, **22** (1987) 76.
4. Faber, K. T. & Evans, A. G., Crack Deflection Processes, *Acta Metall. Mater.*, **31** (1983) 565.
5. Knehans, R. & Steinbrech, R. W., Memory effect of crack resistance during slow crack growth in notched Al_2O_3 bend specimens. *J. Mat. Sci. Lett.*, **1** (1982) 327.
6. Rodel, J., Interaction Between Crack Deflection and Crack Bridging. *J. Eur. Cer. Soc.*, **10** (1992) 143.
7. Lange, F. F., *Fracture Mechanics and Microstructural Design, Fracture Mechanics of Ceramics*, Vol. 4, Plenum Press, New York, 1978, p. 799.
8. Khachaturyan, A. G., *Theory of Structural Transformations in Solids*, Wiley, NY, 1983.
9. Kandil, H. M., Greiner, J. D. & Smith, J. F., Single Crystal Elastic Constants of Yttria-Stabilized Zirconia in the range 20 to 700°C. *J. Am. Cer. Soc.*, **67** (1984) 341.
10. Srawley, J. E., Wide Range Stress Intensity Factor Expressions for ASTM E399 Standard Fracture Toughness Specimens. *Int. J. of Fracture*, **12** (1976) 474.
11. Anstis, G. R., Chantikul, P., Lawn, B. R. & Evans, A. G., A critical evaluation of indentation techniques for measuring fracture toughness. I. Direct crack measurements. *J. Am. Cer. Soc.*, **64** (1981) 533.
12. Garvie, R. C. & Nicholson, P. S., Structure and thermomechanical properties of Partially Stabilised Zirconias in the CaO–ZrO_2 system. *J. Am. Cer. Soc.*, **55** (1972) 152.
13. Jensen, D. G., Estimation of the Size Distribution of Spherical, Disc-like or Ellipsoidal Particles in Thin Films. *J. Phys. D.*, **28** (1995) 549.
14. Jensen, D. G., The orientation relationship between tetragonal zirconia precipitates with regard to elastic interaction energy, *J. Mat. Sci.*, **30** (1995) 5681.
15. Lanteri, V., Mitchell, T. E. & Heuer A. H., Morphology of Tetragonal Precipitates in Partially Stabilized ZrO_2. *J. Am. Cer. Soc.*, **69** (1986) 564.

Journal of the European Ceramic Society 16 (1996) 833–841

0955-2219(95)00211-1
0955-2219/96/$15.00 +.00

Morphology of Lanthanum Carbonate Particles Prepared by Homogeneous Precipitation

Martin L. Panchula & Mufit Akinc

Department of Materials Science & Engineering, Iowa State University, Ames, Iowa 50011, USA

(Received 10 July 1995; revised version received 22 November 1995; accepted 29 November 1995)

Abstract

The synthesis of lanthanide oxide precursor particles through urea decomposition has received considerable attention over the past few years. It was previously reported by several different workers that the synthesis of spherical, monodispersed light lanthanide ceramic precursor particles was consideably more difficult than the precipitation of spherical particles from the heavy lanthanide elements. These difficulties have been overcome to a large extent by proper choice of processing conditions. This paper describes the synthesis conditions for which dispersed spherical particles and plates may be formed of lanthanum, the lightest of the lanthanide elements. The experimental conditions for the synthesis of these particles is given in the form of morphological diagrams and the chemistry and yield of the process is also reported. The process was also analyzed as a function of time in order to observe the supersaturation and growth regimes. The effect of calcining on the morphology of the particles is also discussed.

1 Introduction

It was previously reported by Akinc and Sordelet[1] that lanthanum, cerium, and neodymium powders precipitated as crystalline basic carbonate particles when urea was used as the precipitating agent. Yttrium, on the other hand, and the heavy rare earths,[2] defined in this paper as those heavier than gadolinium, precipitated as spherical, amorphous particles under similar conditions. Recently, it was shown that the light lanthanides can be precipitated as spherical monodispersed particles through the proper choice of initial conditions[3–6] and by the proper choice of supporting anions.[7] These reports demonstrate the sensitivity of particle morphology to subtle variations in experimental conditions.

The growth of monosized, spherical particles has been explained by two mechanisms. The first mechanism is that of spontaneous accumulation of polymeric species and subsequent particle sharpening as a result of radius dependent particle growth during aging. Formation of latex particles was shown to follow this mechanism. The second mechanism is the aggregation of nuclei to form spherical particles. Bogush and Zukoski[8,9] claimed that formation of silica from tetra ethyl ortho silicate (TEOS) follows the aggregation mechanism. Visible proof of the aggregation mechanism has been reported by Celikkaya and Akinc[10] in the precipitation of zinc sulfide particles from thioacetamide solutions where spherical polycrystalline particles were formed. Nanocrystalline aggregates of sphalerite crystallites were observed in SEM and TEM micrographs.

The accepted precipitation mechanism for well developed euhedral particles is based upon the accumulation of ionic species on the surface of nuclei. Preferential growth planes, as determined by surface energy and kinetic restrictions, will then result in euhedral particle (particles with well defined shapes, faces) formation. A number of colloids were precipitated with either spherical or euhedral morphology with relatively subtle changes in experimental conditions such as kinetics of precipitation. It appears that a third mechanism in the formation of spherical particles is operative such that a fast accumulation of ions will also yield spherical particles.

The present work extends the work of Akinc and Sordelet[1] on the synthesis of crystalline euhedral light lanthanides to precipitate spherical monodispersed lanthanum carbonate particles by homogeneous precipitation using urea as the precipitating agent. Morphological diagrams and process yields for a wide range of initial conditions are reported. Additionally, the influence of calcining on the particle morphology and chemistry is also examined.

2 Experimental Procedure

2.1 Materials

The lanthanum stock solution was prepared by dissolving 99·9% pure La_2O_3 (Molycorp) in nitric

acid (Malinckrodt). The solution was then diluted to approximately 0·5 M with respect to La^{3+} ion and filtered through a 0·22 μm Teflon® membrane (Micron Separations, Inc). It is particularly important for homogeneous precipitation studies that no foreign particles which might act as seed crystals enter into the reaction vessel. For this reason, the lanthanum solution was acidified through the addition of excess nitric acid and heated to remove what appeared to be spontaneous lanthanum carbonate formation within the storage container. The urea stock solution, with a concentration of 6·75 M, was prepared by dissolving the appropriate amount of urea in deionized water and filtering through a 0·2 μm Teflon® membrane. This solution was then kept refrigerated to prevent decomposition of urea during storage.

2.2 Powder synthesis

Appropriate amounts of deionized water and lanthanum stock solution were combined in a 400 cm^3 beaker. The pH of this solution was then adjusted at room temperature by adding ammonium hydroxide or nitric acid. The pH of the solution was continuously recorded using a temperature compensated pH meter (Fisher Accumet 810 MP). The beaker was then covered and placed in a circulated hot water bath which was set at 95°C. When the solution reached 95°C, the appropriate amount of the urea stock solution was added to bring the solution up to 250 cm^3 and the beaker resealed and placed in the water bath. The solution was aged for 90 min from the time at which visible nucleation occurred. At the end of the aging period, the beaker was placed in a cold water bath to quench the reaction. Suspension was then centrifuged until a clear supernatant was obtained. The centrifugation was repeated twice with water and once with acetone. After the acetone wash, the precipitate was dried in air at 85°C for overnight.

2.3 Powder characterization

The powder morphology was examined using a scanning electron microscope (JEOL JSM 6100). Thermal decomposition of precursor particles was studied by a thermogravimetric analyzer (Seiko TGA/DTA 300). Approximately 10–40 milligrams of the sample, was heated to 900°C at a rate of 3° min^{-1} in a dry air atmosphere with a flow rate of 100 cm^3 min^{-1}. Crystal structure of the powders was studied by X-ray powder diffraction unit (Scintag XDS 2000). The powder diffraction patterns were compared against JCPDS standards using the Diffraction Management System 2000 software package.

3 Results and Discussion

3.1 Precipitation process

Homogeneous precipitation by urea can be considered as self regulating due to equilibria established between carbonic acid and ammonia which are released by urea decomposition. Dissociation constants of carbonic acid and ammonia are comparable that in the absence of strong acids or bases, the concentrations of OH^- and $CO_3^=$ ions are maintained within a narrow range during precipitation. However, by changing the initial pH of the solution one can affect the quantity of urea which will decompose before supersaturation is achieved. In this way, the chemistry of the solution, the $[OH^-]/[CO_3^=]$ ratio for instance, can be adjusted.

Figure 1 shows the variation of pH with time for solutions with a different initial pH. As the plots clearly depict, the pH of the solutions is essentially identical after the initial 5 min. The nucleation, growth, and cation exhaustion can all be seen by measuring the pH of the system during precipitation. This can be seen most easily at low cation concentrations and relatively high pH solutions. Maxima observed in the early stages represent the critical supersaturation and onset of nucleation. The pH decrease with particle growth is expected as the precipitation of any carbonate will remove $CO_3^=$ ions from the solution, shifting the $HCO_3^- = CO_3^= + H^+$ equilibrium to right and releasing H^+ ions, thus decreasing the pH of the solution. Similarly, if the precipitate involves hydroxides, removing OH^- ions from the medium results in a decrease in pH. Once the cation is exhausted, however, and if there is sufficient urea remaining in solution, the pH will start to increase again signalling the end of precipitation. The differences seen between the low and high initial pH solutions are due to the time it takes for the low initial pH solutions to decompose sufficient urea

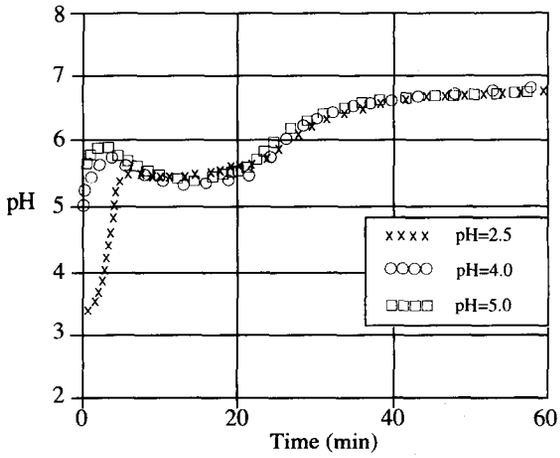

Fig. 1. pH–time curve for lanthanum precipitation from 0·005 M lanthanum solutions of various initial pH (prior to urea addition) and with an initial urea content of 0·054 M and a reaction temperature of 95°C.

to increase the pH to the point where precipitation can occur. This additional time allows more urea to decompose prior to precipitation and this will affect the total carbonate content which will, in turn, affect the ionic strength of the solution. The additional charged species will effectively buffer the solution making the supersaturation region more difficult to detect.

3.2 Morphology

As stated earlier, amorphous spherical particles should be the result of the addition of polymeric, or at least complexing, species to nuclei. On the other hand, the growth of euhedral particles is caused by the addition of ions to the surface of a nucleus with crystalline faceting occurring due to fast and slow growth directions. Lanthanum carbonate particles have been precipitated in this study with both spherical and 'square planar' morphologies (Fig. 2). The morphological diagrams show the effects of the various initial conditions on the resulting morphologies as depicted in Table 1.

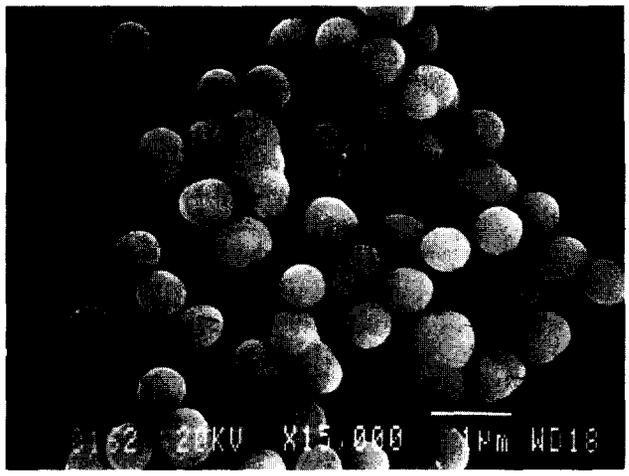

(a)

(b)

Fig. 2. Micrographs of the sperical and square planer morphologies as described above. Notice the spherical particles which have grown on the faces of the square planar precipitates.

Table 1. Plot of particle morphology map as a function of lanthanum ion concentration and initial pH. Reaction temperature T = 95°C. S = Spherical, E = Euhedral, SP = Square planar

Initial pH	*Urea*	*Cation concentration, moles/l*			
		0·005	*0·025*	*0·045*	*0·65*
5·0	0·54	S	E, S	E	—
4·0	0·54	S	E, S	E	—
2·5	0·54	S, E	E, S	E, S	—
1·0	0·54	E	E	E	—
5·0	0·27	S, E	S, E	E	—
4·0	0·27	S, E	SP, S	SP, S	SP, S
2·5	0·27	S, E	SP, E, S	SP, S	SP, S, E
1·0	0·27	E	E		

There are essentially two interesting morphologies created in this system; spheres (S) and square planar (SP) particles. The spheres generally have a smooth surface with few or no surface features present. This suggests an amorphous growth process.

The square planar morphology is perhaps the more interesting. Generally they are 3 μm on a side yet only 0·2 μm thick. In fact, they are translucent to the 20 keV electron beam when viewed perpendicularly to the flat face. A high percentage of the square planar particles have what appear to be spherical particles growing on their faces. Presumably, these particles nucleated and grew after the square planar particles were formed.

The other morphologies mentioned in Table 1 are highly agglomerated with a wide variety of particle morphologies as one would expect from intermixed nucleation and growth processes. The particles described as euhedral are large (> 5 μm) particles with characteristic features exhibited by crystalline materials such as sharp angles and edges.

3.3 Yield

The yield of this process, defined as percentage of initial cation precipitated, is primarily dependent upon the amount of urea decomposed. The amount of urea decomposed at time t is given by the difference between the initial urea concentration, U_0, and urea concentration, U_t, at time t:

$$U_d = U_0 - U_t \tag{1}$$

Where U_d is the concentration of urea decomposed up to time, t.

$$U_t = U_o\,[\exp(-kt)] \tag{2}$$

Substituting this back in eqn (1) results in

$$U_d = U_o\,[1-\exp(-kt)] \tag{3}$$

On the other hand, rate of urea decomposition is given by:[1]

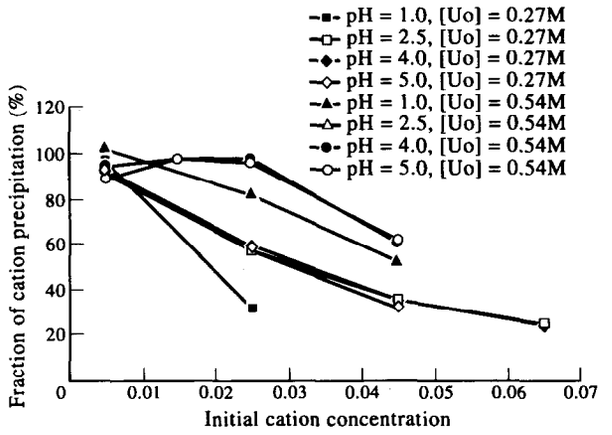

Fig. 3. Yield of the precipitation runs as a function of initial conditions. The reaction temperature was held constant at 95°C.

$$k = (4{\cdot}57 \times 10^{10}\ \text{min}^{-1}) \exp\left(\frac{-96{\cdot}127\ \text{kJ/mole}}{RT}\right) \quad (4)$$

Where R is the gas constant and T is the temperature in degrees Kelvin.

Obviously, both temperature and initial urea concentration can play a large role in the amount of urea decomposed as a function of time. In a related study we showed how temperature, and hence the decomposition rate, affected the yield of neodymium and europium samples.[3] In this paper we show how initial urea concentration and pH affect the yield. As can be seen in Fig. 3, there are four sets of curves. The curves for pH of 2·5, 4, and 5 are grouped together but are separated depending on the concentration of initial urea. The pH=1 samples generally have lower yields than the other pH levels, though this too is dependent on initial urea concentration. The apparent drop in yield at very low concentrations is due to the fact that small sample losses during sample transfer and centrifugation correspond to a larger fraction of the total cations in the solution. The separate curves for the pH=1 condition can only be explained by the fact that much longer times were necessary for the urea to decompose and produce sufficient quantities of hydroxide ions to raise the pH to the point where precipitation could occur. Therefore, initial urea concentration, $[U_0]$, was effectively reduced prior to precipitation. Low initial pH also results in higher $[CO_3^=]/[OH^-]$ ratio during nucleation and growth which will likely alter the chemical composition and morphology of the particles produced.

3.4 Thermal decomposition

The thermal decomposition of the precipitated powder depends upon the chemistry and morphology of the powders. For example, Fig. 4 shows the weight loss on heating of the monodispersed spherical particles (upper curve) and of the square planar precipitates, (lower curve). One subtle difference between the two curves is that the spherical particles appear to have slightly smoother weight loss up to the formation of the dioxycarbonate compared to the square planar particles. This is believed to be due to the degree of crystallinity of the samples and not to any large differences in particle chemistry. Spherical particles also exhibit a small weight loss below 100°C, perhaps due to evolution of adsorbed water. Previous experiences with the light lanthanides precipitated and dried in the same manner as used here have given approximately two waters of hydration for the simple carbonate precipitate. The calculated weight loss data presented in Table 2 are based upon the assumption that the precipitated particles were in the form of $La_2(CO_3)_3 \cdot 1{\cdot}4H_2O$. The experimental values shown in the table are averaged from five TGA runs on powders precipitated under different conditions. The difference between the high and low experimental values at

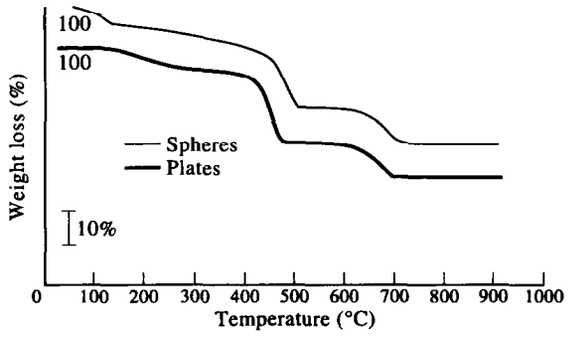

Fig. 4. Weight loss on heating of spherical (upper TGA curve) and square planar (lower TGA curve) lanthanum particles on heating in zero air.

Table 2. Comparison of experimental and calculated weight loss values for precipitated lanthanum carbonate particles with an approximate composition of $La_2(CO_3)_3 \cdot 1{\cdot}4H_2O$

Resultant particle chemistry	*Reaction*	*Calculated weight loss*	*Experimental weight loss*
Dehydrated carbonate	$La_2(CO_3)_3 \cdot 1{\cdot}4H_2O \rightarrow La_2(CO_3)_3$	7·3%	4·9% 50–300°C
Dioxycarbonate	$La_2(CO_3)_3 \rightarrow La_2O_2CO_3$	19·2%	19·8% 423°C
Oxide	$La_2O_2CO_3 \rightarrow La_2O_3$	11·9%	11·7% 630°C

each weight loss step was less than 3%. In Table 2 the sample weight loss from the dehydrated carbonate to the dioxycarbonate and the dioxycarbonate to the oxide are identical within the experimental error.

3.5 X-ray analysis

The crystal structure of the spherical and square planar particles was analyzed by X-ray powder diffraction. The spherical particles gave an amorphous pattern as expected. The square planar particles, however, gave relatively weak diffraction patterns making phase identification difficult (Fig. 5). In addition, because of the two-dimensional nature of the particle growth habit, the relative peak intensities were probably greatly biased. Based upon TGA and chemical analysis, it was expected that the particles would give the lanthanite ($La_2(CO_3)_38H_2O$) diffraction pattern. It appears that the lanthanite structure was lost in favor of an amorphous structure upon drying at 85°C leaving only the minor phase, the monoxycarbonate structure ($La_2O(CO_3)_2xH_2O$) as the crystalline phase. There is some evidence to support the idea that the lanthanite structure does not completely collapse, in that some residual lanthanite peaks including the one at $2\theta=18{\cdot}4°$ survived the drying process. This peak corresponds to (020) plane in the orthorhombic structure. The intensity of this peak varies from sample to sample, possibly the result of different drying conditions. The crystal is a layered structure with lanthanum and carbonate ions forming planes which are separated by planes of water molecules.[11,12] It is possible that certain directions in this highly hydrated crystal structure would collapse first leaving other planes relatively untouched. The observed peak does not correspond to any other lanthanum phase in the JCPDS files. The crystalline phase of anhydrous lanthanum carbonate can only be produced from the lanthanite phase after drying the sample in a vacuum and then heating to 430°C in a 100 kPa CO_2 atmosphere.[13]

The coefficient x for the number of crystalline waters in the monoxycarbonate formula can vary between 1 and 2, just as the TGA analysis suggested. It has been reported by previous workers[14] that drying the eight hydrate lanthanite phase at less than 100°C or placing it in a vacuum results in a primarily amorphous phase due to dehydration. This effect is shown in Fig. 6. The room temperature dried samples exhibit distinct peaks of $La_2(CO_3)_38H_2O$. There are additional, albeit much weaker peaks due to partially hydrated monoxycarbonate, ($La_2O(CO_3)_2xH_2O$). After drying at 85°C the major crystalline phase appears to be the partially hydrated monoxycarbonate, $La_2O(CO_3)_2xH_2O$. The precipitate appears to be mostly amorphous with a small fraction of crystalline phase (monoxycarbonate). Since the particles are small and exhibit large dimensional anisotropy, the peak intensities are questionable. The phase which was assigned as the monoxycarbonate might also be identified as the basic carbonate phase. In fact, chemically it makes no difference whether the particles are monoxycarbonate with one water of hydration, ($La_2O(CO_3)_2H_2O$) or basic carbonate with no waters of hydration, ($2LaOHCO_3$). The basic

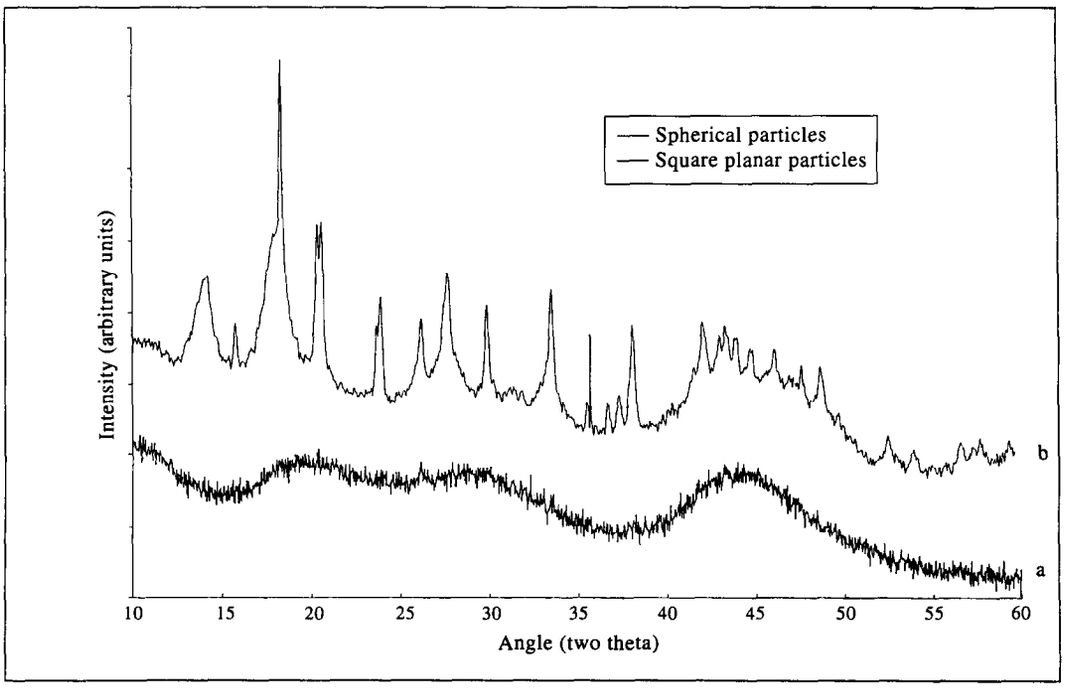

Fig. 5. X-ray diffraction pattern of (a) spherical, (b) square planar particles.

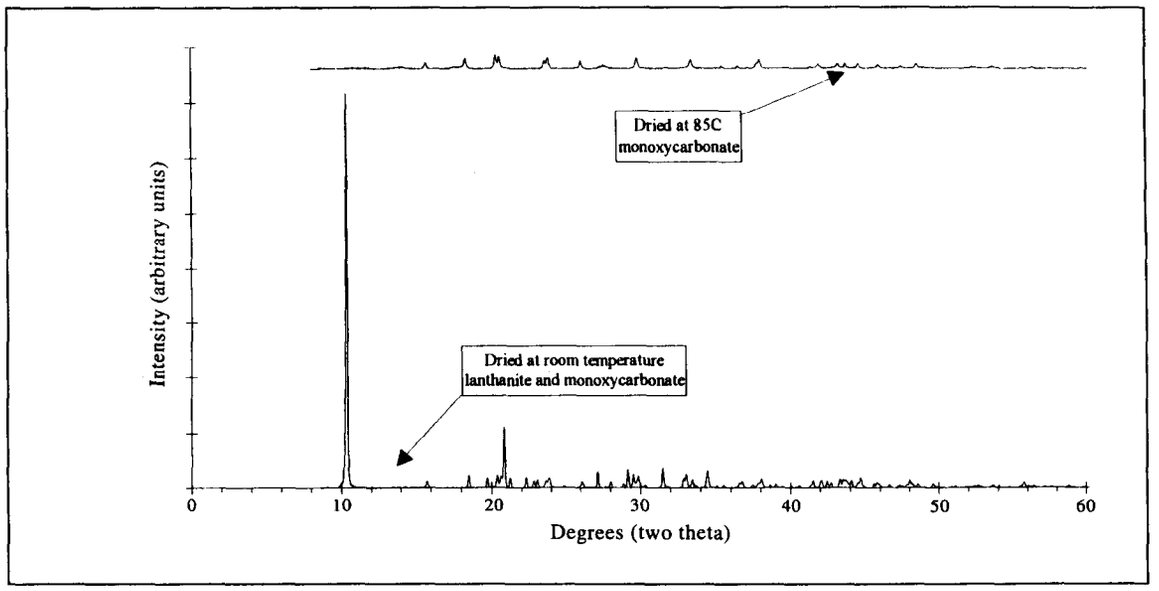

Fig. 6. Effect of drying conditions on crystalline structure as observed through X-ray diffraction

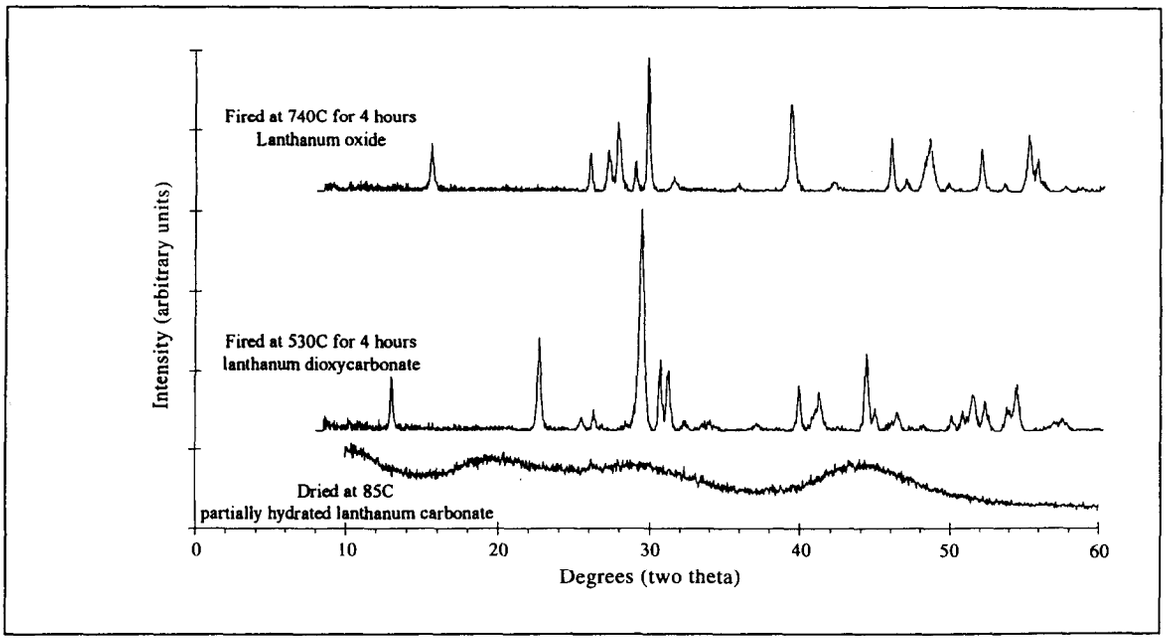

Fig. 7. Effect of firing on crystalline phases and X-ray peak intensity of spherical particles.

carbonate was the only phase observed in heavy lanthanides synthesized by a similar procedure, but without further evidence the structure of this phase is ambigious.

The X-ray diffraction patterns of the powders at 530 and 740°C are shown in Figs 7 and 8. Figure 7 shows that as-precipitated amorphous spherical particles have decomposed and ordered themselves into a dioxycarbonate structure as was predicted by thermogravimetric analysis. The square planar particles show the same trend, with the dioxycarbonate being the stable form at 530°C and the oxide the stable form at 740°C.

3.6 Effect of heating on particle morphology

The influence of calcining on the particle morphology was investigated, heating the spherical and square planar particles in air to 530 or 740°C for 4 h. Both samples were converted to oxide at 740°C. The particle morphology as a function of heat treatment is shown in Figs 9 and 10. The spherical particles became slightly faceted after being heated to 530°C. At 740°C, the particles became crystalline. Monodispersity and overall size and shape of the precursor particles are retained (Fig. 9). The square planar particles showed only subtle changes on being heated to 530°C. The surfaces of the particles became rough

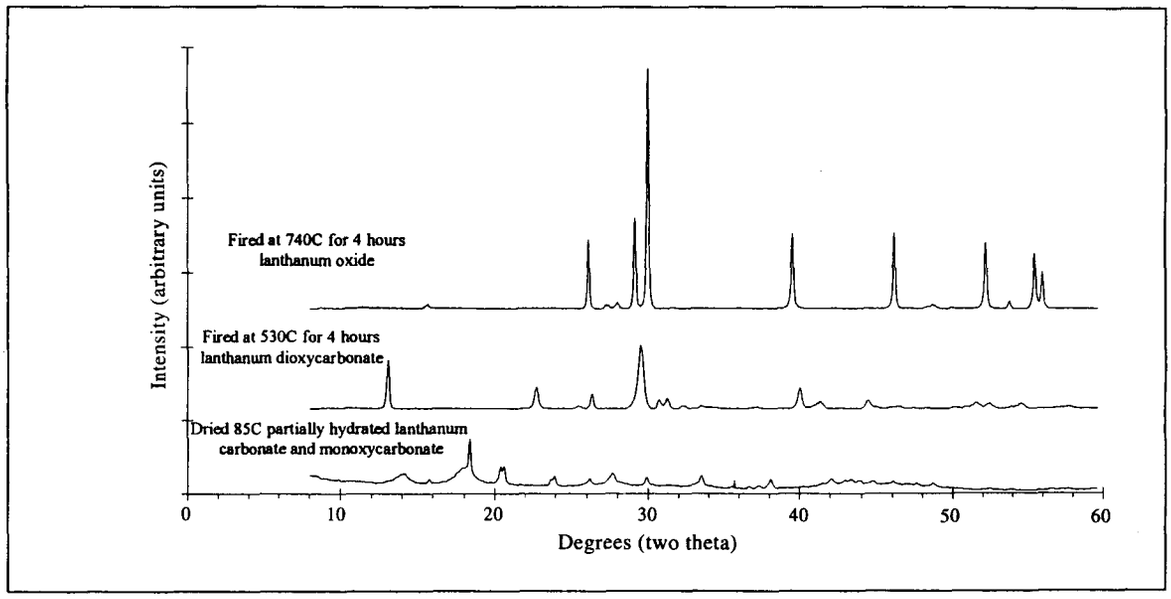

Fig. 8. Effect of firing on crystalline phases and X-ray peak intensity of square planar particles.

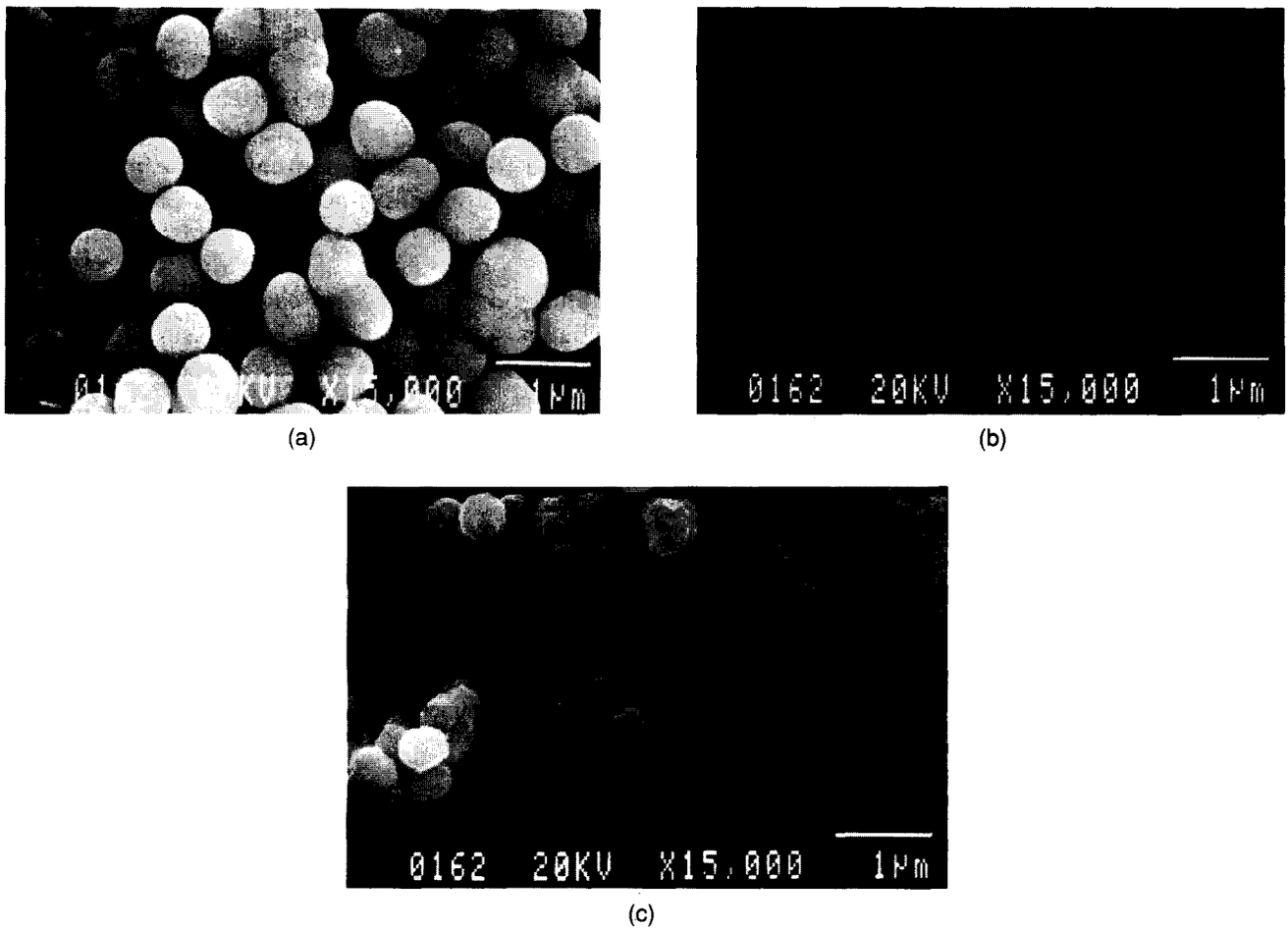

Fig. 9. Effect of heating on spherical lanthanum particle morphology: (a) original particles; (b) after heating to 530°C for 4 h, and (c) after heating to 740°C for 4 h.

and appear to indicate polycrystallinity. At 740°C, the changes are more obvious. The previously smooth surfaces now consist of smaller grains which are sintered together while maintaining the shape of the original plate. The spherical growths on the plates have gone through the same changes as the monodispersed particles shown in Fig. 9 with perhaps more sintering to the surface of the

(a)

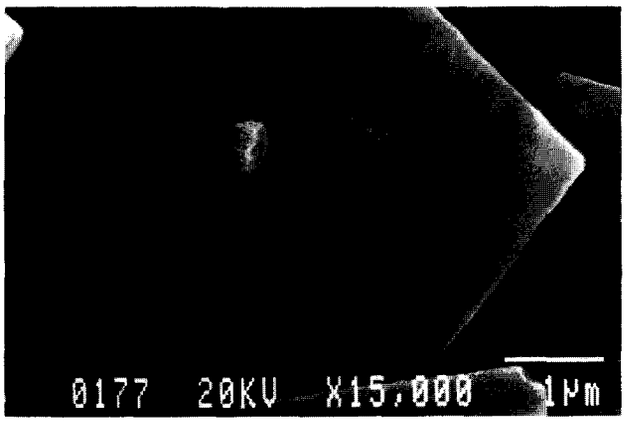

(b)

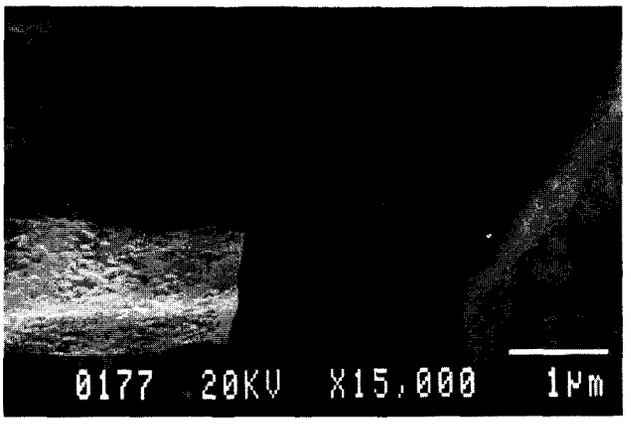

(c)

Fig. 10. Effect of heating on square planar particle morphology: (a) original particles; (b) after heating to 530°C for 4 h, and (c) after heating to 740°C for 4 h.

square planar particles due to the larger initial contact area.

4 Conclusion

Spherical and square planar lanthanum carbonate particles have been synthesized by homogeneous precipitation employing urea as the precipitating agent. It is apparent that the two growth mechanisms are quite different, yet can be achieved in very similar systems. This result underscores the importance of process and variable control when using homogeneous precipitation for the synthesis of ceramic powders. The cause of the different morphologies is derived from two requirements which have been met in different ways resulting in two distinctly different morphologies. The two requirements are the degree of supersaturation before nucleation and the growth rate. At very low cation concentrations and high urea concentrations the supersaturation is relatively large, resulting in a large burst of nuclei and very quick growth. This growth period would be relatively short, lasting only until the remaining cation is completely precipitated. This mechanism has resulted in spherical particles. On the other hand, higher cation concentrations form stable nuclei earlier in the process, thereby keeping the supersaturation level relatively low. Under these conditions a slow growth of the nuclei is expected. Such conditions would allow for formation of euhedral particles. A direct examination of the cation concentration as a function of time would offer great insights into the growth mechanisms of this system and has not been carried out yet. This study, however, provided a method for producing lanthanum carbonate particles of different morphologies and plausible explanation for their formation mechanisms. This study also demonstrated for the first time that spherical, submicron size particles can be synthesized from aqueous solutions at ambient pressures.

References

1. Akinc, M. & Sordelet, D., Preparation of Yttrium, Lanthanum, Cerium, and Neodymium Basic Carbonate Particles by Homogeneous Precipitation. *Advanced Ceramic Materials*, **2** (3A) (1987) 232–8.
2. Akinc, M., Sordelet, D. & Munson, M., Formation, Structure, and Decomposition of Lanthanide Basic Carbonates. *Advanced Ceramic Materials*, **3**(3) (1988) 211–16.
3. Panchula, M. & Akinc, M., Precipitation of Neodymium and Europium Ceramic Precursor Particles through Urea Decomposition. To be published.
4. Kang, Z. C., Li, T. Z. & Eyring, L., The Preparation of Hydroxycarbonate Colloidal Particles of Individual and Mixed Rare Earth Elements. *Journal of Alloys and Compounds*, **181** (1992) 477–82.
5. Chou, K., Lin, C., Hoh, Y. & Miao, Y., Effect of Hydrothermal Synthesis Conditions on the Morphology of Lanthanum Hydroxycarbonate Colloids. *Journal of the Chinese Institute of Chemical Engineering*, **22**(4) (1991) 241–6.
6. Chu, Xi, Chung, W. & Schmidt, L. D., Sintering of Sol–Gel–Prepared Submicrometer Particles Studied by Transmission Electron Microscopy. *Journal of the American Ceramic Society*, **76**(8) (1993) 2115–18.
7. Matijevic, E. & Hsu, W. P., Preparation and Properties of Monodispersed Colloidal Particles of Lanthanide Compounds I. Gadolinium, Europioum, Terbium, Samarium, and Cerium (III). *Journal of Colloid and Interface Science*, **118**(2) (1987) 506–23.

8. Bogush, G. H. & Zukoski, IV, C. F., Studies of the Kinetics of the Precipitation of Uniform Silica Particles through the Hydrolysis and Condensation of Silicon Alkoxides. *Journal of Colloid and Interface Science,* **142** (1) (1991) 1–18.
9. Bogush, G. H. & Zukoski, IV, C. F., Uniform Silica Particle Precipitation: An Aggregative Growth Model. *Journal of Colloid and Interface Science*, **142**(1) (1991) 19–34.
10. Celikkaya, A. & Akinc, M., Preparation and Mechanism of Formation of Spherical Submicrometer Zinc Sulfide Powders. *Journal of the American Ceramic Society*, **73**(8) (1990) 2360–5.
11. Shinn, D. B. & Eck, H. A., The Crystal Structure of Lanthanum Carbonate Octahydrate. *Inorganic Chemistry,* **7**(7) (1968) 1340–5.
12. Dal Negro, A., Rossi, G. & Tazzsoli, V., The Crystal Structure of Lanthanite. *American Minerologist,* **62** (1977) 142–6.
13. Leskela, M. & Niinisto, L., *Handbook on the Physics and Chemistry of Rare Earths*, ed. K. A. Gschneidner & L. Eyring, Chapter 56, Vol 8, North-Holland, New York, 1986.
14. Sawyer, J., Caro, P. & Eyring, L., Hydroxy-carbonates of the Lanthanide Elements, *Revue de Chimie Mineral*, **10** (1973) 93–104.

Journal of the European Ceramic Society 16 (1996) 843–849

S0955-2219(96)00001-5
0955-2219/96/$15.00 + .00

Sintering and Microstructural Investigations on Combustion Processed Mullite

R. Gopi Chandran,[a] B. K. Chandrashekar,[b] C. Ganguly[c] & K. C. Patil[a*]

[a]Department of Inorganic and Physical Chemistry, Indian Institute of Science, Bangalore-560 012, India
[b]Ceramic Technological Institute, Bharat Heavy Electricals Ltd, Bangalore-560 012, India
[c]Radiometallurgy Division, Bhabha Atomic Research Centre, Bombay-400 058, India

(Received 20 September 1994; revised version received 30 November 1995; accepted 5 December 1995)

Abstract

Various grades of mullite have been prepared by the combustion route using different fuels and silica sources of the redox mixture. Sintering behaviour and microstructure of combustion processed mullite have been investigated. Pure mullite sintered at 1650°C showed 3% shrinkage and was porous. The microstructure shows the presence of equiaxed grains. Hot isostatic pressing (100 MPa, 1500°C, 30 min) followed by sintering at 1700°C yielded >95% theoretical density. Mullite with 5 wt% of Y_2O_3 or MgO sintered at 1650°C achieved high density (≈95% theoretical density) with a shrinkage of 18 and 22% respectively. The microstructure showed the presence of anisotropic elongated mullite grains and corundum particles. The enhanced densification of mullite with additives is attributed to the formation of liquid phase which facilitates diffusion.

1 Introduction

Highly pure mullite, containing less than 0·1 wt% of alkali and alkaline-earth oxides, is expected to be a superior high-temperature structural material, since its bending strength and creep resistance do not degrade even at 1200°C or more.[1,2] Similar to other crystalline ceramics with a high degree of covalent bonding, mullite also requires high temperatures for densification. This is due to its relatively low bulk and grain boundary diffusion coefficients.[3] Several processes used for the synthesis of mullite have been reviewed.[3] Recently we reported[4,5] the preparation of mullite by the combustion process using aluminium nitrate, silica fume and urea/diformyl hydrazine mixtures. At present, we report on the sintering behaviour of mullite powders obtained by the combustion of different redox mixtures, e.g. aluminium nitrate, fumed silica/fused silica/TEOS and urea/diformyl hydrazine ($C_2H_4N_2O_2$, DFH)/ carbohydrazide (CH_6N_4O, CH) as well as by the incorporation of extra amount of redox mixture (NH_4NO_3/NH_4ClO_4 and urea).

2 Experimental

Mullite has been prepared by the combustion of aluminium nitrate (98·5%, Glaxo, India), silica fume (99·9%, Chemicals and Plastics, India, surface area ≈200 m^2/g) and urea/DFH fuel according to the procedure described earlier.[4,5] DFH and CH were prepared according to the procedure described in the literature.[6,7] Mullite was prepared by the combustion of stoichiometric amounts of redox mixtures at 500°C. Details of stoichiometry calculation and combustion are given elsewhere.[4]

Various grades of mullite (M1–M7) were obtained by using different fuels, source of silica and addition of extra amount of redox mixture, e.g.:

- M1 — aluminium nitrate (20 g), silica fume (1·066 g) and urea (8 g);
- M2 — aluminium nitrate (10 g), silica fume (0·533 g), ammonium perchlorate (5 g), and urea (6·1 g);
- M3 — aluminium nitrate (10 g), ammonium nitrate (10 g), silica fume (0·533 g) and urea (10·5 g);
- M4 — aluminium nitrate (20 g), silica fume (1·066 g) and carbohydrazide (8·8 g) (CH_6N_4O, CH);
- M5 — aluminium nitrate (20 g), silica fume (1·066 g) and DFH ($C_2H_4N_2O_2$) (8·8 g);
- M6 — aluminium nitrate (20 g), fused silica (1·066 g) and urea (8 g) and
- M7 — aluminium nitrate (20 g) TEOS (2·7 g) and urea (8 g).

The foamy mullite obtained by combustion of redox mixtures was crushed and ground using

* To whom correspondence should be addressed.

an electric agate pestle and mortar for 3 h and used to investigate sintering and microstructure. The mullite powders were uniaxially pressed (50 MPa) to compacts of 13 mm diameter and 3–5 mm thickness, and used for sintering studies. Mullite powder derived by the urea process was milled in a pulverizer using alumina balls (3 h) to study the sintering characteristics in comparison with the unmilled powder. Particle size analysis was done on a Seishin Micron Photosizer model SKC 2000 which operates on the light scattering principle employing sedimentation. Surface area measurements were made by nitrogen adsorption employing a Micromeritics AccuSorb 2100E instrument. The temperature of the incandescent flame which appears during combustion was measured using an optical pyrometer model-120, Toshniwal Company, India. Bulk densities of the sintered compacts were measured by the Archimedes principle using distilled water. The percentage theoretical densities of sintered pellets were calculated assuming the theoretical density of mullite as 3·17 g/cm^3 (JCPDS 15-776). Sintering studies of mullite (M1) were carried out with different additives, e.g. Y_2O_3, La_2O_3, CeO_2, TiO_2, ZrO_2 and MgO. The percentage theoretical density was determined using the density of mullite and additives given in the powder diffraction file.[8] Dilatometric studies were carried out on M1 powder compacted (50 MPa) to a pellet of 11 mm diameter and 4–5 mm thickness using a Netzsch 402 E/7 dilatometer in the temperature range 20–1650°C at a heating rate of 10°/min in N_2 atmosphere. Dynamic shrinkage studies were also carried out on mechanically mixed 5 wt% Y_2O_3 and MgO-M1 powders. Microstructures of the sintered samples were observed using S-360 Cambridge scanning electron microscope (SEM) and chemical composition was determined by an energy dispersive X-ray (EDX) detector attached to the SEM. The morphology of calcined mullite (M1) powders was studied using a Philips EM 301 transmission electron microscope (TEM) operating at 100 kV.

3 Results and Discussion

Various phases present in the combustion derived M1–M7 were identified by the XRD and are summarized in Table 1 along with their densities and particle sizes. The M1, M4 and M5 mullites were essentially weakly crystalline with a broad peak at ≈26° (2θ) in the powder XRD pattern. Complete mullitization occurred at ≈1300°C.[4,5] Mullites M2 and M3 (as-formed) prepared using extra amount of redox mixture (NH_4NO_3/NH_4ClO_4 and urea) were fully crystalline.[4] Changing the source of silicon to fused silica (particle size ≈10 μm) or TEOS in the combustion mixture showed the presence of α-Al_2O_3 and amorphous silica. This could be due to the poor reactivity of fused silica and TEOS. Formation of mullite appears to be facilitated by silica fume due to its greater reactivity coupled with colloid formation. Thus, silica fume appears to be the ideal source of Si for the combustion synthesis of mullite (M1–M3). Further, formation of stoichiometric mullite (3:2) was confirmed by preparing various aluminosilicate powders $xAl_2O_3{\cdot}2SiO_2$, where x = 1–4, by the combustion of aluminium nitrate, silica fume and urea using different mole ratios of Al:Si. The different crystalline phases formed after calcination (1400°C) are shown in Table 2. Stoichiometric mullite (x = 3) gave XRD pattern of pure mullite while the one with excess alumina (x = 4) and

Table 1. The crystalline products of combustion and bulk density*

Mullite	*Phases*	*50% average size (μm)*	*Bulk density (% theoretical)*
M1	Mullite,# θ-Al_2O_3		
Unmilled		8·0	51
Milled		4·0	61
M2	Mullite	2·4	55
M3	Mullite	4·5	55
M4	Mullite#	4·2	61
M5	Mullite#	3·9	57
M6	α-Al_2O_3	5·8	51
M7	Mullite,s α-Al_2O_3	6·3	56

*Sintered at 1600°C, # weakly crystalline, s. small amount.

Table 2. Surface area and phases of aluminosilicate $xAl_2O_3{\cdot}2SiO_2$ (x = 1–4) powders calcined at 1400 °C, 2 h

Aluminosilicate	*Surface area $m^2\,g^{-1}$ (as-formed powders)*	*Phases*
$1Al_2O_3{\cdot}2SiO_2$	201	Mullite Cristobalite Corundum
$2Al_2O_3{\cdot}2SiO_2$	55	Mullite Cristobalite
$3Al_2O_3{\cdot}2SiO_2$(M1)	45	Mullite
$4Al_2O_3{\cdot}2SiO_2$	20	Mullite Corundum

silica (x=1) showed the presence of corundum and cristobalite respectively besides mullite as expected.

The specific surface areas of as-prepared aluminosilicate powders vary from 20 m^2/g to 200 m^2/g (Table 2). The surface area of as-prepared stoichiometric mullite is 45 m^2/g which increased to 200 m^2/g for $1Al_2O_3{\cdot}2SiO_2$. This increase in surface area could be attributed to the amorphous nature of the sample and also due to the very low flame temperature (900°C) compared to the $4Al_2O_3{\cdot}2SiO_2$ (temperature ≈1400°C), which had the lowest surface area, 20 m^2/g. Thus, the surface area of aluminosilicates (Al_2O_3–SiO_2 system) appears to be controlled by the alumina content and processing conditions.

3.1 Dilatometry and sintering of mullite

The dilatometric curve of M1 compact is shown in Fig. 1. The shrinkage curve shows two clearly defined zones:

(i) Negligible shrinkage took place up to 1000°C and

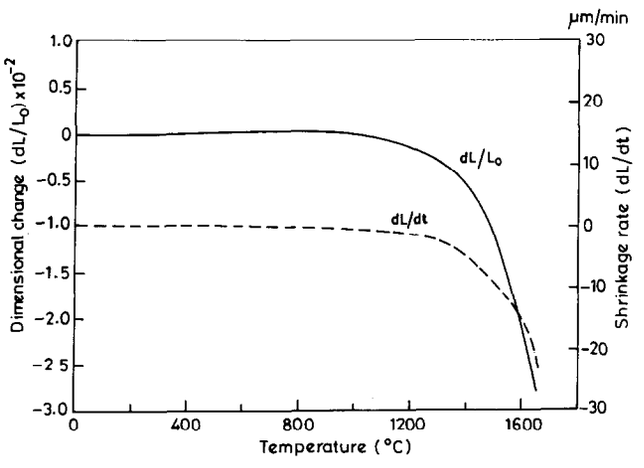

Fig. 1. Dynamic shrinkage curve of M1.

(ii) Between 1100 and 1650°C the total linear shrinkage was less than 3% with a shrinkage rate of ≈25 μm/min.

The green density of M1 uniaxially pressed at 50 MPa was 1·5264 g/cm^3 which on sintering at 1650°C (2 h) became 1·6854 g/cm^3. The milled powder attained a density of 1·9337 g/cm^3. The TEM of M1 particles is shown in Fig. 2. It could

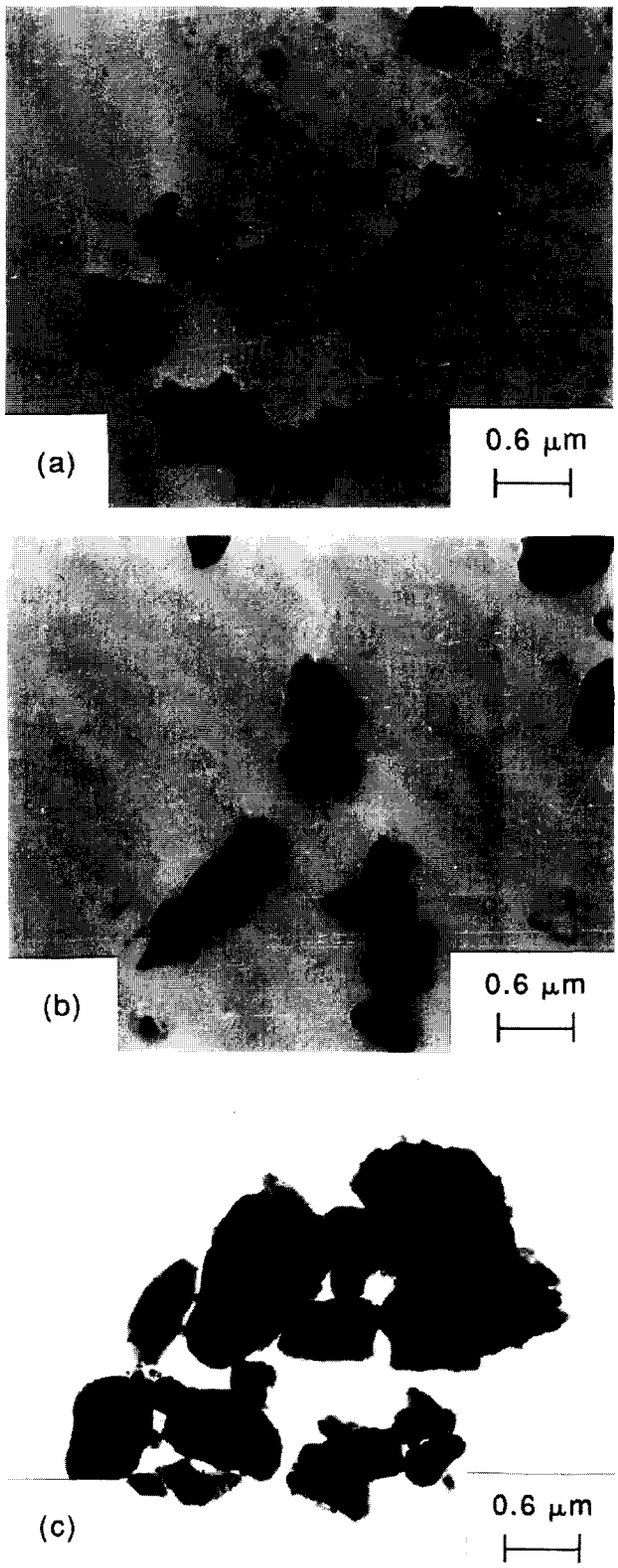

Fig. 2. TEM of M1(a) calcined at 1000°C; (b) calcined at 1200°C and (c) calcined at 1400°C for 1 h.

be seen that the particles have an irregular plate morphology which remains so even after calcination at 1400°C. The low density achieved on sintering could probably be due to the irregular plate morphology of the particles, lower green density and also partly due to the appearance of flame during combustion which induces mullite[9,10] crystallization and neck growth processes. It is interesting to note that combustion derived mullite appears to behave like reaction sintered mullite rather than sol–gel mullite although particle sizes are comparable to sol–gel powders. The as-formed combustion derived powders are crystalline and probably is the reason for lower density achieved as no viscous sintering was possible.

3.2 Effect of processing parameters on particle size and density of mullite

The particle size distributions of the mullite powders M4 and M5 are shown in Fig. 3 and compared with M1. Mullite powders prepared by CH (M4) and DFH (M5) processes have smaller particle size (4 μm). It is comparable to milled mullite M1 (Table 1). Though the powders were fine, the final density of sintered mullite was very low. Lowering the particle size results in increase of the neck growth processes leading to aggregate formation. Aggregates are known[3] to hinder sintering of the compact. In the case of samples wherein mullite crystallites are nucleated, higher density could be attained usually by long milling times[3,9] or hot pressing techniques.[10] Milling appears to help in the breaking of the aggregates ($\geq$0·5 μm) but introduces contamination from the grinding media. Sintered densities of mullite compacts prepared from different size mullites are listed in Table 1. It could be seen that the sintered mullite compacts are porous (Table 1). In addition to reducing the average particle size, sintering can also be enhanced by improving the packing characteristics of the green compact, i.e. increasing green density, decreasing the average pore size and eliminating large defects. Uniaxially pressed samples tend to have relatively large inhomogeneities as a result of the initial packing irregularities created during die filling and the non-uniform stress gradients generated during compaction.[3]

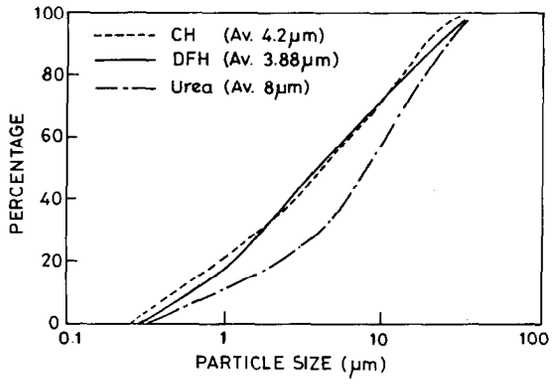

Fig. 3. Particle size distributions (cumulative weight percentage) of mullite prepared using urea (M1), CH (M4) and DFH (M5) processes.

Mullite (M1) when pressed uniaxially and sintered at 1600°C, 2 h achieved a density of 51% theoretical while when pressed cold isostatically (210 MPa) and sintered at 1600°C achieved a density of 63%. Higher density (>95%) could be achieved by hot isostatic pressing (100 MPa, 1500°C, 30 min) followed by sintering at 1700°C, 30 min. The microstructure of the isostatically pressed and sintered M1 (Fig. 4) shows the porous nature of the sample as expected from the density measurements. The microstructure consisted of large agglomerates interconnected by pores (Fig. 4(a)); each aggregate, however, was fully dense and was composed of submicrometer equiaxed grains (Fig. 4(b)). It is generally believed that the presence of a liquid phase causes anisotropic grains. It is known[11] that a metastable SiO_2-rich liquid phase can exist even at temperatures as low as 1250°C in the case of diphasic gels. Mullite processed from colloidal (diphasic) gel[12] is rich in Al_2O_3 resulting

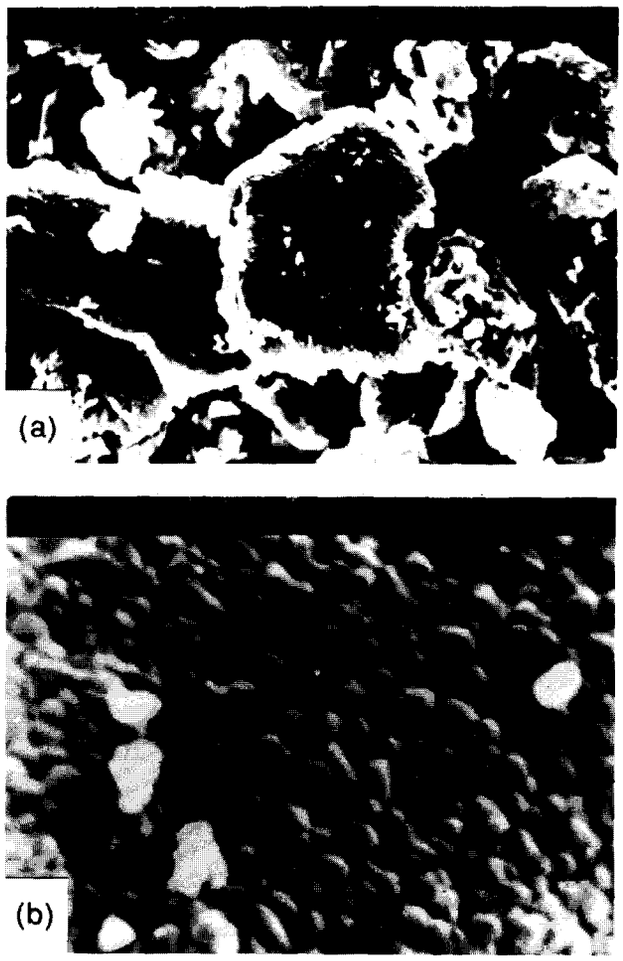

Fig. 4. (a) The microstructure of M1 sintered at 1600°C and (b) microstructure at higher magnification.

Table 3. Bulk density of mullite (M1) + additives sintered at 1650°C

Additive (5 wt%)	*Bulk density (g/cm³)**
—	1·68 (53)
Y_2O_3	3·12 (95·7)
MgO	3·06 (95·9)
TiO_2	2·07 (64·3)
ZrO_2	1·89 (57·4)
CeO_2	2·89 (85·8)
La_2O_3	2·78 (83·2)

*Values in the parentheses correspond to % theoretical density.

in a SiO_2-rich liquid phase. However, there are other reports of equiaxed grains from diphasic gels[13,14] and anisotropic grains from single phase gels.[15–17] Though combustion processed mullite starts from diphasic redox mixture, the microstructure was composed of submicrometer equiaxed grains indicating the absence of liquid phase and hence very low shrinkage during sintering (Fig. 1). Li and Thomson[17] have shown the importance of chemical composition on the morphology of mullite grains. They could make mullite with anisotropic and equiaxed grains from both single phase and diphasic gels by controlling the Al_2O_3/SiO_2 ratio near the stoichiometric mullite.

3.3 Effect of additives on sintering

Additives (0–5 wt%) like MgO, ZrO_2, TiO_2, and rare earth oxides like Y_2O_3, La_2O_3 and CeO_2 have been used to study their effect on the sintering behavior of mullite (M1). The densities of mullite with 5 wt% additives sintered at 1650°C are summarized in Table 1. The final density at 1650°C, 2 h was very low for 5 wt% of TiO_2, ZrO_2 and La_2O_3 and ranges from 1·9 to 2·9 g/cm³. Addition of 5 wt% of CeO_2, however gave a density of 2·89 g/cm³ and its microstructure showed acicular grains. 5 wt% of magnesia and yttria additives gave a highest density of 3·06 and 3·12 g/cm³ respectively and the sintering behaviour of these was studied.

3.4 Dilatometric studies of mullite-MgO/Y_2O_3 (5 wt%)

Dynamic sintering studies of mullite-magnesia (5 wt%) and mullite-yttria (5 wt%) were performed on compacts in the temperature range 25–1650°C. The powders were uniaxially pressed at 50 MPa (without deagglomeration of the platelets) and the shrinkage versus temperature was measured at a constant heating rate of 10°/min. The dilatometric curves of mullite-magnesia (5 wt%)

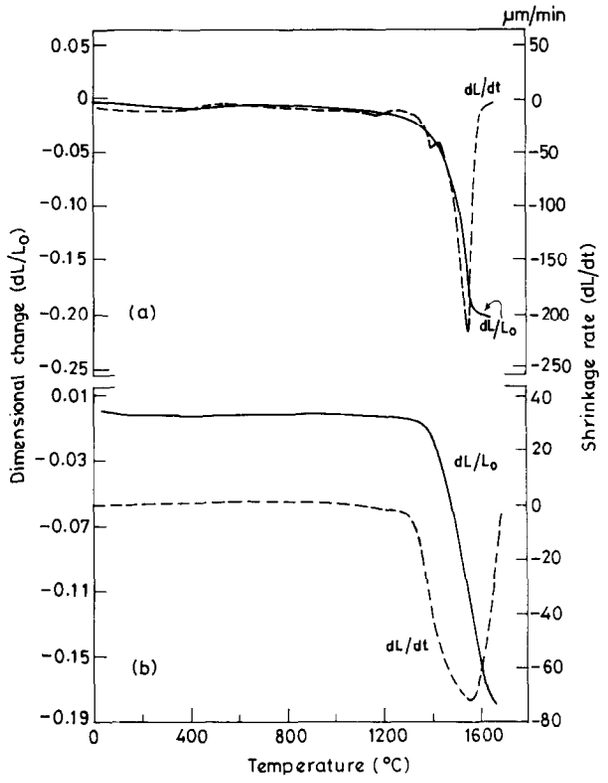

Fig. 5. Dilatometric curves of (a) mullite (M1)-magnesia (5 wt%) and (b) mullite (M1)-yttria (5 wt%).

and mullite-yttria (5 wt%) are given in Fig. 5. Both magnesia- (Fig. 5(a)) and yttria-mullite (Fig. 5(b)) show single step shrinkage. No shrinkage was seen until 1400°C in both the cases, after which a sharp shrinkage was noticed, total shrinkage being 22 and 18% respectively. The shrinkage rate of magnesia- and yttria-mullite was 220 and 75 μm/min respectively at 1650°C. Unlike gel-derived mullite,[18–20] which shows sharp shrinkage before mullitization, combustion derived powders show shrinkage after mullitization. This could be attributed to the formation of liquid phase which helps in the rearrangement of the particles followed by densification. In the gel-derived samples the initial shrinkage before mullite nucleation is attributed to the viscous flow which stops once mullite is nucleated.[18,19]

The dependence of density on the percentage of magnesia and yttria additives at sintering temperature of 1575°C, 2 h is shown in Fig. 6. A steady increase in the density was observed with the increase in percentage of the additives. The variation of density with temperature for 5 wt% of MgO and Y_2O_3-mullite is shown in Fig. 7. It could be seen that the density increases beyond 1400°C as expected from the dilatometric studies (Fig. 5). The final density was above 3·0 g/cm³ at 1650°C. The microstructures of (5 wt%) MgO and Y_2O_3 mullite sintered at 1600°C are shown in Figs 8 and 9 respectively. The mullite with MgO additive

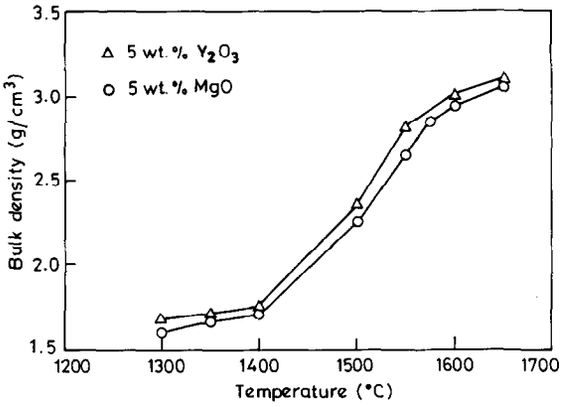

Fig. 6. Dependence of density of mullite on the percentage of magnesia and yttria (1–5 wt%) at 1575°C, 2 h.

show a very dense microstructure with acicular grains, the chemical composition of the grain correspond to that of mullite. Similar observation was made in the case of yttria-mullite (Fig. 9). The microstructures of 5 wt% MgO and Y_2O_3-mullite sintered at 1600°C show the presence of corundum in certain regions of the compact. A typical

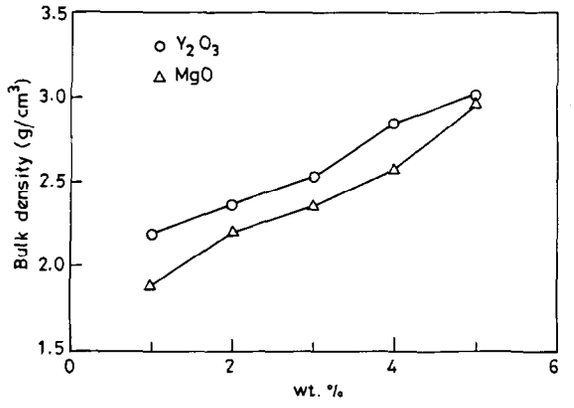

Fig. 7. Variation of density of mullite (M1)-magnesia/yttria (5 wt%) as a function of sintering temperature.

Fig. 8. Microstructure of mullite (M1)-magnesia (5 wt%) sintered at 1600°C, 2 h.

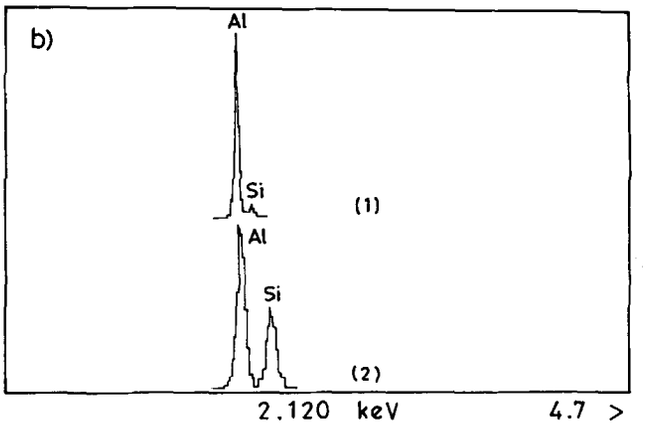

Fig. 9. (a) Microstructure of mullite (M1)-yttria (5 wt%) sintered at 1600°C, 2 h and (b) EDX of the grain marked 1 and 2 in (b).

microstructure of yttria-mullite showing corundum and mullite grains is shown in Fig. 9. It is interesting to note that while the microstructure of pure sintered mullite was composed of submicrometer equiaxed grains (Fig. 4(b)), the one with additives was elongated with large increase in the grain size (Figs 8 and 9). The large increase in the size of mullite grains is probably due to the formation of liquid phase which allow rapid transport of material and much more rapid grain growth similar to the one observed in the case of sodium-doped mullite.[21]

Addition of Y_2O_3 or MgO in the Al_2O_3–SiO_2 system forms a liquid phase at low temperatures and promotes the densification.[22,23] It is interesting to note that densities greater than 3·0 g/cm³ could be achieved at 1650°C, but the density of mullite without the additive was less than 2·0 g/cm³. During sintering some crystalline phases of yttrium silicate or magnesium aluminate spinel were formed in addition to mullite and corundum by the crystallization of the liquid phases as the furnace cooled. In the case of Y_2O_3-mullite crystalline phases of Y-silicate and corundum were observed by Fang and Hwang.[22,23] The liquid phase formed

at higher sintering temperature enhanced the sinterability of mullite powders. During the furnace cooling process, the liquid phase crystallized (by solution–reprecipitation process) and different crystalline phases were obtained depending on the amount of Y_2O_3.[22,23] Yttria and magnesia appear to be the best additives for achieving high density in combustion derived mullite.

4 Conclusions

(i) Pure mullite prepared by the combustion process when sintered at high temperatures (1600°C) was porous and composed of equiaxed grains.
(ii) Mullite could be sintered to high density (95% theoretical) by hot isostatic pressing or by the use of liquid-forming additives like MgO or Y_2O_3.
(iii) Dynamic shrinkage studies of mullite with additives showed the shrinkage to take place after 1400°C, with a total shrinkage of 18 and 22% for yttria and magnesia, respectively.
(iii) The microstructures of magnesia- and yttria-mullite show the presence of anisotropic grains of mullite and alumina particles.

Acknowledgements

The authors thank Mr L. N. Satpathy, BHEL, for his help. One of the authors (RGC) is grateful to the Council of Scientific and Industrial Research (CSIR), New Delhi, India for the award of a Senior Research fellowship.

References

1. Kanzaki, S., Tabata H., Kumazawa, T. & Ohta S., Sintering and Mechanical Properties of Stoichiometric Mullite. *J. Am. Ceram. Soc.*, **68** (1985) C6–C7.
2 Dokko. P. C., Pask, J. A. & Mazdiyasni, K. S., High-Temperature Mechanical Properties of Mullite Under Compression. *J. Am. Ceram. Soc.*, **60** (1977) 150–5.
3. Sacks, M. D., Lee. H. W. & Pask, J. A., A Review of Powder Preparation Methods and Densification Procedures For Fabricating High Density Mullite. In *Mullite and Mullite Matrix Composites, Ceramic Transactions*, Vol. 6, ed. S. Somiya, R. F. Davis & J. A. Pask. The American Ceramic Society Inc., Westerville, OH, 1990, pp. 167–207.
4. Gopi Chandran, R. & Patil, K. C., A Rapid Combustion Method for the Preparation of Crystalline Mullite Powders. *Mater. Lett.*, **10** (1990) 291–5.
5. Gopi Chandran, R., Chandrappa, G. T. & Patil, K. C., Combustion Synthesis of Oxide Materials using Metal nitrates-diformyl hydrazine Redox Mixtures, *Int. J. Self-Prop. High-Temp. Synth.*, **3** (1994) 131–42.
6. Ainsworth, C. & Jones, R. G., Isomeric and Nuclear-substituted β-Aminoethyl-1,2,4-triazoles. *J. Am. Chem. Soc.*, **77** (1955) 621–4.
7. Mohr, E. B., Brezinki, J. J. & Andrieth, L. F., Carbohydrazide. In *Inorganic Synthesis*, Vol. 4, McGraw Hill, New York, 1953, pp. 32–5.
8. Powder Diffraction File, Joint Committee on Diffraction Standards, Swarthmore, PA, 1988.
9. Metcalf, B. L. & Sant, J. H., The Synthesis, Microstructure and Physical Properties of High Purity Mullite. *Trans. J. Brit. Ceram. Soc.*, **74** (1975) 193.
10. Mazdiyasni, K. S., Preparation and characterization of mullite powders from alkoxides and other chemical routes. In *Mullite and Mullite Matrix Composites, Ceramic Transactions, Vol. 6*, The American Ceramic Society Inc., Westerville, OH, 1990, pp. 243–53.
11. Aksay, I. A. & Pask, J. A., Stable and Metastable Equilibria in the System SiO_2–Al_2O_3. *J. Am. Ceram. Soc.*, **58** (1975) 507–12.
12. Pask J. A., Zhang, Y. W., Tomsia, A. P. & Yoldas, B. E., Effect of Sol–Gel Mixing on Mullite Microstructure and Phase Equilibria in the α-Al_2O_3–SiO_2 System. *J. Am. Ceram. Soc.*, **70** (1987) 704–7.
13. Huling, J. C. & Messing, G. L., Hybrid Gels for Homoepitactic Nucleation of Mullite. *J. Am. Ceram. Soc.*, **72** (1989) 1725–9.
14. Wei, W. C. & Halloran, J. W., Phase Transformation of Diphasic Aluminosilicate Gels. *J. Am. Ceram. Soc.*, **71** (1988) 581–7.
15. Li, D. X. & Thomson, W. J., Kinetic Mechanisms for the Mullite Formation From Sol–Gel Precursors. *J. Mater. Res.*, **57** (1990) 1963–9.
16. Mazdiyasni, K. S. & Brown, L. M., Synthesis and Mechanical Properties of Stoichiometric Aluminium Silicate (Mullite). *J. Am. Ceram. Soc.*, **55** (1972) 548–52.
17. Li, D. X. & Thomson, W. J., Mullite Formation From Nonstoichiometric Diphasic Precursors. *J. Am. Ceram. Soc.*, **74** (1991) 2382–7.
18. Osendi, M. I., Baudin, C., de Aza, S. & Moya, J. S., Processing and Sintering of 3:2 Alumina Silica Gel. *Ceram. Int.*, **18** (1992) 365–72.
19. Osendi, M. I., Baudin, C. & de Aza, S., Mullite Material from a 3:2 Alumina–Silica Gel. Part II: Microstructural Evolution. *J. Eur. Ceram. Soc.*, **10** (1992) 399–403.
20. Douy, A., Organic Gels in the Preparation of Silico-aluminate Powders. I: Mullite. *J. Eur. Ceram. Soc.*, **7** (1991) 117–23.
21. Fahrenholtz, W. G. & Smith D. M., Densification and Microstructure of Sodium-Doped Colloidal Mullite. *J. Am. Ceram. Soc.*, **17** (1994) 1377–80.
22. Fang, D. Y. & Hwang, C. S., Effects of Y_2O_3 addition on the Sinterability and Microstructure of Mullite: I. Phase Transformation and Sinterability. J. *Ceram. Soc. Jpn, Int. Ed.*, **100** (1992) 1141–6.
23. Fang, D. Y. & Hwang, C. S., Effects of Y_2O_3 addition on the Sinterability and Microstructure of Mullite: II. Crystallization of Liquid Phase and Grain Growth. *J. Ceram. Soc. Jpn, Int. Ed.*, **101** (1993) 322–6.

Journal of the European Ceramic Society 16 (1996) 851–855

S0955-2219(96)00004-0
0955-2219/96/$15.00 + .00

Constitution of Porcelain Before and After Heat-Treatment. Part II: Aspect Ratio and Size-Distribution of Mullite

S. P. Chaudhuri & P. Sarkar

Special Ceramics Section, Central Glass and Ceramic Research Institute, Calcutta — 700 032, India

(Received 7 August 1995; revised version received 5 December 1995; accepted 12 December 1995)

Abstract

Porcelain samples were prepared with and without the addition of mineralizers. The samples were then heat-treated for 50 h. The aspect ratio and size-distribution (experimental) of mullite crystals were studied in relation to mineralizer and heat-treatment.

1 Introduction

In a recent communication[1] (Part I) it was shown that variations occurred in the mineralogical composition of chemical porcelain before and after heat-treatment at the crystallization temperature of the glassy phase in the material.

The microstructure of the chemical porcelain samples before and after heat-treatment is presented in this paper. The size, size-distribution and shape of the mullite crystals are emphasized and the influence of the mineralizers is also reported.

2 Experimental Procedure

2.1 Sample preparation

Porcelain samples were prepared from a slip made of clay, quartz and feldspar including additional mineralizers by slip casting. The preparation has been described in Part I.[1]

2.2 Electron microscopy

The polished surface of the sample was etched with HF (40%) for 1 min at room temperature, washed with distilled water and dried. A carbon coated plastic replica was prepared. The plastic was dissolved in acetone, the carbon replica was collected on a metal grid and examined by Transmission Electron Microscope (JEM 200 CX, Resolution 1·4 Å, Mag 6,50,000).

2.2.1 Size and shape of mullite crystals

The electron micrographs were illuminated and the length (l) and breadth (b) of mullite crystals seen in the micrographs were measured by a hair divider and scale. 200 crystals were measured from each sample. The aspect ratio (l/b) of the crystals was then derived.

3 Results and Discussion

A brief description of the samples is given in Table 1. The size-distributions of mullite crystals in a few representative samples are displayed in Figs 1 (a–g) where the histograms and continuous curves stand for the experimental size-distribution. The distribution curves are positively skewed.

The mean size and modal size of the mullite crystals increased simultaneously with rise in the concentration of mullite. Both the crystallization and growth of mullite in porcelain were enhanced due to heat-treatment.

The increase in the size of mullite crystals in the samples after heat-treatment is recorded in Table 2, (here the length of mullite crystal is considered as the size). This shows that the added mineralizers influenced the growth of mullite crystals in the samples. It was observed that TiO_2, at low concentration (2·6 wt%) was the most effective oxide in this respect and about 150% increase in the size of mullite crystals could be achieved. The efficiency of TiO_2 decreased, however, at higher concentration and 23% enlargement was found with 8·0 wt% TiO_2.

Cr_2O_3 marginally improved the size of mullite crystals in the heat-treated sample. Incorporation of small amounts of Fe_2O_3, V_2O_5 and Nb_2O_5 in

Table 1. Description of experimental samples

Sample no.	*Description*
1	Base composition (BC)*
2	BC + 8% TiO_2
3	BC + 3% V_2O_5
4	BC + 2·6% Fe_2O_3
5	BC + 2.6% TiO_2
6	BC + 1·5% V_2O_5 + 1·3% Fe_2O_3
7	BC + 1·5% V_2O_5 + 1·3% TiO_2
8	BC + 2.5% Cr_2O_3
9	BC + 2% Nb_2O_5

* BC = 63% clay + 12% quartz + 25% feldspar.

the base composition also helped grow larger mullite crystals. Mixed mineralizers were also used and found to be effective. One such combination, (V_2O_5 + Fe_2O_3), accelerated the influence of the individual components but the other combination, (V_2O_5 + TiO_2), suppressed their activity (Table 2).

The efficiency of mineralizers can be seen to depend on their fluxing action and on their solubility in the glassy phase of the sample. Therefore, a high concentration of TiO_2 (flux) and the low solubility of Cr_2O_3 appeared to be respon-

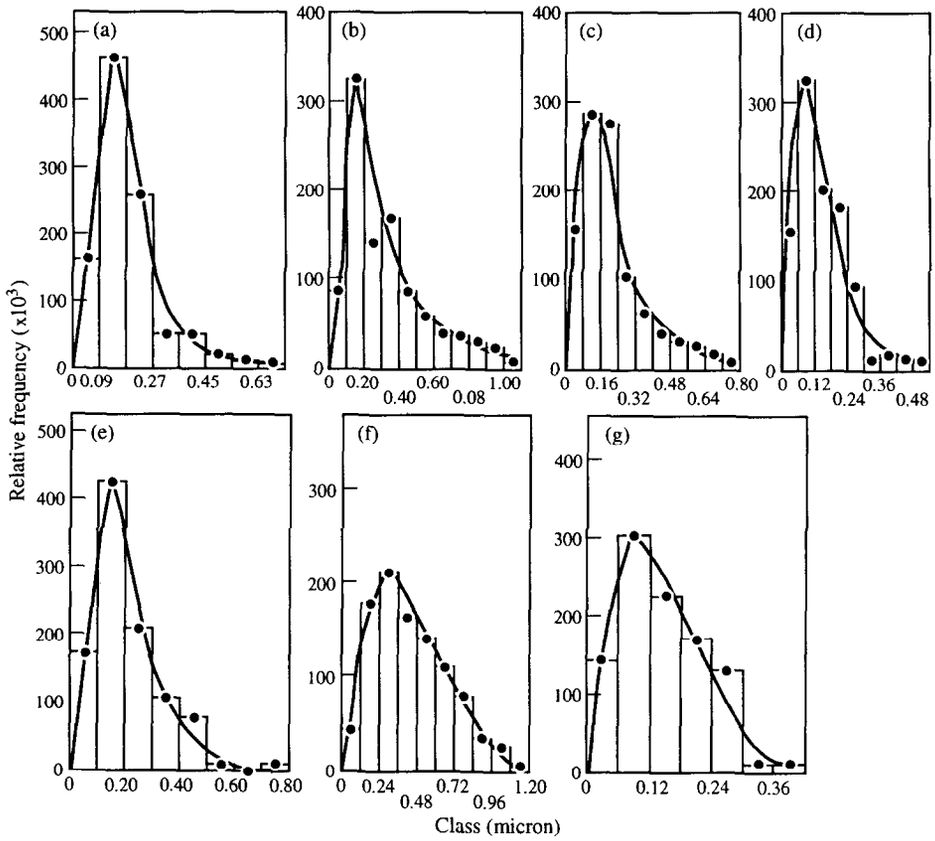

Fig. 1. Size-distribution (experimental) of mullite crystals in porcelain samples: (a) BC + 8·0 wt% TiO_2; (b) BC + 3·0 wt% V_2O_5; (c) BC + 1·5 wt% V_2O_5 + 1·3 wt% Fe_2O_3; (d) base composition; (e) BC + 2·0 wt% Nb_2O_5; (f) BC + 2·6 wt% TiO_2; (g) BC + 8·0 wt% TiO_2. (e) and (g) before heat-treatment and (a), (b), (c), (d) and (f) after heat-treatment.

Table 2. Average size (length) of mullite crystals measured by TEM

Sample no.	*Concentration of mineralizer* (wt%)	*Sample before heat-treatment (B)* (μ)	*Sample after heat-treatment (A)* (μ)	*Increase in average size after heat-treatment* (%)
1	—	0·1364	0·1443	5·8
2	8·0% TiO_2	0·1460	0·1791	22·7
3	3·0% V_2O_5	0·2428	0·3228	32·9
4	2·6% Fe_2O_3	0·1258	0·1772	40·9
5	2·6% TiO_2	0·1790	0·4473	149·9
6	1·5% V_2O_5 + 1·3% Fe_2O_3	0·1298	0·2086	60·7
7	1·5% V_2O_5 + 1.3% TiO_2	0·1233	0·1500	21·7
8	2·5% Cr_2O_3	0·1306	0·1411	8·0
9	2·0% Nb_2O_5	0·2084	0·2550	22·4

Table 3. Average values of aspect ratio (*l/b*) of mullite crystals

Sample no.	*Conc. of mineralizer (wt%)*	*Sample before heat-treatment (B)*	*Sample after heat-treatment (A)*	*Increase in (l/b) after heat-treatment (%)*
1	—	3·1	3·7	19·4
2	8·0% TiO_2	3·5	3·7	5·7
3	3·0% V_2O_5	3·7	5·2	40·5
4	2·6% Fe_2O_3	2·7	4·0	48·1
5	2·6% TiO_2	3·9	6·9	76·9
6	1·5% V_2O_5+ 1·3% Fe_2O_3	3·1	4·1	32·3
7	1·5% V_2O_5 + 1·3% TiO_2	2·8	3·4	21·4
8	2·5% Cr_2O_3	2·9	3·6	24·1
9	2·0% Nb_2O_5	3·7	4·0	8·1

Table 4. Values of skewness of experimental size-distribution curves

Sample no.	*Skewness*	
	Before heat-treatment (B)	*After heat-treatment (A)*
1	0·5701	0·5484
2	0·5549	0·3213
3	0·5270	0·7296
4	0·6110	0·4165
5	0·3962	0·6506
6	0·4985	0·3799
7	0·5561	0·2433
8	0·6176	0·2766
9	0·4182	0·4220

sible for the poor growth of mullite crystals in these samples. At low concentration, TiO_2 was a very good mineralizer. Nb_2O_5 is a good nucleating agent and, thus, improved growth of mullite crystals.

The aspect ratio of the mullite crystals in the heat-treated samples was always higher than in the unheat-treated ones. Irrespective of the added mineralizers, mullite crystals became more acicular in the samples after heat-treatment. In this regard, small amounts (2·6 wt%) of TiO_2 showed excellent performance (Table 3).

It was observed (Table 4) that the effect of heat-treatment was to reduce skewness, i.e. the size-distribution of mullite crystals in the samples became more symmetric as a consequence of heat-treatment.

A few TEM micrographs of selected samples are portrayed in Figs 2 (a–e) to illustrate the effect of heat-treatment. Each sample is represented by two micrographs labelled B and A for before and after heat-treatment conditions, respectively.

4 Conclusions

(1) Heat-treatment of porcelain samples caused mullite crystals to grow particularly in length (higher aspect ratio).

(2) The size-distribution of mullite crystals in porcelain samples was asymmetric but became more symmetric after heat-treatment.

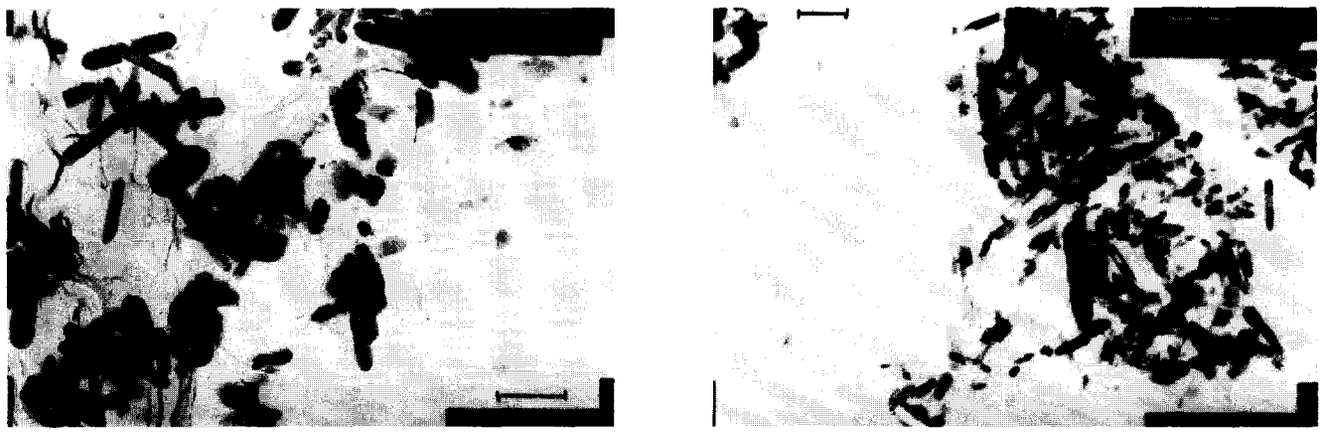

B(a) A(a)

Fig. 2 TEM micrographs of selected porcelain samples: (a) Base composition; (b) BC + 8.0 wt% TiO_2; (c) BC + 2·6 wt% TiO_2; (d) BC + 1·5 wt% V_2O_5 + 1·3 wt% TiO_2; (e) BC + 2·0 wt% Nb_2O_5. BC = Base composition, bar = 0·2 μ, B = before heat-treatment, A = after heat-treatment.

B(b)

A(b)

B(c)

A(c)

B(d)

A(d)

B(e)

A(e)

Fig. 2. Continued

(3) At low concentration level, TiO_2 was the most efficient mineralizer in promoting large acicular mullite crystals.

Acknowledgements

The authors thank Dr B. K. Sarkar, Director of the Institute for his permission to publish the paper. P. Sarkar is grateful to Council of Scientific and Industrial Research, India for a research fellowship granted to him to carry out this investigation.

Reference

1. Chaudhuri, S. P. & Sarkar, P., Constitution of porcelain before and after heat-treatment. Part I: Mineralogical composition, *J. Euro. Ceram. Soc.*, **15** (1995) 1031–5.

Journal of the European Ceramic Society 16 (1996) 857–864

0955-2219(95)0206-5
0955-2219/96/$15.00+.00

A Statistical Analysis of the Influence of Processing Conditions on the Properties of Fused Silica

D Kićević, M. Gašić & D. Marković

The Institute of Nuclear Sciences 'Vinča', Materials Science Laboratory, P.O.B. 522, 11001 Belgrade, Serbia

(Received 29 September 1995; accepted 4 November 1995)

Abstract

In this work the quantitative relations between the properties of sintered fused silica (density, mechanical properties, cristobalite content) and slip preparation parameters as well as sintering conditions (milling balls material, temperature and time of sintering) were established. Multifactorial experimental design was used in order to obtain the respective mathematical models. The response surfaces of these models were analyzed, together with correlations between the compressive and tensile strength and cristobalite content. It was established that the maximum values of mechanical properties for a given material were obtained with 6–8 vol.% of cristobalite in sintered samples.

Les relations quantitatives entre les caractéristiques des échantillons frittés (la densité, les caractéristiques mécaniques, le contenu de cristobalite) et les paramétres de la préparation de la suspension de coulage et les conditions de frittage (le materiel des balles de moulage, la température et le temps de frittage) ont étés établies. Pour obtenir des modèles mathématiques, un dessin expérimentale multifactoriel a été utilisé. Les surfaces de reponse de ces modèles ont été analysées avec la corrélation entre les résistances sous pression et sous tension et le contenu de cristobalite. On a été trouvé que le maximum des caractéristiques mécaniques peut être gagné avec un contenu de cristobalite de 6–8% vol. dans des échantillons frittés.

In dieser Arbeit werden quantitative Zusammenhänge zwischen den Eigenschaften von gesintertem Siliziumdioxid (Dichte, mechanische Eigenschaften, Cristobalitgehalt) und den Bedingungen für die Vorbereitung des Schlickers und für das Sintern (Mahlkugelnmaterial, Sintertemperatur und - zeit) festgestellt. Es werden Vielfaktorenversuchspläne benutzt, um entsprechende statistische Modelle zu erstellen. Echooberflächen dieser Modelle werden zusammen mit Abhängigkeiten zwischen Druckfestigkeit und Zugfestigkeit einerseits und Cristobalitgehalt andererseits analysiert. Es wurde festgestellt, daß die maximalen Werte der mechanischen Eigenschaften für ein Material mit 6–8 vol.% Cristobalit in den gesinterten Proben erreicht wird.

1 Introduction

Fused silica ceramics have found quite broad application due to the good combination of its properties (refractoriness, thermal shock resistance, and good mechanical properties at elevated temperatures).[1–4] The forming of fused silica products is done mostly by slip-casting. The preparation of the slip comprises: (a) wet-milling of coarse fused silica powder to obtain required particle size distribution; (b) slip stabilization for adjusting slip viscosity. After drying the green casts are subjected to sintering, in order to improve mechanical properties.

The fused silica sintering mechanism is viscous flow as for all glassy materials, if there is no significant devitrification to cristobalite. This process depends on many factors: chemical purity, temperature, time, heating conditions, atmosphere, particle size, porosity of green casts etc.[1–5] During sintering of fused silica two processes occur: (a) increase of strength as a result of the strengthening of the contacts between particles and porosity decrease; (b) decrease of strength, as a result of pronounced devitrification, and consequent flaw initiation because of cristobalite phase transformation upon cooling.[5] In this way all parameters that can affect devitrification can affect also sintering.

Indirectly, these two processes are influenced by slip preparation parameters (material of milling balls, mill loading coefficient, rotation speed, solid phase content in the slip, grain size distribution of starting material, pH etc.), through resulting content of impurities (Na_2O, K_2O, CaO, Al_2O_3 etc).[6,7] and grain size distribution of the slip. Using high purity materials, the devitrification problem can be avoided, but in broader applications (metallurgy,

chemical and glass industry and similar) the 'technical grade' fused silica materials of different purity are more frequently used. Therefore, it is necessary for every single material to establish the proper conditions for sintering (temperature, time etc.).[2–5]

In this work, investigation of the influence of most significant process parameters of fused silica sintering (impurity content in casting slip as a result of different milling ball material, sintering temperature and soaking time) on the properties of sintered fused silica (density, open porosity, strength and cristobalite content) was performed. Statistical models, giving quantitative relations between investigated process parameters (influencing factors) and related properties (system responses), were established on the basis of multifactorial experimental design. These quantitative relations enabled the determination of the optimum sintering conditions for investigated material.

2 Experimental Work

The coarse fused silica powder of technical grade purity was used (Elmin, The Netherlands). The properties of this powder are given in Tables 1 and 2.

Slips were prepared by wet-milling of coarse powder in a porcelain mill with silica balls (99% SiO_2) and alumina balls (70% Al_2O_3). Solid content in the slip was 82% mass and deflocculant Dispex 115N (Progress Engineers Ltd, Stoke-on-Trent, UK) was added (1% of solid content). Balls to slip ratio was between 1·25 and 1·5 and rotation speed was 4·2 rad/s (40 rpm). The milling time was 25% shorter for Al_2O_3 balls, for slips having the similar grain size distribution after milling (90–95% smaller than 63 μm, 80–90% smaller than 30 μm).

After milling, the slips were stabilized by rotating for up to 30 h in the mill without balls, when they were ready for casting, having density of 1·83 g/cm^3 and viscosity of about 300 mPas (Brookfield viscometer RVT (spindle 4), Stoughton, Mass. USA).

Slip casting was performed into the impregnated plaster moulds. The obtained casts (ϕ 20 × 100 mm) were dried in air for 24 h, then for 24 h at 110°C and finally 4 h at 180°C. The density of the dry casts was 1·89 g cm^{-3}.

Table 1. Chemical composition of fused silica powder

Component	SiO_2	Al_2O_3	Fe_2O_3	CaO	Na_2O	K_2O
Content (%)	99·02	0·43	0·04	0·43	0·05	0·02

Table 2. Particle size distribution of fused silica powder

Particle size (mm)	<0·3	0·3–0·6	0·6–1	1–2	2–3	>3
Content (%)	1	7	22	37	32	1

The firing of samples was performed in a tubular furnace, in air, with heating rate of 200°C/h. The soaking times at temperatures 1175 and 1275°C were 1 and 3 h. After that samples were quenched down to room temperature in air. Such a cooling procedure was recomended for establishing the optimum sintering conditions.[2]

Density and open porosity of sintered samples were measured by immersion in xylene. Compressive strength was determined by standard measurement on cylindrical samples (diameter 20 mm, height 10 mm). It was calculated from the relationship between crushing force and sample cross area ($D^2\pi/4$). Tensile strength was determined by the diametral compression method[8] on the same samples, but with diametral loading (perpendicular to compressive strength loading). Using special hard paper attachments shear stress concentration was avoided. Tensile strength was calculated from the following relationship:

$$\sigma_{tens} = \frac{2F}{\pi D H} \quad (1)$$

where: σ_{tens} — tensile strength;
F — crushing force;
D — sample diameter;
H — sample height.

Cristobalite content was determined by the modified Harris and Welsh method.[9] This is a quantitative X-ray diffraction method, measuring the integral number of impulses in the interval 2Θ from 21 to 23° (characteristic reflection of the plane (101) for β-cristobalite at 2Θ = 21·94°) on sintered samples and specially prepared standards.[10]

The chemical analysis of green casts, made by atomic absorption spectroscopy, is shown in Table 3. It is evident that higher impurity content is produced with Al_2O_3 balls.

3 Results, Discussion and Statistical Modelling

The properties of samples sintered under different processing conditions are presented in Table 4. A combination of processing parameters was set up following the special design of the experiments, enabling us to investigate the influence of these parameters on sintered fused silica properties through the established statistical models.

3.1 Statistical models and their analysis

The statistical method of multifactorial experimental design[8,9] was used in order to obtain the empirical models for relations between properties of sintered samples (system responses) and some process parameters (influencing factors) in an efficient way, i.e. with as little experimentation as possible. Box–Wilson

Table 3. Chemical composition of the green casts as a function of ball milling material

Ball Milling material	*Composition (%)*						
	SiO_2 (from difference)	Impurities (total)	Al_2O_3	Fe_2O_3	CaO	Na_2O	K_2O
SiO_2	99·17	0·83	0·25	0·04	0·49	0·04	0·01
Al_2O_3	98·75	1·25	0·53	0·05	0·59	0·06	0·02

orthogonal plans[11,12] were used with some adopted modifications because of the specific nature of one influencing factor — ball milling material. A slightly modified matrix plan 2^3 — three factors on two levels was used (the coding of factors and system responses is given in Table 5). Established empirical statistical models have the general form:

$$Y = b_0 + \Sigma b_i x_i + \Sigma b_{ij} x_i x_j + \ldots\ldots\ldots \quad (2)$$

in which regression coefficients (b_i, b_{ij} ...) are obtained from system response data (Table 4), using the following equation:

$$b_0 = \frac{1}{N} \sum_{u=1}^{N} Y_u \quad (3)$$

$$b_i = \frac{1}{N} \sum_{u=1}^{N} X_{iu} Y_u \quad (4)$$

$$b_{ij} = \frac{1}{N} \sum_{u=1}^{N} X_{iu} \cdot X_{ju} \cdot Y_u \quad (5)$$

Control of reproducibility of experiments and evaluation of experimental error were performed by repeating experiments in the plan center (zero level of factors X_2 and X_3), using 95% confidence level. Since one factor, X_1, was milling ball material (SiO_2 or Al_2O_3) which would have as zero level mixture of these two different types, repeating of experiments in the plan center was made separately for both types, taking the greater experimental error as a basis for evaluation of statistical significance of regression coefficients (b_i) by the Student t-test. Model adequacy was verified according to the Fisher F-test,[11,12] comparing the table values of F_t with calculated values of F_r, for respective degrees of freedom.

3.2 Empirical statistical models

It can be seen from Table 4 that the ball milling type, as well as sintering temperature has quite a significant influence on sintering and devitrification processes. The devitrification process is more intensive in the case of Al_2O_3 balls (higher impurities content) and that also has an influence on the sintering process, i.e. on density, porosity and strength of sintered samples.

On the basis of the results shown in Table 4, statistical models were formed, (Table 5).[8,9] They give the relations between sintered samples properties and ball milling type (i.e. impurities content), temperature and time of sintering. In these models, having the general form given by eqn (2), only coefficients with 95% level of significance, according to the Student t-test were included:

$$Y_1 = 1{\cdot}9376 + 0{\cdot}018125\ X_2 + 0{\cdot}009125\ X_3 \ldots\ldots (6)$$

$$Y_2 = 11{\cdot}4 \ldots\ldots\ldots\ldots \quad (7)$$

$$Y_3 = 281{\cdot}1 - 66{\cdot}425\ X_1X_2 - 21{\cdot}675\ X_2X_3 \ldots\ldots (8)$$

$$Y_4 = 13{\cdot}1 - 3{\cdot}725\ X_2 \ldots\ldots\ldots \quad (9)$$

$$Y_5 = 28{\cdot}1 + 11{\cdot}925\ X_1 + 20{\cdot}35\ X_2 + 3{\cdot}95\ X_3 + 7{\cdot}0\ X_1X_2 + 2{\cdot}725\ X_2X_3 \ldots\ldots (10)$$

It can be easily seen that, in the investigated interval of influencing factors, the most pronounced effect was in the case of cristobalite content (Y_5), while in the case of open porosity (Y_2) there is no statistically significant (95%) influence of any factor. The comparison between experimental and

Table 4. The properties of sintered samples as a function of different sintering conditions and ball milling material

Experiment No.	*Ball milling material*	*Sintering temperature (°C)*	*Sintering time (h)*	*Density ($g\ cm^{-3}$)*	*Open porosity (%)*	*Compressive strength (MPa)*	*Tensile strength (MPa)*	*Cristobalite content (vol.%)*
1	SiO_2	1175	1	1·905	12·4	151·0	15·6	1·5
2	SiO_2	1175	3	1·935	10·7	255·1	18·8	4·2
3	SiO_2	1275	1	1·948	10·5	345·4	12·1	20·8
4	SiO_2	1275	3	1·974	9·5	325·2	9·5	38·3
5	Al_2O_3	1175	1	1·915	11·7	363·5	20·4	11·6
6	Al_2O_3	1175	3	1·923	11·6	356·2	12·7	13·8
7	Al_2O_3	1275	1	1·946	13·0	254·2	8·4	62·8
8	Al_2O_3	1275	3	1·955	11·9	198·6	7·7	72·0

Table 5. Coding of factors and system responses

Factors	*Responses*
X_1 — Type of milling balls (Impurity content)	Y_1 — Density (g cm^{-3})
	Y_2 — Open porosity (%)
X_1 = −1 SiO_2 balls	
X_1 = +1 Al_2O_3 balls	Y_3— Compressive strength σ_c (MPa)
X_2 — Sintering temperature	
X_2 = −1 1175°C	Y_4 —Tensile strength
X_2 = +1 1275°C	σ_t (MPa)
X_3 — Sintering time	
X_3 = −1 1 h	Y_5 — Cristobalite content
X_3 = +1 3 h	(vol.%)

calculated values of responses from the models is given in Table 6. By testing of model adequacy, according to Fisher F-test, it was established that all obtained models are adequate ($F_r<F_t$), even the model for open porosity (OP=constant) because of small differences in porosity of sintered samples, Table 6. The compressive strength model shows the influence of all three factors, while in the case of tensile strength only the influence of sintering temperature has the statistical significance. In the case of cristobalite content model there is a significant influence of all factors, including interaction of factors. That fact points out the necessity and possibility of very precise control of cristobalite content in sintered samples.

By projecting the response surfaces on the plane temperature–time it is possible to obtain the contour plots. Figure 1 shows contour plots for density, compressive strength, and cristobalite content. The diagram for density is the same for both milling ball types. For the cristobalite content and compressive strength the diagrams are different because the milling ball type, i.e. impurities content, has a significant influence on the devitrification process.

From the contour plots for compressive strength it is evident that for SiO_2 balls (lower impurities content) the strength continuously increases, and for Al_2O_3 balls (higher impurities content) the strength continuously decreases. This is more illustrative in Fig. 2, where 3D response surfaces for compressive strength and cristobalite content are given. These characteristics cannot be connected with the character of density change, having a continuous increase, and it is even more difficult with a minimum change in the open porosity. In the case of higher cristobalite content the density increase of sintered samples should be attributed to the density change due to the phase transformation because of the difference between density of fused silica (2·20 g·cm^{-3}) and cristobalite (2·33 g·cm^{-3}). In the same way this should be taken into account for the analysis of porosity change. By calculating the density of crystallized fused silica ρ_{th} (the mixture of fused SiO_2 and cristobalite), total and closed porosity, it can be seen that during firing part of the open pore closes (by viscous flow mechanism — typical for the glassy system) but there is almost no change in total porosity, Table 7.

The strength changes of sintered samples evidently could not be the consequence of different porosity. In this case there is a greater influence of strengthening of contacts between particles during sintering, as well as of lower cristobalite content, while the decrease is connected with the exaggerated cristobalite content, when even macro flaws arise.

Analysis of contour plots for compressive strength and cristobalite content for both ball milling types enables us to register the existence of a direct connection between strength change and cristobalite content.

Diagrams of compressive and tensile strength as a function of cristobalite content in sintered samples, for both ball milling types together, are shown in Figs 3 and 4.

Tensile strength is more sensitive to the cristobalite content change in the region of maximum,

Table 6. Adequacy test of statistical models

Experiment No.	*Density (g cm^{-3})* Y_1		*Open porosity (%)* Y_2		*Compressive strength (MPa)* Y_3		*Tensile strength (MPa)* Y_4		*Cristobalite content (vol.%)* Y_5	
	Exp.	*Cal.*	*Exp.*	*Cal.*	*Exp.*	*Cal.*	*Exp.*	*Cal.*	*Exp.*	*Cal.*
1	1·905	1·910	12·4	11·4	151·0	193·0	15·6	16·8	1·5	1·6
2	1·935	1·929	10·7	11·4	255·1	236·3	18·8	16·8	4·2	4·0
3	1·948	1·947	10·5	11·4	345·4	369·2	12·1	9·4	20·8	22·8
4	1·974	1·965	9·5	11·4	325·2	325·8	9·5	9·4	38·3	36·2
5	1·915	1·910	11·7	11·4	363·5	325·8	20·4	16·8	11·6	11·4
6	1·923	1·929	11·6	11·4	356·2	369·2	12·7	16·8	13·8	13·9
7	1·946	1·947	13·0	11·4	254·2	236·3	8·4	9·4	62·8	60·7
8	1·955	1·965	11·9	11·4	198·6	193·0	7·7	9·4	72·0	74·0
F_r	1·6		6·25		3·07		1·6		3·8	
F_t	9·2		9·2		9·2		9·2		9·2	
	Adequate		Adequate		Adequate		Adequate		Adequate	

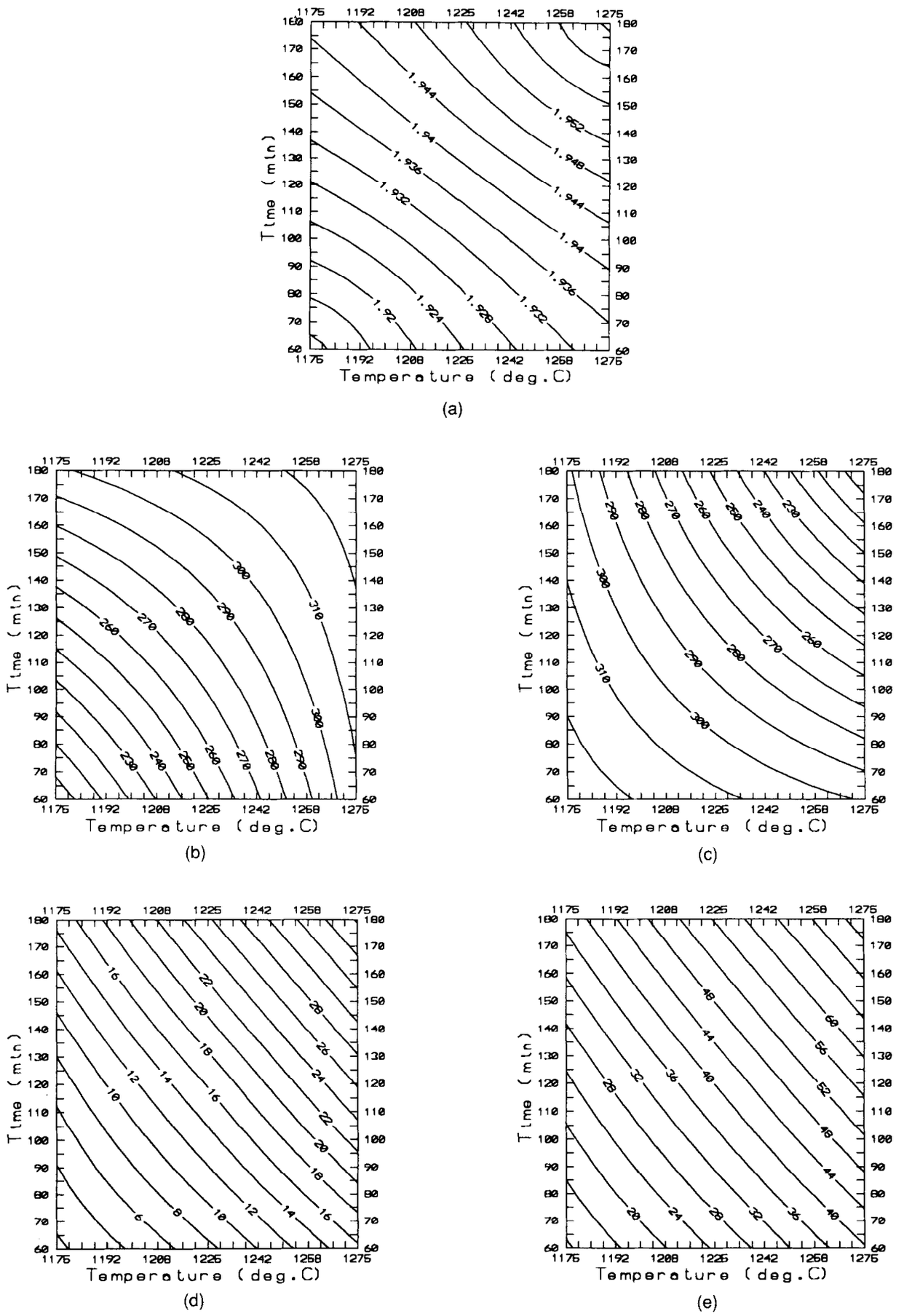

Fig. 1. Contour plots of response surfaces for mathematical models — relations between sintered samples properties and sintering conditions and impurities content. (a) Density (g cm ^{3}); (b) Compressive strength (MPa) — SiO_2 balls; (c) Compressive strength (MPa) — Al_2O_3 balls; (d) Cristobalite content (vol.%) — SiO_2 balls; (e) Cristobalite content (vol.%) — Al_2O_3 balls.

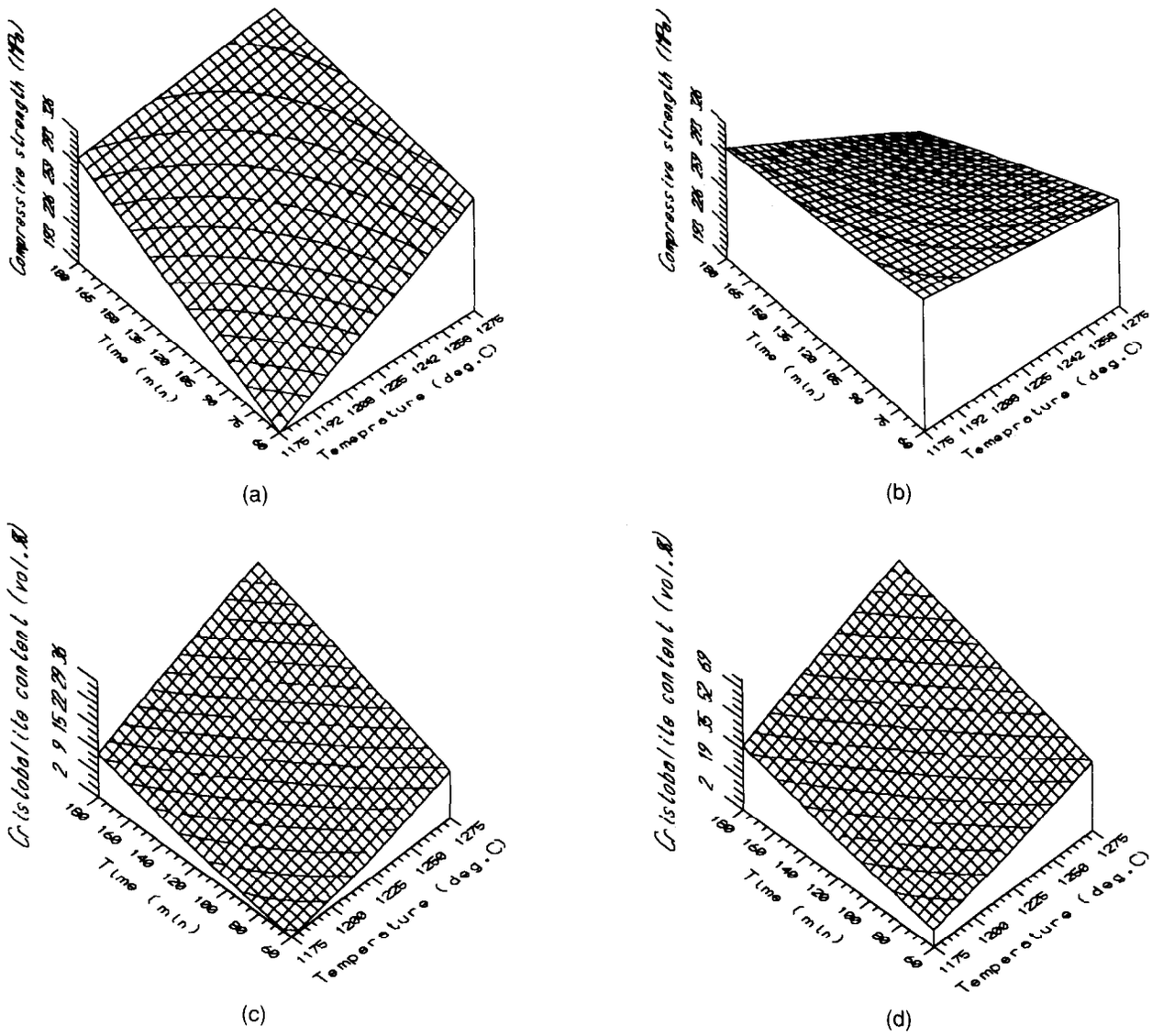

Fig. 2. Response surfaces for compressive strength and cristobalite content as a function of temperature and time of sintering for different ball milling material. (a) Compressive strength (MPa) — SiO_2 balls; (b) Compressive strength (MPa) — Al_2O_3 balls; (c) Cristobalite content (vol.%) — SiO_2 balls; (d) Cristobalite content (vol.%) — Al_2O_3 balls.

Table 7. Analysis of sintered samples porosity

Experiment No.	*Cristobalite content (vol.%)*	ρ_{th} *(g cm* ^{3}*)*	ρ_{exp} *(g cm* ^{3}*)*	*Porosity (%)*		
				Total	*Open*	*Closed*
1	1·5	2·202	1·905	13·5	12·4	1·1
2	4·2	2·205	1·935	12·2	10·7	1·5
3	20·8	2·227	1·948	12·5	10·5	2·8
4	38·3	2·250	1·974	12·3	9·5	2·8
5	11·6	2·215	1·915	13·5	11·7	1·8
6	13·8	2·218	1·923	13·3	11·6	1·7
7	62·8	2·282	1·946	14·7	13·0	1·7
8	72·0	2·294	1·955	14·8	11·9	2·9

so it is possible from Fig. 4 to establish the most convenient cristobalite content very precisely and then, using a contour plot for cristobalite content, to find out the region of optimum combination for sintering conditions. It could be concluded that the optimum content of cristobalite is 6–8 vol.% and in Fig. 1(d) (for SiO_2 balls) the corresponding region of proper combination of sintering

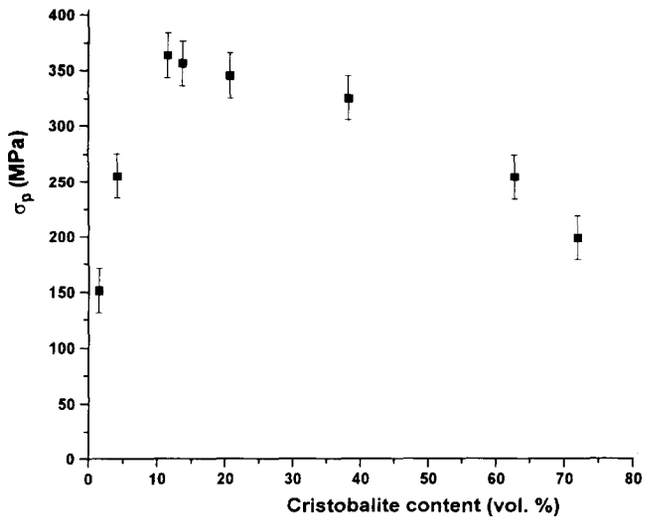

Fig. 3. Compressive strength of sintered samples as a function of cristobalite content.

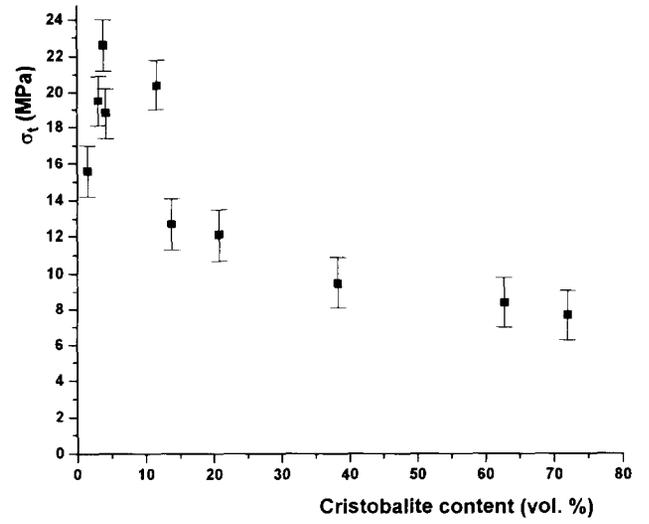

Fig. 4. Tensile strength of sintered samples as a function of cristobalite content.

conditions (temperature and time) should be found near the corner 1175°C, 1 h. It should be pointed out that it is necessary to control the temperature very precisely. For Al_2O_3 balls the optimum region is outside of investigated factorial space (temperatures lower than 1175°C) so further experiments are required to find such a combination for sintering temperature and time.

4 Conclusions

The study of sintering and devitrification processes of fused silica has shown that the interaction of these two processes is strongly dependent on impurities content. Up to a certain level these two processes support each other, and after this the sintering process is retarded by devitrification. Forming of cristobalite causes a density increase of sintered samples while porosity remains practicaly unchanged.

The strength increase is connected with the strengthening of the contacts between grains due to the sintering, by the viscous flow mechanism, and forming of small quantities of cristobalite. The relations between sintered samples properties and sintering conditions and impurities content were established using statistical modelling by the multifactorial experimental design. Using analysis of response surfaces of these models and correlation of the compressive strength and tensile strength with cristobalite content it was established that for 6–8 vol.% cristobalite the strength of sintered samples has the maximum values. Tensile strength is more sensitive to the cristobalite content so this property should be the criterion for establishing the optimum sintering conditions.

Acknowledgements

The authors wish to acknowledge S. Zec for cristobalite content determination in samples. This work was supported by the Scientific Fund of the Republic of Serbia, within the project No. 905.

References

1. Pivinskij, Yu. E. & Romašin, A. G., *Kvarcevaja Keramika*, Metallurgija, Moskva, 1974.
2. Walton, J. D., Sintered Fused Silica, *Interceram*, **2** (1968) 121–122, 133.
3. Kappmeyer, K. K., Russel, C. K. & Hubble, D. H., Refractories for Continuous Casting. *Amer. Ceram. Soc. Bull.*, **53** (1974) 519–523, 527.
4. Ah'jan, A. M., O nekotoryh oblastjah primenenija kvarcevoj keramiki. *Ogneupory* (1982) 4, 40–44.
5. Harris, J. N. & Welsh, E. A., *Fused Silica Design Manual*, Vol. I., Eng. Exp. Station, Georgia Inst. of Technology, Atlanta, 1973.
6. Wagstaff, F. E., Kinetics of Crystallization of Vitreous Silica, PhD Thesis, University of Utah, 1962.
7. Gašić, M., Kićević, D. & Klecko, G., The Structural Changes of Amorphous SiO_2 Powders. In *Contemporary Inorganic Materials*, ed. G. Petzow & W. J. Huppmann. Riederer Verlag GmbH, Stuttgart, 1978, pp. 11–17.
8. Katanić-Popović, J. & Stevanović, M., Measuring the Strength of Brittle Materials by Diametral Compression Method. *Refractories* (in Serb.), **1** (1971) 31–4.
9. Harris, J. N. & Welsh, E. A., *Acceptance Criteria for Slip-cast Fused Silica Radomes*. Tech. Rep. No. 3, Contract N 00017-70-C-4438, Georgia Inst. of Technology, Atlanta, June 1972.
10. Kićević, D., Gašić, M., Zec, S. & Marković, D., X-ray Diffraction Method for Quantitative Determination of Cristobalite in Fused Silica. *J. Serb. Chem. Soc.*, **59** (1994) 185–94.
11. Bondar, A. G. & Statjuha, G. A., *Planirovanie eksperimenta v himičeskoj tehnologiji*, Izd. Viša škola, Kiev, 1976., pp. 6–12, 54–82.

12. Box, G. E. P., Hunter, W. G. & Hunter, J. S., *Statistics for Experimenters — An Introduction to Design, Data Analysis and Model Building*, John Wiley and Sons, New York 1978, pp. 306–22, 510–26.

13. Tecilazić-Stevanović, M., Janaćković, T., Kostić-Gvozdenović, Lj. & Ćirjaković, R., Dependence of the Properties of Cordierite–Mullite Ceramics on Synthesis Conditions. *Ind. Ceramics*, **13** (1993) 31–4.

Journal of the European Ceramic Society 16 (1996) 865–872

0955-2219(95)00207-3
0955-2219/96/$15.00 +.00

Wear Behaviour of Alumina and Sialon in Line Contact Lubricated with Diamond Slurry

E. Jisheng,[a] T. A. Stolarski,[a]* & D. T. Gawne[b]

[a]Department of Mechanical Engineering and [b]Department of Materials Technology, Brunel University, Uxbridge, Middlesex UB8 3PH, UK

(Received 5 April 1995; revised version received 6 November 1995; accepted 13 November 1995)

Abstract

Investigation into the wear behaviour of alumina and sialon was carried out in the line contact configuration lubricated with diamond slurry. The experiments were conducted using different counterface materials, contact loads and size of the diamond abrasive particles in the slurry. The results indicate that the material removal rate depends significantly on the action of the diamond particles and counterface material. Both contact conditions facilitate easy ingress of diamond particles into the interface and the ability of the counterface material to entrap diamond particles contributes to a high rate of material removal.

1 Introduction

Engineering ceramics have found use in many applications, such as engine parts, ball bearings, artificial bone and hip replacements and gyroscopes, because of their good chemical inertness, hardness, high temperature stability and very good wear resistance. These advantages, however, are somewhat compromised by the difficulties in their processing. An example in question is the extremely low material removal rate during conventional grinding, which obviously makes surface finishing processes of ceramics an expensive operation. Increasing use of ceramics in a variety of applications has created a need for better understanding of the mechanisms involved in the grinding process so that an effective grinding method can be developed.

There are many methods of grinding of ceramics. Creep feed grinding, ultrasonic-assisted grinding, energy-beam-assisted grinding, magnetic fluid grinding all serve as examples. However, the dominant and most effective commercial current practice remains diamond slurry grinding.[1] Many researchers have paid a lot of attention to the mechanism of material removal during grinding.[2–4] In the diamond slurry grinding process, some of the key factors responsible for the increase in the material removal rate may be considered in terms of the action of the diamond particles and the characteristics of the counterface materials. Kato[5] studied the grinding process using a rolling contact configuration and a magnetic fluid containing diamond particles. His results show that the material removal rate is almost 40 times higher than that achievable in a non-magnetic environment. Childs *et al.*[6] found that this high material removal rate results from a considerable amount of skidding taking place within the contact region. Stolarski *et al.*[7] pointed out that the high material removal rate occurs when the abrasive action of diamond particles is a dominant mechanism.

In this paper the results of a study into the factors controlling the material removal rate during model grinding experiments are presented. The emphasis is on the understanding of the relationships between effectiveness of material removal and the characteristics of ceramic, counterface material, contact sliding conditions, and the composition of diamond slurries.

2 Experimental Conditions

2.1 Grinding tester

All the tests described in this paper were carried out in the modified Falex machine. Figure 1 shows a ceramic sample together with counterface elements and all dimensions relevant to the experiments reported here. In the configuration used during the experiments presented in this paper, a ceramic specimen in the form of a pin (6.5 mm nominal diameter and 25·4 mm long) was attached to the shaft driven by an electric motor. The specimen was in line contact with two V-shaped blocks and the load on the contact was applied through the

*To whom correspondence should be addressed.

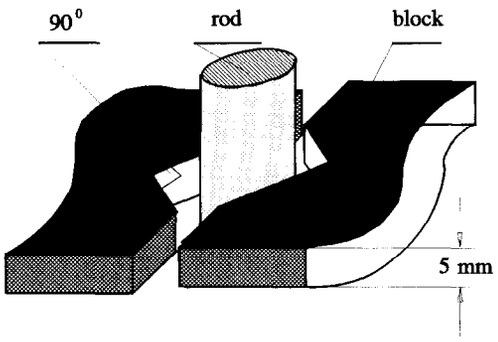

Fig 1. Contact configuration used during the grinding experiments.

blocks. The length of the contact was 5 mm. Both ceramic specimen and V-shaped blocks were submerged in the diamond slurry contained in a specially shaped container. To prevent sedimentation of diamond particles a small stirrer was attached to the ceramic specimen, as there was no magnetic field which could help keep the abrasive particles in suspension.

2.2 Materials

Two types of ceramic, namely sialon and alumina, were tested. Both ceramic materials were supplied as rods 6·5 mm in diameter and 10 mm long. Three different materials were used for the V-shaped blocks: they were mild steel, brass and aluminium alloy. However, the majority of testing was carried out using steel V-blocks. Oil-based diamond slurries with four sizes of diamond particles, namely 1, 6, 15 and 25 μm, were used throughout the experiments.

2.3 Experimental procedure

All experiments were carried out at the speed of 300 rev min^{-1}. The amount of slurry placed in the container was 20 ml and was sufficient to submerge completely the contact between the ceramic rod and the V-shaped counterfaces. The required speed of the ceramic specimen was attained first, then the load on the contact was carefully applied. The load on the contact ranged from 135 to 900 N. The duration of a typical test was 60 min. The temperature in close proximity to the contact zone was continuously monitored using a thermocouple placed at the trailing edge of one of the V-blocks. Before each test all experimental pieces, i.e. specimen, V-shaped blocks and the container, were ultrasonically cleaned in acetone. Both ceramic specimen and V-blocks were weighed before and after the test to obtain an estimate of the rate of material removal. The rate of material removal is expressed as a volume loss of material per unit time calculated on the basis of weight measurements.

2.4 Surface analyses

Scanning electron microscopy (SEM) was used to examine the appearance of the ceramic surface, debris produced during the test and the V-blocks. Optical microscopy was used to examine the metallurgical microstructure of the V-blocks.

3 Results

3.1 Alumina experiments

3.1.1 Effect of applied load and diamond particle size

Results obtained during tests on alumina in contact with steel V-blocks are presented in Fig. 2. In this figure the rates of material removal are plotted against the load on contact for different sizes of diamond particles. The first observation to be made is that the material removal rate increases with the applied load for all sizes of diamond particles. For diamond particle sizes of 1, 15 and 25 μm the change in material removal rate with load is linear. In the case of 6 μm diamond particles, a clear transition in the material removal rate occurring at a load of 450 N can be seen.

The rate of material removal also increases with the size of diamond particles. This is true for 1, 6 and 15 μm diamond particles. A maximum rate of material removal is found to be for 15 μm particles. Further increase in diamond particle size brings about a substantial decrease in material removal rate. In fact, under the load of 675 N, the rate of material removal for 25 μm diamond particles is almost 20 times lower than that recorded for 15 μm particles and approximately five times lower than the removal rate for 1 μm particles.

In Fig. 3 the temperature, recorded by the thermocouple located at the trailing edge of the V-shaped block, is presented in a function of applied load for all four sizes of diamond particles used. It is seen that the temperature increases steadily with

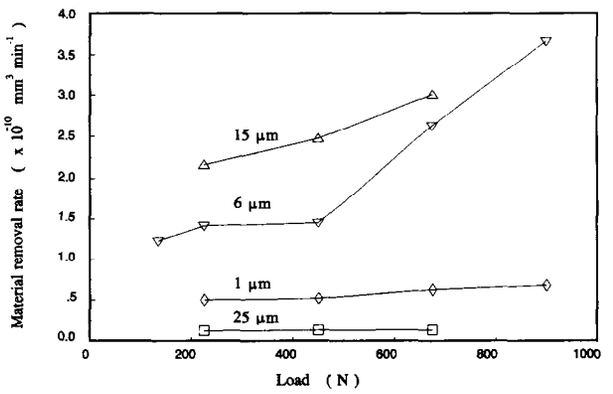

Fig. 2. Material removal rate of alumina as a function of the applied load for different sizes of diamond particles in the slurry. Rotational velocity of the ceramic pin, 300 rev min^{-1}; duration of the test, 60 min.

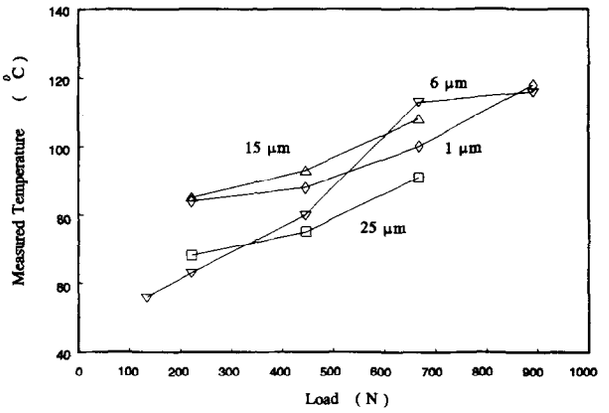

Fig. 3. Temperature within the contact zone as a function of the applied load for alumina and different sizes of diamond particles in the slurry. Rotational velocity of the ceramic pin, 300 rev min^{-1}; duration of the test, 60 min.

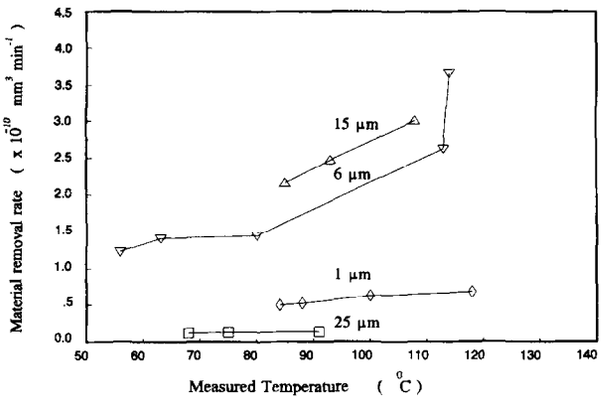

Fig. 4. The relationship between material removal rate and contact temperature for alumina and different sizes of diamond particles in the slurry. Rotational velocity of the ceramic pin, 300 rev min^{-1}; duration of the test, 60 min.

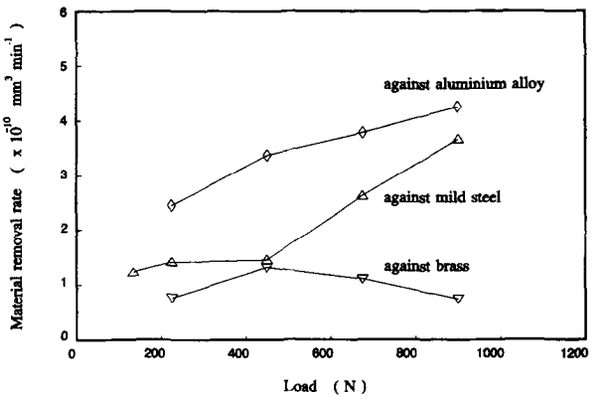

Fig. 5. Variation in the alumina removal rate with the applied load for different counterface materials. Diamond slurry with 6 μm particles; rotational velocity of the ceramic pin, 300 rev min^{-1}; duration of the test, 60 min.

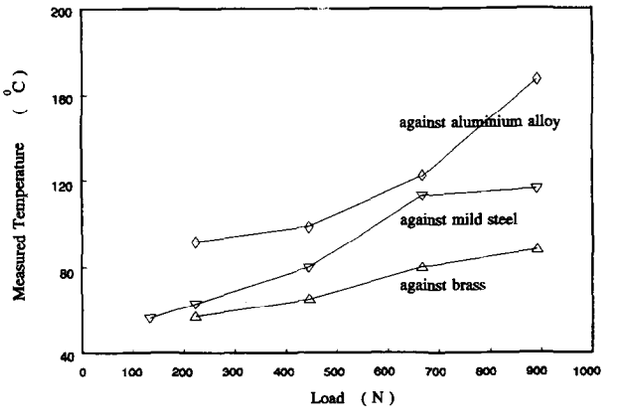

Fig. 6. Temperature within the contact zone as a function of the applied load for alumina and different counterface materials. Diamond slurry with 6 μm particles; rotational velocity of the ceramic pin, 300 rev min^{-1}; duration of the test, 60 min.

the applied load for all sizes of diamond particles used. The highest temperatures were recorded for 15 μm diamond particles followed by 1 μm and 25 μm. The temperature rise during grinding in the presence of 6 μm particles is the lowest up to a load of 300 N, thereafter a very fast increase in temperature with load was observed. At 675 N the temperature for 6 μm particles is the highest.

The relationship between temperature within the contact and the rate of material removal is shown in Fig. 4. It is seen that high rates of material removal are associated with relatively high temperatures. However, this relationship is strongly influenced by the size of the diamond particles.

3.1.2 Effect of counterface material

To examine the effect of counterface material on the efficiency of grinding, V-blocks made of mild steel, aluminium alloy and brass were used during experiments in 6 μm diamond slurry. Figure 5 shows the results obtained. The highest material removal rates were obtained for the aluminium alloy over the whole range of applied loads. The lowest rates were recorded for brass, therefore no more experiments were carried out with V-blocks made of brass. Mild steel produced removal rates

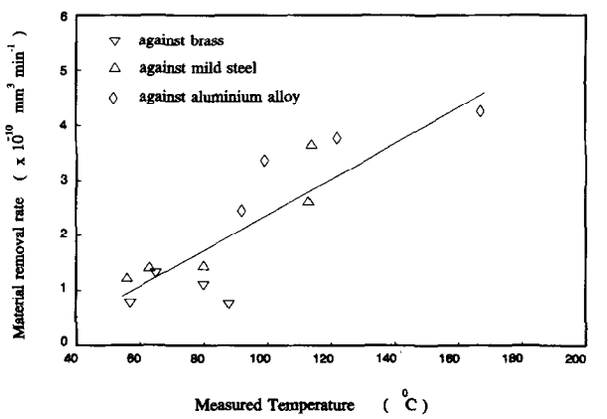

Fig. 7. The relationship between material removal rate and contact temperature for alumina and different counterface materials. Diamond slurry with 6 μm particles; rotational velocity of the ceramic pin, 300 rev min^{-1}; duration of the test, 60 min.

somewhere between these two. This finding points to the importance of retention of abrasive particles within the contact region. It appears that aluminium alloy is the material into which the diamond particles could embed more easily, compared with the other two materials used.

Variations in the contact temperature for all three counterface materials are presented in Fig. 6, while the relationship between contact temperature and the rate of material removal is shown in Fig. 7.

3.2 Sialon experiments

3.2.1 Effect of diamond particles size

The removal rates of sialon for different sizes of diamond particles were investigated at constant load of 900 N. Figure 8 shows the results for mild steel and aluminium alloy counterfaces. It is interesting to note that the maximum rate for the mild steel counterface was achieved when 6 μm diamond particles were used. In the case of the aluminium alloy counterface, the maximum removal rate was obtained for 15 μm diamond particles. Both maximum removal rates are of the same magnitude. The temperatures within the contact area are substantially higher for the aluminium alloy counterface than for the mild steel, as evidenced by the results shown in Fig. 9. For the aluminium alloy counterface the temperature rises steadily with increasing size of the diamond particles. This is not the case for the mild steel counterface where a clear maximum exists. This maximum occurs for 15 μm diamond particles.

3.2.2 Effect of applied load

To find the load at which the rate of material removal is at its highest, grinding experiments on sialon were carried out in 15 μm diamond slurry using both aluminium alloy and mild steel counterfaces. Figure 10 shows the material removal rate plotted against the applied load. Both counterface materials used produce almost linear increase in the material removal rate with increasing load. Again, the aluminium alloy counterface proved to be more effective in material removal than the mild steel counterface under nominally the same

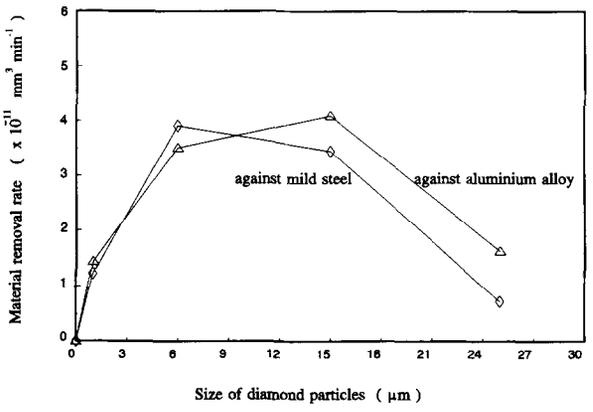

Fig. 8. Sialon removal rate as a function of diamond particles size for different counterface materials. Rotational velocity of the ceramic pin, 300 rev min^{-1}; duration of the test. 60 min.

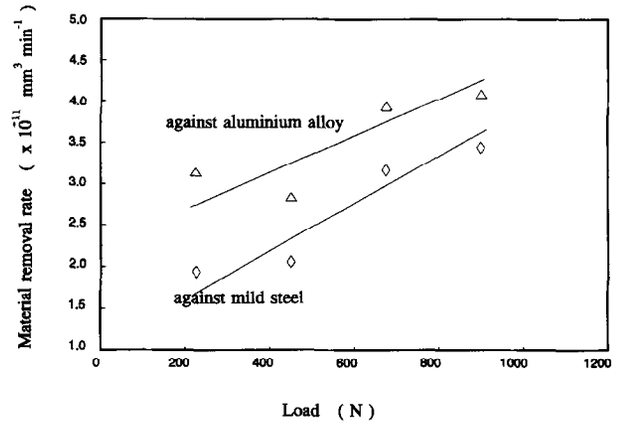

Fig. 10. Sialon removal rate as a function of the applied load for mild steel and aluminium alloy as counterface materials. Diamond slurry with 15 μm particles; rotational velocity of the ceramic pin, 300 rev min^{-1}; duration of the test, 60 min.

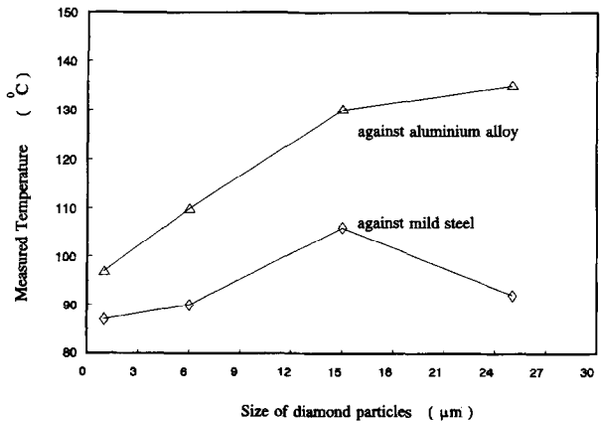

Fig. 9. Temperature within the contact zone as a function of the size of diamond particles in the slurry for different counterface materials. Ceramic material, sialon; rotational velocity of the ceramic pin, 300 rev min^{-1}; duration of the test, 60 min.

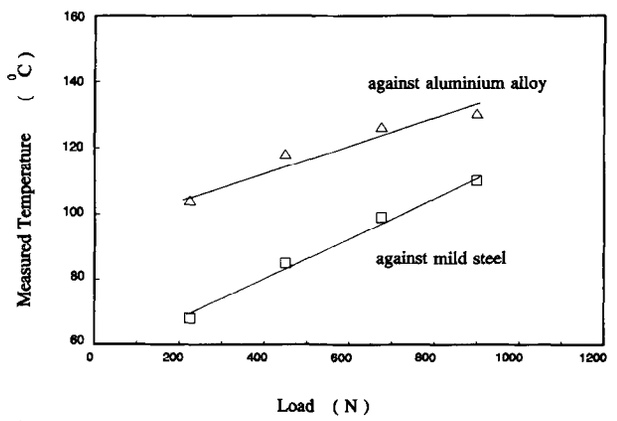

Fig. 11. Temperature within the contact zone as a function of the applied load for sialon in contact with mild steel and aluminium alloy counterface. Diamond slurry with 15 μm particles; rotational velocity of the ceramic pin, 300 rev min^{-1}; duration of the test, 60 min.

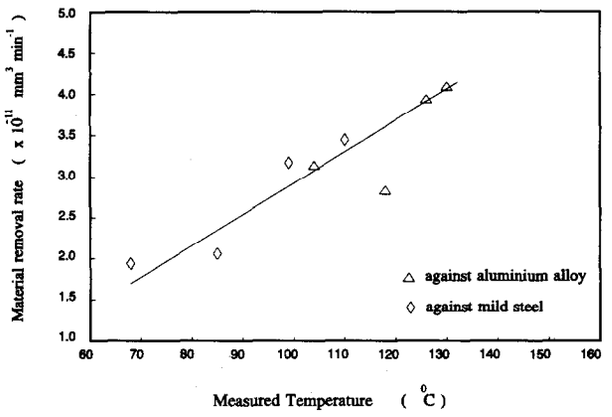

Fig. 12. Relationship between sialon removal rate and contact temperature for mild steel and aluminium alloy counterface. Diamond slurry with 15 μm particles; rotational velocity of the ceramic pin, 300 rev min^{-1}; duration of the test, 60 min.

test conditions. Temperature variations with applied load for both counterface materials used are shown in Fig. 11. The change in temperature with applied load is linear and higher temperatures were recorded for the aluminium counterface. The relationship between material removal rate and temperature within the contact is also linear for both counterface materials used (see Fig. 12).

4 Discussion

4.1 Transition from high to low material removal rate

In general, the rate of material removal of alumina increases linearly with increase in the applied load for 1, 15 and 25 μm diamond particles. However, the alumina removal rate in 6 μm diamond slurry shows a clear transition at a load of 450 N, as shown in Fig. 2. This transition can be explained in terms of the ability of the different sized abrasive particles to embed themselves into the steel counterface under a given load. It appears that, under loads of 450 N and above, 15 μm abrasive particles were able to anchor themselves permanently into the counterface, hence the observed transition in material removal rate. To clarify this behaviour further, microscopy studies of the ceramic microstructure resulting from grinding tests were undertaken. Figure 13(a) shows the appearance of alumina before grinding; Figs 13(b) and 13(c) show surfaces after grinding experiments in 6 μm slurry under 450 N and 900 N, respectively. The grinding direction is from bottom right to top left. Both ground surfaces show the same features characteristic for grinding. Surface grooves are in the direction of grinding and their size (depth and width) is proportional to the applied load. The

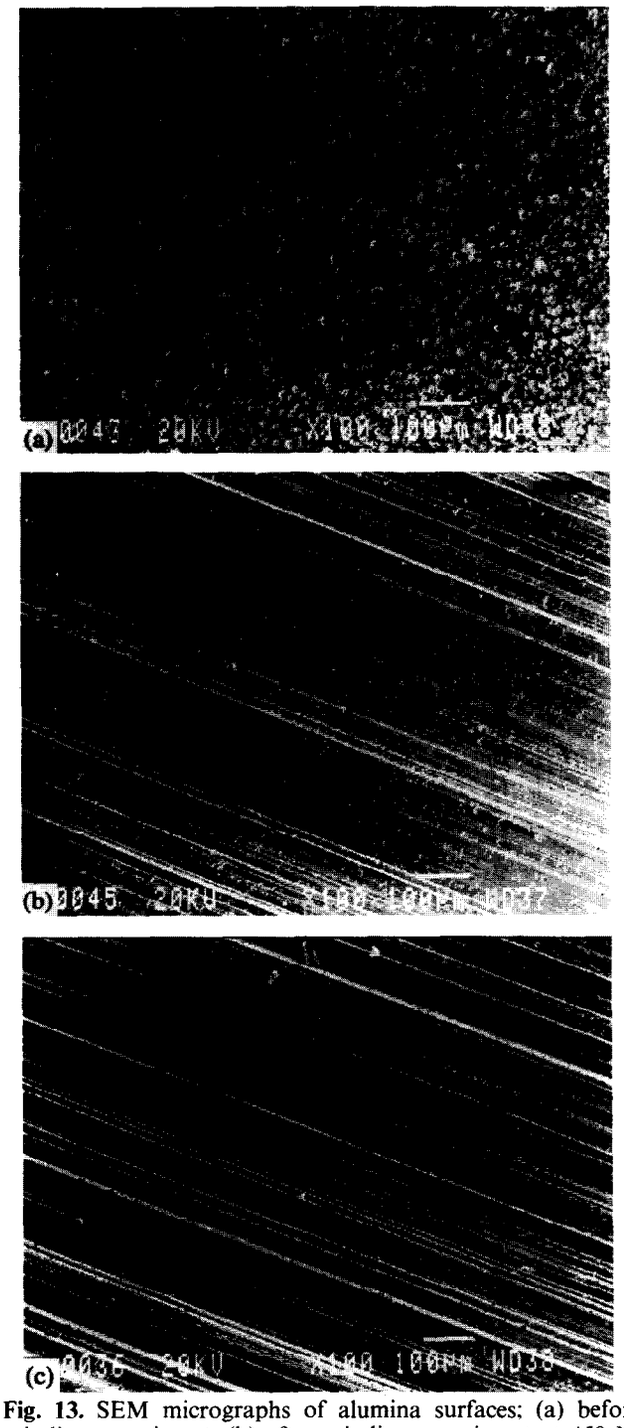

Fig. 13. SEM micrographs of alumina surfaces; (a) before grinding experiment; (b) after grinding experiment at 450 N; (c) after grinding experiment at 900 N. Diamond slurry with 6 μm particles; rotational velocity of the ceramic pin, 300 rev min^{-1}; duration of the test, 60 min.

deeper and wider the grooves, the higher the material removal rate. It can also be said that the high material removal rate is associated with rather poor surface finish.

4.2 Role of diamond particle size in material removal process

It is well known that the rate of material removal depends on the size of abrasive particles used and usually increases with the increase in their size.[7,8]

In this study, however, it was found that the above trend is not exactly observed. As can be seen in Figs 2 and 8, the rate of material removal is clearly lower for 25 μm diamond particles than for 15 μm particles, at which a maximum rate was recorded. This is true for both alumina and sialon.

To provide some explanation for this trend in material removal, it is helpful to consider the number of diamond particles per unit volume of the slurry as this seems to be an important parameter governing the grinding process. It can be easily shown that, on average, in a unit volume of 1 μm slurry there are approximately 16 000 more diamond particles than in the same unit volume of 25 μm slurry.[7] It follows then that 1 μm diamond slurry should give higher material removal rates due to the larger number of diamond particle–ceramic rod contacts per unit time than in the 25 μm slurry. This, however, should be considered in conjunction with possible hydrodynamic effects within the contact area. As there is no direct evidence in support of the explanation given below, therefore it must be regarded as only hypothetical.

The load, speed, grinding slurry liquid and contact geometry could have created conditions under which 15 μm particles were able to enter the contact between the V-block and the ceramic rod and be embedded there, because the fluid film created by the hydrodynamic action was of an appropriate thickness. In case of 1 μm and 6 μm particles the fluid film was apparently too thick, so that they passed through the contact zone without removing much of the material. On the other hand, the fluid film thickness created under similar conditions of load, speed and contact geometry must have been too small for the 25 μm particles so they could not easily enter the contact zone. Hence the material removal rates recorded are significantly lower.

For a high rate of material removal to be achieved during a grinding experiment it was essential that diamond particles could gain easy access to the contact zone and stay there. The retention of particles in the contact zone is only possible if they can embed into the counterface. Figure 14 shows SEM micrographs of the mild steel counterface after grinding experiments on sialon in 6 and 25 μm slurries. It is clearly seen on both micrographs that diamond particles entered the counterface. However, it seems that 6 μm particles penetrated the counterface much more easily and, more importantly, are embedded more firmly [Fig. 14(a)] than 25 μm particles [Fig. 14(b)]. This can be justified by the number of diamond particles seen on the micrographs shown in Fig. 14. A direct consequence of that could be the decrease in material removal rate observed.

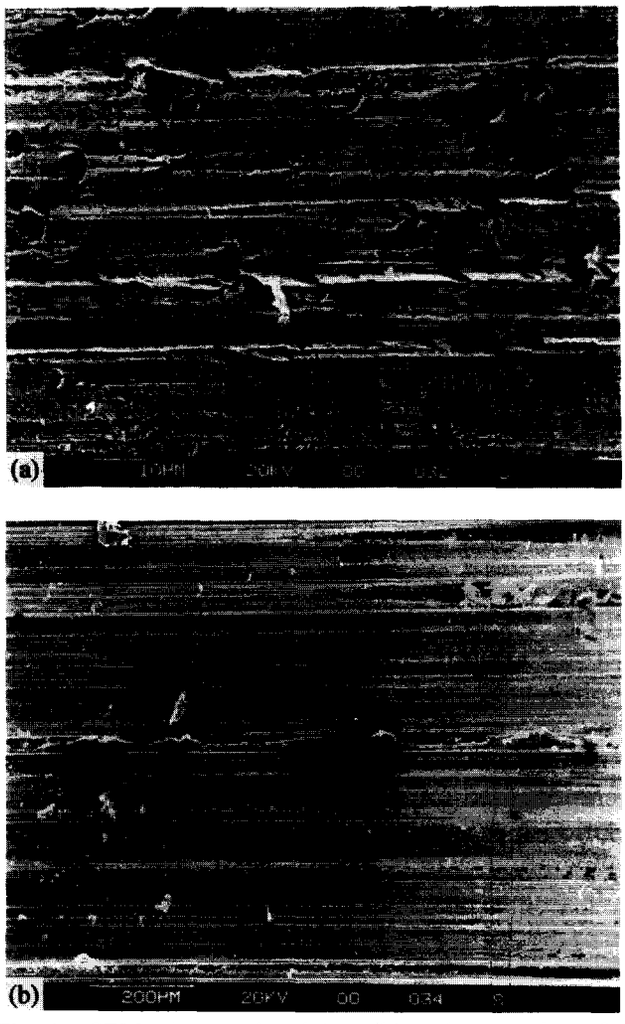

Fig. 14. SEM micrographs of the mild steel counterface after grinding experiment at 900 N and 300 rev min^{-1}; (a) 6 μm slurry: (b) 25 μm slurry.

4.3 Counterface materials

It is clear from Figs 5 and 8 that the counterface material has a considerable effect on the removal rate. In an attempt to explain this, the counterface surface after grinding experiments on sialon in 15 μm diamond slurry at the load of 900 N was examined under a microscope. The results are shown in Figs 15(a) and 15(b) for mild steel and aluminium counterfaces, respectively.

Figure 16 shows the changes in hardness of steel and aluminium counterfaces after a grinding experiment on alumina in 6 μm diamond slurry. It is seen that the surface of the aluminium counterface is considerably harder than its interior [Fig. 16(a)]. The decrease in hardness takes place over the depth of almost 200 μm, after which the hardness remains constant. This points to an appreciable work-hardening of aluminium occurring during grinding and is supported by findings from abrasive wear tests reported by Gahr-Zum.[9] On the other hand, the hardness of the steel counterface does not change at all as evidenced by the results presented in Fig. 16(b).

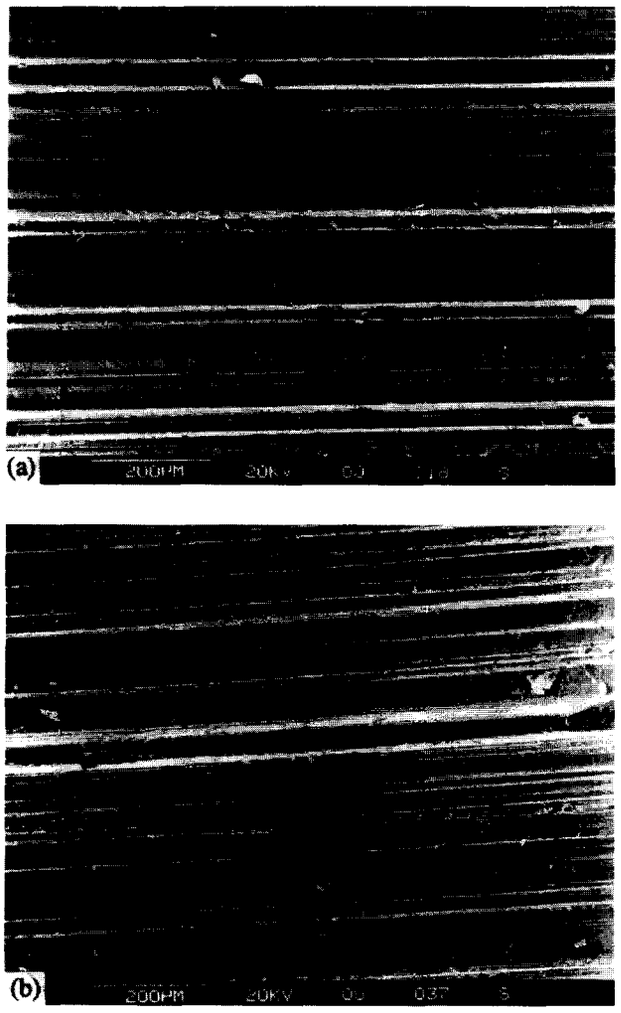

Fig. 15. SEM micrographs of counterface surfaces after grinding experiment at 900 N and 300 rev min^{-1} in 6 μm slurry: (a) mild steel; (b) aluminium alloy.

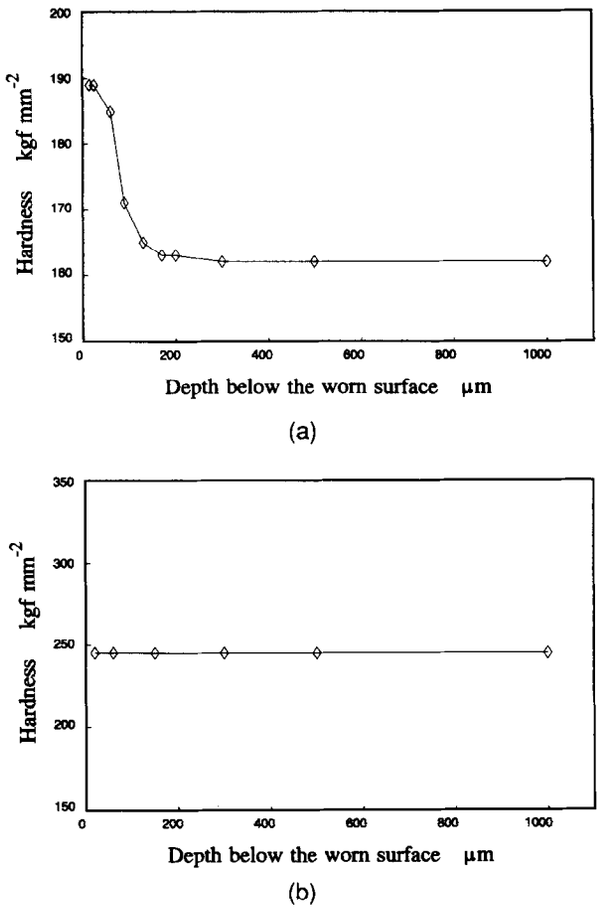

Fig. 16. Hardness profile of counterfaces after grinding experiment at 900 N and 300 rev min^{-1} in 6 μm slurry: (a) mild steel; (b) aluminium alloy.

It could therefore be argued that diamond particles penetrate the aluminium counterface much more easily and have a better chance to be retained by the counterface due to a significant work-hardening effect. This is apparently not the case with the steel counterface. It is not only harder than the aluminium counterface (more difficult ingress into the material for diamond particles) but it also does not undergo any work-hardening, resulting in a poor retention of diamond particles. This is believed to be the main reason why the aluminium counterface is more effective in material removal than the mild steel one.

The third counterface material used during grinding experiments was brass, which was characterized by the lowest hardness among the materials tested. It also gave the lowest material removal rates (see Fig. 5). Figure 17 shows optical images of the cross-section through the brass counterface after a grinding test on alumina in 6 μm diamond slurry. It can be clearly seen that the outermost layer has a different structure than the bulk material. Microhardness measurements revealed that this top layer is softer than the bulk material. In the context of material removal rate it means that this relatively soft layer of material could have acted as a solid lubricant, preventing embedded diamond particles from remaining in the contact zone. As a result, a low rate of grinding was observed.

5 Conclusions

The results presented in this paper lead to the following conclusions.

(1) The rate of wear of alumina and sialon in sliding contact depends on the size of the abrasive particles and the counterface material.
(2) The highest wear rates were achieved for the aluminium counterface followed by the mild steel counterface. The lowest wear rates were obtained for the brass counterface.
(3) Grinding in 15 μm diamond slurry consistently resulted in high material removal rates.
(4) The rate of material removal increases with an increase in the applied load on the contact.

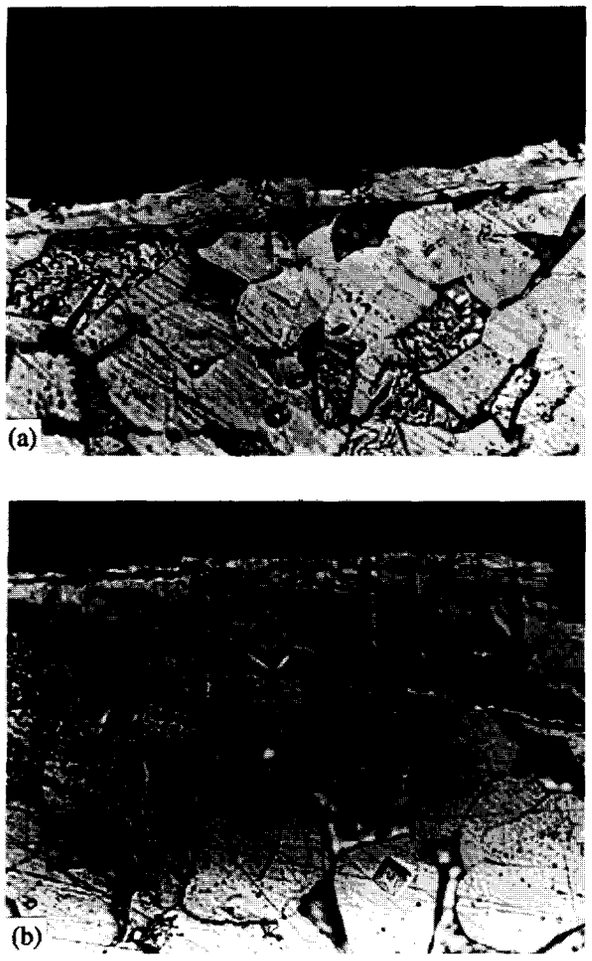

Fig. 17. Optical micrographs of the cross-section through the brass counterface after grinding experiment at 900 N and 300 rev min^{-1} in 6 μm slurry.

(5) The roughness of ground surfaces increases with an increase in the material removal rate.

Acknowledgements

The authors would like to thank the Engineering and Physical Science Research Council and the Defence Research Agency, who jointly funded this research, for permission to publish this paper.

References

1. Wang, J. C. & Hus, S. M., Chemically assisted machining of ceramics. *Trans. ASME J. Tribol.*, **116** (1994) 423.
2. Malkin, S. & Ritter, J. E., Grinding mechanisms and strength degradation for ceramics. *J. Eng. Ind.*, **111** (1989) 167.
3. Rezaei, S. M., Sato, T., Waido, T. & Noguchi, H., Creep feed grinding of advanced ceramics. *Proc. IMechE, J. Eng. Manuf.*, **206** (1992) 93.
4. Van der Berg, P. H. J., Strength and residual stress of Mg-PSZ after grinding. *Wear*, **160** (1993) 301.
5. Kato, K., Tribology of ceramics. *Wear*, **136** (1990) 117.
6. Childs, T. H. C., Jones, D. A., Mahmood, S., Zhang, B., Kato, K. & Umehara, N., Magnetic fluid grinding mechanics. *Wear*, **175** (1994) 189.
7. Stolarski, T. A., Jisheng, E., Gawne, D. T. & Panesar, S., The effect of applied load and abrasive particle size on the material removal rate of silicon nitride artefacts. *Ceram. Int.*, **21** (1995) 355–66.
8. Yamamoto, T., Olsson, M. & Hogmark, S., Three-body abrasive wear of ceramic materials. *Wear*, **174** (1994) 421.
9. Gahr-Zum, K. H., *Microstructure and Wear of Materials*. Elsevier, Amsterdam, 1987, p. 400.

Journal of the European Ceramic Society 16 (1996) 873–883

0955-2219(95)00213-8
0955-2219/96/$15.00 +.00

Reactions Occurring in Post Heat-Treated α/β Sialons: On the Thermal Stability of α-Sialon

Zhijian Shen,[a] Thommy Ekström[b] & Mats Nygren[b]

[a]Department of Materials Science and Engineering, Zhejiang University, Hangzhou 310027, People's Republic of China
[b]Department of Inorganic Chemistry, Arrhenius Laboratory, University of Stockholm, S-106 92 Stockholm, Sweden

(Received 29 September 1995; revised version received 23 November 1995; accepted 29 November 1995)

Abstract

To a powder mixture of an overall α-sialon composition $R_{0.4}Si_{10.2}Al_{1.8}O_{0.6}N_{15.4}$, *with* R= *Nd, Sm, Dy and Yb, were added extra amounts of powder mixtures, (20%), having Si:Al:*R *and O:N atomic ratios of 2:1:1 and 3:1, respectively. Series of α-rich mixed α/β-sialon ceramics containing about 20–30 vol% glassy phase were prepared from these powders by pressureless sintering at 1750°C. The as-prepared samples were subsequently heated at 1750°C and then quenched to room temperature or to 1150, 1300 and 1450°C (with a cooling rate exceeding 400°/min), and were annealed at these temperatures for various times. The samples quenched to room temperature revealed that α-sialon coexists with β-sialon and a liquid phase at 1750°C. The post heat-treatment at the lowest temperature involved a devitrification of the glassy phase and resulted in mixtures of mainly rare earth oxynitrides like the U-phase* $R_3Si_3Al_3O_{12}N_2$, *wollastonite* $RSiO_2N$ *or the B-phase* Dy_2SiAlO_5N. *Post heat-treatment at 1450°C induced a reaction between residual liquid and α-phase in the Nd- and Sm-systems and yielded a mixture of an oxygen- and a nitrogen-rich phase in all systems. Thus the melilite phase,* $R_2Si_{3-x}Al_xO_{3+x}N_{4-x}$, *is formed with all rare earth elements except Yb, which yields* $Yb_4Si_2O_7N_2$. *The oxygen-rich phase in the Nd- and Sm-systems was the aluminate* $RAlO_3$, *while in the Dy- and Yb-systems the garnet phase,* $R_3Al_5O_{12}$, *was formed. Similar results were obtained with samples quenched to 1300°C. These findings suggest that the stability of α-sialon is related to the type of sintering aid used. The phase assemblage found in the as-prepared samples is discussed in view of the findings obtained in the annealing experiments.*

1 Introduction

Sialon ceramics containing α- and/or β-sialon as the main constituents can be prepared by pressureless sintering when an excess of sintering aid(s) is used.[1–4] The observed high toughness of β-sialon is due to the presence of elongated β-crystals and an intergranular glassy phase: in tensile stresses, the cracks will follow tortuous pathways through the microstructure mainly within the latter phase.[5,6] However, the hardness of β-sialon ceramics, as well as the use of these materials at very high temperatures is restricted because of the presence of substantial amounts of residual glassy phase(s) in their microstructures.[4,7] Therefore, the α-sialon ceramics have attracted more attention recently, since they show excellent hardness and offer possibilities of reducing the amount of glassy phase by incorporating the constituents of sintering aids into the crystal lattice.[7,8] Post-sintering heat-treatment has become a frequently used technique for improving the high-temperature properties of sialon ceramics, as this procedure introduces a devitrification of the residual grain-boundary glassy phase.[9–11]

α-Sialon, isostructural with α-Si_3N_4, has an overall composition given by the formula $R_xSi_{12-(m+n)}Al_{m+n}O_nN_{16-n}$, where m(Si–N) are replaced by m(Al–N) and n(Si–N) by n(Al–O). The valence discrepancy introduced by the former substitution mechanism is compensated by the metal ion R^{p+}, where $m=px$.[12–15] The elements R of special interest for engineering α-sialon ceramics intended for use at high temperatures, are Y and the rare-earth elements Nd–Yb.[16] It has been shown that monophasic α-sialons samples are formed in a quite restricted compositional area, which does not vary extensively with the used R-element but does increase somewhat with decreasing size of the rare-earth cations.[14,17] Between the α-sialon plane and the β-sialon phase, $Si_{6-z}Al_zO_zN_{8-z}$, there is an area where α-and β-sialon phases coexist. These composition areas are quite similar in different R–Si–Al–O–N systems and are of special interest because, by carefully adjusting overall compositions

and using a transient liquid phase sintering route, a new kind of '*In situ* reinforced' or 'Self-reinforced' α–β sialon composite can be prepared, with only a minimum amount of residual glassy grain boundary phase.[18]

Recent results reported by different research groups have shown, however, that the α-sialon phase is thermodynamically unstable at lower temperatures in some *R*-sialon systems; i.e. in the presence of an intergranular liquid/glassy phase it tends to transform to β-sialon and other rare-earth-rich grain boundary phase(s).[10,19–21] The instability of the α-sialon at lower temperatures has been attributed to the smaller rare-earth cations being able to occupy the large voids present in the α-sialon structure at the sintering temperature, but not at lower temperatures.[10]

Our recent studies concerning the instability of the α-sialon phase in pure α- and duplex α–β-sialon systems have confirmed that $\alpha \rightarrow \beta$ transformations exist in different rare-earth doped sialon systems.[22–25] However, the decomposition pathway of α-sialon seems to be different in different systems, and it can be related to the preparation conditions used. These studies seem to indicate that the decomposition pathway depends on: (i) the size of the *R* ion; (ii) the composition of the α-sialon itself; (iii) the amount/ composition of the liquid present at the sintering temperature; (iv) the type/ amount of grain-boundary phase(s) formed during the cooling part of the sintering cycle, which in turn seems to depend on the cooling rate applied. Thus, in order to obtain an optimised microstructure all these factors need to be considered.

In this article we will describe the effect of the crystallization/devitrification of residual liquid/ glassy phase on the thermal stability of the α-sialon phase in different rare-earth doped sialon ceramics containing an excess amount of intergranular phase(s). For this purpose a series of α-rich α/β-sialons were prepared, containing an excess of added sintering aids. These materials were post heat-treated in different ways. In order be able to reveal the true phase composition at elevated temperatures and the thermal stability of the α-sialon phase at these temperatures, a furnace set-up was used which allowed very rapid cooling rates. Special attention will be paid to studies of the decomposition pathway of the α-sialon phase.

2 Experimental

α/β-Sialon compacts samples designed to have an excess of a glassy-phase (≥20 vol%) were prepared in the present work. To a powder mixture of the overall α-sialon composition $R_{0.4}Si_{10.2}Al_{1.8}O_{0.06}N_{15.4}$, with *R*= Nd, Sm, Dy and Yb, were added extra amounts of powder mixtures (20%) having Si:Al:*R* and O:N atomic ratios of 2:1:1 and 3:1, respectively. The designed overall compositions of the prepared samples (labelled GAR04 below) are summarised in Table 1.

Specimens were prepared from commercial Si_3N_4(UBE, SN-E10), AlN (H.C. Starck-Berlin, grade A), Al_2O_3 (Alcoa, A16SG), SiO_2 (99·9%, 325 mesh, Johnson Matthey Chemicals Ltd) and R_2O_3 (99·9%, Johnson Matthey Chemicals Ltd). The rare-earth oxide powders were calcined at 1000°C for 2 h before use. In the preparation of the samples, corrections were made for the small amounts of oxygen present in the Si_3N_4 and AlN raw materials. The starting material mixes were milled in water-free propanol for 24 h in a plastic jar, using sialon milling media, and the batch size used was 50 g. Pellets of dried powders (about 5 g) were first compacted in a steel die and then packed with a powder mixture of Si_3N_4, AlN and BN and pressureless sintered at 1750°C for 2 h in a graphite furnace in nitrogen atmosphere. The obtained samples were cooled to room temperature inside the furnace and are called as-prepared samples below.

Selected specimens were subsequently heat-treated in different ways. Some samples were placed in a carbon crucible embedded in the same powder bed as the one used above, and were re-heated up to 1750°C in a graphite furnace in nitrogen atmosphere. After 30 min holding time, the samples were either quenched to room temperature (at a rate of approximately 400°C/min. in the critical temperature range 1650–1000°C) by quickly moving them to a cooling chamber attached to the graphite furnace, or quenched to 1450, 1300, and 1150C, respectively. At these lower temperatures the samples were held for

Table 1. Overall compositions of the starting materials (in wt%)

Sample no.	Nd_2O_3	Sm_2O_3	Dy_2O_3	Yb_2O_3	Si_3N_4	*AlN*	Al_2O_3	SiO_2
GANd04	20·64	—	—	—	62·52	9·22	3·84	3·79
GASm04	—	21·14	—	—	62·21	9·14	3·79	3·72
GADy04	—	—	22·08	—	61·56	9·15	3·64	3·57
GAYb04	—	—	—	22·88	61·04	9·07	3·54	3·47

another 24 h (some samples were post heat-treated at 1450°C for extended times (up to 10 days)) and then quenched. The densities of the sintered specimens were measured according to Archimedes' principle.

The analyses of the crystalline phases present in the prepared samples were based on their X-ray powder diffraction records obtained in a Guinier-Hägg focusing camera with CuKα_1 radiation and Si as internal standard. The obtained photographs were evaluated with a computer-linked SCANPI system,[26] and the cell parameters were determined with the program PIRUM.[27] The z-value of the β-sialon phase, $Si_{6-z}Al_zO_zN_{8-z}$, was obtained from the unit cell dimensions of the samples, using the equations given in Ref. 28.

The phase transformations occurring in a given composition have been semi-quantitatively evaluated as a function of temperature and time have been applied. Thus, the $\alpha/(\alpha+\beta)$ ratio has been used to monitor the decomposition and formation of the α- and β-sialon phases, respectively; the M′/(M′ + A) ratio (M′ = the melilite solid solution $R_2Si_{3-x}Al_xO_{3+x}N_{4-x}$ and A-$RAlO_3$ with R=Nd, Sm and Dy) to monitor the formation of the M′ and A-phases; the M′/(M′ + G) ratio (G= samples of the garnet composition $R_3Al_5O_{12}$ with R=Dy, and Yb) to monitor the formation of the M′- and G-phases in the Dy-system and the G/(G+J) ratio (J=$Yb_4Si_2O_7N_2$) to monitor the formation of the G- and J-phases in the Yb-system. These ratios were obtained from the following relations:

$$\alpha/(\alpha+\beta) = I_{(\alpha)} / (I_{(\alpha)} + I_{(\beta)}) \quad (1(a))$$

$$M'/(M' + A) = I_{(M')} / (I_{(M')} + I_{(A)}) \quad (1(b))$$

$$M'/(M' + G) = I_{(M')} / (I_{(M')} + I_{(G)}) \quad (1(c))$$

$$G/(G+J) = I_{(G)} / (I_{(G)} + I_{(J)}) \quad (1(d))$$

where the integrated intensities $I_{(i)}$ of the following reflections were used: (i) (210) of the α-sialon; (ii) (210) of the β-sialon; (iii) (211) of the melilite solid solution (M′); (iv) (110) of the Nd aluminate, $NdAlO_3$, (200) of the Sm aluminate, $SmAlO_3$; (v) (420) of the garnet; $R_3Al_5O_{12}$ with R= Dy, and Yb; (vi) the peaks with d-values of 3·04 and 2·82 Å for the Yb J-phase, $Yb_4Si_2O_7N_2$.

After application of a carbon coating to the polished surfaces of the produced samples, these surfaces were examined in a scanning electron microscope (JEOL JSM 820, equipped with a Link AN 10000 EDS analyser). For some of the samples the Si, Al and R contents of the α-sialon grains and residual grain boundary glassy phase were determined by EDS analysis, using calibration curves. The final results reported below are averages of at least five experimental determinations.

3 Results and Discussion

3.1 Phase analysis of samples quenched from 1750°C to 1150, 1300 and 1450°C, respectively, and post heat-treated for various times

Crystallization/devitrification of the residual grain-boundary liquid/glassy phase may be achieved via two different post heat-treatment processes, namely, by heat-treatment above the glass transition temperature (T_g) but below the eutectic/liquid forming temperature of the glass, T_e, or by heat-treatment above T_e. The former process is in fact applied in conventional glass-ceramic industrial processes where the glass is devitrified at temperatures above its T_g point but below its softening temperature T_d. In this case the devitrification of the grain-boundary glass phase proceeds mainly within this phase, i.e. the main crystalline phases do not take part in the reactions. However, at temperatures exceeding T_e, a liquid is present in the material, and the crystallization of this liquid phase by heat-treatment in turn promotes reactions between this phase and the main crystalline phase(s), and in addition the liquid provides an effective diffusion pathway for the ions involved.

The liquid forming temperature (T_{lf}) in the R–Al–Si–O–N system is estimated to be around 1350°C,[10, 20, 21] and T_g and T_d of the glasses with the highest nitrogen content in these systems have been reported to be in the ranges 915–950°C and 960–1020°C, respectively.[30–32] Thus, based on these considerations, three post heat-treatment temperatures have been chosen, namely one above T_d but well below T_{lf} (1150°C), one just below T_{lf} (1300°C) and one well above T_{lf} (1450°C).

The XRD indications of phases present in samples quenched from 1750 to 1450°C (with holding times ranging from 4 to 240 h), 1300 (24 h), 1150°C (24 h) and to room temperature are given in Table 2. The table also contains observed unit cell parameters of the hexagonal α-sialon phase. The observed composition from EDS measurements of the α-sialon phase (the m, n and x-values in the formula $R_xSi_{12-(m+n)}Al_{m+n}O_nN_{16-n}$) and the Si, Al and R content in the glassy phase in samples quenched from 1750°C to room temperature are given in Table 3. The aimed-at and observed compositions of the α- and β-sialon are mapped out in Fig. 1. As α-sialon and β-sialon are in equilibrium with each other, the compositions of the obtained α-sialon are close to phase boundary, i.e. more oxygen-rich than the aimed-at composition.

Figures 2 and 3 show the SEM micrographs, obtained in back-scattered electron mode, of the samples quenched to room temperature from 1750°C and from 1450°C after annealing for 24 h.

Table 2. $\alpha/(\alpha+\beta)$ ratios and the crystalline grain boundary phases in samples post heat-treated under different conditions

Sample identification	$\alpha/(\alpha+\beta)$	*GB phase assemblage**								*α-sialon unit cell*	
		M′	*U*	*B*	*J*	*W*	*A*	*G*	*21R*	a(Å)	c(Å)
GANd04											
1750°C quenched	16·3	—	—	—	—	—	—	—	vw	7·814	5·694
1150°C/24 h	14·1	—	mw	—	—	s	—	—	vw	7·814	5·691
1300°C/24 h	0	m	—	—	—	—	s	—	vw	—	—
1450°C/4 h	0	s	w	—	—	—	m	—	vw	—	—
1450°C/24 h	0	s	—	—	—	—	ms	—	vw	—	—
1450°C/120 h	0	m	—	—	—	—	s	—	vw	—	—
1450°C/240 h	0	mw	—	—	—	—	s	—	vw	—	—
GASm04											
1750°C quenched	52·7	—	—	—	—	—	—	—	—	7·811	5·690
1150°C/24 h	34·8	—	w	—	—	mw	ms	—	—	7·810	5·690
1300°C/24 h	27·9	m	—	—	—	—	s	—	—	7·809	5·690
1450°C/4 h	28·8	s	vw	—	—	—	—	—	—	7·811	5·689
1450°C/24 h	3·6	s	—	—	—	—	—	—	—	—	—
1450°C/120 h	0	m					ms	—		—	—
1450°C/240 h	0	m	—	—	—	—	ms	—	—	—	—
GADy04											
1750°C quenched	79·5	ms	—	—	—	—	—	—	—	7·807	5·688
1150°C/24 h	70·1	m	—	w	—	—	m	—	—	7·807	5·687
1300°C/24 h	72·2	m	—	—	—	—	—	s	—	7·805	5·687
1450°C/4 h	57·5	ms	—	—	—	—	—	w	—	7·805	5·684
1450°C/24 h	47·0	s	—	—	—	—	—	mw	—	7·805	5·689
1450°C/120 h	45·0	m	—	—	—	—	—	ms	—	7·805	5·690
1450°C/240 h	36·2	m	—	—	—	—	—	ms	—	7·807	5·688
GAYb04											
1750°C quenched	78·1	—	—	—	—	—	—	—	—	7·804	5·682
1150°C/24 h	61·2	—	—	—	w	—	ms	—	—	7·804	5·683
1300°C/24 h	59·8	—	—	—	w	—	—	s	—	7·800	5·682
1450°C/4 h	64·3	—	—	—	w	—	—	s	—	7·802	5·681
1450°C/24 h	55·7	—	—	—	w	—	—	vs	—	7·800	5·682
1450°C/120 h	55·1	—	—	—	w	—	—	vs	—	7·801	5·683
1450°C/240 h	57·3	—	—	—	w	—	—	vs	—	7·801	5·682

*M′ = the melilite solid solution $R_2Si_{3-x}Al_xO_{3+x}N_{4-x}$ with R=Nd, Sm and Dy; U = the U-phase $R_3Si_3Al_3O_{12}N_2$ with R=Nd, and Sm; B = the B-phase Dy_2SiAlO_5N; J = the J-phase $Yb_4Si_2O_7N_2$; W = the wollastonite phase $RSiO_2N$ with R=Nd, and Sm; A = the aluminate phase $RAlO_3$, with R=Nd, Sm, Dy, Yb; G, the garnet phase $R_3Al_5O_{12}$ with R= Dy, and Yb; 21R = the 21R polytype $Si_xAl_{7-x}O_{3-x}N_{6+x}$.
X-ray intensities: s = strong; m = medium; w = weak; vw = very weak.

Table 3. Composition of the α- and grain-boundary glassy phases, as determined by EDS. The compositions of the precursor powders are also given

Sample	*α-sialon*			*Glassy phase*		
	m	n	x	*Si*	*Al*	R(at %)
Precursor composition	1·2	0·6	0·4	50	25	25
GANd04	1·38	0·39	0·46	45	20	35
GASm04	1·14	0·82	0·38	41	27	32
GADy04	1·11	0·80	0·37	52	20	28
GAYb04	1·11	1·19	0·37	24	52	24

The black areas are β-sialon or 21R polytype grains, the medium grey areas represent α-sialon, and the bright ones a glass phase and/or crystallized rare-earth-rich intergranular phases. It is obvious that the samples quenched from 1750°C predominantly contain elongated β-sialon grains and equiaxied α-sialon grains surrounded by a residual glassy phase. An increase of the amount of the α-sialon and a decrease of the amount of grain-boundary glassy phase with decreasing ion radius of the cation size can also be discerned. Rare-earth-rich crystalline phases, which tend to

segregate into certain areas (see Fig. 3(e)), are formed after annealing at 1450°C for 24 h.

Before discussing the crystallization/devitrification process of the intergranular liquid/glassy phase, the following general observations concerning the thermal stability of the α-sialon phase can be made:

(i) All samples quenched from 1750°C to room temperature contained α- and β-sialon grains and a glassy phase. Additional crystalline grain-boundary phases were only found in the Nd- and Dy-systems, namely 21*R* (in minor amounts) and melilite, respectively.

(ii) The $\alpha/(\alpha+\beta)$ ratio increases with decreasing radius of the R ion in samples quenched from 1750°C to room temperature, e.g. in the order Nd, Sm, Dy and Yb.

(iii) The thermal stability of the α-phase at 1450°C decreases drastically with increasing radius of the *R* ion. In fact, after 240 h post heat-treatment, no α phase is left in the Nd- and Sm-systems, and a decrease of the $\alpha/(\alpha+\beta)$ ratio with the number of hours of heat-treatment is seen in the Dy- and Yb-systems. The main part of the latter decrease is, however, probably due to the β-phase being formed during the devitrification process (see below and Figs. 3(a–d)).

(iv) The lattice parameters of the α-sialon phase vary with the *R* ion used in an expected manner, but they do not seem to vary with temperature or duration of the post heat-treatment within each system, i.e. the composition of the α-phase does not vary with time and temperature of the post heat-treatment. Such a compositional variation has previously been reported to occur in the Nd- and Sm-systems implying that the α-phases

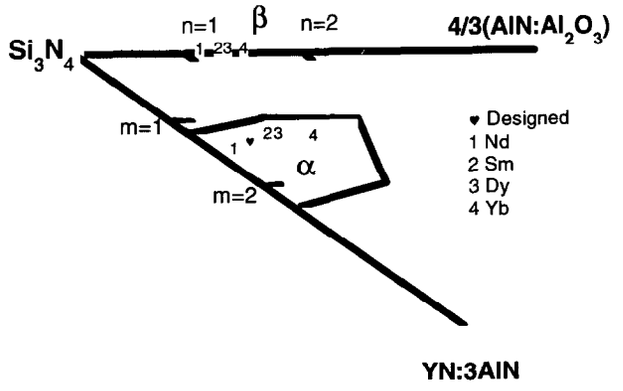

Fig. 1. A schematic illustration of the α-sialon plane in a Jänecke prism of *R*–Si–Al–O–N systems. The location of the designed α-sialon overall composition and the measured compositions of formed α- and β-sialon phases are marked.

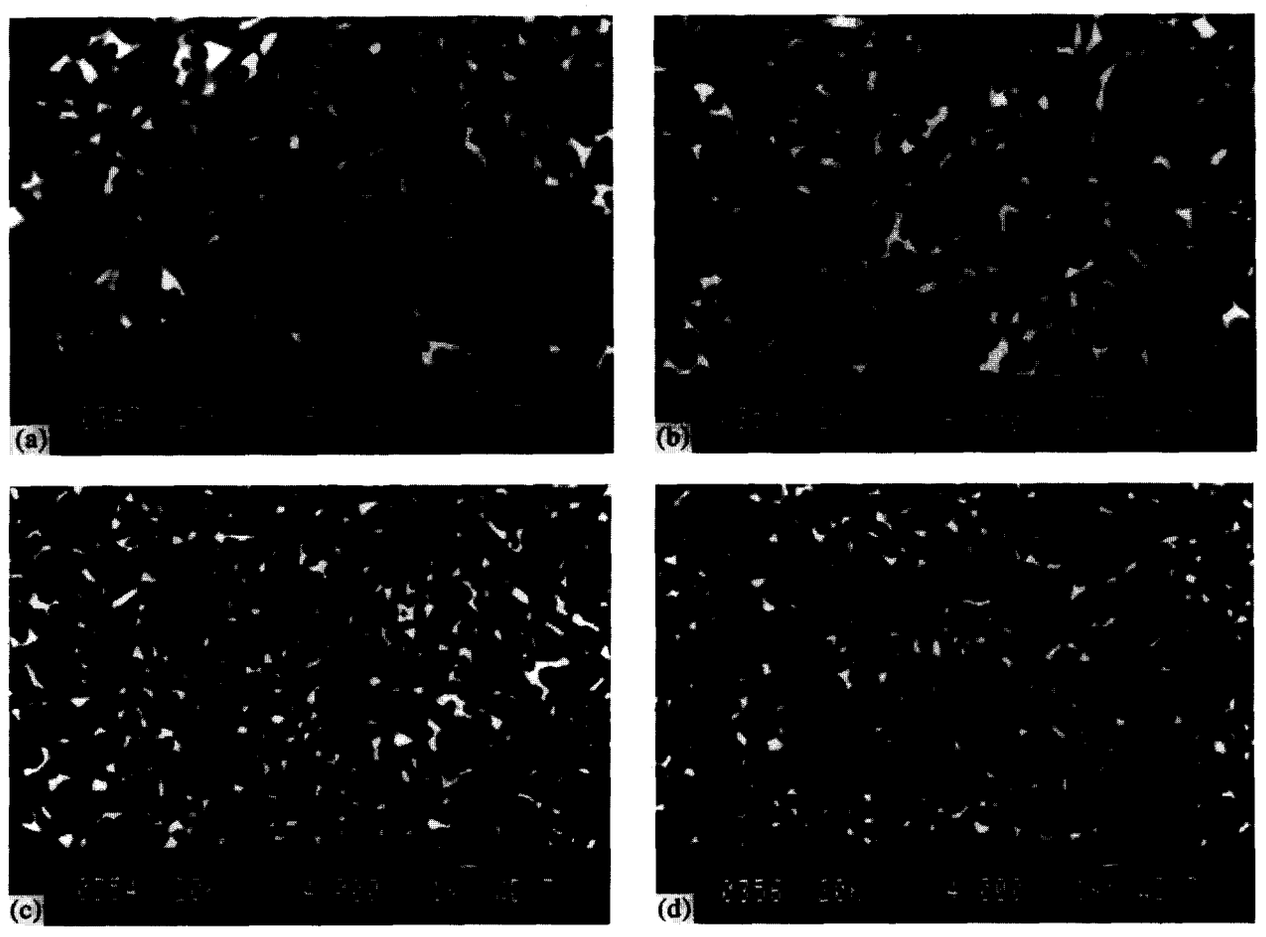

Fig. 2. SEM micrographs obtained in back scattered electron mode, illustrating the microstructure of samples quenched from 1750°C: (a) *GA*Nd04; (b) *GA*Sm04, (c) *GA*d04, and (d) *GA*Yb04.

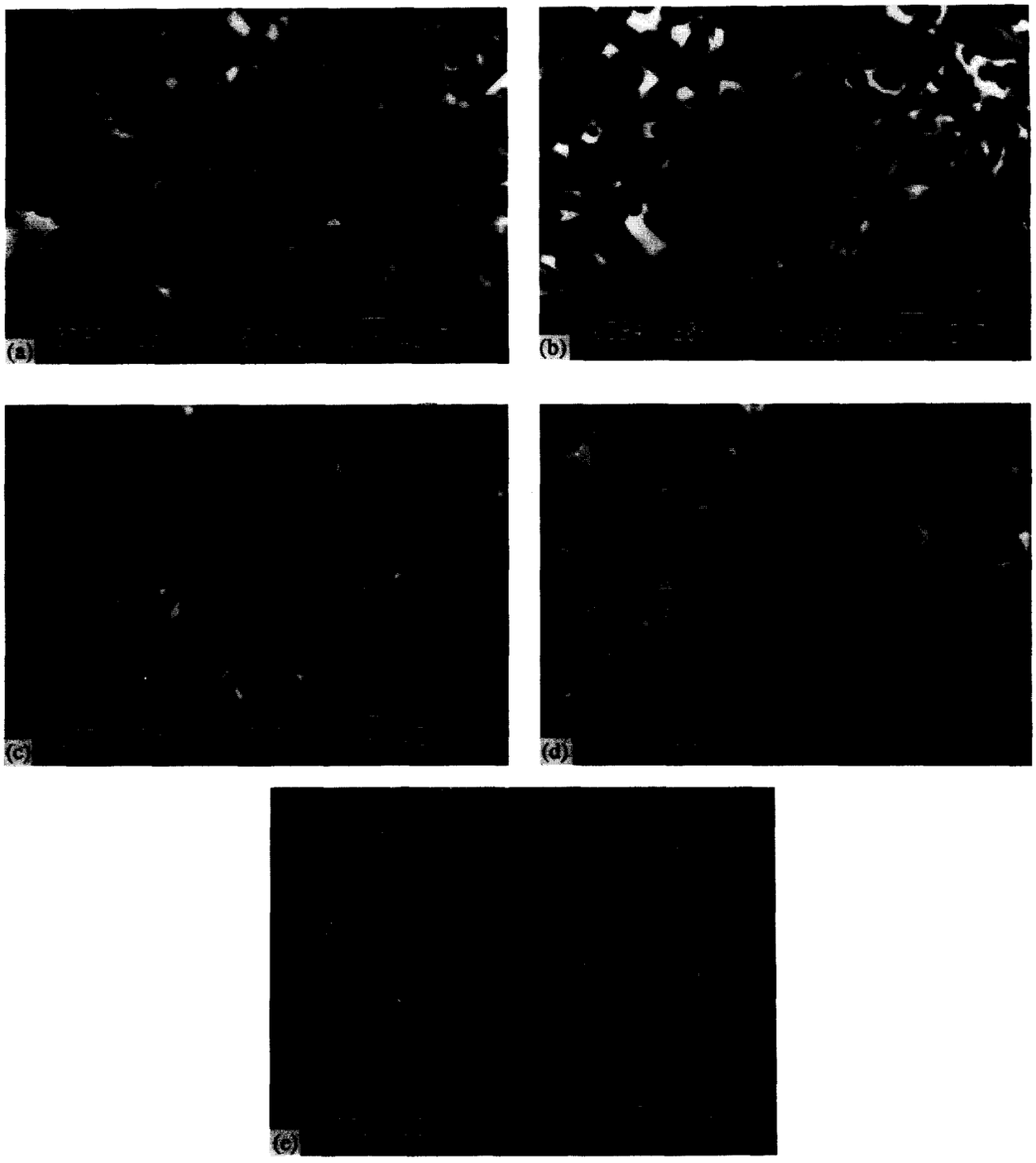

Fig. 3. SEM micrographs of samples heat-treated at 1450°C for 24 h: (a) *GA*Nd04, (b) *GA*Sm04; (c) *GA*Dy04 and (d) *GA*Yb04. The low-magnification micrograph of *GA*Dy04 shows agglomerates of the formed crystalline grain-boundary phases in (e).

lost *R*-elements upon prolonged annealing before they decomposed.[22,23] The compositions of the present α-sialon phases are, however, very close to the borderline of the α-phase area, as seen in Table 3 and Fig. 1, which in turn implies that we cannot expect any compositional variation in the present systems.

3.1.1 Heat-treatment of Nd-sialons

As mentioned above, the samples in the Nd-system, which were quenched from 1700°C to room temperature, contained minor amounts of the 21R phase, and so did all post heat-treated samples. The α-phase in this system decomposes very rapidly at 1450°C. Thus there is no α-phase left after 4 h post heat-treatment, but melilite (M′), $NdAlO_3$ (A) and minor amounts of the U-phase, $R_3Si_3Al_3O_{12}N_2$ are. Prolonged heat-treatment decomposes the U-phase, and more and more A-phase is formed; but if the amount of M′-phase decreases, it decreases at a lower rate than the A-phase is formed. The decrease in the M′(M′+A) ratio with increasing holding times, illustrated in Fig. 4(a), is thus mainly due to progressing A-phase formation. For stoichiometric

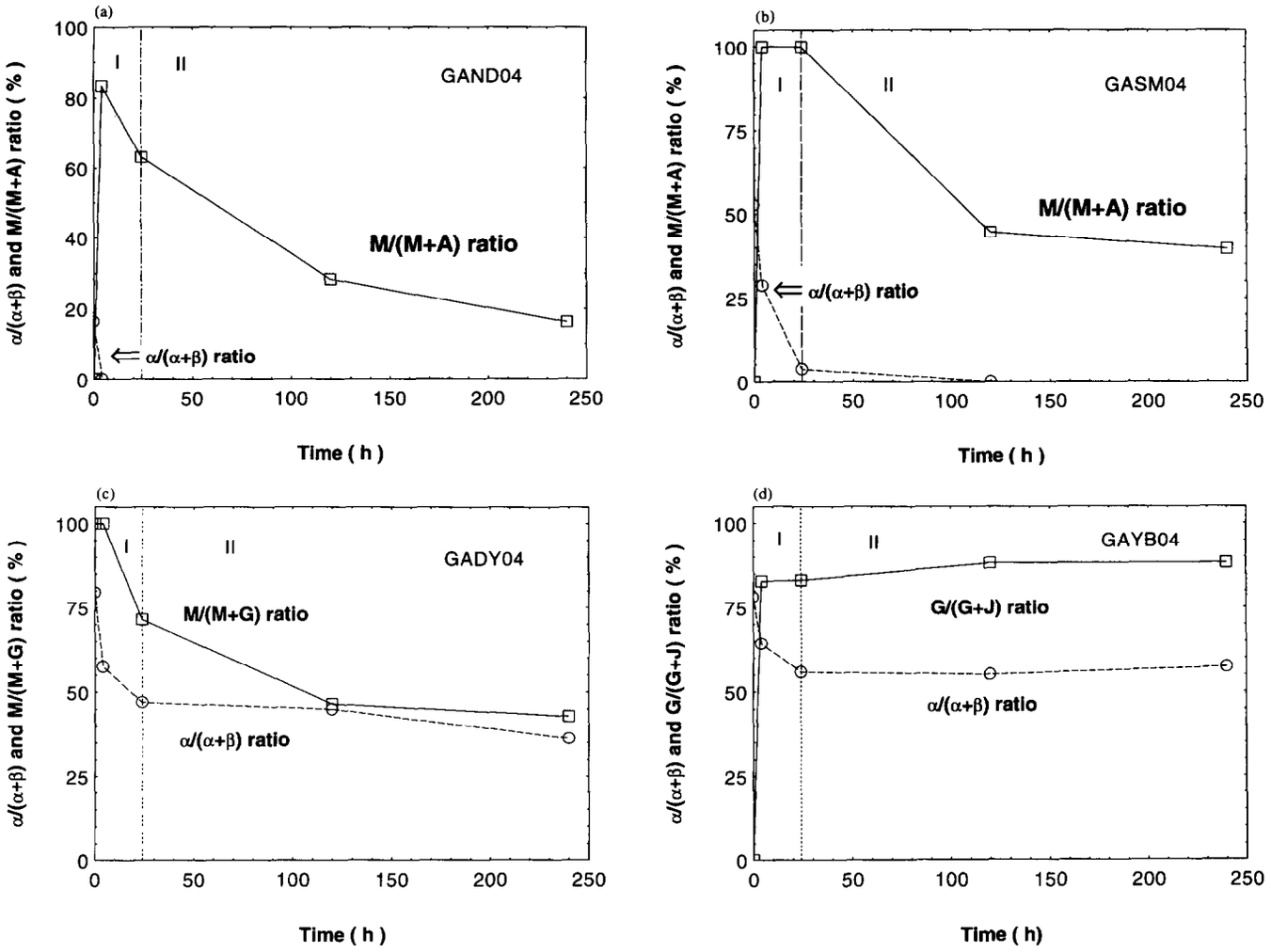

Fig. 4. $\alpha/(\alpha+\beta)$ ratio and grain-boundary phase formation plotted as funtion of the annealing time at 1450°C: (a) *GA*Nd04; (b) *GA*Sm04; (c) *GA*Dy04, and (d) *GA*Yb04.

reasons, β-sialon must also be formed in connection with these reactions. At 1450°C, the crystallization process in the Nd-system thus seems to proceed according to the following pathway:

$$L_1 + \alpha \rightarrow L_2 + M' + A + U + \beta \rightarrow A + M' + \beta \quad (2)$$

where L_1 and L_2 are liquids of different compositions and volume. The final crystallization products besides β-sialon are one pure oxide (A) and one N-rich phase (M′)

At 1300°C, and after 24 h annealing, there is no α-sialon phase left, but some M′-phase and more A-phase has formed. Simultaneously β-sialon is formed for the same reasons as above, yielding an overall devitrification pathway of:

$$\text{Glass} + \alpha \rightarrow A + M' + \beta \quad (3)$$

A quite different phase assembly was observed in the samples post heat-treated at 1150°C for 24 h. The devitrification process at this temperature forms wollastonite, $R\text{SiO}_2\text{N}$, (abbreviated as W below) and the U-phase, $R_3\text{Si}_3\text{Al}_3\text{O}_{12}\text{N}_2$, and because approximately the same $\alpha/(\alpha+\beta)$ ratio is found in this sample as in samples quenched from 1750°C to room temperature (see Fig. 5), this devitrification process does not seem to involve the α-phase, but follows the pathway:

$$\text{Glass} \rightarrow W + U \quad (4)$$

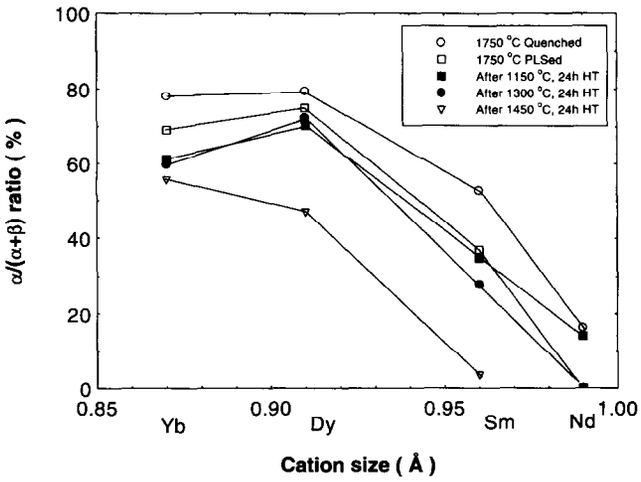

Fig. 5. The $\alpha/(\alpha+\beta)$ ratio in samples exposed to different heat-treatments plotted versus the ion radius of the *R*-ion.

3.1.2 Heat-treatment of Sm-sialons

In the Sm-system, samples quenched from 1750 to 1450°C and annealed at the latter temperature for 4 h did contain α-phase, but the $\alpha/(\alpha+\beta)$ ratio decreased from 52·7 to 28.8% while the M′-phase and minor amounts of the U-phase were simultaneously formed. Upon further heat-treatment, the α-phase and the U-phase were decomposed, and initially more M′ was formed, but later in the crystallization process the A-phase formed and the M′/(M′ + A) ratio remained almost constant from 120 h heat-treatment and further on as seen in Fig. 4(b). As above, β-sialon formed simultaneously. The suggested crystallization pathway at this temperature is thus:

$$L_1 + \alpha \rightarrow L_2 + \mathrm{M}' + \mathrm{U} + \beta \rightarrow \mathrm{M}' + \mathrm{A} + \beta \quad (5)$$

The liquid L_2 has a different composition and volume than L_1. The final crystallization products are the same as above for R=Nd, i.e. one oxygen- and one nitrogen-rich phase.

At 1300°C, and after 24 h post heat-treatment, the A- and β-phases were formed, but $\alpha/(\alpha+\beta)$ ratio was almost the same as after 4 h annealing at 1450°C. Thus, if the α-phase does decompose, its decomposition is substantially lower at this temperature, suggesting the following devitrification pathway:

$$\mathrm{Glass} + (\alpha) \rightarrow \mathrm{M}' + \mathrm{A} + \beta \quad (6)$$

Again, as above, a quite different phase assembly was observed in the samples post heat-treated at 1150°C for 24 h The devitrification process at this temperature thus produces the A-, W- and U-phases. The formation of these phases implies that the β-sialon phase must also be formed. Thus, the decrease in the $\alpha(\alpha+\beta)$ ratio of this sample, compared with that of samples quenched to room temperature from 1750°C (see Fig. 5), might be due to an increasing content of the β-phase. If this assumption is true, our observations suggest the following devitrification pathway at 1150°C in this system:

$$\mathrm{Glass} \rightarrow \mathrm{A} + \mathrm{W} + \mathrm{U} + \beta \quad (7)$$

Post heat-treatment of Sm-sialon compounds has to some extent been studied previously, and it can be concluded that our findings are in agreement with previous results.[9,10]

3.1.3 Heat-treatment of Dy-sialons

It is surprising that the M′-phase is observed in samples in the Dy-system quenched from 1750°C to room temperature. This suggests that the Dy-M′-phase would be thermally more stable than its Nd- and Sm-counterparts, contrary to the general opinion that the thermal stability of the M′-phase decreases with decreasing ionic radius of the R ion. Another possibility would be that the M′-phase present in the as-prepared sample (see below) for some reason did not dissolve during the subsequent heat-treatment at 1750°C. Additional studies to confirm this observation are needed. Anyhow, the α-phase is thermally more stable in this system than in the Nd and Sm ones, as a substantial amount of this phase remains in the sample after annealing at 1450°C for 240 h. A comparison of the $\alpha/(\alpha+\beta)$ ratio in the samples quenched to room temperature and annealed for 4 h at 1450°C suggests that the α-phase is initially involved in the crystallization process. The decrease of the $\alpha/(\alpha+\beta)$ ratio with increasing holding times can be explained by the observation that more β-sialon is formed in conjunction with a grain boundary phase of garnet composition $Dy_3Al_5O_{12}$(G), while the amount of the M′-phase is seemingly constant (see Fig. 4(c)). This suggests that the crystallization process in the Dy-system and in presence of a liquid initially follows the pathway:

$$L_1 + \alpha \rightarrow \mathrm{M}' + \mathrm{G} + \beta \quad (8)$$

while in the latter part of the crystallization process it seems that the dominating reaction is the formation of the G-phase and that this process occurs without the α-phase being involved. The pure oxide phase for Dy is a garnet instead of an aluminate structure, as observed above for Nd and Sm. This is in agreement with earlier findings.[9,10]

Samples annealed at 1300°C for 24 h exhibited almost the same $\alpha/(\alpha+\beta)$ ratio and M′ content as that found in samples quenched to room temperature, but they contained in addition a substantial amount of the G-phase. These observations suggest that the α-phase is not involved in the devitrification process in the glass at 1300°C in the Dy-system, which proceeds as:

$$\mathrm{Glass} \rightarrow \mathrm{G} + \beta \quad (9)$$

The phase assembly observed in the samples post heat-treated at 1150°C for 24 h is quite different from that observed at higher temperatures. The devitrification process at this temperature thus produces A-phase and minor amounts of a grain boundary phase of the composition Dy_2SiAlO_5N (B). The formation of these phases implies that the β-sialon phase must also form, and that the decrease in the $\alpha/(\alpha+\beta)$ ratio in this sample, compared with that of samples quenched to room temperature from 1750°C (see Fig. 5), is most probably due to an increasing content of the β-phase, suggesting the following devitrification pathway:

$$\mathrm{Glass} \rightarrow \mathrm{A} + \mathrm{B} + \beta \quad (10)$$

3.1.4 Heat-treatment of Yb-sialons

Yb does not form any M′-phase, and the most stable grain boundary phase in this system is the G-phase. It is formed in large amounts already after 4 h annealing at 1450°C, in conjunction with the β-phase and minor amounts of $Yb_4Si_2O_7N_2$ (J). The variation of the $\alpha/(\alpha+\beta)$ and G/(G +J) ratios (see Fig. 4(d)) with annealing time indicates that, if the α-phase is involved in the crystallization process, the amount which is decomposed is very small and that, if so, this decomposition occurs only in the very beginning of the process. Furthermore, the rate of crystallization seems to be faster in this system than in the others, as these ratios become almost constant after 24 h annealing. This suggests the following crystallization pathway:

$$L_1 + (\alpha) \rightarrow G + \beta + J \qquad (11)$$

The same pathway seems to be operative at 1300°C, while at 1150°C the devitrification product is A-phase instead of the G-phase.

3.1.5 Concluding remarks concerning the crystallization/devitrification pathway

From these observations it can be concluded:

(i) At least two grain boundary phases are formed in each system: one nitrogen-rich and one oxygen-rich. The N-rich melilite $R_2Si_{3-x}Al_xO_{3-x}N_{4-x}$ is formed for all rare earth elements, except Yb which forms J-phase ($Yb_4Si_2O_7N_2$). The observed oxide was an aluminate ($RAlO_3$) for Sm/Nd and a garnet ($R_3Al_5O_{12}$) for Dy/Yb.

(ii) The phase assembly formed by devitrification of the intergranular glass phase at temperatures slightly above the softening temperature (1150°C) is quite different from that appearing in samples annealed slightly below its liquid-forming temperature (1300°C), which in turn resembles that obtained at temperatures above T_{lf}(1450°C).

(iii) The α-phase is not involved in the devitrification taking place at 1150°C.

(iv) In the Nd- and Sm-systems, the M′- and A-phases are thermodynamically more stable than the α-phase, i.e. at elevated temperatures (T>1150°C) the α-phase decomposes.

(v) If the α-phase is take part in the reactions during the crystallization/devitrification processes in the Dy- and Yb-systems, it does so in the very beginning of the processes and in a limited amount, i.e. the α-phase seems to be thermodynamically stable in these systems.

3.2 Phase analysis of as-prepared samples

The overall composition of the designed sample corresponded to an 80 vol% α-sialon (of the composition GAR04) and a 20 vol% glass content (with a Si:Al:R ratio equal to 2:1:1 and O:N = 3:1). This sample after being pressureless-sintered at 1750°C and cooled to room temperature at a rather slow rate, yielded α/β-sialon ceramics containing about 20–30 vol% glassy phase and different kinds of crystalline grain boundary phases. The phases formed, the lattice parameters of the α- and β-phases and the $\alpha/(\alpha+\beta)$ ratio are shown in Fig. 5 and given in Table 4, respectively.

The phase analysis showed that the Nd sample did not contain any α-phase, but substantial amounts of the M′-phase and minor amounts of the U-phase. The α-phase is present in the Sm sample, but the $\alpha/(\alpha+\beta)$ ratio is lower than those found in the Dy- and Yb-samples. In the Sm sample the M′- and U-phases occur as grain boundary phases, while the M′- and B-phases are formed in the Dy sample. Finally, in the Yb sample the only intergranular phase is the J-phase.

The observation that extremely small amounts of α-phase are present in the Nd sample is in agreement with the annealing experiments, which showed that the α-phase is decomposed in this system. The U- and B-phases are only formed in the low-temperature region (1150°C) in the annealing experiments, while the J-phase is formed both at high and low temperatures. As mentioned above, we always observed one oxygen-rich and one nitrogen-rich phase at the end of our annealing experiments.

Table 4. $\alpha/(\alpha+\beta)$ ratio, grain-boundary phase assemblage and unit cell dimensions of α- and β-sialon in as-prepared samples

Samples	*Density* (g/cm^3)	α/(α+β) (%)	*GB* phase assemblage*					α			β		
			M	*J*	*B*	*U*	*21R***	a(Å)	c(Å)	x****	a(Å)	c(Å)	z****
GAND04	3·566	0	s	—	—	w	w	—	—	—	7·6198	2·9194	0·53
GASM04	3·588	37	ms	—	—	m	—	7·8102	5·6897	0·42	7·6246	2·9203	0·62
GADY04	3·675	75	m	—	m	—	—	7·8070	5·6873	0·39	7·6249	2·9217	0·65
GAYB04	3·681	69	—	mw	—	—	—	7·8032	5·6835	0·40	7·6302	2·9204	0·72

Remarks: *GB, grain boundary; **M, Melilite $R_2Si_{3-x}Al_xO_{3-x}N_{4-x}$ with R=Nd, Sm and Dy; J, J-phase $Yb_4Si_2O_7N_2$;B, B-phase Dy_2SiAlO_5N; U, U-phase $R_3Si_3Al_3O_{12}N_2$ with R=Nd, and Sm; ***α-sialon x-value and β-sialon z-value calculated according to the unit cell dimensions.

X-ray intensities: s, strong; m, medium; w, weak.

In this connection it is interesting to note that no oxygen-rich grain-boundary phase is formed in the as-prepared samples. This observation suggests that the oxygen-rich phases are not formed as long as the nitrogen content of the liquid/glass is high, i.e. nitrogen-rich phases are formed first in the crystallization/devitrification process, and when the oxygen content of the liquid/glass has become high enough, the crystallisation of oxygen-rich intergranular phases starts. The fact that we do not observe any oxygen-rich phases in our as-prepared samples can thus be understood to mean that the cooling rate was too high to allow a more oxygen-rich glassy phase to form.

Our observations thus suggest that the crystallization process in as-prepared samples in the Nd- and Sm-systems follows the pathway:

$$L_1 + \alpha \rightarrow L_2 + M' + U + \beta \quad (12)$$

in the Dy-system:

$$L_1 + M' \rightarrow M' + B + \beta \quad (13)$$

and in the Yb-system:

$$L_1 \rightarrow J + \beta \quad (14)$$

4 Concluding Remarks

As shown above, α-sialon coexists with β-sialon and a liquid phase at 1750°C in Nd-, Sm-, Dy and Yb doped systems, but in the cases of Nd and Sm the α-phase decomposes at lower temperatures. This behaviour has also been observed for Nd- and Sm-α-sialon ceramics containing substantially smaller amounts of intergranular liquid/glassy phases.[22,23] The crystallization/devitrification rate seems to be much faster, though, when the samples contain an excess of the liquid/glass phase, in accordance with earlier indications.[19] If the decomposition of the α-phase is only triggered by the formation of the M′-phase, it is difficult to understand why decomposition does occur in the Nd- and Sm-systems but not with Dy. The Dy-M′-phase can accommodate substantially less Al in its lattice than the Nd- and Sm-M′-phases,[33] and one may speculate that the decomposition rate of the α-phase in the Dy-system is retarded because the formed liquid would otherwise be too Al-rich (see also below). In this connection it should be noted that if one could prepare a Nd- or Sm-α-sialon ceramic without intergranular glass, the α-phase ought to be stable for stoichiometric reasons, because a very nitrogen-rich liquid/glass must be formed besides the M′-phase, and thus seems impossible. The highest observed N-content in a Sm-glass is slightly above 40 eq%.[34]

Our findings show that the phase assembly obtained in as-prepared samples is strongly dependent on: (i) the type of R_2O_3 used as sintering aid; (ii) the amount and composition of the liquid phase formed at the sintering temperature; and (iii) to a greater extent than has previously been realized, on the cooling rate applied.

If the liquid phase formed is nitrogen-rich, as it seems to be in our systems, a nitrogen-rich intergranular phase is formed before an oxygen-rich one, because otherwise the liquid would become too nitrogen-rich. Accordingly, the temperature dependence of the composition variability of the liquid/glass *vis à vis* nitrogen and Al (see above) must also be considered when preparing an α/β-sialon ceramic with designed grain boundary phase(s).

Acknowledgements

This study has been supported by the Swedish Research Council for Engineering Sciences. Zhijian Shen thanks the Swedish Institute for a scholarship during the period when the work was carried out.

References

1. Jack, K. H., Review: Sialons and Related Nitrogen Ceramics, *J. Mater. Sci.*, **11** (1976) 1135–58.
2. Lewis, M. H., Ward, G. & Jasper, C., Sintering Additive Chemistry in Controlling Microstructure and Properties of Nitrogen Ceramics. *Ceram. Powder Sci.*, **2** (1988) 1019–33.
3. Ekström, T., Effect of Composition, Phase Content and Microstructure on the Performance of Yttrium SiAlON Ceramics. *Mater. Sci. Eng.*, **A109** (1989) 341–9.
4. Ekström T. & Nygren, M., Sialon Ceramics. *J. Am. Ceram. Soc.*, **75** (1992) 259–76.
5. Becher, P. F., Microstructural Design of Toughened Ceramics. *J. Am. Ceram. Soc.*, **74** (1991) 255–69.
6. Ekström, T., SiAlON Composite Ceramics. In *Tailoring of Mechanical Properties of Si_3N_4 Ceramics*, ed. M. J. Hoffmann & G. Petzow. Kluwer Acad. Publ., Netherlands, 1994, pp. 149–61.
7. Ekström, T., Hardness of Dense Si_3N_4-Based Ceramics. *J. Hard Mater.*, **4** (1993) 77–95.
8. Cao, G. Z. & Metselaar, R., α-SiALON Ceramics: a review, *Chem. Mater.*, (1991) 242–52.
9. Mandal, H., Thompson, D. P. & Ekström, T., Heat treatment of sialon ceramics densified with higher atomic number rare earth and mixed yttrium/rare earth oxides. In *Proc. Special Ceramics 9*, The Institute of Ceramics, Stoke-on-Trent, UK, 1992, pp. 97–104.
10. Mandal, H., Thompson, D. P. & Ekström, T., Reversible α-β-Sialon Transformation in Heat-treated Sialon Ceramics. *J. Europ. Ceram. Soc.*, **12** (1993) 421–9.
11. Mandal, H., Cheng, Y. B. & Thompson, D. P., α-sialon Ceramics with a Crystalline Melilite Grain-Boundary Phase, Aluminium-Containing Nitrogen Melilite. In *5th International Symposium on Ceramic Materials and Components for Engines*, ed. D. S. Yan, X. R. Fu & S. X. Shi. World Scientific, Singapore, 1995, pp 202–5.

12. Hampshire, S., Park, H. K., Thompson, D. P. & Jack, K. H., α'-Sialon Ceramics, *Nature* (London), **274** (1978) 880–2.
13. Jack, K. H., Silicon Nitride, Sialons, and Related Ceramics. In *Ceramics and Civilization Vol. III, High-Technology Ceramics.* American Ceramic Society, Columbus, OH, 1986, pp. 259–88.
14. Sun, W. Y., Tien, T. Y. & Yen, T.-S., Solubility Limits of α'-Sialon Solid Solutions in the System Si, Al, Y / N, O. *J. Am. Ceram. Soc.*, **74** (1991) 2547–50.
15. Stutz, D., Greil, P. & Petzow, G., Two-Dimensional Solid-Solution Forming of Y-Containing α-Si_3N_4. *J. Mater. Sci. Letters,* **5** (1986) 335–6.
16. Ekström, T., Sialon Ceramics Sintered with Yttria and Rare Earth Oxides. *Mat. Res. Soc. Symp. Proc.,* **287** (1993) 121–32.
17. Huang, Z. K., Tien, T. Y. & Yen, T. S., Subsolidus Phase Relationships in Si_3N_4–AlN–Rare Earth Oxide Systems. *J. Am. Ceram. Soc.*, **69** (1986) C-241–42.
18. Ekström, T., Shen, Z.-J. & Falk L., Dysprosium and Samarium Doped α-β Sialon Ceramics with a Minimum of Residual Glass, submitted to *J. Am. Ceram. Soc.*
19. Ekström T. & Shen, Z.-J. Temperature Stability of Rare Earth Doped α-Sialon Ceramics. In *5th Intern. Symp. on Ceramic Materials and Components for Engine*, ed. D. S. Yan, X. R. Fu & S. X. Shi. World Sci. Publ. Co., 1995, pp. 206–10.
20. Cheng, Y. B. & Thompson, D. P., Preparation and Grain Boundary Devitrification of Samarium α-Sialon Ceramics. *J. Europ. Ceram. Soc.*, **14** (1994) 13–21.
21. Zhao, R. & Cheng, Y., Phase Transformations in Sm(α+β)-SiAlON Ceramics during Post-Sintering Heat Treatments, submitted to *J. Euro. Ceram. Soc.*
22. Shen, Z.-J., Ekström, T. & Nygren, M., Temperature Stability of Samarium Doped α-Sialon Ceramics. *J. Europ. Ceram. Soc.*, **16** (1996) 43.
23. Shen, Z.-J., Ekström, T. & Nygren, M., Homogeneity Region and Thermal Stability of Neodymium Doped α-Sialon Ceramics. *J. Am. Ceram. Soc.*, **79** (1996) 721.
24. Shen, Z.-J., Ekström T. & Nygren, M., Ytterbium Stabilised α-Sialon Ceramics. *J. Phys D: Appl. Phys*, **29** (1996) 893.
25. Shen, Z.-J., Ekström, T. & Nygren, M., Preparation and Properties of Stable Dysprosium Doped α-Sialon Ceramics. Submitted to *J. Mater. Sci.*
26. Anstis, G. R., Chantikul, P., Lawn, B. R. & Marshall, D. P., A Critical Evaluation of Indentation Techniques for Measuring Fracture Toughness: I, Direct Crack Measurements. *J. Am. Ceram. Soc.*, **64** (1981) 533.
27. Johansson, K.-E., Palm, T & Werner, P.-E., An Automatic Microdensitometer for X-ray Powder Diffraction Photographs. *J. Phys.*, **E13** (1980) 1289–91.
28. Werner, P.-E., A Fortran Program for Least-Squares Refinement of Crystal Structure Cell Dimension, *Arkiv för Kemi*, **31** (1969) 513.
29. Ekström, T., Käll, P.-O., Nygren, M. & Olsson, P.-O., Dense Single-Phase β-Sialon Ceramics by Glass-Encapsulated Hot Isostatic Pressing. *J. Mater. Sci.*, **24** (1989) 1853–61.
30. Hampshire, S., Drew, R. A. L. & Jack, K. H., Oxynitride glasses. *Phys. Chem. of Glasses*, **26** (1985) 182–6.
31. Murakami, Y. & Yamamoto, H., Properties of Oxynitride Glasses in the Ln–Si–Al–O–N Systems (Ln=Rare-Earth), *J. of the Ceram. Soc. of Japan, Int. Edition*, **102** (1995) 234–8.
32. Mandal, H., Thompson, D. P. & Ekström, T., Heat Treatment of Ln–Si–Al–O–N glasses. In *Proc. 7th Irish Mater. Forum Conf. IMF7*, ed. M. Buggy & S. Hampshire. Trans. Tech Publications, Switzerland, 1992, pp. 187–203.
33. Wang, P. L., Tu, H. Y., Sun, W. Y., Yan, D. S., Nygren, M. & Ekström, T., On the Solid Solubility of Al in the Melilite Systems $R_2Si_{3-x}Al_xO_{3+x}N_{4-x}$ with R=Nd, Sm, Gd, Dy, and Y. *J. Europ. Ceram. Soc.*, **15** (1995) 689.
34. Tu, H. U., Sun, W. Y., Wang, P. L. & Tan, D. S., Glass-forming region in the Sm–Si–Al–O–N system, *J. Mater. Sci. Letters,* **14** (1995) 1118–22.

Journal of the European Ceramic Society 16 (1996) 885–891

S0955-2219(96)00007-6
0955-2219/96/$15.00 +.00

Structural Investigations of Si/C/N-Ceramics from Polysilazane Precursors by Nuclear Magnetic Resonance

Juliane Seitz,[a] Joachim Bill,[a] Norbert Egger[b] & Fritz Aldinger[a]

[a]Max-Planck-Institut für Metallforschung, Institut für Werkstoffwissenschaft, Pulvermetallurgisches Laboratorium, Heisenbergstrasse, D70569, Stuttgart, Germany
[b]Hoechst AG, Analytisches Laboratorium, Frankfurt, Germany

(Received 13 April 1995; accepted 18 November 1995)

Abstract

Polymeric precursors to Si/C/N-ceramics can be obtained by thermal crosslinking of polysilazanes. The precursor is then pyrolysed at a temperature of 1000°C into the amorphous ceramic. Between 1000 and 2000°C this amorphous state is transformed into the thermodynamically stable phases. The processes during pyrolysis and crystallization are connected with microstructural conversion. Simultaneously, changes of chemical and physical properties take place. The successive conversion of the atomic coordination during the transformation from the polymer into the amorphous ceramic and finally into the crystalline ceramic was studied using solid-state NMR. ^{29}Si-, ^{13}C- and ^{1}H-spectra were recorded. The result is a detailed report of the reactions and changes in structure occuring during ceramization of a polyhydridomethylsilazane and crystallization of its ceramic residue. Furthermore, the amorphous state of this material was compared with a polyvinylsilazane-derived amorphous ceramic.

1 Introduction

As already reported[1–3] thermal crosslinking of inorganic Si/C/N-polymers leads to the formation of infusible polymeric precursors with increased molecular weight. These precursors are pyrolysed into amorphous single-phase materials at 1000°C. Above 1000°C the thermodynamically stable phases silicon carbide and silicon nitride are formed. The resulting SiC/Si_3N_4-ceramics are free of sintering additives. These ceramics are therefore interesting materials for high temperature applications as they have a high thermal and chemical stability.

The changes in chemical structure during the transformation polymer–amorphous material–crystalline ceramic are investigated by means of solid-state NMR. Knowing the reactions during the conversion allows control of the desired attributes of the resulting ceramic by specific variation of the polymer or the reaction conditions. The NMR experiments show the appropriate atomic coordination which gives information about the molecular structure of the samples.

In this report, the polyhydridomethylsilazane NCP 200 (commercial product, Nichimen®, Japan) was studied. The copolymer consists of the structure $[–SiHMe–NH–]_m[–SiMe_2–NH–]_n$ and has a molecular weight of 1100 g/mol. The reactions and intermediates occurring between RT and 1800°C are investigated in detail and the molecular structures for selected temperatures are determined. In addition, the amorphous state of a polyvinylsilazane, named VT 50 (Hoechst AG), was studied and compared with the single-phase material derived from the NCP 200 mentioned above. Polyvinylsilazane VT 50 contains $[–SiVi(NH)_2–]$-structural units and a small number of end groups $[–SiVi(NH)–NMe_2–]$. This polymer has a molecular weight of 800 g/mol.

2 Experimental

Below 1100°C the thermal treatment of the polysilazanes was carried out in quartz tubes in a slight argon flow. The heating rate was 25°C/h. The appropriate temperatures were held for 4 h. Further annealing of the pyrolysed samples at temperatures above 1100°C was carried out for 50 h (heating rate: 120°C/h) in a nitrogen atmosphere using a silicon nitride powder bed.

The NMR-experiments were performed on a Bruker MSL 300 at Hoechst AG, Frankfurt, Germany. The resonance frequency for ^{1}H was 300·13 MHz, for ^{13}C 75·47 MHz and for ^{29}Si

59.60 MHz. All spectra were acquired using magic angle spinning (MAS) with a rotation frequency of 4500 Hz. The excitation of the observed nucleus was 3 μs for ^{1}H, 4 μs for ^{13}C and 5 μs for ^{29}Si when the single pulse technique was used. This technique was applied for the measurement of all samples. All spectra were ^{1}H-decoupled during the data acquisition. The samples heated above 1400°C needed long relaxation times, up to 10 min repetition time was required but time T_1 was not measured explicitly. The number of scans varied and was optimized to get an acceptably good signal to noise ratio. The samples heated below 1100°C were also measured with a crosspolarization sequence (CP). The contact time for ^{13}C and ^{29}Si was 1 and 5 ms respectively. The repetition time was 10 s.

3 Results and Discussion

3.1 NCP 200

3.1.1 Polymer

The ^{13}C-spectrum (Fig. 1) of the polymer shows a sharp peak at 5 ppm which is caused by the carbon of the silylmethyl group Si–$\underline{C}H_3$[4].

The ^{29}Si-spectrum (Fig. 2) shows three sharp signals. The peak with the chemical shift of –22 ppm is assigned to a $\underline{Si}N_2CH$ environment.[5,6] This is proven by the comparison of CP- and one-pulse-spectra. As expected, the $\underline{Si}N_2CH$ signal in the one-pulse-spectrum is weaker than in the CP-spectrum because a signal with a Si–H-bond is detected more strongly in the CP-spectrum. The peak at –5 ppm corresponds to a $\underline{Si}N_2C_2$ surrounding within a six-membered cyclosilazane-ring.[6] For example, a $\underline{Si}N_2C_2$ group in a four- or eight-membered ring would cause a chemical shift of 3·3 ppm or –8·7 ppm respectively.[6] A $\underline{Si}N_2C_2$ group in a chain would have a chemical shift of 2·2 ppm.[5] Such signals are not found in the spectrum. Thus, it is definitely proved that the molecule consists of six-membered rings. As these results show, the polymer has a structure of con-

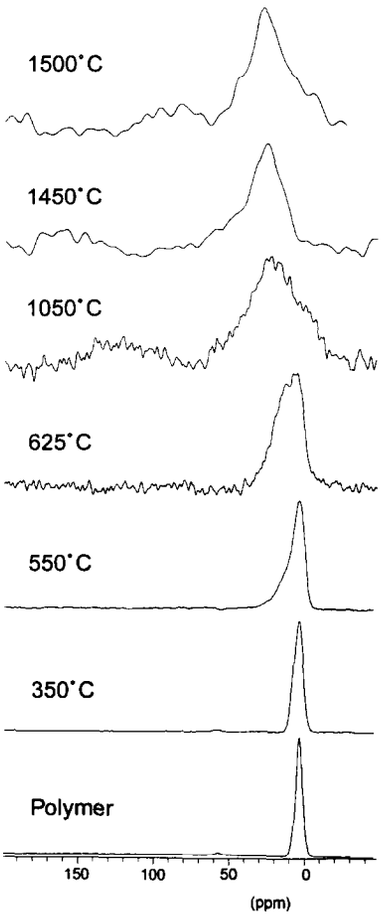

Fig. 1. ^{13}C-NMR-MAS-spectra of NCP 200 and temperature treated derivatives.

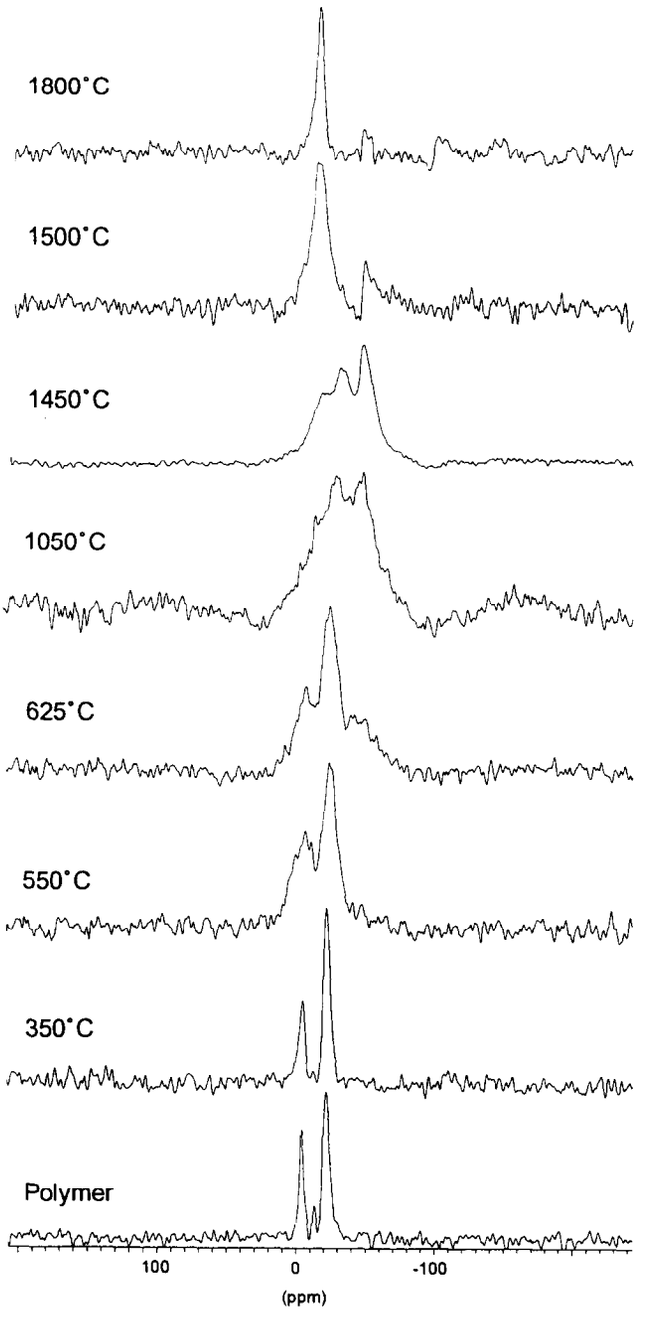

Fig. 2. ^{29}Si-NMR-MAS-spectra of NCP 200 and temperature treated derivatives.

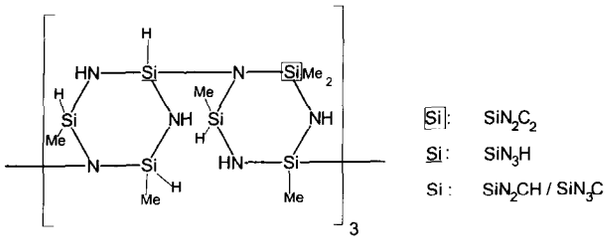

Fig. 3. Chemical structure of the polymer (NCP 200).

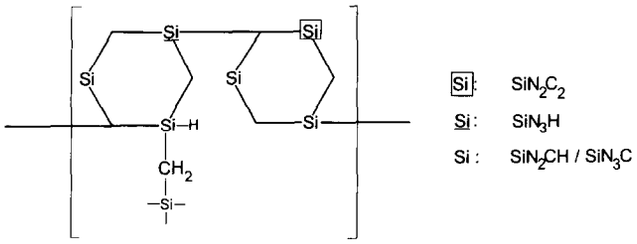

Fig. 4. Chemical structure of the 350°C product (NCP 200).

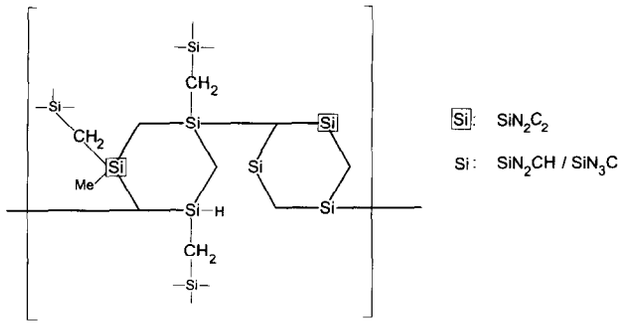

Fig. 5. Chemical structure of the 550°C product (NCP 200).

nected six-membered rings. The bridging Si-atoms could have a $\underline{Si}N_3H$ or $\underline{Si}N_3C$ environment. The peak at –14 ppm is assigned to the bridging $\underline{Si}N_3H$ sites in the six-membered ring. As the signal is weak, the bridging $\underline{Si}N_3H$ sites have a low abundance. The bridging Si-atoms with $\underline{Si}N_3C$ environment have a chemical shift of –23·8 ppm. The small amount of these $\underline{Si}N_3C$ groups is superimposed by the $\underline{Si}N_2CH$ peak at –22 ppm. The relation between $\underline{Si}N_2C_2$ and $\underline{Si}N_2CH$ sites is determined as 1:2 by calculating the appropriate signal areas. The structure proposal of the NCP 200 polymer in Fig. 3 is based on these results. The producer gives a value of 1100 g/mol for the molecular weight average. Thus one average molecule consists of about six six-membered rings.

3.1.2 350°C product

After heat treatment of the polymer at 350°C all the signals in the spectra slightly broaden. The chemical shift of the signal in the ^{13}C-spectra slightly increases. This is caused by the formation of CH_2-bridges shown in the following crosslinking reaction:

$$2\ SiN_2RMe \rightarrow N_2MeSi - CH_2 - SiRN_2 + CH_4\ (H_2) \qquad R = CH_3, H, N \qquad (1)$$

$\underline{C}H_2Si_2$ sites cause a chemical shift of 12 ppm.[7] The ^{13}C-signal has slightly shifted towards the high-field side. This indicates that the crosslinking reaction mentioned above takes place in small amounts.

In the ^{29}Si-spectra, the described reaction causes a slight increase of the line widths. The chemical environment of the appropriate atoms is slightly modified by the crosslinking reaction, which is shown by the broadening of the signals. The chemical shifts and the relation of the peak areas remain essentially unchanged. The structure is shown in Fig. 4.

3.1.3 550°C product

At this temperature, in the ^{13}C-spectra an additional signal at 12 ppm is found as a shoulder, which is attributed to $\underline{C}H_2$-bridges. The crosslinking reaction mentioned above intensifies and hence the number of CH_2-bridges increases.

This reaction can occur with all kinds of Si-species. The ^{29}Si-spectrum shows further broadening of the lines. Thus the signals of the $\underline{Si}N_2CH$ and $\underline{Si}N_3H$ sites combine. The comparison of one-pulse and CP-spectra shows a strong reduction in intensity for the H-amount in the molecule. The Si–H-bonds react more easily than the Si–C-bonds with $Si–CH_3$ to form a CH_2-bridge (see eqns (5) and (6)). Thus the number of $\underline{Si}N_2C_2$ sites increases at the expense of the $\underline{Si}N_2CH$ sites. The ratio of $\underline{Si}N_2C_2$ and $\underline{Si}N_2CH$ is now determined as 1:1 (ratio of the appropriate peak areas). In addition, the Si–H-bonds of the bridging Si-atoms react to form CH_2-bridges. Thus the small amount of $\underline{Si}N_3C$ sites with the chemical shift of –23·8 ppm included in the $\underline{Si}N_2CH$-signal at –22 ppm slightly increases. The structure is shown in Fig. 5.

3.1.4 625°C product

At this temperature, the successive increase of the chemical shift in the ^{13}C-spectrum continues. This is caused by the increased coordination of the C-atoms with Si-atoms.[8] If the known δ-values for $Si–\underline{C}H_3$ (5 ppm),[4] for $Si_2\underline{C}H_2$ (12 ppm)[7] and for $Si_4\underline{C}$ (24 ppm)[4] are interpolated, it is found a δ-value of 18 ppm for the $Si_3\underline{C}H$ site:

$Si–CH_3$	$Si–CH_2–Si$	$Si_2–CH–Si$	Si_4C
5 ppm	12 ppm	18 ppm	24 ppm

Therefore the signal at 15 ppm in the ^{13}C-spectra is assigned to a coordination of the C-atoms with more than two Si-atoms. The $Si_2\underline{C}H_2$-bridges formed in the reactions described above can react with methyl or hydrogen to form $Si_3\underline{C}H$ groups, resulting in the formation of a dense network.

The ^{29}Si-spectrum shows a signal at 43 ppm for the first time which is assigned to SiN_4 sites.[5,9]

These are formed by the following crosslinking reactions of the NH–groups:

$$Si_2N - H + SiN_2R_2 \rightarrow Si_2N - SiN_2R + RH \quad (2)$$

$$Si_2N - H + SiN_3R \rightarrow Si_2N - SiN_3 + RH \quad (3)$$

Consequently, the number of SiN_4 sites determined from the peak area is enhanced by up to 30%. In addition, the amount of $\underline{Si}N_3C$ sites (–24 ppm) increases at the expense of the $\underline{Si}N_2C_2$ sites (–7 ppm). Since the $\underline{Si}N_2CH$ sites and the $\underline{Si}N_3C$ sites have a combined signal and the amount of $\underline{Si}N_2CH$ decreases (reaction of the Si–H-bond with NH or CH_3), the intensity of the signal remains constant. The structure is shown in Fig. 6.

3.1.5 1050°C product, amorphous ceramic

In the ^{13}C- spectrum, the chemical shift of the signal is increased still. It now is found at 24 ppm, which is attributed to $Si_4\underline{C}$.[4] The comparison of one-pulse and CP-spectra shows only a small amount of H-atoms remaining in the molecule. The last H-atom of the $Si_3\underline{C}H$-group reacts, forming the $Si\underline{C}_4$-group.

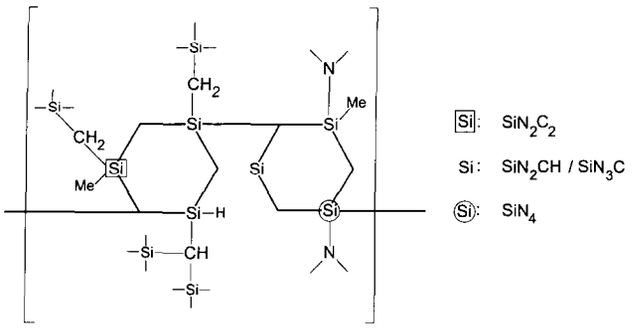

Fig. 6. Chemical structure of the 625°C product.

That is the reason for the reduction of the H-atoms.

Figure 7 shows the ^{29}Si-spectrum fitted with three signals to estimate the intensities of the appropriate components. In general it remains unchanged from the 625°C product. Only the line broadening has continued. The structure (Fig. 8) shows that the basic structure SiN_4, necessary to form the thermodynamically stable phase silicon nitride, has already preformed in the amorphous state.

At the C-atoms all H-atoms are now replaced by Si-atoms. Thus the presupposition to form silicon carbide is made. In the amorphous state, the SiN_4 sites as well as the CSi_4 sites are still fixed in the network.

At lower temperatures, the ^1H-spectra show a methyl-signal becoming continuously weaker as the temperature is increased and the number of H-atoms is decreased. At 1050°C, it is no longer possible to detect this signal. This indicates the reduction of the H-atoms.

3.1.6 1500°C product, crystalline ceramic

In the ^{13}C-spectrum the SiC- signal is found at 27 ppm (corresponding to the measured SiC-sample).

The ^{29}Si-spectrum shows the Si_3N_4- signal at –47 ppm and the SiC- signal at –18 ppm (corresponding to the measured Si_3N_4- and SiC-standards). At this temperature the preformed Si_4C and SiN_4 sites have formed the thermodynamically stable crystalline phases silicon carbide and silicon nitride.[3] The ceramic has changed from the amorphous state into the multiphase state. At the same time a decomposition reaction occurs. Excess carbon reacts with silicon nitride.[10]

$$Si_3N_4 + 3\ C \rightarrow 3\ SiC + 2\ N_2 \quad (4)$$

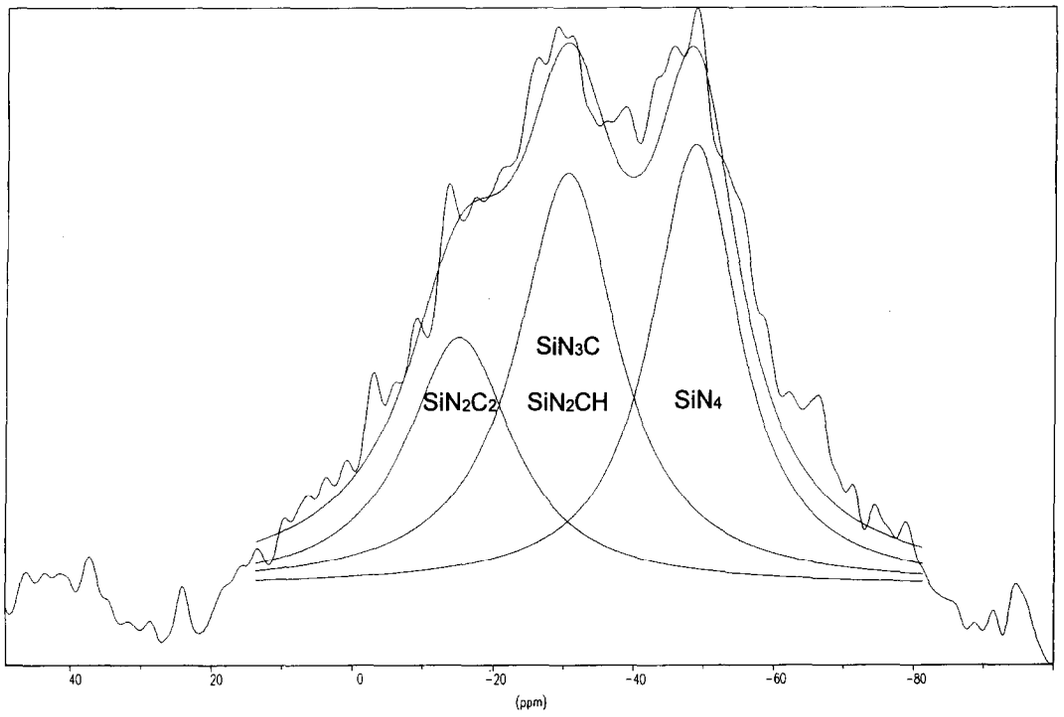

Fig. 7. ^{29}Si-spectrum of the amorphous ceramic fitted with three signals.

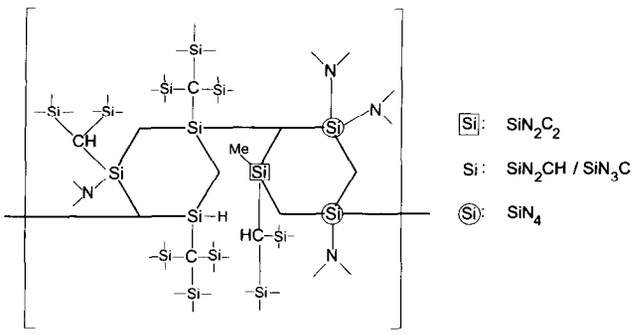

Fig. 8. Chemical structure of the amorphous ceramic.

Table 1. Dissociation energies ΔE (kJ/mol) for 298 K[13]

Element	*H*	*C*	*N*	*Si*
H	436	416	391	323
C	416	345	305	306
N	391	305	159	335
Si	323	306	335	202

The dissociation energy for a C=C-double bond is 615 kJ/mol and for a C ≡ C-triple bond 811 kJ/mol.

As the crystallization temperature increases, the detection of the crystalline phases becomes more difficult.[9] To get an acceptably good signal to noise ratio the repetition time had to be increased up to 10 min for the 1800°C product.

The reactions and structures described above are also confirmed by infrared spectroscopy[11] and energetic calculations. The amounts of energy for the assumed reactions are calculated using the appropriate dissociation energies.[11] Table 1 lists the values for homolytic dissociation.

The following equations show the assumed reactions with the appropriate calculated reaction enthalpy ΔE (kJ/mol).

$$\equiv SiCH_2 - H + H - Si \equiv \rightarrow \equiv SiCH_2 - Si \equiv + H_2 \quad \Delta E = -2 \quad (5)$$

$$\equiv Si - CH_3 + H - CH_2Si \equiv \rightarrow \equiv Si - CH_2Si \equiv + CH_4 \quad \Delta E = 0 \quad (6)$$

$$\equiv Si - H + H - CH(Si \equiv)_2 \rightarrow \equiv Si - CH(Si \equiv)_2 + H_2 \quad \Delta E = -2 \quad (7)$$

$$\equiv Si - CH_3 + H - CH(Si \equiv)_2 \rightarrow \equiv Si - CH(Si \equiv)_2 + CH_4 \quad \Delta E = 0 \quad (8)$$

$$\equiv Si - H + H - C(Si \equiv)_3 \rightarrow \equiv Si - C(Si \equiv)_3 + H_2 \quad \Delta E = -2 \quad (9)$$

$$\equiv Si - CH_3 + H - C(Si \equiv)_3 \rightarrow \equiv Si - C(Si \equiv)_3 + CH_4 \quad \Delta E = 0 \quad (10)$$

$$(\equiv Si)_2N - H + H - Si \equiv \rightarrow (\equiv Si)_2N - Si \equiv + H_2 \quad \Delta E = -55 \quad (11)$$

$$\equiv Si - CH_3 + H - N(Si \equiv)_2 \rightarrow \equiv Si - N(Si \equiv)_2 + CH_4 \quad \Delta E = -54 \quad (12)$$

$$\equiv SiCH_2 - H + H - CH_2Si \equiv \rightarrow \equiv SiCH_2 - CH_2Si \equiv + H_2 \quad \Delta E = +51 \quad (13)$$

$$\equiv SiCH_2 - H + H - N = \rightarrow \equiv SiCH_2 - N = + H_2 \quad \Delta E = +66 \quad (14)$$

$$\equiv SiCH_3 + H_3CSi \equiv \rightarrow \equiv SiCH = CHSi \equiv + 2H_2 \quad \Delta E = +177 \quad (15)$$

$$\equiv SiCH_3 + H_3CSi \equiv \rightarrow \equiv SiC \equiv CSi \equiv + 3H_2 \quad \Delta E = +296 \quad (16)$$

The reactions (5)–(10) describe the successive conversions around the C-atom. With a ΔE-value around 0 they should take place easily at higher temperatures. The NMR investigations that show these reactions to occur at temperatures above 300°C give evidence for this consideration.

A difference was found between the energetic calculations and the NMR results for only reactions (11) and (12). The described reactions of the N–H-bond should occur easily at lower temperatures. However, as the NMR experiments show, they are found only above 600°C. This may be caused by a kinetic effect.

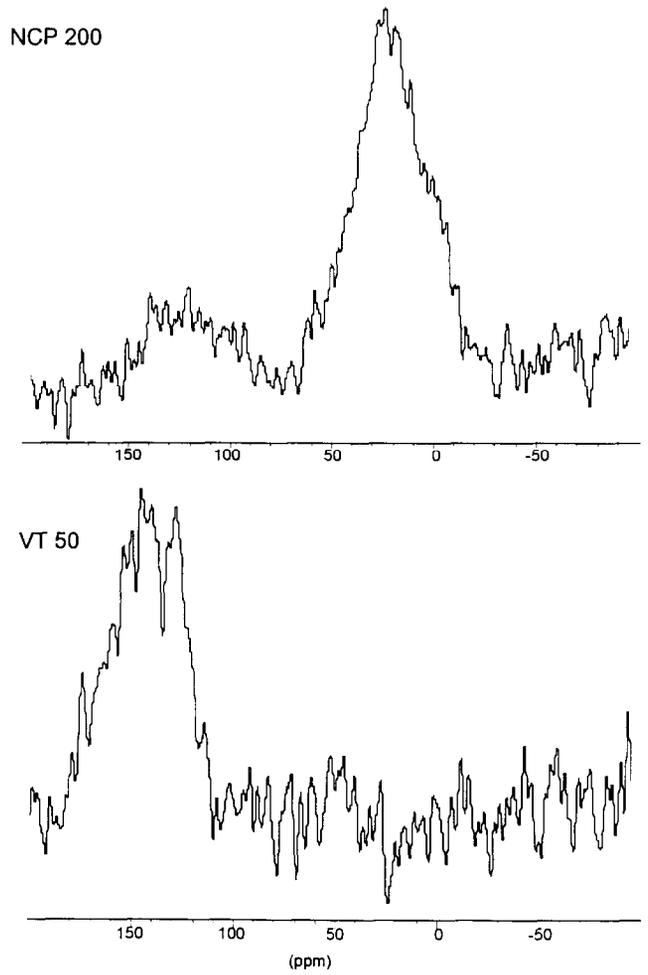

Fig. 9. ^{13}C-spectra of the amorphous ceramics of NCP 200 and VT 50 in comparison.

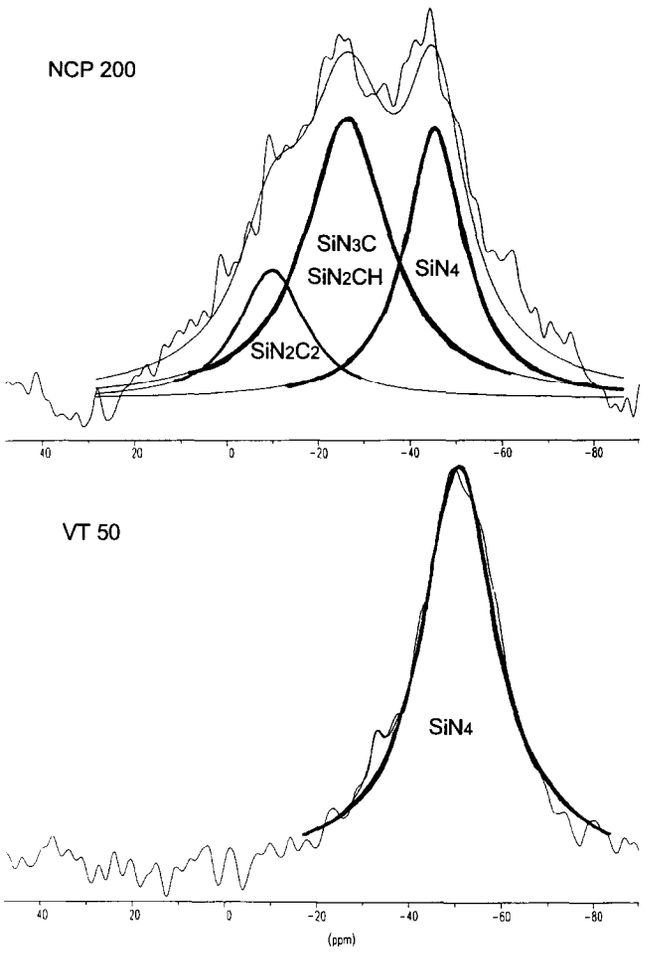

Fig. 10. ^{29}Si-spectra of the amorphous ceramics of NCP 200 and VT 50 in comparison.

The last four reactions (13)–(16) are energetically unfavourable and do not take place, which is in accordance with the results of the NMR investigations.

3.2 VT 50

The ^{13}C-spectra show a significant difference between the two amorphous materials NCP 200 and VT 50. In contrast to NCP 200, a signal centered around 140 ppm is detected in the case of VT 50, indicating a high amount of sp^2-carbon[8]

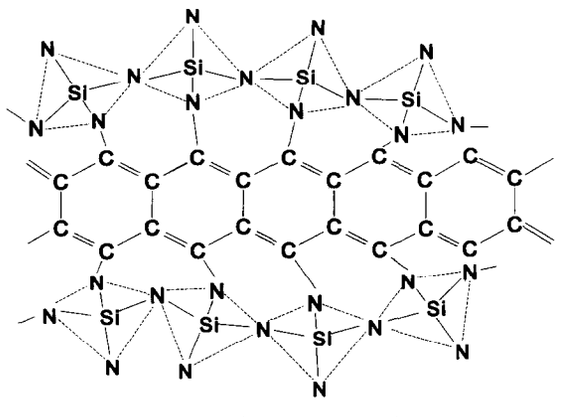

Fig. 11. Structure proposal of the amorphous state obtained by pyrolysis of the polysilazane VT 50 at 1050°C.

(Fig. 9). The vinylic groups of the VT 50 polymer are the reason for the appearance of sp^2-carbon in the amorphous ceramic, resulting in an increased electric conductivity of the amorphous VT 50 in comparison to the amorphous NCP 200 which will be published separately.

The ^{29}Si-spectrum of the amorphous NCP 200 exhibits the signals of the different Si sites described in section 3.1. In contrast to this result, the spectrum of the amorphous VT 50 shows only one single peak that represents $\underline{Si}N_4$ sites (Fig. 10). This difference is caused by the different polymer structure of the VT 50. In the polymer, every Si-atom is surrounded by three N-atoms. Thus in the crosslinking reactions the $\underline{Si}N_4$ sites are directly formed and in the amorphous ceramic nearly all Si-atoms are surrounded by four N-atoms. Another possibility of explaining is the presence of C–N bonds in the end groups of the VT 50 polymer. According to Laine *et al.*[12] C–N bonds support the formation of SiN_4 sites. Figure 11 shows a structure proposal of the amorphous VT 50.

4 Conclusion

The molecular mechanisms occuring during the transformation of the polysilazane NCP 200 into amor-phous and crystalline ceramics in the temperature range between room temperature and 1800°C were determined by solid state NMR spectroscopy. It was possible to suggest structural formulas for the appropriate intermediates. The obtained results confirm with energetic calculations. It was found that NCP 200 crystallizes between 1450 and 1500°C.

The comparison of the NCP 200 with a polyvinylsilazane (VT 50) shows significant differences in the ^{13}C- and ^{29}Si-spectra of the amorphous materials. Pyrolysis of the polymer VT 50 yields a ceramic residue which contains a high amount of sp^2-carbon and SiN_4 sites whereas the NCP 200-derived amorphous state contains various different Si-sites.

References

1. Rice, R., *Ceram. Bull.*, **62** (1983) 889.
2. Seyferth, D. & Wiseman G. H., *J. Am. Ceram. Soc.*, **67** (1984) 132.
3. Frieß, M., Bill, J., Aldinger, F., Szabo, D. V. & Riedel R., *Key Engineering Materials*, **89–91** (1994) 95.
4. Mocaer, D., Pailler, R., Naslain, R., Richard, C., Pillot J. P., Dunogues, J., Gerardin, C. & Taulelle, F., *J. Mater. Sci.*, **28** (1993) 2615.
5. Gerardin, C., Taulelle, F. & Livage, J., *Mat. Res. Soc. Symp. Proc.*, **287** (1993) 233.

6. Yive, N. S. C. K., Corriu, R., Leclercq, D., Mutin, P. H. & Vioux, A., *New J. Chem.*, **15** (1991) 85.
7. Schmidt, W. R., Interrante, L. V., Doremus, R. H., Trout, T. K., Marchetti, P. S. & Maciel, G. E., *Chem. Mater.*, **3** (1991) 257.
8. Soraru, G. D., Babonneau, F. & Mackenzie, J. D., *J. Mater. Sci.*, **25** (1990) 3886.
9. Carduner, K. R., Carter, R. O., Millberg, M. E. & Crosbie, G. M., *Anal. Chem.*, **59** (1987) 2794.
10. Weiss, J., Lukas, H. L., Lorenz, J., Petzow, G. & Krieg, H., *Calphad*, **5** (1981) 125.
11. Frieß, M., PhD thesis, University of Stuttgart (1994).
12. Laine, R. M., Babonneau, F., Rahn, J. A., Zhang, Z.-F. & Youngdahl, K. A., *37th Sagamore Army Materials Conference.*
13. Hollemann, A. F. & Wiberg E., *Lehrbuch der Anorganischen Chemie*, de Gruyter, Berlin–New York, 91–100 Aufl, 1985, p. 139.

Journal of the European Ceramic Society 16 (1996) 893–898

0955-2219(95)00208-1
0955-2219/96/$15.00 +.00

Study of the Behaviour of Aluminium Nitride in the Iron and Steel Industry

J. C. Labbe & A. Laïmeche

Laboratoire de Matériaux Céramiques et Traitements de Surface (CNRS URA 320), Université de Limoges, 123 av. Albert Thomas, 87060 Limoges Cedex, France

(Received 12 September 1994; revised version received 14 November 1995; accepted 29 November 1995)

Abstract

Reactivity studies of different steels with nitride ceramics, and in particular with aluminium nitride, have shown the presence of complex chemical reactions at the solid–liquid and liquid–vapour interfaces. Reaction at the AlN–liquid steel interface shows a decomposition of AlN followed by the oxidation of aluminium, and an AlON phase attack at grain boundaries.

L'étude de la réactivité de différentes nuances d'acier sur les céramiques nitrures et en particulier sur le nitrure d'aluminium, a mis en évidence l'existence d'interactions chimiques complexes aux interfaces liquide–vapeur et solide–liquide. L'interaction à l'interface AlN-acier liquide fait appel d'une part à un mécanisme de décomposition d'AlN avec oxydation de l'aluminium, et d'autre part à l'attaque de la phase AlON aux joints de grains de AlN.

Introduction

The continuous casting of steel presents many advantages, such as economy of energy and best use of raw materials. However, some drawbacks can be found, in particular corrosion of the refractory materials used in foundries, which limits the productivity of installations and affects the steel quality. For these reasons, specialists now are looking toward nitride ceramics and particularly aluminium nitride, which theoretically has good thermochemical stability and low solubility in liquid steel at high temperature (Table 1).

In the present work we are interested in the behaviour of pure AlN in contact with three types of steel: steel A (extra-mild low carbon), steel B (SiCa treated) and steel C (IFS ultra-low carbon). The corrosion problem will be considered in terms of the wettability of AlN surfaces by liquid steels and subsequent interaction as a function of time, temperature and surface porosity.

Theoretical Approach

Solid or liquid reactions can be explained by the surface phenomena of contact angle and surface tension, and by the physicochemical characterization of the intermediate reaction zone.

The simplified fundamental relation [eqn (1)] of Young and Dupre[2] links the contact angle θ to the three surface tensions, σ_{SV}, σ_{SL} and σ_{LV}, of the solid–vapour, solid–liquid and liquid–vapour interfaces, respectively:

$$\sigma_{SV} = \sigma_{SL} + \sigma_{LV}\cos\theta \quad (1)$$

so

$$\cos\theta = (\sigma_{SV} - \sigma_{SL})/\sigma_{LV} \quad (2)$$

σ_{LV} being positive, it is possible to determine the degree of wettability from eqn (2).[3]

$$(\sigma_{SV} - \sigma_{SL}) > 0 \quad \theta < 90°$$
$$(\sigma_{SV} - \sigma_{SL}) < 0 \quad \theta > 90°$$

These mechanical considerations suppose the existence of a solid–liquid interface which can only be possible by thermodynamic considerations when the system is under chemical equilibrium.[4,5] The surface tensions and also the degree of wettability depend on the nature of the reactions at the surfaces. A correlation between the degree of wettability and the presence of a chemical reaction at the interface seems to be possible (Fig. 1) and is accepted by many authors.[6]

Experimental Methods

Wettability apparatus

The equipment employed for the sessile drop method uses an analysis apparatus composed of a furnace, an optical system and a camera coupled with a computer. More details can be found elsewhere.[8]

Table 1. Solubility of some ceramics in liquid iron at 1600°C

Ceramic	*Solubility (mol l^{-1})*
AlN	0·21
BN	0·45
Si_3N_4	1·29
Al_2O_3	$1·02 \times 10^{-3}$
SiO_2	0·018

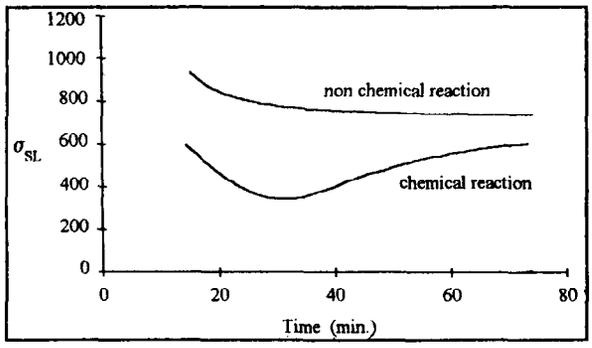

Fig. 1. Evolution of σ_{SL} as a function of time.[6,7]

Finger dipping method

This method consists of dipping AlN samples into different liquid steel baths. Molten steels are contained in small alumina moulds, which could be considered as a small-scale reproduction of the conditions existing in industry.

Materials used

The AlN powder used was produced by H. C. Starck (Berlin) and contains 1·4% oxygen, 33·1% nitrogen and 64·5% aluminium.

We prepared samples of cylindrical form with 35 mm diameter and 4 mm thickness, so that about 12 g of powder was required for each sample. Densification and operating conditions are given in Table 2. The densification of AlN has been studied by Ado *et al.*,[9] who showed that at high temperature (above 1600°C) the formation of AlON phase at grain boundaries is inevitable. This amorphous phase is useful for densification during sintering due to its high diffusion rate. At low temperature (below 1600°C) the AlON phase does not form during sintering. Its absence gives pure sintered material but is detrimental for good densification (see Table 2).

The steel samples employed had a cylindrical form with 6 mm diameter. Their compositions are given in Table 3. Their melting points are 1528, 1515 and 1532°C, respectively.

Table 2. Sintering conditions of pure AlN

P(MPa)	23	18·7	18·7
Temperature (°C)	1820	1600	1550
Time (min)	30	15	20
d_a/d_{th} (%)	97·3	84	78

Table 3. Steel compostion in ppm (major)

	Steel		
	A	*B*	*C*
C	430	1000	60
Si	120	3430	50
Al	450	250	440
Ti	0	110	670
N	46	36	26
Mn	1940	13730	1850

Experimental procedure

Metallic samples were placed on the ceramic substrate in the middle of the furnace in the sight of the camera. The system was kept under vacuum until a temperature of 1490°C was attained, after which argon was introduced in the furnace with a slight gauge pressure. The system was then brought to the working temperature at a rate of 30°C min^{-1}.

For the finger dipping method, small AlN bars with variable density (97·3, 90 and 84%, respectively) were dipped into liquid steels bath for 1 h, under 1 bar pressure of argon (introduced at low temperature), and at temperatures of 1550, 1600 and 1650°C.

Experimental Results

Contact angle

Contact angle is reduced when the temperature increases (Fig. 2) and finally stabilizes above 1580°C at $\theta < 90°$ for steel B and at $\theta > 90°$ for steels C and A; the latter were found to swell between temperatures of 1580 and 1620°C which can be attributed to the formation of gas at the interface.

At constant temperature the wetting angle decreases rapidly during the first 15 minutes (Fig. 3) and then stabilizes at a wetting angle ($\theta < 90°$) for steels A and B and at a non-wetting angle ($\theta > 90°$) for steel C at all temperatures, 1550 or 1570°C.

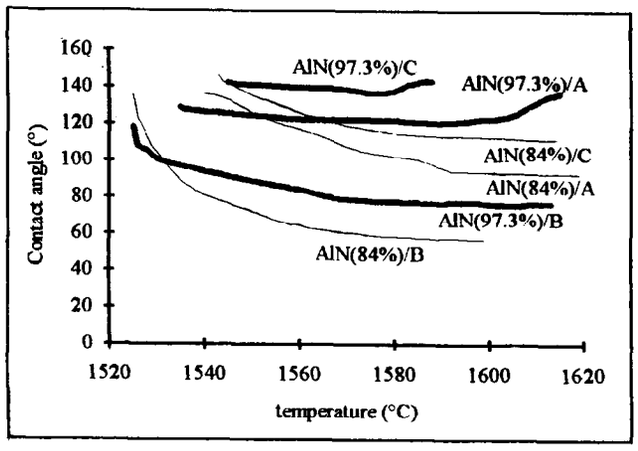

Fig. 2. Contact angle evolution of steel/AlN with temperature.

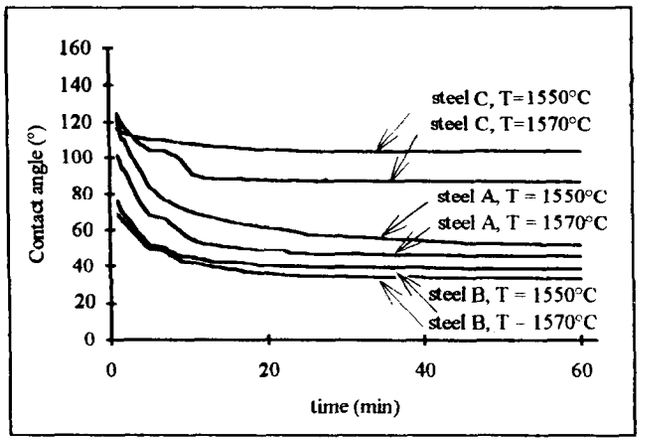

Fig. 3. Contact angle evolution of steel/AlN dense (d/d_{th} = 97·3%).

An increase in porosity decreases the wetting angle considerably, as can be shown by considering the slope $d\theta/dT$ calculated (Fig. 2) after 10 min of heating. For steel A/AlN, the slope varies from –0·1 to –0·85 for temperatures between 1540 and 1580°C, when the ceramic density decreases from 97·3 to 84%. We note that these results are in contradiction with those of Wenzel[10] and Rhee.[11] This can be explained through the fact that an important value of open porosity cannot be assimilated by surface rugosity and that this porosity has altogether different effects.

The effect of atmosphere was studied using the following two conditions:

(1) after having obtained a secondary vacuum of about 5×10^{-2} Pa, argon was introduced at T = 200°C. Argon pressure was kept at $1{\cdot}1 \times 10^5$ Pa;

(2) The furnace was kept under vacuum (6×10^{-2} Pa) up to a temperature of 1490°C and argon gas was introduced into the furnace at this temperature.

In the first case, the wetting angle remains practically constant and non-wetting (Fig. 4) at 1570°C while, in the second case, the angle reduces rapidly to $\theta < 90°$. This different behaviour is due to the presence of a solid layer on the liquid surface, observed just after fusion in the first case and after ~ 40 to 50 min in the second case. This layer probably arises from a reaction between the liquid surface and the impurities present in the atmosphere such as oxygen, prohibiting a normal contact angle evolution. In the case of steel C, this layer makes difficult the formation of a liquid drop.

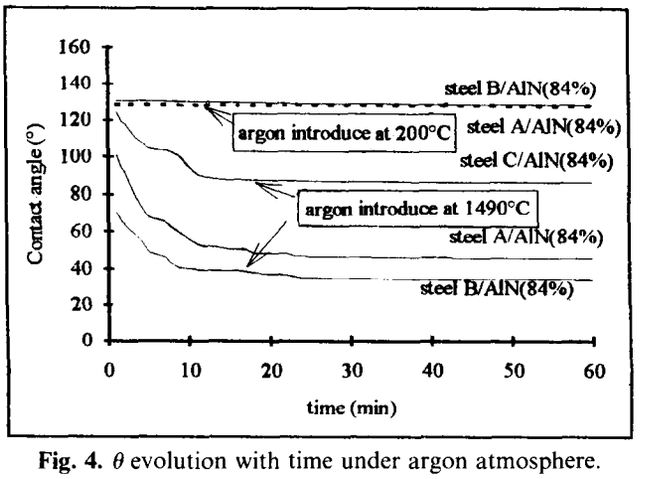

Fig. 4. θ evolution with time under argon atmosphere.

Solid–liquid tension

It is clear that the evolution of the liquid–vapour tension (σ_{LV}) cannot give a complete explanation of the wettability evolution.[12] Therefore, to understand liquid steel behaviour on solid substrates, it is necessary to follow the variation of σ_{SL} as a function of different parameters. A direct measurement of solid–liquid surface tension being impossible, we can only approach its value and its variation using the Young–Dupre equation (1). As done by a number of authors,[13,14] we can give a fixed value to σ_{SV} (1000 mN m^{-1}), θ and σ_{LV} being known through direct measurement or calculation. After that we can only consider the evolution σ_{SL} with respect to different parameters and not its absolute value.

It must be noted that the Young–Dupre equation can only be applied to systems that are in perfect mechanical and thermodynamical equilibrium and to surfaces that are perfectly plane, having very little rugosity. These conditions generally do not prevail during experiments. Thus σ_{SL} values obtained are approximate to a certain extent, but as we are more interested in the evolution of this value rather than its absolute value, we can admit such approximations.

The solid–liquid tension for steels A, B and C over aluminium nitride decreases just after the melting point of the steels (Fig. 5). Generally, high values of σ_{SL} show the presence of a chemical reaction at the interface.[6] At a constant temperature, the solid–liquid tension reaches a minimum value, in each case after 10 min, and becomes stable afterwards (Fig. 6). Experimental curves are

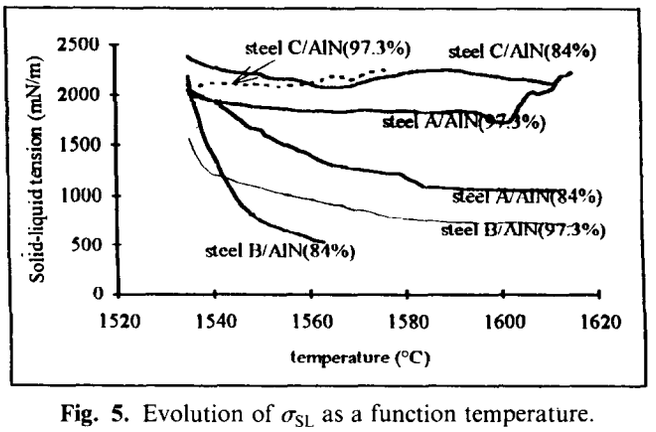

Fig. 5. Evolution of σ_{SL} as a function temperature.

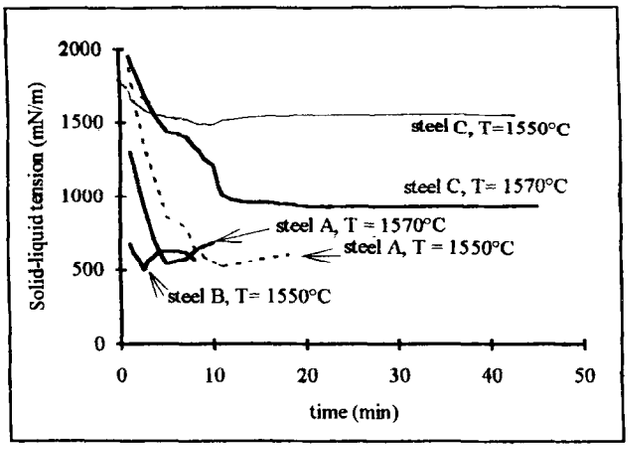

Fig. 6. σ_{SL} evolution of steel/AlN dense (d/d_{th} - 97·3%).

Table 4. The corrosion thickness (mm) of AlN in liquid steels (1 h; 1·1 × 10^5 Pa)

Steel	d/d_{th} (%)					
	97·3		*90*		*84*	
	1550°C	*1650°C*	*1550°C*	*1650°C*	*1550°C*	*1650°C*
A	–	–	0·03	0·65	0	0·1
B	0·22	0·28	0·27	0·2	0	0·06
C	0·16	>0·8	0·8	0·48	0	0·16

characteristic of a chemical reaction at the interface (see Fig. 1).

Porosity has an important influence on the solid–liquid tension (see Fig. 5) and σ_{SL} decreases when the porosity increases. Such behaviour can be explained if we consider that this phenomenon takes place in parallel with the chemical reaction at the interface. While porosity increases, the reaction at the surface gives a higher value of the variation $\Delta\sigma_{SL}$ of σ_{SL}, which is still enhanced by the wetting behaviour of steels A and B.

Results with the finger dipping method confirm these observations and show that higher corrosion values are obtained when the porosity is below 10%. An increase of the corrosion resistance is found when the porosity is around 20% (Table 4).

Discussion and Interpretation of Results

The decrease in θ value during the first 15 min after drop formation at constant temperature, characterizes a system that is out of chemical equilibrium. This behaviour was found at each temperature investigated. It should be noted that a higher porosity (>10%) rapidly decreased the contact angle to a very small value (see Fig. 2). These observations help us to conclude that the wetting angle is controlled by chemical reaction at the liquid steel–AlN interface. The variation of the solid–liquid interfacial tension as a function of time (Fig. 6) passed through a minimum value, for all types of steel. Such an evolution is further evidence for the presence of a chemical reaction at the interface.[6]

Observations made during the experiments —such as the swelling of the liquid drop and the bursting of these drops promoted by gas formation and elimination, and the formation of a solid layer at the liquid drop surface — show the presence of two chemical reactions: one at the solid–liquid interface and the other at the liquid–vapour interface. These will be discussed in the following sections.

Chemical interaction at solid–liquid interface

Scanning electron microscopy (SEM) and energy dispersive analysis by X-rays (EDAX) show that the liquid steel penetrates into the solid surface and also the presence of grains ($r \leq 5$ μm) distributed in the liquid phase. EDAX of these grains reveals a high concentration of Al and O and a very low concentration of N. We can postulate that this oxide is produced by a chemical reaction between AlN or AlON present at grain boundaries and the oxygen dissolved in the liquid steel or present in the nitride as impurities. Both reactions can take place simultaneously.

(1) Oxidation of nitride by oxygen dissolved in the liquid steel. The reaction take place in two stages, decomposition of nitride into Al and N, and oxidation of liquid Al:

$$AlN_{(sol)} \rightarrow [Al_{(liq)}]_{steel} + \frac{1}{2} N_2 \uparrow$$

$$\Delta G_R = -0{\cdot}17 + 7{\cdot}6 \ln[P_{(N_2)}] = -28{\cdot}47 \text{ kJ mol}^{-1}$$

when T = 1820 K and $P_{N_2} = 10^{-7}$ atm

$$2[Al_{(liq)}]_{steel} + 3[O]_{steel} \rightarrow Al_2O_{3(sol)}$$

$$\Delta G^0_R = -498{\cdot}41 \text{ kJ mol}^{-1} \text{ at } 1820 \text{ K}$$

(2) Oxygen attack over AlON present at grain boundaries of sintered AlN, according to the following reactions:

$$2AlON_{(sol)} + [O]_{(steel)} \rightarrow Al_2O_{3(sol)} + N_{2(gas)} \uparrow$$

$$Al_2O_{3(sol)} \xrightarrow{(steel)} [Al_2O_3]_{(steel)}$$

All reactions lead to the formation of Al_2O_3. Theoretically, the steels used are saturated in alumina. The dissolution is probably not possible and we can suggest that Al_2O_3 remains at the interface, and the system advances towards a steel–Al_2O_3 contact. Thus it would be interesting to make some experiments to verify the reaction between steel and Al_2O_3. A study of the behaviour of pure and densified alumina with respect to steels A, B, and C shows[15] that the wetting angle and solid–

liquid tension (Figs 7 and 8) remain practically constant as a function of time. An alumina sample dipped into liquid steel at 1600°C for 10 h does not show any corrosion marks.

In the case of the reaction between steel and AlN, the main difference lies in the fact that the Al_2O_3 phase does not form a protective layer at the AlN surface. Thus a small amount of this alumina is possibly found in the liquid steel drop. The X-ray analysis does not allow us to detect this phase and we can imagine that it is an amorphous form of Al_2O_3. The results of the dipping experiment prove that the attack on the AlON phase present at the grain boundaries is the principal mechanism of corrosion by steels, and when the sintering conditions prevent the formation of AlON phase (temperature <1600°C), the corrosion decreases in a very important way. Thus, a high porosity sample sintered at low temperature presents the best resistance to corrosion (Table 4) in spite of the increase in the contact surface between the steel and the substrate due to the presence of pores.

In addition to AlON reaction, thermodynamic calculations confirm that AlN in all cases reacts with the oxygen present as traces in the furnace atmosphere.[16] This explains the mechanism of corrosion which results in gas (N_2) formation inside the liquid drop and its bursting. If we consider the works of Billy *et al.*[17] and Darbha[18] related to aluminium nitride corrosion, we note that the reaction at the interface resulting in nitrogen formation produces porosity at the interface. This porosity is then filled by liquid steel rich in oxygen, thus promoting further corrosion.

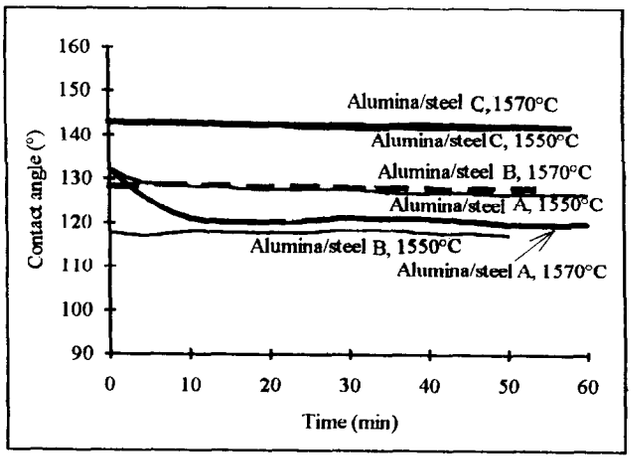

Fig. 7. θ evolution of steel/alumina contact.

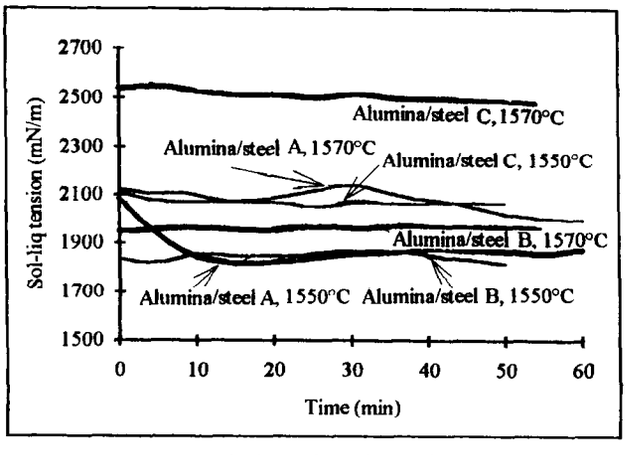

Fig. 8. σ_{SL} evolution of steel/alumina contact.

This type of behaviour is found in all types of steel studied with AlN. This effect was much more enhanced for steel B/AlN because of the presence of silicon which increases the wetting properties of the steel and forms silicon nitride as a result of a reaction with N_2 formed during the decomposition of AlN. This silicon nitride is again soluble in liquid steel[19] and this explains the fact that silicon is not detected at the interface. In the case of steel C, which is rich in titanium, nitrogen reacts with Ti to form TiN. This new phase is corrosion-resistant and helps in reducing or stopping corrosion wherever it forms. Thus we find that corrosion is almost constant at 0·16 mm in the case of steel C, during dipping experiments performed at 1550°C for 1 h.

Chemical interaction at liquid–vapour interface

A high concentration of aluminium and oxygen detected through EDAX shows that an alumina layer forms at the liquid drop surface. Thermodynamic calculations find the same results under our operating conditions. The wetting properties of a steel could then be related to this alumina layer formed at the surface, which keeps the angle of contact at a non-wetting value (Fig. 7) notably in the case of steel C. The speed of formation of this alumina layer depends on the type of steel, and can be rated as: C >> A ≥ B. In the case of steel C it appears 6 to 10 min after melting, and in the case of steel B, 40 min after fusion. Through thermodynamic calculations we find that in steel B, which is poor in aluminium, precipitation starts at 10 ppm of oxygen while it starts at 5 ppm in the case of steel C. This oxide layer has a strong influence on the wetting angle θ. The absence of AlON phase at the surface of samples having 20% porosity adds to the formation of this oxide layer and prevents real contact between steel and the AlN substrate, and thus corrosion is almost stopped (Table 4).

Conclusions

The modification of the contact angle between AlN and liquid steels is controlled by the degree of oxidation of AlN and of AlON present at grain boundaries through oxygen found in:

(1) the initial AlN powder, where it is present at about 1·5 wt%;
(2) the phases formed at the grain boundaries during the sintering of AlN;

(3) the furnace atmosphere where it is present at about 20 ppm, at a temperature between 1500 and 1600°C and at an argon pressure of about 10^5 Pa;
(4) steels, where its concentration varies from each type of steel C >> B ≈ A.

The mechanism of corrosion is complex: at the solid–liquid interface, corrosion takes place after AlN decomposition and alumina formation, and attacks the AlON phases present at grain boundaries. At the liquid–vapour interface, we detect the formation of an oxide layer (alumina) at the liquid drop surface.

For steel rich in Ti, we detect TiN at the solid–liquid interface. The formation of this phase is thermodynamically possible. TiN is corrosion-resistant and gives, where it forms, a higher corrosion resistance to AlN.

References

1. Vandemaele, Y., *Silicates Industriels*, **45**(12) (1980) 249.
2. Young, T., *Phil. Trans. Roy. Soc. London*, **95** (1805) 65.
3. Anerji, E. A., Rohatgi, P. K. & Reif, W., *Metall.*, **38** (1984) 656.
4. Gibbs, J. W., *Trans. Conn. Acad.*, **3** (1878) 343.
5. Johnson Jr., R. E., *J. Phys. Chem.*, **63** (1959) 1655.
6. Aksay, I. A., Hoge, C. E. & Pask, J. A., *J. Phys. Chem.*, **78**(12) (1974) 1178.
7. Delannay, F., Froyen, L. & Deruyttere, A., *J. Mater. Sci.*, **22** (1987) 1.
8. Labbe, J. C., Lachau-Durand, A., Laïmeche, A., Paulyou, V., Tétard, D. & Goujaud, J. F., *High Temp. Chem. Processes*, **1** (1992) 151.
9. Ado, G., Bernache, D. Billy, M., Hahn, K. S. & Lefort, P., *Rev. Chim. Mineral.*, **22** (1985) 473.
10. Wenzel, R., *Ind. Eng. Chem.*, **28** (1936) 988.
11. Rhee, S. K., *J. Am. Ceram. Soc.*, **54**(7) (1971) 334.
12. Coudurier, L., Pique, D. & Eustatopoulos, N., *J. Chim. Phys.*, **84** (1987) 2.
13. Marija, T. & Kolar, D., *J. Am. Ceram. Soc.*, **61** (1978) 5.
14. Sangiriogi, R., Muolo, M. L. & Passerone, A., *Mater. Sci. Monogr.*, **38A** (*High Tech. Ceram. Pt. A*) (1987) 415.
15. Laïmeche, A., Ph D Thesis, University of Limoges, 1993, p. 53.
16. Jones, L. M. & Nocholas, M. G., *J. Mater. Sci. Lett.*, **8** (1989) 265.
17. Billy, M., Jarrige, J., Lecompte, J. P., Mexmain, J. & Yefsah, S., *Rev. Chim. Mineral*, **19** (1982) 673.
18. Darbha, S., *J. Am. Ceram. Soc.*, **73** (4) (1990) 1108.
19. Yefsah, S., Billy, M., Jarrige, J. & Mexmain, J., *Rev. Int. Hautes Temp. Réfract., Fr.*, **18** (1981) 167.

Journal of the European Ceramic Society 16 (1996) 899–906

0955-2219(95)00209-X
0955-2219/96/$15.00 +.00

Effects of Reduction of the Al–Y–O Containing Secondary Phases During Sintering of AlN with YF_3 Additions

Aase Marie Hundere* & Mari-Ann Einarsrud†

Department of Inorganic Chemistry, Norwegian Institute of Technology, University of Trondheim, N-7034 Trondheim, Norway

(Received 26 April 1994; revised 20 November 1995; accepted 29 November 1995)

Abstract

The effect of reduction of the Al–Y–O containing secondary phases forming AlN and YN during sintering of AlN(YF_3) embedded in AlN powder has systematically been studied. The sintering was performed in a graphite furnace at 1880°C. With increased reduction of the secondary phase, the following effects were observed: (a) the chemical composition of the secondary phase changed in the order YAG → YAP → YAM → Y_2O_3 → YN; (b) reduction of the amount or removal of the secondary phase; (c) decreased sinterability of AlN when more than 5 wt% YF_3 was added; (d) reduction in the lattice oxygen content; and (e) increased thermal conductivity. Included in the paper is a discussion of a possible mechanism for the reduction of the secondary phase, which we propose is controlled by the diffusion of gas species (CO/CO_2 and/or Al_2O) through the powder bed and the distance between the AlN samples and a graphite source, as well as a proposed optimal sintering programme for AlN with Al–Y–O containing phases.

1 Introduction

Aluminium nitride (AlN) has attracted much attention, mainly because of its high thermal conductivity. Slack *et al.*[1] estimated the thermal conductivity of an AlN single crystal to be 319 W m^{-1} K^{-1}; however, polycrystalline materials have much lower thermal conductivity (120–240 W m^{-1} K^{-1}) because of oxygen impurities and microstructural defects.

Y_2O_3 and YF_3 are among the most common sintering additives used during liquid-phase sintering of AlN ceramics because a liquid dissolving AlN is formed at the eutectic temperature in the system Al_2O_3–Y_2O_3. Al_2O_3 is normally present as a surface layer of the AlN grains. During heating an Al–Y–O containing phase is formed at around 1100°C due to reaction between the oxide surface layer of the AlN grains and the Y_2O_3/YF_3 additive.[2] The eutectic temperature is around 1800°C,[3] and hence liquid-phase sintering of AlN with Y_2O_3 or YF_3 additives has to be done at a temperature above some 1800°C. The sintering of AlN is most often performed in a nitrogen atmosphere in a graphite furnace using different kinds of crucibles (C, AlN or BN) with or without a protective powder bed (AlN) around the samples.[2,4–13] AlN with Y_2O_3 or YF_3 additives, sintered at the described conditions, contains a range of different secondary phases: $Al_5Y_3O_{12}$ (YAG), $AlYO_3$ (YAP), $Al_2Y_4O_9$ (YAM), Y_2O_3 and YN.[2,4–13] The reducing atmosphere most often present in a graphite furnace due to oxygen impurities, thermal decomposition and/or reduction of oxides is reported to reduce the Al–Y–O containing secondary phases.[5–8,10,12,13]

In this work we have done a systematic study of how the reduction of the Al–Y–O containing secondary phases influences the density, amount and distribution of secondary phases, thermal conductivity and oxygen content of the sintered AlN samples. YF_3 was used as sintering additive to avoid additional oxygen content in the AlN ceramics and to be able to visualize the effect of the reduction of the secondary phase more clearly.

2 Experimental

AlN powder (Tokuyama Soda, grade F) with 0·9 wt% (0·3 wt% lattice dissolved) oxygen and a specific surface area of 3·4 m^2 g^{-1} was used. YF_3 (Pennwalt, 99·99% purity) was used as sintering

*Present address: Elkem a/s Materials, PO Box 126 Vaagsbygd, N-4602 Kristiansand S, Norway.
†To whom correspondence should be addressed.

additive. Five different compositions of samples were used, i.e. with 1, 2, 3, 5 and 10 wt% YF_3. Green bodies of AlN were prepared by a slip-casting technique using isopropanol and the dispersing agent Alkasurf SS-0-75 (Alkaril Chemicals). Mixing of the slurry was performed by an ultrasonic disintegrator (MSE Soniprep 150). All stages in the processing of the green bodies were performed in a dry nitrogen atmosphere glove box (H_2O < 20 ppm) to control the oxygen and impurity content. The green bodies were about 1·5 cm in diameter and 1 cm in height. Before sintering the dispersing agent was removed during 20 h of heating at 150°C in flowing nitrogen. The green density of the samples was about 1·5 g cm^{-3}. The samples were sintered in a nitrogen atmosphere (<5 ppm O_2) in a graphite furnace (total volume about 80 l) at 1880°C for 2 or 6 h. For convenience, the sintering was done with nitrogen flowing through the furnace; however, the gas inlet and outlet were far from the crucible so we can assume stationary conditions around the samples during the sintering.

Three different sintering conditions were employed as shown in Fig. 1: in condition A the AlN sample is embedded in a 'fine' AlN powder bed (grain size <15 μm) in a BN crucible covered by a BN lid (not gastight); in condition B the AlN sample is embedded in a 'coarse' AlN powder bed (grain size <0.5 mm) in a BN crucible covered by a BN lid (not gastight); and in condition C the AlN sample is embedded in a 'fine' AlN powder bed (grain size <15 μm) in a graphite crucible without a lid. The 'fine' powder bed used for sintering condition A reached a higher degree of densification than the 'fine' powder bed used for sintering condition C during the firing. The crucible outer diameter was 52 mm and the height was 64 mm.

The densities of the sintered samples were measured by the liquid immersion method (ASTM C737) using isopropanol. The microstructure was investigated by scanning electron microscopy (SEM) (Zeiss DSM 940). Secondary phases were analysed by a Teller diffractometer (Philips PW 1730/10) and EDS (Noran Instruments, Tracor Series 2). The thermal conductivity was measured to an accuracy within 10% by a laser flash method using a CO_2 laser (Tac 2, 215G). The oxygen content (total and lattice dissolved) was determined by selective hot gas extraction method using a LECO TC 436 analyser by a procedure similar to that described by Thomas and Müller.[14,15] The method allows for separate determination of the lattice dissolved oxygen, oxygen in the secondary phase and the oxygen adsorbed on the surface of the AlN ceramics. The total oxygen content was determined by mixing the AlN samples (crushed <20 μm) with a graphite powder (LECO 501-073) in a nickel basket (LECO 763-065). The nickel basket was placed within a graphite crucible (LECO 782-720) and heated at 2700°C for 50 s. The oxygen content adsorbed on the surface and the oxygen dissolved in the secondary phase were determined by slow heating (6 K s^{-1}) of the AlN samples (ground <20 μm) mixed with graphite powder only in the graphite crucible. The amount of oxygen in the AlN lattice was calculated by difference.[14,15] Typical experimental curves for determination of the total oxygen content and the oxygen content adsorbed on the surface and dissolved in the Al–Y–O secondary phases are given in Fig. 2.

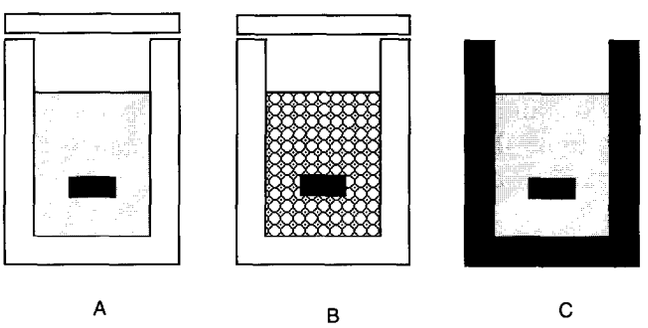

Fig. 1. Schematic representation of the three different sintering conditions. A: AlN sample embedded in a 'fine' AlN powder bed in a BN crucible with a BN lid; B: AlN sample embedded in a 'coarse' AlN powder bed in a BN crucible with a BN lid; C: AlN sample embedded in a 'fine' AlN powder bed in a carbon crucible without a lid.

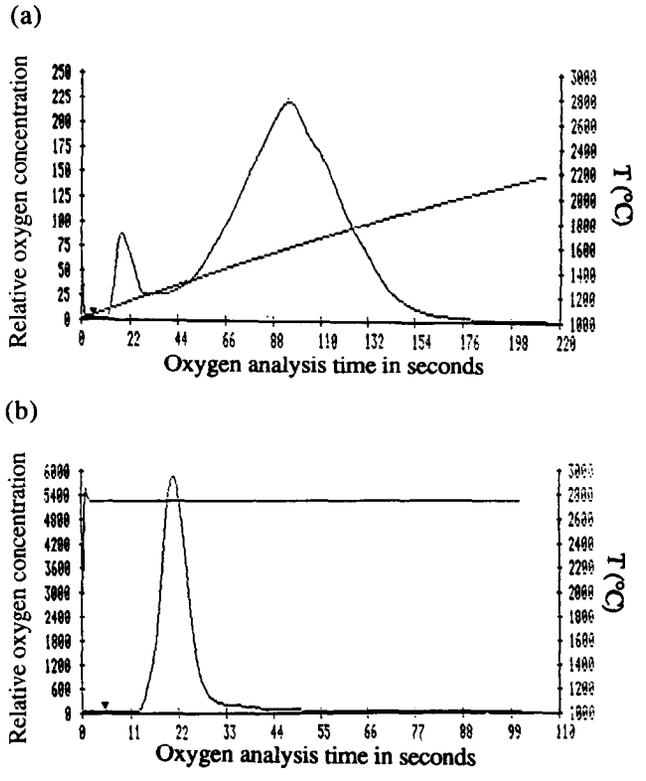

Fig. 2. Experimental curves for determination of the oxygen contents in the AlN ceramics by LECO. (a) Release of oxygen adsorbed on the surface and dissolved in the Al–Y–O secondary phase by slow heating (6 K s^{-1}) and (b) constant heating of the AlN sample at 2700°C for determination of the total oxygen content of the AlN sample.

3 Results and Discussion

3.1 Reduction of the Al–Y–O containing secondary phases

As mentioned above, YF_3 in amounts from 1 to 10 wt% was added to the samples as sintering aid. During heating of the green bodies, Y_2O_3 was presumably formed according to:

$$2YF_3(l) + Al_2O_3(s) = 2AlF_3(g) + Y_2O_3(s) \quad (1)$$

The melting point of YF_3 is reported to be 1155°C.[16] Some YF_3 might evaporate; however, most YF_3 is supposed to react with Al_2O_3 and form AlF_3(g) (AlF_3 sublimes at 1246°C at normal pressure) because only trace amounts of YF_3 were detected in the deposit in the colder regions of the furnace. The evaporation of AlF_3 probably takes place before the AlN powder bed and the AlN samples are densified, because the first maximum in the densification rate of AlN(Y_2O_3) has been observed in the range from 1400°C.[10] However, most of the densification takes place between 1750 and 1800°C,[10] which is well above the sublimation temperature for AlF_3. AlF_3 was deposited as a white powder in the colder regions of the furnace. Other phases observed in trace amounts in the colder regions of the furnace were Y_2O_3 (hexagonal) and AlN. The weight loss of the AlN samples due to thermal decomposition of AlN(s) is considered to be negligible since the protecting embedding was used.

The secondary phases present in the bulk and on the surface of the AlN samples after sintering at conditions A, B and C are shown in Table 1. The secondary phases present in the samples sintered at condition A were generally more rich in Al_2O_3 than the secondary phases in the corresponding samples sintered at condition B. For the samples sintered at condition C a significant difference between the secondary phases on the surface and in the bulk was observed. After 2 h of sintering only Y_2O_3 and YN were identified on the surface, while some Y–Al–O containing phases were present in the bulk. However, after 6 h of sintering, only YN was found on the surface and the bulk was almost completely free of secondary phases with addition of 1 to 3 wt% YF_3. The changes observed in the composition of the secondary phases result from reduction of the Al–Y–O containing phases forming AlN and YN. YN was never observed together with Al_2O_3, in accordance with the phase diagram presented by Sun *et al.*,[17] which stated that YN and Al_2O_3 are not coexistent.

In the following, a discussion of the mechanism for the reduction of the Al–Y–O containing phases is given based on chemical equilibria. For the thermodynamic calculations data are taken from Barin.[16] The sintering temperature (1880°C) is above the eutecticum of the Al_2O_3–Y_2O_3 system;[3] however, the Al–Y–O phases will here be considered as solid species (Al_2O_3 and Y_2O_3) because thermodynamic data are not present in the literature for the liquid phase.

The surface layer of Al_2O_3 on the AlN grains might react with AlN according to:

$$Al_2O_3(s) + 4\,AlN(s) = 3Al_2O(g) + 2N_2(g) \quad (2)$$

The equilibrium pressure of Al_2O(g) at 1880°C and 1 atm N_2 is calculated to be 2×10^{-4} atm. However, due to the small AlN grain size used and the fact that the liquid phase formed is wetting the AlN grains, the partial pressure of Al_2O(g) above the liquid is supposed to be smaller than calculated from the equilibrium due to capillary forces. For reaction (2) to proceed, the Al_2O(g) formed has to be removed from the AlN samples diffusing through the protective AlN powder bed and react with carbon present in the furnace or on the outer graphite crucible (see Fig. 1) to reform AlN according to:

$$Al_2O(g) + C(s) + N_2(g) = 2AlN(s) + CO(g) \quad (3)$$

Using the equilibrium pressure of Al_2O(g) from eqn (2), the calculated equilibrium pressure of CO for eqn (3) is 3.3 atm, and hence the equilibrium position of reaction (3) is driven towards the formation of AlN. However, due to the use of embedding of the samples, the partial pressure of Al_2O(g) at the surface of graphite is much lower

Table 1. Secondary phases present in AlN samples sintered at condition A, B and C. Phases in brackets are observed in trace amounts

Additive YF_3 (wt%)	*Condition A*		*Condition B*		*Condition C*			
	2 h	*6 h*	*2 h*	*6 h*	*2 h surface*	*2 h bulk*	*6 h surface*	*6 h bulk*
1	(YAG)	(YAG)	YAP,YAM	YAM(YAP)	Y_2O_3,YN	YAG	YN	(YN)
2	YAG	YAG	YAM	YAM	Y_2O_3,YN	YAM(YAG)	YN	(Y_2O_3,YN)
3	YAG	YAG	YAP(YAM)	YAP	Y_2O_3,YN	YAP,YAM	YN	(YN)
5	YAG	YAG	YAP(YAM)	YAM(YAP)	Y_2O_3YN	Y_2O_3	YN	Y_2O_3,YN
10	Y_2O_3,YAM	Y_2O_3	YN,Y_2O_3	Y_2O_3	Y_2O_3,YN	Y_2O_3,YN	Y_2O_3,YN	Y_2O_3,YN

than assumed above. The total reaction [eqns (2) and (3)] is:

$$Al_2O_3(s) + 3C(s) + N_2(g) = 2AlN(s) + 3CO(g) \quad (4)$$

It is believed that the rate-determining step for this proposed reaction mechanism (mechanism 1) is the diffusion of the $Al_2O(g)$ through the AlN powder bed towards the graphite source. As the sintering condition is changed from A to B, the diffusion of $Al_2O(g)$ from the AlN samples towards the graphite outside the BN crucible becomes more easy due to less packing density of the AlN powder bed at sintering condition B compared with A. Hence, the secondary phases present in the AlN samples sintered at condition A were more rich in Al_2O_3.

As reaction (4) proceeds, CO gas is formed. From the maximum oxygen content in the nitrogen gas used, the estimated partial pressure of CO in the furnace at the start of the sintering was less than 10^{-5} atm. If all the Al_2O_3 present in the samples and in the powder bed reacted according to reaction (4), the partial pressure of CO in the furnace would be about 10^{-2} atm assuming no flow of nitrogen through the furnace and no pressure gradients in the crucible/furnace. Therefore, quite a high partial pressure of CO might be developed locally inside the crucible especially at sintering condition C, where large amounts of secondary phases were reduced.

Another proposed mechanism is that the CO gas formed might diffuse through the powder bed and react with the $Al_2O(g)$, $Al_2O(g)$ adsorbed on Al_2O_3 or Al_2O_3 in the liquid phase according to eqn (5). For simplicity the reacting aluminium-containing species is assumed to be $Al_2O_3(s)$:

$$Al_2O_3(s) + 3CO(g) + N_2(g) = 2AlN(s) + 3CO_2(g) \quad (5)$$

The calculated equilibrium pressure of CO_2 is 5×10^{-10} atm at 10^{-5} atm CO, which was assumed to be the partial pressure of CO in the furnace due to oxygen impurities. This partial pressure of CO_2 is so low that eqn (5) will not make a significant contribution to the reduction of Al_2O_3. However, CO gas is produced from eqn (3) and this will locally (in the crucible) give a much higher partial pressure of CO and eqn (5) might be of importance. The CO_2 gas formed will diffuse out of the powder bed and react with carbon (crucible/furnace interior) according to:

$$CO_2(g) + C(s) = 2CO(g) \quad (6)$$

For each mole of CO_2 formed, two moles of CO are gained. This means that the partial pressure of CO will increase exponentially if the reaction first is initiated. For this possible reaction mechanism (mechanism 2), the rate-limiting step is believed to be the diffusion of the gas species CO/CO_2 through the AlN powder bed or the limitation might be the equilibrium of eqn (5). Equations (5) and (6) give the same total reaction given in eqn (4). A crucial difference between the reduction of Al_2O_3 according to mechanism 1 [eqns (2) and (3)] and mechanism 2 [eqns (5) and (6)] is where the AlN is formed. According to mechanism 1, AlN is formed on the solid carbon (colder regions of the furnace/crucible). For mechanism 2, the AlN is formed inside or on the surface of the AlN samples. Only very small amounts of AlN were found (identified by X-ray diffraction) deposited on one of the upper radiation shields in the graphite furnace. No broad peaks due to amorphous material were observed in the X-ray diffractograms. These small amounts of AlN could not account for the total amount of Al_2O_3 reduced, especially at sintering condition C. Hence, reduction of Al_2O_3 according to mechanism 2 [eqns (5) and (6)] was probably more important than the reduction according to mechanism 1 [eqns (2) and (3)], especially at sintering condition C. The assumption, stating the importance of the CO gas as the reducing species is strengthened by the detection of CO and CO_2 by mass spectrometry in $AlN(Y_2O_3)$ ceramics reported by Watari *et al.*[6]

In recent work Mitra *et al.*[18] heat-treated dense AlN ceramics with Al–Y–O containing secondary phases at 1900°C for 2 h in a pure nitrogen atmosphere in a W furnace and hence no reducing atmosphere was present. They did not use any embedding of the samples during the heat treatment. Even if their interpretation of the data is questionable, they did not observe a complete depletion of the Al_2O_3 in the secondary phase during this heat treatment or a reduction in the amount of lattice dissolved oxygen which was observed for sintering condition C in this work. We propose that this observed difference is due to the presence of the reducing atmosphere in our work and the significance of CO as a reducing species.

At sintering condition C even large amounts of Y_2O_3 were reduced to YN when all Al_2O_3 was removed from the sample. The total reaction for the reduction of Y_2O_3 is given in eqn (7), where we propose a similar scheme for the reduction of Y_2O_3 with CO as the reducing species to reaction mechanism 2 discussed for Al_2O_3. It should be kept in mind that the partial pressure of CO is considerably higher at the beginning of the reduction of Y_2O_3 compared with Al_2O_3. Large amounts of YN were observed on the surface of the AlN samples, and hence the reducing agent (proposed as CO) must have been present at the surface of the AlN

sample during the reduction of the Y_2O_3.

$$Y_2O_3(s) + 3C(s) + N_2(g) = 2YN(s) + 3CO(g) \quad (7)$$

The possibility for forming volatile Y–O species over Y_2O_3, like $Al_2O(g)$ in the Al_2O_3 system, was also examined. The partial pressure of YO(g), which has been found to be the dominant species above $Y_2O_3(s)$ at high temperature, was calculated to be 10^{-6}–10^{-7} atm at 1880°C using data from Marushkin *et al.*[19] This partial pressure is supposed to be too low to play a major role in the removal of Y_2O_3 from the AlN samples.

To conclude the discussion about the mechanism for the reduction of the Al_2O_3 and Y_2O_3 containing secondary phases in AlN specimens sintered in an AlN powder bed, this reduction is not determined by chemical equilibrium but it is controlled by the diffusion of gas species (i.e. Al_2O and/or CO/CO_2) through the powder bed and the distance between the AlN samples and the graphite source. Therefore, the Al–Y–O containing phases present in the AlN samples sintered at condition A were less reduced than the Al–Y–O containing phases present in the corresponding samples sintered at condition B, due to higher density of the AlN powder bed at sintering condition A. The highly increased reduction of the Al–Y–O containing phases at sintering condition C was probably mainly due to the decreased distance between the AlN samples and the graphite source (the graphite crucible) compared with sintering conditions A and B. We propose reaction mechanism 2 to be dominating at a certain value of the partial pressure of CO (condition C), probably due to a low diffusion rate of $Al_2O(g)$ in the powder bed.

3.2 Densification of the AlN samples

To sinter AlN(YF_3) to nearly 100% density, there has to be Al_2O_3 present as a surface layer on the AlN grains to form a liquid phase in the Al_2O_3–Y_2O_3 system at the sintering temperature. A change in the amount of Al_2O_3 will influence the amount of liquid phase at 1880°C.[3] Using YF_3 as the sintering additive the liquid phase becomes more Y-rich (Y_2O_3 or YN) through two chemical reactions: (a) by reaction between $YF_3(l)$ and $Al_2O_3(s)$ to form $AlF_3(g)$ and $Y_2O_3(s)$ [eqn (1)] and (b) by reduction of Al_2O_3.

Addition of less than 5 wt% YF_3 gave AlN ceramics with densities above 97% for all sintering conditions (Fig. 3). When 5 wt% YF_3 was added, all the Al_2O_3 (about 0·6 wt%) from the surface of the AlN grains should theoretically be removed according to eqn (1), assuming no evaporation of YF_3. This complete removal is not likely to occur because the YF_3 in the green body is not in contact with all the AlN grains. Anyway, the

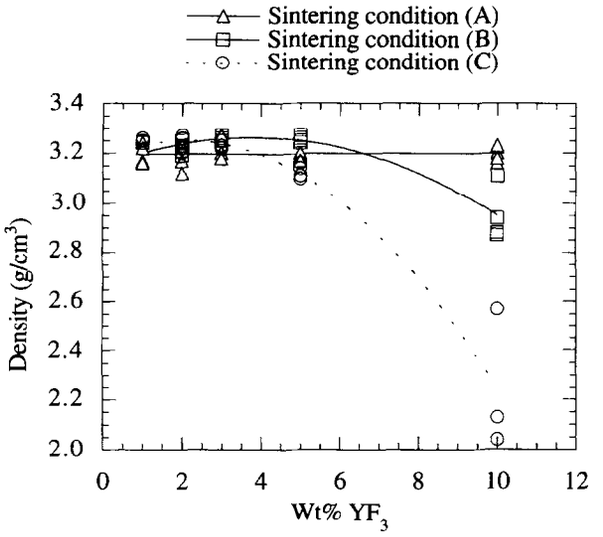

Fig. 3. Density of AlN samples sintered for 6 h as a function of sintering conditions and amount of YF_3 added. The lines are drawn as a guide to the eye.

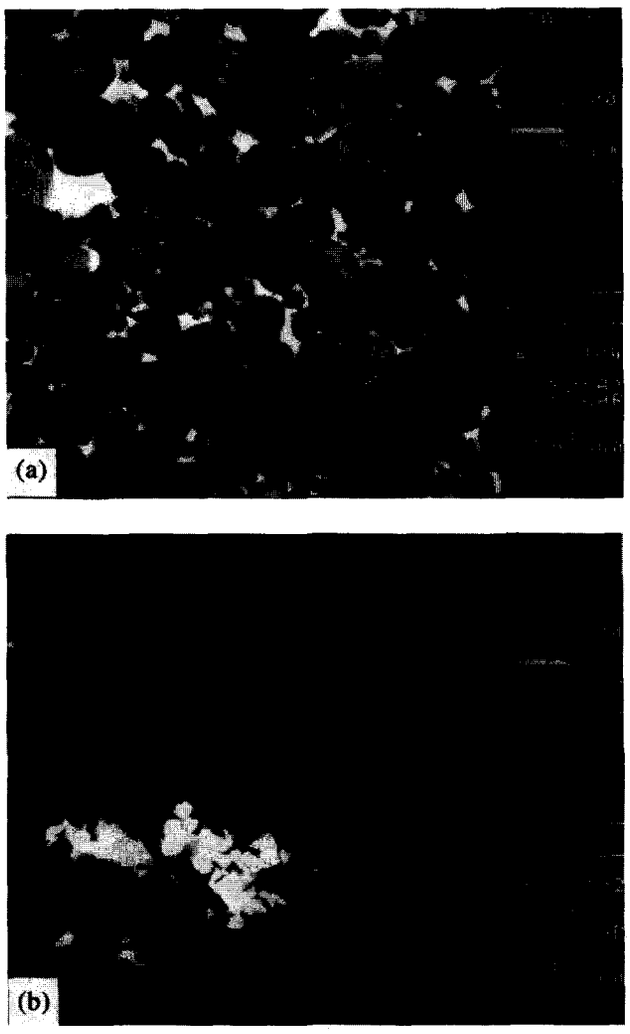

Fig. 4. SEM fractographs of AlN (10 wt% YF_3) samples with electron-backscatter contrast between Y-containing phases (bright) and the AlN grains (dark): (a) sintering condition A; (b) sintering condition C.

amount of Al_2O_3 on the AlN surface will be greatly reduced when the amount of YF_3 added is increasing and a more Y_2O_3-rich secondary phase will be formed. In this situation the influence of the sintering conditions gave rise to large differences in the density and the microstructure, see Figs 3 and 4, respectively. Figure 4 shows fracture surfaces of AlN samples with 10 wt% YF_3 added and sintered at condition A and C for 2 h. The sample sintered at condition A [Fig. 4(a)] shows a well distributed secondary phase (YAM and Y_2O_3) which indicates formation of a liquid phase during the sintering. The sample sintered at condition C [Fig. 4(b)] shows open porosity and an inhomogeneous distribution of the secondary phase (YN and Y_2O_3), which indicate that no/little liquid phase was formed during the sintering. The absence of a liquid phase at the sintering temperature reduces the additional driving force for densification of AlN, which is attained by the liquid-phase mechanism. This explains the reduced density observed for samples with large additions of YF_3 and sintered at condition C (and condition B), (Fig. 3).

3.3 Oxygen content and thermal conductivity of the AlN samples

Previously, increased amount of additive, increased sintering time and type of furnace (C, W, Mo and HIP) were shown to influence the oxygen content in AlN ceramics.[9,11–13,20] The total oxygen content of the AlN samples is given in Table 2 for the samples sintered for 6 h at condition A, B and C, while the oxygen content dissolved in the AlN lattice is given in Fig. 5. The oxygen content in the AlN lattice is found to decrease as a function of increased reduction of the secondary phases, increased amount of additive and increased sintering time. An experimental correlation is found between the composition of the secondary phases present in the AlN ceramics and the oxygen content in the AlN lattice. Samples sintered at condition A contained YAG only as the secondary phase. The oxygen (lattice) content in these samples seems to approach a value of around 0·2 wt% oxygen. The samples sintered at condition B contained YAP and YAM. The oxygen content in the AlN lattice

Table 2. Oxygen content ($[O]_{total}$ in wt%) in AlN samples sintered for 6 h at different sintering conditions

Additive YF_3 (wt%)	*Condition A*	*Condition B*	*Condition C*
1	0·94	0·70	0·28
2	1·10	0·50	0·25
3	0·97	0·61	0·14
5	1·29	0·92	0·25
10	0·90	0·92	–

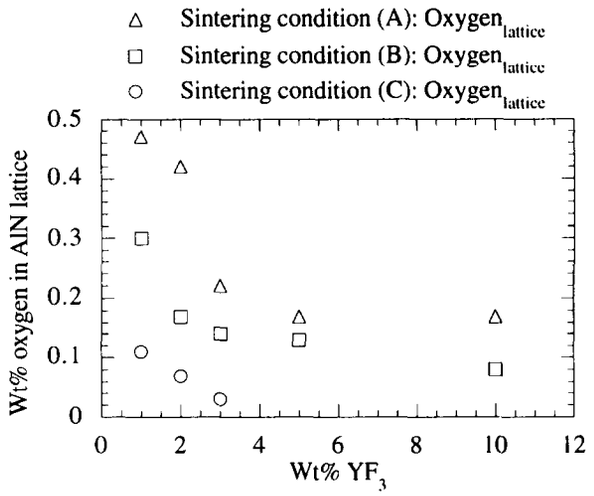

Fig. 5. Oxygen content in the AlN lattice in AlN samples with added YF_3 and sintered for 6 h at condition A, B and C.

reaches a lower value, around 0.1 wt% oxygen. In the samples sintered at condition C, YN and Y_2O_3 were present and the oxygen content approaches zero. The oxygen content of the sample with 5 wt% YF_3 and sintered at condition C is not included in Fig. 5 due to the decreased density of this sample. The presence of the more Al_2O_3-rich secondary phases together with the higher level of oxygen in the AlN grains are in accordance with a thermodynamic model proposed by Virkar *et al.*[4] In this model the lower level of Al_2O_3 in the AlN lattice was determined by the activity of Al_2O_3, $a_{Al_2O_3}$, in the secondary phases. The equilibrium activity of Al_2O_3 dissolved in AlN should be highest in samples containing secondary phases in the region Al_2O_3–YAG and lowest in the region YAM–Y_2O_3.

The thermal conductivities of the AlN samples sintered for 6 h at different sintering conditions are given in Fig. 6. Two trends are predominant: (a) the thermal conductivity increases going from

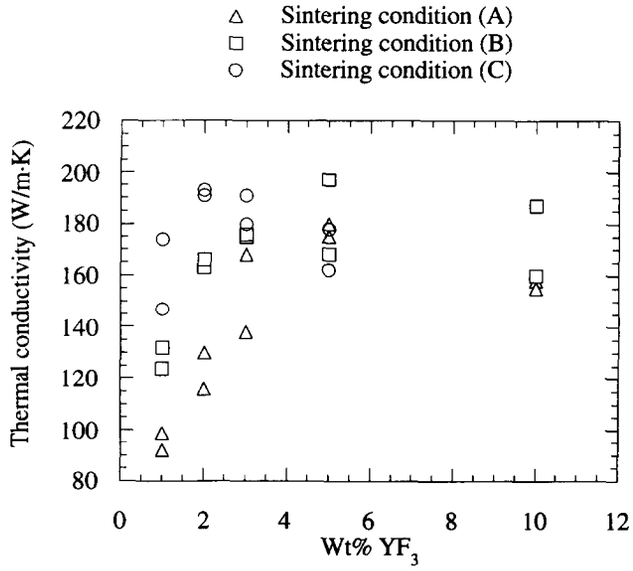

Fig. 6. Thermal conductivity of the AlN samples with added YF_3 and sintered for 6 h at condition A, B and C.

sintering condition A to B to C and (b) the thermal conductivity increases with increasing addition of YF_3 up to about 5 wt%. The decrease in thermal conductivity for the samples with more than 5 wt% YF_3 sintered at condition B and C is most likely due to a decrease in density, see Fig. 3. The oxygen content within the lattice is generally decreasing going from sintering condition A to B to C and decreasing with increasing amounts of YF_3 added, which shows a good correlation between the amount of lattice-dissolved oxygen impurities and the thermal conductivity. This is in accordance with the model proposed by Slack *et al.*[1] and experimental results obtained by others.[9,11,21] However, no correlation between the total amount of oxygen and the thermal conductivity was found. An increasing influence of the secondary phase on the thermal conductivity in the region of very high thermal conductivity (above about 180 W m^{-1} K^{-1}) has been calculated by Buhr and Müller.[11] It is therefore expected to be desirable to be able to remove the secondary phase to obtain a thermal conductivity above about 180 W m^{-1} K^{-1}. This removal can be achieved by choosing proper sintering conditions, e.g. sintering condition C for 6 h. A prolonged reheating at 1900°C in a carbon sagger has previously been used in the literature to remove the Al–Y–O containing secondary phase.[5,8]

On the basis of the results obtained in this work, an optimal sintering programme for AlN with Y-containing additives in a graphite furnace is proposed as follows. The amount of YF_3 added should be below the limit of removing all the Al_2O_3 from the surface of the AlN grains. The reduction of the Al–Y–O containing secondary phase (either by thermal evaporation or reduction with reducing gas species) is kept low during the densification of AlN. This criterion shows the importance of using a powder bed, especially if a graphite furnace is used. In the late part of the sintering, the AlN sample is preferably subjected to a higher partial pressure of reducing species (proposed here to be CO) in order to reduce the secondary phases on the surface of the dense AlN sample, to increase the depletion of oxygen from the AlN lattice and to reduce the amount of secondary phases.

4 Conclusion

Sintering of AlN(YF_3) embedded in AlN powder in a graphite furnace has been studied with respect to reduction of the Al–Y–O containing secondary phases. The secondary phases become more Y-rich (Y_2O_3 or YN) with: (a) increased amounts of YF_3 added, (b) reduced distance between the AlN samples and a graphite source and (c) increased rate of diffusion of gas species (Al_2O, CO and CO_2) through the protective AlN powder bed. When all Al_2O_3 is removed, Y_2O_3 is being reduced to YN. We propose that the mechanism for the reduction of the Al_2O_3 and Y_2O_3 containing secondary phases in AlN specimens sintered in an AlN powder bed is controlled by the diffusion of gas species (CO/CO_2 and/or Al_2O) through the powder bed and the distance between the AlN samples and a graphite source.

The following effects have been observed for increased reduction of the secondary phases: (a) the chemical composition of the secondary phases changes in the order YAG → YAP → YAM → Y_2O_3 → YN; (b) removal of the secondary phases; (c) decreased sinterability of AlN when the amount of YF_3 added increased above 5 wt%; (d) reduction in the lattice oxygen content; and (e) increased thermal conductivity.

Acknowledgements

The authors thank the Research Council of Norway for financial support and Professor K. Motzfeldt for fruitful discussions.

References

1. Slack, G. A., Tanzilli, R. A., Pohl, R. O. & Vandersande, J. W., The intrinsic thermal conductivity of AlN. *J. Phys. Chem. Solids*, **48** (1987) 641–64.
2. Koestler, C., Bestegen, H., Roosen, A. & Boecker, W., Microstructural development during sintering of AlN ceramics. In *Third Euro-Ceramics*, ed. P. Duran & J. F. Fernandez. Faenza Editrice Iberica, 1993, vol. 1, pp. 913–18.
3. Huseby, I. C. & Bobik, C. F., US Patent 4 547 471, 1985.
4. Virkar, A. V., Jackson, B. T. & Cutler, R. A., Thermodynamic and kinetic effect of oxygen removal on the thermal conductivity of aluminium nitride. *J. Am. Ceram. Soc.*, **72** (1989) 2031–42.
5. Ueno, F. & Horiguchi, A., Grain boundary phase elimination and microstructure of aluminium nitride. In *First Euro-Ceramics*, ed. G. de With, R. A. Terpstra & R. Metselaar. Elsevier Applied Science, Amsterdam, 1989, vol. 1, pp. 1383–7.
6. Watari, K., Kawamoto, M. & Ishizaki, K., Sintering chemical reactions to increase thermal conductivity of AlN. *J. Mater. Sci.*, **26** (1991) 4727–32.
7. Lee, R., Development of high thermal conductivity aluminium nitride ceramics. *J. Am. Ceram. Soc.*, **74** (1991) 2242–9.
8. Hirano, M., Kato, K., Isobe, T. & Hirano T., Sintering and characterization of fully dense AlN ceramics. *J. Mater. Sci.*, **28** (1993) 4725–30.
9. Mullot, J., Winter, K., Lecompte, J. P., Müller, G. & Jarrige J., AlN thermal conductivity of tape casting substrates. In *Third Euro-Ceramics*, ed. P. Duran & J. F. Fernandez. Faenza Editrice Iberica, 1993, vol. 3, pp. 1027–31.
10. Buhr, H., Müller, G., Wiggers, H., Aldinger, F., Foley, P. & Roosen, A., Phase composition, oxygen content and thermal conductivity of AlN(Y_2O_3) ceramics. *J. Am. Ceram. Soc.*, **74** (1991) 718–23.

11. Buhr, H. & Müller, G., Microstructure and thermal conductivity of AlN(Y_2O_3) ceramics sintered in different atmospheres. *J. Eur. Ceram. Soc.*, **12** (1993) 271–7.
12. Haase, I. & Himpel, G., Development of single phase aluminium nitride ceramics. *Silicates Industries*, **7/8** (1993) 143–8.
13. Ishizaki, K. & Watari, K., Oxygen behavior of normal and HIP sintered AlN. *J. Phys. Chem. Solids*, **50** (1989) 1009–12.
14. Thomas, A. & Müller, G., Determination of the concentration of oxygen dissolved in the AlN lattice by hot gas extraction from AlN ceramics. *J. Eur. Ceram. Soc.*, **8** (1991) 11–19.
15. Thomas, A. & Müller, G., Alteration of oxygen content during conditioning and sintering of AlN ceramics. *cfi/Ber. DKG*, **67** (1990) 146–9.
16. Barin. I., *Thermochemical Data of Pure Substances Part 1 & 2*, VCH Verlagsgesellschaft mbH, Weinheim, 1989.
17. Sun, W., Huang, Z., Tien, T. & Yen, T., Phase relations in the system Y–Al–O–N. *Mater. Lett.*, **11** (1991) 67–9.
18. Mitra, S., Dutta, G. and Dutta, I., Effect of heat treatment on the microstructure and properties of dense AlN sintered with Y_2O_3 additions, *J. Am. Ceram. Soc.*, **78** (1995) 2335.
19. Marushkin, K.N., Alikhanyan, A.S. & Orlovskii, V.P., The thermodynamic properties of the oxides of zirconium, hafnium and yttrium. *Russ. J. Inorg. Chem.*, **35** (1990) 1181.
20. Kurokawa, Y., Utsumi, K. & Takamizawa, H., Development and microstructural characterization of high-thermal-conductivity aluminium nitride ceramics. *J. Am. Ceram. Soc.*, **71** (1988) 588–94.
21. Slack, G. A., Nonmetallic crystals with high thermal conductivity. *J. Phys. Chem. Solids*, **34** (1973) 321—35.

SHORT REPORTS

0955-2219(95)00212-X

Journal of the European Ceramic Society 16 (1996) 907–910

0955-2219/96/$15.00 +.00

Effect of Cu-Implanted Joining Interface on Oxygen Grain Boundary Diffusion in $SrTiO_3$ Bicrystal

I. Sakaguchi, A. Watanabe & H. Haneda

National Institute for Research in Inorganic Materials, Namiki 1-1 Tsukuba, Ibaraki 305, Japan

(Received 13 March 1995; revised version received 13 November 1995; accepted 29 November 1995)

Abstract

The oxygen tracer diffusion coefficient has been measured across the interface in a $SrTiO_3$ bicrystal by secondary ion mass spectrometry (SIMS). One part of the faces of the bicrystal were carried out on Cu implantation prior to joining. The determined volume and grain boundary diffusion coefficients are $1{\cdot}4 \times 10^{-18}$ m^2/s and $4{\cdot}5 \times 10^{-21}$ m^3/s, respectively. The enhancement of oxygen grain boundary diffusion is found. Dislocation networks and precipitates at the interface are observed using a transmission electron microscope (TEM). This observation suggests that the predominant diffusion path is along the dislocation networks. The enhancement of the oxygen diffusion in the grain boundary is due to the effect of the Cu-implanted layer.

1 Introduction

Strontium titanate ($SrTiO_3$) is widely known as an oxygen sensor at high temperature. The response time depends on oxygen bulk diffusion and the surface exchange processes. Therefore the oxygen diffusion in $SrTiO_3$ is being studied intensively these days. The dependence of the oxygen diffusivity on the oxygen vacancy concentration has been measured in polycrystalline $SrTiO_3$ with the various dopants[1,2] and in the single crystal as well.[3–5] High diffusivity paths for the oxygen in single-crystal $SrTiO_3$ have been shown to play an important role in the redox reaction.[6] Oxygen grain boundary diffusion in (110)–(110) and (100)–(100) bicrystal $SrTiO_3$, joined by hot isostatic pressing (HIP), has been investigated using secondary ion mass spectrometry (SIMS).[7] The data show that the oxygen grain boundary diffusion along the (110) joined sample is one order of magnitude larger than that in the (100) joined sample. This difference in oxygen grain boundary diffusion is explained by the difference in the grain boundary orientation.

The effect of ion implantation on strontium titanate has been extensively investigated. It has been shown that crystallization kinetics of $SrTiO_3$ is affected by the presence of water vapor.[8,9] Simpson *et al.*[10] have shown that water vapor reduces the activation energy of crystallization from 2·1 to 1·0 eV. Moreover, a study involving the implantation of 2 MeV Ar or F ions, suggested that the oxygen vacancies remained in the implanted layer after complete recovery of radiation damage by the thermal annealing.[11]

The objective of this study is to investigate the effect of the implanted layer on the oxygen grain boundary diffusion at the joining interface in a $SrTiO_3$ bicrystal with secondary ion mass spectrometry (SIMS) and transmission electron microscopy (TEM).

2 Experimental

Single-crystal $SrTiO_3$ plates with (110) polished surface and doped with Nb in 1000 ppm (Earth Jewelry Co.) were used in this study. The Cu ions were implanted at an energy of 462 keV with a dose of $1{\cdot}4 \times 10^{15}$ ions/cm^2. The implanted samples were joined in the same crystallographic planes by hot isostatic pressing (HIP). The HIP was completed in 2 h at a temperature of 1573 K and a pressure of 130 MPa.[12] The preparation of $SrTiO_3$ bicrystals has been described by Watanabe *et al.*[12] The joined bicrystal was cut perpendicular to the joining interface with a low speed diamond saw and was polished using a sequence of various grades of diamond pastes to obtain a mirror finish.

Immediately after polishing and cleaning, the sample was loaded into the exchange apparatus. The system was then closed and evacuated, and enriched $^{18}O_2$ was introduced into the manifold at 130 torr pressure. The temperature was increased to 1325 K and maintained at that value for 1800 s. After isotopic exchange of the ^{18}O between the gaseous phase and the samples, the furnace was

switched off. The $^{18}O_2$ was recovered by opening the manifold to an absorption pump which was cooled with liquid nitrogen.

Oxygen isotope profiles were obtained by a CAMECA IMS-4f instrument equipped with a cesium ion source, using a 10 kV, 5 nA, Cs^+ primary ions. The rastered area was 100 × 100 μm. The Cameca normal-induced electron gun was used to stabilize the charge build-up at the sample surface. $^{18}O^-$ and $^{16}O_2^-$ signals from the crater were acquired using a resistive anode encoder (RAE). The ratio of $^{16}O^-/^{16}O_2^-$ was measured using an electron multiplier (EM). The measured bicrystal sample is illustrated in Fig. 1. The spatial resolution of the RAE in this measurement was 3 μm. This value is much larger than the thickness of grain boundary and the Cu-implanted layer. The oxygen profile was collected from the area of 20 × 20 μm including the joining interface in $^{18}O^-$ and $^{16}O_2^-$ images measured by RAE. The oxygen isotope concentration was evaluated as follows; $C = I(^{18}O) / [I(^{16}O) + I(^{18}O)]$, where $I(^{16}O)$ and $I(^{18}O)$ are the intensities of $^{16}O^-$ and $^{18}O^-$ signals, respectively. Depth calibration was performed with a Dektak 3030 surface profiler.

Transmission electron microscopy (TEM) was used to characterize the morphology in the joined interface in bicrystal sample. The sample for TEM observation was first mechanically polished to 30 μm and then ion-milled at room temperature with 4 kV argon ions. TEM images were obtained using a JEOL 2000 EX transmission electron microscope operating at 200 kV.

3 Results and Discussion

The oxygen diffusion profile in the sample annealed at 1325 K for 1800 s is shown in Fig. 2. The oxygen diffusion profile comprised of two parts: volume diffusion up to a depth of 200 nm from the surface and the grain boundary diffusion from a depth of 700 nm. The volume diffusion contribution in the profile was fitted to a solution of diffusion equation for a constant concentration at surface as follows:[13]

$$\frac{C - C_{bg}}{C_s - C_{bg}} = erfc\left(\frac{x}{\sqrt{4D_v t}}\right) \quad (1)$$

where C is the ^{18}O concentration at depth x, C_{bg} the background natural abundance of ^{18}O, and C_s the surface concentration of ^{18}O. This equation assumes equilibrium between the gas phase and the crystal surface and hence a constant C_s value. D_v and t are the volume diffusion coefficient and

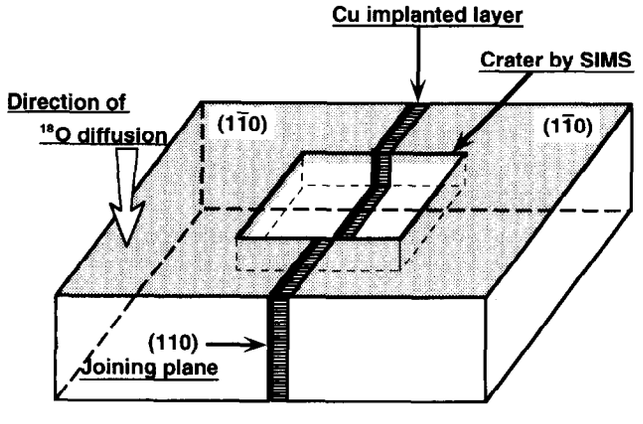

Fig. 1. Schematic diagram of a bicrystal sample.

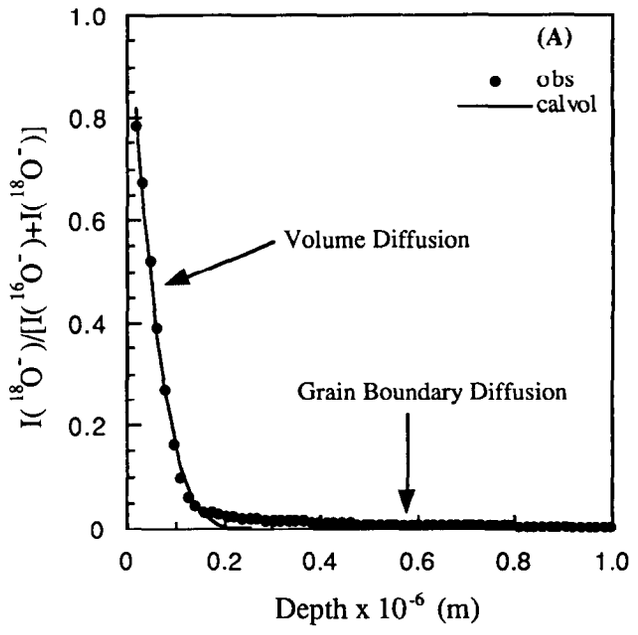

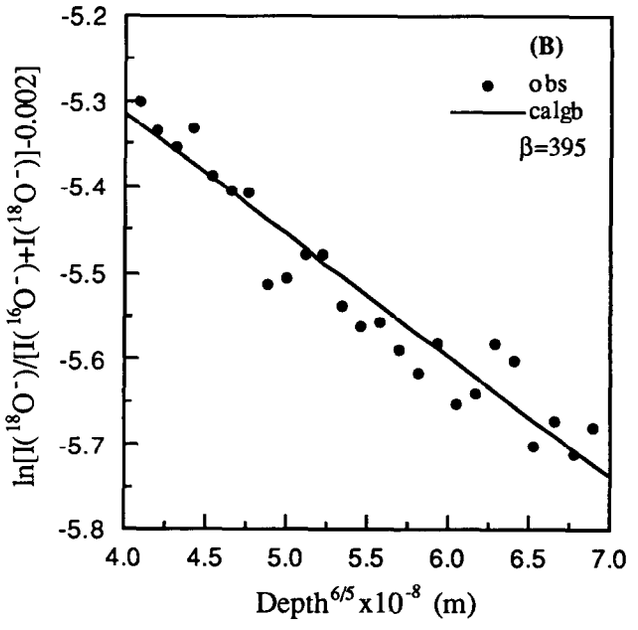

Fig. 2. Oxygen diffusion profiles obtained by SIMS. The solid squares show the oxygen isotope fraction corrected by SIMS. The solid lines indicate the theoretical curves for volume and grain boundary diffusion, respectively. The β factor is obtained from the analysis of reference.[14]

annealing time. The grain boundary diffusion coefficients were determined from the grain boundary model of LeClaire.[14]

$$\delta D_{gb} = 0{\cdot}66\left(-\frac{d\ln C}{dx^{6/5}}\right)^{-5/3}\left(\frac{4D_v}{t}\right)^{1/2} \quad (2)$$

where δ and D_{gb} are grain boundary width and grain boundary diffusion coefficient. The fitted curves shown in Fig. 2 are calculated from the above equations. The values of D_v and δD_{gb} thus obtained are $1{\cdot}4 \times 10^{-18}$ m^2/s and $4{\cdot}5 \times 10^{-21}$ m^3/s, and are shown in Fig. 3. The oxygen grain boundary diffusion along the joining interface in $SrTiO_3$ bicrystal has been reported in our previous study.[7] The value of D_v in this study is in good agreement with the previous result. However, the D_v on oxygen in 1000 ppm Nb-doped $SrTiO_3$ is 4 orders of magnitude smaller than those in pure material.[3] Chan *et al.*[15] have reported the defect chemistry of polycrystalline $SrTiO_3$. At 1000 ppm Nb-doped $SrTiO_3$, the replacement by Nb_2O_5 can be written;

$$Nb_2O_5 + V_{\ddot{O}}(-2TiO_2) \rightarrow 2Nb_{\dot{T}i} + 5O_O \quad (3)$$

This suggests that the oxygen vacancy concentration decreases with the increase in the amount of Nb_2O_5 content. We believe that the difference on D_v between the pure and 1000 ppm Nb-doped $SrTiO_3$ can be explained by the above equation.

As shown in Fig. 3, the value of δD_{gb} is one order of magnitude larger than the previous result. In order to find out the characteristics of the joining interface in the bicrystal sample, a transmission electron microscope analysis (TEM) was carried out. The cross-sectional TEM micrograph near the joining interface in the bicrystal sample is shown in Fig. 4. In this micrograph, dislocations and small precipitates with diameters ranging from 20 to 60 nm are located in the band at a depth of 700 nm below the joining interface. The region from the joining interface to the band has a homogeneous texture. This TEM micrograph indicates that the damaged region of Cu-implantation clearly recovers during the HIP. The dislocation networks at the joining interface were also observed. These dislocation networks were deformed by reacting with the other dislocations. Large cubic precipitates of size 200 nm were observed to be situated mostly at the torsion point of the dislocation networks. The precipitates at the dislocation networks were formed due to the mass transport by the dislocation pipe diffusion. In the implanted sample, small precipitates were located between the large cubic precipitate on the dislocation networks and the defect band. In the non-implanted sample, the large cubic precipitate on the dislocation networks was surrounded by numerous smaller precipitates. There was no precipitate on both sides near the dislocation networks. These precipitates in non-implanted samples seem to suggest that the mass transport between the implanted and non-implanted samples is carried out through the large cubic precipitate on dislocation networks. The formation of dislocation networks at the joining interface relates to the following factors: the misalignment of two samples or the recovery of a Cu-implanted layer. The misalignment of samples occurs due to the rotation of samples for the HIP process. According to previous study,[12] the angle of misalignment in several HIP experiments is about 2°. The effects of

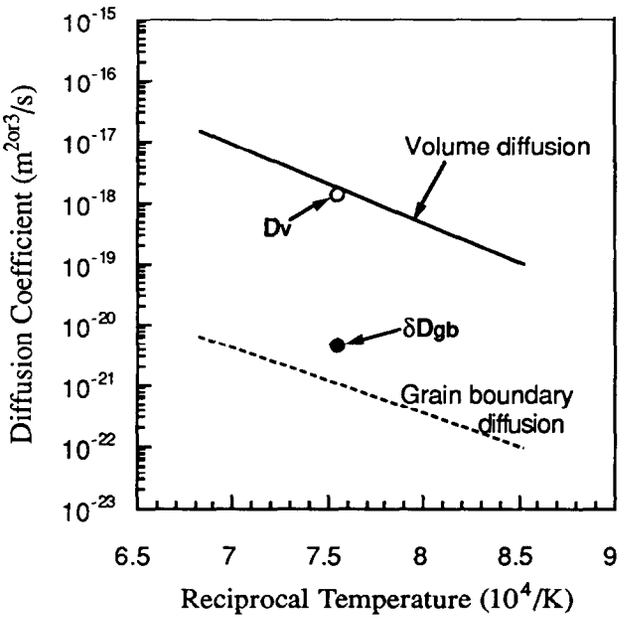

Fig. 3. Temperature dependence of oxygen diffusion coefficient for Nb-doped $SrTiO_3$. The solid and dashed lines show the temperature dependence of volume and grain boundary diffusion of oxygen in our previous result.[7]

Fig. 4. Cross-sectional TEM image in bright field at the joining interface. The upper and lower sides of the joining interface indicate the Cu-implanted and non-implanted samples. The symbols: JI, LP, and SP are the joining interface, large precipitate on the dislocation networks, and small precipitates, respectively.

Cu-implantation are considered to be that the surface region is turned into the amorphous or large amount of dislocation are introduced. The surface state after Cu-implantation has not been investigated. However, the HIP process causes the amorphous region to crystallize epitaxially with the underlying substrate when the surface is turned into the amorphous. The orientation of crystallization is same as that of the substrate. When the surface contains a large amount of dislocations, the HIP process occurs, due to the annihilation of dislocations because the interface acts as the sink for defects. In this case, the orientation of the implanted layer is also same as that of the substrate. It is considered that the formation of dislocation networks at the joining interface is due to the misalignment of the samples.

From the above discussion on the dislocation networks, it is clear that the mechanism of oxygen diffusion at the joining interface is the same as that of the non-implanted $SrTiO_3$ bicrystals (dislocation pipe diffusion).[7] The extent of dislocation pipe diffusion for other diffusion mechanisms are dependent on its density.[16] The dislocation density depends on the tilt angle and is deduced to be of the same order in several HIP experiments. Therefore, the value of the grain boundary diffusion of oxygen in this result is due to the effect of the Cu-implanted layer.

4 Conclusions

The oxygen tracer diffusion across the interface in the $SrTiO_3$ bicrystal has been measured by SIMS and TEM analysis. The determined volume and grain boundary diffusion coefficients are $1{\cdot}4 \times 10^{-18}$ m^2/s and $4{\cdot}5 \times 10^{-21}$ m^3/s, respectively. The enhancement in the oxygen grain boundary diffusion is one order of magnitude. The dislocation networks and precipitates at the joining interface have been observed. The enhancement of the oxygen grain boundary diffusion is due to the effect of the Cu-implanted layer.

Acknowledgments

The authors would like to thank Dr M. Fujimoto of Taiyo Yuden Co. Ltd for useful discussions and Mr Y. Kitami and Mr K. Kurashima of NIRIM for their support during the TEM observations.

References

1. Yamaji, A., Oxygen-ion diffusion in single-crystal and polycrystalline $SrTiO_3$. *J. Am. Ceram. Soc.*, **58** (1975) 152–3.
2. Amante, J. C. & Cawley, J. D., Oxygen tracer diffusion in $SrTiO_3$ and thin films of $YBa_2Cu_3O_{7-x}$ on $SrTiO_3$. In *Point Defects and Related Properties of Ceramics; Ceramic Transactions*, vol. 24, ed. T. O. Mason & J. L. Routbort. The American Ceramic Society, Columbus, OH, 1991, pp. 303–12.
3. Paladino, A. E., Rubin, L. G. & Waugh, J. S., Oxygen ion diffusion in single crystal $SrTiO_3$. *J. Phys. Chem. Solids*, **26** (1965) 391–7.
4. Schwarz. D. B. & Anderson, H. U., Determination of oxygen chemical diffusion coefficients in single crystal $SrTiO_3$ by capacitance manometry. *J. Electrochem Soc.*, **122** (1975) 707–10.
5. Kiessling, U., Claus, J., Borchardt, G., Weber, S. & Scherrer, S., Oxygen tracer diffusion in Lanthanum-doped single-crystal strontium titanate. *J. Am. Ceram. Soc.*, **77** (1994) 2188–90.
6. Waugh, J. S., Paladino, A. E., Dibenedetto, B. & Wantman, R., Effect of dislocations on oxidation and reduction of single-crystal $SrTiO_3$. *J. Am. Ceram. Soc.*, **46** (1963) 60.
7. Sakaguchi, I., Watanabe, A., Hishita, S. & Haneda, H., Oxygen tracer diffusion along joining interface and mechanical damage in bicrystal $SrTiO_3$. *J. Appl. Phys.* (in review).
8. White, C. W., Boatner, L. A., Sklad, P. S., McHargue, C. J., Rankin, J., Farlow, G. C. & Aziz, M. J., Ion implantation and annealing of crystalline oxides and ceramic materials. *Nucl. Instr. and Meth.*, **B32** (1988) 11–22.
9. McCallum, J. C., Rankin, J., White, C. W. & Boatner, L. A., Time resolved reflectivity measurements in Pb-implanted $SrTiO_3$. *Nucl. Instr. and Meth.*, **B46** (1990) 98–101.
10. Simpson, T. W., Mitchell, I. V., McCallum, J. C. & Boatner, L. A., Hydrogen catalyzed crystallization of strontium titanate. *J. Appl. Phys.*, **76** (1994) 2711–18.
11. Sakaguchi, I., Haneda, H., Hishita, S., Watanabe, A. & Tanaka, J., Oxygen diffusion in ion-implanted layer of Nb-doped $SrTiO_3$. *Nucl. Instr. and Meth.*, **B94** (1994) 411–16.
12. Watanabe, A., Haneda, H., Ikegami, T., Tanaka, J. & Shirasaki, S., Solid state bonding of $SrTiO_3$ single crystals using HIP. In *Proceedings of 2nd Japan International SAMPE Symposium*, Japan, 1991, pp. 11–14.
13. Crank, J., *The Mathematics of Diffusion*, Ch. 3.3. Oxford University Press, London, UK, 1975, pp. 28–43.
14. LeClaire, A. D., The analysis of grain boundary diffusion measurements. *Br. J. Appl. Phys.*, **14** (1963) 351–6.
15. Chan, N. H., Sharma, R. K. & Smyth, D. M., Nonstoichiometry in $SrTiO_3$. *J. Electrochem. Soc.*, **128** (1981) 1762–8.
16. Sakaguchi, I., Yurimoto, H. & Sueno, S., Self-diffusion along dislocations in single-crystal MgO. *Solid State Commun.*, **84** (1992) 889–93.

Journal of the European Ceramic Society 16 (1996) 911–914

0955-2219(95)00210-3
0955-2219/96/$15.00 +.00

Viscous Flow of ZnF_2–PbF_2–SiO_2–B_2O_3–GeO_2 glasses and their application to MOS capacitors

Keiji Kobayashi

Toshiba ULSI Research Center, 1-Komukai Toshiba-cho Kawasaki, Japan

(Received 29 September 1995; revised version received 17 November 1995; accepted 29 November 1995)

Abstract

The capacitance and voltage (C–V) characteristics of metal, oxide, and silicon (MOS) capacitors passivated by ZnF_2–PbF_2–SiO_2–B_2O_3–GeO_2 glasses with various water and fluoride contents were investigated. As the OH absorption coefficients of the glass increased, adverse effects on the recovery of hysteresis loops of the C–V curve shifts were observed. The water content was closely related to the fluoride content in these glasses. The viscous flow point of the glass was lowered with an increasing degree of ionic character obtained from Hannay's equation.

1 Introduction

Borophosphosilicate glass films formed from inorganic gas sources have been widely used in high-density integrated circuits such as dielectric insulators.[1–3] The advantageous properties of such films are conformal step coverage, effective protection against alkali ions, and fairly low reflow temperature. Highly doped borophosphosilicate glasses reflow at low temperatures to give step coverage of ultra-high-density integrated circuits, but they also suffer from a tendency to crystallize during the reflow process.[4] Such crystallization is a fatal drawback in the planarization of the ultra-high-density integrated circuits.[4] It has been found that zincborosilicate glasses have even lower flow temperatures than borophosphosilicate glasses, and they do not suffer from the problem of crystallite formation during the reflow process.[5,6] However, both borophosphosilicate and zincborosilicate glasses contain small amounts of water,[7,8] and this adversely affects the C–V characteristics of MOS devices if they are rapidly heated. Past studies have shown that the abnormal C–V curves of MOS capacitors are a result of highly polarizable ions and OH radical in the glass.[8,9]

In this paper, we discuss the relationship between OH^- radical absorption and shifts in the C–V curve for MOS capacitors passivated using non-crystallizable ZnF_2–PbF_2–SiO_2–B_2O_3–GeO_2 glasses with ionic bonds, and investigate the application of these glasses to MOS capacitors.

2 Experimental

ZnF_2–PbF_2–SiO_2–B_2O_3–GeO_2 glasses were prepared for use in the experiments. Batches comprising 1 kg of reagent-grade chemicals were melted at 1300°C for 5 h in an ultra-high-purity platinum crucible with an electric furnace in an oxidizing atmosphere. After homogeneous melting, the glass was poured onto a stainless steel plate and annealed. Infrared transmission spectra were measured using a Digi-Labo spectrophotometer with 10 × 20 × 1 mm plates. Glass flow points were obtained from thermal expansion curves, using a method previously described.[10]

Sputter targets were cut from these samples and ground to 75 mm in diameter and 10 mm thick. Glass films 0·5 μm thick were deposited on a SiO_2 layer (0·3 μm) on Si (100) wafers under 1 kW power and 30 millitorr vacuum sputtering conditions using a Perkin-Elmer vacuum system. The glass thickness was measured by the use of a nanometrics SD9-2000T thickness meter using the Na–D line refractive index (N_D—1·56). Aluminium electrodes were deposited on the glass films. C–V curves for these MOS capacitors were observed at 1 GHz at room temperature, as described previously.[11]

3 Results and Discussion

Low-temperature glass reflow has been studied and used in the planarization of MOS devices and the fabrication of multi-level interconnections.[5,6] It is thought that glass reflow is controlled by

viscosity, which is in turn controlled by composition, chemical bond[12] and structure.[13,14] Namely, glass with 'low connectivity'[12] and 'a released structure'[13] is less viscous than that without such properties. It is to be expected that ionic bonds would give rise to a greater degree of viscous flow than covalent bonds. It seems useful to use Hannay's equation[15] to determine the ionic character of the halide compounds and, moreover, to apply the equation to halide glasses seems a useful way to estimate the bonding states of glass molecules. Hannay and Smyth[15] proposed an experimental equation for ionic bonding as follows;

Degree of ionic character, (%)

$$I_i = 16\,(x_A - x_B) + 3{\cdot}5\,(x_A - x_B)^2 = (x_A - x_B)\,[16 + 3{\cdot}5\,(x_A - x_B)] \quad (1)$$

where $(x_A - x_B)$ is the electronegativity difference for a bond $A - B$ $(x_A > x_B)$.

The ionic character of a glass, I (%), can be described approximately as follows:

$$I = \Sigma I_i M_i \quad (2)$$

where I_i is the ionic character of a single bond $A - B$ making up the glass.

M_i is the mole percentage of the ions making up the glass. The author estimated the ionic character of glasses, using eqns (1) and (2).

The chemical composition (mol%) of various glasses, their absorption coefficients, β_{OH}, ionic character, flow points, T_f, and C–V curve shift, ΔV_G, are listed in Table 1. Infrared absorption spectra for these glasses are given in Fig. 1. The absorption bands around 3·500 cm^{-1} are due to fundamental vibrations arising from OH ions absorption.[16,17]

The relationship between transmittance T_{OH} and reflectivity R_{OH} can be represented as follows:[18]

$$T_{OH}=(1 - R_{OH})^2\,(1 + R_{OH}^2 + R_{OH}^4 + \cdots\cdots) \quad (3)$$

when R_{OH} is small,

$$T_{OH} \fallingdotseq (1 - R_{OH})^2\,(1 + R_{OH}^2) \quad (4)$$

The absorption coefficient β_{OH}[19] resulting from the fundamental vibration due to OH at around 3·500 cm^{-1} is calculated from eqn (5)

$$T_{OH} = [(1 - R_{OH})^2\, e^{-\beta_{OH}t}]/[1 - R_{OH}^2 e^{-2\beta_{OH}t}] \quad (5)$$

where t is the glass thickness.

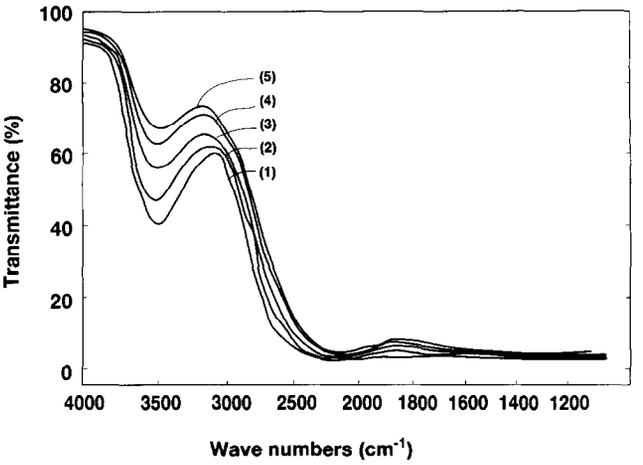

Fig. 1. Infrared absorption spectra for ZnF_2–PbF_2–SiO_2–B_2O_3–GeO_2 glasses: (1) glass no. 1; (2) glass no. 2; (3) glass no. 3; (4) glass no. 4; (5) glass no. 5.

By substituting eqn (4), eqn (5) can be represented as follows:

$$R_{OH}^2(R_{OH}^2 + 1)e^{-2\beta_{OH}t} + e^{-\beta_{OH}t} - R_{OH}^2 = 1 \quad (6)$$

Values of OH^- absorption coefficients β_{OH} are computed from eqn (6). Values of T_{OH}, R_{OH}, and β_{OH} calculated from the infrared absorption spectra in Fig. 1 are also listed in Table 1. Infrared absorption spectra of these glasses are given in Fig. 1, which shows the decrease of OH absorption bands with the increase of fluoride contents in glasses. Fluoride compounds react with water in the batch during melting, as represented in eqn (7)

$$RF_2 + H_2O \rightarrow RO + 2HF\uparrow, \quad (7)$$

where R=Zn, Pb.

Consequently, the reaction of water by fluoride groups in glasses would be advantageous as a means of improving their infrared absorption transmissions in the region of the water peaks.

Thermal expansion curves of ZnF_2–PbF_2–SiO_2–B_2O_3–GeO_2 glasses are given in Figs 2 and 3, which also show the glass flow points. Flow points fell with increasing of ionic character in the chemical bonds. This tendency is clear in Table 1. With regard to the C–V curve shifts in MOS capacitors, when OH absorption coefficients increased, ΔV_G shifts also increased. The C–V characteristics of MOS capacitors passivated with these glasses are

Table 1. Lists of glass compositions, T_{OH}, R_{OH}, β_{OH}, T_f, ionic character I, and ΔV_G

Glass no.	*ZnF_2 (mol%)*	*PbF_2*	*SiO_2*	*B_2O_3*	*GeO_2*	T_{OH} (%)	R_{OH}	β_{OH} (cm^{-1})	I (%)	T_f (°C)	ΔV_G (volt)
1	2	1	37	40	20	40	0·42	0·22	35·7	780	2·1
2	4	2	34	40	20	47	0·35	0·12	36·3	774	1·8
3	6	3	31	40	20	56	0·28	0·06	36·9	768	1·2
4	8	4	28	40	20	62	0·23	0·03	37·4	760	0·8
5	10	5	25	40	20	65	0·21	0·02	38·0	755	0·6

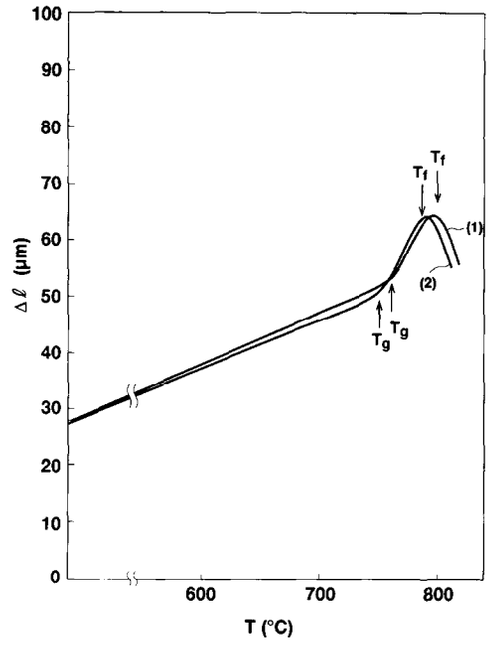

Fig. 2. Thermal expansion curves for ZnF_2–PbF_2–SiO_2–B_2O_3–GeO_2 glasses: (1) glass: no. 1; (2) glass No. 2.

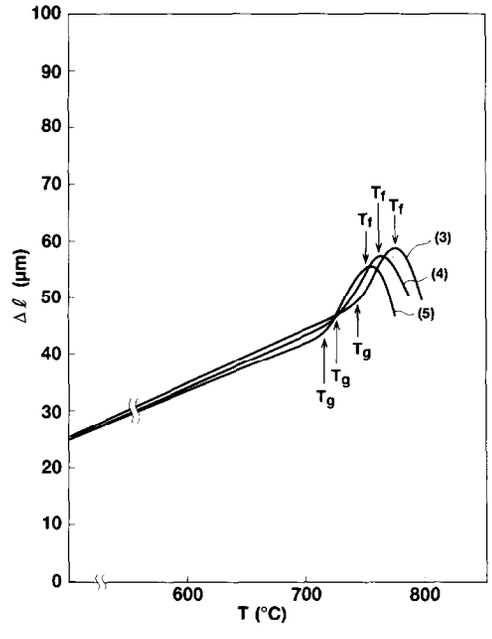

Fig. 3. Thermal expansion curves for ZnF_2–PbF_2–SiO_2–B_2O_3–GeO_2 glasses: (3) glass no. 3; (4) glass no. 4; (5) glass no. 5.

shown in Fig. 4. Figure 4 (1–5), shows the C–V characteristics of MOS capacitors. All the C–V curves for capacitors passivated with these glasses were shifted towards the right. Thus, these peculiar C–V characteristics represent the recovery of C–V curve shifts as the coefficients of OH absorption decrease.

With increasing β_{OH}, the C–V curves shift towards the right. The mean C–V curve shifts, ΔV_G, at the mid-point of forward and backward hysteresis curves are summarized in Table 1.

These shifts in the C–V curves indicate that the total number of positive oxide charges increases.

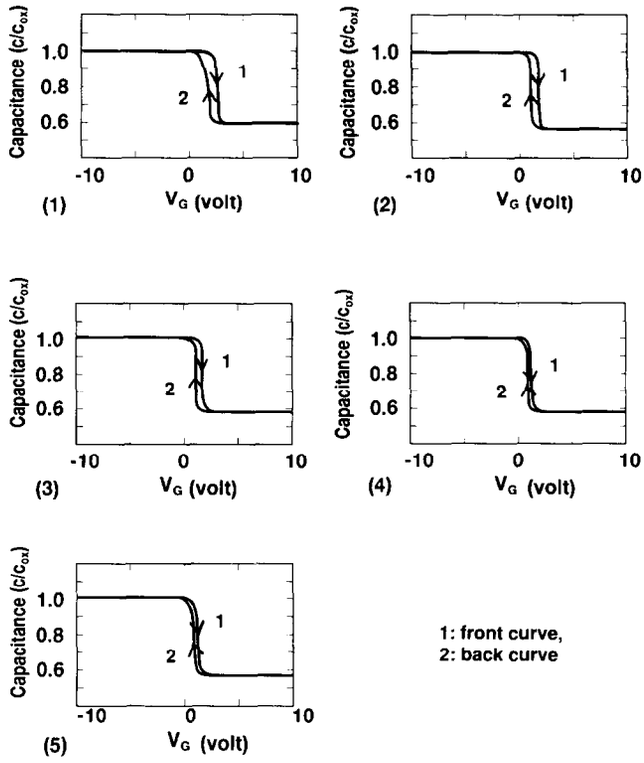

Fig. 4. C–V characteristics of rapidly thermally annealed MOS capacitors passivated with various ZnF_2–PbF_2–SiO_2–B_2O_3–GeO_2 glasses: (1) passivated with glass no. 1; (2) passivated with glass no. 2; (3) passivated with glass no. 3; (4) passivated with glass no. 4; (5) passivated with glass no. 5.

It is reasonable to expect that these positive charges are hydrogen-related vacancies.[9] The loss of hydrogeneous species is related to the disappearance of C–V hysteresis. A hydrogeneous complex is responsible for the carrier trapping mechanism.[9] These shifts are related to hydrogen-related vacancies in water-containing glasses.[9]

4 Conclusion

When the viscous flow point of these glasses became higher, degree of ionic bonding character was reduced and OH absorption coefficient was raised. This tendency may be due to the result of fluoride contents in molten glasses. The viscous flow is reasonably confirmed from the ionic character of bonding state as calculated from Hannay's experimental equation.

The MOS capacitors passivated with ZnF_2–PbF_2–SiO_2–B_2O_3–GeO_2 glasses containing low concentrations of water exhibited the best recovery in their C–V characteristics. With increasing OH absorption coefficient, an adverse effect was seen on the recovery of hysteresis C–V curve shifts. The relationship between recovery from peculiar hysteresis C–V curve shifts and OH absorption coefficient was briefly discussed.

Acknowledgement

The author would like to thank Dr H. Sasaki in Toshiba Research and Development Center for the measurement of infrared absorption spectra.

References

1. Hurley, K. H., *Solid St. Technol.*, **30** (1987) 103.
2. Dickinson, Jr J. E. & deJong, B. H. W. S., *J. Non-cryst. Solids*, **102** (1988) 196.
3. Raley, N. F. & Losee, D. L., *J. Electrochem. Soc.*, **135** (1988) 2640.
4. Schnable, G. L., Fisher, A. W. & Shaw, J. M. *J. Electrochem. Soc.*, **137** (1990) 3973.
5. Kobayashi, K., *J. Non-cryst. Solids*, **88** (1986) 229.
6. Kobayashi, K., *J. Non-cryst. Solids*, (to be published).
7. Kobayashi, K., *J. Electrochem. Soc.*, **131** (1984) 2190.
8. Rojas, S., Gomarasca, R., Zanotti, L., Borghesi, P., Sassela, A., Ottaviani, G., Moro, L. & Lazzeri, P., *J. Vac. Sci. Technol. B*, **10** (1992) 633.
9. Li, S. C., Murarka, S. P., Guo, X. S. & Landford, W. A., *J. Appl. Phys.*, **72** (1992) 2947.
10. Baret, G., Madar, R. & Bernar, C., *J. Electrochem. Soc.*, **138** (1991) 2835.
11. Kobayashi, K., *J. Non-cryst. Solids*, **124** (1990) 229.
12. Kobayashi, K., *J. Non-cryst. Solids*, **159** (1993) 274.
13. Kobayashi, K., *Glass Technol.*, **29** (1988) 253.
14. Kobayashi, K., *Glass Technol.*, **30** (1989) 110.
15. Hannay, N. B. & Smyth, C. P., *J. Amer. Chem. Soc.*, **68** (1946) 171.
16. Shaw, C. M. & Shelby, J. E., *Phys. Chem. Glasses*, **34** (1993) 35.
17. Kobayashi, K., *Glass Technol.*, **34** (1993) 120.
18. Rulller, J. A. & Shelby, J. E., *Phys. Chem. Glasses*, **33** (1992) 177.
19. Naruse, A., *Garasukogaku*, Kyoritsu shuppan, Tokyo, 1959, p. 304 .

Journal of the European Ceramic Society 16 (1996) 915–917

S0955-2219(96)00006-4
0955-2219/96/$15.00 +.00

Exposure to Water Vapor of MOS Capacitors Passivated with PbO-based Glasses

Keiji Kobayashi

Toshiba ULSI Research Center, 1-Komukai Toshiba-cho Kawasaki, Japan

(Received 29 September 1995; revised version received 5 December 1995; accepted 12 December 1995)

Abstract

The capacitance and voltage (C–V) characteristics of metal, oxide, and silicon (MOS) capacitors passivated by PbO-based glasses with various water concentrations and with exposure to water vapor and to heating were investigated. As the OH^- absorption coefficients of the glass increased, adverse effects on the recovery of hysteresis loops of C–V curve shifts were observed. Water vapor had an adverse effect on the hysteresis loops and ΔV_G shifts of MOS capacitors, but they were somewhat improved, following heating at 400°C for 1 h.

1 Introduction

Borophosphosilicate glass films formed from inorganic gas sources have been widely used in high-density integrated circuits as dielectric insulators.[1–3] The advantageous properties of such films are conformal step coverage, effective protection against alkali ions, and fairly low reflow temperature. Highly doped borophosphosilicate glasses reflow at low temperatures to give step coverage of ultra-high-density integrated circuits, but they also suffer from a tendency to crystallize during the reflow process.[4] Such crystallization is a fatal drawback in the planarization of the ultra-high-density integrated circuits.[4] It has been found that zincborosilicate and leadborosilicate glasses have even lower flow temperatures than borophosphosilicate glasses, and they do not suffer from the problem of crystallite formation during the reflow process.[5,6] When leadborosilicate glasses contain small amounts of water and they are exposed to water vapor,[7,8] it is interesting to investigate the C–V characteristics of MOS devices passivated with them. Past studies have shown that the abnormal C–V curves of MOS capacitors are a result of highly polarizable ions and OH^- radical in the glass.[8,9]

In this paper, we discuss the improvement of C–V curves of MOS capacitors passivated with PbO-based glasses exposed to water vapor and investigate the potential for the application of these glasses to MOS devices.

2 Experimental

PbO-based glasses were prepared for use in the experiments. Batches comprising 1 kg of reagent-grade chemicals were melted at 1300°C for 5 h in an ultra-high-purity platinum crucible with an electric furnace in an oxidizing atmosphere. After homogeneous melting, the glass was poured onto a stainless steel plate and annealed. Infrared transmission spectra were measured using a Digi-Labo spectrophotometer with 10 × 20 × 1 mm plates.

Sputter targets were cut from these samples and ground to 75 mm in diameter and 10 mm thick. Glass films 0·5 μm thick were deposited on a SiO_2 layer (0·3 μm) on Si (100) wafers under 1 kW power and 4 Pa vacuum sputtering conditions using a Perkin-Elmer vacuum system. The glass thickness was measured by the use of a nanometrics SD9–2000T thickness meter using the Na–D line refractive index (N_D — 1·56). Aluminium electrodes were deposited on the glass films. C–V curves for these MOS capacitors were observed at 1 MHz at room temperature, as described previously.[10] The MOS capacitors were exposed to water vapor at 80°C for 1 h and heated at 400°C for 1 h in an oxidizing atmosphere.

3 Results and Discussion

The chemical compositions (mol%) of various glasses, their absorption coefficients, β_{OH}, and C–V curve shift, ΔV_G, are listed in Tables 1 and 2. Infrared absorption spectra for these glasses are

Table 1. Lists of glass compositions (mol%)

Glass No	*PbO (mol%)*	*PbF_2 (mol%)*	*B_2O_3 (mol%)*	*SiO_2 (mol%)*
1	37	5	15	43
2	42	0	15	43

Table 2. Lists of T_{OH}, R_{OH}, β_{OH} and ΔV_G: (1) glass no. (1); (2) glass no. (2); (3) glass no. (1) exposed to water vapor at 80°C for 1 h. (4) glass no. (2) exposed to water vapor at 80°C for 1 h; (5) glass no. (1) exposed to water vapor at 80°C for 1 h and heated at 400°C for 1 h; (6) glass no. (2) exposed to water vapor at 80°C for 1 h and heated at 400°C for 1 h

	T_{OH} (%)	R_{OH}	β_{OH} (cm^{-1})	ΔV_G (V)
1	62	0·23	0·03	1·0
2	56	0·28	0·06	1·5
3	38	0·43	0·23	2·5
4	32	0·49	0·38	3·0
5	59	0·26	0·05	1·2
6	50	0·33	0·10	1·6

given in Fig. 1. The absorption bands around 3500 cm^{-1} are due to fundamental vibrations arising from OH ions absorption.[11-13]

The relationship between transmittance, T_{OH}, and reflectivity, R_{OH}, can be represented as follows:[14]

$$T_{OH} \simeq (1 - R_{OH})^2 (1 + R_{OH}^2 + R_{OH}^4 + \cdots\cdots) \quad (1)$$

when R_{OH} is small,

$$T_{OH} \simeq (1 - R_{OH})^2 (1 + R_{OH}^2) \quad (2)$$

The absorption coefficient β_{OH}[15] resulting from the fundamental vibration due to OH at around 3500 cm^{-1} is calculated from eqn (3)

$$T_{OH} = [(1 - R_{OH})^2 e^{-\beta_{OH}t}]/[1 - R_{OH}^2 e^{-2\beta_{OH}t}] \quad (3)$$

where t is the glass thickness.

By substituting eqn (2), eqn (3) can be represented as follows:

$$R_{OH}^2(R_{OH}^2 + 1) e^{-2\beta_{OH}t} + e^{-\beta_{OH}t} - R_{OH}^2 = 1 \quad (4)$$

Values of OH absorption coefficients β_{OH} are computed from eqn (4). Values of T_{OH}, R_{OH}, and β_{OH} calculated from the infrared absorption spectra in Fig. 1 are also listed in Table 2. With regard to the C–V curve shifts in MOS capacitors, when OH absorption coefficients increased, ΔV_G shifts also increased. It has been observed by Li *et al.*[9] that water vapor exercises much adverse influence on the C–V characteristics of MOS capacitors. However, we are able to expect the recovery of hysteresis loops and the ΔV_G shift of C–V curves, following the heating of the MOS capacitors exposed to water vapor.

The C–V characteristics of MOS capacitors passivated with these glasses and the effects of water vapor and heating to MOS capacitors are shown in Fig. 2. The errors of R_{OH}, β_{OH} and ΔV_G values were within ±1% and the hysteresis curves for these MOS capacitors also showed good reproducible capability as required for the MOS device passivations.

In the molten glass, fluoride compound reacts with water in the batch, as represented in eqn (5) and, therefore, the fluoride compound is useful for the removal of OH^- ions in glasses.

$$ZnF_2 + H_2O \rightarrow ZnO + 2HF\uparrow \quad (5)$$

Thus, these peculiar C–V characteristics represent the recovery of C–V curve shifts and the hysteresis loops as the coefficients of OH absorption decrease. Water vapor showed an adverse effect on the C–V hysteresis curves, but the improvement of them was observed, following the heating.

With increasing β_{OH}, the C–V curves shift towards the right. The mean C–V curve shifts, ΔV_G, at the mid-point of forward and backward hysteresis curves are summarized in Table 2.

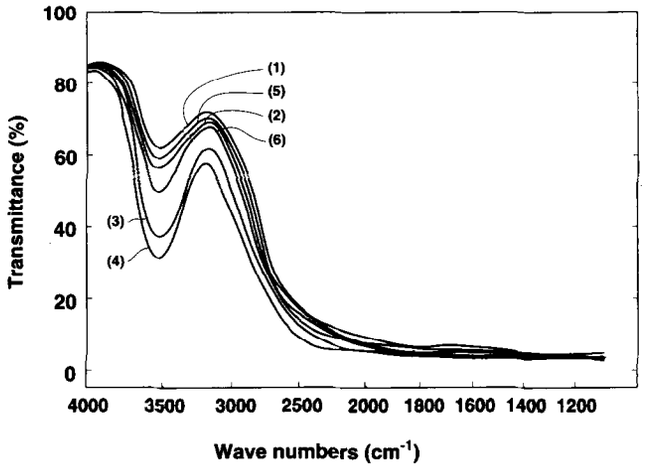

Fig. 1. Infrared absorption spectra for PbO-based glasses: (1) glass no. (1); (2) glass no. (2); (3) glass no. (1) exposed to water vapor at 80°C for 1 h; (4) glass no. (2) exposed to water vapor at 80°C for 1 h; (5) glass no. (1) exposed to water vapor at 80°C for 1 hour and heated at 400°C for 1 h; (6) glass no. (2) exposed to water vapor at 80°C for 1 h and heated at 400°CC for 1 h.

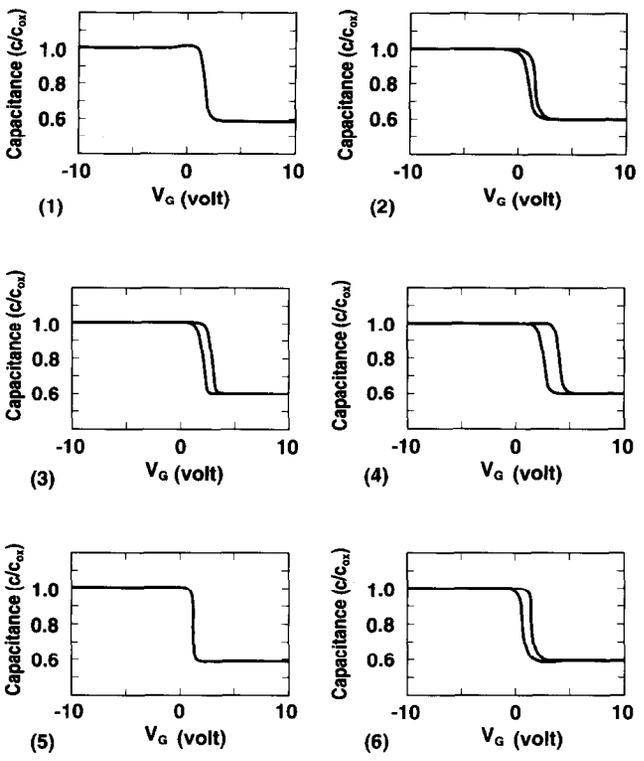

Fig. 2. C–V hysteresis curves of MOS capacitors passivated with PbO-based glasses: (1) passivated with glass no. (1); (2) passivated with glass no. (2); (3) passivated with glass no. (1) and exposed to water vapor at 80°C for 1 h; (4) passivated with glass no. (2) and exposed to water vapor at 80°C for 1 h; (5) passivated with glass no. (1), exposed to water vapor at 80°C for 1 h and heated at 400°C for 1 h; (6) passivated with glass no. (2), exposed to water vapor at 80°C for 1 h and heated at 400°C for 1 h.

These shifts in the C–V curves indicate that the total number of positive oxide charges increases. It is reasonable to expect that these positive charges are hydrogen-related vacancies.[9] The loss of hydrogeneous species is related to the disappearance of C–V hysteresis. A hydrogeneous complex is responsible for the carrier trapping mechanism.[9] These shifts are related to hydrogen-related vacancies in water containing glasses.[9]

4 Conclusion

The MOS capacitors passivated with PbO-based glasses containing low concentrations of water exhibited the best C–V characteristics. With increasing OH absorption coefficient, an adverse effect was seen on the recovery of hysteresis C–V curve shifts. Water vapor exercised much adverse influence on the C–V curves of MOS capacitors, but some improvement of the hysteresis loops and ΔV_G shifts was observed, following the heating of MOS capacitors. After the heating, the recovery of hysteresis and ΔV_G shifts for these MOS capacitors showed good reproducible capability as required for the MOS device passivations. The relationship between the recovery from peculiar hysteresis C–V curve shifts and OH absorption coefficient was briefly discussed.

References

1. Hurley, K. H., *Solid St. Technol.*, **30** (1987) 103.
2. Dickinson Jr., J. E. & DeJong, B. H. W. S., *J. Non-cryst. Solids*, **102** (1988) 196.
3. Raley N. F. & Losee, D. L., *J. Electrochem. Soc.*, **135** (1988) 2640.
4. Schnable, G. L., Fisher, A. W. & Shaw, J. M., *J. Electrochem. Soc.*, **135** (1990) 3973.
5. Kobayashi, K., *J. Non-cryst. Solids*, **88** (1986) 229.
6. Kobayashi, K., *J. Non-cryst. Solids*, **109** (1989) 277.
7. Kobayashi, K., *J. Electrochem. Soc.*, **131** (1984) 2190.
8. Rojas, S., Gomarasca, R., Zanotti, L., Borghesi, A., Sassela, A., Ottaviani, G., Moro, L. & Lazzeri, P., *J. Vac. Sci. Technol. B*, **10** (1992) 633.
9. Li, S. C., Murarka, S. P., Guo, X. S. & Lanford W. A., *J. Appl. Phys.*, **72** (1992) 2947.
10. Kobayashi, K., *J. Non-cryst. Solids*, **124** (1990) 229.
11. Shaw, C. M. & Shelby, J. E., *Phys. Chem. Glasses*, **34** (1993).
12. Kobayashi, K., *Glass Technol.*, **34** (1993) 120.
13. Ruller, J. A. & Shelby J. E., *Phys. Chem. Glasses*, **33** (1992) 177.
14. Naruse, A., *Garasukogaku*, Kyoritsu Shuppan, Tokyo, 1959, p. 304.
15. Zhenhua, L. & Frischat, G. H., *J. Non-cryst. Solids*, **163** (1993) 169.

Journal of the European Ceramic Society 16 (1996) 919–927

S0955-2219(96)00017-9
0955-2219/96/$15.00

RBAO Composites Containing TiN and TiN/TiC

Sven Scheppokat,[a] Nils Claussen[a] & Richard Hannink[b]

[a]Advanced Ceramics Group, Technische Universität Hamburg–Harburg, 21073 Hamburg, Germany
[b]CSIRO Division of Materials Science and Technology, Clayton, Victoria 3169, Australia

(Received 10 October 1995; revised version received 21 December 1995; accepted 3 January 1996)

Abstract

TiC and TiN were tested as candidate materials for particle reinforcement of reaction bonded aluminium oxide (RBAO). As part of the reaction bonding process Al-containing green bodies have to be heated in air in order to oxidize the Al; therefore the oxidation behaviour of any added particles is of critical importance. Previous studies have shown that neither TiC nor TiN is sufficiently oxidation-resistant to withstand the heating cycle necessary to completely oxidize the Al in the process. Therefore, two alternative approaches were investigated. First, TiC and TiN were retained in incompletely reacted RBAO, resulting in an Al_2O_3–TiC/TiN composite with alloy and possibly intermetallic phases. These metal phases were obtained from Al and Ti/Zr which formed when Al reduced TiO_2 and, to a lesser extent, ZrO_2. Second, the reaction of AlN and TiO_2 to form Al_2O_3 and TiN at temperatures above 1350°C was investigated. The resulting material contained Al_2O_3, ZrO_2, TiN and a nitrogen-containing aluminium titanate. © 1996 Elsevier Science Limited.

TiC und TiN wurden als Kandidatmaterialien zur Partikelverstärkung von reaktionsgebundenem Aluminiumoxid (RBAO) untersucht. Da die Al-haltigen Grünkörper als Teil des Prozesses an Luft einer Wärmebehandlung unterzogen werden, ist die Oxidationsbeständigkeit der zugesetzten Partikel von großer Bedeutung. Voruntersuchungen haben gezeigt, daß weder TiC noch TiN ausreichend oxidationsbeständig sind, um den zur Al-Oxidation erforderlichen Heizzyklus zu überstehen. Aus diesem Grunde wurden zwei alternative Verfahren untersucht. Im ersten Verfahren wurden TiC und TiN in unvollständig reagiertem RBAO erhalten. Dies resultierte in einem Al_2O_3–TiC/TiN Verbundmaterial mit Legierungen und möglicherweise intermetallischen Phasen. Diese Phasen enthielten Al und Ti/Zr; die letzteren entstanden bei der Reduktion von TiO_2 und, in geringerem Grad, ZrO_2, durch Al. Im zweiten Verfahren wurde die Reaktion von AlN und TiO_2 zu Al_2O_3 und TiN bei Temperaturen oberhalb 1350°C untersucht. Das dabei entstandene Material enthielt Al_2O_3, ZrO_2, TiN, sowie ein stickstoffhaltiges Aluminiumtitanat.

1 Introduction

The toughening of ceramic materials by incorporating submicrometre-sized particles is of considerable interest because of the dramatic improvements in the mechanical properties of ceramics by adding as little as 5 vol% nanometre-sized particles.[1] For Al_2O_3/SiC, Niihara[1] reported room-temperature increases in toughness from 3·5 to 4·8 MPa $m^{1/2}$. Other workers have found less dramatic, but still significant, improvements of mechanical properties such as bending strength and wear resistance.[2] TiC and TiN offer additional interesting properties because of their hardness and elastic modulus. The low electrical resistivity of TiC and TiN can also make composites containing these materials suitable for electrical discharge machining. Alumina/TiC composites show improved wear resistance and find application for cutting tools, while alumina/TiN composites are promising materials for cutting tools and bearings.

The reaction bonding of aluminium oxide (RBAO) was developed recently at TUHH as a method of fabricating high-strength, fine-grained, low-shrinkage alumina, mullite, or composites of these materials.[3,4] In this process, Al/Al_2O_3 mixtures are attrition-milled in non-aqueous milling media to avoid hydrolysis of the Al. The green bodies are heat-treated in air to oxidize the metal phase to nanometre-sized oxide particles which sinter and bond the original alumina particles. The oxidation of Al is accompanied by a 28% volume increase which partially compensates for the sintering shrinkage. In most cases, ZrO_2 is introduced by the wear of TZP milling balls and helps to control grain growth and improve the mechanical properties. The resulting materials have a fine grain size of approximately 1 μm. The necessity of firing RBAO green bodies in air in order to oxidize the Al makes the oxidation behaviour of any added non-oxide particles a crucial factor. TiN is reported to show

superior oxidation resistance to TiC.[5,6] However, TiN powder has been reported to be completely oxidized at a temperature of 700°C after heating in air at a rate of 5°C min^{-1}.[7] At this temperature, the oxidation of Al in the reaction bonding process is not completed.[3,8] Although the temperature at which complete Al oxidation is achieved will vary with parameters such as milling intensity, compaction pressure and powder composition, a value below 800°C has never been reported. Only in the presence of ZrO_2 does oxidation of Al occur at somewhat lower temperatures than in ZrO_2-free samples.[8]

The purpose of this work was to explore two alternative methods of fabricating TiN and TiN/TiC-containing RBAO composites. In the first method, the fact that Al is capable of reducing the oxides of various other metals was used to fabricate metal/ceramic composites by firing partly reacted RBAO bodies containing Al and metal oxides, such as TiO_2 or ZrO_2, in an inert atmosphere. In our case, Al was reacted with TiO_2, and, to a lesser extent, ZrO_2, to form different intermetallic Al/Ti/(Zr) phases. By firing partly reacted RBAO bodies in an inert atmosphere, it was also possible to retain non-oxide particles in the composite which would otherwise not survive the complete oxidation step.

In the second method, a reaction sintering process was investigated as an alternative approach to achieve TiN-containing RBAO. In this method, instead of directly adding TiN to the precursor powder, TiN was obtained by an exchange reaction during the heating process: AlN and TiO_2 were reacted to form TiN and Al_2O_3 at temperatures above 1350°C.[9,10] The oxidation resistance of AlN up to a temperature of 800°C[11] makes this an interesting route for the reaction bonding process.

2 Experimental

The starting materials and the compositions of the precursor powders used in this work are listed in Table 1. The powder batches were attrition-milled for 6 h at 680 rev min^{-1} in an alumina vessel using 3 mm TZP balls and ethanol as milling medium. A small volume of air was passed into the vessel during milling to ensure complete passivation of the Al phase and allow safe handling of the milled powders. The powders were dried for 2 days in a porcelain bowl at room temperature in a fume-hood and sieved through a 125 μm sieve. Bars were uniaxially pressed at 50 MPa, followed by isopressing at 300 or 200 MPa, with the exception of K5AlN/TiN samples, which were only uniaxially pressed. Phase analysis was carried out using a Siemens X-ray diffractometer and Cu K_α radiation. Differential thermogravimetric analyses and thermogravimetric analyses (DTA/TG) were carried out in air up to 1000°C at a heating rate of 1°C min^{-1}.

The K5TiC samples were heated in air to 480°C; at this temperature the TiC was completely oxidized as indicated by previous DTA/TG data while most of the Al remained unoxidized, followed by sintering in argon at 1600°C for 2 h; this treatment was designated cycle A. The sample of the same batch for scanning electron microscopy (SEM) was sintered at 1550°C for 90 min. In order to fabricate TiN-containing composites, the K5TiNl and K5TiN2 samples were heated in air to 520°C; at 520°C approximately half the original TiN was oxidized according to DTA/TG, followed by sintering in argon at 1600°C for 2 h; this treatment was designated cycle B. To fabricate a TiC-containing composite, the IMC3 samples contained TiO_2 in the precursor powder as an oxygen donor for Al. The presence of TiO_2 eliminated the need for an oxidation step in air and allowed the TiC, pre-added to the composition, to remain unoxidized. These samples were sintered in argon at 1550°C without a prior oxidation step and were designated treatment cycle C. The amount of TiO_2 in the IMG3 composition was calculated to be completely reduced by Al, thus avoiding the formation of aluminium titanate from the remaining TiO_2. The heating/cooling rates for the IMC3 series were 1°C min^{-1} to 1000°C, then 3°C min^{-1} to 1550°C and 10°C min^{-1} to room

Table 1. Powder compositions used in preparation of the samples

Material characteristics, type and source	*Compositions (vol%) and designations*				
	K5TiC	*K5TiN1*	*K5TiN2*	*IMC3*	*K5AlN/TiN*
Al, <50 μm	45	45	45	48	45
Al_2O_3, 0·4 μm, Al6, Alcoa	40	40	40	19	25
ZrO_2, 0·57 μm, HSY 3·0, Daiichi Kigenso	5	5	5	5	5
TiC, 1–1·5 μm, H.C. Starck	10	0	0	7·5	0
TiN no. 1, 2 μm, New Japan Metal Corporation	0	10	0	0	0
TiN no. 2, 45 $m^2 g^{-1}$, Tioxide	0	0	10	0	10
AlN, grain size unknown	0	0	0	0	15
TiO_2, 1 μm, rutile, Aldrich	0	0	0	20·5	0

temperature. The K5AlN/TiN samples were heated in air to 720°C, then sintered in Ar at 1550°C for 1·5 h, designated treatment cycle D.

Powder X-ray diffraction (XRD) was used to monitor the phase content after the various heating cycle procedures.

Bars for mechanical property testing were diamond machined for 3 × 3 mm cross-section. The tension side was polished to a 1 μm finish. Flexural strength was measured in four-point bending using an outer span of 20 mm and an inner span of 7 mm with a crosshead speed of 0.2 mm min^{-1}. Fracture toughness was calculated using the Vickers indentation crack method with loads of 100 N.

3 Results and Discussion

3.1 Oxidation of TiN and TiC particles during RBAO process

DTA/TG data of the K5TiC and K5TiN samples showed no further weight gain after 800°C (see Figs 1 and 2). The DTA/TG data at 800°C correlate well with reported data measured at 820°C on ZrO_2-containing RBAO.[3]

In order to investigate the oxidation behaviour of the TiC and TiN phases, DTA/TG was performed on pure TiC and TiN powders. The DTA data of TiC exhibited a single maximum of the reaction rate at 400°C (see Fig. 3). The TG recorded no further weight gain after 480°C. The DTA data of the TiN powder had two maxima in the reaction rate, one at 470°C and a second more pronounced one at 590°C, with no further weight gain after 680°C (Fig. 4).

The results of the DTA/TG measurements indicate that the oxidation of TiC and TiN is completed by 480°C and 680°C, respectively. These values are considerably lower than the 800°C found necessary to completely oxidize the Al in the reaction bonding process. The oxidation behaviour of TiN in a fabricated composite was also monitored by XRD. After heating a K5TiN2 sample in air to 550°C, TiN could no longer be detected; the material now exhibited strong rutile peaks instead (see Fig. 5) in addition to Al_2O_3 and tetragonal ZrO_2 phases.

As TiN could be clearly identified in the precursor composite batch powder, this result indicates that a substantial fraction of the initial TiN was already oxidized to TiO_2 at 500°C. Aluminium was still detectable in the 550°C-sample, although the intensity of the peaks had diminished considerably. After heating in air to 820°C, the intensity of the rutile peaks had increased further and no remaining Al could be detected. The K5TiC sample showed the same phase composition after heating to 820°C. These results indicate that neither TiC nor TiN is

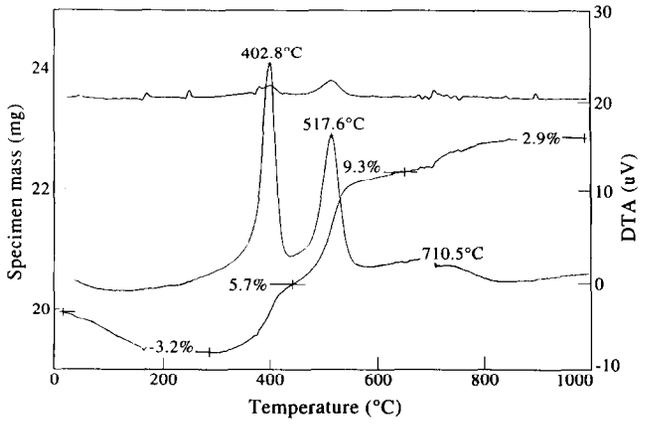

Fig. 1. DTA/TG of K5TiC.

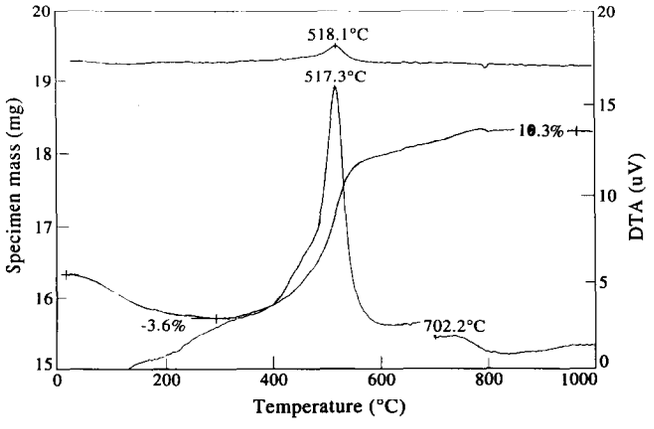

Fig. 2. DTA/TG of K5TiN.

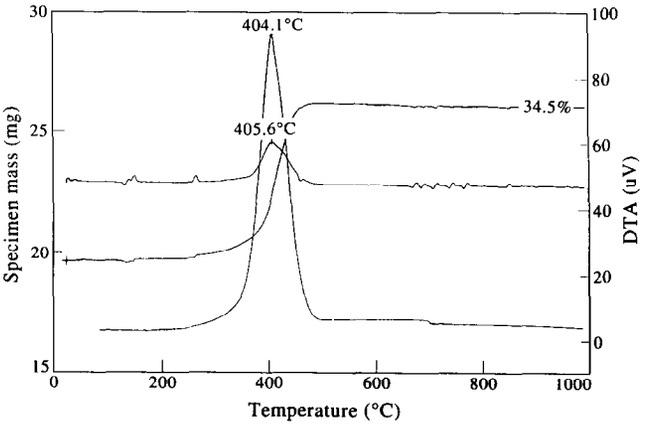

Fig. 3. DTA/TG of TiC.

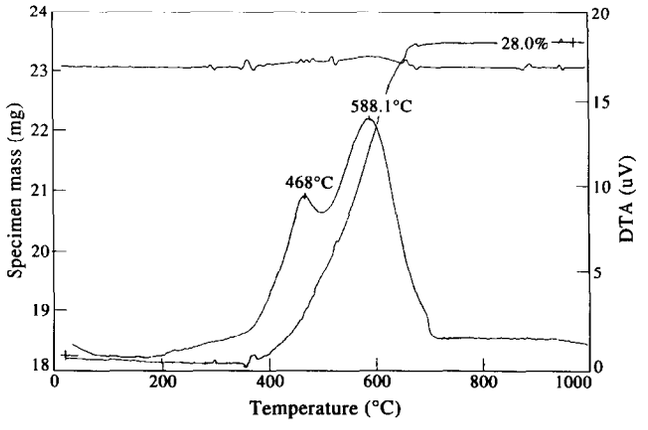

Fig. 4. DTA/TG of TiN.

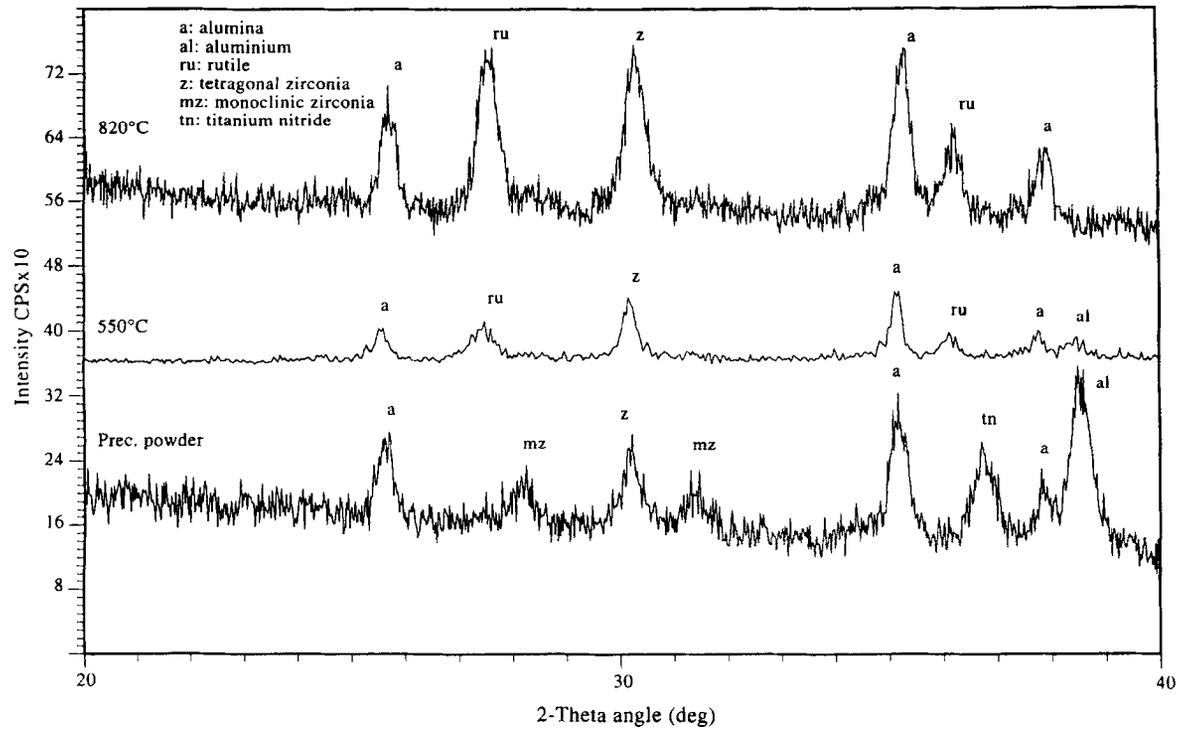

Fig. 5. XRD of K5TiN2 after heating to different temperatures.

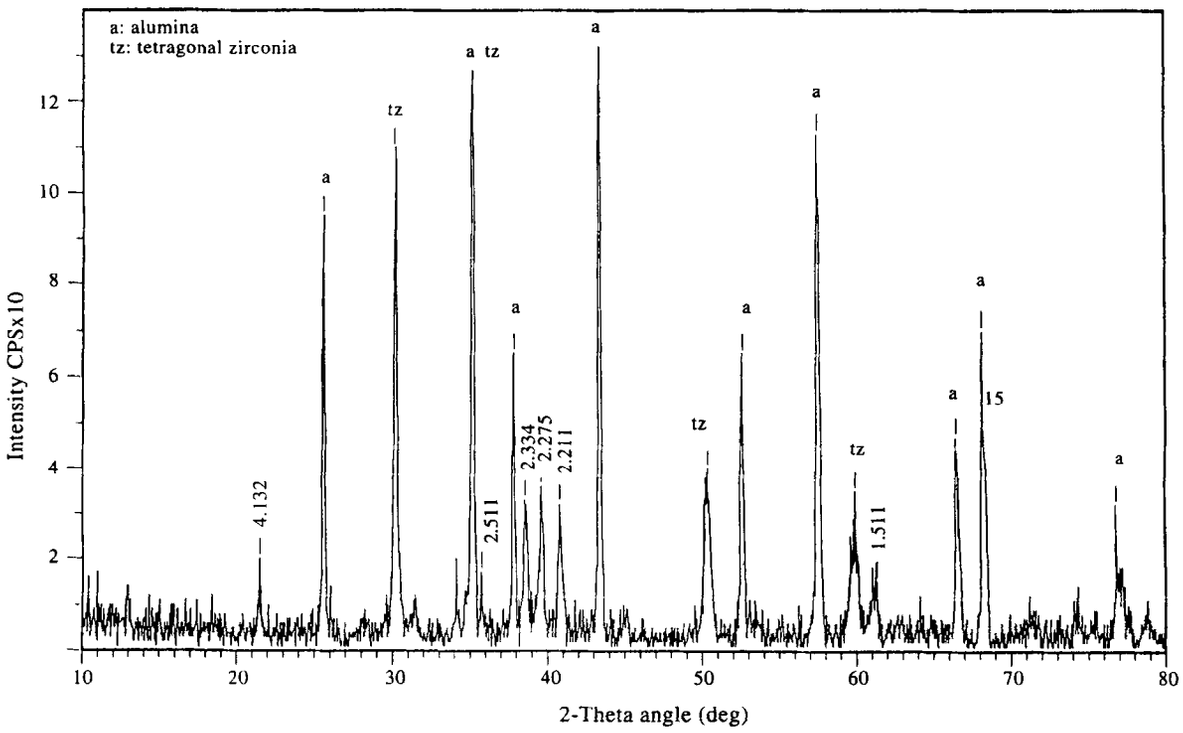

Fig. 6. XRD of K5TiC heated in air to 480°C, then sintered in argon at 1600°C for 2 h.

sufficiently oxidation-resistant to survive the air heating cycle which is necessary to completely oxidize the Al in the reaction bonding process.

3.2 RBAO composite containing intermetallic phases from incomplete precursor reactions

To investigate the consolidation properties of incompletely reacted Ti-containing RBAO, the firing of samples with incompletely oxidized Al was continued in argon, to 1650°C. XRD of a cross-section of a K5TiC sample sintered according to cycle A revealed that, in addition to Al_2O_3 and ZrO_2, several peaks could not be matched to any phase in the JCPDS file (Fig. 6). No peaks of TiO_2, TiC or aluminum titanate were identified in the spectrum. The absence of TiO_2 is reinforced by the fact that the ZrO_2 peaks are not shifted towards higher 2θ values as is commonly observed when ZrO_2 takes

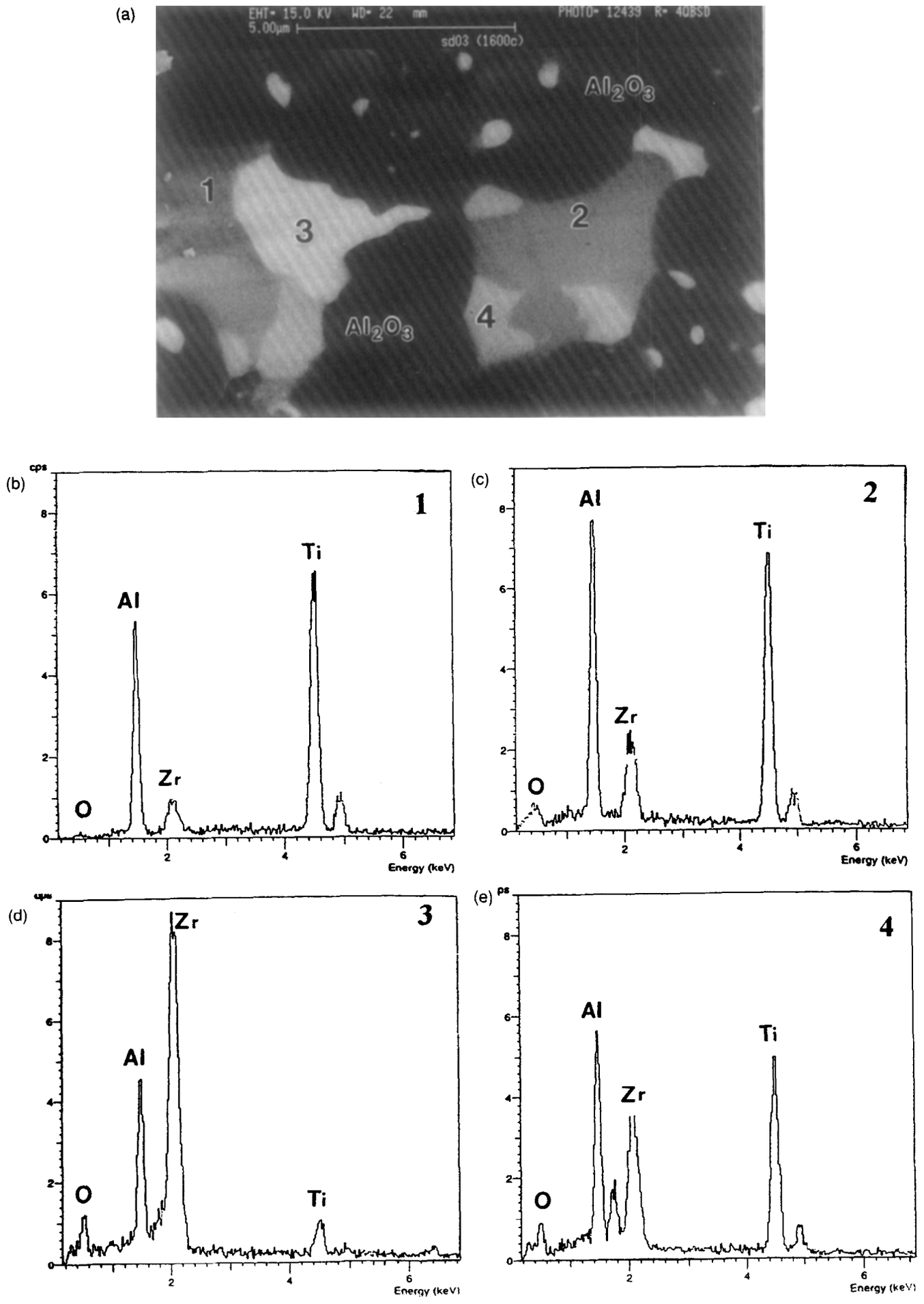

Fig. 7. SEM/EDX of K5TiC heated in air to 480°C, then sintered in argon at 1600°C for 2 h.

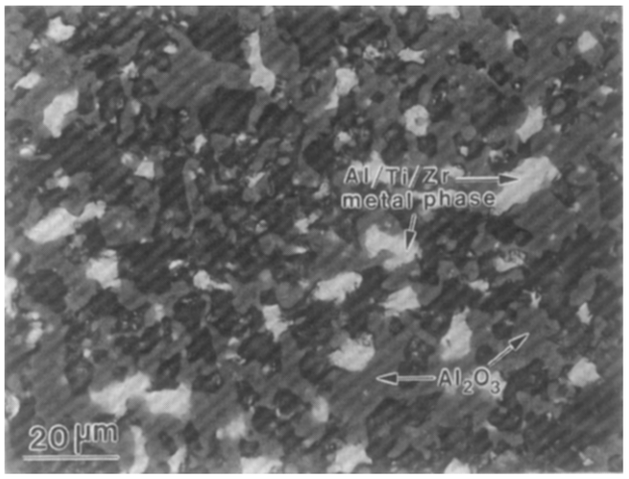

Fig. 8. Optical micrograph of K5TiC heated in air to 480°C, then sintered in argon at 1600°C for 2 h.

up TiO_2 in solid solution,[12] and may also indicate that no TiO_2 was present at high temperatures.

An SEM backscattered electron image and EDX analyses of the material are shown in Figs 7(a)–(e). The EDX analyses, in Figs 7(b)–(e), confirm the presence of different Al/Ti alloy phases. Figure 7(b) shows an Al/Ti phase with small amounts of Zr; estimations of the peak heights indicate that this phase contains Al and Ti approximately in a 1:1 ratio indicating that it may be at the intermetallic composition. A second intermetallic phase which also contains Al and Ti in a 1:1 ratio, but has a higher Zr content is shown in Fig. 7(c). It is possible that there is a third intermetallic phase, Fig. 7(e), but the relatively high oxygen peak measured here makes it possible that this phase is actually zirconia; the presence of Al and Ti peaks in the EDX spectrum could be ascribed to electron-beam spread.

The presence of ternary intermetallic phases explains why no matches for the XRD peaks were found in the JCPDS file, where only binary metallic phases of Al, Ti and Zr are listed. An optical micrograph of the same material sintered according to cycle A is shown in Fig. 8. Sample K5TiC had a bending strength of 240 MPa of a density of 80%.

3.3 RBAO composite containing TiN and TiC from incompletely reacted precursors

K5TiN1 and K5TiN2 samples sintered according to cycle B were 95% dense. XRD of cross-sections indicated the presence of TiN in the sintered material. In the case of K5TiN1, XRD revealed no phases other than alumina, zirconia and TiN (see Fig. 9). In the case of K5TiN1, XRD indicated alumina, zirconia and TiN (see Fig. 9). In the case of K5Tinl, XRD indicated alumia, zirconia, TiN and further peaks that could not be identified. Both materials show micrometre-sized TiN particles in polished optical microscope sections (see Figs 10(a) and (b)). The K5TiN1 sample had a bend strength of 350 MPa, a toughness of 2.4 MPa $m^{1/2}$ and a hardness of 20.4 GPa. The K5TiN2 sample had a bending strength of 280 MPa, a toughness of 2.4 MPa $m^{1/2}$ and a hardness of 14·6 GPa. The hardness of K5TiN1 is higher than that of TiN-free RBAO (20 vol% ZrO_2), which is 17·8 GPa, albeit this hardness difference might be attributed to the higher ZrO_2 content: 5 vol% vs. 20 vol% for the RBAO materials.

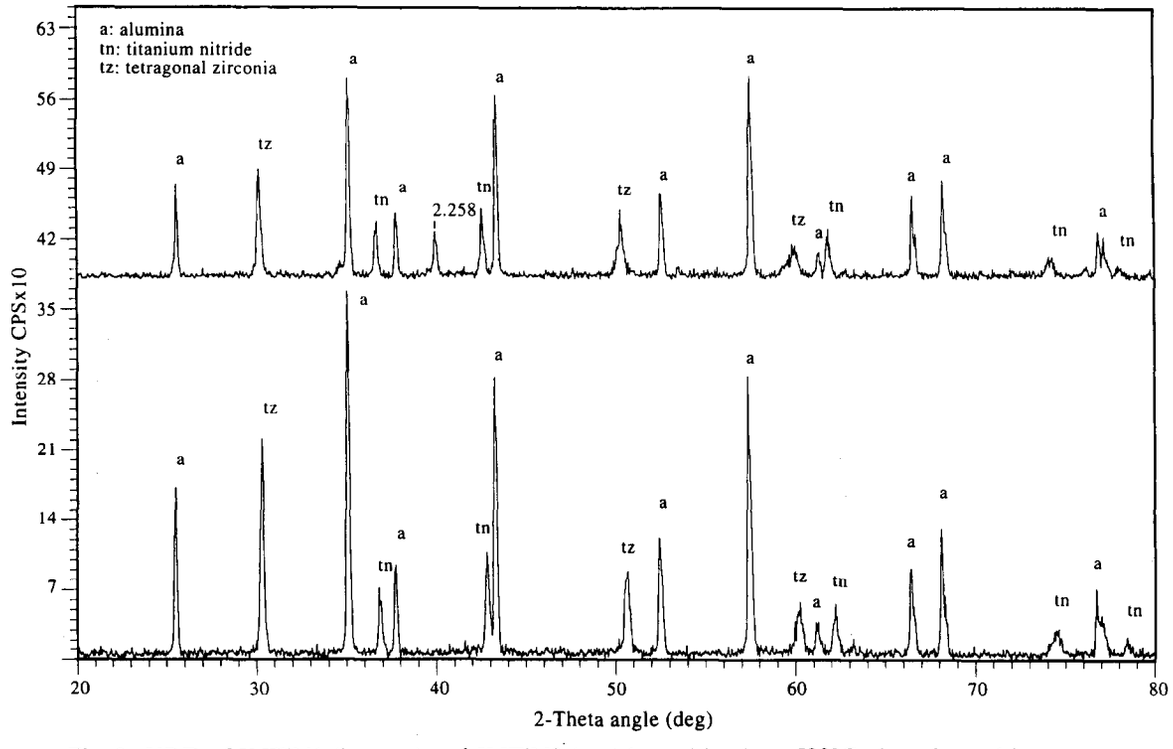

Fig. 9. XRD of K5TiN1 (bottom) and K5TiN2 (top) heated in air to 520°C, then sintered in argon.

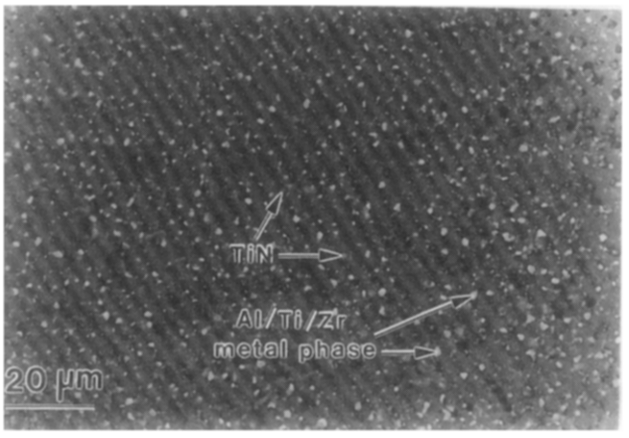

(a)

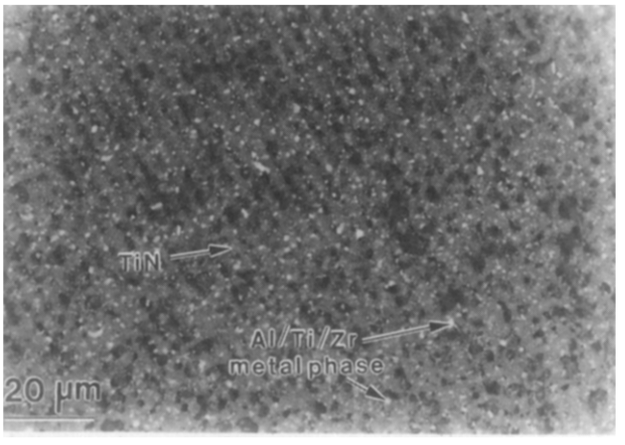

(b)

Fig. 10. Optical micrographs of (a) K5TiN1 and (b) K5TiN2; both samples were sintered in air to 520°C, then sintered in argon at 1600°C for 2 h. Dark matrix material is alumina.

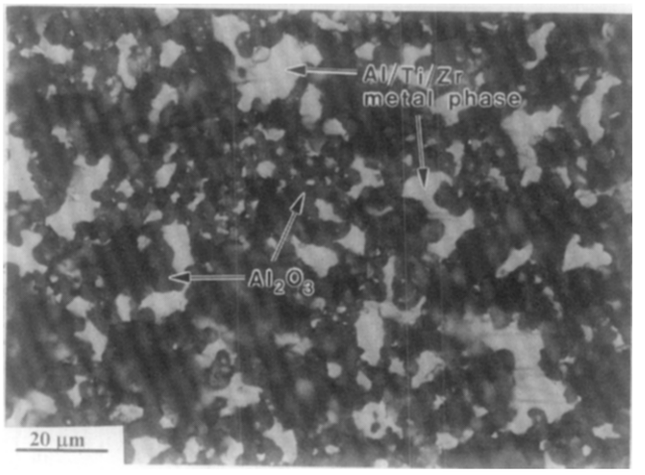

Fig. 12. Optical micrograph of IMC3.

IMC3 samples were 80% dense after sintering and had a bending strength of 170 MPa. The XRD plot of this material is shown in Fig. 11, and the TiC phase can be clearly identified. An optical micrograph of this material is shown in Fig. 12. The metallic phases appear as clusters up to 20 μm in size. The actual grain size could be smaller than the cluster size as the actual grain boundaries were not observed.

3.4 TiN-containing RBAO via reaction of AlN and TiO_2

XRD of a K5AlN/TiN sample indicated no AlN remaining after heating 820°C. The maximum oxidation temperature was reduced to 720°C. XRD of the sample after heating in air to 720°C showed strong rutile peaks, but no remaining TiN, Al or AlN

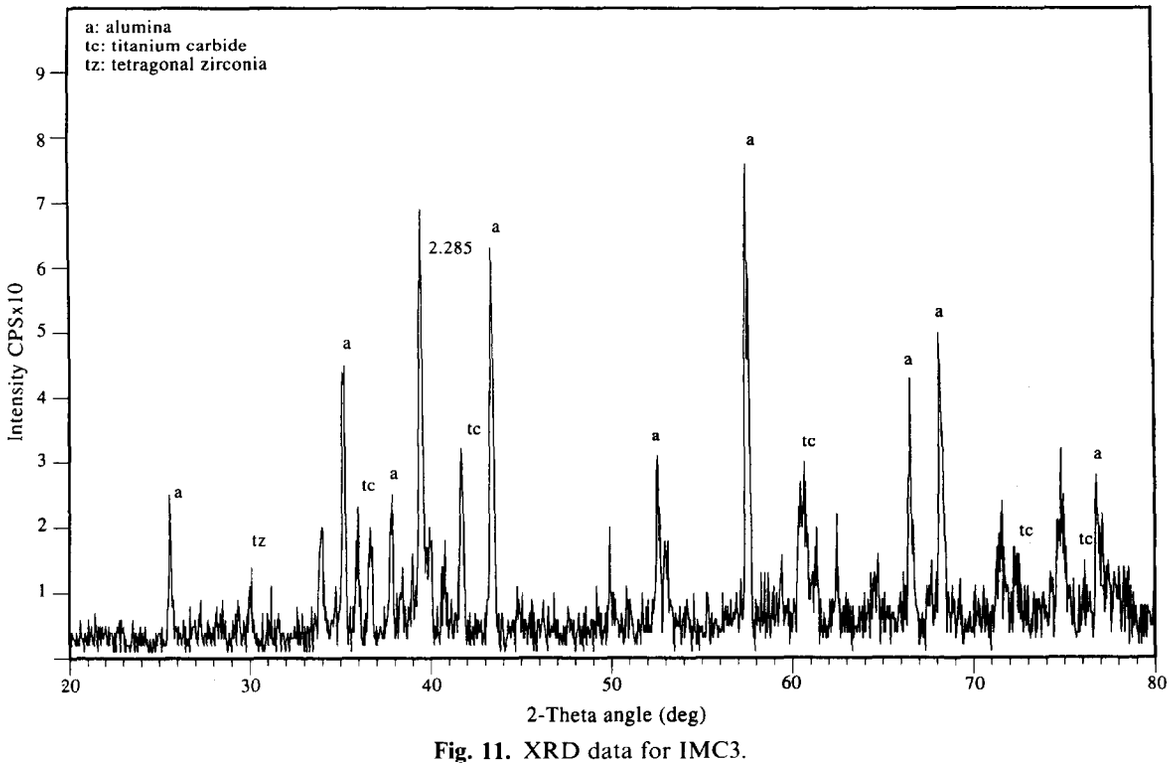

Fig. 11. XRD data for IMC3.

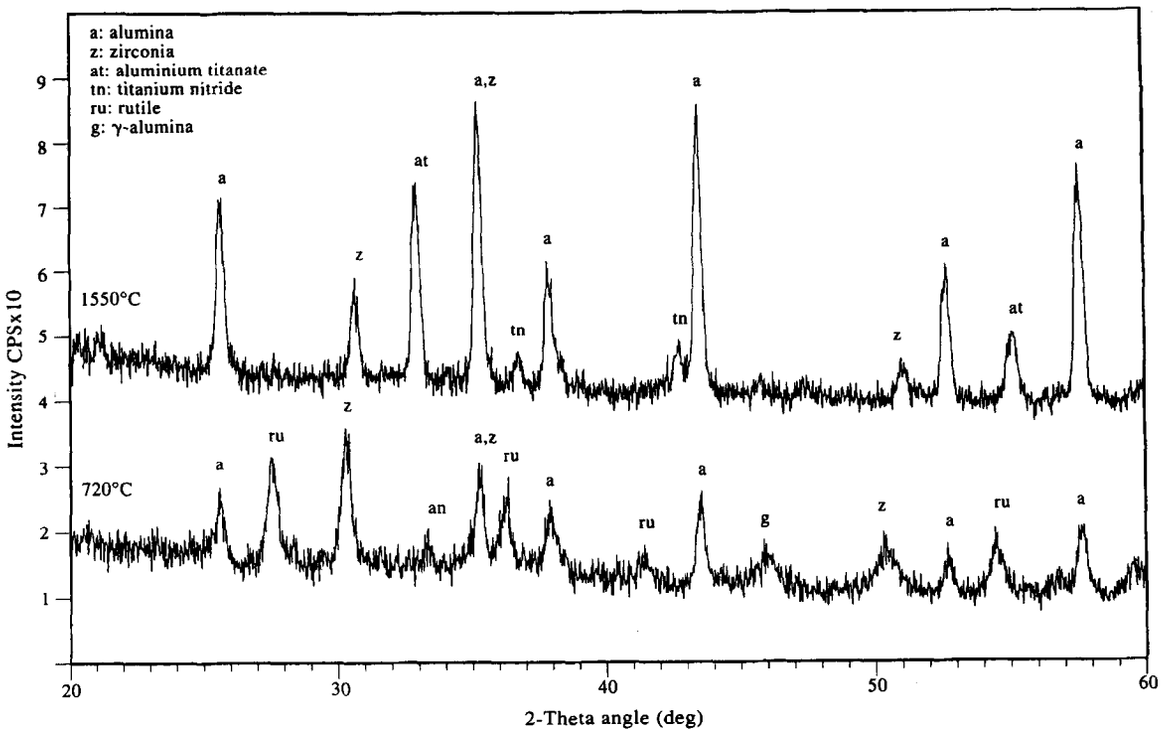

Fig. 13. XRD of K5AlN/TiN after heating in air to 720°C and sintering in argon at 1550°C.

could still be detected. After sintering at 1550°C in argon, XRD revealed alumina, zirconia, a nitrogen-containing aluminium–titanium oxide of pseudo-brookite structure[13] (JCPDS No. 42-1279) and TiN (Fig. 13). The material was black overall but showed gold-coloured TiN grains on polished sections in the optical microscope (Fig. 14). Even though these samples were only uniaxially pressed as no isopress was available at the time that the samples were made, they still achieved a 96% fired density, a flexural strength of 280 MPa and a toughness of 3·3 MPa $m^{1/2}$. The average grain size was approximately 2 μm. Transmission electron microscopy (TEM) examination also indicated that no remaining Al was present in the sample that had only been oxidized up to 720°C and that TiN particles were approximately 1 μm in size (see Fig. 15). EDX analysis in the TEM and SEM showed that, in these samples, zirconia generally contained Ti. The alumina phase of K5AlN/TiN examined by EDX in the TEM appears to be Ti-free, but it must be remembered that the solid solubility limit of 0·27 wt%[14] would be below the limit of EDX detectability. The fact that EDX analysis of the alumina phase in the SEM usually shows some Ti can be attributed to electron-beam spread.

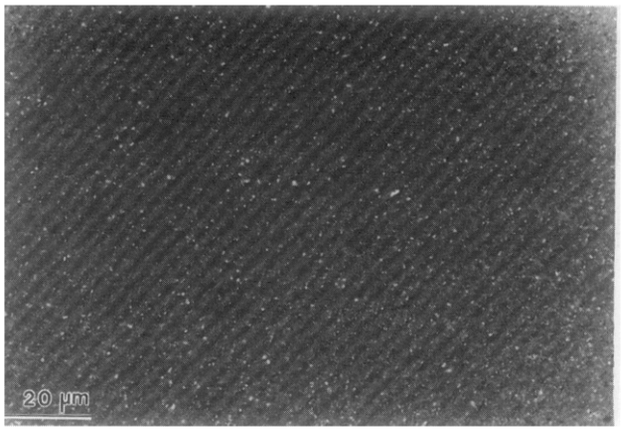

Fig. 14. Optical micrograph of K5AlN/TiN.

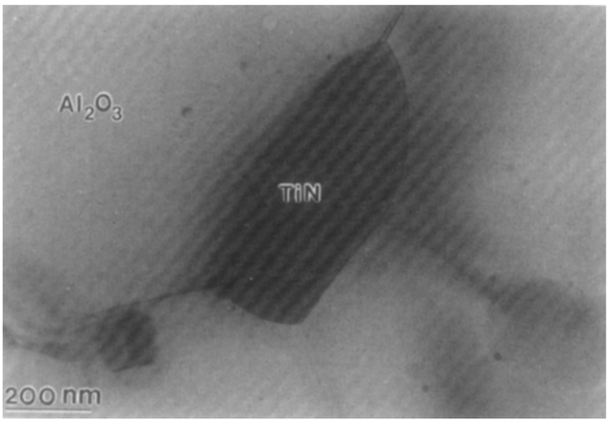

Fig. 15. TEM micrograph of a TiN particle in K5AlN/TiN.

The presence of pseudobrookite (PB) could indicate that the reaction of AlN and TiO_2 to form Al_2O_3 and TiN had not gone to completion, as PB has been previously reported as an intermediate step in the reaction.[10] Another possibility for the presence of PB was that, although in the initial precursor powder the molar ratio of TiN to AlN was 1·5:2 (a ratio that has been reported to result in a low PB content[9]), the TiN:AlN ratio was changed because part of the AlN oxidized during

heating in air. When the molar ratio was changed to result in a more TiO_2-rich composition as previously observed, the amount of PB also increased.[9]

In order to fabricate TiN-containing RBAO via the reaction described here, the originally added TiN was permitted to completely oxidize to TiO_2. As TiO_2 later reacts to form TiN again, it should be possible to add TiO_2 to the green compact in the first place. However, the reaction TiO_2 to TiN is accompanied by 39% volume shrinkage. Therefore, the initial addition of TiN has the advantage of compensating for this shrinkage by introducing an equal volume increase from the oxidation of TiN to TiO_2 first.

4 Summary and Conclusions

The present work has shown that TiC and TiN are not sufficiently oxidation-resistant to survive the heating cycle that is generally used to achieve complete oxidation of Al in the RBAO process. However, if the oxidation step is arrested before completion and the samples are subsequently sintered in an inert atmosphere, TiN- and TiC-containing ceramic/metal composites can be readily obtained. The metallic phase in these composites consists of various Al/Ti/Zr alloy phases, possibly intermetallic, that are formed when the remaining unoxidized Al reduces TiO_2 and ZrO_2.

A ceramic/metal/TiN-containing composite was obtained which achieved a hardness of 20·4 GPa and a flexural strength of 350 MPa. (Table 2 lists the physical properties of samples prepared in this study.) This strength is lower than that of conventional RBAO, where strengths of more than 600 MPa are commonly achieved. Through careful process control it should be possible to obtain a variety of cermet/TiN compositions by starting from one precursor powder composition and adjusting the temperature at which the reaction sintering atmosphere is changed from air to inert gas. Such control would change the ratio of the Al to TiO_2 phases in the pre-sintered sample and lead to different volume contents and compositions of alloy/intermetallic phases in the consolidated materials.

A method for fabricating TiN-containing RBAO has been proposed. While retention of TiN through addition to the precursor powder was not successful due to TiN completely oxidizing before Al oxidation was completed, the reaction of AlN and TiO_2 to form Al_2O_3 and TiN at temperatures >1350°C could be successfully employed for the RBAO process used here because AlN is more oxidation-resistant than TiN. The grain size of the TiN phase obtained was approximately 1 μm; however smaller grain sizes should be possible by adjusting processing parameters.

Table 2. Physical properties of the RBAO–TiN and TiN/TiC-containing composites

Sample	*Fired density (%)*	*Hardness (GPa)*	*Bend strength (MPa)*	K_{IC} *(MPa m$^{1/2}$)*
K5TiN1	95	20	350	2·4
K5TIN2	95	14·6	280	2·4
IMC3	80		170	
K5AlN/Tin	96		280	3·3

Acknowledgements

Special thanks are due to Dr S. Lathabai for valuable discussions and help with numerous practical aspects, without which much of this work would not have been possible. Thanks are also due to Dr D. Hay for help with the XRD, and to Mr P. Curtis for accumulating the DTA/TG data. The authors wish to thank Deutsche Forschungsgemeinschaft (DFG) for their support under contract number Cl 52/23-1.

References

1. Niihara, K., New design concept of structural ceramics. *J. Ceram. Soc. Jpn, Int. Edn*, **99**(10) (1991) 945–52.
2. Walker, C. N., Borsa, C. E., Todd, R. I., Davidge, R. W. & Brook, R. J., Fabrication, characterisation and properties of alumina matrix nanocomposites. In *Novel Synthesis and Processing Ceramics, Br. Ceram. Proc. 53*, ed. F. R. Sale. The Institute of Materials, London, 1994.
3. Wu, S., Holz, D. & Claussen, N., Mechanisms and kinetics of reaction-bonded aluminum oxide ceramics. *J. Am. Ceram. Soc.*, **76**(4) (1993) 970–80.
4. Holz, D., Wu, S., Scheppokat, S. & Claussen, N., Effect of processing parameters on phase and microstructure evolution in RBAO Ceramics. *J. Am. Ceram. Soc.*, **77**(10) (1994) 2509–17.
5. Kochergina, A. A. & Fedoseev, D. V., Oxidation of untradispersed powders of titanium carbide and titanium nitride. *Inorg. Mater.*, **26**(3) (1990) 549–50. Translated from *Izvestiya Akademii Nauk SSSR, Neorganicheskie Materialy*, **26**(3) (1990) 648–9.
6. McKee, D. W., The oxidation of dispersed refractory metal compounds and their behaviour as carbon oxidation catalysts. *Carbon*, **24**(3) (1986) 331–6.
7. Bellosi, A., Tampieri A. & Liu Y.-Z., Oxidation behaviour of electroconductive Si_3N_4–TiN composites. *Mater. Sci. Eng.*, **A127** (1990) 115–22.
8. Holz, D., Processing and characterisation of reaction-bonded Al_2O_3–ZrO_2 ceramics. PhD Thesis, TUHH, Hamburg, 1994, (in German).
9. Mukerji, J. & Biswas, S. K., Synthesis, properties and oxidation of alumina–titanium nitride composites, *J. Am. Ceram. Soc.*, **73**(1) (1990) 142–5.
10. Mocellin, A. & Bayer, G., Chemical and microstructural investigation of high-temperature interactions between AlN and TiO_2. *J. Mater. Sci.*, **20** (1985) 3697–704.
11. Bellosi, A., Landi, E. & Tampieri, A., Oxidation behaviour of aluminium nitride. *J. Mater. Res.*, **8**(3) (1993) 565–72.
12. Bannister, M. J. & Barnes, J. M., The solubility of TiO_2 in ZrO_2. In *Proc. of the Twelfth Australian Ceramics Conference*, 1986, pp. 241–5. The Australian Ceramic Soc.
13. Perera, D. S. & Bowden, M. E., Nitrogen-containing aluminium titanate. *J. Mater. Sci.*, **26**(6) (1991) 1585–7.
14. Hwang, C.-S., Nakagawa, Z. & Hamano, K., Microstructure and mechanical strength of TiO_2-doped Al_2O_3-ceramics fired in vacuum atmosphere. *J. Ceram Soc. Jpn., Int. Edn*, **101**(5) (1993) 1025–30.

Journal of the European Ceramic Society **16** (1996) 929–935

S0955-2219(96)00019-2
0955-2219/96/$15.00

The Use of Lithium as a Dopant in the Directed Melt Oxidation of Aluminium

X. Gu & R. J. Hand*

Department of Engineering Materials, University of Sheffield, Sir Robert Hadfield Building, Mappin Street, Sheffield S1 3DJ, UK

(Received 12 October 1995; revised version received 21 December 1995; accepted 3 January 1996)

Abstract

A Li source has been used to initiate directed melt oxidation of Al; the Li source used was Li_2CO_3. Growth both into free space, in which case Li_2CO_3 powder was placed on the metal surface, and into preform bodies comprising pure particulate α-Al_2O_3 mixed with a doping amount of Li_2CO_3, has been examined. In both cases it is shown that Li may initiate the directed oxidation reactions in the absence of any other dopants and that Li is therefore an effective dopant for the production of Al_2O_3/Al by the directed melt oxidation process. The products were characterized using scanning electron microscopy, transmission electron microscopy and X-ray diffraction. A cyclic reaction sequence for Al_2O_3/Al composite growth in the Li-doped system is postulated. This process is initiated by the formation of $LiAl_5O_8$ which aids the breakdown of the stable oxide film that would normally form on aluminium in a similar fashion to magnesium aluminium spinel in the Mg-doped system. The process involves motion of Li from within the growth to the reaction front; this can occur because of the high vapour pressure of Li at the reaction temperature. The effects of the preform body on these cyclic reactions are also considered.

Introduction

The directed melt oxidation process involves the directed growth of a composite product from a bulk molten metal via oxidation of the melt by a vapour-phase oxidant (e.g air).[1] This composite comprises an interconnected ceramic reaction product and, usually, several per cent of residual metal. The product may be shaped by growing the product either into a defined empty space or into a shaped region containing a preform comprising a loosely packed filler, ceramic fibres or whiskers. In this paper we distinguish the two cases by referring to bodies produced by growth into free space as 'unreinforced bodies' and to ones produced by growth into a preform body as 'reinforced bodies'.

The growth of products by directed melt oxidation depends crucially on the presence of dopants, which initiate and maintain the process. These dopants may be introduced by alloying with the pure parent metal or externally in the form of elemental or oxide powders.

Much of the published literature on this process has used alloys to introduce the doping elements. For example, growth of Al_2O_3/Al composites from Al alloys containing Mg either alone or in conjunction with Si has been studied by several authors.[1–3] More recently, the use of external doping with Mg or MgO powders has received some attention.[4,5]

It has been shown that Mg, either in elemental form or as part of a compound, can initiate directed melt oxidation reactions in the Al_2O_3/Al system. For example, Xiao and Derby[4] have shown that MgO may be used as an external dopant to initiate growth with pure Al, and that oxide growth occurs in the temperature range 1100–1400°C, with no incubation period. Our previous work,[5] in which Mg powder was used as external dopant for directed oxidation of pure Al, also showed that only Mg is necessary to initiate and sustain the reaction growth. Mg can initiate growth in the Al_2O_3/Al system as it promotes the formation of a non-protective oxide layer at the interface between the growth oxide and oxidant. This layer plays an important role in the subsequent directed oxidation cyclic reaction sequence. By comparison Si seems only to accelerate the reaction process, probably by modifying the viscosity of the aluminium melt.[2] Na and Sn have also been examined as possible dopants; Na can initiate the process although it leads to low quality products and Sn apparently has similar effects to Si.

In the current work we have examined the possibility of using Li to initiate directed melt oxidation growth in the Al_2O_3/Al system. Li was chosen

*To whom correspondence should be addressed.

as a potential dopant because examination of the periodic table reveals that, in general, on moving diagonally across the periodic table the elements have certain similarities. This is because as one moves across a period, the charge on the ions increases and the size decreases, causing the polarizing powder to decrease, whereas on moving down a group, the size increases and polarizing power increases. On moving diagonally these two effects partly cancel each other, so that there is no marked change in properties. The type and strength of bond formed and the properties of the compounds are therefore often similar, although the valency is different. The similarities between diagonally related pairs of elements are usually weaker than those within a group, but they are quite pronounced for the following pairs of elements.[6] Li and Mg; Be and Al; B and Si. Therefore, there are some similarities in the properties of Mg and Li which were expected to allow Li to be used as dopant in directed oxidation of aluminium; in particular, both Mg and Li have very high vapour pressures at high temperature and they both form spinel structures with Al_2O_3.

In this paper the use of Li_2CO_3 as an externally applied lithium source in the directed melt oxidation of aluminium has been examined. Both unreinforced and α-Al_2O_3 particulate-reinforced bodies have been produced. In both cases, a detailed description of the microstructure is provided.

Experimental Procedure

A block of 99·8% pure Al (Alcan) was placed in a cavity shaped in an alumina crucible using fine alumina powder. Between 1·25 and 7·50 wt% (based on the weight of Al) reagent grade Li_2CO_3 powder (Fisons) was either applied directly on the surface of the Al block for composites grown into free space, or mixed with fine pure α-Al_2O_3 (A17, Alcoa) for composites grown into a preform body. The respective experimental arrangements are given in Figs 1(a) and 1(b).

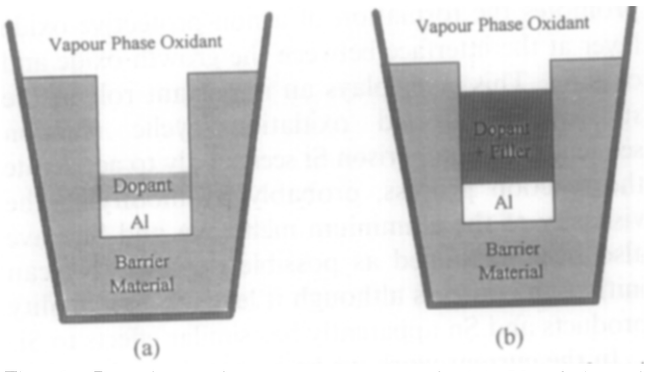

Fig. 1. Experimental arrangements used. (a) Unreinforced bodies: dopant directly placed on the Al block. (b) Reinforced bodies: dopant mixed with filler and the mixture placed above the Al block.

The prepared systems were heated in air at 200°C h^{-1} in a muffle furnace to a soaking temperature of 700, 900 or 1180°C. Samples fired to 700 and 900°C were held at these temperatures for 3 h, whereas samples fired to 1180°C were held at this temperature for 35 h. In all cases the samples were cooled to room temperature inside the furnace.

Fired samples were sectioned parallel or perpendicular to the growth direction and the different regions analysed by qualitative X-ray diffraction. These samples were subsequently mounted in epoxy resin, ground and diamond polished to 1 μm, before carbon coating for examination using scanning electron microscopy (SEM; Jeol JSM 6400) and energy dispersive spectroscopy (EDS; Link Analytical 6276). For transmission electron microscopy (TEM), the samples were punched to 3 mm discs, mechanically thinned to around 20 μm, ion milled at 6·0 keV until perforation, coated with carbon, and examined in a Philips EM420 at 100 keV.

Results

Growth into free space

Small, soft, black compacts were produced when samples containing 2·47 or 7·41 wt% Li_2CO_3 were fired to 700°C for 3 h. XRD (Fig. 2) showed that these compacts consisted of Al, Li_2CO_3, α-$LiAlO_2$,

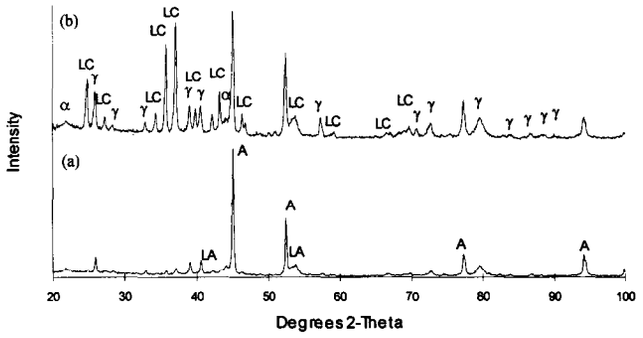

Fig. 2. XRD traces of samples fired for 3 h at 700°C: (a) Al–2·47 wt% Li_2CO_3; (b) Al–7·41 wt% Li_2CO_3 (A, Al; LC, Li_2CO_3; α, α-$LiAlO_2$; γ, γ-$LiAlO_2$; LA, $LiAl_5O_8$).

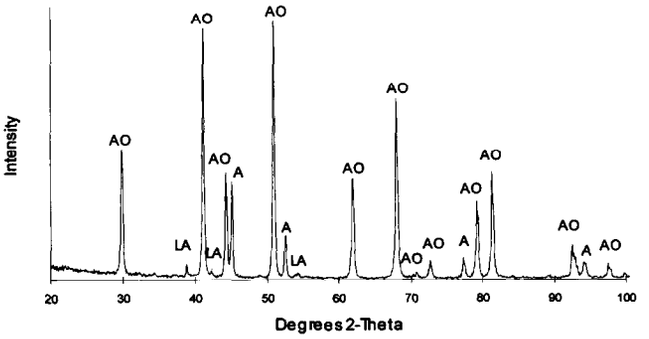

Fig. 3. XRD trace of Al–1·23 wt% Li_2CO_3 sample fired for 35 h at 1180°C (A, Al; AO, Al_2O_3; LA, $LiAl_5O_8$).

γ-$LiAlO_2$ and $LiAl_5O_8$, and that, within the limits of detection, no Al_2O_3 had been produced.

In samples doped with 1·23 wt% Li_2CO_3 and fired at 1180°C, Al_2O_3/Al growth was obtained; the Al block was totally exhausted after a soaking time of 35 h. Growth proceeded not only upwards from the top surface of the Al block but sideways into the barrier material. A section cut parallel to the growth was analysed by XRD which showed (Fig. 3) that the product was mainly Al and α-Al_2O_3; in addition, a small amount of $LiAl_5O_8$ was detected. Cross-sections of the growth product were also analysed by SEM. At the top of the sample there was a thick layer comprising Al pockets within a ceramic matrix (Fig. 4). Beneath this thick layer there was a series of thinner alternating dense and less dense layers (Fig. 5). The dense layers contained Al channels and the less dense ones contained no Al. In the centre of this sample (Fig. 6), an interconnected matrix was obtained. At the bottom of the sample (Fig. 7), further alternating dense and less dense layers were found. In addition, in the base of the product, the presence of Li-containing phases can be inferred from the backscattered electron image, as well as a small amount of AlN, which was identified by EDS (Fig. 8). Around the outermost surface of these samples, a thin Li-containing layer was observed (Fig. 9).

Although it is very difficult to identify the ceramic oxide as Al_2O_3 or $LiAl_5O_8$ using EDS since lithium

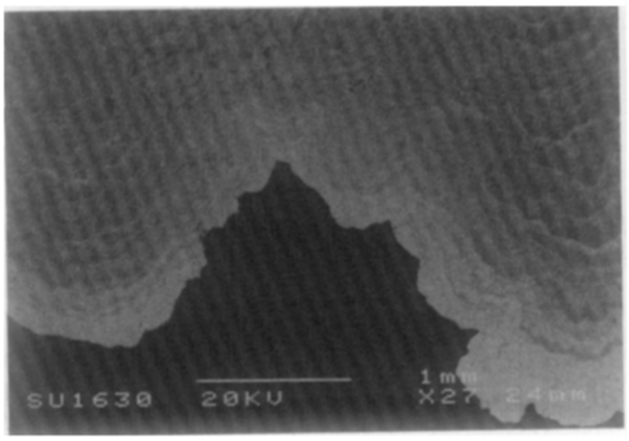

Fig. 4. SEM micrograph of the Al–1·23 wt% Li_2CO_3 sample fired to 1180°C for 35 h, showing a thick matrix layer at the top.

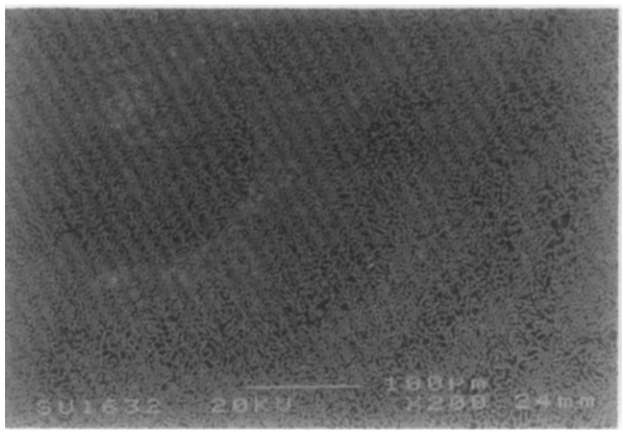

Fig. 5. SEM micrograph of the Al–1·23 wt% Li_2CO_3 sample fired to 1180°C for 35 h, showing alternating dense and less dense layers.

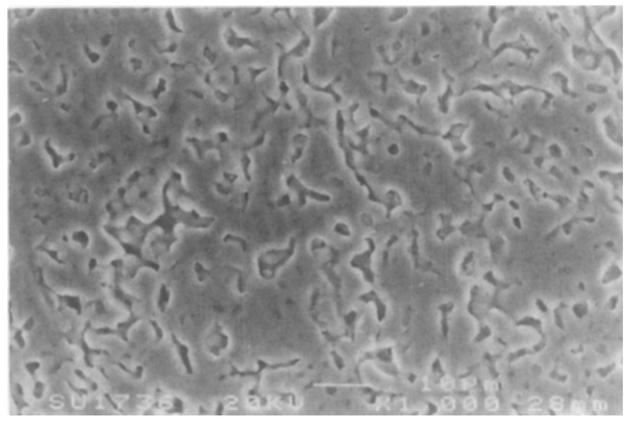

Fig. 6. SEM micrograph of the Al–1·23 wt% Li_2CO_3 sample fired to 1180°C for 35 h, showing interconnected Al_2O_3/Al matrix in the centre region.

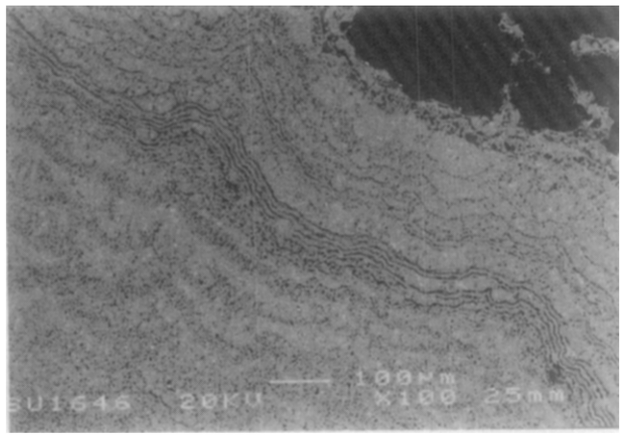

Fig. 7. SEM micrograph of the Al–1·23 wt% Li_2CO_3 sample fired to 1180°C for 35 h, showing alternating dense and less dense layers at the bottom of the product.

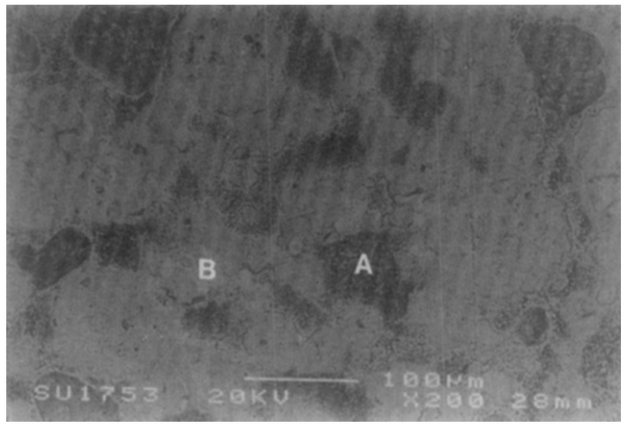

Fig. 8. Backscattered electron image of the Al–1·23 wt% Li_2CO_3 sample fired to 1180°C for 35 h, showing a Li-containing phase (dark feature — A) and AlN (light feature — B).

is too light, TEM showed up differences between these two phases. High-angle $LiAl_5O_8$–$LiAl_5O_8$ grain boundaries were commonly observed (Fig. 10), which was similar to the high-angle $MgAl_2O_4$–$MgAl_2O_4$ grain boundaries reported by Breval *et al.* on the Mg-doped system.[7] It was also found that many

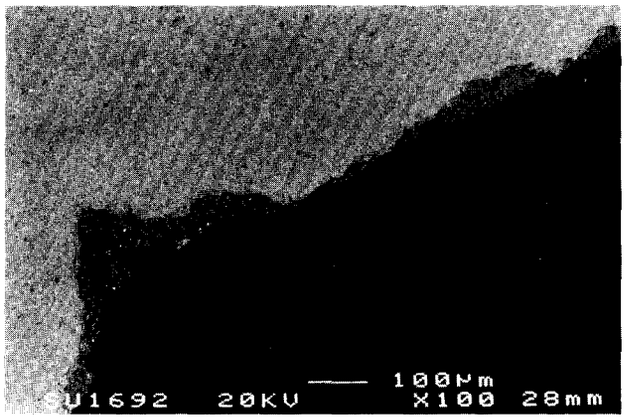

Fig. 9. SEM micrograph of the surface of a sample fired to 1180°C for 35 h, showing a thin, Li-containing layer on the surface.

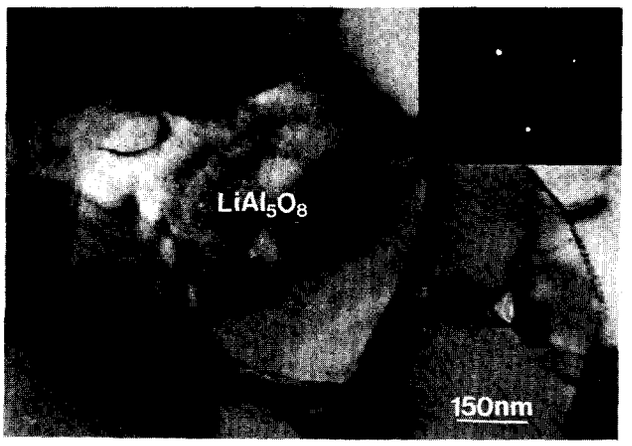

Fig. 10. TEM micrograph of a $LiAl_5O_8$ feature showing a high-angle $LiAl_5O_8$–$LiAl_5O_8$ grain boundary. Diffraction pattern shows $LiAl_5O_8$ [1 9 $\bar{2}$ $\bar{3}$].

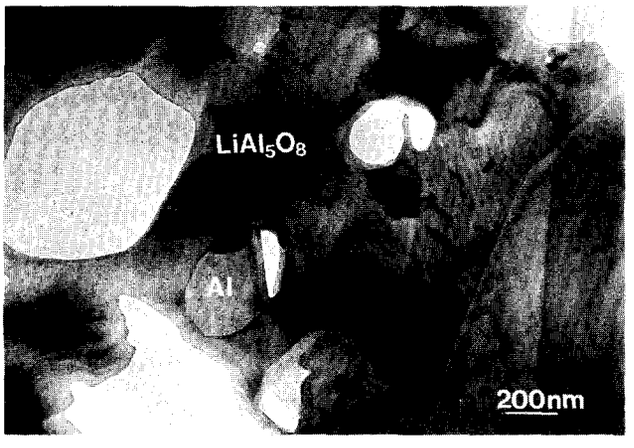

Fig. 11. TEM micrograph showing inclusions of Al within $LiAl_5O_8$ matrix.

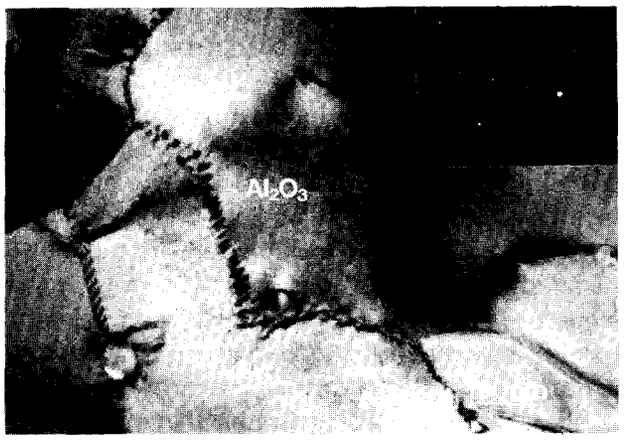

Fig. 12. TEM micrograph of Al_2O_3 feature showing low-angle Al_2O_3–Al_2O_3 grain boundary and high-angle Al_2O_3–Al grain boundary. Diffraction pattern shows Al_2O_3 [00$\bar{6}$].

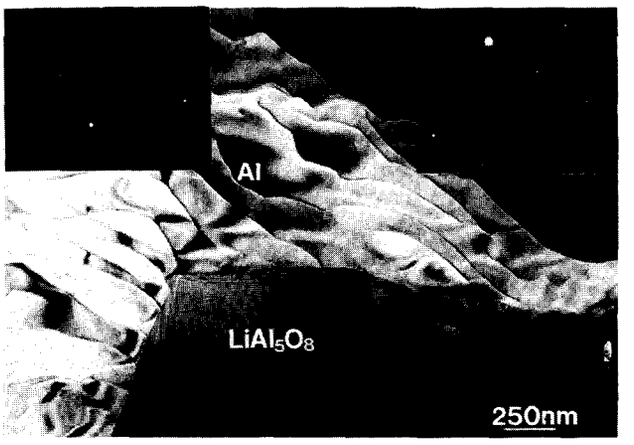

Fig. 13. TEM micrograph showing Al channel between $LiAl_5O_8$ crystals. Diffraction patterns show Al [0 $\bar{1}$ 3] (right) and $LiAl_5O_8$ [0 4 $\bar{3}$] (left).

inclusions of unoxidized Al remained within the $LiAl_5O_8$ matrix (Fig. 11). Low-angle grain boundaries were observed between Al_2O_3 grains (Fig. 12) and Al pockets were found set in the Al_2O_3–Al_2O_3 grain boundaries with a high-angle Al–Al_2O_3 phase boundary. This was also in agreement with the features seen in the directed melt oxidation of Al–Mg alloys.[1,3,7] Some thin channels of aluminium were also found (Fig. 13), which separate neighbouring $LiAl_5O_8$ crystals rather than Al_2O_3 crystals reported in the Mg-doped system by Newkirk *et al.*[1]

Growth into a preform body

Apart from a small amount of surface oxidation of the aluminium blocks, no growth was found in samples containing either 2·47 or 7·41 wt% Li_2CO_3 that had been heated to 900°C for 3 h. XRD showed, however (Fig. 14), that after firing the filler powder mixture consisted of α-Al_2O_3, α-$LiAlO_2$, γ-$LiAlO_2$ and $LiAl_5O_8$. The greater the initial Li_2CO_3 content, the more γ-$LiAlO_2$ was obtained in the fired mixture.

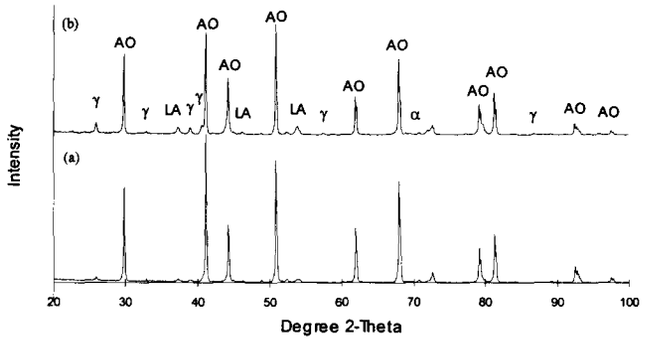

Fig. 14. XRD traces of Al_2O_3 particle-reinforced samples fired for 3 h at 900°C: (a) Al–2·47 wt% Li_2CO_3; (b) Al–7·41 wt% Li_2CO_3 (A, Al; α, α-$LiAlO_2$; γ, γ-$LiAlO_2$; LA, $LiAl_5O_8$).

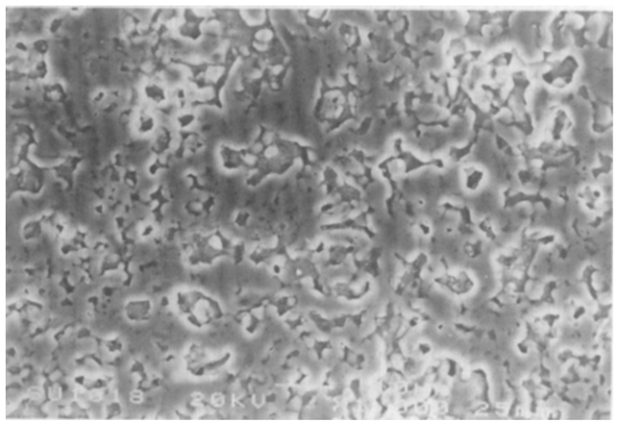

Fig. 15. SEM micrograph of Al_2O_3 particle-reinforced Al–1·23 wt% Li_2CO_3 sample fired to 1180°C for 35 h.

In systems doped with between 1·24 and 7·41 wt% Li_2CO_3 that had been heated to 1180°C for 24 or 35 h, irregular growths were obtained in the lower part of the dopant/filler mixture and part of the aluminium block was consumed. On inspection of the cross-section, it was difficult to distinguish between alumina filler and growth. The section was analysed by XRD which showed that although $LiAl_5O_8$ was present in addition to α-Al_2O_3 and Al, no $LiAlO_2$ was present. The fired mixture above the growth product consisted of α-Al_2O_3 (filler) and $LiAl_5O_8$. Unlike the unreinforced body, there were no alternating dense/less dense layers within the micro-structure of the reinforced body. A lithium aluminate phase was concentrated on the surface of the product body and, within the growth, an interconnected Al_2O_3/Al matrix that contained filler Al_2O_3 particles (0·3 μm diameter) and unoxidized Al channels was formed (Fig. 15).

Discussion

Ginsberg and Datta[8] claimed that lithium confers a greater reactivity to aluminium melt than any other alloying element. Small amounts of lithium (3 wt%) dramatically alter the nature of the molten alloy to the extent that traditional materials of construction used in the melting and transfer of aluminium alloy are rendered inadequate. Furthermore, rapid reaction of lithium with oxygen and water from the ambient atmosphere renders the oxide crust that forms on the molten metal non-protective, leading to severe volatilization of lithium, necessitating processing under an inert atmosphere. This removal of coherent film from the molten alloy also allows intimate contact with particles and promotes wetting and infiltration.[9]

Butler and co-workers[10,11] showed that a binary Al–3 wt% Li alloy developed surface films of spinel oxides such as $LiAl_5O_8$ and γ-$LiAlO_2$ in oxygen-containing environments around 500°C. Under pure oxygen γ-$LiAlO_2$ and α-Al_2O_3 developed at around 700°C on alloys containing relatively low levels of Li. X-ray analysis[12] of oxide films grown in air at 750°C on Al–0·3 wt% Li and Al–1·2 wt% Li indicated that γ-AL_2O_3 was present in addition to γ-$LiAlO_2$. Field and co-workers[11,13] studied the oxidation of liquid Al–3 wt% Li alloy under different environments. In dry air the oxidation sequence with increasing temperature was $Li_2O \rightarrow Li_2CO_3 \rightarrow$ γ-$LiAlO_2$. In wet air, Li_2O and Li_2CO_3 were stable up to 500°C but above this temperature a mixture of cubic spinel $LiAl_5O_8$ and $LiAlO_2$ existed. The surface of molten Al–3 wt% Li appeared to behave chemically like pure lithium and thus Al played only a minor role during oxidation. Oxidation was not limited by Li diffusion but controlled by the nucleation and growth of crystalline reaction products at the metal–oxide interface.

In this work, pure aluminium and an external Li_2CO_3 dopant, rather than an Al–Li alloy, have been used. XRD of Li_2CO_3 fired at 600°C, and DTA traces of Li_2CO_3 heated from room temperature to 1180°C, show that Li_2CO_3 is very stable even above 660°C (the melting point of aluminium) and that the decomposition reaction occurs around 730°C. Thus, in the directed melt oxidation process below 730°C, Li_2CO_3 may react directly with the protective Al_2O_3 oxide layers that will be present on the pure aluminium:

$$Li_2CO_3 + Al_2O_3\ (\text{film}) \rightleftharpoons 2LiAlO_2 + CO_2 \quad (1)$$

or

$$Li_2CO_3 + 5Al_2O_3\ (\text{film}) \rightleftharpoons 2LiAl_5O_8 + CO_2. \quad (2)$$

These reactions can aid the breakdown of stable oxide film in a similar fashion to magnesium aluminate spinel, $MgAl_2O_4$, in the Mg-doped system.[5]

On the other hand, above the melting point of aluminium, molten aluminium may also react directly with Li_2CO_3 to form $LiAl_5O_8$ or $LiAlO_2$, i.e.

$$4Al + 2Li_2CO_3 + 3O_2 \rightleftharpoons 4LiAlO_2 + 2CO_2 \quad (3)$$

$$20Al + 2Li_2CO_3 + 15O_2 \rightleftharpoons 4LiAl_5O_8 + 2CO_2. \quad (4)$$

As Li_2O is never observed it is thought that these reactions occur preferentially to the high-temperature decomposition of the carbonate to the oxide.

Lithium aluminates are therefore formed on the surface of the parent metal and aluminium liquid continues to penetrate this lithium aluminate layer by capillary action and react with lithium aluminates. Byker *et al.*[14] claimed that $LiAl_5O_8$ spinel is stable over a substantial range of stoichiometry and thus any $LiAlO_2$ could be transformed to $LiAl_5O_8$ on contact with excess Al:

$$LiAlO_2 + 4Al + 3O_2 \rightleftharpoons LiAl_5O_8. \quad (5)$$

$LiAl_5O_8$ can also react with liquid Al to produce Al_2O_3

$$LiAl_5O_8 + Al \rightleftharpoons 3Al_2O_3 + Li \quad (6)$$

The resulting Li vaporizes easily to the reaction front and would reform $LiAl_5O_8$ again producing the Li-rich layer seen on the outermost surface of the products:

$$Li + 5Al + 4O_2 \rightleftharpoons LiAl_5O_8. \quad (7)$$

This cycle of oxidation reactions leads to the directed oxidation Al_2O_3/Al body growth although some Li may be lost to the environment.

As the lithium aluminate layer is constantly being broken down and reformed, the orientation of lithium aluminate grains formed at a later time is not related to those formed earlier. High-angle grain boundaries are therefore observed in the lithium aluminate layer (Fig. 10). By comparison, after the initial development of an Al_2O_3 layer there is always Al_2O_3 present in the system. Hence the orientation of subsequently grown Al_2O_3 is related to the pre-existing Al_2O_3 grains, and low-angle grain boundaries are seen between Al_2O_3 grains (Fig. 12).

Within the base of growth product the oxygen content may be exhausted so that the remaining Al liquid may react with nitrogen (present in air which was used as the oxidizing atmosphere) to form AlN.[5]

In the Al_2O_3/Al growth into a preform body, fine Al_2O_3 particles were used as filler. Before the directed melt oxidation reactions started, the following reactions between Al_2O_3 filler and Li_2CO_3 would occur:

$$Li_2CO_3 + Al_2O_3 \text{ (filler)} \rightleftharpoons 2LiAlO_2 + CO_2 \quad (8)$$

and

$$Li_2CO_3 + 5Al_2O_3 \text{ (filler)} \rightleftharpoons 2LiAl_5O_8 + CO_2. \quad (9)$$

When aluminium liquid infiltrates into the mixture of dopant and reinforcement, $LiAlO_2$ leads to breakdown of the Al_2O_3 protective layer on the aluminium surface by the following reaction:

$$LiAlO_2 + 2Al_2O_3 \text{ (film)} \rightleftharpoons LiAl_5O_8. \quad (10)$$

Thus $LiAl_5O_8$ could start to react with aluminium liquid, resulting in a cyclic directed melt oxidation reaction sequence similar to that outlined above.

Conclusions

Composite Al_2O_3/Al ceramics have been obtained by directed melt oxidation of pure aluminium externally doped with a Li source (Li_2CO_3). Products have been produced by directed melt oxidation into both free space and particulate preforms comprising pure α-Al_2O_3. As no other dopants were present, Li can initiate directed oxidation reactions and is therefore an effective dopant for the production of Al_2O_3 from Al by directed melt oxidation.

With Li the directed melt oxidation process was initiated by the formation of $LiAl_5O_8$, which aids the breakdown of the stable oxide film that would normally form on aluminium. Subsequently the process involves motion of Li from within the growth to the reaction front; this can occur because of the high vapour pressure of Li at the reaction temperature. Thus, a Li-containing non-protective lithium aluminate layer was formed on the outward surface of product growth. This layer was instrumental in developing the subsequent cyclic reaction sequence in a similar fashion to the Mg-doped directed oxidation system.

Acknowledgement

This work was undertaken whilst one of us (X.G.) was in receipt of a Sheffield University Scholarship.

References

1. Newkirk, M. S., Urquhart, A. W. & Zwicker, H. R., Formation of lanxide ceramic composite materials. *J. Mater. Res.*, **1** (1986) 81–9.
2. Nagelberg, A. S., Observations on the role of Mg and Si in the directed oxidation of Al–Mg–Si alloys. *J. Mater. Res.*, **7** (1992) 265–8.
3. Aghajanian, M. K., Macmillan, N. H., Kennedy, C. R., Luxzcz, S. J. & Roy, R., Properties and microstructures of lanxide Al_2O_3–Al ceramic composite materials. *J. Mater. Sci.*, **24** (1989) 658–70.
4. Xiao, P. & Derby, B., Alumina/aluminum composites formed by the directed oxidation of aluminum using magnesia as a surface dopant. *J. Am. Ceram. Soc.*, **77** (1994) 1961–70.
5. Gu, X. & Hand, R. J., The production of reinforced aluminium/alumina bodies by directed melt oxidation. *J. Eur. Ceram. Soc.*, **15** (1995) 823–31.
6. Lee, J. D., in *Concise Inorganic Chemistry*. D. Van Nostrand Company Ltd, London, 1965, pp. 69–76.
7. Breval, E., Aghajanian, M. K. & Luszcz, S. J., Microstructure and composition of alumina/aluminum

composites made by directed oxidation of aluminum. *J. Am. Ceram. Soc.*, **73** (1990) 2610–14.
8. Ginsberg, H. & Datta, P. K., Dross formation in commercial aluminium and aluminium alloy melts in relation to the oxygen supply. *Aluminium*, **42** (1966) 681–7.
9. Weiranuch, D. A. Jr & Graddy, G. E. Jr, Wetting and corrosion in Al–Mg–Si–O system. In *Proc. Int. Symp. on Advances in Refractories for the Metallurgical Industries*, Winnipeg, Canada, 1987, ed. M. A. J. Figand. Pergamon Press, New York, 1988.
10. Scanans, G. M. & Butler, E. P., Direct observation of oxidation of aluminium and aluminium alloys. In *Proc. 4th Int. Cong. HVEM*, Toulouse, 1975, pp. 341–4.
11. Field, D. J. & Butler, E. P., Liquid metal oxidation of Al–3 wt% Li. In *Aluminum–Lithium Alloy II, Proc. 2nd Int. Aluminum–Lithium Conf.*, AIME, 1983. The Metallurgical Society of AIME, Warrendale, PA, 1983, pp. 667–73.
12. Kouzmichev, L. V., Myzlin, L. Y., Radin, A. Y. & Goopiev, B. D., Oxidation of aluminium/lithium alloys and method of protection. *Tekhnol. Legk. Splavov Nauchno-Tech Byul Vilsa*, **8** (1975) 18–22.
13. Field, D. J., Scamans, G. M. & Butler, E. P., The high temperature oxidation of Al–Li alloy. In *Aluminum–Lithium Alloy II, Pro. 2nd Int. Aluminum–Lithium Conf.*, AIME, 1983. The Metallurgical Society of AIME, Warrendale, PA, 1983, pp. 657–66.
14. Byker, H. J., Eliezer, I., Eliezer, N. & Howald, R. A., Calculation of a phase diagram for the $LiO_{0.5}$–$AlO_{1.5}$ system. *J. Phys. Chem.*, **83** (1979) 2349–55.

Journal of the European Ceramic Society 16 (1996) 937–943

S0955-2219(96)00008-8
0955-2219/96/$15.00

Mechanical Properties of Alumina–Metal–Zirconia Nano-Micro Hybrid Composites

Ch. Laurent,[a] A. Rousset,[a] P. Bonnefond,[a,b] D. Oquab[b] & B. Lavelle[b]

[a]Laboratoire de Chimie des Matériaux Inorganiques, URA CNRS 1311, Université Paul-Sabatier, 31062 Toulouse Cedex, France
[b]Laboratoire des Matériaux, URA CNRS 445, Institut National Polytechnique de Toulouse (ENSCT), 31077 Toulouse Cedex, France

(Received 24 February 1995; revised version received 14 December 1995; accepted 5 January 1996)

Abstract

Al_2O_3 and Al_2O_3–2 wt% $Fe_{0.8}Cr_{0.2}$ nanocomposite powders were wet-mixed with different ZrO_2 or Y-ZrO_2 powders. The influence of the ball-milling medium and mixing duration on the microstructure and the amount of tetragonal zirconia retained after hot-pressing are discussed. The fracture strength and fracture toughness of the alumina–metal–zirconia specimens are lower than that of the alumina–metal and alumina–zirconia composites. This could result from a partial annihilation of the different reinforcement mechanisms involved and also from interactions between zirconia and the metallic phase. There is no correlation between the mechanical properties and the amount of tetragonal zirconia. However, the amount of tetragonal to monoclinic transformation at the surface of the specimens during grinding prior to the mechanical tests seems to be a key parameter. © 1996 Elsevier Science Limited.

1 Introduction

Nanocomposites consisting of nanometric metal particles dispersed within the grains of an alumina matrix have been found to exhibit higher strength and higher toughness than alumina,[1–6] even with a metal content as low as 2 wt% (so about 1 vol%).[2] Although this is not fully understood yet, it seems probable that plastic stretching of the ductile particles,[7] and crack deflection are the main reinforcement mechanisms.

A more popular way to improve the mechanical properties of alumina is based on the dispersion of micrometric zirconia grains as a discrete second phase; zirconia-toughened alumina (ZTA) ceramics have been widely studied (see Wang and Stevens[8] for a review), and several reinforcement mechanisms have been identified, including stress-induced (tetragonal to monoclinic, t → m) phase transformation toughening, microcrack toughening, compressive surface stresses and crack deflection. The combination of these mechanisms is related to the microstructure of the ZTA material, and notably to the extent of agglomeration of the zirconia particles.[8]

Niihara *et al.*[9] have shown that the hybridization of microcomposites and nanocomposites could result in a further improvement in both the strength and toughness. Thus, the aim of this work was to study the mechanical properties of a composite containing both intragranular metal nanoparticles and micrometric zirconia-based particles located in the grain boundaries of alumina.

Results reported in the literature[10–19] on the elaboration of ZTA by mechanical mixing greatly differ regarding the influence of elaboration parameters, such as the ball-milling duration and the nature of the dispersion medium, on the mechanical properties. The first part of this paper deals with the preparation of the alumina–metal–zirconia composite by wet-mixing an Al_2O_3–2 wt% $Fe_{0.8}Cr_{0.2}$ nanocomposite powder prepared in this laboratory with a commercial ZrO_2 powder. $Fe_{0.8}Cr_{0.2}$ is a notation for metal particles containing 80 at% of iron and 20 at% of chromium.

2 Experimental

Details for the synthesis of nanocomposite powders were given in a previous study.[20] Briefly, a solid solution between the requested amounts of the rhomboedral sesquioxides Al_2O_3, Fe_2O_3 and Cr_2O_3 was prepared from the decomposition and

calcination of an oxalate precursor. Pure α-Al_2O_3 was also prepared by the same method. Hydrogen reduction at 1050°C of the solid solution gave rise to the Al_2O_3–2 wt% $Fe_{0.8}Cr_{0.2}$ nanocomposite powder.

A commercial zirconia powder (CERAC Z-1042, monoclinic, average size 10·6 μm, minimum size 0·2 μm, maximum size 20 μm) was mixed and sonicated for 30 min with the nanocomposite powder (average size 2 μm, minimum size 0·2 μm, maximum size 10 μm) in different media: 'acid' water (pH = 5), 'basic' water (pH = 8) and ethanol. The powder/liquid volume ratio was fixed to 50/50 to reduce the risk of differential sedimentation.[19] This was followed by ball-milling, using zirconia balls and vessel, for different times (10, 60 and 360 min). The zirconia content was fixed to 13 wt%. In some cases the Z-1042 powder was dry ball-milled for 60 min prior to sonication ('preground' zirconia). The powders were oven-dried (80°C) and their average size (in volume) was measured using sedimentation granulometry in isopropanol. Transmission electron microscopy (TEM) was also performed to investigate the microstructure. The powders for TEM examination were sonicated in ethanol and a drop of the dispersion was deposited on to a copper grid coated with a collodion film.

The powders were uniaxially hot-pressed in graphite dies at 1450°C under vacuum. The dense specimens (20 mm in diameter and 1 mm thick) were ground successively to 45 and 6 μm with diamond suspensions and a final polish was carried out using 'colloidal' silica (0·05 μm). Relative densities were calculated from the mass and dimensions of the dense composites and found to be equal to or higher than 99%.

Phase identification was performed with X-ray diffraction (XRD) patterns analysis (CoKα = 0·17902 nm) on unground (U), 45 μm-ground (G) and silica-polished (P) specimens. The relative amounts of tetragonal and monoclinic zirconia were calculated from the XRD patterns using the well-known Garvie–Nicholson equation.[21] P specimens were also observed by scanning electron microscopy (SEM). Thin foils for TEM observations were prepared by mechanical grinding and Ar ion-milling.

After a set of preparation parameters has been chosen, mechanical tests were conducted on G specimens. The transverse fracture strength (σ_f) was determined by the three-point-bending test on parallelepipedic specimens (1·6 × 1·6 × 18 mm^3) machined with a diamond saw. The fracture toughness (K_{Ic}) was measured by the SENB method on similar specimens notched using a diamond wire 0·1 mm in diameter. The calibration factor proposed by Brown and Srawley[22] was used to calculate the SENB toughness from the experimental results. Cross-head speed was fixed at 0·1 mm/min. The values given for σ_f and K_{Ic} are the average of measures on seven and six specimens respectively.

Several other zirconia-based powders have been used for these tests: a commercial ZrO_2–5·3 mol% Y_2O_3 powder (CERAC Z-1065, cubic, average size 7·0 μm, minimum size 0·3 μm, maximum size 20 μm), and four products prepared in this laboratory by hydrolysis of $ZrCl_4$ (and YCl_3) aqueous solutions:[23] ZrO_2 (tetragonal) calcined at 500 and 800°C and ZrO_2–2 mol% Y_2O_3 (tetragonal) calcined at 500 and 800°C. The average size of these four powders was about 5·5 μm (minimum size 0·2 μm, maximum size 20 μm), but crystallinity was improved in those calcined at 800°C. A specimen containing only 6·5 wt% of Z-1042 zirconia was also tested.

Table 1 summarizes the characteristics of the zirconia-based powders and gives a letter code for the designation of specimens prepared with these powders.

3 Results and Discussion

3.1 Preparation

The microstructure of the Al_2O_3–2 wt% $Fe_{0.8}Cr_{0.2}$ nanocomposite powder prior to mixing with zirconia is shown in Fig. 1(a). Most of the metal particles are homogeneously dispersed within the alumina grains and are smaller than 3 nm in size. Some larger (5–10 nm) metal particles are located in the pores of the matrix. It has been shown in a previous study[24] that both the alumina grains and the

Table 1. Composition, designation, structure, and average size (as determined by sedimentation granulometry) of the zirconia-based powders

Composition	*Designation*	*Structure*	*Average size (μm)*
ZrO_2(Z-1042)	A13 or A6·5	Monoclinic	10·6
ZrO_2–5·3 mol% Y_2O_3	B	Cubic	7·0
ZrO_2(500°C)	C	Tetragonal	5·5
ZrO_2(800°C)	D	Tetragonal	5·5
ZrO_2–2 mol% Y_2O_3(500°C)	E	Tetragonal	5·4
ZrO_2–2 mol% Y_2O_3(800°C)	F	Tetragonal	5·5

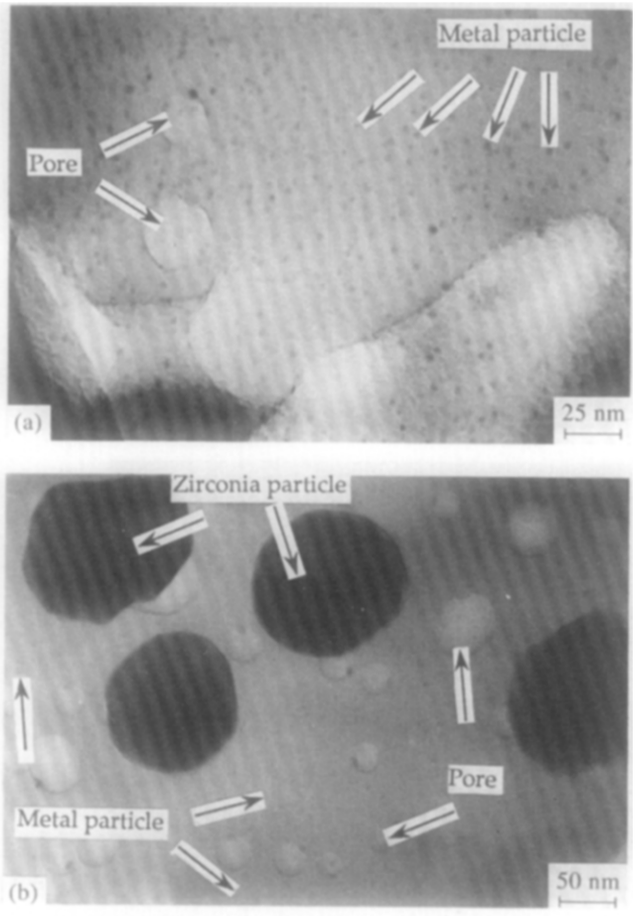

Fig. 1. TEM micrographs showing the microstructure of the Al_2O_3–2 wt% $Fe_{0.8}Cr_{0.2}$ nanocomposite powder (a) and of the alumina–metal–zirconia powder after 60 min ball-milling (b). Some metal particles, pores and zirconia particles are indicated by arrows.

metal particles are monocrystalline and that the intragranular particles are epitaxied in the alumina matrix. The alloy particles are in the stable α form.[20] A TEM micrograph of the alumina–metal–zirconia powder is presented (Fig. 1(b)): it can be seen that metallic dispersion was not affected by the 60 min ball-milling and that 100–150 nm large zirconia particles are located at the surface of the nanocomposite powder grains. The decrease of the powder grain size with the increase in ball-milling duration will be described later in this paper.

The dense composites microstructure as observed by SEM is the same, irrespective of the dispersion medium used: for 10 min ball-milling (Fig. 2(a, b)) there is an inhomogeneous distribution of zirconia agglomerates, the size of which ranges from a few micrometers to 60 μm. As expected, a more even distribution is achieved with the increase in ball-milling time to 60 min, the size of the zirconia agglomerates being lower than 10 μm (Fig. 2(c, d)). Ball-milling for 360 min only results in a slight re-agglomeration of the zirconia particles (Fig. 2(e,f)).

XRD patterns analysis revealed the presence of α-Al_2O_3, t-ZrO_2, m-ZrO_2 and α-$Fe_{0.8}Cr_{0.2}$. The {110} metal peak is very weak and the calculation of the average size of the metal particles using Scherrer's method is not possible. Since a high content of tetragonal zirconia is known to be beneficial with respect to the mechanical properties, we have plotted the t-ZrO_2 content as deduced from XRD measurements on unground (U) specimens versus the average size of the composite powder (Fig. 3). Ball-milling the starting powders for 10, 60 and 360 min reduces the average grain size to about 3, 2 and 1·5 μm respectively; the size distribution is also reduced (maximum size lower than 7 μm after 60 and 360 min ball-milling). However, this has no influence on the amount of tetragonal zirconia retained after hot-pressing, since the higher measured value is equal to 30% and all values are within the 14–30% range. The data presented in Fig. 3 also show little difference between the dispersion media, but more t-ZrO_2 is generally obtained using 'pre-ground' zirconia. Thus, it appears that whatever the elaboration process, agglomeration of the zirconia particles in our dense materials is strong enough to allow a majority of particles to undergo the spontaneous (t $\rightarrow$ m) phase transformation during cooling from the hot-pressing temperature.

Due to the development of high stresses during grinding, which favour the tetragonal-to-monoclinic (t $\rightarrow$ m) phase transformation, the t-ZrO_2 content is found to be markedly lower in G specimens (ranging between 12 and 26%). The values measured in P specimens are very close to that in U specimens, showing that P values are representative of the bulk t-ZrO_2 content and that the lower G values are only due to grinding. The compressive stresses that develop at the surface of the material owing to the volume increase associated with the (t $\rightarrow$ m) transformation are known to be beneficial with respect to fracture strength.[25] Thus, to quantify the grinding-induced (t $\rightarrow$ m) phase transformation we have defined R as the ratio of the t-ZrO_2 content in G specimens to the t-ZrO_2 content in U specimens. R is not dependent on the ball-milling time (for example R = 0·88, 0·88 and 0·86 for 10, 60 and 360 min mixing in ethanol respectively); however R is equal to about 0·76 when 'pre-ground' zirconia was used, except in 'basic' water in which values close to 0·87 are still measured. This could indicate that higher stresses would be necessary to further transform the t-ZrO_2 particles in specimens prepared in this medium.

According to this preliminary study, the following set of preparation parameters has been chosen: 'pre-grinding' of the zirconia-based powder, mixing with the nanocomposite powder in 'basic' (pH = 8) water (30 min sonication followed by 60 min ball-milling), and oven-drying.

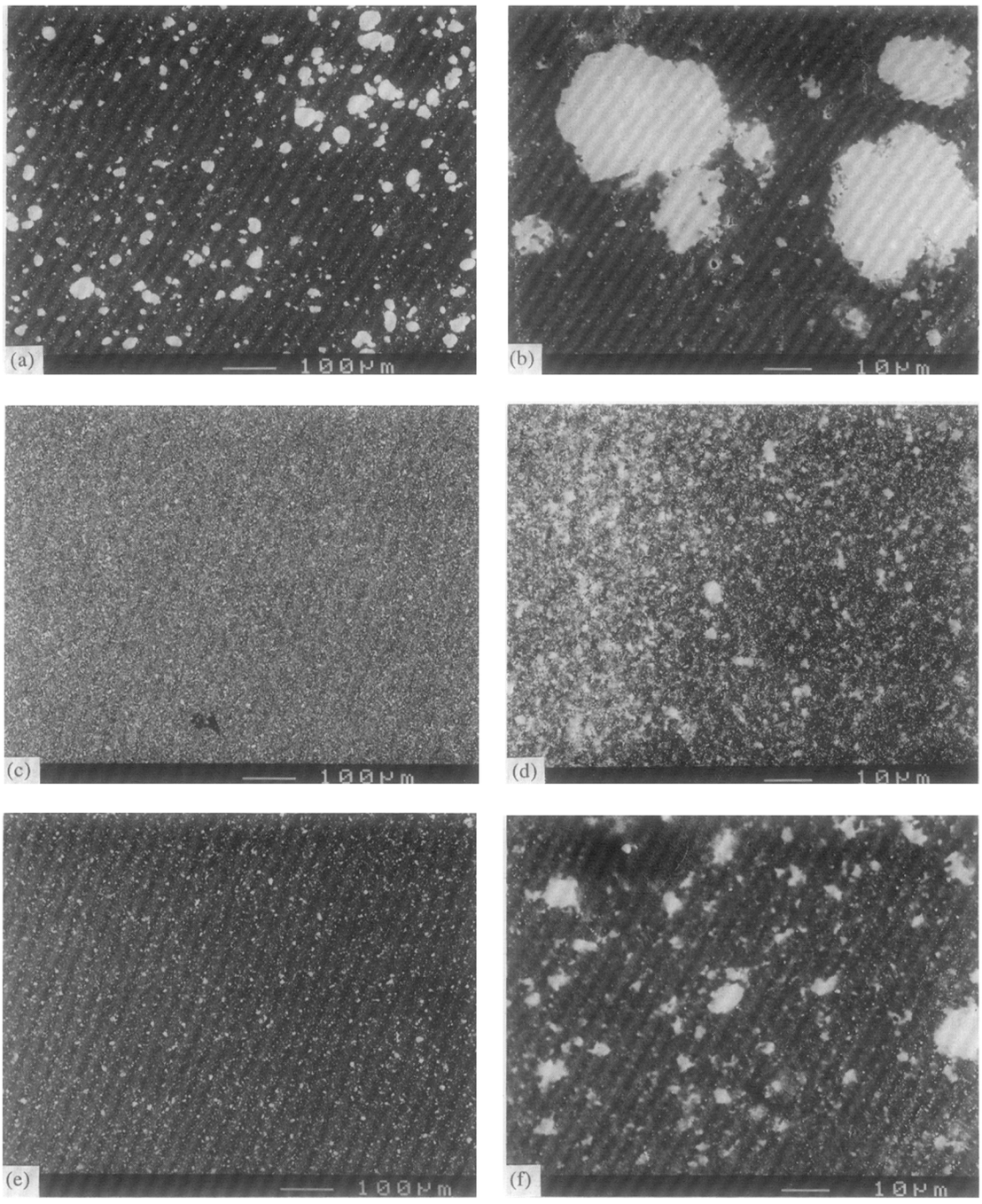

Fig. 2. SEM micrographs showing the microstructure of silica-polished (P) specimens after 10 min ((a),(b)), 60 min ((c),(d)) and 360 min ((e),(f)) ball-milling (the dispersion medium was found to have no or very little influence).

A TEM micrograph of the A13 composite prepared according to this process and hot-pressed in vacuum at 1450°C is shown in Fig. 4. The zirconia particles are mainly located at the grain boundaries and triple grain junctions of the alumina matrix. The shape of some is elongated because their formation results from agglomeration of several particles (see the particle in the upper right hand corner of Fig. 4). The alumina grains are micrometric in size (1 μm for this particular grain, but in fact closer to 2 μm) and seem to be quite porous, but some of the larger holes probably correspond to the location of zirconia particles entrapped in the alumina grain that were extracted during ion-milling; accordingly, some of the smaller holes could correspond to the location of nanometric metal particles. Some metal particles smaller than 20 nm can be seen on Fig. 4.

3.2 Mechanical properties

In order to discriminate the effects on mechanical properties of zirconia on the one hand and of metal nanoparticles on the other hand, an alumina–zirconia (Z-1042) specimen (denoted H hereafter) was also prepared. The t-ZrO_2 content measured in G specimens, R ratio, and results of the mechanical tests, including those previously published[2] of the Al_2O_3–2 wt% $Fe_{0.8}Cr_{0.2}$ nanocomposite

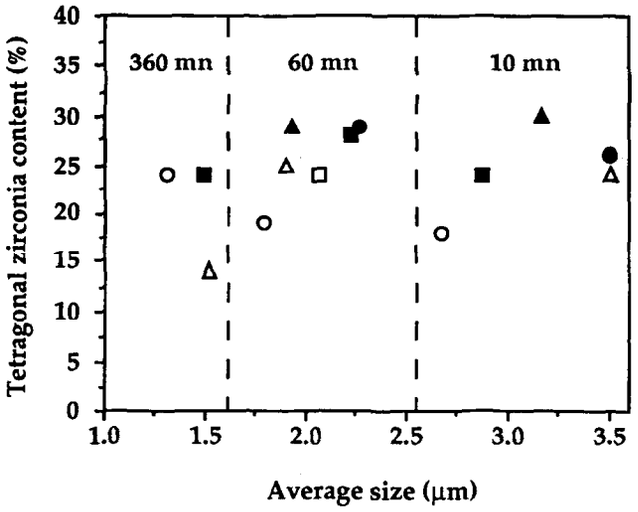

Fig. 3. Amount of tetragonal zirconia in unground (U) specimens versus the average size of the composite powder as determined by sedimentation granulometry. Full symbols denote dry ball-milling of the zirconia powder before sonication. Circle: water (pH = 5); square: water (pH = 8); triangle: ethanol. Ball-milling duration is indicated.

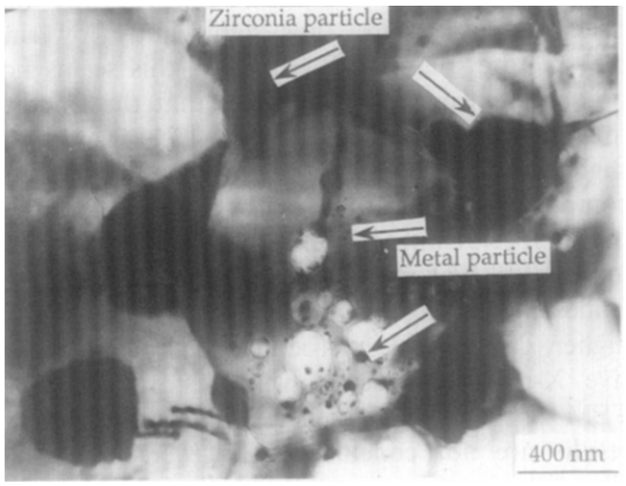

Fig. 4. TEM micrograph of the A13 alumina–metal–zirconia dense composite. Some metal particles and zirconia particles are indicated by arrows.

(denoted N hereafter) and alumina, are listed in Table 2. The size of the alumina grains in these latter composites is close to 2 μm and thus similar to that found in the alumina–metal–zirconia specimens.

It should be noted that the amount of tetragonal zirconia is fairly low, even when using tetragonal zirconia starting powders (C, D, E, F). However, the t-ZrO_2 content is much higher (34 and 51% in G and U specimens respectively) when a lower amount of zirconia is dispersed in alumina (A6·5). These results confirm that our preparation method does not allow the zirconia particles to disperse homogeneously enough at the surface of the nanocomposite to prevent agglomeration during hot-pressing. The minimum value of R is 0·67 (in A6·5) and the maximum is 1, i.e. no transformation (in E). The trend is that R decreases with the increase in t-ZrO_2, which seems to indicate that a higher proportion of these particles would also be available to undergo the (t $\rightarrow$ m) phase transformation during grinding. However, this is not strictly followed, due probably to the microstructural and compositional differences that exist between our composites.

The mechanical properties of the alumina–zirconia composite (H, σ_f = 712 MPa and K_{Ic} = 5·4 MPa$\sqrt{m}$), as well as those achieved using cubic zirconia (B, σ_f = 590 MPa and K_{Ic} = 4·5 MPa$\sqrt{m}$), which is known to not promote the mechanical reinforcement,[26] are similar to that found in the literature.[8,26] In particular, it should be noted that the fracture strength of the alumina–zirconia composite (H) is of the order of that of the metal-alumina nanocomposite (N), showing the validity of our wet-mixing preparation method with respect to preparing composite material with reasonably high strength and toughness.

Concerning the hybrid composites, all fracture strength values are lower than that of the reference materials (H and N), and all K_{Ic} values are lower than that of the nanocomposite. The fracture strength of specimen A6·5, which contains a higher amount of tetragonal zirconia, is higher than that of A13, but there is otherwise no correlation between the mechanical properties and the t-ZrO_2 content.

Table 2. Fracture strength, fracture toughness, tetragonal zirconia content (G specimens), and R ratio (see text). Values for Al_2O_3 and N are from Reference 2. Standard deviation on σ_f and K_{Ic} values is indicated between brackets

Specimen	σ_f *(MPa)*	K_{Ic} *(Mpa*$\sqrt{m}$*)*	*t-ZrO_2 content (%)*	*R*
Al_2O_3	335 (20)	4·4 (0·3)	—	—
N	690 (127)	6·5 (0·2)	—	—
H	712 (40)	5·4 (0·4)	16	0·70
A6·5	620 (124)	5·5 (1·0)	34	0·67
A13	572 (40)	5·7 (0·4)	22	0·82
B	590 (62)	4·5 (0·3)	100% cubic	—
C	510 (28)	5·2 (0·6)	22	0·88
D	612 (16)	5·6 (0·5)	19	0·79
E	486 (36)	5·0 (0·4)	17	1·00
F	582 (31)	6·0 (0·5)	15	0·79

On the contrary, it is interesting to note that both the lower σ_f and K_{Ic} are achieved with specimen E, which do not exhibit (t → m) phase transformation during grinding (R = 1). Plotting fracture strength versus R (Fig. 5(a)) suggests that the higher σ_f is obtained for an optimal value of R (about 0·74). A similar evolution is observed for K_{Ic} (Fig. 5(b)). This could represent an optimal combination of stress-induced (t → m) transformation toughening and compressive surface stresses, the microcrack toughening mechanism being roughly of the same importance in all specimen, which contain a similar amount of monoclinic zirconia.

R could also be related to the transformation zone depth whose influence is discussed by Kosmac *et al.*[27] Our results are in qualitative agreement with theirs, since they have shown that the higher toughness is not obtained for the larger transformation zone depth, but for a particular combination of several factors: zone depth, t-ZrO_2 content and size of the zirconia particles.

Obviously, the additive effect that was expected from the hybridization of nano- and microcomposites is not observed. The lower mechanical properties achieved with the alumina–metal–zirconia composites could result from a partial annihilation of the different reinforcement mechanisms: indeed, SEM observations (Fig. 6) show that the fracture is mostly intergranular, while it is essentially

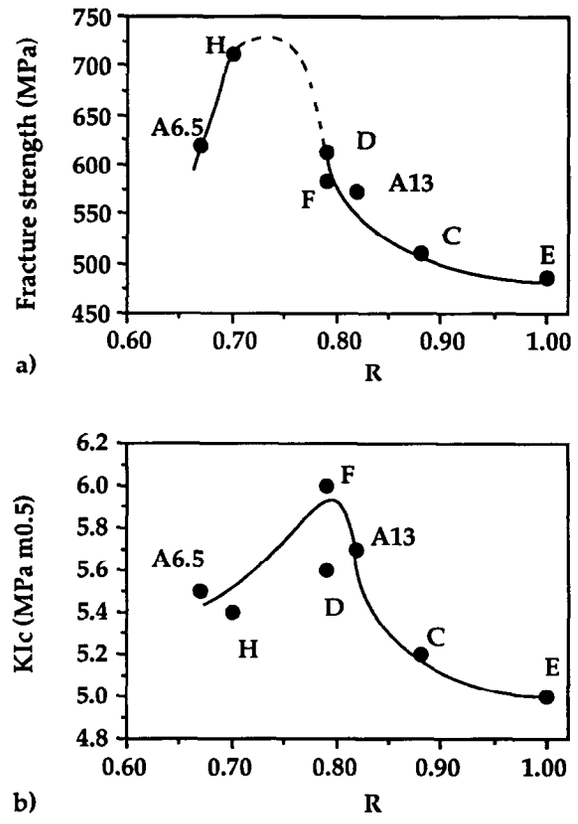

Fig. 5. Fracture strength (a) and fracture toughness (b) versus R ratio (see text). Dashed part of the curve is only speculative.

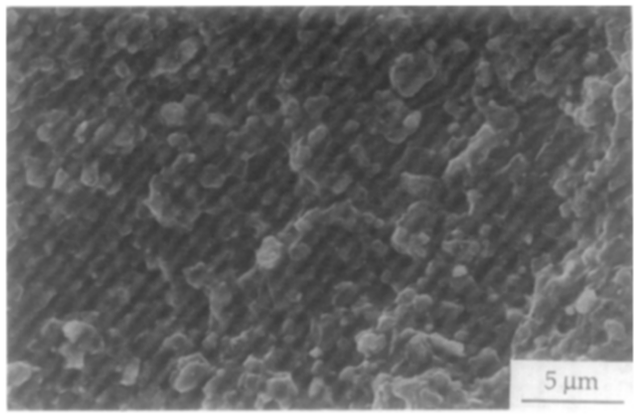

Fig. 6. SEM micrograph showing the fracture surface of an alumina–metal–zirconia composite.

intragranular in the absence of zirconia.[28] Thus, mechanisms involving the metal particles, which are located within the matrix grains, would be far less operative. On the other hand, the metal nanoparticles could favour the coalescence of the residual microcracks due to the (t → m) transformation taking place during cooling from the hot-pressing temperature, thus significantly lowering the fracture toughness.[8] However, this seems not probable since one can observe that the fracture toughness of specimens A6·5, A13, D and F is slightly higher than that of the alumina–zirconia composite (H). The diffusion at high temperatures of Fe species into zirconia, which is known[29] to increase the volume difference between the monoclinic and tetragonal phases, could provoke a higher, detrimental, microcracking. Energy dispersive X-ray spectroscopy was performed during TEM observations to check this point, but the results are not conclusive. However, Tuan and Chen[30,31] recently reported that interactions between micrometric silver and zirconia particles do not favour the additive effect.

4 Conclusions

'Nano-micro hybrid composites' have been prepared by wet-mixing and hot-pressing a zirconia powder and a 2 wt% metal–alumina nanocomposite powder. The nanometric metal particles are dispersed within the matrix grains and the zirconia particles are located at the grain boundaries of alumina. Owing to the agglomeration of zirconia particles, the amount of tetragonal zirconia is fairly low (≤ 30%) even when using t-ZrO_2 starting powders; however, it was observed to increase when using a lesser amount of zirconia. The validity of the chosen elaboration method (60 min ball-milling in pH 8 water) is demonstrated by the mechanical properties achieved with the 13 wt%

zirconia–alumina composite (without metal): σ_f = 712 MPa and K_{Ic} = 5·4 MPa$\sqrt{m}$).

Instead of the expected additive strengthening and toughening effects, annihilation of the reinforcement mechanisms occurs in the hybrid composites. Explanations for this may be found in the microstructure of the material and also in interactions between zirconia and the metallic phase. The amount of tetragonal to monoclinic transformation at the surface of the specimens during grinding prior to the mechanical tests was identified to be a key parameter, showing the importance of the effect of compressive surface stresses in these materials.

References

1. Devaux, X., Laurent, Ch., Brieu, M. & Rousset, A., Propriétés microstructurales et mécaniques de nanocomposites à matrice céramique. *C. R. Acad. Sci. Paris*, **312** Série II (1991) 1425–30.
2. Devaux, X., Laurent, Ch., Brieu, M. & Rousset, A., Ceramic matrix nanocomposites. In *Composites Materials*, eds A. T. Di Benedetto, L. Nicolais & R. Watanabe. Elsevier Science Publishers B. V., Amsterdam, 1992, pp. 209–14.
3. Laurent, Ch., Devaux, X., Brieu, M. & Rousset, A., Microstructural and mechanical properties of alumina–iron–chromium alloys nanocomposites. In *Euro-Ceramics II*, eds G. Ziegler & H. Hausner. Deutsche Keramische Gesellschaft e. V., Köln, 1992, pp. 1679–83.
4. Breval, E., Deng, Z., Chiou, S. & Pantano, C. G., Sol–gel prepared Ni–alumina composite materials. Part I. Microstructure and mechanical properties. *J. Mat. Sci.*, **27** (1992) 1464–8.
5. Sekino, T., Nakahira, A., Niihara, K. & Nawa, M., Fabrication of Al_2O_3/W nanocomposites. *KONA Powder and Particle*, **10** (1992) 192–7.
6. Sekino, T., Nakahira, A., Nawa, M. & Niihara, K., Fabrication and mechanical properties of tungsten metal dispersed Al_2O_3 based nanocomposites. In *Proceedings of the International Conference Ceramics adding the Value:Austceram 92*, ed. M. J. Bannister, CSIRO, Australia, 1992, pp. 745–50.
7. Evans, A. G., High toughness ceramics. *Mat. Sci. Eng. A*, **105–106** (1988) 65–75.
8. Wang, J. & Stevens, R., Review. Zirconia-toughened alumina (ZTA) ceramics. *J. Mat. Sci.*, **24** (1989) 3421–40.
9. Niihara, K., Nakahira, A. & Sekino, T., New nanocomposite structural ceramics. *Mat. Res. Soc. Symp. Proc.*, **286** (1993) 405–12.
10. Brodhag, C., Bach, J. P., Thevenot, F. & Deletter, M., Microstructure of zirconia-toughened alumina obtained through different precursor routes. *Mat. Sci. Eng. A*, **109** (1989) 53–9.
11. Tomaszewski, H. & Kulczycki, A., Effect of Y_2O_3 partial stabilization on thermomechanical properties of Al_2O_3–ZrO_2 ceramic. In *Advanced Structural Inorganic Composites*, ed. P. Vincenzini, Elsevier Sci. Pub. B. V., Amsterdam, 1991, pp. 391–400.
12. Samdi, A., Grollier-Baron, Th., Roubin, M. & Durand, B., Etude des conditions de dispersion optimale de poudres de zircone obtenues par pyrolyse d'acétates de zirconium. *Powder Tech*, **66** (1991) 237–42.
13. Yoshimatsu, H., Miura, Y., Osaka, A., Kawasaki, H. & Omori, S., Mechanical properties of zirconia–alumina composite ceramics prepared from Zr–Al organometallic compounds. *J. Mat. Sci.*, **25** (1990) 5231–6.
14. Hoshi, Y., Obitu, M., Awano, M. & Takagi, H., Al_2O_3–PSZ ceramics with high flexural strength and high fracture toughness. *Interceram*, **32** (1990) 84–7.
15. Homerin, P., Thévenot, F., Orange, G., Fantozzi, G., Vandeneede, V., Leriche, A. & Cambier, F., Mechanical properties of zirconia toughened alumina prepared by different methods. *J. Phys.*, C1, **47** (1986) 717–21.
16. Carlstrom E. & Lange F. F., Mixing of flocced suspensions. *J. Am. Ceram. Soc.*, **67** (1984) C-169–70.
17. Bleier, A. & Westmoreland, G., Chemical and physical principles of processing that effect microstructure of Al_2O_3–ZrO_2 composites. *Mat. Res. Soc. Symp. Proc.*, **121** (1988) 145–54.
18. Leuwerink, T. H. P., Den Exter, P., Winnubst, A. J. A. & Burggraaf, A. J., Characteristics of wet chemically prepared zirconia/alumina ceramics. In *Advanced Structural Inorganic Composites*, ed. P. Vincenzini, Elsevier Sci. Pub. B. V., Amsterdam, 1991, pp. 619–28.
19. Glennie, D. & Konsztowicz, K. J., Homogenization of dense acqueous suspensions of ZTA composites. In *Advanced Structural Inorganic Composites*, ed. P. Vincenzini, Elsevier Science Publishers BV, Amsterdam, 1991, 629-36.
20. Devaux, X., Laurent, Ch. & Rousset A., Chemical synthesis of metal nanoparticles dispersed in alumina. *Nanostruct. Mater.*, **2** (1993) 339–46.
21. Garvie, C. & Nicholson, P. S., Phase analysis in zirconia systems. *J. Am. Ceram. Soc.*, **55** (1972) 303–5.
22. Brown, W. F. & Srawley, J. E., *Plane Strain Crack Toughness Testing of High Strength Metallic Materials.* ASTM Spec. Tech. Pub., 410, ASTM, Philadelphia, PA, USA, 1966.
23. Haberko, K., Characteristics and sintering behaviour of zirconia ultrafine powders. *Ceramurgia International*, **5** (1979) 148–53.
24. Devaux, X., Laurent, Ch., Brieu, M. & Rousset, A., Iron–alumina interface in ceramic matrix nanocomposites. *J. All. Comp.*, **188** (1992) 179–81.
25. Lange, F. F., Transformation toughening. Part 4. Fabrication, fracture toughness and strength of Al_2O_3–ZrO_2 composites. *J. Mat Sci.*, **17** (1982) 247–54.
26. French, J. D., Chan, H. M., Harmer, M. P. & Miller, G. A., Mechanical properties of interpenetrating microstructures: the Al_2O_3/c-ZrO_2 system. *J. Am. Ceram. Soc.*, **75** (1992) 418–23.
27. Kosmac, T., Swain, M. V. & Claussen, N., The role of tetragonal and monoclinic ZrO_2 particles in the fracture toughness of Al_2O_3–ZrO_2 composites. *Mat. Sci. Eng.*, **71** (1985) 57–64.
28. Laurent Ch., Contribution à l'étude de nanocomposites à matrice céramique. Alumine - alliages fer–chrome et alumine–zircone–fer et alliages fer–chrome. Doctoral Thesis, Université Paul-Sabatier, Toulouse, France, 1994.
29. Beck, H. P. & Kaliba, C., On the solubility of Fe, Cr and Nb in ZrO_2 and its effects on the thermal dilatation and polymorphic transitions. *Mater. Res. Bull.*, **25** (1990) 1161–8.
30. Tuan, W. H. & Chen, W. R., Enhancing the mechanical performance of alumina through the addition of metallic and ceramic inclusions. In *Third Euro-Ceramics* Vol. 3, eds P. Duran & J. F. Fernandez, Faenza Editrice Iberica S. L., 1993, pp. 713–18.
31. Tuan, W. H. & Chen, W. R., The interactions between silver and zirconia inclusions and their effect on the toughening behaviour of Al_2O_3/(Ag + ZrO_2) composites. *J. Eur. Ceram. Soc.*, **14** (1994) 37–43.

Journal of the European Ceramic Society 16 (1996) 945–952

S0955-2219(96)00015-5
0955-2219/96/$15.00

Low-temperature Sintering and Microstructural Development of Nanocrystalline Y-TZP Powders

P. Durán, M. Villegas, F. Capel, P. Recio & C. Moure

Instituto de Cerármica y Vidrio (CSIC), Electroceramics Department, 28500 Arganda del Rey, Madrid, Spain

(Received 29 September 1995; revised version received 12 December 1995; accepted 5 January 1996)

Abstract

Powders of yttria-doped tetragonal zirconia (3 mol%) with a narrow pore size distribution and ultrafine particle size (~9 nm) have been prepared by the mixed organic + inorganic precursors coprecipitation method. The compaction behaviour of almost agglomerate-free calcined powders was studied, and their sintering behaviour using both isothermal and non-isothermal techniques was evaluated. Fully dense nanoscale ceramics with an average grain size below 95 nm were obtained after sintering at 1200°C for 20 min or at 1150°C for 4 h. Several stages were identified in the whole densification process: it was found that a particle rearrangement process assisted by sintering pressure is the densification mechanism in the earlier sintering step (up to 800°C), and grain boundary diffusion was the dominant mechanism for densification up to 1180°C. Activation energy values of 130 ± 20 and 300 ± 40 kJ mol^{-1}, respectively, were calculated for these densification mechanisms. The almost complete absence of agglomerates in the calcined powders and the homogeneous pore structure of the green compacts are the two main factors leading to low-temperature fully densified Y-TZP bodies. © 1996 Elsevier Science Limited.

1 Introduction

The use of advanced ceramics for structural applications or as electronic components will become more generalized when all the problems associated with their development, such as poor sinterability without aids, normally low densities, internal flaws and degraded mechanical properties as a consequence of the internal holes, can be solved. Much effort has been made over the years to circumvent the above-mentioned obstacles, and, today, the control of both powder synthesis and subsequent sintering to achieve high density and ultrafine grained microstructure in the sintered bodies is still one of the major challenges in the processing of ceramic materials. To the latter end, the use of nanocrystalline ceramic powders could be the key for achieving much lower sintering temperatures, better microstructures, improved mechanical and electrical properties and, as a consequence, higher reliability.

Different methods such as sol–gel,[1,2] hydrothermal synthesis,[3] spray pyrolysis[4] or, more recently, electrochemical synthesis[5] are used for making nanocrystalline ceramic powders. Although the solution methods present some disadvantages related mainly to the drying and purity of the powders, their low cost and relatively good reproducibility make them more attractive from the viewpoint of a possible industrial application. Thus, in spite of some difficulties, the aqueous coprecipitation methods are the most widely used to prepare nanoscale ceramic powders.

In the case of fully stabilized tetragonal Y_2O_3–ZrO_2 ceramics (Y-TZP), it is well known that the room-temperature phase stability, strength and toughness depend strongly on a critical grain size (<0.8 μm), and that the requirement is so strict when Y-TZP ceramics are exposed to humid atmospheres that the above critical grain size has to be reduced to ~0·25 μm.[6,7] Because of this, the production of nanostructured ceramics is very interesting not only for the above advantages but also because, when coupled with attention to forming methods, it is favourable for achieving superplastic behaviour at relatively high temperatures.[8,9]

The present work was undertaken to study the sintering behaviour and the microstructural development of a nanocrystalline Y-TZP (3 mol% Y_2O_3) powder prepared by a mixed organic–inorganic precursors coprecipitation method.

2 Experimental Procedure

2.1 Powder preparation

The preparation of amorphous Y-TZP (3 mol% Y_2O_3) powders was carried out by dissolving, in the adequate proportions, yttrium nitrate [$Y(NO_3)O_3 \cdot 5H_2O$] and zirconium tetrabutoxide [$Zr(C_4H_9O)_4 \cdot C_4H_9OH$] in slightly acidulated isopropyl alcohol. Complete coprecipitation of the Y^{3+} and Zr^{4+} cations was achieved by mixing with an excess of 12 N aqueous ammonia solution using a procedure similar to that previously reported to obtain Er-TZP amorphous powders;[10] the details of the basic procedure were described in the previous report and will not be repeated here. However, we would like to emphasize some points: (1) the order of addition of the reactants was that of dropping the above acidic cation solution to the stirred, aqueous ammonia solution, resulting in a simultaneous and homogeneous coprecipitation under the precipitation conditions (pH > 9); (2) the sequence of the washing process was water → water + isopropyl alcohol mixture → anhydrous isopropyl alcohol for two or three times; and (3) the washed powders were calcined at 500°C for 1 h. These and all the other powder preparation steps mentioned elsewhere[10] have to be rigorously controlled in order to achieve unagglomerated or weakly agglomerated nano-sized Y-TZP powders.

2.2 Powder characterization

Crystallite sizes of calcined powders were determined by means of the X-ray line broadening (XRLB) method[11] using an X-ray diffractometer (Siemens D5000), Cu K_α radiation and a scan rate of 0·5° min^{-1}. The crystallite size, D, was calculated from the Scherrer equation:

$$D = 0.9\lambda/(\beta \cos\theta)$$

where λ is the wavelength of the X-rays, θ is the diffraction angle and β is the calibrated width of the diffraction peak at half-maximum at the selected 2θ. Particle size and shape were also examined by transmission electron microscopy (TEM; ME-300, Philips) and scanning electron microscopy (SEM; DSM-950, Carl Zeiss). Specific surface area was measured by the BET (Accusorb 210E, Micromeritics) method, and the amorphous powders were also characterized by means of dynamic thermal analysis/thermogravimetric analysis (DTA/TG; Netzsch STA-409).

2.3 Powder compaction and sintering

After calcining, the powders were isopressed at different compaction pressures up to 350 MPa, and the compaction behaviour was studied by measuring the changes in density with increased isostatic pressure. The pore size distribution in both the green and the sintered compacts was calculated by mercury porosimetry (Autopore II 9215). Sintering kinetics were studied by non-isothermal experiments using constant-rate heating (CRH) dilatometry (Netzsch DIL 402E/7) at a heating rate of 5°C min^{-1} from 200 to 1400°C. Isothermal sintering was performed at different temperatures at a heating rate of 5°C min^{-1}. After sintering, the samples were quickly cooled to room temperature. The density of the sintered samples was measured by Archimedes' method with water, and grain size was measured by X-ray line broadening and/or by SEM using the interception method.[12]

3 Experimental Results

3.1 Powder characteristics

As shown in Fig. 1, the thermogravimetry curve shows that only about 12% total weight loss occurs on heating, which is much smaller than that corresponding to a well formed Y–Zr hydroxide. This result and the exothermic peak centred at ~140°C in the DTA curve indicate that the majority of the adsorbed water has been eliminated during the drying at 300°C to remove residual anhydrous isopropyl alcohol.[10] The exothermic peak at 440°C in the DTA curve indicates that the crystallization of tetragonal zirconia starts at about 400°C and ends at about 500°C, in fairly good agreement with previous results.[13] For this reason, as mentioned above, the coprecipitated powders were calcined at a temperature at which the complex Y–Zr hydroxide would completely transform to tetragonal zirconia and for a short time, to avoid excessive crystallite growth.

The as-prepared powders were amorphous as determined by X-ray diffraction, and the powders calcined at 500°C for 1 h were not well crystallized tetragonal yttria-doped zirconia solid solution. The surface areas of the isopropyl alcohol washed coprecipitated yttria–zirconia powders were in the range 200–250 $m^2\ g^{-1}$. The calcined powders had surface areas S_{BET} in the range 80–90 $m^2\ g^{-1}$ and a crystallite size of ~9 nm as calculated by XRLB analysis. The crystallite diameter calculated from S_{BET}, using the equation $D = 6/(\rho_t \cdot S_{BET})$ in which ρ_t is the theoretical density, was in the range 10–12 nm. A TEM micrograph of the calcined powders (see Fig. 2) shows a weakly agglomerated powder in which an average crystallite size of ~10 nm could be measured, in close agreement with the above measurements. Some agglomerate-like chains (three to five

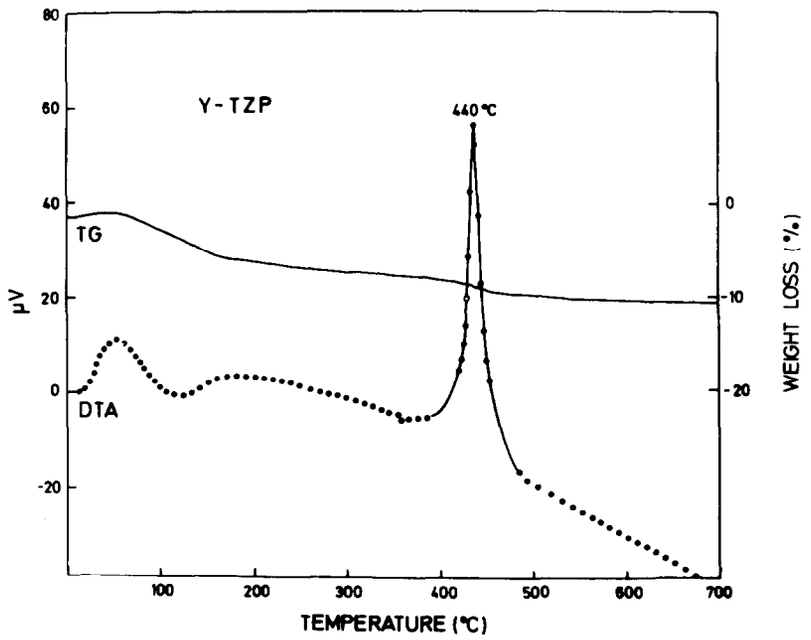

Fig. 1. DTA/TG curves for Y-TZP coprecipitated powders.

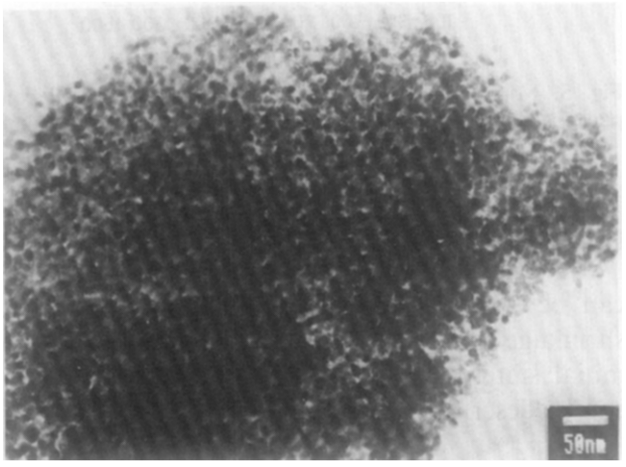

Fig. 2. Transmission electron micrograph of Y-TZP calcined powders.

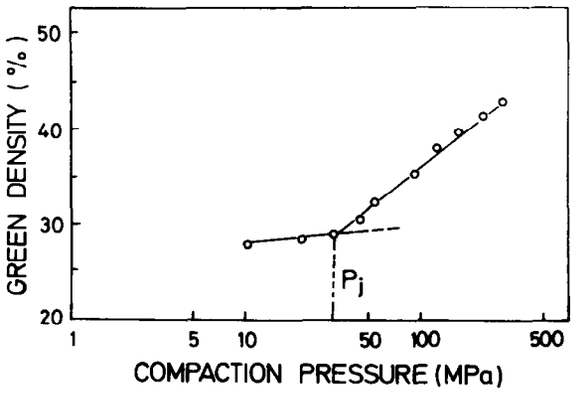

Fig. 3. Compaction behaviour of the nano-sized Y-TZP calcined powders.

primary crystallites apparently welded by necks or overlapped) can be observed. These characteristics reveal that, after calcining, the powder is in a loose state with high internal porosity which facilitates the destruction of the smaller agglomerates during milling.

3.2 Compaction behaviour

The compaction response of the calcined powders was studied by plotting the relative density of the green compacts vs. the logarithm of the applied pressure;[14] as shown in Fig. 3, a curve with two linear regions was obtained. In the first one, for compaction pressures lower than 40 MPa, variation in densification was barely achieved and this is consistent with a rearrangement of the soft agglomerates during pressing. The low break point (P_j < 40 MPa) in the curve, which is related to the agglomerate strength,[15] gives an idea of the weakness of the agglomerates which easily deform as a result of their lower strength.

In the second linear part of the curve (Fig. 3), the relative density increases with the compaction pressure, the agglomerates are deformed or fractured and the interagglomerate porosity, if any, is eliminated. No advantage in the sintering process is gained by exceeding 250 MPa (~43% dense), and at the end a coherent compact structure with a narrow pore size distribution is obtained (see Fig. 4). This result is consistent with the above assumption of a high internal powder porosity leading to green compacts with inter- and intraagglomerate pores with the same dimensions.

Given that the average pore diameter (~6 nm) and the average crystallite size (9–10 nm) are quite similar, the simpler cubic rearrangement for the crystallites in the green compacts could be assumed. From the average crystallite size, the calculated pore diameter (assuming spherical crystallites) is approximately 4 nm for such a cubic

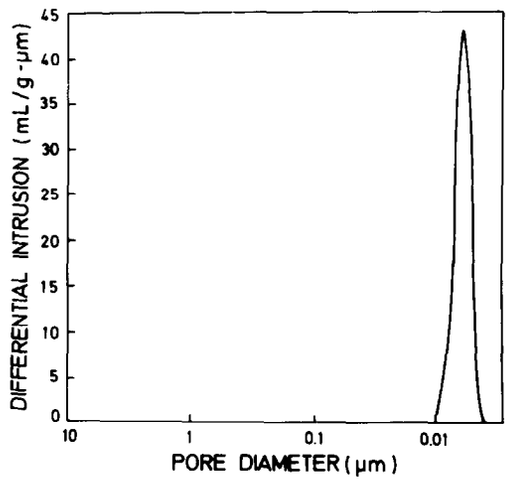

Fig. 4. Pore size distribution in the Y-TZP green compacts.

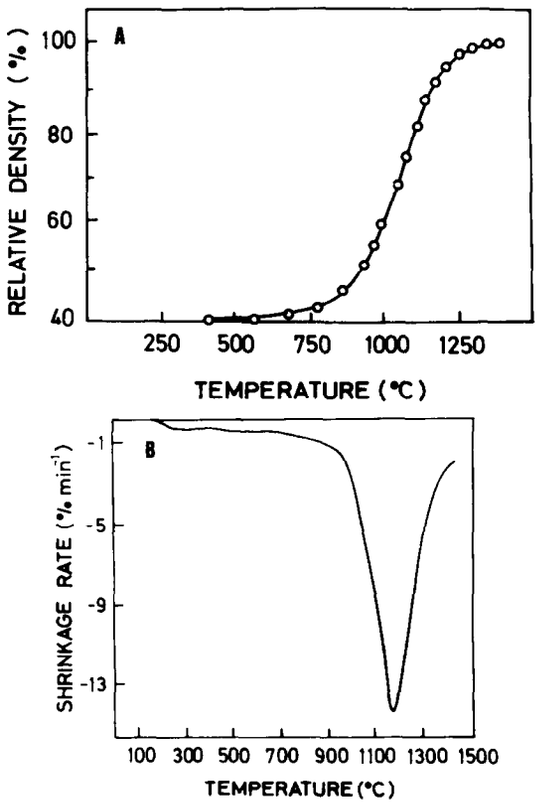

Fig. 5. Non-isothermal sintering behaviour of Y-TZP compacts: (A) densification vs. temperature; and (B) shrinkage rate curve.

arrangement. This value is in reasonable agreement with the observed mode size of 6 nm in Fig. 4. This result and the low green density of the compacts (~43% theoretical density), which is considerably below the value for a close-packed structure, lead us to assume the presence of many small packing defects — undetected by Hg porosimetry — between the crystallite arrangements leading to packing inhomogeneities (dislocations, grain boundaries, some agglomerates that are not destroyed, etc.) in the green compacts. Since (as mentioned above) the crystallite size calculated from S_{BET} and by XRLB is almost the same and the pore size distribution in green compacts shows a single mode size of 6 nm, it can be concluded that the calcined powder is agglomerate-free and the porosity in our compacts is mainly intercrystallite.

3.3 Constant-rate heating densification experiments

Non-isothermal densification experiments in air showed that the compacts start to shrink at ~500°C, the temperature for 4% shrinkage being ~800°C, and that the shrinkage process (total shrinkage ~26%) is complete at approximately 1250°C. In terms of the relative density, calculated from the initial green density and the shrinkage data, Fig. 5(A) shows that, up to ~1000°C (12% shrinkage), a densification of only 15% (from 43 to 58% theoretical density) takes place. In the short temperature interval of 250°C, between 1000 and 1250°C, a strong shrinkage and a rapid densification (97% theoretical density) were achieved. At ~1275°C the density was as high as 99·9%. According to the experimental curve obtained for densification rate during sintering, shown in Fig. 5(B), the maximum densification rate is found at a temperature as low as 1180°C, proving the high sinterability of the prepared compacts. The presence of only one maximum in the densification rate curve confirms the single mode and narrow pore size distribution in the compacted samples.

Sintering kinetics for Y-TZP powder compacts can be analysed on the basis of initial sintering shrinkage. According to Young and Cutler,[16] the initial sintering theory with constant-rate heating can be described by the expression:

$$\ln\left(\frac{\Delta l/l_o}{T}\right) = \frac{-nQ}{RT} + C$$

where $\Delta l/l_0$ is the fractional shrinkage of the compact at temperature T, Q is the activation energy, and C and n are constants related to the powder geometry and the sintering mechanism, respectively. RT has its usual meaning. Figure 6 shows a plot of the experimental data for $\ln(\Delta l/l_0)/T$ vs. $1/T$ and, as was expected for compacts which are relatively inhomogeneous in packing, the Arrhenius plot is not completely linear over the whole range of densification.

This result suggests that the densification process can be divided into several stages. In a first stage, up to ~800°C, if it is assumed that $n = 0{\cdot}3$ in the above equation, which is the value for a grain boundary diffusion mechanism, an activation energy of 130 ± 20 kJ mol^{-1} was calculated: this is too low to be associated with such a diffusion mechanism at the early stage of densification. According to the results of Fig. 5(B), the low shrinkage rate at this densification stage seems to be better correlated to a rearrangement process in

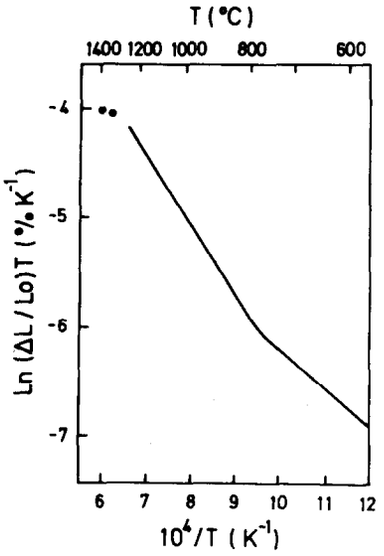

Fig. 6. Arrhenius plot of logarithm of shrinkage vs. the reciprocal of temperature.

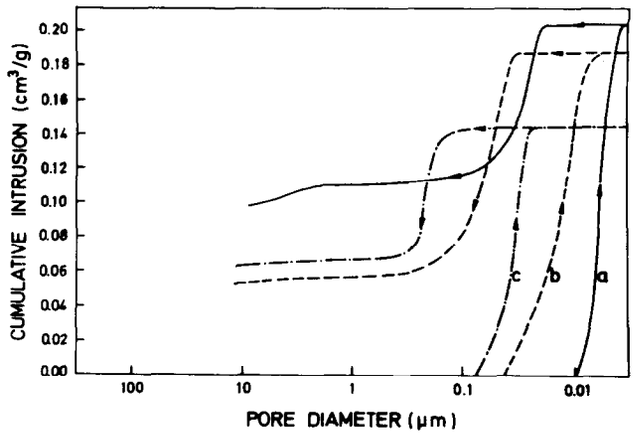

Fig. 7. Hysteresis curves of mercury porosimetry for (a) as-pressed Y-TZP compacts, (b) sintered at 620°C, and (c) sintered at 980°C.

which the porosity of the intercrystallite arrays is transported to the surface of the crystallite arrays with a subsequent densification of the crystallite arrays. This results in a slight densification of the compact in which a change of both the microstructure and the morphology of the pores has been produced.

To confirm the above assumption, a study of the intruded–extruded mercury was made by mercury porosimetry[17] on as-pressed compacts and those sintered at 620 and 980°C. As shown in Fig. 7, a different intruded/extruded mercury ratio was found and this was lower in the case of the compacts sintered at 980°C (average pore diameter = 30 nm) than in those sintered at 620°C (average pore diameter = 15 nm) or in the as-pressed compacts. This means that some entrapment of mercury in pores took place in the latter case mainly due to the small entrance openings, and the fact that a larger volume of mercury was extruded during the depressurizing process indicates that both the entrance size and the interior are quite similar in the former cases. This result and the microstructure in Fig. 8 lead us to assume that an evolution of the pore shape, from spheroidal to interconnected columnar or cylindrical, occurs with temperature. In conclusion a new pore configuration at the end of the early sintering stage, as consequence of the particle rearrangement process, seems to exist. Such a rearrangement process assisted by the sintering pressure as the driving force[18,19] can be considered as the main mechanism responsible for the early densification stage.

A second densification stage seems to be present between ~800 and 1180°C in which an extremely high shrinkage rate takes place (see Fig. 5(B)). From $n = 0{\cdot}25$ reported elsewhere for this temperature range[20] and the slope calculated in Fig. 6, a value of $Q = 300 \pm 40$ kJ mol^{-1} for the activation energy was calculated. This is somewhat higher than the values reported by Theunissen *et al.*[21] (275 kJ mol^{-1}) for a commercial Y-TZP powder and by Durán *et al.*[10] (270 ± 40 kJ mol^{-1}) for a nanoscale Er-TZP powder. Although the activation energy reported here is somewhat lower than that corresponding to a single grain boundary diffusion mechanism[22] (385 kJ mol^{-1}), such a diffusion mechanism is more effective for densification than volume diffusion and, therefore, grain boundary diffusion was assumed to be the main densification mechanism present between 800 and 1180°C. Over this temperature interval a rapid densification takes place, the relative density increasing from about 48 to 97% theoretical density. It is believed that, favoured by the new pore configuration and the sintering pressure, the pores are rapidly eliminated along the grain boundaries, at least in the beginning of this second densification stage. The little grain growth observed at this point indicates that the mobility of the pores was much higher than that of the grain boundaries. Thus the pores, being much smaller than the grain size, and their mobility are believed to have a pinning effect for the grain boundaries and, hence, for grain growth. With increasing relative density and after a certain pore coalescence, the effect of sintering pressure becomes incrementally smaller.[19] Theunissen *et al.*[21] reported a sintering pressure of 70 MPa at 900°C and suggested that at this stage, densification can still be considerable. At 1180°C the relative density was higher than 95% and the average pore diameter was 70 nm: this indicates that the pore surface curvature is small and, therefore, the sintering pressure and its effect on densification will also be very small.[18]

Above 1180°C, a third densification stage could be present. Almost complete densification, about 99·9% theoretical density, is attained and normal

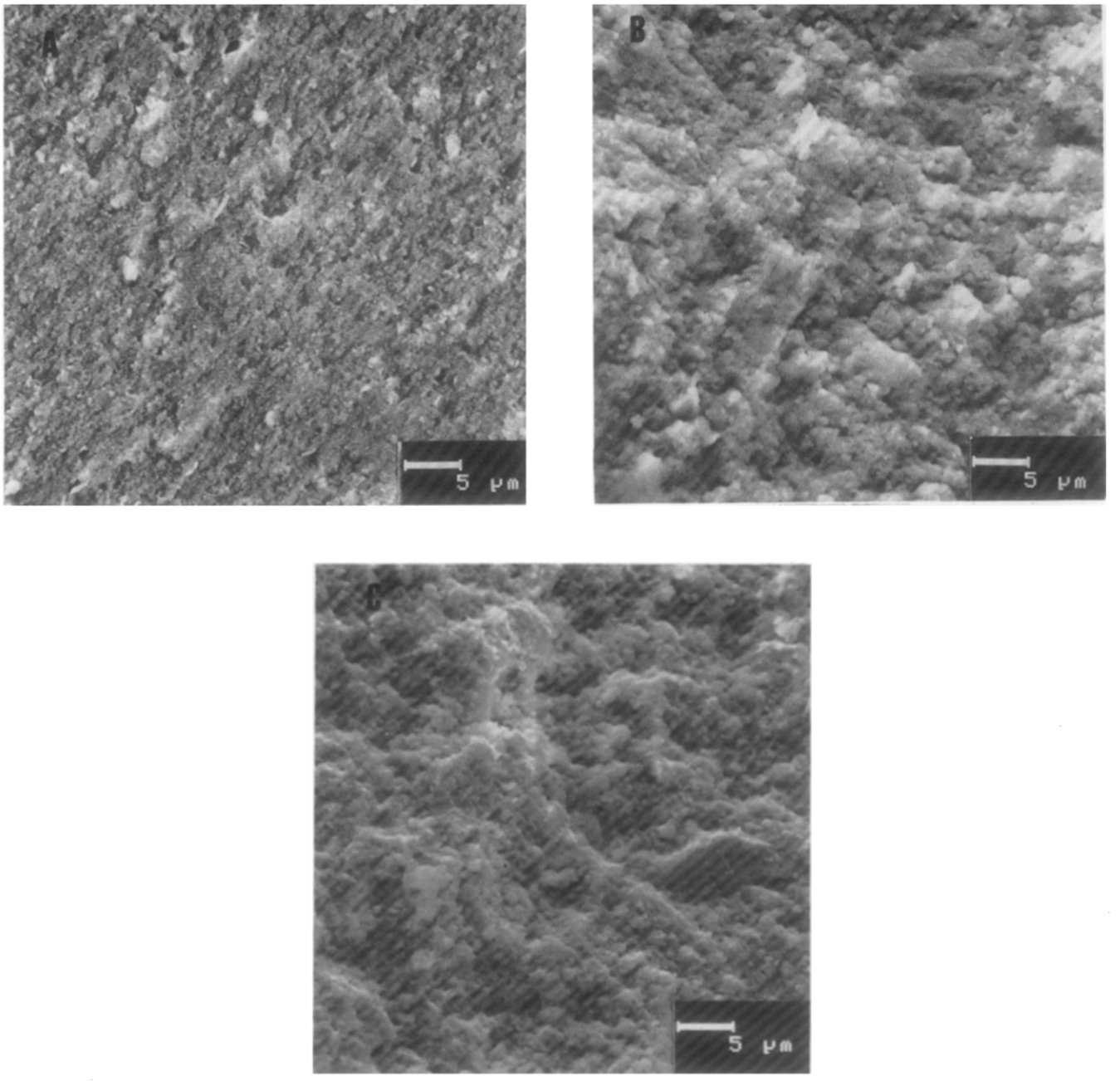

Fig. 8. Microstructure of fracture surfaces in Y-TZP compacts: (A) as-pressed, (B) sintered at 620°C, and (C) sintered at 980°C.

grain growth was observed. At this sintering stage volume diffusion was assumed as the main densification mechanism.

3.4 Isothermal densification

Isothermal sintering behaviour of the Y-TZP powder compacts was studied at temperatures for which the densification was nearly complete and the grain size in the nanometre range. Thus, one of these experiments was performed at the second densification stage (i.e. at 1150°C) and the other at 1200°C (i.e. at the third densification stage). Figure 9 shows the isothermal densification curves for samples sintered at the chosen temperatures. As can be observed, the time dependence of the density was very different at and above 1150°C. At this temperature the density increased continuously, whereas above it the Y-TZP ceramics were fully dense within the first 10–15 min. In the samples sintered at 1150°C, starting with a relative density of 55%, a relative density of 95% was obtained after only 50 min of heat treatment and fully dense bodies were achieved after 4 h. A grain size as low as 85 nm was measured at this point.

In the case of the samples sintered at 1200°C, fully dense Y-TZP ceramics were obtained for sintering times shorter than 20 min with a grain size still below 100 nm. The rapid initial densification confirms the statement that a particle rearrangement process assisted by sintering pressure[23] plays

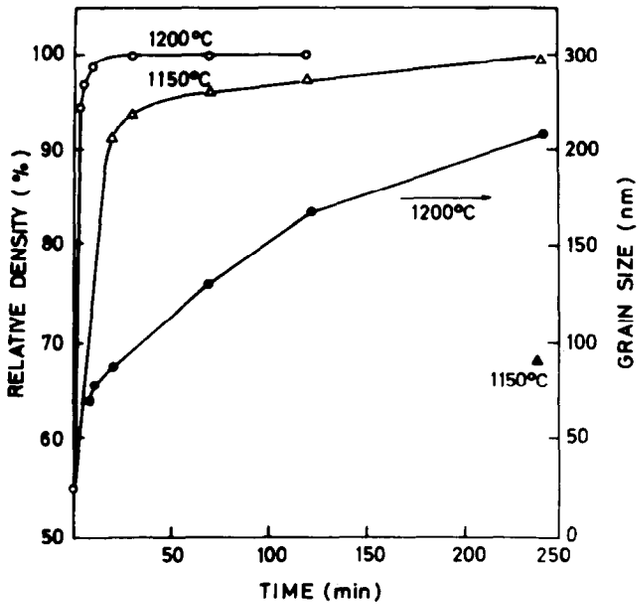

Fig. 9. Isothermal densification behaviour and grain size of Y-TZP compacts as functions of temperature and time.

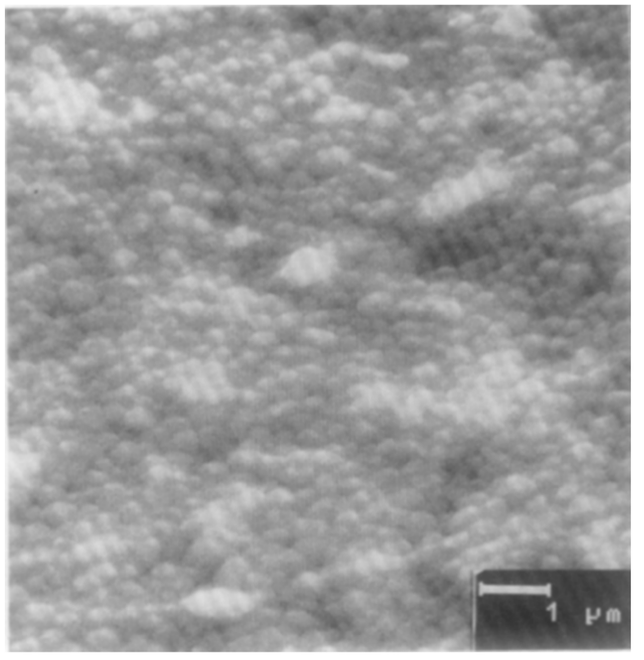

Fig. 10. Microstructure of fully dense Y-TZP compact sintered at 1200°C for 240 min.

an important role in rapid pore elimination at the early densification stage. For longer sintering times the relative density remains constant and relatively rapid grain growth takes place. A grain size of 210 nm was measured after 4 h of sintering (see Fig. 10), which indicates that at this temperature volume diffusion is probably the most important diffusion mechanism. The fact that Y-TZP fully dense ceramics have been obtained at low temperatures (1150–1200°C) with a grain size within the nanometre range (<100 nm) makes it an interesting material for superplastic forming applications. Nanostructured Y-TZP and YCe-TZP ceramics with relatively high densities (90–93% theoretical density) sintered at a temperature as low as 1100°C, using sinter forging as a pressure-assisted densification technique, have recently been reported.[24]

4 Conclusions

From the above experimental results, the following conclusions may be drawn.

(1) Highly sinterable Y-TZP calcined powders, having specific surface areas as high as 90 $m^2\ g^{-1}$ and an average crystallite size of 8–10 nm, can be prepared by the mixed organic and inorganic precursors coprecipitation method.

(2) Owing to the unusual characteristics of the Y-TZP calcined powders (very small and soft arrays of three to five particles) and the sharp pore size distribution in the green compacts, fully dense ceramics with a grain size in the nanometre range (<100 nm) were obtained at a sintering temperature as low as 1150°C for 4 h or at 1200°C for much shorter (~20 min) sintering times.

(3) From the constant-rate heating sintering experiments several (at least three well defined) densification steps could be established but it was very difficult to determine the start and the end of each of them. A first step comprising a particle rearrangement process assisted by sintering pressure seems to be present up to ~800°C. The low activation energy value calculated for this densification step (130 ± 40 kJ mol^{-1}) cannot be associated with any of the known diffusional mechanisms. A second densification step, in which rapid densification (≥ 95% dense) occurs with slow grain growth, takes place between 800 and 1180°C, and it was considered as the most important in the whole densification process. The activation energy value calculated for this second densification step (300 ± 40 kJ mol^{-1}) could be well correlated to grain boundary diffusion as the main densification mechanism. Finally, a third densification step is considered to exist above 1180°C in which almost fully dense Y-TZP ceramics were achieved. At this densification step a normal grain growth process occurred, and volume diffusion was assumed to be the dominant densification mechanism.

(4) From the isothermal sintering experiments at 1150 and 1200°C, it can be stated that the rapid initial densification indicates an important role of the particle rearrangement

in the early densification step, supporting the above contention. Such a particle rearrangement process led to a new pore configuration which favoured both pore elimination along the grain boundaries and rapid densification during the first minutes in the second sintering stage.

(5) The small crystallite size of the Y-TZP calcined powders, the small crystallite arrays in the compacts, and the low activation energy for densification leading to dense ceramics at low temperature, in spite of the low green compact density, reveal the usefulness of the mixed organic–inorganic precursors precipitation method for preparing highly sinterable Y-TZP powders.

Acknowledgement

This research was supported in part by the European Commission under contract JOUE-044C.

References

1. Mackenzie, J. D., Applications of sol–gel methods for glass and ceramics processing. In *Ultrastructure Processing of Ceramics, Glasses and Composites*, eds L. L. Hench & D. R. Ulrich. Wiley, New York, 1984, pp. 15–26.
2. Barringer, E. A. & Bowen, H. K., Formation, packing and sintering of nanodisperse TiO_2 powders. *J. Am. Ceram. Soc.*, **65** (1982) c-199–201.
3. Zhou, Y. C. & Rahaman, M. N., Hydrothermal synthesis and sintering of ultrafine CeO_2 powders. *J. Mater. Res.*, **8** (1993) 1680–6.
4. Dubois, B., Ruffier, R. & Odier, P., Preparation of fine spherical yttria stabilized zirconia by the spray pyrolysis method. *J. Am. Ceram. Soc.*, **72** (1989) 713–15.
5. Zhou, Y. C., Phillips, R. J. & Switzer, J. A., Electrochemical synthesis and sintering of nanocrystalline cerium oxide powders. *J. Am. Ceram. Soc.*, **78** (1995) 981–5.
6. Lange, F. F., Transformation-toughened ZrO_2: Correlations between grain size control and composition in the system ZrO_2–Y_2O_3. *J. Mat. Sci.*, **17** (1982) 240–2.
7. Winnubst, A. J. A. & Burggraaf, A. J., The aging behaviour of ultrafine-grained Y-TZP in hot water. In *Advances in Ceramics, Vol. 24A, Science and Technology of Zirconia III*, eds S. Somiya, N. Yamamoto & H. Yanagida. The American Ceramic Society, Inc., Columbus, OH, 1989, pp. 39–47.
8. Panda, P. C., Wang, J. & Raj. R., Sinter forging characteristics of fine-grained zirconia. *J. Am. Ceram. Soc.*, **71** (1988) c-507–9.
9. Boutz, M. M. R., Winnubst, A. J. A., Burggraaf, A. J., Nauer, M. & Carry, C., Low temperature superplastic flow of Y-TZP. *J. Eur. Ceram. Soc.*, **13** (1994) 103–11.
10. Durán, P., Recio, P., Jurado, J. R., Pascual, C. & Moure, C., Preparation, sintering and properties of translucent Er_2O_3 doped tetragonal zirconia. *J. Am. Ceram. Soc.*, **72** (1989) 2088–93.
11. Klug, K. P. & Alexander, L. E., *X-Ray Diffraction Procedures*. John Wiley and Sons, New York, 1974.
12. Fullman, R. L., Measurement of particle size in opaque bodies. *J. Metals, Trans. AIME*, **197** (1953) 447–52.
13. Navarro, L., Recio. P. & Durán, P., Preparation and properties evaluation of zirconia-based/Al_2O_3 composites as electrolytes for solid oxide fuel cells systems. *J. Mater. Sci.*, **30** (1995) 1931–8.
14. Niesz, D. E., Benet, R. B. & Snyder, H. J., Strength characterization of powder aggregates. *Am. Ceram. Soc. Bull.*, **51** (1972) 677–80.
15. Matsumoto, R. L. K., Analysis of powder compaction using compaction rate diagram. *J. Am. Ceramic. Soc.*, **73** (1990) 465–8.
16. Young, W. S. & Cutler, I. B., Initial sintering with constant rate of heating. *J. Am. Ceram. Soc.*, **53** (1970) 659–63.
17. Petzow, G. & Exner, H. E., Particle rearrangement in solid state sintering. *Z. Metalled*, **67** (1976) 611–8.
18. Raj, R., Analysis of the sintering pressure. *J. Am. Ceram. Soc.*, **70** (1987) c-210–11.
19. Venkatachari, K. R. & Raj, R., Shear deformation and densification of powder compacts. *J. Am. Ceram. Soc.*, **69** (1986) 499–506.
20. Olmo, L. D., Durán, P. & Moure, C., Sintering of a Yttria-stabilized zirconia. In *Materials Science Monographs, Vol. 14, Sintering Theory and Practice*, eds D. Kolar, S. Pejonik & M. M. Ristic. Elsevier, Amsterdam, The Netherlands, 1982, pp. 401–8.
21. Theunissen, G. S. A. M., Winnubst, A. J. A. & Burggraaf, A. J., Sintering kinetics and microstructure development of nanoscale Y-TZP ceramics. *J. Eur. Ceram. Soc.*, **11** (1993) 315–24.
22. Jorgensen, P. J., Diffusion-controlled sintering oxides. In *Sintering and Related Phenomena*, eds G. C. Kuzynski, N. A. Hooton & C. F. Gibbon. Gordon and Breach, New York, 1967, pp. 401–22.
23. GrootZevert, W. F. M ., Winnubst, A. J. A., Theunissen, G. S. A. M. & Burggraaf, A. J., Powder preparation and compaction behaviour of fine-grained Y-TZP. *J. Mater. Sci.*, **25** (1990) 3449–55.
24. Boutz, M. M. R., Winnubst, L., Burggraaf, A. J., Nauer, M. & Carry, C., Low temperature sinter forging of nanostructured Y-TZP and YCe-TZP. *J. Am. Ceram. Soc.*, **78** (1995) 121–8.

Journal of the European Ceramic Society **16** (1996) 953–959

S0955-2219(96)00013-1
0955-2219/96/$15.00

On the Brittle-to-Ductile Transition of Y-PSZ Single Crystals

A. D. Vasilev, S. A. Firstov, A. V. Shinkaruk, O. A. Babiy & A. V. Sameliuk

Department of Physics of Strength and Plasticity of Materials, Francevich Institute for Problems of Materials Science, Kyiv, 252680, Ukraine

(Received 7 June 1995; revised version received 13 December 1995; accepted 5 January 1996)

Abstract

The fracture behaviour (fracture mechanisms, fracture toughness, and strength) of yttria-partially stabilized zirconia (Y-PSZ) single crystals has been investigated between room temperature and 1700°C. Cleavage was the fracture mechanism acting over the entire temperature interval studied, with some plastic elements arising at temperatures of 1000°C and above, accounting for the increasing fragmentation with temperature observed for the precipitation-hardened materials. Fragmentation is ensured from interdomain cleavage on {1 0 0} and {1 1 0} planes. No subcritical cracks were observed. The strength and fracture toughness follow behaviour typical for materials with a pronounced brittle-to-ductile transition. After a gradual decrease between room temperature and 1000°C, both properties show a sharp increase under elevated temperatures, followed by a sharp decrease. This increase is associated with dislocation plasticity revealed in delaminations along {1 1 0} and {1 0 0} planes. The lower temperature limit of the brittle-to-ductile transition was estimated as 1000°C. A higher limit was not reached and the transition of Y-PSZ [1 0 0] single crystals into a ductile state probably occurs at about 2000–2100°C. The mechanism of ductile fracture is presumably intergranular sliding of grains, formed in the course of plastic deformation, from domain microstructure.

1 Introduction

For a long time, zirconia as well as zirconia ceramics were considered as materials only for low-temperature application. Mainly for this reason their high-temperature mechanical and fracture behaviour has not been the subject of intensive systematic study. Lack of interest in high-temperature behaviour was due to the belief that the mechanical properties of some zirconia materials drop too drastically with temperature,[1,2] therefore investigators generally did not extend testing to high temperatures to determine the behaviour above 1000–1200°C.

At the same time, an investigation of the brittle-to-ductile transition of different refractory materials, metallic and ceramic, has shown that after some decrease in properties, properly tailored brittle materials can develop a pronounced enhancement of strength and fracture toughness at high temperatures.[3] For polycrystalline materials, this enhancement depends strongly on the chemical composition of the grain boundaries as well as the grain size. Granular structure facilitates the transition of a body from a brittle state into a ductile one via high-temperature intergranular sliding. Before it can fall into a ductile state, the single crystalline material has to form a new dislocation, similar to a polycrystalline structure, during the predeformation stage. Only after this event can the single-crystal material use the intergranular sliding mechanism of failure.[4]

This phenomenon has received little investigation in the case of zirconia ceramics, and is the reason why this study was undertaken. The specific objective was to obtain systematic data on the fracture mechanisms of yttria- partially stabilized zirconia (Y-PSZ) single crystals during the temperature-induced brittle-to-ductile transition, using tests for strength and fracture toughness of a limited number of samples.

2 Material and Experimental Techniques

As materials for the study, partially stabilized (by 6 mol% of yttria) zirconia single crystals, grown by scull melting in the Francevich Institute for Problems of Materials Science, were used.

Since the scull-melting technique gives comparatively small crystals with a high scatter of directions, only a limited number of specimens, that were nearly similar in composition, was available for analysis. We succeeded in finding about 30 samples to study, to a first approximation, the temperature dependence of the strength of smooth

and notched samples, using only one sample for each temperature selected in both tests.

Samples of dimensions 3 × 4 × 45 mm, oriented (using the X-ray technique) along the [1 0 0] direction, were cut by a diamond saw, carefully ground and polished with diamond abrasives of up to 1.0 μm grain size. The processed samples, with a discrepancy of [1 0 0] directions of approximately 10' were annealed in air at 1600°C for 8 h and furnace-cooled. They were then tested in a three-point bend in a vacuum of ~10^{-3} Pa at temperatures between room temperature and 1700°C, with a loading frame rate of ~10^{-3} m min^{-1}. Samples for fracture toughness testing were notched with a diamond saw to a radius of ~50 μm.

The structure of the thin sample sections was examined using transmission electron microscopy (TEM; Jeol JEM 100 CX II). Fracture mechanisms were studied by scanning electron microscopy (SEM; Jeol Superprobe-733).

3 Results and Discussion

TEM shows that the materials under study consisted of three {1 1 2} type tetragonal variants or ferroelastic domains[5] with sizes of 2 × 0·2 μm, as seen in the dark-field images of Figs 1(a), (b) and (c) and the electron diffraction pattern of Fig. 1(d). The twin boundaries lay in the (1 1 0) planes of a pseudo-cubic symmetry. The dark-field image of {1 1 2} type reflections for the [1 1 1] beam reveals that {1 1 2} tetragonal variants have slightly different volumes due to the release of mechanical stresses.

The temperate dependences of flexural strength and fracture toughness for the partially stabilized tetragonal zirconia single crystals, derived using only one sample for each temperature, are shown in Fig. 2. Nevertheless, it can be seen that the data lie on curves that are typical for materials with a pronounced brittle-to-ductile transition.[3] Strength decreases from ~1000 to 400 MPa within a temperature range between 300 and 1000°C, after which it increases rather sharply up to ~1.2 GPa with the maximum at 1300–1500°C. At 1700°C the single crystals again have a bend strength of ~700 MPa. Similarly to bend strength, the fracture toughness decreases from 7 to 4 MPa $m^{1/2}$ in the temperature interval between room temperature and 1300°C. After 1300°C K_{1c} increases rather sharply, reaching 18 MPa $m^{1/2}$ at 1700°C. The high-temperature maximum as well

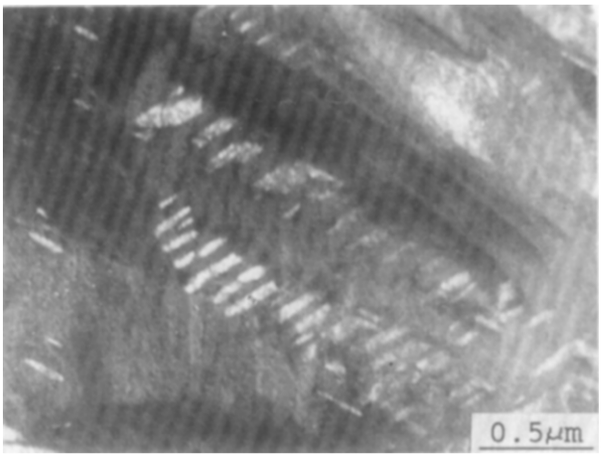

(a)

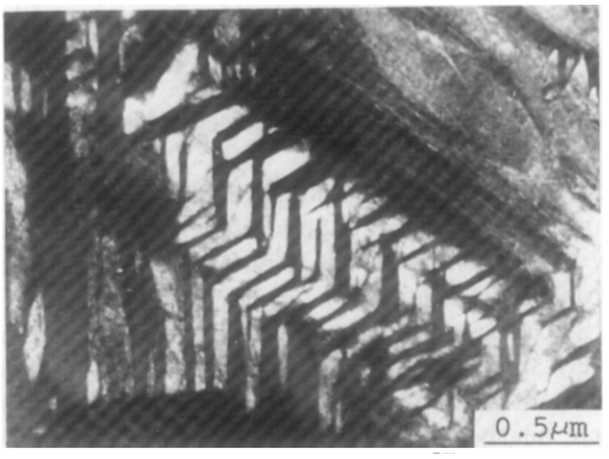

(c)

(b)

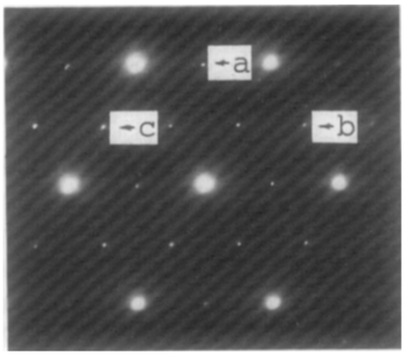

(d)

Fig. 1. (a), (b), (c) TEM dark-field images and (d) diffraction pattern of three {1 2 2} tetragonal twin variants of partially stabilized zirconia single crystals in a [1 1 1] zone axis.

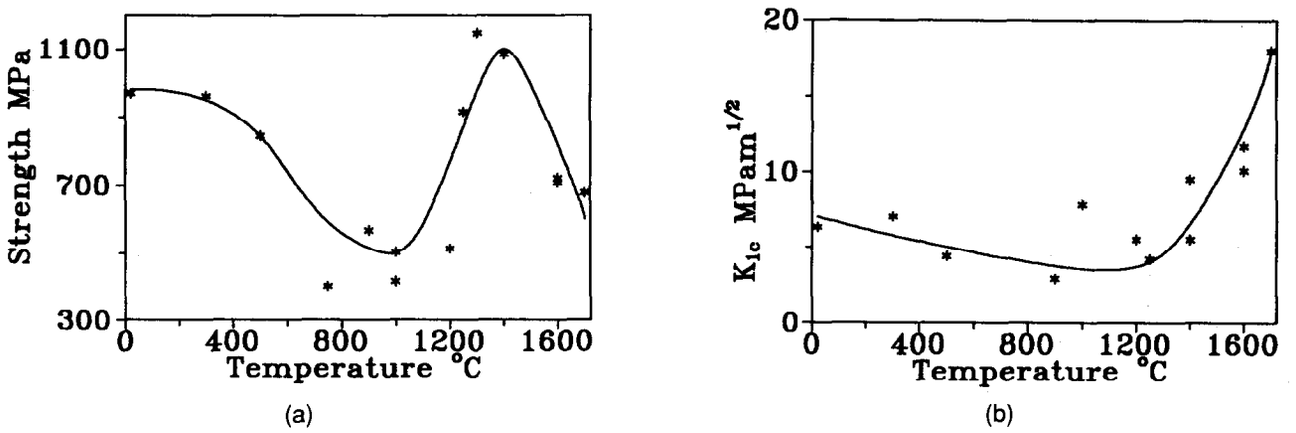

Fig. 2. Temperature dependences of the flexural strength and fracture toughness of partially stabilized zirconia single crystals.

as the following decrease of fracture toughness will probably be achieved at higher temperatures. This means that the maximum of fracture toughness is achieved at a temperature 300–400°C higher than that of bend strength. The low-temperature part of our data is close to that published earlier.[1]

Fractographical analysis shows that the main fracture mechanism is cleavage. This acts over the entire temperature interval investigated, from room temperature up to 1700°C, in both types of samples: notched and unnotched. No subcritical cracks preceding cleavage were observed.

3.1 Unnotched samples

The fracture surface features of the unnotched samples may be detailed as follows.

(1) Fracture originates from the side surfaces

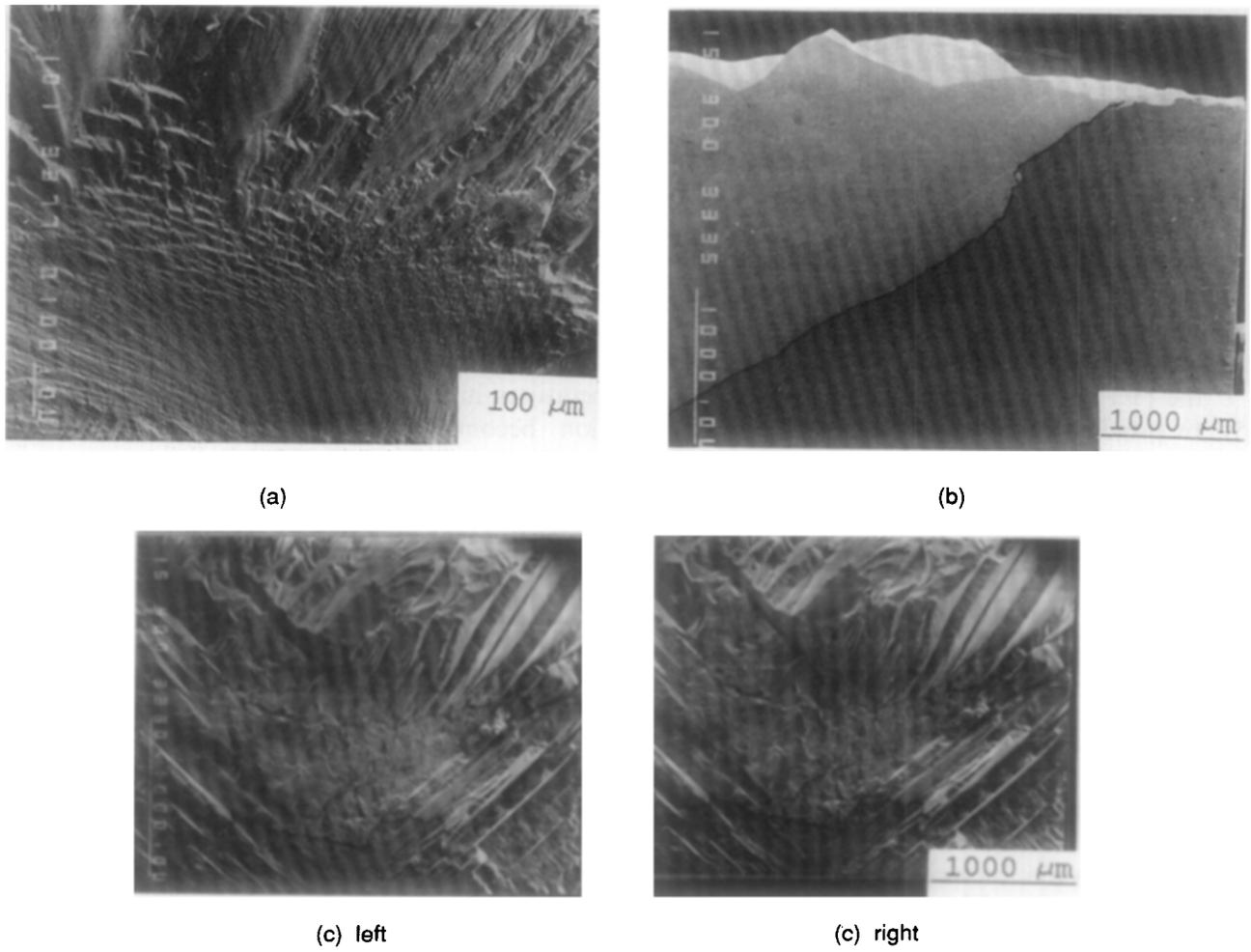

Fig. 3. SEM micrographs of fracture surfaces of Y-PSZ single crystals tested for strength at different temperatures. (a) Cleavage and Wallner lines at 900°C, cracking starts from the sample side surface; (b) view of crack branching on the sample side surface at 1600°C; (c) double branching and rough delaminating cracks in the fracture surface. Stereopair: (d) fan-like pattern in fracture surface at 1250°C; (e) recrystallized surface layer at 1600°C.

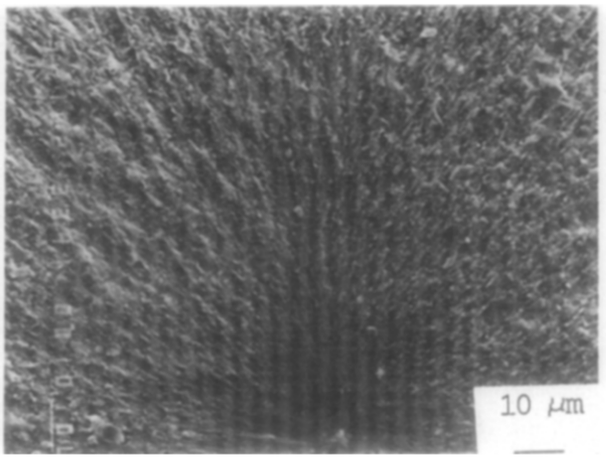

(d)

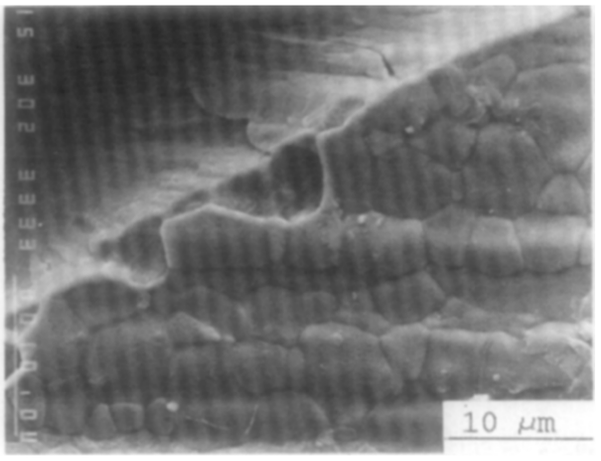

(e)

Fig 3. Continued.

of the samples in all cases [Figs 3(a), 3(c), 3(d)]. Cracks begin from stress concentrators such as grinding flaws or edges, and at the beginning actually lie in the crystallographic surfaces close to {1 0 0} as shown earlier.[1] Sometimes, cracks lying in {1 1 0} planes may be observed in side surfaces.

(2) Up to 1000°C the fracture surfaces have no distinguishing features except for chop–offs opposite the original side of the sample and Wallner lines [Fig. 3(a)].

(3) Beginning at 1000°C, dynamic crack branching with an angle of about 30–35° may be seen [Figs 3(b), 3(c)]. Some samples show double branching [stereopair in Fig 3(c)].

(4) Also beginning from 1000°C, rough delaminating cracks may be seen [Fig. 3(c)]. Samples tested at 1700°C additionally show fine cracks; these are transverse to the rough and deep cracks. Delaminating cracks lie in the {1 1 0} planes.

(5) In principle, the second phases (as well as some likenesses of them) in zirconia single crystals should give rise to some fragmentation of the cleavage surface.[6] This may actually be seen under higher magnification in all samples, as will be demonstrated later for notched samples [see, for example, Figs 4(a) and (b)].

(6) For all the temperatures studied, the directions of cleavage, crack propagation in the {1 0 0} planes is practically indifferent to the crystallographic orientations of the crystals. This conclusion follows from the fan-like pattern in the fracture surface [Fig. 3(d)].

(7) The surface defects acting as origins of cleavage at temperatures of 1400°C and above are probably intergranular cracks of the recrystallized surface layer, and are clearly seen on the surface of high-temperature samples [Fig. 3(e)]. The thickness of the recrystalized surface layer is ~1–3 μm and its structure inherits the directions of scratches on the sample surface resulting from mechanical processing with diamond powders. Recrystallized grains with a size of ~2–10 μm peel off during crack propagation.

3.2 Notched samples

The predefined location of the process-zone, as well as the suppression of common plastic deformation by the notch, almost completely eliminates some features that are visible on the fracture surfaces of smooth, unnotched samples. First of all, for the notched samples, the fracture surface is rather flat over the temperature interval between room temperature and 1300°C. Only hems and a slight growth of fragmentation sharpness with temperature may be seen ([Figs 4(a) and 4(b)]). Dynamic crack branching is only observed at temperatures higher than 1300°C, whereas delamination becomes slightly visible only at 1700°C [compare Figs 4(c) and (d)].

Thus the fractographical analysis clearly shows that, in spite of the flexural strength passing its high-temperature maximum, the transition of the tetragonal PSZ single crystals of the [1 0 0] orientation into the plastic state is not completed at 1700°C because the fracture mechanism is not changed. Cleavage takes place in the {1 0 0} plane as well as {1 1 0}. The lower-temperature boundary of the brittle-to-ductile transition, in accordance with Ref. 3, may be determined as ~1000°C, at which temperature some marks of plastic deformation can be found in the fracture surface. Such marks are delaminating cracks [Fig. 3(c)]; the number and their delaminating ability grow with temperature. Delaminating cracks are parallel to the {1 1 0} planes and are probably original, lying in those planes where the boundaries of domain microstruc-

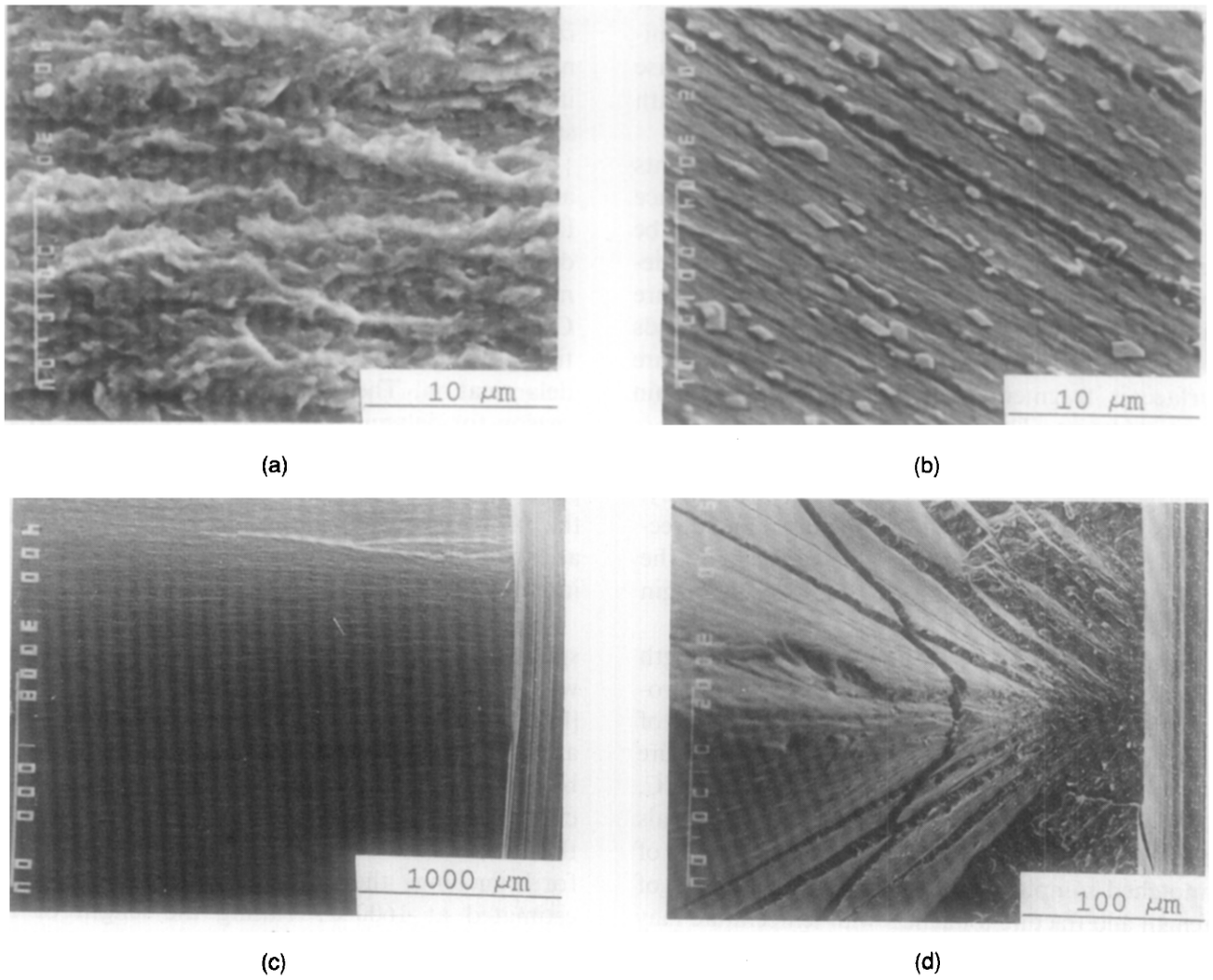

Fig. 4. SEM micrographs of fracture surfaces of Y-PSZ single crystals tested for fracture toughness at different temperatures. (a) Low-temperature fragmentation of cleavage surface at 20°C; (b) high-temperature fragmentation of cleavage surface at 1700°C; (c) crack starts from the notch at 20°C; (d) crack branching and delamination at 1700°C.

ture are located. By analogy with refractory metals, e.g. Mo,[6] microplasticity may result in crack nucleation, namely in boundaries. These cracks divide the crystal into microcrystals separated by delaminating interfacial cracks. Every delaminating microcrystal deforms separately. Some of them may develop rather high plasticity preceding fracture and fail in a ductile manner with the formation of knife-like fracture as seen in the stereopair of Fig. 5. As may be observed, some parts of the knife may fail, equally, as well as the cleavage.

Microplasticity resulting in delaminations may be the reason for the strength enhancement with temperature, due to relaxation of stresses. Increasing

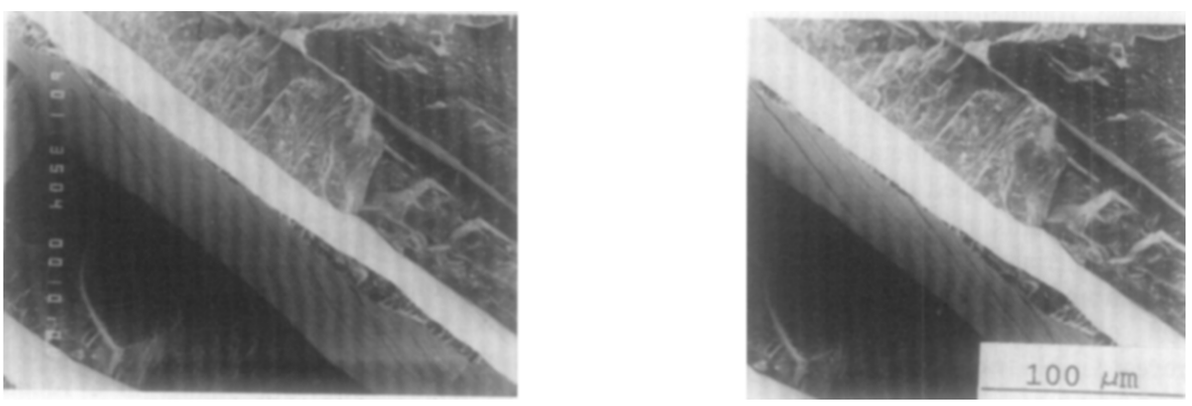

Fig. 5. The knife-like fracture in Y-PSZ single crystals at 1700°C. Stereopair.

delaminations result in decreasing strength at higher temperatures. During this time, the delaminations promote the fracture toughness increase observed in the fracture toughness behavior with temperature.

Delaminations are practically the only elements of ductile fracture observed on the fracture surface at 1000°C. For this reason, this temperature may be determined as the lower boundary of the brittle-to-ductile transition. Therefore the temperature range from low temperatures to 1000°C corresponds to the area of brittle fracture. The cleavage fracture surface is fragmented by boundaries of domain microstructure. The fragmentation becomes more visible with temperature, revealing the growing role of interdomain boundaries at high temperatures. Cleavage planes are of the {1 1 0} or {1 1 0} family. Cracks propagate in the {1 0 0} plane in any direction without any preference, as evidenced by the fan-like pattern of fracture in the area of origin [Fig. 3(d)].

Comparing fracture toughness and strength behaviours (Fig. 2), it is possible to see their proportional reductions with temperature: the factor of reduction is about 2·3. In the very wide temperature interval from room temperature up to about 1200°C, the fracture toughness of Y-PSZ single crystals behaves in the same manner as the strength of unnotched samples. These identical behaviours of strength and fracture toughness with temperature may indicate the independence of fracture toughness, determined in practice from the concept of $K_{1c} = \sigma\sqrt{\pi c}$, on the parameters of the rather blunt notch. This may be correct in the case where fracture behaviour is controlled by inner, stronger concentrators of stresses than outer ones. The outer concentrators localize the place of failure, whereas actual fracture stresses are produced by inner defects. Such defects may be mainly microcracks; those in our case have an interdomain or interphase nature. Exactly which interphase, interdomain microcracks determine the mechanical behaviour of Y-PSZ single crystals is indicated by the views of cleavage fracture surfaces with intensive fragmentation and delamination [Figs 3(c), 4(a) and 4(b)]. Fragmentation of the cleavage surface by dislocations only cannot give such an intensive and developed fragmentation. Strongly deformed ionic[4] or metallic[6] single crystals do not reveal the developed delaminating relief of fracture surface. This is typical for dispersion-strengthened materials with weakly cohesive particles delaminating from the matrix under loading.[6] Even steels containing well-known iron carbides do not reveal visible fragmentation of the cleavage surface.

Fragmentation of the cleavage fracture surface in Y-PSZ single crystals results from the special defect structure of these crystals. Defects are localized in the {1 0 0} and {1 1 0} planes, forming a network of boundaries (Fig. 1). The crystal loses its homogeneity and assumes the so-called domain structure with the stressed boundaries lying in the {1 0 0} and {1 1 0}, crystallographic planes, which at that time are revealed as cleavage planes. All this facilitates strong microcracking along these interdomain boundaries, thereby ensuring the important mechanism of fracture toughness enhancement. Crystallographic tetragonal–monoclinic transformation also facilitates microcracking and subsequent delamination. The fact that microcracking is the reason for delamination may be confirmed by the appearance of delaminating cracks containing clearly visible cleavage steps in Fig. 5. Growing with temperature, the dislocation microplasticity intensifies the process of damage accumulation by boundaries and thereby also facilitates the nucleation of interdomain cracks.

The transition to ductile fracture under the specified loading condition begins at ~1000°C with the appearance of rough delaminating cracks [Fig. 3(c)]; the dynamic cleavage crack branching also becomes apparent at this point. The angle of branching, as may be observed in Fig. 3(b), is close to 35°. Taking into account the assumption that twice the elastic deformation energy is needed for branching,[7] the surface energy of fracture was estimated at 1600°C. Taking the length of the cleavage crack before branching to be 0·3 mm [Fig. 3(c)] the surface energy for cleavage was found to be equal to 500 J m^{-1}; this corresponds to a fracture toughness of 11·7 MPa $m^{1/2}$, measured with notched samples.

Unfortunately, we did not succeed in observing the ductile fracture of Y-PSZ single crystals. The upper temperature limit probably lies far above 1700°C and the temperature required could not be attained with testing equipment available. In full analogy with the fracture behaviour of model ceramics, namely NaCl single crystals,[4] and being based on plastic delamination as a forerunner of the plastic nucleation of intergranular (interdomain) cracks, we conclude that intergranular sliding of grains formed in the process of plastic deformation preceding fracture, might be the mechanism by which ductile fracture (like dimple fracture) occurs at elevated temperatures. The transition of Y-PSZ {1 0 0} single crystals into ductile fracture might occur between 2000 and 2100°C.

It was found also that recrystallization of the damaged, mechanical processing surface layer takes place at temperatures of 1600°C (i.e. 0·64 times the melting temperature) and higher in a vacuum of 10^{-3} Pa, leading to peeling of the polycrystalline scale (~1–3 μm) under loading [Fig. 3(e)]. In principle,

this indicates that there is a possibility to control the structure as well as the properties of zirconia ceramics by high-temperature plastic deformation and heat treatment.

4 Conclusions

Y-PSZ [1 1 0] single crystals exhibit a pronounced brittle-to-ductile transition that occurs at temperatures between 1000 and 2000–2100°C. At around 1400°C the samples possess a strength that is 20–30% greater than at low-temperature and more than twice the fracture toughness. Cleavage was the fracture mechanism over the whole range of temperatures studied, its action probably extending up to 2100°C. Cleavage planes are the {1 0 0} and {1 1 0} habit ones. The cleavage surface is fragmented by interdomain boundaries as is attributed to precipitation–hardened materials. Fragmentation and delamination at elevated temperatures result from microcracking along interdomain boundaries lying in the {1 0 0} and {1 1 0} planes. Plastic deformation enhances fragmentation. Cleavage crack propagation is independent of crystallographic orientation. Dynamic crack branching takes place in the brittle-to-ductile transition and was observed in both notched and unnotched samples after some plastic deformation. No subcritical cracks preceding cleavage were observed. Recrystallization of a surface layer damaged by mechanical processing occurs at 1400°C and above. Single crystals are covered by a polycrystalline peeling film. Intergranular cracks nucleating in this film originate cleavage in the bulk of specimens. The probable mechanism of ductile fracture at temperatures near 2000°C is intergranular sliding of grains formed during plastic deformation preceding fracture.

In this case of brittle fracture by cleavage, the temperature dependence of fracture toughness is proportional to that of strength. Mechanical behaviour is determined only by the inner defects; these are interdomain microcracks also resulting in fragmentation of the cleavage surface. The notches in samples for fracture toughness tests only localize the place of fracture and prevent general yielding of the samples under elevated temperatures, thereby shifting the upper limit of the brittle-to-ductile transition to higher temperatures (up to 2000–2100°C).

Acknowledgements

This research was supported by the State Committee of Science and Technology of Ukraina under Program 07.04.01, 'New materials and components based on zirconia'. The authors would also like to thank Dr O. Bakun for performing the mechanical testing experiments and Mr R. Sculthorp for making our English more understandable.

References

1. *Transformation Toughening of Ceramics*, eds D. J. Green *et al.* CRC Press Inc., USA, 1993, pp. 126–37.
2. Tikare, V. & Heuer, A. H., Temperature-dependent indentation behavior of transformation-toughened zirconia based ceramics. *J. Am. Ceram. Soc.*, **74** (1991) 593–9.
3. Vasilev, A. D., The temperature dependence of fracture toughness of materials undergoing a brittle–ductile transition. In *Proc. European Conf. on Fracture Behavior and Design of Materials and Structures*, ed. D. Firrao. EMAS Ltd, London, 1990, pp. 92–7.
4 Betekhtin, V. I., Bakhtibaev, A. N., Vasilev, A. D., *et al.*, Fractographical investigation of fracture mechanisms of NaCl single crystals undergoing a brittle–ductile transition. In *Proc. European Conf. on Fracture Behaviour and Design of Materials and Structures*, ed. D. Firrao. EMAS Ltd, London, 1990, pp. 556–9.
5. Than, C.J., Range, F.F. & Ruhle, M., Ferroelastic domain switching in tetragonal zirconia single crystals. Microstructural aspects. *J. Am. Ceram. Soc.*, **74** (1991) 807–13.
6. Vasilev, A.D., Scanning electron fractography of body centered cubic (BBC) metals. *Scanning Electron Microsc. III*, (1988) 917–32.
7. Broek, D., *Elementary Engineering Fracture Mechanics*. Noordhoff International Publishing, Leyden, 1974, 256 pp.

Journal of the European Ceramic Society 16 (1996) 961–973

S0955-2219(96)00012-X
0955-2219/96/$15.00

Sintering Behaviour and Ionic Conductivity of Yttria-Doped Ceria

Jan Van herle,* Teruhisa Horita,† Tatsuya Kawada, Natsuko Sakai, Harumi Yokokawa & Masayuki Dokiya

National Institute of Materials and Chemical Research, 1-1 Higashi, Tsukuba Science City, 305 Ibaraki, Japan

(Received 29 September 1995; revised version received 11 December 1995; accepted 5 January 1996)

Abstract

Highly sinterable yttria-doped ceria powder $(YO_{1.5})_x(CeO_2)_{1-x}$ *(*$x = 0.1$–0.33*) was fabricated by an optimized coprecipitation route. Compacted bodies could be sintered to impermeability at 1200°C and near full density at 1300°C, among the lowest temperatures reported for doped ceria densification. Ceria diffusion is important above 1400°C. Excellent conduction properties were observed: high ionic conductivity (6·5 S* m^{-1} *at 750°C for* $Ce_{0.8}Y_{0.2}O_{1.9}$*), low activation energy (0·7 eV) and vanishing grain-boundary resistance. © 1996 Elsevier Science Limited.*

1 Introduction

Doped ceria is a solid electrolyte that is becoming increasingly attractive for use in solid oxide fuel cells (SOFC) because of its high oxygen ion conductivity, among other advantages. Whereas the routinely used but less conducting yttria-stabilized zirconia (YSZ) electrolyte has long been established in SOFC application in terms of fabrication methods, mechanical strength and chemical stability, these topics are now under investigation for the ceria-based materials.

In terms of a fabrication method, we focused on the powder preparation of doped ceria for tape casting,[1] which is a practical, industrial technique. The simple and reliable doped ceria preparation method yields active powder that is sinterable to high densities at low temperatures. High density, which was found difficult to achieve for ceria even at high temperatures until recently,[1] results in better mechanical and conduction properties.

*Present address: Ecole Polytechnique de Lausanne, Dpt. Chemistry, Institute of Physical Chemistry II, 1015 Lausanne, Switzerland.
†To whom correspondence should be addressed.

As for chemical stability in the SOFC environment, a popular solution tends towards the combination of doped ceria with a thin protective layer of the established and very stable YSZ electrolyte.[2,3] This goal in turn re-emphasizes the requirement for ceria to densify at lower temperatures than usually employed (1600°C) if, for example, cofiring of a double-layered tape-cast ceria–zirconia structure is pursued. Low temperature cofiring (<1500°C) is necessary to avoid interdiffusion. For the same reason, yttrium is used as a dopant rather than the more popular gadolinium or samarium, since the thin zirconia is yttria-doped. Furthermore, ceria is known to exhibit evaporation — or dissociation — problems at high temperature.[4]

In this study, sintering of compacts of $Ce_{0.667}Y_{0.333}O_{1.833}$ (33YDC) is investigated at temperatures between 1200 and 1600°C, with attention to densification and evaporation of the samples. A composition with a high yttrium content was purposely chosen since it supposedly densifies with greater difficulty than compositions of lower dopant concentration.[5]

Low grain boundary conductivity is also a well-known problem of ceria-based electrolytes.[6–9] It sometimes dominates the overall conductivity at low temperature, and may persist up to operation temperature (700°C). For SOFC application, the grain-boundary resistivity should ideally vanish at the projected operating temperature. The grain-boundary resistivity is reported to be a strong function of the dopant content.[9–11]

Powders in the composition range 10–33% $YO_{1.5}$ dopant concentration were synthesized and sintered to fully dense compacts in order to study the grain-boundary and total conductivity of YDC as a function of the composition. The maximum in ionic conductivity is generally believed to lie at around 5% oxygen vacancy concentration,[12] hence around 20% doping with the trivalent yttrium, but experimentally reported to range between 8

and 20% of $YO_{1.5}$ doping, depending on the temperature.[10,13–18]

Finally, an example of the correlation between density and conductivity will be given, illustrating the relevance of pursuing high density for solid electrolytes to ensure, apart from mechanical strength, the best conduction properties.

2 Experimental

The YDC powders (10–33% $YO_{1.5}$–CeO_2) were prepared by the oxalate coprecipitation method. The detailed procedure is published elsewhere.[1] In summary, it involves addition of a concentrated Ce–Y-nitrate aqueous solution (1 mol l^{-1}) under stirring to a neutral dilute oxalic acid aqueous solution (0·05 mol l^{-1}). The resulting precipitate is vacuum-filtered, washed with water and ethanol, and calcined at 700°C. This temperature was optimal to yield very compactable powder and normal shrinkage, resulting in crack-free pellets of high density. Powders of accurate composition were prepared from standardized metal nitrate solutions. The metal content of individual cerium and yttrium nitrate solutions was determined by complexometric titration with 0·01 M EDTA solution, using xylenolorange as the indicator. Direct titration could be carried out using an acetic acid/sodium acetate buffer to stabilize the solution at pH 5.

2.1 Sintering behaviour

Pellets of 33YDC, with or without prior ball milling of the powders, were pressed at 200 MPa (20 mm diameter, 1–2 mm thick) and fired at 1200–1600°C for the sintering behaviour study. Densities were measured by Archimedes' method (H_2O) and expressed as relative to the experimentally determined X-ray density [1]. Scanning electron microscopy (SEM) analysis of all samples was conducted in a Hitachi S-800 electron microscope model with an energy-dispersive X-ray (EDX) facility. With respect to the problem of ceria loss at high temperature, the metal ratio of 2:1 for Ce:Y in the $Ce_{0.667}Y_{0.333}O_{1.833}$ composition provided a convenient reference for semi-quantitative EDX analysis.

2.2 Ionic conductivity

Pellets of 10, 15, 20, 25 and 33YDC were fired fully dense at 1500°C for the conductivity study. Ionic conductivity in air at temperatures between 300 and 1000°C was measured by impedance spectroscopy in a small tubular oven. Silver electrodes of 10 mm diameter were applied by brushing silver paint symmetrically on opposite sides of the pellets using a masking technique. Four Pt wire contacts, two per electrode, were fabricated by thermocompression bonding using additional silver paint. During measurement the temperature was closely monitored by three thermocouples kept in the vicinity of the sample. The frequency range 1·3 MHz down to 5 Hz (Yokogawa Hewlett Packard 4192ALF Impedance Analyzer, Japan) or else 3 MHz down to 1 Hz (Solartron 1260, Schlumberger Electronics) was covered. Standard fitting techniques with ZARC elements[19] were used (ZView Windows 1.1, Scribner Assoc. Inc., USA) for precise grain-boundary and intragrain conductivity determination.

3 Results

3.1 Sintering behaviour of 33YDC and SEM analysis

The typical average particle size of calcined powders of all compositions (10–33YDC) was determined to be 0·7 μm. Submicrometre-sized powder is essential for ceria to sinter at normal temperatures.[1,20] The average particle size was reduced to 0·5 μm by wet milling with zirconia balls in 2-propanol (12–24 h), further improving the sinterability. Achieved relative densities as a function of the sintering temperature are displayed in Fig. 1. High density of >98% is reached at 1400°C and 1300°C for 'as-calcined' and milled powders, respectively. The sintering time at maximum temperature for all samples presented in this study was 4 h. Each pellet was placed on a zirconia or alumina fibre cloth in an open alumina crucible and fired in air, when not mentioned otherwise.

3.1.1 'As-calcined' powder

Figures 2 and 3 show surface and fracture views of 33YDC pellets fired between 1200 and 1500°C

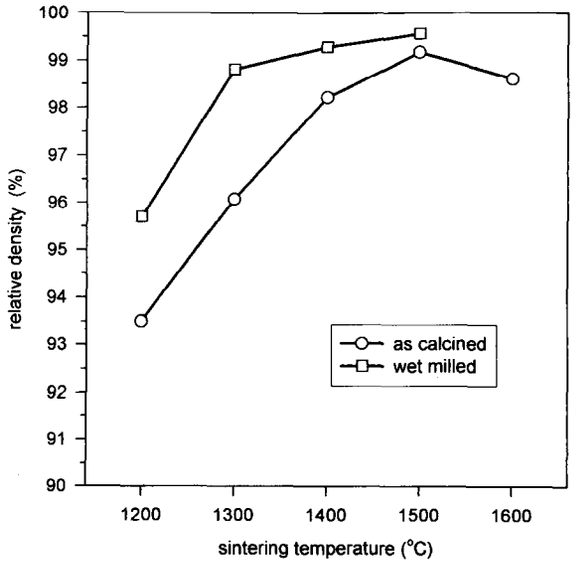

Fig. 1. Relative density of sintered 33YDC compacts (200 MPa) for various sintering temperatures (4 h), for both calcined and milled standard powder batches.

(4 h) at heating and cooling rates of 100°C h^{-1}. During sintering at 1200°C [Figs 2(a) and (b)], no grain growth has occurred yet. The particles are basically of the same size as in the starting powder. Nevertheless, 93% density was achieved at this unusually low temperature for ceria, illustrating the excellent sinterability. During sintering at 1300°C [Figs 2(c) and (d)], densification has started as clearly visible from the fracture view [Fig. 2(d)]. The grains remain very small, as evident from the surface view [Fig. 2(c)] which is identical for 'bottom' and 'top' faces of the pellets. At this temperature, closed porosity (96%) and hence impermeability is already reached. After sintering at 1400°C, the sample has fully densified [Fig. 3(c)]; grains have grown and packed together to a near dense surface [Figs 3(a) and (b)]. The top and bottom faces are not entirely identical as a minor porosity is noted at the bottom side. This phenomenon is pronounced after sintering at 1500°C, where the top face of the pellet has grown fully dense while the bottom face shows a high porosity [Figs 3(d) and (e)]. The grain growth has further increased significantly compared with firing at 1400°C. (Note that the magnification of the surface view at 1400°C is different from that of the other micrographs.)

The porosity phenomenon was identified as resulting from ceria diffusion into the underlying material. EDX measurement on the bottom face of Fig. 3(e) showed a Ce:Y ratio as low as 2:3, compared to the 2:1 ratio measured in the bulk of the sample. The porous surface layer was just a few micrometers deep, as a detailed view in Fig. 4 of the bottom and top edges of such a sample,

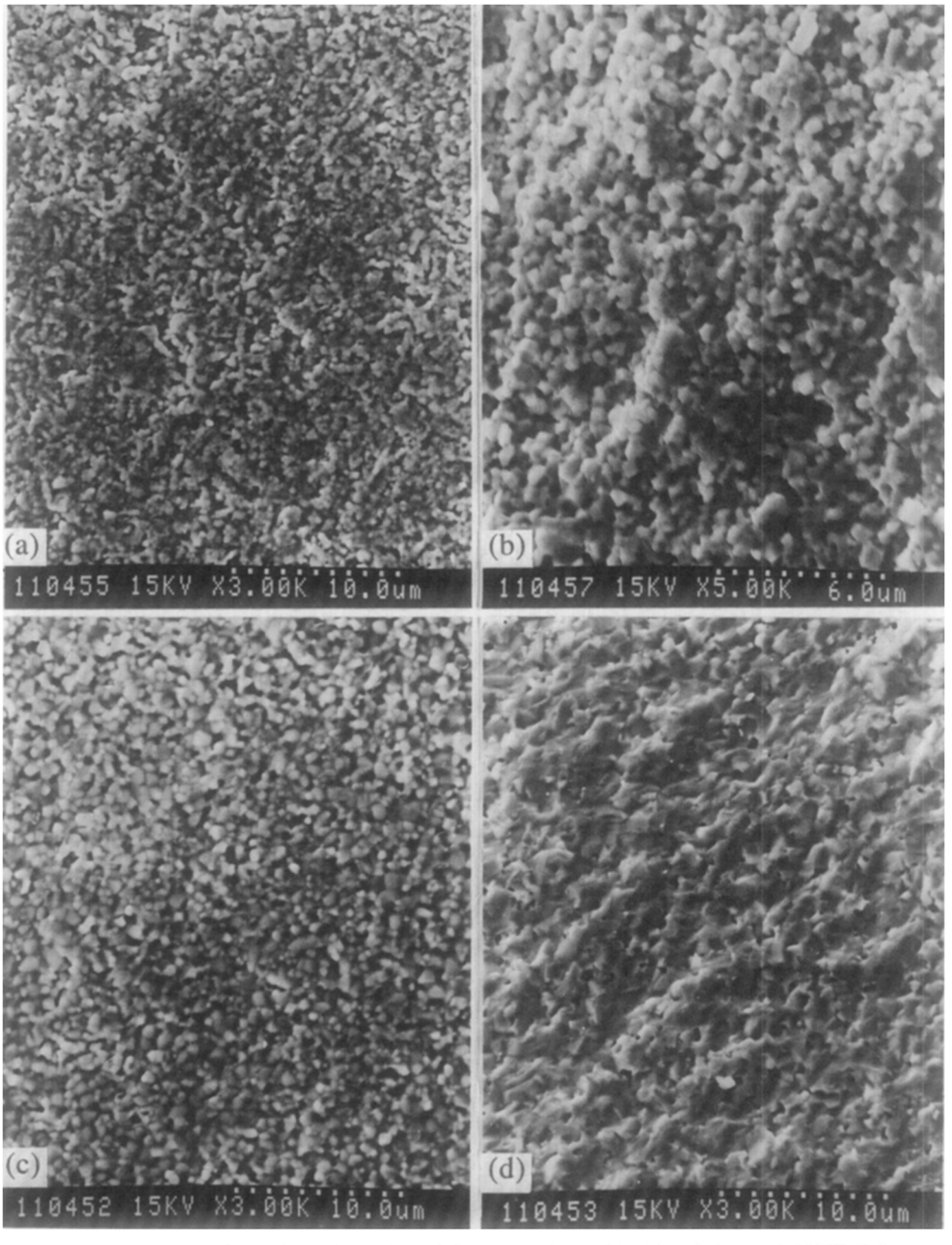

Fig. 2. SEM micrographs showing surface views (a), (c) and fracture views (b), (d) of sintered 33YDC from as-calcined powder: (a), (b) 1200°C, 4 h; (c), (d) 1300°C, 4 h.

fired at 1500°C, shows. This observation is of relevance for the application in SOFC, where reactions at the electrode/electrolyte interface play a major part in the power generation. The contact between an electrode layer with such a porous ceria-based electrolyte face might result in a large polarization loss, as the conductivity of the porous layer enriched in yttrium is considerably less than in the bulk of the sample. Therefore this loss of ceria into the substrate material during sintering at temperatures >1400°C has to be addressed.

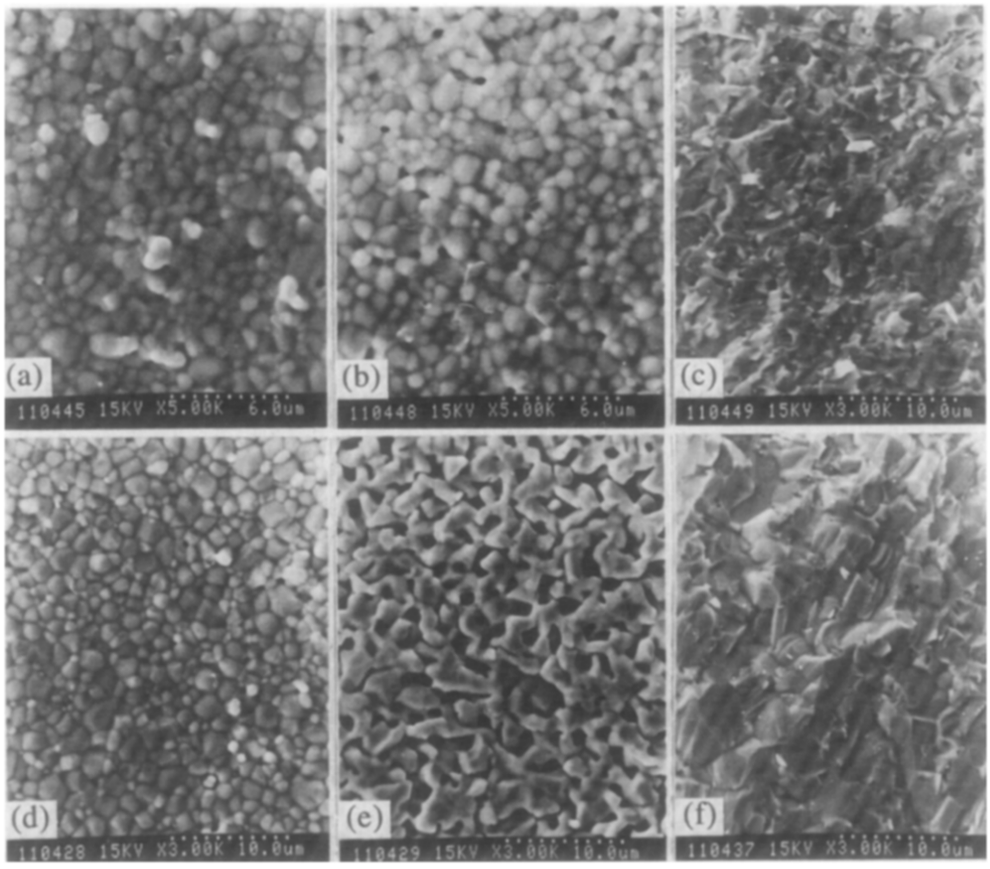

Fig. 3. SEM micrographs showing top (a), (d) and bottom (b), (e) surface views and fracture views (c), (f) of sintered 33YDC pellets from as-calcined powder: (a), (b), (c) 1400°C, 4 h; (d), (e), (f) 1500°C, 4 h.

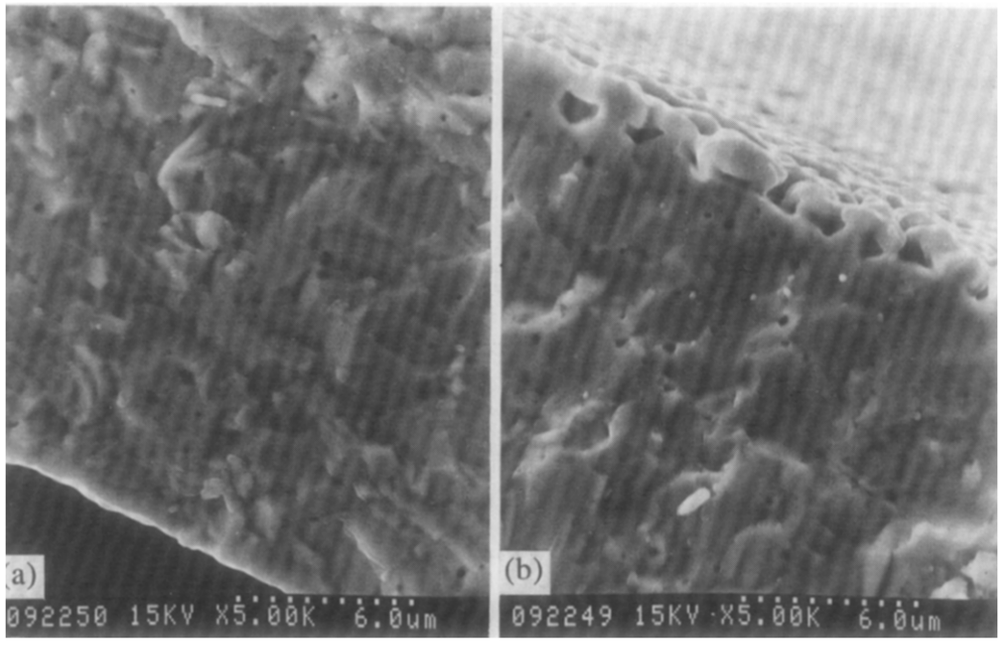

Fig. 4. SEM micrographs showing fracture views near the top surface edge (a) and near the bottom surface edge (b) of a 33YDC pellet sintered at 1500°C freely in air, without a powder bed.

3.1.2 Effect of sample embedding

As a logical solution to this problem, pellets were put on a powder bed of coarse 33YDC, entirely covered with it, and sintered at 1500°C. The SEM results of surface views of such samples are presented in Figs 5(a) and (b), which should be compared with Figs 3(d) and (e). It can be seen that the ceria loss has been entirely suppressed by this simple procedure. The bottom and top faces are equally dense.

The use of only a powder bed instead of complete embedding results in the grain growth on the 'protected', i.e. lower, face being slightly enhanced, compared with that on the upper face which was not covered with the coarse powder. This is explicitly visible from Figs 5(c) and (d) of a sample that was fired at 1500°C using a powder bed only. The grain sizes were estimated to be 1·9 and 2·2 μm for top and bottom faces, respectively.

3.1.3 Effect of heating rate

As longer times at high temperature aggravate the diffusion problem, the effect of faster heating rates, effectively shortening the residence time, was studied on samples that were not covered with additional powder on either side.

Top and bottom faces of pellets fired at 1500°C for 4 h at heating/cooling rates of 250 and 500°C h^{-1} are presented in Fig. 6, together with those for the case of a pellet fired at 100°C h^{-1} to 1500°C. It can be easily seen that faster heating rates improve densification and suppress ceria loss from the bottom

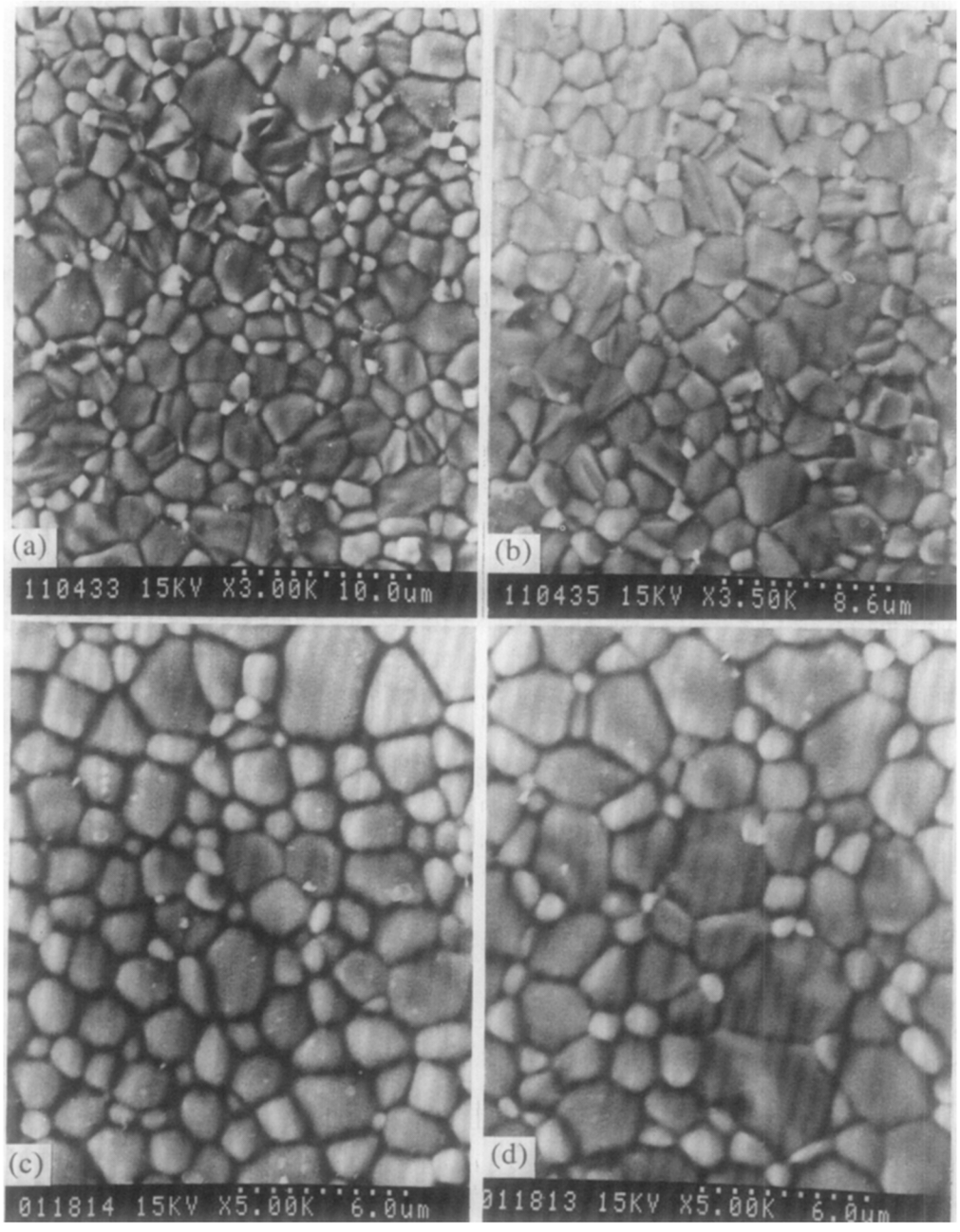

Fig. 5. SEM micrographs showing top surface views (a), (c) and bottom surface views (b), (d) of sintered 33YDC from as-calcined powder at 1500°C (4 h): (a), (b) sample entirely embedded in YDC powder; (c), (d) sample placed on a YDC powder bed only.

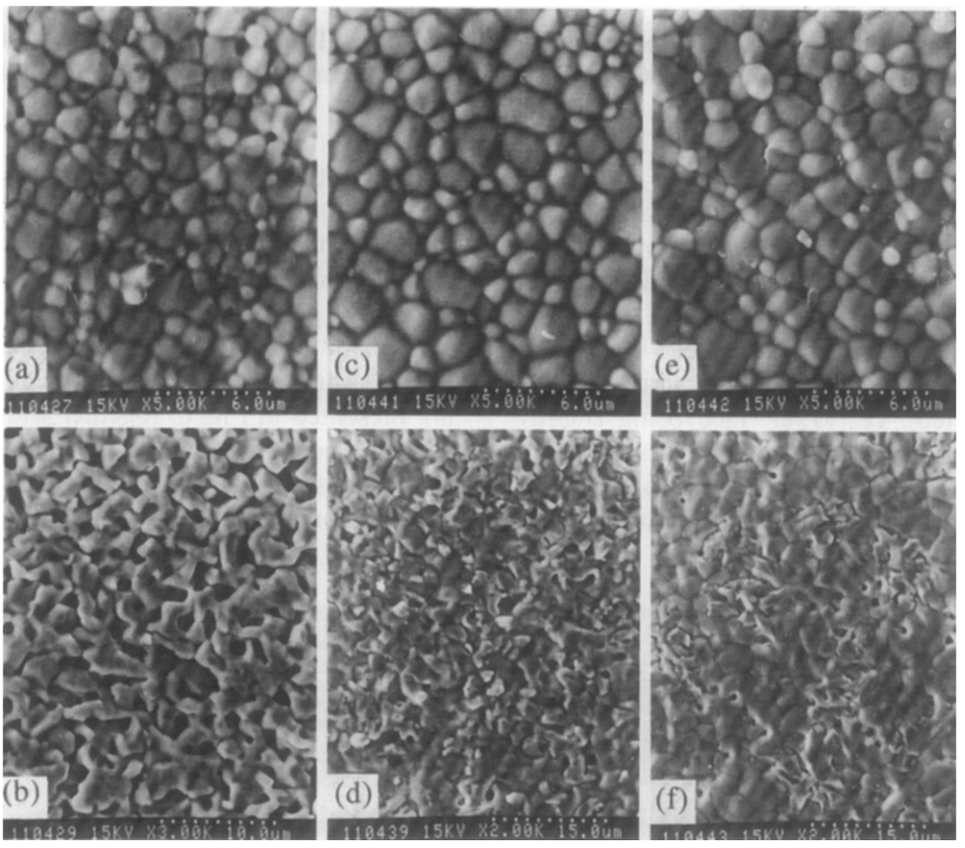

Fig. 6. SEM micrographs showing top (a), (c), (e) and bottom (b), (d), (f) surface views of sintered 33YDC pellets at 1500°C (4 h) from as-calcined powder at different heating/cooling rates: (a), (b) 100°C h^{-1}; (c), (d) 250°C h^{-1}; (e), (f) 500°C h^{-1}.

face, though not entirely. A slight increase in grain growth is observed. EDX measurements from the bottom faces of these samples gave Ce:Y ratios of 0·7 (100°C h^{-1} rate), 1·1 (250°C h^{-1}) and 1·3 (500°C h^{-1}), confirming quantitatively the suppression of ceria loss. This series of experiments demonstrates that ceria samples, in contact with other materials, can be fired safely only up to 1400°C. This should therefore be a target temperature for cofiring of ceria with other materials. Tape-cast ceria must therefore be densified at 1400°C, as we achieved and reported in another paper.[20] For isolated ceria samples, protection against ceria loss is required, e.g. by using a powder embedding or even only a powder bed, above this temperature.

3.1.4 Effect of ball milling

33YDC powder milled in 2-propanol for 12–24 h with zirconia balls in polyethylene containers, was pressed into pellets and subjected to a similar series of sintering conditions as for calcined powder. Interest was focused on the improved densification at low temperature (see Fig. 1). The samples were fired at temperatures between 1200 and 1600°C for 4 h at heating/cooling rates of 100°C h^{-1}, and without using any powder bed.

A SEM analysis is presented in Fig. 7 for top faces, bottom faces and fracture views for all sintering temperatures. At 1200°C the powder has already densified to a gas-impermeable body (Fig. 7iii), though grain size has remained small (Fig. 7i, ii). After sintering at 1300°C, the samples are near fully dense (Fig. 7vi) and grain growth was initiated (Fig. 7iv, v). In effect, the ball milling step lowers the sintering temperature by approximately 100°C with respect to the calcined powder, to achieve a similar microstructure and density. During firing at 1400°C, grain growth further increases (Fig. 7vii, viii), and at 1500°C ceria loss from the bottom face is again noted (Fig. 7xi): the Ce:Y ratio as determined by EDX was 1:1 for this sample. The problem becomes very serious at 1600°C (Fig. 7xiv), Ce:Y ratio of 0·4, where a significant increase in grain size is also observed.

In Ref. 5 it was suggested that the yttrium dopant acts as a grain growth inhibitor. In that work, the densest samples were achieved only for low $YO_{1.5}$ concentrations of 1–6%. The small grain sizes observed in this work for ceria doped with 33% of $YO_{1.5}$ seem to confirm that report. The data are plotted in Fig. 8 as estimated average grain size vs. the sintering temperature. Significant growth is not noticed until temperatures above 1500°C. However, high density could still be reached in this work at normal temperatures, despite the high yttrium content and the

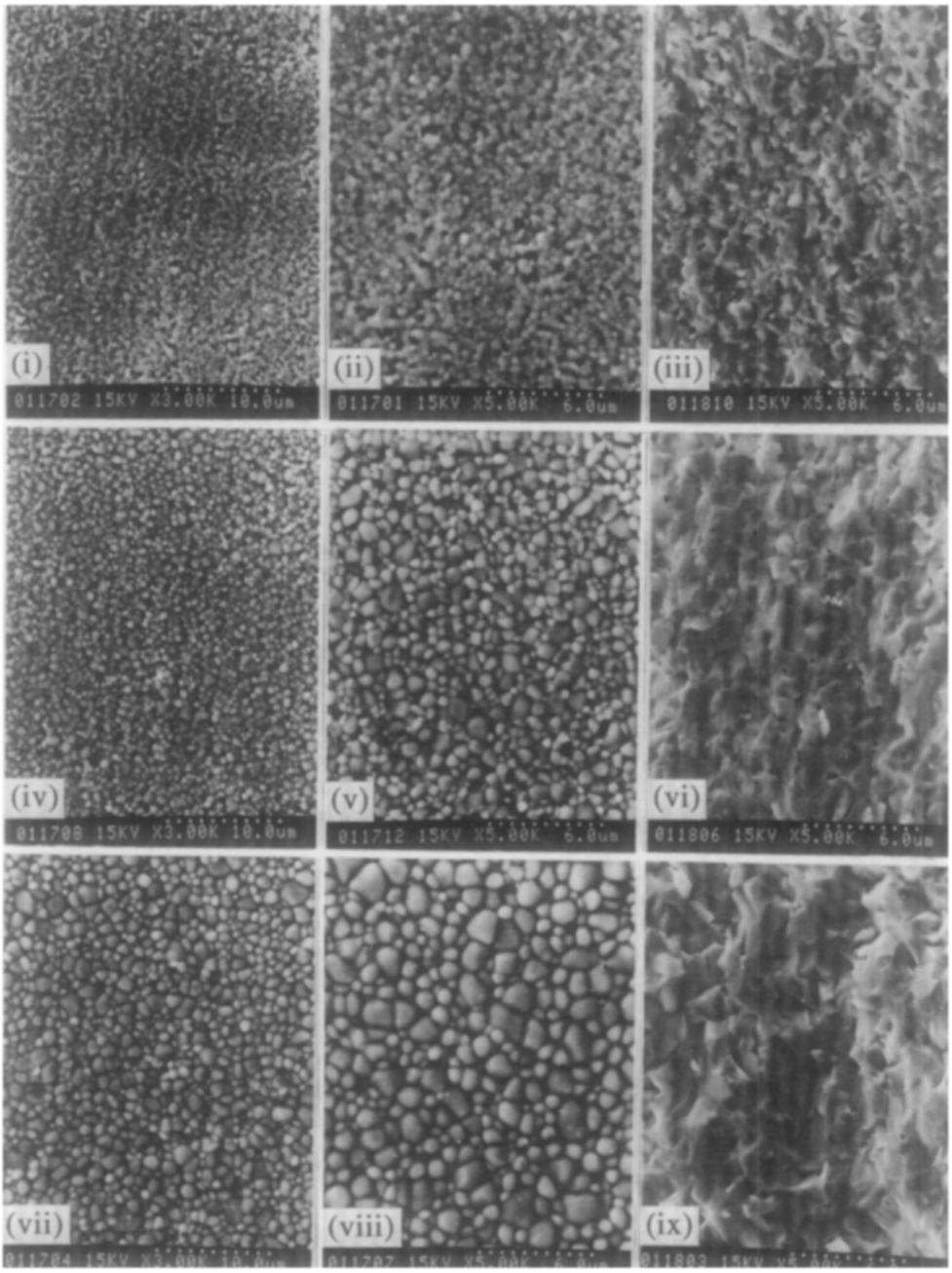

Fig. 7. SEM micrographs showing top (left column), bottom (middle column) and fracture views (right column) for sintered 33YDC pellets (4 h) from wet milled powder (2-propanol): (i)–(iii) 1200°C; (iv)–(vi) 1300°C; (vii)–(ix) 1400°C; (x)–(xii) 1500°C; (xiii)–(xv) 1600°C.

small grain size, indicating that our preparation procedure yields very active powder. This is confirmed by the fact that we were able to sinter to high density any doped ceria powder synthesized according to our procedure, independent of the composition within the range 10–33 mol% $YO_{1.5}$, or even of the dopant (Y, Gd or Sm).[21] This implies an advantage expected in terms of mechanical strength: a structure composed of fewer very much larger grains is weaker than one of many small grains, as it provides extended surfaces along which cracking can occur. Hence the densification feasibility at lower temperature presents advantages not only of practical sintering and lessening of interdiffusion, but also of better control of the mechanical properties.

3.2 Ionic conductivity

Powders of 10, 15, 20, 25 and 33 mol% $YO_{1.5}$–CeO_2 were prepared (calcination at 700°C), pressed at 200 MPa and fired at 1500°C while embedded in powder of the same composition, in order to yield fully dense samples for the conductivity measurements. A summary of the powder and compact characteristics is given in Table 1. As pointed out above, no differences in these characteristics with varying dopant content were noted, confirming a wide applicability of our powder preparation procedure.

3.2.1 Impedance spectroscopy vs. four-point method

Four-point dc measurements were carried out on sample rods in order to verify the total conductivity

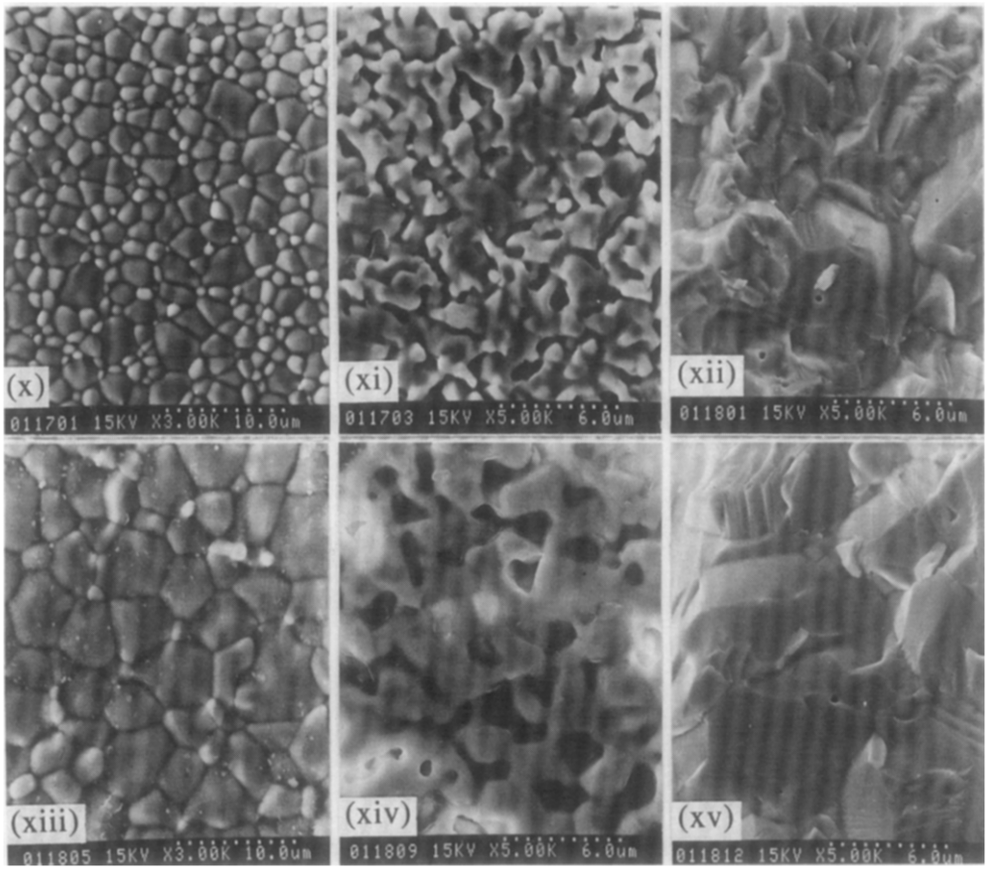

Fig. 7. Continued.

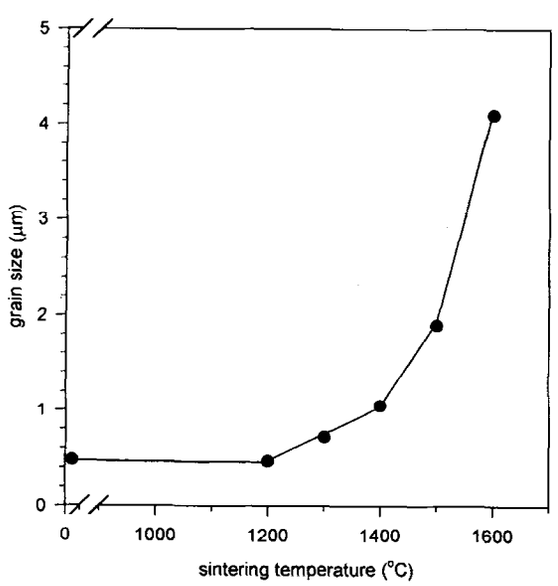

Fig. 8. Average grain size of sintered 33YDC bodies as a function of sintering temperature.

values obtained from the impedance data. Whereas this worked well for samples of high yttrium content (33YDC), a slow voltage transient phenomenon was observed after application of the current step with samples of lower yttrium content (10YDC). This phenomenon was observed and explained by previous workers.[22] Therefore impedance measurements were consistently employed for all samples, especially since grain-boundary conductivity can be decoupled from the total conductivity in the same measurement.

3.2.2 Platinum vs. silver electrodes

Silver paint electrodes (Nilaco Co., Japan) were preferred over platinum paint (TR-7905 Tanaka Kikinzoku Kogyo, Japan), since the silver electrode response was much better resolved from the grain-boundary response of the ceria electrolyte. The overlap between the latter and the platinum electrode frequency regime was rather strong, which complicated accurate determination of the total electrolyte resistance intercept. A comparison is given in Fig. 9 for a sample of 10YDC — which showed the largest grain-boundary resistance of the composition range studied — with (a) Pt electrodes and (b) Ag electrodes. Clearly, in Fig. 9(b), fitting of the second arc is more readily accomplished.

The frequencies are indicated as powers of 10 in Hz on these plots. Also, all impedance graphs shown were normalized to the same geometrical factor of 1 mm electrolyte thickness (10 mm electrode diameter), to make them comparable.

Since the grain-boundary contribution vanishes with high dopant content ($\geq 25\%$ $YO_{1.5}$), as reported before[9] and as confirmed in this work, the nature of the electrode chosen for such samples was not

Table 1. Overview of characteristic data of YDC powders of varying dopant content. d_{50} = average agglomerate size by volume, from particle-size distribution measurement in H_2O; d_{crys} = primary particle size estimated from X-ray diffraction line broadening; BET = powder surface area by N_2 adsorption; a = cubic lattice constant; ρ_{XRD} = theoretical density; ρ_{exp} = observed relative density of samples fired at 1500°C (4 h) in air

(%) $YO_{1.5}$	d_{50} (μm)	d_{crys} (nm)	BET ($m^2 g^{-1}$)	a (Å)	ρ_{XRD} ($g\ cm^{-3}$)	ρ_{exp} (%)
10	0·72	19	17·1	5·4056 ± 0·0012	6·991	99·1
15	0·71	21	20·6	5·4048 ± 0·0010	6·870	99·0
20	0·76	19	15·3	5·4016 ± 0·0107	6·753	99·4
25	0·76	23	17·1	5·4026 ± 0·0077	6·630	99·6
33	0·75	16	16·0	5·3939 ± 0·0008	6·452	99·2

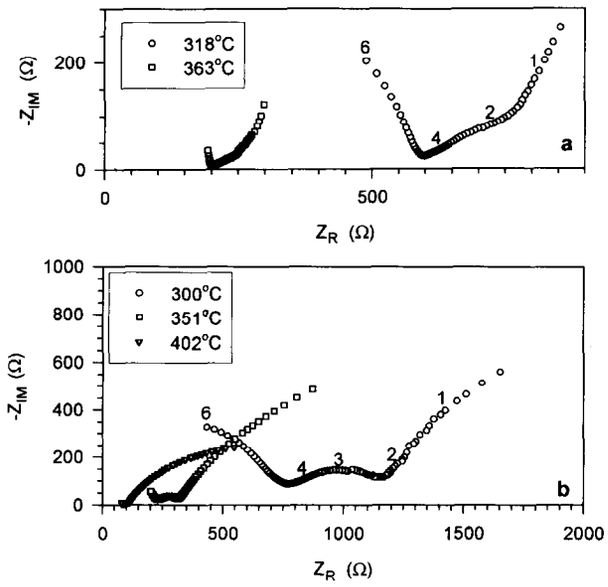

Fig. 9. Impedance diagram in air at low temperature for a 10YDC electrolyte: (a) with platinum electrodes; (b) with silver electrodes.

relevant for the measurement of the total electrolyte resistance from the real axis intercept. In the following, results on the 10, 15, 20 and 25% $YO_{1.5}$–CeO_2 material will be presented with silver electrodes, and on the 33YDC material with platinum electrodes.

3.2.3 Examples of impedance spectra

Figures 10 and 11 present two series — one at lower temperature, the other at higher temperature — of impedance responses of cells with electrolytes of the different compositions under study. Figures 9 and 10 show the results obtained with pellets of 10–33YDC in the low temperature range 300–400°C. Three arcs are distinguished, identified as bulk electrolyte semicircle (highest frequency), electrolyte grain-boundary semicircle (intermediate frequency regime) and electrode response (lowest frequency region).

Two tendencies are apparent from this series: (1) the grain boundary arc is biggest for the lower dopant concentrations, vanishing for the higher dopant regime; and (2) the total resistance (electrolyte intragrain + grain-boundary resistances) increases with increasing dopant content at this low temperature.

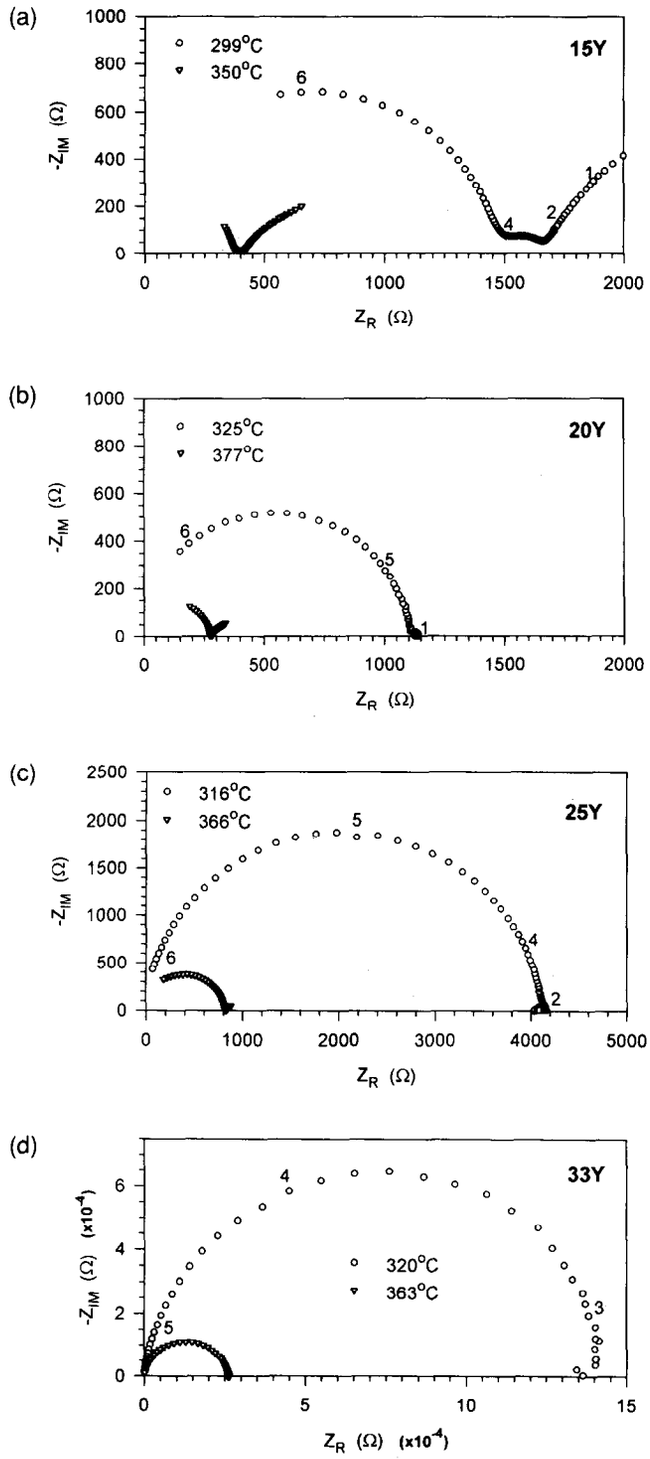

Fig. 10. Impedance diagrams in air at lower temperature (around 350°C) for different electrolytes: (a) 15YDC, (b) 20YDC, (c) 25YDC and (d) 33YDC.

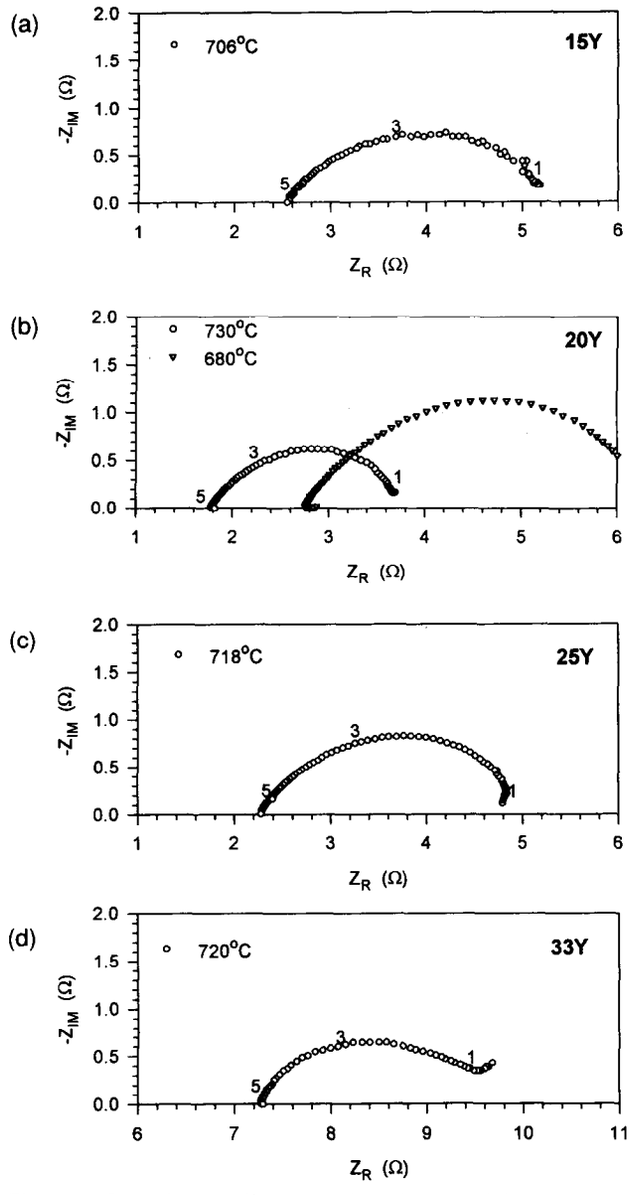

Fig. 11. Impedance diagrams in air at higher temperature (around 700°C) for different electrolytes: (a) 15YDC, (b) 20YDC, (c) 25YDC and (d) 33YDC.

Figure 11 shows the results obtained with pellets of 15–33YDC at temperatures around 700°C, a realistic SOFC operation temperature with doped ceria cells. Only the electrode response is observed at this temperature. Its shape and value are very similar and reproducible for the different pellets. The resistance is lowest for the composition 20YDC.

Data over a range of temperatures are presented in the next few graphs, elaborating more clearly the conclusions obtained from Figs 10 and 11.

Figure 12 shows the percentage of grain-boundary contribution to the total resistivity for the compositions 10–20YDC. For compositions of higher Y content no grain-boundary response was detected. The contribution is largest for the lower Y dopant concentrations at the lowest temperatures, but vanishes rapidly with increasing Y content and temperature.

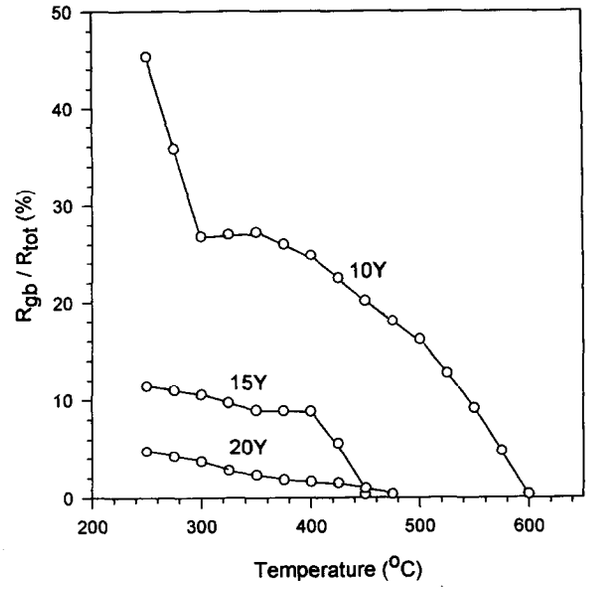

Fig. 12. Grain-boundary resistivity R_{gb} as a percentage of the total resistivity R_{tot} of YDC for different compositions, as a function of temperature.

It is to be noted that, to simplify calculations, only the geometrical electrode area and electrolyte thickness were adopted to calculate a grain-boundary 'resistivity' value from the measured resistance, rather than the real grain boundary surface and thickness which can only be estimated with difficulty. A more precise treatment using modelling has been given elsewhere.[10] Nevertheless, the relevant conclusion here is that the grain-boundary contribution becomes negligible for any Y composition studied at the projected operation temperature (>600°C). This re-illustrates the quality of our pellets and coprecipitated starting powder.

Figure 13 shows the measured total ionic conductivities of all samples over the temperature range covered as a typical Arrhenius graph. The composition giving maximum conductivity shifts with increasing temperature to one of higher Y content. This is more clearly visible from Fig. 14, where interpolated conductivity values are replotted in 100°C intervals vs. the composition. Conductivity at 300°C is a maximum at 10YDC (but may be higher at lower dopant compositions), at ~500°C at 15YDC, at 700°C at 20YDC, and at 25YDC at above 1000°C. Hence, for SOFC application at around 700°C with a doped ceria electrolyte, 20YDC is the most suitable composition in terms of ionic conductivity; this finding confirms an earlier prediction[12] and lies in the range of results of most other workers, who found maximum conductivity for the compositions 15YDC to 18YDC.[10,15,16,18] However, the conductivity difference to other compositions being small (very broad maximum in Fig. 14), properties other than conductivity, like mechanical strength, may become decisive for choosing the most suitable dopant content overall.

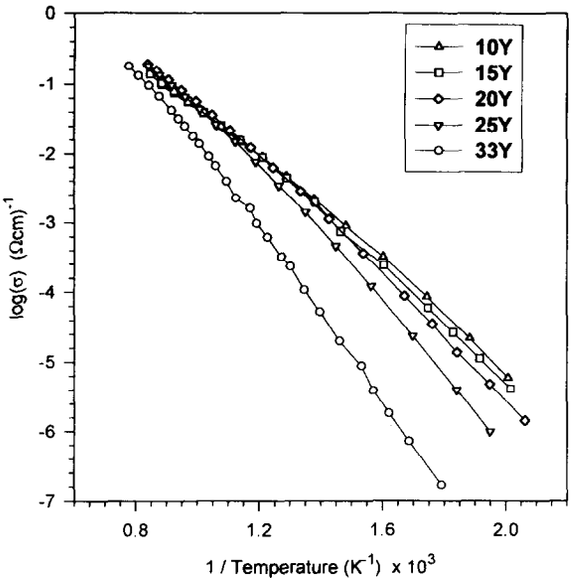

Fig. 13. Arrhenius plot over 300–1000°C of the ionic conductivity in air for YDC of the compositions used in this study.

The Arrhenius plots of Fig. 13 break up into two straight-line portions, one at low temperature (<500°C) and one at high temperature (>600°C). The activation energies for these two portions vary significantly with the Y dopant concentration, as presented in Fig. 15. Two activation energies on the same Arrhenius plot have been frequently identified before for doped ceria electrolytes.[7,10,12,23] The result of Fig. 15 differs slightly from some reports,[10,24] where the high temperature activation energy was constant in the dopant range 1–15% $YO_{1.5}$. Attractive values of 0·6–0·7 eV in the high-temperature portion of interest were observed for the samples of 10–20YDC, among the lower values observed for YDC.

The conductivity of YDC in air measured in this work is among the highest reported so far.

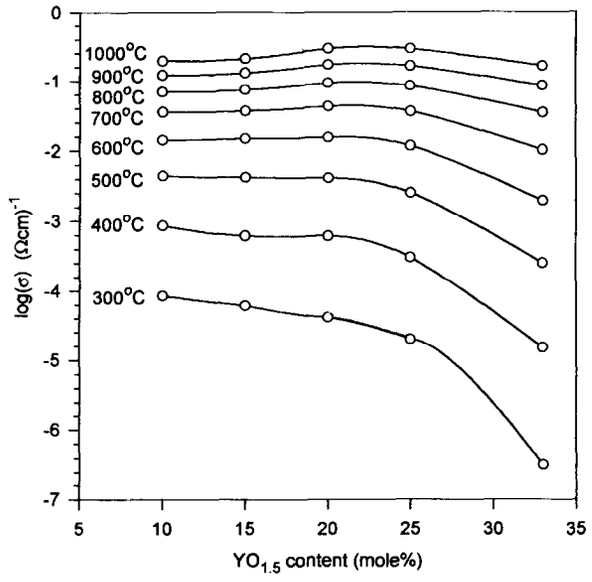

Fig. 14. Ionic conductivity of YDC in air as a function of temperature and dopant content. The composition showing maximal conductivity shifts with temperature.

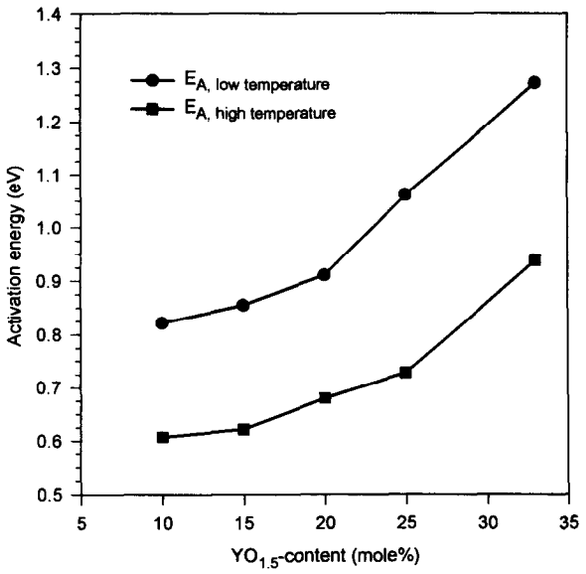

Fig. 15. Activation energies E_a for the ionic conductivity of YDC in air at low (<500°C) and high (>600°C) temperatures as a function of the dopant content, as obtained from the Arrhenius plots (Fig. 13).

Table 2 presents a comparison with literature data at 750°C, a representative operating temperature. We attribute this (1) to the optimal coprecipitation procedure giving a highly homogeneously dispersed dopant in the sample, thus yielding optimal conduction properties,[23] and (2) to the high density of the samples (99%), which has rarely been achieved in the past. A remaining porosity of a few percent or more cannot be accounted for by a simple proportional correction as is often assumed.[12,16,26] An example is given in Fig. 16, where a perfectly dense 33YDC pellet is compared in an Arrhenius plot with the ionic conductivity of a pellet of only 91%

Table 2. Ionic conductivities (σ) of YDC in air at 750°C obtained in this study, compared with literature values

Compound	σ ($S\ m^{-1}$)	*Ref.*
8·5YDC	1·2	7
20YDC	1·9	12
11YDC	2·0	9
16YDC	2·1	18
20YDC	2·2	2
15YDC	3·3	10
10YDC	3·7	25
18YDC	4·0	16
10YDC	4·7	11
20YDC	5·5	17
20YDC	6·5	This work
20GdDC	2·6	12
18GdDC	2·8	18
20GdDC	3·3	2
10GdDC	5·9	24
18GdDC	6·5	23
20GdDC	6·7	27
20SmDC	3·1	12
18SmDC	4·0	18
20SmDC	6·1	2
20SmDC	6·9	17

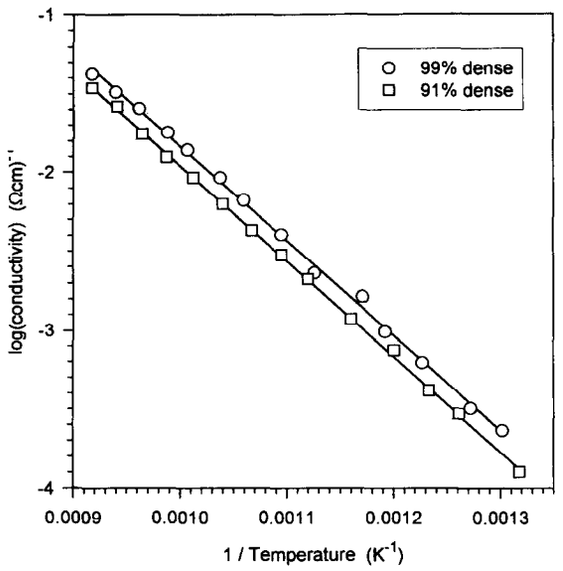

Fig. 16. Ionic conductivity (500–800°C) for 33YDC bodies of different density.

density, prepared by firing at 1100°C. On average the conductivity of the latter is worse by >25%, rather than the proportional porosity correction of ≈ 10%.

Our values for dense YDC even compare well, as Table 2 shows, with those reported for the more popular Gd- and Sm-doped cerias, generally recognised as the better conductors and hence used in preference. When abundance, price, ionic conductivity, high temperature reactivity and sinterability are considered,[21] we feel that the use of YDC compared with that of GdDC and SmDC is being neglected somewhat, more so since combination of YDC with a thin YSZ electrolyte layer should be less troublesome with respect to interdiffusion at high temperature.

4. Summary

Highly sinterable yttria-doped ceria powder was prepared, allowing densification at temperatures several hundred degrees lower than those employed in the majority of cases so far, and independent of the dopant concentration. The cerium component becomes very mobile above 1400°C, resulting, for example, in samples featuring porous surface layers if not properly protected by a powder bed. Following the high degree of densification and homogeneity of the samples, excellent conduction properties were noticed, approaching those of the more expensive Gd- and Sm-doped ceria. The conductivity maximum at 700°C, though very broad, lay at the composition around 20YDC. Lower temperature densification demonstrated in this work provides advantages in energy cost, cofiring and mechanical property control.

Acknowledgement

This work was supported by the Science and Technology Agency, Japan, which is most gratefully acknowledged.

References

1. Van herle, J., Horita, T., Kawada, T., Sakai, N., Yokokawa, H. & Dokiya, M., Yttria doped ceria: powder preparation and sintering of compacts. *J. Am. Ceram. Soc.*, submitted.
2. Eguchi, K., Setoguchi, T., Inoue, T. & Arai, H., Electrical properties of ceria-based oxides and their application to solid oxide fuel cells. *Solid State Ionics*, **52** (1992) 165–72.
3. Mehta, K., Hong, S.-J., Fue, J.-F. & Virkar, A. V., Fabrication and characterization of YSZ-coated ceria electrolytes. In *Proc. 3rd Int. Symp. on Solid Oxide Fuel Cells*. Honolulu, Hawaii, May 1993, eds. O. Yamamoto & S. C. Singhal. The Electrochemical Society, Inc., pp. 93–103.
4. Piacente, V., Bardi, G., Maluspina, L. & Desideri, A., Dissociation energy of CeO_2 and Ce_2O_2 molecules. *J. Chem. Phys.*, **59** (1973) 31–6.
5. Upadhyaya, D. P., Bhat, R., Ramanathan, S., Roy, S. K., Schubert, H. & Petzow, G., Solute effect on grain growth in ceria ceramics. *J. Eur. Ceram. Soc.*, **14** (1994) 337–41.
6. Zhen, Y. S., Milne, S. J. & Brook, R. J., Oxygen ion conduction in CeO_2 ceramics simultaneously doped with Gd_2O_3 and Y_2O_3. *Science of Ceramics*, **14** (1988) 1025–30.
7. Chiang, C. K., Bethin, J. R., Dragoo, A. L., Franklin, A. D. & Young, K. F., Inhomogeneity contribution to the electrical properties of Y-doped CeO_2 ceramics: comparison of ac and dc measurements. *J. Electrochem. Soc.*, **129** (1982) 2113–19.
8. Gerhardt, R. & Nowick, A. S., Grain-boundary effect in ceria doped with trivalent cations: I, electrical measurements. *J. Am. Ceram. Soc.*, **69** (1986) 641–6.
9. Wang, D. Y. & Nowick, A. S., The grain-boundary effect in doped ceria solid electrolytes. *J. Solid State Chem.*, **35** (1980) 325–33.
10. ElAdham, K. & Hammou, A., Etude des Propriétés electriques de solutions solides à base de dioxyde de cérium. *J. Chim. Phys.*, **79** (1982) 633–44.
11. Subbarao, E. C. & Maiti, H. S., Solid electrolytes with oxygen ion conduction. *Solid State Ionics*, **11** (1984) 317–38.
12. Dirstine, R. T., Blumenthal, R. N. & Kuech, T. F., Ionic conductivity of calcia, yttria, and rare-earth doped cerium dioxide. *J. Electrochem. Soc.*, **126** (1979) 264–9.
13. Wang, D. Y., Park, D. S., Griffith, J. & Nowick, A. S., Oxygen ion conductivity and defect interactions in yttria-doped ceria. *Solid State Ionics*, **2** (1981) 95–105.
14. Sarkar, P. & Nicholson, P. S., Ac conductivity and conductivity relaxation studies in the CeO_2–Y_2O_3 system. *Solid State Ionics*, **21** (1986) 49–53.
15. Catlow, C. R. A., Transport in doped fluorite oxides. *Solid State Ionics*, **12** (1984) 67–73.
16. Pascual, C., Jurado, J. R., Arroyo, G. F., Del Olmo, L., Moure, C. & Duran, P., Electrical conductivity of solid solutions in the systems CeO_2–CaO and CeO_2–Ln_2O_3 (Ln = La, Nd, Sm, Gd, Er, Y). *Science of Ceramics*, **12** (1984) 729–34.
17. Yahiro, H., Baba, Y., Eguchi, K. & Arai, H., High temperature fuel cell with ceria-yttria solid electrolyte. *J. Electrochem. Soc.* **135** (1988) 2077–81.
18. Balazs, G. B. & Glass, R. S., Ac impedance studies of rare earth oxides doped ceria. *Solid State Ionics*, **76** (1995) 155–62.
19. MacDonald, J. R., *Impedance Spectroscopy*. John Wiley & Sons, New York, 1987, pp. 90–5.

20. Van herle, J., Horita, T., Kawada, T., Sakai, N. Yokokawa H. & Dokiya, M., Yttria doped ceria: tape casting. *J. Am. Ceram. Soc.*, submitted.
21. Van herle, J., Horita, T., Kawada, T., Sakai, N., Yokokawa, H. & Dokiya, M., Low temperature fabrication of (Gd,Sm,Y)-doped ceria electrolyte. *Solid State Ionics*, submitted.
22. Chiang, C. K., Dragoo, A. L. & Franklin, A. D., Slow transient phenomenon in Y-doped CeO_2. In *Fast Ion Transport in Solids*, eds. P. Vashishta, J. Mundy & G. Shenoy. North Holland Elsevier, 1979, pp. 661–3.
23. Riess, I., Braunshtein, D. & Tannhauser, D. S., Density and ionic conductivity of sintered $(CeO_2)_{0\cdot82}(GdO_{1\cdot5})_{0\cdot18}$. *J. Am. Ceram. Soc.*, **64** (1981) 479–85.
24. Hohnke, D. K., Ionic conduction in doped oxides with the fluorite structure. *Solid State Ionics*, **5** (1981) 531–4.
25. Mogensen, M., Lindegaard, T., Hansen, U. R. & Mogensen, G., Physical properties of mixed conductor solid oxide fuel cell anodes of doped CeO_2. *J. Electrochem. Soc.*, **141** (1994) 2122–8.
26. Tuller, H. L. & Nowick, A. S., Ionic conductivity of doped cerium dioxide. In *Proc. Conf. on High Temperature Solid Oxide Electrolytes*, August 1983, ed. F. Salzano. Brookhaven Nat. Lab. Assoc. Univ. Inc., Upton, NY, pp. 177–85.
27. Kudo, T. & Obayashi, H., Oxygen ion conduction of the fluorite-type $Ce_{1-x}Ln_xO_{2-x/2}$ (Ln = lanthanide). *J. Electrochem. Soc.*, **122** (1975) 142–7.

Journal of the European Ceramic Society 16 (1996) 975–984

S0955-2219(96)00009-X
0955-2219/96/$15.00

Slip Casting of Submicron $BaTiO_3$ Produced by Low-Temperature Aqueous Synthesis

Marco Alvazzi Delfrate,[a] Jacques Lemaitre,[a]* Vincenzo Buscaglia,[b] Marcello Leoni[b] & Paolo Nanni[c]

[a] Ecole Polytechnique Fédérale de Lausanne (EPFL), Laboratoire de Technologie des Poudres, MX-Ecublens, CH-1015 Lausanne, Switzerland
[b] Istituto di Chimica Fisica Applicata dei Materiali, CNR, Area della Ricerca, via de Marini 6, I-16149 Genova, Italy
[c] Istituto di Chimica, Facoltà di Ingegneria, Università di Genova, P. le Kennedy, I-16129 Genova, Italy

(Received 24 April 1995; revised version received 15 December 1995; accepted 5 January 1996)

Abstract

Two submicron $BaTiO_3$ powders of different stoichiometries, prepared by an aqueous method have been characterized and submitted to chemical, thermal and mechanical treatments in order to optimize the processing conditions. Acid cleaning at different pH values, calcinations at different temperatures and ultrasonication were performed. The resulting powders were characterized by TGA, SEM, specific surface area, XPS and particle size analysis.

Fired samples were obtained via slip casting and isothermal or non-isothermal sintering. Densification was studied by dilatometric measurements.

Acid cleaning treatments caused desintering phenomena and low fired density, while high density samples with an homogeneous fine grained microstructure were obtained from powders calcined at 950°C.

Deux poudres submicroniques de $BaTiO_3$ de stoechiométries différentes, préparées par synthèse en milieux aqueux, ont été caractérisées et soumises à des traitement chimiques, thermiques et mécaniques pour optimiser la mise en oeuvre. Des lavages acides à différents pH, des calcination et des traitements aux ultrasons ont été effectués. Les poudres résultantes ont été caractérisées par TGA, SEM, mesure de surface spécifique, XPS et granulométrie.

Des corps compacts ont été obtenus par coulage en barbotine et frittage isotherme ou non isotherme. Le comportement au cours du frittage a été étudié par dilatométrie.

Les lavages acides ont provoqué des phénomènes de défrittage et des basses densités, tandis que des échantillons de haute densité présentant une microstructure fine et homogène ont été obtenus à partir de poudres calcinées à 950°C.

1 Introduction

Barium titanate is a ferroelectric material widely employed in the fabrication of multilayer capacitors (MLC), because of its high permittivity. The general trend in ceramic capacitor production is to decrease size and price while preserving or, if possible, increasing performances. This goal can be achieved by a careful control of microstructure and impurity content. Several preparation routes, alternative to the classic solid state reaction $BaCO_3 + TiO_2 \rightarrow BaTiO_3$, have been developed in order to obtain submicron and monodispersed powders, which would produce high density, regular, small grain microstructure free of anomalous grain growth. Among them, the hydrothermal processes[1] are particularly interesting because they allow the production of pure and fine powders and an easy introduction of specific dopants.

The surface of the resulting $BaTiO_3$ powders is contaminated by carbonates, whose presence can be due to the synthesis itself, to the subsequent washing and drying treatments, and to exposure to atmospheric CO_2. This layer, which can promote the formation of agglomerates, has been found to be detrimental to formation and sintering of some commercial powders.[2,3]

Barium titanate powders were prepared by low-temperature (80°C) aqueous synthesis in ICFAM-CNR Genova according to the following reaction:[4]

$$Ba(OH)_2 \cdot H_2O + TiCl_4 + 4NaOH \rightarrow BaTiO_3 + 4NaCl + 4H_2O.$$

NaOH is in 1·5 stoichiometric excess to neutralize HCl and keep the pH high. After 5 h digestion at

* To whom correspondence should be addressed.

constant temperature, the suspension was cooled down and washed several times with distilled water until neutrality was reached. These powders present high specific surface areas, a cubic lattice according to X-ray diffraction (XRD), but lower symmetry and bulk hydroxyl groups according to Raman spectroscopy,[5] and a nearly spherical morphology; the presence of carbonates was detected by XRD. Cristallite size control can be achieved by changing some reaction parameters, such as temperature and digestion time. Sintered samples were prepared by forming such powders by isostatic pressing, obtaining satisfactory ceramic and dielectric properties.[6]

The aim of this work is to optimize the processing conditions and surface treatments of these powders, in order to obtain slip-cast products with good ceramic properties (fine monodispersed grains and high density).

2 Experimental Procedures

Two different batches with different stoichiometries were used: batch BTN5, prepared with stoichiometric quantities of reactants, has a ratio Ti/(Ba+Sr) = 1·05, as measured by plasma spectrometry (ICP) after fusion in $Li_2B_4O_7$; batch BTN8, prepared with an excess of $Ba(OH)_2$, gives Ti/(Ba+Sr) = 0·99; small amounts of Na, probably incorporated during the synthesis, are also detected (≅ 1000 ppm).

Thermal, chemical and mechanical treatments were performed, in order to break agglomerates and obtain high green-density samples.

Partial elimination of water and of carbonates was performed by calcining the powders in a tube furnace for 1 h in air at two different temperatures, either 600 or 950°C (heating rate 10°C/min), using alumina crucibles.

Chemical treatment was performed on non-deagglomerated calcined powder (Batch BTN5) in order to finish the surface decontamination treatment.[2]

Three cleaning solutions were used:

(i) Boiled demineralized water, as a reference;
(ii) pH = 4·5: 0·36 M buffer solution of 50 mol% acetic acid (Merck 100%) + 50 mol% ammonium acetate (Merck 98%) in boiled demineralized water;
(iii) pH = 3·0: 0·30 M buffer solution of 60 mol% nitric acid (Merck 100%) + 40 mol% ammonium citrate (Merck 98%) in boiled demineralized water.

Two grams of powder were cleaned with 55 ml of cleaning solution; these amounts were determined from $BaCO_3$ contents in raw powder, estimated from thermogravimetric (TGA) measurements, and assuming the consumption of 20% of the acid during dissolution.

The suspensions were stirred at 150 rpm and maintained at fixed temperature.

The effects of acid cleaning conditions on the impurity content of the raw powder (namely [C] and [S]) were studied using a 2^4 statistical factorial design. The factors investigated were: (a) pH of the cleaning solution (3–4·5); (b) solution renewal after 2 h of cleaning (no–yes); (c) washing time (8–16 h); and (d) temperature (30–40°C).

After cleaning, the powder suspensions were centrifuged at 4000 rpm for 10 min. The supernatant was discarded and replaced by boiled demineralized water. Washing was repeated until constant conductivity (Schott CG858) of the supernatant was obtained.

Deagglomeration was performed by ultrasonicating 2·5 g of powder suspended in 50 ml of boiled demineralized water for 10 min at constant temperature (Bandelin UW 200 ultrasonic horn).

In order to avoid powder reagglomeration due to capillary forces upon drying, the deagglomerated suspensions were freeze-dried (CHRIST Alpha 1-4), and finally kept in a dessicator under a primary vacuum using $CaCl_2$ as a desiccant (32% relative humidity) until constant weight was reached.

Liquid limits (i.e. the minimum liquid/solid ratio necessary to obtain a free flowing mixture) were determined using 2·00 g of powder mixed with 200 μl of dispersing liquid, vibrating for 1 min at 35 Hz and adding successive 20 μl aliquots of dispersing liquid until the resulting dispersion flows under its own weight.

Slip cast specimens were prepared by mixing 2·00 g of powder with a volume of dispersing solution in excess by 50 μl/g over the measured liquid limit (aqueous solution of PAA with a neutralization ratio R = $[NH_3]/[PAA]$ = 1·5).[7] The slips were vibrated for 1 min at 35 Hz, ultrasonicated (P = 300 W, 7 l bath) for 10 min and outgassed for 1 min under a vacuum. The slips were cast in a silicone rubber mould placed on a flat gypsum base prevented against direct contact with the specimens by inserting a 0·2 μm cellulose membrane. Samples were prepared in this way in the form of blocks (approximately 12·5 × 6·5 × 6·5 mm) for dilatometry measurements, or in the form of discs for microscope observation. The samples were withdrawn from the mould after some hours, and dried to constant weight over $CaCl_2$ in a desiccator.

The processing parameters were studied using a 2^{5-1} statistical factorial design. The factors investigated were: (a) PAA concentration in the slip solution (0·8–1.0%); (b) calcination temperature (600–950°C), (c) cleaning medium (water–acid) — acid cleaning conditions giving the lowest carbon

content according to acid cleaning experience were chosen; (d) powder batch (BTN5-BTN8); and (e) ultrasonic horn power (80–120 W).

Thermogravimetric and differential thermal analyses (TGA-DTA) were performed simultaneously under flowing oxygen atmosphere (SETARAM 92-16.18): 200 mg of powder were weighed in a platinum crucible, and the temperature was raised up to 1000°C at 10°C/min and then up to 1400°C at 5°C/min.

Specific surface areas were measured by N_2 adsorption according to the BET model (Micromeritics type GEMINI 2360). Two grams of powder previously outgassed for 1 h at 200°C in flowing N_2, were used for each measurement.

Granulometry: a 20 mg powder suspension dispersed in a polyacrylic acid aqueous solution ([PAA] = 0·01% and R = 1·5) was used to determine the particle size distributions (HORIBA CAPA-700 cuvet photo centrifuge). Before measurement the suspensions were ultrasonicated for 10 min (P = 150 W, 7 l bath).

Evolved gas analyses (EGA) were carried out on a specific carbon + sulphur analyser (LEYBOLD-HERAEUS type CSA 2003): 0·1 g of powder, mixed with melting agents (1 g Fe + 0·5 g W) to ensure complete decomposition, were placed in a crucible in an induction furnace with flowing oxygen. After H_2O separation, the evolved gases were analysed by infra-red detectors specially calibrated for CO_2 and SO_2.

X-ray photoelectron spectroscopy measurements (XPS), (PERKIN ELMER Phi 5500 ESCA system, MgKα line 15 KeV-350 W) were carried out using several milligrams of powder placed on an indium substrate; the signal curves were fitted using Gaussian peaks summation and Shirley baseline subtraction.

Isothermal sintering (Lynn HT 1800G furnace) was carried out for 2 h at different temperatures, corresponding to densification and de-densification peaks, and different heating rates (1 and 10°C/min) were used to reach the sintering temperature.

Green and fired densities were measured by Archimedes' method, using isopropanol as an immersion liquid, and assuming the theoretical density of $BaTiO_3$ to be 6·02 g.cm^{-3}. For green density measurements, the samples were first saturated in a vacuum with isopropanol.

Dilatometric curves were measured under dry air (SETARAM DHT) using the following heating cycle: 10°C/min up to 800°C, 3·3°C/min up to 1400°C and 5°C/min down to room temperature. Intermediate densities were calculated from dilatometric curves corrected for thermal expansion and calibrated on measured final densities.

X-ray diffraction (XRD) (SIEMENS Kristalloflex 805 diffractometer, Ni-filtered Cu–Kα wavelength) was performed with a scanning step of 0.04 2θ and a 4 s sampling time for each point with digital collection of the resulting pattern.

Scanning electron microscopic observations (SEM) were performed by conventional methods (JEOL 6300 and CAMBRIDGE S-360), for both powder and sintered specimen observations. Sintered samples were polished and either thermally (heating up to 1200°C at 20°C/min) or chemically etched (10 min in a 1:1:2 mixture of HCl 37%, H_2O_2 and water).

Statistical analysis: the results of the statistical factorial experiments were analysed by the ANOVA method. The statistical significance of the observed effects is reported as the probability p of a Type I error (i.e. the risk to consider, by mistake, an effect as significant).

3 Results

3.1 X-ray diffraction

XRD spectra of raw powders show a cubic structure as reported in the literature for hydrothermal powders:[8] the diffraction profiles of powders calcined at 950°C tend to shift towards the tetragonal form, but the transition is completed for sintered samples. This effect can be attributed to the presence of internal OH giving sufficient elasticity to the structure to appear cubic to XRD analysis[5,8] and/or to the grain size.[9] $BaCO_3$ peaks are visible for both raw powders and disappear after 950°C treatment.

Second phase peaks are eliminated by both the acid cleaning treatments (pH = 3 and pH = 4·5) and by calcination at 950°C, while calcination at 600°C is ineffective.

3.2 Thermogravimetric analysis

Both raw powders exhibit very similar TGA behaviour (Fig. 1). Chemical and thermal treatments considerably modify the weight loss derivative (Fig. 2). The first DTG peak (150°C) is due to reversibly adsorbed water or CO_2. The second peak (250–300°C), which is partially reduced by acid cleaning, decreases significantly upon calcination at 600°C and is completely eliminated after calcination at 950°C. This behaviour can be related to the elimination of OH groups present in the crystal lattice, as observed by IR spectroscopy.[5] The peak at 950°C disappears after acid cleaning or after calcination at 950°C, while it is left unchanged by calcination at 600°C; therefore, it can be ascribed to the decomposition of $BaCO_3$ also observed by XRD.[2]

3.3 Differential thermal analysis

The DTA signal is noticeably affected by thermal and chemical treatments; Fig. 3 clearly shows the

presence of a liquid phase at about 1300°C for the acid cleaned powders.

3.4 Specific surface area

Specific surface measurements of raw and thermal treated powders are reported in Table 1: no substantial differences are observed between the two batches, both presenting high specific surfaces. After calcination at 950°C the specific surface area is reduced by 70%, of the original value, while calcination at 600°C causes only a 5–10% decrease.

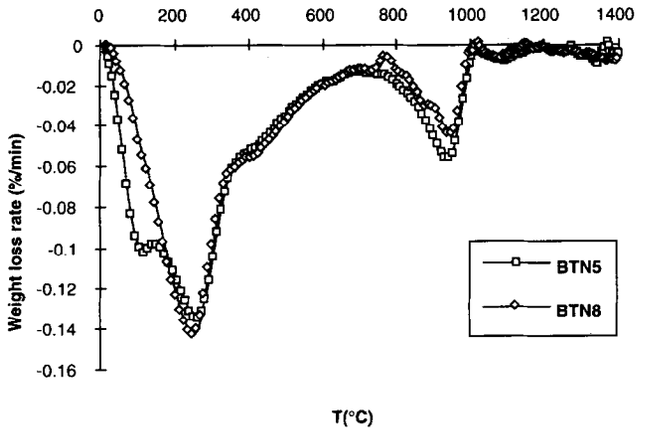

Fig. 1. Weight loss rate curves of raw powders.

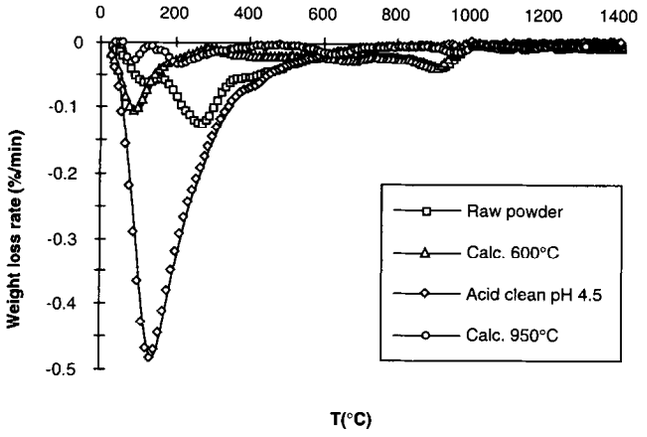

Fig. 2. Weight loss rate curves of powders from BTN5 batch, after various treatments.

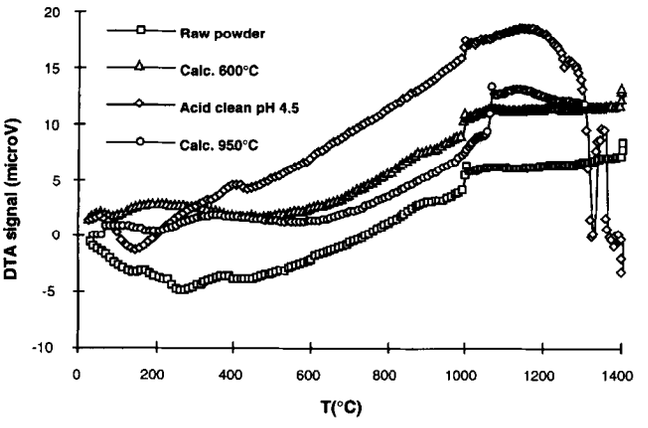

Fig. 3. DTA curves of powders from BTN5 batch, after various treatments.

3.5 Carbon and sulfur contents

EGA measurements have been carried out on raw or thermally treated powders, and powders treated chemically under different conditions: the results are reported in Table 2.

Calcination at 950°C considerably reduces the carbon content while calcination at 600°C gives only a very slight reduction. The sulfur content is low for all the samples (<13 ppm), none of the investigated factors having a significant effect ($p > 0.05$).

As shown in Fig. 4, the most important factor affecting the amount of residual carbon is the washing pH (factor D). Upon washing at pH = 3, precipitation of a sparingly barium citrate salt presumably occurs, thereby increasing the carbon content of the samples; the effect is stronger at a higher washing temperature (factor C); increasing the number of wash runs decreases the carbon content ($p < 0.01$).

The residual carbon content is much lower at pH = 4·5; the results were analysed separately, and are presented in Fig. 5. Here, the residual carbon increases with the wash time (factor B), and with temperature (factor C) ($p < 0.05$); the wash number (factor A) has no significant effect ($p > 0.10$). Thus, in order to minimize the residual carbon content, a single wash at 30°C for 8 h has been applied in the subsequent work.

3.6 XPS analysis

Surface Ba, Ti, O, C and Na contents were determined by XPS analysis on raw and treated powders;[11] the results are summarized in Table 3.

The Na content, calculated from the Na_{1s} transition decreases from about 3% for raw and calcined powders down to 1·1% for powders cleaned with the citric buffer and 0·6% for powders cleaned with the acetic buffer. The carbon content, calculated from the C_{1s} transition, increases from about 14·5% for the raw powders, up to 25% for the powders calcined at 950°C, and 38% for the powders cleaned with the citric buffer.

The Ba/(Ba + Ti) ratio was calculated from the $Ba_{3d5/2}$ and Ti_{2p} transitions. It decreases from about 40% for the raw powders and the powders calcined

Table 1. Specific surface area for raw, 600 and 950°C calcined powders

	Batch	
Treatment	*BTN5*	*BTN8*
Raw	27·2	27·5
Calcined, 600°C	25·9	24·7
Calcined, 950°C	8·5	8·0

Table 2. Residual carbon and sulfur concentrations after different treatments

Test number	*Treatment*	*Wash number*	*Wash time (h)*	*Temperature (°C)*	*pH*	*[C] (wt%)*	*[S] (ppm)*
1	'1'	1	8	30	3·0	6·55	12
2	a	2	8	30	3·0	4·68	7
3	b	1	16	30	3·0	8·61	5
4	ab	2	16	30	3·0	4·91	9
5	c	1	8	40	3·0	10·71	3
6	ac	2	8	40	3·0	6·70	3
7	bc	1	16	40	3·0	10·80	11
8	abc	2	16	40	3·0	8·31	3
9	d	1	8	30	4·5	0·20	2
10	ad	2	8	30	4·5	0·20	1
11	bd	1	16	30	4·5	0·23	4
12	abd	2	16	30	4·5	0·23	2
13	cd	1	8	40	4·5	0·27	1
14	acd	2	8	40	4·5	0·29	1
15	bcd	1	16	40	4·5	0·29	13
16	abcd	2	16	40	4·5	0·28	8
	Raw powder	—	—	—	—	0·27	1
	Calcined, 600°C	—	—	—	—	0·24	3
	Calcined, 900°C	—	—	—	—	0·04	3

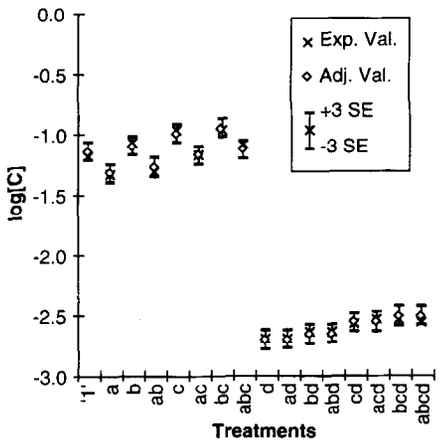

Fig. 4. Carbon content after acid washing (p <0·01).

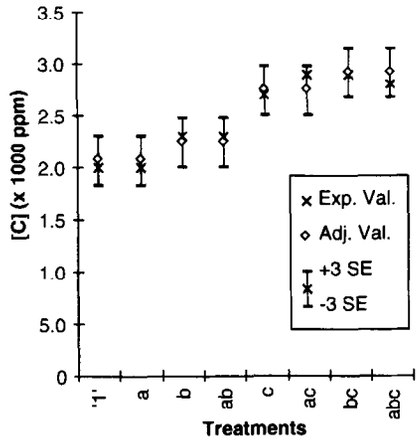

Fig. 5. Carbon content after acid washing at pH = 4·5 (acetic buffer, p <0·05).

at 600°C, down to 33% for the powders cleaned with the acetic buffer, indicating that this treatment has dissolved Ba in the form of Ba^{2+} ions. On the other hand this ratio increases up to about 50% for the powders calcined at 950°C and for those cleaned with the citric buffer. The shapes of the O and C peaks were not investigated in detail, because of their high sensitivity to atmospheric contamination.

The $Ba_{3d5/2}$ peak was resolved as the superimposition of two Gaussian components separated by 1·5 ± 0·1 eV, corresponding respectively to the titanate (the higher energy peak) and the carbonate matrix (the lower energy peak): the ratio $BaCO_3/BaTiO_3$ was calculated from these peaks.[2] Washing in the citric buffer increases the relative height of the carbonate peak, and consequently the thickness of the carbonate layer, by a factor of 10, while 950°C calcination leads to a 50% increase, and acetic buffer cleaning leads to a 40% decrease.

Table 3. XPS analysis (at%) of raw, calcined and acid cleaned powders

Treatment	*C (at%)*	*O (at%)*	*Ba (at%)*	*Ti (at%)*	*Na (at%)*	*Ba / (Ba + Ti)*	*$BaCO_3$ / $BaTiO_3$*
Raw	14·5	58·5	9·8	14·1	3·1	0·41	0·45
Calcined, 600°C	15·3	55·1	10·5	15·8	3·3	0·40	0·50
Calcined, 950°C	24·9	50·4	11·2	9·9	3·6	0·53	0·77
Cleaned, pH3	37·6	47·8	6·8	6·8	1·1	0·50	5·13
Cleaned, pH 4·5	13·5	59·0	9·0	18·0	0·6	0·34	0·30

3.7 Powder morphology

SEM observations showed irregular agglomerates of particles smaller than 100 nm, for both raw and 600°C calcined powders (Fig. 6). Conversely, calcination at 950°C results in compact and large agglomerates, up to 20 μm in size. Sintering has already started and the elementary particles are necked to each other, thereby reducing the specific surface (Fig. 7).

3.8 Green densities

Calcination at 950°C also reduces the liquid limit, while increasing significantly the green density up to 60% of the theoretical density (p <0·01), even though this green density is still lower than the one expected for randomly packed monosized spheres.[12]

On the other hand, the effects of stoichiometry, cleaning solutions (water or acetic buffer), PAA concentration in the dispersing solution, and ultrasonic horn power on these properties were found to be unsignificant (p >0·05).

3.9 Particle size distribution

The particle size distribution of the powder calcined at 950°C, treated with the ultrasonic horn and freeze dried, was measured with correction for light scattering;[13] this was the powder giving the highest green densities (Fig. 8). The median in volume distribution is 0·14 μm, but some agglomerates which can cause low green densities are still present.

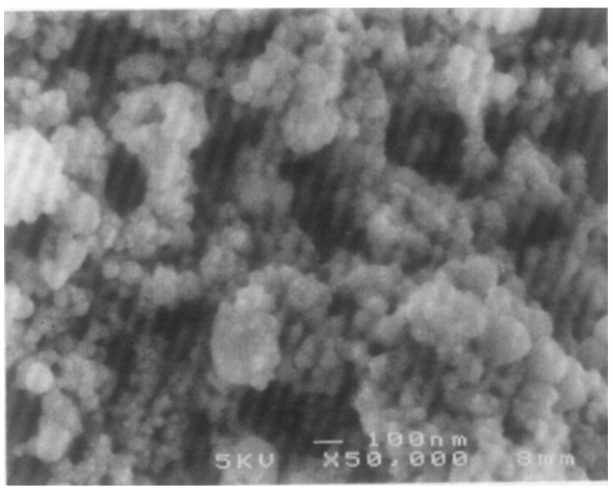

Fig. 6. SEM micrograph of raw powder from BTN5 batch.

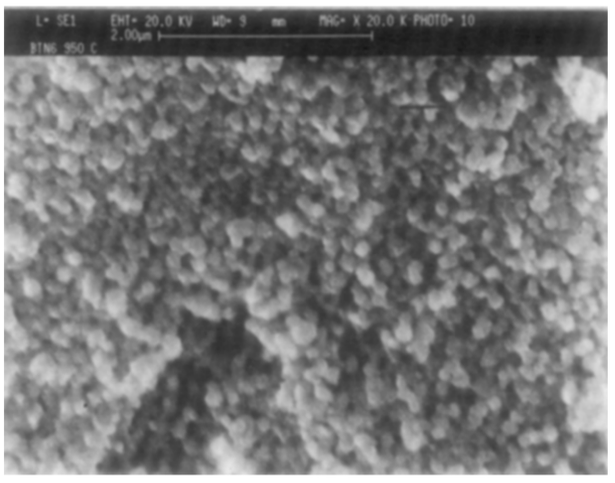

Fig. 7. SEM micrograph of powder from BTN5 batch calcined at 950°C.

3.10 Dilatometry

Dilatometric curves for BTN5 batch are reported in Figs 9 and 10, and in Figs 11 and 12 for BTN8 batch; the main features of these curves are summarized in Table 4. The two batches have the same sintering behaviour, except for the sintering and de-sintering (when present) peak temperatures. De-sintering is always observed with acid cleaned powders, and never with powders washed with demineralized water. For this reason, lower final densities are obtained with acid cleaned powders. The de-sintering phenomenon is less pronounced for the powders calcined at 600°C, probably due to a higher fraction of open porosity at the de-sintering temperature.

Samples from powders calcined at 950°C present starting and maximum densities higher than those calcinated at 600°C: the final density of water cleaned samples ranges between 91–93% and 95–96%, and between 67–74% and 82–86% for acid cleaned samples. Calcination at 950°C decreases by a factor of 2 times the height of the lower temperature sintering peak, because part of the shrinkage has already taken place during the calcination treatment.

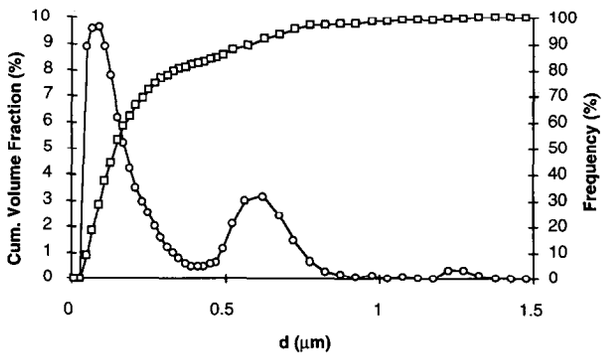

Fig. 8. Particle size distribution of powder from BTN5 batch calcined at 950°C.

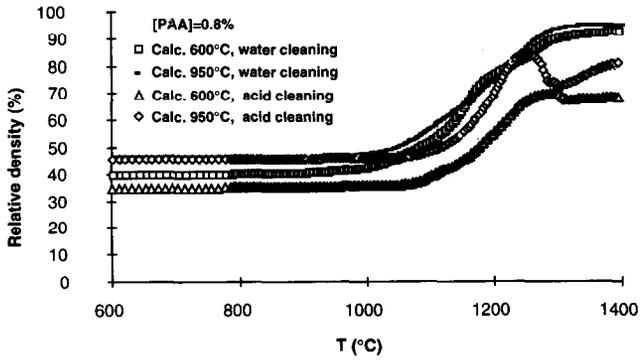

Fig. 9. Densification curves of calcined powders from BTN5 batch.

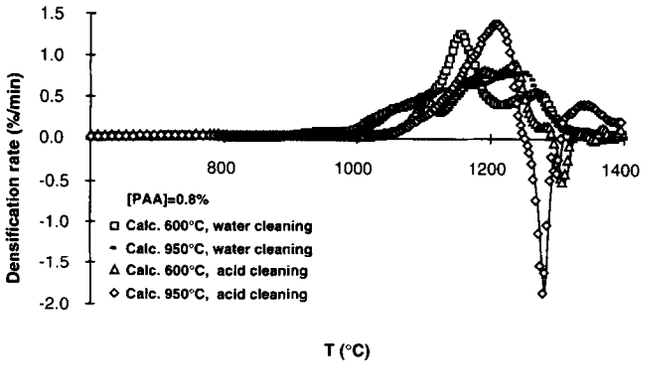

Fig. 10. Densification rate curves of samples from BTN5 batch.

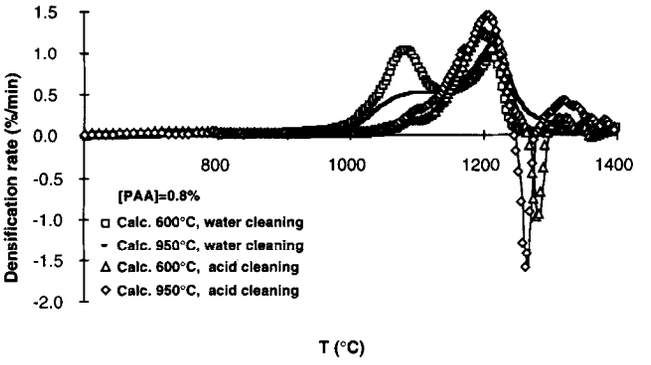

Fig. 12. Densification rate curves of samples from BTN8 batch.

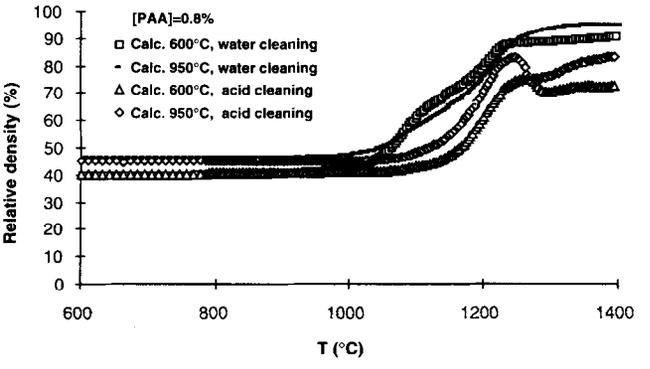

Fig. 11. Densification curves of samples from BTN8 batch.

3.11 Microstructure of sintered samples

SEM observations on non-isothermally sintered samples reveal a coarse-grained structure for water cleaned samples (Fig. 13), whereas acid cleaned samples present coarser grains and pores, probably caused by desintering (Fig. 14). Water cleaned samples sintered 2 h at the first densification peak temperature (Fig. 15) have a very fine grain size (<1 μm), although densification is not complete (≅ 93% theoretical density). The samples sintered at the second densification peak temperature exhibit higher densities: 95 and 97%, depending on the heating rate (10 and 1°C/min, respectively). SEM inspection of these samples reveals a homogeneous and fine-grained microstructure (Fig. 16), although some formation defects are still present (Fig. 17), which decrease density and cause local grain growth. The grain size distribution was measured for these samples: both present a log-normal monomodal distribution. The mean apparent grain diameter, calculated from the measurement of the areas of 350 grains (assuming spherical shape), was 1·4 ± 0·7 μm for the denser sample and 1·2 ± 0·6 μm for the second one.

4 Discussion

No effect on powder and compact properties was detected when the Ti/(Ba + Sr) ratio goes from 1·05 to 0·99, except for a shift in the sintering peak temperatures, which are higher for the Ti-rich batch. Impurities can probably account for this anomalous effect, as the stoichiometry would rather explain the opposite behaviour. Sintering of the raw powders starts at lower temperatures (about 900°C), and induces initially a reorganization of the crystallites together with a reduction of the surface area.

Calcination at 600°C does not lead to substantial changes in the raw powders. It eliminates the irreversible TG loss at 250–300°C and reduces the powder specific surface by about 5–10%. The decrease in surface area is accompanied by an increased surface carbon content, as revealed by XPS measurements: this effect is due to a redistribution of the carbon present on a smaller area, resulting in a

Table 4. Main characteristics of non-isothermal sintering for samples obtained from calcined powders after acid or water cleaning

	Pretreatment conditions		*Sintering characteristics*		
Batch	*Calcinated temperature (°C)*	*Cleaning*	*Maximum density ($\%D_{th}$)*	*Sintered peak (°C)*	*De-sintered peak (°C)*
BTN5	600	Water	93	1157	—
BTN5	950	Water	95	1247	—
BTN5	600	pH 4·5	69	1238	1311
BTN5	950	pH 4·5	83	1210	1280
BTN8	600	Water	91	1082	—
BTN8	950	Water	96	1215	—
BTN8	600	pH 4·5	74	1201	1281
BTN8	950	pH 4·5	82	1208	1264

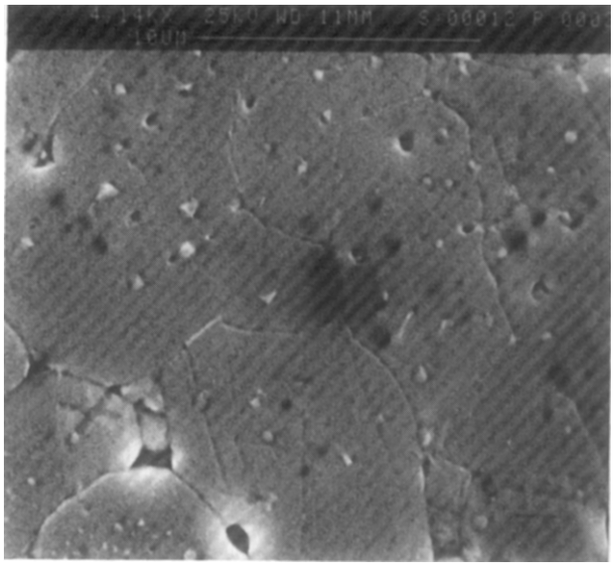

Fig. 13. SEM micrograph of sample non-isothermally sintered (1400°C); BTN8 powder calcined at 950°C and water cleaned.

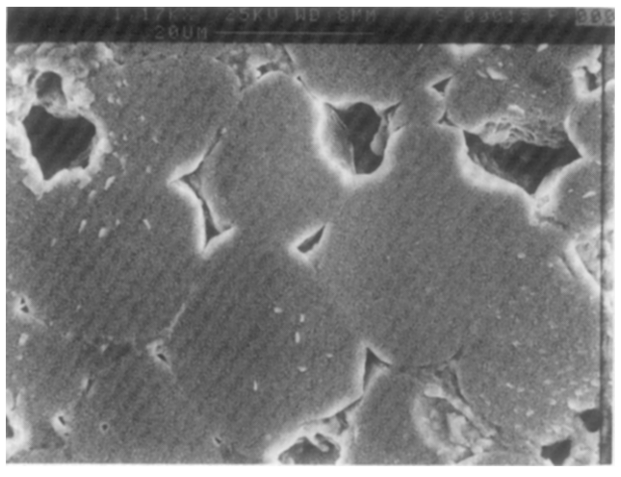

Fig. 14. SEM micrograph of a non-isothermally sintered sample (1400°C); BTN8 powder calcined at 950°C and cleaned with acetic buffer.

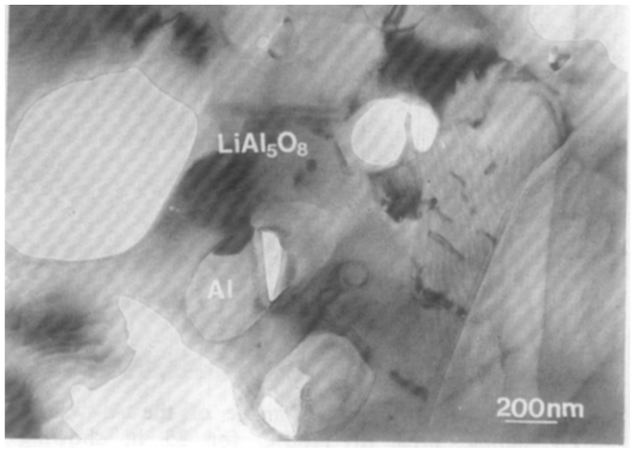

Fig. 15. SEM micrograph of an isothermally sintered sample (2 h, 1167°C, slow heating rate: 1°C/min); BTN5 powder calcined at 950°C and water cleaned (93% theoretical density).

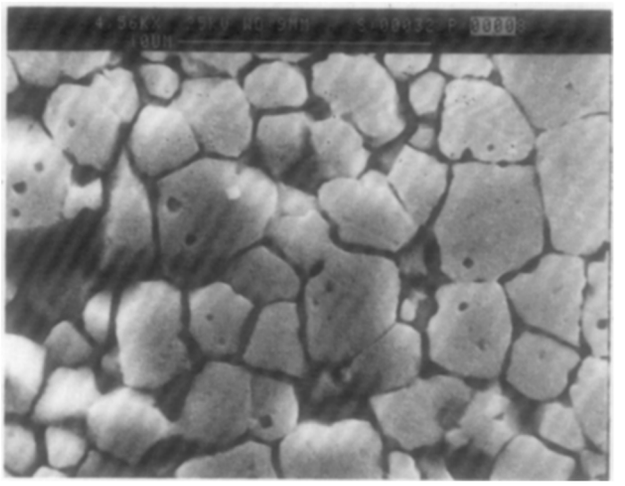

Fig. 16. SEM micrograph of an isothermally sintered sample (2 h, 1247°C, slow heating rate: 1°C/min); BTN5 powder calcined at 950°C and water cleaned (97% theoretical density).

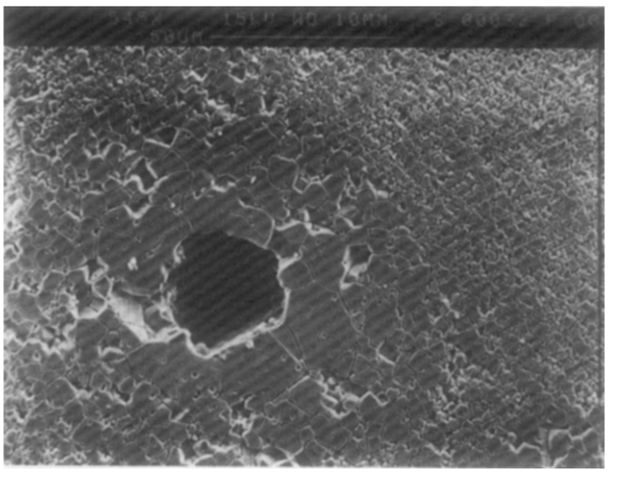

Fig. 17. SEM micrograph showing a forming defect in an isothermally sintered sample (2 h, 1247°C, slow heating rate: 1°C/min); BTN5 powder calcined at 950°C and water cleaned (97% theoretical density).

thicker carbonate layer. EGA measurements provide evidence for a reduction of about 10% in total carbon content. As a consequence, $BaCO_3$ is still present after this thermal treatment.

Calcination at 950°C reduces the surface area by about 70%, thereby increasing the carbon content detected by XPS. However the total carbon content measured by EGA is decreased dramatically from 0·27% down to 0·04%, and TG losses are markedly reduced. $BaCO_3$ is therefore almost completely decomposed, as confirmed by XRD, and the carbon is reduced to a reversibly bounded surface layer. Sintering is already active at this temperature, so that a strong agglomerate can form by inter-crystallite necking, as shown by SEM.

Green bodies made of powders calcined at 950°C have higher densities than those made of powders calcined at 600°C; in any case, however,

the green densities obtained are still low, due to formation defects. The better quality of the green bodies prepared from powders calcined at 950°C leads to higher sintered densities, even though the shrinkage starts at higher temperature. Formation defects and residual agglomerates in water-washed samples are responsible for lower than expected sintered densities, as they lead to the formation of pores with a higher-than-critical coordination number. SEM observation reveals the presence of pores in samples made from powders calcined at 600 or 950°C, though in smaller number for the latter temperature. Despite this residual porosity, densities up to 97% have been achieved at the peak temperature of densification (≅ 1250°C), after 2 h sintering (heating rate 1°C/min). This sintering temperature was quite low, due to the high surface area of the powders, which provides the driving force for shrinkage. The microstructure of these samples is quite interesting, because no evidence for abnormal grain growth is visible and the grain size is quite small (<2 μm).

Acid cleaning at pH = 3, precipitating barium citrate, caused an increase in carbon content instead of the decrease expected: for this reason the citric buffer cannot be recommended as a cleaning medium. The acid cleaning at pH = 4·5 was successful in eliminating partly the surface C and Na, but also dissolved some Ba from the surface. As a result, a Ti-rich surface is formed leading to the development of a liquid phase at about 1300°C, as detected by DTA. In fact, the BaO–TiO_2 system presents a eutectic composition melting at 1317°C,[10] whose melting temperature can be lowered by the presence of impurities.

No effect of chemical treatment was detected on green densities: acid cleaning does not seem to enhance de-agglomeration when the powders are treated with a US horn.

The surface modifications caused by acid cleaning, namely the elimination of a Ba-rich surface layer, lead to a sintering behaviour dramatically different from that of water cleaned powders. The shrinkage start is delayed and a de-sintering step appears, leading to markedly lower final densities. The delay of the onset of densification (from 900 to 1000°C) has been observed previously,[3] and can be ascribed to a more complete consolidation without shrinkage taking place when impurities are removed from the powder surface. The presence of a de-sintering step, absent in water cleaned powders, can be ascribed to the formation of a large amount of liquid phase. The liquid formed enhances the plasticity of the material, allowing a de-sintering process that can be due to CO_2 release[14] and to inhomogeneous densification:[15] lower densities are therefore obtained for acid cleaned powders.

5 Conclusion

The aim of the present work was to investigate the influence of surface treatments in order to obtain dense and small grained sintered samples. Acid cleaning with acetic buffer, which proved a useful method to increase the density of samples prepared from low specific surface area powders (<2 m^2/g),[3] degrades the ceramic properties of high specific surface powders synthesized by low-temperature aqueous precipitation. In fact, green densities are not enhanced compared to powders merely treated by ultrasonication and, in addition, de-sintering considerably reduces the final density. The removal of Ba from the surface should therefore be avoided.

Powders calcined at 950°C, water cleaned and ultrasonicated, can be sintered up to 97% of the theoretical density at relatively low temperatures (≅ 1250°C), with a fine grained homogeneous microstructure. The microstructure obtained is particularly favourable for dielectric properties, especially by comparison to results of similar treatments on commercial powders:[3] research on this promising synthesis route should therefore be continued. Higher fired densities can be obtained by enhancing green density, through elimination of forming defects and agglomerates that are still present. In order to avoid forming defects, the rheological properties of the casting slip should be optimized. Elimination of the agglomerates requires a stronger de-agglomeration technique such as ball-milling, but pollution effects from grinding media must be considered. In addition, the synthesis method, allowing the control of the crystallite size by changing some processing parameters, can also help to enhance the green density.

Acknowledgements

The authors would like to thank Dr C. Hérard and Dr P. Bowen for useful discussions, Mr B. Senior for SEM powder observations, Mr N. Xanthopulos for XPS measurements and Mr F. Rossetti for EGA analysis.

The financial support of the Swiss National Fund for Scientific Research (project no 21-29'914·90) is gratefully acknowledged by J. L.

COTRAO (Communauté de Travail des Alpes Occidentales) is acknowledged for a grant by M.A.D.

References

1. Dawson, W. J., Hydrothermal synthesis of advanced ceramics powders. *Am. Ceram. Soc. Bull.*, **67** (1988) 1673–8.
2. Hérard, C., Faivre, A. & Lemaitre, J., Surface decontamination treatments of undoped $BaTiO_3$. Part I: powder and green properties. *J. Europ. Ceram. Soc.*, **15** (1995) 135–43.

3. Hérard, C., Faivre, A. & Lemaitre, J., Surface decontamination treatments of undoped $BaTiO_3$. Part II: influence on sintering. *J. Europ. Ceram. Soc.*, **15** (1995) 145–53.
4. Nanni, P., Leoni, M., Buscaglia, V. & Aliprandi, G., Low temperature aqueous preparation of barium metatitanate powders. *J. Europ. Ceram. Soc.*, **14** (1994) 85–90.
5. Busca, G., Buscaglia, V., Leoni, M. & Nanni, P., Solid state and surface spectroscopic characterization of $BaTiO_3$ fine powders. *Chemistry of Materials*, **6** (1994) 955–61.
6. Alvazzi Delfrate, M., Leoni, M., Nanni, L., Melioli, E., Watts, B. E. & Leccabue, F., Electrical charaterization of $BaTiO_3$ made by hydrothermal methods. *J. Mater. Sc. Mater. in Electronics*, **5** (1994) 153–6.
7. Chen, Z.-C., Ring, T. A. & Lemaitre, J., Stabilization and processing of aqueous $BaTiO_3$ suspension with polyacrylic acid. *J. Amer. Cer. Soc.*, **75** (1992) 3201–8.
8. Hennings, D. & Schreinemacher, S., Characterization of hydrothermal barium titanate. *J. Europ. Ceram. Soc.*, **9** (1992) 41–6.
9. Uchino, K., Sadanaga, E. & Hirose, T., Dependence of the crystal structure on particle size in barium titanate. *J. Amer. Cer. Soc.*, **72** (1989) 1555–8.
10. Jaffe, B., Cook, W. R. & Jaffe, H., *Piezoelectrics Ceramics*, Academic Press, London and New York, 1971.
11. Hung, C. C., Riman, R. E. & Caracciolo, R., An XPS investigation of hydrothermal and commercial barium titanate powders. In *Ceramic Powder Science III*, **12** (1990) 17–25.
12. Nolan, G. T. & Kavanagh, P. E., Computer simulation of random packings of spheres with log–normal distributions. *Powder Technology*, **76** (1993) 309–16.
13. Bowen, P., Dirksen, J. A., Humphrey-Baker, R. & Jelinek, L., An approach to improve the accuracy of submicron particle size distribution using the Horiba CAPA-700. *Powder Technology*, **74** (1993) 67–71.
14. Demartin, M., Hérard, C., Lemaitre, J. & Carry, C., Grain growth and swelling of hot pressed $BaTiO_3$ during annealing treatments. In *Proceedings of Third Euro-Ceramics*, eds Duran P. & Fernandez J. F., Faenza editrice iberica, Madrid 1993, pp. 775–80.
15. Sudre, O. & Lange, F. F., The effect of inclusions on densification: III the desintering phenomenon., *J. Amer. Cer. Soc.*, **75** (1992) 3241–51.

Journal of the European Ceramic Society 16 (1996) 985–988

S0955-2219(96)00018-0
0955-2219/96/$15.00

Reactive Coating of Magnetite by a $PbO–B_2O_3–SiO_2$ Glass

Frank Müller,* Hanns P. Steier & José S. Moya

Instituto de Ciencia de Materiales de Madrid (ICMM-CSIC), Cantoblanco, 28049 Madrid, Spain

(Received 8 August 1995; revised version received 21 December 1995; accepted 3 January 1996)

Abstract

The wetting behaviour of a $PbO–B_2O_3–SiO_2$ glass on a pure magnetite substrate was studied in air and CO_2 atmosphere from room temperature to 600°C. The decrease in contact angle observed at 590°C was explained by considering the formation of an oxidized layer (~20 μm) during the wetting experiment. The final coating was proved to be free of cracks due to the small residual stress at the interface because of the low thermal expansion mismatch. © 1996 Elsevier Science Limited.

1 Introduction

Stoichiometric spinels have the general structure $A[B_2]X_4$, where A refers to cations in tetrahedral sites, B to cations in octahedral sites and X to anions that are essentially cubic close-packed. For example, the ferrites MFe_2O_4 — where M represents a solvent metal cation such as Mn^{2+}, Fe^{2+}, Co^{2+}, Ni^{2+} and Cu^{2+} — are a family of commercially important magnetic oxides. They all have magnetic spins exhibiting partial or completely inverse structures. The ferric ions on the tetrahedral sites have magnetic spins which are antiparallel to those on the octahedral sites. This arrangement gives the ferrites either antiferromagnetic or ferrimagnetic properties.[1]

Magnetic ceramics, most often represented by ferrites, are becoming increasingly important materials for electronic components. In recording media, ferrites are used to store information, either analogue as in music or speech recording or digital for computer and information processing. Therefore this material must be capable of being permanently magnetized locally but must be capable of being read or demagnetized without much difficulty.[2]

The aim of this investigation was to obtain a physically and chemically stable glass coating in order to protect magnetite (Fe_3O_4) substrate from environmental effects and also to improve its wear resistance. Glasses from the $PbO–B_2O_3–SiO_2$ system have been selected for this purpose.

2 Experimental

The following starting materials were used for the glass preparation: reagent grade $PbCO_3$ (Merck, D), and BO_2O_3 (Merck, D) and glassy silica (Vesuvius, E) powder (99.99%, < 10 μm). Based on the $PbO–B_2O_3–SiO_2$ phase diagram[3,4] (Fig. 1), as well as the data reported by Nagesh,[5] the following composition was selected: 70 wt% PbO, 20 wt% B_2O_3 and 10 wt% SiO_2. Batches of ~50 g of glass powder were obtained using the following procedure:

(i) dry mixing in an alumina ball mill for ~15 min;
(ii) the mixture was then melted in a silica–alumina crucible at 1000°C for 30 min with a heating rate of 10°C min^{-1}; and
(iii) the melt was water-cooled, then dried at 100°C for 2 h, and subsequently dry ball-milled down to 37 μm.

After this operation, wet chemical analysis performed on the glass powder by means of inductively coupled plasma analysis (ICP) found: SiO_2, 10·74; Al_2O_3, 2·40; PbO, 65·30; B_2O_3, 21·0 (in wt%).

Magnetite powder (Aldrich Chemie, D) with 5 μm average particle size was used. This powder was attrition-milled in isopropanol for 1 h, using Si_3N_4 balls. After drying at 70°C for 24 h, the powder was sieved down to 63 μm in order to eliminate agglomerates. The average particle size was determined by scanning electron microscopy (SEM) to be ~2 μm. The powder was subsequently cold-isostatically pressed at 200 MPa into a cylindrical block with ~12 mm diameter. Based on the data reported by Yamaguchi *et al.*,[6] it was sintered at 1175°C for 2 h in a flux of CO_2 (0.4 l min^{-1}). The sintered samples were cut and polished down to 1 μm for optical

*Permanent address: Friedrich-Alexander-Universität, Erlangen, Germany.

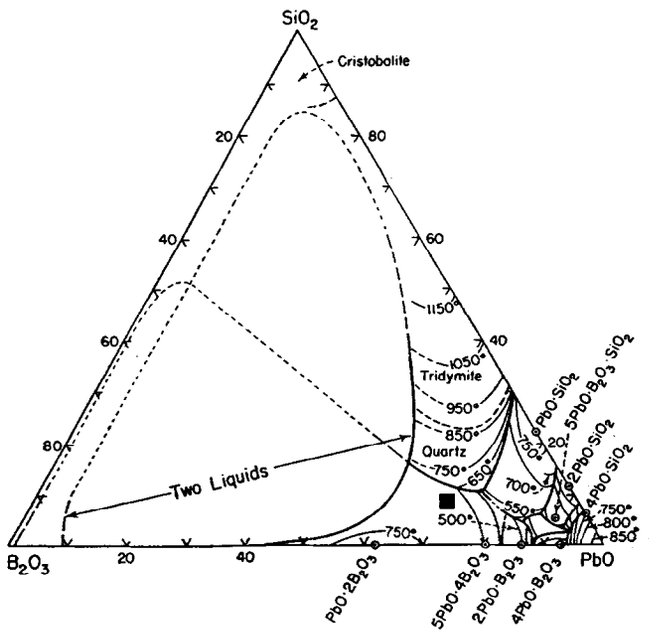

Fig. 1. Phase equilibrium diagram of the $PbO–B_2O_3–SiO_2$ system (■, glass composition).

microscope- and SEM observation. The wetting behaviour of the glass on the polished magnetite surface was studied using an optical high-temperature microscope. Analysis of cross-sections was performed by energy dispersive spectroscopy in the SEM (SEM-EDS).

An ink containing glass powder (<37 μm) was obtained by mixing it with ethylene glycol (33 wt%). The polished surfaces of magnetite sintered blocks were coated with this suspension by screen printing and heat-treated at different temperatures in air and CO_2 atmospheres.

The thermal expansion of the glass and the magnetite blocks (5 × 5 × 5 mm) was determined in the temperature range from room temperature to 350°C.

3 Results and Discussion

The thermal expansion coefficients of the glass and magnetite were found to be $8{\cdot}1 \times 10^{-6}$ and $8{\cdot}3 \times 10^{-6}$ °C^{-1}, respectively.

Figures 2 and 3 show a SEM micrograph of the fractured surface of the magnetite and the XRD pattern of the polished surface. It can be seen that the average grain size of the sintered pure magnetite block with ~88% theoretical density is ~2 μm. Figure 4 presents high-temperature micrographs of the $PbO–B_2O_3–SiO_2$ glass on magnetite obtained at different temperatures and times, while in Fig. 5 the contact angle vs. time at 590°C in air is plotted. As observed, at this temperature a very low contact angle (<20°) is obtained after 1 h treatment, which indicates a high wettability. A similar trend was observed in CO_2. The main difference in the microstructure observed between both treatments (air, CO_2) was the bubble content of the glass (Fig. 6).

Figure 7 shows a SEM micrograph of the glass-magnetite cross-section, where it can be seen that the obtained glassy coating (~ 60 μm) is almost free of bubbles. The surface layer (~20 μm) in contact with the glassy coating was found to be haematite (Fe_2O_3) by both SEM-EDS and XRD thin film analysis. The corresponding XRD thin film analysis of a glass-free magnetite substrate after heating at 590°C for 1 h in both air and CO_2 shows the presence of a haematite layer (Fig. 8). This fact is in agreement with the $FeO–Fe_2O_3$ equilibrium diagram,[7] i.e. at this particular temperature magnetite is stable only at

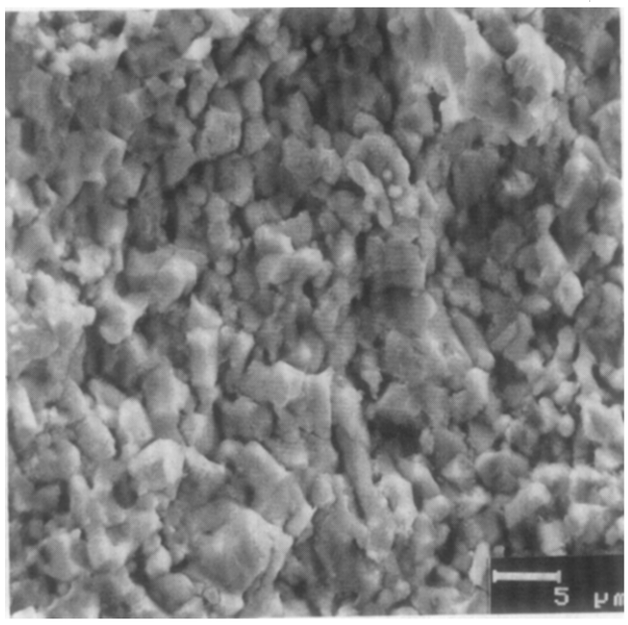

Fig. 2. SEM micrograph of the fracture surface of magnetite after sintering at 1175°C.

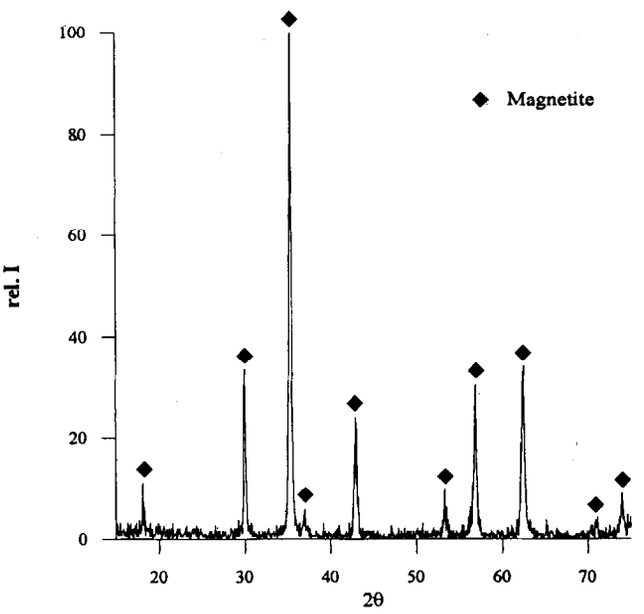

Fig. 3. XRD pattern of the polished surface of magnetite after sintering at 1175°C.

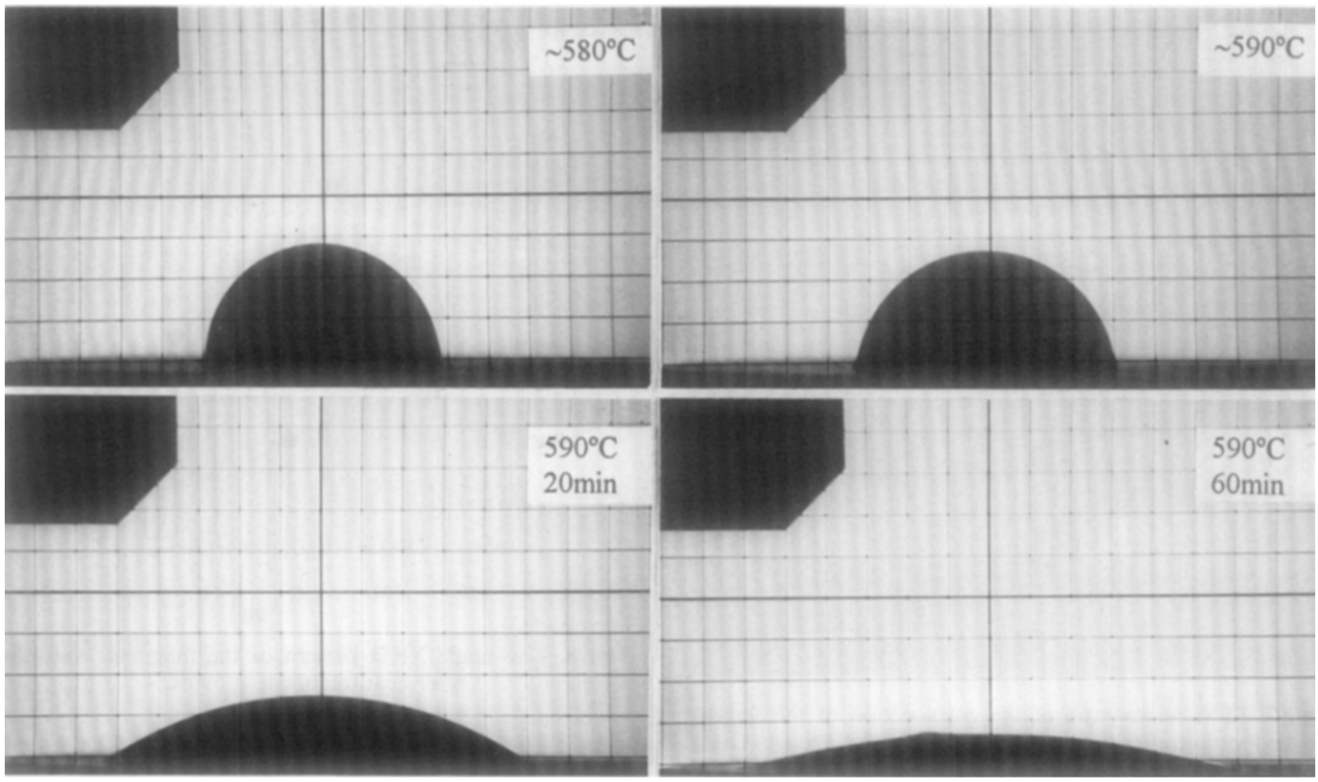

Fig. 4. Optical high-temperature micrographs of $PbO–B_2O_3–SiO_2$-glass on magnetite.

$P_{O_2} < 10^{-20}$ atm. In a pure CO_2 atmosphere this low P_{O_2} partial pressure is not reached.

The wetting behaviour of this particular glass (Figs 4 and 5) on the magnetite substrate can be understood by considering that oxidation of the magnetite surface layer with the formation of haematite, which takes place in air and CO_2 during the wetting experiments at 590°C (Fig. 8), is the driving force for the observed reactive wetting.[8] According to Young's equation $\gamma_{SV}-\gamma_{SL} = \gamma_{LV}\cos\theta$, where γ_{SV} and γ_{LV} are the surface free energies of the solid/vapour and liquid/vapour, γ_{SI} is the interfacial energy of the solid/liquid and θ is the contact angle, θ will tend to zero as γ_{SI} decreases. During oxidation γ_{SI} is decreasing, and consequently, decreases in the contact angle have been observed (Fig. 5). Thus, we can conclude that the oxidation of the magnetite surface was the driving force for the spreading of the glass at 590°C.

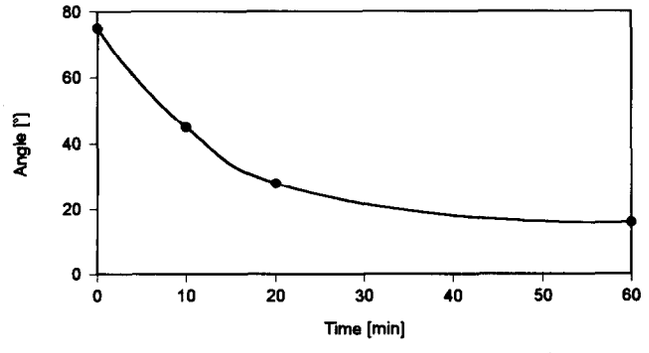

Fig. 5. Contact angle vs. time at 590°C in air.

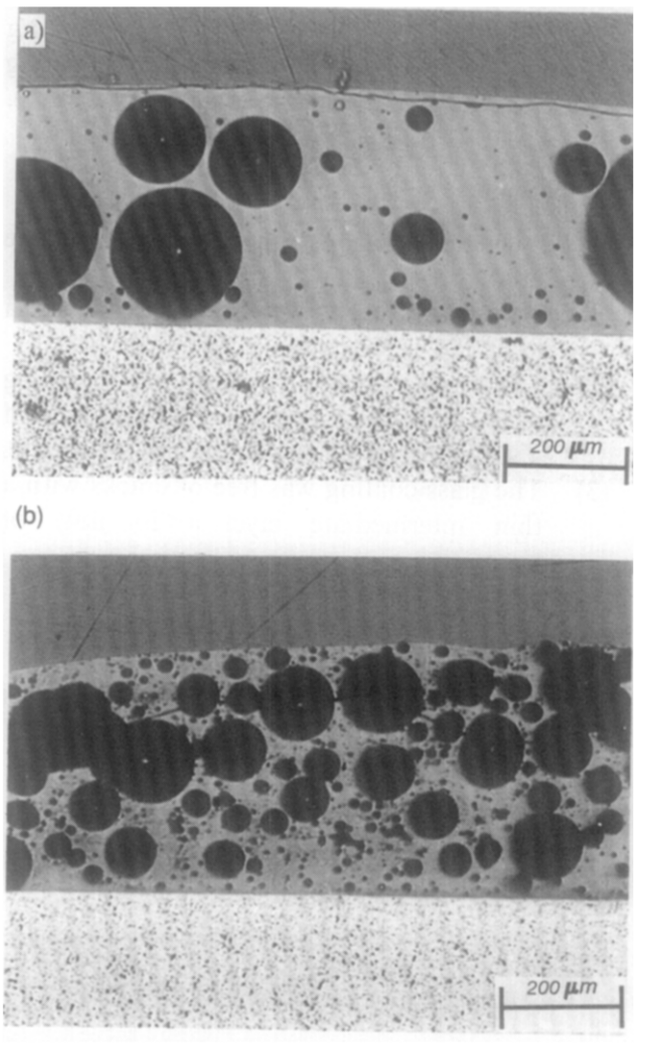

Fig. 6. Optical micrographs of the cross-sections of samples after the sessile drop experiment at 590°C for 1 h in (a) air and (b) CO_2.

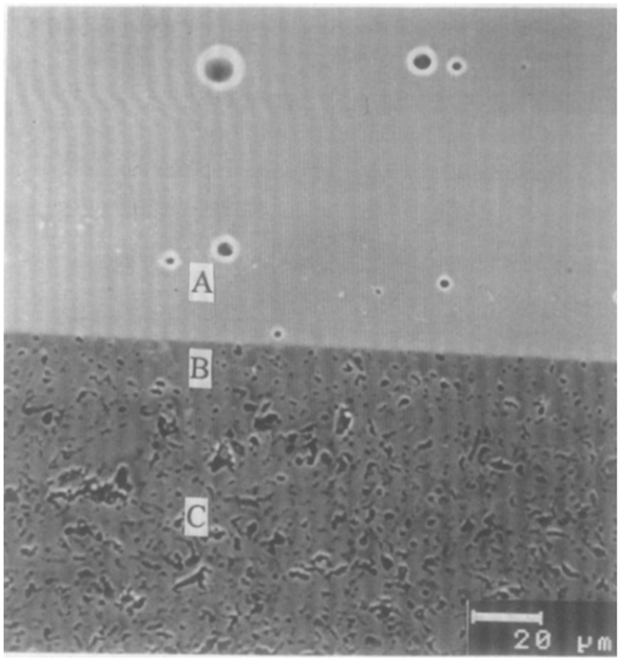

Fig. 7. SEM micrograph of the cross-section of the screen-printed sample after heating in air at 590°C for 1 h. (A) Glass coating; (B) haematite intermediate layer; (C) magnetite substrate.

Due to the small mismatch (<3%) between the thermal expansion coefficients of the glass coating and the magnetite substrate, a perfect glass coating free of cracks at the interface was obtained (Fig. 7).

4 Conclusions

The following conclusions can be drawn from the present study.

(1) It is possible to coat magnetite by a $PbO–B_2O_3–SiO_2$ glass at 590°C in air.

(2) The driving force for wetting and spreading of the glass was found to be the oxidation of a surface layer of magnetite into haematite.

(3) The glass coating was free of cracks with a thin intermediate layer (<20 μm) of haematite.

Acknowledgements

This work was supported by CICYT (Spain) under contract MAT. 94-0974. F. Müller thanks COMETT for financial support. H. P. Steier thanks the Commission of the European Communities. The authors thank A. P. Tomsia for the helpful discussion.

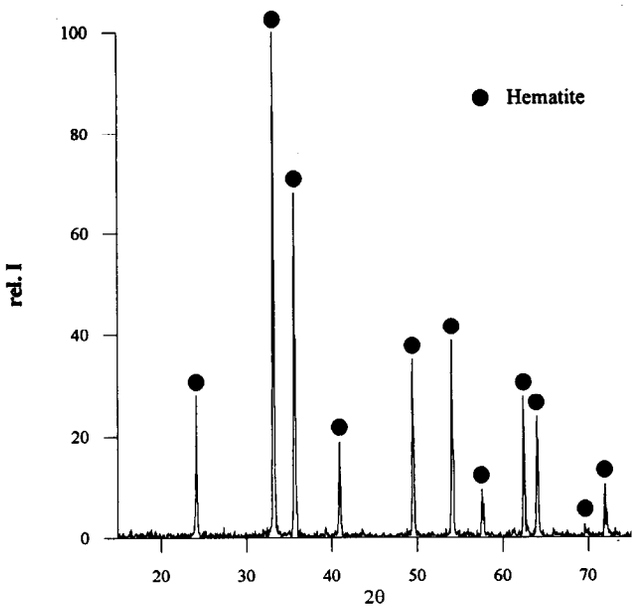

Fig. 8. Low-angle XRD pattern of the magnetite substrate after heat treatment at 590°C.

References

1. *Engineered Materials Handbook, Vol. 4: Ceramics and Glasses*. ASM International, Metals Park, OH, 1991.
2. Levinson, L. M., Electronic ceramics. In *Magnetic Ceramics*, ed. A. Goldman, Marcel Dekker Inc., New York, 1987, p. 47.
3. Geller, R. F. & Bunting, E. N., *J. Res. Natl. Bur. Standards*, **23**(8) (1939) 279.
4. *Phase Diagrams for Ceramists*. American Ceramic Society, Westerville, OH, Fig. 740.
5. Nagesh, V. K., Electrical conduction in metal–glass composite materials. *Report LBL-5172*, Lawrence Berkeley Laboratory, CA, 1976.
6. Yamaguchi, T., Ishii, T. & Mochizuki, A., Effect of additives on magnostrictive properties of magnetite. *Funtai Oyobi Funmatsuyakin*, **24**(8) (1977) 236–41.
7. Muan, A., The effect of oxygen pressure on phase relations in oxide systems. In *Phase Diagrams: Materials Science and Technology, Vol. 6-II*, ed. A. Alper. Academic Press, 1970, pp. 1–19.
8. Dalgleish, B. J., Saiz, E., Tomsia, A. P., Cannon, R. M. & Ritchie, R. O., Interface formation and strength in ceramic–metal systems. *Script. Met.*, **31**(8) (1994) 1109–14.

Journal of the European Ceramic Society **16** (1996) 989–993

S0955-2219(96)00022-9
0955-2219/96/$9.50

Preparation of Micro-Coiled ZrC Fibres by Vapour Phase Metallizing of Micro-Coiled Carbon Fibres

S. Motojima,[a] H. Asano[a] & H. Iwanaga[b]

[a]Department of Applied Chemistry, Faculty of Engineering, Gifu University, Gifu 501-11, Japan
[b]Faculty of Liberal Arts, Nagasaki University, Nagasaki 852, Japan

(Received 26 June 1995; revised version received 4 January 1996; accepted 8 January 1996)

Abstract

Micro-coiled ZrC fibres were prepared by the vapour phase metallizing of micro-coiled carbon fibres using a $ZrCl_4$ + H_2 + Ar gas mixture at 1100–1250°C. The preparation conditions, morphology and bulk electrical resistivity of the obtained ZrC coils were examined. The coiling morphology of the source coiled carbon fibres was fully preserved even after this treatment. The bulk resistivity of the coiled ZrC fibres decreased with bulk density and was 10^{-1} s^{-1} cm at 0·8 g cm^{-3}. © 1996 Elsevier Science Limited.

1 Introduction

Raw materials with a micro-coiled or helical morphology are not currently available. The helical morphology of DNA and some vine plants affords living bodies with essential functional roles. Accordingly, we could expect novel functional properties from such coiled materials. Addamiano[1] and Kang *et al.*[2] reported the preparation of micro-coiled SiC fibres using an impurity-activated chemical vapour deposition (CVD) process. Vogt *et al.*[3] prepared regularly micro-coiled Si_3N_4 fibres by the CVD process. We have obtained regularly micro-coiled Si_3N_4 fibres by the metal impurity-activated CVD process using Si_2Cl_6,[4–7] SiO_2 + C or SiO[8] as the Si source at 1200–1500°C. However, the growth of the micro-coiled fibres from the vapour phase was extremely accidental with low reproducibility. Johansson and Schweitz[9] prepared a boron spring by a laser-assisted CVD process using a three-dimensional micropositioning system. Macro-coiled ceramic springs or windings of above 5 mm in coil diameter were prepared by conventional calcination and sintering of an extruded polymer–ceramic suspension winding.[10] However, preparation of micro-coiled springs or fibres using these processes is very difficult.

We obtained regularly micro-coiled carbon fibres by the catalytic pyrolysis of acetylene with high coil yield and reproducibility.[11–15] Generally, carbon can easily be vapour phase metallized followed by solid-state diffusion to form the corresponding metal carbides. Accordingly, the metallization treatment of micro-coiled carbon fibres is considered to be the most promising process for obtaining micro-coiled fibres of the metal carbides. Coiled fibres of SiC[16] or TiC[14,15] were obtained by the CVD process or the metallizing of the coiled carbon fibres. However, their preparation conditions, morphology and characteristics have not been examined. The metal carbides have good properties such as high thermal and chemical stabilities, super-high hardness and high electrical conductivity. Thus their micro-coiled fibres are potential candidates for fillers in electromagnetic shielding materials, elastic packing or filter materials resistant to high temperatures and/or harsh or corrosive environments, and for micromechanical elements such as microsprings and micro sensors.

ZrC whiskers were prepared by the metal impurity-activated CVD process.[17–19] However, the deposition of coiled ZrC fibres has not been reported.

In this work, micro-coiled ZrC fibres were obtained by the vapour phase metallizing of the micro-coiled carbon fibres obtained by the catalytic pyrolysis of acetylene. The preparation conditions, morphology and electric resistivity of the coiled ZrC fibres were examined.

2 Experimental

Source micro-coiled carbon fibres (abbreviated as 'carbon coils' hereafter) were prepared by the Ni-metal catalysed pyrolysis of acetylene. The detailed preparation procedures and conditions

are given in Ref. 12. The used carbon coils are 1–5 μm in coil diameter and 50–500 μm in coil length. The source carbon coils were placed in a mullite boat which was located in the central part of a horizontal reaction tube (mullite, 20 mm i.d.). The carbon coils were vapour phase zirconized under a $ZrCl_4 + H_2 + Ar$ atmosphere at 1100–1250°C. The $ZrCl_4$ gas was prepared *in situ* by the chlorination of Zr sponge at 700°C and was carried by Ar into the reaction tube. Gas flow rates of $ZrCl_4$, H_2 and Ar were fixed at 5 sccm (ml s^{-1}), 100 sccm and 40 sccm, respectively.

3 Results and Discussion

3.1 Preparation of micro-coiled ZrC fibres

Figure 1 shows the influence of the square root of the zirconizing time on the zirconizing ratio of the source carbon coils as a function of reaction temperature. The zirconizing ratio was obtained from the weight gain due to zirconizing. The zirconizing ratio increased linearly with increasing zirconizing times irrespective of zirconizing temperature. Furthermore, it can be seen that the zirconizing ratio was only 25% after 4 h of zirconizing time at 1250°C. That is, the carbon coils were zirconized only near the surface under the conditions used in this work. The obtained zirconized carbon coils (abbreviated as 'ZrC coils' hereafter) have a carbon core which was not zirconized. The ZrC layers formed on the surface of the carbon coils were very dense without pores. The density of the formed ZrC layers was not examined. However, the above result suggests that the rate-determining step is diffusion of the Zr or carbon atoms through the formed ZrC layers.

The representative morphology of the ZrC coils obtained after zirconizing for 1 h at 1200°C is shown in Fig. 2. It was observed that the coiling morphology of the source carbon coils was fully preserved after zirconizing under any of the zirconizing conditions, except for a slight diameter increase in the carbon fibres. Carbon coils having a rectangular cross-section as well as those with the common circular cross-section as shown in Fig. 2 were sometimes observed in the source carbon coils. Flat or ribbon-like carbon coils were also zirconized with full preservation of the morphology to form flat or ribbon-like ZiC coils. Figure 3 shows various types of the flat or ribbon-like ZrC coils. Grain growth or secondary crystal growth on the surface of the ZrC coils was not observed even after zirconizing the carbon coils at 1250°C for 2 h, as shown in Fig. 4(b). The grain size of the ZrC observed on the surface was about 10 nm.

The X-ray diffraction (XRD) profiles of the ZrC coils obtained after a 60 min zirconizing time at 1100–1250°C are shown in Fig. 5. Apparent peaks indicating ZrC were not observed at 1100°C. Small peaks of $ZrCl_2$ as well as the apparent large peaks of ZrC were observed at 1200–1250°C. The $ZrCl_2$ decomposes above 350°C to form metal Zr and $ZrCl_4$. Accordingly, these peaks of $ZrCl_2$ may be caused by the contamination of the specimen by the $ZrCl_2$ by-product when the temperature was lowered. Figure 6 shows the XRD profiles of the ZrC coils obtained

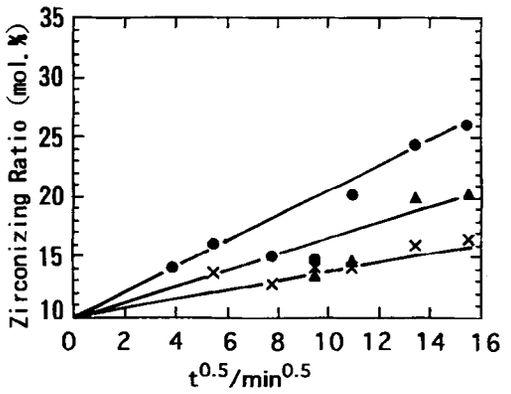

Fig. 1. Effect of square root of zirconizing time on the zirconizing ratio of the carbon coils. $ZrCl_4$ gas flow rate: 1·5 sccm, H_2 flow rate: 70 sccm, Ar flow rate: 40 sccm. Zirconizing temperature: ●, 1250°C, ▲, 1150°C, ×, 1100°C.

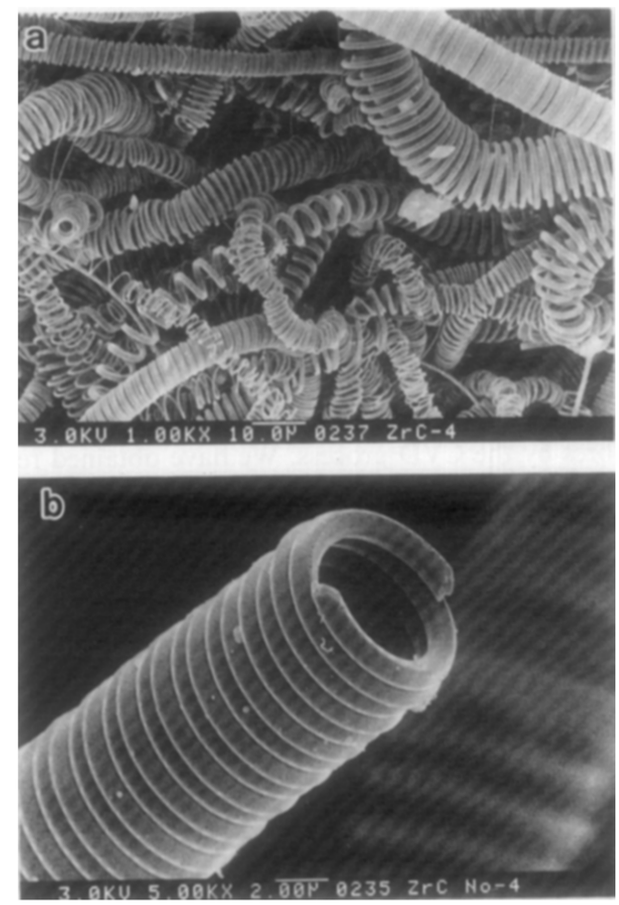

Fig. 2. Representative morphology of the ZrC coils (a) and the enlarged view (b).

after 15–120 min at 1250°C. Apparent peaks of ZrC were observed for a 15 min zirconizing time, and peaks were sharper with increasing zirconizing time.

Figure 7 shows a transmission electron micrograph (dark-field image) and electron diffraction profile. A halo ring (H) as well as Debye–Sherrer rings (A–D) are observed in Fig. 7(b). The source carbon coils used have an amorphous state, and this halo ring is caused by the unzirconized core part of the carbon coils. It is considered that the ZrC coils obtained in this work were only partly zirconized carbon coils, and the ZrC layers formed on the surface had a polycrystalline state.

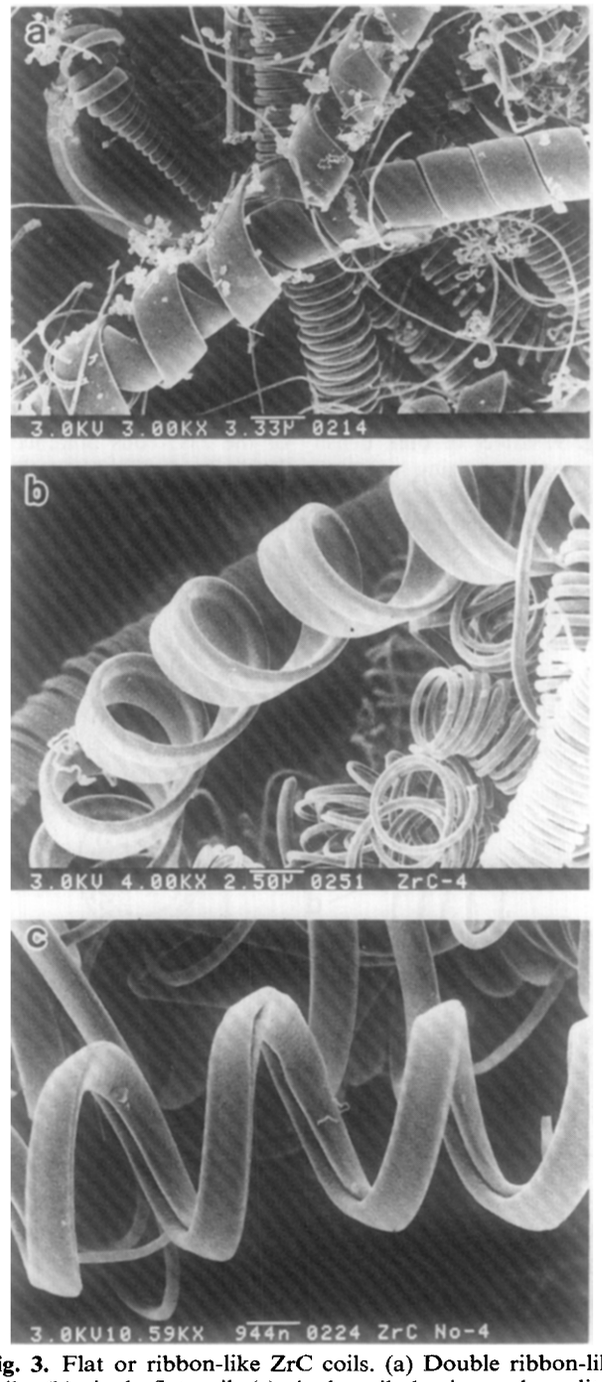

Fig. 3. Flat or ribbon-like ZrC coils. (a) Double ribbon-like coils, (b) single flat coil, (c) single coils having a deep ditch on the inside.

3.2 Bulk electrical resistivity of the ZrC coils

The bulk electrical resistivity of the ZrC coils was measured using a 10 mm i.d. cylindrical measurement cell. The effect of bulk density of the ZrC coils obtained at various zirconizing temperatures on the bulk electrical resistivity is shown in Fig. 8, in which zirconizing time was fixed for 120 min. The resistivity of the ZrC coils decreased

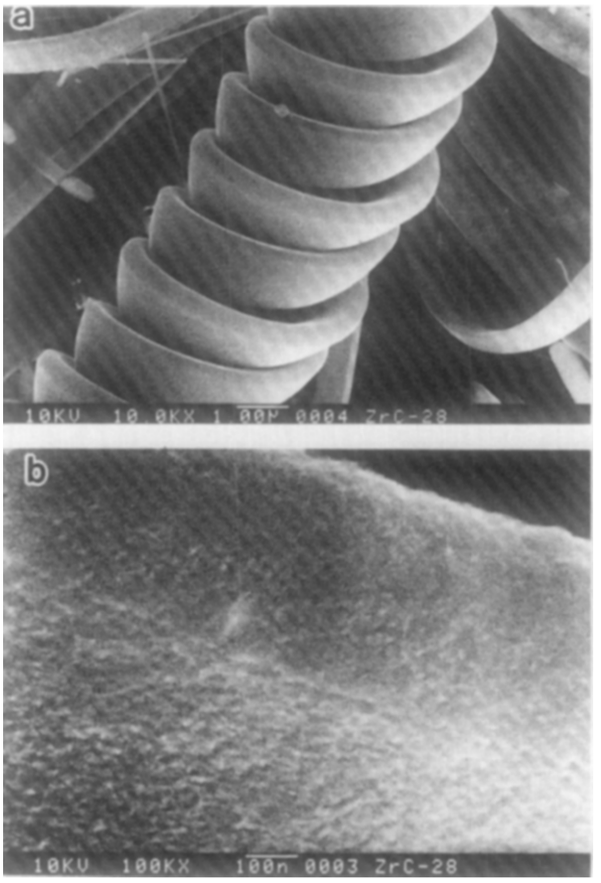

Fig. 4. ZrC coils having a rectangular cross-section (a) and the enlarged view (b).

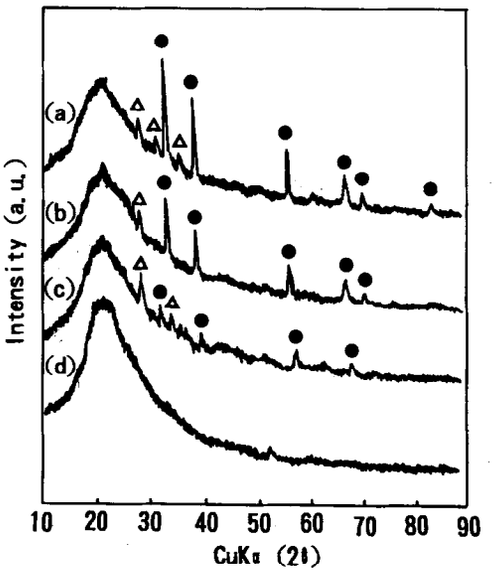

Fig. 5. XRD profiles of the ZrC coils obtained at various zirconizing temperatures. Zirconizing time: 60 min. Zirconizing temperature: (a) 1250°C, (b) 1200°C, (c) 1150°C, (d) 1100°C. ●, ZrC; Δ, $ZrCl_2$.

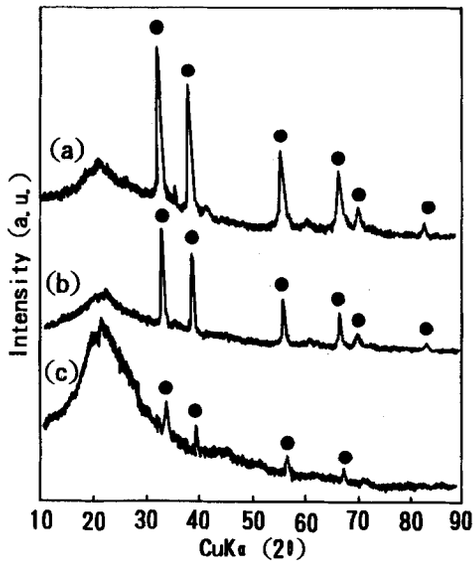

Fig. 6. XRD profiles of the ZrC coils obtained at various zirconizing times. Zirconizing temperature: 1250°C. Zirconizing time: (a) 180 min, (b) 120 min, (c) 15 min. ●, ZrC.

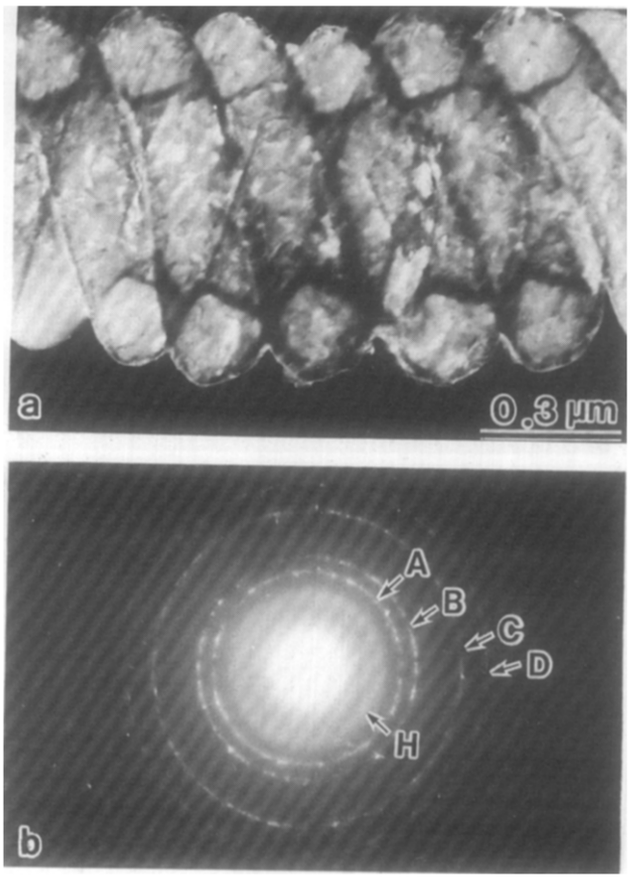

Fig. 7. Dark field image (a) and electron diffraction profile of the ZrC coils (b). A (111), B (200), C (220), D (311). H indicates halo pattern.

with increasing zirconizing time. No apparent effect of zirconizing temperature on the bulk resistivity was observed. The effect of zirconizing time on the bulk resistivity of ZrC coils is shown in Fig. 9, in which the zirconizing temperature was fixed at 1250°C. The bulk resistivity of the ZrC coils decreased with increasing zirconizing

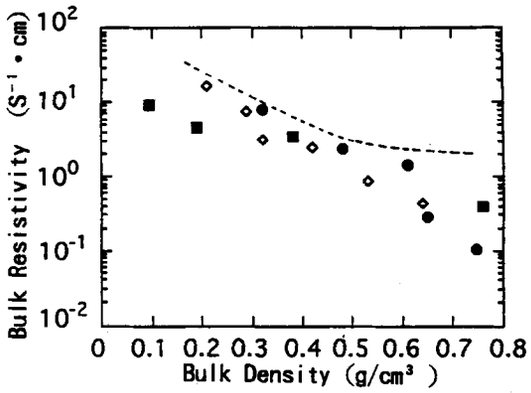

Fig. 8. Effect of bulk density of the ZrC coils obtained at various zirconizing temperatures on the bulk electrical resistivity. Zirconizing time: 180 min. Zirconizing temperature: ●, 1250°C; ■, 1200°C; ◊, 1150°C. ----, Source carbon coils.

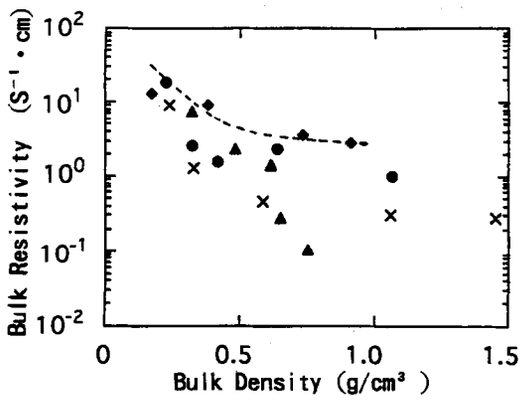

Fig. 9. Effect of bulk density of the ZrC coils obtained at various zirconizing times on the bulk electrical resistivity. Zirconizing temperature: 1250°C. Zirconizing time: ●, 15 min; ◆, 60 min; ×, 120 min; ▲, 180 min. ----, Source carbon coils.

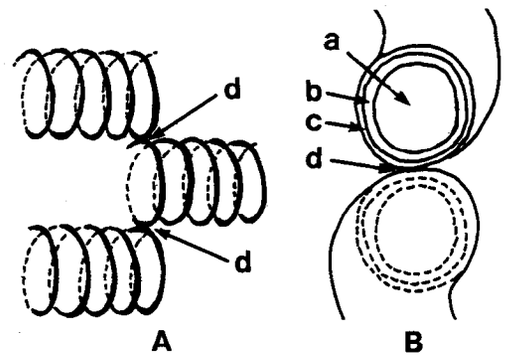

Fig. 10. Schematic contact conditions of the bulk ZrC coils (A) and the enlarged cross-section (B). a, Carbon core; b, ZrC clad; c, Zr-oxide layers; d, contact part.

time and attained a low value of about 10^{-1} s^{-1} cm at 0·8 g cm^{-3} for 120 min zirconizing time. The electric contact conditions in the bulk ZrC coils and the cross-section of the contact part are shown schematically in Fig. 10. It is postulated that very thin zirconium oxide layers are formed on the surface of the ZrC layers (ZrC clads). Accordingly, the bulk electrical resistivity of the ZrC coils, R, can be estimated by the equations

$$\frac{1}{R_b} = \frac{1}{R_c} + \frac{1}{R_z} + \frac{1}{R_o} \quad (1)$$

$$R = R_b + R_a + R_c \quad (2)$$

where R_b, R_c, R_z and R_o are the electrical resistivity of the ZrC coils, source carbon coils (carbon core), ZrC layers (ZrC clad) and zirconium oxide layers formed on the ZrC clad, respectively, and R_a is a contact resistivity between the ZrC coils. The density and electrical resistivity of the ZrC clad as well as the carbon core are not known. The densities of the $ZrC_{1.0}$ single crystal and amorphous carbon is 4·0 g cm^{-3} and about 2·0 g cm^{-3}, respectively. The carbon coils are in an amorphous state. The ZrC coils obtained at 1250°C for 120 min have a ZrC clad with 20% of the total cross-section, and the density of the ZrC coils is estimated to be 2·4 g cm^{-3}. The electrical resistivities of the $ZrC_{0.97}$ crystal and vapour-grown straight carbon fibres are 5×10^{-4} s^{-1} cm (Ref. 20) and 1×10^{-3} s^{-1} cm (Ref. 21), respectively.Accordingly, the electrical resistivity of the ZrC coils is estimated to be $3{\cdot}6 \times 10^{-4}$ s^{-1} cm. This value is two orders of magnitude lower than that of 1×10^{-1} s^{-1} cm obtained for the bulk ZrC coils with a bulk density 0·8 g cm^{-3}, as can be seen in Fig. 8. The bulk ZrC coils with a bulk density of 0·8 g cm^{-3} are more expanded (by about three times) than the ZrC coils with a density of 2·4 g cm^{-3}. Therefore, the area of the contact point between each ZrC coil, through which electric current is conducted, may be smaller than that for the cross-section of a ZrC coil, which may result in an increased electrical resistivity. Furthermore, zirconium oxide layers formed on the surface of the ZrC clads may act as a large barrier for electrical conduction. That is, the observed electrical resistivity of the bulk ZrC coils is larger than that estimated theoretically because of the small contact area between each ZrC coil and the presence of oxide layers.

4 Conclusions

Micro-coiled ZrC fibres were prepared by vapour phase zirconizing of micro-coiled carbon fibres, and their preparation conditions, morphology and bulk electrical resistivity were examined. The coiling morphology of the source carbon coils was fully preserved under all zirconizing conditions. The bulk resistivity of the coiled ZrC fibres decreased with bulk density and was 10^{-1} s^{-1} cm at 0·8 g cm^{-3}.

Acknowledgements

This work was supported by the Kawasaki Steel 21st Century Foundation, Iketani Science and Technology Foundation, Murata Science Foundation and Yazaki Memorial Foundation for Science and Technology.

References

1. Addamiano, A., *J. Cryst. Growth*, **58** (1982) 617–22.
2. Kang, T.-K., Park, S.-D., Rhee, C.-K. & Kuk, Il-H., *Proc. 6th Japan–Korea Ceramic Seminar* (1989, Kobe), pp. 249–53.
3. Vogt, U., Hofmann, H. & Kramer, V., *Key Eng. Mater.*, 89–91 (1994) 29–34.
4. Motojima, S., Ueno, S., Hattori, T. & Goto, K., *Appl. Phys. Lett.*, **54** (1989) 1001–3.
5. Motojima, S., Ueno, S., Hattori, T. & Iwanaga, H., *J. Cryst. Growth*, **96** (1989) 383–9.
6. Iwanaga, H., Kawaguchi, M. & Motojima, S., *Jpn J. Appl. Phys.*, **32** (1993) 105–15.
7. Iwanaga, H., Iwasaki, T., Motojima, S. & Takeuchi, S., *J. Mater. Sci. Lett.*, **9** (1990) 731–4.
8. Motojima, S., Yamana, T., Araki, T. & Iwanaga, H., *J. Electrochem. Soc.*, **142** (1995) 3141–8.
9. Johannson, S. & Schweitz, J.-A., *J. Appl. Phys.*, **72** (1992) 5956–63.
10. Wright, J. K., Thomson, R. M. & Evance, J. R. G., *J. Mater. Sci.*, **25** (1990) 149–56.
11. Motojima, S., Kawaguchi, M., Nozaki, K. & Iwanaga, H., *Appl. Phys. Lett.*, **56** (1990) 321–3.
12. Motojima, S., Kawaguchi, M., Nozaki, K. & Iwanaga, H., *Carbon*, **29** (1991) 379–85.
13. Motojima, S., Hasegawa, I., Kagiya, S., Momiyama, M., Kawaguchi, M. & Iwanaga, H., *Appl. Phys. Lett.*, **62** (1993) 2322–3.
14. Motojima, S., Kawaguchi, M., Nozaki, K. & Iwanaga, H., *Proc. 11th Int. Conf. CVD* (1990, Seattle), pp. 573–9.
15. Motojima, S., Hasegawa, I., Kawaguchi, M., Nozaki, K. & Iwanaga, H., *J. Chem. Vapor Deposition*, **1** (1992) 136–56.
16. Unpublished data.
17. Naito, K., Kamegashira, N. & Fujiwara, N., *J. Cryst. Growth*, **45** (1978) 506–10.
18. Tamari, N. & Kato, A., *Nippon Kagaku Kaishi, J. Chem. Soc. Jpn*, (1977) 650–5.
19. Tamari, T. & Kato, A., *J. Less-Common Met.*, **58** (1978) 147–60.
20. Endo, M., *Chemtech*, (1988) 568–76.
21. In *Tugoplakie Soedineniya*, eds G. V. Samsonov & I. M. Vinitskii. Moskva, 1976.

Journal of the European Ceramic Society 16 (1996) 995–999

0955-2219(95)00010-6
0955-2219/96/$15.00

Phase Formation of Ca-α-sialon by Reaction Sintering

J. W. T. van Rutten, H. T. Hintzen & R. Metselaar*

Centre for Technical Ceramics, Laboratory of Solid State Chemistry and Materials Science, Eindhoven University of Technology, PO Box 513, 5600 MB Eindhoven, The Netherlands

(Received 11 September 1995; revised version received 13 December 1995; accepted 5 January 1996)

Abstract

In this study the reaction sintering route for the formation of Ca-α-sialon with a composition on the line $Si_3N_4/CaO{\cdot}3AlN$ ($Ca_{0.8}Si_{9.6}Al_{2.4}O_{0.8}N_{15.2}$, m = 1·6, n = 0·8) has been investigated. This is compared with the hot-pressing of Ca-α-sialon and the reaction sintering of Y- or lanthanide-α-sialons. The reaction follows the same sequence: first, the formation of a Ca-rich α-sialon phase (m = 1·9) which is gradually transformed to a Ca-α-sialon with a lower Ca concentration (m = 1·2). The gehlenite phase ($Ca_2Al_2SiO_7$, melilite group) is observed as an intermediate product. A potential advantage of Ca-α-sialon over Ln-α-sialon ($Si_3N_4/\frac{1}{3}Ln_2O_3{\cdot}3AlN$, where Ln = Y, lanthanide) is liquid phase formation at a lower temperature, which has a positive influence on the processing temperature. Moreover, Ca is cheaper than the lanthanides. The solubility of Ca in the α-sialon is in agreement with values found in the literature. © *1996 Elsevier Science Limited.*

1 Introduction

Sialon ceramic materials have many potential applications because of their good mechanical and chemical properties such as strength, hardness, thermal shock resistance and wear resistance. The sialon ceramics can be divided into two categories: β-sialon with the general formula $Si_{6-z}Al_zO_zN_{8-z}$ where $0 < z < 4{\cdot}2$,[1,2] and α-sialon with the general formula $Me_{m/val}Si_{12-(m+n)}Al_{m+n}O_nN_{16-n}$ (where Me = metal like Y, lanthanides, Ca, Mg, Li; val = valency of the metal).[3] The α- and β-sialon materials have similar structures to α- and β-Si_3N_4. The z, m and n parameters are substitution numbers for Al and O. Among the α-sialon materials Y-α-sialon has been studied most extensively,[3–6] with Ln-α-sialon (Ln = lanthanide) materials being less well studied. However, most lanthanides are quite expensive and therefore this work is focused on a less expensive alternative, i.e. Ca-α-sialon.

In a previous paper, the preparation of Ca-α-sialon by a carbothermal reduction and nitridation process was reported.[7] In this paper the reaction route for the formation of Ca-α-sialon by reaction sintering is described. The results are compared with results found in the literature concerning the hot-pressing of Ca-α-sialon and reaction sintering of Ln-α-sialon (Ln = Y, lanthanide) to see what are the similarities and differences in reaction paths.

2 Experimental Methods

To determine the reaction sequence during reaction sintering, several experiments were carried out. The aim was to prepare Ca-α-sialon with composition $Ca_{0.8}Si_{9.6}Al_{2.4}O_{0.8}N_{15.2}$ (m = 1·6, n = 0·8). As starting materials, Si_3N_4 (LC-12N, Starck; $\alpha/(\alpha+\beta)$ > 95%, oxygen content 2 wt%), AlN (Starck, grade C; oxygen content 2 wt%) and CaO [freshly decomposed $CaCO_3$ (Merck p.a.)] were used. No correction was made for the oxygen content of the nitride starting materials. All firing experiments were performed with the same batch of mixed starting materials. The mixing of these powders was performed in isopropanol in polyethylene bottles on a roller bench (for 48 h) with Si_3N_4 milling balls. Subsequently the powder was dried and pressed into tablets; first uniaxially at 51·7 MPa followed by isostatic pressing at 250 MPa. The firing of the samples was performed in a graphite resistance nitriding furnace at a pressure of 1·3 bar (maximum) of nitrogen. The temperature was increased from room temperature to 800°C at 10°C min^{-1} in vacuum, and kept constant for 15 min to decompose the $CaCO_3$. Then the temperature was raised (10°C min^{-1}) to the maximum temperature which was varied in the range 1300–1700°C. At 900°C

*To whom correspondence should be addressed.

the vacuum was replaced by a nitrogen atmosphere. After reaching the maximum temperature the samples were cooled down immediately (10°C min^{-1}), so no soaking time was used. The tablets (five for each temperature) were embedded in a powder mixture of 55 wt% Si_3N_4, 20 wt% AlN, 5 wt% CaO (decomposed $CaCO_3$) and 20 wt% BN to prevent decomposition of the starting materials at elevated temperatures. BN was added to this mixture to prevent sintering of the powder bed mixture.

Densification during heat-up was measured using dilatometry. This was performed in a graphite resistance furnace in a static nitrogen atmosphere (heating rate 5° min^{-1}, no soaking time at maximum temperature). A 15 min holding time at 1350°C was implemented, thereafter shrinkage rate started to drop. The difference in heating rates in the dilatometry and reaction sintering experiments was used to get a clear separation of the different shrinkage rate maxima. The dilatometer was set up to measure horizontal displacement. The samples were pressed into bars with the aid of polyethylene glycol as a binder material, first uniaxially and then isostatically at 250 MPa. The size of the bars was approximately 15 × 5 × 5 mm^3. To remove the binder and decompose the $CaCO_3$ to CaO and CO_2, the bars were carefully heated up in air to 900°C and soaked for 1 h. The dilatometer samples were not used for further investigation. Only samples with a weight loss <5% were used for further analysis.

The samples were analysed by X-ray diffraction (Rigaku, Geigerflex, Cu $K\alpha$ radiation, 0·0125° min^{-1}, 2θ = 10–97°, 5 s counting time, 35 kV, 20 mA). For X-ray diffraction the tablets were powdered as fine as possible by mortar and pestle. The determination of phase composition by X-ray diffraction was performed qualitatively by estimation of the intensities of peaks in the diffractograms belonging to various compounds. To determine the cell parameters, the peaks with the highest intensity were generally chosen. It would have been better to use the peaks at high reflection angles, but the intensity of these peaks was too low. The computer program REFCEL[8] was used to calculate the cell parameters. The d- or 2θ-values and the $h\ k\ l$-values of the 10 strongest peaks ($h\ k\ l$ = 1 0 1, 2 0 1, 1 0 2, 2 1 0, 2 1 1, 3 0 1, 2 2 2, 3 2 1, 4 1 1, 3 2 2) were used as input for this program.

3 Results and Discussion

3.1 Shrinkage behaviour

It is generally accepted that the shrinkage during densification of α-sialon occurs as a consequence of liquid phase sintering, which proceeds in three stages:[3]

(1) primary particle rearrangement, immediately following the formation of liquid phase, brought about by solid particles sliding over each other under the action of capillary forces;
(2) a solution/precipitation process which will occur if the solid particles have sufficient solubility in the liquid phase; and
(3) coalescence and closed pore elimination.

By reaction of SiO_2 and Al_2O_3 on the surface of the nitride starting materials with CaO, a liquid phase can be formed at the eutectic temperature.

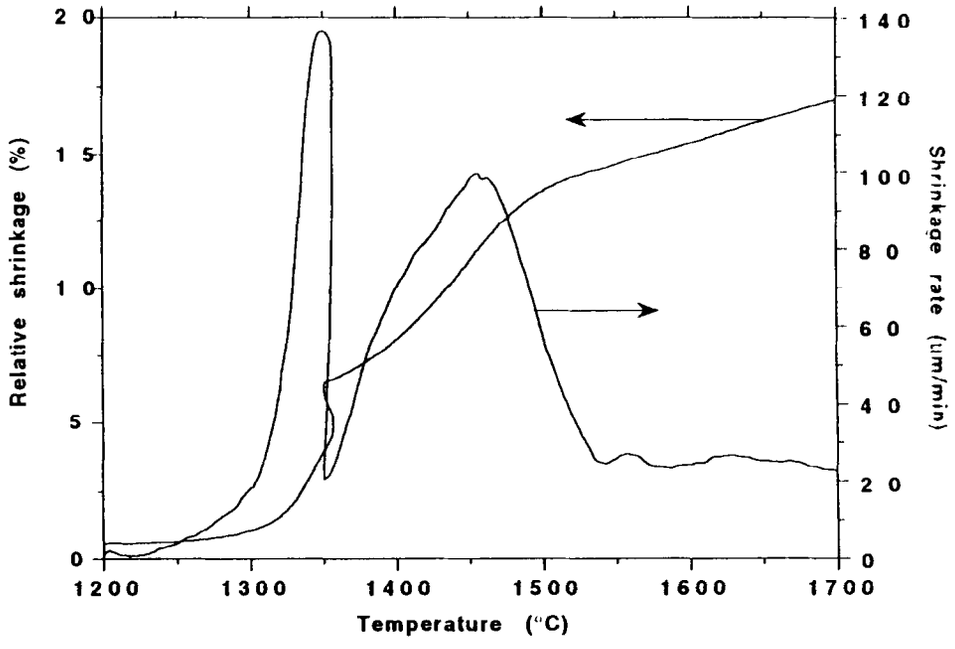

Fig. 1. Dilatometer curve of reaction mixture of CaO, Si_3N_4 and AlN with a composition $Ca_{0.8}Si_{9.6}Al_{2.8}O_{0.8}N_{15.2}$. The kink in the shrinkage curve at the holding temperature of 1350°C (15 min) is a result of an overshoot when it is reached. The final density of this sample is 95% of the theoretical density.

According to the $CaO–SiO_2–Al_2O_3$ phase diagram the lowest eutectic temperature is 1170°C.[9] To increase the amount of liquid phase the temperature should be somewhat higher, in agreement with the fact that shrinkage starts at about 1225°C (Fig. 1) due to particle rearrangement. The amount of liquid phase increases further at higher temperatures, more so because dissolution of nitrogen lowers the eutectic temperature.[10] As a result, a maximum shrinkage rate is observed at about 1350°C (Fig. 1), which corresponds with the temperature (1360°C) reported for this stage during reaction hot-pressing of Ca-α-sialon.[11] Reaction sintering of Si_3N_4/AlN/Y_2O_3 compositions on the line $Si_3N_4/\frac{1}{3}\,Y_2O_3{\cdot}3AlN$ shows the first shrinkage rate maximum at a significantly higher temperature of 1500°C[12] to 1550°C.[13] At about 1450°C the second shrinkage rate maximum can be discerned for Ca-α-sialon (Fig. 1), which is ascribed to the occurrence of the solution/precipitation mechanism (stage 2). The temperature observed for this stage agrees with the value reported for the second shrinkage step during reaction hot-pressing of Ca-α-sialon.[11] Chen and co-workers[11,14,15] pointed out that the position of the second peak is closely related to the temperature at which the major nitride component in the mixture is wetted by the liquid phase. For Si_3N_4, which is the major component in our reaction mixture, complete wetting was observed at 1450°C, corresponding with the second peak in Fig. 1. For the Ca system preferential wetting of the nitride starting material present in the largest amount (i.e. Si_3N_4) takes place,[14] whereas for the Y system preferential wetting of the AlN starting material occurs.[15] From the present study and our earlier research on Y-α-sialon,[16] we conclude that the densification during reaction sintering is quite similar to that during reaction hot-pressing observed by Chen and co-workers.[11,14,15]

3.2 Phase formation

Powder X-ray diffraction was used to analyse the phase composition of the tablets. The amounts of the crystalline phases are presented in Fig. 2 as a function of the reaction sintering temperature. The figure shows that the formation of Ca-α-sialon starts at a temperature between 1300 and 1400°C. This is related to the formation of a significant amount of liquid phase at 1350°C, as deduced from the first peak in the shrinkage curve. From the dilatometer curve it was concluded that at 1450°C the solution/precipitation mechanism plays a dominant role. This corresponds with the temperature in Fig. 2 where the amounts of the raw materials, Si_3N_4 as well as AlN, start to decrease significantly. β-Si_3N_4, which was near the detection limit, was no longer detectable above 1300°C. AlN disappears in the range 1500–1600°C. α-Si_3N_4 can still be determined at 1600°C. The amount of Ca-α-sialon increases with increasing temperature until near-complete conversion at 1700°C. Only one crystalline intermediate product could be determined: this is $Ca_2Al_2SiO_7$ (gehlenite) or more likely a compound with the general formula $Ca_2Al_{2-x}Si_{1+x}O_{7-x}N_x$, according to the calculated cell parameters which are different from that of pure gehlenite. This product is observed at 1300°C and can be detected until 1600°C, at which temperature it is completely dissolved. The amount, however, is near the detection limit. The presence of this intermediate phase is in agreement with the results Hewett *et al.*[17] reported for the reaction hot-pressing of Ca-α-sialon. Besides this gehlenite intermediate they also found a very small amount of M-phase ($2CaO{\cdot}Si_3N_4{\cdot}AlN$) at low temperatures (up to about 1400°C), which was not detected in our samples. In our investigation $CaSiO_3$ appears between 1400°C and 1500°C and remains in the mixture even at 1700°C. It may be formed during cooling, and its presence in the end product is ascribed to the surface oxygen present on the nitride starting materials. It can be calculated that the oxygen content of the nitride raw materials corresponds with 2–3 wt% $CaSiO_3$ in the end product. According to this calculation the *m*-value of the resulting Ca-α-sialon shifts a little, from 1·6 to 1·4 at minimum. According to Hintzen *et al.*[18] the *m*- and *n*-values can be calculated from the relations:

$$a\ (\text{Å}) = 7{\cdot}749 + 0{\cdot}0023\ n + 0{\cdot}0673\ m \qquad (1)$$

$$c\ (\text{Å}) = 5{\cdot}632 - 0{\cdot}0054\ n + 0{\cdot}0550\ m. \qquad (2)$$

From these relations it can be seen that the *m*-value is the dominant parameter; therefore the *n*-value is not calculated.

At the beginning of the reaction (1400°C) the cell parameters of the Ca-α-sialon material are large (a = 7·883 Å, c = 5·731 Å, see Table 1) which is ascribed to the formation of a Ca-rich Ca-α-sialon material. From the eqns (1) and (2) the *m*-value can

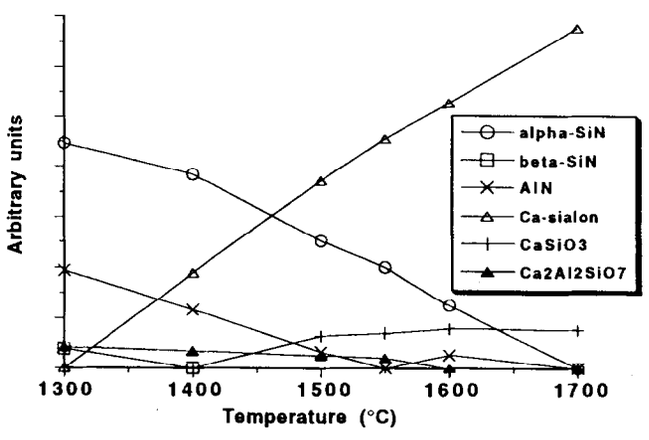

Fig. 2. Phase composition of product after firing at different temperatures.

Table 1. Influence of sintering temperature on the lattice parameters of Ca-α-sialon, and the m-values calculated with equations (1) and (2)

Temperature (°C)	a (*Å*)	c (*Å*)	m_{cal}
1400	7·883	5·731	1·9
1500	7·865	5·725	1·7
1550	7·845	5·700	1·4
1600	7·842	5·685	1·3
1700	7·830	5·694	1·2

be calculated to be 1·9. This m-value is smaller than 2·8 which is reported as the upper limit of the solubility of Ca in α-sialon.[19] The presence of still large amounts of Si_3N_4 and AlN at 1400°C also is in agreement with the presence of Ca-α-sialon with a high Ca concentration. For increasing sintering temperatures the lattice parameters of the Ca-α-sialon become smaller (Table 1). This corresponds to a decreasing m-value (Fig. 3), and indicates the formation of Ca-α-sialon with lower Ca concentrations at higher temperatures. The final Ca-α-sialon composition (1700°C) has small lattice parameters (a = 7·830 Å, c = 5·694 Å) resulting in m = 1·2. From the comparison of the experimentally found m-value (1·2) with the m-value expected from the weighed-out starting composition (1·4–1·6), it can be concluded that 75–85% of the amount of calcium is incorporated in the Ca-α-sialon lattice. Such percentages are generally found for Ca-α-sialon systems.[18] The reaction is finished according to the cell parameters calculated from the samples fired at 1700°C, in agreement with the presence of nearly single-phase Ca-α-sialon. The decrease of the cell parameters of Ca-α-sialon during the reaction corresponds with the results that Sun *et al.*[20] reported for reaction sintering of Ca-α/β-sialon composite materials. In the latter case, however, the shift of the boundary between the single-phase α-region and the two-phase α/β-region with temperature may also play an important role.

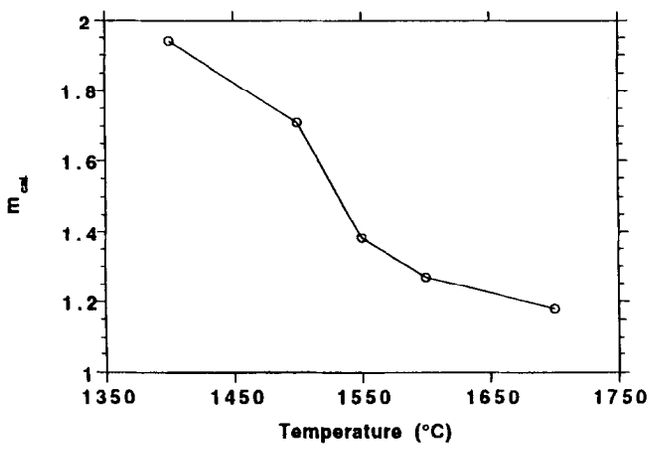

Fig. 3. Influence of sintering temperature on the m-values calculated from the measured lattice parameters using eqns (1) and (2).

3.3 Reaction mechanism

From the results discussed so far, the following reaction mechanism can be derived.

$$CaO + Al_2O_3 / AlN + SiO_2 / Si_3N_4 \rightarrow \text{Ca–Si–Al–O–N liquid} + \text{gehlenite} \quad \sim 1350°C \quad (3)$$

$$\text{Ca–Si–Al–O–N liquid} + Si_3N_4 + AlN + \text{gehlenite} \rightarrow \text{Ca-}\alpha\text{-sialon}\,(m = 1{\cdot}9) + \text{Ca–Si–Al–O–N liquid} + \text{gehlenite} \quad \sim 1400°C \quad (4a)$$

$$\text{Ca-}\alpha\text{-sialon}\,(m = 1{\cdot}9) + Si_3N_4 + AlN + \text{Ca–Si–Al–O–N liquid} + \text{gehlenite} \rightarrow \text{Ca-}\alpha\text{-sialon}\,(1{\cdot}2 < m < 1{\cdot}9) + \text{Ca–Si–Al–O–N liquid} + \text{gehlenite} \quad \sim 1400\text{–}1550°C \quad (4b)$$

$$\text{Ca-}\alpha\text{-sialon}\,(1{\cdot}2 < m < 1{\cdot}9) + \text{Ca–Si–Al–O–N liquid} + \text{gehlenite} \rightarrow \text{Ca-}\alpha\text{-sialon}\,(m = 1{\cdot}2) + CaSiO_3 \quad > 1550°C. \quad (5)$$

Reaction (3) occurs at about 1350°C, reaction (4) in the range 1400–1550°C and reaction (5) if the temperature is higher than 1550°C. The SiO_2 and Al_2O_3 in eqn (3) are present on the surface of the starting Si_3N_4 and AlN powder.

The reaction scheme proposed in this study is similar to that observed by Watari *et al.*[13] for reaction sintering of Ln-α-sialons (Ln = Y, Er, Yb). They proposed a reaction sequence, starting with lanthanide oxides (Y, Er, Yb), in which first a liquid phase is formed, subsequently α-sialons with high concentrations of lanthanide ions and finally α-sialons with low lanthanide concentrations. In this case a melilite-like compound ($Ln_2Si_3O_3N_4$) is also found as an intermediate, in agreement with results found by Cao and co-workers for reaction sintering of Y-sialon materials.[3,12,16] There are strong similarities between the reaction sequence proposed for Ln-α-sialons and the work described in the present paper for Ca-α-sialon. In both cases a melilite like compound $M_2(Al,Si)_3(O,N)_7$ (M = Ca, Y, lanthanide) was observed as an intermediate product, but there is no end product present which can be exchanged by $CaSiO_3$ in their reaction sequence.

Potential advantages of Ca-α-sialon are the lower processing temperature (densification) and the much cheaper starting materials.

4 Conclusions

Reaction sintering of a mixture of CaO, Si_3N_4 and AlN on the line Si_3N_4/CaO·3AlN ($Ca_{0·8}Si_{9·6}Al_{2·4}O_{0·8}$

$N_{15\cdot2}$, $m = 1\cdot6$, $n = 0\cdot8$) starts at a temperature of about 1350°C due to the formation of a Ca–Si–Al–O–N liquid, as deduced from shrinkage rate measurements. At about 1450°C the solution precipitation mecha-nism is dominant, promoting the formation of Ca-α-sialon. First, a Ca-α-sialon is formed which contains more Ca than aimed at ($m = 1\cdot9$). Subsequently this Ca-rich α-sialon reacts with the Si_3N_4 and AlN still present until finally $m = 1\cdot2$ is reached, indicating that not the total amount of Ca is incorporated in the α-sialon matrix. As an intermediate product $Ca_2Al_{2-x}Si_{1+x}O_{7-x}N_x$ (gehlenite, belonging to the melilite group) was found. This is comparable to the inter-mediate products in the formation of Ln-α-sialon (Ln = Y, lanthanide) where $Ln_2Si_3O_3N_4$ melilite phases are formed. In the final product, besides Ca-α-sialon, $CaSiO_3$ was observed due to the presence of oxygen in the nitride starting materials, which was not corrected for. Potential advantages of Ca-α-sialon over Ln-α-sialon are the lower processing temperature and the much cheaper starting materials.

Acknowledgement

The authors wish to thank P. P. Geluk for his contribution to the practical work of this study.

References

1. Oyama, Y. & Kamigaito, O., *Jpn J. Appl. Phys.*, **10** (1971) 1637.
2. Jack, K. H. & Wilson, W. I., *Nature (Lond.) Phys. Sci.* **238** (1977) 28.
3. Cao, G. Z. & Metselaar, R., *Chem. Mater.*, **3** (1991) 242–52.
4. Wang, H., Sun, W.-Y., Zhuang, H.-R. & Yen, T.-S., *J. Eur. Ceram. Soc.*, **13** (1994) 461–5.
5. Haviar, M. & Dobdova, J., *Ceram. Acta*, **6** (1994) 15–20.
6. Sun, W.-Y., Tien, T.-Y. & Yen, T.-S., *J. Am. Ceram. Soc.*, **74** (1991) 2753–8.
7. van Rutten, J. W. T., Terpstra, R. A., van der Heijde, J. C. T., Hintzen, H. T. & Metselaar, R., *J. Eur. Ceram. Soc.*, **15** (1995) 599–604.
8. Rietveld, H. M., *Calculation of Cell Constants*, University of Amsterdam, Oct. 1972.
9. *Phase Diagrams for Ceramists*, ed., E. M. Levin, C. R. Robbins, H. F. McMurdie & M. K. Reser. American Ceramic Society, Columbus, Ohio, 1964, Fig. 630.
10. Hampshire, S. & Jack, K. H., *Proc. Brit. Ceram. Soc.*, **31** (1980) 37–49.
11. Menon, M. & Chen, I-.W., *J. Am. Ceram. Soc.*, **78** (1995) 553–9.
12. Cao, G.Z., Preparation and characterization of α-sialon. PhD thesis, Eindhoven University of Technology, The Netherlands, 1991.
13. Watari, K., Yasuoka, M., Valecillos, M. C. & Kanzaki, S., *J. Eur. Ceram. Soc.*, **15** (1995) 173–84.
14. Menon, M. & Chen, I-.W., *J. Am. Ceram. Soc.*, **78** (1995) 545–52.
15. Hwang, S-.L. & Chen, I-.W., *J. Am. Ceram. Soc.*, **77** (1994) 165–71.
16. Cao, G.Z., Metselaar, R. & Ziegler, G., in *Ceramics Today — Tomorrow's Ceramics*, ed. P. Vincenzini, Elsevier Science Publishers, Amsterdam, 1991, pp. 1285–92.
17. Hewett, C. L., Cheng, Y-.B., Muddle, B. C. & Trigg, M. B., *Austceram*, (1994) 1001–6.
18. Hintzen, H. T., Vrolijk, J. W. G. A., van Rutten, J. W. T & Metselaar, R., to be published.
19. Huang, Z.-H., Sun, W.-Y. & Yan, D.-S., *J. Mater. Sci. Lett.*, **4** (1985) 255.
20. Sun, W. Y., Walls, P. A. & Thompson, D. P., *Non-oxide Technical and Engineering Ceramics*, ed. S. Hampshire, Elsevier Applied Science, London, 1986, Ch. 8, pp. 105–17.